Lecture Notes in Civil Engineering

Lakshman Nandagiri
M. C. Narasimhan
Shriram Marathe *Editors*

Recent Advances in Civil Engineering

Select Proceedings of CTCS 2021

Springer

Lecture Notes in Civil Engineering

Volume 256

Lecture Notes in Civil Engineering (LNCE) publishes the latest developments in Civil Engineering - quickly, informally and in top quality. Though original research reported in proceedings and post-proceedings represents the core of LNCE, edited volumes of exceptionally high quality and interest may also be considered for publication. Volumes published in LNCE embrace all aspects and subfields of, as well as new challenges in, Civil Engineering. Topics in the series include:

- Construction and Structural Mechanics
- Building Materials
- Concrete, Steel and Timber Structures
- Geotechnical Engineering
- Earthquake Engineering
- Coastal Engineering
- Ocean and Offshore Engineering; Ships and Floating Structures
- Hydraulics, Hydrology and Water Resources Engineering
- Environmental Engineering and Sustainability
- Structural Health and Monitoring
- Surveying and Geographical Information Systems
- Indoor Environments
- Transportation and Traffic
- Risk Analysis
- Safety and Security

To submit a proposal or request further information, please contact the appropriate Springer Editor:

– Pierpaolo Riva at pierpaolo.riva@springer.com (Europe and Americas);
– Swati Meherishi at swati.meherishi@springer.com (Asia - except China, and Australia, New Zealand);
– Wayne Hu at wayne.hu@springer.com (China).

All books in the series now indexed by Scopus and EI Compendex database!

More information about this series at https://link.springer.com/bookseries/15087

Lakshman Nandagiri · M. C. Narasimhan · Shriram Marathe
Editors

Recent Advances in Civil Engineering

Select Proceedings of CTCS 2021

Springer

Editors
Lakshman Nandagiri
Department of Water Resources and Ocean Engineering
National Institute of Technology Karnataka
Mangalore, India

M. C. Narasimhan
Department of Civil Engineering
National Institute of Technology Karnataka
Mangalore, India

Shriram Marathe
Department of Civil Engineering
N.M.A.M. Institute of Technology
Karkala, Karnataka, India

ISSN 2366-2557 ISSN 2366-2565 (electronic)
Lecture Notes in Civil Engineering
ISBN 978-981-19-1861-2 ISBN 978-981-19-1862-9 (eBook)
https://doi.org/10.1007/978-981-19-1862-9

This Springer imprint is published by the registered company Springer Nature Singapore Pte Ltd.
The registered company address is: 152 Beach Road, #21-01/04 Gateway East, Singapore 189721, Singapore

Organizing Committee

Patron

Sri. N. Vinaya Hegde, Chancellor, Nitte-Deemed to be University President, Nitte Education Trust, Mangaluru

Steering Committee

Sri. Vishal Hegde, Pro-Chancellor, Nitte-Deemed to be University, Mangalore
Dr. N. R. Shetty, Chancellor, Central University, Karnataka
Dr. Omid Ansary, Senior Associate Dean and Professor, Penn State University, USA
Dr. Samson Ojoawo, Professor, Ladoke Akintola University of Technology, Nigeria
Dr. Shripad T. Revankar, Professor, Purdue University, USA
Dr. Takamoto Itoh, Vice Dean, Mechanical Engineering, Ritsumeikan University, Japan
Dr. Prakash Kumar, Professor, Department of Biological Science, National University of Singapore
Dr. Harish Kumar Madhyastha, Professor, University of Miyazaki, Japan

General Chair

Dr. Niranjan N. Chiplunkar, Principal

General Co-chairs

Dr. I. R. Mithanthaya, Vice Principal and Dean (Academics), NMAMIT Nitte
Dr. Srinivasa Rao B. R., Vice Principal and Controller of Examinations, NMAMIT Nitte

Chief Conveners

Dr. Sudesh Bekal, Dean (R&D), NMAMIT Nitte
Dr. Muralidhara, P. G. Coordinator, NMAMIT Nitte

Organizing Committee

Dr. G. Srinikethan, Director (R&D—Technical), Nitte-Deemed to be University
Dr. A. N. Parameswaran, Director, IIC, NMAMIT Nitte
Mr. Yogesh Hegde, Registrar, NMAMIT Nitte
Dr. Subrahmanya Bhat, Professor and Dean (Student Welfare, ISO and IQAC Coordinator), NMAMIT Nitte
Dr. K. Rajesh Shetty, Dean (Admission and Alumni Affairs), NMAMIT Nitte
Dr. Srinivas Pai, Deputy Controller of Examinations, NMAMIT Nitte
Dr. Uday Kumar Shenoy, Chief Warden (Gents Hostel), NMAMIT Nitte
Dr. Veena Devi Shastrimath V., Chief Warden (Ladies Hostel), NMAMIT Nitte
Dr. Srinath Shetty K., Resident Engineer, NMAMIT Nitte
Dr. Vaman Rao, Head, Department of Biotechnology Engineering, NMAMIT Nitte
Dr. Shashikantha Karinka, Head, Department of Mechanical Engineering, NMAMIT Nitte
Dr. Rashmi Hegde B., Head, Department of Humanities, NMAMIT Nitte
Dr. Kumudakshi, Associate Professor and Head, Department of Mathematics, NMAMIT Nitte
Dr. Shivaprasad Shetty M., Assistant Professor and Head, Department of Chemistry, NMAMIT Nitte
Dr. Shobha R. Prabhu, Assistant Professor and Head, Department of Physics, NMAMIT Nitte
Dr. H. Divakar Bhat, Librarian, NMAMIT Nitte
Mr. Krishnaraja Joisa, Public Relations Officer, NMAMIT Nitte

Programme Chair

Dr. Arun Kumar Bhat, Professor and Head, Department of Civil Engineering, NMAMIT, Nitte

Organizing Secretary

Dr. Shriram P. Marathe, Assistant Professor, Department of Civil Engineering, NMAMIT, Nitte

Organizing Co-secretary

Mr. Thushar S. Shetty, Assistant Professor, Department of Civil Engineering, NMAMIT, Nitte

Web Coordinator

Mr. Janakaraj M., Assistant Professor, Department of Civil Engineering, NMAMIT, Nitte

Conference Advisory Committee

Dr. Md. Rezaul Karim, Professor in Department of Civil Engineering, Director of IQAC, Dhaka University of Engineering and Technology, Gazipur, Bangladesh
Dr. Mukesh Kashyap, Senior Lecturer (Construction Management), School of Architecture Design and the Built Environment, Nottingham Trent University, England
Dr. Narendra Kumar Samadhiya, Professor, Department of Civil Engineering, Indian Institute of Technology Roorkee and President, Indian Geotechnical Society (IGS), New Delhi
Dr. S. Mohan, Chair Professor, Department of Civil Engineering, Indian Institute of Technology Madras, Chennai
Dr. G. L. Sivakumar Babu, Professor, IISc, Bengaluru
Dr. Dharamveer Singh, Associate Professor, IIT, Bombay
Dr. H. N. Ramesh, Professor and Principal, UVCE, Bengaluru

Dr. Puttaraju, Professor and Vice Chancellor, Mandya University, Karnataka
Dr. Vipul Prakash, Professor, IIT, Roorkee

Technical Advisory Committee

Dr. Annappa, IEEE Mangalore Sub Section Chair
Dr. A. U. Ravishankar, Professor, Department of Civil Engineering, NITK
Dr. Lakshman Nandagiri, Professor, Department of Water Resources and Ocean Engineering, NITK
Dr. M. C. Narasimhan, Professor, Department of Civil Engineering, NITK
Dr. Varghese George, Professor, Civil Engineering Department, NITK, Surathkal
Dr. Purushotham Sarvade, Professor and Head, Department of Civil Engineering, MIT, Manipal
Dr. G. P. Chandradhara, Professor and Head, Civil Engineering Department, Sri Jayachamarajendra College of Engineering, Mysuru
Dr. Balakrishna Rao K., Professor, Department of Civil Engineering, MIT, Manipal
Dr. Chandrashekhar A., Professor and Head, Department of Civil Engineering, KVGCE, Sullia
Dr. Ganesh Mogaveer, Professor and Head, Department of Civil Engineering, MITE, Moodabidre
Dr. H. Ajith Hebbar, Professor and Head, Department of Civil Engineering, Alva's Institute of Engineering and Technology, Moodubidire, Mangalore
Dr. K. Swaminathan, Professor and Head, Department of Civil Engineering, NITK
Dr. Kiran Kumar Shetty, Professor, Department of Civil Engineering, MIT, Manipal
Dr. Narayana Sabahit, Professor and Registrar, MAHE, Manipal
Dr. R. Shivashankar, Professor, Department of Civil Engineering, NITK
Dr. Ramakrishna Hegde, Professor and HOD, Department of Civil Engineering, Srinivas University, Mangalore
Dr. S. V. Dinesh, Professor and Head, Department of Civil Engineering, SIT Tumakuru
Dr. Sandeep J. Nayak, Professor and Head, Department of Civil Engineering, SMVITM, Bantakal
Dr. Ananda V. R., Professor and Head, Department of Civil Engineering, VCET, Putturu

List of Reviewers

Dr. Durga Prasad J., Ex-Professor, Nitte Meenakshi Institute of Technology
Mr. Subrahmanya V. Bhat P., Ambruni Architects and Structural Consultants, Pangala
Dr. Shivaprasad K. N., JSS Science and Technology University, Mysuru
Mr. Joel Santhosh, RAKNOR LLC, UAE
Dr. Santhosh L. G., Ramaiah Institute of Technology, Bengaluru
Mr. Vinod N. Tamburi, Reva University, Bengaluru
Mr. Thilak L. N., JSS Academy of Technical Education
Mr. Hemanth Kamplimat, Nirma University
Dr. Sanjith J.,Adhichunchanagiri Institute of Technology
Dr. A. U. Ravi Shankar, National Institute of Technology Karnataka, Surathkal
Dr. Nitendra Palankar, KLS Gogte Institute of Technology, Belagavi
Dr. Shriram Marathe, NMAM Institute of Technology NITTE
Dr. P. C. Srinivas, Government Engineering College, Kushal Nagar
Dr. Mohan S., Indian Institute of Technology Madras, Chennai
Dr. R. Sridhar, SJB Institute of Technology
Dr. Vivek S., JSS Academy of Technical Education, Bengaluru
Dr. Radha Krishna, RV College of Engineering, Bengaluru
Dr. Jagadish Vengala, Prasad V. Potluri Siddhartha Institute of Technology, Vijayawada
Dr. Saranya P., NMAM Institute of Technology NITTE
Dr. S. V. Dinesh, Siddaganga Institute of Technology, Tumkuru
Dr. Hema H. C., CMR Institute of Technology, Bengaluru
Dr. Arunkumar Yadav, CMR Institute of Technology Bengaluru
Dr. Aarti S. Bhatt, NMAMIT, NITTE
Dr. Subrahmanya Ishwar Bhat, NMAM Institute of Technology NITTE
Dr. N. K. Samadhiya, IIT Roorkee
Dr. Arun Kumar Bhat, NMAM Institute of Technology NITTE
Dr. Somanath M. Basutkar, R V College of Engineering, Bengaluru
Dr. P. S. Raghuprasad, J.S.S. Science and Technology University
Dr. N. C. Balaji, The National Institute of Engineering, Mysuru
Dr. M. C. Narasimhan, National Institute of Technology Karnataka, Surathkal

Dr. N. P. Rajamane, Centre for Advanced Concrete Research, SRM Institute of Science and Technology
Dr. Rajesh Gratian D'souza, Yenepoya Institute of Technology
Dr. Bhojaraja B. E., NMAM Institute of Technology NITTE
Dr. R. Sathyanathan, SRM Institute of Science and Technology, Kattankulathur
Dr. S. K. Prasad, Vidyavardhaka College of Engineering
Dr. Vinayak Gajananrao Mutalik Desai, KLS Gogte Institute of Technology
Dr. Kumar Raju B. C., Sapthagiri College of Engineering
Dr. Sanjeev Sangami, Jain College of Engineering, Belagavi
Dr. Ramesh Bhat, NMAM Institute of Technology NITTE
Mr. Prasanna P. Rao, Srinivas University College of Engineering and Technology
Mr. Sachin Kukian, Middle East College, UAE
Dr. Saubhagya Kumar Panigrahi, VSSUT BURLA
Mr. Ranjith A., NMAM Institute of Technology NITTE
Dr. Radhakrishnan K., NMAM Institute of Technology NITTE
Dr. Harishchander Anandaram, Amrita Vishwa Vidyapeetham Coimbatore, Tamil Nadu, India
Dr. Shiva Kumar G., Dayananda Sagar College of Engineering, Bengaluru
Dr. Mithun B. M., NMAM Institute of Technology NITTE
Dr. Goutham Sarang, VIT Chennai
Dr. Manjunath G. R., Sapthagiri College of Engineering
Dr. Rama R. Subrahmanian, Dayananda Sagar of Architecture
Dr. Namrata D. Jariwala, S V National Institute of Technology, Surat
Ms. Deekshitha K., NMAM Institute of Technology NITTE
Dr. Vikas Kumar, Central University of Haryana, Mahendergarh
Dr. Krishna Murari Soni, Central Public Works Department (Retired)
Dr. G. Beulah Gnana Ananathi, Anna University, Chennai
Dr. Payal Mehta, Indus University, Ahmedabad
Mr. Y. R. Suresh, Jyothy Institute of Technology, Bengaluru
Dr. Kundan Meshram, Guru Ghasidas Vishwavidyalaya (A Central University) Bilaspur (C.G.)
Dr. Babloo Chaudhary, NITK Surathkal
Mr. Prof Ar. Pramod M. Gawari, School of Planning And Architecture
Dr. Shivakumar J. Nyamathi, Department of Civl Engineering, UVCE, Bangalore University
Dr. Yogeshwar V. Navandar, National Institute of Technology (NIT), Calicut
Mr. Likhit M. L., Vemana Institute of Technology, Bengaluru
Mr. Adithya Shenoy, MIT, Manipal
Mr. V. S. Sanjay Kumar, NATPAC
Dr. Katta Venkataramana, NITK Surathkal
Dr. Sujatha Unnikrishnan, Christ (Deemed to be University)
Dr. Ganesha Mogaveera, MITE Moodabidri
Dr. Raghava Gopala Setty, Nitte Meenakshi Institute of Technology, Bengaluru
Dr. G. Srilakshmi, Sapthagiri College of Engineering
Mrs. Elavarasi V., Vemana Institute of Technology

Dr. Suman Kundapura, A J Institute of Engineering and Technology
Dr. Udayakumar G., NMAM Institute of Technology NITTE
Dr. Neethu Urs, Dayananda Sagar College of Engineering
Dr. Shankar H. Sanni, Basaveshwar Engineering College, Bagalkot
Dr. Prasanna Kumar P., BMS College of Engineering
Dr. Omar Alobaidi, Middle East college, UAE
Dr. Dr. Rajakumara H. N., BMS Institute of Technology and Management
Dr. Shivakumar B. R., NMAM Institute of Technology, NITTE
Dr. Anil Kumar, Central Road Research Institute, Delhi
Dr. Vinayak Shet, NMAM Institute of Technology, NITTE
Dr. Vikas Mendi, RV College of Engineering, Bengaluru
Dr. Roshan Fernandes, NMAM Institute of Technology, NITTE
Dr. Raghavendra Holla, MIT Manipal
Mr. Janakaraj M., NMAM Institute of Technology, Nitte
Dr. Varghese George, National Institute of Technology Karnataka, Surathkal
Dr. Muneera C. P., MES Kuttippuram
Mr. Chintaman Bari, Sardar Vallabhbhai National Institute of Technology (SVNIT)
Dr. Basuraj Bhowmik, Gandhi Institute of Technology and Management
Mrs. Deepthishree S. A., Sahyadri College of Engineering and Management, Mangalore
Dr. Akshatha Shetty, Metasite (Geenus Communications), Australia
Mr. Subrahmanya R. M., Vivekananda College of Engineering and Technology, Putturu
Er. Dr. Rama Raju Kunadharaju, CSIR-Structural Engineering Research Centre, Chief Scientist (Retired)
Dr. Krishnamurthy M. P., Nitte Meenakshi Institute of Technology, Bengaluru
Dr. Prof. Bashir Ahmed Mir, National Institute of Technology Srinagar, J&K
Dr. K. S. Shivaprakasha, NMAM Institute of Technology, Nitte
Mr. Anil Kumar Bhat, NMAM Institute of Technology, Nitte
Dr. Sangeetha D. M., A. J. Institute of Engineering and Technology
Dr. Mahesh G. B., MITS Madanapalle
Dr. Nalini Rebello, Sahyadri College of Engineering
Dr. Prathap Kumar M. T., RNS Institute Of Technology, Bengaluru
Dr. Anisha P. Rodrigues, NMAM Institute of Technology, Nitte
Dr. H. B. Balakrishna, Bangalore Institute of Technology
Dr. Naveen B. O., The National Institute of Engineering, Mysuru
Dr. Sujay Raghavendra Naganna, Siddaganga Institute of Technology
Dr. Ramesh B. R., Nitte Meenakshi Institute of Technology, Bengaluru

List of Session Chairs

Dr. Rajamane N. P., Former Head, AML-CSIR-SERC
Dr. S. Mohan, Institute Chair professor, Indian Institute of Technology Madras, Chennai
Dr. Prasad S. K., Professor and Head, Vidyavardhaka College of Engineering, Mysuru
Dr. P. C. Srinivasa, Associate professor, Government Engineering College Kushalnagar, Kodagu
Dr. Radhakrishna, Professor and Head, RV College of Engineering, Bengaluru
Dr. Santhosh L. G., Assistant Professor, M. S. Ramaiah Institute of Technology, Bengaluru
Dr. Gopala Setty Raghava, Professor, Nitte Meenakshi Institute of Technology, Bengaluru
Dr. Saubhagya Kumar Panigrahi, Associate Professor, VSSUT BURLA
Dr. Narasimhan M. C., Professor, NITK, Surathkal
Dr. Nitendra Palankar, Associate Professor, KLS Gogte Institute of Technology, Belagavi
Dr. Basuraj Bhowmik, Assistant Professor, GITAM School of Science and Technology, GITAM University Bengaluru
Dr. Goutham Sarang, Assistant Professor (Sr), VIT Chennai, Chennai
Dr. A. U. Ravi Shankar, Professor, NITK, Surathkal
Dr. Bashir Ahmed Mir, Professor, National Institute of Technology Srinagar, J&K
Dr. Lakshman Nandagiri, Professor, NITK, Surathkal
Dr. Mithun B. M., Assistant Professor, NMAM Institute of Technology NITTE
Mr. Manjunath M., Assistant Professor, NMAM Institute of Technology NITTE
Dr. Shriram Marathe, Assistant Professor, NMAM Institute of Technology NITTE
Mr. Ranjith A., Assistant Professor, NMAM Institute of Technology NITTE
Dr. A. N. Parameswaran, Professor, NMAM Institute of Technology NITTE
Mr. Shaik Kabeer Ahmed, Assistant Professor, NMAM Institute of Technology NITTE
Dr. Arun Kumar Bhat, Professor, NMAM Institute of Technology NITTE
Dr. I. R. Mithanthaya, Professor, NMAM Institute of Technology NITTE
Dr. Srinath Shetty K., Professor, NMAM Institute of Technology NITTE

Dr. Radhakrishnan K., Professor, NMAM Institute of Technology NITTE
Dr. Saranya P., Assistant Professor, NMAM Institute of Technology NITTE
Dr. G. Udayakumar, Professor, NMAM Institute of Technology NITTE
Dr. Bhojaraja B. E., Associate Professor, NMAM Institute of Technology NITTE

Preface

N.M.A.M. Institute of Technology, Nitte, Karnataka, India, organized the International Conference on Emerging Trends in Engineering (ICETE 2021) on November 19 and 20, 2021, which is the 11th International Conference being organized since 2011. From the year 2019, in an effort to focus on the specific issues associated with various engineering disciplines, the idea of a multi-conference platform has been mooted.

ICETE 2021—a multi-conference platform—was a collection of several international conferences with the themes specific to various engineering streams. Besides, there was an opportunity for the students and research scholars of various branches of engineering and technology, and industrial professionals to present and discuss research papers.

Civil Engineering Trends and Challenges for Sustainability (CTCS-2021) was organized by the Department of Civil Engineering, N.M.A.M. Institute of Technology, Nitte, under the umbrella of ICETE-2021. CTCS-2021 was a platform for exchange of knowledge from both individual and interdisciplinary researchers pertaining to Civil Engineering Challenges and Sustainability. This International Conference aimed to bring together the researchers, scientists, engineers, scholars and students in an International forum for the dissemination of original research results in the domain areas of Civil Engineering.

This Proceedings Volume contains the full-length research papers, experience reports and empirical study plans. All of these submissions went through a rigorous peer-review process commensurate with their track. In all, 293 research papers were submitted, with each of them being reviewed by a minimum of two experts. Upon peer-review, 95 papers were accepted for presentation in the Conference. Presentations were reviewed and ranked by the track chairs and discussed with the industry and practice chairs in order to ensure suitable theme sessions were available. Subsequently, after the final quality checks, 69 articles were accepted (with an overall

acceptance rate of 24%) for the publication in the Lecture Notes in Civil Engineering (Springer).

Surathkal, India — Lakshman Nandagiri
Surathkal, India — M. C. Narasimhan
Karkala, India — Shriram Marathe

Contents

About the Editors

Dr. Lakshman Nandagiri is a Professor in the Department of Applied Mechanics and Hydraulics at the National Institute of Technology Karnataka, Surathkal. He has an academic career spanning over 34 years. He possesses a Bachelor's degree in Civil Engineering (University of Mysore, 1983), a Master's degree in Hydraulics (University of Mysore, 1986), and a Doctoral degree in Water Resources Engineering (IISc, 1994). His main areas of research interest are surface water hydrology, hydrological modeling using remote sensing/GIS, vadose zone hydrology, and irrigation and drainage engineering. He has to his credit over 80 technical papers in journals/conference proceedings and has guided 08 doctoral candidates and over 50 M.Tech./B.Tech. dissertations. He has completed 07 R&D projects and several consultancy assignments in the area of hydraulics and water resources engineering and remote sensing/GIS. Prof. Nandagiri has a keen interest in promoting research culture and ethical values amongst students and has delivered a large number of popular lectures on these topics. He is a reviewer for several reputed international and national journals and associate editor for the *ISH Journal of Hydraulic Engineering* (Taylor and Francis).

Dr. M. C. Narasimhan is a proud alumnus of University BDT College of Engineering, Davangere, India [B.E. (Civil Engineering)—1982]. He obtained his masters and a doctoral degree from Indian Institute of Technology Madras, India, during the years 1985 and 1993, respectively. He started his teaching career at the National Institute of Technology Karnataka (NITK), [formally, Karnataka Regional Engineering College, KREC], Surathkal, Mangalore, India, as a lecturer in the Department of Applied Mechanics and Hydraulics in the year 1985 and was promoted as a professor in the Department of Civil Engineering in the year 2002. His research interests are in the areas of concrete technology, special concretes, structural behaviour of RCC, steel and composite constructions, and numerical methods in structural analysis. He has completed a number of R&D and consultancy projects in his department. He has guided more than fifty five postgraduate students for their dissertations and eight students for their doctoral thesis. He has a large number of research publications to his credit in leading journals or presented and included in proceedings of reputed international conferences. He has been a reviewer of papers submitted to leading international research journals like *Construction and Building Materials*, *Cement and Concrete Composites*, *Thin-Walled Structures*, *Journal of Cleaner Production* and *Journal of Building Engineering*, etc. He has chaired technical sessions at international conferences held at Curtin University, Miri, Malaysia, IIT-Delhi, BITS-Pilani, etc. He is an associated member in the sectional committee on special structures, Bureau of Indian Standards, New Delhi. He is also a life member of leading professional organizations like Institution of Engineers (India), Indian Concrete Institute, Association of Consulting Civil Engineers, Indian Society for Technical Education, and Indian Society for Earthquake Technology.

Dr. Shriram Marathe is an Assistant Professor in the Department of Civil Engineering at NMAM Institute of Technology NITTE. He has competed his Ph.D. degree at VTU Belagavi in the area of alkali activated concrete pavements. He completed his M.Tech. (Transportation Engineering) from National Institute of Technology Karnataka, Surathkal, and Master Facilitator Degree (MFLHRD) in Human Resources Development from CLHRD, Mangalore. His areas of research interests include alkali-activated concrete applications to pavements, stabilization of sub-grade soil, road safety, pavement material characterization, and pavement design. He has guided several projects for B.E. and M.Tech. dissertations. He also successfully executed one funded research project on "Study and to Develop Cost-Effective and Green Masonry Block Using Industrial Waste Materials", funded by NITTE Education Trust. Till date, he has about 50 research publications out of which 10 articles are published in scopus indexed journals (Three Q1 articles). Further, he also filed a patent on his invention entitled, "Sustainable Pervious Alkali Activated Concrete Paver Block Pavement for Ground water Recharge" on 29-07-2020. He also served as conference secretary and successfully completed the CTCS-2020, International Conference held at NMAMIT Nitte during December 2020. Further, he is also serving as a potential reviewer for *International Journal of Pavement Research and Technology* published by Springer Nature, *Construction and Building Materials* published by Elsevier B V, *Case Studies in Construction Materials* published by Elsevier B V and *Cogent Environmental Science* published by Taylor & Francis Online. Being a resource person, he has delivered several technical talks at various graduate schools. He is a life member of Indian Roads Congress (IRC) New Delhi, Indian Geotechnical Society (IGS) New Delhi, Indian Society for Technical Education (ISTE), Indian Society of Systems for Science and Engineering (ISSE), Technical Institute for Engineers (India), and Kannada Sahithya Parishadh, Karnataka. He worked as Departmental Co-ordinator (Civil Engineering) for NAAC, NBA, IQAC, Industry Institute Interaction, ISTE, IE(I), and IOV related works.

Suggested Modification in Bedding, Specimen Surface and Load Transferring Plate of Standard ACI 544—2R RBDWI Test in Fibrous Concrete—SIFCON and Prepacked Aggregate

K. Ramakrishnan, S. R. Depak, and K. R. Hariharan

Abstract An alternative configuration test was performed with the help of fibre-reinforced concrete made from steel and polypropylene fibres, for the ACI (American Concrete Institute) 544-2R. Repeated Ball Drop Weight Impact (RBDWI) test. Two types of samples, one being PAFC (Pre-Packed Aggregate Fibrous Concrete) and SIFCON (Slurry Infiltrated Concrete), were employed instead of conventional concrete. The notched specimen contributed to the crack control and hindered the generation of random cracks. The line and cross specimen led to a failure with less blows of a concrete specimen. Thus, by adopting line notched specimens, we may minimize the number of specimens needed for testing.

Keywords RBDWI impact test · Sand bedding · Coarse bedding · ACI 544-2R · Fibre-reinforced concrete · Hooked end steel fibre · Polypropylene fibre

1 Introduction

Different sorts of loads are persistent because of the design or as well because of seismic events in a structure when in manystructural components. The building is also sensitive to security hazards such as traffic accidents and mishaps or explosions [1]. These all have a substantial influence on the overall system, resulting in catastrophic structural failures.

Structures are established throughout the globe that are associated with a range of meteorological variations from scorching deserts to cold winter, from drylands to shore buildings that have diverse effects. The offshore structure has huge waves

K. Ramakrishnan (✉) · S. R. Depak · K. R. Hariharan
School of Civil Engineering, SASTRA Deemed to be University, Thanjavur, India
e-mail: ramakrishnan@civil.sastra.edu

S. R. Depak
e-mail: 121049003@sastra.ac.in

K. R. Hariharan
e-mail: 121049008@sastra.ac.in

L. Nandagiri et al. (eds.), *Recent Advances in Civil Engineering*, Lecture Notes in Civil Engineering 256, https://doi.org/10.1007/978-981-19-1862-9_1

which affect the structure consistently. In high elevation installations, there are wind loads and in the cold climates, there are snow loads.

The structure is often susceptible to the powerful impact of the crash of a moving object, such as transport or vehicles, sometimes by water on offshore structures, sometimes by the wind in a building of high rise or at instances by a fusion reaction in a power station, and all of these loads have an adverse effect on much of the structure [2]. Sometimes impact damage may or may not result in a building failure. We must be prepared for the worse. For different reasons, various impact tests are performed in different methods. These values are then employed in the assessment of the concrete impact tolerance. Various impact tests such as the Charpy Pendulum Test and Drop Weight tests. The Drop Weight Test is the most often utilized due to its simpler and less expensive operation. These tests are quite costly to carry out.

As discussed earlier, fibre reinforced concrete cannot execute the normal ACI (American Concrete Institute) test [3] and 544-2R test [4, 5] in different ways and must be adjusted due to the change in strength, for different reasons. On further examination of fibre reinforced concrete, several tests also have weakness. The fault is in the analytical section, as the results are excessively dispersed. To lower this, they thus need to develop a method for employing diverse reinforced concrete fibre variants. In order to better regulate the test findings, several improvements to the testing technique are also implemented.

A concrete incorporating reinforced fibre is a form of concrete that comprises fibrous components such as steel fibre, synthetic fibre and natural fibres that strengthen the material's structural stability. The absorbed impact is much bigger than regular concrete. This is due to the bridging of the concrete fibres. The steel fibre, due to its ductility and strength, is one of the strongest fibres utilized in research. In the field of fibrous concrete, there are also many kinds of steel fibres accessible. The integrity of the concrete is substantially improved when improved with fibre. This in turns leads to strength increase also. This also improves their total capability for higher energy dissipation.

The project was begun to identify a technique of minimizing the total time needed to finish the research by minimizing the number of tested specimens. This is done by minimizing the dispersion of outcomes [6]. A novel way of dispensing the load equally using knives such as load transferring plates is, therefore, devised, which also comprises notches on the specimen. Many academics are interested to work in this field to bring about improved outcomes so that the way we perceive the technology has a tremendous effect. The scope of this research work is enormous in future as many things remain unknown till now. The reason for this is attributed to the various constraints in the technology adopted. This study provides a fresh perspective into how the material interacts and tests its limitations.

2 Standard RBDWI Test by ACI-544-2R

This test is straightforward to perform and was initially developed to determine the material's impact resistance. Its methods lead us to record the number of blows it takes when the specimen is unsuccessful. It also demands that we record at the time of the first crack. The ACI takes us to a 152 mm diameter, 63.5 mm thick cylinder specimen of 4.5 kg weight, which drops freely from 450 mm while the specimen sits on a laterally fixed metal base plate platform [7]. A 63.5 mm ball is also put on the specimen to correctly distribute the load onto the specimen. The recordings are made at the appearance of the initial and final cracks, until then, the test is continued. The stoppage of testing is, when the split expanded wide enough to touches the side lugs. (Fig. 1).

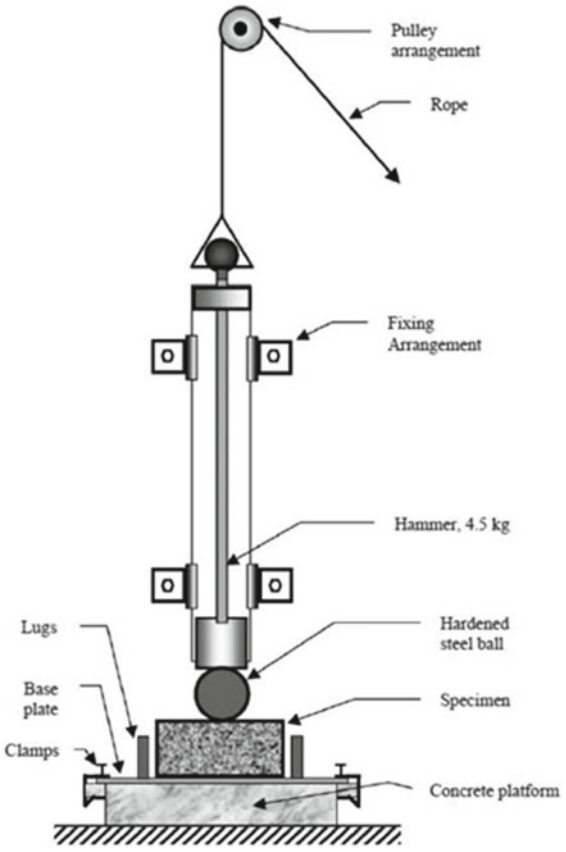

Fig. 1 Experimental setup recommended by ACI

3 Reasons to Modify the Testing Procedure

The following results will necessitate revisions in the present standard ACI 544-2R testing techniques.

The hardened steel ball only transfers the load to the centre of the specimen where the decreasing weight operates. We know that cement is a heterogeneous substance consisting of several ingredients, but it cannot be known whether it is crammed or distributed uniformly throughout the specimens. The results discovered might create an enormous difference [8]. This test configuration causes the cracks to randomly form around the specimen to be verified for exact results after each blow, which also takes time. When parts touch the side lugs after failure, the ACI recommends stopping the experiment. It can sometimes lead to erroneous data; we may stop before the specimen fails or we may continue after failure. The ACI gives various alternatives for either casting a sample of the necessary dimension or cutting the standard cylinder from standard concrete compressive strength cylinders.

4 Suggested Modifications for the Standard ACI 544-2R RBDWI Testing Method

The modifications suggested are as follows.

1. Using different bedding under the specimen instead of the usual steel base plate. Sand bedding and Coarse bedding.
2. Using a notched specimen instead of the usual specimen without a notch. Line and cross notch.
3. Using knife-like load transferring plates instead of a hardened steel ball. A line and cross knife load transferring plate.

4.1 Sand Bedding

Due to its high quality, the sand bedding was deployed to uniformly transmit the weight. Usually, its fineness ranges between 80 and 200 microns. The sample is held in a cylindrical mould substantially bigger than the subject with a diameter of typically 200 mm $\times$ 20 mm $\times$ 100 mm. The sand from the base onto which the specimen is put is filled entirely for 20 mm. Then up to half the specimen height say up to 30 mm, the sides are filled with sand so that it is immersed in the sand bedding. To get the sight of the split, it was filled up to half the height of the cylinder Fig. 7c.

Fig. 2 Modified cross and line notch specimens

4.2 Coarse Bedding

The coarse bedding is similar to the sand bedding but is merely coarse. The size of the aggregate used in this section was 12.5 mm. In the cylindrical mould, the specimen is maintained in the base same as sand bedding but is filled with 12.5 mm aggregate on the sides. Then the first crack and the last crack was taken correspondingly Fig. 7b.

4.3 Modification of Specimen and the Loading Pattern

The amendment referred to here is illustrated by notches on the specimen. They are produced when casting the specimens using 2 mm thick, 150 mm long steel plates with a height of 30 mm. This overlay is applied during casting on the specimen and then removed once the concrete has been hardened, to prevent damage later. In the experiment, there are two types of notches used, namely line and cross notches. After the initial setting period, twenty-eight days after drying, notches are removed and cured in a cured tank. The specimens are whitewashed to observe the initial breaking more accurately before testing Fig. 7.

The test technique is also changed with the knife-line and cross, such as load transfer plates. The insertion of the knife plate into the notches of the exemplar initiates the testing operation. The mass can then fall free of charge towards the back of the plate and the blows are recorded (Figs. 2, 3, 4, 5 and 6).

4.4 Preparation of Grout and Aggregate Used

The preparation of the grout was done by using the mix ratios obtained. The ratios used are the same as provided in Tables 4 and 5. The sand cement ratio used were 1 and 0.45 for sand–cement ratio and water–cement ratio, respectively [9]. The

Fig. 3 Knife like load transferring plates

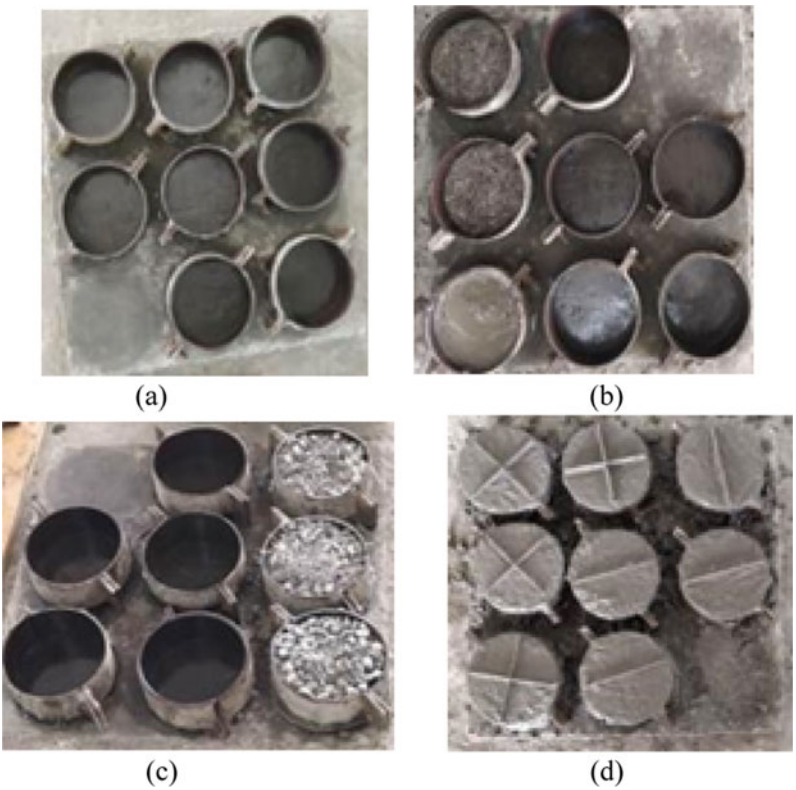

Fig. 4 Preparation of Specimen, **a** Empty Moulds, **b** moulds filled with fibre and grout, **c** filling the top layer, **d** finished specimens with notches being placed

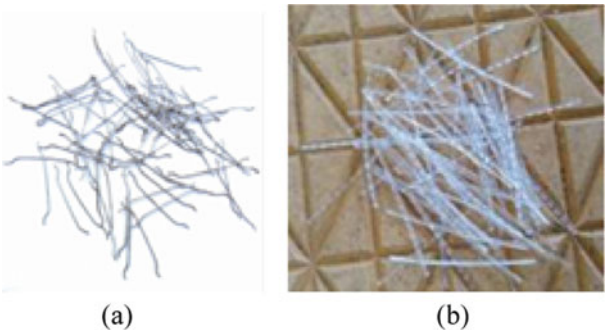

Fig. 5 **a** Hooked end Steel Fibre, **b** polypropylene fibre used in the experiment

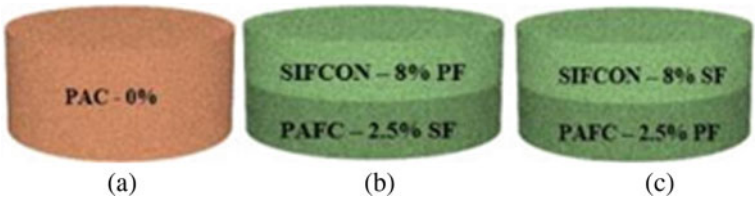

Fig. 6 **a** Prepacked aggregate concrete without any fibre, **b** top layer SIFCON with 8% PF and bottom layer PAFC with 2.5% SF, **c** top layer SIFCON with 8% SF and bottom layer PAFC with 2.5% PF

superplasticizer was also added with 0.35% and 0.5% for conventional mix and fibrous mixes, respectively. The image represents the preparation of grout (Fig. 8).

5 Verification of the Experiment

The experimental effort involves the casting and testing using the test technique RBDWI of the cylindrical specimens. The specimens have a diameter of 150 mm, with a height of 64 mm as required by the ACI. For the experiment, three groups included standard concrete were classified: SIFCON with high-level polypropylene fibres and PAFC with bottom-level steel fibre and SIFCON with top-level steel fibres and PAFC with bottom-level polypropylene fibres. The testing included three different bedding namely coarse bedding, sand bedding and no bedding. All of them possessed SIFCON layer fibre at 8%, and PAFC layer fibres at 2.5%. Three specimens of a total of 54 specimens are cast in each type. The calculated mix proportions are 0.45 for water–cement, 1 for conventional concrete and 0.5 for fibrous concrete, and the sand–cement ratio is 0.35 for superplasticizer.

The experiment is conducted by casting specimens using PPC concrete (Tables 1 and 2) of 53 grade, sand (Table 3), coarse aggregate of 12.5 mm (Table 3) and

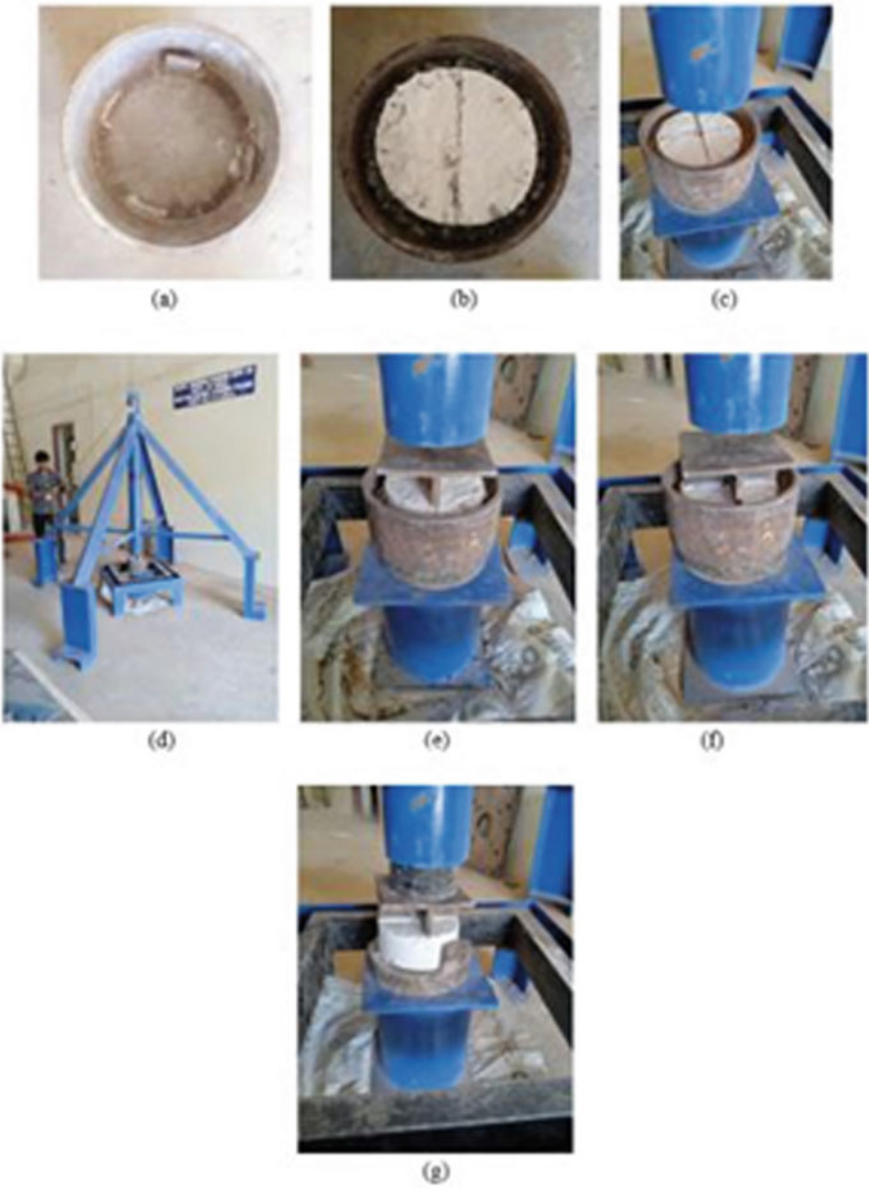

Fig. 7 **a** Setup without bedding, **b** setup with Coarse Bedding, **c** setup with sand bedding, **d** RBDWI testing equipment, **e** setup with line knife load transferring plate, **f** setup with cross knife load transferring plate, **g** setup with cross knife load transferring plate without bedding

Fig. 8 Preparation of grout

Table 1 Chemical properties of cement used

S. No	Oxide	Cement
1	Lime-to-Silica ratio, alumina, iron oxide	0.89
2	Aluminium to iron oxide ratio	0.68
3	Magnesia %	5.48
4	Sulphuric Anhydride %	2.74
5	Chloride content %	0.089
6	SO_3 (Sulphur trioxide)	2.01
7	f-CaO (Calcium Oxide)	0.76
8	Specific gravity	3.15
9	Total loss on ignition %	4.3

Table 2 Physical properties of cement used

S. No	Property	Cement
1	Fineness in m^2/kg	225
2	Soundness by Le Chatelier method in mm	10
3	Average compression strength (N/mm^2) after3 days	27
4	Average compression strength (N/mm^2) after 7 days	37
5	Average compression strength (N/mm^2) after 28 days	53
6	Specific surface in m^2/kg	362

Table 3 Physical properties of Steel Fibre, Polypropylene Fibre, Sand and Coarse aggregate

S. No	Property of material	Value
1	Density of Steel Fibre	7850 kg/m^3
2	Density of Polypropylene Fibre	910 kg/m^3
3	Sand grain size range	80–200 μm
4	Dry bulk density of sand	1500 kg/m^3
5	Specific gravity of sand	2.65
6	Fineness of sand	5.24
7	Specific gravity of coarse aggregate	2.67
8	Coarse aggregate density	800 kg/m^3

superplasticizer. Steel and polypropylene fibres have also been used (Table 3). The grout is prepared and injected into the aggregate and the fibre as shown in Fig. 4. The first layer is filled, followed by the second layer. Depending on the mix composition, the operation was followed in the same way (Tables 4 and 5).

6 Results and Discussions

The results from the impact assessment is shown in Table 6. Three specimens were cast in each type [10]. The results were interpreted in the table revealing the first and final cracks by using the average specimens called R1 and R2. The energy of the impact differs with the height of the mass. For all of the examined specimens, we employed the same height which shows that the energy of impact of the specimens is the same. By the usage of a knife-like load transmission plate, the results were obtained a little quicker because of the stress consistency achieved by the sand bedding [11]. During the test, the sand particles were dissipated from the cylindrical container associated with repetitive impact. After a few blows, this had to be addressed to get the intended results. When sand particle in the sand bedding was continuously dissipated and disappeared due to repetitive blows, the variation in the height of the spcimen is carefully noted [12]. The results show that the dispersion of results is reduced by utilizing sand bedding (Fig. 13). Only in the linear specimens this effect is differently visible. The overall dispersion of the data was significantly modified with the noted specimens. This was achieved by the efficient use of different kinds of bedding and notch. As may be seen in Figs. 8, 9 and 10 in the graph findings. Compared with cross notches, the line notch has produced superior outcomes (Figs. 11 and 12).

The previous research showed that, after many blows from the emergence of the initial break, the specimens frequently fail [13]. This is caused by the brittle nature of the material and its rigidity. But this is not the case with the High-Performance Concrete, the initial and ultimate crack of impact numbers is extremely different.

Table 4 Mix composition for line notched specimens with different bedding

Group	Mix Id	s/c	w/c	Fibre dosage (%)		Concrete type		Type of fibre		SP (%)	Type of notch and bedding
				Top layer	Bottom layer	Top layer	Bottom layer	Top layer	Bottom layer		
1	CC-LN-NB	1	0.45	0	0	PAC	PAC	0	0	0.35	Line notch, no bedding
	SP-P-LN-NB	1	0.45	8	2.5	SIFCON	PAFC	PF	SF	0.5	
	SP-S-LN-NB	1	0.45	8	2.5	SIFCON	PAFC	SF	PF	0.5	
2	CC-LN-CB	1	0.45	0	0	PAC	PAC	0	0	0.35	Line notch, coarse aggregate bedding
	SP-P-LN-CB	1	0.45	8	2.5	SIFCON	PAFC	PF	SF	0.5	
	SP-S-LN-CB	1	0.45	8	2.5	SIFCON	PAFC	SF	PF	0.5	
3	CC-LN-SB	1	0.45	0	0	PAC	PAC	0	0	0.35	Line notch, sand bedding
	SP-P-LN-SB	1	0.45	8	2.5	SIFCON	PAFC	PF	SF	0.5	
	SP-S-LN-SB	1	0.45	8	2.5	SIFCON	PAFC	SF	PF	0.5	

Table 5 Mix composition for cross notched specimens with different bedding

Group	Mix Id	s/c	w/c	Fibre dosage (%)		Concrete type		Type of fibre		SP (%)	Type of notch and bedding
				Top layer	Bottom layer	Top layer	Bottom layer	Top layer	Bottom layer		
4	CC-CN-NB	1	0.45	0	0	PAC	PAC	0	0	0.35	Cross-notch, no bedding
	SP-P-CN-NB	1	0.45	8	2.5	SIFCON	PAFC	PF	SF	0.5	
	SP-S-CN-NB	1	0.45	8	2.5	SIFCON	PAFC	SF	PF	0.5	
5	CC-CN-CB	1	0.45	0	0	PAC	PAC	0	0	0.35	Cross-notch, coarse aggregate bedding
	SP-P-CN-CB	1	0.45	8	2.5	SIFCON	PAFC	PF	SF	0.5	
	SP-S-CN-CB	1	0.45	8	2.5	SIFCON	PAFC	SF	PF	0.5	
6	CC-CN-SB	1	0.45	0	0	PAC	PAC	0	0	0.35	Cross-notch, sand bedding
	SP-P-CN-SB	1	0.45	8	2.5	SIFCON	PAFC	PF	SF	0.5	
	SP-S-CN-SB	1	0.45	8	2.5	SIFCON	PAFC	SF	PF	0.5	

Table 6 RBDWI test results recorded during the impact test

Type of notch and bedding	Group	Mixture id	Impact numbers						Average		SD	COV	IDI
			Specimen1		Specimen2		Specimen3						
			R1	R2	R1	R2	R1	R2	R1	R2			
Line notch no bedding	1	CC-LN-NB	16	19	19	21	20	22	18	21	1.53	7.39	1.13
		SP-P-LN-NB	41	424	50	457	52	486	48	456	31.02	6.81	9.56
		SP-S-LN-NB	54	682	68	728	75	777	66	729	47.51	6.52	11.10
Line notch coarse bedding	2	CC-LN-CB	20	28	28	30	29	31	26	30	1.53	5.15	1.16
		SP-P-LN-CB	54	550	56	592	72	626	61	589	38.07	6.46	9.71
		SP-S-LN-CB	75	886	89	904	98	926	87	905	20.03	2.21	10.37
Line notch sand bedding	3	CC-LN-SB	32	34	32	35	37	38	34	36	2.08	5.84	1.06
		SP-P-LN-SB	92	565	116	592	130	634	113	597	34.77	5.82	5.30
		SP-S-LN-SB	190	1046	226	985	252	1102	223	1044	58.52	5.60	4.69
Cross-notch no bedding	4	CC-CN-NB	16	19	19	22	21	23	19	21	2.08	9.76	1.14
		SP-P-CN-NB	44	408	48	452	51	495	48	452	43.50	9.63	9.48
		SP-S-CN-NB	54	666	74	745	77	801	68	737	67.83	9.20	10.79
Cross-notch coarse bedding	5	CC-CN-CB	24	26	28	29	29	31	27	29	2.52	8.68	1.07
		SP-P-CN-CB	59	619	70	612	72	715	67	649	57.55	8.87	9.68
		SP-S-CN-CB	84	932	99	985	115	1101	99	1006	86.43	8.59	10.13
Cross-notch sand bedding	6	CC-CN-SB	48	58	53	66	62	66	54	63	4.62	7.29	1.17
		SP-P-CN-SB	156	701	172	779	189	818	172	766	59.57	7.78	4.44
		SP-S-CN-SB	284	1250	297	1324	348	1434	310	1336	92.59	6.93	4.31

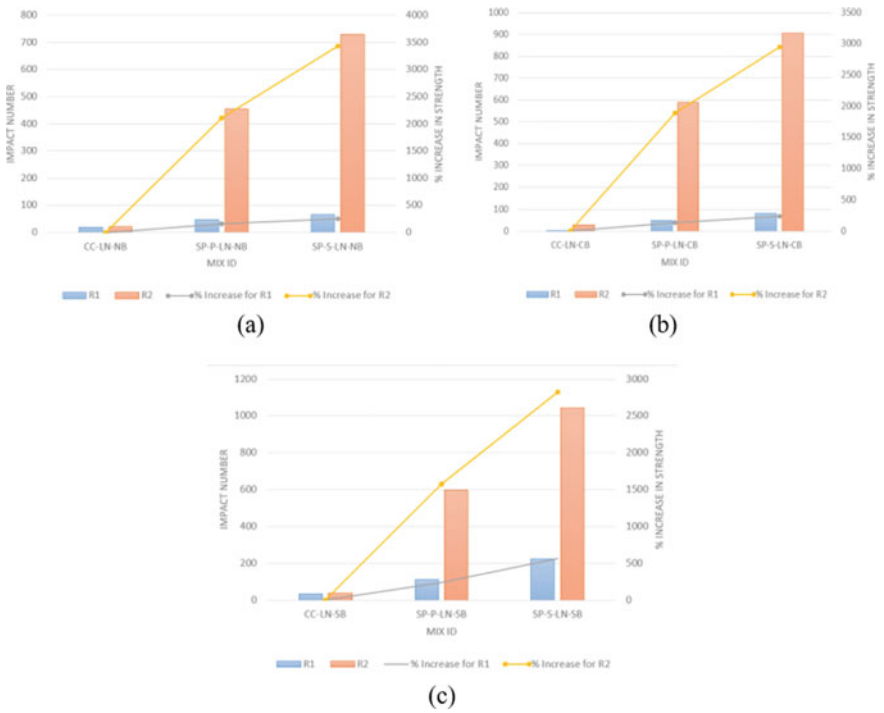

Fig. 9 Initial and final cracking of line notch specimens, **a** no bedding, **b** coarse bedding, **c** sand bedding

The reason for this is, the nature of the combination of different fibre materials, the availability of fine materials and the type of bedding. Table 6 shows that in the first crack, the number of blows increased from 19–21 for initial cracks to 348–1400 for final cracks. The number of blows results in an increase in Table 6. The time and effort required to cast the sample has considerably increased the time to produce failure of the specimens. In comparison to the samples analyzed, the specimen obtained more strength and ductility.

7 Failure Pattern

The failure pattern (Fig. 14) gives us sensitive information when observed correctly. In the previous fibrous concrete tests, the material was discovered to be brittle after the first fracture was shown [14]. This normally happens after 3 to 5 hits, mainly after the first break occurs, the specimen is occasionally divided into several parts. Therefore, it is recommended to use notched specimens to alter the direction of the fracture so that the crevices are properly regulated. The failure crack patterns obtained

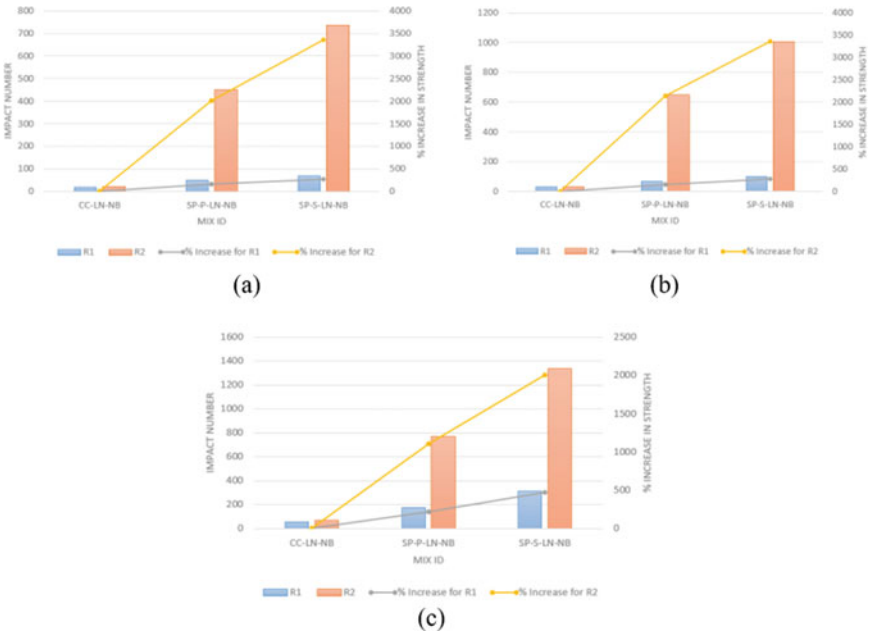

Fig. 10 Initial and final cracking of cross notch specimens, **a** no bedding, **b** coarse bedding, **c** sand bedding

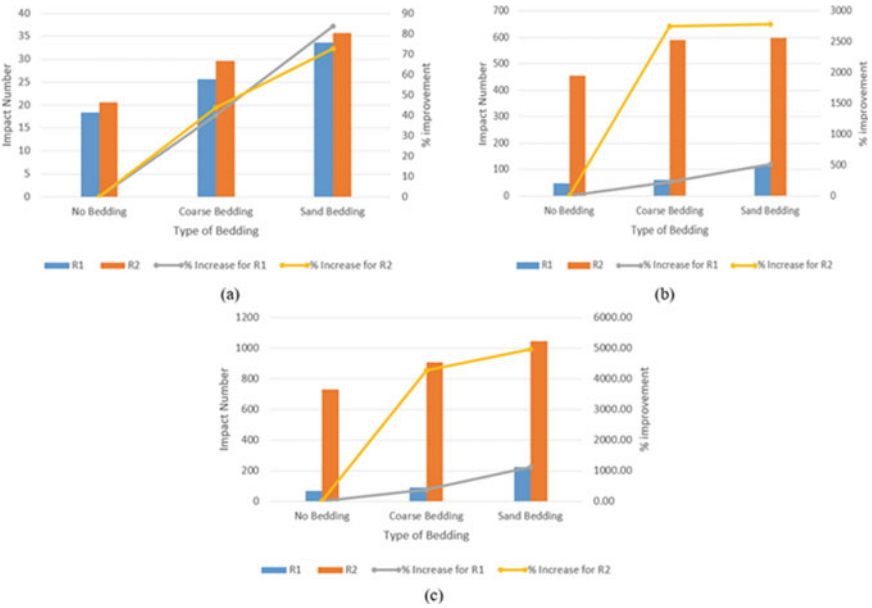

Fig. 11 Effect of bedding type on the line notch specimens, **a** conventional type, **b** SP-P type, **c** SP-S type

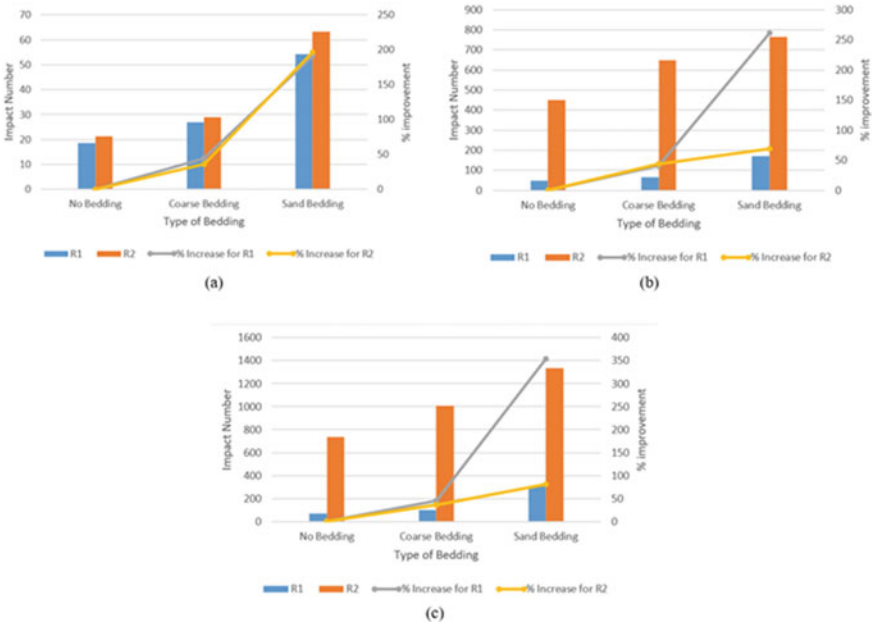

Fig. 12 Effect of bedding type on the cross notch specimens, **a** conventional type, **b** SP-P type, **c** SP-S type

when evaluating different bedding and pruning modes are illustrated in Fig. 13 [15]. Since the line notch and the cross notch specimen have improved crack control, a more systematic failure approach has been demonstrated.

Due to the effect of the knife-like load transfer plate, the fractures caused by the notches followed the same course [16]. Some new ones began to occur on the sides of the specimens after a certain distance travelled by the cracks, which increased with more effects and had a greater effect on the specimen [17]. In specimens, even secondary cracks are visible, perhaps because of the weak surface matrix in the surface layers of the specimens.

The enormous differences between the initial and ultimate fracture values are shown, revealing that the specimens have projected increased bridging actions, which implies higher ductility. Important observations were also made on the changing of bed type [18]. There are fewer secondary breaks in the specimens above the sand bedding, this is because the sand bedding shows the impact energy that might provide us greater control of the breaks and also identify them (Fig. 14d). The specimens with sand bedding had a higher impact than the ones without any bedding or rough bedding [19]. The sand bedding is, therefore, found to absorb more energy than the coarse bedding, and the steel base plate gives us more control over the spread of fractures [20].

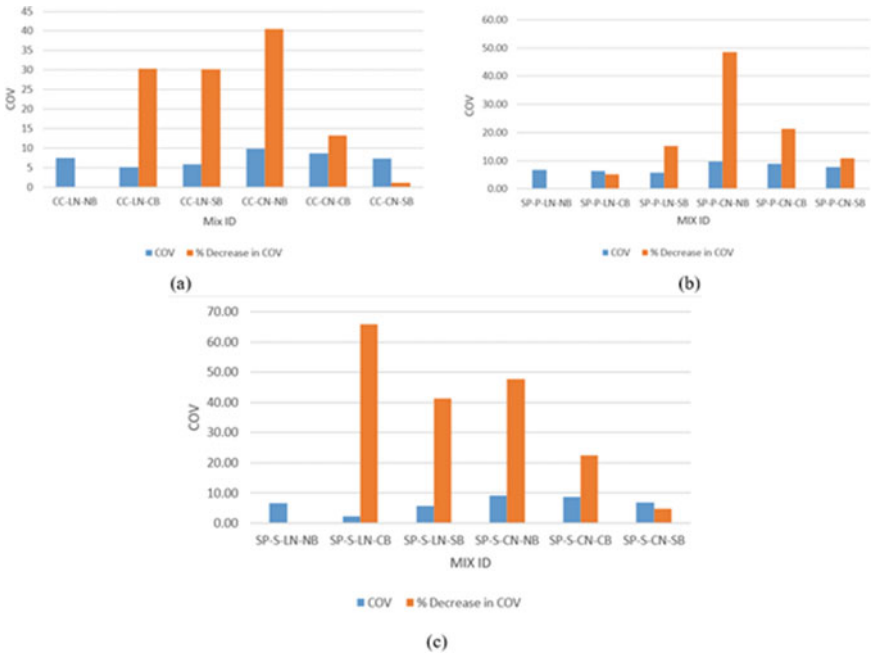

Fig. 13 Co-efficient of variation graph with different bedding and notch types, **a** conventional type, **b** SP-P type, **c** SP-S type

8 Conclusion

In this study on RBDWI fibre-reinforced concrete tests, the suitability of these new amendments proposed for the repeated testing method ACI 544 -2R was evaluated [21]. The adjustment encompasses the employment of knife-like specimens and transfer plate only for screening of the specimens. The study has been conducted and thus the progress has been made. The following findings were drawn from the experimental inquiry.

The usage in all classed groups in the experiment of sand bedding has yielded a reduced dispersion of data. But the percentages vary from sample to sample. There are variances. The dispersive decrease was mostly observed in a linear sample.

Crack control is enhanced using notched specimens and knife-like transfer plates. The splits began and spread across the notch's projections. Accurate measurement of the spread of crack would offer a distinct criterion for the result to be adopted or to be rejected. The filtering of such specimens would likewise reduce the dispersion of the result.

Thanks to its interactions with the notched surface, the line notched specimens have achieved failure sooner. The cross notch hence has a greater area that allows for the dissipation of energy in two directions because it's a cross. This also changes the specimen shape where the knife plate interacts. This can influence what findings

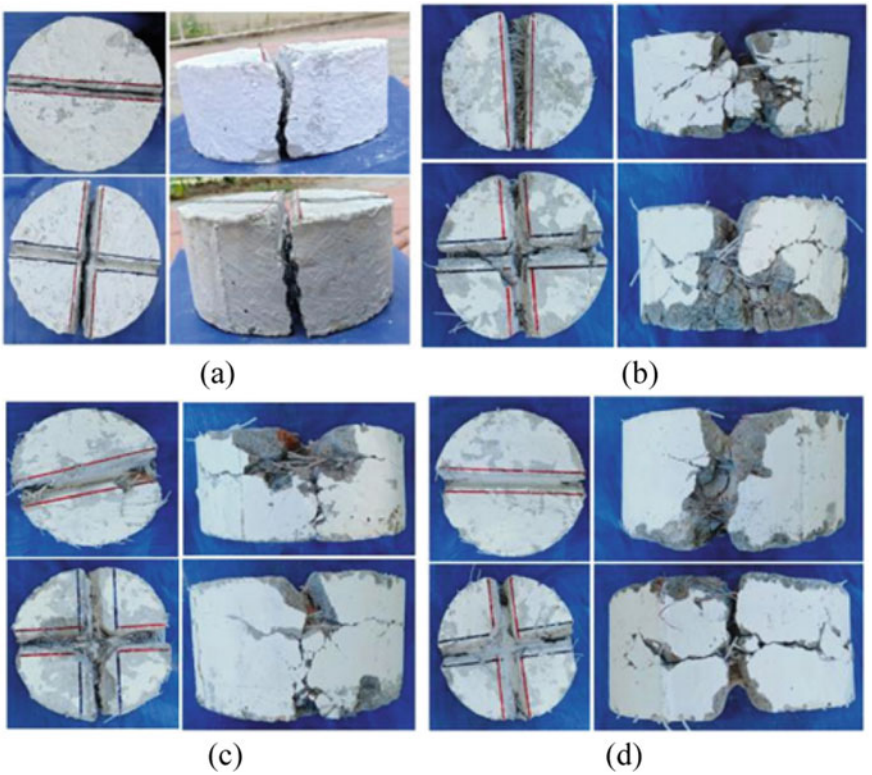

Fig. 14 Fibrous concrete failure pattern, **a** conventional mix, **b** no bedding-line and cross notch, **c** coarse bedding-line and cross notch, **d** Sand bedding-line and cross notch

can be negligible in cross notch specimens. This is not true for the line specimens as the contact area is smaller and only projected in a straight line. Therefore, a line notch is noted for the speedier failure.

The advantages and disadvantages of discoveries produced in history is still to be validated. Thus, any recommended experimental change can be further enhanced and deliver better findings or can even create a new door in the field of research.

Acknowledgements The authors would like to thank the School of Civil Engineering, SASTRA Deemed to be University, Thanjavur, India, for their support to complete the project.

References

1. Badr AF, Ashour AK, Platten (2006) Statistical variations in impact resistance of polypropylene fibre-reinforced concrete. Int J Impact Eng 32:1907–1920

2. Mwasha A, Ramnath R (2018) Manufacturing concrete with high compressive strength using recycled aggregates. J Mater Civil Eng 30(8)
3. ACI 544.1R-96 (2002) Report on fiber reinforced concrete. American Concrete Institute ACI, USA
4. ACI 544.2R-89 (1999) Measurement of properties of fiber reinforced concrete. American Concrete Institute ACI, USA
5. ACI 544.6R-15 (2015) Report on design and construction of steel fiber reinforced concrete elevated slabs. American Concrete Institute ACI, USA
6. Chen B, Liu JY (2004) Residual strength of hybrid-fiber-reinforced high-strength concrete after exposure to high temperatures. J Cement Concr Res 34:1065–1069
7. Yoo D-Y, Banthia N (2017) Mechanical and structural behaviours of ultra-high-performance fiber-reinforced concrete subjected to impact and blast. Constr Build Mater 149:416–431
8. Aydin AC (2007) Self-compact ability of high volume hybrid fiber reinforced concrete. J Constr Build Mater 21:1149–1154
9. Banthia N, Gupta R (2004) Hybrid fiber reinforced concrete fiber synergy in high strength matrices. J Mater Struct 37:707–716
10. Schrader EK (1981) Impact resistance and test procedure for concrete. ACI Mater J 78(2):141–146
11. Nili M, Afroughsabet V (2010) The effects of silica fume and polypropylene fibers on the impact resistance and mechanical properties of concrete. Constr Build Mater 24:927–933
12. Nataraja MC, Dhang N, Gupta AP (1999) Statistical variations in impact resistance of steel fiber-reinforced concrete subjected to drop weight test. Cem Concr Res 29:989–995
13. Song PS, Wu JC, Hwang S, Sheu BC (2005) Assessment of statistical variations in impact resistance of high-strength concrete and high-strength steel fiber reinforced concrete. Cem Concr Res 35:393–399
14. Song PS, Wu JC, Hwang S, Sheu BC (2005) Statistical analysis of impact strength and strength reliability of steel-polypropylene hybrid fiber-reinforced concrete. Constr Build Mater 19:1–9
15. Yu R, van Beers L, Spiesz P, Brouwers HJH (2016) Impact resistance of a sustainable ultra-high performance fibre reinforced concrete (UHPFRC) under pendulum impact loadings. Constr Build Mater 107:203–215
16. Abirami T, Loganaganandan M, Murali G, Fediuk R, Sreekrishna RV, Vignesh T, Januppriya G, Karthikeyan K (2019) Experimental research on impact response of novel steel fibrous concretes under falling mass impact. Constr Build Mater 222
17. Rahmani T, Kiani B, Shekarchi M, Safari A (2012) Statistical and experimental analysis on the behaviour of fiber reinforced concretes subjected to drop weight test. Constr Build Mater 37:360–369
18. Gopalaratnam VS, Shah SP (1986) Properties of steel fibre reinforced concrete subjected to impact loading. ACI Mater J 83(14):117–126
19. Suaris W, Shah SP (1983) Properties of concrete subjected to impact. J Struct Eng 109 (7):1727–1741 (ASCE)
20. Wang CQ, Wu KR (2005) Research on the hybrid effect of different geometrical size hybrid fiber reinforced concrete. J. Build Mater 8(3):15–20
21. Liu X, Dai S (2012) Determination method of the beam depth of tapered steel. J Sci J Archit 2(1):22–26

Spatial SWOT Analysis: An Approach for Urban Regeneration

Sumana Jayaprakash and Vimala Swamy

Abstract Urban regeneration projects encompass a wide variety of interventions to improve the conditions and intensify the use of an existing urban area, which has degraded with continuous use, overuse, changing social context, land values, and markets. The dilapidation of building structures and aging infrastructure systems add to the degraded condition. Identification of the need for intervention with an in-depth study of the existing situation is the first step that leads to the framing of the strategic goals of the Urban Regeneration project. A SWOT analysis evaluates the internal strengths and weaknesses and the external threats and opportunities of the context in consideration. The internal analysis is used to identify characteristics inherent to the context and the external analysis is used to identify opportunities and threats that can be effectively utilized for enhancing the quality of the urban environment. Hence, SWOT analysis as a tool is employed to assess the capacity of the urban area to execute a plan or achieve its goals. The limitations have been identified, and modifications proposed to remodel the traditional tool with the mapping on the SPACE matrix in the context of Urban Regeneration. The result of the analysis determined the operational strategy to be adopted for the Urban Regeneration intervention. This research paper aims to (1) examine the efficiency of the SWOT tool concerning its applicability to Urban Regeneration Intervention (2) Identify the limitations of the existing practices as applicable to Urban Regeneration Projects (3) Propose a spatial SWOT Analysis mapped on a SPACE matrix with proposed strategies for the Urban Regeneration Intervention for the city of Hassan. The limitation of the work was that the area specific dynamic factors had not been considered.

Keywords SWOT analysis · Characteristics · Strategy · Urban context

S. Jayaprakash (✉)
Department of Civil Engineering, Malnad College of Engineering, Hassan, Karnataka, India
e-mail: sj@mcehassan.ac.in

V. Swamy
School of Architecture, REVA University, Bengaluru, Karnataka, India
e-mail: svimala309@gmail.com

L. Nandagiri et al. (eds.), *Recent Advances in Civil Engineering*, Lecture Notes in Civil Engineering 256, https://doi.org/10.1007/978-981-19-1862-9_2

1 Introduction

Urban Regeneration is a comprehensive and integrated vision and action to resolve urban problems to bring about a re-orientation in the economic, physical, social, and environmental conditions in an area that has been degraded and requires improvement [1]. Regeneration of underutilized urban land in cities also contributes to creating communities that are economically sustainable and environmentally friendly. Revitalizing urban areas can increase inclusiveness by providing affordable housing and open spaces for the urban community. Urban regeneration projects are complex due to their multi-sectoral and multi-stakeholder nature. These projects require a stable local government and a capable institutional structure well aligned to long-term processes that can sustain initiatives for a long time regardless of political factors [2]. A world bank report states that it is difficult to finance urban regeneration projects, as the private sector investment in regeneration projects is overpowered with risks when compared with new development [3]. Urban regeneration is a crucial factor in city policies and management, environmental protection, life quality improvement, and sustainable development. It has grown beyond the scope of a field of study and has become crucial for developing urban policies [4].

In this perspective, the planning process should be intertwined with the decision-making process. The assessment of urban transformation scenarios represents a complex decision problem that calls for different conflicting aspects, including the definition of shared goals for possible solutions and their effects according to different development scenarios [5].

The project proposal is to develop a model for defining and evaluating the area for Urban Regeneration that need to be prioritized for intervention. Apply the model for Hassan City core area to Restore the Historic Identity of the traditional Urban fabric core with the Devigere tank as the focus (Physical planning) with the creation of public open space integrating the various public functions (social aspects) aligned with the environmental factors as an economically sustainable Urban Regeneration Intervention.

SWOT Analysis is adopted as a strategic planning tool to evaluate internal and external influences on a vision or specific goal. It is a tool for a company or organization to assess its capacity to execute a plan or achieve an attainable goal [6]. SWOT stands for: Strengths: attributes of criteria that are helpful in the achievement of the objective. Weaknesses: attributes that weaken the attainment of the goal. Opportunities: external factors which can be a catalyst for the achievement of the objectives. Threats: external conditions, which restrict or prohibit the attainment of the goal [7].

2 SWOT Analysis

In the present context, the decision is not a one-shot activity but a procedural one, extended over a while. A spectrum of feasible solutions is available from which

choices emerge. Given the present nature of public planning and policymaking, it is clear that many conflicting issues and interests exist where the market mechanism does not exclusively determine the social value of the impacts of public decisions. It thereby implies that the use of new evaluation methods in physical planning is imperative. SWOT as an evaluation tool is increasingly efficient in the evaluation process of Urban Regeneration projects.

In the SWOT Analysis, Strengths and weaknesses refer to the existing conditions of the site, which are either helpful or harmful to achieving the goals of the project. Strengths are favorable conditions that need to be built upon, whereas weaknesses are unfavorable conditions that need to be taken care of in the concept and plan. Opportunities and threats refer to potential future consequences on the site. Opportunities are inherent improvements and favorable conditions that the project will seek to achieve. Threats are the potential barriers that may obstruct the implementation of projects [8]. In particular, the initial phase is related to the structuring of the decision problem to identify possible alternative solutions for reaching the goal. This phase constitutes the development of the SWOT analysis [9].

The SWOT Analysis is a final statement of internal and external influences on the community understanding in a four-quadrant table. The SWOT's potential to address the multi-dimensions of issues and multi-stakeholders is a valuable tool in the brownfield revitalization process. It focuses on both the internal and the external factors, and aids in the identification of specific proposals in the strategic plan. It identifies priority areas and activities for development. The SWOT analysis may be used in any decision-making situation to meet the desired end-state (objective). Conclusions are to be arrived at to maximize strengths and opportunities by matching strengths to opportunities and converting threats or weaknesses to strengths or opportunities. The threats and weaknesses should be minimized or avoided.

However, the SWOT analysis is just one method of categorization and has its weaknesses. A holistic approach to conceptualize what is crucial in achieving objectives can end up as lists of priorities that lack an in-depth understanding. SWOT Analysis presents a mere list of factors as to micro and macro environment; moreover, it is cumbersome to use qualitatively listed factors in decision-making. The qualitative examination of the internal and external factors can only be the beginning of in-depth analysis of the planning process. In a group brainstorming session, individual prejudices and personal experiences of trivial issues can be voiced by individuals or small groups among the participants, overpowering the theme of discussion and thereby deviating from the cause. The inability to articulate the point of view in alignment with the goal can portray an incomplete or incorrect strength or weakness. It does not present the conclusions critically, and with clear prioritization, for example, weak opportunities may appear to balance threats. SWOT Analysis is a technique that has a general perspective and presents a generic solution. Detailed and specific issues are not the focus of SWOT Analysis, but the other analyses that would follow. The decision arrived at in a SWOT Analysis may be unreliable, all bound up with aspirations, biases, and hope of the individuals involved. It is a situation analysis that can be only a start point for a more comprehensive review. There is also the complexity in interpreting the result and applying it in the planning and design process. An in-depth

scientific analysis of the site situation, technical understanding of the issues, policies governing the problem, and a trained research mindset are required if the SWOT analysis results must derive appropriate and realistic conclusions. The researcher will also be responsible for the analysis and technically prove the derivation of the conclusions. In general SWOT, collective pooling makes it impossible to trace the logical derivation of the specific conclusions from the pooled collective ideas. The ideas presented in a meeting of various stakeholders are not necessarily well thought out by each one. It may be a quick response to the issue in consideration in a given slot of the brainstorming session [8].

SWOT Analysis is an analysis tool that has a problem in terms of quality and measurements. In applying SWOT Analysis, innumerable factors get identified. However, quantity does not mean quality. It is not possible to identify the priorities as portrayed by the participants in SWOT Analysis, work out the details, and translate them into development concepts, thereby presenting conflicts in different dimensions. The data may be unreliable for analysis as it could be vague due to the inability to track the logic of the statements [10].

The importance of individual SWOTs becomes evident by the value of the strategies to be generated based on it. A SWOT item that produces valuable inputs is more crucial than the one with no valuable inputs. It is important to carefully identify individual SWOT items as subsequent steps in the planning for the achievement of the selected objective.

As Comino rightly points out, the problem is that an indicator by itself provides little information unless it is associated with a system of indicators, able to provide systematic information for assessment. A set of indicators consists of several indicators correlated from a logical and functional point of view. It describes and provides information on several associated phenomena, interpreted in a coordinated way [11]. Working out a SWOT Analysis is more than an exercise of making four lists. The valuable part of SWOT Analysis is determining what story the four lists tell about the existing situation and considering what actions are needed [10].

It is illogical to work on a base of collective responses and ideas compiled in a session or two. A structured format of the SWOT in terms of priorities and at macro and a microscale is also not the outcome of the SWOT, making it cumbersome in incorporating the conclusions as unrelated bits of inputs.

In Urban Regeneration projects mapping, the SWOT analysis on the map can be a possible solution to overcome the limitations of SWOT. Spatial SWOT mapping offers the opportunity to make the process contextual and specific to the area in consideration. The SWOT indicators mapped by spatial distribution can effectively guide decision-makers to accurately analyze the context to a greater depth, than with the conventional SWOT [11].

3 The Study Area

Hassan is located in the midway of the Bengaluru-Mangaluru National highway. The study area is the Inner city of Hassan, and part of the research project is part of academic work (Fig. 1).

The area around the historically significant Devigere tank area, in the center of the city (no. 9 on the map) with the stretch of land extending up to the Maharaja Park, is considered. This belt of about 750 m long and 250 m wide (Area of approximately 0.3sqm) and reflects the transition zone separating the traditional old Urban Fabric from the new. Northwards, from the Devigere tank, the belt contains the city bus stand, cinema theaters, Institutional buildings, markets, parks, open spaces, commercial areas, etc., and presents a series of challenges and opportunities for Urban Regeneration Intervention. It is the center of the city with mixed land uses, characterized by old buildings and a closely-knit urban fabric, and a good amount of pedestrian and vehicular movement. The traditional Urban fabric core area of the

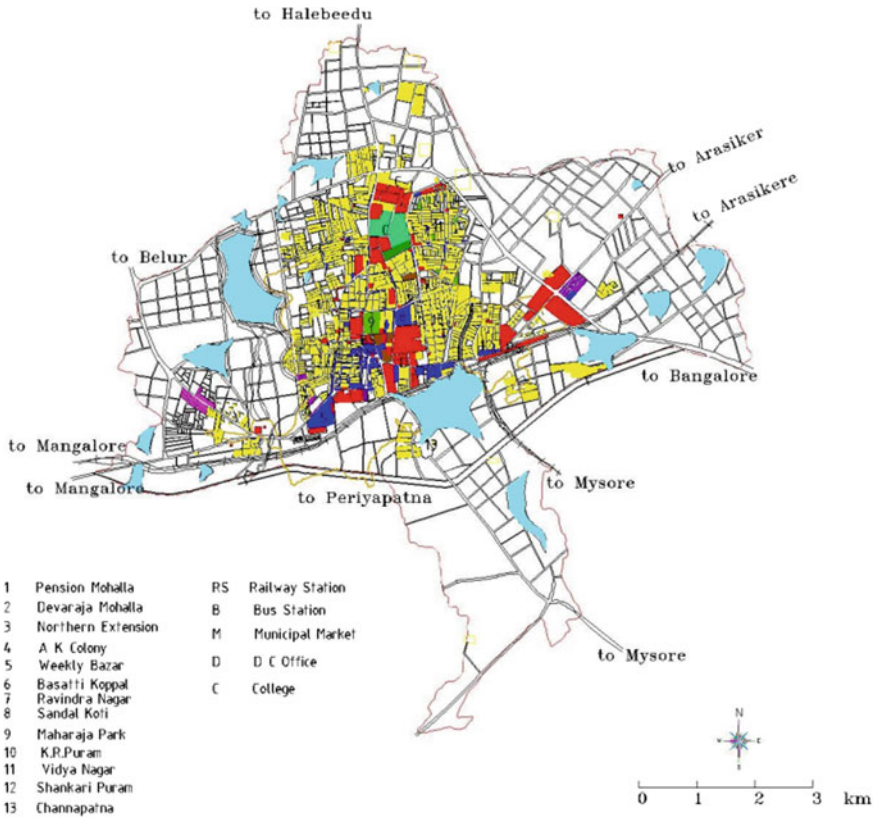

Fig. 1 Map of Hassan, Karnataka

Devigere tank is to be the focus of Physical planning to create public open spaces and integrate the various public functions which include the social aspects, aligned with the environmental factors for an economically sustainable Urban Regeneration Intervention (Fig. 2).

Fig. 2 Devigere tank surroundings, Hassan

4 Methodology

SWOT Analysis technique was used to identify the internal factors of strengths and weakness and the external factors of opportunities and threats. The following steps have been followed: (1) Mapping the SWOT factors on the base map by the researcher. (2) Appropriating scores to the various factors. (3) Mapping of the SPACE matrix. (4) Identifying the design strategies to be adopted. The methodology adopted focused on Spatial SWOT Analysis as a technique for a comprehensive understanding of the study area. The conclusive set of maps represents the strengths, weaknesses, opportunities, and threats mapped on the aerial map containing physical features. The methodology adopted proposes a baseline spatial SWOT map, which is scientifically aligned with the policies and includes all the complexities of the context. These maps serve as a starting point for educating the stakeholders, inviting suggestions, and incorporating overlays of viewpoints of the various interest groups.

4.1 Mapping the SWOT Factors on the Base Map by the Researcher

The approach adopted overcomes the limitations of the conventional SWOT analysis by incorporating the following three aspects. The novel design of the SWOT analysis is oriented to the strategic plan of the Urban Regeneration project. Google Earth Maps available on the internet create easy access to valuable and accurate information.

The three aspects adopted are by considering the dimensions of economic, social, environmental, physical, and mobility factors. A multidimensional focus on the five factors confines and concentrates focus on the key issues. Specific solutions obtained are employed to strengthen the strategic goals. Sub-criteria analysis of the five dimensions stated above helped to arrive at precise and holistic integrated objectives at both the macro and the microscale. The spatial mapping of the issues on the area plan gave a better understanding by relating to the physical planning aspects.

The five dimensions and the sub-criteria factors considered for the SWOT Analysis are discussed in Table 1.

4.2 Appropriating Scores to the Various Factors

The various factors of the four quadrants (strengths, weakness, opportunities, and threats) were rated by the researcher on a scale of 1 to 5, in terms of their importance, 5 being the highest score and 1 being the lowest score. The average score of each of the four factors of SWOT was the score to be used for locating the position in the appropriate quadrant.

Table 1 The five dimensions and sub-criteria

Dimension	Physical	Environmental	Economic	Social	mobility
Sub Criteria factors	Area and Identity	Inner city location and site	Image and Identity	Accessibility	Bicycle, pedestrian
	Streets and squares	Green spaces	Resource mobilization	connectedness	Car
	Building forms	Eco sensitive design	Implementation	Scale and safety	Public transport

Source author analysis

4.3 Mapping of the SPACE Matrix

The average of the internal factors (strengths and weakness) and external factors (opportunities and threats) then plotted on the SPACE matrix facilitated the working out of specific strategic goals of the Urban regeneration Intervention.

4.4 Identifying the Design Strategies to Be Adopted

The location points positioned in the appropriate quadrant were joined together. The quadrant in which the area covered by the obtained figure is maximum is the strategy determined by that quadrant as per the SPACE matrix principles of aggressive, conservative, defensive, and competitive.

5 The Process Carried Out

5.1 Mapping the SWOT Factors/rating

See Fig. 3.

5.2 Appropriating Scores to the Various Factors

See Figs. 3, 4, 5, and 6; Tables 2, 3, 4, 5, and 6.

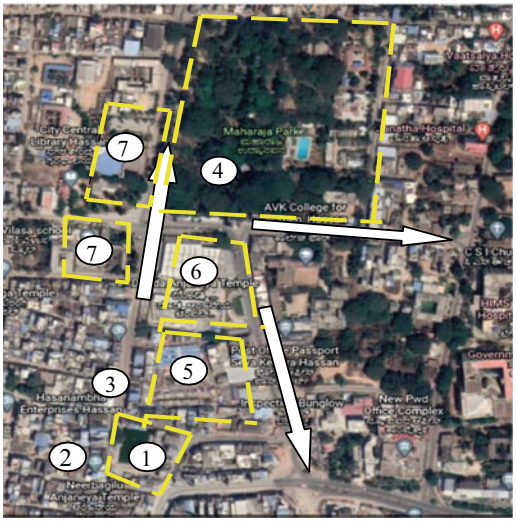

	STRENGHTS:
1.	Devigere Tank
2.	Compact Planning
3.	Old low-rise structures
4.	City level park
5.	City level Market
6.	City Bus Stand
7.	Institutional buildings
	Zones of the area
	City Level Linkages

Area of intervention: Hassan

URBAN REGENERATION

Fig. 3 SWOT analysis: strengths mapped by author. *Source* https://www.google.com/earth/

	WEAKNESS:
1.	Aging building structures
2.	Spill to street activities
3.	Underutilized FAR
4.	Inadequate parking
5.	Unsafe spaces
6.	No bicycle tracks
7.	No footpaths
	No street edge design
	No Zonal Linkages
	Inadequate Parking

Area of Intervention : Hassan

URBAN REGENERATION

Fig. 4 SWOT analysis: weakness mapped by author. *Source* https://www.google.com/earth/

5.3 Mapping of the SPACE Matrix

The strategic position and action evaluation (SPACE) is a management tool to analyze and derive the strategy for intervention. The SPACE matrix has four quadrants, where

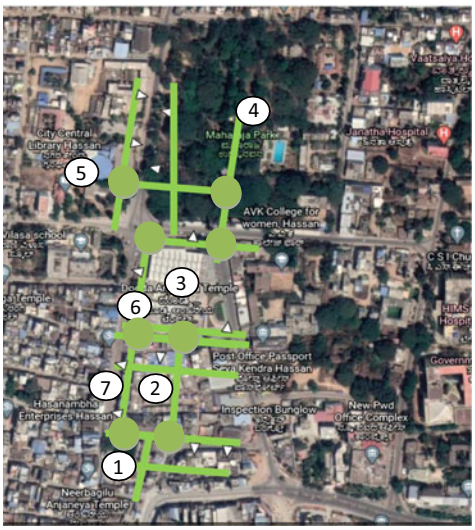

	OPPORTUNITIES
1.	Historic zone
2.	Shopping zone
3.	Transit zone
4.	Recreational zone
5.	Institutional zone
6.	Commercial zone
7.	Informal vending zone
	Street edge design
	Design of Nodes

Area of Intervention : Hassan

URBAN REGENERATION

Fig. 5 SWOT analysis: opportunities mapped by author. *Source* https://www.google.com/earth/

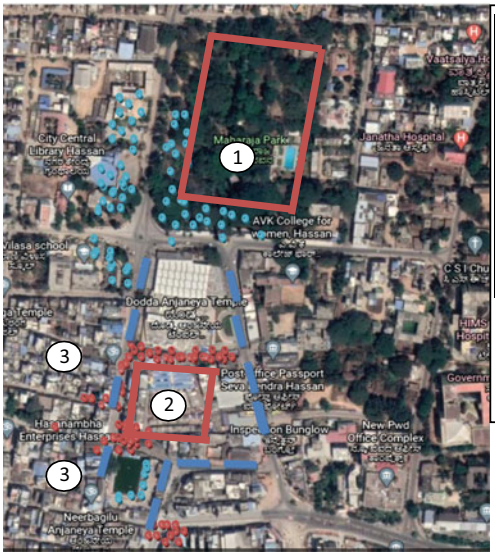

	THREATS
1.	Maintenance
2.	Participatory planning challenge
3.	Tenant occupied challenge
	Increasing parking
	Overcrowded zones
	Underutilized zones
	Inappropriate new growth

Area of Intervention: Hassan

URBAN REGENERATION

Fig. 6 SWOT analysis: Threats mapped by author. *Source* https://www.google.com/earth/

each quadrant proposes a specific type of strategy to be adopted by the mapping of the internal and external factors. The four strategies include aggressive, conservative, defensive, and competitive [12]. It is plotted on the x and y-axis. The internal factor

Table 2 Flow chart of the methodology

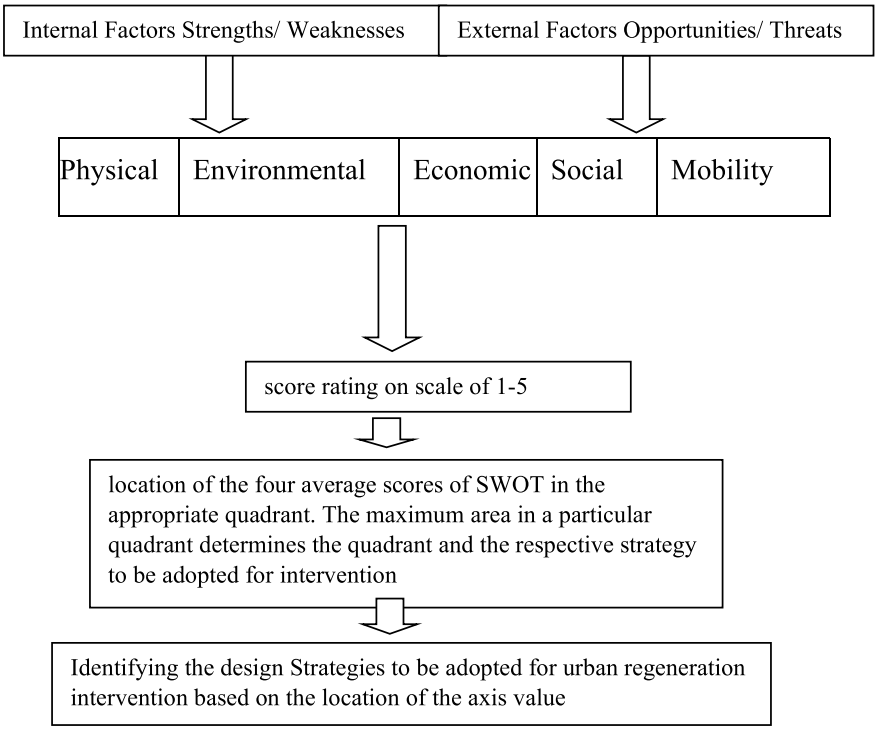

scores are plotted on the x-axis and the external factor scores are plotted on the y-axis, the scores range from 0 to 5 and 0 to −5 on the positive and negative sides, respectively (Table 7).

5.4 Results: Identifying the Design Strategies to be Adopted

The strategic positions of the four quadrants are as follows. The first quadrant is an aggressive position having both internal strength and external opportunities. The second quadrant is the conservative position, which is characterized by internal weakness and external opportunities. The third quadrant is the defensive position having both internal weakness and external threats. The fourth quadrant is a competitive position having internal strength but facing external threats. Having plotted the average of the Internal and External factors score, as shown below the suggested design strategy to be adopted is a conservative strategy (Graph 1).

Table 3 Strengths: (mapping on base map and tabulation: Author's work)

S1 Physical	Strengths	Scores
Area and Identity	Historic precinct, market, bus stand, park, Institutions. Mixed land uses with living and work spaces	4
Streets & squares	Interzone of Walking habit among people, Shopping convenience,	1
Building forms	Site profile Unconventional space standards	3
S2 Environment		
Inner city location	Reduces pressure on land use and conserves Greenfield sites	4
Green spaces	Historic and environmental setting of urban fabric	3
Eco design	Mixed use zone reducing pollution of travel. Compact planning	2
S3 Economic		
Image and Identity	Presence of historic water body and temple precints. Old Low rise structures, allows for new identity for the area	1
Resource mobilization	Capitalizing on the Historic setting. Potential of economic development by public private participation	1
Implementation	Financial affordability of owners to repair/ build new	2
S4 Social		
Accessibility	People friendly city level Center with amenities	2
Connectedness	Adjacency of major functions like market, bus stand	3
Scale and safety	Close knit community and contextual social characters	1
S5 Mobility		
Bicycle	Presence of bicycle users of all age groups	2
pedestrian	Walking is the way of life	2
Car	As distances are short, Local users preference of two wheelers	2
Public transport	Small scale of city, hence low public movement	3
	Total	2.25

6 Discussions and Conclusions

SWOT analysis traditionally carried out in one or two brainstorming sessions is a limiting factor for the researcher to base his analysis for the Design stage. The conclusions arrived at by the stakeholders are a basket of random pointers based on individual partial understanding, which may not aid in the framing of a meaningful objective. A sound SWOT Analysis requires an in-depth study of the subject and a research mindset. Hence, it should be carried out by the researcher. The results are to be presented to the stakeholders for additional inputs or criticisms.

The limitations presented by SWOT analysis as a traditional tool can be overcome to contextualize Urban Regeneration projects. The brief pointers as indicated for the four quadrants of the SWOT in the traditional method are to be replaced by five

Table 4 Weakness: (mapping on base map and tabulation: Author's work)

W1 Physical	Weakness	Scores
Area and Identity	Aging commercial spaces, backing the unused historic precinct	−4
Streets and squares	No area level recreational space, no defined pedestrian paths. No interlinkages/sequencing of spaces	−3
Building forms	No street edge Design, P arking problems, over spilling	−1
W2 Environment		
Inner city location	Old and dilapidated structures	−3
Green spaces	Quality open green spaces. No natural env strong features. Waste management poor	−4
Eco design	Existing policy does not specify eco sensitive measures	−3
W3 Economic		
Image and Identity	FAR unutilized. No large influential public development to foster improvement	−2
Resource mobilization	Unexplored urban development	−1
Implementation	Old and dilapidated building fabric	−3
W4 Social		
Accessibility	Crowdedness	−2
connectedness	Streets are encroached upon	−4
Scale and safety	Spaces not designed and unsafe	−3
W5 Mobility		
Bicycle	No bicycle tracks. No provision for differently abled	−2
pedestrian	No proper footpaths. No provision for differently abled	−2
Car	Lack of parking spaces	−1
Public transport	No space allotment for local buses. No provision for differently abled	−3
	Total	−2.56

factors, namely Physical, Economic, Environmental, Social, and mobility with the sub-criteria for each of the factors. The scoring of the factors makes it possible to analyze the specific factors at the sub-criteria level, resulting in a precise, operational, applicable response to the quadrant in question in the SPACE matrix.

In the traditional presentation of the conclusions as a group of words/ phrases, SWOT results make it complicated to interpret and apply the same in the planning and designing process. The area plan is the context where these interpretations are to be operational, and the SWOT results prove ineffective in comprehensive interpretation relating to the area plan. This is overcome by the spatial mapping of the criteria on the SPACE matrix by relating the criteria to the physical planning aspects.

The analysis clearly states the strategic position to be adopted for intervention. As the location of the strategic position is in the 3rd quadrant, the conservative strategy should be adopted. It is the integration of the weakness with the opportunities. The

Table 5 Opportunities: (mapping on base map and tabulation: Author's work)

O1 Physical	Opportunities	Scores
Area and Identity	Defined linkages to city. Located between old and new	2
Streets and squares	Definition of pedestrian network Integration of activities with the recreational open. space. Market land underutilized	3
Building forms	Appropriate byelaws Building typology and street edge design	3
O2 Environment		
Inner city location	Develop/ Demonstrate an integrated land reuse, densification, appropriate sustainable use	3
Green spaces	Focus on the water body can integrate conservation and city identity. Incorporate green / env features	4
Eco design	To develop eco sensitive building footprint	2
O3 Economic	Develop city Center with new identity	2
Image and Identity	Tourist attractions Increase building density. Financially sustainable integrated projects	4
Resource mobilization	Innovative Private investment strategies, educational, recreational, innovative projects for resource mobilization	3
Implementation	Area specific Policies Use of TDR. Innovative proposals	2
O4 Social		
Accessibility	Provide open space with social amenities, street furniture. Design response to the young age group and the old	2
Connectedness	In between zones and building spaces as creative zones of recreation. Street furniture and places of interaction/ rest	3
Scale and safety	Building and boundary edge design can foster informal events	2
O5 Mobility		
Bicycle	Design cycle tracks, Increase in bicycle users	2
Pedestrian	Provide walking network, street furniture connected to transit	2
Car	Encourage two-wheeler and bicycle use by innovative uses	1
Public transport	Formalize the existing public travel. Integrated transport	2
	Total	2.62

area is confronted with opportunities listed out in the SWOT mapping, which need to effectively be exploited. However, the urban area in consideration has internal weaknesses as listed in the spatial SWOT mapping. Combining the weakness and the opportunities the intervention strategies emerge (W1O1, W2O2, W3O3, W4XO4, W5O5).

The decision was arrived at as the results of the SWOT analysis in the Urban Regeneration Intervention:

- To preserve and promote the appropriate use of existing historic properties and areas, such as the city center, and to enable citizens to be aware of and appreciate the history and development of Hassan.

Table 6 Threats: (mapping on base map and tabulation: Author's work)

T1 Physical	Threats	Scores
Area and Identity	Inappropriate new land use / building can change the character	−2
Streets and squares	Consistency of design across all proposals for the area. Roads in-between zones challenges the pedestrian network	−2
Building forms	Land pooling can disrupt the existing pattern of fabric and change the character of the place	−1
T2 Environment		
Inner city location	Inappropriate new growth. Parking issues at junctions	−4
Green spaces	Maintenance. Attitude of users. Spilling by vendors,	−3
	Overcrowded and underutilized spaces	−1
Eco design	Apprehension/ traditional attitude toward development	−2
T3 Economic		
Image and Identity	Participatory approach to planning and Design	−2
Resource mobilization	Private sector if not aligned with public interest can overpower the historic scenario	−2
Implementation	Tenant occupied buildings complex to upgrade/ rebuild, uncertain funding. Changing political scenario	−2
T4 Social		
Accessibility	Increase in stealing and misuse at night	−3
Connectedness	Formalizing the vendors may not solve the street encroachment	−1
Scale and safety	New forms of development if not guided can disrupt the character	−2
T5 Mobility		
Bicycle	Less number opting to use bicycles due to stealing of bicycle from parking places. Visibility of bicycles in the dark	−3
Pedestrian	Vendors occupying footpaths. Shopkeepers spilling over	−2
Car	Increasing number of cars. Parking problems	−4
Public transport	Informal public transit spill on to the roads. Overcrowding	−2
	Total	−2.37

Table 7 SWOT: average scores and axis value

	Average scores	Axis value
Internal factor score strengths	2.25	−0.15
Weakness	−2.56	
External factor score opportunities	2.62	0.12
Threats	−2.37	

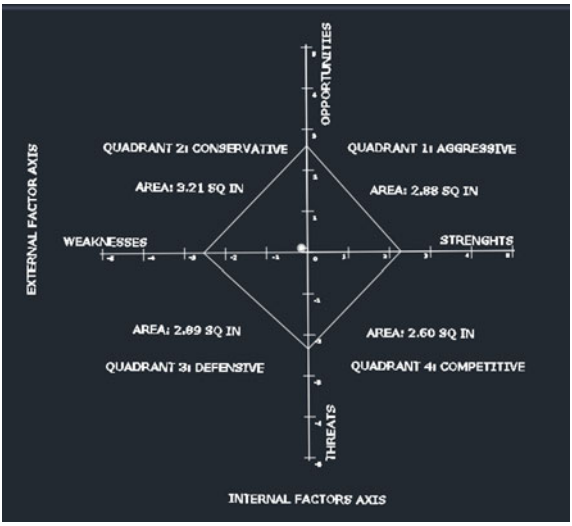

Graph 1 Plotting scores on axis

- To provide for a community of mixed land use development that includes eating places, offices, and home-work places.
- To provide efficient and effective town services along with recreational opportunities, at a level that is accessible to all users.
- Design a sustainable community through energy conservation, alternative energy efforts, and waste management.
- To design economically sustained projects with effective public–private partnerships and innovative policy planning. To adopt appropriate integrated mobility systems that encourage and provide for bicycle and pedestrian networks and well-connected zones for various activities.

The above opportunistic strategies are weakened by internal factors such as the absence of concern for the historic precinct, absence of bylaws for its protection. No area level recreational space, no defined pedestrian paths, and absence of interlinkages/sequencing of spaces. It is characterized by old and dilapidated building structures and a lack of public motivation along with unexplored urban development. Mobility is poor with a lack of parking spaces and no defined pedestrian movement. These inherent weaknesses will have to be taken into consideration while exploring the opportunities for Urban Regeneration of the area.

This model of SWOT analysis can be effectively applied to the Urban Regeneration project, as it presents a spatial macro analysis picture in a holistic manner, which can be translated into design and operational terms. It also presents the objectives for the Urban Regeneration Intervention without the problem of misinterpreting the results of the SWOT.

This paper presented an approach to holistically understand the efficiency of SWOT in the evaluation stage of the Urban Regeneration Strategic Planning Stage. The SWOT tool though effective in the generalized identification of the strengths,

weakness, opportunity, and threats seems ineffective as a tool in the process of defining the strategic goals of Urban Regeneration. Hence, the limitations have been identified and modifications were proposed to remodel the traditional tool of SWOT in the context of Urban Regeneration by application of the SPACE matrix. Spatial SWOT analysis baseline mapping is considered the first step in understanding the urban issues. This baseline map serves to educate the stakeholders. The scoring of the various internal and external factors allows for the location of the scores of SWOT spatially in the four quadrants of the SPACE matrix and the final location of the strategic position. This position determines the design strategy to be adopted for intervention. These proposals are to be mapped on the baseline map for further understanding and analysis.

The limitation of the work has been that it has not focused on the dynamic spatial aspect integral to Urban Regeneration Plan. It presents a promising future direction for research including factors of microanalysis of the urban area. With the inclusion of the dynamic spatial factors like the everyday changes in the area and carrying out the SWOT analysis of the area in a more detailed level, a holistic approach to spatial SWOT analysis can be achieved.

References

1. Roberts P, Sykes H (eds) (1999) Urban regeneration: a handbook. Sage
2. Indicators-Programme-Monitoring-Human-Settlements-Volume-1 (n.d.) Retrieved from http://globalhousingindicators.org/sites/globalhousingindicators.org/files/97119175-Indicators-Programme-Monitoring-Human-Settlements-Volume-1.pdf
3. Amirtahmasebi R, Orloff M, Wahba S, Altman A (2016) Regenerating urban land: a practitioner's guide to leveraging private investment. Urban Development Series. World Bank, Washington, DC. https://doi.org/10.1596/978-1-4648-0473-1. License: Creative Commons Attribution CC BY 3.0 IGO
4. Natividade-Jesus E, Almeida A, Sousa N, Coutinho-Rodrigues J (2019) A case study driven integrated methodology to support sustainable urban regeneration planning and management 11(15):4129
5. Della Spina L (2019) A multi-level integrated approach to designing complex urban scenarios in support of strategic planning and urban regeneration. Vols. https://doi.org/10.1007/978-3-319-92099-3_27
6. SWOT Analysis Report, Goshen Master Plan update. https://www.uvlsrpc.org/files/9913/7037/4504/swotGOSH013111_final.pdf. Accessed 23 Dec 2020
7. Sammut-Bonnici T, Galea D (2017) SWOT analysis (October), 5–9. https://doi.org/10.1002/9781118785317. Weom120103
8. SWOT Analysis—City of Pittsburg. Jan 31, 2011. http://www.ci.pittsburg.ca.us/Modules/ShowDocument.aspx?documenti d=1347. Accessed 23 Dec 2020
9. Bottero M, Armando A, Bonino M, Frassoldati F, Bruno E, Federighi V (2016) A hybrid evaluation approach for designing complex urban scenarios: application for the T.I.T. area (China). In: Procedia—social and behavioral sciences, pp 929–935
10. Gürel E (2017) SWOT analysis: a theoretical review. J Int Soc Res 10:994–1006
11. Comino E, Ferretti V (2016) Indicators-based spatial SWOT analysis: supporting the strategic planning and management of complex territorial systems. Ecol Indicators 60:1104–1117

12. Ommani AR (2011) Strengths, weaknesses, opportunities and threats (SWOT) analysis for farming system businesses management: case of wheat farmers of Shadervan District, Shoushtar Township, Iran. Afr J Bus Manage 5(22):9448–9454

Assessment of Concrete Workability Using Conical Funnel

B. G. Anand Kumar

Abstract Concrete is one of the major and widely used construction materials which is used to construct earthquake-resistant structures, high-rise buildings, flyovers and bridges, dams, etc. Workability is a property of concrete that determines the flowing ability or the working ability of concrete. So, it becomes an important property to be determined for construction and research purposes. There are various laboratory methods to assess the workability of the concrete for industrial and research purposes. The present work focuses on the development of a single apparatus called Conical Funnel which can assess all the workability criteria for normal compacting concrete and self-compacting concrete (SCC). This research paper also focuses on the feasibility studies of various trial studies on normal and self-compacted concrete and also uses regression analysis to find out the correlation between the output of conventional apparatus and Conical Funnel apparatus.

Keywords Concrete · Workability · Normal conventional concrete · Self-Compacting Concrete (SCC) · Coarse Aggregate (CA) · Fine Aggregate (FA) · Conical funnel · Compaction Factor (CF) · Regression analysis · Coefficient of correlation

1 Introduction

The Workability of the concrete can be defined in a number of ways as there is no proper definition of this term. It can be defined as the: (1) flowing ability of the concrete, (2) filling ability of concrete, (3) transporting ability of the concrete, (4) pumping ability of the concrete, (5) finishing ability of the concrete, (6) mixing ability of the concrete, and (7) compacting/consolidating ability of the concrete.

There are various methods to assess the workability of the normal as well as self-compacting concrete (SCC). Various testing apparatus are used in workability methods. Even though the concrete production industry is strengthened with the

B. G. Anand Kumar (✉)
Department of Civil Engineering, Rashtreeya Vidyalaya College of Engineering, Bengaluru, Karnataka, India
e-mail: anandkumarbg@rvce.edu.in

L. Nandagiri et al. (eds.), *Recent Advances in Civil Engineering*, Lecture Notes in Civil Engineering 256, https://doi.org/10.1007/978-981-19-1862-9_3

advancement in mass production of concrete mixes, easy assessment of the workability of concrete mixes in field conditions is a major concern. The introduction of modern and consequently called HPC (high-performance concrete) mixes that is prone to minute change in mix proportions of concrete, made to assess workability critically. In reality, NRMCA (National Ready Mixed Concrete Association) has conducted an appraisal to classify the requirement for an improved test method to describe the workability of HPC. Even after 80 years of R & D in the concrete industry to assess the workability of concrete mixes, the industry is still facing uncertainty in developing a good testing method to evaluate the appropriate rheological property of mixes of concrete rapidly and precisely. Presently, the conventional workability test methods available to assess normal/conventional concrete mixes are: (1) Slump cone, (2) Compaction factor (CF), and (3) Vee-Bee consistometer test. To assess the workability of SCC (Self consolidating/Compacting), the most commonly used test methods are (1) J-Ring test, (2) L-Box test, (3) U-Box test, (4) Fill Box test, (6) V-Funnel test, (7) Orimet test, (8) Inverted Slump flow test, etc.

This paper describes the development of a new single apparatus to assess the workability of concrete, called Conical Funnel. It also describes the study of various statistical parameters and finds a correlation between conventional apparatus and conical funnel apparatus. Also, the conclusion will be drawn on the basis of results obtained and the calculation of mathematical regression analysis.

2 Theory and Concept of Conical Funnel

This part describes a brief of guidelines of assessment of workability, factors affecting workability and rules required for development of new workability gadget.

2.1 Principle of Measurement of Workability

There are no solo test device or technique that can assess all fresh concrete properties. Despite the fact that there are a few techniques accessible to evaluate workability, the working capacity of concrete is discovered depending on a few conditions. Workability of the concrete blend is by and large arranged into three classifications, in particular, Class I, II, and III. The greatest number of concrete workability testing techniques is falling in class II and III. They are:

Class I (Qualitative): By and large the concrete workability testing techniques that fall in this classification will be just in a clear way; with no push to measure, for example, Workability. Streaming capacity, compacting capacity, finishing capacity and Pumping capacity.

Class II (Quantitative): By and large the concrete workability testing strategies that fall in this classification will be utilized as a simple quantitative presentation of

conduct in a specific arrangement of situations [1]. For example, Droop, Compaction factor, Vee Bee Time, droop stream test, and so on.

Class III (Quantitative Fundamental): By and large the concrete workability testing techniques that fall in this class will be utilized especially in concurrence with a run of the mill definition, i.e., Consistency, Mobility, Fluidity, and so on.

2.2 Factors Affecting Workability

- W/C ratio: Water content is essential to solidify proportion (w/c ratio) is high, higher the workability and the other way around.
- Aggregate's size: On the off chance that the measure of coarser totals utilizing is more or less the fine totals in substantial blend, workability of concrete mix will be lower and the other way around.
- Supplementary material used in concrete: The utilization of steel or engineered strands will diminish the concrete workability effectively.
- Weather conditions: The temperature and wind are the two fundamental properties of the common climate condition that may influence the concrete workability. Higher the temperature and wind, loss of water content structure the concrete blend will happen that may cause the decrease in workability of concrete new property and the other way around.
- Chemical admixtures: Promoters, retarders, and superplasticizers are a portion of the synthetic admixtures most regularly used in the substantial blend. Promoters will decrease the workability of concrete mixes; retarders and superplasticizers will be helpful to improve the workability of fresh concrete.
- Shape of aggregates: The rounded aggregates and smaller sizes in the concrete will pose a better workability property than angular aggregates and larger size aggregates, respectively.
- Sand to aggregates ratio: Higher the sand to aggregate ratio betters the workability of concrete and vice versa.

2.3 Criteria for Developing New Workability Test Device

- Cost-effective: Introductory expense and upkeep cost of a gadget will be less while created in a bunch, and furthermore, it ought to be serious with the present existing gadgets on the lookout/merchants.
- Less complexity: New testing device must be adequately simple to perform tests on concrete lying on the field. Even though the test might describe results in the provision of plastic viscosity and yield stress, on-site people not aware of the rheology of concrete must also be able to understand the obtained values and make a prompt decision. The use of nomographs and rooted electronic tools can smooth the progress of interpretation of the results in the field.

- Speed of the test conduction should be upgraded. Which may assist with assessing the workability on-site, test results are obtained on site itself and easy to measure workability of all kind of concrete mixes.
- Parameters measured: Latest test device developed must assess the dynamic property of low to moderate concrete workability mixes and should suitably evaluate concrete mixes that illustrate a high thixotropy.
- Dimension and Weight: The instrument should be small and lighter in weight this would enhance the speed of test.
- Toughness: Test instrument should be adequately tough and rugged to use often in a field condition. Depending on the precision of the apparatus, a decision can be made to use the apparatus in the field, research laboratory, and for concrete mix proportioning.
- Dimension and Weight: The instrument must be tiny and light in overall weight so that anyone on the jobsite can move around it easily.
- Man Power: Test shall be performed with minimum man power quickly and with easy methodology so that a performer can also be able to perform other duties on the jobsite.
- Electricity: Since many of the construction sites and laboratories have electricity readily available. Alternatively, rechargeable batteries are also to be used in the worst cases. Preferably, mechanically operated devices are encouraged on the site to avoid the dependency on electricity.

3 Methodology

First, a preliminary survey on available workability assessment devices was done, then a review of existing literature work was done. After going through the literature review, some general problems were identified and details and design data of workability devices were collected. After this, the design development of the device was done followed by the fabrication of the device. After the fabrication of the new workability device, trials were done with normal concrete and SCC. After completing the trials, correlations between different statistical parameters were established and conclusions were drawn.

3.1 Material for Concrete Mix Proportioning

Ingredients required for concrete-like cement, coarse aggregates and fine aggregates (M-Sand) are procured from the available various nearest vendors [2]. The OPC-53 grade cement, coarse aggregates of 20 mm downsize and fine aggregates of 4.75 mm downsize are used in this study to produce the concrete mix. Superplasticizers of Master Glenium Sky 8233 have been used, which is of high range water reducing

admixture added to the concrete mixture [3]. Master Glenium Sky 8233 has a recommended dosage range between 0.5 and 2 percent of cementations material for the most concrete mixes. Class F fly ash is used in the SCC mix. It was used as a 33% replacement for cement.

3.2 Trial Studies on Device

The trial studies on normal conventional concrete and SCC are made and these results were correlated with the existing and most commonly used test methods for both normal conventional concrete and SCC. The tests that were carried out with their corresponding correlated test results for the normal conventional concrete are (1) Conical funnel results correlated with Slump cone test. (2) Conical funnel results correlated with Compaction factor test.

The tests that were carried out with their corresponding correlated test results for the SCC are (1) Conical funnel correlated with Slump flow, (2) Conical funnel correlated with V-Funnel, and (3) Conical funnel correlated with J-Ring.

4 Experimental Studies

Mild steel is used to fabricate the instrument because the device is in a trial state. Mild Steel is economical and helps to reduce the overall weight of the device. The instrument is fabricated to a conical shape, it consists of two main portions, i.e., (1) Bottom cylindrical portion and (2) Top conical frustum. Bottom of the cylindrical portion is of diameter of 135 mm it is considered as 6 times the average size of aggregates and height of 150 mm is adopted. Top conical frustum with bottom diameter of 135 mm, top diameter of 370 mm and height of 470 mm. These values were restricted due to the side slope of the conical funnel and volume. The overall height of the funnel is 620 mm. There are two removable cages that were provided in the funnel, i.e., the first cage is at the position of 385 mm from the bottom of the conical funnel. The second cage is at the position of 150 mm from the bottom (at the junction of the bottom cylindrical portion and top conical frustum) of the conical funnel. Only during the study of self-compacting concrete, these cages were placed in the conical funnel in their respective positions, whereas normal conventional concrete is evaluated in this conical funnel without cages in it. Here placing cage/mesh is felt feasible in the funnel during the trials to self-compacting concrete but not to normal conventional concrete. A sliding gate valve is provided at the bottom of the conical funnel orifice. The size of the gate valve is 180 × 285 mm. The valve is watertight. The sliding gate valve is adopted because of its simple fabrication process, low cost, and as it is easy to handle by the users of the conical funnel. The overall volume of the conical funnel is 0.0262 m^3. Since the offset is provided at the top by 100 mm, concrete is poured

up to that offset mark. The volume of concrete used in this instrument is 0.0172 m^3 (without adding the wastage) (Figs. 1 and 2).

Since the conical funnel instrument is in the trial stage, the cages with different bar spacing, as shown in Fig. 3, were considered in this study. The 12 mm diameter bars and 10 mm diameter bars of both directions were rejected due to unconvinced results; the loss in volume of the concrete is high. Similarly, 12 mm diameter bars of the single direction were used in the trial study and the results obtained are not satisfactory.

The cage/mesh finalized for the study is shown in Fig. 4. The trial studies were taken on all the cages to evaluate the characteristics of self-compacting concrete.

The stand to hold the conical funnel is shown in Fig. 5. The stand designed as four legged angle sections of ISA 25 × 25 × 2 mm are used to make this stand.

To hold the conical funnel in position from a definite height, a four-legged stand is fabricated. The overall height of the stand adopted is 900 mm; it is to provide enough space for receiving container (bucket) to receive concrete from the funnel. Also, an

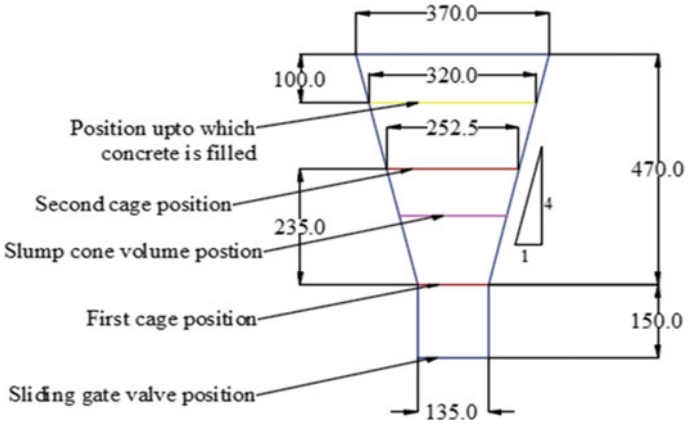

Fig. 1 Front view of the conical funnel (elevation) (all dimensions in mm)

Fig. 2 Top view of the conical funnel (plan) (all dimensions in mm)

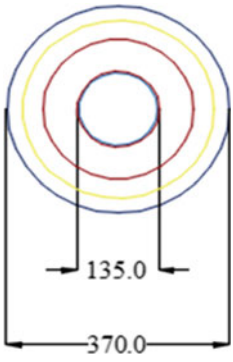

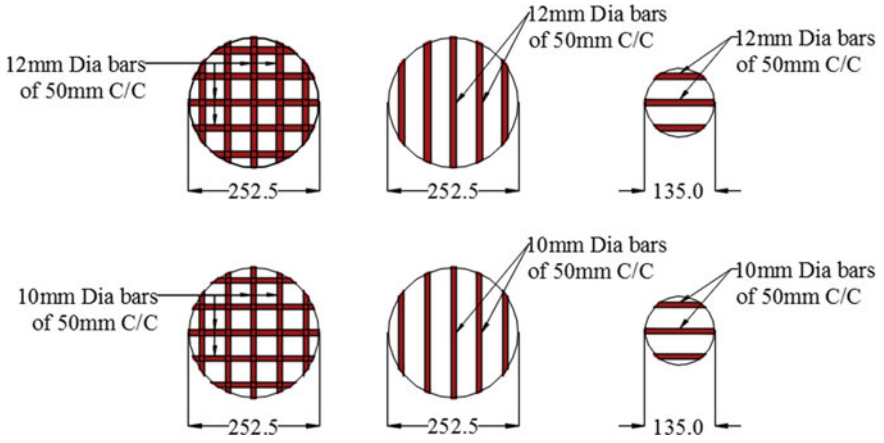

Fig. 3 Trial stage cage/mesh (all dimensions in mm)

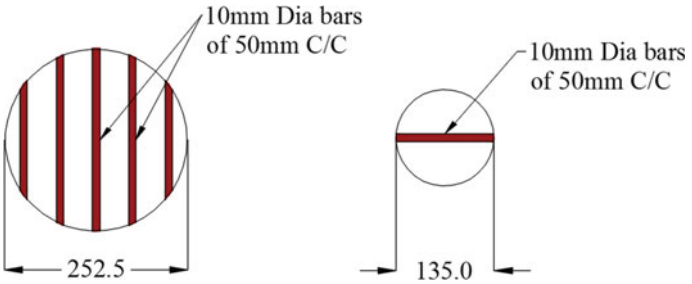

Fig. 4 Finalized first and second cage/mesh (all dimensions in mm)

average height person can able to pour the concrete in a conical funnel firmed in the stand. ISA 25 × 25 × 2 mm four-legged stand is provided to withstand the upcoming load from a conical funnel full of concrete. Also, stand should not get buckled and deformed due to load coming on it. The conical funnel will be firmed in the ring provided at the top of the stand. The diameter of the ring is 280 mm and the ring is made with a 12.5 mm diameter bar. The top diameter of the ring is decided based on the position of the conical funnel that needs to be seated on the stand. Circular flay Disc of 48 mm diameter and 2 mm thickness was used at the bottom of each leg of the stand. This is because to place a stand on the ground fairly without sharp impressions on the floor.

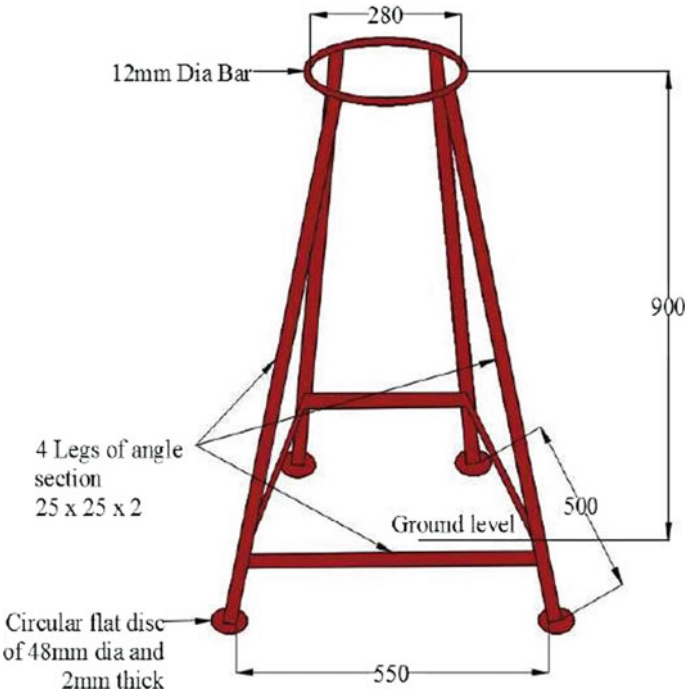

Fig. 5 Conical funnel stand (all dimensions in mm)

4.1 Mix Proportions of Normal Conventional Concrete

In the normal conventional concrete mix proportion, no additives were added. To achieve the slump, ingredients used in the concrete mixes are cement, CA, FA or M-Sand and water. The mix proportions for normal conventional concrete were shown in Table 1. The mix proportions were arrived for this normal conventional concrete as per BIS-10262-2009 and BIS-456-2000.

Table 1 Normal conventional concrete mix proportions

Mix No	Cement (kg/m^3)	CA (kg/m^3)	FA (kg/m^3)	Water (l/cm^3)	Targeted slump (mm)
1	413.33	1161.9	671.11	186	25–50
2	430.23	980.86	757.84	215	75
3	443.23	965.73	746.15	221.6	100
4	455.68	949.08	733.29	227.84	125
5	468.22	1095.2	721.59	234.11	150
6	480.72	918.8	709.90	240.38	175

Table 2 SCC concrete mix proportion

Material	Control mix
Cement in kg/m^3	382.5
Fly ash in kg/m^3	71.64
Fine Aggregate in kg/m^3	910.00
Coarse Aggregate in kg/m^3	684.28
Water in l/cm^3	215.71
Superplasticizer %	0.6

4.2 Mix Proportions of Self-compacting Concrete

In the self-compacting concrete (SCC), the mix proportions were arrived from "Nan-Su" method of SCC mix proportioning [4]. The mix proportions for SCC were shown in Table 2.

4.3 Test Procedure Using Conical Funnel Apparatus

4.3.1 Flow Test for Normal Conventional Concrete

Here the test procedure describes the average flows through time of concrete and average flow through speed of the concrete from the orifice of the conical funnel.

Apparatus: (1) Conical funnel, (2) The discharge orifice, (3) Container to receive the discharged concrete below the conical funnel and (4) Stopwatch.

Procedure: (1) Volume of concrete required for this experiment including 10% of wastage is 0.018 m^3. (2) The conical funnel without cages is considered in this experimental procedure (3) The funnel is cleaned and the inner surface is to be oiled. (4) The valve should be closed before pouring the concrete. (5) Conical funnel and stand should be vertical. Which shall be verified using spirit level for more accuracy (6) Pour concrete in the conical funnel up to 100 mm offset of the funnel from the top. (7) Once the concrete is filled in the funnel, the valve below the orifice must be released and the stopwatch is started immediately as the valve is released. Record time (to nearest μ seconds) required to pass the entire concrete through the funnel is recorded. (8) Flow through time is defined as the time that is required by the concrete to flow through the conical funnel. (9) Average speed of concrete from the funnel orifice is calculated.

Formulae

1. Average flow through time in conical funnel $= 1.26/t_0$ m/s
2. Average flow through speed in V-funnel $= 2.05/t_0$ m/s

where t_0 average flow through time in seconds.

Here, 1.26 and 2.05 are the two constants obtained for conical funnel and V-funnel, respectively. For conical funnel, constants were obtained by dividing the

volume of 0.018 m^3 by the cross-section of the orifice. Similarly, v-funnel constants were obtained by dividing the volume of 0.01 m^3 by the cross-section of the orifice (i.e., 0.065 × 2).

4.3.2 Compaction Factor Test Using Conical Funnel Apparatus

To determine the compaction factor of the concrete mix using conical funnel apparatus/arrangements.

Apparatus: (1) Conical funnel and stand, (2) The discharge orifice of the conical funnel should be watertight, (3) Cylinder to receive the discharged concrete below the conical funnel and (4) Weighing machine.

Procedure: (1) Volume of concrete required for this experiment including 10% wastage is 0.00583 m^3. (2) The conical funnel without cages is considered in this experimental procedure. (3) The funnel is cleaned and the inner surface is to be oiled. (4) The valve should be closed before pouring the concrete. (5) Conical funnel and stand should be vertical. (6) Pour the concrete into the funnel up to the mark of slump cone volume position. (7) The standard height of fall of concrete into the cylinder placed below is 460 mm. (8) Using the weighing machine, the weight of the dully compacted concrete mix in the cylinder is determined. (9) The fully compacted weight of concrete is noted by compacting the concrete into three layers in the cylinder. (10) Each layer should be compacted with 25 number of blows using a tamping rod (10 mm diameter and 60 cm height).

Formula: Compaction factor = Partially compacted concrete/Fully compacted concrete.

4.3.3 Flow-Through Test for Self-compacting Concrete (SCC)

The test procedure describes the average flows through time of concrete and average flow through speed of the concrete from the orifice of the conical funnel.

Apparatus (1) Conical funnel, mesh/cages and stand, (2) The discharge orifice of the conical funnel should be watertight, (3) Container to receive the discharged concrete below the conical funnel and (4) Stopwatch. **Procedure**: (1) Volume of concrete required for this experiment including 10% of wastage is 0.018 m^3. (2) The conical funnel with cages is considered in this experimental procedure. (3) The funnel is cleaned and the inner surface is to be oiled. (4) The cages are oiled and placed in their respective position. (5) The valve should be closed before pouring the concrete. (6) Conical funnel and stand should be vertical. Shall be verified using spirit level for more accuracy. (7) Then pour the concrete in the conical funnel up to 100 mm offset of the funnel from the top. (8) Once the concrete is filled in the funnel, the valve below the orifice must be released and the stopwatch is started as soon as the valve is released; the time required to pass the entire concrete through the funnel is recorded. (9) The flow-through time is the time required by the concrete to flow through the conical funnel. (10) Average speed is calculated by the formulae

Table 3 Correlating slump with conical funnel flow

Slump (mm)	Conical funnel flow through test result (s)	Average flow through time (s)	Average flow through speed (m/s)
75–100	–	–	–
100–125	5–8	6.5	0.193
125–150	4–6	5	0.252
150–175	3.5–5	4.25	0.296
175 to above	Less than 4	3.5	0.36

1. Average flow through time in conical funnel $= 1.26/t_0$ m/s
2. Average flow through speed in V-funnel $= 2.05/t_0$ m/s

where t_0 average flow through time in seconds.

5 Results and Discussion

5.1 Conical Funnel Results Correlated with Slump Cone Test

Mix proportions tabulated in Table 4.6 depicts normal conventional concrete. The slump ranging between 75 to 100 mm, 100 to 125 mm, 125 to 150 mm, 150 to 175 mm, above 175 mm and corresponding conical funnel results obtained are tabulated, respectively, in Table 3.

The concrete mix ranging slump below 100 t is evaluated as the mix gets stuck in the conical funnel. The slump ranging above 100 mm can be described using a conical funnel instrument.

5.2 Conical Funnel Results Correlated with Compaction Factor Test

The volume of the concrete for this compaction factor test is taken as 0.00583 m^3. The mix proportion for the considered volume is as given in Table 4.

Initially, 1 L of water was considered for the mentioned volume of concrete, then 150 ml of water was added each time to determine the compaction factor test results.

Table 4 Concrete mix proportion for compaction factor test

Volume (m^3)	Cement (kg)	CA (kg)	FA (kg)	Water (L)
0.00583	2.41	6.775	3.912	1.084

Table 5 Correlating compacting factor (CF) test result

CF using CF apparatus	CF using conical funnel
0.808	0.805
0.830	0.829
0.847	0.837
0.877	0.863
0.904	0.899
0.932	0.929

Table 6 Regression statistic value of CF test

Regression statistic	Values
Multiple R	0.994317
R square	0.988677
Adjusted R square	0.985834
Standard error	0.005533
p-value	4.83E-05
Observations	6

From Table 5, it is clearly evident that there is not much deviation in the readings of compaction factor from the Conventional Apparatus test and Conical funnel test. As it can be visualized that there are slight variations in the readings obtained from both the apparatus. So, to localize the errors, and to find various statistical parameters, a study of regression analysis is done through MS Excel.

From Table 6, we get the Multiple R, R square value and probability of errors. The Multiple R is called the coefficient of correlation which predicts the closeness of the two sets of statistical values and the R square is called the coefficient of determination which predicts how many values lie in the regression line. If both the values of Multiple R and R square lie between 0.9 and 1.0, it means that the output would be better. As per Table 6, the value of multiple *R* is 0.994317. It lies in the range of 0.9–1.0 which clearly indicates that the value of both the apparatus is close. Similarly, the R square value is 0.988667 which implies that 98.8% of fits with the standard results. The value of the probability of errors should be less than 0.05 always. As per Table 6, the *p*-value is 4.83 × e-05 which shows that the results are reliable. From the above results, we can conclude that the conical funnel can be used for the determination of the compaction factor [5].

5.3 Conical Funnel Correlated with Slump Flow for SCC

The volume of the concrete considered for this compaction factor test is 0.0175 m^3. The mix proportion for the considered volume is as given in Table 7.

From Table 8, it is clearly evident that there is not much deviation in the readings of slump flow from the Conventional Slump Cone test and Conical funnel test. As it

Table 7 SCC mix proportion for slump flow test

Volume (m^3)	Cement (kg)	Flyash (kg)	CA (kg)	Water (l)
0.0175	6.69	1.254	11.975	15.925

Table 8 Correlating slump flow value test result (SCC)

Water (l)	SP (%)	Slump (mm)	Conical funnel flow (mm)
3.0	0.3	335	305
3.3	0.4	405	390
3.5	0.5	510	515
3.7	0.5	570	580
3.9	0.6	660	670

Table 9 Regression static value of slump flow test (SCC)

Regression statistic	Values
Multiple R	0.999117
R square	0.998234
Adjusted R square	0.997645
Standard error	7.08742
p-value	3.15E-05
Observations	5

can be visualized that there are slight variations in the readings obtained from both the apparatus. So, to localize the errors, and to find various statistical parameters, a study of regression analysis is done through MS Excel.

As per Table 9, the value of multiple R is 0.999117. It lies in the range of 0.9–1.0 which clearly indicates that the value of both the apparatus is close. Similarly, the R square value is 0.998234 which implies that 99.8% of fits with the standard results [6]. The *p*-value is 3.15 × e-05 which shows that the results are reliable. From the above results, we can conclude that the conical funnel can be used for the determination of Slump Flow.

5.4 Conical Funnel Correlated with V-funnel

The volume of the concrete considered for this compaction factor test is 0.033 m^3. The mix proportion for the considered volume is as given in Table 10. As per the guidelines of the EFNARC, the fresh properties of the concrete should be evaluated within 8 min from its freshly prepared time.

From Table 11, it is clearly evident that there is not much deviation in the readings of time from the V-Funnel Apparatus test and Conical funnel test. As it can be

Table 10 Concrete mix proportion for V-funnel factor test

Volume (m^3)	Cement (kg)	Flyash (kg)	CA (kg)	FA (kg)
0.033	12.62	2.364	22.581	30.03

Table 11 Correlating V-funnel and Conical funnel flow through test results

Water (l)	SP (%)	V-funnel flow (s)	Conical funnel flow (s)	V-funnel speed (m/s)	Conical funnel speed (m/s)
6.2	0.3	31	28	0.066	0.045
6.4	0.4	15	13	0.136	0.0969
6.6	0.5	11.32	9.51	0.18	0.133
6.8	0.6	8.8	7.11	0.233	0.177
7.10	0.6	8	6.69	0.256	0.188

Table 12 Regression static value of slump flow test (SCC)

Regression statistic	Values
Multiple R	0.999897
R square	0.999794
Adjusted R square	0.999725
Standard error	0.146318
p-value	1.26E-06
Observations	5

visualized that there are slight variations in the readings obtained from both the apparatus. So, to localize the errors, and to find various statistical parameters, a study of regression analysis is done through MS Excel.

As per Table 12, the value of multiple R is 0.999897. It lies in the range of 0.9–1.0 which clearly indicates that the value of both the apparatus is close. Similarly, the R square value is 0.999794 which implies that 99.9% of fits with the standard results. The p-value is 1.26 × e-06 which shows that the results are reliable. From the above results, we can conclude that the conical funnel can be used for the determination of the time taken for the flow of concrete [7].

5.5 Conical Funnel Correlated with J-Ring

The volume of the concrete considered for this compaction factor test is 0.0175 m^3. The mix proportion for the considered volume is given in Table 5.19. As per the guidelines of the EFNARC [6], the fresh properties of the concrete should be evaluated within 8 min from its freshly prepared time (Tables 13 and 14).

Table 13 SCC mix proportion for J-ring test

Volume (m^3)	Cement (kg)	Flyash (kg)	CA (kg)	Water (l)
0.0175	6.69	1.254	11.975	15.925

Table 14 Correlating J-ring test results

Water (l)	SP (%)	J-ring test (H_2/H_1)	Conical funnel test (H_2/H_1)
3.0	0.3	0.32	0.43
3.3	0.4	0.52	0.50
3.5	0.5	0.60	0.56
3.7	0.5	0.89	0.89
3.9	0.6	0.97	0.95

Table 15 Regression statistic value of J-ring test

Regression statistic	Values
Multiple R	0.979380
R square	0.959185
Adjusted R square	0.945580
Standard error	0.055367
p-value	0.003543
Observations	5

From the graph (Fig. 5.8), it is clearly evident that there is not much deviation in the readings from Abram's Cone test and conical funnel test. As it can be visualized that there are slight variations in the readings obtained from both the apparatus. So, to localize the errors, and to find various statistical parameters, a study of regression analysis is done through MS Excel.

As per Table 15, the value of multiple R is 0.97938. It lies in the range of 0.9–1.0 which clearly indicates that the value of both the apparatus is close. Similarly, the R square value is 0.959185 which implies that 95.9% of fits with the standard results. The p-value is 0.003543 which shows that the results are reliable. From the above results, we can conclude that a conical funnel can be used for the determination of Slump flow through J ring.

5.6 Advantages and Disadvantages of Conical Funnel

Advantages: (1) Using the conical funnel alone fresh properties of both normal conventional concrete and self-compacting concrete were described. (2) Found economical in comparison with other conventionally available and commonly used apparatus. Also, the instrument is light in weight. (3) Single person can handle the

instrument to evaluate the fresh concrete properties. Due to simple procedure. (4) Independent to power and electricity as it is operated mechanically. (5) Operators with minimum knowledge of concrete rheology are able to handle the instrument without any complications. (6) Instrument is best suited for both onsite and laboratory conditions. The instrument is lightweight and portable. (7) Helps to evaluate the self-compacting properties like flowability or filling ability and passing ability. (8) Instrument is found ideal for high workable mixes. (9) The test procedures are dynamic and thus it is more appropriate than the static tests.

Disadvantages: (1) The volume of concrete required for these concrete test procedures is relatively high. Operational errors may occur during experimental work, i.e., during stopwatch handling, miss placing of cages, the instrument is not vertical, etc. (2) Flow-through test cannot be conducted on low workable concrete mixes. The apparatus is not completely standardized and it is still in the trial stage.

6 Conclusion

From the conducted research, calculations and obtained results, the following conclusions were drawn: (1) The developed conical funnel was feasible to evaluate the workability of both normal conventional concrete and SCC [8]. (2) Based on the research results, it was found that the developed conical funnel apparatus is feasible to study the conventional concrete of slump ranging above 100 mm for flow-through test on conventional concrete. (3) The results obtained for conventional compaction factor apparatus are approximately 98.8% same compared with the test results and regression analysis using the developed device, hence the developed device was found advantageous due to its lightweight and high portability. (4) The experimental results show that there is a good correlation between V-funnel and conical funnel, i.e., 99.9%. However, the flow-through speed of concrete in the conical funnel is less in comparison with V-funnel, it may be because of the presence of cage/mesh which acts as obstacle to concrete flow. (5) From the study, it was clear that slump flow and conical funnel flow results for a mix of higher concrete flow are found compatible. (6) From the research, it was observed that the j-ring test results with a conical funnel achieved a 3% higher value on average as a whole compared to the J-ring test results using a slump cone. (7) By comparing the available conventional test methods, the developed conical funnel is economical, results are obtained quickly in-situ and the instrument is light in weight. (8) Both self-compacting properties like filling ability or flowability and passing ability can be evaluated with the developed conical funnel apparatus.

7 Scope and Opportunities

The scope of the present paper is to describe various opportunities in developing one such device which may evaluate the workability of normal/conventional concrete and self-compacting concrete mixes. Along with workability, the apparatus needs to be improvised further for Fibre Reinforced Concrete (FRC) and Geopolymer Concrete to evaluate the fresh property of concrete. BIS-10262-2019 illustrates various mixed proportioning guidelines utilizing supplementary materials, no specific workability evaluation has been mentioned in the code.

References

1. Koehler EP, David W (2003) Summary of concrete workability test measure. ICAR Report, Fowler university of Texas at Austin, vol 105, issue 1, pp 1–71
2. Faroug F, Szwabowski J, Wild S (2015) Influence of superplasticizer on workability of concrete. J Mater Civil Eng ASCE 11:151–157
3. Cook MD, Tyler Ley M, Ghaeezadah A (2016) Effect of aggregate concepts on the workability of slip formed concrete. J Mater Civil Eng ASCE 23:1–10
4. Su N, Hsub K-C, Chai H-W (2001) Simple mix design method for self-compacting concrete, vol 3. Elsevier, pp 1799–1807
5. Hadavand B, Imaninasab R (2019) The influence of construction and demolition waste materials on workability and mechanical properties of concrete using statistical analysis innovative infrastructure solution, vol 4, issue 29. Springer, Heidelberg, pp 2–11
6. EFNARC (2002) Specification and guidelines for self-compacting concrete. ISBN 0 9539733 4 4@EFNARC
7. Concrete Mix Proportioning- Guidelines. BIS 10262-2019. Determination of conventional concrete mix proportioning
8. Leemann A, Hoffmann C (2005) Properties of self-compacting and conventional concrete differences and similarities journal of concrete research, vol 57, issue 6. Elsevier, pp 315–319

Phycoremediation: An Advanced Treatment Approach for Domestic Wastewater

Nandini Moondra, R. A. Christian, and N. D. Jariwala

Abstract Conventional municipal wastewater leads to sludge generation leading to additional treatment costs. In addition, the secondary treatment is not efficient in removing nutrients, which calls for additional treatment costs associated with the tertiary treatment. Incorporating the tertiary treatment will affect the overall economics of the municipalities. Thus, the present study was performed to study the impact of phycoremediation on treating raw domestic wastewater. Different microalgal concentrations were operated at 11 h contact period. *C. vulgaris* was used as a microalgal species for the study. Various physicochemical parameters were analyzed to assess the working of the microalgal system. Among the different microalgal concentrations studied, 30% concentration had the best reduction, with >90% reductions for NH_3-N and PO_4-P and >85% reductions for COD and BOD. The study revealed the benefits of the phycoremediation technique, which can be an eco-friendly and practical solution to the challenges of the conventional treatment system.

Keywords Biological treatment · Chlorella vulgaris · Domestic wastewater · Eco-friendly · Nutrient removal · Photo-synthetic effect

1 Introduction

Sustainable development is questioned as 40% of water lack will be faced by 2030 in various regions globally. This setback may arise from uncontrollable water usage and release in nearby receiving bodies without adequate treatment [1]. The untreated/partially treated wastewater contains organic and inorganic matters, toxic to humans and the aquatic ecosystem.

In India, only 40% of the sewage generated is treated, resulting in 60% of untreated or partially treated sewage being released into the river. Nonetheless, the greater part of the current sewage treatment in agricultural-based nations faces troubles with

N. Moondra (✉) · R. A. Christian · N. D. Jariwala
Civil Engineering Department, Sardar Vallabhbhai National Institute of Technology, Surat, India
e-mail: nandini7808@yahoo.in

L. Nandagiri et al. (eds.), *Recent Advances in Civil Engineering*, Lecture Notes in Civil Engineering 256, https://doi.org/10.1007/978-981-19-1862-9_4

nutrient expulsion at low costs [2]. Also, extensive methodology, carbon transmission, and additional sludge treatment generated during various treatments are severe setbacks of the conventional system [3].

Investigations have proposed microalgae as a biological treatment that proficiently eliminates high and fluctuating concentrations of organics and nutrients present in various wastewaters [4, 5]. In addition, nitrogen, phosphorus, and various trace metals such as Fe, Mn, and S present in municipal wastewater act as food to microalgae [4].

In the present study, *C. vulgaris* was utilized to treat domestic wastewater due to its attributes like (a) high development rate, (b) quick expulsion rate, and (c) highly riched biomass [5]. The disinfectant property of microalgae is also an added advantage to remove toxic microorganisms. The phycoremediation system has low capital and operating cost. These benefits make it more noticeably internationally. However, the literature also reveals that the significant expense related to the method is the harvesting of biomass [6].

After analyzing the gaps in the acceptability of the system, the present study was focused on working on a few challenges by investigating the viability of the phycoremediation system in removing nutrients along with other physicochemical parameters at lower HRT and in the open to sky conditions. In this study, the workability of a phycoremediation system was observed to treat raw domestic wastewater under light/dark conditions.

2 Methodology

C. vulgaris was used as a microalgal strain for the study, which was provided by an Ahmedabad-based consultancy. A batch study was performed with a total volume of 1800 mL, combining raw wastewater and microalgal concentrations (Fig. 1). In the study, six different concentrations of microalgae were studied, ranging between 20

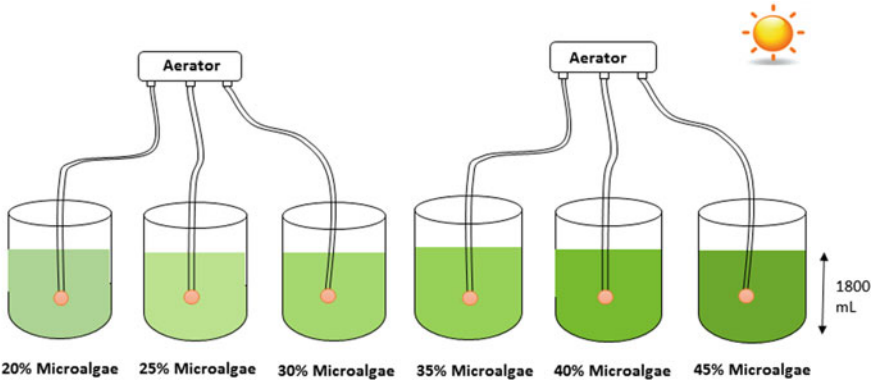

Fig. 1 Experimental setup

Table 1 Different microalgal concentrations and corresponding dry weight

Microalgal concentration (%)	Dry weight (mg/L)
20	1.80
25	2.25
30	2.75
35	3.15
40	3.60
45%	4.05

and 45%. Each concentration has an increment in 5% microalgae than the previous. Six different microalgal concentrations studied were 20% (360 mL microalgae + 1440 mL raw wastewater), 25% (450 mL microalgae + 1350 mL raw wastewater), 30% (540 mL microalgae + 1260 mL raw wastewater), 35% (630 mL microalgae + 1170 mL raw wastewater), 40% (720 mL microalgae + 1080 mL raw wastewater), and 45% (810 mL microalgae + 990 mL raw wastewater), and their respective dry weight is illustrated in Table 1.

The study was conducted in an outdoor condition. The study was conducted in the month of June–July. Temperature variation during the study was between 21 and 24 °C. The number of trials conducted for each set of experiments (20–25%, 30–35%, and 40–45%) was 24, respectively. The retention time for the study was 11 h (aeration followed by settling). Physico-chemical analysis was done on the supernatant drawn after settling.

The sewage pumping station near the experimental site was the source of domestic wastewater for the study. Parameters such as BOD, COD, PO_4-P, NO_3-N, NH_3-N, pH, EC, TS, TSS, and TDS were analyzed. Each sample was analyzed twice, and the average was considered for analysis to reduce the instrument and human errors in the study.

3 Result and Discussion

The study was conducted in three combinations (20% and 25%), (30% and 35%), and (40% and 45%). Variations in characteristics of domestic wastewater during the study are tabulated in Table 2.

High COD (>92%), NH_3-N (>85%), and phosphorus removal (30%) were obtained at 6 days and 10 days HRT [7]. The phycoremediation system effectively reduced the various parameters analyzed at low HRT during the present experimental study.

NH_3-N concentration in the effluent lowered to 1.62 mg/L (84.58%), 1.00 mg/L (90.51%), 0.39 mg/L (96.60%), 0.43 mg/L (96.26%), 3.34 mg/L (77.11), and 2.71 mg/L (77.91%), when treated with 20%, 25%, 30%, 35%, 40%, and 45% microalgal concentration, respectively. Figure 2a depicts variation in the reduction of NH_3-N

Table 2 Variations in raw wastewater characteristics

Parameter	Set I (20% and 25%)		Set II (30% and 35%)		Set III (40% and 45%)	
	Min	Max	Min	Max	Min	Max
pH	6.58	7.56	6.8	7.45	6.8	7.82
EC (mS/cm)	1.69	2.65	1.96	2.53	1.91	2.55
TDS (mg/L)	910	1260	980	1290	940	1230
TSS (mg/L)	926	1710	1140	2010	1006	1897
TS (mg/L)	1836	3045	2120	3095	1946	2987
COD (mg/L)	160	315	243.2	313.2	184.4	326
BOD (mg/L)	60.8	119.7	93.48	119.1	93.5	119.2
PO_4-P (mg/L)	1.47	3.72	2.01	3.72	1.62	3.32
NH_3-N (mg/L)	10.01	12.32	10.08	16.24	10.64	17.64
NO_3-N (mg/L)	0.23	1.28	0.45	1.23	0.23	1.28
DO (mg/L)	BDL	0.40	BDL	0.40	BDL	0.40

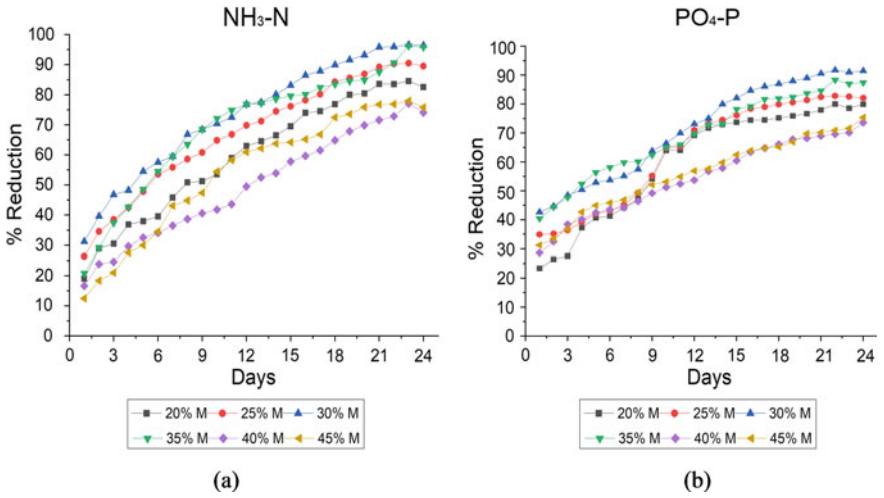

Fig. 2 Reductions in nutrients at various microalgal concentrations

at different concentrations. Microalgae burn-through NH_3-N among all N structures accessible [8]; NH_3-N consumed is fused into protein for microalgal development.

Similarly, for PO_4-P, promising reductions were observed in all concentrations. PO_4-P concentration in the effluent lowered to 0.42 mg/L (80.00%), 0.34 mg/L (82.84%), 0.17 mg/L (91.73%), 0.25 mg/L (88.36%), 0.49 mg/L (73.59%), and 0.45 mg/L (75.35%), when treated with 20%, 25%, 30%, 35%, 40%, and 45% microalgal concentration, respectively. Figure 2b illustrates PO_4-P reduction at different concentrations. Microalgae consumes phosphorus as orthophosphate [9].

In addition to nutrient removal, phycoremediation is quite effective in organics removal. COD removal reached to 79.17% (48 mg/L), 84.72% (35.2 mg/L), 85.13% (40.00%), 84.27% (46.55 mg/L), 73.89% (61.20 mg/L), and 72.92% (56.20 mg/L) after treatment with different microalgal concentrations, respectively. Figure 3a illustrates COD reductions during the study. COD reduction in the presence of microalgae results in cooperative connection with the heterotrophic microscopic organisms [10] as microbes use the oxygen delivered by algae as a finished result for their development and endurance. In any case, COD evacuation was marginally lesser than the nutrients, as the development of nitrates interferes with COD reduction [11]. COD and TKN removal were about 86% and 97% at an HRT of 2 days when the microalgal-bacterial consortium was used to treat municipal pre-settled wastewater [12].

Phycoremediation technique effectively reduced PO_4-P, NH_3-N, and COD concentration to 97.89%, 98.81%, and 88.24%, respectively, from the primary-treated effluent's of an urban STP at the identical HRT, practiced for secondary treatment [9]**.** A lab-scale mode in SBR mode (HRT = 48 h.) comprising *Chlorella vulgaris* and activated sludge used to treat synthetic wastewater led to 88% and 15% removal of COD and TN, respectively [13]. *Chlorella vulgaris* reduced PO_4-P, NH_3-N, and COD concentration to 98.32, 97.26, and 84.71%, respectively, without any external aeration from the primary-treated municipal wastewater [11]**.**

Likewise, BOD removal reached to 85.20% (12.96 mg/L), 89.14% (9.50 mg/L), 89.56% (11.61 mg/L), 88.83% (12.56 mg/L), 82.01% (20.30 mg/L), and 82.19% (20.50 mg/L) after treatment with different microalgal concentrations, respectively. Figure 3b illustrates reductions in BOD at different concentrations. However, the

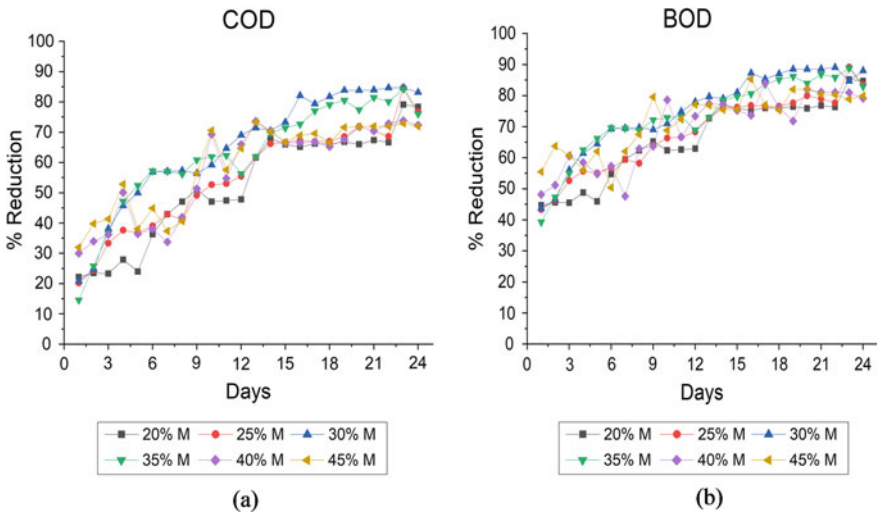

Fig. 3 Reductions in organics at the different microalgal concentration

reduction in BOD was much higher than in the conventional system because of the ample amount of DO present, enhancing the degradation of organic matter.

Among solids, TSS had the greater reduction, i.e., up to 39.28% (895 mg/L), 34.70% (890 mg/L), 30.87% (912 mg/L), 33.67% (970 mg/L), 26.94% (925 mg/L), and 25.35% (940 mg/L) after treatment with 20% to 45% microalgal concentration, respectively. The formation of algal bacterial flocs resulted in a reduction in solids. TDS and EC had a similar reduction. *C. Vulgaris* used for domestic wastewater treatment at 3 days HRT led to COD, and nutrient and TS removal during the study was around 85% [14].

The study revealed that challenges of the conventional system could be resolved if the phycoremediation technique is incorporated into the traditional system. As the nutrients and organics concentration in the effluent was far below the desirable limit, the study also revealed that the increment in microalgal concentration led to increased removal efficiency of physicochemical parameters to a certain extent. Excess microalgae can harm the treatment process. Light availability and temperature varying between 20 and 30 °C are the primary conducive environmental conditions required for the system.

NH_3-N had the highest removal among all the parameters because N comprises 10% algal biomass and phosphorus only 1%. DO reached 7 mg/L in the system comprising 20%, 25%, and 30% microalgal concentration. Whereas for the systems with 35% and 40% microalgal concentration, DO reached 7.6 mg/L and 7.8 mg/L in the case of 45% microalgal concentration. The increase in DO was due to the external aeration and microalgal presence.

Similarly, a pH increase was found in the effluents of all the systems. The pH increase in the effluent was contributed because of the photosynthetic effect, which was to a certain extent counterbalanced by nitrification [15]. However, increased pH contributed to nutrient removal as DO increment enhanced the organic removal. Effluent pH in all the concentrations studied was higher than 8.

The study revealed that combining microalgae in conventional treatment can be eco-friendly and helpful in minimizing the electricity cost (as microalgae can lead to aeration) and resolving other setbacks of the conventional system. In addition to this, the study also addressed that the phycoremediation technique can effectively work at lower HRTs.

4 Conclusion

The study also revealed that the increase in microalgal concentration does not lead to higher removal of pollutants. Among various microalgal concentrations analyzed, 30% microalgal concentration had the highest reductions in both nutrients and organics. Removal efficiency reached >90% for nutrients and >85% for organic matter when 30% concentration was used to treat raw municipal wastewater. Thus, 30% microalgal concentration was observed as the optimum concentration for the

study. Reductions in the algal system were contributed by high pH and DO concentration in the effluent. Thus, the algal system reduces the eutrophication in the receiving bodies and can enhance the self-cleansing capacity of the water body. An appropriate treatment unit includes limited human and financial resources, reliable treatment, system economic feasibility, less energy demand, and social acceptance. Therefore, research combining microalgae with conventional wastewater treatment can be the best-suited treatment option. In addition to this, this system also eliminates the need for tertiary treatment and can answer various challenges of the present treatment systems practiced in developing countries.

References

1. FG Acien Fernandez C Gomez-Serrano JM Fernandez-Sevilla 2018 Recovery of nutrients from wastewaters using microalgae Front Sustain Food Syst 2 59 71
2. SK Kumar HU Dahms EJ Won JS Lee KH Shin 2015 Microalgae—a promising tool for heavy metal remediation Ecotoxicol Environ Saf 113 329 352
3. T Saeed B Paul R Afrin A Al-Muyeed G Sun 2016 Floating constructed wetland for the treatment of polluted river water: a pilot scale study on seasonal variation and shock load Chem Eng J 287 62 73
4. S Aslan IK Kapdan 2006 Batch kinetics of nitrogen and phosphorus removal from synthetic wastewater by algae Ecol Eng 28 1 64 70
5. FG Acien 2016 Wastewater treatment using microalgae: how realistic a contribution might it be to significant urban wastewater treatment? Appl Microbiol Biotechnol 100 9013 9022
6. O Tricolici C Bumbac C Postolache 2014 Microalgae-bacteria system for biological wastewater treatment J Environ Prot Ecol 15 1 268 276
7. Quijano G, Arcila JS, Buitron G (2017) Microalgal-bacterial aggregates: applications and perspectives for wastewater treatment. Biotechnol Adv 35(6):772–781
8. N Moondra ND Jariwala RA Christian 2021 Integrated approach of phycoremediation in wastewater treatment Insight Water Conserv Manage 5 1 8 12
9. N Moondra ND Jariwala RA Christian 2021 Role of phycoremediation in domestic wastewater treatment Water Conserv Manage 5 2 35 39
10. SR Subashchandrabose B Ramakrishnan M Megharaj 2011 Consortia of cyanobacteria/microalgae and bacteria : Biotechnological potential Biotechnol Adv 29 6 896 907
11. N Moondra ND Jariwala RA Christian 2021 Microalgae based wastewater treatment: a shifting paradigm for the developing nations Int J Phytorem 23 7 765 771
12. P Foladori S Petrini M Nessenzia G Andreottola 2018 Enhanced nitrogen removal and energy saving in a microalgal-bacterial consortium treating real municipal wastewater Water Sci Technol 78 1 174 182
13. G Gutzeit A Weber M Engels U Neis D Lorch 2018 Bioflocculent algal–bacterial biomass improves low-cost wastewater treatment Water Sci Technol 52 12 9 18
14. S Petrini P Foladori F Beghini F Armanini N Segata G Andreottola 2020 How inoculation affects the development and the performances of microalgal-bacterial consortia treating real municipal wastewater J Environ Manage 263 110427 110436
15. G Schumacher I Sekoulov 2003 Improving the effluent of small wastewater treatment plants by bacteria reduction and nutrient removal with an algal biofilm Water Sci Technol 48 2 373 380

Expert System Classifier for RS Data Classification

B. R. Shivakumar and B. G. Nagaraja

Abstract Classification of remote sensing (RS) imagery has been a primary source for mapping applications. Many classification algorithms have been developed in the past four decades to aid this purpose. Most of these classifiers are designed to operate on a single source of data and therefore, fail to operate on multi-source information. An expert system classifier, on the other hand, is solely designed to take advantage of the multi-source data and thereby brings a new dimension to the classification approach. Unlike most other classifiers, the expert system classifier is constructed and operated solely based on the domain knowledge of the expert himself/herself. In this paper, we illustrate the construction of an expert system classifier using multi-source RS imagery for the classification perspective. From the results obtained, we note that expert system classifiers can produce excellent results on par with many traditional classifiers.

Keywords Expert system classifier · Remote sensing · Land cover mapping · Image classification · Inference engine

1 Introduction

With the advent of satellite technology, remote sensing (RS) has grown tremendously in the last three decades. From a period in which it was next to impossible for the public to lay hands on satellite imagery, the field of remote sensing has grown so much that many government agencies distribute refined RS data to the public free of cost. The sensors used in remote sensing have also undergone great advancements in this era. At the beginning of the RS science, imaging sensors captured Earth information in as few as 3–5 spectral bands. Today, advanced imaging sensors such

B. R. Shivakumar (✉)
NMAM Institute of Technology, Nitte 574110, India
e-mail: shivkumarbr@nitte.edu.in; shivkumarbr@gmail.com

B. G. Nagaraja
KLE Institute of Technology, Hubli 580027, India

L. Nandagiri et al. (eds.), *Recent Advances in Civil Engineering*, Lecture Notes in Civil Engineering 256, https://doi.org/10.1007/978-981-19-1862-9_5

as hyperspectral sensors collect information using more than 200 spectral bands [1, 2].

This development of RS science has been greatly used by almost every application of environmental science. From basic applications such as mapping and change detection, remote sensing data have now been used in most advanced and critical of the environmental applications such as vegetation phenology distribution [3, 4], water current monitoring in oceans [5, 6], urban settlement monitoring [7, 8], forest fire monitoring [9, 10], military surveillance [11, 12] and so on. To aid these applications, researchers around the globe have dedicated themselves to developing new algorithms for successful information extraction from RS data.

Land cover mapping is one of the most common yet primary applications in remote sensing. In mapping, the RS data is used to create meaningful land use land cover (LULC) classes by employing suitable classification algorithms. Literature [13–15] indicates the design and development of a great number of classification algorithms ranging from traditional hard classifiers that work on conventional Boolean logic to advanced soft classifiers such as Fuzzy-based classifiers. However, the evolution of classifiers has not yet stopped mainly because of the availability of different types of RS data available today.

Most of the RS data classifiers available today are supervised classifiers. In such classifiers, the analyst collects signature information about the LULC classes available on the data and feeds them as training data to the classification algorithm [16, 17]. In doing so, the analyst is forced to accept the results produced by the classification algorithm and may have to occasionally face the wrath of their disadvantages. Hence came the knowledge-based expert system classifiers.

It is possible to describe a knowledge-based expert system as a system that uses human knowledge to solve problems that would usually require human intelligence [18, 19]. Expert systems can effectively and accurately address problems in a narrow problem area [20] and operate at the level of an expert [21]. It was the team at the Stanford Heuristic Programming Project headed by Edward Feigenbaum who officially introduced expert systems [22]. An expert system is generally a computer inference system that emulates the decision-making abilities of a computer [23]. To solve complex problems, they are constructed by reasoning through knowledge bodies, interpreted primarily as *if-and-then* rules. They were used for problem-solving as early as the 1970s and saw huge success during the 1980s [24]. They were among the first truly successful types of artificial intelligence software [25].

This study has a two-fold objective: (i) to construct an expert system classifier based on multi-source RS imagery, (ii) analyze the classification performance of the expert system classifier and compare it with other conventional classifiers. To realize these objectives, we have made use of Anderson's [26] level 1 and level 2 classes in the study area considered.

The rest of the paper is structured as follows. In Sect. 2, the RS data products used and the study area is presented. Section 3 presents the discussion of the expert system classifier and its construction for the study area considered. Section 4 presents and discusses the results obtained during the conduction of the study. Conclusions drawn from the results are discussed in Sect. 5.

2 Data Products and Study Area

In this study, we have made use of data captured from two sensors: Landsat 8 and Cartosat-1. Landsat 8 carries two push-broom type passive imaging sensors namely operational land imager (OLI) and thermal infrared sensor (TIRS). Through these sensors, Landsat 8 collects medium resolution multispectral imagery of global landmass in 11 spectral bands [27]. OLI sensor has 9 spectral bands, while TIRS has 2 spectral bands. In this study, we have used the first 8 spectral bands of the OLI sensor for creating the primary data source.

The first of the Cartosat series of satellites designed, launched, and maintained by the Indian Space Research Organization (ISRO) was Cartosat-1. It is a satellite for earth observation located in a sun-synchronous orbit and is used primarily to collect cartographic data from the Indian subcontinent. Data from this satellite is available for worldwide distribution from Bhuvan [28] portal.

The study area of the Kumta Taluk boundary is shown in Fig. 1. It is located in the south-western part of the Indian subcontinent and is categorized under coastal agro-climatic zone [29]. It is bordered by the state of Goa and Belagavi district to the north, the districts of Dharwad and Haveri to the east, the districts of Shivamogga and Udupi to the south, and the Arabian Sea to the west. The study area is mainly characterized by the Western Ghats and more than 50% of the study area is covered by vegetation. Abundant rainfall during the long monsoon season assures thick vegetation growth on the hilly terrain. The study area mainly exhibits seven LULC classes; water body,

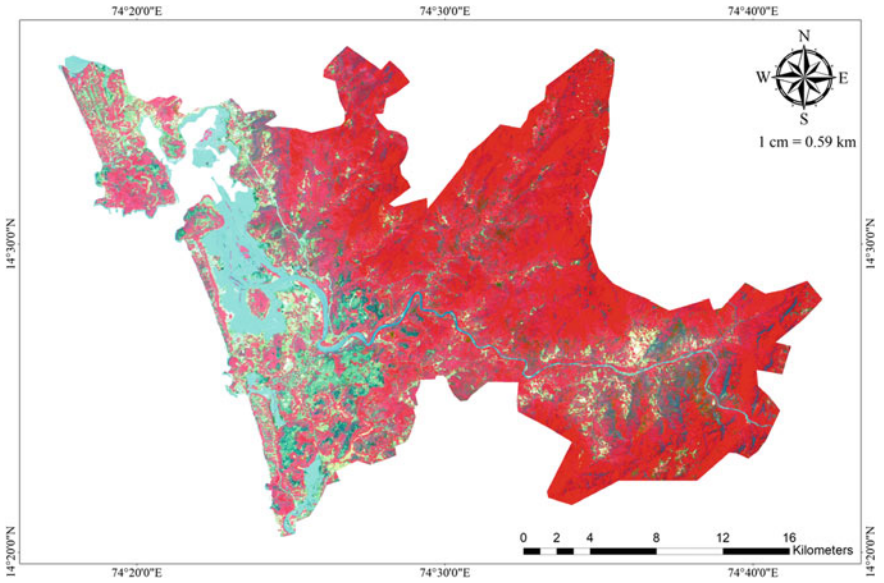

Fig. 1 Map of the study area (band combination [3–5]) (Data courtesy U.S. Geological Survey Earthexplorer [32])

kharif, built-up, scrubland, deciduous forest, evergreen forest, and double-crop and plantations. These classes were elaborately analyzed in our previous papers [30, 31] for their spatial and spectral distribution.

The study area exhibits the first two levels of Anderson's LULC classification system [26]. The LULC classes can be categorized into two types: spatial and spectral. Each category can be further subdivided into dominant and subservient classes. Spatially dominant classes are those that are found in majority terms on the study area. On the other hand, spectrally dominant classes are those that have clear and superior spectral signatures. Evergreen forest, scrub land, kharif, and water body classes can be classified under spatially dominant classes while the others are categorized under spatially subservient classes. It should be noted that spatially subservient classes are found scarcely on the study area. Further, evergreen forest, water body, and scrub land form the spectrally dominant classes. The remaining classes fall under spectrally subservient classes. It should be noted that spectrally subservient classes have similar spectral signatures as that of some of the spectrally dominant classes and therefore overlap them in the spectral space. Among the classes identified, we note that evergreen forest and double crop classes are spectrally similar making the LULC classification challenging. Also, kharif, built-up, and scrub classes indicate considerable overlapping in the spectral space. Considering the amount of spectral overlapping, the study area is regarded as heterogeneous.

3 Expert System Classifier

In general, an expert system is composed of two subsystems: the inference engine and the knowledge base. A knowledge base is a compilation of information expressed in the form of facts and rules. An inference engine is an automatic system of reasoning that analyses the existing knowledge base, establishes applicable rules, and then creates new knowledge in the knowledge base [33]. The inference engine applies the rules to the evidence and deduces fresh evidence [34]. The inference engine operates in two modes: forward chaining and backward chaining mode. How the inference engine selects a mode of operation depends on whether the value is powered by the antecedent (left) or consequent (right) [35]. In forward chaining, the antecedent fires and asserts the consequent while the framework looks at potential conclusions in backward training and operates backward to see if they may be accurate. A generic expert system consists of the components indicated in Fig. 2.

Expert systems based on knowledge accumulate and store information known to humans in a knowledge base. This knowledge is then used to create a set of heuristic rules to solve problems in the real world. The efficiency of the solution depends on the expert's domain knowledge. An expert may attain knowledge through experiments or real-life experiences or case studies. A knowledge engineer is a subsystem that evaluates the domain expert and extracts as many rules and conditions relating to the current problem (hypothesis) as possible. A knowledge engineer generally has three sub-blocks: hypotheses, rules, and conditions. A hypothesis is a problem whereby

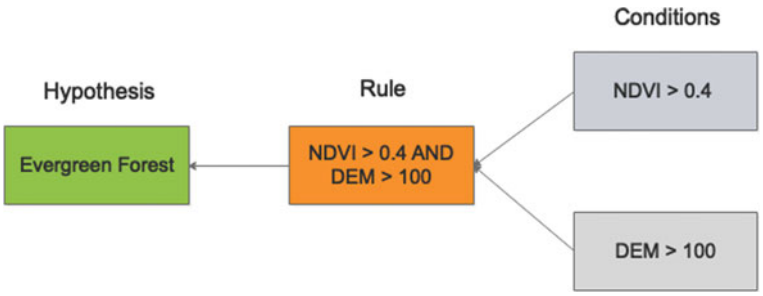

Fig. 2 A generic expert system structure

an expert tries to find a solution by applying rules and conditions. To provide a solution to the hypothesis, the rules and conditions function on the knowledge base. For example, for the study area considered, NDVI > 0.4 and elevation >100 m define the evergreen forest class. These form the requirements for the expert system. If Evergreen Forest was to be found in the study area, the decision rule would then be NDVI > 0.4 AND elevation >100 m. The pixels in the study area that meet these requirements are assigned to the evergreen forest class.

Expert systems have evolved to incorporate modern techniques with the advent of technology [36]. Some of these methods are;

- Maintenance of the truth: The framework relates to the facts contained in the database. If a fact changes, then the relevant information in the database is altered accordingly [37].
- Hypothetical reasoning: The database is split into several sections so that various parallel possibilities can be explored by the inference engine [37].
- Uncertainty systems: The information in the database is correlated with the likelihood that a rule with a finite probability of occurrence is associated with each fact [37].
- Ontology classification: Expert systems can reason not just about object values but also about object structures by adding object classes to the knowledge base [38].

3.1 Inference Engine

To establish any method by which conclusions are drawn, reasoning and inference are essential [25]. On an inference engine, the expert system is modeled and fed with rules, conditions, and hypotheses. The spatial data is evaluated using Boolean AND logic for one or more conditional statements within a rule. To accept the hypothesis, it is important for all the conditions inside a rule to be satisfied. The hypothesis would be dismissed even if one of the conditions inside a rule is not satisfied. Some inference systems inculcate confidence values to conditions within a rule. Adding

trust values makes it more robust. Estimating confidence values, however, is difficult and relies on the expert's knowledge of the topography of the study region.

To interpret the rules, an inference system can use forward- or reverse-chain, or both. Through each stage, the expert is able to monitor the quality of the inference system. It helps the expert systems to account for their class assignments. This is a good feature of the expert systems [39]. An inference engine can be customized by using an expert system shell. Expert system shells are equipped with an inference mechanism and allow the entry of information in a specified format.

The ability to use information from different platforms and sources is an important advantage of expert systems. For the creation of expert systems, one may use two or more input data sets. Currently, for establishing rules and conditions, online databases are also available. There can be other formats for online databases; raster or vector data, graphs, charts, photographs, text, etc. It is important to provide structured metadata in the database. Using two methodologies, an expert may construct rules and conditions: (i) using the expert's knowledge and (ii) using an inductive machine learning algorithm based on training data. To construct an expert classifier, it is possible to use both methodologies.

3.2 Band Ratioing

Sometimes, because of factors such as elevation, slope, shadows, changes in illumination intensity, and sun angle, the pixel values of spectrally similar classes may differ. These factors affect the capacity of the expert to correctly interpret the surface materials. Ratio transformations can be used to solve this challenge to reduce the impact of the above-said factors on environmental conditions [18]. In extracting unique information that is not found in individual spectral bands, the band-ratio technique is more effective [40].

Mathematically, band ratioing can be expressed as

$$B_{i,j,r} = \frac{B_{i,j,k}}{B_{i,j,l}} \tag{1}$$

where $B_{i,j,k}$ and $B_{i,j,l}$ are the (i, j) th pixel values in band k and l, respectively, and $B_{i,j,r}$ is the (i, j) th pixel in the band ratioed image.

Equation (1) can lead to unexpected results at times. For example, if $B_{i,j,l}$ is zero, a $B_{i,j,r}$ response will not fit the system. The brightness values of $B_{i,j} = 0$ across bands can be reset to 1 to solve this issue. Alternatively, you can apply a small value, such as 0.1, to both the numerator and the denominator. The overall result is not influenced by this action [18]. It is not always easy to pick two bands for ratioing. In general, the analyst explores all possible ratio choices and selects the bands that produce the results that are most attractive. To identify the optimal bands for band ratioing, the Optimum Index Factor (OIF) and Sheffield Index can be used [41, 42].

3.3 Expert System Construction

To build an expert system, information from any type of RS source can be used. Only a few sources of data, however, provide relevant information. Therefore, before building an expert system, it is important to identify these relevant sources. Since this paper aims to classify RS data, the primary data source will be satellite imagery of the study area. This study uses Landsat 8 data of the Kumta study area as the primary source of data. An analyst can decide, depending on the application, to use more data sources for constructing the expert system. Several other data source variables/factors characterizing the topography, vegetation phenology, etc., of the study area, can provide additional insight. Apart from these external information sources, an expert may perform mathematical operations on the data to obtain new data.

We did extensive testing of all data sources before the expert system was built and chose the ones that produced the most attractive results. They are individual band images from Landsat 8 data, band ratio images constructed from Landsat 8 data, Cartosat-1 elevation detail, and NDVI values computed from Landsat 8 data bands. Upon analyzing the band ratioed images, we noted that the water bodies are indicated with bright pixels in B4/B6 imagery, the Kharif class was highlighted with brighter pixels in B7/B2 imagery, and the Scrub Land class with medium intensity pixels in B7/B2 imagery. Other band ratio images did not provide any useful information and hence are omitted from the analysis.

Evergreen Forest class covers the largest portion of the study area. It is characterized by high altitude and high NDVI values. The rule for the Evergreen Forest class uses Band-7 and NDVI values. It is noted that Band-7 highlights the vegetation classes excellently. Pixel values of Band-7 that represent the Evergreen Forest class were found to be in the range 10 and 3400. These values were found by analyzing individual data bands. The rule for Evergreen Forest class is $10 \leq \text{Band} -7 \leq 3400$ AND NDV I ≥ 0.3. The expert engineer for the Evergreen Forest class is indicated in Fig. 3.

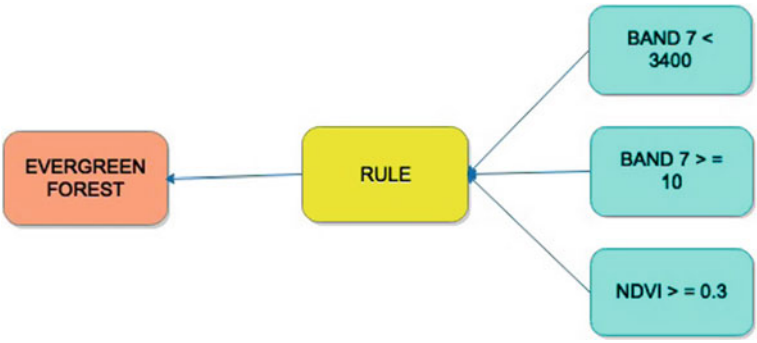

Fig. 3 Expert engineer for evergreen forest

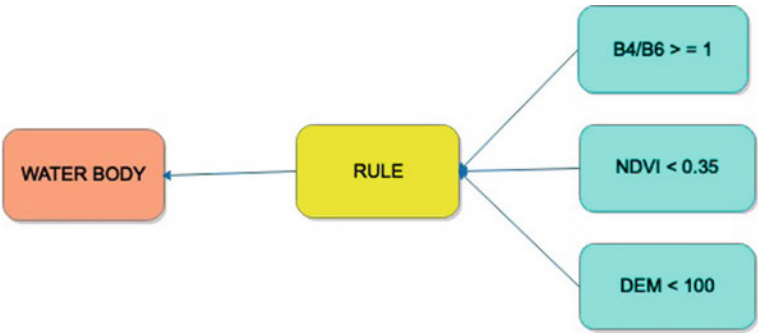

Fig. 4 Expert engineer for water body

Water Body class would have very low values of NDVI and generally. Water Bodies are found profoundly at lower elevations. Therefore, we combined B4/B6, NDVI, and DEM to create a rule for the water body. It is given by $B4/B6 \geq 1$ AND NDVI < 0.35 AND DEM < 100. The expert engineer for the Water Body class is indicated in Fig. 4.

Deciduous Forest class covers only a very small region in the study area towards the eastern part of the study area. Deciduous Forest was extracted using four variables: Band-6, Band-7, NDVI, and DEM. The decision rule for extracting Deciduous Forest class is $6000 \leq \text{Band} - 6 \leq 8000$ AND DEM ≥ 70 AND $10 \leq \text{Band} - 7 \leq 4100$ AND NDV I ≤ 0.3. The expert engineer for the Deciduous Forest class is indicated in Fig. 5.

Analysis of the study area revealed that Scrub Land regions were found generally at lower elevations ($\leq$20). Hence, we used two variables to extract the Scrub Land class: B7/B2 and DEM. Also, since the band ratioed image B7/B2 highlights Scrub Land with medium intensity pixels, a range was found for representing Scrub Land. The decision rule for Scrub Land is $0.75 \leq$ B7/B2 ≤ 1.5 AND DEM ≤ 70. The expert engineer for the Scrub Land class is indicated in Fig. 6.

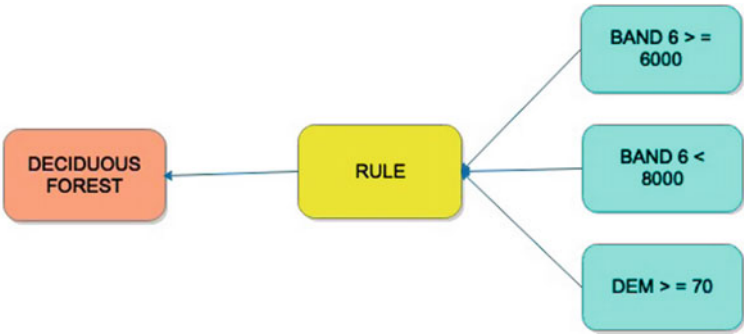

Fig. 5 Expert engineer for deciduous forest

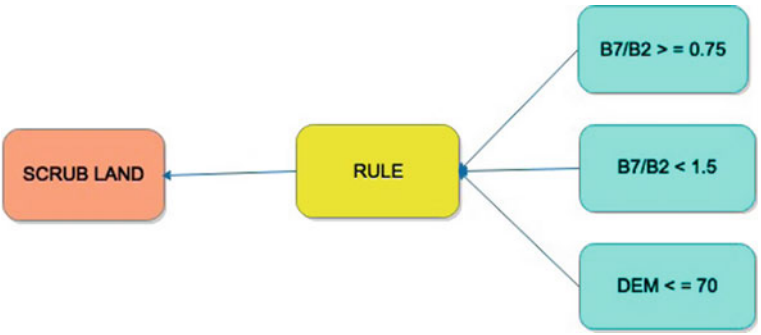

Fig. 6 Expert engineer for Scrub Land

As stated earlier, the B7/B2 band ratioed image excellently highlighted the Kharif class. Hence, no other parameters were used for extracting the Kharif class. By detailed analysis of the data, the decision rule for Kharif is set as B7/B2 $\geq$ 1.5. The expert engineer for the Kharif class is indicated in Fig. 7. For extracting the Built-Up class, Band-4 alone was used. Band-4 highlighted Built-Up areas on the data excellently with bright pixels. By analyzing the data, the rule for the Built-Up class was set as Band-4 > 5200. The expert engineer for the Built-Up class is indicated in Fig. 8.

Double Crop and Plantations class is a derivative of Evergreen Forest class and therefore has very similar characteristics. Therefore, to extract the Double Crop class, the rules used for the Evergreen Forest class were applied first and by further analyzing the data a new rule was formed. The Rule for Double Crop class is 10 $\leq$ Band $-7 \leq$ 3400 AND NDV I $\geq$ 0.3 AND Band $-7 \leq$ 1300 AND DEM < 5 AND 0.61 $\leq$ NDV I $\leq$ 0.67. The expert engineer for the Double Crop and Plantations class is indicated in Fig. 9.

Fig. 7 **Ex**pert engineer for Kharif

Fig. 8 Expert engineer for built up

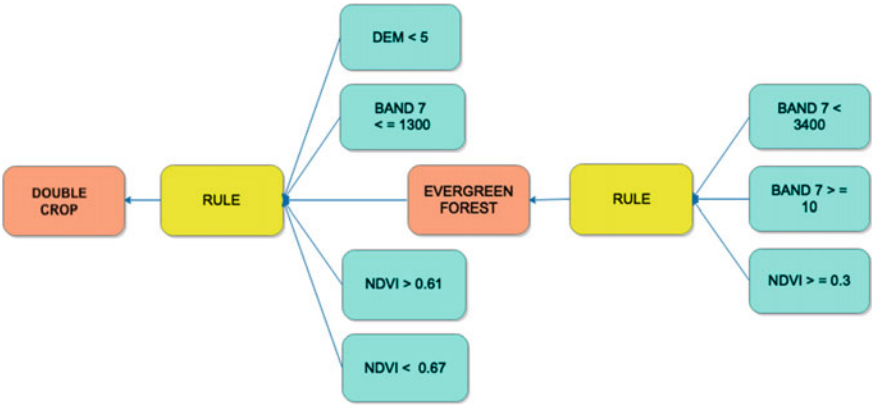

Fig. 9 Expert engineer for double crop and plantations

Table 1 Expert system rules for LULC classes of Kumta study area

Class	Rule
Kharif	B7/B2 $\geq$ 1.5
Built-up	Band $-4 > 5200$
Scrub land	$0.75 \leq$ B7/B2 ≤ 1.5 AND DEM ≤ 70
Evergreen forest	$10 \leq$ Band $-7 \leq 3400$ AND NDVI ≥ 0.3
Water body	B4/B6 ≥ 1 AND NDV I < 0.35 AND DEM < 100
Deciduous forest	$6000 \leq$ Band $-6 \leq 8000$ AND DEM ≥ 70 AND $10 \leq$ Band $- 7 \leq 4100$ AND NDVI ≤ 0.3
Double crop	$10 \leq$ Band $-7 \leq 3400$ AND NDV I ≥ 0.3 AND Band $-7 \leq 1300$ AND DEM < 5 AND $0.61 \leq$ NDV I ≤ 0.67

4 Results and Discussion

The thematic map produced by the expert system classifier was subjected to a rigorous accuracy assessment procedure to quantify the classification results. A total of 1000 pixels were selected using the stratified random technique to conduct an accuracy assessment. These results of accuracy assessment are indicated in Table 2. The number of pixels selected for each classifier is listed under the reference total (RT) column in Table 2. The classifier assigns each pixel to one of the LULC class, and the number of pixels assigned to each LULC class is listed under classification totals (CT) in Table 2. Out of these classified pixels, the number of correctly classified pixels are listed under the number correct (NC) column in Table 2. The producer's accuracy is the ratio of NC and RT and gives the perspective of what the classifier thinks as the correct pixel assignment. The user's accuracy is the ratio of NC and RT and provides the perspective of what the user thinks is the correct pixel assignment. In remote sensing studies, user's accuracy is regarded as the better accuracy metric

Table 2 Accuracy assessment results of expert system classifier for Kumta study area

Class name	RT	CT	NC	PA (%)	OE(%)	UA (%)	CE (%)	Kappa
Evergreen forest	603	620	540	89.55	10.45	87.10	12.90	0.6750
Deciduous forest	28	12	7	25.00	75.00	58.33	41.67	0.5713
Water body	78	79	73	93.59	06.41	92.41	07.59	0.9176
Kharif	75	91	60	80.00	20.00	65.93	34.07	0.6317
Scrub land	112	171	76	67.86	32.14	44.44	55.56	0.3744
Built up	15	10	5	33.33	66.67	50.00	50.00	0.4924
Double crop and plantations	89	17	6	06.74	93.26	35.29	64.71	0.2897
Totals	1000	1000	767					
Overall classification accuracy	76.70	Overall kappa value	0.6064					

RT Reference totals, *CT* Classified totals, *NC* Number correct, *PA* Producer's accuracy, *OE* Omission error, *UA* Users accuracy, *CE* Commission error

and hence we use user's accuracy for analyzing the classification results. Omission error (OE) is the error incurred during accuracy assessment in the classifier's perspective and commission error is the error incurred during accuracy assessment in the user's perspective. Finally, the Kappa statistic indicates the extension of the accuracy assessment results to the rest of the pixels on the thematic map.

The expert system classifier extracted spectrally dominant classes with excellent class accuracies while their spectral counterparts were extracted with reasonable accuracies. The expert system classifier has successfully separated the spectrally overlapping class pairs reasonably well. The overall classification accuracy and overall kappa value produced by the expert system classifier are 76.70% and 0.6064, respectively. Comparing the kappa value of the classified map with those defined by Richards [17], the classification performance can be termed good.

Water Body and Evergreen Forest classes were extracted with excellent class accuracies greater than 80%. Very few misclassifications were recorded for these two classes. Kharif and Deciduous Forest classes were also extracted with acceptable class accuracies although many of the pixels of these classes were misclassified to Scrub Land class. The Scrub Land class itself has produced large misclassifications with Evergreen Forest and Double Crop classes.

Deciduous Forest and Built-Up classes form the subservient classes in the study area. These classes were poorly extracted from many other classifiers we had previously tested [43]. Expert system classifier has extracted these two classes with considerably higher-class accuracies highlighting its ability to separate spectrally overlapping classes as well as subservient classes on the data. Although the classifier did

Table 3 Classification accuracy assessment results of several other classifiers over the study area

Classifier	OCA (%)	OKV
Maximum likelihood classifier	75.40	0.5773
Minimum distance-to-means classifier	54.20	0.3856
Mahalanobis distance classifier	58.40	0.4302
Neural network classifier	77.40	0.6040
Support vector machine (linear Kernel)	77.70	0.6136
Classification and regression tree	79.40	0.6482
Iterative dichotomizer 3	78.60	0.6350
Fuzzy based MLC	77.00	0.6069

OCA Overall classification accuracy, *OKV* Overall Kappa value

not meet the estimated class accuracy for the data, the overall classification accuracy is lesser than the estimated value by only $\approx 2\%$.

To assess the classification performance of expert system classifier, we compared it with several other classifiers as shown in Table 3. It should be noted that expert system classifier produced considerably better classification performance that minimum distance-to-mean and Mahalanobis distance classifiers. Further, its performance is on par with the mathematically sound maximum likelihood classifier. However, it falls short in performance compared to advanced classifiers listed in Table 3. It should be noted that these advanced classifier results are for the input parameter combination, and under several conditions, expert system classifier performed better than advanced classifiers (discussed in our previous work [43]).

4.1 Observations

The expert systems provide several advantages such as (i) Defining new rules which are simple and easy to understand, evaluate, and edit. (ii) They are simple to manage. This is achieved in two ways: removing the need for code writing and introducing new rules to the system in a short period [33]. (iii) Ability to operate on integrated sources of data that are difficult for traditional algorithms [44].

Expert system classifiers have many advantages over other classifiers [45, 46]: (i) By working backward to determine how the decision was made, it is possible to assess the performance of an expert system [47]. It is much simpler compared to other classification strategies such as neural networks, where the decision principle is regulated by the weights in the hidden layer. (ii) A decision tree can simulate and predict hierarchical and non-linear relations between the input variables and use them to make membership predictions; (iii) Literature shows that decision trees can effectively handle high-dimensional data sets such as hyperspectral imagery [48].

There is a fair range of drawbacks of expert systems as well. The problem of acquiring knowledge is the most fundamental issue in expert systems. Field experts

are rare and difficult to find as well. Although it is simple to understand and easy to develop expert systems, they are not as powerful as coding languages. Another issue expert system usually face is the size of the database. The processing complexity increases with larger databases. The right number of rules that are compatible with each other is also difficult to find. Generally, such problems lead to a satisfactory formulation. It is difficult to prioritize rules to operate them efficiently or to overcome ambiguities if the expert system allows the probability to be correlated with facts. To solve these challenges and instill feedback mechanisms, the current generation of expert systems uses innovative approaches based on machine learning.

5 Conclusions

Land cover mapping has been one of the most basic applications of remote sensing imagery. In this paper, we have illustrated the construction of an expert system classifier using multi-source RS data for classification application. The most daunting requirement of the expert system classifier is the expert himself/herself. It requires the analyst to have profound knowledge of the terrain characteristics of the data as well as to apply the knowledge successfully. The analyst is also expected to know the system, and the software platform on which the expert classifier is implemented. When one gets these things correctly, as our results indicate, one can expect highly reliable classification results from an expert system classifier.

Another important aspect of the expert system classifier is that the classification results depend rightly on the construction of the classifier itself. Misinterpretation of the hypothesis or variables or the decision rules can be catastrophic and must be carefully built. In this study, the expert system classifier extracted the dominant classes considerably well while also extracting the subservient classes with reasonably good class accuracies. We intend to further explore the capabilities of the expert system classifier by employing additional multi-source data sets in our future investigations.

Acknowledgements This work was supported by N.M.A.M. Institute of Technology, Nitte, Karnataka, India, and K.L.E. Institute of Technology, Hubli, Karnataka, India.

References

1. Jensen JR (1986) Introductory digital image processing: a remote sensing perspective. Technical Report University of South Carolina, Columbus
2. Mather PM, Koch M (2011) Computer processing of remotely-sensed images: an introduction. Wiley
3. Reed BC, Schwartz MD, Xiao X (2009) Remote sensing phenology. In: Phenology of ecosystem processes. Springer, pp 231–246

4. Vrieling MM, Darvishzadeh R, Skidmore AK, Wang T, Zurita-Milla R, Oosterbeek K, O'Connor B, Paganini M (2018) Vegetation phenology from sentinel-2 and field cameras for a dutch barrier island. Remote Sens Environ 215:517–529
5. E Akbari SK Alavipanah M Jeihouni M Hajeb D Haase S Alavipanah 2017 A review of ocean/sea subsurface water temperature studies from remote sensing and nonremote sensing methods Water 9 12 936
6. V Levizzani E Cattani 2019 Satellite remote sensing of precipitation and the terrestrial water cycle in a changing climate Remote Sens 11 19 2301
7. R Kar GO Reddy N Kumar S Singh 2018 Monitoring spatio-temporal dynamics of urban and peri-urban landscape using remote sensing and gis–a case study from central india Egyptian J Rem Sens Space Sci 21 3 401 411
8. MS Saleem SR Ahmad MA Javed 2020 Impact assessment of urban development patterns on land surface temperature by using remote sensing techniques: a case study of lahore, faisalabad and multan district Environ Sci Pollut Res 27 32 39865 39878
9. L Hua G Shao 2017 The progress of operational forest fire monitoring with infrared remote sensing J Forestry Res 28 2 215 229
10. MA Matin VS Chitale MS Murthy K Uddin B Bajracharya S Pradhan 2017 Understanding forest fire patterns and risk in nepal using remote sensing, geographic information system and historical fire data Int J Wildland Fire 26 4 276 286
11. Xing H, Feng H, Fu J, Xu X, Yang G (2017) Development and application of hyperspectral remote sensing. In: International conference on computer and computing technologies in agriculture, Springer, pp 271–282
12. Bachagha N, Wang X, Luo L, Li L, Khatteli H, Lasaponara R (2020) Remote sensing and gis techniques for reconstructing the military fort system on the roman boundary (tunisian section) and identifying archaeological sites. Remote Sens Environ 236:111418
13. D Lu Q Weng 2007 A survey of image classification methods and techniques for improving classification performance Int J Remote Sens 28 5 823 870
14. Laha N Pal R, Das J (2006) Land cover classification using fuzzy rules and aggregation of contextual information through evidence theory. IEEE Trans Geosci Remote Sens 44:1633–1641
15. Li WF, Dong X (2015) Research on the classification of high resolution image based on object-oriented and class rule. Int Arch Photogrammetry, Remote Sens Spatial Inf Sci-ISPRS Arch 40(7):75–80
16. Jensen JR (2015) Introductory digital image processing: a remote sensing perspective. Prentice Hall Press
17. Richards JA (2013) Remote sensing digital image analysis, vol 5. Springer
18. Jensen JR (2000) Introductory digital image processing: a remote sensing perspective
19. AI P (2002) Expert systems
20. Waterman D (1986) A guide to expert systems
21. Liebowitz J (1988) Introduction to expert systems. Mitchell Publishing, Inc.
22. Feigenbaum EA (1977) The art of artificial intelligence. 1. themes and case studies of knowledge engineering. Technical Report Stanford Univ CA Dept of Computer Science
23. Jackson P (1998) Introduction to expert systems 3rd
24. Leondes CT (2001) Expert systems: the technology of knowledge management and decision making for the 21st century. Elsevier
25. SJ Russell P Norvig 2016 Artificial intelligence: a modern approach Pearson Education Limited Malaysia
26. Anderson JR (1976) A land use and land cover classification system for use with remote sensor data, vol. 964. US Government Printing Office, 1976. 27. USGS, "Landsat 8 oli and tirs and their uses"
27. "Landsat 8 OLI and TIRS and their uses." U.S. Geological Survey. Accessed March 03, 2021. https://www.usgs.gov/media/images/landsat-8-oli-and-tirs-and-their-uses
28. "National Remote Sensing Centre: Government of India." Indian Geo Platform of ISRO. Accessed March 19, 2021. https://bhuvan.nrsc.gov.in/home/index.php

29. T Ramachandra B Setturu S Chandran 2016 Geospatial analysis of forest fragmentation in uttara kannada district, india Forest Ecosystems 3 1 10
30. BR Shivakumar SV Rajashekararadhya 2018 Investigation on land cover mapping capability of maximum likelihood classifier: a case study on north canara, india Proced Comput Sci 143 579 586
31. BR Shivakumar SV Rajashekararadhya 2018 An investigation on land cover mapping capability of classical and fuzzy based maximum likelihood classifiers Int J Eng Technol 7 2 939 947
32. EarthExplorer U "Us department of the interior," *US Geological Survey*. https://www.earthexplorer.usgs.gov
33. Hayes-Roth F, Waterman DA, Lenat DB (1983) Building expert system
34. Nwigbo Stella N, Chuks AO (2011) Expert system: a catalyst in educational development in nigeria
35. Arman N (2007) Fault detection in dynamic rule bases using spanning trees and disjoint sets
36. W Mettrey 1987 An assessment of tools for building large knowledge-based systems AI Mag 8 4 81 81
37. R MacGregor MH Burstein 1991 Using a description classifier to enhance knowledge representation IEEE Expert 6 3 41 46
38. Berners-Lee T, Hendler J, Lassila O (2001) The semantic web. a new form of web content that is meaningful to computers will unleash a revolution of new possibilities. Sci Am 284(5):3
39. K Darlington 1996 Basic expert systems Inf Tech In Nurs 8 9 11
40. Satterwhite M (1984) Discriminating vegetation and soils using landsat mss and thematic mapper bands and band ratios. Technical report, Army Engineer Topographic Labs Fort Belvoir Va
41. P Chavez Jr 1984 Image processing techniques for thermatic mapper data Proc ASPRS-ACSM Tech Papers 2 728 742
42. C Sheffield 1985 Selecting band combinations from multi spectral data Photogramm Eng Remote Sens 58 6 681 687
43. Shivakumar BR (2020) Study and analysis of pixel-based classification of remote sensed data using different classifiers. PhD thesis, Visvesvaraya Technological University, Belagavi
44. BK Wong JA Monaco 1995 Expert system applications in business: a review and analysis of the literature (1977–1993) Inf Manage 29 3 141 152
45. M Hansen R Dubayah R DeFries 1996 Classification trees: an alternative to traditional land cover classifiers Int J Remote Sens 17 5 1075 1081
46. R DeFries JC-W Chan 2000 Multiple criteria for evaluating machine learning algorithms for land cover classification from satellite data Remote Sens Environ 74 3 503 515
47. F Qiu J Jensen 2004 Opening the black box of neural networks for remote sensing image classification Int J Remote Sens 25 9 1749 1768
48. RL Lawrence A Wright 2001 Rule-based classification systems using classification and regression tree (cart) analysis Photogramm Eng Remote Sens 67 10 1137 1142

Applications of Geospatial Technologies and Wetspass Model in Groundwater Recharge Estimation in Sana River Catchment, Kembata Tembaro Zone, Southern Ethiopia

Deginet Danebo, Abunu Atilebachew, Abel Abebe, and Muralitharan Jothimani

Abstract Estimating groundwater recharge is critical for water resource appraisal and management. In the present study WetSpass model and GIS tools were used to determine water balance components' temporal and spatial changes (surface runoff, actual evapotranspiration, and groundwater recharge) in the Sana watershed Kembata Tembaro Zone, Southern Ethiopia. In the current study, biophysical and hydro-meteorological parameters such as land use/cover, soil texture, elevation, and slope were included in the model. The data mentioned above sets were calibrated per the Wetspass model requirements. The spatial–temporal variation of the mean annual rainfall of 1358.6 mm was segmented into 20.6% (280 mm) of surface runoff (Qo), 59.76%(811.6 mm) of actual evapotranspiration, and 19.65% (267 mm) of water that annually recharges the groundwater system, according to the model results. The model's results show that the area's hydro-meteorological and biophysical variance controls the temporal and geographical variability of the catchment's water balance components. The current study provides policymakers and water resource experts with critical information on groundwater availability for sustainable development in the present study area.

Keywords Groundwater recharge · Ethiopia · Kembata tembaro zone · Sana catchment · Wetspass model

1 Introduction

Water is essential for life, and it must be supplied in adequate quantities and of sufficient quality to meet expanding demands for domestic, agricultural, and industrial

D. Danebo · A. Abebe · M. Jothimani (✉)
Department of Geology, Arba Minch University, Arba Minch, Ethiopia
e-mail: muralitharangeo@gmail.com

A. Atilebachew
Faculty of Water Resources and Irrigation Engineering, Arba Minch University, Arba Minch, Ethiopia

L. Nandagiri et al. (eds.), *Recent Advances in Civil Engineering*, Lecture Notes in Civil Engineering 256, https://doi.org/10.1007/978-981-19-1862-9_6

processes [1, 2]. On the earth, freshwater is an inadequate, vital, versatile, and natural resource, and demand is growing worldwide due to urban, economic, and population growth [3]. Surface water is unpredictable since it is prone to seasonal variations and pollution. On the other hand, groundwater is more suitable in quantity, is commonly accessible, and is characteristically secured against direct contamination [4]. Proper groundwater resource planning and management regarding availability, consumption, and environmental roles are critical for augmenting groundwater resources [3].

Due to the rapidly rising and conflicting demand for a resource, access to clean water has become a challenge in many parts of the world, particularly in dry regions of emerging countries. Population growth and urbanization are increasing rapidly in developing countries, and they are putting a strain on current water supplies in terms of capacity, sustainability, and contamination [5]. Ethiopia also has a lot of surface water resources. There are 12 significant river basins in the country. Nine of these are wet river basins, one is a lake basin, and the other two are dry river basins with almost no water flow [6]. Despite these country's assets, location-specific expertise and insight into the groundwater system remain critical for local communities' residential and economical water demands [6].

Monitoring annual and seasonal variations in water resources, particularly runoff, evaporation, transpiration, and recharge is critical for effective and long-term groundwater management [7]. Identification of the watershed's hydrological and biophysical parameters is required for accurate groundwater resource quantification. The ability to predict the potential of groundwater resources is closely related to the amount of groundwater recharge available, which is critical for groundwater resource management [8]. Groundwater recharge is when water percolates through the soil and reaches the water table to replenish the aquifer, either naturally or artificially. Its evaluation is a significant difficulty in establishing the long-term productivity of aquifers in arid and semi-arid locations [9].

For reliable measurement of groundwater resources, a complete understanding of an area's physical and biological properties, as well as its climatic circumstances, is required [10]. There are several ways for estimating groundwater resources [11]. Groundwater recharge has also been approximated using the water-balance approach, the water budget model method, or utilizing conservative chemical tracers, including chloride [12, 13]. Under quasi-steady conditions, the WetSpass system is a regionally dispersed simulation model for energy and water exchange among soil, plants, and the atmosphere. It predicts surface runoff, evaporation and transpiration, and groundwater recharge patterns [14]. Groundwater recharge evaluation in a specific region is essential in resolving problems linked to water resource management and various environmental sustainability planning employing other hydrological models, such as the WetSpass model and remote sensing and GIS technologies [6].

The WetSpass method has been used to assess groundwater recharge in many locations worldwide by the following scholars [15, 16]. The following authors used the wetspass model to determine the surface and groundwater potential in different parts of Ethiopia, Diredawa town [8], Geba Basin, Ethiopia [17], Raya Basin, Ethiopia [18], Adigrat area, and Northern Ethiopia [19]. Groundwater recharge, runoff, and

evapotranspiration have not been estimated in detail in the present study area, Sana catchment, Kembata Tembaro Zone, and Southern Ethiopia. Hence, the present was conducted to evaluate the total groundwater recharge in the current study area using the GIS-based WetSpass model.

2 Materials and Methods

2.1 Study Area

The present study area, the Sana catchment, Kembata Tembaro Zone, is located in the upper part of the Omo Gibe basin. And it is located in the Southern National and Nationalities Region (SNNPR) of Ethiopia. Geographically, Sana catchment is bounded between 6°95′00″ to 7°30′00″N latitude and 37°30′00″ to 37°60′00″E longitude with its areal extent of 921 km^2. Diverse topographic conditions characterize in the present study area. The upstream area is characterized by mountainous terrain with highly steep slopes and undulating topography, while the downstream region is characterized by gentle topography, and the slope varies from 0° to 76°. The mean annual precipitation of the catchment is 1358.6 mm. From June to September, the Sana catchment receives around 70.8 and 29.2% from October to May. The Sana catchment's minimum and maximum mean annual temperatures are 11.7 °C and 27.5 °C, respectively. The current research area's critical land use/land cover (LULC) categories are farmland, grassland, forests, settlements, and water bodies. The present study area significantly covers the following soil types: loam sand, silty clay loam, sandy clay loam, and clay soils dominate the current study area. Figure 1 shows the study area location map.

2.2 Data Sources

The study's primary data sources are climatic as well as remote sensing data. Meteorological data such as temperature, rainfall, and wind speed required for the study were collected from National Meteorological Agency (NMA). And also, hydrological maps and geological maps of the Omo-Gibe basin were collected from the Ethiopian Geological Survey (EGS). The topographic/elevation grid map and the slope map have been derived from SRTM DEM with 30 * 30 m spatial resolution. The ArcGIS 10.6 software was used to prepare, manipulate, and analyze the digital data as a raster cell. All raster input data of the meteorological, water table, land use/cover, soil, DEM, and slope grid maps were prepared by using ArcGIS software. Cloud free Landsat OLI 8 satellite images of 07-January-2019 were downloaded from the (https://earthexplorer.usgs.gov/) website to prepare the LULC map. Figure 2 shows the methodology flow chart. Table 1 shows the data and their sources used in the present study.

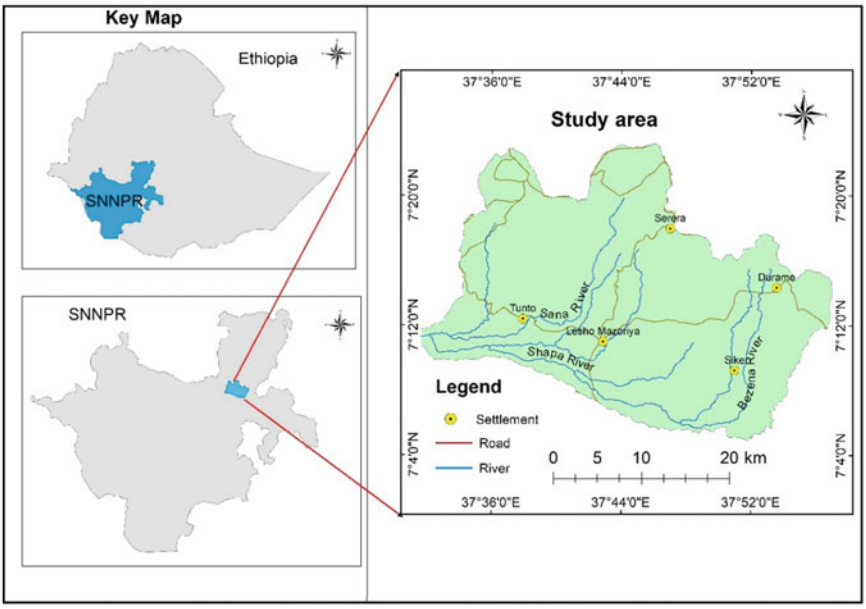

Fig. 1 Study area

2.3 Thematic Layer Preparation

Physiography and drainage. The elevation map of the Sana catchment was derived from the Shuttle Radar Topography Mission (SRTM) dataset (digital elevation model). To delineate the study area's catchment and drainage network, terrain features at each grid cell were extracted from the DEM, including flow accumulation, flow direction, stream order, elevation, and stream network from the spatial analysis tool of ArcGIS software. The lowest topographic relief of the study area is 752 m at the mouth of the Sana catchment, and the highest is 3020 m (Fig. 3) in the upper stream part like Mount Hambaricho. The drainage pattern network of the Sana catchment was processed from DEM data. The study area's drainage patterns are mainly dendritic and show a parallel drainage network in some parts. The most extended branch is about 59 km.

Rainfall. The period 2000–2019 is used to process weather data (precipitation, evapotranspiration, temperature, and wind speed), with an overall average for every annual sampling interval, i.e., the winter and summer seasons, which correspond to October to May and June to September, respectively. Rainfall point data were collected from NMA. It is a widely measured meteorological element within and nearby the study area. One of the most critical parameters for a distributed hydrological water balance model is rainfall. From the selected six meteorological stations, rainfall records were collected 19 years from 2000–2019. Based on these records, the summer, winter, and mean annual rainfall distribution of the Sana catchment have

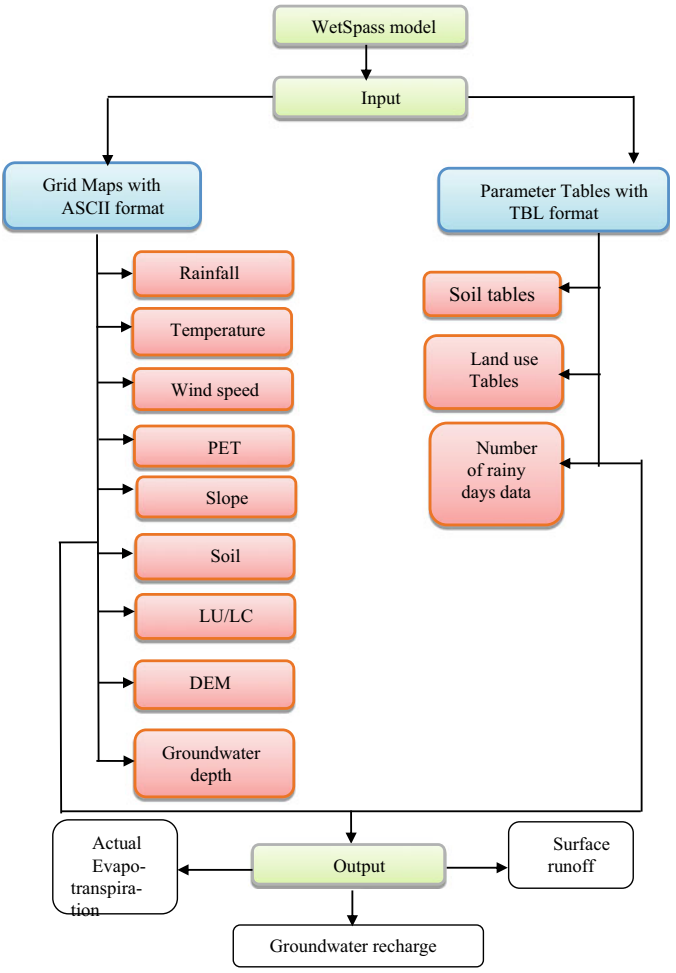

Fig. 2 Methodology flow chart

been computed through the ArcGIS interpolation tool. The minimum, maximum, and mean annual rainfall is 1202.7 mm, 1519.9, and 1358.6 mm. The summer season accounts for 70.8 percent (961.8 mm) of precipitation, and winter seasons account for 29.2% (396.7 mm) of the catchment's total annual rainfall.

Wind speed and temperature. Wind speed is one of the influencing factors of evaporation, when the increase of wind speed, resulting in the removal of saturated vapour, affects the evaporation rate. The magnitude of summer, winter, and annual wind speed varies from 1 to 1.29 m/s, 1.2– 1.4 m/s, and 1.14–1.35 m/s. Wind speed is relatively low, especially in the rainy season.

The temperature is an important parameter that governs the rate at which water molecules leave from the surface through evaporation, change in water surface

Table 1 WetSpass model input data sources

Raster input maps	Source
DEM (Digital elevation model)	Shuttle radar topography mission (SRTM)
Rainfall	Ethiopian meteorological agency
Soil	Ministry of water, irrigation, and energy, Ethiopia
Slope	SRTM DEM
LULC	https://earthexplorer.usgs.gov/, dated 07-January-2019
PET	Calculated using Hargreaves equations
Groundwater level	Ministry of water, irrigation, and energy, Ethiopia
Temperature	Ethiopian meteorological agency
Wind speed	Ethiopian meteorological agency

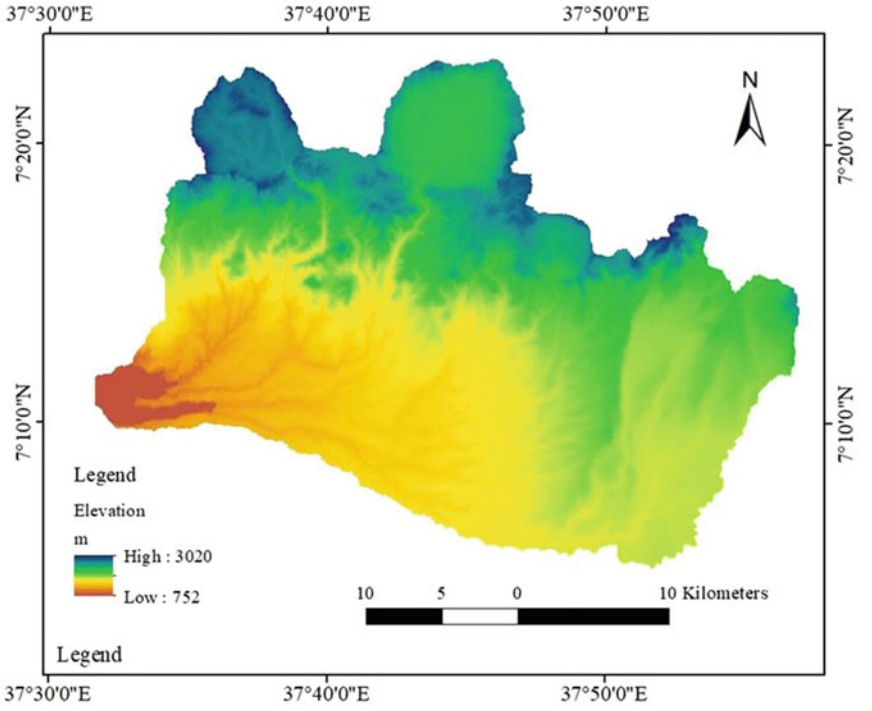

Fig. 3 Study area's elevation map

temperature, and water entering the ground surface. Variation of temperature in the study can be influenced by altitude. Temperature data of the catchment was taken from six-gauge stations, and the mean annual temperature of the catchment was calculated. The study area's annual lowest and maximum and mean temperatures are 11.7 °C, 27.5 °C, and 19. 97 °C respectively.

LULC. One of the significant input factors for the WetSpass model is land use/land cover. The present area's LULC map was prepared from satellite imageries, and field observations checked its accuracy. The datasets from USGS Earth Explorer of Landsat OLI 8 Level-1 image dated 07-January-2019 were downloaded from the website (https://earthexplorer.usgs.gov/), supervised image classification technique was adopted to prepare LULC map of the present study area. 187 field-based control points field were collected using GPS to check the accuracy of the prepared LULC map. The overall accuracy was utilized to measure classification accuracy, and the data's overall accuracy is 85.66 percent, with a kappa coefficient is 0.83. The following are the major LULC types present in the study area: agricultural land, grassland, forest, settlements, and water bodies account for about 74%, 10.9%, 14.3%, 0.6%, and 0.2%, respectively. Figure 4 shows the study area's LULC map.

Soil Texture. Soil texture is the most basic soil characteristic that influences soil properties such as the rate of infiltration, soil moisture, runoff, interflow, erosion,

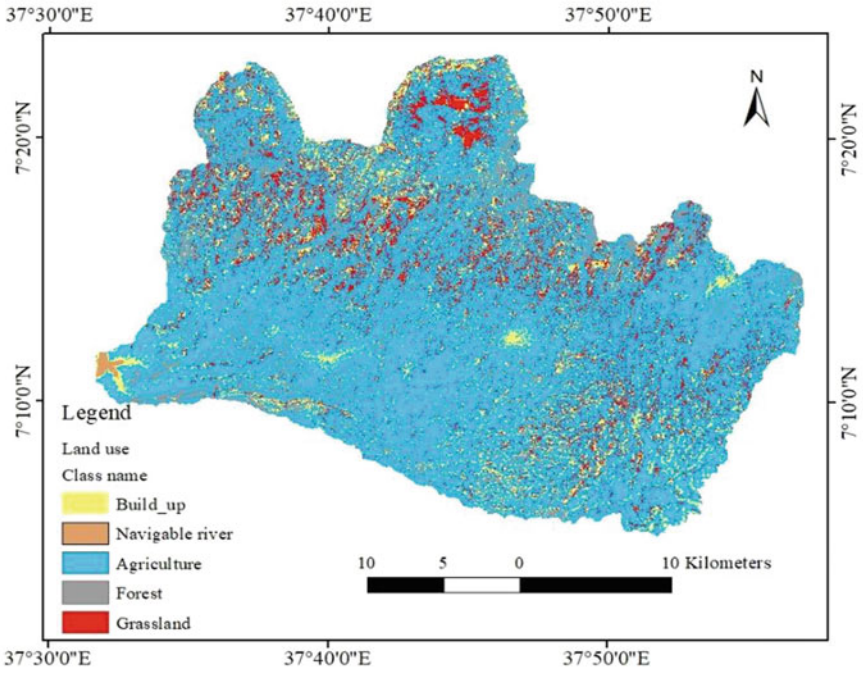

Fig. 4 LULC map

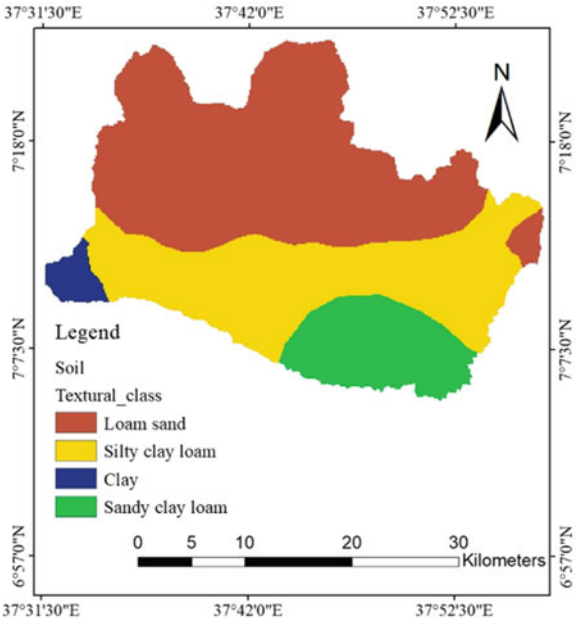

Fig. 5 Soil map

and root penetration. The texture of soil and its permeability is significate in groundwater recharge estimation. The soil map for the research region was received from Ethiopia's Ministry of Water Resources, Irrigation, and Energy (MoWIE). The current study area discovered loamy sand, silty clay loam, sandy clay loam, and clay soil types. The soil map for the research region is depicted in Fig. 5.

2.4 WetSpass Model Description

Wetspass model is used to assess groundwater systems (recharge-discharge interactions) on a more substantial scale, frequently quasi-steady-state [14]. It simulates geographic and temporal patterns of water balance components such as evapotranspiration, surface runoff, and groundwater recharge within a catchment using meteorological data, land use/cover, groundwater level, slope, elevation, and soil map of a region [20, 21]. The WetSpass model is used in this work to calculate spatial groundwater resources at annual and seasonal scales. The overall water balance of each raster cell was calculated using [14] formulae. To calculate the total evapotranspiration, Eq. (1) was employed.

$$ET_{\text{raster}} = a_v ET_v + a_s E_s + a_o E_o + a_i Ei \tag{1}$$

"Where ETraster is the total evapotranspiration at the raster cell, av, as, ao, and ai, are area components of vegetated, bare-soil, open-water, and impervious, respectively, [14]". The following sets of formulas were used to calculate surface runoff, evapotranspiration, and recharge.

In two processes, surface runoff (Sv) was computed. The potential surface runoff (S_v–pot) was determined in the first stage by multiplying a coefficient by the precipitation minus the interception, i.e., Eq. (2).

$$S_v\text{–pot} = C_{sv}(P - I) \tag{2}$$

C_{sv} is a surface runoff coefficient for vegetated infiltration areas and is a function of soil type, slope, and vegetation. Surface runoff (Sv) occurs in an area of saturated groundwater discharge areas. The surface runoff coefficient in this area is relatively high and presumed to be constant due to its dependence on the slope rather than soil, vegetation type, and the area's proximity to the river.

The potential surface runoff (Sv-pot) was determined in the second stage by comparing precipitation intensities to soil infiltration capabilities. According to [14], the formula Eq. (3) of infiltration derived by Horton's is valid only where the intensity of rainfall at the whole time exceeds infiltration.

$$\text{Sv} = \text{CHor Sv-pot} \tag{3}$$

CHor is a coefficient for parameterizing seasonal precipitation that contributes to surface runoff or Hortonian overland flow (HOF). Surface runoff is influenced by rainfall intensity in groundwater discharge zones. As a result, CHor equals 1.0 because all rainfall intensities contribute to surface runoff. High-intensity storms can only produce surface runoff in recharging zones.

The WetSpass-M model simulated seasonal and annual groundwater recharge as a final output of water balance computation by following equation Eq. (4).

$$\text{P} = \text{I} + \text{Sv} + \text{ETv} + \text{Gwr} \tag{4}$$

where P is the mean annual precipitation [LT-1], I is the interception of rainfall by vegetation [LT-1], Sv is the surface overland flow [LT-1], ETv is the actual transpiration vegetation cover [LT-1], and Gwr is the recharge amount of groundwater [LT-].

The final output for the WetSpass model is estimating the spatially distributed groundwater recharge, which can be calculated from the water balance by Eq. (5):

$$\text{Gwr} = P - \text{Sv} - \text{ETv} - I \tag{5}$$

where P is the mean annual precipitation, Sv is the surface overland flow, Gwr is the total amount of groundwater recharge, I indicates the interception by vegetation, and ETv is the actual evapotranspiration [LT-1] calculated as the sum of transpiration

Tv. Es is the evaporation from bare soil found in between the vegetation. Precipitation, temperature, land use/cover, soil type, slope, topography (elevation), groundwater level, and other input parameters utilized in the WetSpass model determine groundwater recharge.

2.5 Water Balance Per Raster Cell

At the raster cell level, long-term water balance computations for a given basin were done. Using long-term mean annual hydro-meteorological and biophysical factors, the model replicates spatial–temporal water balance components such as groundwater recharge, surface runoff, and actual-evapotranspiration. The total water balance, per raster cell and season, was calculated using the following water balance equations Eqs. (6–8) for vegetated (a_{av}), bare-soil (a_s), open-water (a_o), and impervious parts (a_i) of a raster cell [14].

$$ET_{\text{raster}} = a_v ET_v + a_s E_s + a_o E_o + a_i E_i \tag{6}$$

$$S_{\text{raster}} = a_v S_v + a_s S_s + a_o S_o + a_i S_i \tag{7}$$

$$R_{\text{raster}} = a_v R_v + a_s R_s + a_o R_o + a_i R_i \tag{8}$$

ET_{raster}, S_{raster}, and R_{raster} represent the total evapotranspiration, surface runoff, and recharge in a raster cell.

2.6 Wetspass Model Input Data Preparation

Generally, the WetSpass model requires two inputs: to start its running process and simulate the catchment's water balance component. I. All raster grid maps were converted into (ASCII file format) in the conversion tool of ArcGIS. II. Parameter soil, land use/cover, and rainy-day table data were prepared (TBL file format).

The WetSpass model requires raster data that is spatially distributed. Data from the weather, such as rainfall, temperature, and wind speed, was converted to a raster format. The spatial interpolation method was applied in ArcGIS software to convert the raster format for mentioned above meteorological data sets. Then the raster data format of gridded maps was converted into ASCII file format using a conversion tool in ArcGIS. Also, groundwater level grid maps were prepared using well-compilation data. Potential evapotranspiration data is required for the model, which was calculated by using the Hargreaves method. To run the model, four types of parameter tables (soil, number of the rainy day, summer, and winter land use/cover parameter tables) were needed. Those parameter tables were prepared appropriately (TBL) for the

valuable model running process in notepad software. As an input to the model, soil parameter, summer, and winter land use/land cover data sets were generated as attribute lookup tables.

3 Results and Discussions

3.1 Output of WetSpass

WetSpass model produces various seasonal and annual spatial distributed hydrological parameters such as grid maps of surface runoff, actual evapotranspiration, groundwater recharge, interception, transpiration, and evaporation. The simulated results of the model were produced in three-phase (for summer, winter, and annual).

3.2 Surface Runoff

WetSpass-model uses different input parameters and variables to simulate the water balance component. Annual and seasonal surface runoff for the Sana catchment was simulated. Surface runoff within the catchment shows variations over an area that depends on the areal rainfall distribution, soil texture, topography, slope, availability of vegetation, and other meteorological parameters. The minimum, maximum, and mean annual surface runoff by the WetSpass model was 0.4 mm/year, 757 mm/year, and 280 mm/year, respectively. From the catchment's total annual precipitation (1358.5 mm), the average yearly surface runoff accounts for 20.6% (280 mm). The summer season (June to September) accounts for about 58.5% of surface runoff, while the winter season accounts for the remaining 41.5% (October to May). Rainfall is higher in the wet season (June to September) than in the dry season (October to May), resulting in more summer runoff than winter runoff because precipitation exceeds soil infiltration capacity. The rainfall is less than the catchment's soils' infiltration capacity during the dry months, resulting in less surface runoff. The runoff spatial distribution map of the Sana catchment is shown in Fig. 6.

3.3 Actual Evapotranspiration (AET)

The overall precipitation does not enter the groundwater system by infiltration and percolation; plants intercept some rainwater, a process called an interception, evaporation from the soil surface, and overland flow during saturation of soil surface stream channel. Actual evapotranspiration is the amount of water lost from plants due to transpiration, transpiration of the vegetative cover, and evaporation from the bare

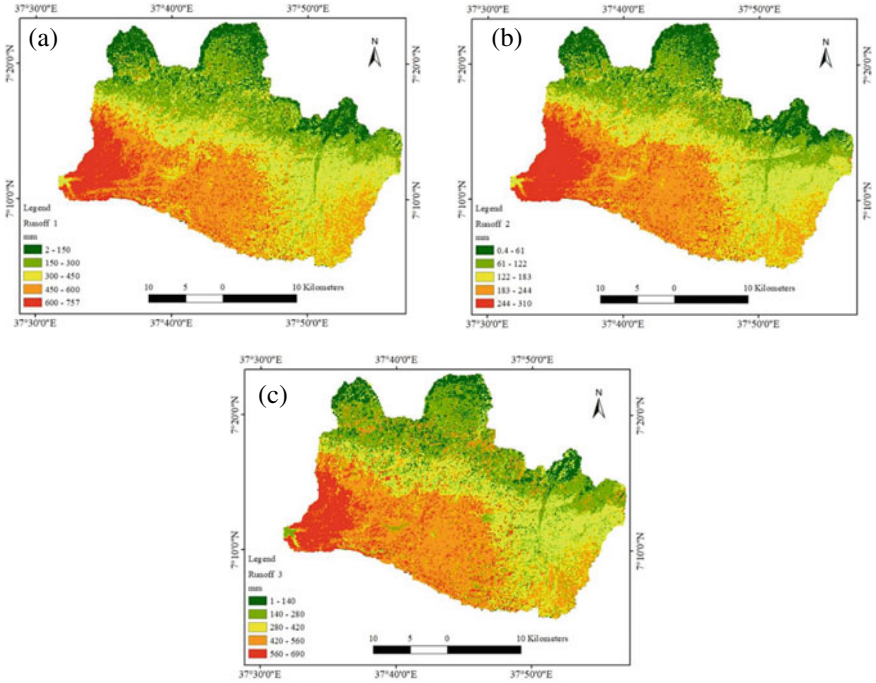

Fig. 6 Study area's surface runoff map **a** summer, **b** winter, and **c** annual

soil between the vegetation. The model computes actual evapotranspiration values. The catchment's mean annual interception is around 35.4 mm, with the lowest and highest values of total annual interception ranging from 0 to 269.4 mm. The amount of precipitation lost due to interception depends on the kind and condition of vegetation, the intensity of plantings, and the season of the year. The ability of vegetative interception values varies according to their class. Forests may intercept more than 20–40% of yearly precipitation, but grasslands ecosystems can intercept 10–20% of total rainfall [13].

According to the model, the average yearly evaporation from bare soil between the plants in the research area is 609 mm. The lowest and maximum values are 0 mm and 1011 mm, respectively. As a result, evapotranspiration plays a key role in loss of moisture within the watershed. This is owing to the catchment's strong sun radiation and dry winds. Vegetation cover average transpiration ranged from 0 to 908 mm, with a mean of 167.2 mm. The simulated output of the WetSpass model reveals that the Sana catchment's minimum, maximum, and long-term mean annual amount of precipitation lost by actual-evapotranspiration is 361, 1102 mm, and 811.6 mm, respectively. Actual-evapotranspiration is the most abundant water balance component in the Sana catchment, accounting for approximately 59.75% of total water balance.

When considering the whole catchment, the highest evapotranspiration values were detected in the topographically lower part of the catchment and vice-versa. And, it is due to the high radiation rate and the dry wind availability in the lower elevated area with their respective land use/covers and soil types in the present study area. Therefore, the simulated model depends on the atmospheric condition, soil texture's ability to hold water, and the availability of vegetation types within the study area.

3.3.1 Groundwater Recharge

Groundwater recharge originates from the land surface through infiltration. The amount of infiltration and percolation of water into the groundwater system depends on different controlling factors such as the slope of an area, land-use/cover, soil texture and contents of organic matter, precipitation intensity and its rate, temperature, and temperature, and groundwater level. The simulated result of the estimated long-term monthly Spatio-temporal distribution of groundwater recharge in the Sana catchment was calculated by subtracting surface runoff and actual-evapotranspiration from the total precipitation using the following equation Eq. (9).

$$R = P - \mathrm{AET} - Qo \tag{9}$$

R is the recharge, P is the precipitation, AET is the evapotranspiration, and Qo is the surface runoff.

According to the WetSpass-simulation model's results, the long-term minimum and maximum values of annual groundwater recharge of the Sana catchment range from 0 to 800 mm with a mean of 267 mm; this accounts for about 19.65% of the total annual precipitation. Nearly 85% or (226.95 mm) of the mean yearly groundwater recharge occurred in the rainy (Jun to September) season, and the dry (October to May) season accounts for the remaining 15% or 40.05 mm. The groundwater recharge map of the Sana catchment is shown in Fig. 7. Table 2 provides an overall summary of the water balance component of the study area, and the model results show that approximately 19.65% of the annual average rainfall goes to recharge the groundwater. At the same time, the remaining portion leaves the study area via evapotranspiration (59.75%) and surface runoff (20.6%).

The controlling factors that made temporal variation are due to different climatological and biophysical input parameters. During summer seasons, the intensity, duration, and number of precipitations are higher than in the winter season, increasing the soil's moisture content, and accelerating groundwater recharge. From the simulated result of the model, there is a high amount of recharge values detected along with loam, and the lowest values were seen with clay soil as discussed in Fig. 3.6; this is due to its physical properties of soil such as hydraulic conductivity, texture, and porosity. Spatial variability in these hydro-physical properties of soil can affect the pathway and water movement rates through the unsaturated zone.

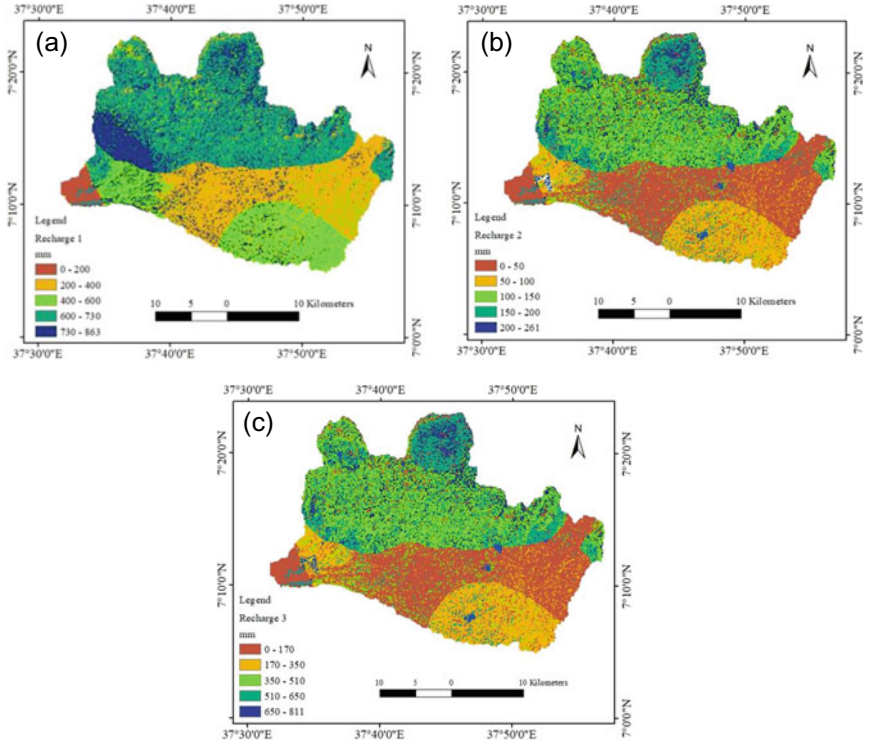

Fig. 7 Study area's groundwater recharge map **a** summer, **b** winter, and **c** annual

Table 2 Summary of the simulated water balance components within the study area

Water balance components	Values in mm			
	Minimum	Maximum	Mean	%
Precipitation	1202.7	1519.9	1358.6	100
Actual-evapotranspiration	361	1102	811.6	59.75
Runoff	2	923	280	20.6
Groundwater recharge	0	800	267	19.65

An area's land use/cover changes significantly affect hydrological processes such as groundwater recharge and evapotranspiration (ET). Considering its response to hydrologic characteristics of an area is very important. Agriculture is the most dominant from the land use/cover of the catchment. And, a high rate of surface runoff with a low amount of groundwater recharge through agricultural dominate areas than forest-covered areas. The characteristic of the area's geological formation and its structural density can also affect the rate and amount of groundwater recharge.

Along the upper part of the study area, dominantly lacustrine sediments and highly weathered rhyolite resulting a higher amount of groundwater recharge, and the lower part of the catchment along with Dino group and Nazret formation receives a lower amount of groundwater recharge. Therefore, the upper part of the catchment gets a higher amount of groundwater recharge and ultimately flow to the lower elevated area forming high discharge springs at the escarpment; this is due to the combined effects of soil type, land use/cover, topography, climatological variability, slope, geology, and lineament density of an area. The groundwater recharge spatial distribution map of the Sana catchment is shown in Fig. 7.

4 Model Verification

Water balance components simulated by WetSpass may be validated using a variety of ways, including river flow monitoring. In the present study, runoff results from the wetspass model were verified by using field-based runoff data. Consequently, the model validation result is presented in Fig. 8. And the significance level is used to assess the observed and WetSpass model-generated results (R^2). The observed and simulated baseflows have a coefficient of determination (R^2) of 0.98, indicating that the consistency between measurements and model simulations is within acceptable limits.

Further, the present study outcome was compared with prior studies conducted in adjacent areas with similar hydro-meteorological settings. The study was conducted by [22] in the Abya-Chamo lakes basins, Ethiopia, and [23] showed the study in Bilate catchment, southern Ethiopia. Both mentioned above catchments are the adjacent catchment to the present study area, and the study's results are very close to the current simulation in the Sana catchment, Ethiopia. In light of the constraints of

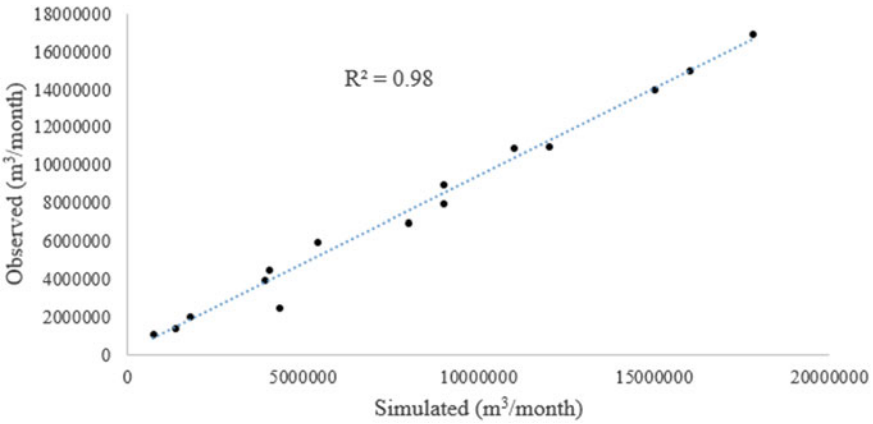

Fig. 8 Comparison between observed data in Sana gauge station and simulated flow data

hydrological and meteorological data, as well as the variable topography and rainfall in the current research region, the WetSpass model simulations and observed flow data were found to be relatively accurate.

5 Conclusions

The WetSpass model, which is GIS-based, is a geographically distributed physical model that considers meteorological, hydrological, and biophysical factors. The input parameters were prepared using GIS tools and remote sensing data. The WetSpass model was used to successfully define recharge regions, actual evapotranspiration, and surface runoff. The groundwater recharge zone for this study was defined using the study area's site-specific hydrologic, hydro-geologic, hydrometeorology, and physiographic data. The WetSpass model successfully simulated groundwater recharge estimation in the Sana watershed for yearly and seasonal circumstances. According to the model's simulated results, groundwater recharge and other water balance components fluctuate geographically and temporally owing to variations in the catchment's dispersed soil texture, land-use/cover, physiography, slope, and hydro-meteorological characteristics.

The integrated GIS and remote sensing techniques with WetSpass model results indicate a high amount of groundwater recharge potential corresponds to alluvial plains, especially around Wagebeta depression, lacustrine sediments deposit, and fractured valleys high lineaments density and gentle slope areas concerning land use/cover and soil texture. Based on the model result, the summer, winter, and mean annual long-term groundwater recharge of the Sana catchment were 189 mm, 78 mm, and 267 mm, respectively. The minimum and maximum values of groundwater recharge were detected to be 0 mm and 863 mm. From the paper result, 70.8% of the mean annual precipitation (1358.6 mm) occurs in the summer seasons and 29.2% (1358.6 mm) in the winter season. In contrast, 19.65% of total annual rainfall (1358.6) percolate to the groundwater system.

The mean annual evapotranspiration and surface runoff values of the Sana catchment are 811.6 mm and 280 mm, respectively. At the same time, 59.75% of total precipitation is lost through evapotranspiration, and 20.6% is through surface runoff. The sensitivity analysis of the different input variables was conducted, and most of the variables are highly sensitive in the Sana catchment. From the model results, rainfall, potential evapotranspiration, soil type, land use/cover, slope, hydro-climatological parameters of the study area are the essential terms affecting the amount and rate of the different water balance components. The present study's output will be helpful for planners and administrators for sustainable groundwater development in the current study area.

Acknowledgements The authors would like to express their appreciation to the Department of Geology, Arba-Mich University, for their permission to pursue this research. Further, the authors

would also like to thank the Ethiopian National Meteorological Agency, Ministry of Water and Irrigation, and Geological Survey of Ethiopia for their kindness in carrying out this research.

References

1. Shanableh A, Merabtene T (2015) Geomatics for mapping of groundwater potential zones in the northern part of the United Arab Emiratis— Sharjah City. Sens Spatial Inf Sci. 581–586 (2015). https://doi.org/10.5194/isprsarchives-xl-7-w3-581-2015
2. Arefayne SH, Abdi S (2015) Groundwater exploration for water well site locations using geophysical survey methods. J Waste Water Treat Anal 7(1):1–7. https://doi.org/10.4172/2157-7587.1000226
3. Karimi P, Bastiaanssen WGM (2013) Spatial evapotranspiration, rainfall, and land use data in water accounting—Part 1: Rev Acc Hydrol Earth Syst Sci. https://doi.org/10.5194/hess-19-507-2015
4. Fenta AA, Kifle A, Gebreyohannes T, Hailu G (2014) Spatial analysis of groundwater potential using remote sensing and GIS based multi-criteria evaluation in Raya Valley, northern Ethiopia. Hydrogeol J 23(1):195–206. https://doi.org/10.1007/s10040-014-1198-x
5. Sykes JF (2006) The impact of climate change on groundwater 28.1. Water Resour 28:1–42
6. Meresa E, Taye G (2018) Estimation of groundwater recharge using GIS-based WetSpass model for Birki watershed, the eastern zone of Tigray, Northern Ethiopia. Sustainable Water Res Manag 5(4):1555–1566. https://doi.org/10.1007/S40899-018-0282-0
7. Obuobie E (2008) Estimation of groundwater recharge in the context of future climate change in the White Volta River Basin, West Africa. https://bonndoc.ulb.uni-bonn.de/xmlui/handle/20.500.11811/3712
8. Tilahun K, Merkel BJ (2009) Estimation of groundwater recharge using a GIS-based distributed water balance model in Dire Dawa, Ethiopia. Hydrogeol J 17:1443–1457. https://doi.org/10.1007/s10040-0090455
9. Yongxin XU, Beekman H (2018) Review: groundwater recharge estimation in arid and semi-arid southern Africa. Hydrogeol J 27:1–15. https://doi.org/10.1007/s10040-018-1898-8
10. Dragoni W, Sukhija BS (2013) Climate change and groundwater: a short review. Geolog Soc London, Spec Publ 288:1–12
11. Ahmadi T, Ziaei AN, Davary K, Faridhosseini A, Izadi A (2012) Estimation of groundwater recharge using various methods in Neishaboor Plain. In: Iran C Hadi (ed) Groundwater modelling and management under uncertainty Taylor & Francis Group London vol 9, p 15
12. Scanlon BR, Healy RW, Cook PG (2002) Choosing appropriate techniques for quantifying groundwater recharge. Hydrogeol J 10:18–39. https://doi.org/10.1007/s10040-0010176-2
13. Christoph S, Kallioras A, Piepenbrink M, Pfletschinger H, Al-Ajmi H, Engelhardt I, Saud M (2011) New approaches to quantify groundwater recharge in arid areas. Int J Water Resour Arid Environ 1:33–37
14. Batelaan O, De Smedt F (2007) GIS-based recharge estimation by coupling surface-subsurface water balances. J Hydrol 337(3–4), 337–355. https://doi.org/10.1016/j.jhydrol.2007.02.001
15. Mogheir Y, Ajjur S (2013) Effects of climate change on groundwater resources (Gaza strip case study). Int J Sustain Energy Environ 1(8)136–149
16. Graf R, Jan P (2014) Estimation of shallow groundwater recharge using a GIS-based distributed water balance model. Quaest Geograph 33(3)
17. Gebreyohannes T, Smedt FD, Walraevens K, Gebresilassie S, Hussien A, Hagos M, Gebrehiwot K (2013) Application of a spatially distributed water balance model for assessing surface water and groundwater resources in The Geba Basin, Tigray, Ethiopia. J Hydrol 499:110–123. https://doi.org/10.1016/j.jhydrol.2013.06.026

18. GH Kahsay, Gebreyohannes T, Gebremedhin MA (2019) Spatial groundwater recharge estimation in Raya basin, Northern Ethiopia: an approach using GIS based water balance model. Sustain Water Resour Manag 5:961–975. https://doi.org/10.1007/s40899-018-0272-2
19. Zeabraha A, yohannes T, Mariyam F (2020) Application of a spatially distributed water balance model for assessing surface and groundwater resources: a case study of Adigrat area, Northern Ethiopia. Sustain. Water Resour Manag 6:73. https://doi.org/10.1007/s40899-020-00424-5
20. Aish AM (2010) Estimation of water balance components in the Gaza Strip with GIS based WetSpass model. Civ Environ Res 6:11
21. Armanuos AM, Negm A, Yoshimura C, Valeriano OCS (2016) Application of WetSpass model to estimate groundwater recharge variability in the Nile Delta aquifer. Arab J Geosc 9:553. https://doi.org/10.1007/s12517-016-2580-x
22. Dagnachew DM (2018) Evaluation of surface and Groundwater availability under changing climate in abaya-chamo lakes basin, Ethiopia. Unpublished PhD thesis, Addis Ababa University, Ethiopia
23. Bitsiet DA (2015) groundwater recharge estimation using wetspass model in upper Bilate catchment: South-Western escarpment of Main Ethiopian Rift. Unpublished M.Sc thesis, Addis Ababa University, Ethiopia

Relational Study of $PM_{2.5}$ Surface Concentration with MODIS Level 3 AOD Data Over India

Haritha P. Scaria, Premkumar Avanthika, Anna Mary Jose, J. S. Alisa, Anagha Sadasivan, and George K. Varghese

Abstract $PM_{2.5}$, a principal constituent of particulate matter, is the most deadly form of air pollution attributing to significant number of health problems. For a country like India with a vast topographical distribution, the existing number of ground-based stations for monitoring of pollutant concentration is inadequate. With the advent of technology, remote sensing-based monitors have been able to capture the pollutant concentrations of any region. Using a combined Dark Target and Deep Blue (DTB) Terra and Aqua Moderate Resolution Imaging Spectroradiometer (MODIS) Level 3 aerosol optical depth (AOD) product and surface $PM_{2.5}$ measurements from Central Pollution Control Board (CPCB) monitors, we provide a decade (2010–2020) of assessment of AOD–$PM_{2.5}$ relationships all over India by graphical analysis and simple linear regression analysis. This study analyse the factors which can affect the relationship observed between the two datasets over various regions and at different times. Region-wise, state-wise and season-wise analyses for correlation were carried out. In addition, analyses were also carried out based on pollutant concentration levels and for 2020 lockdown period. Regardless of the classification, the two datasets were found to have a high correlation to one another. In general, Northern regions tend to show higher correlations, however the relation was found to be independent of concentration of pollutants. Post-monsoon and winter season showed comparatively higher correlation. The regression analysis for a general equation all over India yielded a linear equation with $R^2 = 0.92$ and a root mean square error of 26.84 $\mu g/m^3$. Overall, our evaluation shows that MODIS Level 3 data estimates of $PM_{2.5}$ on an annual time scale using simple linear models are reliable.

Keywords $PM_{2.5}$ · CPCB · MODIS Level 3 · Air quality monitoring · Aerosols

H. P. Scaria · P. Avanthika · A. M. Jose · J. S. Alisa · A. Sadasivan · G. K. Varghese (✉)
National Institute of Technology, Calicut, India
e-mail: gkv@nitc.ac.in

L. Nandagiri et al. (eds.), *Recent Advances in Civil Engineering*, Lecture Notes in Civil Engineering 256, https://doi.org/10.1007/978-981-19-1862-9_7

1 Introduction

Air quality monitoring has become of utmost importance with increasing pollution trends across the world. Dangerous effects of pollution have led to the need of monitoring various pollutants in the atmosphere. Among the various air pollutants, those that are amenable to long-range transport without any transformation, like very fine particles are of particular concern. $PM_{2.5}$ (particulate matter with particle size less than or equal to 2.5 μm), a principal constituent of particulate matter, is the most deadly form of air pollution attributing to significant number of premature deaths and also causing other health problems due to their capability to enter deep into the organs like lungs and brain and the bloodstreams [1]. It is a significant component contributing to deterioration of air quality over the Indian subcontinent. There are studies linking the increased mortality over the Indian region to particulate pollution [2]. Hence there is a need for monitoring near-ground concentration of $PM_{2.5}$ with extensive regional coverage.

In India, ground based measurements are done by the Central Pollution Control Board (CPCB). This ground-based monitoring network consists of more than 230 continuous monitoring sites and over 650 manual monitoring sites [3] deployed in the urban centres. Even though the ground-based monitoring sites seems large in number, it is not sufficient for air quality management. Based on the CPCB guidelines [4] and 2011 census [5], it is estimated that there is a need for 4000 continuous monitoring stations (2800 in the urban areas and 1200 in the rural areas of the districts) to spatially, temporally, and statistically represent the pollution in the urban and the rural areas of India [6].

Measurement of exposure to air pollutants in any given area with accuracy is a demanding task because of the extremely complex extraction processes, scarce ground monitoring in many regions [7], high cost of setting up such ground monitoring stations, and interrupted measurements in many of the setup stations throughout the year. The location of available networks adds up to the disadvantage of using data from ground monitors to estimate exposure. Monitoring stations are mainly located in areas of high air pollution and population density. Thus, the measurements from monitoring stations that are positioned primarily for regulatory purposes may not include the areas that is representative of either individual or community-level exposure. Therefore, most epidemiological studies of air pollution are based in urban areas mainly owing to this sample size considerations and also because of the design of monitoring networks. Ambient monitors also lack full temporal coverage for a range of pollutants in addition to the lack of spatial coverage [8]. These limitations render surface measurements inadequate for air quality management and hence restricts the epidemiological community from using these data alone for the consistent generation of indigenous evidence of air pollution health impacts [9, 10]. For these reasons, there is a need to use other sources like satellite measurements to acquire estimates of exposures across India.

Satellite data concentrates on upper atmosphere measurements. Capable of retrieving aerosol information at regional scale (>1000 km) and fine spatial resolution (10 km), satellite remote sensing has showed its value for the air quality community, both in areas with sparse ground observations [11] and in the denser networks of ambient monitors.

In India, CPCB stations that measure pollutant concentration are spread mostly across urban centres and are scarce in remote areas, hence evaluating pollutant concentration at desired locations may not be feasible. Compared to ground measurements, satellite imagery, proves to be an essential aid in monitoring aerosols and their transport patterns owing to their large spatial coverage and reliable repeated measurements [12]. Hence, a comparative analysis of both ambient air quality data and satellite data can provide reliable data and information to observe pollutant emissions and study how pollution episodes evolve over hours, days, and weeks, interacting with weather patterns as they move across the landscape.

This paper presents a relational study of $PM_{2.5}$ surface concentration with MODIS Level 3 AOD data all over India for a decade (2010–2020). A graphical analysis of the data collected is made to study the various factors that can influence the relation between CPCB and satellite measured values. For the analyses, year-wise, month-wise, state-wise, season-wise, concentration-wise, and region-wise categorization of data was done. The influence of the COVID-19 lockdown was also analysed. Although data for one decade was used for obtaining the relationship between AOD and the ground monitored $PM_{2.5}$, due to the enormity of data, the last two years data (2019–20) only were used for some of the other relational analyses.

2 Data Sets

2.1 Satellite AOD Data

The study utilized satellite data from Terra and Aqua Moderate Resolution Imaging Spectroradiometer (MODIS) collection 6.1 (C6.1). These MODIS instruments provide two daytime observations (10:30 a.m. from Terra and 1:30 p.m. from Aqua) [13]. The known official aerosol retrieval algorithms for the MODIS products includes the Dark Target (DT) algorithm over land and ocean and the Deep Blue (DB) algorithms over land. Further, to enhance the data coverage, a new dataset DTB (a combination of DT and DB) was introduced over land by a simple approach that leverages the strengths of DT and DB algorithms [14].

MODIS has provided two official aerosol products based on the above algorithms. Level-3 daily (MxD08_D3, where x represents O for Terra and Y for Aqua), eight-day (MxD08_E3), and monthly (MxD08_M3) products at a $1° \times 1°$ horizontal resolution and Level-2 daily (swath) products at 10-km (MxD04_L2) and 3-km (MxD04_3K) resolutions are two kinds of long-term and global coverage aerosol

products operationally provided by MODIS. All of the Level 3 aerosol products provide three datasets: DT, DB and DTB datasets [14].

On a global scale, among the collection 6.1 Level 3 products DTB datasets provided maximal data samples along with showing the highest correlations with AERONET AOD data among the three datasets. Also, among the collection 6.1 products, DTB products were found more apt compared to the other two for South Asia. As a whole, DTB products were found to show the correct aerosol changes more precisely and were strongly recommended for studies related to aerosols at the global scale [15].

In this study, we made use of the DTB Level 3 daily (MxD08_D3) MODIS AOD data at 550 nm measured at 10 km resolution processed as the collection 6.1 data set from both Aqua and Terra. The time averaged values of the daily products for the annual data for 2010–2020 was collected from both Aqua and Terra, and the mean of the both was used for the work. The same satellite data product was used for the monthly datasets for the years 2019 and 2020. The required MODIS AOD data used were collected from the Giovanni online data system, developed and maintained by the NASA GES DISC [16].

2.2 Surface Measurements

The surface concentrations of $PM_{2.5}$ were collected from CPCB. CPCB is a statutory organization that serves as a field formation and also provides technical services to the Ministry of Environment and Forests through the provisions of the Environment (Protection) Act, 1986. The CPCB collects, compiles, and publishes technical and statistical data relating to water and air pollution to improve their quality. These measures devised are for the effective prevention, control, or abatement of pollutants. The CPCB stations monitor $PM_{2.5}$ mass concentrations using the Tapered Element Oscillating Microbalance (TEOM). This instrument utilizes a vibrating glass tube whose frequency depends on the mass of $PM_{2.5}$ deposited on it.

In India, there are over 230 continuous monitoring stations set up by CPCB. Figure 1 shows the 164 CPCB stations taken for the study. In addition to the deficiency of not providing continuous data, the manual monitoring sites sample only twice a week. Hence only the data from automatic monitoring stations were used for this study. The annual averages of $PM_{2.5}$ concentrations for a decade from 2010 to 2020 and monthly averages for the years 2019 and 2020 were collected from the CPCB website.

3 Methodology

Methodology adopted is simple linear regression. This study looks into the cases that can possibly affect the relation between $PM_{2.5}$ ground concentration and satellite

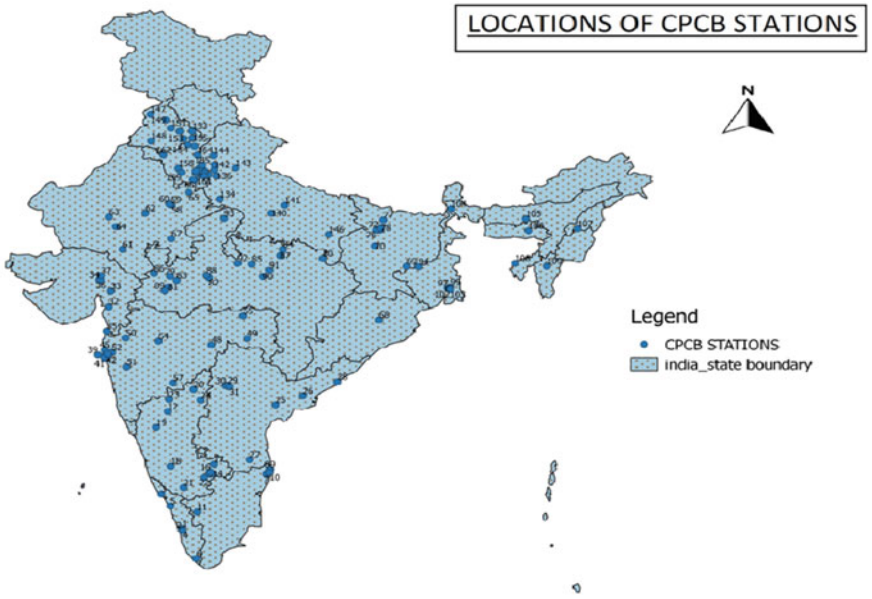

Fig. 1 Locations of 164 CPCB stations across India

derived AOD along with an attempt to generate a simple general equation explaining the relation. Figure 2 summarizes the steps followed in this study.

The steps included are:

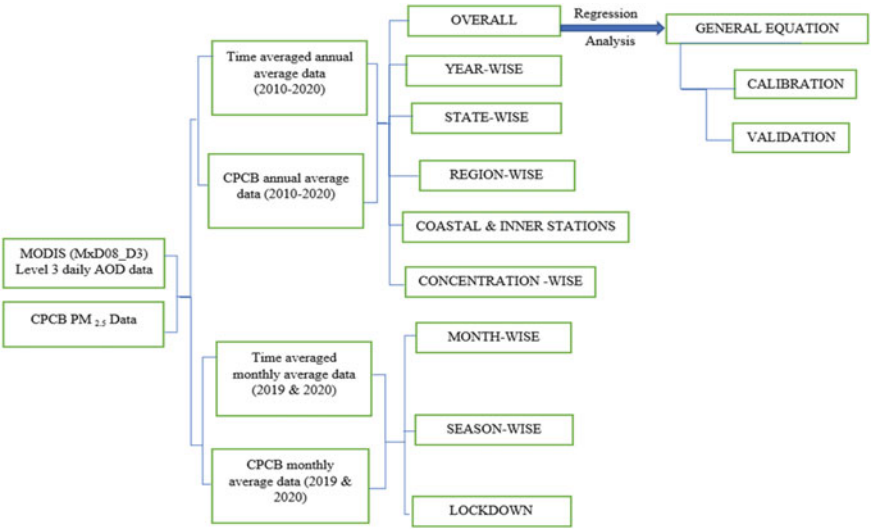

Fig. 2 Flow chart depicting steps followed

1. In this study, we made use of the DTB Level 3 daily (MxD08_D3) MODIS AOD data at 550 nm data set from both Aqua and Terra and the mean of the two were considered. Ground measurements were collected from CPCB.
2. The annual average data from CPCB and satellite for the year 2010–2020 and the monthly average for the years 2019 and 2020 was collected for the 164 selected CPCB stations spread all over India.
3. Then a graphical analysis of the data was done by categorizing the data into overall, year-wise, month-wise, state-wise, region-wise, concentration-wise, season-wise, lockdown period, coastal and inner stations. The R^2 values were tabulated.
4. Then from the overall data a general equation relating annual average $PM_{2.5}$ concentration and AOD was obtained using simple linear regression analysis which was calibrated and validated.
5. The annual average datasets from 2010 to 2019 were taken for the calibration with a total of 300 observations. Since most of the observations were clustered under specific intervals, the total CPCB data was classified into different classes with a step size of 2; the lowest interval being 20-22 $\mu g/m^3$ and the highest interval being 118-120 $\mu g/m^3$. This approach was adopted to minimize the error and ensure uniform accuracy at different concentrations. A linear scatter plot was drawn with the mean of the CPCB values from each interval and the corresponding mean satellite data, with the CPCB values on the Y axis and the satellite observed values on the X axis. The best fit line for this scatter plot was taken as the general equation.
6. For validation, the obtained equation from the previous step was used to predict the CPCB data values for the rest of 2019 and 2020. The correlation values, standard error values, F-test and t-test values were obtained using the data analysis tool of MS Excel.
7. Also, various statistical evaluators like the Mean Absolute Error (MAE), Root Mean Square Error (RMSE) and Mean Bias Error (MBE) were manually calculated for checking the prediction accuracy. These evaluators were calculated as follows:

$$\mathrm{MBE} = \frac{1}{N}\sum_{i=1}^{N}(c_{p,i} - c_{o,i}) \tag{1}$$

$$\mathrm{MAE} = \frac{1}{N}\sum_{i=1}^{N}\left|c_{p,i} - c_{o,i}\right| \tag{2}$$

$$\mathrm{RMSE} = \sqrt{\frac{1}{N}\sum_{i=1}^{N}(c_{p,i} - c_{o,i})} \tag{3}$$

where MBE is the mean bias error.
MAE is the mean absolute error.

RMSE is the root mean square error.
N = Number of observations.
$c_{p,i}$ is the *i*th predicted value.
$c_{o,I}$ is the *i*th observed value.

An additional test was conducted to assess the dependability of the equation. To evaluate air quality models, one index factor of two (FAC2) test was put forth by Chang and Hanna [17], in order to correlate derived data directly with the observed data. According to this, a model performance is considered good if the proportion of data that falls within the range of $0.5 \leq C_P/C_o \leq 2$ is equal to or more than 0.5. The derived and observed datasets were utilized for the test, and the results were noted.

4 Results and Discussion

4.1 Graphical Analysis

Graphical evaluation of MODIS AOD was performed against $PM_{2.5}$ from CPCB. The total datasets were divided and studied under different categories in order to understand the relation better. The study yielded the following results.

Overall Graph. The overall graph plotted between CPCB and satellite data over a decade (2010–2020) showed a significant correlation with R^2 value of 0.83 as shown in Fig. 3a. A rough estimate of all the datasets together thus ensures a significant correlation. The procedure is thus extended to other categories.

Year-wise Graphs. Different temporal divisions were done to study the datasets in which graphs were plotted for individual years from 2015 to 2020 to check the

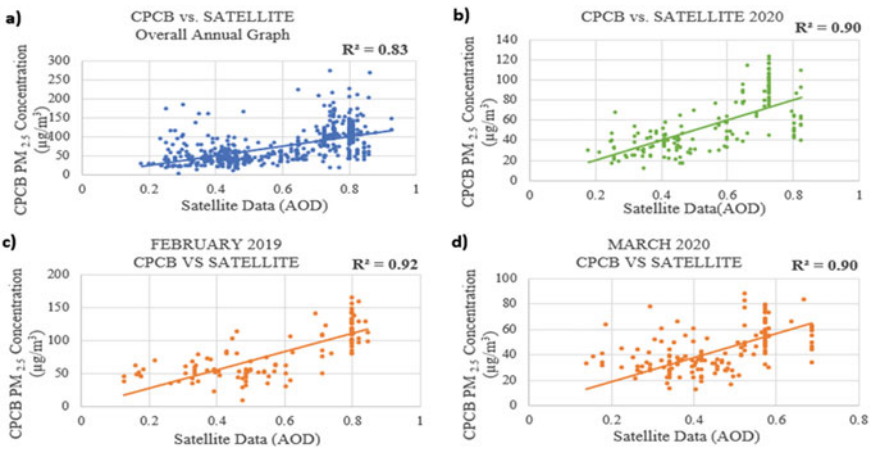

Fig. 3 $PM_{2.5:}$ Comparing concentrations ($\mu g/m^3$) from CPCB and MODIS satellite data: **a** overall annual graph, **b** year 2020, **c** February 2019, **d** for March 2020

Table 1 R^2 values for year-wise graphs

Year	2015	2016	2017	2018	2019	2020
R^2	0.85	0.84	0.69	0.82	0.91	0.90

Table 2 R^2 values for month-wise graphs for the year 2019 and 2020

Month	Jan	Feb	Mar	Apr	May	Jun	Jul	Aug	Sep	Oct	Nov	Dec
2019	0.90	0.92	0.89	0.81	0.77	0.75	0.81	0.81	0.87	0.90	0.91	0.83
2020	0.86	0.89	0.90	0.78	0.74	0.80	0.76	0.72	0.85	0.81	0.88	0.84

correlation. In India $PM_{2.5}$ monitoring (CPCB) started in 2009, but the network expanded nationally only after 2015–2016 [9]. Thus, due to the lack of adequate CPCB data for individual year from 2010 to 2014, year-wise graphs were not plotted for those years. Table 1 shows the results obtained from the year-wise graphs. The R^2 values varied between 0.82 and 0.91, except for 2017, where it was observed to be 0.69. Of all these years, 2019 showed the highest correlation of R^2 value of 0.91. Figure 3b shows the graph plotted for year 2020.

Month-wise Graphs. As the second set of temporal divisions, the datasets were categorised month-wise and analyzed for the years 2019 and 2020, the years when the highest correlations were noticed. Table 2 gives the results obtained from the month-wise graphs. The R^2 values varied from 0.72 to 0.92 for all the months of 2019 and 2020 indicating good correlation. February 2019 showed the highest correlation of 0.92 amongst all the observations. Figure 3c and d shows the graphs plotted for February 2019 and March 2020 respectively. The starting months and the ending months of the year tend to have a higher correlation compared to the remaining months and that can be attributed to the favorable conditions for dispersion during the middle months of the year in some regions in India [9].

Season-wise Graphs. As for the next analysis, monthly datasets from 2019 and 2020 were categorised seasonally and graphs were plotted. Figure 4 shows the graphs plotted for the season-wise analysis. The seasons considered are as follows: winter (December-February), pre-monsoon (March–May), monsoon (June–September), and post-monsoon (October–November). The R^2 value varied from 0.71 to 0.86 for season-wise analysis for the year 2019–2020, indicating a significant correlation. The graphs plotted for post-monsoon and winter seasons showed a comparatively higher correlation than the rest of the seasons with R^2 value 0.86. The highest correlations observed during winter and post monsoon seasons could be attributed to the decreased cloud coverage and the reduced wind velocity causing unfavourable conditions of dispersion [18].

Lockdown Period. The results of graphs plotted for before, during and after lockdown period showed significant relations with R^2 values ranging from 0.55–0.85 except for the post lockdown period. A decreasing trend for the R^2 values is seen from pre-lockdown period to post lockdown period. The results are summarized in Table 3.

Table 3 R^2 value for pre-lockdown, lockdown and post-lockdown graphs

Period	Pre-lockdown	Lockdown	Post-lockdown
R^2	0.86	0.76	0.55

The temporal division wise analysis showed that the starting and ending months of the year are showing higher correlation than rest of the months. Along with the temporal divisions, spatial divisions were also studied. The data were classified regionally (north and south), state-wise and as coastal and inner stations for observing any patterns.

Region-wise Graphs. The total stations across India were divided into two regions with respect to Tropic of Capricorn, passing through the centre of the country. The region to the north of Tropic of Capricorn was considered as northern region and that to south was considered as southern region. The results obtained from the region wise analysis of correlation between CPCB and satellite data shows that the stations under the northern region of India tend to show better correlation than that of southern stations. Figure 5a and b depicts the graph plotted for the southern and northern regions respectively with northern region having comparatively higher correlation of 0.85. This observation can possibly be due to the greater number of ground stations across many states included in the northern region.

State-wise Graphs. Stations were grouped according to state boundaries and the observations were noted. Table 4 depicts the results observed for the state-wise correlation analysis. Out of all the studied states, Punjab, Haryana, Chandigarh, Northeast India, Orissa, Jharkhand, Kerala, and Andhra Pradesh showed a high correlation with R^2 values above 0.9. Apart from states like Gujarat, Karnataka, and Tamil Nadu that have R^2 values below 0.7, all other states showed a significant correlation with R^2

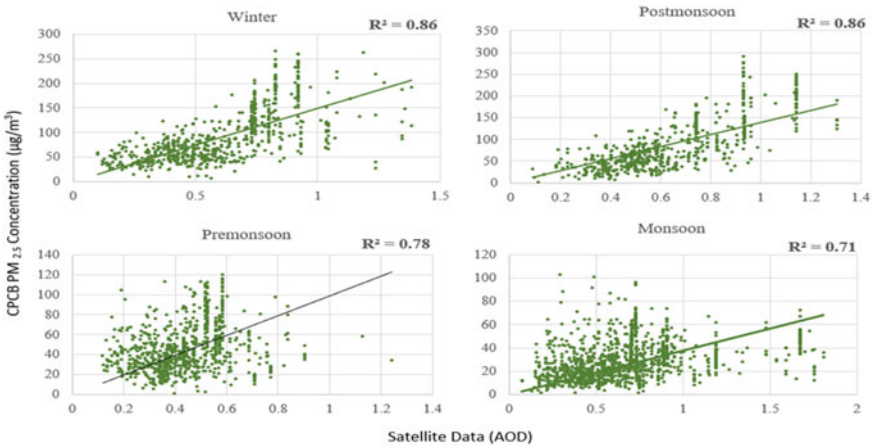

Fig. 4 $PM_{2.5}$: Comparing concentrations ($\mu g/m^3$) from CPCB and MODIS satellite data: winter season, post-monsoon season, monsoon season and pre-monsoon season (from top left in clockwise direction)

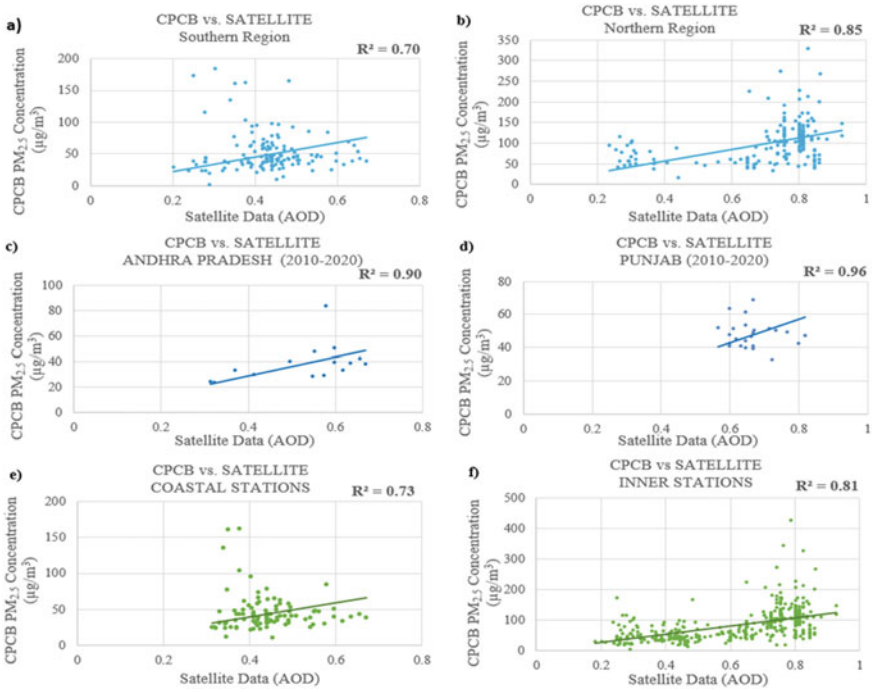

Fig. 5 $PM_{2.5:}$ Comparing concentrations ($\mu g/m^3$) from CPCB and MODIS satellite data: **a** southern region, **b** northern region, **c** Andhra Pradesh, **d** Punjab, **e** Coastal stations and **f** Inner stations

values above 0.7. Many states in the northern region of India showed very high correlation, whereas only some states in the southern region showed similar correlation. Figure 5c and d gives the graphs plotted for Andhra Pradesh ($R^2 = 0.90$) and Punjab ($R^2 = 0.96$) respectively.

Most of the states that are a part of the Indo Gangetic Plains, which is a very highly polluted area due to the dense population that contributes to the continuous emission of pollutants from a range of anthropogenic activities, coupled with unfavorable topography [9], showed a very high correlation between the CPCB concentration and the satellite values.

Inner and Coastal Stations Graphs. Though the R^2 values of both coastal and inner stations showed good correlation between the satellite and the CPCB values, the inner stations had better correlations ($R^2 = 0.81$) than the coastal stations ($R^2 = 0.73$) as shown in Fig. 5e and f. The difference observed between the R^2 values of the coastal regions and the inner region could be due to the presence of the sea near coastal stations. The sea breeze could affect the movement of pollutants [19]. It can also be due to the lesser number of observations of coastal stations compared to the inner stations.

The overall results of region-wise, state-wise and coastal and inner stations-wise analysis showed a significant correlation in most cases. The season wise analysis

Table 4 R^2 value for state-wise graphs

States	R^2	No. of observations
Kerala	**0.95**	9
Tamil Nadu	0.70	22
Karnataka	0.59	34
Andhra Pradesh	**0.90**	15
Telangana	0.90	12
Maharashtra	0.89	60
Gujarat	0.64	14
Rajasthan	0.84	40
Madhya Pradesh	0.80	40
Bihar	0.84	22
West Bengal	0.83	28
Delhi	0.71	121
Punjab	**0.96**	24
Uttar Pradesh	0.89	49
Haryana and Chandigarh	**0.96**	19
Northeast, Orissa and Jharkhand	**0.94**	12

showed highest correlations during winter and post monsoon seasons and the stations in northern region and the states in northern parts of India showed better correlation in the region-wise and state-wise analysis respectively. This could also be attributed to the higher concentration of $PM_{2.5}$ pollution during the winter and post monsoon seasons generally and also in northern parts of India compared to other regions [19]. Thus, a concentration-wise analysis was done to check if correlation was dependent on concentration.

High and Low CPCB Pollutant Concentration Graphs. The mean of the CPCB datasets was considered as the threshold value for concentration-wise analysis. Thus, the values below 65 $\mu g/m^3$ were considered low concentration and that above were considered as high concentration. The results obtained for analysis of correlation among low and high concentration values showed a similar significant correlation of $R^2 = 0.89$ as shown in Fig. 6. This indicates that regardless of the concentration of pollutants there is significant correlation between the satellite and CPCB measured values of $PM_{2.5}$. This means, in spite of whether a region is having many polluting industries or is a rural settlement, the satellite measured $PM_{2.5}$ have good correlation with the CPCB measured values. Since most of the cases taken showed a significant relationship between the two datasets, a general relation between the ground annual average value of $PM_{2.5}$ and the satellite AOD value for the whole of India was derived. A simple linear regression model was established to explain the ground measurements by using satellite measurements.

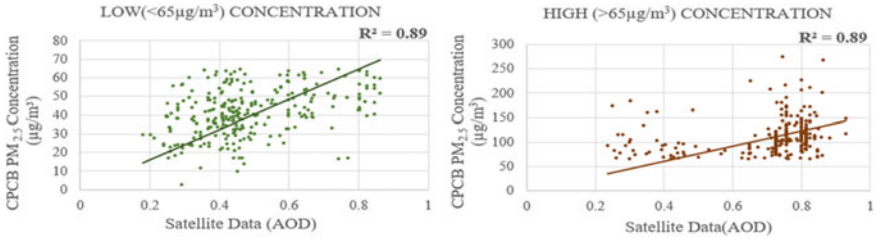

Fig. 6 $PM_{2.5:}$ Comparing concentrations ($\mu g/m^3$) from CPCB and MODIS satellite data: for low concentration (left), for high concentration

4.2 Regression Analysis

General Equation. The final linear equation relating annual average value of $PM_{2.5}$ and satellite AOD was obtained as given in Eq. (4).

$$PM_{2.5} = 131.54 \times AOD \tag{4}$$

The R^2 value of the fit was 0.92 which indicates that the equation accounts for about 92% of the CPCB value's variance. Figure 7a represents the graph of the equation obtained.

Prediction Accuracy. To validate the obtained equation, a plot between the observed and the modelled values was drawn, and it showed a significant relation with $R^2 = 0.91$. Figure 7b represents the validation plot between the predicted and observed values.

A regression analysis of the same gave the standard error as 25.31 $\mu g/m^3$, indicating a typical size of the residuals. The value obtained for the distance between the data points and fitted values are considerable compared to the range of chosen datasets. The t-stat and p-value obtained were within the limits for a good model. The p-value is very miniscule proving Eq. (4) to be statistically significant. Also, the Significance F value, or the p-value for the F-test of overall significance, was obtained as a very small value than any reasonable significance level. Consequently,

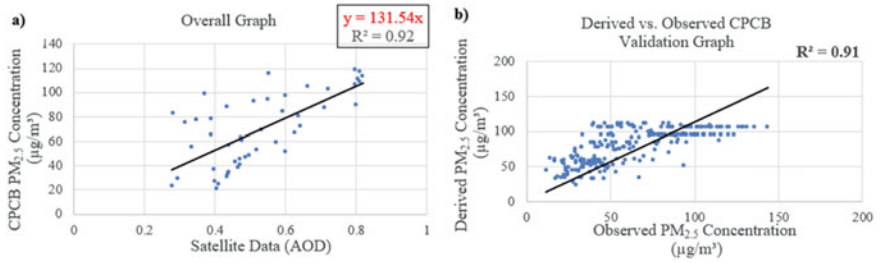

Fig. 7 Graph plotted for **a** calibration of equation, **b** validation of equation

Table 5 Overall regression statistics (2019–2020)

R square	0.91
Standard error	25.31 μg/m^3
Observations	239
F	2316.16
Significance *F*	2.53E−124
t Stat	48.13
p-value	1.21E−124

Table 6 Error indices

MAE (μg/m^3)	21.46
RMSE (μg/m^3)	26.84
MBE (μg/m^3)	−16.29

we can conclude that the equation is statistically significant. Table 5 summaries the regression statistics for predicted datasets.

The Mean Absolute Error was obtained as 21.46 μg/m^3 and the Root Mean Square Error was obtained as 26.84 μg/m^3. Mean Bias Error was computed to be −16.29 μg/m^3, which shows that the equation has a tendency to underestimate the value. Table 6 summaries the calculated error indices.

The FAC2 test was also done to check the reliability of the model. 0.85 proportion of the data falls under the range of $0.5 \leq C_P/C_o \leq 2$ which satisfies the condition for the model performance to be considered good (the proportion of data which falls within the range of $0.5 \leq C_P/C_o \leq 2$ should be ≥ 0.5 to consider it a good model performance).

5 Conclusion

In the reported study we attempted a relational analysis of $PM_{2.5}$ surface concentration with MODIS Level 3 AOD data all over India for a decade (2010–2020). The Satellite measured data over India showed good correlation with ground monitored data. The correlation was not seen to be significantly influenced by the factors considered. This would mean that a single equation can be adopted to relate AOD to ground-level $PM_{2.5}$. Although the simple linear equation that was derived tends to underestimates the actual ground concentration of $PM_{2.5}$, 85% of the simulated values was found to fall within FAC2 of the observed value. That is, in general, the equation can be utilized for rough estimates of ground $PM_{2.5}$ for all over India. Thus, such a model will help in circumventing the issues associated with the shortage of ground-monitoring stations to a great extent. It has a potential to make $PM_{2.5}$ monitoring cheap leading to better environmental quality.

Acknowledgements We wish to acknowledge Central Pollution Control Board (CPCB) for their open access to $PM_{2.5}$ data and also the Giovanni online data system, developed and maintained by the NASA GES DISC for making the data available for public use from where the required MODIS AOD data used to carry out the study were collected.

References

1. Navinya CD, Vinoj V, Pandey SK (2020) Evaluation of PM2.5 surface concentrations simulated by NASA's MERRA version 2 aerosol reanalysis over india and its relation to the air quality index. Aerosol Air Qual Res 20(6):1329–1339
2. Apte JS, Marshall JD, Cohen AJ, Brauer M (2015) Addressing global mortality from ambient PM2.5. Environ Sci Technol 49(13):8057–8066
3. Central Pollution Control Board (2020) Government of India, "CPCB," [Online]. Available: https://cpcb.nic.in/. Accessed 15 Sept 2020
4. Central Pollution Control Board (2003) Ministry of environment and forests, Guidelines for ambient air quality monitoring, National Ambient Air Quality Monitoring Series: NAAQMS
5. Ministry of Home Affairs (2020) Government of India, Census of India—Office of the Registrar General and Census Commissioner, India [Online]. Available: https://censusindia.gov.in/2011common/censusdata2011.html. Accessed 15 Sept 2020.
6. URBANemissions.info [Online]. Available: https://urbanemissions.info/india-air-quality/india-ambient-monitoring-data/. Accessed 15 Sept 2020
7. Shaddick G, Thomas ML, Green A, Brauer M, Donkelaar AV, Burnett R, Chang HH, Cohen A, Dingenen RV, Dora C, Gumy S, Liu Y, Martin R, Waller LA, West J, Zidek JV, Prüss-Ustün A (2017) Data integration model for air quality: a hierarchical approch to the global estimation of exposures to ambient air pollution. J Roy Stat Soc: Ser C (Appl Stat) 67(1):231–253
8. Brauer M, Guttikunda SK, Nishad KA, Dey S, Tripathi SN, Weagle C, Martin RV (2019)Examination of monitoring approaches for ambient air pollution: A case study for India. Atmos Environ 216
9. Dey S, Purohit B, Balyan P, Dixit K, Bali K, Kumar A, Imam F, Chowdhury S, Ganguly D, Gargava P, Shukla VK (2020) A satellite-based high-resolution (1-km) ambient PM2.5 database for India over two decades (2000–2019): applications for air quality management. Remote Sens 12(23)
10. Gordon T, Balakrishnan K, Dey S, Rajagopalan S, Thornburg J, Thurston G, Agrawal A, Collman G, Guleria R, Limaye S, Salvi S, Kilaru V, Nadadur S (2018) Air pollution health research priorities for India: perspectives of the Indo-U.S. communities of researchers. Environ Int 119:100–108
11. Gupta P, Christopher SA, Wang J, Gehrig R, Lee Y, Kumar N (2006) Satellite remote sensing of particulate matter and air quality assessment over global cities. Atmos Environ 40:5880–5892
12. Mishra RK, Agarwal A, Shukla A (2020) Predicting ground level PM2.5 concentration over delhi using landsat 8 satellite data. Int J Remote Sens 42(3):827–838
13. Wang J, Christopher SA (2003) Intercomparison between satellite-derived aerosol optical thickness and PM2.5 mass: implications for air quality studies. Geophys Res Lett 30(21)
14. Wei J, Lia Z, Peng Y, Sun L (2019) MODIS Collection 6.1 aerosol optical depth products over land and ocean: validation and comparison. Atmos Environ 201:428–440
15. Wei J, Peng Y, Guo J, Sun L (2019) Performance of MODIS Collection 6.1 Level 3 aerosol products in spatial-temporal variations over land. Atmos Environ 206:30–44
16. NASA (2020) Giovanni, Earthdata [Online]. Available: https://giovanni.gsfc.nasa.gov/giovanni/. Accessed 2020 Sep 15
17. Chang JC, Hanna S (2004) Air quality model performance evaluation. Meteorol Atmos Phys 87:167–196

18. Guttikunda SK, Calori G (2013) A GIS based emissions inventory at 1 km × 1 km spatial resolution for air pollution analysis in Delhi, India. Atmos Environ 67(2013):101–111
19. Chen Y, Wild O, Conibear L, Ran L,. He J, Wang L, Wang Y (2020) Local characteristics of and exposure to fine particulate matter (PM2.5) in four Indian megacities. Atmospheric Environ: X 5:100052

Behavior of Fully and Partially Encased Stone Column in Black Cotton Soil

Mahantesh Neelawani and Prasanna Patil

Abstract In general, expansive soils are subjected to high volume changes as a consequence of variations in water content. In the dry season, these soils undergo shrinkage, which causes deep cracks in the soil. Thus, these soils are extremely troublesome for geotechnical engineers, so it is essential to implement the ground improvement techniques. The single-column behavior in expansive soil with and without encasement was discussed in this laboratory model study. The load tests were conducted in a steel tank measuring 50 cm × 50 cm × 50 cm. For the whole study, the column measures 30 mm in diameter and 300 mm in depth and is made of stone chips. The addition of a column increases ultimate strength by 225%. To enhance the strength and rigidity of the column, an encasement using non-woven geotextile was adopted. According to the load tests, a partially encased column improves ultimate strength by 275% and a fully encased column improves ultimate strength by 340%. A conventional column is associated with a lower load limit ratio, whereas a fully encased column is associated with a higher ratio. However, partially encased columns have a minor improvement. The behavior of a column in black cotton soil is influenced by climatic fluctuations, particularly at the 1D to 3D depths. Therefore, the encasement is adopted and lime was injected into the soil bed up to 150 mm deep to reduce the shrinking and swelling characteristics of the soil around the column.

Keywords Stone column · Non-woven geotextile · Black cotton soil · Fully and partial encasement

M. Neelawani (✉)
Madanapalle Institute of Technology and Science, Madanapalle, Andhra Pradesh, India
e-mail: mahanteshneelawani@mits.ac.in

P. Patil
Basaveshwar Engineering College, Bagalkot, Karnataka, India

L. Nandagiri et al. (eds.), *Recent Advances in Civil Engineering*, Lecture Notes in Civil Engineering 256, https://doi.org/10.1007/978-981-19-1862-9_8

1 Introduction

In the past, land that was encountered on site by soft clay or weak soil was ignored for any kind of construction work but as urbanization grows, demand for the land is rising. This scenario leads to a new era in the civil industry; thus, engineers forced the ground to accept the project requirements. The common behavior of black cotton soil is swelling and shrinkage as a result of climatic activity; due to this, it loses supportive strength and became critical for construction work. In the northern part of Karnataka, India, most of the land is composed of black cotton soil. If urbanization development work is carried out in such regions, engineers will face a difficult situation; due to low capacity and excessive settlement of the soil, this increases the cost and time of the construction work; therefore, ground improvement work is extremely essential. Several kinds of ground development methods are adopted depending on the soil, structure, degree of improvement, and load magnitude. Among the several types of ground improvement methods, stone column has shown to be the most cost-effective, especially in clay soil, because they serve as reinforcing components [1–3]. The reason for the effective popularity of the stone column in the civil industry is it optimizes capacity limit and ground rigidity, decreases the liquefaction potential, and also enhances the consolidation rate by minimizing the drainage flow; therefore, stone column is very much suitable for cohesive soil having undrained shear strength ranging from 7 to 50 kPa [4–7]. The stone column develops its capacity from the neighboring soil confinement. When the columns are established in the weak clay bed, because of the poor lateral confinement of the surrounding clay, the column will not take notable capacity. If the stone columns were not restrained by the surrounding soft or weak soil, column would bulge in excessively, and the soil would knead out into the voids of the stones. In these circumstances, granular columns require extra repression for development in their presentation. One of the techniques to give imprisonment to the column is adopting the individual columns with reasonable geosynthetic material as outlined in Fig. 1. The geosynthetic encasement elevates extra repression to granular piles and expands the solidness of the segment by forestalling the coarse aggregates' loss into the encompassing delicate soil and preserving the aggregates' drainage and frictional characteristics [1, 2, 8–10].

Most of the literature authors focused to investigate the rate of strength improvement and the rate of settlement reduction in the ground after adopting the column through several experimental and numerical methods. In general, the maximum capability of the column depends upon the neighboring soil reaction against the bulging of the column, and it was observed that it is limited to 4D depth [3]. The conventional one's settlement was very high compared to the encased one, and the quality of the encasement material had a considerable impact on the settlement of the ground [7, 8]. This technique of ground improvement method can be adopted for various structures, such as retaining walls, oil storage tanks, earthen dams, raft foundations, and other structures. When there is a considerable settlement and the column portion is individually loaded, the column bulges by 0.5 to 1 times its own diameter. The load

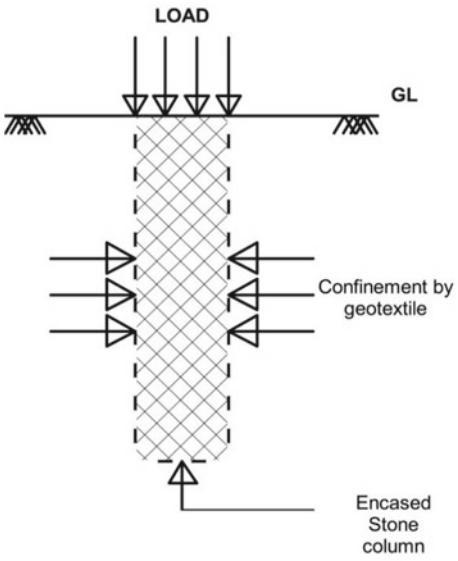

Fig. 1 Geosynthetic encased stone column

settlement characteristic is substantially straight when both the column and the neighboring area were considered for the load application, and it is possible to achieve the steadiness of the ground when compared to the column region individually loaded [10, 11]. When the column segments are immersed in particularly weak or delicate soil, they may fail or fail to meet the specified bearing limit; hence, higher lateral confining pressures are generated by encasing the column section and providing encasing up to 2 times of column's diameter, which is considered notably enough for the enhancement of load-bearing limit and even with partially geosynthetic encasement the presentation of column discovered prominent [8, 12]. To better comprehend the column's performance, it is vital to analyze its failure pattern. The column usually fails in one of three ways: bulging, bearing failure, or punching. Bulging is frequent in long types of columns and has been reported in the majority of cases [6]. The main objective of the study is the behavior of stone column in black cotton soil. However, the behavior of column differs based on climatic changes especially from 1 to 3D depth in black cotton soil. The portion of the column that is positioned in the active zone of moisture content variations, during the dry season, loses contact with the soil owing to shrinkage property, and column bulging may occur. Thus, the encasement is adopted to protect against the effect of the active zone of moisture content fluctuations in two ways; one is to cover the active zone only and another one is to cover the stone column fully and along with that lime was injected around the column. Most of the literature proved positive conclusions on the stone column but less study was observed on the performance of the column in expansive clay.

Fig. 2 Black cotton soil

2 Materials

2.1 Black Cotton Soil

Expansive clay was taken at a depth of one meter beyond the topsoil level by direct excavation nearby the Bagalkot railway station, North Karnataka, India, as shown in Fig. 2. The soil was air- and sun-dried before being crushed and sieved through a 425-micron sieve to determine the basic tests for evaluating the physical properties of soil and sieved through a 4.75 mm sieve for bed preparation. The physical properties of expansive soil were identified using their respective IS codes and are presented in Table 1.

2.2 Stone Chips

The stone chips of sizes between 2 and 10 mm were used for the column construction, as shown in Fig. 3. Stone chips that were passed through a sieve size of 10 mm and preserved on a 2 mm were adopted. Following their respective IS codes, the physical properties of stone chips were determined and the properties of stone chips are shown in Table 2.

Table 1 Properties of soil

Parameter	Value
Gravel	1%
Sand	9%
Silt and clay	90%
Natural moisture content	24%
Specific gravity	2.65
Liquid limit	78.3%
Plastic limit	32.5%
Plasticity index	45.8%
Free swell index	70%
Optimum moisture content	22%
Maximum dry density	1.7 g/cc
In-situ field density	1.4 g/cc
Cohesion	0.3 kg/cm^2
Internal friction angle	9^0
IS classification	CH

Fig. 3 Stone chips

2.3 Geotextile

Non-woven geotextile was employed in this case, as shown in Fig. 4. As the neighboring soil confinement is not sufficient, to provide additional lateral confinement, geotextile was utilized. Table 3 shows the geotextile properties.

Table 2 Properties of stone chips

Parameter	Value
Specific gravity	2.7
Impact value	13%
Crushing value	19%
Cu	3.2
Cc	1.2
Unit weight	22 KN/m^3
Friction angle	42°

Fig. 4 Non-woven geotextile

Table 3 Properties of geotextile

Parameter	Value
Unit weight	637.4 gsm
Thickness	4.50 mm
Tensile strength-length wise	1834.8 N/50 mm
Tensile strength-transverse Wise	1171.4 N/50 mm
Resistance to punching	4630.6 N

2.4 Lime

Lime is a popular addition used to control expansive soil behavior, significant improvement in soil texture and structure by lowering plasticity and increasing pozzolanic strength. The flexibility of the soil will diminish when it transitions to a granular mass; at that time, the connections between the soil particles will grow stronger due to cation exchange, which occurs between the ions of soil particles and the lime's calcium ions, Fig. 5 shows lime. In this case, lime is grouted into the

Fig. 5 Lime

Table 4 Properties of lime

Chemical property	
Component	Percentage by weight
CaO	73.3
MgO	0.9
Fe_2O_3	0.8
Al_2O_3	0.6
SiO_2	1.9
Na_2O	0.4–0.5
CO_2	2.5
$CaCO_3$	2.4
Ignition loss	24
Physical properties	
Property	Value
Specific gravity	2.2
Bulk density (kN/m^3)	4.2

ground to minimize the shrinkage and swelling behavior of soil around the column caused by climatic activities. Table 4 shows the lime properties.

2.5 Grouting Material

For lime grouting, a 60 ml needle was adopted as shown in Fig. 6 as a fluid tank of

Fig. 6 60 ml needle

lime water blend. The maximum pressure which can be applied by hand through the needle is about 3 kN/m^2 [13].

3 Methodology

3.1 Model Dimensions

The model tank dimension was determined by the stress distribution of the soil (2:1). Considering that a 30 mm diameter foundation was located at the top of a 300 mm depth column, the necessary width of the tank was 330 mm based on the stress distribution of the soil. Hence, the model tank's dimensions were set at 500 × 500 × 500 mm. The D/d ratio should be between 12 and 40; in the field, the diameter typically ranges from 0.6 to 1 m, and crushed stone aggregates range from 25 to 50 mm; in the current model test, the diameter is 30 mm, and the size of the crushed stone aggregates (stone chips) passes through 10 mm and is retained on a 2 mm IS Sieve with a mean diameter of 2.5 mm, so the D/d ratio is 12. Since the optimum L/d ratio for a stone column is 10, the column's depth was set at 300 mm.

Fig. 7 Soil bed

3.2 Black Cotton Soil Bed

To eliminate sticking between both the soil and the inside surface of the model steel tank, oil was entirely coated within the test tank. The soil was mixed thoroughly in the blending tray with 24% water, and in the model tank, the mixed material was placed in three layers of 10 cm thickness, and manual compaction was performed to reach a field density of 1.4 g/cc as shown in Fig. 7. After filling the tank with soil to the appropriate field density, it was covered with a polythene sheet for 24 h to reduce moisture loss and improve soil bed maturity.

3.3 Lime Grouting

To produce lime water mix, 50 gm lime was combined with 80% water by weight and properly mixed. To eliminate the swelling behavior of the soil, a little amount of lime water mix was produced and lime grouting was used. After the soil had matured, a lime water mix was grouted manually through a 60 ml needle, producing 2 mm diameter holes with a depth of 15 cm around the column in a triangle pattern as shown in Fig. 8 and it was left for 48 h to attain the proper reaction between soil and lime.

3.4 Formation of Stone Column

Throughout the whole test, a stone column of 300 mm in length and 30 mm in diameter was constructed while maintaining the L/D ratio constant at 10 [11, 14,

Fig. 8 Lime grouting

15]. An end bearing stone column was used. The column was constructed using the dry technique method. After preparing the bed in the test tank, using an auger a hole was made according to column dimensions afterward pvc pipe casing was installed. Aggregates ranging in size from 2 to 10 mm were poured in three layers into the pvc pipe casing using a funnel. Each layer was compacted with a 60 cm long and 1.6 cm diameter tamping rod, tamping from 2.5 cm height with 25 blows after each pouring of comparable amount of aggregates. After the construction of the column it was allowed for 24 h to promote the bond between the column and surrounding soil.

3.5 Formation of Fully Encased Column

After the formation of a column hole in the soil bed, a stitched non-woven geotextile with the same dimensions as the column was inserted into the hole with the assistance of a pvc pipe casing having a smaller diameter than the stone column, so that the geotextile adhered securely to the soil. Furthermore, the column was formed by filling and compacting particles.

3.6 Formation of Partially Encased Column

The unreinforced portion of the column was first formed through filling with compacting stone aggregates, and then a stitched non-woven geotextile with the same dimensions as the column was inserted into the hole with the assistance of a pvc pipe casing having a smaller diameter than the stone column, so that the geotextile adhered securely to the soil. Furthermore, the column was created by filling and compacting particles.

3.7 Experimental Setup

After column construction, a circular footing of 30 mm in diameter and 10 mm in thickness was placed on the stone column, and the proving ring linked to the loading jack came into contact with the footing through a round steel ball. The dial gauge was placed on the footing to record the settlement. Loading was performed in accordance with IS 15284 (Part 1):2003. The load was applied using a jack screw linked to a 100 kN proving ring, with care intended to prevent impact, fluctuation, or eccentricity. The settlement was recorded using a dial gauge with a sensitivity of less than or equal to 0.02 mm positioned on the footing. Each loading step was 1/5th rotation until the settlement amount was less than 0.05 mm/h, at which point the further loading phase was applied. The maximum load test was maintained at least a minimum of 12 h after settlement stabilization for the rate of 0.05 mm/h. A load settlement curve was drawn from the measured settlements for each increment of load at 1, 2, 4, 8, 16, 30 min and 1, 2, 3, 4 h, and so on up to the required settlement.

4 Experimental Results and Discussion

4.1 Load Tests

The current investigation is based on laboratory model evaluations. Three experiments were run using a stone column with a diameter of 30 mm and a depth of 300 mm. The studies were undertaken to investigate the performance of conventional column as well as to evaluate the effectiveness of encased columns with geotextile by adopting fully (100%) and partially (50%) encasements as shown in Fig. 9. In addition, an untreated soil bed load test was performed to determine its ultimate bearing capability without any treatment. Table 5 shows the summary of the load test conducted.

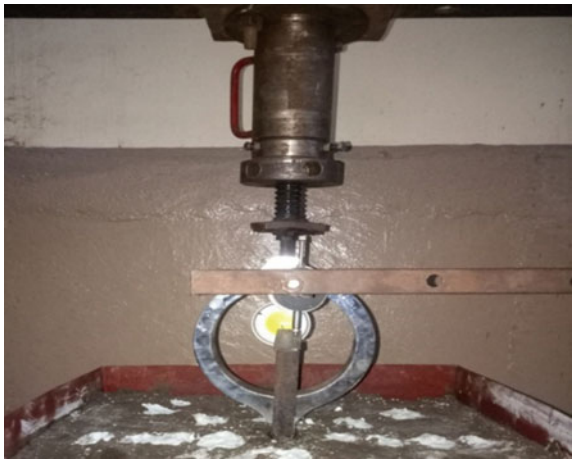

Fig. 9 Load test

Table 5 Summary of load test conducted

S. No.	Test notation	Diameter (mm)	Length (mm)	Column type	Encasement length (%)
1	UTBCS	–	–	–	–
2	OSC	30	300	End bearing	–
3	FESC	30	300	End bearing	100
4	PESC	30	300	End bearing	50

UTBCS Untreated black cotton soil; *OSC* Ordinary stone column; *FESC* Fully encased stone column; *PESC* Partially encased stone column

4.2 UTBCS Load Test

On the soil bed, a circular footing of 30 mm in diameter and 10 mm in thickness was placed, and the proving ring linked to the loading jack came into contact with the footing through a round steel ball for the application of the required load and settlements were recorded with a dial gauge as shown in Fig. 10. Following the conclusion of the test, a load versus settlement graph was drawn to assess the ultimate carrying capability of the soil, as shown in Fig. 11.

4.3 OSC Load Test

After the construction of the column, a circular footing of 30 mm in diameter and 10 mm in thickness was placed, and the proving ring linked to the loading jack came into contact with the footing through a round steel ball for the application of the required load and settlements were recorded with a dial gauge as shown in Fig. 12.

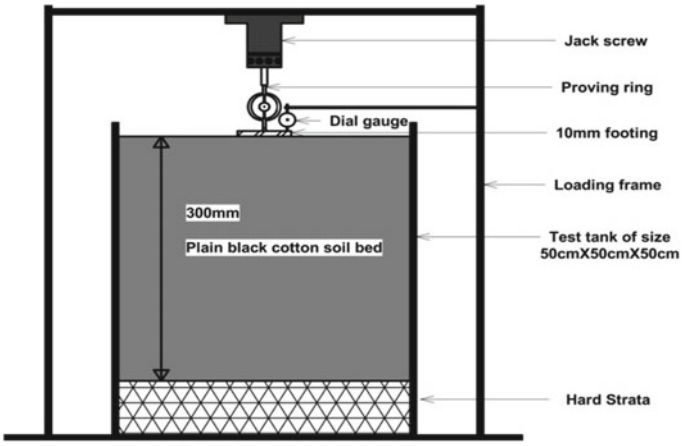

Fig. 10 Schematic view of UTBCS load test

Fig. 11 Load settlement graph of UTBCS

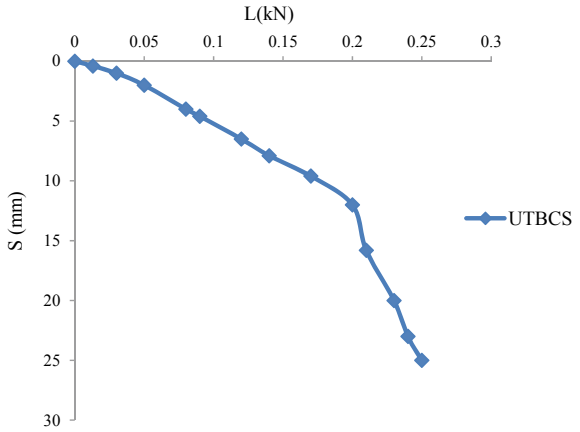

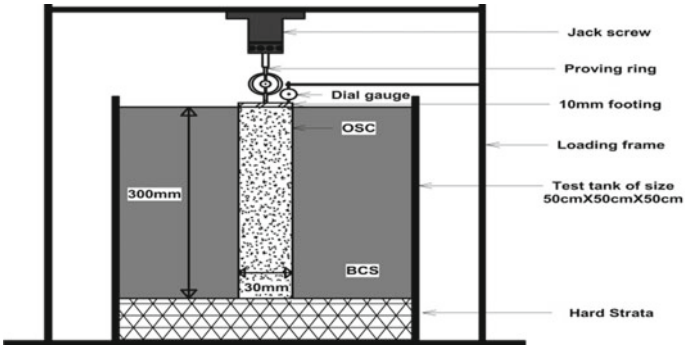

Fig. 12 Schematic view of OSC load test

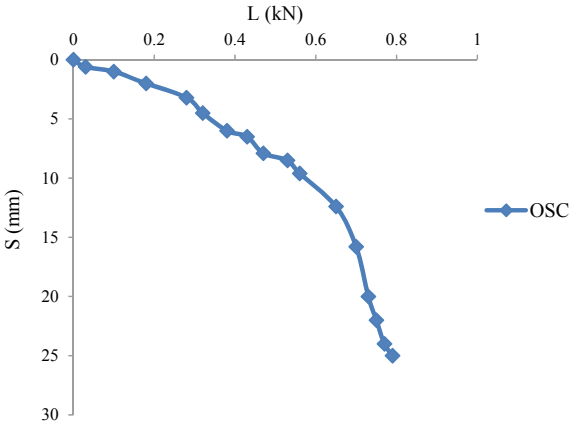

Fig. 13 Load settlement graph of OSC

Following the examination, a load versus settlement graph was generated to evaluate the ultimate capability of the soil as shown in Fig. 13.

4.4 PESC Load Test

Load tests were carried out on the partially encased column. Non-woven geotextile was adopted for the partial encasement as shown in Fig. 14. Once the load test was completed, the load settlement curve was plotted as shown in Fig. 15.

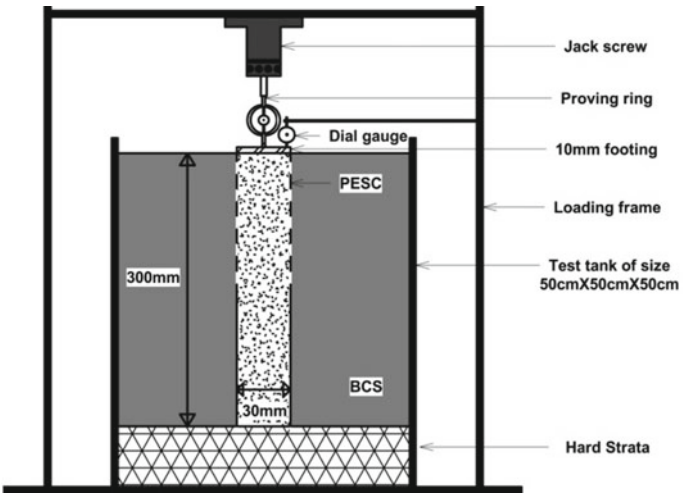

Fig. 14 Schematic view of PESC load test

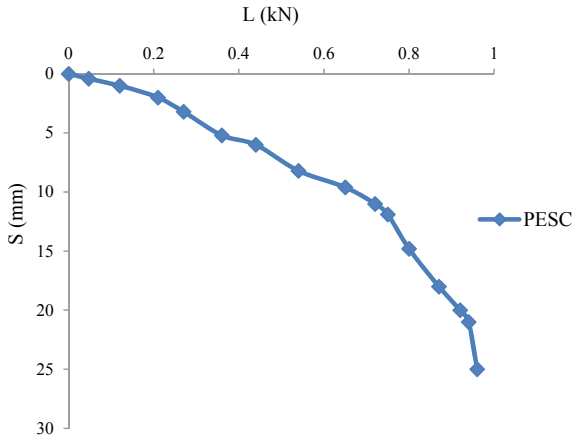

Fig. 15 Load settlement graph of PESC

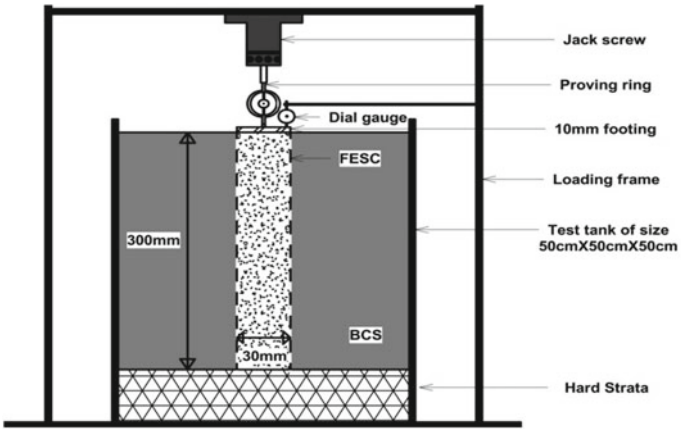

Fig. 16 Load settlement graph of FESC

4.5 FESC Load Test

An investigation on FESC was done by performing load tests. Non-woven geotextile was adopted as the encasing material as shown in Fig. 16 after the test load settlement curve has been plotted as shown in Fig. 17.

4.6 Comparisons of Load Test

Different types of columns have varying degrees of strength and resistance to load. As per the results of a load test, the ultimate strength of a plain soil bed is 0.20

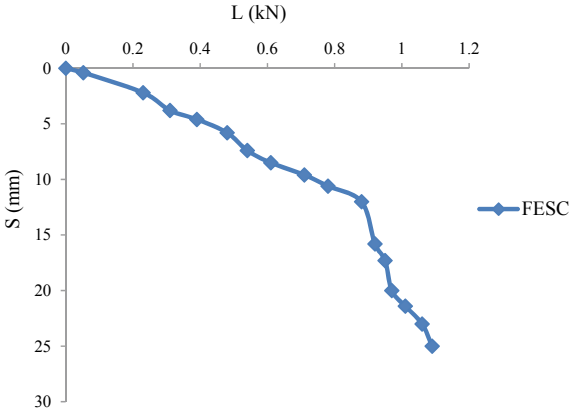

Fig. 17 Load settlement graph of FESC

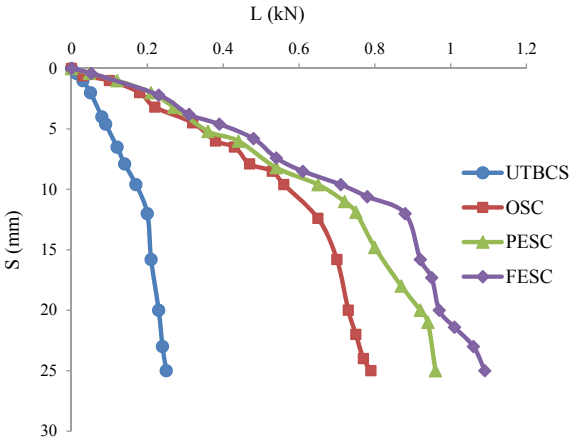

Fig. 18 Load settlement graph of all tests

kN. The ultimate strength of a column in the soil bed is 0.65 kN, which is a 225% improvement over the strength of plain soil. Partially encased column possesses ultimate strength of 0.75 kN which is a 275% improvement in the strength compared to the plain soil. Fully encased column gives ultimate strength of 0.88 kN which is a 340% improvement in the strength of the ground compared with plain soil. Figure 18 shows the load settlement graph of all tests (Fig. 18).

4.7 Enhancement of Load Limit Ratio

The load limit ratio is the proportion of the treated soil strength to the untreated soil strength at a specific soil settlement. In this scenario, a lower load limit ratio is linked with a conventional column, whereas a greater ratio is linked with a fully

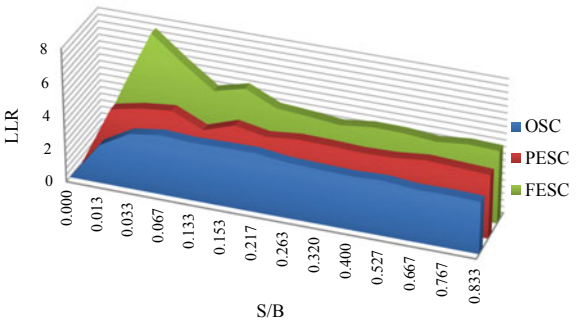

Fig. 19 Load limit ratio versus settlement ratio

encased column. For encased column, the load limit ratio is notably enhanced due to encasement enhanced lateral pressure around the column. In comparison between fully and partially encased, a fully encased column has a higher load limit ratio. In the conventional and partially encased column, the load limit ratio is larger at 6% settlement whereas in the fully encased column, it is larger at 3% as shown in Fig. 19.

4.8 Outcomes of Load Test

In the current study, conventional columns have less strength improvement as well as a lower load limit ratio at any given settlement; whereas fully encased columns have a major improvement. A partially encased column has more strength than a normal column, but it is not as noticeable. The failure pattern of columns is also seen by pouring pop after the test into the column hole; a bulging pattern is noticed in the conventional one, and a very slight linear pattern is observed in both fully and partially encased columns. Table 6 shows the outcomes of the load test.

Table 6 Outcomes of load test

Test	Ultimate bearing capacity (kN)	Improvement in strength		Load limit ratio	
		12 mm settlement	25 mm settlement	12 mm settlement	25 mm settlement
UTBCS	0.20	–	–	–	–
OSC	0.65	225%	192	3.25	3.16
PESC	0.75	275%	284	3.75	3.84
FESC	0.88	340%	336	4.40	4.36

5 Conclusions

The above study shows stone column behavior in a black cotton soil bed; as stated in the literature, the behavior is completely dependent on the surrounding soil; nonetheless, the following are the important findings of the current study:

1. A conventional column gains the soil limit by 3.25 times, but a partially and fully encased column gains the soil limit by 3.75 times and 4.40 times, respectively.
2. The capability of the column is considerably increased by adopting the non-woven geotextile encasement; the fully encased column has 35.4% and 17% more strength than the conventional and partially encased columns, respectively.
3. The partially encased column possesses 15.4% greater strength than the ordinary one; however, it is not as noticeable improvement.
4. Adoption of fully encased columns gives higher strength to the soil compared with partial and ordinary columns.
5. A bulging pattern is observed in the conventional one, and a very slight linear pattern has been found both in fully and partially encased columns.

References

1. Murugesan S, Karpurapu R (2007) Model tests on geosynthetic-encased stone columns. Geosynthet Int 14(6):346–354 (2007). https://doi.org/10.1680/gein.2007.14.6.346
2. Kumar R, Jain PK (2013) Expansive soft soil improvement by geogrid encased granular pile. Int J Emerg Technol 4(1):55–61
3. Hugher JMO, Withers NJ (1974) Reinforcing of soft cohesive soils with stone columns. Ground Eng (7):42–49
4. Alamgir M, Miura N, Poorooshasbm Madhav MR (1996) Deformation analysis of soft ground reinforced by columnar inclusions. Comput Geotech 18(4):267–290. https://doi.org/10.1016/0266-352X(95)00034-8
5. Deb K, Behera A (2017) Rate of consolidation of stone column–improved ground considering variable permeability and compressibility in smear zone. Int J Geomech (17). https://doi.org/10.1061/(ASCE)GM.1943-5622.0000830
6. IS 15284: Part-1 (2003) Design and construction for ground improvement—guidelines, Part-1: stone colums. Indian Standards, Bureau of Indian Standards, New Delhi
7. Malarvizhi SN, Ilamparuthi (2007) Comparative study on the behavior of encased stone column and conventional stone column. Soil Found (47):873–885. https://doi.org/10.3208/sandf.47.873
8. Murugesan S, Karpurapu R (2006) Geosynthetic encased stone columns: numerical evaluation. Geotext Geomembr (24): 349–358. https://doi.org/10.1016/j.geotexmem.2006.05.001
9. Jayarajan J, Karpurapu R (2020) Bearing capacity and settlement response of ordinary and geosynthetic encased granular columns in soft clay analysis and design charts. Ind Geotech J (51):231–253. https://doi.org/10.1007/s40098-020-00457-9
10. Ambily AP, Shailesh RG (2007) Behavior of stone columns based on experimental and FEM analysis. J Geotech Geoenviron Eng 133:405–415. https://doi.org/10.1061/(ASCE)1090-0241(2007)133:4(405)
11. Ambily AP, Gandhi SR (2004) Experimental and theoretical evaluation of stone column in sofy clay. ICGGE 201–206

12. Murugesan S, Karpurapu R (2008) Performance of encased stone columns and design guidelines for construction on soft clay soils. Geosynthet Civ Env Eng (1):729–734. https://doi.org/10.1007/978-3-540-69313-0_133
13. Fattah MY, AI-Saidi A, Jebur MM (2015) Improvement of bearing capacity of footing on soft clay grouted with lime-silica fume mix. Geomechan Eng (8):113–132. https://doi.org/10.12989/gae.2015.8.1.113
14. Mitra S, Chath BC (1999) Stone columns and design limitations. In: Proceeding of Indian geotechnical conference held at Culcutta, pp 201–205
15. Arora S, Kumar, Jain PK (2014) Load settlement behavior of granular pile in black cotton soil. Int J Adv Wengineering Technology. 7(3):773–781

Applications of Geospatial Technologies and Frequency Ratio Method in Groundwater Potential Mapping in Iyenda River Catchment, Konso Area, Rift Valley, Ethiopia

Muralitharan Jothimani, Abel Abebe, and Gosaye Berhanu

Abstract The present study aimed to map the potential groundwater zones in the Iyenda river catchment, Konso area, Rift Valley, Ethiopia. The potential groundwater zones were defined in this study using a frequency ratio (FR) model. The following nine thematic layers were considered in the present study, such as lithology, lineament density, slope, drainage density, land use/land cover (LULC), topographic wetness index (TWI), normalized difference vegetation index (NDVI), drainage density, rainfall, and soil types. The above-mentioned thematic layers were prepared using primary and satellite data in the ArcGIS software environment. During fieldwork, thirty-four water points, including deep bore wells, springs, and hand pump locations, were collected using GPS. In the FR model, 24 well points were used to calculate the success rate, and the rest ten well points were used to calculate the prediction rate. Groundwater prospect zones were further categorized into three groups: very good, moderate, and very low. Low groundwater prospective zones account for 39.23% of the current study, whereas medium and high potential groundwater zones account for 38.33 and 22.44%. The area under curve (AUC) technique was used to examine the accuracy of the potential groundwater zones. The AUC value for the success rate prediction rate is 0.735 and 0.732, respectively, and the same indicates the model produces excellent results in the current study. The findings of this study may aid in effective water resources management in the present study area, allowing planners and decision-makers to design suitable groundwater development plans for a sustainable environment.

Keywords Groundwater potential · Geospatial · Frequency ratio · Iyenda catchment · Konso area · Ethiopia

M. Jothimani (✉) · A. Abebe · G. Berhanu
Department of Geology, Arba Minch University, Arba Minch, Ethiopia
e-mail: muralitharangeo@gmail.com

L. Nandagiri et al. (eds.), *Recent Advances in Civil Engineering*, Lecture Notes in Civil Engineering 256, https://doi.org/10.1007/978-981-19-1862-9_9

1 Introduction

Groundwater is one of the world's most essential and renewable natural resources. In many places globally, groundwater is extensively used for household, commercial, and agricultural purposes [1]. The reliance on groundwater is increasing all the time. These rising demands frequently lead to overexploitation, putting a considerable strain on this finite freshwater supply [2, 3]. The water table has been steadily declining as a result of groundwater exploitation [4].

Furthermore, owing to inappropriate irrigation patterns, dense population, and climatic change, groundwater problems have intensified, primarily in many parts of the world [5]. Ethiopia has had tremendous economic growth, including an average yearly growth rate of 8%; from 1998 to 2016, the pace of urbanization expanded by 10%, resulting in fast urbanization rates ranging from 6 to 20%. This expansion has resulted in uncontrolled migration from rural areas to major urban centers searching for work, significantly impacting current infrastructures, especially water supply [6]. Ethiopia is known as East Africa's "water tower". However, water is frequently unavailable when it is needed due to considerable temporal and geographical fluctuations in rainfall and complicated aquifers. Ethiopia's groundwater contributes little to its agricultural growth [7].

Groundwater sources like bore wells, springs, and shallow wells provide domestic water to most Ethiopian towns and villages. Groundwater accounts for more than 70% of Ethiopia's water supply [8]. Despite this, just 34% of the population has access to safe drinking water. It implies that groundwater development and use must be in great demand in the country. But there is an absence of comprehensive knowledge about Ethiopia's groundwater potential. And there is a significant gap in estimating groundwater reserves in Ethiopia [8]. In Ethiopia, several complex variables hinder the efficient and effective use of groundwater. The most critical is the absence of accurate hydrological data, a lack of comprehension of aquifer architecture and features, and technical constraints [9].

As a result, it is vital to comprehend the structure of aquifers and explore cost-effective, comprehensive, and user-friendly methodologies and processes for groundwater detection, extraction, and monitoring [9]. Ethiopia's aquifers are very intricate, low-storage aquifers that are segregated. The complex geological nature is to account for this. As a result, conventional groundwater investigation methods in Ethiopia will be time-consuming and costly [10]. Groundwater is underutilized in Ethiopia due to increased development and operating costs and a failure to understand groundwater dynamics [11]. In Ethiopia, groundwater is mainly used for domestic purposes. There have been a few instances of groundwater being utilized for farming and other non-domestic purposes. There has been minimal research on groundwater potentiality for agriculture and other non-domestic purposes [12]. There are very few regional studies on geospatial technologies in Ethiopia to delineate groundwater potential [10].

Various elements, such as geology, soil, geological structures, land use/land cover (LULC), topography, and rainfall, influence groundwater occurrence. It is easier

to predict a region's groundwater potential using various techniques considering all of these elements [13]. Before a groundwater borehole can be dug or drilled, several approaches such as geophysical, hydrogeological, geological, and spatial methods have been employed to analyze a suitable location for groundwater potential. Furthermore, several of these approaches are too costly and challenging to implement. However, spatial technology has aided in developing a method for groundwater investigations [14, 15]. Satellite images are utilized to create the following layers: lithology, landscapes, LULC, stream, slope, Normalized Difference Vegetation Index (NDVI), Topographic Wetness Index (TWI), geological structures, and so on, which serve as the basis for determining the potential groundwater zone [16].

The following researchers from across the world, including Ethiopia, employed remote sensing (RS) and Geographic Information System (GIS) technology to delineate prospective groundwater zones, including in Karur district, Tamil Nadu, India, by using AHP methods [17]; in the Leylia–Keynow watershed, southwest of Iran [18]; in Tirunelveli Taluk, South Tamil Nadu, India [19]; in Guna tana landscape, upper Blue Nile Basin, Ethiopia [20]; and Jemma River basin, Ethiopia [10]. Various scholars have used different models in potential groundwater mapping worldwide, such as the logistic regression model [21], multi-criteria decision evaluation [22, 23], random forest model [24, 25], evidential belief function [24], frequency ratio [26–28], weights of evidence model [29, 30], and drainage morphometric analysis [31, 32].

With this background, using remote sensing data, GIS technologies, and a probability-based frequency ratio technique, the current research aims to map the possible groundwater zones in the Iyenda river catchment, Konso area, Southern Ethiopia. The frequency ratio (FR) method is a data-driven framework and bivariate statistical technique for assigning rating (r) values to each class through the computation of spatial links among dependent variables (springs and wells) and the independent variable (thematic layers). In this present study, nine significant factors were taken into account, including lithology, lineament density, drainage density, Slope, NDVI, TWI, LULC, and rainfall. So far, no study has been conducted using this method and data sets in the present study area. The current study results may be helpful for researchers to carry out further research, planners, and administrators for locating suitable sites for drilling water wells.

2 Materials and Methods

2.1 Study Area

The present study area, the Iyenda river catchment, is situated in Southern Nations, Nationalities, and People (SNNPR) regional state, Rift Valley, Ethiopia. It is located geographically between 37° 15′ 28″ and 37° 35′ 15″ E longitude and 5° 18′ 28″ to 5° 39′ 29″ N latitude. The present study area covers a total area of 576 km^2. Gidole,

Gato, and Konso are the significant settlements. Figure 1 shows the location map of the present study area. The study area has rugged topography and elevation ranging between 1055 and 2576 m, and the terrain slope is between 0° and 51° (Fig. 2). The

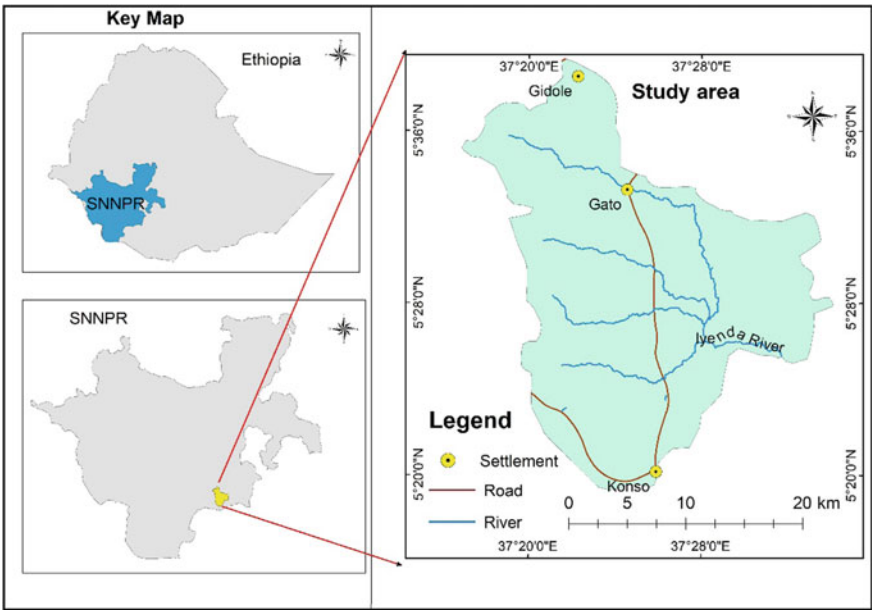

Fig. 1 Study area

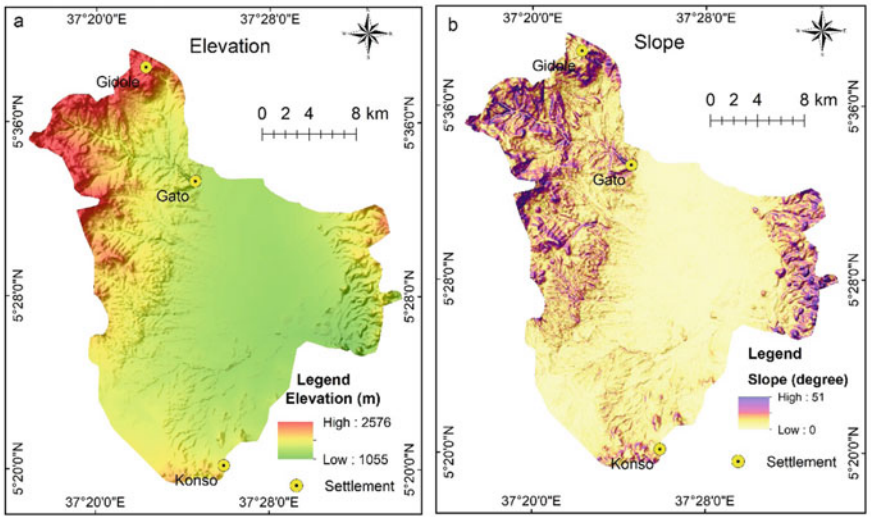

Fig. 2 Topography and slope map

present study area's northwest and southwest rift margins have a higher elevation, rugged topography, steep slope in the current location, and vice versa in the rift floor, which divided rift margins.

2.2 Data Collection and Preparation of Thematic Layers

The present study aims to use remote sensing data, GIS tools, and the frequency ratio approach to identify possible groundwater zones in Ethiopia's Iyenda river watershed. The methodology flow chart for the present study is shown in Fig. 3. The multiple thematic layers were produced by utilizing several data sets, including remote sensing data, secondary information, and field observations, to carry out the present study. The ArcGIS 10.8 software's many features were used to prepare thematic layers and conduct data analysis. The WGS-84, UTM-37 N projection system was used to project all of the data sets. The data and sources utilized in this investigation are listed in Table 1.

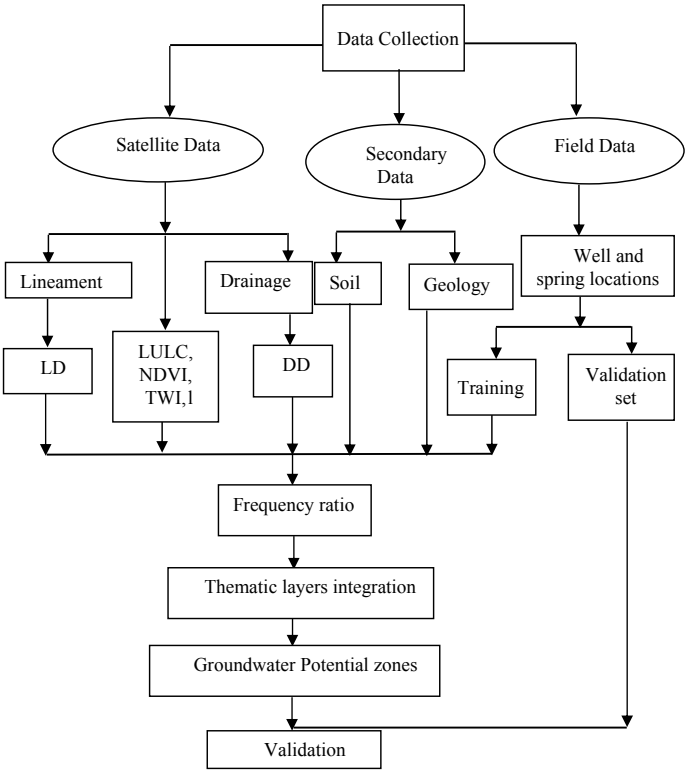

Fig. 3 Methodology flow chart

Table 1 Input data and its sources

S.No.	Thematic layer	Data	Data source
1	Geology	Geological map of Ethiopia, Landsat-8 OLI (30 m spatial resolution)	Geological Survey of Ethiopia, https://earthexplorer.usgs.gov/
2	Elevation and slope	SRTM-DEM (30 m spatial resolution)	https://earthexplorer.usgs.gov
3	Lineament	Landsat-8 OLI (30 m spatial resolution)	https://earthexplorer.usgs.gov
4	Soil	Shape file	Food and Agriculture Organization
5	Drainage	Toposheets, SRTM-DEM	Ethiopian Mapping Agency, https://earthexplorer.usgs.gov
6	Topographic wetness index	SRTM-DEM	https://earthexplorer.usgs.gov
7	Rainfall	Grid	https://chrsdata.eng.uci.edu/
8	Well/Spring locations	GPS reading	Field work
9	NDVI	Landsat-8 OLI (30 m spatial resolution)	https://earthexplorer.usgs.gov

2.3 Thematic Layers Preparation

The following thematic layers were used, such as lithology, lineament density, slope, TWI, soil, rainfall, drainage density, LULC, and NDVI in the present study. Lithology is recognized as one of the most significant markers of hydrogeological characteristics since it affects aquifer materials' permeability and porosity [33]. Initially, the lithological contact of the present study area was demarcated using a Geological map prepared by the Ethiopian Geological Survey. Hornblende gneiss, basalt, and alluvial deposits are the central rock units present in the study area. The above-mentioned rock units were further classified based on their weathering nature. And the same was identified using false-color composite of the Landsat-8 OLI satellite image. The rift margins comprise the differently weathered basalts and hornblende gneiss, and alluvial deposits cover the rift floor (Fig. 4b).

In hard rock fractured aquifer areas, lineaments regulate groundwater ingress and serve as a transmission medium [34]. The present research area lineaments were identified and extracted from a Landsat-8 OLI satellite image through a visual interpretation approach based on the image's tonal contrast. Further, the lineaments were extracted in the satellite data, where the linear drainages with moisture content appeared as black tonal contrast. The lineament density (km/km^2) map was created with ArcGIS software's line density tool, and the same were classified into five classes natural break method viz (0–0.25, 0.26–0.51, 0.52–0.77, 0.78–1.03, and 1.04–1.29). The present study area's lineament density map is shown in Fig. 4a.

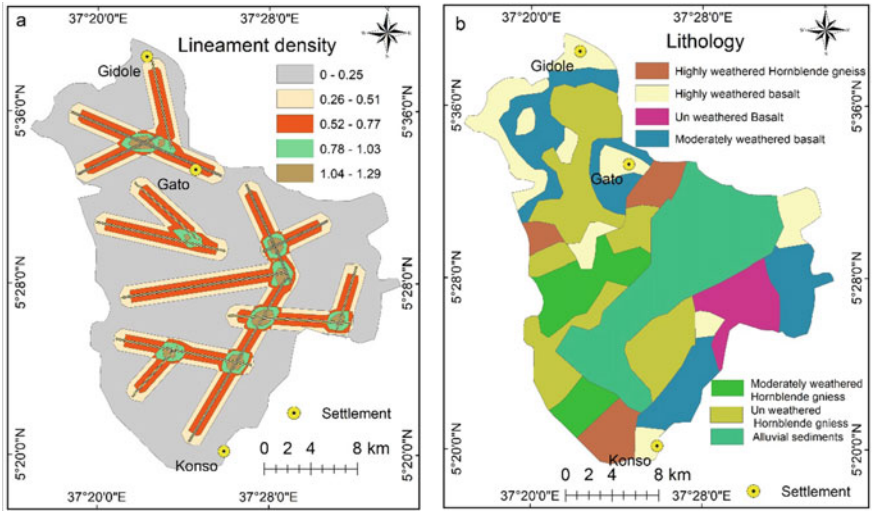

Fig. 4 Lineament density and lithology map

In general, water moves slowly over moderate slopes, allowing for more significant infiltration into the substrate. The present study area's slope map research region was created using ArcGIS 9.3's Spatial Analysis tools and a DEM. On the other hand, the steep slope increased run-off and decreased infiltration into the surface [35]. SRTM-DEM with 30 m spatial resolution data was used to prepare the slope layer of the present study area. The minimum and maximum slope of the current study area are 00 and 540, respectively. Using ArcGIS software's natural break technique, the slope layer has been further categorized into five groups (0–4.66, 4.67–9.74, 9.75–16.03, 16.04–23.94, and 23.95–51.74). Figure 2b shows the slope map of the present study area, and it has been observed that the rift margins have a steep slope compared to the rift floor.

Drainage density, which negatively correlates to soil and rock permeability, is an important indicator in evaluating the potential groundwater zones. High drainage density levels cause run-off and thus indicate a limited groundwater occurrence. In contrast, if lineaments or fractures control the drainage system of any area, then high drainage density areas are potential for groundwater occurrences [28]. The present study area's drainage system is controlled by structural features [32]. SRTM-DEM data and Archydro toolset of ArcGIS software were used to automatically extract the present study area's drainage, as procedures suggested by Maidment [36]. The drainage density (km/km^2) map was created with ArcGIS software's line density tool, and the same was classified into five classes natural break method viz (0–0.42, 0.42–0.84, 0.85–1.26, 1.27–1.68, and 1.69–2.10). The drainage density map for the current study area is given in Fig. 5a.

The LULC of a particular region has a significant impact on groundwater occurrence [37]. Surface run-off and flooding are more in the built-up areas, primarily

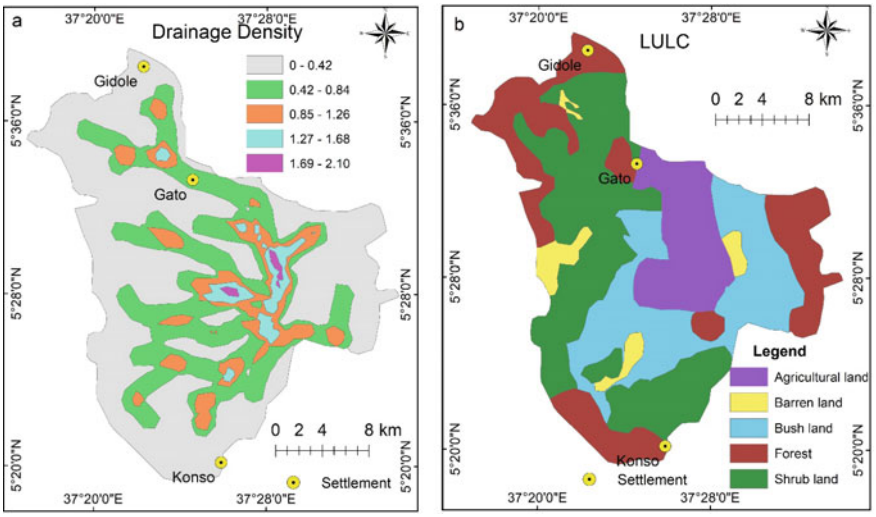

Fig. 5 Drainage density and LULC map

made up of impervious surfaces. On the other hand, agricultural areas are less prone to flood due to the positive relationship between vegetation density and infiltration capacity [38]. The LULC map in this study was created using a false-color composite of the Landsat-8 (OLI) image. Based on the fieldwork, the LULC of the current study area was classified through visual interpretation.

The agricultural field was identified based on the FCC satellite image's rectangle shape, color, and texture [39]. The built-up land has pale bluish-white, fine texture, and uniform shape and size [40]. Forest areas were dark reddish with a fine to medium texture and irregular and varied in size. Barren land was generally identified by its light to dark blue tone and gritty texture [41]. The primary LULC types in the study area are farm and bushland, forest, shrubland, and barren land. The forest is covered in the higher elevation in the rift margins where the rainfall is high, and shrubland is also covered significantly in the rift margins. The present study area's LULC map is shown in Fig. 5b.

The amount of rain that occurs significantly affects groundwater recharge in any region [28]. In the present study, rainfall data in the grid format for the year 2000–2020 was downloaded from the PERSIANN (Precipitation Estimation from Remotely Sensed Information using Artificial Neural Networks) developed by the Center for Hydrometeorology and Remote Sensing (CHRS) at the University of California, Irvine (UCI). The weblink for downloading the rainfall data is https://chrsdata.eng.uci.edu/. For twenty years (2001–2020), average rainfall data was downloaded as a grid format with a spatial resolution of 4 km × 4 km. The minimum and maximum rainfall of the present study area are 521 mm and 623 mm, respectively. The same was classified into five categories, as shown in Fig. 6a.

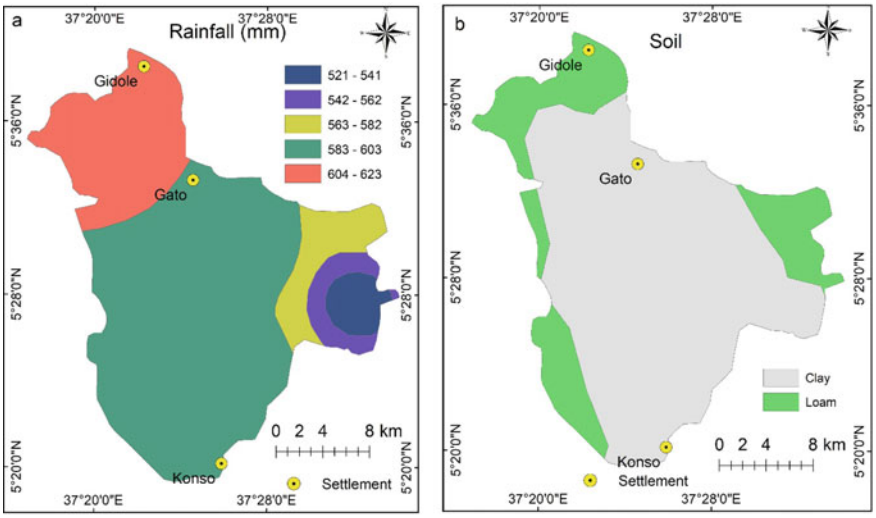

Fig. 6 Rainfall and soil map

The type of soil has a vital role in determining possible groundwater zones. Soil mapping often entails identifying soil types with distinguishable features. The soil data for the current research area was retrieved from the Food and Agriculture Organization [42]. The present study area covered clay (76%) and loam (24%) majorly. A soil map is shown in Fig. 6b.

The examination of the normalized difference vegetation index (NDVI) is considered as an approximate estimate of the quantity of vegetation present and the potential for groundwater across a given area [43]. The NDVI of the present location was calculated using the following Eq. (1).

$$\text{NDVI} = (\text{Near infrared} - \text{Red})/(\text{Red} + \text{Near-infrared}) \quad (1)$$

In this study, the NDVI was calculated using ArcGIS software's raster calculator. −0.15 and 0.44 are the minimum and maximum NDVI values further, classified into three categories. The maximum values were observed where forest and bushland have occurred. In contrast, negative or minimum values were found around the settlement and barren land. Figure 7a shows the NDVI map.

The topographic wetness index (TWI) evaluates the hydrologic process' topographic control. TWI is a metric that assesses the potential of wetlands. Wetland potential is shown in areas with a high positive TWI value. The zones show the erosion potential with a low TWI value [44]. The SRTM-DEM and TWI tool in QGIS 3.18 software were used to prepare the TWI for the present study. The minimum and maximum TWI values for the current study are 3.59 and 21.84, respectively. The same was classified into three categories Fig. 7b. The rift floor and drainages have medium and high TWI values, respectively.

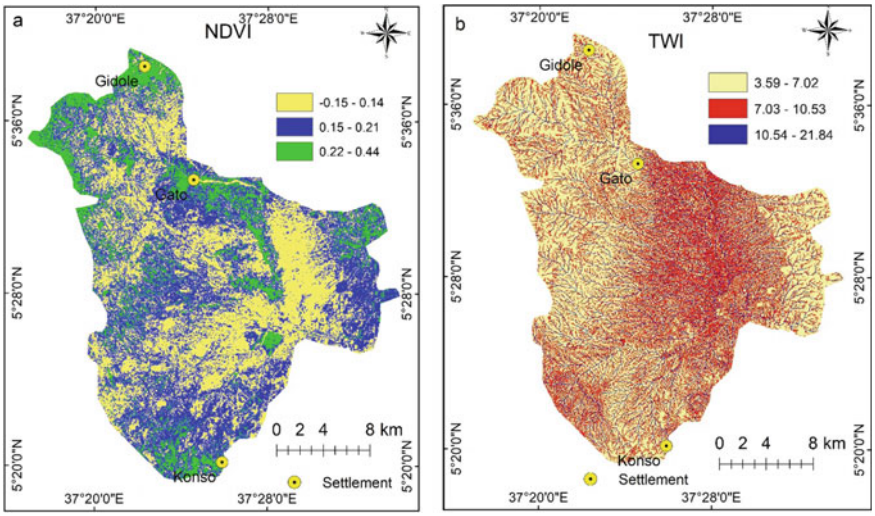

Fig. 7 NDVI and TWI map

Thirty-four well locations were located using GPS during fieldwork. Among these, 15 are springs and the remaining 12 and 7 are hand pumps and deep boreholes, respectively. Figure 8 shows the spatial distribution of springs, deep boreholes, and springs in the present study area. Seventy per cent (24 wells) of the 34 sample locations were chosen as training data sets for utilizing the FR model to map possible groundwater zoning. The remaining 30% of the samples (10 wells) were utilized for model validation.

2.4 Frequency Ratio Model and Identification of Potential Groundwater Zone

The frequency ratio (FR) method is a bivariate statistical technique widely used to establish the probability relationships among the dependent and independent variables in geospatial assessments [45]. The method examines the statistical connection between borehole locations and the factors that influence the occurrence of groundwater. In practice, the FR was computed using the following Eq. (2).

$$\mathrm{FR} = (A/B)/(C/D) \tag{2}$$

where A—the number of training wells/springs in the particular sub-thematic feature, B—the total number of wells/springs in the study area, C—the number of pixels in the sub-thematic class, and D—the total number of sub-thematic class's pixels in the study area.

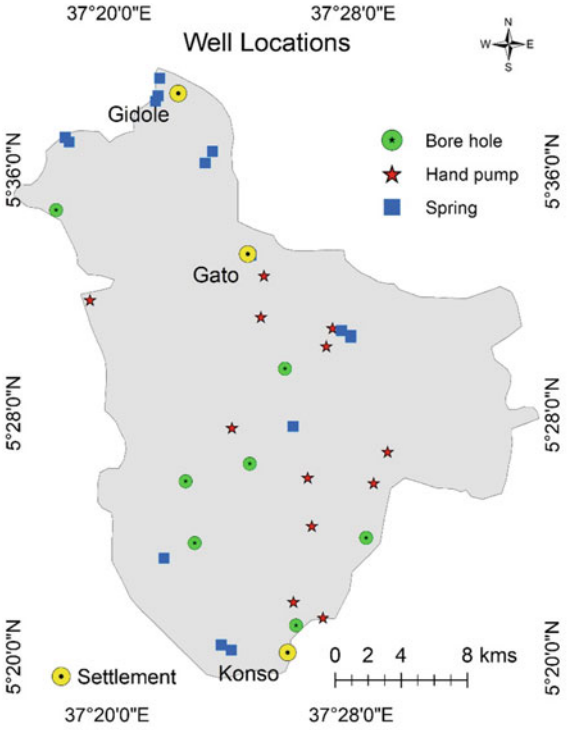

Fig. 8 Well locations map

Table 2 shows the entire weight determination computation for individual parameters. The probability of groundwater in a specific pixel may be calculated by adding the pixel values in the ArcGIS software as per Eq. (3):

$$\text{GWPI} = \sum \text{Li}_{\text{fr}} + \text{Ld}_{\text{fr}} + \text{Sl}_{\text{fr}} + \text{Dd}_{\text{fr}} + \text{Lulc}_{\text{fr}} + \text{NDVI}_{\text{fr}} + \text{Twi}_{\text{fr}} + \text{Rf}_{\text{fr}} + \text{So}_{\text{fr}} \tag{3}$$

where GWPI—groundwater potential index, fr—frequency ratio, Li—lithology, Ld—lineament density, Sl—slope, Dd—drainage density, Lulc—land use/land cover, NDVI—normalized difference vegetation index, Twi—topographic wetness index, Rf—rainfall, and So—soil.

Table 2 Frequency ratio calculation for potential groundwater mapping

Factor	Number of pixels	Domain percentage	No. of wells	Percentage of well	FR
Lithology					
Highly weathered hornblende gneiss	42,585	6.65	3	12.50	1.88
Moderately weathered hornblende gneiss	57,665	9.84	0	0.00	0.00
Un weathered hornblende gneiss	148,249	23.16	4	16.67	0.72
Highly weathered basalt	89,091	13.92	6	25.00	1.80
Moderately weathered basalt	113,973	17.81	3	12.50	0.0.70
Un weathered basalt	35,395	5.53	1	4.17	0.75
Alluvial sediments	153,155	23.09	7	29.17	1.26
Lineament density (km/km^2)					
0–0.25	398,590	62.27	15	62.50	1.00
0.26–0.51	103,071	16.1	4	16.67	1.04
0.52–0.77	107,617	16.81	5	20.83	1.24
0.78–1.03	19,139	2.99	0	0	0
1.04–1.29	11,696	1.83	0	0	0
Slope in degrees					
0–4.66	263,378	41.4	14	58.33	1.41
4.67–9.74	173,792	27.32	6	25.00	0.92
9.75–16.03	111,475	17.52	3	12.50	0.71
16.04–3.94	61,061	9.6	1	4.17	0.43
23.95–1.74	26,537	4.17	0	0	0
Drainage density (km/km^2)					
0–0.42	383,291	59.88	12	50.00	0.84
0.43–0.84	174,215	27.22	6	25.00	0.92
0.85–1.26	60,213	9.41	5	20.83	2.21
1.27–1.68	19,867	3.1	1	4.17	1.34

(continued)

Table 2 (continued)

Factor	Number of pixels	Domain percentage	No. of wells	Percentage of well	FR
1.69–2.10	2527	0.39	0	0	0
LULC					
Agricultural land	87,181	13.62	6	25	1.84
Bush land	152,396	23.81	6	25	1.05
Forest	154,648	24.16	6	25	1.03
Shrub land	218,678	34.16	6	25	0.73
Barren land	27,210	4.25	0	0	0
NDVI					
−0.15–0.14	248,831	38.87	9	37.5	0.96
0.15–0.21	293,080	45.79	6	25	0.54
0.22–0.44	98,202	15.34	9	37.5	2.44
TWI					
3.59–7.02	395,669	62.3	13	54.16	0.86
7.03–10.53	193,179	30.42	7	29.17	0.95
10.54–1.84	46,274	7.29	4	16.67	2.28
Rainfall (mm)					
521–541	24,633	3.85	0	0	0
542–562	26,350	4.12	0	0	0
563–582	49,841	7.79	1	4.17	0.53
583–603	403,351	63.01	17	70.83	1.12
604–623	135,938	21.24	6	25	1.17
Soil					
Loam	153,450	23.97	6	25	1.04
Clay	486,663	76.03	18	75	0.98

3 Results and Discussions

3.1 Analysis of the Relationship Between Frequency Ratio and Thematic Layers

Frequency ratio values were computed for each selected thematic layer based on the association with observed well and spring locations. The frequency ratio between lithology and observed well and spring locations shows that highly weathered Hornblende gneiss and weathered basalt have a high-frequency value of 1.88 and 1.80 respectively, compared to other lithological features. The high-frequency ratio value of 1.24 was found where the lineament density value is 0.52–0.77 km/km^2. The

frequency value is decreasing when the slope angle is increasing. The association between high-frequency value and drainage density indicates that high-frequency value is concentrated where medium and high drainage density occurs in the present study area. The frequency value is high where agricultural land is present and zero in the barren land LULC classes. The high-frequency ratio value of 2.44 is observed in the high NDVI and vice versa in the low NDVI. The high-frequency ratio value of 2.28 is found where the high topographic wetness index (10.54–21.84) is observed. The inverse relationship was observed between rainfall and the frequency ratio values. Table 2 displays the frequency ratio value of various thematic layers and categories.

3.2 Groundwater Potential Assessment

The frequency ratio values for the present study ranged between 5.34 and 14.77, and the same was classified into three potential groundwater categories such as high (5.34–8.37), medium (8.38–10.11), and high (10.12–14.77). 39.23% of the present study covers the low groundwater potential zones, and 38.33% and 22.44% are the medium and high groundwater potential zones, respectively. Figure 9 shows the groundwater potential map of the present study area. It is observed from the

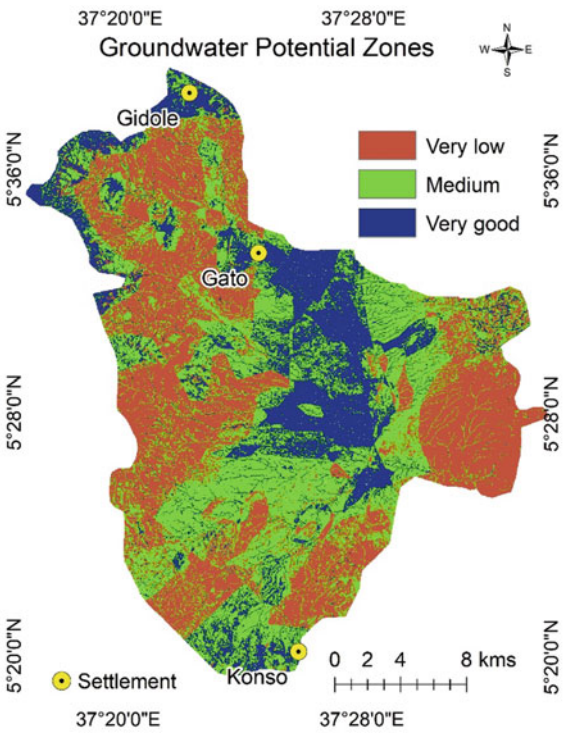

Fig. 9 Groundwater potential map

groundwater potential map that the majority of the groundwater high potential zones have occurred in the central part, and that is the rift floor and Gidole area where the plateau is present with high rainfall. Generally, the high and medium groundwater potential zones occurred where lithologically the study area covers highly weathered hornblende gneiss, weathered basalt, and alluvial deposits. And further, the results show that high and medium groundwater zones were found where medium lineament density, medium to high drainage density, less slope, high NDVI, rainfall and TWI, and loam soil occur in the present study area. In contrast, the low groundwater potential zones occurred where barren rock, high slope, less rainfall, unweathered rock, less TWI, and NDVI were found in the present study area.

3.3 Model Validation

Validation is recognized as a crucial phase in the modeling process because of its scientific significance. The receiver operating characteristics (ROC) curve technique is a widely accepted method to validate the groundwater potential mapping's results [46]. The area under curve (AUC) values range from 0.5 to 1.0, with a number around 1.0 suggesting the highest level of precision and a value around 0.5 showing the model's unreliability [24]. It has been categorized into the following categories based on the link between AUC value and prediction accuracy, excellent (0.9–1.0), very good (8–0.9), good (0.7–0.8), average (0.6–0.7), and poor (0.5–0.6) [24].

The success and prediction rate curves in this investigation were calculated using the AUC technique. The success rate was assessed at 0.735, utilizing the AUC values obtained using a training set of 24 springs, hand pumps, and bore wells to measure the success rate curve (Fig. 10). However, because the success rate is estimated using the same training data set used to create the groundwater potential zone model, it is not an acceptable approach for assessing a model's prediction capacity [25]. Consequently,

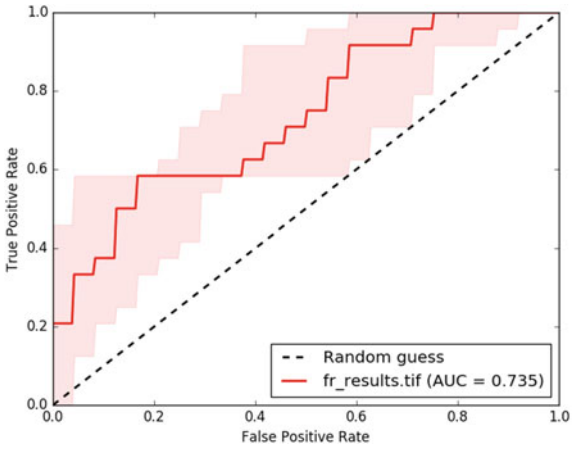

Fig. 10 Success rate curve

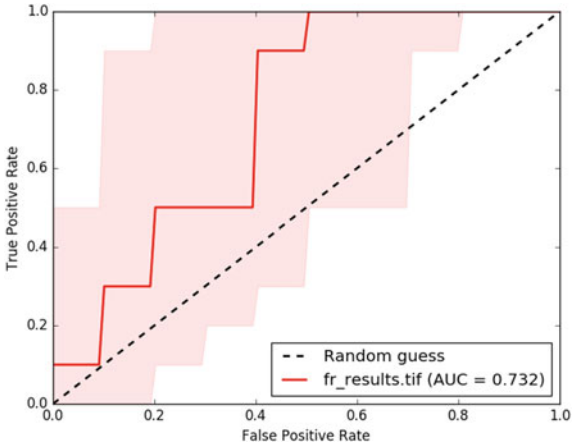

Fig. 11 Predication rate curve

the prediction rate curve was calculated using ten well locations not included in the frequency ratio model used to produce groundwater potential zone mapping. The AUC of the prediction rate curve is 0.732. (Fig. 11). The present AUC analysis has proven that the present model had excellent results.

4 Conclusions

Groundwater potential zone mapping is a prominent field of study, particularly in dry and semi-arid environments. Globally, many approaches for assessing regional groundwater potential have been used. Groundwater potential index maps were created in the present research utilizing the frequency ratio technique with remote sensing data, primary and secondary data, and GIS tools. Nine significant thematic layers regulating the groundwater recharge were mapped. The frequency ratio method was adopted for allocating rating (r) values to each class by computing spatial connections between dependent variables (springs and wells) and the independent variable (thematic layers). The weighted linear combination approach was used to combine the nine theme layers to determine possible groundwater zones. According to the study results, 39.23% of the current study includes low groundwater potential zones, 38.33% covers medium groundwater potential zones, and 22.44% covers high groundwater potential zones. The output of the present study was validated through the AUC method. The success and prediction rate AUC values suggest that the technique employed in this investigation was highly successful. Finally, the findings of this study demonstrated that the FR model might indeed be utilized successfully in the groundwater potentiality mapping.

Acknowledgements The authors would like to thank the Arba Minch University, Ethiopia, for funding the present research (Grant No. GOV/AMU/TH4/GEOL/02/2011).

References

1. Nampak H, Pradhan B, Abd Manap M (2014) Application of GIS based data driven evidential belief function model to predict groundwater potential zonation. J Hydrol 513:283–300
2. Chen W, Li H, Hou E, Wang S, Wang G, Panahi M, Niu C (2018) GIS-based groundwater potential analysis using novel ensemble weights-of-evidence with logistic regression and functional tree models. Sci Total Environ 634:853–867
3. Arulbalaji P, Padmalal D, Sreelash K (2019) GIS and AHP techniques based delineation of groundwater potential zones: a case study from southern Western Ghats, India. Sci Rep 9(1):1–17
4. Das S (2019) Comparison among influencing factor, frequency ratio, and analytical hierarchy process techniques for groundwater potential zonation in Vaitarna basin, Maharashtra, India. Groundwater Sustain Dev 8:617–629
5. Ahmed N, Hoque MAA, Pradhan B (2021) Spatio-temporal assessment of groundwater potential zone in the drought-prone area of Bangladesh using GIS-based bivariate models. Nat Resour Res. https://doi.org/10.1007/s11053-021-09870-0
6. Mengistu HA, Demlie MB, Abiye TA (2019) Review: groundwater resource potential and status of groundwater resource development in Ethiopia. Hydrogeol J 27:1051–1065. https://doi.org/10.1007/s10040-019-01928-x
7. Semu M (2012) Agricultural use of groundwater in Ethiopia: assessment of potential and analysis of economics, policies, constraints and opportunities. IWMI, Addis Ababa Ethiopia
8. Berhanu KG, Hatiye SD (2020) Identification of groundwater potential zones using proxy data: case study of Megech watershed, Ethiopia. J Hydrol Reg Stud 28:100676. https://doi.org/10.1016/J.EJRH.2020.100676
9. Moges DM, Bhat HG, Thrivikramji KP (2019) Investigation of groundwater resources in highland Ethiopia using a geospatial technology. Model Earth Syst Environ 5:1333–1345. https://doi.org/10.1007/s40808-019-00603-0
10. Ahmad I, Dar MA, Teka AH, Teshome M, Andualem TG, Teshome A, Shafi T (2020) GIS and fuzzy logic techniques-based demarcation of groundwater potential zones: a case study from Jemma River basin, Ethiopia. J Afr Earth Sci 169:103860. https://doi.org/10.1016/J.JAFREARSCI.2020.103860
11. Tolche AD (2021) Groundwater potential mapping using geospatial techniques: a case study of Dhungeta-Ramis sub-basin, Ethiopia. Geol Ecol Landscapes 5(1):65–80. https://doi.org/10.1080/24749508.2020.1728882
12. MacDonald AM, Bonsor HC, Dochartaigh BÉÓ, Taylor RG (2012) Quantitative maps of groundwater resources in Africa. Environ Res Lett 7(2):024009. British Geological Survey Groundwater Programme Internal Report Ir/10/103. https://doi.org/10.1088/1748-9326/7/2/024009
13. Das S, Pardeshi SD (2018) Morphometric analysis of Vaitarna and Ulhas river basins, Maharashtra, India: using geospatial techniques. Appl Water Sci 8:158. https://doi.org/10.1007/s13201-018-0801-z
14. Kumar T, Gautam AK, Kumar T (2014) Appraising the accuracy of GIS-based multi-criteria decision making technique for delineation of groundwater potential zones. Water Resour Manag 28(13):4449–4466. https://doi.org/10.1007/s11269-014-0663-6
15. Al-Shabeeb AA, Al-Adamat R, Al-Fugara A, Al-Amoush H, Al-Ayyash S (2018) Delineating groundwater potential zones within the Azraq basin of central Jordan using multi-criteria GIS analysis. Groundwater Sustain Dev 7:82–90. https://doi.org/10.1016/j.gsd.2018.03.011
16. Senapati U, Das TK (2021) Assessment of basin-scale groundwater potentiality mapping in drought-prone upper Dwarakeswar River basin, West Bengal, India, using GIS-based AHP techniques. Arab J Geosci 14:960. https://doi.org/10.1007/s12517-021-07316-8
17. Muralitharan J, Palanivel K (2015) Groundwater targeting using remote sensing, geographical information system and analytical hierarchy process method in hard rock aquifer system, Karur district, Tamil Nadu, India. Earth Sci Inf 8:827–842. https://doi.org/10.1007/s12145-015-0213-7

18. Mohammadi-Behzad HR, Charchi A, Kalantari N, Nejad AM, Vardanjani HK (2018) Delineation of groundwater potential zones using remote sensing (RS), geographical information system (GIS) and analytic hierarchy process (AHP) techniques: a case study in the Leylia–Keynow watershed, southwest of Iran. Carbonates Evaporites 34(4):1307–1319. https://doi.org/10.1007/S13146-018-0420-7
19. Muniraj K, Jesudhas CJ, Chinnasamy A (2020) Delineating the groundwater potential zone in Tirunelveli Taluk, South Tamil Nadu, India, using remote sensing, geographical information system (GIS) and analytic hierarchy process (AHP) techniques. Proc Natl Acad Sci India Sect A Phys Sci 90(4):661–676. https://doi.org/10.1007/S40010-019-00608-5
20. Andualem TG, Demeke GG (2019) Groundwater potential assessment using GIS and remote sensing: a case study of Guna tana landscape, upper blue Nile Basin, Ethiopia. J Hydrol Reg Stud 24:100610. https://doi.org/10.1016/J.EJRH.2019.100610
21. Pourtaghi Z, Pourghasemi HR (2014) GIS-based groundwater spring potential assessment and mapping in the Birjand Township, southern Khorasan Province, Iran. Hydrogeology 22:643–662. https://doi.org/10.1007/s10040-013-1089-6
22. Razandi Y, Pourghasemi HR, Neisani NS, Rahmati O (2015) Application of analytical hierarchy process, frequency ratio, and certainty factor models for groundwater potential mapping using GIS. Earth Sci Inf 8(4):867–883. https://doi.org/10.1007/s12145-015-0220-8
23. Jothibasu A, Anbazhagan S (2016) Modeling groundwater probability index in Ponnaiyar River basin of South India using analytic hierarchy process model. Earth Syst Environ 2:109. https://doi.org/10.1007/s40808-016-0174
24. Naghibi A, Pourghasemi HR (2015) A comparative assessment between three machine learning models and their performance comparison by bivariate and multivariate statistical methods for groundwater potential mapping in Iran. Water Resour Manag 29(14):5217–5236. https://doi.org/10.1007/s11269-015-1114-8
25. Zabihi M, Pourghasemi HR, Pourtaghi ZS, Behzadfar M (2016) GIS-based multivariate adaptive regression spline and random forest models for groundwater potential mapping in Iran. Environ Earth Sci 75:665. https://doi.org/10.1007/s12665-016-5424-9
26. Davoodi MD, Rezaei M, Pourghasemi HR, Pourtaghi ZS, Pradhan B (2015) Groundwater spring potential mapping using bivariate statistical model and GIS in the Taleghan watershed Iran Arab. J Geosci 8:913–929. https://doi.org/10.1007/s12517-013-1161-5
27. Manap MA, Nampak H, Pradhan B, Lee S, Sulaiman WNA, Ramli MF (2012) Application of probabilistic-based frequency ratio model in groundwater potential mapping using remote sensing data and GIS. Arab J Geosci 7(2):711–724. https://doi.org/10.1007/S12517-012-0795-Z
28. Guru B, Seshan K, Bera S (2017) Frequency ratio model for groundwater potential mapping and its sustainable management in cold desert, India. J King Saud Univ Sci 29(3):333–347. https://doi.org/10.1016/J.JKSUS.2016.08.003
29. Nejad SG, Falah F, Daneshfar M, Haghizadeh A, Rahmati O (2017) Delineation of groundwater potential zones using remote sensing and GIS-based data-driven models. Geocarto Int 32(2):167–187
30. Sahoo S, Munusamy SB, Dhar A, Kar A, Ram P (2017) Appraising the accuracy of multiclass frequency ratio and weights of evidence method for delineation of regional groundwater potential zones in canal command system. Water Resour Manag 31(14):4399–4413
31. Jothimani M, Abebe A, Dawit Z (2020) Mapping of soil erosion-prone sub-watersheds through drainage morphometric analysis and weighted sum approach: a case study of the Kulfo River basin, Rift valley, Arba Minch, Southern Ethiopia. Model Earth Syst Environ 6:2377–2389. https://doi.org/10.1007/s40808-020-00820-y
32. Jothimani M, Abebe A, Duraisamy R (2021) Drainage morphometric analysis of Shope watershed, Rift Valley, Ethiopia: remote sensing and GIS-based approach. IOP Conf Ser Earth Environ Sci 796(1):012009. https://doi.org/10.1088/1755-1315/796/1/012009
33. Ayazi MH, Pirasteh S, Arvin AKP, Pradhan B, Nikouravan B, Mansor S (2010) Disasters and risk reduction in groundwater: Zagros Mountain southwest Iran using geo-informatics techniques. Dis Adv 3(1):51–57

34. Anbazhagan S, Balamurugan G, Biswal TK (2011) Remote sensing in delineating deep fracture aquifer zones. In: Anbazhagan S, Subramanian SK, Yang X (eds) Geoinformatics in applied geomorphology. Taylor and Francis, CRC Press, pp 205–229
35. Prasad RK, Mondal NC, Banerjee P, Nandakumar MV, Singh VS (2008) Deciphering potential groundwater zone in hard rock through the application of GIS. Environ Geol 55(3):467–475
36. Maidment D (2002) ArcHydro GIS for water resources. ESRI Press, Redlands, CA
37. Bhattacharya AK (2010) Artificial ground water recharge with a special reference to India. Int J Res Rev Appl Sci 4:214–221
38. Das S, Gupta A, Ghosh S (2017) Exploring groundwater potential zones using MIF technique in semi-arid region: a case study of Hingoli district, Maharashtra. Spat Inf Res 25(6):749–756. https://doi.org/10.1007/s41324-017-0144-0
39. Lone MS, Nagaraju D, Mahadavesamy G, Siddalingamurthy S (2013) Applications of GIS and remote sensing to delineate artificial recharge zones (DARZ) of groundwater in HD Kote taluk, Mysore district, Karnataka, India. Int J Remote Sens Geosci 2(3):92–97
40. Lillesand T, Kiefer RW, Chipman J (2007) Remote sensing and image interpretation. Wiley, Hoboken
41. Rajaveni SP, Brindha K, Elango L (2015) Geological and geomorphological controls on groundwater occurrence in a hard rock region. Appl Water Sci 7(3):1377–1389. https://doi.org/10.1007/s13201-015-0327-6
42. Food and Agriculture Organization (FAO) (1997) The digital soil and terrain database of East Africa (SEA), via delle Terme di Caracalla, Rome, Italy
43. Sar N, Khan A, Chatterjee S (2015) Hydrologic delineation of ground water potential zones using geospatial technique for Keleghai river basin, India. Model Earth Syst Environ 1:25. https://doi.org/10.1007/s40808-015-0024-3
44. Teshome A, Halefom A, Ahmad I (2020) Fuzzy logic techniques and GIS-based delineation of groundwater potential zones: a case study of Anger river basin, Ethiopia. Model Earth Syst Environ. https://doi.org/10.1007/s40808-020-01035-x
45. Bonham-Carter GF (1994) Geographic information systems for geoscientists, modeling with GIS. Pergamon Press, Oxford
46. Pradhan B (2013) A comparative study on the predictive ability of the decision tree, support vector machine and neuro-fuzzy models in landslide susceptibility mapping using GIS. Comput Geosci 51:350–365

Study on Variation of Leaf Temperature at Different Stages of Growth of Brinjal Crops

Nazmin Sultana, Uddipta Ghosh, Ranajit Kumar Biswas, Debargha Banerjee, Kankita Das, Ishita Roy, and Syed Ealham Hossain

Abstract The experiment was conducted at the Instructional Farm of Faculty of Agricultural Engineering, BCKV, Mohanpur, Nadia, West Bengal, during the year 2018 to study the variation of leaf temperature at different stages of growth of brinjal crops. The leaf and air temperatures were taken by handheld infrared thermometer at 12.00 and 4.00 p.m., and the corresponding soil moisture at 15 cm depth of crop field was measured by the gravimetric method during the study period. The data were processed for leaf temperature (at 12.00 and 4.00 p.m.), air temperature (at 12.00 and 4.00 p.m.) and the difference between leaf and air temperatures (at 12.00 and 4.00 p.m.) corresponding to soil moisture. The leaf temperature at 12.00 and 4 p.m. was used to develop the relation with corresponding soil moisture. The standard deviations of these two sets of data were found as 1.042 and 0.27, respectively. The standard deviation between the observed and estimated values was found as 7.21 and 9.67 at 12.00 p.m. and 4.00 p.m., respectively; while comparing the level of adequacy in estimating the soil moisture by using the leaf and the difference between leaf and air temperatures, the later one was found much better, though both of the practices are acceptable within the desired level of accuracy. The statistical analysis of soil moisture content versus the difference between leaf and air temperatures explained the estimated values of soil moisture for noon and evening times by an average of 91.61% and 96.86%, respectively.

Keywords Leaf and air temperatures · Brinjal · Infrared thermometer · Soil moisture · Gravimetric method · Standard deviations

N. Sultana · R. K. Biswas
Department of Soil and Water Engineering, Bidhan Chandra Krishi Viswavidyalaya, Mohanpur, Nadia, West Bengal 741252, India

U. Ghosh (✉) · D. Banerjee · K. Das · I. Roy · S. E. Hossain
Department of Civil Engineering, JIS College of Engineering, Kalyani, Nadia, West Bengal 741235, India
e-mail: uddiptaghosh04@gmail.com

L. Nandagiri et al. (eds.), *Recent Advances in Civil Engineering*, Lecture Notes in Civil Engineering 256, https://doi.org/10.1007/978-981-19-1862-9_10

1 Introduction

Agricultural production, particularly grain production, has risen in lockstep with the creation and use of irrigation facilities throughout the years. The irrigation potential has risen at a pace of around 342.30% throughout the Previous Twelve Five Years Plan, from 1950–51 to 2017–18, compared to a 500% growth in cereal output (CWC 2017) [1, 7]. Because of the large number of tube wells in the irrigated region, groundwater has contributed roughly 60% of the improved irrigation potential [6]. Brinjal (*Solanum melongena* L.), or eggplant, is one of the most important indigenous vegetable crops grown in India and other parts of the world. India is the second largest producer of brinjal after China with production of 15.57 million tons from an area of 0.71 mha [2]. Irrigation is one of the essential inputs for brinjal cultivation. According to the ICAR; about 80% of the current water use is drawn by agriculture. Irrigated area of the country is nearly 48.8% of the 140 million hectare (mha) of agricultural land in India. The remaining 51.2% is rain-fed [4]. In West Bengal, the total cultivable area is about 56 lakh ha which is 63% of its geographical area and has 62% irrigation area of the net cropped area [3]. Indian farmers are mostly adopting the conventional method of irrigation, i.e. surface irrigation and due to this, the available water resources are not being used judiciously. These may lead to the erroneous calculation of irrigation water requirements. Irrigation scheduling has conventionally aimed to achieve an optimum water supply for productivity, with soil water content being maintained close to field capacity [8]. Scheduling irrigation is the process of determining when to irrigate and how much to irrigate. Selecting the appropriate time span in between two types of irrigation and applying the required volume of water in each irrigation ensures saving of water, minimizing energy use, higher crop yield and lower production costs [5]. Several methods of measuring plant water stress, for monitoring the irrigation scheduling, are directly related to the plant status. Handheld Infrared thermometer is used for measuring the leaf temperature. It is a comparatively handy and low-cost instrument. There is a relation between the leaf temperature and soil moisture content. If this relation is suitably developed for a crop, then the scheduling of irrigation will be much easier. With the above in view, the present study was undertaken to determine the leaf temperature of brinjal plants at different times of the day, soil moisture at the time of determining the leaf temperature and also establish a relationship among soil moisture, leaf temperature and air temperature in brinjal.

2 Materials and Methods

The study was conducted at the Instructional Farm of Faculty of Agricultural Engineering, BCKV, Nadia, West Bengal, during the year 2018. Daily Meteorological data were collected from Agricultural Meteorology and Physics Department, B.C.K.V., Mohanpur, Nadia. The soil's physical characteristics were analyzed for its bulk

density, porosity, textural class, water holding capacity and soil moisture versus tension. Brinjal seedlings (cv. Krishna hybrid) were collected from a local nursery. This is a popular brinjal variety used widely in West Bengal. The 20 days old seedlings were planted. The area needed for the experiment was cleaned and the soil clods were broken to get a good tilth and the furrow was made. The soil was added with 4 kg *safola* and 2 kg *mustard cake* dust. After mixing with soil, water was applied in good quantity for settlement of the soil and incorporation of the fertilizer in the soil. The brinjal seedlings were collected from a local nursery and transplanted in the field when the soil was found ready. The field was kept as much as possible free from weed by hand weeding. *Krilaxyl Gold* insecticide was used as the plant protection measured at the early stage of the plant. At the panicle initiation stage, *Krilaxyl* and *Tiger 10* insecticides were used to control fungal diseases and insects and pests like thrips, aphids and shoot borer. The mature, well-colored, suitable fruits were picked as and when they were matured. The first picking was done 65 days after the planting and thereafter further pickings were done as the fruits mature at 5–7 days intervals. Leaf temperature was measured with the help of a handheld *Telatemp* model MT-5 infrared thermometer. The infrared thermometer was used for measuring canopy and plant temperatures. It detected minute difference between crop canopy and surrounding air temperature. The instrument focused toward the object whose temperature was measured and displayed immediately indicating the temperature of the object. The temperature difference between the target and the air could be measured by pressing the trigger. The comparison has been expressed as percentage explained or percentage deviation.

3 Results and Discussions

The Bouyoucos Hydrometer method of determination of soil texture revealed that the relative portions of soil particles for the examined sample were 37.3% of clay content, 27.8% of silt content and 38.3% of sand content (Table 1). These percentages were located on a USDA soil texture triangle and classified as clay loam (Tables 2 and 3).

The outcome reveals that at 0 cm (0 bars) tension, the soil moisture is 61.13%. This value is approximately equal to the field capacity of the soil. With increased

Table 1 Particle size distribution results from Bouyoucos hydrometer method

Soil aggregates	Percentage distribution
Silt + clay	65.1%
Clay	37.3%
Silt	27.8%
Sand	38.3%
Soil textural class	Clay loam

Table 2 Results of soil parameters measured by the core sampler

Soil physical characteristic	Value	Unit
Bulk density	1.31	g/cm^3
Particle density	2.58	g/cm^3
Porosity	47.23	%
Maximum water holding capacity	48.3	%

Table 3 Volumetric soil moisture contents at various tensions as recorded using the porous plate apparatus

Tension (cm)	Volumetric moisture content (%)
0	61.13
11.5	56.86
21	52.88
31.5	49.67
61	43.56
83.5	39.63
98	36.42
140	33.84

tensions, the soil moisture was seen to decrease. The equation fitting the curve is $\theta = 99.811x^{-0.235}$ with the R^2 value being 0.984 in the case of tension in terms of centimeters of water column (Fig. 1). This high value of the correlation coefficient indicates a good fit of the plotted data. The equation can be used to derive the different tensions corresponding to the moisture contents measured in different treatments as per the experiment.

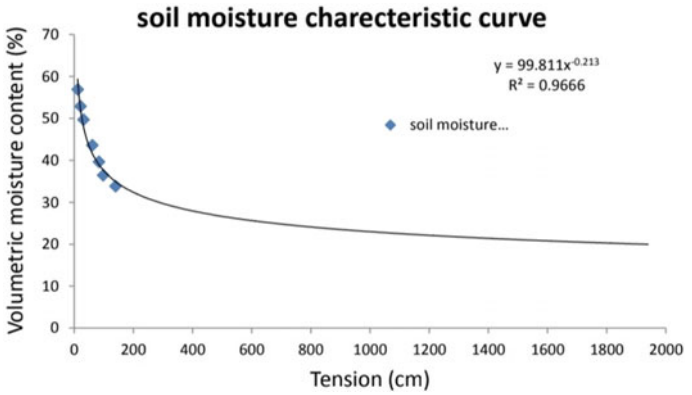

Fig. 1 Soil moisture characteristic curve

4 Soil Moisture in Between Leaf and Air Temperatures

The data collected for leaf and air temperatures at 12 p.m. and 4 p.m. and the corresponding soil moisture contents is been described in Tables 4 and 5 representing the temperature variation between the leaf and air and the corresponding soil moisture (θ).

Table 4 Leaf temperature and air temperature with moisture content at 12 p.m, and 4 p.m.

Date	DAP	Leaf temp. at 12 p.m.	Air temp. at 12 p.m.	Volumetric moisture content	Leaf temp. at 4 p.m.	Air temp. at 4 p.m.	Volumetric moisture content
29-Mar	1	31	35	33.13	29	32	32.75
02-Apr	5	31.6	35.7	29.24	29.2	32.5	27.52
03-Apr	6	32	36.6	27.15	29	31.9	26.65
04-Apr	8	31.6	36	32.18	29.1	32.2	30.2
05-Apr	9	32	36.2	26.97	30	33.2	26.14
06-Apr	10	31.1	35.3	28.18	29.5	34	27.25
09-Apr	13	32.5	36.8	33.12	30	33.6	31.28
10-Apr	14	31.2	36.5	38.14	29	32.7	35.45
11-Apr	15	31.2	36.6	32.21	29	32.9	30.22
12-Apr	16	32.8	37	26.85	30	34	26.20
13-Apr	17	33.5	38.8	42.84	31	34.2	40.21
16-Apr	20	31.8	36.4	25.65	29.6	33	24.60
17-Apr	21	32.6	37	23.31	30.4	34	22.10
18-Apr	22	33.6	38.8	31.65	30.1	35	30.52
19-Apr	23	32.6	37.4	27.24	30	34	26.45
20-Apr	24	32.5	37	25.57	31.2	35	24.32
23-Apr	27	35.6	40.8	32.23	32.3	36	30.32
24-Apr	28	34.8	40	27.14	32.5	36	26.20
25-Apr	29	35.9	40.9	24.91	32.9	37	31.30
26-Apr	30	36	41.5	30.21	33.4	37	29.12
27-Apr	21	35.2	42.2	26.34	33.7	37	25.62
03-May	27	34.2	40.6	27.34	33.2	37	26.68
04-May	28	35.9	40.9	32.97	32.3	37	31.36
07-May	31	36.2	42.4	29.67	34.1	38	28.76
08-May	32	35.8	41.8	29.72	33	37	28.35
10-May	34	36.6	42	31.22	34	37.8	30.21
11-May	35	36.7	42.7	32.28	33.4	37	31.63
12-May	36	34.3	40	29.12	33	37	28.56
13-May	37	36.1	43.2	29.1	33	36.7	28.36

Table 5 Variation of leaf temperature and air temperature with moisture content at 12 p.m. and 4 p.m. by ascending order

Volumetric moisture content at 12 p.m.	Variation of leaf and air temperatures at 12 p.m.	Variation of leaf and air temperatures at 4 p.m.	Volumetric moisture content at 4 p.m.
23.31	7.2	4	22.85
24.91	7.1	4	24.2
25.57	6.9	3.9	24.43
25.65	7	3.6	25.56
26.34	6.8	3.7	25.87
26.85	6.4	3.6	25.75
26.97	6.1	3.5	26.1
27.14	6.2	3.7	26.12
27.15	6	3.4	26.14
27.24	5.5	3.3	26.23
27.24	5.1	3.5	26.65
27.34	5.2	3.7	27.25
28.18	5	3.6	27.94
29.12	4.6	3.4	28.05
29.67	4.8	3.7	28.17
29.72	4.7	3.6	29.26
30.21	4.5	3.2	29.45
31.00	4.6	3.3	29.98
31.65	4.5	3.2	30.2
32.18	4.4	3.1	30.22
32.21	4.3	3.2	30.32
32.28	4.2	3.3	30.52
32.97	4	3	30.67
33.12	4.1	3.1	30.67
33.13	4.2	3	30.98
34.54	4.3	3	32.75
38.14	4	2.9	35.45

The leaf temperature at 12 p.m. and 4 p.m. was used to develop the relation with corresponding soil moisture. The equation was developed as below. From Fig. 2, at 12.00 p.m.:

$$T = 0.1664\theta^2 - 12.775\theta - 272.35, \quad R^2 = 0.7692 \tag{1}$$

From Fig. 3, at 4.00 p.m.:

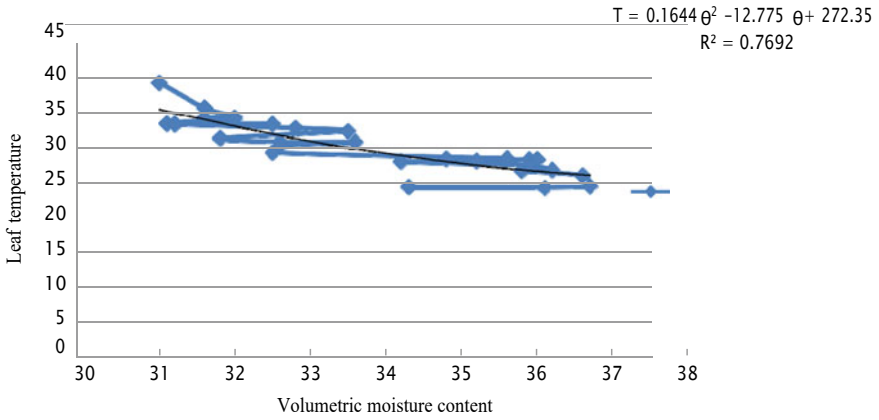

Fig. 2 Volumetric moisture content versus leaf temperature at 12 p.m.

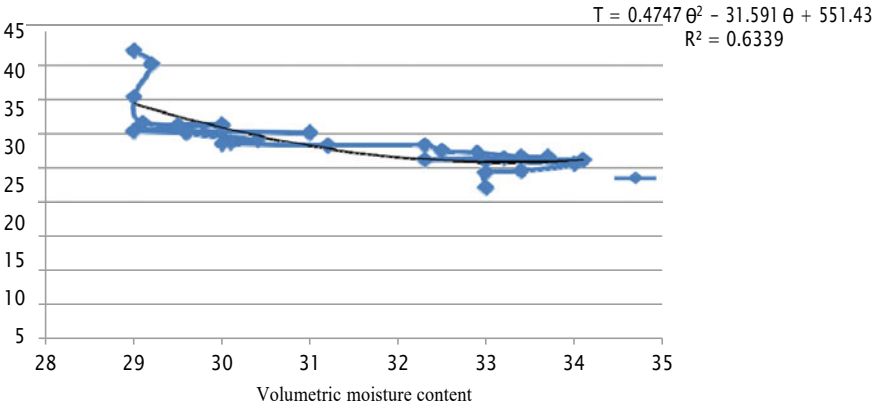

Fig. 3 Volumetric moisture content versus leaf temperature at 4 p.m.

$$T = 0.474\theta^2 - 31.5\theta + 551.4, \quad R^2 = 0.634 \tag{2}$$

Similarly, the data for variation of temperature between leaf and air were used to develop the equation. The equations are as below.

From Fig. 4, at 12.00 p.m.:

$$T = 0.0253\theta^2 - 1.8073\theta + 36.29, \quad R^2 = 0.9006 \tag{3}$$

From Fig. 5, at 4.00 p.m.:

$$T = 49.218\theta^{-0.8}, \quad R^2 = 0.7827 \tag{4}$$

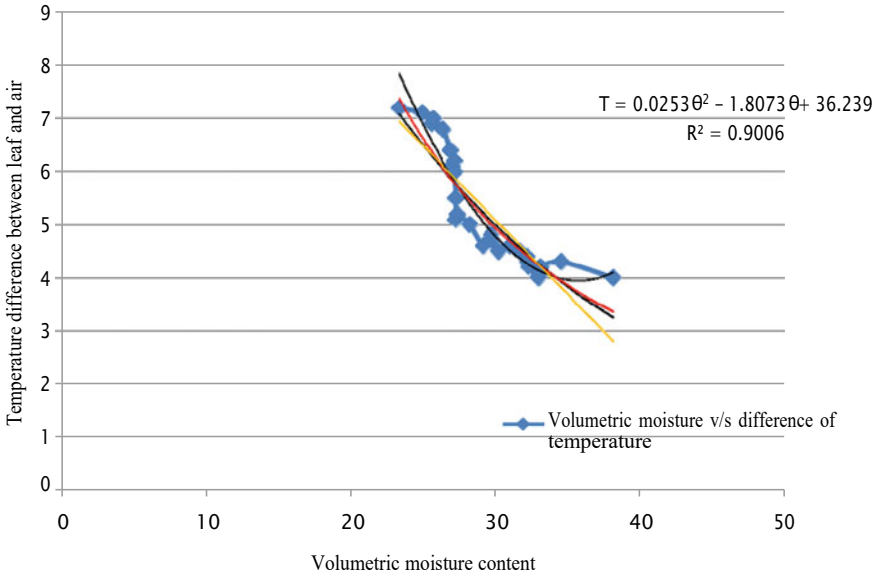

Fig. 4 Volumetric moisture versus difference between air temperature and leaf temperature at 12 p.m.

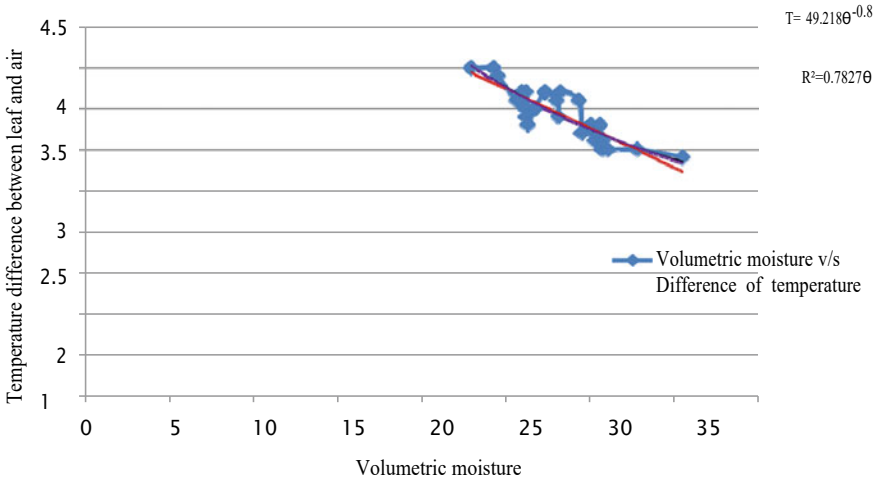

Fig. 5 Volumetric moisture versus difference between air temperature and leaf temperature at 4 p.m.

The temperature difference between the leaf and air corresponding to soil moisture gave the better fit equations in polynomial and power form to 12.00 p.m. and 4.00 p.m., respectively, unlike for the case of using leaf temperature both the equation were in polynomial form. The equation was developed for to generate the values corresponding to observed values. The standard deviation of these two sets of data was found to be 1.042 and 0.27, respectively (Table 6).

Table 6 Standard deviation between observed and estimated values of difference between leaf and air temperatures at 12 p.m. and 4 p.m.

Soil moisture (θ) at 12 p.m.	Difference between leaf and air temp. (observed) at 12 p.m.	Difference between leaf and air temp. (estimated) at 12 p.m.	Soil moisture (θ) at 4 p.m.	Difference between leaf and air temp. (observed) at 4 p.m.	Difference between leaf and air temp. (estimated) at 4 p.m.
23.31	7.2	7.857	22.85	4	4.027
24.91	7.1	6.918	24.2	4	3.846
25.57	6.8	6.659	24.43	3.9	3.817
25.65	7	6.527	25.56	3.6	3.682
26.34	6.8	6.187	25.75	3.7	3.660
26.85	6.4	5.952	25.87	3.6	3.646
26.97	6.1	5.898	26.1	3.5	3.621
27.14	6.2	5.824	26.12	3.7	3.618
27.15	6.1	5.820	26.14	3.4	3.616
27.24	6	5.781	26.23	3.3	3.606
27.24	5.5	5.781	26.65	3.5	3.561
27.34	5.1	5.738	27.25	3.7	3.498
28.18	5.2	5.400	27.94	3.6	3.428
29.12	5	5.064	28.05	3.6	3.418
30.21	4.6	4.730	28.17	3.4	3.406
31.00	4.8	4.526	29.26	3.7	3.304
31.65	4.7	4.381	29.45	3.6	3.287
32.18	4.5	4.279	29.98	3.2	3.241
32.21	4.4	4.274	30.2	3.1	3.222
32.28	4.3	4.262	30.22	3.2	3.220
32.97	4.2	4.154	30.32	3.3	3.212
33.12	4	4.134	30.52	3.1	3.195
33.13	4.1	4.132	30.67	3	3.182
34.54	4.2	3.998	30.98	3	3.157
38.18	4.3	4.116	32.75	2.9	3.019
	STDEV = 1.04201707			STDEV = 0.27194216	

It was therefore said that the estimation of soil moisture from the difference between leaf and air temperatures is better in the evening than in the noon. The standard deviation between the observed and estimated values was found to be 7.21 and 9.67 at 12.00 and 4.00 p.m., respectively (Table 7); while comparing the level of adequacy in estimating the soil moisture by using the leaf and the difference

Table 7 Standard deviation of leaf temperature observed and estimated values at 12 p.m. and 4 p.m.

Soil moisture (θ)	Leaf temp. at 12 p.m. (observed)	Leaf temp. at 12 p.m. (estimated)	Soil moisture (θ)	Leaf temp. at 12 p.m. (observed)	Leaf temp. at 12 p.m. (estimated)
33.13	31	28.872	32.75	29	28.248
29.24	31.6	35.599	27.52	29.2	35.225
27.15	32	43.182	26.65	29	39.372
32.18	31.6	29.628	30.2	29.1	27.805
26.97	32	43.965	26.17	30	42.024
28.18	31.1	39.098	27.25	29.5	36.421
33.12	32.5	28.877	31.28	30	27.099
38.14	31.2	34.364	35.45	29	36.692
32.21	31.2	29.595	30.22	29	27.780
26.85	32.8	44.498	26.20	30	41.851
42.84	33.5	54.006	40.21	31	71.556
25.65	31.8	50.334	24.60	29.6	52.501
23.31	32.6	64.344	22.10	30.4	74.931
31.65	33.6	30.299	30.52	30.1	27.459
27.24	32.6	42.799	26.45	30	40.445
25.57	32.5	50.756	24.32	31.2	54.671
32.23	35.6	29.574	30.32	32.3	27.662
27.14	34.8	43.225	26.20	32.5	41.851
24.91	35.9	54.389	24.30	32.9	52.098
30.21	36	33.023	29.12	33.4	29.823
26.34	35.2	46.366	25.62	33.7	45.381
27.34	34.2	42.379	26.68	33.2	39.214
32.97	35.9	28.959	31.36	32.3	27.099
29.67	36	34.383	28.76	34.1	30.083
29.72	35.2	34.249	28.35	33	32.063
31.22	34.2	30.974	30.21	34	27.793
32.28	35.9	30.873	31.63	33.4	27.152
29.12	36.2	35.960	28.56	33	31.386
29.1	35.8	36.021	28.36	33	28.685
	STDEV = 7.213038			STDEV = 9.679491918	

between leaf and air temperatures, the later one is found much better, though both of the practices are acceptable within the desired of level of accuracy.

5 Statistical Analysis

Equations 3 ($T = 0.0253\theta^2 - 1.8073\theta + 36.29, R^2 = 0.9006$) and 4 ($T = 49.218\theta^{-0.8}$, $R^2 = 0.7827$) were further processed. The details of these are shown in Tables 8 and 9. The difference between leaf and air temperatures explained the estimated values of soil moisture at 12 p.m. and 4.00 p.m. by an average of 94.70% and 96.86%. It is therefore concluded that the difference between leaf and air temperatures is an acceptable method of estimating soil moisture.

6 Summary and Conclusions

The current study was conducted in the summer of 2018 at the Instructional Farm of Agricultural Engineering, BCKV, Mohanpur, Nadia, with the goal of discovering the relationship between leaf and air temperatures and soil moisture. Brinjal was chosen as the experimental crop. During the research period, the leaf and air temperatures were recorded using a handheld infrared thermometer at 12.00 p.m. and 4.00 p.m., and the equivalent soil moisture at 15 cm of the crop field was determined using a gravimetric technique. The differences in leaf and air temperatures, as well as soil moisture content, were found to be linked with standard deviations of 12 p.m. and 4 p.m., respectively. As a result, it was discovered that predicting soil moisture using leaf and air temperatures was a bit better in the evening. Between actual and estimated values, the connection formed between soil moisture content and leaf and air temperatures was statistically evaluated. The predicted values of soil moisture for midday and evening time were explained by 94.70% and 96.86%, respectively, by the relationship between soil moisture and leaf and air temperatures. The results of this study suggest that leaf and air temperatures can be utilized to estimate soil moisture content in crop fields.

Table 8 Statistical test for difference between leaf and air temperatures observed and estimated data at 12 p.m.

Observed data (Y_0)	Estimated data (Y_E)	${Y_0}^2$	${Y_E}^2$	$(Y_0/N)^2$	$S_T = {Y_0}^2 - (Y_0/N)^2$	$S_E = (Y_0 - Y_G)^2$	Percent explained = $(S_T - S_E)/S_T \times 100$
4	3.846	16.00	14.794	0.667	15.333	1.206	92.133
3.9	3.817	15.21	14.569	0.0264	15.184	0.641	95.778
3.6	3.682	12.96	13.557	0.0225	12.937	0.0067	99.94
3.7	3.660	13.69	13.439	0.0238	13.666	0.0016	99.98
3.6	3.646	12.96	13.293	0.0225	12.937	0.0021	99.98
3.5	3.621	12.25	13.112	0.0213	12.228	0.0146	99.98
3.7	3.618	13.69	13.089	0.0238	13.666	0.0067	99.98
3.4	3.616	11.56	13.075	0.0201	11.539	0.0466	98.23
3.3	3.606	10.89	13.003	0.0189	10.871	0.0936	96.26
3.5	3.561	12.25	12.681	0.0213	12.228	0.0037	98.62
3.7	3.498	13.69	12.236	0.0238	13.666	0.0408	99.71
3.6	3.428	12.96	11.751	0.0225	12.907	0.0296	99.8
993.6	3.418	12.96	11.623	0.0225	12.937	0.0331	99.83
3.4	3.406	11.56	11.601	0.0201	11.539	0.088	97.52
3.7	3.304	13.69	10.916	0.0238	13.666	0.157	98.88
3.6	3.287	12.96	10.804	0.0225	12.934	0.0979	99.46
3.2	3.241	10.24	10.501	0.0177	10.222	0.0017	99.98
3.1	3.222	9.61	10.381	0.0167	9.593	0.0144	98.65
3.2	3.212	10.24	10.317	0.0177	10.222	0.0014	98.67
3.3	3.195	10.89	10.208	0.0189	10.871	0.011	98.49
3.1	3.182	9.61	10.125	0.0167	9.593	0.00672	99.99
3	3.157	9	9.967	0.0156	8.983	0.0246	98.62
2.9	3.019	8.41	9.114	0.0146	8.395	0.0142	98.36
							Avg. = 94.70%

Table 9 Statistical test for difference between leaf and air temperatures observed and estimated data at 4 p.m.

Observed data (Y_0)	Estimated data (Y_E)	${Y_0}^2$	${Y_E}^2$	$(Y_0/N)^2$	$S_T = {Y_0}^2 - (Y_0/N)^2$	$S_E = (Y_0 - Y_G)^2$	Percent explained = $(S_T - S_E)/S_T \times 100$
4	3.846	16.00	14.794	0.667	15.333	1.206	92.133
3.9	3.817	15.21	14.569	0.0264	15.184	0.641	95.778
3.6	3.682	12.96	13.557	0.0225	12.937	0.0067	99.94
3.7	3.660	13.69	13.439	0.0238	13.666	0.0016	99.98
3.6	3.646	12.96	13.293	0.0225	12.937	0.0021	99.98
3.5	3.621	12.25	13.112	0.0213	12.228	0.0146	99.98
3.7	3.618	13.69	13.089	0.0238	13.666	0.0067	99.98
3.4	3.616	11.56	13.075	0.0201	11.539	0.0466	98.23
3.3	3.606	10.89	13.003	0.0189	10.871	0.0936	96.26
3.5	3.561	12.25	12.681	0.0213	12.228	0.0037	98.62
3.7	3.498	13.69	12.236	0.0238	13.666	0.0408	99.71
3.6	3.428	12.96	11.751	0.0225	12.907	0.0296	99.8
993.6	3.418	12.96	11.623	0.0225	12.937	0.0331	99.83
3.4	3.406	11.56	11.601	0.0201	11.539	0.088	97.52
3.7	3.304	13.69	10.916	0.0238	13.666	0.157	98.88
3.6	3.287	12.96	10.804	0.0225	12.934	0.0979	99.46
3.2	3.241	10.24	10.501	0.0177	10.222	0.0017	99.98
3.1	3.222	9.61	10.381	0.0167	9.593	0.0144	98.65
3.2	3.212	10.24	10.317	0.0177	10.222	0.0014	98.67
3.3	3.195	10.89	10.208	0.0189	10.871	0.011	98.49
3.1	3.182	9.61	10.125	0.0167	9.593	0.00672	99.99
3	3.157	9	9.967	0.0156	8.983	0.0246	98.62
2.9	3.019	8.41	9.114	0.0146	8.395	0.0142	98.36
							Avg. = 96.86%

References

1. Acharya SS (2010) Indian agriculture and food security: current concerns and lessons. Asian J Agric Dev Southeast Asian Reg Cent Grad Study Res Agric (SEARCA) 7(1):1–22
2. Anonymous (2014) Area and production of brinjal cultivation in India. Indian Horticulture Database—2013, National Horticulture Board, Ministry of Agriculture, Government of India. http://nhb.gov.in/area-pro/Indian%20Horticulture%202013.pdf
3. Anonymous (2016) West Bengal agriculture an overview. http://matirkatha.net/wp-content/uploads/2016/07/West-Bengal-Agriculture-an-Overview.pdf
4. Anonymous (2019) Growing gap in irrigation potential and usage major challenge. https://www.

downtoearth.org.in/news/agriculture/growing-gap-in-irrigation-potential-and-usage-major-challenge-66580
5. Biswas RK (2015) Irrigation and agricultural drainage engineering. New Delhi Publishers, p 598
6. Gandhi VP, Bhamoriya V (2011) Groundwater irrigation in India: growth, challenges and risks. Indian infrastructure report. Oxford University Press, New Delhi, pp 90–117
7. Jain R, Kishore P, Singh DK (2019) Irrigation in India: status, challenges and options. J Soil Water Conserv 18(4):1–11
8. Jones HG (2004) Irrigation scheduling: advantages and pitfalls of plant-based methods. J Exp Bot 55:2427–2436
9. CGWB (2017) Dynamic Ground Water Resources of India New Delhi, Central Ground Water Board (CGWB), NIL. http://cgwb.gov.in/Documents/Dynamic%20GWRE-2013.pdf

The Effect on Mechanical and Microstructure Properties by Varying GGBS Content and NaOH Solution Concentration in Alkaline Solution of Fly-Ash-Based Self-compacting Geopolymer Concrete

B. R. Arun, N. H. Vedamurthy, P. S. Nagaraja, and Srishaila Jagalur Mahalingasharma

Abstract In this research, mechanical and microstructural properties of Fly-ash-based self-compacting geopolymer concrete (SCGC) were investigated for shear strength and impact strength by substituting Fly Ash with Ground Granulated Blast Furnace Slag (GGBS) by 0, 30, 50 and 70% and by using alkali solutions such as sodium hydroxide and sodium silicate in the ratio 1:2.5 for different NaOH solution molarities like 8, 10 and 12 M. An iterative procedure was utilized to arrive at the SCGC design mix by completing workability tests like slump flow in compliance with European Federation of National Associations Representing for Concrete (EFNARC) criteria. After obtaining the requisite flow, the concrete was poured into the moulds and cured for 24 h at 70 °C in the oven, with ambient treatment occurring for the remainder of the test days. A constant binding content of 400 kg/m^3 and a fluid to binder ratio of 0.47 by mass have been maintained for all molarities, while the superplasticizer dosage of 3% has remained constant. And by compromising on strength, the extra water content was adjusted to provide the desired flow. With increasing molarity and GGBS, the slump flow was reduced. As GGBS content and molarity increased, engineering properties such as shear and impact strength increased, and this was justified with microstructure analysis. As compared to the other replacement level, the replacement of 70% of the Fly Ash with GGBS at 12 M showed higher structural strength. Hence, fly ash and GGBS in a ratio of 50:50 could be a better CO_2-reducing alternative to traditional OPC concrete in connection to cost and sustainability.

B. R. Arun (✉)
Civil Engineering Department, AIEMS, Bangalore, India
e-mail: arunuvce2012@gmail.com

N. H. Vedamurthy · P. S. Nagaraja
Civil Engineering Department, UVCE, Bangalore, India

S. J. Mahalingasharma
Civil Engineering Department, RYMEC, Ballari, India

L. Nandagiri et al. (eds.), *Recent Advances in Civil Engineering*, Lecture Notes in Civil Engineering 256, https://doi.org/10.1007/978-981-19-1862-9_11

Keywords High calcium fly-ash geopolymer concrete (HCFGC) · Fly ash (FA) · Self-compacting geopolymer concrete (SCGC) · Molarities (M) · Specific gravity (S.G.) · Water absorption (W.A.) · Fluid-to-binder ratio (F/B) · Fineness modulus (F.M.)

1 Introduction

Concrete is a potential resource for a variety of projects owing to its structural capabilities and strength. The total consumption is about twenty billion tons, which for every living human being is equal to two tones [1]. In such enormous amounts, human beings ingest. Most construction activities in India are done with concrete, as it is easily available and moulding can be done even by unqualified labour. Therefore, for every human being, concrete becomes a very important material. Cement is a binder that forms a protective bind with other compounds. India is the world's second-largest cement major exporter, factoring for 6.9% of global cement output. India has approximately 420 million tons (MT) of cement production capacity (as of July 2017), which is expected to reach 550 million tons by 2025, according to Indian cement industry research. The cement industry has realized the necessity to reduce concrete creation's ecological consequences while also taking into account the issues that come with it. Cement processing is responsible for over 80% of overall greenhouse gas emissions in concrete, according to Flower and Sanjayan [2]. Portland cement production accounts for around 7% of global emissions [3, 4] and global greenhouse gas emissions are about 50 Gt per year [5] (6.6 tonnes per person). This is the result of kiln calcination and fossil fuel combustion throughout the manufacturing process, according to Roy et al. [6]. Furthermore, according to Berry et al. [4], Portland cement production is a high-energy operation.

The use of alkaline and aluminosilicates to make cement is known as geopolymer by French research scientist Davidovits. As a cement matrix, geopolymer technology performs similarly, but with significantly lower greenhouse gas pollutants, boosted fire and chemical tolerance, and easier scrap disposal. A recent development is the use of geopolymers in modern industrial applications, becoming increasingly popular due to their intrinsic environmental and technical advantages.

Geopolymer concrete, which uses Fly Ash and alkali as the binding agent instead of OPC, is springing up as new material that is friendly to the environment for sustainable development. This effort yields two benefits: reduced CO_2 emissions from OPC processing and more effective operation of industrial waste in the form of Fly Ash, slag and other materials. OPC replacement levels need to be increased and industrial by-products used as supplementary cementing materials should be maximized. SCGC is a new group of non-traditional, modern free binders and self-compacting materials that do not segregate and flow into locations and obstructions by themselves, hence self-compacting geopolymer concrete is a potential field in this approach.

2 Literature Review

In geopolymer concrete, superplasticizer is a key component. On the other hand, Topark-Ngarm et al. [7] have studied HCFGC at room temperature and analysed the effect of extra water, superplasticizer (SP), retarders on the mix to study flow, setting time and compressive strength. The ratio of Alkali liquid to the Fly Ash was 0.5, and the ratio of Sodium Hydroxide solution to Sodium Silicate solution was 1.0, and the concentration of sodium hydroxide solution was fixed at 10 molarity. The superplasticizer used in the study was sulphonate-based and the retarder used was Sika Plastiment, and it was added to the mix by 1, 3 and 5% by mass of Fly Ash and extra water dosage added was 2, 4 and 6% by mass of Fly Ash.

The flow of geopolymer concrete was found to have ramped up when extra water and retarder admixture were added, but when SP was added the flow decreased because chemicals in SP reduced the amount of liquid in the process. Setting time increased when SP and retarder were added but decreased when extra water was added; this is because extra water reduces NaOH concentration and reacts with the calcium in Fly Ash and forms a hydration reaction instead of polymerization. The compressive strength of HCFGC cured at room temperature decreased when extra water and chemical admixtures were added. The average compressive strength ranged from 21.1 to 39.9 MPa when compared to a controlled mix without any extra water and chemical admixture.

Variables such as workability and durability of fly-ash-based geopolymer concrete have been studied in various studies by Hardjito and Rangan [8] and Wallah and Rangan [9] as well as Rangan [10]. The inclusion of a superplasticizer based on naphthalene by up to 4% of Fly Ash by mass increases the workability, and a slight degradation of compressive strength can be seen after an increase in SP dosage by 2%. The slump value also increases as the water content increases. A higher Molarity of sodium hydroxide solution and a higher ratio of sodium hydroxide solution to sodium silicate solution results in higher compressive strengths and also stressed the curing temperature that as the curing temperature increases from 30° to 90 °C the strength also increases but the strength increase from 70 °C is not that significant and also curing hours place a very important role; as the curing hours increase from 4 to 96 h, the strength also increases, but after 48 h the strength increase is not that significant. Geopolymer concrete that has been thermally cured, on the other hand, shows very little strength gain over time.

3 Materials Used

3.1 Fly Ash

The physical and chemical characteristics of the Fly-Ash sample taken for this study are provided in Tables 1 and 2. Fly-Ash samples were found to meet IS 3812: 1981 requirements.

In Fig. 1, scanning electron microscope images of Fly Ash are reproduced. Most of the Fly-Ash particles are smooth and spherical, as shown by these photos. The X-ray diffractogram analysis in Fig. 2 shows that the alumino-silicate-glass matrix has crystalline phases of quartz and mullites. The base hump denotes the existence of reactive silica, which defines fly ash's pozzolanic potential and its ability to respond rapidly with accessible calcium hydroxide to generate cementitious hydration products.

Table 1 Fly ash's physical characteristics

Colour	Grey
S.G.	2.1
Surface area	310 m^2/kg
Bulk density	1.1 gm/cc

Table 2 Chemical composition of fly ash

S. No.	1	2	3	4	5	6	7	8	9
Parameter	SiO_2	Fe_2O_3	Al_2O_3	MgO	CaO	Na_2O	K_2O	SO_3	Loss on ignition (% by mass)
Quantity (wt%)	62.63	3.93	23.35	0.46	2.04	0.032	0.03	1.34	0.39

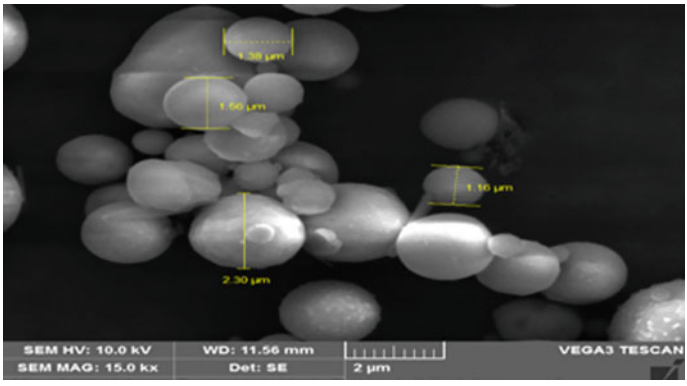

Fig. 1 SEM micrographs of fly-ash specimen

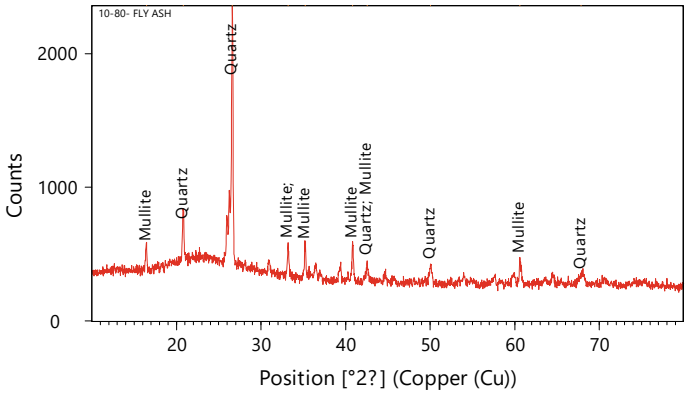

Fig. 2 X-ray diffractogram pattern of fly ash

Table 3 GGBS physical characteristics

Colour	Specific gravity	Surface area
Light grey	2.7	450 m^2/kg

Table 4 Chemical composition of GGBS

Parameter	SiO_2	CaO	Al_2O_3	MgO	Fe_2O_3	Mno	Sulphide sulphur
Quantity (wt%)	33.77	33.77	13.24	8.46	0.05	0.65	2.23

3.2 Ground Granulated Blast Furnace Slag (GGBS)

The GGBS proposed to be used in the present investigation is from JSW, Ballari, Karnataka. Tables 3 and 4 display the physicochemical characteristics. The test results of the chemical composition of GGBS and the requirements are as per IS: 12089-1987 [11].

SEM micrographs of GGBS in Fig. 3 show more or less angular, flaky and elongated in shape. XRD of the GGBS. Figure 4 shows the significant amorphous phase of calcium, silica and aluminaoxides.

3.3 Alkaline Activators

As an alkaline solution, a blend of sodium hydroxide and sodium silicate was used in this study. Both of these substances are available for commercial purposes. Solvents derived from sodium, on the other hand, were cheaper than those derived from potassium. Sodium silicate aids in the dissolution of the binder components more easily. As a result, both alkalis were of industrial quality. Sodium hydroxide in pellet form

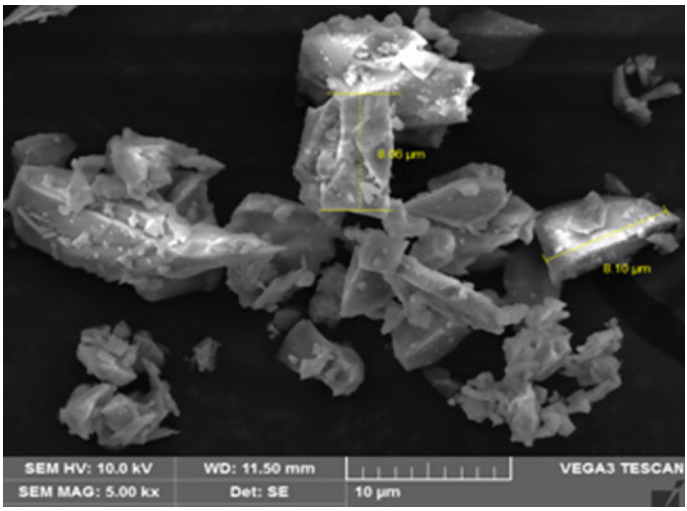

Fig. 3 SEM micrographs of GGBS specimen

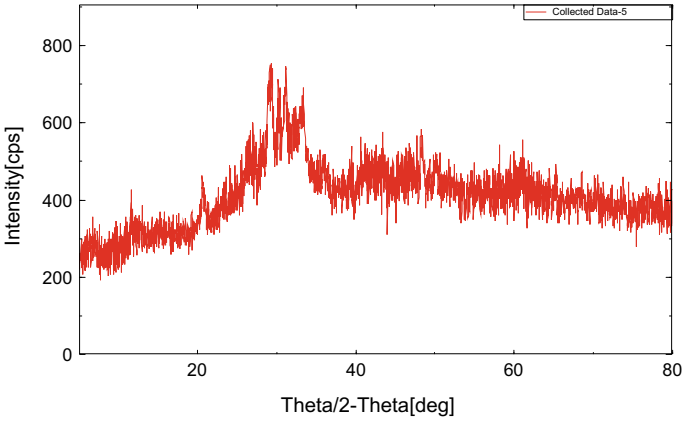

Fig. 4 X-ray diffractogram pattern of GGBS

used in the study is 99% pure and has a specific gravity of 2.11. The pH of the silicate solution is 12 and it is driven by a range of factors including the amount of silica in the solution, as shown in Table 5. The ratio of sodium hydroxide solution to sodium silicate solution is fixed at 2.5 for all of the experiments in the study.

Table 5 Composition of sodium silicate solution

Sp. gravity	Na_2O %	SiO_2 %	Water %
1.55	14.34	29.55	56.11

3.4 Superplasticizer

A contemporary group of polycarboxylic ether-based additive GLENIUM B233 was used.

3.5 Aggregates

The M-sand that verified zone 2 had an S.G. of 2.57, a Water Absorption (W.A.) of 2.21%, and an Fineness Modulus (F.M.) of 2.66, while the crushed coarse aggregate had an S.G. of 2.66, a W.A. of 0.63% and an F.M. of 6.83.

3.6 Mix Proportions

Twelve Fly-Ash blends were swapped with GGBS at 0, 30, 50 and 70% by mass for this study. As stated in Table 6, mix Mix1–Mix2–Mix3–Mix4 corresponds to 8 molarity concentration, mix Mix5–Mix6–Mix7–Mix8 corresponds to 10 molarity concentration and mix Mix9–Mix10–Mix11–Mix12 corresponds to 12 molarity concentration. For all combinations, the (F/B) ratio was kept at 0.47 by mass and the maximum amount of binder was established at 400 kg/m^3. The requisite working qualities of SCGC were achieved by keeping the Superplasticizer content at 3% for Mix1, Mix5 and Mix9 and 4% for the remaining combination, and Table 6 shows additional water content based on binding mass molarities.

4 Engineering Properties and Test Results of SCGC

4.1 Test Result of SCGC on Slump Flow

Slump flow must be within 650–800 mm of the acceptable threshold as given by EFNARC. Table 7 shows the results for various molarities, and Fig. 5 illustrates the same. As GGBS granules are flat, elongated and have a large surface area, as shown in Fig. 3, the rate of flow reduces as the amount of GGBS increases, leading to a high supply of water and, as a result, a loss in concrete workability; however, all readings stayed within a prescribed tolerance. The effectiveness of the SCGC decreases as the dosage of sodium hydroxide goes up from 8 to 12 M.

Table 6 Mix proportion

Mix proportion	Fly ash (kg/m^3)	GGBS (kg/m^3)	M-sand (kg/m^3)	Coarse aggregate (kg/m^3)	(F/B) ratio	Molarity (M)	S.P (%)	Extra water (%)
Mix1 (FA 100%)	400	0	872	706	0.47	8 M	3	1
Mix2 (FA 70% and GGBS 30%)	280	153.6	872	706	0.47	8 M	4	1
Mix3 (FA 50% and GGBS 50%)	200	256	872	706	0.47	8 M	4	4
Mix4 (FA 30% and GGBS 70%)	120	358.4	872	706	0.47	8 M	4	9
Mix5 (FA 100%)	400	0	872	706	0.47	10 M	3	2
Mix6 (FA 70% and GGBS30%)	280	153.6	872	706	0.47	10 M	4	2.5
Mix7 (FA 50% and GGBS 50%)	200	256	872	706	0.47	10 M	4	5.5
Mix8 (FA 30% and GGBS 70%)	120	358.4	872	706	0.47	10 M	4	10
Mix9 (FA 100%)	400	0	872	706	0.47	12 M	3	3.5
Mix10 (FA 70% and GGBS 30%)	280	153.6	872	706	0.47	12 M	4	4
Mix11 (FA 50% and GGBS 50%)	200	256	872	706	0.47	12 M	4	7
Mix12 (FA 30% and GGBS 70%)	120	358.4	872	706	0.47	12 M	4	12

Table 7 Workability test results

Mix No.	Mix1	Mix2	Mix3	Mix4	Mix5	Mix6	Mix7	Mix8	Mix9	Mix10	Mix11	Mix12
Slump flow (mm)	700	690	690	685	695	685	682	670	690	675	670	660

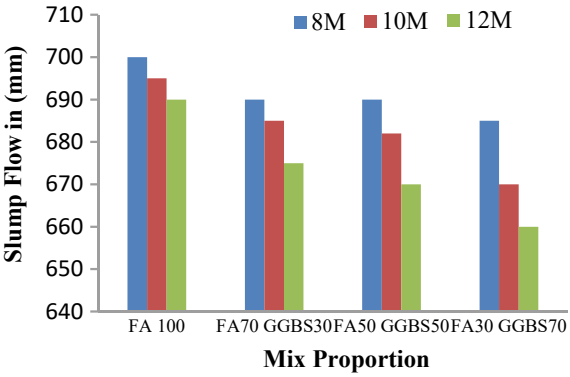

Fig. 5 Slump flow test for various molarities

4.2 Test Result of SCGC on Shear Strength

Shear strength tests on an L-shaped shear test specimen on self-compacting geopolymer concrete were done devoid of a stated code, as advised by Bairagi and Modhera [12] and Baruah and Talukdar [13]. Before the concrete was poured, a steel block with a cross-section of 90 mm × 60 mm and a height of 150 mm was inserted into 150 mm side-cube moulds. Figure 6 shows the details of shear test specimens. The sample was mounted in a CTM system and specimen failure is shown in Fig. 7 and loading was applied until the specimen failure was reached.

SCGC's shear strength increases when the GGBS content rises and the Fly-Ash content falls, as illustrated in Fig. 8. However, the strength of all mix proportions increases gradually and marginally after 28, 56 and 90 days.

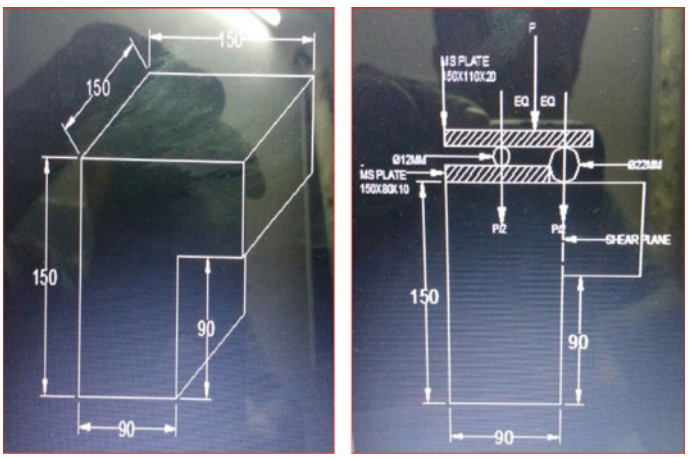

Fig. 6 Details of shear test specimen

Fig. 7 Failure of shear test specimen in CTM machine

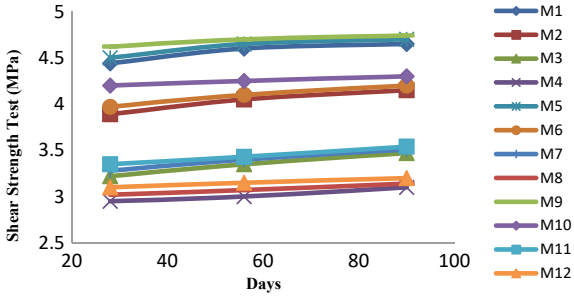

Fig. 8 Shear strength w.r.t. different binder components and molarity

At the end of 90 days, the percentage strength gain for (30%–50%–70%) replacement of Fly Ash by GGBS for 8 M, 10 M and 12 M compared to control mix FA100 is around 4.3–18.2%–30.4%, 4.2%–18.2%–28.9% and 2.9%–8.1%–18.5%.

At the close of 90 days, the percentage boost in strength from 8 to 10 M and from 10 to 12 M for Mix1 and Mix2 series is 2.1% and 14.8%, respectively. The Mix3 and Mix4 series have a 2.2% and 5.0% boost in strength, accordingly.

The maximum concrete shear strength given in IS 456-2000 [14] is approximately 2.5 MPa for (conventional) concrete grade M20. Therefore, it can be observed from Fig. 10 that for 8 M and 10 M samples for 50% and 70% Fly-Ash replacement with GGBS, all specimens achieved strength above 2.5 MPa and for 12 M all formulations

achieved shear strengths around 2.6–3.2 MPa. In view of this, geopolymer concrete based on oven-cured Fly-Ash–GGBS can be considered to perform satisfactorily.

4.3 Test Result of SCGC on Impact Strength Test

By means of Schruder's impact test machine, the impact strengths of self-compacting geopolymer concrete have been obtained. As a result, samples with a diameter of 150 mm and a thickness of 60 mm (high) were employed. The experiment is placed in Schruder's impact assessment apparatus, and a 45.4 N hammer (ball) is lowered from a height of 457 mm, as shown in Fig. 9. The number of blows that must occur for the initial and final breakdown to occur is recorded. The final failure is to create cracks enough in the sample to impact at least three out of four sections of concrete on the base plate.

The compressive, tension and flexural strength test are subjected to a low-stress rate, and the behavior of concrete subjected to a high-stress rate and the energy absorption can be known by impact test. The experimentation is to study the Impact resistance of SCGC by the incorporation of mineral admixture in various proportions. Table 8 demonstrates the impact strengths and eventual failure of specimens at 28, 56 and 90 days for various replacements of Fly Ash by GGBS in SCGC, as recommended by ACI Committee 544 [15].

Table 9 displays the percentage increase in impact energy of SCGC compared to the control mix Mix1 for 8 M, Mix5 for 10 M and Mix9 for 12 M for all testing days.

Impact resistance was improved in comparison to Fly Ash, which has a surface area of around 310 m^2/kg, due to its strong wrapping ability and porous structure of GGBS, which is around 450 m^2/kg, as shown in Table 3. Furthermore, the SEM

Fig. 9 Impact test setup and failure of impact specimen

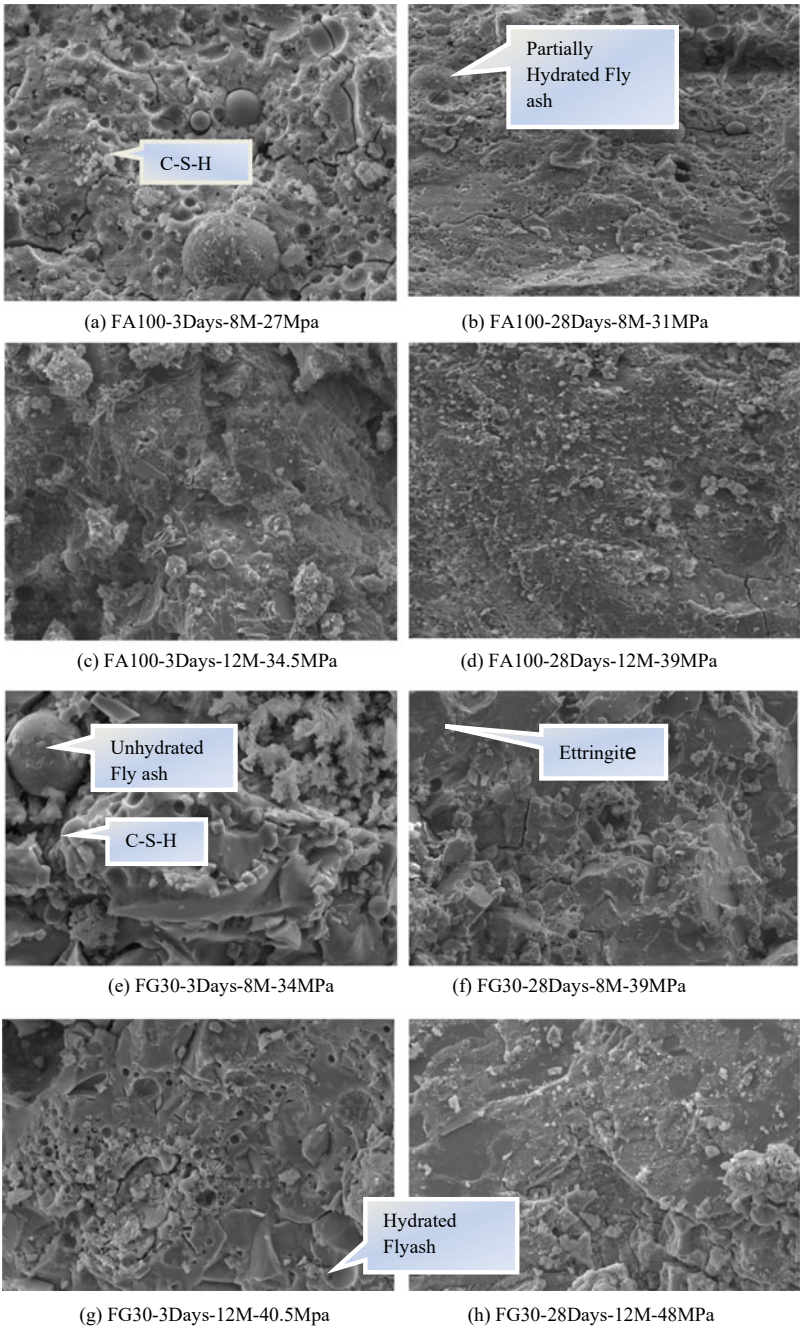

Fig. 10 SEM images of fly ash/GGBS-based SCGC w.r.t. different binder composition and molarity

Table 8 Impact energy of fly ash/GGBS-based SCGC

Mix	Molarity	28 days		56 days		90 days	
		First crack, N m	Final crack, N m	First crack, N m	Final crack, N m	First crack, N m	Final crack, N m
Mix1	8 M	1058	1141	1183	1245	1328	1390
Mix2		1141	1203	1245	1307	1411	1452
Mix3		1224	1307	1328	1369	1452	1514
Mix4		1390	1452	1432	1494	1535	1597
Mix5	10 M	1141	1224	1266	1307	1432	1494
Mix6		1203	1266	1348	1390	1514	1556
Mix7		1286	1348	1432	1473	1597	1660
Mix8		1432	1473	1514	1577	1722	1763
Mix9	12 M	1183	1245	1348	1432	1473	1535
Mix10		1266	1307	1411	1473	1535	1597
Mix11		1328	1390	1514	1577	1639	1722
Mix12		1494	1556	1618	1680	1763	1867

Table 9 % Increase (+) or % decrease (−) in impact energy

Mix	Molarity	% Increase (+) or % decrease (−) in the impact energy of SCGC at 28 days		% Increase (+) or % decrease (−) in the impact energy of SCGC at 56 days		% Increase (+) or % decrease (−) in the impact energy of SCGC at 90 days	
		First crack, N m	Final crack, N m	First crack, N m	Final crack, N m	First crack, N m	Final crack, N m
Mix1	8 M	0	0	0	0	0	0
Mix2		7.84	5.43	5.24	4.97	6.25	4.46
Mix3		15.68	14.54	12.25	9.95	9.33	8.92
Mix4		31.37	27.25	21.04	20	15.58	14.89
Mix5	10 M	0	0	0	0	0	0
Mix6		5.43	3.43	6.47	6.35	6.35	4.14
Mix7		12.70	10.13	13.11	12.70	12.70	11.11
Mix8		25.5	20.34	19.58	19.78	20.65	18
Mix9	12 M	0	0	0	0	0	0
Mix10		7	4.97	4.67	2.86	4.20	4.03
Mix11		12.25	11.64	12.31	10.12	11.26	12.18
Mix12		26.28	24.97	20	17.31	19.68	21.62

picture of GGBS in Fig. 3 reveals that flakier and longer particles make GGBS particles more packable.

Due to increased sodium hydroxide concentration, the increase in molarity increased SCGC's energy absorption. In addition, the energy absorption capacity was greater when Fly Ash was replaced with GGBS at 70%, regardless of the molarity, on all test days.

The percentage gain in strength at ultimate failure from 8 to 10 M and from 10 to 12 M for 70% substitution of Fly Ash with GGBS at 90 days is 10.39% and 5.89%, accordingly. This implies that self-compacting geopolymer concrete based on oven-cured Fly Ash–GGBS performs well in terms of impact strength.

5 Microstructure Studies

5.1 Evaluation of Microstructure and Compressive Strength with Age w.r.t. Different Binder Composition and Molarity

The micrographs (Fig. 10a, b, e, f), (8 M) and (Fig. 10c, d, g, h), (12 M) of hardened geopolymer concrete samples, taken after 3 days and 28 days of compressive strength tests, for FA100 mix (Fly Ash 100%) and FG30 mix (Fly Ash 30% and GGBS 70%), respectively, reveal microstructural morphology with respect to binder composition and molarity.

In micrograph (a) for 100% Fly Ash at 8 M when tested at 3 days, the Fly-Ash particles are spherical as shown in Fig. 1, of different sizes and dissolved to a different extent which can be seen distributed throughout. Some of the Fly-Ash particles appear to have dissolved almost completely, while large number of particles have partially dissolved. Completely un-reacted spherical particles are visible.

In micrograph (b) for 100% Fly Ash at 8 M when tested at 28 days, we can see that the un-reacted and marginally reacted Fly-Ash particles seem to be bonded in the matrix. And when compared with micrograph (a), only a few un-reacted spherical particles are visible and hence the geopolymer matrix in (b) is more compact than in (a), and the strength attained is more than 3 days at 28 days (31 MPa).

When compared to micrographs (a) and (b) in micrographs (c) and (d), the matrix appears to be more homogeneous with surface continuity. Correspondingly, the compressive strengths have also increased due to the maximum dissolution of the binder components in alkaline liquid with 12 M NaOH. The strength attained at 3 days and 28 days is of order 34.5 MPa and 39 MPa, respectively.

In image (e), a few undissolved Fly-Ash particles do exist in spite of much better dissolution and the reaction of both Fly Ash and GGBS. Voids, discontinuous micro-cracks and partially dissolved GGBS particles are also visible. The strength gained at 3 days is around 34 MPa. This is due to more CaO percentage as shown in Table 4.

However, the microstructure of micrograph (f) is far more compact because at later stages GGBS content led to the formation of higher geopolymeric and CSH gel, resulting in much higher strength development of around 39 MPa at 28 days.

In micrographs (g and h) due to the high concentration of NaOH, the un-reacted Fly-Ash particles are almost absent; dissolution of Fly Ash and GGBS is more complete and uniform. Micro-pores and semi-spherical cavities as a result of the breakdown of Fly-Ash particles at this stage can be seen in micrograph (g). Still, the matrix appears to be dense and compact giving strength in excess of 40.5 MPa and 48 MPa, respectively.

Thus, significant progressive morphological changes take place with a progressive increase in GGBS content as shown in micrographs (e)–(h) compared to micrographs (a) and (b) resulting in better strength performance.

According to Song et al. [16], the alkaline activated slag microstructure was highly smooth, uniform and interconnected-solid in all samples. Increased alkali doses, on the other hand, contributed to more degree of reactivity and more sealed pores, resulting in a less porous microstructure.

6 Conclusion

1. With the addition of GGBS and molarity concerning the reference mix (fly ash 100%), slump flow values decreased and all the values were within the limits of EFNARC guidelines.
2. With age, oven-cured SCGC centred on fly ash/GGBS gain strength for all binder fractions and molarities.
3. At all ages, shear strength increases with an increase in GGBS and a decrease in Fly Ash. Unaffected by the mix, an increase in molarity also increases shear strength. These strengths vary from 5 to 10% of the respective compressive strength.
4. The increase in GGBS and molarity increased the energy absorption and hence increased the impact resistance of SCGC, and energy absorption capacity was more for 70% replacement of fly ash with GGBS irrespective of any molarity for all the days of testing.
5. The microstructure images reveal a very dense structure and correspondingly higher strength with age. A similar observation is made with an increase in GGBS content and also with an increase in the molarity of NaOH solution.
6. From both competitiveness and cost standpoints, a Fly Ash:GGBS proportion in the spectrum of 50:50, regardless of molarity, appears to be desirable.

References

1. McCaffrey R (2002) Climate change and cement industry. Global Cement and Lime Magazine, environmental special issue, 15–19
2. Flower DJM, Sanjayan JG (2007) Greenhouse gas emissions due to concrete manufacture. Int J Life Cycle Assess 12:282–288
3. Mehta PK (2001) Reducing the environmental impact of concrete. Concr Int 23:61–66
4. Berry M, Cross D, Stephens J (2009) Changing the environment: an alternative "Green" concrete produced without Portland cement. In: World of coal ash (WOCA) conference, Lexington, KY, USA
5. Ritchie H, Roser M (2020, May 11) Greenhouse gas emissions. Our World in Data. Retrieved 22 June 2021
6. Roy DM (1999) Alkali-activated cements opportunities and challenges. Cem Concr Res 29:249–254
7. Topark-Ngarm P, Sata V, Chindaprasirt P (2012) Effects of admixtures on high calcium geopolymer concrete cured at room temperature. In: The 4th KKU international engineering conference
8. Hardjito D, Rangan BV (2005) Development and properties of low-calcium fly-ash-based geopolymer concrete. Research report GC1. Faculty of Engineering, Curtin University of Technology, Perth, Australia
9. Wallah SE, Rangan BV (2006) Low-calcium fly-ash-based geopolymer concrete: long-term properties. Research report GC2. Curtin University of Technology, Perth, Australia
10. Rangan BV (2008) Fly-ash-based geopolymer concrete. Research report GC4, Curtin University of Technology, Perth, Australia
11. IS: 12089-1987 (1987) Specification of granulated slag for the manufacture of Portland slag cement. Bureau of Indian Standards, New Delhi
12. Bairagi NK, Modhera CD (2001) Shear strength of fiber-reinforced concrete. ICI J 47–53
13. Baruah P, Talukdar S (2007) A comparative study of compressive, flexural, tensile and shear strength of concrete with fibres of different origins. Indian Concr J 17–24
14. IS 456: 2000 (2000) Plain and reinforced concrete-code of practice. Bureau of Indian Standards, India
15. ACI Committee 544 (1996) State of the art report on fibre reinforced concrete. ACI Committee 544 report 544. 1R-96. American Concrete Institute, Detroit
16. Song S, Sohn D, Jennings HM, Mason TO (2000) Hydration of alkali-activated ground granulated blast furnace slag. J Mater Sci 35:249–257

An Experimental Study on Self-Compacting Concrete by Using Silica Fume and Fly Ash

B. S. Shruthi and Anilkumar

Abstract Self-Compacting Concrete (SCC) is a new type of concrete that wouldn't require vibration for laying or compaction. Fine materials, such as silica fume and class F fly ash, are used to provide the desired properties of the concrete. The SCC increases constructability, lowers skilled workers' wages, provides a smooth and clear surface quality, and speeds up project timelines. One way to reduce the cost of self-compacting concrete is to include cementitious materials like Silica Fume (SF) and class Fly Ash (FA). It also minimizes the heat related to hydration. This work provides experiments on compressive strength (compression tests for double-blended and triple-blended), split tensile test, flexural strength of SCC containing various mineral admixtures, workability aspects such as slump flow, T500, and V-funnel flow time tests, and modulus elasticity tests. In particular, (OPC 53) and M35 concrete grades have been used in this research. The approach used is that mineral admixtures are substituted with silica fume 5% and 10% and fly ash 25%, 30%, and 35% by weight of Portland cement is inserted, and performance is evaluated and compared to normal Portland cement. Mineral admixtures were examined for their influence on self-compacting concrete workability, compressive strength, splitting tensile strength, flexural strength, and modulus of elasticity. Adopted water-cement ratio of 0.45 and manufactured sand are used as fine aggregates and coarse aggregates with a size of 12.5 mm and powder content of 520 kg/m^3 (as per IS code 10262-2019) is selected as binder material (fine aggregate and cement). Poly-carboxylate ether is used them. As an outcome, the superplasticizer accelerated the pace of the concrete; there has been a general improvement in the flow and filling capabilities of self-compacting concrete. And SF10FA30 does have maximum strength for 28 days than other mixes, whereas SF5FA25 seems to have a higher modulus of elasticity than other mixes.

Keywords Fly ash · Freshness parameters · Strength parameters · Silica fume · Modulus of elasticity · Self-compacting concrete

B. S. Shruthi (✉) · Anilkumar
Nitte Meenakshi Institute of Technology, Yelahanka, Bangalore 560064, India
e-mail: shruthi.bs@nmit.ac.in

L. Nandagiri et al. (eds.), *Recent Advances in Civil Engineering*, Lecture Notes in Civil Engineering 256, https://doi.org/10.1007/978-981-19-1862-9_12

1 Introduction

SCC is characterized as a concrete that can be poured and compacted with little or no vibration effort while being cohesive enough and being handled without segregation or bleeding [1]. Mineral additives such as cement and chemical admixtures such as superplasticizers and viscosity modifiers have been used to create SCC. Self-compacting concrete is a new combination of cement that flows easily. By its outstanding consolidation, homogeneity, and reliability, SCC is more common in RMC facilities in recent years. Both in fresh and hardened concrete, it is critical to understand the role of the various components utilized in the mix. Self-compacting concrete is claimed to have greater fluidity and separation. Its need for water and the workability of concrete influence particle shape and size distribution, particle packing effect, and smoothness of surface textures. From 1997 to 2000, substantially flowable concrete was applied in underwater concreting of unreinforced and moderately reinforced low-grade building elements. Okamura introduced the SCC idea to Japan in 1986 at a university. Thus, Prof. Ozawa of the University of Tokyo was the first to offer SCC in Japan in 1988. In 1994, the Japan Society of Civil Engineers issued the first guiding papers. Professor Okamura modified the nomenclature of concrete from one type of HPC being used worldwide to self-compacting concrete in 1997. The North American conference coordinated the first-ever design and implementation of SCC in November 2002. SCC was sponsored by a multinational project leading manufacturer from 1997 to 2000. Admixtures are the byproduct of industry; the cost of that materials is less than that of cement.

2 Methodology

The goal of this study is to see if self-compacting concrete can be made using regular Portland cement and substituted in an attempt to understand the difference in cementitious materials, with fly ash and silica fume. The mix proportions for M35 grade concrete were calculated according to IS 10262: 2019 [2] and trials were carried out using regular Portland cement and substituting it containing fly ash at 25, 30, and 35% by weight of cement, and silica fume at 5 and 10% by weight of cement. Basic assays were conducted to evaluate the quality of the materials, as well as workability tests to ensure the fluidity of the composite, and Superplasticizer also was performed to boost workability. SCC's toughened capabilities are also demonstrated. This result obtained test results in the parameters of fresh and hardened self-compacting concrete were compared to improve the performance of concrete in workability and strength (compression test (CS) for double-blended and triple-blended mix). SCC is being used to cast concrete cubes, cylinders, and beams. The strength parameters are assessed at 7 and 28 days of age (triple-blended mix), and the specimen's modulus of elasticity is computed at 28 days.

Table 1 Properties of cement

S. No.	Test conducted	Test performed	FA	SF
1	Specific gravity	2.98	2.23	2.24
2	Normal consistency	29.5%	–	–
3	Initial setting time	120 min	–	–
4	Final setting time	230 min	–	–
5	Fineness	3.38%	26.72%	22.23%
6	Soundness	2 mm	–	–

3 Experimental Investigation

3.1 Components

3.1.1 Ordinary Portland Cement

The OPC grade 53 is utilized in this project, which complies with IS 12269: 2013 and for physical tests as per IS 4031: 1996 [3] (Table 1).

3.1.2 Sand

Manufactured sand made from the stone crusher plant nearby conforming to IS 383: 2016 is used [4, 5] (Table 2).

3.1.3 Coarse Aggregate (CA)

Coarse aggregate of 12.5 mm downsized aggregate conforming to IS 383: 2016 is used [4] (Table 3).

3.1.4 Superplasticizer

Poly-carboxylate ether superplasticizer manufactured by Buildplast Super conforming to IS 9103: 1999 is used (Table 4).

3.2 Mix Proportioning

Mix design of concrete M35 grade is a method of addition of ingredients like cement, coarse, and fine aggregates in different quantities to obtain preferred outcomes.

Table 2 Properties of sand

S. No.	Tests conducted		Results obtained
1	Specific gravity		2.604
2	Water absorption		0.78%
3	Fineness modulus value		
IS sieve sizes	Cumulative percentage		
	Retained	Passing	
4.75 mm	0	100	Observation: as per the IS code, fine aggregate come under zone II
2.36 mm	9.80	90.20	
1.18 mm	36.40	63.60	
600 µm	59.53	40.47	
300 µm	84.53	15.47	
150 µm	97.30	2.70	
075 µm	99.70	0.30	
Pan	100	0	

Table 3 Tests conducted on CA

S. No.	Tests conducted		Results obtained
1	Shape		Angular
2	Specific gravity		2.73
3	Water absorption		0.64%
4	Particle size distribution		
IS sieves	Cumulative %	Cumulative %	
	Retained	Passing	
16.00 mm	0.00	100	Observation: as per the obtained value, CA comes under graded aggregate
12.50 mm	0.38	99.62	
10.00 mm	31.76	68.24	
4.75 mm	97.84	2.16	

Table 4 Properties of superplasticizer

S. No.	Properties	Results
1	Color	Brownish liquid
2	pH	6.80
3	Specific gravity	1.08
4	An existence of chloride	<0.2%
5	Entrainment of air	>1.5%

Table 5 Triple-blended mixes

Materials are in kg/m^3									
Data	Grade	Cement	FA	SF	Water	FA	CA	SP %	W/C %
Control	M35	444.44	–	–	195	944.50	748.02	1.0	0.45
SF5FA25	M35	311.11	111.11	22.22	200	944.50	720.61	1.5	0.45
SF5FA30	M35	288.89	133.33	22.22	200	944.50	710.34	1.5	0.45
SF5FA35	M35	260.01	151.66	22.22	195	958.37	732.34	1.0	0.45
SF10FA25	M35	288.88	111.11	44.44	200	944.50	704.34	1.5	0.45
SF10FA30	M35	266.68	133.33	44.44	200	944.50	690.23	2.0	0.45
SF10FA35	M35	244.45	155.55	44.44	200	944.50	688.23	1.5	0.45

Table 6 Double-blended mixes

Data	Grade	Cement	FA	SF	Water	Fine	Coarse	SP	W/C
SF5	M35	422.22	–	22.22	200	944.50	720.61	1.0	0.45
SF10	M35	400.00	–	44.44	200	944.5	704.34	1.5	0.45
FA25	M35	333.33	111.11	–	200	944.50	720.61	1.5	0.45
FA30	M35	311.10	133.33	–	200	944.50	710.34	1.5	0.45
FA35	M35	288.88	155.55	–	195	944.50	732.34	1.0	0.45

Chemical admixtures were also used in concrete because it improves the attributes of workability and strength. The mix design is produced in accordance with IS 10262-2019 [2] and IS 456-2000. Mineral admixtures such as FA and SF are employed, while chemical admixtures are preferred. In this, poly-carboxylate ether gives a good performance to concrete. Zone-II conforming fine aggregates are used. M-sand is used is the replacement of the natural river sand and a coarse aggregate of downsized 12.5 mm is adopted to reduce the water content superplasticizer used (Tables 5 and 6).

4 Results and Discussion

4.1 Workability Test

4.1.1 Slump Test

This is carried out in accordance with IS code 1199 part 6 [6] for the triple-blended mix. Control mix slump value reached with w/c ratio of 0.42 and for blended it is of 0.45; workability rises as admixture concentration increases. SF5FA25, SF5FA30,

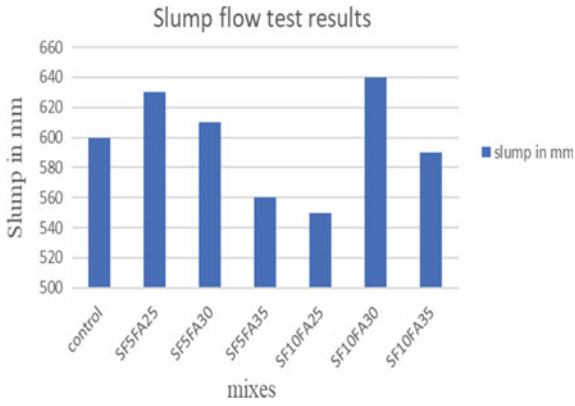

Fig. 1 Slump flow results

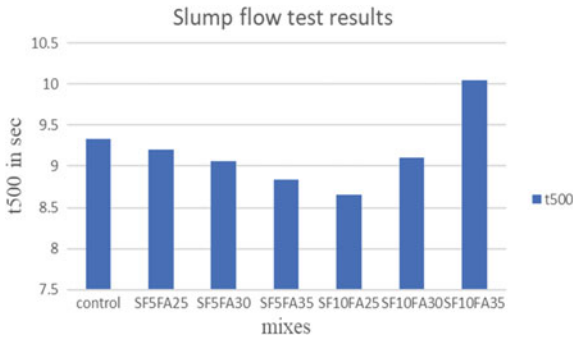

Fig. 2 Slump flow time for 50 cm diameter

and SF10FA30 have high filling capabilities. This falls under the SF1 category of unreinforced concrete (Figs. 1 and 2).

4.1.2 V Funnel Testing

This is done as per the IS 1199 part 6 for the blended mix proportions. Viscosity and filling ability are determined by this testing for the SCC. For the basic mix, V funnel time is more when compared with other trial mixes. It comes under the V1 class because the SCC pass from the funnel in < or = to 8 s (Figs. 3 and 4).

Fig. 3 V funnel test

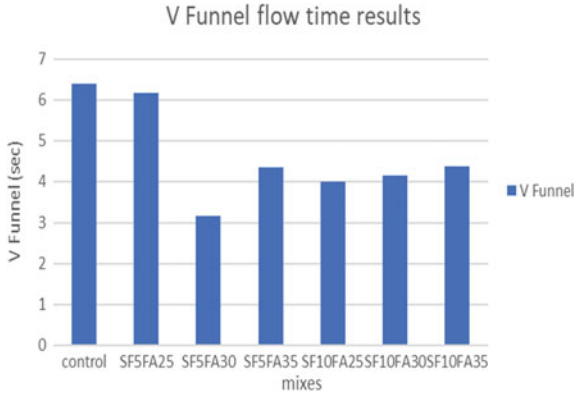

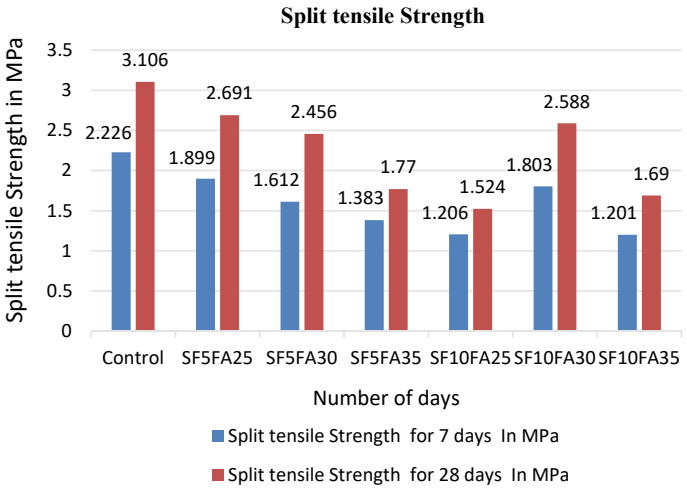

Fig. 4 Split tensile strength

4.2 Hardnesned Properties of Concrete

4.2.1 Compressive Strength for Triple-Blended Mixes

For the size of the beam, 150 mm * 150 mm * 150 mm are used in this test. IS 516: 1959 [7] is used to calculate compressive strength for varying percentages of Fly Ash and Silica Fume. The following are the results of these mixes after 7 and 28 days of curing. The graph depicts the results of three trial tests for the control and triple-blended mix. The control mix that had been used for 7 and 28 days produces the highest compressive strength values of 27.01 MPa and 33.811 MPa, respectively. The greatest compressive strength value for a triple-blended 5 percent SF mix is SF5FA25 for 7 days and SF5FA30 for 28 days, correspondingly, with the ultimate

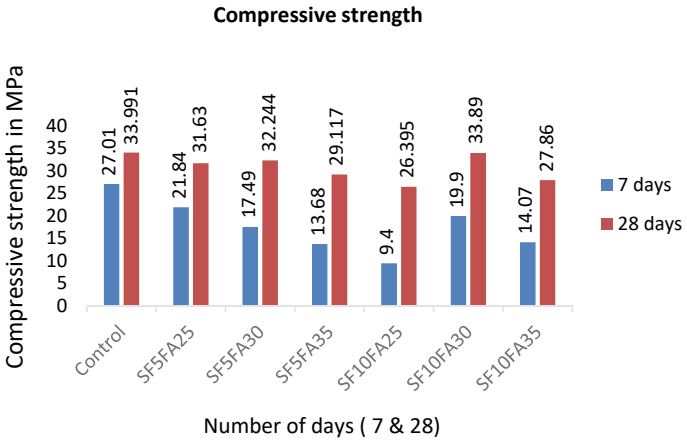

Fig. 5 Compressive strength

load value for a 10 percent SF mix being SF10FA35 for 7 days and SF10FA30 for 28 days. Triple-blended mix is made by using OPC, FA, and SF. Less FA and SF content gives higher strength than the higher content of both. The heat of hydration is less due to less pozzolanic reaction of FA and reduced Calcium oxide content. Because of its fineness and the nature of proper packing, SF provides early strength. When SF interacts with cement, calcium silicate hydrate is formed. When SF10FA30 was compared to the control mix and triple-blended mix, after 28 days, SF10FA30 had reached 99% of the strength of the control mix (Fig. 5).

4.2.2 Compressive Strength of Mixes that have been Double Mixes of FA and SF for 28 Days for Double Blended Mixes

Double-blended mixes of FA and OPC. The highest compressive strength value obtained for in SF10 when compared with the other mix proportions. Figure 6 gives the strength value for 28 days. And mix proportions.

4.2.3 Split Tensile Testing

The IS 5816: 1999 [8] Split tensile procedure is done on a 150 mm diameter, 300 mm height cylinder. The tensile strength of concrete is evaluated for varying ratios of admixture blended mix for curing durations of 7 and 28 days.

When compared to triple-blended mixes, SF5FA25 achieves the maximum strength in 7 days and 28 days, indicating that as the number of days spent curing increases, so does strength, with a 13.45% increase in 28 days compared to blended mixes (Fig. 7).

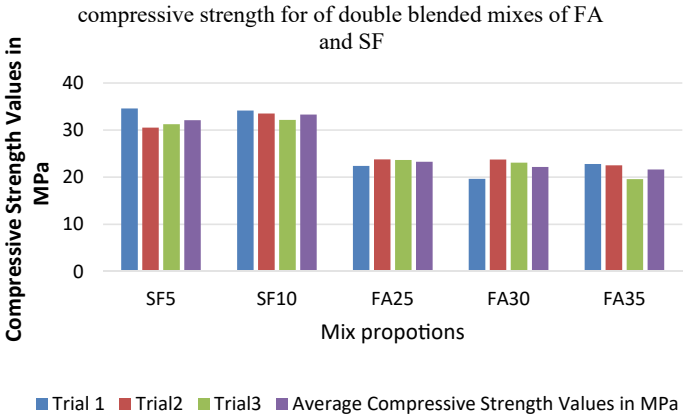

Fig. 6 CS of double-blended mixes of FA and SF for 28 days

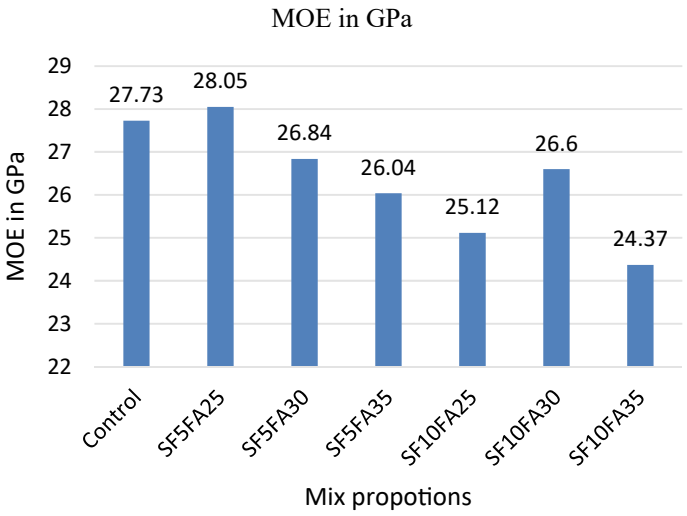

Fig. 7 Modulus of elasticity

4.2.4 Flexural Test

In respect of beam size, 10 × 10 × 50 is used in this test as per IS 516: 1959 [7]. This beam is used to calculate the flexural strength of the SCC. Testing is carried out for 7- and 28-day cure periods. Three trials should be conducted to get accurate results on the flexural strength of SCC. Control mix showed higher strength when compared with remaining triple-blended mixes of 7- and 28-day curing period. Curing period should be increased in SCC to get higher flexural strength values. Control mixes will giving higher strength than other blended mixes of 7 and 28 days (Fig. 8).

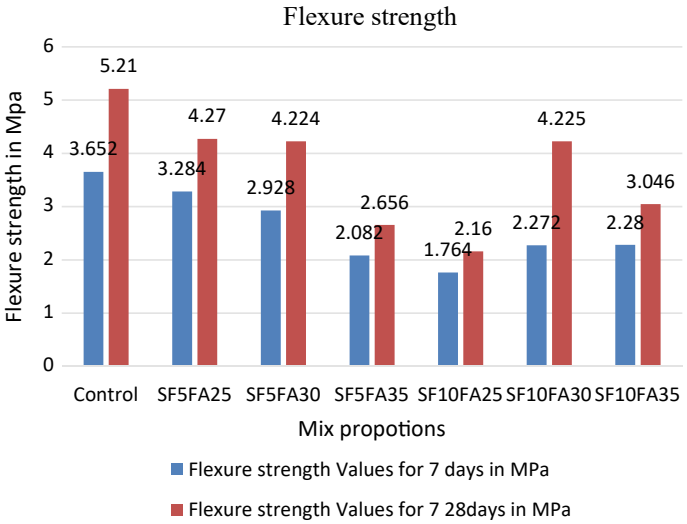

Fig. 8 Flexural test

4.2.5 Modulus of Elasticity Testing (MOE)

A cylinder with a diameter of 150 mm and a height of 300 mm is employed in this sample, and three trials are run for different ratios. MOE for varying percentages of Fly Ash and Silica Fume in SCC, MOE values were determined using IS 516: 1959. The graph depicts several MOE findings for 28 days of age. The control mix has a pressure of 27.73 MPa. Sample SF5FA25 had the highest pressure measurement of 28.05 MPa. A smaller percentage of FA and SF addition yields a better value (Fig. 7).

The accompanying Fig. 9 reveals that the initial tangent modulus is 3.0840E−05 MPa and the secant modulus of elasticity is 1000 MPa.

5 Conclusion

The outcomes of the above graphs, such as strength, workability, and modulus of elasticity testing were obtained by running several tests on cement with a Fly Ash content of 25, 30, and 35% and a Silica Fume content of 5 and 10%. Triple-blended mix of SCC and a double-blended mix for compressive strength are discussed below the addition of Fly Ash and Silica Fume to SCC improves the workability of the mixes SF5FA25 and SF10FA30.

1. The inclusion of FA and SF in SCC promotes the workability of the SF5FA25 and SF10FA30 blends.
2. The 28-day cube strength of SCC is boosted when both FA and SF are included in SCC blends.

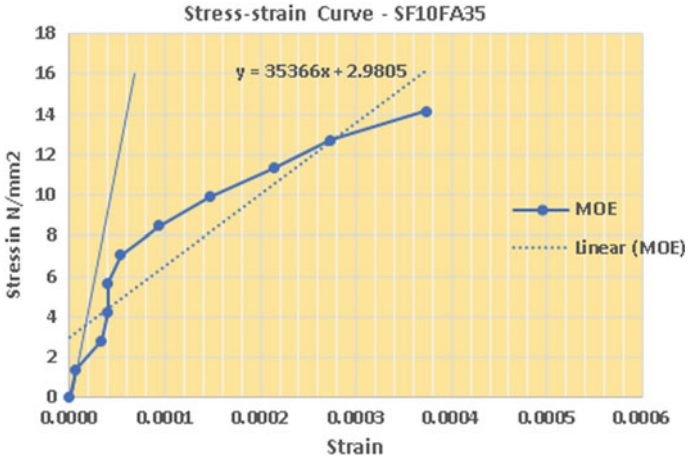

Fig. 9 Modulus of elasticity curve for SF10FA35

3. Use of SF5FA25 mixes gives the 98% compressive strength and flexural and split tensile and same as compared with control mix, bases on the results as mix as optimum mix SF5FA25.
4. As the percentage of Fly Ash increases in a mix, it leads to an increase in the strength values. The compressive strength of the control mix is 27.01 MPa. Tensile and flexural strength are better again for the control mix, having values of 2.226 and 3.648 MPa for 28 days of age.
5. The control mix does have a good tensile strength than the other blended mixes, with a value of 33.991 MPa. Tensile and flexural strength are also higher for solely the control mix. Tensile and flexural strength values are 15 and 22% higher, respectively, than SF5FA25.
6. Concrete's strength may rise as the curing period lengthens. The compressive strength value of the control mix is increased by approximately 26% from 7 to 28 days of curing.
7. Double-blended mixes of SF in 5 and 10%, FA in 25%, 30%, and 35% in SCC. The obtained results are better when compared to the blended mixes.
8. The SF5FA25 mix has a higher MOE than the other mixes, at 28.03 MPa against 27.73 MPa for the control mix. For smaller amounts in the blended mix, SF, like FA and cement mixed mixes, gives superior strength values.
9. SF5FA25 in all aspects is considered as an optimum mix proportion.

References

1. Song HW, Byun KJ, Kim SH, Choi DH (2001) Early-age creep and shrinkage in self-compacting concrete incorporating GGBFS. In: Proceedings of the second international RILEM symposium

on self-compacting concrete, Japan, pp 413–422
2. IS 10262: 2019 (2019) Recommended guidelines for concrete mix design. Bureau of Indian Standards, New Delhi
3. IS 12269: 2013 (2013) Ordinary Portland cement, 53 grade-specification. Bureau of Indian Standards, New Delhi
4. IS 383: 2016 (2016) Coarse and fine aggregate for concrete-specification. Bureau of India Standards, New Delhi
5. IS 4031 (part 1): 1996 (1996) Method of physical tests for hydraulic cement, reaffirmed 2005. Bureau of Indian Standards, New Delhi
6. IS 1199 (Part 6): 2018 (2018) Fresh concrete-methods of sampling, testing and analysis. Bureau of Indian Standards, New Delhi
7. IS 516: 1959 (1959) Methods of test for strength of concrete, reaffirmed 2004. Bureau of Indian Standards, New Delhi
8. IS 5816: 1999 (1999) Splitting tensile strength of concrete, reaffirmed 2004. Bureau of Indian Standards, New Delhi
9. IS 269: 2015 (2015) Ordinary Portland cement-specification. Bureau of Indian Standards, New Delhi

Feasibility of Utilization of ECC Mix in Pavement Construction

Arjun Patil and Sarah Mariam Abraham

Abstract Engineered cementitious composites are a class of high-performance fiber-reinforced cementitious composites with strain hardening and multiple cracking properties. The specialty of engineered cementitious composite is its tensile strain carrying capacity to be 300–500 times that of conventional concrete. Analysis results suggest that engineered cementitious composite can greatly extend the service life of the structure due to its high fatigue and ductility performance. This has led to the wide acceptability of engineered cementitious composite and has the potential to be used as an overlay, interlayer, and even as a surface course in pavement construction. The present paper discusses the advantages and disadvantages of engineered cementitious composite in comparison to conventional concrete in terms of strength and durability characteristics, life cycle costs, and field applications. It has summarized the performance of engineered cementitious composite in different courses of the pavement. In this study, an empirical relation has been derived for a relation between flexural strength and compressive strength of the engineered cementitious composite.

Keywords Engineered cementitious composite · Fatigue life · Ductility · Flexural strength · Compressive strength · Strength relation

1 Introduction

Engineering Cementitious Composites (ECC) was developed by Prof. Victor Li at the University of Michigan in the year 1993. It is a type of fiber-reinforced cementitious composite having the property of high tensile ductility. It has a tensile strain in the range of 300–500 times more than conventional concrete [1]. ECC is also known as bending concrete due to its capability of withstanding bending stress. ECC has both strain hardening and multiple cracking properties. Generally, the failure in concrete is brittle which is promoted due to the formation and propagation of a single crack. In ECC, instead of one single huge crack, there is the formation of multiple microcracks

A. Patil (✉) · S. M. Abraham
Department of Civil Engineering, Birla Institute of Technology and Science Pilani, Pilani, India
e-mail: h20200080@pilani.bits-pilani.ac.in

L. Nandagiri et al. (eds.), *Recent Advances in Civil Engineering*, Lecture Notes in Civil Engineering 256, https://doi.org/10.1007/978-981-19-1862-9_13

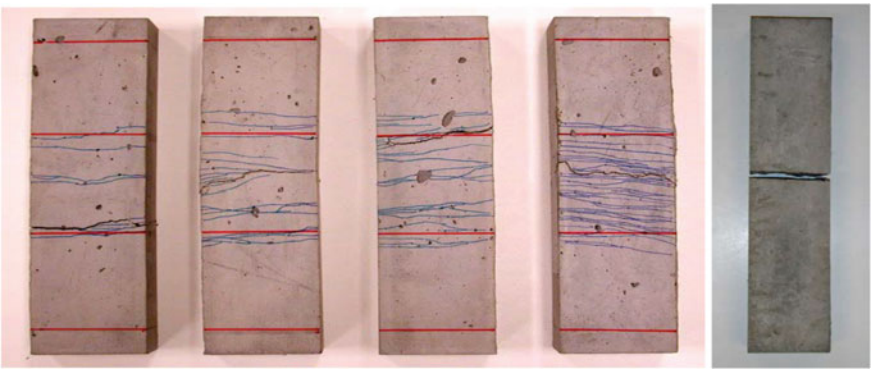

(a) (b)

Fig. 1 Crack pattern of **a** 4 ECC samples and **b** 1 conventional concrete sample. Adapted from [1]

throughout the body of the structural member as shown in Fig. 1. ECC improves the deformation characteristics as it is more ductile. The durability of pavement was checked by subjecting ECC and conventional concrete samples to monotonic and fatigue loading [1].

This results in the dissipation of the applied load more effectively and thus increases the life span of the member. This behavior of the material is due to the absence of coarse aggregates in the mix, higher binder content (usually fly ash and cement), presence of fibers, and higher workability due to the utilization of a super-plasticizer. ECC has been widely used in various structures like roads, bridges, and even earthquake-resistant structures. They have been used in countries like Japan, Europe, and the USA. It was first used in Michigan, to design a bridge deck slab, and it has been performing better than conventional concrete [2].

It is imperative to understand the behavior of ECC mixes in terms of their mixture preparation, mechanical properties, crack propagation, climatic conditions, and their-contribution toward sustainability. The objective of the paper is to collectively assess the research studies conducted on ECC and recognize the disparity with conventional concrete and whether the universal strength relations would cater to ECC.

2 Literature Review

Research regarding various strength parameters and behavior of the material under different atmospheric conditions has been conducted by researchers [3]. Studies vary depending on the materials incorporated in the mix design of ECC which subsequently influences the strength characteristics and behavior in non-ideal conditions. Selection of any type of mix would depend on it being ecological, economical, and an asset to the society which could be assessed using Life Cycle Analysis and pragmatic application of the same. A brief review of materials, strength, and durability

characteristics, impact on environment, and field applications is described in this section.

2.1 Fibers

Fibers form an integral part of ECC mix whereas in the conventional concrete mix, they acts as a supplementary material. The incorporation of fibers in an ECC mix can be a boon as well as a curse since it is responsible for improving the ductility of a structural member by holding the matrix together, but excess of it could cause a reduction in workability and impact the overall ductility of the composite [4]. So, it has been recommended to use not more than 2% by weight of the fibers in the mix [4].

Fibers of Polyvinyl alcohol (PVA), Carbon, Steel, Nylon-6, glass, Polyethylene (PE), Nylon-66, Basalt, Aramid, Polyethylene Terephthalate, and Polyacrylonitrile (PAN) have been studied for use in ECC composite [3, 5–8]. Some important factors like the cost and tensile strength were studied and represented by Figs. 2 and 3 [7]. The compatibility of fibers with ECC plays a prominent role in the performance of the same.

Steel: In terms of the cost of steel fibers, it is the cheapest in comparison to the rest. Figure 2 shows the cost of the fibers per unit mass. It was found that steel

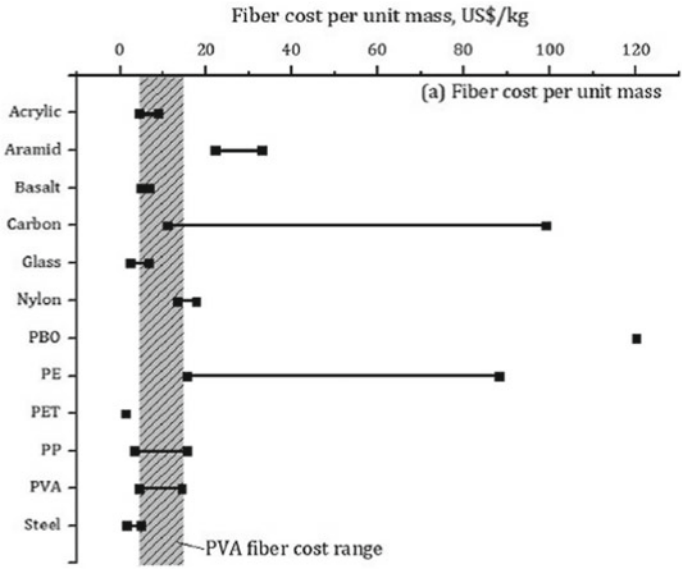

Fig. 2 Cost of fibers per unit mass. Adapted from [7]

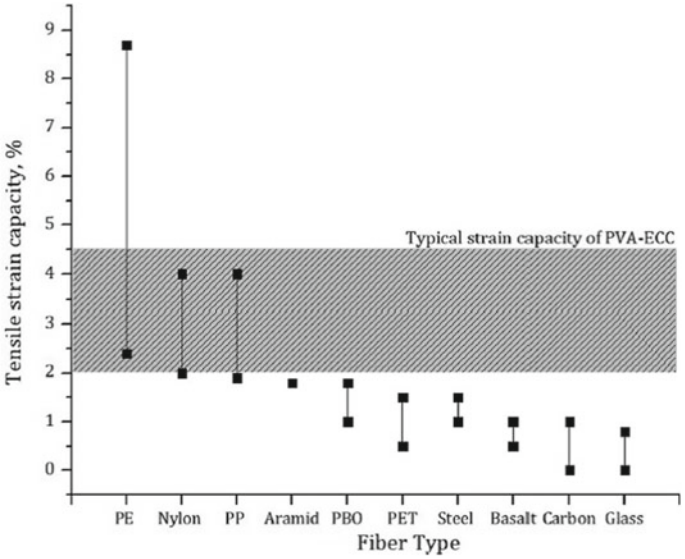

Fig. 3 Tensile strain capacity for different fibers. Adapted from [7]

formed a better bond with the matrix when compared with other fibers making the crack width be least as well.

It was found that the higher the aspect ratio and volume of the steel fibers used, the more will be the flexural strength and toughness of the mix [9]. It is generally not advised to use 20–50 micrometer diameter steel fiber as they can injure workers and puncture tires [7]. The optimum aspect ratio of steel fiber is hard to be determined and hence detailed research is required.

It was concluded that twisted fibers were more effective than hooked fibers in promoting the composite load carrying capacity, effective energy absorption capacity, and multiple cracking behavior [10]. Overall, the more the percentage of deformed steel fibers, the more is the effective bond, and hence more is the composite flexural strength and toughness [7].

It was also found that steel was naturally resistant to alkaline nature which would be beneficial since concrete mixes are ideal in a pH of 12–13.5 [11]. Cement is alkaline in nature and thrives in its surrounding. However, when fibers are exposed to an alkaline environment, they deteriorate [8].

Polypropylene [PP]: PP fiber when compared with PVA fiber has lower modulus and thus higher elongation at break. Due to this, it promotes higher ductility in cement composite [7]. PP fibers form a weak bond with ECC when compared with that of the PVA-ECC sample. This is due to its nature being more hydrophobic when compared to that of PVA fibers [7]. Exposing PP fibers to plasma changes the nature of PP fiber from hydrophobic to hydrophilic, which in turn improves the adhesion between the fiber and ECC matrix [7].

PP fibers are resistant to alkaline environments [7]. The aging effect of PP fibers caused by oxidation can lead to fiber embrittlement and can be improved by using the chemical stabilization of fibers through pretreatment [12]. It has comparable tensile ductility but less tensile strength when compared to that of Polyvinyl alcohol (PVA) fibers. The low cost and high chemical stability have made it to be a potential replacement for PVA in the future.

Polyethylene [PE]: PE fibers are thermoplastic in nature and hence have good toughness, abrasion resistance, and impact resistance [6]. It was found that the addition of PE fibers decreased the drying shrinkage of cementitious material. The reduction in drying shrinkage was more than 10% [13]. This was also the reason for the reduction in crack width and crack area as the content of the fiber increased [14].

As the aspect ratio or the volume of fibers increases in the mix, it has been found that it increased the flexural strength, shear strength, deflection, and elastic modulus [6]. However, this comes at the cost of a reduction of workability and an increase in non-homogeneity of the matrix as it is difficult to disperse the fibers uniformly [6].

A reduction in compressive strength was noted with the incorporation of PE fibers. Li et al. (2020) in an experiment showed that the incorporation of 1% of PE fibers decreased compressive strength by 7% when compared with the regular ECC sample [6]. PE fibers increased air voids from 0.4 to 1.2% in the mixture and to rectify it a new vibration method for mixing the fibers is recommended [6].

Nylon 66 And Polyacrylonitrile: Research was conducted for studying Nylon 66 and Polyacrylonitrile (PAN) fibers [5]. PAN fiber composites were found to possess higher flexural strength while Nylon 66 fiber composite had higher deflection as depicted in Fig. 4.

The deflection was 7 Times that of PAN and 140 times that of normal concrete specimen [5]. This increase in deflection of the specimen resulted in higher toughness which is about 70 times that of the control sample [5].

Pull-out strength required for PAN fibers was more than that of Nylon fiber due to the stronger bonding of PAN with the matrix as shown in Fig. 5. This bonding was due to the mechanical and chemical characteristics of the PAN fiber. The kidney shape of the PAN fibers leads to an increase in the lateral surface of the fiber which

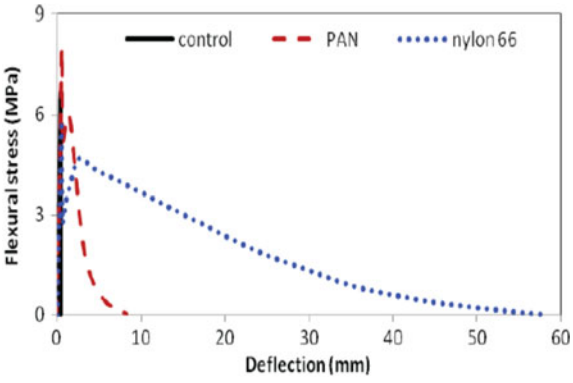

Fig. 4 Flexural stress versus deflection of nylon 66 and PAN. Adapted from [5]

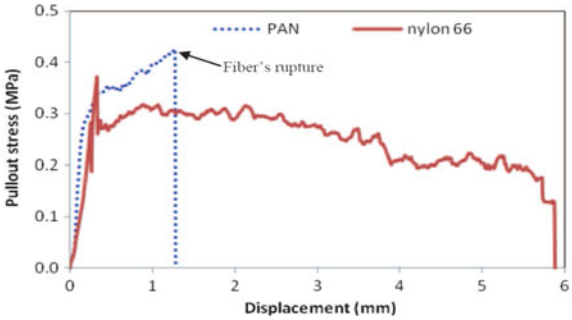

Fig. 5 Pullout stress (Mpa) versus displacement for nylon 66 and PAN fibers. Adapted from [6]

enhances the pull-out strength [15]. Also, it was reported that as the Nylon 66 fiber higher modulus of rupture and molecular weight, there is less chemical interaction between the Nylon 66 fiber and the mix, when compared to that of the PAN fiber and the concrete mix [5]. Nylon 66 fiber came out as a whole when the composite went under test, while PAN fiber broke.

2.2 Tensile Strength

One of the major issues with conventional concrete including Fiber-Reinforced Concrete (FRC) is it undergoes brittle failure when exposed to fatigue loading [1]. Conventional concrete has a strain capacity of less than 0.01% [1] leading to pavement surface failures due to reflective cracking, fatigue cracking, and joint spalling. ECC being highly ductile and possessing an average strain capacity of 2.5% [1] as shown in Fig. 5 can improve the pavement's resistance to such failures.

This has promoted the usage of ECC in various structural applications including bridges, roads, and even earthquake-resistant buildings [16, 17] (Fig. 6).

ECC has been used in bridge construction and was observed to have a significant reduction in cracks on the pavement surface [2] since the pavement was capable to handle variations due to temperature and moisture. This has also led the expansion

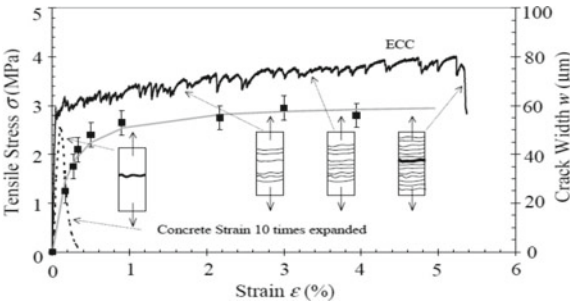

Fig. 6 Stress versus strain graph of a normal concrete road and ECC. Adapted from [17]

joints to be of little to no use [9]. A study by Qian and Li conducted a Finite Element Analysis on both conventional and ECC composites. The study concluded that the thickness required for the conventional concrete sample is 1.8–2.7 times that of ECC [1]. Li conducted research on bridge deck slab of reinforced ECC (RECC) and normal reinforced concrete, in which they were subjected to a high fatigue load [2]. This resulted in 0.6 mm of cracks in the latter, whereas the microcracks didn't exceed 50 μm of crack width in the former.

While the utilization of recycled asphalt shingles (RAS) in ECC showed that it compromised the flexural strength of the composite, there was a considerable change in maximum load and midspan deflection of the composite when more than 50% of silica sand in ECC was replaced with recycled asphalt (RAS). Similar results were reported by Hossiney [18], after utilization of more than 40% recycled asphalt (RAS) in conventional concrete. The reason for this can be attributed to the increase in voids due to reduced bonding of recycled asphalt (RAS) and concrete interface.

2.3 Compressive Strength

It was found that the compressive strain carrying capacity of ECC was 0.45–0.65% higher than that of conventional concrete [17]. The 28-day compressive strength of ECC generally varies from 30 to 90 MPa, depending on the mix design [17]. The relatively low elastic modulus of ECC ranging from 20 to 25 GPa [17] promises less resistance to deformation and subsequently lowers the accumulation of tensile stress. The brittle failure pattern of conventional and high-strength concrete was not the characteristic failure of an ECC sample, under compressive loading but rather at an angle of 45° as shown in Fig. 7, and could be categorized as a "ductile compressive failure" [17].

While there was no reduction in compressive strength of ECC when compared to conventional concrete [17], a 20.6% reduction of compressive strength was reported in the composite when silica sand was fully replaced by RAS. This observation was

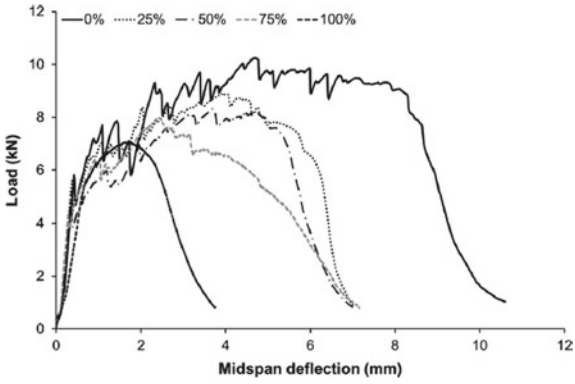

Fig. 7 Load deflection curve of ECC-recycled asphalt (RAS) composites. Adapted from [19]

also resonated in studies conducted by Hossiney et al. and Huang et al. with respect to conventional concrete due to the development of a weak Interfacial Transition Zone.

However, only a 20.6% reduction in compressive strength was observed for ECC-RAS composite [19] in comparison to conventional concrete incorporating RAS, where the latter observed a 50% reduction. This may be attributed due to higher content of fine aggregate and lower water–binder ratio leading to lower void content of the mix [19].

2.4 Exposure to Climatic Conditions

Concrete structures including pavements are subjected to non-ideal environmental conditions like extreme weather leading to freezing and thawing, tropical climates, undesirable entities in groundwater, soil, or even the materials used for preparing the mix. Li [17] conducted the freeze and thaw test on a non-air entrained specimen of conventional concrete and ECC specimen as per ASTM 666 [20] where the specimens shall be subjected to numerous cycles of freeze and thaw. It was observed that the conventional concrete deteriorated after 110 cycles of freeze and thaw, whereas ECC did not show signs of deterioration after 300 cycles. Hence, ECC achieved a durability factor of 100 whereas conventional concrete had a durability factor of 10. This indicates the potential of ECC to withstand changes under extreme fluctuating weather conditions and can protect the structure from frost damage.

Various other tests were conducted by Li in 2007 [17] conducted tests which included exposing the ECC specimen to tropical climate and chloride for replicating different field conditions. When the ECC specimen was exposed to tropical climate conditions, the early age strain capacity of the specimen dropped from 4.5% to 2.75% which is about 250 times the normal concrete [17]. Chlorides are present in groundwater, soil, and binders of mix and have the capability of destroying the protective layer of reinforcement, leading to corrosion [11]. Minimum steel requirements in rigid pavements include tie bars and dowel bars in plain jointed rigid pavements according to IRC 58–2015. Hence, the application of ECC as a viable pavement material should not cater to corrosion due to chloride penetration. After exposing the ECC specimen to chloride, the crack width increased from 40 to 100 μm [17]. The reason was pointed out to be most likely because of the chemical interaction between the bonds of the ECC matrix and chloride content added for the test [11]. It was reported that after the incorporation of fibers in the mix, there is an increase in the chloride migration coefficient of the mix [21]. Since chloride penetrates more in the composite, the crack width has been found to increase [21].

2.5 *Life Cycle Analysis*

Life cycle analysis for ECC composite was conducted [22] and it was found that ECC overlay had double service life when compared with a conventional concrete overlay. The cost of construction is reduced by 55.7% when compared with hot mix asphalt (HMA) overlay and by 39.2% when compared with unbonded concrete layer (UBOL) [22]. Greenhouse gas emissions reduced by 35% [22] as shown in Fig. 8 and primary energy consumption reduced by 75% when compared with Hot Mix Asphalt pavement (HMA) [22] as shown in Fig. 9. Overall, ECC performs much better both economically and environmentally.

Fig. 8 Comparison of concrete specimen manufactured by using ECC and normal concrete, respectively. Adapted from [2]

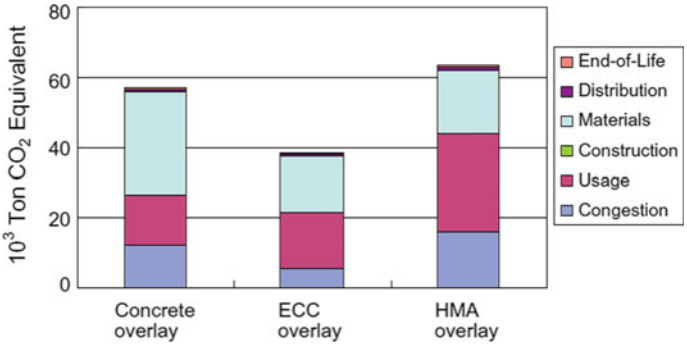

Fig. 9 Greenhouse gases liberated while construction of an overlay with concrete, ECC, and HMA. Adapted from [22]

2.6 Green ECC

Research to utilize waste material and to obtain optimum ECC mix to be used for construction was conducted by Li et al. [23]. It was found by their research that even after incorporating over 70% of the industrial waste, the overlay thickness required of the ECC material was half that of conventional concrete mix. The design also leads to a reduction in industrial waste of fly ash from coal-fired thermal power plants, sand, and slags from various metal casting processes, carpet fibers, cement kilns from cement production, polystyrene beads, etc.

As the virgin material used for the production of ECC was reduced by 74%, it also leads to a reduction in primary energy consumption by 21% [23]. Due to optimum utilization of materials in ECC mixes, it leads to a staggering reduction of 58% in cost [22]. In terms of greenhouse gas emissions, ECC mixtures brought a reduction of 55% in terms of CO_2 emissions [23].

In the research with substitution of silica sand with recycled asphalt (RAS) [19], it was reported that there was a reduction of about 2.2% with 100% substitution. This also leads to a reduction in costs incurred by 14.5%. The test results can be summarized by the image below.

To understand the overall performance of the ECC-recycled asphalt (RAS) composite in comparison with the ECC composite, composite index (Ci) was used. Composite index takes embodied carbon, cost, compressive strength, and durability into account and can be represented by the below formula.

$$\text{Ci} = \frac{\text{Embodied Carbon} \times \text{Cost}}{\text{Compressive Strength} \times \text{Absorption}} \tag{1}$$

It was shown by this study [19] that a sample consisting of 50% replacement of silica sand and a sample with 0% replacement of silica sand would give approximately the same value of Ci, which takes the above-mentioned four factors into account. The following image shows the value of Ci for different mixes in the study.

2.7 Application of ECC as an Interlayer

Reflective cracking is one of the types of failure that needs to be considered while constructing the pavement. When an overlay is constructed over an existing cracked pavement surface, there is a high probability of crack propagation on the overlay because of existing cracks due to the concentration of stress at those cracks. This is due to the repeated loading of vehicles and less flexibility of the material.

Since ECC has excellent crack resistance and is more ductile, it is being thought of as a layer to arrest crack propagation. In an experiment, the feasibility of ECC as an interlayer between the already existing conventional concrete layer and hot mix asphalt layer was checked [24]. It was found that the provision of ECC as an

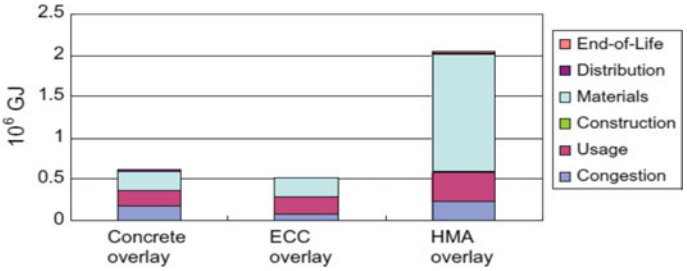

Fig. 10 Primary energy expenditure involved in the construction of overlay with concrete, ECC, and HMA. Adapted from [22]

interlayer increased the fatigue life of the overall pavement by 30–47 times [24] due to a reduction in strain concentration caused by multiple cracking eventually leading to an increase in the service life of the pavement by 17–21 times [24]. The layer was subjected to horizontal tensile strain under fatigue loading and no cracks were formed in the ECC interlayer. Cracks were directly formed on the topmost hot mix asphalt layer [24] as shown in Fig. 10.

2.8 Application of a ECC as an Overlay

ECC has also been looked at as an overlay material. Maa and Zhang suggest an ultra-thin overlay to be used on an existing pavement surface to increase the service life of the pavement [25]. It has been incorporated into an Airfield [25]. The ultimate flexural load carried by ECC samples was higher than that of the conventional concrete sample [25] as shown in Fig. 11. The maximum load point displacement was reported as 0.5 mm for the conventional concrete sample, while it was 3.5 mm for the ECC sample [25]. The test was conducted under quasi-static flexural loading. It was also concluded that using interfacial delamination is useful to successfully induce characteristics of

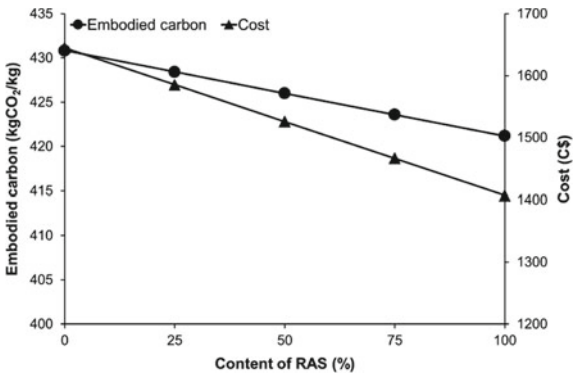

Fig. 11 Effect of recycled asphalt (RAS) on cost and embodied carbon of ECC. Adapted from

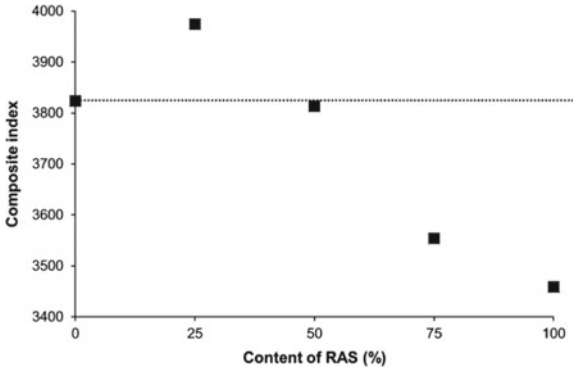

Fig. 12 Variation of composite index with varying content of recycled asphalt (RAS). Adapted from [19]

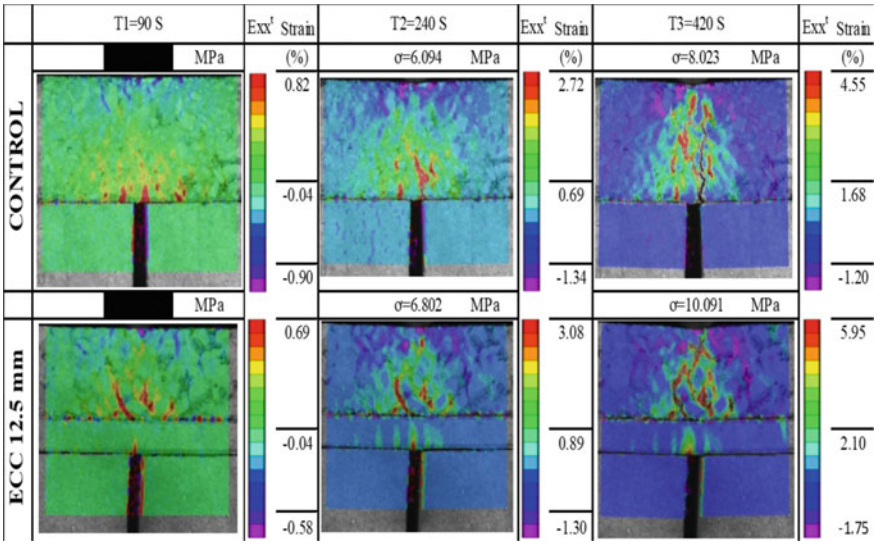

Fig. 13 Distribution of horizontal tensile stress in HMA and ECC specimens. Adapted from [24]

multiple cracking, strain hardening, and delay the development of reflective cracking [25] as shown in Figs. 12, 13, 14 and 15.

2.9 Relation Between Flexural and Compressive Strengths For ECC

The flexural strength could be predicted from compressive strength in the absence of former test results as given below [Reference of IS 456]

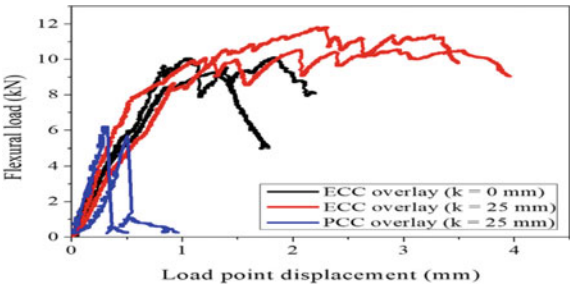

Fig. 14 Flexural load versus load point deflection of **a** PCC overlay with interfacial delamination **b** ECC overlay with interfacial delamination of 25 mm **c** ECC overlay without interfacial delamination. Adapted from [25]

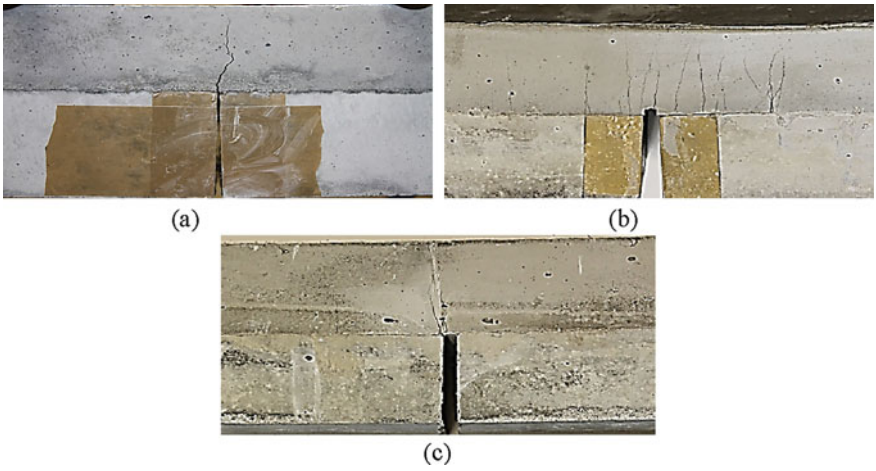

Fig. 15 **a** PCC overlay with interfacial delamination **b** ECC overlay with interfacial delamination of 25 mm **c** ECC overlay without interfacial delamination. Adapted from [25]

$$\text{Flexural Strength}(f_r) = 0.7\sqrt{f_{\text{ck}}}, \tag{2}$$

where f_{ck} represents the compressive strength of the mix.

The present paper attempts to ascertain whether Eq. (1) caters to the ECC mixture and develops a suitable relationship. For deriving an empirical relationship between flexural strength and compressive strength, research data from [26] was used. Non-linear regression was conducted on the sample size of 36 to derive a relation which best suits the data.

It was found that flexural strength had a higher correlation with that of the w/b (water-to-binder) ratio of the mix and the compressive strength of the mix as shown in Table 1. However, compressive strength had also good relation with that to the w/b ratio, and hence to avoid multicollinearity, only compressive strength was considered to derive the equation for computing flexural strength.

The best non-linear regression equation was decided based on mean square error (MSE). These non-linear regressions were carried on Minitab and the best equation

Table 1 Pairwise pearson correlations

Sample 1	Sample 2	N	Correlation	95% CI for ρ	p-Value
s/b	w/b	36	−0.000	(−0.329, 0.329)	1.000
SP/b (%)	w/b	36	−0.000	(−0.329, 0.329)	1.000
$D_{\max}$(lm)	w/b	36	−0.500	(−0.712, −0.205)	0.002
F_{ck}	w/b	36	−0.803	(−0.895, −0.644)	0.000
Mr	w/b	36	−0.852	(−0.922, −0.726)	0.000
SP/b (%)	s/b	36	0.000	(−0.329, 0.329)	1.000
$D_{\max}$ (lm)	s/b	36	−0.000	(−0.329, 0.329)	1.000
F_{ck}	s/b	36	−0.202	(−0.498, 0.135)	0.236
Mr	s/b	36	−0.063	(−0.384, 0.271)	0.714
$D_{\max}$ (lm)	SP/b (%)	36	0.000	(−0.329, 0.329)	1.000
F_{ck}	SP/b (%)	36	0.363	(0.039, 0.618)	0.030
Mr	SP/b (%)	36	0.114	(−0.223, 0.427)	0.508
F_{ck}	$D_{\max}$ (lm)	36	0.229	(−0.108, 0.518)	0.180
Mr	$D_{\max}$ (lm)	36	0.049	(−0.284, 0.372)	0.775
Mr	F_{ck}	36	0.808	(0.652, 0.898)	0.000

is the following.

$$f_r = 0.4156 X f_{ck}^{0.8131} \tag{3}$$

The scatterplot of f_r versus f_{ck} and the regression line of the above equation is shown in Fig. 16.

f_r predicted is calculated by using Eq. (3) and the predicted value for data from [26, 27] was plotted against it in Figs. 17 and 18, respectively.

The calculated least mean square error (MSE) is 0.38 after incorporating Eq. (2) into data from [26] as shown in Fig. 19 The validation of Eq. (3) was carried out

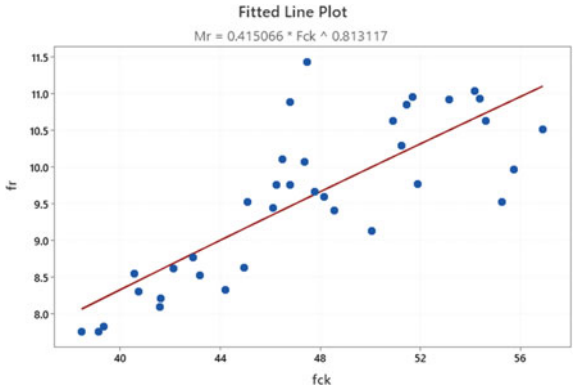

Fig. 16 Scatter plot and regression line of f_r versus f_{ck}

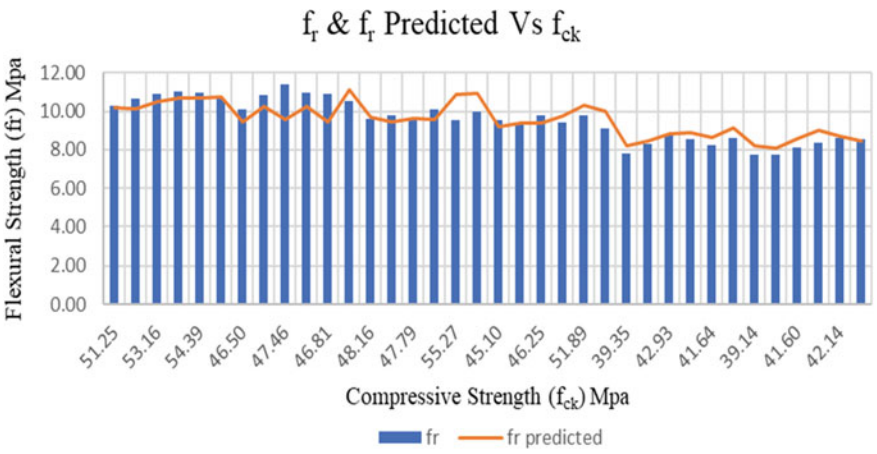

Fig. 17 Development of relationship of f_r versus f_{ck}

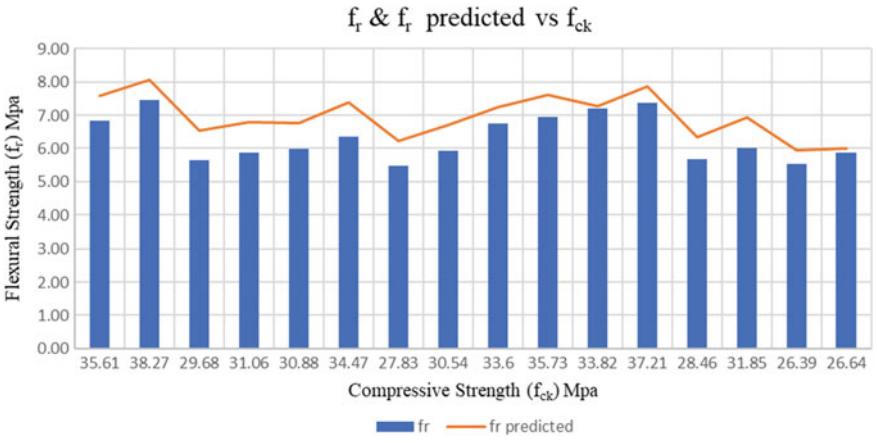

Fig. 18 Validation of f_r versus f_{ck}

using strength values as per Kallepalli Bindu Madhavi et al. [27] and the mean square error (MSE) was 0.49 as shown in Fig. 20.

3 Conclusion

(1) Study on fibers concluded that the volume of fibers in ECC is recommended to be below 2% by weight of the mix. A higher percentage of fibers reduces the workability of the mix and hence the ductility of the overall composite. The

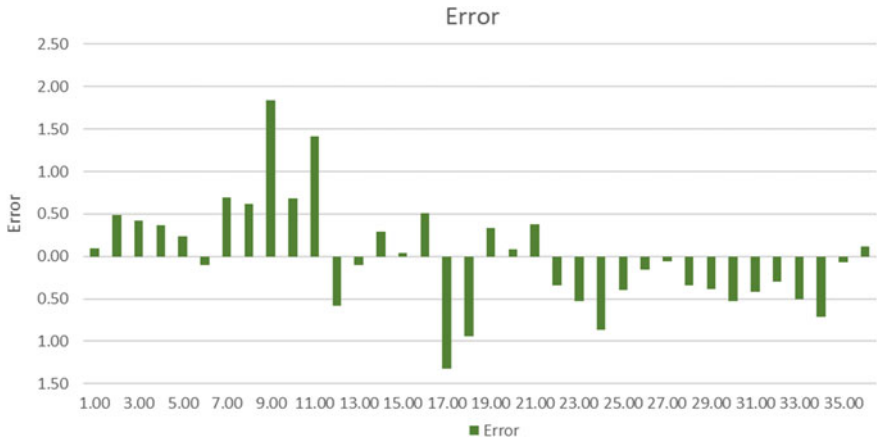

Fig. 19 Error for data during development

Fig. 20 Error for validation data

aspect ratio of the fibers plays an important role in the performance of the ECC composite. More research needs to be conducted to find the optimum aspect ratio for respective fibers to be used in ECC composites.

(2) After examination of the physical characteristics of the ECC mix, it was found that the performance of ECC in terms of tensile strength, compressive strength, freeze and thaw, and when exposed to chloride is better than conventional concrete. This also leads to a reduction in tensile and shear reinforcement required.

(3) Incorporation of ECC in overlay construction increased the service life of the pavement when compared with that of the HMA and UBOL. Due to this, even though the material required for ECC was more, there was cost saving in the long run. ECC can be used as an overlay and an interlayer since it has better stress dispersing characteristics, better ductility, and can delay the phenomenon of reflective cracking.
(4) Even though the energy intensity and the quantity of the material used for ECC are more, due to half the thickness of the pavement required for ECC and more service life, the overall energy utilized for construction of overlay was less. This also leads to less greenhouse gas emissions when compared to HMA and UBOL overlay. Industrial waste like fly ash, slag from metal casting process, carpet fibers, and cement from cement kiln can be utilized in the construction of ECC, which reduced the overall cost of construction.
(5) By correlating different parameters of the mix, it was concluded that flexural strength has a high correlation with water-to-binder ratio of the mix and to the compressive strength of the composite.

References

1. Qian S, Li VC (2008) Durable pavement with ECC. In: 1st International conference on microstructure related durability of cementitious composites Nanjing, China
2. Li M (2014) Engineered cementitious composites for bridge decks. University of Houston, USA
3. Halvaei M, Jamshidi M*, Latifi M, Behdouj Z (2013) The effect of nylon fibers on mechanical properties of engineered cementitious composites (ECCs)
4. Akkari A (2011) Evaluation of a polyvinyl alcohol fiber reinforced engineered cementitious composite for a thin-bonded pavement overlay. Minnesota Department of Transportation MN/RC
5. Halvaei M, Jamshidi M, Latif M (2014) Effect of polymeric fibers on mechanical properties of engineered cementitious composite (ECC). In: Proceedings of the 12th Asian textile conference (2014)
6. Zhou S *, Xie L, Jia Y, Wang* C (2020) Review of cementitious composites containing polyethylene fibers as repairing materials. Polymers MDPI J
7. Zhang D, Yu J, Wu H, Jaworska B, Ellis BR, Li VC (2020) Discontinuous micro-fibers as intrinsic reinforcement for ductile engineered cementitious composites (ECC). Composite Part B. January
8. Coricciati, Corvaglia P, Mosheyev G (2009) Durability of fibers in aggressive alkaline environment
9. Nataraja M, Dhang N, Gupta A (1999) Stress–strain curves for steel-fiber reinforced concrete under compression. Cement Concr Compos 21(5–6):383–390
10. Kim D-J, Naaman AE, El-Tawil S (2009) High performance fiber reinforced cement composites with innovative slip hardending twisted steel fibers. Int J Concr Struct Mater 3(2):119–126
11. Shetty MS (2019) Concrete technology theory and practice. S.Chand and Company limited
12. Richaud E, Fayolle B, Davies P (2018) Tensile properties of polypropylene fibers. In: Handbook of properties of textile and technical fibres. 2d edn. Elsevier
13. Pesic N, Zivanovic S, Garcia R, Papastergiou P (2) Mechanical properties of concrete reinforced with recycled HDPE plastic fibres. Constr Build Mater 115:362–370

14. Alhozaimy AM, Shannag MJ (2009) Performance of concretes reinforced with recycled plastic fibres. Mag Concr Res 61:293–298
15. Pakravan HR, Jamshidi M, Latifi M (2010) Performance of fibers embedded in a cementitious matrix. J Appl Polym Sci 116:1247–1253
16. Zhanga Z, Huc J, Mac H (2019) Feasibility study of ECC with self-healing capacity applied on the long-span steel bridge deck overlay. Int J Pavem Eng 20(8):884–893
17. Li VC (2008) Engineered cementitious composites (ECC)—material, structural, and durability performance. In: Nawy E (ed) Concrete construction engineering handbook, Chapter 24, published by CRC Press
18. Hossiney N, Tia M, Bergin MJ (2010) Concrete containing RAP for use in concrete pavement. Int J Pavement Res Technol.https://doi.org/10.6135/ijprt.org.tw/2010.3(5).251
19. Adesina A, Das S (2021) Sustainable utilization of recycled asphalt as aggregates in engineered cementitious composites. Construct Build Mater 283:122727
20. Standard Test Method for Resistance of Concrete to Rapid Freezing and Thawing: ASTM C666
21. Hu X, Guo Y,* Jianfu Lv, Mao J (2019) The mechanical properties and chloride resistance of concrete reinforced with hybrid polypropylene and basalt fibres. Mater Basel. https://doi.org/10.3390/ma12152371
22. Qian SZ, Li VC, Zhang H, Keoleian GA (2013) Cement and concrete composites: life cycle analysis of pavement overlays made with engineered cementitious composites. Cement Concrete Compos 35
23. Lepech MD, Keolein GA, Qian S, Li VC (2008) Design of green engineered cementitious composites for pavement overlay applications. In: Biondini ad Frangopol (eds) Life-cycle civil engineering
24. Khattak MJ, Zhang Q (2019) Mitigating reflective cracking through the use of a ductile concrete interlayer. transportation consortium of South-Central States
25. Maa H, Zhang Z (2020) Paving an engineered cementitious composite (ECC) overlay on concrete airfield pavement for reflective cracking resistance. Construct Build Mater 252
26. S_ahmaran M, Bilici Z, Ozbay E, Erdem TK, Mohamed Lachemi HEY (2013) Improving the workability and rheological properties of engineered cementitious composites using factorial experimental design. Composites: Part B 45
27. Bindu K, Mandala M, Rajesh VV, Suresh K (2016) Experimental study on bendable concrete. Int J Eng Res Technol (IJERT) IJERTV5IS100400 5(10). http://www.ijert.org ISSN: 2278–0181
28. Huang B, Shu X, Burdette EG (2006) Mechanical properties of concrete containing recycled asphalt pavements. Mag Concr Res. https://doi.org/10.1680/macr.2006.58.5.313
29. Zhang Q, Khattak MJ (2020) Mitigating reflective cracking through the use of a ductile concrete layer. Transport consortium of South Central States. Construct Build Mater 259:120383
30. Zhao Y, Jiang J, Ni F, Zhou L (2019) Fatigue cracking resistance of engineered cementitious composites (ECC) under working condition of orthotropic. Appl Sci
31. Kabele P, Novak L, Nemecek J, Pekar J (2007) Multiscale experimental investigation of deterioration of fiber-cementitious composites in aggressive environment

Experimental and Analytical Comparative Analysis on Effectiveness of Different Wrapping Techniques for Two Way RC Slabs Using Different International Guidelines

B. S. Shubhalakshmi, H. N. Jagannath Reddy, R. Prabhakara, and Arjun Kasi

Abstract Enhancement of strength and performance of building members is the need of hour for the existing structures. Every time the slab strengthening is the most challenging task, since very few techniques are available as on date and the productivity of those are under research stage (Hollaway in Constr Build Mater 24:2419–2445, 2010) [1]. In this scenario, fibre reinforced polymer composites promotes the research activity due to the various advantages of these materials over steel (Anakal et al., in Int J Adv Sci Eng Technol 6(1), 2018) [2]. The Fibre Reinforced Composites (FRP) such as CFRP (Carbon Fibre Reinforced Polymer) composite and GFRP (Glass Fibre Reinforced Polymer) composite materials used, seems to be not so economical in the present situation of technology and its application. However, Basalt fibres which are very much used in different engineering fields and their application are limited in Structural and construction industries. In this work, strengthening of RC slabs was done using wrapping technique using Basalt Fibre Reinforced Polymer (BFRP) composites by means of hand layup method and wet layup technique. Unidirectional knitted fibres were attached to the surface of the slab in different configurations (plus and square), in a way that the FRP and the RC slab performs as single structure when subjected to load. The effectiveness of the retrofitting method was measured by means of the deflection and crack width on working loads attained by the RC slabs. The deflection and crack width on working loads obtained from the experiment were compared with guidelines of ACI 440.2R-17 (ACI 440.2R-17, Guide for the design and construction of externally bonded FRP systems for strengthening concrete structures) [3], ISIS CANADA Design Manual

B. S. Shubhalakshmi (✉)
Dayananda Sagar Academy of Technology and Management, Bangalore, Karnataka, India
e-mail: shubhalakshmibs@gmail.com

H. N. Jagannath Reddy
Bangalore Institute of Technology, Bangalore, Karnataka, India

R. Prabhakara
Structural Engineering, VTU, Belagavi, Karnataka, India

A. Kasi
B.M.S. College of Engineering, Bangalore, Karnataka, India

L. Nandagiri et al. (eds.), *Recent Advances in Civil Engineering*, Lecture Notes in Civil Engineering 256, https://doi.org/10.1007/978-981-19-1862-9_14

No. 3 (ISIS CANADA Design Manual No. 3 2007, Reinforcing concrete structures with fibre reinforced polymers) [4], Fib Bulletin14 (Fib Bulletin14-2001, Externally bonded FRP reinforcement for RC structures) [5], CNR DT 200 R1/2013 (CNR DT 200 R1/2013, Guide for the design and construction of externally bonded FRP systems for strengthening existing structures) [6] /CNR-DT 200/2004 (CNR-DT 200/2004, Guide for the design and construction of externally bonded FRP systems for strengthening existing structures) [7] and TR55 (TR55, Design guidance for strengthening concrete structures using fibre reinforced composite materials) [8]. The observations made are presented along with a comparative statement of analytical and experimental results.

Keywords Strengthening · Fibres · Wrapping · FRP · GFRP · CFRP · BFRP

1 Introduction

The infrastructure projects are performed using the RC structures because of the convenience of the materials and well recognised practice of construction [9]. The performance of the structure is influenced by the behaviour of the structural elements when subjected to external loading. Slab members are subjected to dead load, live load and partition load, sometimes concentrated loads along with the impact effect. In the dimensions of the slab, the depth is very minor when compared over the other two dimensions, this marks the slab structurally flexible when compared with the other structural elements. It was also witnessed that the failure of structures has increased due to the inadequate maintenance, heavy loading because of change in the functionality aspects of the structure or the design requirements, inappropriate practice of standard code and unsuitable environmental condition, ageing or corrosion. It has been perceived that the strengthening techniques enrich the quality of performance of structural element and enhance the service life of the structures. The rise in need for the enhancement of strength has given the chance for the invention to the research of new techniques and new materials developments in the areas of strengthening of structures [10]. Various techniques are implemented in practice to strengthen the RC slabs. The appropriate method to strengthening of slab depends on the mechanical properties of strengthening material, design provisions, level of failure in member, the economic efficiency and the feasibility of the material [1].

The application of Basalt fibre, was restricted only in the field of aerospace and automotive industries, found a new approach in the civil engineering field. Strengthening of members using basalt fibre in various ways was a reward in the field of construction [11]. The strengthening techniques using FRP need to be authenticated with analytical study using the guidelines or standard codes. Only limited codes or guidelines are available for the strengthening techniques of externally bonded FRP reinforcements.

2 Literature

Establishing a new approach in the Civil Engineering field, strengthening of structures using basalt fibre in various ways was a methodology in the field of construction. BRM (Basalt Reinforced Mortar) for column jacketing was researched by Ludovico et al. [12] and concluded that it performed well. The basalt fibres and glass fibres reinforced with epoxy resin were treated under sea water solution which was investigated by Wei et al. [13] and observed that the stability against the chemicals was the same for BFRP and GFRP in seawater. Li-jun et al. [14] conclude that continuous beams reinforced with 1–3 films of BFRP sheets at the tension faces of concrete were prone to bending type of failure whereas the beams reinforced with 1 to a few films of BFRP sheets show excellent ductility. Singaravadivelan et al. [15] concluded that there had been increase in the flexural strength significantly by usage of BFRP and there will be a brittle failure if the number of BFRP layers were increased more than two. Zhishen et al. [16] investigated on the basalt fibres and concluded that there was a great compatibility between the matrix and steel which resulted in having a good mechanical properties, resistance to fatigue and performs well under high temperature. Anandakumar et al. [17] showed that the cube, cylinder and prism specimens with double wrapping of basalt fibre give better performance when compared with conventional and single wrapped specimens. Experimental investigation conducted by Elsanadedy et al. [18] on the beams, used TRM to strengthen the beams and concluded that there was an enhancement in the flexural capability of the beams in the range of 39–91%. The concrete specimens were verified at diverse age level for the mechanical properties by Gore Ketan and Suhasini Kulkarni [19] and found the optimum range of basalt fibre content to increase the performance of high strength concrete (HSC). The FRP-retrofitted structure was tested on shake table which was carried out by Ma et al. [20] and presented that the, ductility, shear capacity and energy dissipation capacity (hysteretic) of every level were significantly enhanced and that the joint failure mode (beam-column) was disallowed and the member practiced much less destruction associated with the actual member.

Maariappan and Singaravadivelan [21] used two different codes for reinforcement detailing (IS 456:2000 and IS 13920:1993) and concluded that the strengthened specimens performed well when linked with the performance of un-strengthened specimens. Basalt FRP rebars were used as an internal reinforcement for prestressed members by Pearson et al. [22] and it was concluded that the losses in prestress was nearly the same or little less with BFRP when compared to steel. Sfarra et al. [23] performed the tests on the basalt fibre and e-glass fibre for impact falling weight (IFW) using non-destructive testing techniques and it experimented that the basalt fibre executed in an improved way compared to the glass fibre under impact falling weight.

An investigation on the Fibre Reinforced Polymer reinforced ECC and ECC/concrete composite beams with different reinforcement ratios was performed by Yuan et al. [24] and it was concluded that for the FRP reinforced ECC beams demonstrated improved flexural properties in comparison with FRP Reinforced

Concrete beams. Dhand et al. [25] presented an evaluation on basalt fibres material for reinforcement and discussed to use it as a replacement to the glass fibres and it was concluded with a discussion on the improvement of mechanical, chemical and thermal challenging properties for the applications in specific industries. Fiore et al. [26] discussed the practicality of using the basalt fibre as reinforcement material and the industrial applications of basalt fibre reinforced composites with reference to the research papers. The behaviour of RC beams subjected to monotonic load and fatigue load (low cycle) was investigated by Gopinath et al. [27] and it was established that the strengthened beam enhanced the ductility by 84.5% and energy absorption by 162% compared to the reference beam. Larrinaga et al. [28] analysed the Basalt Textile Reinforced Mortar (TRM) subjected to uniaxial tensile stress and it was observed that the stiffness, cracking and tensile strengths were improved using basalt as a strengthening material. High et al. [29] incorporated the chopped Basalt fibres to enrich the mechanical behaviour of concrete and from the research it was established that the utilisation of basalt fibres in concrete enhanced the compressive stress and the modulus of rupture of concrete.

Very limited literatures are available for the authentication of the strengthening techniques using FRP. Ebead and Marzouk [30] instigated ACI 440.2R [31] (ACI Committee 440 2002) code for the validation of maximum load carrying capability beside the experimental values. Experimentation was accompanied on the performance of two-way slabs retrofitted with Carbon FRP strips and Glass FRP laminates. It was determined that the final load carrying capacity using ACI code was at satisfactory level with the experimental results. A comparative investigation on the guidelines of externally bonded FRP strengthened beam using three different codes or guidelines was conducted by Dola and Ahmed [32]. Flexural moment capacity was confirmed using ACI 440.2R-17 [3], ISIS CANADA design manual [4] and TR-55 [8]. A study on the parameters such as FRP reinforcement, FRP modular ratios and FRP ultimate strength were matched with the moment capacity using all the three codes or guidelines. It was concluded that the effect of these parameters differs depending on the analysis, assumptions and procedures of strengthening.

2.1 Research Gap

1. From the literature it was estimated, that very few research was carried on the flexural strength enhancement of the two-way slabs using Fibre Reinforced Polymers as an externally bonded reinforcement with plus and square type of wrapping configurations.
2. Basalt fibre has been used in different structural members in the form of bars as a replacement to steel bars. There are very limited research works were done on the two-way slabs using basalt fibre fabrics as a strengthening material.

2.2 *Objectives of the Work*

The work presented here contemplates to fulfil the following objectives:

1. To conduct experimentation on the flexural performance of two-way Reinforced concrete slabs under uniformly distributed load and retrofitted with Fibre Reinforced Polymer composites.
2. To demonstrate variation in the flexural behaviour of strengthened slabs over control specimen.
3. To estimate the flexural parameters experimentally obtained over available codes.

3 Materials

The practice of FRP materials has increased in the retrofitting of RC structures mainly because to its mechanical behaviour such as high strength/weight ratio, high stiffness/weight ratio, noncorrosive, high durability, acceptable presentation characteristics, comfort of application and low life cycle costs [33]. The mechanical behaviour of Basalt fibre such as density is 2.7–2.8 g/cm^3, hardness in the range of 5–9 on Mohr's scale, the modulus of elasticity ranges between 85 and 87 GPa abrasion resistance, resistance against low and high temperatures, acid and solvent resistance, fire resistant, retention of moistness is 0.1% at 65%, low and high temperature resistant and vibration protection [34].

The strengthening of slabs was carried out using the FRP sheets in correlation with epoxy adhesives. The adhesives (primer, concresive and saturant) were acquired from BASF India Limited, Bengaluru. Basalt FRP from Nickunj Eximp Private limited, Mumbai. The properties of Basalt FRP as per the Manufacturer's specification are tabulated in Table 1.

The adhesives were in two parts, base and hardener, both were mixed as per the guidelines given by the manufacturer. The adhesives used are primer, concresive and saturant. The properties of adhesives are tabulated in Table 2.

Table 1 Properties of FRPs given by the manufacturer specifications [35, 36]

Technical data of fibre	Basalt (BUF 601-111)
Elasticity Modulus (GPa)	105
Tensile strength (MPa)	2100
Density (g/cc)	2.67
Ɛ ultimate (%)	2.6
Thickness (mm)	0.1
Orientation	Unidirectional
Cost	Rs.750/kg

Table 2 Properties of adhesives given by the manufacturer [37–39]

Technical data of adhesives	Primer	Concresive	Saturant
Colour	Brown	Cement grey	Translucent blue
Mixed density (kg/l)	1.07	1.75	1.13
Strengths	Bond strength-1 MPa (ASTM D4541 [40])	7 days Compressive strength-60 MPa-ASTM D695 [41]	7 days Compressive strength-60 MPa (ASTM D579 [42]) Tensile strength-17 MPa (BS 6319, part 7 [43]) Flexural strength-35 MPa (BS 6319, part-3 [44])
Volume solids (%)	100	–	100
Pot life (min)	40	105	30
Tack free time (h)	6	7	3

4 Methodology

Designing of M20 grade concrete was done in accordance with IS 10262-2009 [45] by trial mixes. Mix proportions by weight (kg/m^3) are given in Table 3.

The design procedure and detailing was followed in accordance with IS 456-2000 [46] and SP 34-1987 [47]. In this work, OPC-53 Grade, following to IS 12269-1987 [48] was utilised and the requirements as per IS 12269-2013 [49] and IS 8112-1989 [50] were verified by conducting the standard experiments in the Laboratory. Nearby by available clean sand (river) passing through Standard Sieves was used and the material was verified for all the properties as specified in IS 383-1970 [51] and IS 2386 (Part-III)-1963 [52]. The coarse aggregates utilised for the work are angular (crushed) aggregate conforming to IS 383-1970 [51]. The coarse aggregate utilised for the work are12 mm and down size. The properties of coarse aggregates were tested in the laboratory and were within the permissible limits of IS 2386 (Part-III)-1963 [52] and IS 2386 (Part-IV)-1963 [53]. The reinforcing steel bars utilised in this work were High Yield Strength Deformed-HYSD bars of Fe-415 grade with the characteristic tensile strength-415 MPa for all the specimens and was certified to IS 1786-2008 [54].

Table 3 Mix proportions by weight

Water/cement ratio	Water (kg/m^3)	Cement (kg/m^3)	Fine aggregate (kg/m^3)	Coarse aggregate (kg/m^3)
0.5	194.68	431.64	895.03	809.27
0.5	0.451	1	2.07	1.87

The dimension of the slab adopted for the design was 1070 mm × 1070 mm × 90mm. The effective depth (d) of the slab was 70 mm. The detailing was maintained with the IS detailing code SP-34 [47] represented in Fig. 1.

Totally 6 specimens were casted, 2 specimens each for un-strengthened or control slabs, wrapping with plus and square techniques. The slabs were loaded to its design load and released and these slabs were considered as control specimens or un-strengthened slabs. For the remaining slabs, FRP was wrapped on the bottom face of the slab with the wrapping techniques (plus and square type) (Fig. 2a, b). In the plus wrapping configuration, the fibre layers were uni-directional, the sheets were attached along the longitudinal and the transverse direction. In square type of wrapping configuration, the FRP layers were attached along longitudinal direction only.

Retrofitting of RC slabs was conducted using hand layup methods (wet layup). Unidirectional knitted fibres were glued to the face of the slab, in such a technique the

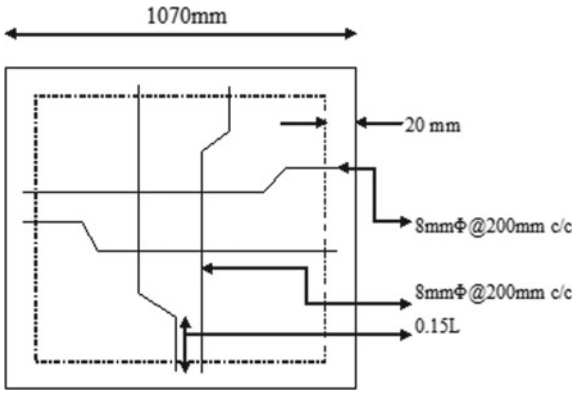

Fig. 1 Reinforcements of the RC slab

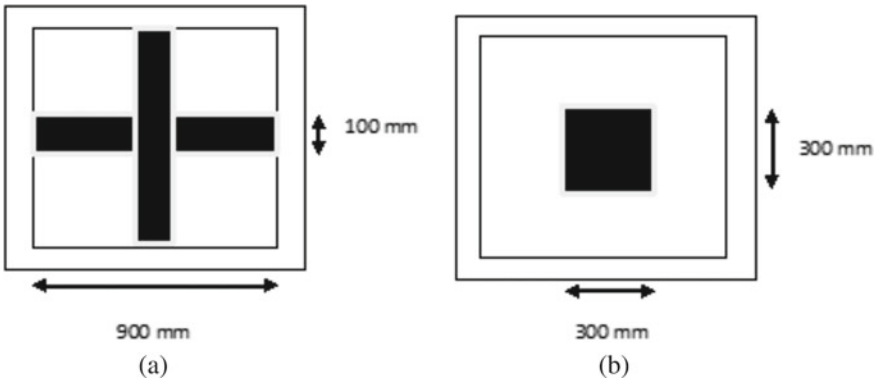

Fig. 2 **a** Represents plus wrapping technique and **b** represents square wrapping technique

Fibre Reinforced Polymer composite and the RC slab acts as a homogeneous member, when load was applied. It was mentioned to follow few stages for retrofitting of fibres as given by the company, so that the FRP attached RC slabs perform as one unit under the action of loads. The bonding among FRP and concrete face was adequately sturdy to support the transfer of stress from Concrete to the Fibre Reinforced Polymer. The succeeding stages, in accord to the company's guidelines [55–57] are followed.

1. Preparation of Surface: Before the attachment of fibres, the concrete surface must be even and no roughness, patches or defects must be present on the concrete surface. The smooth surface was achieved by grinding the surface of the slab by hand machine grinder.
2. Primer application: Here the MBrace primer system was utilised for penetrating the minute openings in the structure of cementitious substrates and to give a high bond base coat. After ensuring the good surface profile, the primer was applied on the surface of the slabs.
3. Filler application: The filler putty used was Concresive 2200, a non-slumping epoxy bedding compound and bonding agent. It helps in levelling the surface, filling the gap and concrete repair applications.
4. Dimensioning of the FRP fabric: The fabrics of basalt fibre was cut into the requisite size and shape, to fasten it to the slab face for the retrofitting work.
5. Saturant application-first layer: MBrace saturant was the epoxy resin, which was used in combination with FRP sheets.
6. Positioning of fabric sheets: Carefully measured and cut basalt fabric was positioned on the individual chosen slab specimens.
7. Saturant application -second layer: On top of the Fibre Reinforced Polymer fabric layers, the second coat of MBrace saturant was applied, when the first layer of saturant remained damp.
8. Air curing: The retrofitted slabs were permitted for a 7 days air curing as represented in Fig. 3a, b.

Fig. 3 **a** Represents plus type of wrapping configuration retrofitted slabs placed for air curing and **b** represents square type of wrapping configuration retrofitted slabs placed for air curing

5 Experimental Setup

An experimental setup was made using a 25 T loading frame with the loading jack which was secured on top of the specimen for the application of the load. All the slab specimens were subjected to udl with simple support. The uniformly distributed load outcome on the slab was given using the I-channel loading, which were dispersed as sixteen pointed loads at equal distances so that the deflection was not affected as represented in Fig. 4a, b. The deformation below the slab was noted with the help of dial gauges. The entire arrangement for the slab testing under laboratory environment is shown in Fig. 5. The experimentation was carried out on all the specimens and then the comparative study was done by taking an average of specimens with the same wrapping configurations used for the retrofitting.

Enhancement in the load was noted with a steady rise at an interval of four kN. This steady rise in the weight on the slab and the deformation in the slab were recorded throughout the test using the prior fixed 5 dial gauges.

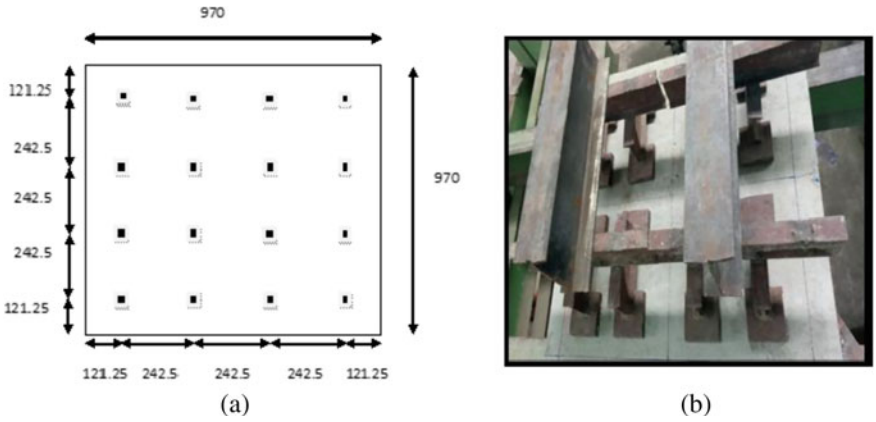

Fig. 4 **a** Load spreader and **b** I-channel sections for load distribution

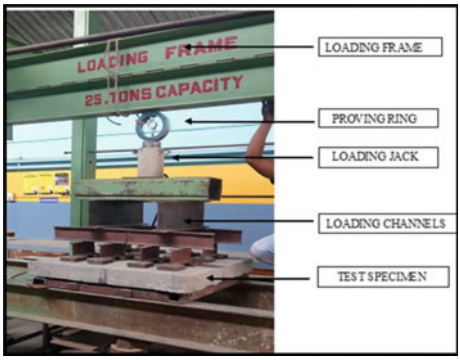

Fig. 5 Laboratory experimental setup

6 Results and Discussion

After completing the experimentation in the laboratory, the crack pattern obtained from the experimental investigation for slab specimens retrofitted with plus and square type of wrapping configurations using BFRP has been represented in Figs. 6, 7 and 8 respectively.

In Table 4, the first cracking load and respective deflection for every slab specimens were presented and in Table 5, the ultimate load and respective failure deflection for the entire slab specimens were tabulated.

An analytical investigation was done using the International guidelines for strengthening aspects with FRP of the slab members to compare the deflection and crack width at the working load for strengthened slabs with the experimental results.

(a) (b)

Fig. 6 **a** Crack patterns for control slab specimen 1 and **b** crack patterns for control slab specimen 2

(a) (b)

Fig. 7 **a** Crack patterns for plus wrapped slab specimen 1 and **b** crack patterns for plus wrapped slab specimen 2

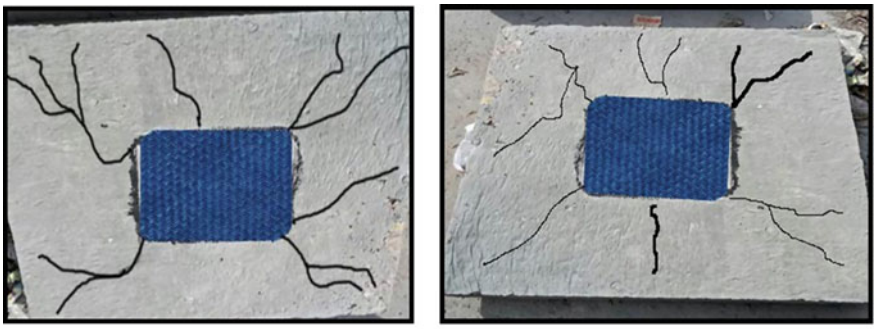

Fig. 8 **a** Crack patterns for square wrapped slab specimen 1 and **b** crack patterns for square wrapped slab specimen 2

Table 4 Cracking load and deflection at first crack of all the slab specimens

S. No	Specimen	First cracking load (kN)	Deflection at first crack (mm)
1	Control slab specimen 1	32	3.09
2	Control slab specimen 2	26	2.189
3	Plus wrapped specimen 1	40	2.678
4	Plus wrapped specimen 2	46	4.273
5	Square wrapped specimen 1	36	2.146
6	Square wrapped specimen 2	40	3.584

Table 5 Ultimate load and deflection at failure of all the slab specimens

S. No	Specimen	Ultimate load (kN)	Deflection at failure (mm)
1	Control slab specimen 1	120	19.972
2	Control slab specimen 2	124	19.487
3	Plus wrapped specimen 1	164	18.298
4	Plus wrapped specimen 2	172	21.031
5	Square wrapped specimen 1	156	16.016
6	Square wrapped specimen 2	160	16.361

Deflection at working load: The average deflection at working load has been evaluated using five international guidelines for plus and square wrapping configuration specimens.

The procedure to calculate the deflection at working load using the guidelines are specified in the different sections and are as follows, ACI 440.2R-17 (Section 10.2) [3], ISIS CANADA Design Manual No. 3 (Section 7.5.2) [4], Fib Bulletin14 (Section 4.6.3) [5], CNR DT 200 R1/2013 (same procedure was followed as done in Fib Bulletin 14 [5]) [6]/CNR-DT 200/2004 [7] and TR55 (BS 8110-2, Section 3.7.2 [58]) [8] and is represented in Table 6 along with the Bar chart in Fig. 9.

Table 6 was witnessed that when the deflection at working load was compared among the International guidelines there was a variation with respect to the type of slab specimens.

Crack width at working load: The predicted crack width at working load has been evaluated according to five International guidelines are tabulated in Table 7. The procedure to calculate the crack width at working load using the guidelines is specified in the different sections and are as follows, ACI 440.2R-17 (Section 10.2) [3], ISIS CANADA Design Manual No. 3 (Section 7.4.3) [4], Fib Bulletin14 (Section 4.6.4) [5], CNR DT 200 R1/2013 (same procedure was followed as done in Fib Bulletin 14 [5]) [6]/CNR-DT 200/2004 [7] and TR55 (BS 8110-2, Section 3.8.3

Table 6 Prediction of deflection at working load as per the International guidelines

S. No	Specimen	$\Delta_{(Exp)}$ (mm)	$\Delta_{(ACI)}$ (mm)	$\Delta_{(ISIS)}$ (mm)	$\Delta_{(Fib)}$ (mm)	$\Delta_{(CNR)}$ (mm)	$\Delta_{(TR)}$ (mm)
Plus wrapping configuration specimens							
1	S/BFRP/Plus	10.32	6.85	6.45	8.3	8.39	7.41
Square wrapping configuration specimens							
2	S/BFRP/Square	9.62	6.37	6.00	8.09	7.39	4.32

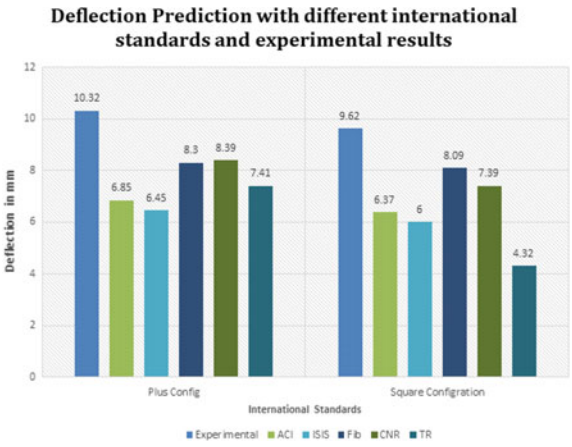

Fig. 9 Bar chart representing deflection prediction with different International standards and experimental results

Table 7 Prediction of crack width at working load as per the International guidelines

S. No	Specimen	$w_{(Exp)}$ (mm)	$w_{(ACI)}$ (mm)	$w_{(ISIS)}$ (mm)	$w_{(Fib)}$ (mm)	$w_{(CNR)}$ (mm)	$w_{(TR)}$ (mm)
Plus wrapping configuration specimens							
1	S/BFRP/Plus	0.32	0.18	0.19	0.15	0.12	0.12
Square wrapping configuration specimens							
2	S/BFRP/Square	0.24	0.21	0.22	0.12	0.11	0.10

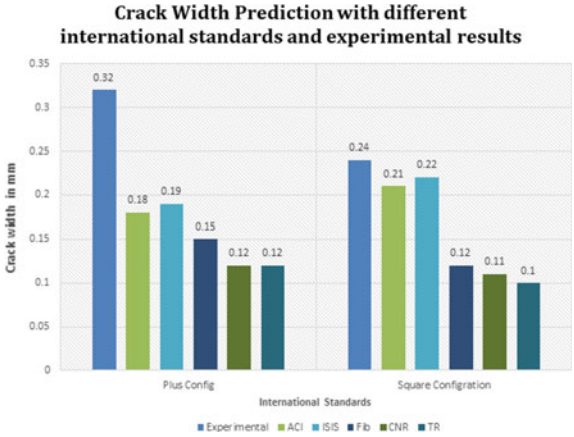

Fig. 10 Bar chart representing the crack width prediction with different International standards and experimental results

[58]) [8] and it is compared with the result from the experimental analysis (average of three specimens is considered) and is represented with the Bar chart in Fig. 10.

Table 7 was witnessed that the crack width at working load from the experimental investigation was more compared over the International guidelines.

7 Conclusions

1. The ultimate flexural strength of retrofitted slab specimens was enhanced by 27 and 23% in plus and square wrapping techniques, respectively, when compared with control slab specimens.
2. The deflections recorded at working load in the experimental investigation for plus and square wrapping configurations of retrofitting seem to be approximately near, therefore the effectiveness of the configurations assumed seems to be potential and gives the right information about the configurations placed.
3. The crack width measured at working load in the experimental investigation for plus wrapping configuration was more compared over the square wrapping configuration of retrofitting systems.

4. The deflections and crack width at working load from the experimental investigation were higher compared over the International guidelines ACI 440.2R-17 [3], ISIS Design Manual No. 3 [4], Fib Bulletin14 [5], CNR DT 200 R1/2013 [6]/CNR-DT 200/2004 [7] and TR55 [8].

References

1. Hollaway LC (2010) A review of the present and future utilization of FRP composites in the civil infrastructure with reference to their important in-service properties. Constr Build Mater 24:2419–2445
2. Anakal A, Arjun K, Shubhalakshmi BS (2018) Retrofitting of reinforced concrete slabs using different FRP's—a critical review. Int J Adv Sci Eng Technol 6(1). Special Issue 1, ISSN(p) 2321-8991, ISSN(e) 2321-9009
3. ACI 440.2R-17, Guide for the design and construction of externally bonded FRP systems for strengthening concrete structures. Reported by ACI Committee 440
4. ISIS CANADA Design Manual No. 3 2007, Reinforcing concrete structures with fibre reinforced polymers. ISIS Canada research network, Version 2, Manual No. 3, ISBN 0-9689006-6-6
5. Fib Bulletin14-2001, Externally bonded FRP reinforcement for RC structures. Fib Bulletin-14, Task group 9.3-FRP reinforcement for concrete structures, International Federation for structural concrete
6. CNR DT 200 R1/2013, Guide for the Design and Construction of Externally Bonded FRP Systems for Strengthening Existing Structures, CNR—Advisory Committee on Technical Recommendations for Construction. National Research Council, Rome
7. CNR-DT 200/2004, Guide for the design and construction of externally bonded FRP systems for strengthening existing structures, CNR-Advisory committee of technical recommendations for construction, National Research Council, Rome.
8. TR55, Design Guidance for Strengthening Concrete Structures Using Fibre Reinforced Composite Materials, Network group for composites in construction, London.
9. Shubhalakshmi BS, Jagannatha Reddy HN, Prabhakara R, Kasi A (2020) Performance-based economic evaluation of retrofitted slabs with different FRP's and different configurations. Springer Nature Singapore Pte Ltd. 202,1 Narasimhan MC et al (eds) Trends in civil engineering and challenges for sustainability, Lecture notes in civil engineering, vol 99, pp 323–331. https://doi.org/10.1007/978-981-15-6828-2_25
10. Shubhalakshmi BS, Jagannatha Reddy HN, Arjun K (2016) Flexural strength of two-way RC slabs retrofitted with basalt fibre reinforced polymer (BFRP). Int J Eng Sci Res Technol 5(8):207–213. ISSN 2277-9655
11. Pendhari SS, Kant T, Desai YM (2008) Application of polymer composites in civil construction: a general review. Compos Struct 84:114–124
12. Di Ludovico M, Prota A, Manfredi G (2010) Structural upgrade using basalt fibres for concrete confinement. J Compos Constr 14(5):541–552
13. Wei B, Cao H, Song S (2011) Degradation of basalt fibre and glass fibre/epoxy resin composites in seawater. Corrosion Sci 53:426–431
14. Li-jun O, Zhou-dao L, Wei-zhen C (2012) Flexural experimental study on continuous reinforced concrete beams strengthened with basalt fibre reinforced polymer/plastic. J Shanghai Jiaotong Univ (Sci.) 15(5):613–618
15. Singaravadivelan R, Sakthieswaren N, Muthuramu KL (2012) Experimental investigation on the behaviour of flexural strengthening of beam using basalt fibre. In: International conference on automotive, mechanical and materials engineering (ICAMME'2012), Penang (Malaysia), pp 85–89

16. Zhishen W, Xin W, Gang W (2012) Advancement of structural safety and sustainability with basalt fibre reinforced polymers. In: Proceedings of CICE 2012 6th international conference on FRP composites in civil engineering at international institute for FRP in construction (IIFC), Rome, Italy
17. Anandakumar R, Selvamony C, Kannan SU (2014) Retrofitting of concrete specimens and reinforced concrete piles using basalt fibres. Int J Eng Sci Invent 2(8):01–05
18. Elsanadedy HM, Almusallam TH, Alsayed SH, Al-Salloum YA (2013) Flexural strengthening of RC beams using textile reinforced mortar—experimental and numerical study. Composite Struct 97:40–55
19. Gore Ketan R, Kulkarni SM (2013) The performance of basalt fibre in high strength concrete. J Inform Knowl Res Civil Eng 2(2):117–124
20. Ma G, Li H, Wang J (2013) Experimental study of the seismic behavior of an earthquake-damaged reinforced concrete frame structure retrofitted with basalt fibre-reinforced polymer. J Composites Constr 04013002 1-10
21. Maariappan G, Singaravadivelan R (2013) Studies on behaviour of RCC beam-column joint retrofitted with basalt fibre reinforced polymer sheet. Glob J Res Eng Civil Struct Eng 13(5). Version 1.0
22. Pearson M, Donchev T, Salazar J (2013) Long-term behaviour of prestressed basalt fibre reinforced polymer bars. In: The 2nd international conference on rehabilitation and maintenance in civil engineering. Procedia Eng 54:261–269
23. Sfarra S, Ibarra-Castanedo C, Santulli C, Paoletti A, Paoletti D, Sarasini F, Bendada A, Maldague X (2013) Falling weight impacted glass and basalt fibre woven composites inspected using non-destructive techniques. Composites: Part B 45:601–608
24. Yuan F, Pan J, Leung CKY (2013) Flexural behaviors of ECC and concrete/ECC composite beams reinforced with basalt fibre-reinforced polymer. J Composites Constr 17(5):591–602
25. Dhand V, Mittal G, Rhee KY, Hui D (2014) A short review on basalt fibre reinforced polymer composites. Composites: Part B
26. Fiore V, Scalici T, Di Bella G, Valenza A (2014) A review on basalt fibre and its composites. Composites: Part B
27. Gopinath S, Murthy AR, Iyer NR, Prabha M (2014) Behaviour of reinforced concrete beams strengthened with basalt textile reinforced concrete. J Industr Textiles 1–11
28. Larrinaga P, Chastre C, Biscaia HC, San-Jose JT (2014) Experimental and numerical modeling of basalt textile reinforced mortar behavior under uniaxial tensile stress. Mater Des 55:66–74
29. High C, Seliem HM, El-Safty A, Rizkalla SH (2015) Use of basalt fibres for concrete structures. Constr Build Mater 96:37–46
30. Ebead U, Marzouk H (2004) Fibre-reinforced polymer strengthening of two-way slabs. ACI Struct J 101(5):650–659
31. ACI 440.2R-02, Guide for the Design and Construction of Externally Bonded FRP Systems for Strengthening Concrete Structures, Reported by ACI Committee 440
32. Dola TA, Ahmed MdZ (2015) A comparative study on beam strengthened with externally bonded FRP material. Int J Sci Eng Res 6(2):1325–1332
33. Bakis CE, Bank LC, Brown VL, Cosenza E, Davalos JF, Lesko JJ, Rizkalla SH, Triantafillou TC (2002) Fibre-reinforced polymer composites for construction-state-of-the-art review. J Composites Constr 6(2):73–87
34. Wu G, Gu DS, Wu ZS, Jiang JB, Hu XQ (2007) comparative study on seismic performance of circular concrete columns strengthened with BFRP and CFRP composites. In: Smith ST (ed) Asia-Pacific conference on FRP in structures (APFIS 2007). International Institute for FRP in Construction
35. BASF Application guidelines: MBrace fabric, BASF-The Chemical Company, Technical sheet, BASF, 2009
36. Basalt fabric, Nickunj Eximp Private limited, Mumbai
37. BASF, MasterBrace 4500 Brochure
38. BASF, MasterBrace P 3500 Brochure
39. BASF, MasterBrace ADH 2200 Brochure

40. ASTM D 4541; Standard Test Method for Pull-Off Strength of Coatings Using Portable Adhesion Testers
41. ASTM D 695; Standard Test Method for Compressive Properties of Rigid Plastics
42. ASTM D 579; Standard Specification for Greige Woven Glass Fabrics
43. BS 6319-7:1985; Testing of resin and polymer/cement compositions for use in construction. Method for measurement of tensile strength
44. BS 6319-3:1990; Testing of resin and polymer/cement compositions for use in construction. Methods for measurement of modulus of elasticity in flexure and flexural strength
45. IS 10262-2009; Guidelines for concrete mix design proportioning. Bureau of Indian Standards, New Delhi
46. IS 456-2000; Plain and reinforced concrete—code of practice. Bureau of Indian Standards, New Delhi
47. SP 34-1987; Handbook on concrete reinforcement and detailing. Bureau of Indian Standards, New Delhi
48. IS 12269-1987; Specification for 43 grade ordinary Portland cement. Bureau of Indian Standards, New Delhi
49. IS 12269-2013; Specification for 53 grade ordinary Portland cement. Bureau of Indian Standards, New Delhi
50. IS 8112-1989; Specification for 43 grade ordinary Portland cement. Bureau of Indian Standards, New Delhi
51. IS 383-1970; Specification for coarse and fine aggregates from natural sources for concrete. Second revision, Bureau of Indian Standards, New Delhi
52. IS 2386 (Part-III)-1963; Methods of test for aggregates for concrete (Specific gravity density, voids, absorption and bulking). Bureau of Indian Standards, New Delhi
53. IS 2386 (Part-IV)-1963; Methods of test for Aggregates for concrete, Mechanical properties. Bureau of Indian Standards, New Delhi
54. IS 1786-2008; High strength deformed steel bars and wires for concrete reinforcement. Bureau of Indian Standards, New Delhi
55. Retrofitting products, MBrace: a composite strengthening system
56. MasterBrace Composite Strengthening Systems Solutions, Master Builder Solutions Brochure BASF MBrace composite strengthening systems, BASF Construction Chemicals—Building systems, Technical sheet, Form No. 1030493, BASF 9/06, 2006
57. Retrofitting products, MBrace: a composite strengthening system. Indian Concr J 517–518, 2002
58. BS 8110-2:1985; Structural use of concrete. Part 2: Code of practice for special circumstances.

Retrofit Guidelines Towards Achievement of Net Zero Energy in a University Building

Advika Shetty, K. S. Samarth, Shrihari K. Naik, Hritik Tej M. Setty, and K. Hannah

Abstract A zero energy building (ZEB) is a type of sustainable structure that can meet its energy needs by producing the required quantity by itself, that is, the energy demand of such a building is met through installation of renewable energy sources as a part of the building as well as by reducing the existing consumption through other passive strategies in order to ensure a high performance than conventional structures. Some of the advantages of moving towards zero energy buildings are decreased operation or maintenance costs, lower impact on the environment and more energy security, and a higher resilience in cases such as power outages and blackouts as well as natural disasters. The energy consumption of new buildings as well as pre-existing buildings can be decreased through retrofits for energy efficiency, energy conservation programs, reduction of plug loads, and integrated structural design. However, to proceed with retrofitting, there is a prerequisite of understanding the characteristics of the retrofits and careful planning as it is complex. Many methods of building retrofitting have been investigated previously to achieve near-zero energy or zero energy status. Therefore, the primary focus of this project lies in the review and proper assessment of available retrofitting technologies and how these can be applied to a pre-existing institutional structure in a university campus and their corresponding effect of the current energy consumption of the selected structure. Further investigation on the possibility of adopting these techniques requires thorough studies to be carried out through numerical simulations or experiments.

Keywords Net zero energy buildings (nZEB) · Revit modeling · Revit insight · Solar panels · University building retrofitting

1 Introduction

One of the world's primary concerns has been the environmental impact of the release of greenhouse gas emissions which accompany increasing energy consumption rates

A. Shetty (✉) · K. S. Samarth · S. K. Naik · H. T. M. Setty · K. Hannah
PES University, Bengaluru, KA 560085, India
e-mail: shettyadvika@gmail.com

L. Nandagiri et al. (eds.), *Recent Advances in Civil Engineering*, Lecture Notes in Civil Engineering 256, https://doi.org/10.1007/978-981-19-1862-9_15

in all activities. The building and/or construction sector accounted for 36% of final energy use and 39% of energy and process-related carbon dioxide emission, 11% of which resulted from manufacturing building materials and products such as steel, cement, and glass [1]. There is a need to reduce these harmful effects and proactively counter them in order to decrease their repercussions on climate change as a whole. Among the strategies that have been practiced to decrease energy consumption all over the world in the last few years, one that has had a significant is the net zero energy building concept. The nZEB design concept aims at designing green or sustainable structures, mostly in terms of energy usage. The concept of nZEBs is reliant majorly on the below two aspects:

- Generation of renewable energy and;
- Saving of energy [2]

While energy will still be a requirement to power the daily operation of such a building, despite the implementation of energy effective measures, the use of renewable sources will greatly decrease the necessity for outside supply.

Sustainable development in the building sector requires the renewable energy utilization and the integration of energy efficiency in buildings. While it is simpler to integrate energy saving technologies such as BIPV systems, curtain walls, trombe walls, solar chimney, and passive evaporative system, it is also of importance that pre-existing buildings are steadily converted into Zero Energy buildings to ensure longevity in the building industry. Extension of the life of an already existing building through renovation has been an oft-used strategy to increase life time without much expenditure or with a relatively lower payback time. Renovations have proven time and time again to be a cost-effective method of making a structure more sustainable and energy-efficient. The energy consumption of a building is affected by multiple factors such as window-to-wall ratio, wall structure, and building orientation in addition to the prevalent weather conditions of the location.

Possible retrofit solutions come in both internal and external variations as well as passive and active technologies. Examples of passive retrofits are orientation, daylighting, natural ventilation, phase change materials, and insulation. Energy efficient technologies include HVAC (heating, ventilation, and air conditioning systems), lighting and other appliances, and DHW (domestic hot water) generation systems from renewable sources like solar, PV panels, wind turbines, etc. Energy efficient measures can be grouped into three categories for their implementation into existing structures during any retrofitting procedures. These are as follows:

1. Building envelope
2. Internal conditions
3. Building service systems [3]

The more common and widespread technologies applied onsite are PV (photovoltaic), BIPV (building integrated photovoltaic) and solar, thermal, and wind turbines.

This study examines the feasibility and potential of retrofitting a university building in order to transform it into a NZEB using Autodesk Revit and Revit

Insight. Revit is a comprehensive workflow software used by professionals across the construction sector to create real-world structures and buildings [4]. The primary use of Revit is in BIM (building information modeling). Revit constitutes several tools which can be adopted in planning and tracking the various phases of a building's life cycle, from conceptualization to excavation to construction and finishing execution, and operation/maintenance to its demolition. It can be used as a very powerful collaboration tool between different disciplines in the building design sphere. The different disciplines that use Revit approach the program from their own perspectives. Each of these perspectives is focused on completing that domain's task.

In this paper, a university building of 13 floors is chosen and survey is carried out through the building to find out intensity of light in individual rooms. Further, the building is modeled based on the data collected and provisions for retrofits are investigated both through examples of previously modified or retrofitted buildings and through simulations using software in order to check for feasibility of these renovations in the Indian scenario considering both cost as well as environmental impact.

2 Methodology

2.1 Survey of Selected Building with Luxmeter

Luxmeter is a simple light meter used for measuring illuminance in a particular area. The lux is the SI derived unit of illuminance, measuring luminous flux per unit area. Luxmeter is a simple device which shows the illuminance of an area in seconds. Lux reading of all areas (including corridor areas, stairwells, lift areas, staff rooms, and classrooms) are measured. Retrofitting with light systems is done wherever the lux value is found to be lesser than the minimal value. Retrofitting is done by either providing larger windows or demolishing unnecessary non-load bearing walls installation glass windows can be done or lights which utilize renewable energy sources where natural light is not available.

2.2 Building Modeling and Power Optimization Through Revit

Revit is a building information modeling software used to make 3D and parametric object-based designs [5]. The building's design is first designed on Revit, where the building is kept location and altitude specific. Revit Insight's environment analysis performs all the Ecotect tasks such as solar analysis, thermal performance, sun and shadow studies, weather data analysis, and energy analysis. The changes or optimization required in lighting and ventilation can be made on the software and checked

if the problem is rectified. All of Revit's environment analysis performance is time and weather specific. For example, sun and shadow studies show details for all the seasons and at very hour of the day.

2.3 Investigation of Retrofit Options

All the retrofitting options obtained from all the articles are taken into consideration keeping the cost and benefit in mind. Retrofitting options like EPS and XPS are used to improve thermal efficiency while PVC frames and double-glazed windows are used to achieve more lighting. Retrofitting is done using Insight benchmarks for modeling and analysis. The retrofitting options are short-listed according to the requirement and the weather of that region. Shortlisting is done considering efficiency and budget. If two retrofit options A and B are ideal, where option A is 10% more efficient than option B, but option B is cheaper and affordable. Option B is considered the best retrofit option. Retrofitting is done such that the room or the area receives optimum natural light and ventilation, and electricity consumption drops nearly to zero.

2.4 Cost Analysis

The total cost of power consumed on an annual basis in the selected building is determined. The total expenditure for the modifications after analysis through Revit Insight is calculated. The payback period for these changes is determined by correlating the values found. This helps in ascertaining the feasibility of the undertaken project if implemented practically.

3 Luxmeter Survey and Analysis of Lux Values

The lux (symbol: lx) in the International System of Units (SI) is a measure of Illuminance, which is the total amount of light that falls on a surface, that measures the luminous flux per unit area. One lux is adequate to one lumen per square meter. A specific amount of light will illuminate a surface more indistinctly if it is spread over a large area, so illuminance is inversely proportional to area when the luminous flux is held constant. Table 1 illustrated the technical specifications of the luxmeter used and Fig. 1 shows the TM203 luxmeter.

General trends observed after luxmeter survey:

- Classrooms at the west side of the building have a general trend of being better lit than on the east.

Table 1 Specifications of TM203 luxmeter

Display	2000 count, large LCD display	
Sensor	Silicon photodiode and filter	
Measuring range	20, 200, 2000, 20,000, 200,000 lx 20, 200, 2000, 20,000 Footcandles	
Accuracy	± 3%	
Angle deviation	30 degrees	± 2%
	60 degrees	± 6%
	80 degrees	± 25%
Power supply	9 V NEDA 1604, IEC 6F22, JIS 006P battery x1pc	
Battery life	About 200 h	
Dimensions	38 (H) × 55 (W) × 172 (L) mm 1.5 (H) × 2.2 (W) × 6.8 (L) inch	
Weight	250 g (including battery)	

- Natural light values reduce on the lower floors due to the presence of surrounding buildings.
- Staircases with double windows do not require any extra lighting as they are bright throughout the day.
- Classrooms and staff rooms at the building corners require minimal lighting as they have windows on two sides of the outer faces of the building.
- The distribution of the natural light intensities is shown in Fig. 2.

4 Modeling Using Revit

Revit is used to model the building as per official plans retrieved from the estate office. All elements of these plans are accurately incorporated into the Revit model. Floor plans are first modelled and the three-dimensional view of the same is presented as the final model. Figures 3 and 4 illustrate the model as constructed on Revit.

5 Investigation of Retrofit Options and Strategies

5.1 Solar Panels

The term ‘solar panel’ is the layman’s term for a photovoltaic or PV module. Such photovoltaic cells, when embedded to each other to form an assembly, are referred to as a PV module after mounting in a framework to be installed. The source of energy for these cells is sunlight, through which they generate direct current electricity. A PV panel is a collection of such modules, and an array is a system of these PV panels.

Fig. 1 TM203 luxmeter

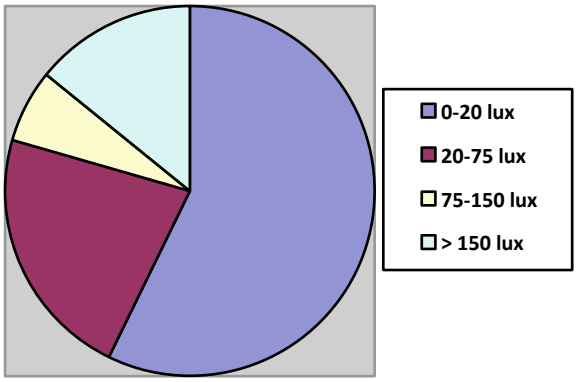

Fig. 2 Distribution of natural light intensities

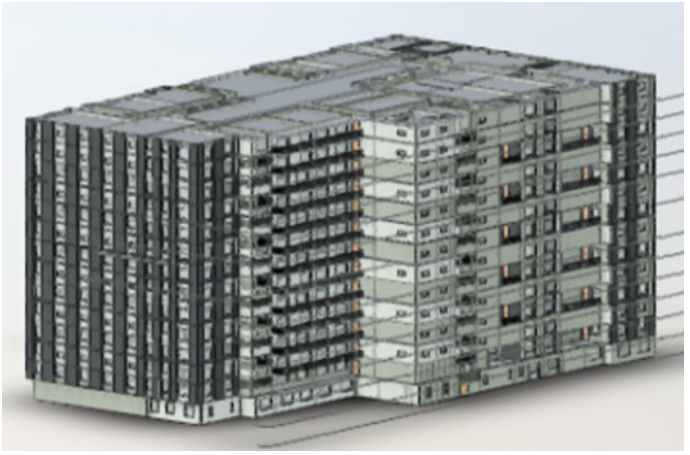

Fig. 3 Western view of 3D model

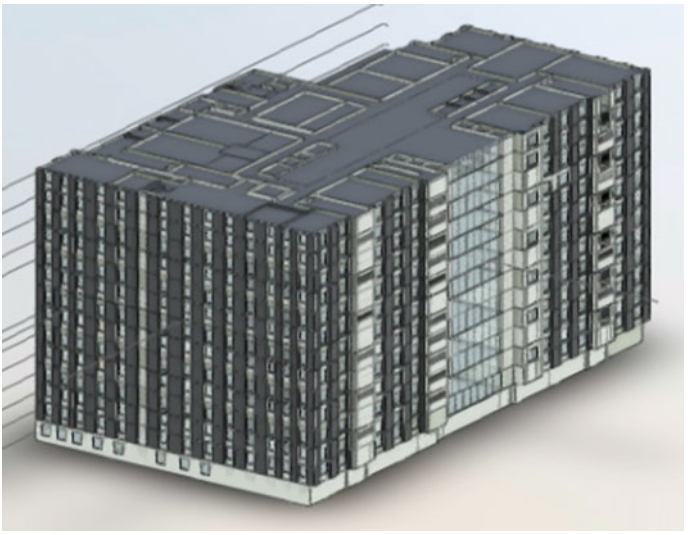

Fig. 4 Eastern view of 3D model

A PV system is one that supplies solar-generated electricity through these arrays to any electrical equipment that it is connected to. In order to perform optimally, it is necessary for a solar panel to be constructed using similar modules and to also be oriented in a direction perpendicular to that of direct sunlight. The primary challenge that arises in perfectly implementing this technology is the price per unit of the electricity produced. Due to the continuous fall of the price of solar-generated

electrical power in several countries, it has become more economical as compared with ordinary fossil fuel electricity produced in electricity grids.

5.2 Green Roofing

Traditionally, roofs have also been made of elements such as aluminum or iron sheets, ceramic tiles, concrete, leaves, and/or grass. Over the years however, techniques have been found to maintain gardens in roof tops while also serving their original purpose. Green roofs, or living roofs as they are termed, are where the building roof is covered in vegetation, either partly or wholly. The building top, which constitutes the roof, is modified and fitted to grow plants, which can be purely aesthetic and decorative in purpose such as flowering plants, or even food crops. Green roofs are gaining traction in the sustainable construction domain as they ensure savings in terms of both spacing as well as environmental consciousness.

5.3 XPS and EPS Panels

XPS is a type of façade panel board that is manufactured in a continuous extrusion process to produce foam insulation of closed cell form. However, manufacturing of EPS is by enlarging the round beads inside a mold, then fusing the beads together by heating while applying pressure. Both products have supporters claiming the advantages of one over the other, but it is important to understand each product's unique characteristics which make it more fit for specific types of structures. This can be made clearer by examining each product's resistance to fire and water, thermal and moisture protection, and suggestions for workably designed projects. The most widely adopted insulation for structural insulated panels (SIPs) is EPS, insulated concrete forms (ICFs), and exterior insulation and finishing systems (EIFs). When compared to EPS, XPS only has a moderately better thermal performance. The thermal insulation performance of XPS and EPS is near enough when XPS and EPS have nearly the same densities. Nevertheless, XPS is more expensive even when it has the same density as EPS. In areas where materials with a lower density are needed, EPS is generally favored, the material is not suited in case it is not manufactured beneath a certain density. Use of XPS as a lesser compact material in similar building cases might possibly prove to be more expensive.

5.4 HVAC Commissioning

To ensure that all HVAC systems in a building are at peak performance levels, continuous commissioning is necessary. The commissioning process is intended

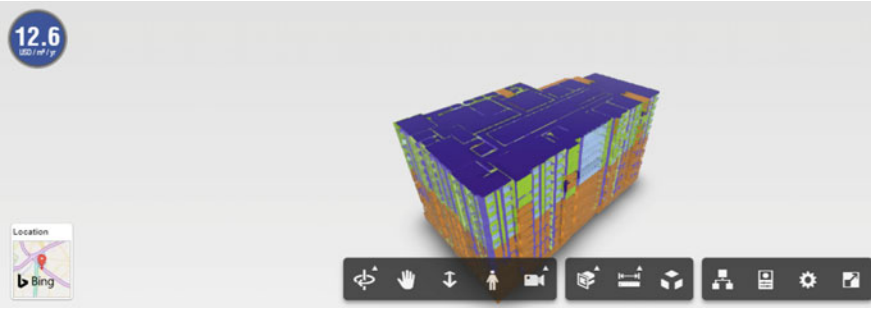

Fig. 5 Building performance analysis using insight—current scenario

for optimization of energy use in existing buildings, to resolve operational problems and provide improved comfort levels. The useful life of HVAC equipment can also be extended significantly through continuous commissioning. Continuous commissioning will also greatly increase HVAC efficiency. HVAC commissioning also plays an important role in identifying retrofits for existing institutional buildings as well as central plant facilities and commercial structures.

6 Energy Analysis Using Revit Insight

Revit Insight is a cloud-based service from Autodesk which can be used for energy analysis and building performance analysis [6]. Various factors can be adjusted based on the changes to be implemented in the improved model. These parameters are window-to-wall ratio in all four directions of the structure as Insight takes exact location into consideration to determine climate and position of the sun throughout the day, wall construction, roof construction, infiltration, lighting efficiency, daylighting controls, occupancy controls, plug load efficiency, HVAC systems and their efficiency, efficiency of the type of PV panels installed and the surface coverage of the same. These parameters are first analyzed for the initial state of the building, i.e., the current consumption (as illustrated in Fig. 5), and that of the building in an improvised scenario, i.e., if the suggested retrofits are implemented (as displayed in Fig. 6) which gives us a comparison of how much energy can be saved.

7 Cost Analysis

The purpose of conducting a cost analysis on the proposed retrofits is to ensure that the suggested modifications are within the estimated payback period. By justifying the expenditure on the changes as detailed previously, it is possible to declare the feasibility of taking up such a project practically. With a 74% decrease in energy

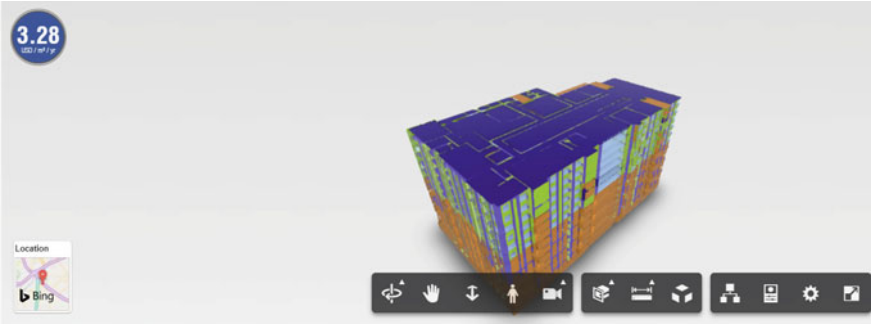

Fig. 6 Building performance analysis using insight—improvised scenario

Table 2 Current electrical consumption details

Item	Number	Consumption (kWh)
Computer	2100	300,000
Projector	175	4550
Tube light	2660	77
Fan	700	130
Air conditioner	950	950
Elevators	6	17,850

through retrofits, electricity costs are greatly decreased. On approximate analysis, the average consumption for 8 hours a day with 260 working days annually is found to be (Table 2):

The total electrical consumption is estimated as an annual usage of 323,557 kWh, rounded off to 324,000 kWh. At a rate of Rs. 6.5 per unit, the average cost annually would be around Rs. 2,103,120. In this 74% of the requirement is eliminated through retrofitting. Therefore, only Rs. 546,811 is the annual electricity cost. The money spent on the retrofits would be as outlined below:

1. Solar Panels:

The technical specifications of the chosen solar panel for simulation are shown in Tables 3 and 4. Each panel costs Rs. 5200 per sq.m. including installation cost. 1380 sqm is to be covered with PV panels. Therefore, the total cost of the panels and installation would be Rs.7176000.

2. Dimension and Material Changes for Windows:

Trp LoE fittings costing Rs. 80 per sq.ft. are to be installed. The total number of windows to be retrofitted are 28 in the southern walls and 15 in the eastern walls per floor which adds up to 559 windows. Breaking up and replastering and painting costs approximately Rs. 1000 per window. Therefore, the total cost of this retrofitting process is Rs. 603434.

Table 3 Solar panel type and description

Brand	Systovi
Product family	R—VOLT
Product group	On top PV
Width (mm)	1679.5
Height (mm)	1019.5
Depth (mm)	24.9
Type	Single object

Table 4 Technical data of solar panel

Rated power	300 Wc
Size	1679.5 × 1019.5 × 24.9 (L × I × H)
Weight	17 kg
Certification	IEC 61,215 et 61,730
Efficiency	18%
Material	Anodized aluminum frame and toughened glass
Resistance	Wind and snow loads resistance of 2400 Pa

3. HVAC changes are calculated to come in at Rs. 900,000.
4. Daylight and occupancy controls can be installed at a lumpsum cost of Rs. 798,000.

Therefore, the total investment is estimated to be around Rs.9477434, which is the electricity savings done in 7 years. It can be concluded that the initial expenditure for the retrofits can be made up with savings on power bills and should therefore be implemented.

8 Observations

Figure 7 gives the comparison between the performances of both models, i.e., in its current state and the model post the retrofitting activities. It can be inferred from this image that the maximum performance improvement that can be simulated using Revit Insight is 73.97%. The use of further retrofits such as building façade changes, use of exterior wall paint for sun protection and roof cooling, paneling with XPS or EPS and green roofing can still improve the building in order for it to qualify as a net zero energy structure.

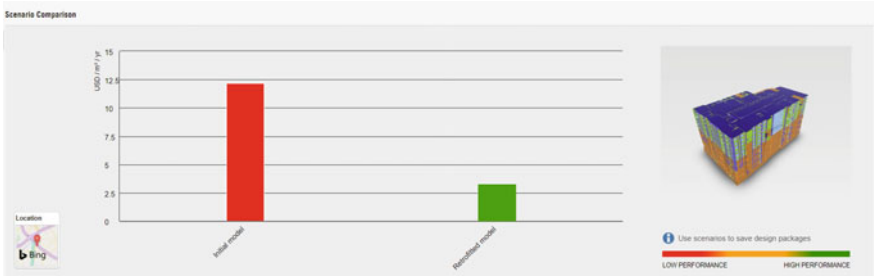

Fig. 7 Comparison of current energy consumption versus projected energy consumption after retrofits

9 Conclusion

While the concept of ZEBs is seeing a rise in prominence across new constructions, the use of it as a green strategy to save the current electrical usage and the attached heavy carbon footprint has not been examined in detail. There are a minimal number of case studies that have implemented the same in already existing buildings. The aim of the research undertaken in this paper was to fill these gaps that exist in this aspect of civil engineering in a methodical way which can further be improved upon to act as a guideline for new, upcoming structures within the university or even serve the purpose of modifying other existing buildings within the campus. A unique factor to be considered in modifying a university building is that its primary use time is within daylight hours, thereby reducing the necessity for electrical consumption in the night time. The location also gives another parameter of slightly unpredictable weather which is a challenge in strictly determining what kind of cooling or heating would be required now or in the near future.

By using the retrofits and simulating the same on Revit Insight, it can be observed that the building energy requirements can be significantly reduced and even further changes can be made to achieve net zero energy for pre-existing buildings. In conclusion, it is evident that the concept of zero energy buildings is one that must be introduced in the Indian scenario and especially with the future of the country as it must eventually become the norm for combatting severe climate change effects which have become rampant in harming the ecosystem.

10 Future Scope

It is observed that it is possible to decrease 74% of current energy requirement of a structure that functions as an institutional facility by simple retrofitting methods and strategies to save consumption. While 74% is an exceptional number to start with, bringing it to 100% should be the future goal for all civil engineers. In view of this, it is understood that using extra measures such as green roofing and wall retrofits such

as XPS and/or EPS panels can further improve the number to at least 90%, while decreasing overall carbon footprint as well as justifying expenditure as the payback period is estimated to be much lesser than the expected life cycle time of the building. Software such as gbXML or DOE2 can be employed in the simulation of the other mentioned retrofits to accurately understand their feasibility as well as conduct cost analysis [7].

11 Highlights

- A university building is chosen for analysis and simulating retrofitting.
- The chosen structure is surveyed for areas of improvisation in terms of natural light intensity and other variables.
- The building is modeled using Revit.
- Further, the model is analyzed for energy and power consumption through Revit Insight.
- Possible retrofits are studied to be implemented in the simulation.
- Revit is used to remodel the building and the consumption of power is decreased to 26% of the existing value.
- The initial low performing model is transitioned to a high performance, retrofitted model.
- Cost analysis is conducted in order to justify feasibility of taking up the project practically.

References

1. UN IEA (2019) Global status report for buildings and construction (2019). Available at https://www.gbpn.org/china/newsroom/2019-global-status-report-buildings-and-construction. Access date 15 (2020)
2. Pless S, Torcellini P (2010) Net-zero energy buildings: a classification system based on renewable energy supply options. No. NREL/TP-550–44586. National Renewable Energy Lab (NREL), Golden, CO (United States)
3. Ma Z et al (2012) Existing building retrofits: Methodology and state-of-the-art. Energy Build 55:889–902
4. Garagnani S (2013) Building information modeling and real-world knowledge: a methodological approach to accurate semantic documentation for the built environment. In: 2013 digital heritage international congress (DigitalHeritage). vol 1. IEEE
5. Wong K, Qing F (2013) Building information modelling (BIM) for sustainable building design. Facilities
6. Deepa K et al (2019) Energy analysis of buildings
7. Fratila LC (2019) Building information modeling for energy retrofitting. In: Retrofitting for optimal energy performance. IGI Global, pp 176–194

Experimental Studies on Pull-Out Behavior of Piles

V. Divya

Abstract Tall and off shore structures are often subjected to uplift forces due to the action of wind, water waves, and seismic loads. In such cases pile foundations are used for the effective transfer of load to the underlying soil. The ultimate shaft resistance of a single model pile in two different types of soils has been evaluated and compared in the present study. The experimental studies are carried out in a prefabricated model tank having a height of 600 mm and diameter of 290 mm. Steel solid piles of varying diameter and surface characteristics are driven in model tank and have been subjected to tensile load. The tests are carried out on piles for length to diameter ratios of 12, 20 and 30 inside the model tank. The test results stipulate the significant role of characteristics such as length to diameter ratio, moisture content, and interfacial friction in altering the shaft resistance of the piles. Comparative studies are also performed to assess the variation of pile soil interaction in two different types of soil used in the present study.

Keywords Shaft resistance · Interfacial friction · Model piles · Lateritic soil · Red soil

1 Introduction

Pile foundations are generally provided at sites where compressible soft strata exist to a larger depth from the ground surface. They are also provided in order to mitigate the problems faced due to the presence of expansive soils as well as to withstand the horizontal forces in the foundation. The increase in population across the world has been creating a huge demand for enhanced infrastructure and hence expansive soils have also been subjected to numerous high-rise constructions works. Many high-rise structures such as transmissions towers, mooring systems, tall chimneys, bridge abutments, and multi-storied buildings are subjected to heavy lateral loads due to the action of wind and wave forces. In such cases, piles also serve as a convenient

V. Divya (✉)
Department of Civil Engineering, CMR Institute of Technology, Bengaluru, India
e-mail: divyaadarsh82@gmail.com

L. Nandagiri et al. (eds.), *Recent Advances in Civil Engineering*, Lecture Notes in Civil Engineering 256, https://doi.org/10.1007/978-981-19-1862-9_16

measure to arrest/control the uplift/tensile forces in both marine and land conditions. Hence, the analysis of uplift capacity of piles becomes significant during the design of foundations for such structures. The resistance to the uplift /tensile forces is obtained through the skin friction occurring between the pile shaft and the surrounding soil material. This resistive force can be increased further by under-reaming or by belling-out the bottom of the piles. The pull-out resistance of a pile is also found to vary for static and varying forces such as that of wind and seismic loads. Most of the research work related to the pull-out resistance of piles have been carried out on cohesionless soils or expansive soils. The present study deals with the experimental investigation on the pull-out capacity of solid piles on two different types of soil. The effect of moisture content on the pull-out/ tensile capacity of the piles has been studied and compared in the current work. Further, surface characteristics and interfacial friction between the pile soil also has been estimated and comparative studies performed.

2 Literature Studies

The uplift capacity of piles has been studied and reported by many researchers in the past. Most of the reported work have been analyzed in expansive soils which possess shrinkage and swelling properties. A theoretical method for the evaluation of uplift capacity of driven circular piles in sand was proposed by Chattopadhyay and Pise [1]. The relevance and inter relationship between parameters such as length to diameter ratio, pile soil friction angle, and angle of shearing resistance on the ultimate uplift load were compared and reported by them. The pull-out behavior of Granular Pile Anchors (GPA) with varying length to diameter ratio on expansive clay was studied by Rao et al. [2]. They reported a reduction in heave of the expansive soil as a result of uplift resistance offered by the pile soil interface. They also observed from their results that the failure pull-out load increased with reduction in length to diameter ratio. The uplift behavior of a transmission tower foundation using finite element method was investigated by Hao et al. [3]. Based on their analysis they reported shallow mode of footing failure when length to diameter ratio is less than or equal to 2 and that the ultimate uplift capacity is independent of the extended angle of the footing base. The analytical studies for determining the uplift capacity of piles in cohesionless soil were conducted by Deshmukh et al. [4] and concluded that the critical embedment ratio plays a significant role in the prediction of pile uplift characteristics. They also proposed a semi-analytical method for the prediction of uplift capacity up to the critical embedment ratio. Experimental studies on uplift capacity of single and group piles in cohesionless soils were investigated by Gaaver [5]. Their study revealed the significance of embedment depth to diameter ratio and soil properties in defining the ultimate uplift resistance of single piles. They also observed a decrease in group efficiency of piles with increase in number of piles in the group and pile embedment depth to diameter ratio. The pull-out characteristics of piles in submerged floating tunnels at different inclinations were analyzed using numerical simulations by Jiang and Li [6]. Based on their studies they concluded that

maximum pull-out resistance and hence the lateral confinement of soil mass against the pile shaft could be achieved when the pile inclination is 30°. The comparative studies between laboratory and analytical models to evaluate the uplift forces in expansive soil were performed by Soundara and Robinson [7]. Their results indicated that interfacial shear stress follows a triangular distribution along the pile shaft. The computational limit analysis to evaluate the uplift capacity of circular piles in sand was utilized by Ukritchon and Keawsawasvong [8]. The comparative studies indicated that proposed correlation for the prediction of uplift capacity of piles in soil having high friction angle was in accordance with existing methods. The effect of embedment length to diameter ratio, shaft diameter, and angle of the enlarged base in predicting the uplift capacity of under-reamed piles in dry sand using artificial neural network (ANN) was investigated by Moayedi and Rezaei [9]. Their results stipulated a highly accurate and precise ANN model for the prediction of tensile capacity of piles with least error. The efficiency of GPA against pull-out forces in expansive soils was researched upon by Abhishek [10]. Their studies highlighted the significance of elastic modulus of soil in altering the pull-out resistance of GPA. Laboratory investigations were performed by Sharma and Sharma [11] to estimate the pull-out behavior of geogrid reinforced GAP in stabilized expansive soil. They observed that pull-out load increased with increase in relative density of the granular materials and was observed to be the maximum for geogrid reinforced GPA in stabilized soil. The pile load test was conducted and the effect of skin friction on bearing resistance of bored piles was analyzed by Wada [12]. It was concluded based on the results that skin friction is largely influenced by the displacement of pile shaft.

3 Pile Soil Interaction

The pile soil interaction problems had been analyzed for single and pile groups with the help of experimental and analytical models. The studies conducted in the past offered an improved understanding for closely spaced piles subjected to both vertical and lateral loads. This phenomenon was observed to be dependent on embedment length to diameter ratio (L/d), surface and material characteristic of pile, friction angle at the soil pile interface, method of installation, ground conditions, etc. The curved failure surface, of a pile subjected to uplift, was assumed to pass through soil mass adjoining the pile shaft. According to [1] an axisymmetric mass of soil will also move along with the pile shaft during the uplift of a circular pile hence resulting in a curved failure surface (Fig. 1).

In Fig. 1 P_u represents the ultimate uplift load, L being the length of the pile shaft and $\ominus$ indicates the inclination of the failure surface. The maximum extent of the failure surface from the pile shaft occurs when the pile friction angle reaches the shearing resistance of the surrounding soil mass. In pile soil interaction analysis, it is assumed that the ultimate uplift force is achieved when the mobilized shear strength of the soil balances with overburden pressure and self-weight of the pile.

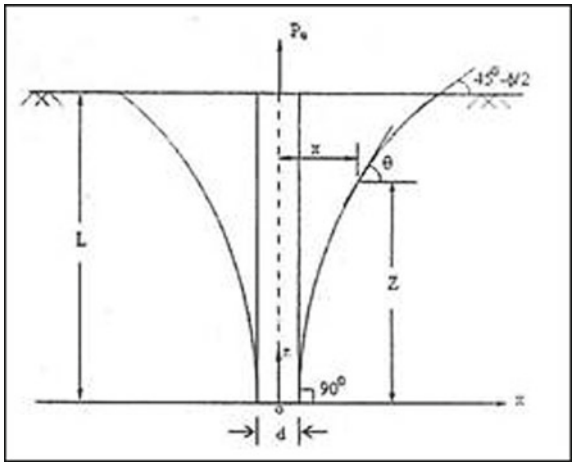

Fig. 1 Pile shaft with curved failure surface [1]

4 Methodology

The methodology adopted in the current work can be sequenced as:

(1) Fabrication of a model tank.
(2) Characterization of the soils for index and engineering properties.
(3) Fixing the moisture contents and length to embedment ratio (L/D) at which pull-out forces would be estimated.
(4) Estimation and comparative studies of the pull-out capacity, interfacial friction, and pile displacements corresponding to the selected moisture contents for both the soils.

The model tank for carrying out the laboratory investigations is fabricated based on experimental requirements. The soils used in the current study, viz., lateritic and red soils, are identified and transported from the field. Since there would be disturbance experienced by the surrounding soil during pile installation and pull-out, disturbed soil samples are used in the present study. The soils are then characterized to understand its index and engineering properties. Based on literature studies, the moisture content and length to embedment ratio of piles at which uplift capacity would be estimated are prefixed. Experimental studies are carried out to evaluate the pull-out capacity, pile soil interfacial friction, and magnitude of pile displacements corresponding to the prefixed moisture contents. The obtained results are then analyzed and comparative studies are performed for lateritic and red soils.

5 Materials Used

5.1 Model Tank

The fabricated model steel tank is cylindrical in shape with an inner diameter of 290 mm and height of 600 mm. The thickness of the steel tank is 10 mm. As per [13] the influence zone of the pressure bulb is 2.5 times pile stem diameter away from the shaft periphery. The model tank used in the current study is adequately large to incorporate the confinement pressure of the pressure bulb created by the pile shaft.

5.2 Model Piles

The model piles used in the current study are made of mild steel of 20 and 50 mm circular cross section. The experiments are carried out on 20 and 50 mm diameter steel solid piles having smooth and corrugated or rough surface characteristic. The embedment length (L) taken for 20 mm diameter (D) pile is 600 and 400 mm, respectively, whereas a length of 600 mm is taken in case of 50 mm diameter pile. Hence L/D ratios for 20 mm piles are 30 and 20, respectively, and that for 50 mm pile is 12.

5.3 Lateritic Soil (LS)

The lateritic soil used in the current study is obtained from Quilon district, Kerala. The sample is obtained at a depth of 2 m from the ground surface and is finely grounded before subjecting to the laboratory tests. The pulverized sample is oven dried for 24 h prior to experimental investigations. Table 1 represents the index and engineering properties of lateritic soil.

5.4 Red Earth (RE)

The red soil, collected from Bengaluru district, Karnataka, is secured from a depth of 1.5 m below the top soil. Red soil is typically rich in iron content and clayey particles. The soil sample is pulverized and oven dried prior to tests in order to ensure uniformity. Table 1 represents the index and engineering properties of red earth used in the present study. Figure 2 shows the compaction curve for lateritic soil and red earth.

Table 1 Properties of soil samples

Property	Lateritic soil (LS)	Red earth (RE)
Color	Dark brown	Brick red
Specific gravity	2.67	2.69
Liquid limit, %	31.5	42
Plastic limit. %	20.7	26
Plasticity index. %	10.8	16
IS classification	CL	CI
Maximum dry density, g/cc	1.864	1.620
Optimum moisture content, %	17.8	18.2
Angle of shearing resistance, degrees	29	24

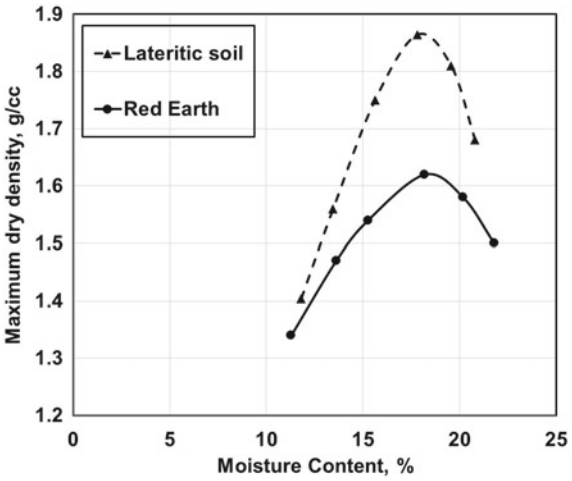

Fig. 2 Compaction characteristics of lateritic soil and red earth

6 Experimental Results and Discussions

The experiment is carried out for dry side of optimum, wet side of optimum and maximum dry densities, the former two being taken at 95 percentage of the maximum dry density. The soil bed is prepared in the model tank for the desired unit weight after which the pile is driven inside at the prefixed L/D ratio. The top end of the pile is attached to Universal Testing Machine and dial gauges are fixed to measure the pile displacements. Tests on model piles are conducted under strain-controlled conditions to understand their uplift behavior. The ultimate uplift load/resistance is achieved when the embedded model pile is moved out of the prepared soil bed.

6.1 Variation of Pull-Out Resistance with Moisture Content

Figures 3 and 4 represent the variation of pull-out capacity with moisture content in lateritic soil and red earth for embedment length to diameter (L/D) ratios of 30 and 12, respectively. The maximum pull-out load is attained for rough pile in lateritic soil at a moisture content corresponding to maximum dry density. As the soil moisture content increases beyond this optimum range, the pull-out load is observed to decline. This trend is generated owing to the fact that shear strength of the soil reduces when compacted at wet side of optimum and thereby enables easy displacement of the pile.

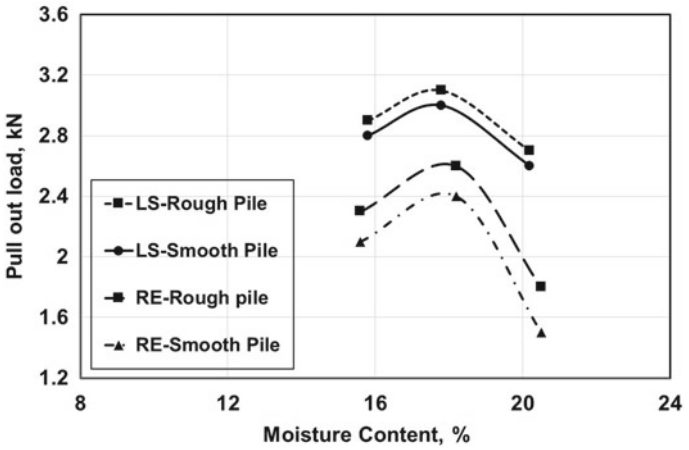

Fig. 3 Variation of pull-out load with moisture content for L/D = 30

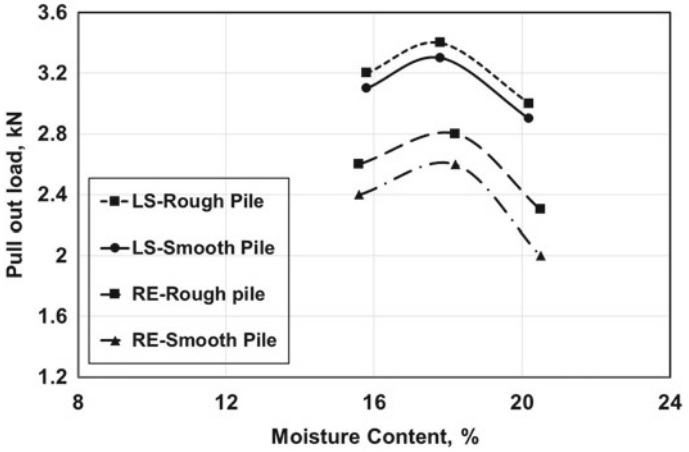

Fig. 4 Variation of pull-out load with moisture content for L/D = 12

Table 2 Pull-out load for lateritic soil and red earth

Soil type	Moisture content, %	L/D ratio	Rough pile, kN	Smooth pile, kN
Lateritic soil (LS)	15.8	30	2.9	2.8
	17.8		3.1	3
	20.2		2.7	2.6
	15.8	12	3.2	3.1
	17.8		3.4	3.3
	20.2		3.0	2.9
Red earth (RE)	15.6	30	2.3	2.1
	18.2		2.6	2.4
	20.5		1.8	1.5
	15.6	12	2.6	2.4
	18.2		2.8	2.6
	20.5		2.3	2.0

The L/D ratio of the pile is also found to possess a significant role in improving the uplift capacity. As the pile diameter increases, larger is the uplift resistance detected. Hence, it can be inferred from the results that pull-out resistance is a function of surface and material characteristics of pile as well as the soil properties. Table 2 represents the experimental results of pull-out load for both L/D ratios.

6.2 Variation of Interfacial Friction with Moisture Content

The interfacial friction is assessed by subjecting a representative steel plate to direct shear test under three confining pressures of 50, 100 and 150 kPa. The samples for the tests are prepared at dry, maximum, and wet side of maximum densities. The variation in effective interfacial friction for smooth and rough pile material corresponding to the prefixed moisture contents is shown in Fig. 5 and the corresponding values are tabulated in Table 3.

It can be observed from the results that interfacial friction increases with increase in moisture content up to the optimum value. However, as the pores get completely saturated with water, soil loses shear strength and hence the interfacial friction between the pile and soil reduces. With respect to dry density of the surrounding soil, the interfacial friction exhibited incremental proclivity. This frictional tendency may also be attributed to the change in soil structure from flocculated to that of the dispersed. Further, it is also observed that lateritic soil offered higher frictional resistance when compared with that of red earth. The higher interfacial friction generated could be owed to the presence of more gravels or sand and well-graded distribution of particles in lateritic soil in contrast to poorly graded red earth.

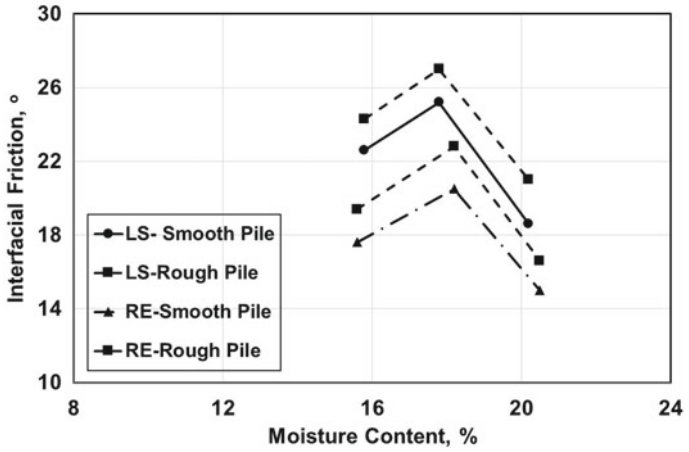

Fig. 5 Variation of Interfacial friction with moisture content

Table 3 Interfacial friction for lateritic and red earth

Soil type	Moisture content, %	Rough pile, δ, degrees	Smooth pile, δ, degrees
Lateritic soil (LS)	15.8	24.3	22.6
	17.8	27	25.2
	20.2	21	18.6
Red earth (RE)	15.6	19.4	17.6
	18.2	22.8	20.5
	20.5	16.6	15

6.3 Variation of Skin Friction with Moisture Content

The skin friction resistance of the embedded model piles is estimated using Eq. (1).

$$Q_s = K^* \sigma_y^* \tan \delta^* \mathrm{A_s} \tag{1}$$

where Q_s = skin friction of the pile, K = earth pressure coefficient, σ_v = average effective overburden pressure over the embedded depth of pile, δ = interfacial friction angle, A_s = embedded pile surface area.

Figures 6, 7 and 8 show the variation of skin friction in model piles for embedment length to diameter ratios of 30, 20 and 12, respectively. It can be inferred based on results that skin friction is dependent on surface characteristics and diameter of the pile. With increase in pile diameter, the skin friction exhibited significant upsurge. This increment is up to 162% for rough piles and up to 154% for smooth piles embedded in lateritic soil (when compared between L/D = 30 and L/D = 12). In case of red earth, the increment spotted is up to 166 and 150% in rough and smooth

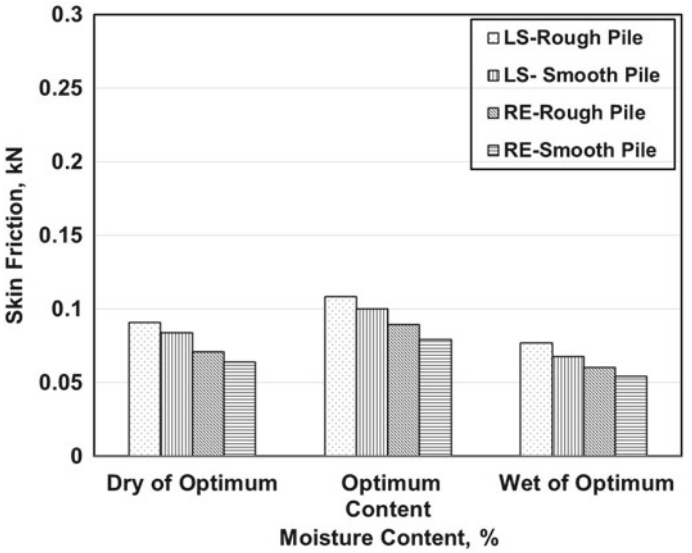

Fig. 6 Variation of pile skin friction with moisture content for L/D = 30

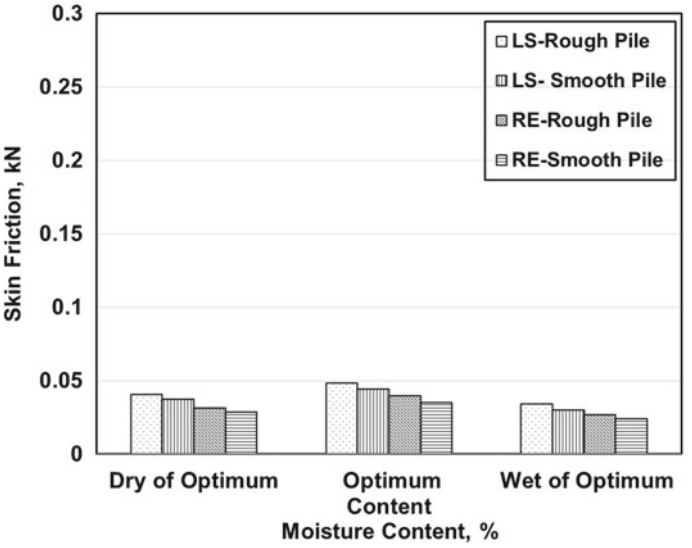

Fig. 7 Variation of pile skin friction with moisture content for L/D = 20

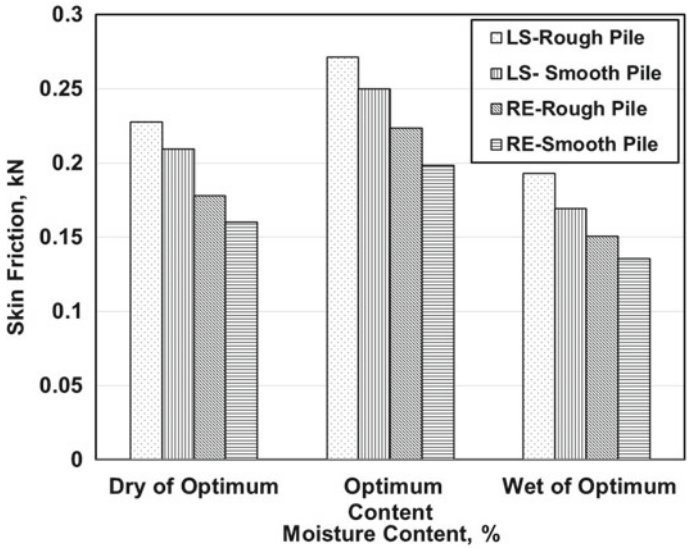

Fig. 8 Variation of pile skin friction with moisture content for L/D = 12

piles, respectively. Further, the moisture content of the soil is also found to influence pile skin resistance. The skin friction is generated with displacement in pile shaft and is observed to attain its maximum value at the optimum moisture content. A further increase in moisture content resulted in skin friction being reduced to its residual strength. Based on the test results, it is incidental that skin friction decreases with decrease in pile embedment length for the same cross-sectional area of the pile. Hence the maximum skin friction can be confirmed as a parameter of embedded length, diameter of pile, and soil properties.

7 Conclusions

Based on the current study following conclusions are deduced:

(1) Pull-out capacity of pile is influenced by the presence of moisture content in the soil as well as pile cross-sectional area. The maximum uplift resistance is achieved at optimum content corresponding to maximum dry density.
(2) The effective interfacial friction increases with increase in soil moisture content up to optimum limit. Rough piles embedded in lateritic soil display higher frictional resistance than in red soil.
(3) The skin friction generated is observed to be a function of embedment depth to diameter ratio of the pile and moisture content of the surrounding soil. It reduces to its residual strength at wet of optimum moisture content.

(4) Piles possessing rough surface behavior exhibit higher performance rate in terms of pull-out resistance, interfacial, and skin friction.
(5) Apart from factors such as surface and material characteristics of pile and embedment depth to diameter ratio, the characteristics of soil surrounding the pile also has a significant influence in the estimation of uplift capacity of piles.

References

1. Chattopadhyay BC, Pise PJ (1987) Uplift capacity of driven piles in sand. J Inst Eng Civ Eng Div 68:89–91
2. Rao AS, Phanikumar BR, Babu RD, Suresh K (2007) Pullout behavior of granular pile-anchors in expansive clay beds in situ. J Geotech Geoenvironm Eng 133:531–538. https://doi.org/10.1061/(ASCE)1090-0241(2007)133:5(531)
3. Hao D, Chen R, Fan G (2012) Ultimate uplift capacity of transmission tower foundation in undisturbed excavated soil. Energy Proc 17:1209–1216. https://doi.org/10.1016/j.egypro.2012.02.228
4. Deshmukh VB, Dewaikar DM, Choudhury D (2010) Computations of uplift capacity of pile anchors in cohesionless soil. Acta Geotech 5:87–94. https://doi.org/10.1007/s11440-010-0111-6
5. Gaaver KE (2013) Uplift capacity of single piles and pile groups embedded in cohesionless soil. Alexandria Eng J 52:365–372. https://doi.org/10.1016/j.aej.2013.01.003
6. Jiang X, Li K (2016) Research on pull-out mechanical characteristics of pile foundation in submerged floating tunnel. Procedia Eng 166:389–396. https://doi.org/10.1016/j.proeng.2016.11.570
7. Soundara B, Robinson RG (2017) Hyperbolic model to evaluate uplift force on pile in expansive soils. KSCE J Civ Eng 21:746–751. https://doi.org/10.1007/s12205-016-1001-8
8. Ukritchon B, Keawsawasvong S (2019) Design equations of uplift capacity of circular piles in sands. Appl Ocean Res 90:101844.https://doi.org/10.1016/j.apor.2019.06.001
9. Moayedi H, Rezaei A (2019) An artificial neural network approach for under-reamed piles subjected to uplift forces in dry sand. Neural Comput Appl 31:327–336. https://doi.org/10.1007/s00521-017-2990-z
10. Abhishek SRK (2019) A numerical study of granular pile anchors subjected to uplift forces in expansive soils using PLAXIS 3D. Indian Geotech J 49:304–313. https://doi.org/10.1007/s40098-018-0333-3
11. Sharma A, Sharma RK (2019) An experimental study on uplift behaviour of granular anchor pile in stabilized expansive soil. Int J Geotech Eng 00:1–14. https://doi.org/10.1080/19386362.2019.1597481
12. Wada A (2004) Scholars ' mine skin friction and pile design. pp 0–6
13. Bureau of Indian Standards (1985) Code of practice for design and construction of pile foundations. Part 4: Load test on piles. IS2911 (Part 4)

Reviewing the Mechanical Properties of FA and GGBS-Based Geo-polymer Concrete Containing Recycled Concrete Aggregates

Ritik Saxena and S. P. Singh

Abstract As in today's construction industry, concrete is the key component of construction material used worldwide. But the problem of overconsumption of natural resources, heavy emission of CO_2, and high consumption of energy while manufacturing are the challenging obstacles in production. Therefore, various studies are performed to get a sustainable and economical construction material that replaces conventional Ordinary Portland Cement (OPC) from industrial wastes like Fly Ash (FA) and Granulated Blast Furnace Slag (GGBS), also using Recycled Concrete Aggregate (RCA) of demolished structures in place of natural coarse and fine aggregate. Hence, the final outcome has resulted in a sustainable construction material that is formed by the alkali activation of source materials like GGBS and FA with a combination of metal hydroxide and silicate known as Geopolymer Concrete (GPC); that is eco-friendly for the environment through suppressing the issues of waste disposal and global warming. This paper presents a literature review on the mechanical properties of FA and GGBS-based GPC. The mechanical properties that have been reviewed include compressive strength, flexural strength, split tensile strength, and modulus of elasticity. The optimum proportion of RCA, aluminosilicate, activating solution, molar concentration, water to binder ratio (w/b), rest period and curing temperature, etc. are reported to generate an efficient mix. Also, various existing gaps and future scope are discussed as per the comprehensive literature survey.

Keywords Geopolymer · Fly ash · GGBS · Recycled concrete aggregate · Mechanical properties · Sustainable · Activating solution · Water to binder ratio

R. Saxena (✉) · S. P. Singh
Dr B R, Ambedkar National Institute of Technology, Jalandhar, India
e-mail: ritiks.ce.20@nitj.ac.in; ritik1998saxena@gmail.com

S. P. Singh
e-mail: spsingh@nitj.ac.in

L. Nandagiri et al. (eds.), *Recent Advances in Civil Engineering*, Lecture Notes in Civil Engineering 256, https://doi.org/10.1007/978-981-19-1862-9_17

Abbreviations

OPC	Ordinary Portland cement
FA	Fly ash
GGBS	Ground granulated blast furnace slag
GPC	Geopolymer concrete
RCA	Recycled concrete aggregate
w/b	Water to binder ratio
CC	Conventional concrete
SCM	Supplementary cementitious material
CSH	Calcium silicate hydrate
NaOH	Sodium hydroxide
Na_2SiO_3	Sodium silicate
f_{ck}	Characteristic compressive strength
f_{ct}	Split tensile strength
E_c	Elastic modulus
MPa	Mega Pascal
GPa	Giga Pascal

1 Introduction

The rapid industrialization and urbanization is the leading factor behind the increased demand for concrete in the world. Though concrete is a wonderful material due to its excellent mechanical properties, prompt accessibility of its constituent materials, ability to mould in any shape, etc. [1–3]. The main binding material in conventional concrete (CC) is OPC. Although the production of this substance requires a high amount of energy, approximately every ton of OPC consumes 4GJ energy and release 1 ton of CO_2 towards the environment [4]. Therefore, it is solely responsible for a total of 7% emission of greenhouse gas whose impact gives rise in global warming up to 4% over the earth [4]. Hence, to reduce this heavy consumption of cement with the help of a supplementary cementitious material (SCM) is a big concern. This problem can be tackled by partial replacement of OPC using the waste generated from the iron and steel-making industries like FA and GGBS, in this way, the challenge of disposing of them safely has been solved. In addition to this, the natural aggregate covers the major volume of CC usually extracted from the quarries of hard rock and pits of sand and gravel through mining [5]. This is causing a drastic effect on mineral deposits as well as overconsumption has resulted in the scarcity of natural aggregate. In contrast, the availability of huge construction and demolition waste generated from old and damaged structures has become a leading concern for society and the environment. Though vast investigation proves that partial substitution of natural aggregate using RCA can significantly reduce shortage and disposal constraints [6–8]. However, several pieces of literature have established

that concrete containing (RCA) over a certain limit shows weaker mechanical properties than concrete containing natural aggregate [9, 10]. Furthermore, recent work on improving the performance of recycled aggregate has made the use of recycled aggregates easier [11, 12]. As the conventional components involved in the manufacturing of concrete lead to exploitation of the environment. In order to eliminate this significant issue, various researches have already been conducted. Best efforts bring to the development of another type of adhesive substance in the form of Geopolymer, which is produced by a polycondensation reaction between aluminosilicates such as FA and GGBS with alkali activators consisting of a combination of metal hydroxide and silicates [13]. The predominant cementitious compound in this inorganic substance is geopolymeric gel, as opposed to Portland cement, which has a hydrated gel of calcium silicate (CSH) as the main binding component [14]. It is also estimated that geopolymer concrete prepared with fly ash can reduce the consumption of energy up to 60% and CO_2 emission by 80% [15]. Observations imply that heat curing of GPC with low-calcium FA at an elevated temperature ranging from 50 to 90 °C resulted in high-level cementing characteristics [16]. On the other hand, curing of GPC at ambient temperature with added calcium content in the FA also shows better cementitious strength [17]. Various studies have proved that GGBS is an efficient material for improving the properties of GPC. According to Nath and Sarker [18] experimental works, for every 10% replacement of GGBS in GPC with fly ash used as primary binder constituent improves the compressive strength of concrete by 10 MPa that can be observed in Table 4. It is also observed that GGBS acts as the catalyst and accelerates the chemical reaction resulting in rapid strength development [19–21]. It is due to ingestion that GGBS increases the amount of free calcium ion in the geopolymer matrix; hence, dissolution of FA together with geopolymerization gets promoted. Sata et al. [22] performed various experiments with previous GPC in which natural aggregate is replaced by crushed concrete and brick waste and uses varying concentrations of alkali solution formed by NaOH. In comparison to CC containing only natural aggregate, the observatory results for such previous concrete demonstrate inferior mechanical parameters including compressive strength and splitting tensile strength. Although the mechanical characteristics of GPC made with crushed aggregate improved when the NaOH concentration was increased. It is investigated that GPC is an eco-friendly construction material that can convert a lot of residual waste into cost-effective and consumable products but its strength and durability properties depend on various parameters. The primary goal of this research is to review the mechanical properties of GPC made from industrial and demolition waste. Also, the impact of the variation in quality and quantity of various ingredients and their optimum percentage required to design a high strength mix of GPC is discussed.

2 Process and Mechanism of Geopolymerization

In 1978, Davidovits defined geopolymer as an amorphous substance formed by the polycondensation reaction of a highly concentrated alkaline solution with aluminosilicates source material [13]. Geopolymer consists of a vast ability to serve as third-generation cementitious material by replacing conventional binding materials such as lime and OPC. The chemical reaction that turns silica-rich industrial waste material into an advanced binding substance is called geopolymerization. Various industrial residual wastes or agriculture products such as FA, GGBS, metakaolin, red mud, volcano ash, glass powder, silica fumes, rice husk ash, etc. are the rich sources of aluminosilicates used as a binder in GP [23]. Together with the source material, the activating solution takes part in a polymeric reaction consisting of hydroxide and silicates of potassium (K) or sodium (Na) to form a 3-D tecto-aluminosilicate network [24]. The empirical formula for the molecule of geopolymer is given by Eq. (1):

$$Mn[-(SiO_2)z - AlO_2]n.wH_2O \tag{1}$$

Here, M stands for positively charged ions like Na^+, Ca^{2+}, or Li^+; n represents the degree of polycondensation; z is the subscript that can be 1,2,3,4 or any greater value showing molar ratio, and w is bonded water content. This type of poly structure combination is called poly(sialate) in which sialate chemically represents silicon-oxo-aluminate. Here, the presence of positively charged ions (K^+, Ca^+, Li^+, Na^+ or NH^{4+}) must require to make an equilibrium with negatively charged aluminium ions in a fourfold coordinate system [25]. The mechanism of geopolymerization consists of two major phenomena that are alkali activation and polycondensation of aluminosilicate gel, which is followed by proper curing at high temperature for better mechanical properties [26].

The basic steps involved in the geopolymerization process can be ordered as follows:

1. Initially, aluminium (Al) and silica (Si) ions present in the inorganic precursor get dissolved with the help of activating solution resulting in tetrahedral units of (SiO_4) and (AlO_4).
2. Further tetroxide reaction results in the disintegration of Si–O–Si bonds, as well as alternate linking of Al atoms, develops Si–O–Al geopolymeric precursor as reported in Eq. (2):

$$(Si_2O_5, Al_2O_2)_n + nH_2O \xrightarrow{KOH,NaOH} n(OH)_3 - Si - O - Al^{(-)} - (OH)_3 \tag{2}$$

3. The reactive nature of aluminosilicate gel catalyzes the polycondensation reaction hence form a 3D ring framework of geopolymer network known as poly(sialate) shown in Eq. (3):

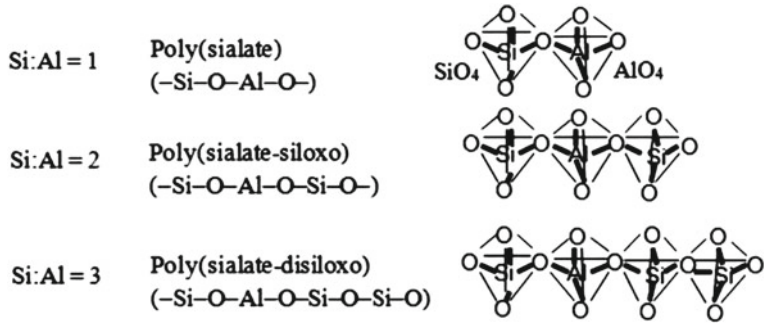

Fig. 1 Basic 3D structural combination of polysialates [27]

$$n(OH)_3 - Si - O - Al^{(-)} - (OH)_3 \xrightarrow{KOH,NaOH} (Na,K)(-\underset{|}{Si} - O - \underset{|}{Al}^{(-)} - O + 3nH_2O \tag{3}$$

4. The adequacy of geopolymerization with enhanced properties also requires elevated curing conditions after a sufficient rest period.

The main element of the geopolymer matrix is poly(sialate) consisting of a huge network of Si–O–Al, which are attached by sharing alternate oxygen atoms. The resulting degree of crystallinity with the final form of 3D chain and ring framework depends on the molar ratio between Si/Al. There are three types of poly(sialate) forms during geopolymerization, which can be categorized based on the particular proportion of Si/Al can be seen in Fig. 1.

3 Materials Involved

Sources of various materials used for the manufacturing of GPC are highly responsible to decide the output strength. Geopolymer is synthesized with the combination of (Si) and (Al) rich source materials that are activated through high concentration (Na) or (K)-based alkali activators. Most of the materials that are professionally involved are the by-products of metal industries and thermal power plants. Even though its proper utilization is still far away.

3.1 Fly Ash

FA is a derivative of inflammable and inorganic materials found in pulverized coal that is captured from flue gases in the chimney of the coal power plant through separators or fabric filters [28]. FA is currently produced more than 300 million tonnes over the world. However, it is only consumed in small amounts up to (10–30%), primarily as a component of concrete and infill material for embankments and foundations [28]. Numerous observations concluded that (Class F) FA with low calcium content produced by the combustion of Anthracite and bituminous coal is sufficient for obtaining desired results in GPC [29]. This form of FA has a specific gravity of 2.2–2.8 with particle size of 1–150 μm. Table 1 shows the variation in chemical compounds present in FA taken from different sources used by several researchers.

3.2 Granulated Blast Furnace Slag

GGBS is produced at steel mills by employing the phenomenon of rapid cooling of molten slag using water while the manufacturing of iron [36]. Blast furnace slag can be classified as foam-based slag, palletized slag, GGBS, and air-cooled slag, depending on the procedures used in the production [37]. In GGBS, about 98% of particle is passed from a 45-micron sieve. The range of particles present in GGBS is approximately (0–5) mm and in the case of palletized slag, it is between 0 and 20 mm [38]. Several results are already recorded with the incorporation of furnace slag in GPC. Study of Kurklu et al. [39] compiled that slag is the remarkable strength-building factor in geo-polymer-based concrete. Gupta et al. [30] experiments using 100% replacement of GGBS with 0–3% superplasticizer give up to 20.7 MPa compressive strength in just 7 days and 40.2 MPa in 28 days as shown in Table 4. Ling et al. [40] investigated the bonding strength of GPC in which furnace slag is proved to be the best filler content in reducing the cracks and imparting the high durability for the concrete specimen. Due to the inclusion of slag in geopolymer matrix, the mixing of calcium content is accelerated by which more CSH gel is synthesized that provides high strength in concrete. Many literature reviews convince that GGBS leaves a sustainable impact on the environment. Slag in concrete reduces the need for sodium silicate, resulting in lower energy usage and diminish carbon footprint during the manufacturing of GPC [41]. Table 2 listed the compositions of chemical constituents found in GGBS and their variation depending on different industrial resources.

Table 1 Chemical compositions of different constituents of fly ash

Oxides	FA (wt%)					
	Nakul et al. [30]	Yong et al. [31]	Faiz et al. [32]	Akbarnezhad et al. [33]	Mesgari et al. [34]	Ganesh et al. [35]
Silicon dioxide (SiO_2)	61.74	65.90	51.11	66.65	66.65	47
Aluminium oxide (Al_2O_3)	25.23	24.00	25.56	22.47	22.47	30
Iron oxide (Fe_2O_3)	5.98	2.87	12.48	3.54	3.54	12.4
Calcium oxide (CaO)	2.15	1.59	4.30	1.64	1.64	2.84
Titanium oxide (TiO_2)	–	0.92	1.32	0.88	0.88	–
Phosphorus oxide (P_2O_5)	–	0.19	0.89	0.11	0.11	–
Magnesium oxide (MgO)	0.32	0.42	1.45	0.65	0.65	0.83
Sulphur trioxide (SO_3)	0.27	–	0.24	0.10	0.10	0.5
Sodium oxide (Na_2O)	–	0.49	0.77	0.58	0.58	0.51
Potassium oxide (K_2O)	–	1.44	0.70	1.75	1.75	0.45
Manganese oxide (MnO)	–	0.06	0.15	0.06	0.06	–
Loss of ignition (LOI)	2.15	1.53	0.57	1.66	1.66	–

3.3 Recycled Concrete Aggregate (RCA)

Waste aggregate generated from a scrap of old buildings or accidental damages accumulated by a natural disaster can be reprocessed to use as concrete aggregate. Quality and amount of cement mortar previously adhered to the surface of recycled aggregate, as well as the recycling methods utilized, determine the attributes of such aggregate [42]. Because the mechanical characteristics of RCA are heavily affected by the replacement ratio and water content; hence, these parameters should be decided with proper validation [43]. The main factors that are responsible to decide the compressive strength of RCA are the (w/b) ratio, replacement percentage

Table 2 Various percentages of chemical oxides found in GGBS

Oxides	GGBS (wt%)					
	Nakul et al. [30]	Yong et al. [31]	Akbarnezhad et al. [33]	Mesgari et al. [34]	Ganesh et al. [35]	Pradip et al. [18]
Silicon dioxide (SiO_2)	31.36	36.00	31.52	31.52	31.25	32.46
Aluminium oxide (Al_2O_3)	13.16	13.80	12.22	12.22	14.06	14.3
Potassium oxide (K_2O)	–	0.27	0.33	0.33	–	0.33
Calcium oxide (CaO)	39.21	42.60	44.53	44.53	33.75	43.1
Iron oxide (Fe_2O_3)	2.34	0.30	1.14	1.14	2.8	0.61
Titanium oxide (TiO_2)	–	0.8	1.03	1.03	–	0.55
Phosphorus oxide (P_2O_5)	–	0.10	0.02	0.02	–	0.02
Sulphur trioxide (SO_3)	1.40	0.56	3.24	3.24	–	4.58
Magnesium oxide (MgO)	6.56	5.80	4.62	4.62	7.03	3.94
Sodium oxide (Na_2O)	–	0.21	0.21	0.21	–	0.24
Manganese oxide (MnO)	–	0.40	0.36	0.36	–	–
Loss of ignition (LOI)	1.68	−1.00	0.79	0.79	–	0.09

of RCA with naturally produced concrete aggregate, and the absorbed moisture content present in the aggregate [44]. At constant w/b ratios, studies also show a clear relationship between compressive strength and replacement ratio of RCA used in the mix design of concrete [45, 46]. With 100% elimination of traditional aggregate with RCA, many studies reported a significant drop of 12–25% in compressive strength concrete [47]. Table 3 is depicting the changes in specific gravity with water absorption of RCA as per a comprehensive literature review.

3.4 Alkali Activating Solutions

Alkali activators play an important role in transforming the huge amount of waste generated from power plants and metal industries into a cost-effective and sustainable construction material. There are two combinations of alkali activators used in

Table 3 Changes in water absorption versus specific gravity of RCA

Properties of RCA	Sata et al. [22]	Koushkbaghi et al. [48]	Hu et al. [31]	Shaikh et al. [32]	Peem et al. [49]	Saravanakumar et al. [50]	Hoai-Bao et al. [51]
Specific gravity	2.53	4.3	2.18	1.24	2.26	2.54	2.6
Water absorption	4.58	1.9	6.78	4.9	5.9	6.5	5.8

practices, one is based on liquid activating solution and the other is powder activating solution Re (Fig. 2). Liquid-based activating solution can be generated with the mixture of ($NaOH + Na_2SiO_3 + H_2O$) or by combining ($NaOH +$ silicon dioxide (SiO_2) $+ H_2O$) [38]. The strength parameters of GPC that are designed by such an activating solution fluctuate with changes in molarity [52]. The second kind of activating agent consists of NaOH and Na_2SiO_3, which are mixed in the dry phase without the use of water resulting in easier handling of geopolymer binder. It reduces the loss in workability and provides consistent mechanical properties [52]. Alkali activators are responsible to enhance the mechanical characteristics of GPC by playing a significant role in the hydration process. According to observation maximum, NaOH to binder ratio is kept at 2.6% as optimum [38]. It is estimated that about 38–62 kg of NaOH is used to generate per ton of GPC together with partial replacement of OPC. This reduces the final cost of production and enhances the mechanical properties of concrete [53]. In this research, a thorough investigation of the mechanical characteristics of GPC is carried out at various molar concentration of alkali activating solutions and their combined results are presented.

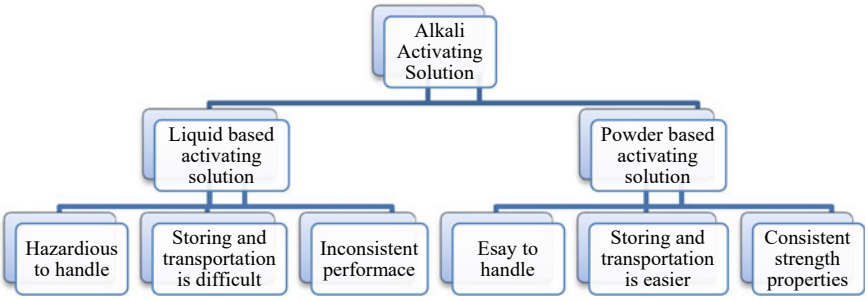

Fig. 2 Properties of activating solutions

3.5 Superplasticizer

The use of a superplasticizer is intended to decrease the water requirement of concrete without affecting workability up to greater than 30% as per usual observation. Rheological and mechanical attributes of GPC are also significantly influenced by superplasticizers [54]. There are various forms of superplasticizer available such as naphthalene-based, modified polycarboxylate-based, acrylic polymer-based, modified lignosulfonates, multi-carboxylatethers, melamine based, etc. An experiment with GPC containing 100% GGBS and addition of 1%, 2%, and 3% dose of polycarboxylate-based superplasticizer resulted in increasing compressive strength by 38.1, 38.9, and 40.2 MPa, respectively, for 28 days of testing. Similar improving results are also obtained with 50% GGBS and FA content with superplasticizer for both tensile and compressive strength [30]. Vora and Dave [55] experimental results found that only 2% inclusion of naphthalene-based superplasticizer provide 32 MPa strength within 3 days of testing, which is superior then strength obtained for 3 and 4% addition. Jithendra and Elavenil [56] also observed similar progressive trends in mechanical properties of GPC for 2 and 3% dosages of superplasticizer as compared to results of 4–6%. Several studies imply that the effect of 1–3% dosages of superplasticizer is positive over the mechanical properties of GPC [55–61]. Therefore, the optimum amount of superplasticizer is necessary to improve different properties of GPC but a higher amount cannot be economical and favourable for better results [62].

4 GPC Mix Design

The design procedure of this latest construction material known as GPC has already been subjected to extensive research, still, there is no globally approved standards mix percentage is available with respect to codal provisions. Researchers usually considered the required performance and application as the basic criteria to decide the trial mix of GPC. In 2010, Lloyd and Rangan made the first attempt to provide a way for designing GPC that included FA instead of OPC cement. IS 10262-(2019) and IS 456-(2000) are used to provide basic assumptions and design criteria as per Indian standards. The total amount of aggregate usually taken in the design of GPC is equal to 77% of the total mass of concrete in which fine aggregate is approximated as 30% of the entire mix. This proportion of aggregate is in comparison to the CC in which aggregate content varies from 70 to 80% of the total mass of concrete [29]. Minimization of voids and maximization of bulk density is the main concern of aggregate proportioning. Various replacement percentages of RCA with natural aggregate are used to investigate the strength and durability of GPC. The different molar concentrations of alkali compounds used in the ratio ranging from (1:1) to (1:2.5) between NaOH and Na_2SiO_3 are used to prepare activating solution 24 h before casting as shown in Table 4, depending on the material of geo polymerization

Table 4 Optimum proportion of various ingredients required to achieve superior mechanical properties

Authors	Binder	Different ratios and percentage	Molar ratio	Curing condition	Replacement percentage of RCA	Compressive strength (MPa)			Flexural strength (MPa)	Split tensile strength (MPa)	Modulus of elasticity (GPa)
						7 days	28 days	28 days	28 days	28 days	28 days
Faiz et al. [32]	100 % fly ash	Na_2SiO_3/NaOH = 2.5	8 M	Heat-cured at 60 °C for 1 day	15%	40.6	41.8	–	–	4.1	20
					30%	37.4	37.6			3.9	15
					50%	35	36.8			3.7	14
Ahmed et al. [104]	80% GGBS and 20% silica fume	Na_2SiO_3/NaOH = 2 Water/binder = 0.19 Alkali/aluminosilicate = 0.35	8 M	Ambient cured for 28 days	100% natural aggregate	51	79	–	–	–	–
Sanjayan et al. [75]	100% fly ash	Na_2SiO_3/NaOH = 2.5 alkali/aluminosilicate = 0.45	8 M	Heat-cured at 60 °C for 18 h	100% natural aggregate	–	69.8	–	–	5	35.5
Hu et al. [31]	70% FA and 30% GGBS	Na_2SiO_3/NaOH = 2.0	12 M	Heat-cured at 75 °C for 1 day	0%	45.4	51	52.3	5.01	4.77	22.32
					50%	36	40.9	43	4.36	4.16	17.96
					100%	34.1	37.9	38.1	4.22	3.54	17.03
Akbarnezhad et al. [33]	81% FA and 18% GGBS	Na_2SiO_3/NaOH = 2.5 Water/binder = 0.35 Alkali/aluminosilicate = 0.55	12 M	Water cured for 7 days	20%	–	48.8	–	5.5	–	25
					50%		47		5		22.5
					100%		41		4.5		20

(continued)

Table 4 (continued)

Authors	Binder	Different ratios and percentage	Molar ratio	Curing condition	Replacement percentage of RCA	Compressive strength (MPa)			Flexural strength (MPa)	Split tensile strength (MPa)	Modulus of elasticity (GPa)
						7 days	28 days	28 days	28 days	28 days	28 days
Sasalatti el at. [105]	80% FA and 20% GGBS	Na_2SiO_3/NaOH = 1.25 Water/binder = 0.45 Alkali/aluminosilicate = 0.4	12 M	Ambient cured for 28 days	100% natural aggregate	3.3	23.11	–	4.06	2.45	25
Chithambr et al. [35]	80% FA and 20% GGBS	Na_2SiO_3/NaOH = 2.5	13 M	Heat-cured at 90 °C for 1 day	100% natural aggregate	37.5	41.3	–	5.3	3.8	–
Albitar et al. [78]	100% fly ash	Na_2SiO_3/NaOH = 1.5 Alkali/aluminosilicate = 0.37	14 M	Heat-cured at 70 °C for 1 day	100% natural aggregate	–	50	–	5.3	4.23	30.88
Adejo et al. [79]	100% metakaolin	Na_2SiO_3/NaOH = 2.5	16 M	Heat-cured at 60 °C for 1 day	20%	27.5	31.5	–	–	2.75	–
					30%	25	28			2.4	
					40%	24	26.5			2.3	

and the desired compressive strength [63]. A conventional blending technique is used to mix different ingredients of GPC. Initially, the fine and coarse aggregate (both recycled and natural aggregate) are mixed for 1–2 min in dry conditions subsequently aluminosilicates such as FA and GGBS are added, followed by another 2–3 min of homogeneous mixing. The alkali solution is then slowly added to the prepared binder and aggregate mixture to activate the hydration process through uniform mixing in the wet phase [31]. A concrete specimen is cast as per the mould dimensions and put in the rest period of 5–6 days [64]. Various forms of curing are supplied by adjusting the surrounding temperature, such as ambient curing at room temperature and steam/hot curing at raised temperature, to see how the mechanical characteristics of concrete change after 7 days, 14 days, and 28 days, respectively, as given in Table 4.

5 Mechanical Properties of GPC

These are the performance evaluation characteristics of concrete that are used to decide the commercial value of the product. Compressive strength is the leading indicator used to define the strength of concrete. The ratio of alkali activators to aluminosilicates, molar concentration, percentage of superplasticizer, rest period, and temperature of curing, as previously reported, are the important parameters affecting the compressive strength of GPC [55, 64]. The method and tools used in compressive strength testing for GPC and CC are the same but the only difference is the curing methodology, which is different for GPC and CC. OPC concrete receives conventional water curing, whereas GPC receives ambient or hot curing [65]. Because the direct tensile strength of concrete cannot be determined by experiment hence the indirect approach of flexure and split tensile strength are used to determine an approximate value. The bending capacity of a concrete structure is measured by its flexural strength. According to several national and international design codes, the flexural strength of concrete can be predicted by using empirical relations linking to compressive strength [21, 66]. Split tensile strength is another significant attribute of concrete that measures the extent and size of cracks that occur due to tensile load [67]. Also, the modulus of elasticity is an excellent indicator of concrete strength and performance; therefore, it is used to determine the stiffness and flexibility of the material. The empirical formula given in various standards of codes implies that the elastic modulus can be computed by using the 28-day compressive strength of a concrete specimen [66, 68].

5.1 Compressive Strength

Strength properties of GPC are highly influenced by fineness fraction of FA because it catalyzes alkali activation due to the massive agility of particles smaller than 43 μ

[29]. Finer particles of FA consist of the greater surface area hence provide a stronger Al–Si bond leading to better polymerization of aluminosilicate source material [2]. The fineness of particles provides a positive impact on both workability as well as the compressive strength of concrete [69]. Studies found that larger aggregate produces interfacial fissures with water accumulation that creates internal bleeding and voids, resulting in lower strength of concrete [70]. The compressive load-carrying capacity of concrete is also altered by the substitution of natural aggregate with RCA. The use of 100% natural aggregate increases the strength of GPC up to 9% while curing period of 7–28 days. It is very much comparable with strength of CC obtained at age of 28 days as shown in Re (Fig. 5). However, 50 and 100% replacement by RCA causes a significant 9–16% and 25–30% respective decrement in compressive strength of GPC as in comparison to CC at the age of 28 days as represented by Table 4 [32, 50, 71]. It is already stated that GGBS increases the formation of CSH gel in concrete thus provides better compressive strength over fly ash. In an observation, 10%, 20%, and 30% addition of GGBS as binder with FA provided an improvement in compressive strength of combination by 67%, 79%, and 100%, respectively, in comparison to the mixture without GGBS also shown in Table 4 [31]. It is too noted that a higher ratio of alkali to source material is also responsible to enhance the compressive strength up to a particular range. However, the amount of activating solution increase beyond a certain limit causes a rise in the w/b ratio that can lead to reduced strength of concrete [65, 72]. Observation concluded that sufficient ratio between water to binder content should be 0.25–0.35. Significantly with the addition of water, a very high ratio produces a separated mix, whereas a too low ratio due to lack of water content produces a viscous-dry mix proportion that is undesirable for workability [55, 73]. Various researchers have concluded that increasing the molarity of the activating solution increases the affinity of Al–Si ions for each other, resulting in long chains of polymerized reaction that improve the compressive strength of GPC [74]. As there are various conflicting results are available with respect to any particular ratio of molar concentration and its effect on compressive strength. Overall results revealed that its effect remains positive as the ratio varies from 8 to 16 M at various test conditions [31–33, 35, 74–79]. In a study comparing the strength properties of geopolymer samples generated by utilizing 10, 12, 14, and 16 M concentrations of alkali solution and cured over longer periods, the compressive strength for 16 M concentration after 28 days of curing was 46 MPa Re (Fig. 3)**,** which is stronger than the others [77]. However, the rising of molar ratio beyond the limit creates a reverse effect due to increasing (OH^-) ions, which lead to the precipitation of aluminosilicate gel at the beginning of geopolymerization [80]. The ratio of Na_2SiO_3/NaOH in GPC varies from 1.5 to 3.5 as shown in Table 4. The strength properties of concrete are found more consistent and cost-effective at a ratio of 2.5 Re (Fig. 4) [32, 74]. It has been discovered that a higher percentage of sodium ions can produce sodium carbonate as a result of atmospheric carbonation, which is a barrier to geopolymerization [81]. The amount of superplasticizer used to promote workability at low water content could also induce alterations in compressive strength. As per studies, a superplasticizer content of nearly 2% is sufficient to improve compressive strength and produce a cost-effective paste [74]. After casting of concrete specimen sufficient rest period is

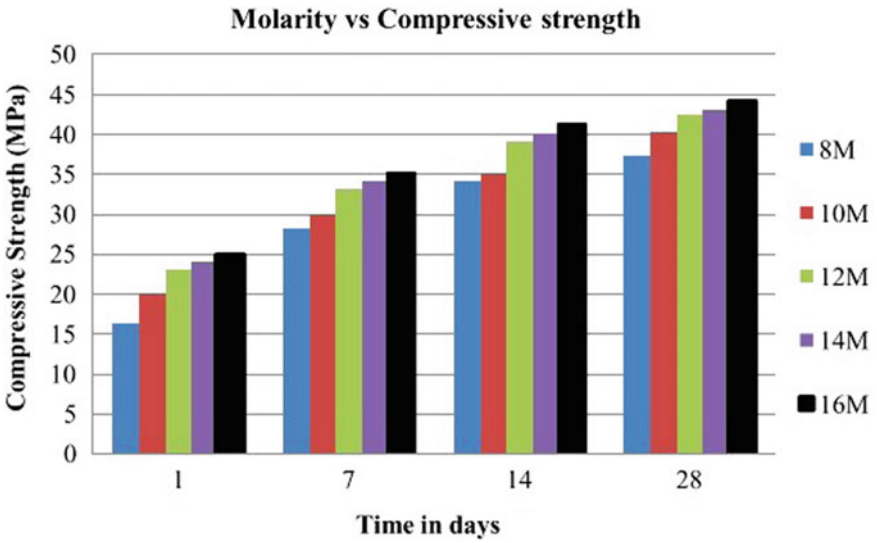

Fig. 3 Influence of various molar concentration on compressive strength [77]

also provided before curing of GPC at elevated temperature. Studies revealed that optimum compressive strength is achieved at 4 days rest period in comparison to results of 1, 2, 3, and 5 days [64]. The curing of GPC is an important step to obtain proper polymerization and higher strength. It is curing temperature and duration of curing that is a deciding factor for attaining optimum pace in strength gaining and peak value of compressive strength for GPC. It is usually seen that at 90 °C curing temperature and 12 h of curing is sufficient to gain the maximum amount of strength in comparison to 80, 100, and 120 °C temperature with variation in curing period of 6, 18, 24 h as shown in Table 4 [82, 83]. Higher temperatures and longer curing times can also help to increase the rate of strength gain; however, after 12 h of curing at a considerably higher temperature, there is no discernible difference in the rate of strength gain. The experimental result also proves that at 60 °C of temperature, the strength gaining pace increases continuously for all periods [84].

5.2 Flexural Strength

The bonding of gel aggregate in the microstructure zone of the concrete matrix has a significant impact on the flexural strength of GPC. It especially depends upon the criteria of propagation of micro-cracks during elevated curing temperature in the gel-aggregate zone of GPC. Low calcium FA blended with GPC producing stronger gel-aggregate bond and a smaller number of micro-crack resulted in higher flexural

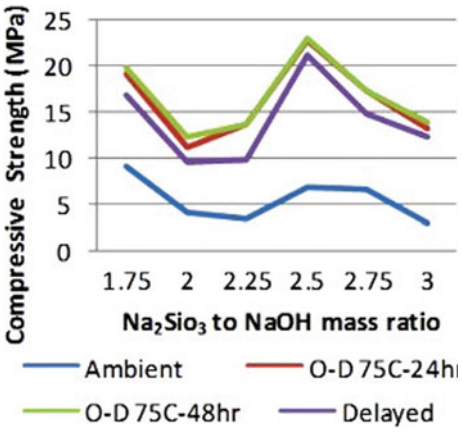

Fig. 4 Changes in compressive strength of GPC at different ratios of Na_2SiO_3/NaOH [85]

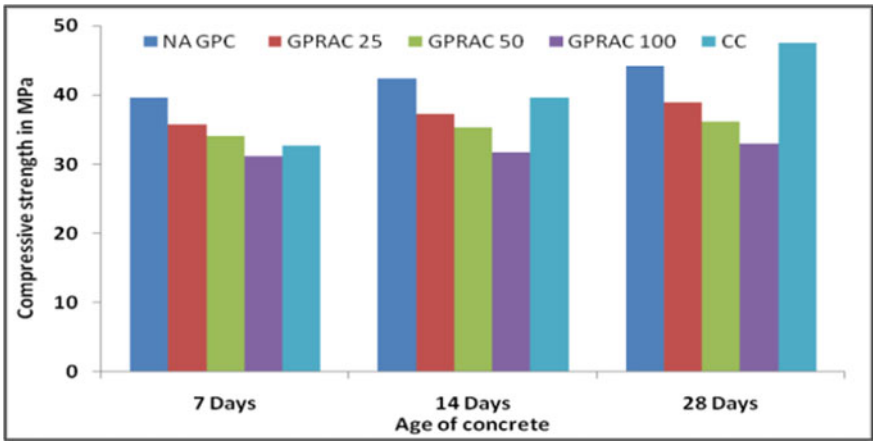

Fig. 5 Compressive strength of GPC produced with various RCA percentages [50]

strength [86]. It also depends upon the particles present in the FA actively participating in the hydration and geo-polymerization reaction of GPC in order to generate a denser mix. Flexural strength of CC and GPC designed with 100% natural aggregate usually shows slight difference in magnitude as per results obtained by other authors [33, 34, 75]. However, as the amount of RCA included in the design mix in replacement of natural aggregate creates a negative impact on flexural strength [49]. According to a review of the literature, replacing natural aggregate with RCA by 20%, 50%, and 100% indicated flexural strength reductions of 0.4%, 8.2%, and 15.2%, respectively, as given in Table 4 [33]. This reduction in flexural strength can be compensated by the addition of GGBS in GPC. It has been observed that the addition of 10–30% GGBS resulted in an increment of flexural strength by 30–43% for concrete with 100% natural aggregate, 51–64% for the concrete mixture with

50% RCA and it rises up to 54–92% for a concrete mixture containing 100% RCA Re (Fig. 6) [31]. Inclusion of GGBS to GPC with RCA increases tensile strength by 0.6 N/mm^2 and flexural strength by 5% as compared to OPC concrete with slag [87, 88]. The presence of silica oxide (SiO_2) in the source material of GPC gives a slight improvement in the flexural strength of GPC. Flexural strength of GPC modified with SiO_2 rich content was found to be lower than CC having natural limestone [49]. There are various standard codes that describe flexural strength as an empirical

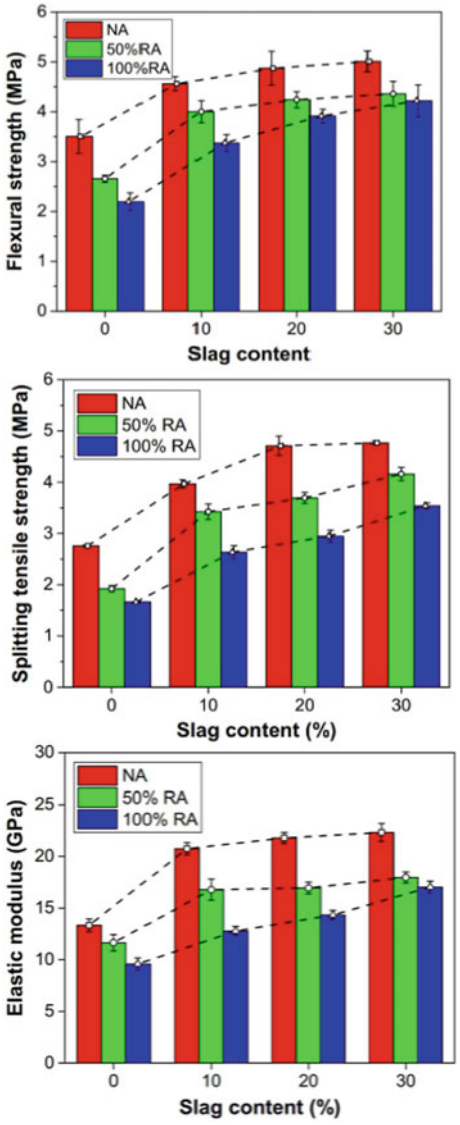

Fig. 6 Effect of slag content and RCA on flexural strength, splitting strength and elastic modulus [31]

formula with reference to compressive strength of concrete. The modulus of rupture (f_{cr}) in reference to the characteristic strength of concrete (f_{ck}) is calculated applying IS 456 (design specification for simple and reinforced concrete) [68] as:

$$f_{cr} = 0.7\sqrt{f_{ck}} \tag{4}$$

ACI 318 (building code of structural applications) [66] provides another equation that connects the modulus of rupture (f_{cr}) and compressive strength (f_c) is given by:

$$f_{cr} = 0.62\sqrt{f_c} \tag{5}$$

Also, the empirical relationship between 28 days of mean flexural strength (f_{ms}) and cylindrical strength of concrete (f_c) is given by Eurocode 2 (concrete structure design code) [89]:

$$f_{ms} = \max\left[\left(1.6 - \frac{h}{1000}\right) f_a;\ f_a\right] \tag{6}$$

$$\begin{cases} f_a = 0.3(f_c)^{2/3}, & f_c \le 50 \text{ MPa} \\ f_a = 2.12\left(1 + \left(\frac{f_{cm}}{10}\right)\right)^{2/3}, & f_c \ge 50 \text{ MPa} \end{cases} \tag{7}$$

$$f_{cm} = f_c + 8 \tag{8}$$

Here, (f_a) stands for the axial tensile strength in mega pascal (MPa), (f_{cm}) denotes the average value of concrete compressive strength in MPa, and h signifies the entire depth of a particular specimen of concrete in millimetre (mm).

5.3 Split Tensile Strength

The experimental procedure used to evaluate splitting strength of GPC is same as for CC. In comparison to CC made with OPC cement, the magnitude of splitting strength for GPC including FA was observed to be greater [33]. It is also observed that experimental results for split tensile strength of GPC are more optimum as compared to predicted results through various empirical relations given in different design codes [90]. The effect of RCA and GGBS replacement on such indirect fracture strength of GPC is comparable to that reported in flexural and compressive strength Re (Fig. 6) [31]. The results for splitting strength of CC and GPC designed by natural aggregate show a difference of 10–20% under similar test conditions [50, 75, 91, 92]. Studies reveal that 50 and 100% inclusion of RCA in GPC resulted in the loss of splitting strength by 0.54–1.01 MPa and 1.09–1.76 MPa for respective mix designs as given in Table 4. Such loss in strength can be reimbursed with the help of GGBS. Slag content of 10%, 20%, and 30% improves splitting strength by

0.97, 1.28, and 1.87 MPa, respectively, Re (Fig. 6) [31]. Various practical studies concluded the magnitude of split tensile strength is comparatively lower than flexural strength by 3–28% as shown in Table 4 [31, 93–95]. The inclusion of steel fibres with GGBS significantly improves the splitting strength by suppressing the post cracks that occur due to tensile stresses. However, the weight percentage of fibre used in the design mix has very less effect on both compressive and splitting strength [96]. It is observed that splitting strength fluctuates due to the quantity and amount of alkali compounds utilized in the activating solution. Molar concentrations ranging from 8 to 14 M boost the split tensile strength, but the impact on GPC is negative once this threshold is exceeded [31–33, 35, 68, 69, 72, 73]. This is because the higher molarity of NaOH causes loose interaction between paste and aggregate. Variation in the ratio between Na_2SiO_3 and NaOH included in the mix proportion is also responsible to change the splitting strength of GPC. According to research, the splitting strength improves with every 0.5 increase in the ratio of Na_2SiO_3/NaOH from 1:1 to 2:1 can be seen in Table 4 [31, 32]. There are various empirical equations that are available to compare the experimental in order to standardize the obtained result. According to ACI 318 [66] structure building code, the empirical formula that establishes a relation between an indirect strength of concrete in tension for splitting (f_{ct}) and compressive strength (f_c) as well is given by:

$$f_{ct} = 0.56\sqrt{f_c} \tag{9}$$

Similarly, Eurocode 2 [89] also provides an empirical expression to analyze a predicted value splitting strength ($f_{ct,sp}$) by using:

$$f_a = 0.9 f_{ct,sp} \tag{10}$$

5.4 Modulus of Elasticity

Elastic modulus is a serviceability parameter that regulates deformation and imparts stiffness to concrete structures. The slope of the linear section of the stress–strain diagram is used to calculate it. The majority of research demonstrates that GPC containing RCA has a lower elastic modulus than CC made from fresh aggregates [33, 74, 91]. There are various factors responsible for the lower value of elastic modulus hence to increase its magnitude, the inclusion of maximum size aggregate as well as lowering the water/cement ratio are effective approaches to improve test results [97]. Replacement of RCA with natural aggregate usually resulted in decreased modulus of elasticity. An observed experimental result shows a maximum downfall of elastic modulus is about 42% for GPC containing 50% replacement of RCA [32]. The presence of micro-cracks and porous interfacial transition zone at the boundary of old mortar and aggregate are the significant factors that are responsible to reduce elastic modulus [98–101]. It is seen in research that 50 and 100% replacement of RCA with

natural coarse aggregate leads to 20 and 40% approximate downfall in the elasticity of recycled aggregate concrete but there is no harmful effect is noticed up to 20% replacement Re (Fig. 6) [31, 34]. Further investigation found that GPC containing RCA shows a lesser volume of permeable voids in comparison to CC containing RCA [34]. The literature review concluded that there is a linear relationship found between pore volume and modulus of elasticity; therefore, a denser mix of GPC provides a higher elasticity [102]. As the elasticity modulus of concrete tends to increase with time as the ultimate strength increase but follows the variation in the ratio of increment [86]. The elastic modulus is heavily influenced by the testing environment and the type of aggregate used, even though GPC has a lower elastic modulus than OPC concrete by 23–50% for the identical conditions and aggregate [75, 103]. The predicted value of elastic modulus can be calculated by using the existing model given by the standard research institute for normal-weight concrete. ACI 381[66] provides the following empirical expression considering any given sample of concrete mix that correlates elastic modulus (E_c) with characteristic compressive strength (f_c):

$$E_c = 4700(f_c)^{1/2} \tag{11}$$

Another existing model is given by Eurocode 2 [89] to correlate 28 days elastic modulus (E_c) of concrete in (MPa) with a specified grade of concrete (f_c) in form of its compressive strength (MPa):

$$E_c = 2.2 \times 10^4 (f_c/10)^{1/3} \tag{12}$$

In comparison to the value computed using the aforementioned conventional formulae for GPC, the actual experimental value of elastic modulus is reported to be 30–60% lower by various researchers [21, 31].

6 Major Outcomes, Limitations, and Future Scope

There are several research that have been carried out for reducing the consumption of OPC and natural aggregate causing a deteriorative effect on environment and natural resources. The development of GPC provides an excellent alternative technique to eliminate the harmful effect of OPC using eco-friendly industrial and agriculture waste in the form of binder by incorporating scrap material of old structures. In this way, the heavy load on natural resources and their scarcity can be adjusted.

The current research looks into the impact of different constituents of GPC that causing the variation in mechanical properties. Significant conclusions drawn from regress literature survey and comparative analysis of their experimental results are as follows:

- An increment in the amount of RCA beyond a certain limit shows a drastic impact on all mechanical properties of GPC. The strength criteria benefit with an optimum

substitution of 20–30% natural aggregate but 50–100% inclusion of RCA can cause 9–30% decrement in Compressive strength, 8–16% decrement in flexural strength, 0.54–2 MPa decrement in split tensile strength and 20–40% decrement in Modulus of elasticity as per analysis.

- Addition of GGBS in concrete increases the amount of CSH gel, which is responsible for improving strength characteristics of GPC. Up to 30% incorporation of GGBS in place of fly ash with 1–3% superplasticizer is efficient to provide high compressive, flexural and splitting strength in concrete.
- In order to polymerize the source material, the molar concentration of alkali solution is important. Therefore, the recommended range of molarity as per analysis should lie between 8 and 16 M as it makes stronger bonding of Al–Si ions and improves compressive and tensile strength of concrete. However, at a high molar ratio, strength decreases due to the accumulation of (OH^-).
- The acceptable proportion of alkali compounds lies in the ratio of (2.5:1) for Na_2SiO_3/NaOH for achieving the expected strength and economic mix design of GPC. Together with w/b ratio should be in the range of 0.25–0.35.
- A sufficient rest period is necessary for the polymeric reaction in GPC between aluminosilicates and alkali activators. Studies concluded that 4 days rest period is optimum to improve compressive strength of GPC.
- Curing is the most important process for strength development; therefore, proper period and temperature are necessary for the gradual release of heat and reducing surface cracking of concrete specimen. For GPC elevated curing up to 90 °C temperature for 12 h period provides high compressive strength beyond this the results are not significant as per investigation.

Though GPC consists a huge advantage over other conventional materials used in the construction and infrastructure industry but its widespread commercial application and implementation are still require a lot of relevant performance data and standard equations consistent with alternative materials used to prepare the strength-oriented mix design of GPC. There is a lack of a specific proportion of chemical components needed to produce silica-rich source material. Variable characteristics of aluminosilicates available in the market or produced in metal industries are responsible to fluctuate long-term mechanical properties of GPC. Also, the availability of current source material primarily depends on the production rate of secondary materials like coal and steel that is a risk for a continuous supply chain. Proper methodologies and relevant testing must be developed for enhancing the substitution percentage of RCA by compensating all the weaknesses associated with the microstructure zone in comparison to fresh aggregate. High-level precautions required to handle activating material, the necessity of high molar concentration, and the absence of a fixed percentage of alkali compounds are significant research areas that have to be further investigated. Susceptibility towards elevated temperature while curing in a strict control environment to impart high compressive strength is also an obstacle behind its mass consumption.

In order to establish GPC as a globalized engineering material, various high-priority steps must be taken to improve on-site feasibility and practical application rather than laboratory results:

- More research is needed to understand how aluminosilicates and alkali activators behave in the microstructure zone during the geopolymerization process.
- Emphasizing more focus on variation in properties of each element required to develop a combined product.
- Individual research on formulating mathematical equations and empirical models to define the significance of various mechanical and durability properties of GPC.
- Critical evaluation of field performance in respect to laboratory results must be analyzed to predict better engineering properties.
- Development of separate material with respect to the exposer conditions and strength requirement according to particular engineering structure.
- Standard tests and proven specifications regarding the design and construction of any structure particularly using GPC should be prepared for approval.
- More research on low-cost alkali-activators and admixtures must be required to generate an overall economical mix design.
- Refinement in the standard proportions must be identified to overcome the restriction of controlled environment and elevated curing temperature for gaining high strength.

References

1. Ojha A, Chouhan V, Gupta L, Goswami S (2020) A case study on project performance of railway underpass construction project in Jaipur, India. In: AIP conference proceedings 2204.https://doi.org/10.1063/1.5141542
2. Patankar SV, Ghugal YM, Jamkar SS (2015) Mix design of fly ash based geopolymer concrete. In: Advances structural engineering materials volume three, pp 1619–1634.https://doi.org/10.1007/978-81-322-2187-6_123
3. Ojha A, Gupta L (2018) Study on the information technology impact questionnaire ITIQ on the construction industry in India, pp 552–557. https://doi.org/10.1061/9780784482025.056
4. Malhotra VMMP (2002) High-performance, high-volume fly ash concrete: materials, mixture proportioning, properties, construction practice, and case histories. ETDEWEB
5. https://www.greenspec.co.uk/building-design/aggregates-for-concrete
6. SC Kou CS Poon HW Wan 2012 Properties of concrete prepared with low-grade recycled aggregates Constr Build Mater 36 881 889 https://doi.org/10.1016/J.CONBUILDMAT.2012.06.060
7. SW Tabsh AS Abdelfatah 2009 Influence of recycled concrete aggregates on strength properties of concrete Constr Build Mater 23 1163 1167 https://doi.org/10.1016/J.CONBUILDMAT.2008.06.007
8. R Zaharieva F Buyle-Bodin F Skoczylas E Wirquin 2003 Assessment of the surface permeation properties of recycled aggregate concrete Cem Concr Compos 25 223 232 https://doi.org/10.1016/S0958-9465(02)00010-0
9. SFU Ahmed 2013 Existence of dividing strength in concrete containing recycled coarse aggregate J Mater Civ Eng 26 784 788 https://doi.org/10.1061/(ASCE)MT.1943-5533.0000864

10. FUA Shaikh HL Nguyen 2013 Properties of concrete containing recycled construction and demolition wastes as coarse aggregates J Sustain Cem Mater 2 204 217 https://doi.org/10.1080/21650373.2013.833861
11. C Shi Y Li J Zhang 2016 Performance enhancement of recycled concrete aggregate—a review J Clean Prod 112 466 472 https://doi.org/10.1016/j.jclepro.2015.08.057
12. G Dimitriou P Savva MF Petrou 2018 Enhancing mechanical and durability properties of recycled aggregate concrete Constr Build Mater 158 228 235 https://doi.org/10.1016/J.CONBUILDMAT.2017.09.137
13. J Davidovits 1989 Geopolymers and geopolymeric materials J Therm Anal 352 35 429 441 https://doi.org/10.1007/BF01904446
14. JL Provis RJ Myers CE White 2012 X-ray microtomography shows pore structure and tortuosity in alkali-activated binders Cem Concr Res 42 855 864 https://doi.org/10.1016/J.CEMCONRES.2012.03.004
15. P Duxson JL Provis GC Lukey JSJ Deventer van 2007 The role of inorganic polymer technology in the development of "green concrete" Cem Concr Res 37 1590 1597 https://doi.org/10.1016/J.CEMCONRES.2007.08.018
16. P Nath PK Sarker 2015 Use of OPC to improve setting and early strength properties of low calcium fly ash geopolymer concrete cured at room temperature Cem Concr Compos 55 205 214 https://doi.org/10.1016/J.CEMCONCOMP.2014.08.008
17. JL Provis 2018 Alkali-activated materials Cem Concr Res 114 40 48 https://doi.org/10.1016/J.CEMCONRES.2017.02.009
18. P Nath P Sarker 2014 Effect of GGBFS on setting, workability and early strength properties of fly ash geopolymer concrete cured in ambient condition Constr Build Mater 66 163 171 https://doi.org/10.1016/J.CONBUILDMAT.2014.05.080
19. F Puertas S Martínez-Ramírez S Alonso T Vázquez 2000 Alkali-activated fly ash/slag cements. Strength behaviour and hydration products Cem Concr Res 30 1625 1632 https://doi.org/10.1016/S0008-8846(00)00298-2
20. El-Hassan H, Ismail N (2017) Effect of process parameters on the performance of fly ash/GGBS blended geopolymer composites. 7:122–140.https://doi.org/10.1080/21650373.2017.1411296
21. NK Lee HK Lee 2013 Setting and mechanical properties of alkali-activated fly ash/slag concrete manufactured at room temperature Constr Build Mater 47 1201 1209 https://doi.org/10.1016/J.CONBUILDMAT.2013.05.107
22. V Sata A Wongsa P Chindaprasirt 2013 Properties of pervious geopolymer concrete using recycled aggregates Constr Build Mater 42 33 39 https://doi.org/10.1016/J.CONBUILDMAT.2012.12.046
23. MS Reddy P Dinakar BH Rao 2016 A review of the influence of source material's oxide composition on the compressive strength of geopolymer concrete Microporous Mesoporous Mater 234 12 23 https://doi.org/10.1016/J.MICROMESO.2016.07.005
24. Davidovits J, France S (2019) Geopolymer chemistry and sustainable development geopolymer chemistry and sustain able development. The Poly (sialate) terminology: a very useful and simple model for the promotion and understanding of green-chemistry
25. MMAB Abdullah LY Ming HC Yong MFM Tahir 2018 Clay-based materials in geopolymer technology Cem Based Mater https://doi.org/10.5772/INTECHOPEN.74438
26. Sambucci M, Sibai A, Valente M (2021) Recent advances in geopolymer technology. A potential eco-friendly solution in the construction materials industry: a review. J Compos Sci 5:109.https://doi.org/10.3390/JCS5040109
27. Davidovits J (2002) 30 Years of successes and failures in geopolymer applications. Market trends and potential breakthroughs. Geopolymer 2002 conference, pp 1–16
28. Joshi RC (2010) Fly ash—production, variability and possible complete utilization. Indian geotechnical conference—GEOtrendz
29. Rajalakshmi R, Revathi P (2016) Geo-polymerization of recycled concrete aggregate—a review. Int J Adv Eng Res Dev 3. https://doi.org/10.21090/IJAERD030646

30. N Gupta A Gupta KK Saxena 2021 Mechanical and durability properties of geopolymer concrete composite at varying superplasticizer dosage Mater Today Proc 44 12 16 https://doi.org/10.1016/J.MATPR.2020.05.646
31. Y Hu Z Tang W Li 2019 Physical-mechanical properties of fly ash/GGBFS geopolymer composites with recycled aggregates Constr Build Mater 226 139 151 https://doi.org/10.1016/J.CONBUILDMAT.2019.07.211
32. FUA Shaikh 2016 Mechanical and durability properties of fly ash geopolymer concrete containing recycled coarse aggregates Int J Sustain Built Environ 5 277 287 https://doi.org/10.1016/J.IJSBE.2016.05.009
33. A Akbarnezhad M Huan S Mesgari A Castel 2015 Recycling of geopolymer concrete Constr Build Mater 101 152 158 https://doi.org/10.1016/J.CONBUILDMAT.2015.10.037
34. Mesgari S, Akbarnezhad A, Xiao JZ (2020) Recycled geopolymer aggregates as coarse aggregates for Portland cement concrete and geopolymer concrete: effects on mechanical properties. Constr Build Mater 236.https://doi.org/10.1016/J.CONBUILDMAT.2019.117571
35. AC Ganesh M Muthukannan 2021 Development of high performance sustainable optimized fiber reinforced geopolymer concrete and prediction of compressive strength J Clean Prod 282 124543 https://doi.org/10.1016/J.JCLEPRO.2020.124543
36. Aziz IH, Abdullah MMAB, Mohd Salleh MAA et al (2020) Strength development of solely ground granulated blast furnace slag geopolymers. Constr Build Mater 250.https://doi.org/10.1016/J.CONBUILDMAT.2020.118720
37. (2016) FHWA research and technology evaluation gusset plates final report
38. Assi LN, Carter K, Deaver E, Ziehl P (2020) Review of availability of source materials for geopolymer/sustainable concrete. J Clean Prod 263.https://doi.org/10.1016/J.JCLEPRO.2020.121477
39. G Kürklü 2016 The effect of high temperature on the design of blast furnace slag and coarse fly ash-based geopolymer mortar Compos Part B Eng 92 9 18 https://doi.org/10.1016/J.COMPOSITESB.2016.02.043
40. Y Ling K Wang W Li 2019 Effect of slag on the mechanical properties and bond strength of fly ash-based engineered geopolymer composites Compos Part B Eng 164 747 757 https://doi.org/10.1016/J.COMPOSITESB.2019.01.092
41. G Habert JB D'Espinose De Lacaillerie N Roussel 2011 An environmental evaluation of geopolymer based concrete production: reviewing current research trends J Clean Prod 19 1229 1238 https://doi.org/10.1016/J.JCLEPRO.2011.03.012
42. M Malešev V Radonjanin G Broćeta 2014 Properties of recycled aggregate concrete Contemp Mater 2 239 249 https://doi.org/10.7251/COMEN1402239M
43. K McNeil THK Kang 2013 Recycled concrete aggregates: a review Int J Concr Struct Mater 7 61 69 https://doi.org/10.1007/S40069-013-0032-5
44. A Ajdukiewicz A Kliszczewicz 2002 Influence of recycled aggregates on mechanical properties of HS/HPC Cem Concr Compos 24 269 279 https://doi.org/10.1016/S0958-9465(01)00012-9
45. KH Younis FF Jirjees G Khoshnaw B Haidar Ali 2019 Experimental study on performance of recycled aggregate concrete: effect of reactive mineral admixtures Int J Civ Eng Technol 10 2566 2576
46. KH Younis SM Mustafa 2018 Feasibility of using nanoparticles of SiO_2 to improve the performance of recycled aggregate concrete Adv Mater Sci Eng https://doi.org/10.1155/2018/1512830
47. Garcia-Lodeiro I, Palomo A, Fernández-Jiménez A (2015) Crucial insights on the mix design of alkali-activated cement-based binders. In: Handbook of alkali-activated cements, mortars and concretes, pp 49–73.https://doi.org/10.1533/9781782422884.1.49
48. M Koushkbaghi P Alipour B Tahmouresi 2019 Influence of different monomer ratios and recycled concrete aggregate on mechanical properties and durability of geopolymer concretes Constr Build Mater 205 519 528 https://doi.org/10.1016/J.CONBUILDMAT.2019.01.174
49. Nuaklong P, Jongvivatsakul P, Pothisiri T et al (2020) Influence of rice husk ash on mechanical properties and fire resistance of recycled aggregate high-calcium fly ash geopolymer concrete. J Clean Prod 252.https://doi.org/10.1016/J.JCLEPRO.2019.119797

50. Saravanakumar P, Saravanakumar P (2018) Strength and durability studies on geopolymer recycled aggregate concrete. Int J Eng Technol 7:370–375. https://doi.org/10.14419/ijet.v7i2.24.12087
51. HB Le QB Bui L Tang 2021 Geopolymer recycled aggregate concrete: from experiments to empirical models Mater (Basel, Switzerland) 14 1 22 https://doi.org/10.3390/MA14051180
52. K Neupane 2016 Fly ash and GGBFS based powder-activated geopolymer binders: a viable sustainable alternative of Portland cement in concrete industry Mech Mater 103 110 122 https://doi.org/10.1016/J.MECHMAT.2016.09.012
53. Assi L, Carter K, Deaver E (Eddie) et al (2018) Sustainable concrete: building a greener future. J Clean Prod 198:1641–1651.https://doi.org/10.1016/J.JCLEPRO.2018.07.123
54. M Palacios YF Houst P Bowen F Puertas 2009 Adsorption of superplasticizer admixtures on alkali-activated slag pastes Cem Concr Res 39 670 677 https://doi.org/10.1016/J.CEMCONRES.2009.05.005
55. PR Vora UV Dave 2013 Parametric studies on compressive strength of geopolymer concrete Procedia Eng 51 210 219 https://doi.org/10.1016/j.proeng.2013.01.030
56. C Jithendra S Elavenil 2019 Role of superplasticizer on GGBS based geopolymer concrete under ambient curing Mater Today Proc 18 148 154 https://doi.org/10.1016/J.MATPR.2019.06.288
57. WP Triwulan J Jaya Ekaputri 2016 Addition of superplasticizer on geopolymer concrete ARPN J Eng Appl Sci 11 14456 14462
58. Vahini M, Manjunatha K, Venkatesh, Meti B (2019) Study on effect of superplasticizer on GGBS blended geopolymer concrete. Energy Earth Sci 2:53. https://doi.org/10.22158/EES.V2N2P45
59. Raju T, Ramaswamy KP, Saraswathy B (2020) Effects of slag and superplasticizers on alkali activated geopolymer paste effects of slag and superplasticizers on alkali activated geopolymer paste. In: IOP conference series earth and environmental science 5th international conference on modeling and simulation in civil engineering, 491. https://doi.org/10.1088/1755-1315/491/1/012042
60. Demie S, Nuruddin MF, Ahmed MF, Shafiq N (2011) Effects of curing temperature and superplasticizer on workability and compressive strength of self-compacting geopolymer concrete. In: National postgraduate conference—energy and sustainability: exploring the innovative minds, NPC.https://doi.org/10.1109/NATPC.2011.6136362
61. Patil SG, Manojkumar (2013) Factors influencing compressive strength of geopolymer concrete. IJRET Int J Res Eng Technol 372–375
62. IR Mithanthaya S Marathe NBS Rao V Bhat 2017 Influence of superplasticizer on the properties of geopolymer concrete using industrial wastes Mater Today Proc 4 9803 9806 https://doi.org/10.1016/J.MATPR.2017.06.270
63. Kumar S, Gautam PD, Sarath Chandra Kumar B (2019) Effect of alkali activator ratio on mechanical properties of GGBS based geopolymer concrete. Int J Innov Technol Explor Eng 8:947–952. https://doi.org/10.35940/IJITEE.J9539.1081219
64. Oyebisi S, Ede A, Olutoge F et al (2019) Effects of rest period on the strength performance of geopolymer concrete. IOP Conf Ser Mater Sci Eng 640.https://doi.org/10.1088/1757-899X/640/1/012056
65. Ramesh V, Srikanth DK (2020) Mechanical properties and mix design of geopolymer concrete—a review. E3S Web Conf 184. https://doi.org/10.1051/E3SCONF/202018401091
66. Committee A (2014) Building code requirements for structural concrete (ACI 318–14) commentary on building code requirements for structural concrete (ACI 318R-14) an ACI standard and report
67. Split Tensile Strength of Concrete as per IS 5816 (1999)|Definition, test procedure, apparatus list, formula. https://www.civilalliedgyan.com/2020/03/split-tensile-strength-test-of-concrete.html. Accessed 25 Jul 2021
68. IS456:2000, Plain and reinforced concrete-code of practice, Bureau of Indian Standard, New Delhi, pp 1–100

69. Guades EJ, Taduyo OG, Sobreviga MD (2016) Compressive strength of geopolymer concrete: influence of size of gravel. In: 6th International conference on advanced in engineering science and applied mathematics, pp 30–33. https://doi.org/10.15242/IIE.E1216009
70. Sharma A, Ahmad J (2017) Factors affecting compressive strength of geopolymer concrete-a review. Int Res J Eng Technol 04
71. Shaikh FUA, Odoh H, Than AB (2015) Effect of nano silica on properties of concretes containing recycled coarse aggregates. 168:68–76.https://doi.org/10.1680/COMA.14.00009
72. P Nath P Sarker 2014 Use of OPC to improve setting and early strength properties of low calcium fly ash geopolymer concrete cured at room temperature Cem Concr Compos 55 205 214 https://doi.org/10.1016/J.CEMCONCOMP.2014.08.008
73. Patankar SV, Jamkar SS, Ghugal YM (2013) Effect of water-to-geopolymer binder ratio on the production of fly ash based geopolymer concrete. Int J Adv Technol Civ Eng 79–83. https://doi.org/10.13140/2.1.4792.1284
74. Hardjito D, Rangan BV (2005) Development and properties of low-calcium fly ash-based geopolymer concrete. Res Rep GC 1
75. Z Pan JG Sanjayan BV Rangan 2011 Fracture properties of geopolymer paste and concrete Mag Concr Res 63 763 771 https://doi.org/10.1680/MACR.2011.63.10.763
76. MNS Hadi NA Farhan MN Sheikh 2017 Design of geopolymer concrete with GGBFS at ambient curing condition using Taguchi method Constr Build Mater 140 424 431 https://doi.org/10.1016/J.CONBUILDMAT.2017.02.131
77. SK Das AK Mohapatra AK Rath 2014 Geo-polymer concrete-green concrete for the future-a review Int J Civ Eng Res 5 21 28
78. M Albitar P Visintin MSM Ali M Drechsler 2015 Assessing behaviour of fresh and hardened geopolymer concrete mixed with class-F fly ash KSCE J Civ Eng 195 19 1445 1455 https://doi.org/10.1007/S12205-014-1254-Z
79. Jacob A, Ephraim K, Mohammad A (2020) Properties of metakaolin based geopolymer concrete made with recycled concrete aggregate. Int J Res Innov Appl Sci 57–63
80. P Topark-Ngarm P Chindaprasirt V Sata 2014 Setting time, strength, and bond of high-calcium fly ash geopolymer concrete J Mater Civ Eng 27 04014198 https://doi.org/10.1061/(ASCE)MT.1943-5533.0001157
81. VFF Barbosa KJD MacKenzie C Thaumaturgo 2000 Synthesis and characterisation of materials based on inorganic polymers of alumina and silica: sodium polysialate polymers Int J Inorg Mater 2 309 317 https://doi.org/10.1016/S1466-6049(00)00041-6
82. MR Nagral T Ostwal MV Chitawadagi 2014 Effect of curing temperature and curing hours on the properties of geo-polymer concrete Int J Comput Eng Res 04 2250 3005
83. Jamdade PK (2016) Effect of temperature and time of curing on strength of fly ash based geopolymer concrete. Int J Innov Res Sci Eng Technol (An ISO 5:9269–9274). https://doi.org/10.15680/IJIRSET.2016.0506085
84. SV Patankar YM Ghugal SS Jamkar 2014 Effect of concentration of sodium hydroxide and degree of heat curing on fly ash-based geopolymer mortar Indian J Mater Sci 2014 1 6 https://doi.org/10.1155/2014/938789
85. SV Joshi MS Kadu 2012 Role of alkaline activator in development of eco-friendly fly ash based geo polymer concrete Int J Environ Sci Dev 3 417 421 https://doi.org/10.7763/IJESD.2012.V3.258
86. Gunasekara MPC, Law D, Setunge S (2016) Long term engineering properties of fly ash geopolymer concrete. Proceedings of the 4th international conference on sustainable construction materials and technologies, pp 85–94
87. Gupta L, Suresh G (2018) Determination of indirect tensile strength of bituminous concrete mix prepared using stone dust and cement as filler materials. Sustain Civ Infrastruct 249–261.https://doi.org/10.1007/978-3-319-61633-9_16
88. L Gupta A Bellary 2018 Comparative study on the behavior of bituminous concrete mix and warm mix asphalt prepared using lime and Zycotherm as additive Mater Today Proc 5 2074 2081 https://doi.org/10.1016/J.MATPR.2017.09.203
89. (2004) Eurocode 2: design of concrete structures (EN 1992-1-1:2004). 1

90. B Singh G Ishwarya M Gupta SK Bhattacharyya 2015 Geopolymer concrete: a review of some recent developments Constr Build Mater 85 78 90 https://doi.org/10.1016/J.CONBUILDMAT.2015.03.036
91. Hasnaoui A, Ghorbel E, Wardeh G (2019) Comparison between Portland cement concrete and geopolymer concrete based on metakaolin and granulated blast furnace slag with the same binder volume. Acad J Civ Eng 37:127–132
92. Ahmed HQ, Jaf DK, Yaseen SA (2020) Flexural capacity and behaviour of geopolymer concrete beams reinforced with glass fibre-reinforced polymer bars. Int J Concr Struct Mater
93. P Nuaklong V Sata P Chindaprasirt 2016 Influence of recycled aggregate on fly ash geopolymer concrete properties J Clean Prod 112 2300 2307 https://doi.org/10.1016/J.JCLEPRO.2015.10.109
94. P Nuaklong V Sata A Wongsa 2018 Recycled aggregate high calcium fly ash geopolymer concrete with inclusion of OPC and nano-SiO_2 Constr Build Mater 174 244 252 https://doi.org/10.1016/J.CONBUILDMAT.2018.04.123
95. K Parthiban K Saravana Raja Mohan 2017 Influence of recycled concrete aggregates on the engineering and durability properties of alkali activated slag concrete Constr Build Mater 133 65 72 https://doi.org/10.1016/J.CONBUILDMAT.2016.12.050
96. S Bernal R Gutierrez De S Delvasto E Rodriguez 2010 Performance of an alkali-activated slag concrete reinforced with steel fibers Constr Build Mater 24 208 214 https://doi.org/10.1016/J.CONBUILDMAT.2007.10.027
97. Neville AM (1995) Properties of concrete, 4th ed. Pearson Education Limited
98. M Etxeberria E Vázquez A Marí 2006 Microstructure analysis of hardened recycled aggregate concrete Mag Concr Res 58 683 690
99. A Katz 2004 Treatments for the improvement of recycled aggregate J Mater Civ Eng 16 597 603 https://doi.org/10.1061/(ASCE)0899-1561(2004)16:6(597)
100. N Otsuki S Miyazato W Yodsudjai 2003 Influence of recycled aggregate on interfacial transition zone, strength, chloride penetration and carbonation of concrete J Mater Civ Eng 15 443 451 https://doi.org/10.1061/(ASCE)0899-1561(2003)15:5(443)
101. CS Poon ZH Shui L Lam 2004 Effect of microstructure of ITZ on compressive strength of concrete prepared with recycled aggregates Constr Build Mater 18 461 468 https://doi.org/10.1016/J.CONBUILDMAT.2004.03.005
102. Liu MYJ, Alengaram UJ, Jumaat MZ, Mo KH (2014) Evaluation of thermal conductivity, mechanical and transport properties of lightweight aggregate foamed geopolymer concrete. Energy Build Complete 238–245. https://doi.org/10.1016/J.ENBUILD.2013.12.029
103. Fernandez-Jimenez AM, Palomo A, Lopez-Hombrados C (2006) Engineering properties of alkali-activated fly ash concrete. Aci Mater J 106–112.https://doi.org/10.1061/jsfeaq.0001744
104. AMA Blash DTVSV Lakshmi 2016 Properties of geopolymer concrete produced by silica fume and ground-granulated blast-furnace slag Int J Sci Res 5 319 323
105. Sasalatti V, Radhakrishna (2020) Mechanical properties of geopolymer concrete with alternative materials. NBM CW Infra Constr Mag

Structural Damage Detection for Plates Using Flexibility Based Strain Energy Method

B. U. Darshan, H. Siddesha, and T. Rajanna

Abstract Plates like structural elements are commonly found in many structural applications and may undergo injury or damages during its service life. Identification, characterization, and detection of damages at the early stages in a plate structure avoid the further growth of damages and prevent the structural failure. In this paper, the strain energy and flexibility matrix-based damage detection procedure is adopted to detect single as well multiple damages in a plate structure. Toward this, a 4-noded plate element is utilized to discretize the rectangular plate with 6° of freedom (dof) at every node. The flexibility matrix is calculated using the natural frequency and mode shape. This method detects the damage in the plate by an increase in flexibility matrix of the damaged one. The damage indicator is then computed by evaluating the changes in strain energy of a structural plate using the coefficients of the flexibility matrices. The modal parameters were extracted from the FE analysis software Abaqus. Nine illustrative examples with damages at various locations are induced by decreasing the modulus of elasticity at the specified elements in plate structure, in order to determine the effectiveness of the method. The numerical result shows that the adopted damage detection procedure can be able to locate the structural damages in plates with lower modes, and the magnitude of the evaluated damage index depends on the severity of the damage.

Keywords Damage detection · Flexibility matrix · Structural health monitoring · Natural frequencies · Mode shapes · Strain energy

1 Introduction

Plate structures are one among the important structural elements in steel structures like towers, bridges, buildings in civil, and airplane body, ships, automotive, oil plants

B. U. Darshan · H. Siddesha (✉)
Department of Civil Engineering, Siddaganga Institute of Technology, Tumkur 572103, India
e-mail: sh@sit.ac.in

T. Rajanna
Department of Civil Engineering, BMS College of Engineering, Bengaluru 560019, India

L. Nandagiri et al. (eds.), *Recent Advances in Civil Engineering*, Lecture Notes in Civil Engineering 256, https://doi.org/10.1007/978-981-19-1862-9_18

in mechanical disciplines. Occurrence of any type of damage in these structures may lead to loss of human lives. The most important challenges in the field of structural health monitoring are to detect damages in the early stages so that the life of the damaged structure can be improved or extended for few more years and, the loss of human lives can be saved. Damages are the most common cause for structural failure like, material ageing, wear, creep, fatigue, and certain unavoidable events such as earthquakes. If the damages that take place in these structures are not detected in a timely manner, it may have disastrous consequences. As a result, over the last three decades particular attention with utmost priority was paid to preventing structural component failures by detecting the damages in structure by using several methods. Several researches in civil, aeronautical, and mechanical engineering fields are particularly interested in monitoring the structural health of the system using the characteristics of vibration measurements.

Damage localization is more important in the health monitoring phase after the presence of damage has been recognized. Zhong and Yang [1] utilized the natural frequencies to detect the damages and its location is estimated by mode shape curvature technique. Nicknam et al. [2] suggested a new method to detect the defects by the change in mode shapes and natural frequencies of the damaged plate using a colonial competitive algorithm as an optimization strategy. Navabian et al. [3] introduced the mode-shaped derivative-based index method based on derivative of modes for the detection of damages in plate structures. Arun Kumar and Mallikarjuna Reddy [4] employed a damage identification method for plates and beam structures based on frequency response function curvatures. They also demonstrated that it is difficult to localize the damages using natural frequencies alone. Hilmy et al. [5] investigated the shift in natural frequency due to the presence of void's in a clamped plate. The results also showed that the natural frequency is a function of location of the voids present in the plate. Nasiri et al. [6] extracted the natural frequencies and mode shapes of multilayer composite plates under free boundary conditions. The features are used as the input data for artificial intelligence to detect the damage severity. Vo-Duy et al. [7] demonstrated the damage detection procedure using modal strain energy and improvised differential evolution algorithm for detecting the damages in the laminated composite plate layer. Masoumi and Ashory [8] employed generalized flexibility matrix and 2D discrete wavelet transform to detect the damage in plate structures. Dinh-Cong et al. [9] utilized modified differential evolution algorithm in the optimization procedure to detect the damage in plate. The objective function is formulated based on the discrepancy between the flexibility matrix determined from modal testing and the corresponding one determined from the numerical model. Zakian et al. [10] performed the dynamic analysis of plate structure using finite cell method. The particle swarm optimization is utilized to solve the optimization problem for damage identification.

Kazemi et al. [11] proposed new damage indicator based on the variation of modal flexibility and the load–deflection differential equation for the plate structure to locate various faults. Then artificial neural network technology is used to identify the magnitudes of the fault. Xu et al. [12] employed 2D mode shape curvature method to detect the damages in plates. Wu and Law [13] introduced Uniform Load

Surface (ULS) curvature to localize the damage in plates. In the computation of ULS curvature, Chebyshev polynomial approximation is employed. Araujo dos Santos et al. [14] adopted numerical methodology for identifying the damages in laminated plate structure using the first-order shear deformation. The proposed model detects the multiple damages without the prior knowledge of the damaged areas. Rucka and Wilde [15] employed 1D continuous wavelet transform and 2D continuous wavelet transform to detect the damages in beams and plates. The defected locations are localized without using the characteristics of the structure. Cho et al. [16] developed the damage detection method for plates based on the assumed mode method. The vibrational characteristics of plates with openings and edge constraints are evaluated. Hossain et al. [17] studied the variation of modal parameters due to the cutouts at different locations in a plate. Xu et al. [18] proposed a different non-prototype-based approach for detecting damages in plate which uses mean, principal, and Gaussian curvature mode shapes. Zima and Rucka [19] implemented guided wave-based technique and ellipse-based binary damage imaging algorithm to detect the linear cracks of variable length in plates. Kwak and Han [20] introduced the Independent Coordinate Coupling Method (ICCM) for detecting the damage in plates with rectangular or circular holes. Chandrashekhar and Ganguli [21] derived a new method to identify the damages in plate using modal curvatures and fuzzy logic with noisy data. The method also works well even though some modal data is missing.

2 Previous Studies on Flexibility Method

Nobohari and Seyedpoore [22]proposed flexibility matrix and strain energy concepts for damage localization in 2D framed structure. Montazer and Seyedpoore [23] showcased flexibility method to find the position and extent of damages in trusses. Reynders and De Roeck [24] introduced quasi-static flexibility matrix for damage identification in beam structures. Pandey and Biswas [25] demonstrated the utilization of changes in flexibility matrices for detecting damage in beams. Bernagozzi et al. [26] developed the damage detection procedure using modal flexibility-based deflections for a rectangular plan-symmetric 3D building structures.

Siddesha and Hegde [27] showed the advantages of generalized flexibility matrix over the original flexibility matrix in the damage identification of members in frame due to the settlement of support. Shih et al. [28] used the changes in flexibility and strain energy before and after damage of flexural members for assessing the structural health of beam and plate structure. Sung et al. [29] investigated the damage identification in cantilevered beam type structures by using damage induced inter-storey deflections obtained from flexibility matrix. Yang [30] described a new approach for identifying damages using flexibility disassembly for a spring mass system, 2D frame, and truss structure. Li et al. [31] compared generalized flexibility and original flexibility method for damage identification in beam structure. The results indicate that generalized flexibility method showed better performance in damage identification. Weng et al. [32] presented a sub-structuring method which uses the

sub-structural flexibility matrices. Grande and Imbimbo [33] employed mode shapes to formulate multistage approach for 3D structure. The damage locations are determined from the flexibility method. Zhang et al. [34] developed a flexibility-based damage detection procedure to identify the damages in 3D frame without using its mass. Changes in flexibility are utilized by Bernal [35] to identify the damages in beam and truss problems. Yang and Sun [36] proposed a novel approach for locating and quantifying the structural damage by using best achievable flexibility change. Kim et al. [37] employed modal flexibility method to evaluate the damages in beams. Zare et al. [38] developed an optimization scheme from the flexibility matrix and Modal Assurance Criterion to determine the damage severity in truss and shear storey models. An orthogonal projector is developed by Weng et al. [39] from the generalized stiffness and flexibility matrices.

Large amounts of research have been carried out in damage localization of beams, frames, and truss structures either by reducing the modulus of elasticity or by reducing the stiffness in certain elements using flexibility method and strain energy concept. However, less investigation is done using the flexibility and strain energy concept for plate structures in the area of structural health monitoring. Hence, in the current study, flexibility method along with strain energy concept is extended for a plate structure for assessing the severity in the damaged elements in the plate structure.

3 Damage Detection Procedure

Dynamic responses are used as one among the non-destructive structural damage identification method. This is due to the fact that structural damage is linked with stiffness, mass, modal, and damping properties. Damages are typically detected by comparing the structural responses of healthy or intact structure with unhealthy or damaged structure. The present method is based on flexibility-based strain energy method. This concept was originally adopted for 2D frame and truss by Nobohari and Seyedpoore [22] for assessing the damage severity. In the present study, this method is extended for 2D plate structure for the assessment of damage severity.

The flexibility matrix can be used to determine the presence of damage in the damaged element by observing the variation of the displacement along its dof. The flexibility matrix is computed by "Eq. (1)" using just a few vibrating modes of the structure.

$$\mathrm{Fl} = \sum_{i=1}^{nd} \frac{1}{\omega_i^2} \varphi_i . \varphi_i^T \quad i = 1 \ldots nd \tag{1}$$

The flexibility coefficients of this matrix are determined for intact and damaged structure along its global dof separately. The displacement generally increases for a damaged structure due to the variation in modal properties. This increase or change

in flexibility matrix can be used to indicate the damaged elements by the inverse analysis.

Where

φ_i ith mode shape vector.
nd total degrees of freedom of the complete plate structure.

The flexibility strain energy fse of the eth element in ith column in flexibility matrix can be expressed as

$$\text{fse}_i^e = \tfrac{1}{2} f_i^{eT}.K^e.f_i^e \quad \begin{matrix} e = 1 \ldots ne, \\ i = 1 \ldots nd \end{matrix} \tag{2}$$

where

K^e represents the stiffness matrix for eth element of the plate structure.
f_i^e represents the vector of nodal displacements of element e for the column i.

The total flexibility strain energy of the plate structure for ith column can be calculated by adding the fse of all elements, i.e., ne. This is given in "Eq. (3)"

$$\text{fse}_i = \text{fse}_i^{e1} + \text{fse}_i^{e2} + \cdots + \text{fse}_i^{ne} = \sum_{e=1}^{ne} \text{fse}_i^e \tag{3}$$

It is preferable to normalize the fse of the elements with respect to the total fse of the plate structure. Hence, $n$fse can be written as

$$n\text{fse}_i^e = \frac{\text{fse}_i^e}{\text{fse}_i} \tag{4}$$

The normalized fse of the eth element for ith column of the flexibility matrix is $n\text{fse}^e$. Then taking the mean of "Eq. (4)" to the nd columns is chosen as the efficient parameter as

$$mn\text{fse}^e = \frac{\sum_{i=1}^{nd} n\text{fse}_i^e}{nd} \tag{5}$$

As the structural plate element is damaged, FSE increases due to the increase of the flexibility matrix. Further, $mn\text{fse}^e$ also increases. The parameter $mn\text{fse}^e$ is evaluated once for the intact structure $(mn\text{fse}^e)^h$ and, once for the damaged structure $(mn\text{fse}^e)^d$, respectively. The FSEBI^e in "Eq. (6)" is represented as damage index for the damage location of the element damaged.

$$\text{FSEBI}^e = \max\left[0, -\left(\frac{(mn\text{fse}^e)^d - (mn\text{fse}^e)^h}{(mn\text{fse}^e)^h}\right)\right] \tag{6}$$

The damage index is greater than zero for the damaged element and it is equal to zero for intact element.

4 Numerical Analysis

A rectangular plate of dimension 0.56 × 0.48 × 0.002 m with fixed boundary conditions is considered in the present study. The material properties for plate are Young's modulus, $E = 192$ GPa, Poisson's ratio, $\mu = 0.25$, Density, $\rho = 7430$ kg/m^3. "Plate dimensions are shown in Fig. 1".

The plate model is created in the FE software Abaqus Simulia. The properties of the plate material are assigned as mentioned and, the plate has been meshed into 14 × 12 along two directions. Each element dimension is 0.04 × 0.04 m and, the total number of elements is 168 consisting of 195 nodes. S4R element type is chosen for modeling each plate element. This is a 4-noded element with 6 dof at each node. "Figure 2 shows the dof of the plate element". "The total dof is 1170. Six damage cases are considered and are presented in Table 1". In this numerical analysis, damages are induced by reducing the modulus of elasticity at the selected elements.

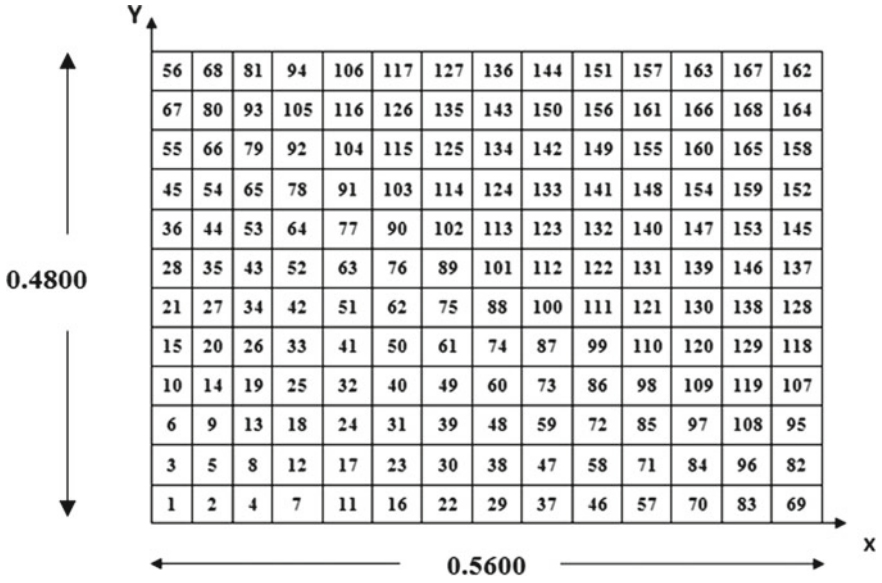

Fig. 1 Plate dimensions in mm

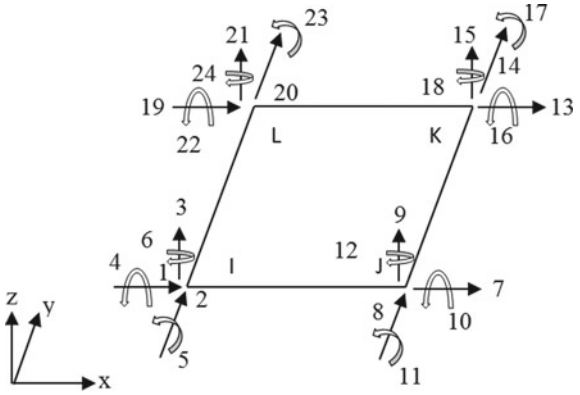

Fig. 2 Degrees of freedom

5 Results

5.1 Natural Frequencies and Mode Shapes

"The natural frequencies for various damage cases mentioned in Table 1 are represented in Table 2". UD represents undamaged natural frequency. It is observed that the natural frequency decreases for $D1$–$D9$ in comparison with UD. This is due to reduction in stiffness of the selected damaged element.

The natural frequencies indicate only the presence of damage in plate. The first natural frequency and its mode shape are used to formulate the flexibility matrix. Later, damage sites are identified by the flexibility strain energy method for various damage cases of the plate. "The mode shapes of the plate are shown in Fig. 3".

5.2 Damage Detection Results

"Figures 4, 5, 6, 7, 8, 9, 10, 11, and 12 show the damage detection results for single and multiple element damage cases". For all the damage cases, the damage index is obtained for the damaged elements. The damage index less than 0.12 is ignored while selecting the damaged elements. In the damage case $D1$, single element 26 is damaged for a severity of 56%. The ratio of damage index to damage severity (D_i/D_s) for the element 26 is 84%. In the damage case $D2$, single element 125 is damaged for a severity of 56%. The ratio of damage index to damage severity (D_i/D_s) for the element 125 is 87.5%.

For the damage case $D3$, the two elements 34, 43 are damaged with a severity of 56%. The D_i/D_s for these two elements is 87.5%. For the damage case $D4$, the elements 39, 48 elements are damaged with a severity of 56%. The D_i/D_s for these two elements is 85.7%. However in $D5$, the elements 26 and 120 are damaged with a severity of 20%. Hence, the D_i/D_s for these two elements is 75%. However in $D6$,

Table 1 Damage cases

Elements	$D1$	$D2$	$D3$	$D4$	$D5$	$D6$	$D7$		$D8$	$D9$			
	26	125	34, 43	39, 48	26, 120	30, 135	39, 125	48, 134	34, 43, 130, 139	34, 43	39, 48	125, 134	130, 139
Damage severity (%)	56	56	56	56	20	20	25	57	57	46	40	50	57

Table 2 Natural frequencies

Modes	UD	*D*1	*D*2	*D*3	*D*4	*D*5	*D*6	*D*7	*D*8	*D*9
1	66.65	66.60	66.63	66.59	66.61	66.62	66.59	66.59	66.53	66.47
2	124.80	124.54	124.59	124.15	124.38	124.65	124.69	124.21	123.52	123.03
3	153.03	152.84	152.39	152.67	151.57	152.91	153.02	151.21	152.32	150.29

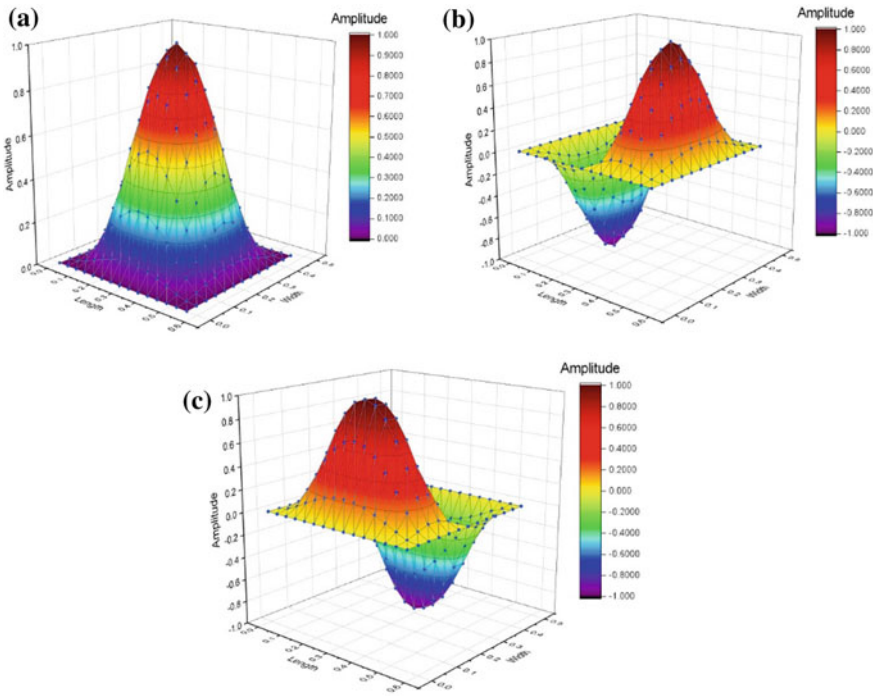

Fig. 3 Mode shapes. **a** First mode, **b** second mode, **c** third mode

the elements 30 and 135 are damaged with a severity of 20%. Hence, the D_i/D_s for these two elements is 90%. In *D*7, four elements are damaged, namely, 39, 125, 48, and 134 with a damage severity of 25% and 57%. For the damaged elements 39, 125, and 48, 134 the D_i/D_s is 72% and 85.9%, respectively. In *D*8, the number of damaged elements is 34, 43, 130, and 139. The damage severity for these elements is 57%. The D_i/D_s is 85% for all these four elements. Eight elements are damaged in *D*9 with a damage severity of 46%, 40%, 50%, and 57%. For the damaged elements 34 and 43, D_i/D_s is 83.1% and for 39 and 48 elements, D_i/D_s is 70%. However for 125, 134, and 130, 139, the D_i/D_s is 72% and 85% respectively. Hence, the least D_i/D_s in these damage cases is 70%.

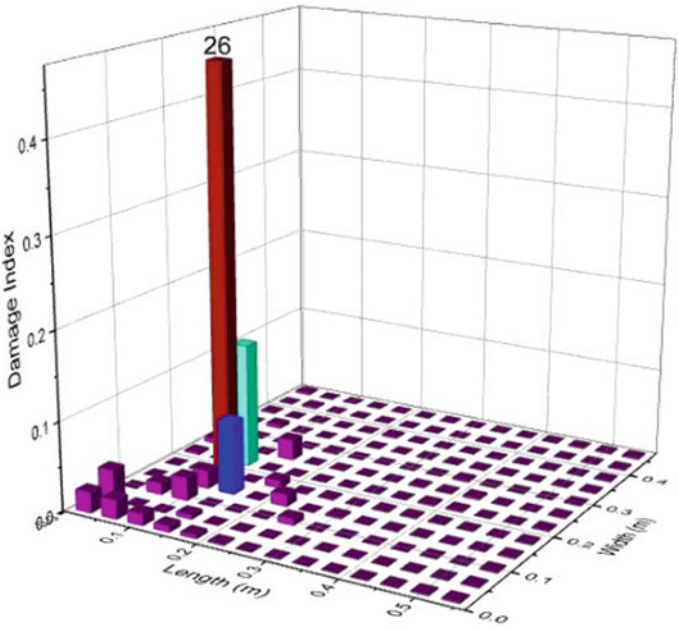

Fig. 4 Damage detection results for *D*1

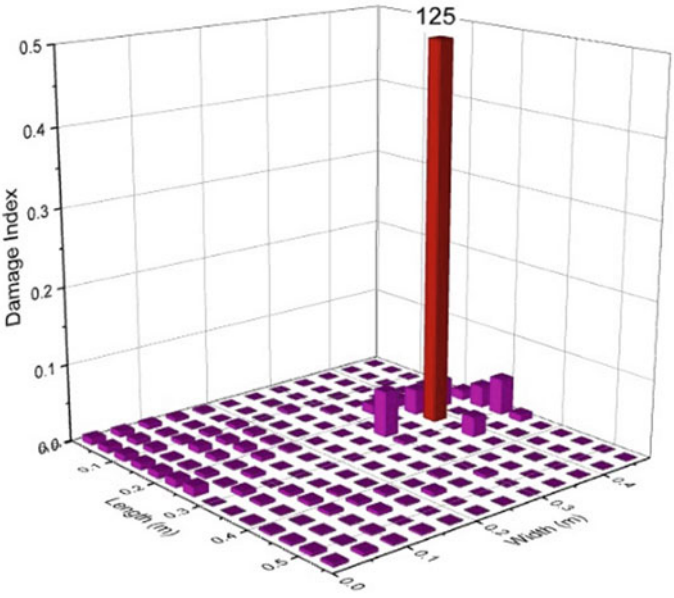

Fig. 5 Damage detection results for *D*2

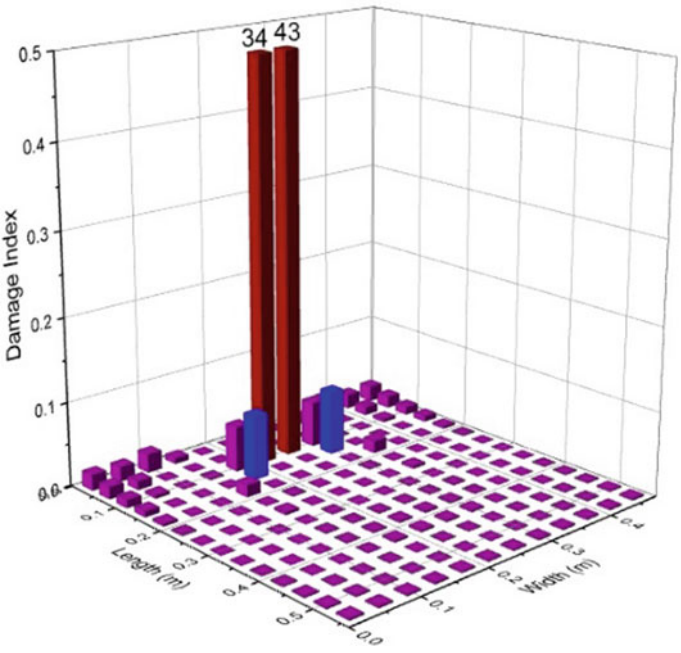

Fig. 6 Damage detection results for *D*3

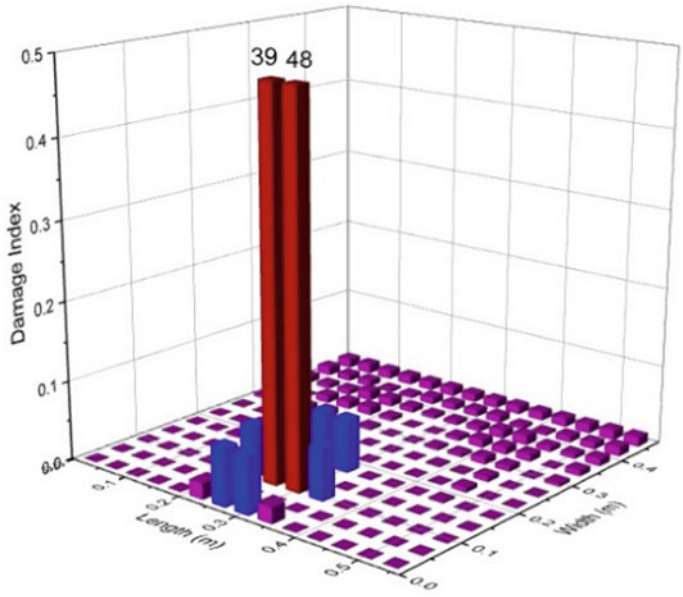

Fig. 7 Damage detection results for *D*4

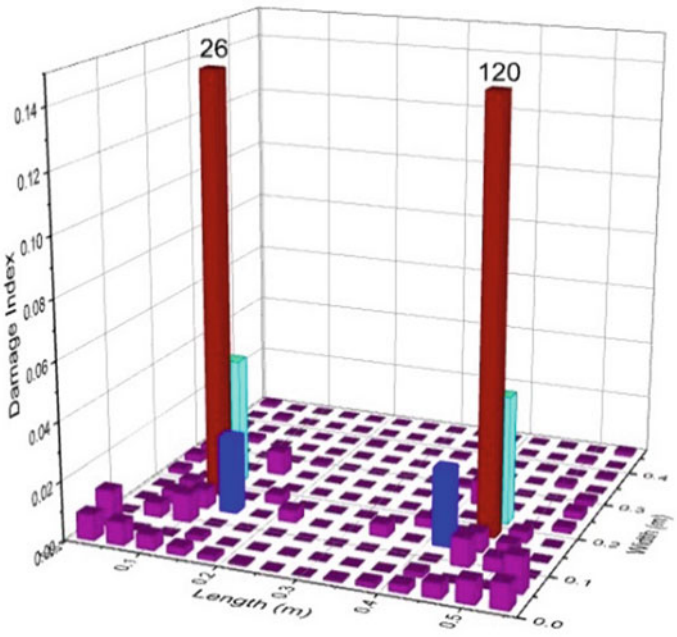

Fig. 8 Damage detection results for *D*5

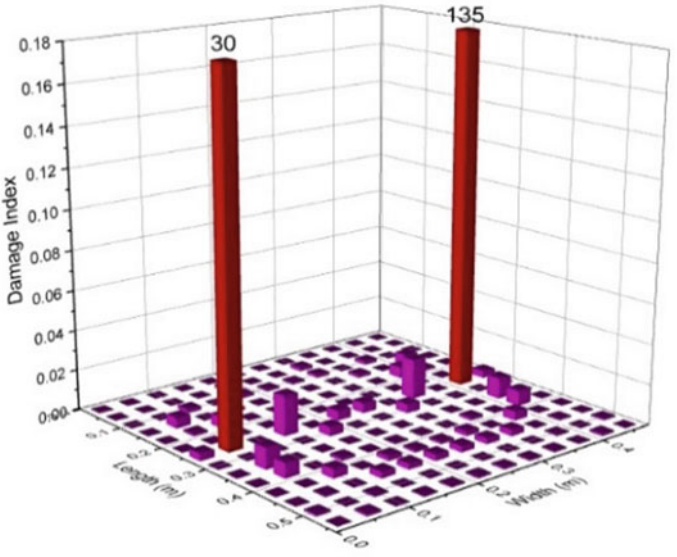

Fig. 9 Damage detection results for *D*6

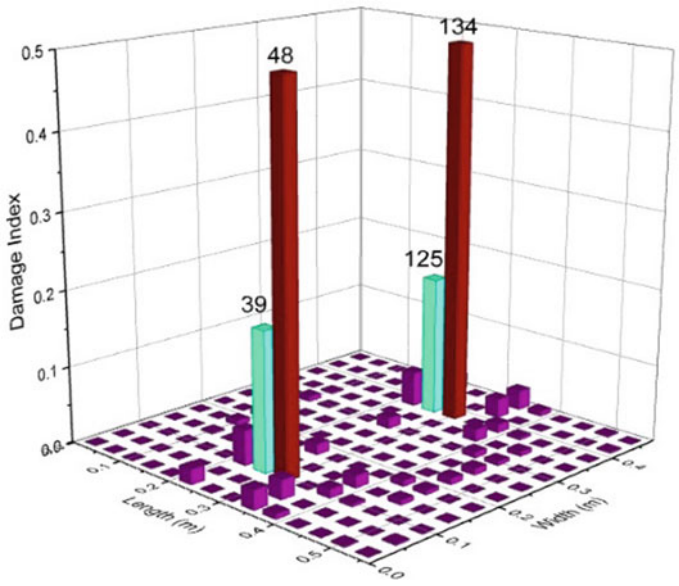

Fig. 10 Damage detection results for *D*7

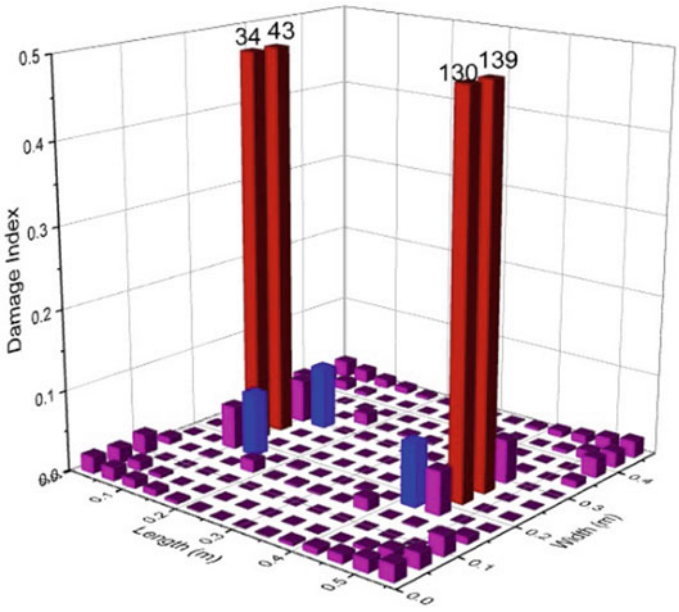

Fig. 11 Damage detection results for *D*8

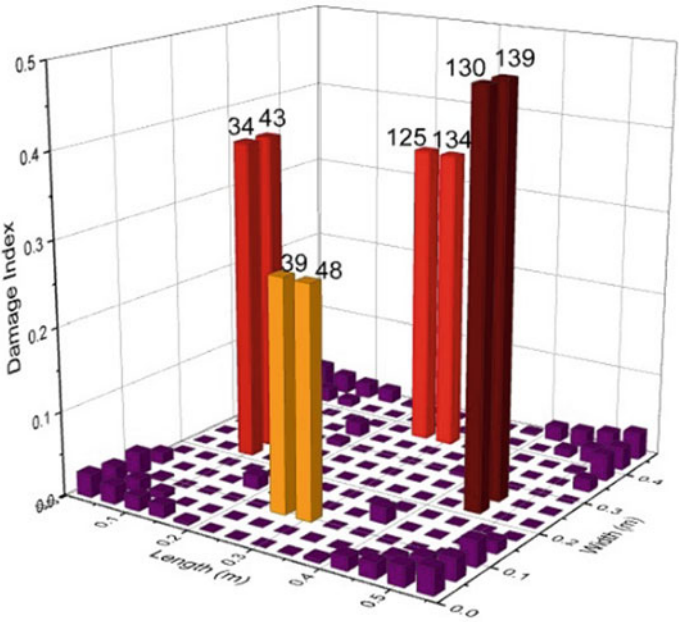

Fig. 12 Damage detection results for *D*9

6 Conclusions

In this paper, the flexibility strain energy-based method is extended for detecting the damages in plate structure. Nine damage cases, which includes single and multiple element damage cases. The damage index is computed by utilizing the first mode of vibration. The numerical results indicate that flexibility strain energy-based method is effective and detects the damage in the damaged elements. However, the ratio of damage index to damage severity is more than 70%. Hence, the flexibility strain energy-based method can be used effectively for damage detection in plate structures.

References

1. Zhong H, Yang M (2016) Damage detection for plate-like structures using generalized curvature mode shape method. J Civ Struct Health Monit 6(1):141–152
2. Nicknam A, Hosseini MH, Bagheri A (2011) Damage detection and denoising in two-dimensional structures using curvelet transform by wrapping method. Arch Appl Mech 81:1915–1924
3. Navabian N, Bozorgnasab M, Taghipour R, Yazdanpanah O (2016) Damage identification in plate-like structure using mode shape derivatives. Arch Appl Mech 86:819–830

4. Arun Kumar K, Mallikarjuna Reddy D (2016) Application of frequency response curvature method for damage detection in beam and plate like structures. IOP Conf Ser Mater Sci Eng 149:1–11
5. Hilmy I, Wahab MMA, Adesta EYT, Firdaus T (2015) Damage detection based on the natural frequency shifting of a clamped rectangular plate model. J Phys Conf Ser 628:1–7
6. Nasiri MR, Mahjoob MJ, Aghakasiri A (2011) Damage detection in a composite plate using modal analysis and artificial intelligence. Appl Compos Mater 18(6):513–520
7. Vo-Duy T, Ho-Huu V, Dang-Trung H, Dinh-Cong D, Nguyen-Thoi T (2016) Damage detection in laminated composite plates using modal strain energy and improved differential Evolution Algorithm. Procedia Eng 142:181–188
8. Masoumi M, Ashory MR (2013) Damage identification in plate-type structures using 2-D spatial wavelet transform and flexibility-based methods. Int J Fract 183(2):259–266
9. Dinh-Cong D, Vo-Duy T, Ho-Huu V, Dang-Trung H, Nguyen-Thoi T (2017) An efficient multi-stage optimization approach for damage detection in plate structures. Adv Eng Softw 112:76–87
10. Zakian P, Nadi M, Tohidi M (2021) Finite cell method for detection of flaws in plate structures using dynamic responses. Structures 34:327–338
11. Kazemi S, Fooladi A, Rahai AR (2010) Implementation of the modal flexibility variation to fault identification in thin plates. Actaastronautica 66(3–4):414–426
12. Xu W, Cao M, Ostachowicz W, Radzieński M, Xia N (2015) Two-dimensional curvature mode shape method based on wavelets and Teager energy for damage detection in plates. J Sound Vib 347:266–278
13. Wu D, Law SS (2004) Damage localization in plate structures from uniform load surface curvature. J Sound Vib 276(1–2):227–244
14. Araujo dos Santos JV, Mota Soares CM, Mota Soares CA, Pina HLG (2000) Development of a numerical model for the damage identification on composite plate structures. Compos Struct 48(1–3):59–65
15. Rucka M, Wilde K (2006) Application of continuous wavelet transform in vibration-based damage detection method for beams and plates. J Sound Vib 297(3–5):536–550
16. Cho DS, Vladimir N, Choi TM (2013) Approximate natural vibration analysis of rectangular plates with openings using assumed mode method. Int J Naval Archit Ocean Eng 5(3):478–491
17. Hossain N, Ahshan KHN, Hossain MZ, Islam MS (2015) Effect on natural frequency of a simply supported plate due to circular cutouts. In: 10th global engineering, science and technology conference, BIAM Foundation, Dhaka, Bangladesh
18. Xu YF, Zhu WD, Smith SA (2017) Non-model-based damage identification of plates using principal, mean and Gaussian curvature mode shapes. J Sound Vib 400(1):626–659
19. Zima B, Rucka M (2016) Guided waves for monitoring of plate structures with linear cracks of variable length. Arch Civ Mech Eng 16(3):387–396
20. Kwak MK, Han S (2007) Free vibration analysis of rectangular plate with a hole by means of independent coordinate coupling method. J Sound Vib 306(1–2):12–30
21. Chandrashekhar M, Ganguli R (2009) Structural damage detection using modal curvature and fuzzy logic. Struct Health Monit 8(4):267–282
22. Nobahari M, Seyedpoor SM (2013) An efficient method for structural damage localization based on the concepts of flexibility matrix and strain energy of a structure. Struct Eng Mech 46(2):231–244
23. Montazer M, Seyedpoor SM (2014) A new flexibility-based damage index for damage detection of truss structures. Shock Vib 2014(2):1–12
24. Reynders E, De Roeck G (2010) A local flexibility method for vibration-based damage localization and quantification. J Sound Vib 329(12):2367–2383
25. Pandey AK, Biswas M (1995) Experimental verification of flexibility difference method for locating the damage in structures. J Sound Vib 184(2):311–328
26. Bernagozzi G, Ventura CE, Allahdadian S, Kaya Y, Landi L, Diotallevi PP (2020) Output-only damage diagnosis for plan-symmetric buildings with asymmetric damage using modal flexibility-based deflections. Eng Struct 207:1–27

27. Siddesha H, Hegde MN (2017) Structural damage detection in framed structures using under foundation settlement/rotation of bases. Tech Sci Press 12(1):17–41
28. Shih HW, Thambiratnam DP, Chan THT (2009) Vibration based structural damage detection in flexural members using multi-criteria approach. J Sound Vib 323(3–5):645–661
29. Sung SH, Koo KY, Jung HJ (2014) Modal flexibility-based damage detection of cantilever beam-type structures using baseline modification. J Sound Vib 333(18):4123–4138
30. Yang QW (2010) A new damage identification method based on structural flexibility disassembly. J Vib Control 17(7):1000–1008
31. Li J, Wu B, Zeng QC, Lim CW (2010) A generalized flexibility matrix-based approach for structural damage detection. J Sound Vib 329(22):4583–4587
32. Weng S, Zhu H-P, Xia Y, Mao L (2013) Damage identification by the eigen parameter decomposition of structural flexibility change. Mech Syst Sig Process 34(1–2):19–38
33. Grande E, Imbimbo M (2016) A multi-stage approach for damage detection in structural systems based on flexibility. Mech Syst Signal Process 76–77:455–475
34. Zhang J, Xu JC, Guo SL, Wu ZS (2013) Flexibility-based structural damage detection with unknown mass for IASC-ASCE benchmark studies. Eng Struct 48:486–496
35. Bernal D (2014) Damage localization and quantification form the image changes in flexibility. J Eng Mech 140(2):279–286
36. Yang QW, Sun BX (2011) Structural damage identification based on best achievable flexibility change. Appl Math Model 35(10):5217–5224
37. Kim BH, Joo HJ, Park T (2007) Damage evaluation of an axially loaded beam using modal flexibility. KSCE J Civ Eng 11(2):101–110
38. Zare Hosseinzadeh A, Ghodrati Amiri G, Seyed Razzaghi SA, Koo KY, Sung SH (2016) Structural damage detection using sparse sensor installation by optimization procedure based on the modal flexibility matrix. J Sound Vib 381:65–82
39. Weng S, Zhu H-P, Li P-H, Xia Y, Ye L (2016) Construction of orthogonal projector for the damage identification by measured sub structural flexibility. Measurement 88:441–455

Determination of Saturated Hydraulic Conductivity in Unsaturated Zone from Field and Lab Methods

B. M. Vasanth Kumar and P. N. Chandramouli

Abstract In many geotechnical and hydrological studies, there is a significant increase in the field investigation of hydraulic properties in unsaturated zone. Hydraulic conductivity is one such parameter that is used as an input in many physically based models. As hydraulic conductivity is a highly spatially variable property, estimating the representative values are required for any modeling processes. The present study aimed at determining the saturated hydraulic conductivity (K_s) at two different land covers by Guelph permeameter in the field, permeability tests in the lab, and the Rawls–Brakensiek regression equation as a function of textural properties of the soil. Also, the study involves the comparison of the K_s values measured from field, lab, and Rawls regression equation. The results of this study indicate that, although there is slight variability in the results of hydraulic conductivity measurement methods, the graphical plots show a good correlation between the field, lab, and estimated values by Rawls equation.

Keywords Unsaturated zone · Saturated hydraulic conductivity · Guelph permeameter · Laboratory methods · Textural-based models

1 Introduction

Unsaturated zone is the integral part of hydrological cycle which controls the interrelationship between the various water balance components, namely, precipitation, infiltration, evapotranspiration, and groundwater recharge. As the percolation takes place through this zone, it is most important to study the hydraulic properties of the soil to know the behavior of solute transport, drainage, and irrigation systems design. As the precipitated water infiltrates through the vadose zone and recharges the aquifer, hydraulic properties are also significant in estimating ground water recharge.

To determine hydraulic conductivity, several direct and indirect methods have been developed in the field as well as in lab. The direct method includes the determination

B. M. Vasanth Kumar (✉) · P. N. Chandramouli
Department of Civil Engineering, The National Institute of Engineering, Mysuru 570008, India
e-mail: vasanthaprameya@gmail.com

L. Nandagiri et al. (eds.), *Recent Advances in Civil Engineering*, Lecture Notes in Civil Engineering 256, https://doi.org/10.1007/978-981-19-1862-9_19

of hydraulic conductivity through various methods such as auger hole method, single-ring infiltrometer, double-ring infiltrometer, Guelph permeameter method, etc.

Gallichand et al. [6] compared the three measurement methods such as Guelph permeameter and single auger hole method in the field, and falling head permeameter method in lab for determining hydraulic conductivity. The results of this study show a lower K_s value for falling head permeameter than the other two methods. The reasons for lower hydraulic conductivity were explained by the factors such as disturbance of the cores, smaller sampling volume, soil anisotropy, and macropores existence.

Kanwar et al. [9] conducted the field experiments to evaluate the performance of the two techniques to measure hydraulic conductivity at field using Guelph permeameter (constant head method) and velocity permeameter (falling head method). The experiments were conducted at field for different sites and depths by using these two techniques and also laboratory measurements were made using constant head permeability method. The comparison of the results shows almost similar values between these two techniques and also laboratory values show a higher value of K_s than the Guelph permeameter method because of the presence of the macropore flow.

Gribb et al. [7] compared the soil hydraulic property measurement methods. Saturated hydraulic conductivity was determined in the field with Guelph permeameter and in the lab using falling head permeameter. The results of GP yield a higher value of K_s than the falling head permeability test at all sites. This is due of the fact that K_s values were determined in the lab on smaller specimens, whereas during the field measurements, the soil structure may encounter macropores, wormholes, etc. Furthermore, the GP test produces the K_s values based on the radial flow and vertical flow out of a borehole. The vertical K_s is often less than the horizontal K_s in case of natural soils. As a result, the GP produces a higher value of K_s than the vertical K_s measured by the Falling head test.

Jačka et al. [8] has compared the three saturated hydraulic conductivity measurement methods in the shallow sub surface layer, namely Guelph permeameter, single-ring infiltrometer, and the lab permeameter. This study yields a slightly higher mean values of the lab permeameters than the other two methods. The presence of the macropores and full saturation of the soil sample during were led to higher K_s values in the lab permeameter method.

Mahapatra and Jha [12] evaluated the values of K_s by four pedotransfer functions such as Campbell, Rawls–Brakensiek, Cronican–Gribb and Rosetta Models 2 and 3 on the layered vadose zones with the limited data availability. Guelph permeameter has been used in the field to determine saturated hydraulic conductivity. The results were concluded that the Model-3 of Rosetta gave a comparable value of K_s to some extent and the Rawls–Brakensiek equation yields a good value of K_s at deeper lateritic layers of vadose zone with finer sandy clay loam texture.

The present study focuses on the determination of saturated hydraulic conductivity in Western Ghat regions at two different land covers, namely, forested and grassland areas by Guelph permeameter and lab permeability tests. In addition, the soil basic physical properties such as % sand, % silt, % clay, bulk density, and porosity were determined as a function of depth and space and are input parameters for Rawls–Brakensiek regression equation used to estimate saturated hydraulic conductivity in

the current research. The K_s values so obtained, are useful as input parameters for many Rainfall–Runoff models and in understanding the characteristics of different depths of vadose zone.

2 Material and Methods

2.1 Study Area

In the present study, two different sites were selected in Beedalli and Heggade Mane located in the Somwarpet Taluk of Kodagu district as shown in Fig. 1a–c. The study areas are located in the Western Ghat region having North latitude 12° 40′ 10″ and East longitude 75° 43′ 32″. The soils of the region are of heterogeneous profile and the principle soil types being reddish brown forest soil, grayish sandy loam soil, and mixed soils.

2.2 Investigation Sites

In the present study, two different sites with different land covers were selected to measure the hydraulic conductivity. The first site (Site-1) is forested area located in the Beedalli region as shown in Fig. 1b and second site (Site-2) is grass land area located in the Heggade Mane region as shown in Fig. 1c which are at 24 km away from the Somawarpet Taluk. Experimental works were carried out at different locations and at three depths, i.e., at 150, 300, and 600 mm in these two sites.

2.3 Determination of Soil Physical Properties

At each location and depth, soil samples were collected to determine the physical properties of soils such as texture, bulk density, particle density, and porosity. The undisturbed soil cores (100 mm diameter and 130 mm height) were taken at each depth to determine the bulk density of soil. Particle size distribution of the soil samples collected from each site were made using wet sieve analysis and hydrometer analysis and particle size distribution curves were constructed. From the % Sand, % Silt, and % Clay so obtained, the soil samples were classified in to different textural classes according to the United States Department of Agriculture (USDA) soil texture classification system. Particle density of soils were determined in the laboratory using density bottle method.

The porosity of the soil at each depth was calculated using the expression (1):

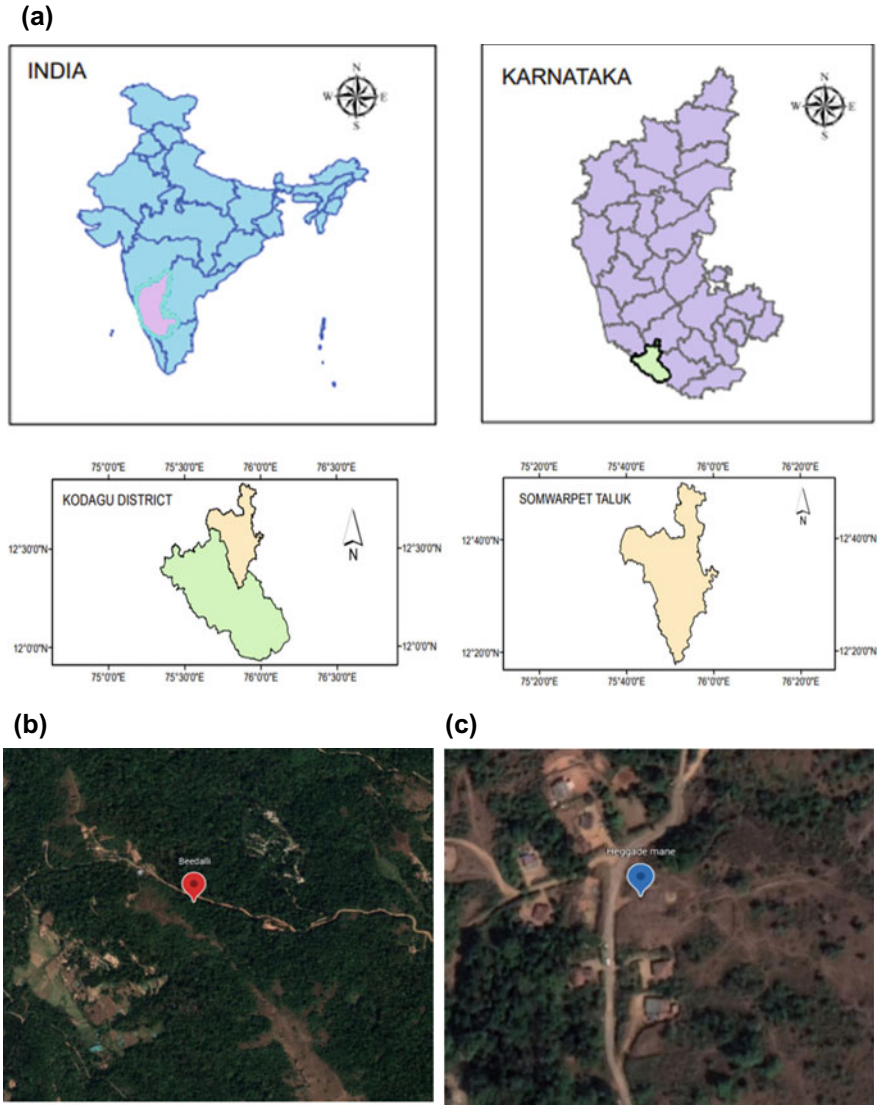

Fig. 1 **a** Study areas at Somawarpet Taluk, Kodagu district. **b** Beedalli, Somwarpet Taluk (site-1; forested area). **c** Heggade Mane, Somwarpet Taluk, (site-2; grassland area)

$$\text{Porosity} = 1 - (\text{Bulk Density}/\text{Particle Density}) \quad (1)$$

2.4 Determination of Saturated Hydraulic Conductivity

Hydraulic conductivity has been determined in the field using the Guelph permeameter, permeability tests in the laboratory and by the Rawls regression equation based on the textural properties of the soil.

2.4.1 Measurement of Saturated Hydraulic Conductivity in Field

Guelph permeameter has been used to determine field saturated hydraulic conductivity at different locations and depths. It is a constant head permeameter which employs the Mariotte principle and is based on the assumption of three dimensional steady-state flows from a cylindrical auger hole in the unsaturated soil [14]. There are different procedures available to measure the steady-state infiltration rates in terms of field saturated hydraulic conductivity and equilibrium time estimates [1]. The instrument measures both horizontal and vertical K_{fs} by measuring the steady-state flow rate at specified depths in which the constant depth of water is maintained. Figure 2 represents the experimental setup of the instrument at site-1 and site-2. At first, the well hole was prepared to a required depths with the help of auger before making the measurements. Then, the instrument was set at 150 mm depth having the radius of the hole 300 mm. The experiments were carried out for two heads (5 and 10 cm) for same auger hole and at the same depths till a steady-state condition were achieved. The steady-state flow rates so obtained has been used to determine the saturated hydraulic conductivity using the following Eq. (2):

$$K_s = G_2 Q_2 - G_1 Q_1 \tag{2}$$

Fig. 2 Guelph permeameter setup at site-1 and site-2

$$Q_1 = R_1 \times 35.39 \tag{3}$$

$$Q_2 = R_2 \times 35.39 \tag{4}$$

$$G_1 = \frac{H_2 C_1}{\pi\left(2H_1H_2(H_2 - H_1) + a^2(H_1C_2 - H_2C_1)\right)} \tag{5}$$

$$G_2 = \frac{H_1 C_2}{\pi\left(2H_1H_2(H_2 - H_1) + a^2(H_1C_2 - H_2C_1)\right)} \tag{6}$$

where K_s represents the saturated hydraulic conductivity; H_1 and H_2 are the heads maintained at 5 cm and 10 cm, respectively; R_1 and R_2 represent the steady-state flow rates at 5 cm and 10 cm head, respectively; a represents the radius of the well; C_1 and C_2 are the dimensionless shape factors that depends on H/a ratio and soil texture-structure category [14, 16].

2.4.2 Determination of Saturated Hydraulic Conductivity Using Laboratory Method

Saturated hydraulic conductivity has been determined in the laboratory using variable head permeability tests as described by Klute and Dirksen [10]. The undisturbed soil specimens were collected from the field using the cores of 100 mm diameter and 130 mm height. The cores were driven in to the soil vertically with the help of rammer and the samples were covered with the filter paper. First, the samples were saturated in the laboratory by allowing the water, once a steady-state flow rate is reached the hydraulic conductivity calculations were made using the Eq. (7).

$$K = \frac{2.30aL}{A(t_2 - t_1)} \log_{10}\left(\frac{h_1}{h_2}\right) \tag{7}$$

where K is the hydraulic conductivity or coefficient of permeability (cm/s); a is the cross-sectional area of stand pipe (cm^2); L is the length of the mold (cm); A is the cross-sectional area of mold (cm^2); $t = (t_2 - t_1)$ is the time interval (s) during which the head reduces from h_1 to h_2.

2.4.3 Estimation of Saturated Hydraulic Conductivity Using Rawls Regression Equation

In the present study, Rawls–Brakensiek regression equation [13] has been used to estimate the saturated hydraulic conductivity. The input parameters are percentage sand, percentage clay, and porosity values in fraction. The Rawls–Brakensiek regression equation has obtained from the wide soil texture data base and is given in the

Eq. (8).

$$K_s = \exp\big[19.52348(\phi) - 8.96847 - 0.028212C + 0.00018107S^2 - 0.0094125C^2 - 8.395215(\phi^2) + 0.077718S(\phi) - 0.00298S^2(\phi^2) + 0.019492C^2(\phi^2) + 0.0000173S^2C + 0.02733C^2(\phi) + 0.001434S^2(\phi) - 0.0000035C^2S\big] \quad (8)$$

where K_s is the saturated hydraulic conductivity of the soil sample in cm/h, 'ϕ' is the porosity expressed in fraction, 'C' represents the clay percentage, and S represents the sand percentage. Equation (8) is applicable only for the soils with sand percent greater than 5% and lesser than 70% and clay percent greater than 5% and lesser than 60%.

3 Results and Discussions

3.1 Physical Properties of Soil

The soil physical properties, namely, texture, bulk density, and porosity for the two study sites with varying depths are summarized in Tables 1 and 2. The site-1 has a sandy clay loam type and site-2 has sandy loam type texture. At both the sites, higher percentage of sand can be seen and the percentage clay in site-2 is more when compare to site-1. The bulk density values show the increase in the values with depths. The porosity values at site-1 varies from 37 to 55.5%, whereas at site-2 it varies from 32.5 to 48.3%.

3.2 Comparison of the Results of Saturated Hydraulic Conductivity Obtained from Field, Lab, and Estimated Values by Rawls Equation

Table 3 represents the comparison of results of saturated hydraulic conductivity obtained from the field using Guelph permeameter; Lab using the permeability tests; Rawls–Brakensiek equation based on the textural properties. The saturated hydraulic conductivity is considered log normally distributed [2, 11] and hence the geometric mean has been considered. The mean values of K_s obtained from field, lab, and textural properties show the slight variations at both the sites. The K_s values of lab permeability tests show lesser values than the field method. This is because of the fact that, Guelph permeameter measures both horizontal and vertical K_s, whereas the permeability tests in lab measure only vertical K_s. Figures 3 and 4 represent

Table 1 Physical properties of soil at Beedalli site

Site	Depth (mm)	% Sand	% Silt	% Clay	Bulk density (g/cm^3)	Porosity (%)	Textural class
	150	59	20	21	1.2	55.5	Sandy clay loam
1	300	54	20	26	1.22	55	Sandy clay loam
	600	47	28	25	1.56	41.1	Sandy clay loam
	150	64	22	14	1.18	55.3	Sandy clay loam
2	300	60	27	13	1.21	54.2	Sandy clay loam
	600	57	25	18	1.67	37	Sandy clay loam
	150	60	26	14	1.25	48.7	Sandy loam
3	300	57	19	22	1.32	45.1	Sandy clay loam
	600	52	21	27	1.42	44.5	Sandy clay loam
	150	60	34	6	1.19	55.3	Sandy loam
4	300	57	29	14	1.23	53.5	Sandy loam
	600	47	28	25	1.42	46.4	Sandy clay loam

Forested land

the graphical plots of K_s obtained from field, lab, and textural methods for site-1 and site-2, respectively, with field K_s as the reference. Though there is a slight variability in the K_s values, the scatter plots between the field, lab, and estimated values using Rawls equation show the good fit line for both the sites as given in the Figs. 3 and 4. This shows that the saturated hydraulic conductivity from the lab and the Rawls–Brakensiek equation are almost comparable with that of the field values.

4 Conclusion

Saturated hydraulic conductivity has been determined using Guelph permeameter in the field, permeability tests in the lab, and Rawls–Brakensiek regression equation based on textural and porosity data. The results of K_s obtained from the lab permeability tests gave slightly lesser values than the field method because of smaller sampling size and also the permeability tests measure only vertical $K_{s,}$ but the Guelph permeameter method measures combined vertical and horizontal K_s. The

Table 2 Physical properties of the soil at Heggade Mane site

Site	Depth (mm)	% Sand	% Silt	% Clay	Bulk density (g/cm^3)	Porosity (%)	Textural class
	150	65	28	7	1.35	37.8	Sandy loam
1	300	61	30	9	1.48	35.1	Sandy loam
	600	60	25	15	1.68	36.7	Sandy loam
	150	67	21	12	1.37	48.3	Sandy loam
2	300	65	21	14	1.43	45.9	Sandy loam
	600	60	26	14	1.58	40.3	Sandy loam
	150	65	28	7	1.30	48.2	Sandy loam
3	300	61	31	8	1.38	43.6	Sandy loam
	600	58	27	15	1.57	40.6	Sandy loam
	150	61	34	5	1.41	46.7	Sandy loam
4	300	62	29	9	1.58	39.2	Sandy loam
	600	57	25	18	1.60	32.5	Sandy loam

Grass land

results indicate that, the saturated hydraulic conductivity at 150 mm depth is higher when compared to 300 and 600 mm depths at both sites. Also, the K_s values at first two depths at the forested areas were much higher when compared to the grass land areas. This may be due to the presence of macropores in the forested region. The mean values of saturated hydraulic conductivity estimated from the Rawls–Brakensiek regression equation and lab method were compared with the field values as shown in Table 3. Though the comparison of the results given in Table 3 shows a slight variation in the K_s values, the graphical plots between the field, lab, and estimated values shown in Figs. 3 and 4 show a good fit line, i.e., the values obtained from the three methods are in good accordance with each other.

Table 3 Comparison of the results of K_s

Site	Depth (mm)	Method	N^*	Mean, K_s (cm/h)	Range (cm/h)
1	150	GP	4	14.55	8.43–20.81
		Lab	3	12.41	7.27–16.85
		Rawls equation	4	10.18	5.71–16.05
	300	GP	4	7.98	4.07–16.12
		Lab	3	7.16	2.94–14.81
		Rawls equation	4	5.97	2.38–10.29
	600	GP	4	0.87	0.37–1.63
		Lab	3	0.56	0.84–4
		Rawls equation	4	0.69	0.35–1.03
2	150	GP	4	4.86	2.63–7.68
		Lab	3	3.92	1.49–7.07
		Rawls equation	4	4.77	1.80–9.76
	300	GP	4	2.64	0.91–5.39
		Lab	3	2.35	0.84–4
		Rawls equation	4	2.31	0.84–6.27
	600	GP	4	0.97	0.29–2.14
		Lab	3	0.93	0.6–1.52
		Rawls equation	4	0.88	0.25–1.73

N^* = Number of experiments

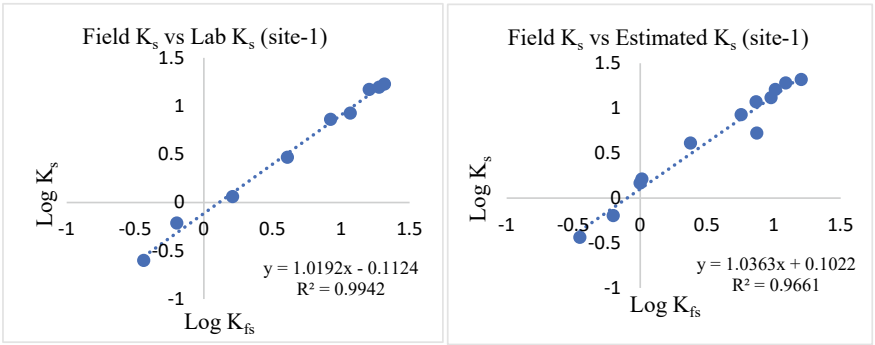

Fig. 3 Scatter plots for field, lab and estimated K_s for site-1

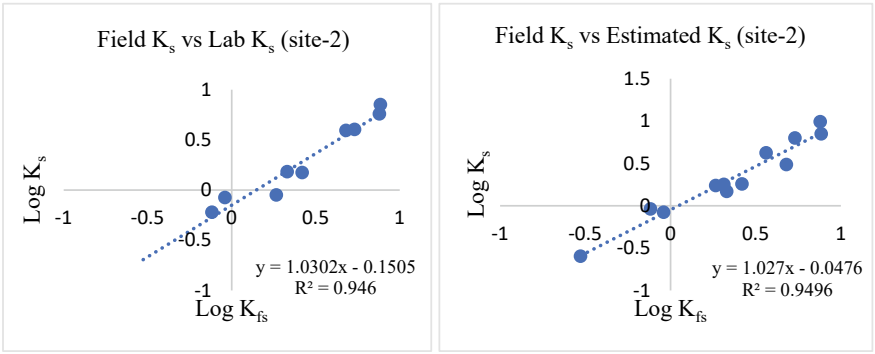

Fig. 4 Scatter plots for field, lab and estimated K_s for site-2

Bibliography

1. Bagarello V, Giordano G (1999) Comparison of procedures to estimate steady flow rate in field measurement of saturated hydraulic conductivity by the Guelph permeameter method. J Agric Eng Res 74(1):63–71
2. Bouwer H, Jackson RD (n.d.) Determining soil properties 58
3. Elrick DE, Reynolds WD, Tan KA (1989) Hydraulic conductivity measurements in the unsaturated zone using improved well analyses. Groundwater Monit Rem 9(3):184–193
4. Elrick DE, Reynolds WD (1992) Methods for analyzing constant-head well permeameter data. Soil Sci Soc Am J 56:320–323. https://doi.org/10.2136/sssaj1992.03615995005600010052x
5. Feki M, Ravazzani G, Barontini S, Ceppi A, Mancini M (2020) A comparative assessment of the estimates of the saturated hydraulic conductivity of two anthropogenic soils and their impact on hydrological model simulations. Soil Water Res. 15:135–147. https://doi.org/10.17221/33/2019-SWR
6. Gallichand J, Madramootoo CA, Emight P, Barrington SF (1990) An evaluation of the Guelph permeameter for measuring saturated hydraulic conductivity. Trans ASAE 33:1179–1184. https://doi.org/10.13031/2013.31455
7. Gribb MM, Kodesova R, Ordway SE (2004) Comparison of soil hydraulic property measurement methods. J Geotec. Geoenviron Eng 130:1084–1095. https://doi.org/10.1061/(ASCE)1090-0241(2004)130:10(1084)
8. Jačka L, Pavlásek J, Kuráž V, Pech P (2014) A comparison of three measuring methods for estimating the saturated hydraulic conductivity in the shallow subsurface layer of mountain podzols. Geoderma 219–220:82–88
9. Kanwar RS, Rizvi HA, Ahmed M, Horton R, Marley SJ (1990) Measurement of field-saturated hydraulic conductivity by using Guelph and velocity permeameters. Trans ASAE 32:1885
10. Klute A, Dirksen C (1986) Hydraulic conductivity and diffusivity: laboratory methods. In: Klute A (ed) SSSA book series. Soil science society of America, American Society of Agronomy, Madison, WI, USA, pp 687–734. https://doi.org/10.2136/sssabookser5.1.2ed.c28
11. Lee DM, Elrick DE, Reynolds WD, Clothier BE (1985) A comparison of three field methods for measuring saturated hydraulic conductivity. Can J Soil Sci 65:563–573. https://doi.org/10.4141/cjss85-060
12. Mahapatra S, Jha MK (2019) On the estimation of hydraulic conductivity of layered vadose zones with limited data availability. J Earth Syst Sci 128:75. https://doi.org/10.1007/s12040-019-1101-1
13. Rawls WJ, Brakensiek DL (1989) Estimation of soil water retention and hydraulic properties. In: Morel-Seytoux HJ (ed) Unsaturated flow in hydrologic modeling. Springer Netherlands, Dordrecht, pp 275–300. https://doi.org/10.1007/978-94-009-2352-2_10

14. Reynolds WD, Elrick DE (1985) In-situ measurement of field-saturated hydraulic hydraulic conductivity, sorptivity and the alpha-parameter using the Guelph permeameter. Soil Sci 140(4):292–302
15. Soil moisture Equipment Corporation (1987) 2800KI operating instructions. Soil moisture Equipment Corp., Santa Barbara, CA, USA
16. Zhang ZF, Groenevelt PH, Parkin GW (1998) The well-shape factor for the measurement of soil hydraulic properties using the Guelph permeameter. Soil Tillage Res 49:219–221. https://doi.org/10.1016/S0167-1987(98)00174-3

Analyzing Compliance of Façade Passive Fire Resistance as Per ASTM E2307

Harsh Kumar Chaurasia, Chetan, Aman Kumar, Sadiya Sulthana, Muttana S. Balreddy, and Deepanjan Sengupta

Abstract Glass façade construction is increasing at a rapid rate with more attention to aesthetics, energy efficiency, green concept, etc. but the fire safety factor has completely been neglected. A high-rise façade is a very crucial element in case of a fire incident, poses a greater fire hazard. However, they can easily allow the fire to transfer from lower floor to upper floors of the building through the gap present in between the slab edge and glass façade. This study promotes fire safety in the façade structures. The study is based on cellulosic fire and mainly concentrates on the chimney effect, which is very common in residential, commercial, and institutional buildings, etc. Following fire safety, passive fire protection is considered for the study. The study says in the buildings with glass façade, proper compartmentation must be adopted by ensuring proper fire stopping done at spandrel sections in compliance with test conditions. This can be implemented with proper installation of fire stop in all necessary areas such as unsealed openings and joints to prevent fire spread. A real spandrel of a building has been analyzed and re-drawn in AutoCAD software as per fire safety norms of ASTM E2307 and further engineering judgements have been made for the same as per International Firestop Council guidelines which are also reflected in IS 12458-2019. The study also includes basic analysis on cause of some major fire incidents in India, key points on building fire safety provision of passive fire protection. NBC-2016 is also referred to get an insight about the important clauses which promotes the façade fire safety.

Keywords Façade spandrel · Passive fire protection · Engineering judgements · ASTM E2307 · IS 12458-2019 · NBC 2016

H. K. Chaurasia · Chetan · A. Kumar · S. Sulthana · M. S. Balreddy (✉)
Siddaganga Institute of Technology, Tumakuru 572103, India
e-mail: msb@sit.ac.in

D. Sengupta
HILTI-India, Gurugram, India

L. Nandagiri et al. (eds.), *Recent Advances in Civil Engineering*, Lecture Notes in Civil Engineering 256, https://doi.org/10.1007/978-981-19-1862-9_20

1 Introduction

Fire is essential for the development of human society and also it is a significant part of human civilization. Among the different types of disasters, fire poses a serious threat to life and property in urban and rural areas. When a flammable material gets sufficient heat in presence of oxygen, then becomes fuel for the fire. The possibility of a fire in a tall building is always an area of concern because it has the potential for higher rate of life and asset loss. The fire can be of two types namely Cellulosic fire and Hydrocarbon fire but our area of focus is Cellulosic fire. Cellulosic fire is a general fire which occurs without any hydrocarbon products like petrol, diesel, etc. In standard temperature curve it reaches 500 °C in just 5 min [1, 2].

In past few decades, there were many fatal fire incidents that occurred around the globe such as a fire in the Jiaozhou Road, Shanghai, China in the year 2010 cost 58 lives and 71 injuries, Grenfell Tower, London, UK in 2017 costs 72 deaths and 70 injuries [3], Windsor Tower, Madrid, Spain in 2005 caused 7 injuries, and a fire incident in Mantralaya building which was the administrative headquarters of the state government of Maharashtra in South Mumbai, India in year 2012, due to a faulty electrical circuit, the fire broke out in the 7 storey block that killed 5 people and injured more than 20.

In India, 35 Indians die daily in a fire, according to the National Crime Records Bureau (NCRB), according to the report 11,037 cases reported in 2019 which caused injuries to 441 persons and 10,915 deaths [4]. Fire occurs due to various reasons such as electrical faults, lighters, gas stoves, and so on. No matter what's the cause of fire, these fires are always fatal, leading to the loss of many lives and valuable assets. The key area of focus is the gap present between a building slab edge and a façade spandrel which allows the fire and smoke to spread from lower floor to upper floors of the building. And out of multiple combustible products, the smoke is so grave as humans cannot see or locate the route of escape and moreover it contains highly poisonous gases. A fire happened in June 2013 at the IndusInd Bank building in Mumbai, had clearly mentioned that the most common cause of fire fatalities was smoke inhalation rather than the flames themselves. As per newspaper reports, the fire and smoke transfer inside the building from lower to upper floors through the gap. This situation arose due to lack of passive fire protection between glass façade and concrete slab. The perimeter fire barrier is a solution which sits behind façade and in between the slab edge and façade itself to hinder the spread of fire, heat, and the smoke by converting it in single compartment. Compartmentation is an important term to impede the spread of fire in any building. It is basically of two types such as vertical and horizontal compartmentation. In the process, the building will be divided into a series of fire tight boxes which is termed as 'compartments' with the help of fire barrier on fire resistant walls on all sides, including the top and bottom [5–7].

The case study is presented on few fire incidents in India such as Carlton Tower (Bangalore), Rolta Technology Park (Mumbai), ESIC Hospital (Mumbai), and Sunrise Hospital of Dreams Mall (Mumbai) because actual fires are valuable as case studies in many branches of the fire scientific community. Fire investigation

and analyzing that information are useful tools for gathering knowledge and experience on characteristics of fires like how fires occur? And why do they unfold the way they do? Fire investigation allows for the collection and analysis of important data and information. While investigating fire, smoke is also an important component to consider which contains toxic components which can directly lead to death once people inhale it during fire. The information can be used for the evaluation of regulations; it can also be used in the field of fire safety [8].

A proper investigation of these accidents is an important tool to obtain learning in different disciplines of safety areas and has been successfully implemented in residential and commercial building structures which are mostly build of façade spandrel [9, 10].

In modern Indian cities, glass façade or glazing construction is experiencing rapid growth in recent years because it looks snazzy and clean [3]. But according to a fire inspection done on the buildings in Mumbai, Maharashtra in 2015-July 2018, there were 50% buildings with violation. BMC and fire brigade also have set rules which is to be considered while designing any buildings with glass facades. As per these established rules, the distance between glass façade and building structure must not be more than 300 mm and the smoke seals should be made up of non-combustible material which has to be laid in between slab edge and glass façade [11]. The Indian Standard codes which are available for façade design and safety names as IS 1642-1989, IS 3548-1988, and IS 8183-1993 are outdated and even not in practice by designers and consultant because of lack of knowledge and its importance. But also these codes are not detailed and integrated, cross referencing it the challenge. Fire safety is very important in glass buildings and also it is equally important to understand the benefits of tested systems and Engineering Judgement (EJ).

2 Case Study

2.1 Carlton Tower, Bengaluru

Carlton Towers was built in 1999, and has two towers on all ‘A’ with seven floors and ‘B’ with six floors. The accident happened in Tower ‘A’, but the other’s outlook also took a hit.

Although the fire department had issued a no-objection certificate to Carlton Towers under the National Building Code 2005, a fatal fire broke out which resulted in 9 fatalities and 60 injuries in the fire of 23rd February 2010. The fire began from lift service cable on second floor and spread through the duct with smoke inundating the remaining floors. Among the total people died, 3 of them got panicked and jumped from the upper floors by breaking the window to escape from the blaze [12]. The fire was brought under control and the building was evacuated in close to 120 min (2 h) of struggle. The scores of people fainted after inhaling the smoke. The factors behind

Fig. 1 Carlton tower [14, 15]

this incident are such as the disregard of the standards on building and fire safety, poor awareness of fire safety and mitigation strategies, poor government monitoring and corruption, and also the spectators who had blocked the fire fighters' way [13] (Fig. 1).

2.2 Sunrise Hospital of Dreams Mall, Mumbai

The Hospital was situated on LBS Marg in Bhandup (West), Mumbai. The fire broke out on March 26, 2021 on the first floor, with no smoke outlet due to mall's glass façade, the smoke quickly crawled to next floor, i.e., third floor, from where it entered into ventilation ducts of the hospital. According to CCTV footage, the smoke entered through the rear end of the hospital at 11:10 pm, where the VIP suites were located. The smoke spread across and occupied the entire third floor where the hospital was located which, over one lakh square meters of area, in just 5–10 min of time.

At the time of incident, there was 35 on duty staffs available in hospital, few patients were on high-flow oxygen support, it was not possible to separate them from ventilator and nurses could not stay with them due to dense smoke, and also 76 Covid-19 patients, there was a natural misgiving about touching them. The smoke in the building was so dense that no one can see the person ahead of them and the smoke at a time made its way into patient's oxygen tube. But around 70 Covid-19 patients were rescued safely and shifted to another hospital.

The fire caused total 11 deaths, including Covid-19 patients [16] (Fig. 2).

Fig. 2 Sunrise hospital of Dreams Mall [16]

2.3 ESIC Hospital, Mumbai

The ESIC Hospital was built in 1973, situated in Marol, Andheri (East). The hospital had 325 beds ground floor plus six-storey installed with a glass façade and only one fire extinguisher on each floor. A fire broke out in the building on 17th December 2018 at around 4 pm. In the primary investigations, it was found that the sprinkler system and fire alarm were not functioning. The fire official also said that the building materials kept at ground floor for renovation work caught fire and also the glass façade prevented smoke from escaping out of ground floor as the windows were shut, and instead moved to higher floors where lung patients were admitted, who got suffocated and died. The further fire investigation of fire brigade inspected that there was no fire resistant door installed in staircase area, and electric duct that should be sealed was left open. 11 people including a two-month old girl died and 146 people got injured in the fire. The fire was brought into control at 7:35 pm.

Environmentalist Rishi Agarwal added that the glass in difficult to handle, there should be stringent building codes for the use of glazing and violation should be punished. Green building norms also recommend that the glass windows should have openable panel, instead of fixed ones [17] (Fig. 3).

2.4 Rolta Technology Park, Andheri, Mumbai

Rolta Technology park was a façade structure located at Andheri, Mumbai. It was a four-storey commercial structure, and the fire took place, at around 11:30 am, in a

Fig. 3 ESIC hospital [18]

server room on the third floor and escalated quickly from floor three to floor four. The stairwells were filled with smoke due to the packed structural design and firefighting systems were not functioning either. The situation was grave because of aluminum cladding, glass façade, and lack of ventilation in the building. Although no one died, the fire-damaged electric wiring, furniture, computers, and records which was stored in server room on the second floor [19] (Fig. 4).

Fig. 4 Rolta Technology Park [20]

3 Passive Fire Protection

Passive fire protection comprises limiting down the improvement of a fire and its fast spread by utilizing combustible and flammable structure materials. These actions are identified with the response of materials like a divider, floor, roof, and façade cladding and the materials nearby the uncovered surface. When a fire occurs, it must be detected and extinguished as soon as possible. Active fire protection, including fire identification, alarm and dousing, and smoke and warmth extraction, assumes an indispensable part.

At the point when the fire has been completely formed and is gone into its subsequent stage, then, at that point, passive fire protection guarantees the structure strength for a particular timeframe. This action alludes to the imperviousness to fire of development components, which should have the option to support their stacking or isolating capacities for a specific time frame, to have the option to clear the tenants, and to permit the intercession of the crisis administrations. The compartmentation of the structure is a sort of division of the structure into little volumes which can be delimited by dividers with adequate imperviousness to fire. For the most part, compartmentation is of two sorts names as vertical and horizontal compartmentation. At the point when a structure gets built, there are straight joints between the neighboring underlying components and furthermore, have various administrations going through dividers and floors that make voids around the infiltration. Such joints and voids can provide the path to fire, smoke, and heat to transfer from one section to another section of the building. So, these joints and voids should be appropriately sealed to contain the fire in particular area for a certain time period. These seals should be designed to resist the fire for at least 2-h (i.e., *F*-rating). This time period helps in evacuation of occupants. Various fire protection systems include fire barriers, firestops, fire door, and fire/smoke dampers. A firestop is one of the parts of passive fire protection which is used to seal the joints and openings around a fire-rated wall or a floor assembly. Various codes and standards test and recommend to use passive fire protection. Some passive fire protection systems are shown below.

Damper

Fire Door

Firestop

Cable Transit System

Use of passive fire protection system is shown in Fig. 5

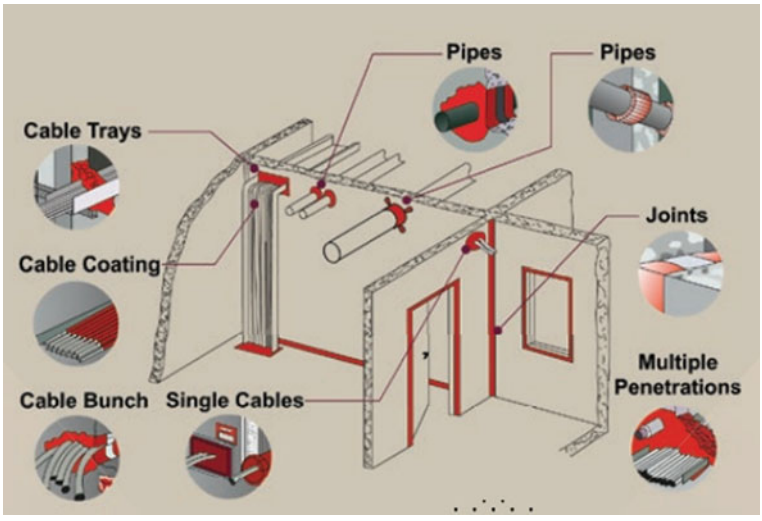

Fig. 5 Passive fire protection (compartmentation) * Copyright HILTI-India

3.1 Key Considerations for Designing the Perimeter Barrier and Firestop Requirement [21]

- The products should be properly tested and certified to prove its ability to prevent the spread of flame, gases or smoke, and heat.
- All products should have equal insulation and integrity ratings which will be normally 120 min.
- The products should be installed under compression; it must be capable of accommodating movement of a façade.
- Perimeter barriers must be installed to provide horizontal compartmentation for every floor.
- Products should be fitted tightly around all bracketry to restrict the smoke from passage. All potential gaps must be sealed with the sealant which carries same insulation and integrity rating as the perimeter barrier.
- The maximum frontal deflection of the curtain walls should not exceed L/200 or 15 mm, whichever is lesser, under the declared wind load.

4 A Brief Summary of Codebooks

The available Indian Standard codes to design glazing structures and fire safely building are IS 1642:1989; lay down the essential requirements of fire safety of buildings with respect to details of construction [22], IS 3548:1988; covers glazing work in buildings including techniques used in glazing [23], and IS 8183:1993; prescribes the requirements and methods of sampling and test for bonded mineral wool for thermal insulation [24]. But available codes are so old, that they are not even in practice by designers and consultants. These codes are not integrated and detailed, cross referencing is the challenge. In India, fire safety is not a major concern of designers and consultant which leads to higher life and asset losses.

Now India has two biggest game changers for firestop which are NBC 2016, Part 4, Fire and Life Safety [25] and IS 12458-2019; fire resistance of through penetration firestops-method of test [26], giving a clear idea about firestop and its need in buildings. But the industry is not aware of their importance. NBC 2016 defined compartmentation and firestop. It also defines two different types of firestop assemblies such as for through penetrations and for joints. IS 12458:2019 deals with the fire resistance through penetration firestops and also provides guidance on providing engineering judgement based on profound codebook test. However, Indian standards don't have any codebook for joints in façade spandrel. The different components of façade spandrel are shown in Fig. 6.

ASTM E2307 is a highly integrated and detailed code available on fire safety. Its testing methods measure the ability of perimeter fire barrier systems to prevent interior fire spread. A perimeter fire barrier is the fire protection which resists the spread of fire from lower floor to upper floors between the exterior wall assembly (typically

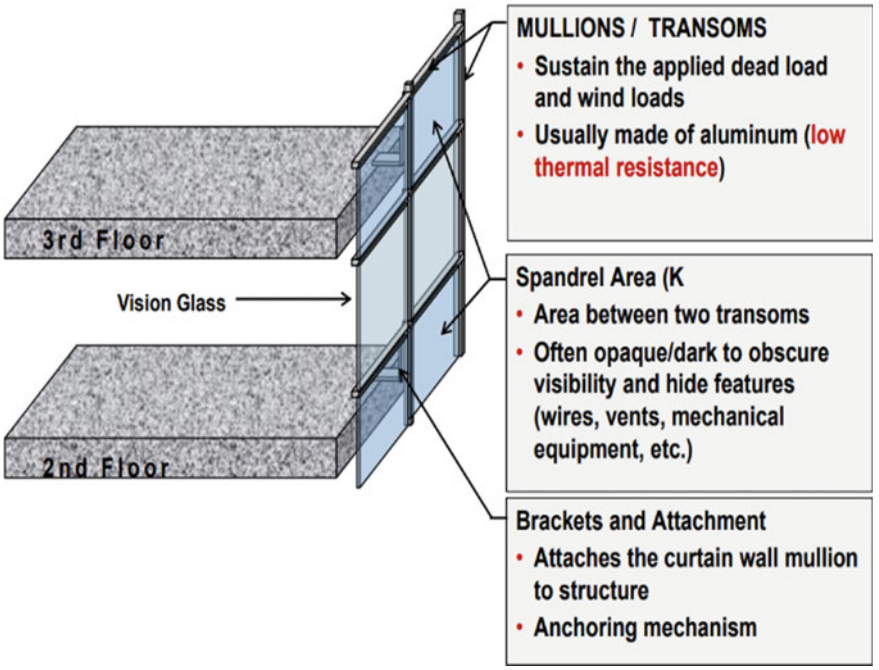

Fig. 6 Components of façade spandrel * Copyright HILTI-India

non-rated) and floor assembly within the building. Its temperature increases exponentially. The exterior perimeter of building is subjected to wind load and seismicity [27] (Fig. 7).

The fire can transfer through two effects in a building such as Chimney effect and Leapfrog effect. When the fire transfers from the gap then its known as Chimney effect

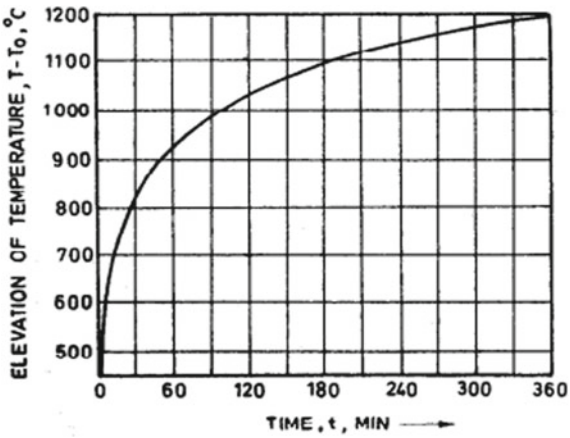

Fig. 7 Standard time–temperature rise curve [28]

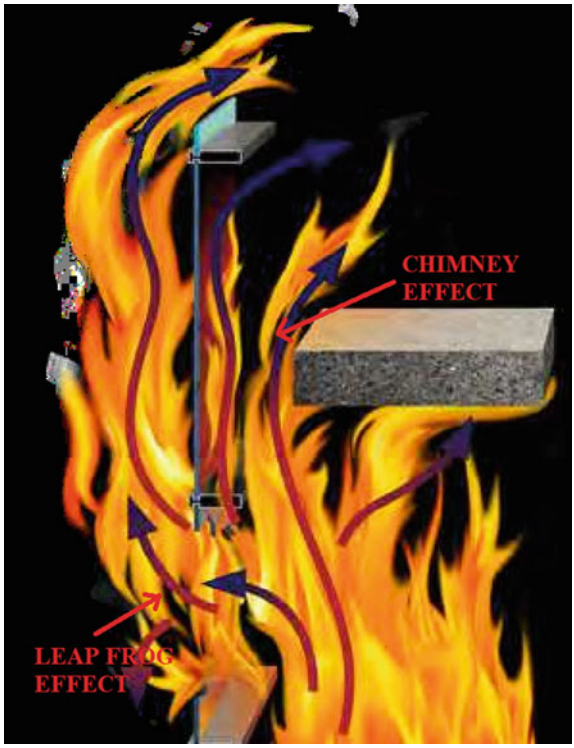

Fig. 8 Fire transfer paths [29]

and if the fire transfers through the building perimeter then its known as Leapfrog effect (Fig. 8).

National Building Code of India 2016 says since India doesn't have its own code for façade firestop design, the most researched and widely accepted code for fire safety MFPA 101 for Indian context. In terms of façade fire safety, MFPA 101 clause 8.3.5.4 and IBC mentions to use ASTM E2307.

5 Preventive Measure in a Potential Fire

A structure was investigated which was built in the year 2007. In the examination, we have tracked down that the structure has a glass facade introduced at stair-well which assumes a significant part in the evacuation during the fire. The different panels dimensions are shown in Fig. 9.

The gap between slab and glass panel was packed with aluminum sheet as shown in Fig. 10.

The sides of aluminum sheet were not properly fixed which can be clearly explained in Fig. 11.

Fig. 9 Actual façade

Fig. 10 Façade spandrel

Fig. 11 Façade spandrel gap

The gap size between the slab and glass panel was 65 mm which is much sufficient to transfer fire and smoke. The front view and gap is shown in Fig. 12.

5.1 Engineering Judgements

The Engineering Judgements for the described building was made based on HI/BPF 120-12 certificate [30] and the drawing with passive fire prevention is also shown with *F*-rating of assembly of 2 h (Fig. 13).

1. Spandrel or vision glass and aluminum mullion curtain wall assembly with minimum spandrel height of 18″ (non-fire-rated).
2. Concrete floor assembly (1-h or 2-h fire rating):

   (A) Concrete floor assembly (minimum 6″ thick)

3. [Optional, not shown] aluminum shadow box.
4. Steel back pan (minimum 22 ga.) constructed with minimum 1-1/2″ return legs. Back pan to completely fill spandrel and shall be mechanically fastened to aluminum framing members per Intertek approved joint system HI/BPF 120-12.
5. Minimum 3″ (75 mm) foil faced or unfaced curtain wall insulation (mineral wool minimum 128 kg/m^3 density) to completely fill back pan, insulating all fastening points. Curtain wall insulation to be tightly fit, compressed a minimum 1/8″ (3 mm) in all directions and secured to steel back pan with minimum 12 ga. Steel pins a minimum ½” longer than the thickness of the curtain wall insulation pins to be installed in minimum two rows at 12″ (300 mm) C/C.
6. Minimum 6″ (150 mm) thickness mineral wool safing (minimum 64 kg/m^3 density) compressed 33%, flush with top surface of floor assembly.

Fig. 12 Gap between slab edge and spandrel, and front elevation

7. Minimum 3.2 mm (WET) thickness Hilti CFS-SP WB firestop joint spray to completely cover mineral wool, overlapping minimum ½" onto adjacent assemblies.

Note: Fire-rating of assembly is dependent on the performance of curtain wall assembly under fire conditions.

The preventive measures suggested above can improve the building performance during fire.

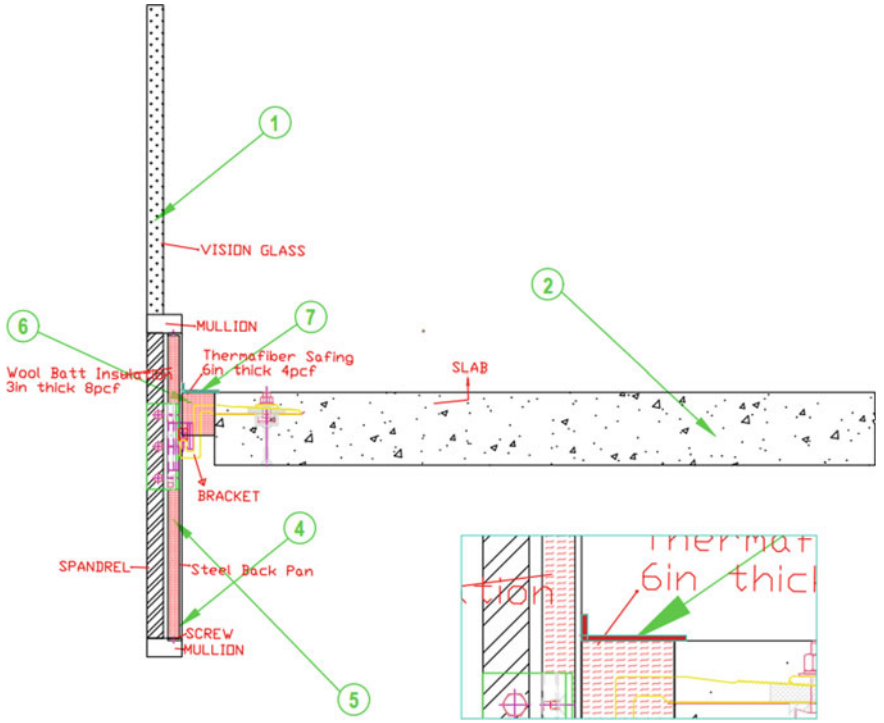

Fig. 13 Suggested system with passive fire protection

5.2 Limitations of Thermafiber Safing

Thermafiber safing has ability to resist smoke and fire but it is unable to hinder the path of UV rays [31].

6 Conclusion

Actual fire events were analyzed, showing the use of combustible insulation in exterior wall claddings without appropriate fire and protection barriers would potentially invoke the fire to spread quickly and can lead to severe fire damage and loss. If the experimental facility is not available to test the facade designs, then engineering judgments (EJ) can be referred to design a more appropriate fire protection for the buildings. We have used HI/BPF 120-12 to make the EJ of the drawing that has been discussed section above. The detailed description of passive fire protection and its necessity is also mentioned. And the lagging of the Indian Standard Bureau has been discussed to show the major need to revise or publish a stringent code for façade

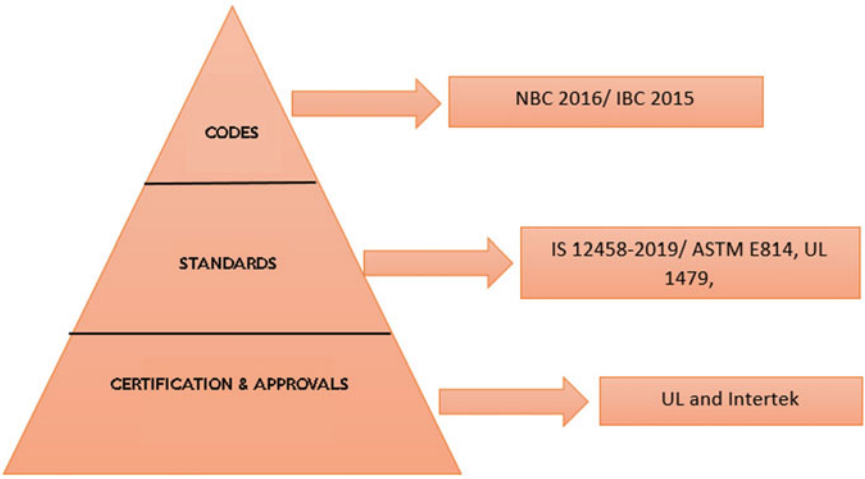

Fig. 14 Suggested flow of designing passive fire protection

spandrel design and fire protection in glazed building. The flow diagram is shown in Fig. 14.

Codes which are available in Indian Standard and which must be developed are mentioned below.

	Indian Standard	Number	ASTM	Number
Penetration	✓	12458-2019	✓	E814
Joints	✗	✗	✓	E1966
Structural Glazing	✗	✗	✓	E2307

Acknowledgements The authors would like to thank HILTI India for their help in arriving to the engineering judgement based on the Intertek certificates.

References

1. Law A, Bisby L (2020) The rise and rise of fire resistance. Fire Saf J 116:103188
2. Law A, Kanellopoulos G (2020) The rise and fall of UK's spandrel panel. Fire Saf J 115:103170
3. Wegrzynski W, Antosiewic P, Burdzy T, Tofilo P, Papis BK (2020) Experimental investigation into fire behaviour of glazed facades with pendant type sprinklers. Fire Saf J 115:103159
4. Accidents Deaths and Suicides in India (2019) Chapter 1, Accidents in India, National Crime Records Bureau

5. Srivastava G, Nakrani D, Ghoroi C (2020) Performance of combustible facade systems with glass, ACP and firestops in full-scale, real fire experiments. Fire Technol 56:1575–1598
6. Gandhi P, Jagdish V, Karthikeyan G, Chakravarthy A, Nakrani D, Ghoroi C, Srivastava G (2017) Performance of glass-ACP façade system in a full-scale real fire test in a G+2 structure. Procedia Eng 210:512–519
7. Stec AA, Hull TR (2011) Assessment of the fire toxicity of building insulation materials. Energy Build 43:498–506
8. Chow WK (2005) Building fire safety in far east. Archit Sci Rev 48(4):285–294
9. Hansen ND, Steffensen FB, Valkvist M, Jomaas G, Van Coile R (2018) A fire risk assessment model for residential high-rises with a single stairwell. Fire Saf J 95:160–169
10. Peng L, Ni Z, Huang X (2013) Review of the fire safety of exterior wall claddings in high-rise buildings in China. Procedia Eng 62:663–670
11. https://firesafetynation.com/bmc-and-fire-brigade-rules-for-buildings-with-glass-facades/
12. Carlton Tower, Bangalore: http://surl.li/akjye
13. Carlton Tower, Bangalore: http://surl.li/akjyh
14. Carlton Tower, Bangalore: http://surl.li/akjyc
15. Carlton Tower, Bangalore: http://surl.li/akjyk
16. Sunrise Hospital of Dreams Mall: http://surl.li/akjyr
17. ESIC Hospital, Mumbai: http://surl.li/akjyx
18. ESIC Hospital, Mumbai: http://surl.li/akjyz
19. Rolta Technology Park: http://surl.li/akjze
20. Rolta Technology Park: http://surl.li/akjzg
21. https://wfmmedia.com/passive-fire-protection-building-facades/
22. IS 1642:1989, Fire safety of buildings (general): details of construction-code of practice (first revision). Bureau of Indian Standards, New Delhi
23. IS 3548:1988, Code of practice for glazing in buildings (first revision). Bureau of Indian Standards, New Delhi
24. IS 8183:1993, Bonded mineral wool-specification (first revision). Bureau of Indian Standards, New Delhi
25. "National Building Code of India—Part 4: Fire and Life Safety (2016)" Bureau of Indian Standards, New Delhi
26. IS 12458:2019, Fire resistance of through penetration firestops-method of test (first revision). Bureau of India Standards, New Delhi
27. ASTM E2307, 2020 Edition, April 1, 2020—Standard test method for determining fire resistance of perimeter fire barriers using intermediate-scale, multi-story test apparatus
28. IS 12458:1988, Method of fire resistance test of firestops. Bureau of India Standards, New Delhi
29. https://www.wconline.com/articles/92757-assessing-leap-frog-risk-a-new-testing-method
30. Intertek Certificate: HI/BPF 120-12, (2017)
31. Thermafiber Safing: Product Data Sheet https://www.owenscorninglibrary.ca/wp-content/uploads/2020/02/600010C-Thermafiber-Safing-Data-Sheet-EN.pdf

Performance of RCC Column Retrofitted with CFRP Wrappings and the Wrappings with Steel Angle-Batten Jacketing Under Blast Loading

Mohd Shariq, Mehtab Alam, and Asif Husain

Abstract Blasts and accidental explosions are being reported more frequently than before with grievous injuries and loss of lives and damage to the structure, increasing the concern of disaster management authority officials. Structural engineers apprehend that such events may trigger progressive structural collapse leading to huge loss of property and its consequences and therefore the blast performance of important load-carrying members such as columns becomes the topic of interest. Blast performance and blast-resistant design are being given importance for the structure likely to be the target of insurgents by various researchers and engineers. In a framed structure system, the safety of columns being the principal element against blast loading is extremely important for the stability of the structure. The present study focuses on how best can we enhance the blast performance of the reinforced concrete (RC) columns of an existing building. One 3000 mm long, 300 mm × 300 mm RC column carrying an axial load of 950 kN subjected to the 82 kg TNT equivalent blast loading tested experimentally has been first analyzed using the ABAQUS/CAE software. The concrete damage plasticity (CDP) model including the strain rate effect is used to model the concrete material behavior to blast loading. To enhance the performance of the column, (1) CFRP wrappings over the (i) seismic confining regions, (ii) seismic and mid-height regions, and (iii) entire length, and (2) jacketing with steel angles at the corners throughout the column length and connected with battens on the wrappings are considered. Results in terms of displacement, damage, and stresses are compared and discussed. Considered provisions lead to a novel technique of retrofitting the RCC columns with CFRP wrappings with steel angle and batten jacketing over the seismic confining regions and mid-height against blast loading.

M. Shariq (✉) · A. Husain
Department of Civil Engineering, Faculty of Engineering and Technology, Jamia Millia Islamia, New Delhi, Delhi 110 025, India
e-mail: shariqqq786@gmail.com

A. Husain
e-mail: ahusain2@jmi.ac.in

M. Alam
Department of Civil Engineering, Netaji Subhas University of Technology, New Delhi, Delhi 110 073, India
e-mail: mehtab.alam@nsut.ac.in

L. Nandagiri et al. (eds.), *Recent Advances in Civil Engineering*, Lecture Notes in Civil Engineering 256, https://doi.org/10.1007/978-981-19-1862-9_21

Keywords Blast loading · RC columns · Carbon fiber-reinforced polymer (CFRP) wrapping · Steel angles · Battens · Displacement · Damage

1 Introduction

The world is experiencing continuing high and low-intense blast explosions, caused either by bombs or gas cylinders, or other sources. The casualties and economic depletion that these explosions give rise to are huge [1–8]. Most recently in June 2021, an explosion took place in a gas company in the city of Shiyan (Hubei Province of China), which caused 25 casualties and injuries to 138 others. Another blast explosion took place in the city of Moghbazar (Dhaka, Bangladesh) where a gas cylinder exploded and took seven lives, and injured a dozen others [9]. It also caused intense damage to several surrounding buildings causing huge economic losses. In the year 2020, the well-known Beirut explosion occurred at Beirut port. The blast in the chemical caused more than 200 casualties and injured about 7000 people [10]. It also led to a financial and economic loss of up to $15bn and left around 3,00,000 people homeless [10]. Such explosions are increasing globally and attracting the attention of engineers and researchers to investigate the effect of blast loading on different elements of building structures. RC column being a key load-carrying member in a concrete building structure is of prime importance. Several techniques and strategies are available in the open literature to retrofit/strengthen the existing RC columns of a building vulnerable to blast loading. In this study, a novel method of strengthening the existing RCC columns wrapped with C-FRP sheets over the region(s) likely to suffer more damage and jacketed with steel angles at the corners throughout the length and connected with wide battens on the sheet is proposed. Steel of two different grades (Fe250 and Fe300) and thickness (5 and 8 mm) are considered. Some researchers had worked on improving the strength of the column and the other building components are as follows. Heffernan et al. [11] investigated a square RC column with 2100 mm in length and a cross-section of 150 × 150 mm. The compressive strength of the concrete is 44 MPa. The column was reinforced with 4 bars of 10 mm diameter as longitudinal reinforcement having a yield strength of 450 MPa and ultimate strength of 630 MPa, and ties of 6 mm diameter with 100 mm spacing in the transverse direction with yield and ultimate strength of 450 and 630 MPa, respectively. The RC column was strengthened in the longitudinal and transverse direction using different configurations of SRP and CFRP. The investigation was done by using C-4 explosives of different magnitudes—49, 65, 90, and 100 kg at standoff distances of 4 and 5.25 m. The study concluded that the columns strengthened with SRP emerged to be more ductile than those reinforced using CFRP. RC column of diameter 600 mm with concrete of compressive strength 30 MPa and 4000 mm height was examined by Elsanadedy et al. [12]. The column was reinforced with 16 bars of 16 mm diameter and 500 MPa yield strength, and 10 mm diameter ties at 200 mm c/c and 500 MPa yield strength. Furthermore, two layers each of 1 mm thick CFRP were applied to the column in the circumferential direction and longitudinal direction. Multiple blast

charges of 100, 200, 500, and 1000 kg TNT equivalent were used at standoff distances of 1, 4, and 15 m, and the numerical model was developed using the finite explicit software LS DYNA. Results showed that the column retrofitted with CFRP reduced the peak lateral displacement, and by increasing the number of layers of CFRP, the capacity of the column to bear high intense blasts was improved.

Burrell et al. [13] investigated eight columns where two columns were constructed using self-consolidated concrete (SCC) and the other six columns were constructed using steel-fiber-reinforced concrete (SFRC). The cross-section of each column was 152 × 152 mm with a length of 2468 mm. Four bars of 11.30 mm diameter were provided as longitudinal reinforcement having a yield strength of 483 MPa and 6.30 mm diameter stirrups with a spacing of 75 mm c/c as transverse reinforcement without seismic detailing. However, 38 mm spacing with seismic detailing was used with a yield strength of 604 MPa. The compressive strength of concrete varied from 40.50 to 56.60 MPa. The axial load was 294 kN. The columns were tested using shock-tube-induced simulated blast loading. The research concluded that the use of SFRC improved blast performance of the column resulting in maximum reduction of residual displacement and increased damage tolerance. Jacques et al. [14] examined four RC columns with a cross-section of 300 × 150 mm and a length of 2440 mm. Eight bars of 10 mm diameter were provided as longitudinal reinforcement having yield and ultimate strength of 445 and 550 MPa, respectively, and ties of 6.30 mm diameter at 150 mm c/c having yield and ultimate strength of 582 mm and 670 mm, respectively. Different compressive strengths of concrete were used for multiple models varying from 30.40 to 38.50 MPa. Three cases were considered taking 1.18 mm thick GFRP layer(s) along the column length on tension face and transverse wrapping over the entire column: (1) one layer along the column length and one layer of transverse wrapping, (2) five longitudinal layers and one layer of transverse wrapping, and (3) five longitudinal layers and three transverse layers. The columns were tested using shock-tube-induced simulated blast loading. It was discovered from the investigation that the specimens where a maximum number of GFRP sheets were applied reflected the best results. Kyei and Braimah [15] examined the performance of 300 × 300 mm square axially loaded RC columns, without and with seismic reinforcement over the confining regions, and confining as well as mid-height regions, subjected to 82 kg TNT load at a scaled distance of 1.0 m/kg$^{1/3}$. The columns were reinforced with 4 bars of 25 mm diameter of yield strength 500 MPa. The compressive strength of the concrete was 30 MPa. It was discovered through the investigation that the column with seismic reinforcement over the confining as well as mid-height regions gave superior blast performance. Dong et al. [16] analyzed the blast performance of 3000 mm long, 300 × 300 mm RC columns of compressive strength 40 MPa retrofitted with 0.17 mm thick wrappings of CFRP, AFRP, and GFRP under 8 kg TNT at 0.80 m standoff distance. The columns were reinforced with 4 bars of 20 mm diameter as longitudinal reinforcement of yield strength 450 MPa and transverse seismic reinforcement over the top and bottom regions. The study concluded that the column retrofitted with the CFRP wrapping over the entire column showed the finest performance. Rajkumar et al. [17] used different shapes of RC columns in this study to understand the effect of the blast. A column with

an 85 × 85 mm cross-section was selected for the study, with a height of 900 mm. The column was longitudinally reinforced by 8 bars of 3.2 mm diameter each, with 450 MPa yield strength, and it was laterally reinforced by 1.6 mm diameter, with the spacing of 100 mm and yield strength of 400 MPa. The width of the hexagonal, octagonal and radius of a circular column are obtained by equating its volume with the volume of the square. The study concluded that the circular column diminishes the effect of blast load more significantly as compared to the square, hexagonal, and octagonal RC column.

Yan et al. [18] performed experimental and numerical investigations on RC square columns of 150 × 150 mm cross-section with concrete of 30 MPa compressive strength reinforced with 4 bars of 12 mm diameter of yield strength 400 MPa and 6 mm diameter stirrups of yield strength 554 MPa at 180 mm spacing. The length of the column was 1700 mm. The columns were retrofitted with a CFRP sheet of thickness 2 mm applied (1) on both tension and compression faces, and (2) two sheets on the tension face and a single sheet on the compression face. The columns were examined under close-in explosion with TNT charge masses of 0.80, 1.00, and 1.40 kg TNT at scaled distances of 0.54, 0.40, and 0.45 m/kg$^{1/3}$. Results from the study reflected that the CFRP sheet ameliorated the blast performance of the column, and reduced the maximum and residual displacements with diminished spalling. It was discovered that on providing CFRP reinforcement on both faces of the column, diagonal shear damage escalated, which in turn shifted the damage mode from flexural to shear failure. Hu et al. [9] conducted a field test on RC columns of cross-section 200 × 200 mm and 2500 mm length in the concrete of compressive strength 50.16 MPa, consisting of 4 bars of 20 mm diameter of grade HRB335 (466.70 MPa) as longitudinal reinforcement and transverse reinforcement in the form of 10 mm diameter stirrups at 150 mm c/c of yield strength 483.50 MPa to examine the effect on the anti-blast performance of the columns applying 0.167 mm thick CFRP composite wrapping. Three different retrofitting schemes, namely, A type: single layer of longitudinal strips on middle 2100 mm length, B-type: longitudinal and transverse strips each with single layer on middle 2100 mm length, and C-type: three bands of transverse strips with double layers of 350 mm length each with 525 mm spacing between them were tried. The explosive employed was rock emulsion of 18.20 kg weight equivalent to 11.10 kg TNT at a scaled distance of 0.67 m/kg$^{1/3}$. It was deduced from the investigation results that the retrofitted column of Type-A performed best by increasing its residual axial load-carrying capacity (43%) with reference to the residual load-carrying capacity of the un-retrofitted column.

2 Numerical Modeling

A computer software package, ABAQUS/CAE 2019, has been employed in the study to investigate the blast performance of the 300 × 300 mm RC columns having a clear span of 3000 mm carrying an axial load of 950 kN. The longitudinal reinforcement in the column has been provided in the form of 4 bars of 25 mm diameter of yield

strength 500 MPa [15]. The compressive strength of the concrete is 30 MPa [15]. A total of 16 finite element models are developed. The first model (C-UR) is of conventional un-retrofitted RC column with lateral seismic reinforcement in the form of 10 mm diameter stirrups at 75 mm c/c over the top and bottom regions (600 mm) and 150 mm c/c over the remaining region. The first letter in the designation of column no. represents the square column (C); the second letter denotes either the un-retrofitted or retrofitted column (UR: un-retrofitted, and R: retrofitted); the third letter represents the retrofitting technique used (CF: CFRP wrappings, and CF + ST: wrappings with steel angles connecting with wide battens; T&B: over the top and bottom 600 mm regions; T, B&M: top, bottom, and middle regions; and EL: over the entire column); the first numeral describes the thickness of angles and battens; and the second numeral indicates the yield strength of angles and battens. The description of the models is given in Table 1. The concrete is discretized with the C3D8R explicit elements with a 10 mm seed size [19]. The re-bars are embedded in the concrete using the EMBEDDED_REGION constraint command. The wrappings, angles, and battens are tied with the column surfaces using the TIE_CONSTRAINT command [19]. The bottom of the column is assumed fixed, while no translational degree of freedom restraint in the direction of applied axial load at the top [15]. The thickness of the CFRP wrapping is 2 mm. Concrete has a tensile strength of 3 MPa, Young's modulus of 26.60 GPa, and Poisson's ratio of 0.20 [15]. The mass density, ultimate tensile strength, yield strength, Young's modulus, and Poisson's ratio of the steel reinforcement bars are 7850 kg/m^3, 545, 500 MPa, 210 GPa, and 0.30, respectively [15]. The properties of CFRP are taken from Phan-Vu et al. [20].

2.1 Explosion Loading

An explosion is defined as a prompt elevation of volume and dissemination of energy in a paramount form [21–23]. It is the result, not the cause, of a rapid expansion of gases that may occur from physical or mechanical change. Owing to any blast explosion, an abrupt oxidation reaction takes place, which releases a huge volume of energy in the form of light, heat, and sound for a short span of time [1, 2, 23]. Figure 1a reflects the pressure profile of a blast, which begins with the value of pressure as atmospheric pressure at one point. At a time t_A (time of arrival) the blast wave reaches the point of interest. At time t_A, explosive burst takes place and causes instant increase in the pressure, valued at P_i (peak overpressure), which takes place for a short stretch of time [3, 4, 23]. This peak pressure holds the highest amplitude in the entire blast episode history, which makes it consequential for use on the blast face [5, 21, 23]. The time period during which the value of pressure is more than the atmospheric pressure is called positive phase duration t_d [24–27]. After a short period of time, the time pressure substantially diminishes and causes the value of pressure to reach equal to the atmospheric pressure [6–8]. In due course, the value of pressure starts declining further and becomes lower than the atmospheric pressure, and starts generating vacuity, making the pressure negative. The duration where the

Table 1 Description of the models

Column ID	W	SA-B	W_P	B_P	Y_{SA-B} (MPa)	t_{SA-B} (mm)	t_W (mm)
C-UR	No	No	–	–	–	–	–
C-R (CF: T&B)	Yes	No	T&B	–	–	–	2
C-R (CF: T, B&M)	Yes	No	T,B&M	–	–	–	2
C-R (CF: EL)	Yes	No	EL	–	–	–	2
C-R (CF + ST5, 250: T&B)	Yes	Yes	T&B	T&B	250	5	2
C-R (CF + ST5, 250: T, B&M)	Yes	Yes	T,B&M	T,B&M	250	5	2
C-R (CF + ST5, 250: EL)	Yes	Yes	EL	T,B&M	250	5	2
C-R (CF + ST5, 300: T&B)	Yes	Yes	T&B	T&B	300	5	2
C-R (CF + ST5, 300: T, B&M)	Yes	Yes	T,B&M	T,B&M	300	5	2
C-R (CF + ST5, 300: EL)	Yes	Yes	EL	T,B&M	300	5	2
C-R (CF + ST8, 250: T&B)	Yes	Yes	T&B	T&B	250	8	2
C-R (CF + ST8, 250: T, B&M)	Yes	Yes	T,B&M	T,B&M	250	8	2
C-R (CF + ST8, 250: EL)	Yes	Yes	EL	T,B&M	250	8	2
C-R (CF + ST8, 300: T&B)	Yes	Yes	T&B	T&B	300	8	2
C-R (CF + ST8, 300: T, B&M)	Yes	Yes	T,B&M	T,B&M	300	8	2
C-R (CF + ST8, 300: EL)	Yes	Yes	EL	T,B&M	300	8	2

* *Note W*: wrapping of C-FRP; SA-B: steel angle-batten jacketing; W_P: placement of the wrapping; B_p: placement of steel battens; Y_{SA-B}: yield strength of steel angles and battens; t_{SA-B}: thickness of the angles and battens; t_W: thickness of the wrapping; T&B: top and bottom regions (600 mm); T,B&M: top, bottom, and mid-height regions; EL: entire length of the column (throughout)

value of pressure has been lesser than the atmospheric pressure is known as negative phase duration [27–37]. The time history of air blast wave pressure of the blast mechanism was explicated by Wu and Hao [23], who proposed an empirical formula to find the value of air blast wave parameters like arrival time, rising time, positive phase duration, etc.

$$t_A = 0.34 S^{1.4} W^{-0.2} / C_a \tag{1}$$

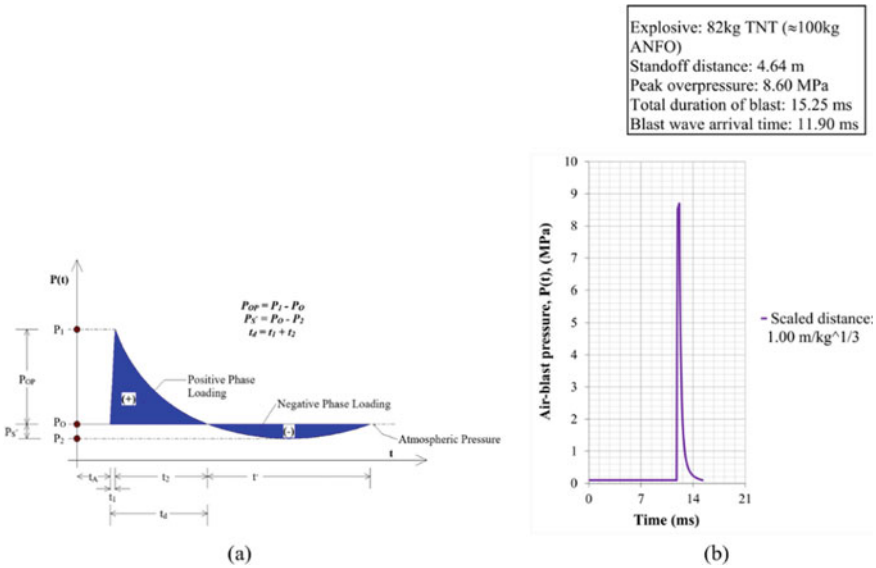

Fig. 1 **a** Idealized blast time history and **b** experimentally recorded history for 82 kg TNT load

Here, W = explosive charge (kg); S = detonation distance (m); C_a = speed of sound in air = 340 m/s; t_A = arrival time of blast wave (s).

$$t_1 = 0.0019\left(\frac{s}{w^{0.33}}\right)^{1.30} \tag{2}$$

$$t_2 = 0.0005 S^{0.72} W^{0.16} \tag{3}$$

$$t_d = t_1 + t_2 \tag{4}$$

$$P(t) = \left\{ \begin{array}{ll} P_a, & (0 \le t < t_A) \\ P_a + P_i\left(\frac{t}{t_i}\right), & (t_A \le t \le t_1) \\ P_a + P_i\left(1 - \frac{t-t_1}{t_2}\right) \cdot exp\left(-\frac{\xi(t-t_1)}{t_2}\right), & (t_1 \le t) \end{array} \right\} \tag{5}$$

Here, t_1 = rising time (sec); t_d = duration of positive phase (sec); t_2 = decreasing time (sec); P_a = atmospheric pressure = 0.1 MPa; P_i = peak overpressure (MPa); $\boldsymbol{\xi}$ = decay coefficient. The decay coefficient can be determined by using the following equations:

$$\boldsymbol{\xi} = \left\{ \begin{array}{ll} 3.02 P_i^{0.38} + 6.85 P_i^{0.79} \cdot \exp\left(-4.55 \frac{t-t_1}{t_2}\right), & (t_1 \le t \le t_d) \\ 1.96 P_i^{0.25} + 0.176 P_i \cdot \exp\left(-0.73 P_i^{-0.49} . \left(\frac{t-t_d}{t_2}\right)\right), & (t_d < t) \end{array} \right\} \tag{6}$$

for $P_i \leq 1.0$; and

$$\xi = \begin{Bmatrix} 1.62P_i^{0.30} + 5.13P_i^{0.28} \cdot \exp\left(-1.05P^{0.37}.\left(\frac{t-t_1}{t_2}\right)\right), \ (t_1 \leq t \leq t_d) \\ 0.74P_i^{0.17} + 2.71P_i^{0.28} \cdot \exp\left(-0.26P_i^{0.33}.\left(\frac{t-t_1}{t_2}\right)\right), \ (t_d < t) \end{Bmatrix} \quad (7)$$

for $1 < P_i \leq 100$. As per the IS4991:1968 [38], IS6922:1973 [39], TM5-1300(1990) [40], and ASCE/SEI 59-11 (2011) [41] guidelines of blast design, only the positive pressure phase can be used for the investigation and composition of the concrete structure. The guidelines have been framed because it has been discerned and culminated in multiple researches that the value of the negative (suction) pressure phase is much lesser than the atmospheric pressure, on account of which it adds no value in designing the structure [21–23, 38, 39, 41]. Furthermore, these values are also presumed to neglect the damage responses. Therefore, the negative pressure phase is forsaken in designing concrete structures, and only the positive phase is scrutinized and contemplated (Fig. 1b).

2.2 Concrete Damage Plasticity (CDP) Model

The CDP (concrete damage plasticity) is a continuum, plasticity-based damage model for concrete [19, 42]. The model is used for modeling concrete and quasi-brittle material that is utilized in different types of structures, including beams, columns, trusses, plates, solids, and more. The CDP model portrays and reflects the inelastic behavior of concrete, and functions on the isotropic damage elasticity postulation [19, 42–44]. The model assumes two concrete failure mechanisms: crushing of concrete in compression and cracking of concrete in tension. The damages or cracks caused in the fracturing process under the CDP model can be particularized by the plasticity model [3, 24, 42, 45]. The uniaxial tensile and compressive response of concrete is conjectured to be controlled by the damage plasticity, which is shown in Fig. 2 [19]. In uniaxial tension, the stress–strain response illustrates a linear relationship until the value of failure stress reaches (σ_{t0}). Beyond failure stress, micro-cracks are established, which are microscopically outlined with a stress–strain response [19, 25]. This further persuades strain localization in the concrete structure. In uniaxial compression, the response is linear until the value of the initial yield is (σ_{c0}). In the plastic region, the response is predominantly identified by stress handling, followed by strain-softening beyond the ultimate stress (σ_{cu}). These failure surfaces are controlled by two hardening variables, $\epsilon_c^{pl,h}$ (compressive equivalent plastic strain) and $\epsilon_t^{pl,h}$ (tensile equivalent plastic strain) [26, 27, 42]. The automatic function in ABAQUS/CAE converts the uniaxial stress–strain curve into stress versus inelastic strain curve [19]. The uniaxial compression and tensile reaction of concrete are reflected utilizing the statistical equations under compression and tensile loading in the CDP model [19].

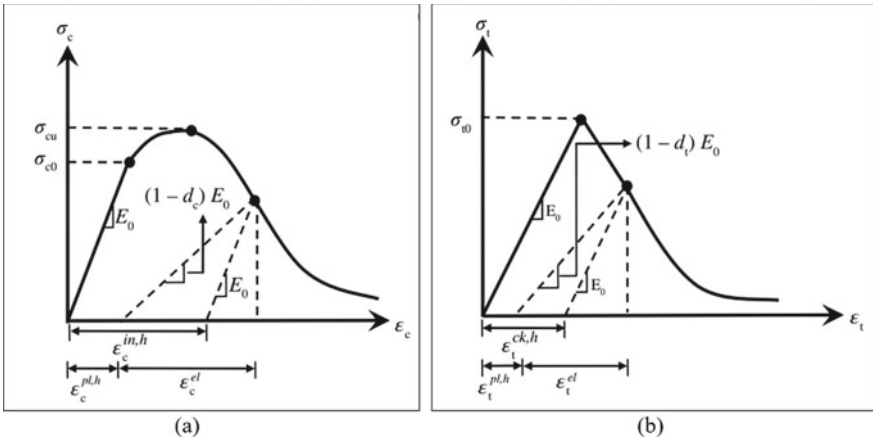

Fig. 2 Uniaxial loading condition for concrete response: **a** Compression and **b** tension

$$\sigma_c = (1 - d_c)E_0\left(\epsilon_c - \epsilon_c^{pl,h}\right) \tag{8}$$

Here, σ_c = nominal compressive stress (MPa), σ_{cu} = ultimate compressive stress (MPa), ϵ_c = compressive strain $\left(\epsilon_c^{pl,h} + \epsilon_c^{el}\right)$, $\epsilon_c^{pl,h}$ = compressive equivalent plastic strain, ϵ_c^{el} = elastic compressive strain

$$\sigma_t = (1 - d_t)E_0\left(\epsilon_t - \epsilon_t^{pl,h}\right) \tag{9}$$

Here, σ_t = nominal tensile stress (MPa), σ_{t0} = failure stress (MPa), ϵ_t = tensile strain $\left(\epsilon_t^{pl,h} + \epsilon_t^{el}\right)$, ϵ_t^{el} = elastic tensile strain. The model assumes that the reduction of the modulus of elasticity of the material can be expressed in terms of a scalar degradation variable, d as

$$E_a = \left(1 - d_{i=c,t}\right)E_0 \tag{10}$$

E_u = reduced modulus of elasticity (MPa), E_0 = initial elasticity modulus of concrete (MPa), d_c and d_t are two damage variables ranging from zero (undamaged material) to one (total loss of strength). A study conducted by Hafezolghorani et al. [42] concluded the values for the CDP model of M30 grade concrete, which included plasticity parameters, Young's modulus, and stress versus inelastic strain data, that have been used as input parameters in this investigation.

3 Results and Discussion

Maximum displacement and crack pattern of the column C-UR under the considered TNT load are found in close agreement with the experimental results [15] (Table 2 and Fig. 3). The maximum transverse displacement of the reference column C-UR is 34.68 mm and the damage dissipation energy is 769.67 J (Table 3). Intense crushing of the concrete has been observed near the top and bottom regions of the column as compared to the crushing in the mid region of the column (Fig. 7).

3.1 Application of CFRP Wrappings (2mm)

- The computed maximum transverse displacement of the columns C-R(CF:T&B), C-R(CF:T,B&M), and C-R(CF:EL) are 28.38 mm, 7.76 mm, and 3.97 mm, respectively, and the corresponding damage dissipation energy of these columns are found to be 692.70 J, 384.83 J, and 230.90 J (Table 3 and Figs. 4, 5 and 6). On using CFRP, maximum transverse displacement was reduced by 18.16, 77.62 and 88.55%, respectively, and damage dissipation energy was reduced by 10, 50 and 60% with respect to the reference column C-UR.

Table 2 Comparison of maximum transverse mid-height displacement (mm) of reference column C-UR

Kyei and Braimah, 2017 result	ABAQUS/CAE result	Percentage difference
36.00	34.68	3.67 (<4)

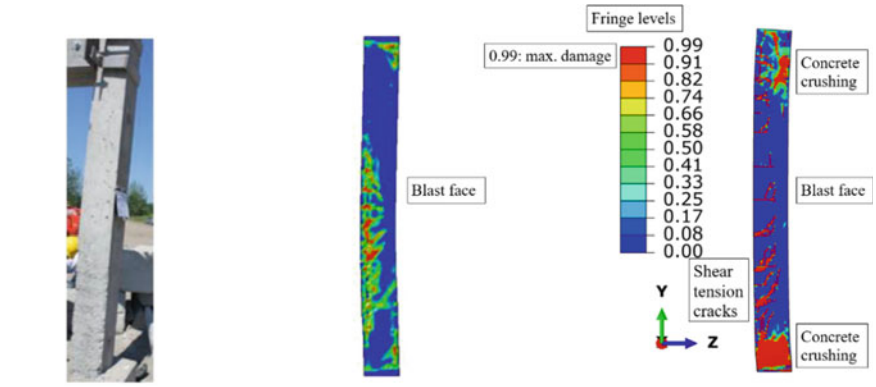

(a) Experimentally tested axially loaded RC column under 100 kg ANFO explosion (Kyei and Braimah, 2017)

(b) Tension Damage profile obtained using LS-DYNA under 100 kg ANFO explosion (Kyei and Braimah, 2017)

(c) Tension Damage profile obtained using ABAQUS/CAE under 100 kg ANFO explosion (Present study)

Fig. 3 Comparison of crack patterns of column C-UR

Table 3 Maximum transverse displacement and damage dissipation energy (DDE) of the columns

Column ID	Max. Disp. (mm)	DDE (J)
C-UR	34.68	769.67
C-R (CF: T&B)	28.38 ([a]18)	692.70 ([a]10)
C-R (CF: T, B&M)	7.76 ([a]78)	384.83 ([a]50)
C-R (CF: EL)	3.97 ([a]89)	230.90 ([a]70)
C-R (CF + ST5, 250: T&B)	26.11 ([a]25)	482.43 ([a]37)
C-R (CF + ST5, 250: T, B&M)	3.54 ([a]90)	225.14 ([a]71)
C-R (CF + ST5, 250: EL)	3.43 ([a]90)	155.39 ([a]80)
C-R (CF + ST5, 300: T&B)	25.07 ([a]26)	477.45 ([a]38)
C-R (CF + ST5, 300: T, B&M)	3.35 ([a]90)	204.12 ([a]73)
C-R (CF + ST5, 300: EL)	2.95 ([a]91)	154.16 ([a]80)
C-R (CF + ST8, 250: T&B)	23.59 ([a]32)	468.48 ([a]39)
C-R (CF + ST8, 250: T, B&M)	2.92 ([a]92)	190.52 ([a]75)
C-R (CF + ST8, 250: EL)	2.61 ([a]92)	147.50 ([a]81)
C-R (CF + ST8, 300: T&B)	22.5 ([a]35)	456.83 ([a]41)
C-R (CF + ST8, 300: T, B&M)	2.64 ([a]92)	145.73 ([a]81)
C-R (CF + ST8, 300: EL)	1.86 ([a]95)	129.75 ([a]83)

[a]Percentage decrease (%) w.r.t reference column C-UR

- The steel bars of the columns C-R(CF:T&B), C-R(CF:T, B&M), and C-R(CF:EL) facing the blast experience maximum compressive stress of 152.30, 94.10, and 55 MPa, respectively, while the bars on the tension side carry maximum stress 123.36, 63.15, and 12.66 MPa (Fig. 9).
- The maximum tensile stress in the stirrups reduces significantly in the regions wrapped by the CFRP (Fig. 9). The percentage reductions are found to be 7.78, 5.58 and 65.60% with respect to reference column C-UR.

3.2 CFRP Wrappings with Steel Angles and Wide Battens (5mm)

- Application of the steel angles and wide battens of thickness 5 mm diminishes the maximum transverse displacement of columns C-R (CF + ST5,250:T&B), C-R (CF + ST5,250:T,B&M) and C-R(CF + ST5,250:EL) by 8, 54, and 13.50%,

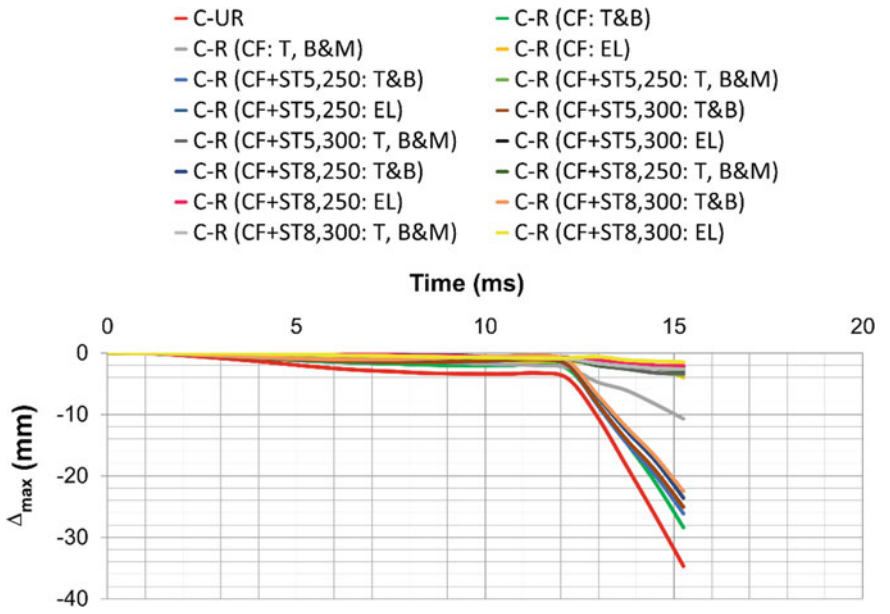

Fig. 4 Maximum displacement–time histories

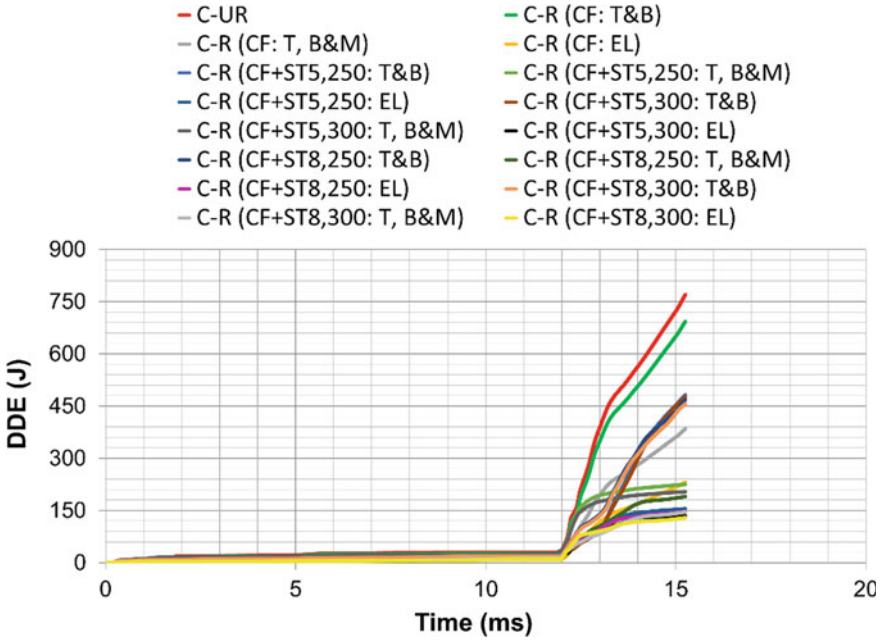

Fig. 5 Damage dissipation energy histories

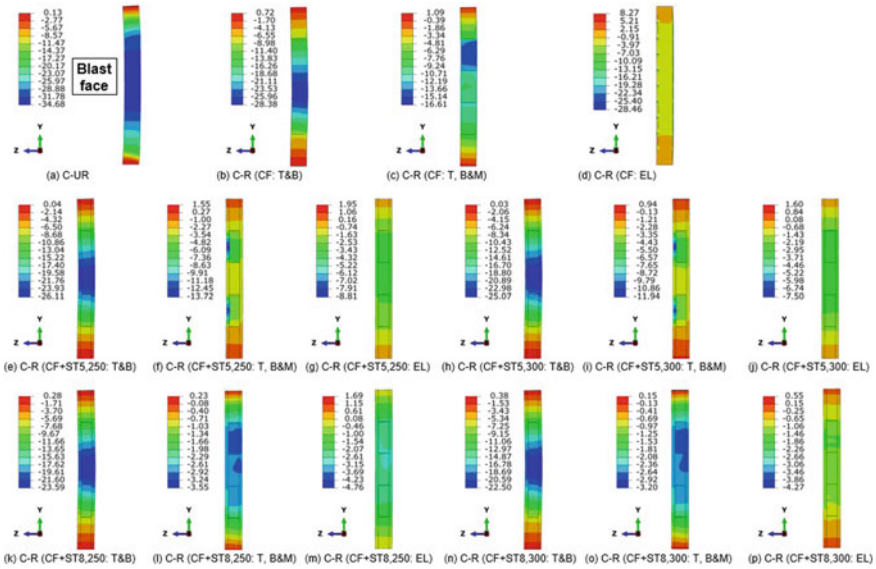

Fig. 6 Transverse Z-displacement (mm) of different FE models considered

respectively, with respect to columns C-R(CF:T&B), C-R(CF:T,B&M), and C-R(CF: EL) (Table 3 and Fig. 6).

- On increasing the yield strength (300 MPa) of angle and battens assembly, the stresses in the re-bars reduced but marginally (Table 4).
- CFRP dissipates energy and assembly of angle and battens imparts stiffness to the column.
- CFRP wrapping is found to be very effective to control the concrete crushing/cracking of the concrete, while the assembly of angles and battens control displacement (Figs. 7 and 8).

3.3 CFRP Wrappings with Steel Angles and Wide Battens (8 mm)

- Application of the assembly of the steel angles and wide battens of 8 mm thickness reduces the maximum transverse displacement of the column C-R(CF + ST8,250:T&B), C-R(CF + ST8,250:T,B&M), and C-R(CF + ST8,250:EL) by 9.65, 17.51, and 24%, respectively, with respect to the column C-R(CF + ST5,250:T&B), C-R(CF + ST5,250:T,B&M), and C-R(CF + ST5,250:EL) and decreases by 16.87%, 62.37%, and 34.25% with respect to the columns C-R (CF:T&B), C-R(CF:T,B&M), and C-R(CF:EL) (Table 3).

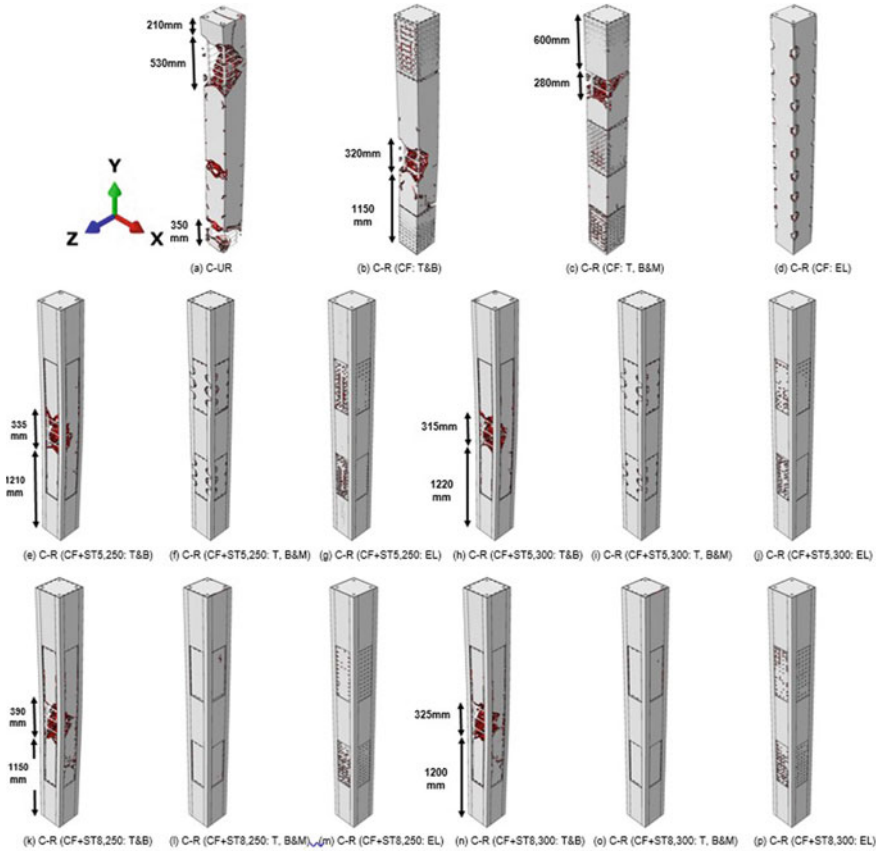

Fig. 7 Crushing of concrete of the columns (t = 15.25 ms) [**Note* Empty space in the figures shows the crushed concrete]

- Due to obvious reasons, a considered increase in the strength of the assembly from 250 to 300 MPa is not as effective as an increase in thickness of the assembly from 5 to 8 mm.
- Blast performance of the column C-R(CF + ST8,300:EL), i.e., retrofitted with the CFRP wrapping over the entire column, and steel angle section at the corners connected with battens of thickness 8 mm and yield strength 300 MPa is found to be the most superior with regards to concrete crushing and cracking (Figs. 4, 5, 6, 7, 8 and 9).

Table 4 Maximum principal stresses (MPa)

Column ID	Steel bars facing the explosion	Steel bars on the tension side	Stirrups
C-UR	−141.24	+ 108.54	+ 233.43
C-R (CF: T&B)	−152.30	+ 153.99	+ 215.25
C-R (CF: T, B&M)	−94.10	+ 89.36	+ 220.40
C-R (CF: EL)	−55.00	+ 23.93	+ 80.31
C-R (CF + ST5, 250: T&B)	−141.86	+ 148.76	+ 206.89
C-R (CF + ST5, 250: T, B&M)	−64.65	+ 68.76	+ 202.17
C-R (CF + ST5, 250: EL)	−52.68	+ 42.88	+ 61.99
C-R (CF + ST5, 300: T&B)	−134.33	+ 148.81	+ 205.44
C-R (CF + ST5, 300: T, B&M)	−63.81	+ 68.69	+ 201.19
C-R (CF + ST5, 300: EL)	−50.33	+ 34.45	+ 62.71
C-R (CF + ST8, 250: T&B)	−140.98	+ 97.77	+ 217.15
C-R (CF + ST8, 250: T, B&M)	−95.38	+ 85.71	+ 176.25
C-R (CF + ST8, 250: EL)	−48.53	+ 30.62	+ 57.00
C-R (CF + ST8, 300: T&B)	−137.95	+ 99.56	+ 218.32
C-R (CF + ST8, 300: T, B&M)	−96.02	+ 70.19	+ 153.19
C-R (CF + ST8, 300: EL)	−43.95	+ 12.77	+ 31.67

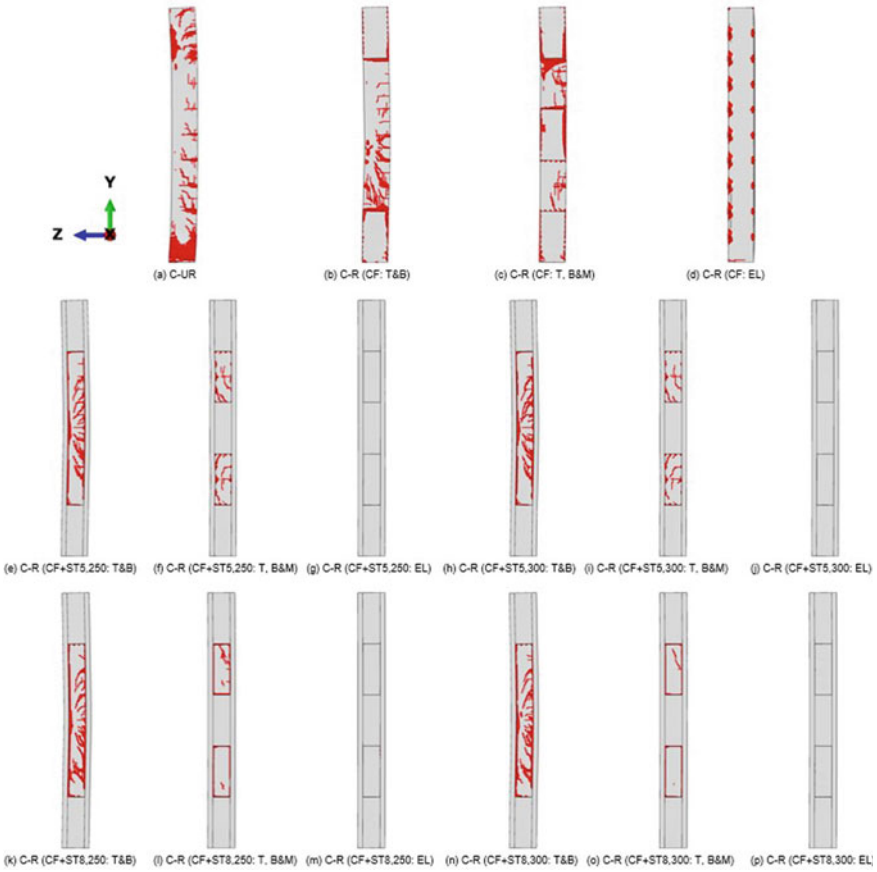

Fig. 8 Concrete spalling and cracking on the side face of the columns ($t = 15.25$ ms)

4 Conclusions

To improve the blast performance of the existing RC columns of square cross-section, researchers used different strengthening techniques. In the present work, the CFRP wrappings (2 mm) with steel angles connecting with wide battens with yield strength 250 and 300 MPa and thickness 5 and 8 mm are used to enhance the performance of the axially loaded RC columns with seismic reinforcement over the top and bottom regions (600 mm) subjected to the explosive loading of 82 kg TNT. The novel technique reported in this paper presents retrofitting of the exposed existing square RCC columns of the building likely to be more vulnerable to the threat of blast loading and their failure may destabilize the structure triggering a partial or catastrophic structural collapse. Results showed that the application of the wrapping over the entire column significantly improves the deflection response and damage resistance; however, the wrapping with steel angle and batten jacketing over the seismic confining regions

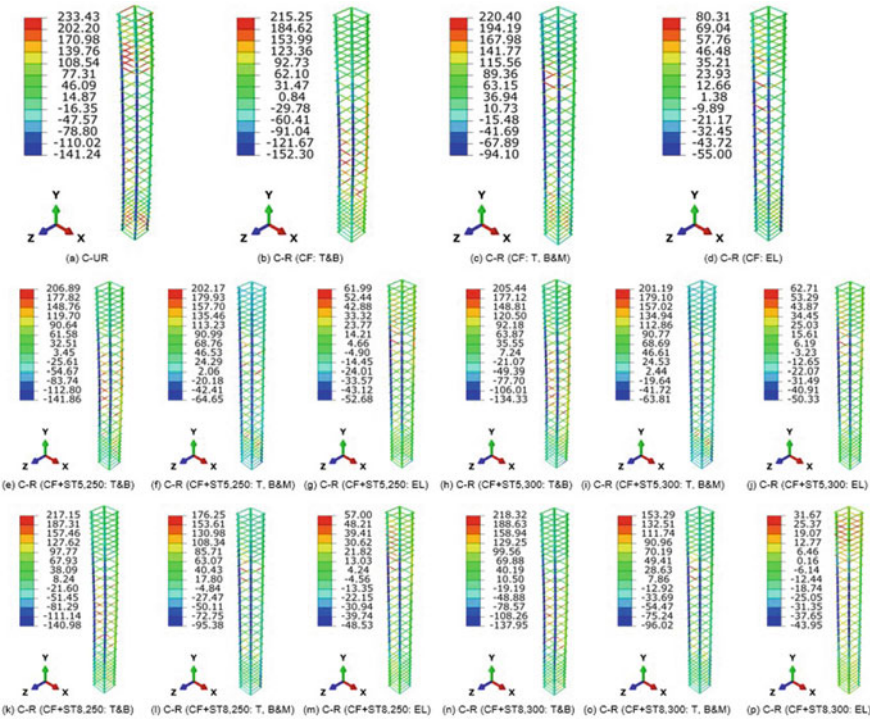

Fig. 9 Distribution of the principle stresses in the reinforcements of different column models considered ($t = 15.25$ ms)

and mid-height further ameliorates the blast performance of the column. Higher yield strength of the angle sections and battens are not found to be contributing to reducing the maximum displacement in comparison to the higher thickness of the angles and battens. It is concluded that the RC column retrofitted with 2 mm thick CFRP wrapping with steel assembly of thickness 8 mm and yield strength 300 MPa gives the most superior blast performance and makes the column almost blast-resistant against considered 82 kg TNT charge weight at scaled distance 1.0 m/kg$^{1/3}$.

References

1. Anas SM, Alam M, Umair M (2020) Performance of one-way composite reinforced concrete slabs under explosive-induced blast loading. In: 1st international conference on energetics, civil and agricultural engineering 2020, vol 614. ICECAE 2020, Tashkent, Uzbekistan. https://doi.org/10.1088/1755-1315/614/1/012094
2. Anas SM, Alam M, Umair M (2021) Experimental and numerical investigations on performance of reinforced concrete slabs under explosive-induced air-blast loading: a state-of-the-art review. Struct Elsevier 31:428–461. https://doi.org/10.1016/j.istruc.2021.01.102

3. Anas SM, Alam M, Umair M (2021) Performance of one-way concrete slabs reinforced with conventional and polymer re-bars under air-blast loading. In: Chandrasekaran S, Kumar S, Madhuri S (eds) Recent advances in structural engineering. Lecture notes in civil engineering, April 2021, vol 135. pp 179–191. https://doi.org/10.1007/978-981-33-6389-2_18
4. Anas SM, Ansari MdI, Alam M (2020) Performance of masonry heritage building under air-blast pressure without and with ground shock. Aust J Struct Eng 21(4):329–344. https://doi.org/10.1080/13287982.2020.1842581
5. Anas SM, Ansari MI, Alam M (2021) A study on existing masonry heritage building to explosive-induced blast loading and its response. Int J Struct Eng 11(4):387–412. https://www.inderscienceonline.com/doi/abs/10.1504/IJSTRUCTE.2021.118065
6. Anas SM, Alam M, Umair M (2022) Out-of-plane response of clay brick unreinforced and strengthened masonry walls under explosive-induced air-blast loading. In: Kolathayar S et al (eds) Resilient infrastructure, lecture notes in civil engineering 2022, vol 202. Springer, Singapore. https://doi.org/10.1007/978-981-16-6978-1_37
7. Anas SM, Alam M, Umair M (2022) Influence of charge locations on close-in air-blast response of pre-tensioned concrete U-girder. In: Kolathayar S et al (ed) Resilient infrastructure, lecture notes in civil engineering 2022, vol 202. Springer, Singapore. https://doi.org/10.1007/978-981-16-6978-1_40
8. Anas SM, Alam M (2021) Comparison of existing empirical equations for blast peak positive overpressure from spherical free air and hemispherical surface bursts. Iranian J Sci Technol Trans Civil Eng. https://doi.org/10.1007/s40996-021-00718-4
9. Hu Y, Chen L, Fang Q, Kong X, Shi Y, Cui J (2021) Study of CFRP retrofitted RC column under close-in explosion. Eng Struct 227
10. Ain UQ, Alam M, Anas SM (2022) Behavior of ordinary load bearing structure under distant large explosion, beirut scenario. In: Kolathayar S et al (eds) Resilient infrastructure, lecture notes in civil engineering 2022, vol 202. Springer, Singapore. https://doi.org/10.1007/978-981-16-6978-1_19
11. Heffernan P, Wight G (2008) Blast testing of CFRP and SRP strengthened RC columns. In: Structure under shock and impact. pp 95–104
12. Elsanadedy HM, Almusallam TH, Abbas H, Al-salloum YA, Alsayed SH (2011) Effect of blast loading on CFRP- Retrofitted RC column—a numerical study. Latin American J Solid and Struct 55–81
13. Burrell RP, Aoude H, Saatcioglu M (2014) Response of SFRC columns under Blast loads. J Struct Eng 04014209:1–15
14. Jacques E, Lloyd A, Imbeau P, Quek J (2015) GFRP-Retrofitting reinforced concrete columns subjected to Simulated Blast loading. J Struct Eng 04015028:1–13
15. Kyei C, Braimah A (2017) Effect of transverse reinforcement spacing on the response of reinforced concrete columns subjected to blast loading. Eng Struct 142:148–164
16. Dong J, Zhao J, Zhang D (2020) Numerical evaluation of reinforced concrete columns retrofitted with FRP for blast mitigation. Adv Civil Eng
17. Rajkumar D, Senthil R, Kumar BBM, Gomathi KA, Velan SM (2020) Numerical study on parametric analysis of reinforced concrete column under blast loading. J Perform Constr Facil 04019102:1–12
18. Yan J, Liu Y, Xu Z, Li Z, Huang F (2020) Experimental and numerical analysis of CFRP strengthened RC Column subjected to close-in blast loading. Int J Impact Eng 146
19. ABAQUS/CAE FEA program (2017) Concrete-damaged plasticity model, explicit solver, three-dimension solid element library. ABAQUS DS-SIMULIA User Manual
20. Phan-Vu P, Tran TD, Pham MT, Dang DT, Ngo-Huu C, Nguyen-Minh L (2021) Distinguished bond behaviour of CFRP sheets in unbonded post-tensioned rein-forced concrete beams versus single-lap shear tests. Eng Struct Elsevier 234
21. Goel DM, Matsagar AV (2014) Blast-resistant design of structures. Practice Period Struct Design Construct ASCE 19(2):1–9
22. Hao H, Hao Y, Li J, Chen W (2016) Review of the current practices in blast resistant analysis and design of concrete structures. Adv Struct Eng 19(8):1193–1223

23. Wu C, Hao H (2005) Modelling of simultaneous ground shock and air blast pressure on nearby structures from surface explosions. Int J Impact Eng 31:699–717
24. Ahmadi E, Alam M, Anas SM (2022) Blast performance of RCC slab and influence of its design parameters. In: Kolathayar S et al. (eds) Resilient infrastructure, lecture notes in civil engineering 2022, vol 202. Springer, Singapore. https://doi.org/10.1007/978-981-16-6978-1_31
25. Anas SM, Alam M (2021) Air-blast response of free-standing: (1) Unreinforced Brick Masonry Wall, (2) Cavity RC Wall, (3) RC Walls with (i) Bricks, (ii) Sand, in the cavity: a macro-modeling approach. In: Marano GC, Ray Chaudhuri S, Unni Kartha G, Kavitha PE, Prasad R, Achison RJ (eds) Proceedings of SECON'21. SECON2021. Lecture notes in civil engineering, vol 171. Springer, Cham, pp 921–930. https://doi.org/10.1007/978-981-33-6389-2_18
26. Anas SM, Alam M, Umair M (2021) Performance of on-ground double-roof RCC shelter with energy absorption layers under close-in air-blast loading. Asian J Civil Eng. https://doi.org/10.1007/s42107-021-00395-8
27. Anas SM, Alam M, Umair M (2021) Air-blast and ground shockwave parameters, shallow underground blasting, on the ground and buried shallow underground blast-resistant shelters: a review. Int J Protect Struct. https://doi.org/10.1177/20414196211048910
28. Anas SM, Alam M (2022) Performance of simply supported concrete beams reinforced with high-strength polymer re-bars under blast-induced impulsive loading. Int J Struct Eng 12(1):62–76. https://www.inderscienceonline.com/doi/abs/10.1504/IJSTRUCTE.2022.119289
29. Anas SM, Alam M, Umair M (2022) Strengthening of braced unreinforced brick masonry wall with (i) C-FRP wrapping and (ii) steel angle-strip system under blast loading. Materials Today: Proceedings. https://doi.org/10.1016/j.matpr.2022.01.335
30. Anas SM, Shariq M, Alam M (2022) Performance of axially loaded square RC columns with single/double confinement layer(s) and strengthened with C-FRP wrapping under close-in blast. Materials Today: Proceedings. https://doi.org/10.1016/j.matpr.2022.01.275
31. Anas SM, Alam M, Umair M (2022) Effect of design strength parameters of conventional two-way singly reinforced concrete slab under concentric impact loading. Materials Today: Proceedings. https://doi.org/10.1016/j.matpr.2022.02.441
32. Anas SM, Alam M (2022) Performance of brick-filled reinforced concrete composite wall strengthened with C-FRP laminate(s) under blast loading. Materials Today: Proceedings. https://doi.org/10.1016/j.matpr.2022.03.162
33. Shariq M, Alam M, Husain A, Anas SM (2022) Blast performance enhancement of RC square column jacketed with steel angle sections and wide battens. Asian J Civil Eng, Springer (Article in press)
34. Tahzeeb R, Alam M, Muddassir SM (2022) A comparative performance of columns: reinforced concrete composite and composite with partial C-FRP wrapping under contact blast. Materials Today: Proceedings. https://doi.org/10.1016/j.matpr.2022.03.367
35. Anas SM, Shariq M, Alam M, Umair M (2022) Evaluation of critical damage location of contact blast on conventionally reinforced one-way square concrete slab applying CEL-FEM blast modeling technique. Int J Protective Struct (Article in press)
36. Anas SM, Alam M, Umair M (2022) Performance based strengthening with concrete protective coatings on braced unreinforced masonry wall subjected to close-in explosion. Materials Today: Proceedings, Elsevier (Article in press)
37. Anas SM, Alam M, Shariq M, Umair M (2022) Damage response of conventionally reinforced two-way spanning concrete slab under eccentric impacting drop weight loading. Defence Technology (Article in press)
38. IS 4991 (1968) Criteria for blast resistant design of structures for explosions above ground. Bureau of Indian Standard, New Delhi, India
39. IS 6922 (1973) Criteria for safety and design of structures subjected to underground blasts. Bureau of Indian Standards, New Delhi, India
40. TM 5–1300(1990) Structures to resist the effect of accidental explosions. Technical manual, Joint Department of the Army, the Navy, and the Air Force, US

41. ASCE/SEI 59–11(2011) Blast protection of buildings. American Society of Civil Engineers, U.S.
42. Hafezolghorani M, Hejazi F, Vaghei R, Saleh M, Karimzade K (2017) Simplified damage plasticity model for concrete. Struct Eng Int 68–78
43. Jahami A, Temsah Y, Khatib J (2019) The efficiency of using CFRP as a strengthening technique for reinforced concrete beams subjected to blast loading. Int J Adv Struct Eng
44. Lee J, Shin H, Min K, Yoon (2018) Flexural assessment of blast-damaged RC beams retrofitted with CFRP sheet and steel fibre. Int J Polym Sci
45. Ye L, Yue Q, Zhao S, Li Q (2002) Shear strength of reinforced concrete columns strengthened with carbon fibre reinforced plastic sheet. J Struct Eng 1527–1534

Simulation Modeling of Impact of Multi-class Heavy Vehicles on Traffic Flow Characteristics of Multi-lane Highways Under Mixed Traffic Conditions Using VISSIM Software

K. R. Kamala, Vidya Rajesh, Sandeep Singh, and P. Sharmila

Abstract The heavy vehicle's interactivity with the remaining classes of vehicles in the traffic stream is constantly rising and their impact becoming pronounced day by day. Unlike other vehicle categories, the heavy vehicle's operational characteristics vary widely and their impact on the traffic flow is high. The impact of heavy vehicles (HVs) on the traffic flow is high due to their larger dimensions and different operational capability compared to other classes of vehicles. The lane-changing and overtaking behavior of the rear vehicles to the HVs are more frequent, which raises safety concerns. Various studies are undertaken continuously to study their influence on the mixed traffic flow condition. Our study is aimed at analyzing the heavy vehicle's influence on traffic flow speed and capacity of a highway section using simulation analysis with VISSIM software. The traffic flow data of National Highway 83 was collected using the Transportable Infra-Red Traffic Logger (TIRTL) for a period of 24 h. A base model was created using VISSIM to replicate the field conditions. Four classes of heavy vehicles were taken for the study purpose. Macroscopic fundamental diagrams (MFDs) were used to analyze the before and after flow at the arrival of HVs. Statistical analyses were done to validate the model and arrive at the results. The field and simulation results were compared. Significant impacts were observed in the after characteristics compared to before characteristics of the traffic stream at the arrival of HVs. Few strategies were recommended to regulate and control the operations of HVs.

Keywords Heavy vehicles · Mixed traffic flow · VISSIM software · Macroscopic fundamental diagrams

K. R. Kamala · V. Rajesh (✉)
School of Civil Engineering, SASTRA DEEMED to be University, Thanjavur 613401, India
e-mail: vidyarajesh123@gmail.com

S. Singh · P. Sharmila
Department of Civil Engineering, National Institute of Technology, Tiruchirappalli, India

L. Nandagiri et al. (eds.), *Recent Advances in Civil Engineering*, Lecture Notes in Civil Engineering 256, https://doi.org/10.1007/978-981-19-1862-9_22

1 Introduction

Traffic on Indian roads is highly mixed in nature with wide variations in the static and dynamic characteristics of vehicles [1]. Among the different classes of vehicles, the interactions of the commercial vehicles have a greater influence on the characteristics of traffic flow on a highway section [2]. We see that there is a rapid growth in the multi-class heavy vehicles (HVs) which causes a hindrance to the smooth traffic flow. Although HVs comprise a small proportion of traffic stream, they can have the potential impact on macroscopic and microscopic traffic flow characteristics. It also affects the lane-changing behavior of other classes of vehicles greatly. The safety concerns during overtaking of HVs and other vehicles by HVs are high [3]. The traffic parameters such as speed, flow, and density of the different classes of heavy commercial vehicles are calculated by considering the average of before passing vehicles and after passing vehicles. Heavy vehicles' frequent interaction with other vehicles leads to a decline in the flow and speed, eventually causing traffic breakdown [4]. Additionally, the abreast driving behavior of HVs during lane-changing and overtaking has been a concern of safety being unaddressed for a long time [5]. There is an immediate need to address the issues related to the operation and management of HVs on highways to deal with the traffic conditions in this new paradigm. It is necessary to fully assess the impacts on the parameters that are influenced by the multi-class HVs for effective and efficient implementation of the designed strategies. In this project, we aimed in finding the impact of the heavy commercial vehicles on the traffic speed and capacity of the vehicles on the highways using a simulation of a model created with VISSIM software. We classified heavy vehicles into different groups based on Indian conditions and codes. The variation in the volume of the impact of those groups with respect to one another is being examined. Our objective is to develop a simulation model to predict the multi-class heavy vehicle's influence on characteristics of traffic flow using VISSIM software and to validate the developed micro-simulation model.

2 Literature Review

2.1 Heavy Commercial Vehicles: Following Behavior and Interactions with Other Class Vehicles

Majid Sarvi [2] discussed the following behavior of the heavy commercial vehicles and their comparison with the passenger car, and the effect of heavy commercial vehicles on the capacity and overall performance of the congested freeway sections. A detailed trajectory analysis has been carried out for analyzing the following behavior of 120 heavy vehicles and to understand their following behavior mechanism. Passenger cars were found to travel back of heavy vehicles. Heavy vehicles adopt longer time and distance headways when following the other vehicles

compared to the car-following-car situation. The throughput of the freeway section is reduced and headway tends to be more because of the influence of heavy vehicles. Thus, by impacting the flow negatively and bringing up safety concerns, they make it inevitable to address and manage their interaction with the traffic flow, especially during congested flow conditions.

2.1.1 Operational Characteristics

The physical and operational characteristics of HVs vary significantly from other classes of vehicles. They require more time to start and stop, i.e., for acceleration and deceleration with respect to their weight and dimension than other classes. This affects the speed and flow of the traffic in a highway section, thereby rendering it difficult to achieve its design capacity. Bokare and Maurya [6] analyzed the acceleration and deceleration behavior of heavy vehicles. The acceleration–deceleration (A/D) distance and A/D time were observed to be directly proportional to the maximum speed of the vehicle. The acceleration values decreased with an increase in speed, thereby giving a negative exponential relation. The deceleration values increased with a decrease in speed after reaching a maximum value at critical speed giving rise to a dual regime model. Thus, under high speeds, it is more likely to cause deadly accidents while at low velocities it affects the total throughput of the highway section.

2.1.2 Lane-Changing Behaviour and Safety Concerns

Moridpour et al. [5] examined the average time taken and lane-changing maneuvres in a highway lane under heavy traffic conditions. The HVs maintained constant speed on a whole and they were slower than the other vehicles in the stream. The front and rear gaps of HV were more compared to any other vehicle due to various factors like the visibility of drivers (of both truck and rear vehicle), safety concerns, etc. These factors increased the average time taken to traverse a highway section. The lane-changing behavior was more frequent when the number of HVs increased in the lane and under higher traffic densities, potentially increasing the number of accidents and decreasing road safety.

2.1.3 Influence of HVs on Traffic Stream

Pokulwaret al. [7] studied the movement of heavy vehicles in the urban roads using video filming technique. They found three factors contributing to the impact of heavy vehicles on the roads like size, operating capabilities of Heavy vehicles, the physical impact on the nearby cars and the psychological effect on the drivers of those cars. In the traffic stream when the heavy vehicles comes in contact with smaller dimension vehicles it affects the traffic flow, speed, travel time and density. Due to this when the heavy vehicles travel with slow speed there is a formation of queue on the back

of heavy vehicles thereby decreasing the lane capacity. They found some similarities between free-flow and congested traffic flow concerning heavy vehicles and found that heavy vehicles are responsible for congestion and other complications on the urban roads often. Gao et al. [8] controlled the rate of mixing of large vehicles in the traffic stream. The statistical analysis revealed that they have a negative logarithmic linear correlation. Their traffic flow influence is more as volume increases.

2.1.4 Passenger Car Units versus Volume–Capacity Ratio

Bains et al. [9] modeled traffic flow on Indian expressways using the micro-simulation model, VISSIM by evaluating passenger car units (PCUs) of different vehicle categories at different volume levels. They evaluated the capacity of expressways and studied the effect of vehicle composition on PCU values. Patil et al. [10] studied the vehicle composition and analyzed the capacity of the highways. They too assessed that the PCU of different vehicle classes varied with the volume for different flow values. The dynamic nature of the PCU values gave more accurate results compared to the assumption of static values for PCUs. They too found out that the PCU values decreased for a vehicle type when their proportion increased in the traffic stream. Kumar and Agarwal [11] estimated the capacity of a six-lane highway using the VISSIM software. The PCU values decreased for all the vehicle types with the increase in the V/C ratio. By developing a relationship based on the speed, flow, and area occupancy, they proposed a generalized equation for determining mixed-flow capacity.

2.1.5 Calibration of VISSIM and Analysis

Siddharth and Ramadurai [12] used sensitivity analyses to find the VISSIM parameters that affected the driver behavior under Indian heterogeneous traffic conditions. They calibrated the traffic model using the Visual C++ COM interface of VISSIM software (automatic calibration). ANOVA and the elementary effects method were used in the sensitivity analysis. The optimal combination of sensitive parameters during calibration was found using a genetic algorithm.

3 Methodology

Based on the availability of traffic data, we collected the raw data of the traffic streams in National Highway 83 (Trichy–Thanjavur Highway) in Tamil Nadu which was taken near NIT Trichy. The study area was chosen such that the instrument (TIRTL) used to get the traffic data was placed and operated without any interruption either to the traffic flow or to the instrument itself.

3.1 Data Collection

Data of the lane traffic was collected using IR sensor-based instrument, Transportable Infrared Traffic Logger (TIRTL). The TIRTL consists of two electronic devices, namely, the transmitter and receiver were placed on either side of the roadway and two infrared light waves pass from the transmitter to the receiver continuously. The receiver records the time whenever the tires of the vehicle block and unblock these beams. Using these time and distance between the two beams, the speed of the vehicle and other parameters are calculated. Thus, it was set up across the lane under study and 24 h of traffic data was collected. TIRTL is connected to the system which records and interprets the data automatically and we got the output file from the system in the Excel format. The raw data consists of various parameters, like time, lane, average speed, heading direction, headway, spacing, clearance, class of vehicle, etc. For more details on the data collection, the studies by Singh et al. [13–15] may be referred.

3.2 Data Extraction

Commercial vehicles can be classified into different categories based on their gross vehicle weight (GVW). The vehicle classes taken for the study purpose in our project are:

(1) Heavy commercial vehicles (HCVs)
(2) Medium commercial vehicles (MCVs)
(3) Small commercial vehicles (SCVs) and light commercial vehicles (LCVs)

Their GVW ranges between 7.5 metric tons and below for SCV and LCVs, 7.5 and 16.2 metric tons for MCVs and 16.2 metric tons and above for HCVs. The data needed for the further project is extracted from the raw data file. The data of four different classes of commercial vehicles were separated from other classes of vehicles. HCV, MCV, LCV and SCV constituted 3.25%, 13.24% and 8.19% (LCV and SCV combined) in NH 83. The average speed and the count of the vehicles before and after 1 min of the arrival of HVs were calculated.

3.3 Development of Macroscopic Fundamental Diagrams

The macroscopic fundamental diagrams (MFDs) are diagrams that give the relation between traffic flow (vehicles/h), traffic density (vehicles/km), and velocity (km/h). This is used to analyze the behavior of traffic flow under various conditions like free flow and congested situations. Figure 1 shows the graphical representation of the relation between speed, density, and flow. Thus, the MFDs were drawn using the extracted dataset. The extracted raw data was refined by manually removing the

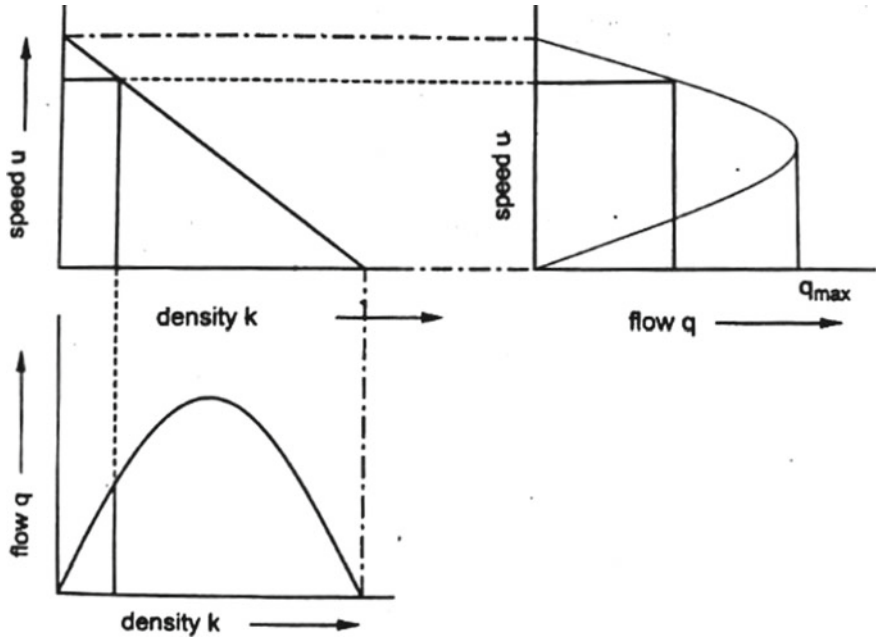

Fig. 1 Fundamental diagram of traffic flow

extremities. Speed–flow–density plots were established for the refined dataset. Flow is obtained from the count value obtained for 1 min and is converted to get the flow per hour. The density is obtained by dividing the flow by the average speed of the flow. They are obtained for all the classes under study with respect to their before and after characteristics. These values were used to get the relation in the form of MFDs. The speed–density (v–k) plot was represented by a linear function while speed–flow (v–q) and flow–density (q–k) plots were represented by a polynomial function of order 2. This is the first and most simple traffic stream model proposed by Greenshield. Eq. (1) defines the maximum flow given by the Greenshield equation.

$$Q_{\max} = \left(K_j \times V_f\right)/4 \tag{1}$$

where K_j is the jam density, V_f is the free flow velocity, and $Q_{\max}$ is the maximum capacity of a section.

The free flow velocity is obtained from the statistical software EasyFit. EasyFit is simulation software used for analyzing the statistical data and it provides us with the probabilistic distributions for the data sample. The 98th percentile value of the cumulative distribution of the speed data of any section is taken to be the maximum free flow speed of that section under the given conditions which is obtained using that software.

The jam density is obtained from the equations formed as a result of establishing Greenshield relation between the speed and density in the MFD graph. It is obtained under the condition of jamming, i.e., zero velocity. Thus, the linear relationship gives the jam density values. Hence, the maximum capacity is obtained by substituting the above-obtained values in the Greenshield equation, thereby giving capacity values to find the impact of various classes of HVs. Thus, the statistical analysis using the data obtained from the field is carried out which was compared with simulation results later.

3.4 Modeling in VISSIM

The raw traffic data we obtained consists of 16 vehicle types on the whole from which the heavy vehicles were categorized into four groups based on Indian standards. The different vehicle types observed were two-wheelers, three-wheelers, bicycles, HCV-articulated trucks, HCV rigid trucks, LCV, LMV, MAV four-axle articulated trucks, MAV four-axle rigid trucks, MAV five-axle articulated trucks, MAV five-axle rigid trucks, MAV six-axle articulated trucks, MCV, SCV, Tractor and Tractor with trailer. The traffic data had both peak and low flow periods. From the 24 h data, the peak flow period between 9:00 and 10:00 AM was taken for the hourly design flow to create a basic model using VISSIM software. PTV VISSIM [16] is microscopic multi-modal traffic flow simulation software, which helps in reproducing real-world conditions in traffic simulation.

The link was modeled over a segment of National Highway 83 near NIT Trichy (from where the data was recorded) using Google Maps access. The lane was designed over a plain terrain and the stretch was assumed to be straight without curves or slopes.

A single link was drawn for a stretch of 1000 m with two lanes for we have one traffic direction data, i.e., data of traffic flowing from Trichy to Thanjavur.

The different types of vehicles observed in the flow data were inserted for the modeling. Relative vehicle compositions were calculated with respect to their composition in the traffic for that hour which is internally evaluated to get the absolute percentage values for each category. The vehicle inputs were defined for the link, i.e., the direction in which the vehicle enters the link and the desired vehicle composition is added as per our need. The volume of the flow was taken to be the peak hour flow to get more efficient results.

The cumulative distribution function of the average speed data of the traffic stream was drawn using EasyFit statistical software for all the vehicle classes. EasyFit is a data-analyzing software used for basic probabilistic and statistical analyses. It handles large datasets and helps in comparing various predictive models of the same dataset. It helps in fitting a large number of distributions to our dataset and thereby enables us to choose the best fit. The 15th and 85th percentile of the cumulative distribution of speed data were taken to be the minimum and maximum speed limits for each vehicle category, which are then given as input for the different vehicles.

- Different vehicle types are grouped under the same class if they incorporate similar physical and driver behavior characteristics. There are six default classes of vehicles in VISSIM. In our vehicle categories, commercial vehicles were grouped under trucks, a class for the three-wheeler was added and others were divided accordingly.
- When the needed vehicle models are not available in the VISSIM directory, the heavy vehicle models (3D models) were downloaded and added to the types based on the physical characteristics of the vehicle. The average values of the dimensions were taken to create each model.
- Deceleration, car-following model, lane-changing behaviors, lateral behavior, etc. were given as per the Indian conditions. Wiedemann 74 model was used for the car following model which is more suitable for urban roads.
- The acceleration behavior of the various classes of vehicles was given based on the previous study works and analyses that incorporated Indian mixed traffic conditions.
- The data collection points were taken on both ends and middle of the link to get the evaluation results.
- Thus, the basic model was created by giving all the inputs mentioned above for every category of the vehicle in the traffic stream.

3.5 Calibration and Multi-run Simulation of the Model

The model was calibrated to Indian traffic conditions based on the previous research works and reference papers and it was checked with the field data to replicate the field conditions. A simulation was run six times, with each run lasting for 3600 s (1 h duration) for any hourly data under consideration. The minimum number of runs recommended is six for reliable results. Different random speed values were adopted for every simulation run of the multi-run simulation. Figure 2 shows a sample image of the running simulation.

3.6 Analysis of Impact of Heavy Vehicles

Thus, from the results the peak hour model (basic model) was validated after much iteration of the input data. Once after the validation, the same basic model was used to get the results of all the other hours. The simulation was run for all the 24 h data using the validated base model. The vehicle composition and relative flow of the vehicles were changed for each hour based on the field data. From the 24 h data we got, the relative proportions of the heavy vehicles under study were found which was comparable with the field data.

(1) Heavy commercial vehicles (HCV): 2.95%
(2) Medium commercial vehicles (MCV): 13.32%

Fig. 2 An image of running simulation

(3) Light and small commercial vehicles (LCV and SCV): 8.03%

The statistical analysis of the simulated data was done using macroscopic fundamental diagrams (speed–density plot, speed–flow plot, and flow–density plot) and was compared with the plots of field data.

4 Statistical Analysis

The empirical analysis is done with the raw data obtained directly from the field. The Greenshields parameters (free flow speed, jam density, and maximum capacity) are found from the MFDs and are evaluated to get the results. The free flow speed before and after passing of the heavy vehicles was found using EasyFit software. The cumulative distribution function of the speed data before and after the arrival of HVs is obtained and the 98th percentile value of this distribution is considered as the free flow speed, before and after the arrival of HVs. The average speeds (of different vehicles) of the traffic stream fed in the software to get the 98th percentile value and is taken to be the before free flow speed with which a vehicle can travel without hindrance from any class of HVs or other vehicles. The extracted after speeds of the different heavy vehicle classes were given as input to get the free flow speed after the arrival of HVs. There was a significant reduction observed in the free flow speed between the different before and after speeds. The MFDs were drawn in the Excel

sheets for all the classes in highway data to get various relations between speed, density, and flow using Greenshield theory.

From the study, significant reductions were observed in the traffic capacity of the lane which is under study. Heavy commercial vehicles (HCVs) were found to have more impact on the macroscopic traffic behavior, i.e., they have highly reduced the traffic capacity of a section compared to other commercial vehicles like LCVs and MCVs with respect to their large dimensions. The impact of the vehicles understudy in their reducing order is HCV > MCV > LCV/SCV. The reduction in traffic capacity of NH83 for HCV, MCV, and LCV/SCV is 31.84%, 25.57%, and 21.22%, respectively. A reduction in the density is observed, which resulted in the reduction of capacity. The macroscopic fundamental diagrams (MFDs) of HCV (see Fig. 3 a–c), MCV (see Fig. 4a–c), and LCV/SCV (see Fig. 5 a–c) are shown. Table 1 gives the speed and capacity reductions of the empirical analysis.

5 Simulation Analysis

The simulation analysis is done with the results obtained from the simulation of the basic model after its validation. The process is similar to the empirical analysis once the results are extracted from the validated model. The results were obtained from the basic model for peak hour data. Six runs wre conducted for every class of a vehicle and its average is taken as the final value. The speed data was checked for the replication of the field conditions using a statistical test called paired t-test for validation. The actual speeds from the field data and the average speeds obtained from simulation are compared and their deviation is observed from descriptive statistics analysis.

5.1 Validation of the Basic Model

Simulated speed values were compared with the field data using paired t-test to validate the model. The paired t-test is a statistical procedure to determine if the mean difference between two sets of observations is zero. This test has two competing hypotheses—null hypothesis and alternative hypothesis. If the p-value $\leq \alpha$, the difference between the means is statistically significant (reject the null hypothesis). If the p-value $> \alpha$, the difference between the means is not statistically significant (fails to reject the null hypothesis).

We assumed an α-value of 0.05 and the p-values were found to be greater than 0.05. The paired t-test yielded the t-statistic value of 0.807. The t-statistic–critical value for a significance level of 0.05 for 13 degrees of freedom is 2.16. Our t-statistic value is less than the t-critical value, which implies that there is no significant difference between the observed and simulated speeds. Thus, our basic model was validated which was further used for running the simulation for the remaining 23 h data. The

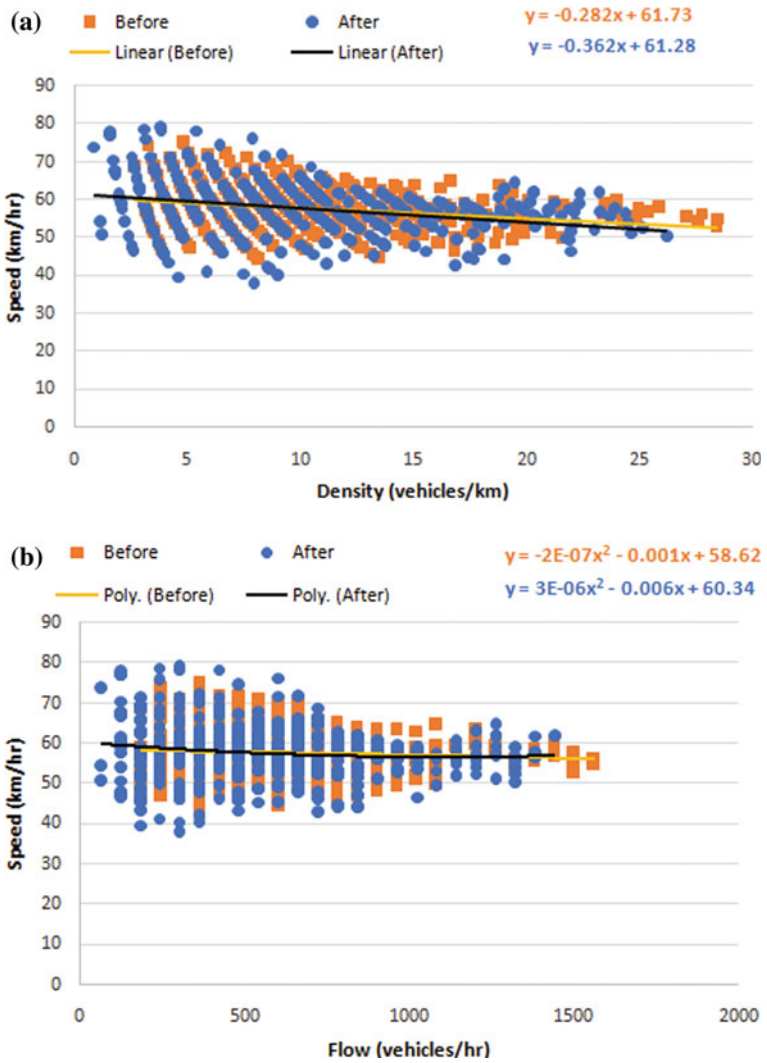

Fig. 3 **a** Speed–density plot of HCV. **b** Speed–flow plot of HCV

actual speeds from the field data and the average speeds obtained from simulation are compared and their deviation is observed from descriptive statistics analysis. The 95% confidence interval was found to be ± 1.608. Table 2 gives the paired t-test results performed between field and simulation speeds and Table 3 gives their descriptive statistics. The tests were done using MS Excel.

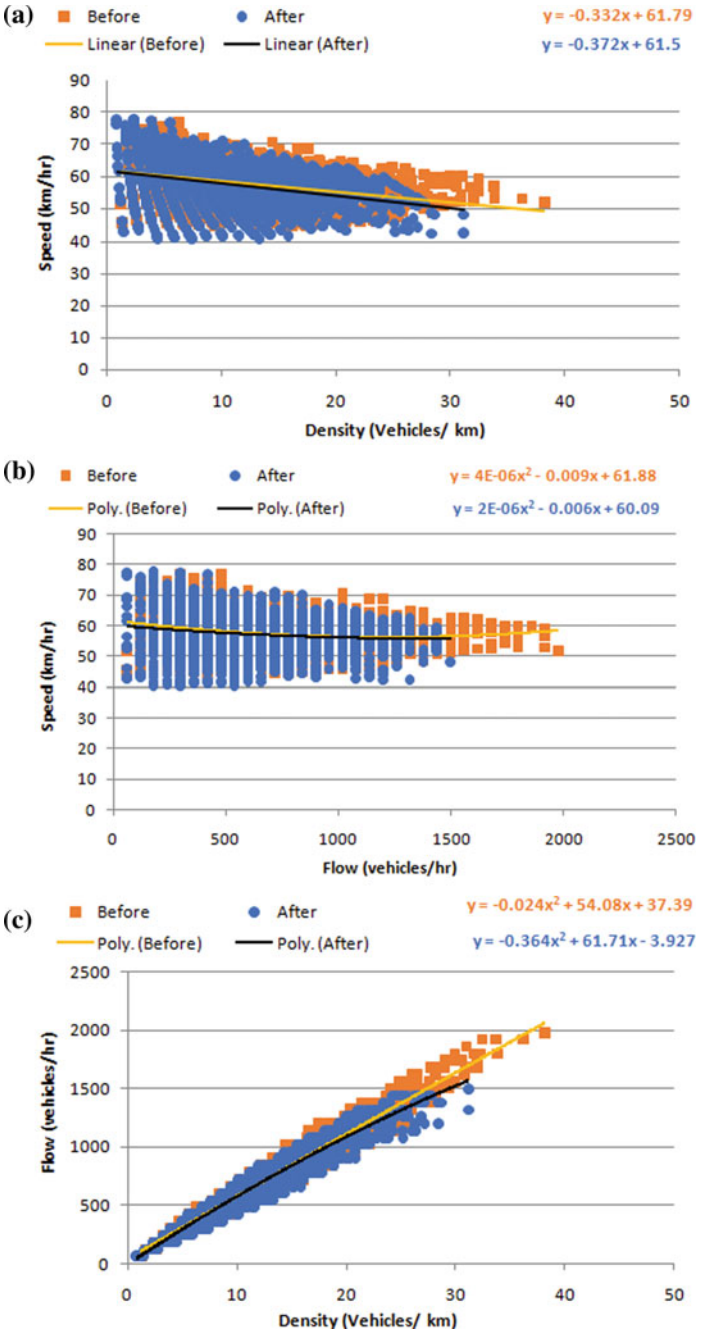

Fig. 4 **a** Speed–density plot of MCV. **b** Speed–flow plot of MCV. **c** Flow–density plot MCV

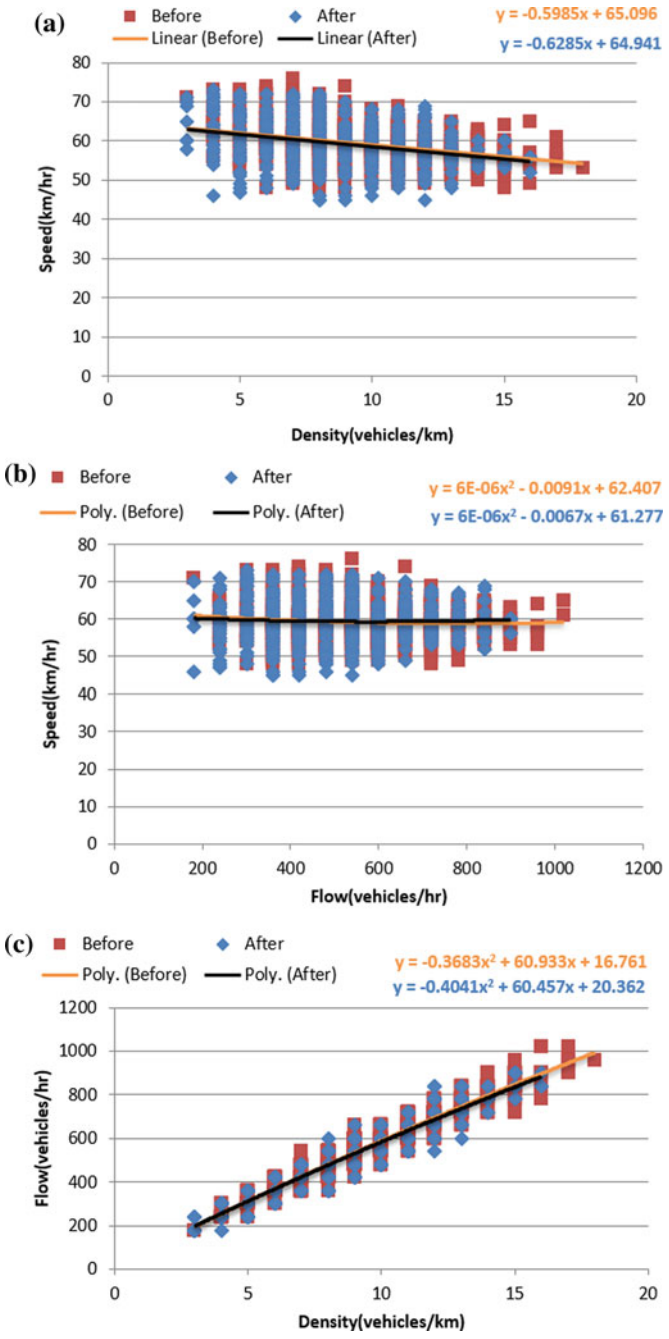

Fig. 5 **a** Speed–density plot of LCV/SCV. **b** Speed–flow plot of LCV/SCV. **c** Flow–density plot of LCV/SCV

Table 1 Empirical results: speed and capacity results

Heavy vehicle types	Speed reduction (%)	Capacity reduction (%)
HCV	11.67	31.84
MCV	16.09	25.57
LCV/SCV	16.14	21.22

Table 2 Paired t-test results

Parameters	Variable 1 (simulated speed)	Variable 2 (field speed)
Mean	51.77995	51.17921
Variance	127.0275	155.2751
Observations	14	14
Pearson correlation	0.977428	
Hypothesized mean difference	0	
df	13	
t Stat	0.807059	
P(T <= t) one-tail	0.217075	
t-Critical one-tail	1.770933	
P(T <= t) two-tail	0.43415	
t-Critical two-tail	2.160369	

Table 3 Descriptive statistics

Parameters	Values
Mean	0.60074
Standard error	0.744357
Median	0.016475
Standard deviation	2.78513
Sample variance	7.756952
Kurtosis	9.060443
Skewness	2.631785
Range	12.62125
Minimum	−3.17158
Maximum	9.449667
Sum	8.410367
Count	14
Confidence level (95.0%)	1.608086

5.2 Analysis of Traffic Data

The validated basic model (peak hour model) was used to run the analysis for all the remaining hours. From the 24 h simulation results, the speed and frequency of the different classes of vehicles were recorded separately and the needed classes were extracted from the whole dataset along with the required before and after speeds as described for statistical analysis of field data. The free flow speeds are calculated as mentioned earlier in statistical analysis for the whole data and different classes. The macroscopic fundamental diagrams were drawn in Excel for all the classes to get the speed and capacity reductions in the same way as mentioned in the statistical analysis. The MFDs of HCV (see Fig. 6 a–c), MCV (see Fig. 7a–c), and LCV/SCV (see Fig. 8a–c) are shown. Table 4 gives the speed and capacity reductions of the simulation analysis.

6 Comparison Between Field and Simulation Results

The speed and capacity reductions were approximately similar between field and simulated traffic flows. HCVs were found to have more impact on the traffic flow characteristics than any other class of heavy vehicles with respect to their huge dimensions in both cases. Thus, the presence of commercial vehicles on the highways has a greater impact on the traffic speed, density, and capacity. The percentage of speed and capacity reductions of the field and simulated traffic flows are compared in Tables 5 and 6, respectively.

7 Conclusion and Further Work

It is observed that the impact of heavy vehicles on the traffic speed, flow, and density of highways from a macroscopic point of view. In this paper, speed–flow–density characteristic plots under the mixed traffic conditions were plotted using the results of both field data and their respective simulation data analysis. The capacity of the highway has been calculated using the MFDs (on the basis of Greenshields linear model) pertaining to a different class of commercial vehicles. It is evident from the analysis that the traffic speed and capacity are affected by the movement of the commercial vehicles. The overall speed and capacity reductions were 11.67, 16.19, 16.14% and 51.8%, 25.57%, 21.22% for HCV, MCV, and LCV/SCV, respectively. The simulated basic model can be used to analyze traffic flow patterns and with a few modifications it can be used to replicate the field conditions of different highways. It can be used as a reference for any traffic plans in the future. The operation, control, and management of heavy vehicles traffic on the highways are of utmost importance now as we know how heavy vehicles affect the other vehicles. The following are

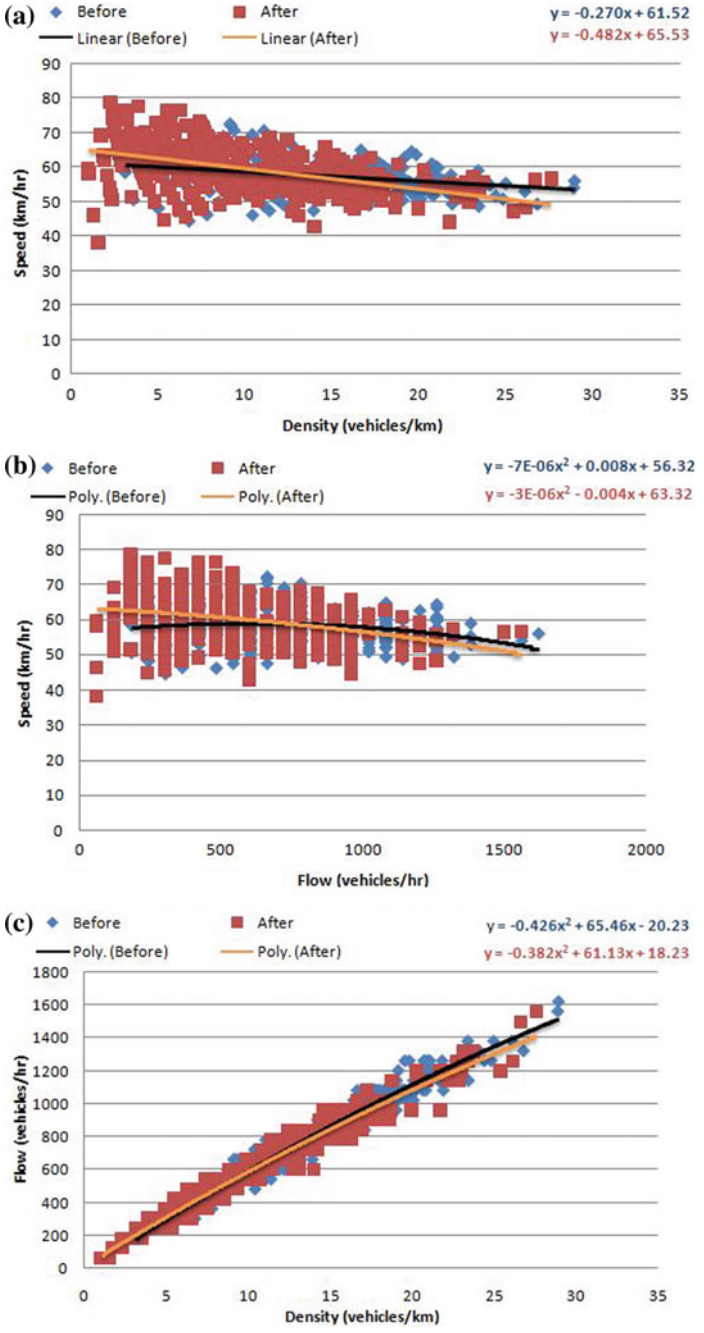

Fig. 6 **a** Speed–density plot of HCV. **b** Speed–flow plot of HCV. **c** Flow–density plot HCV

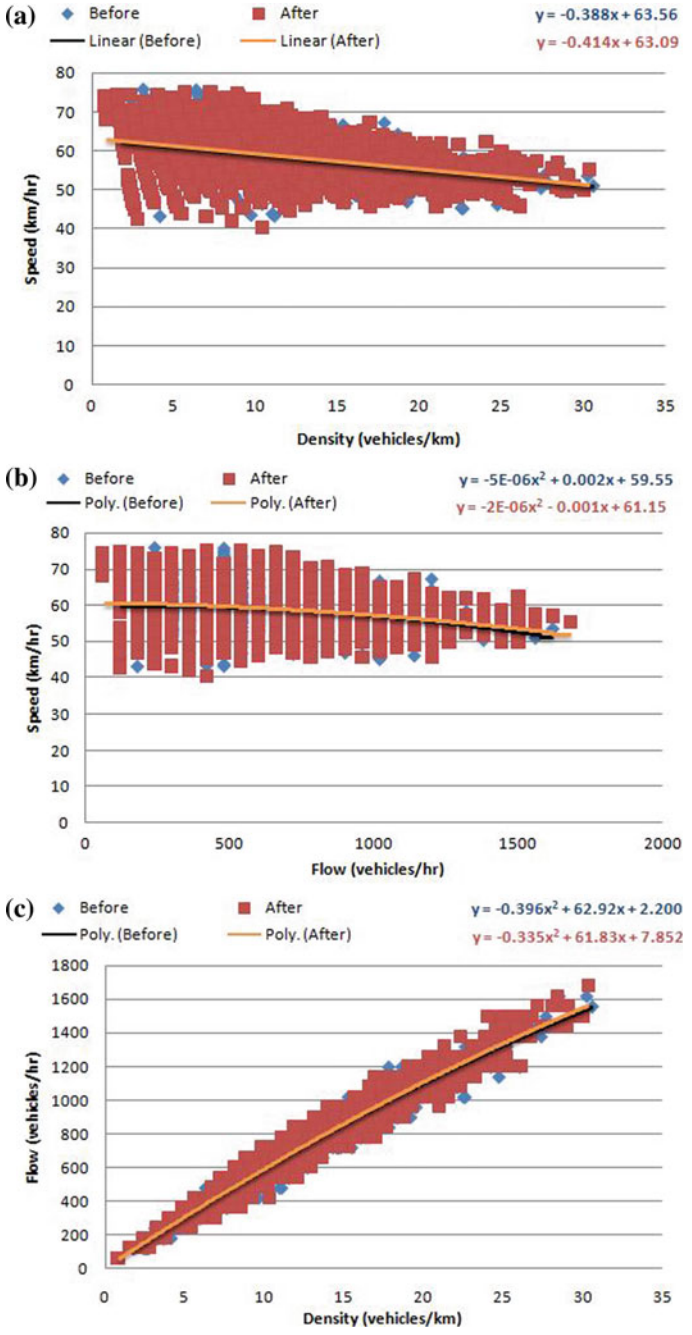

Fig. 7 **a** Speed–density plot of MCV. **b** Speed–flow plot of MCV. **c** Flow–density plot MCV

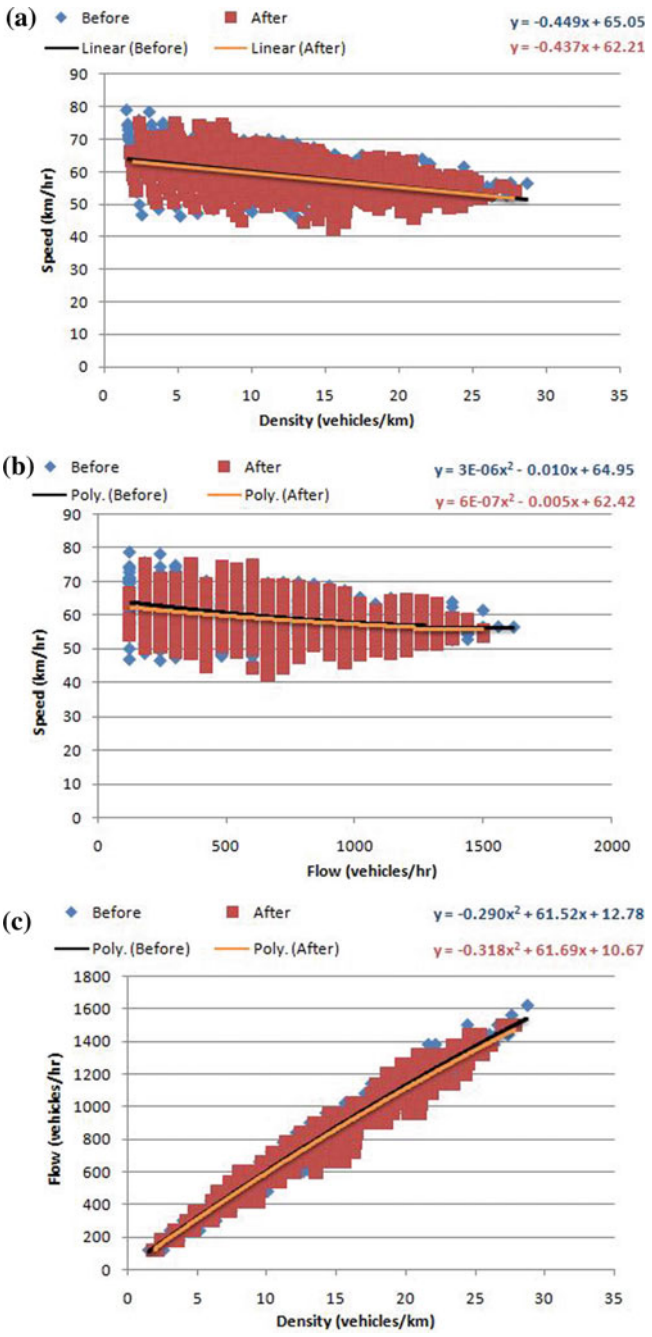

Fig. 8 **a** Speed–density plot of LCV/SCV. **b** Speed–flow plot of LCV/SCV. **c** Flow–density plot of LCV/SCV

Table 4 Simulation results: speed and capacity results

Heavy vehicle types	Speed reduction (%)	Capacity reduction (%)
HCV	15.56	49.63
MCV	18.42	24.39
LCV/SCV	19.68	21.34

Table 5 Speed reductions

Heavy vehicle types	Field (%)	Simulated (%)
HCV	11.67	15.56
MCV	16.09	18.42
LCV/SCV	16.14	19.68

Table 6 Capacity reductions

Heavy vehicle types	Field (%)	Simulated (%)
HCV	51.84	49.63
MCV	25.57	24.39
LCV/SCV	21.22	21.34

some of the strategies to regularize the HVs traffic on highways: Penalizing the over speeding HVs and abruptly overtaking HVs; Intelligent transportation system-based (ITS) techniques such as number plate recognition and video-camera installation for monitoring movement of HVs; Stringent legislative rules and amendment of Motor Vehicles Act (MVA) to control the day and night movement of HVs; Providing exclusive lanes for HVs; and Instructing HV drivers to follow lane discipline and to occupy curb lane.

References

1. Singh S, Santhakumar SM (2021) Empirical analysis of impact of multi-class commercial vehicles on multilane highway traffic characteristics under mixed traffic conditions. Int J Transport Sci Technol. https://doi.org/10.1016/j.ijtst.2021.07.005
2. Sarvi M (2011) Heavy commercial vehicles-following behavior and interactions with different vehicle classes. J Adv Transp 47:572–580
3. Singh S, Santhakumar SM (2021) Platoon-based impact assessment of heavy-duty vehicles on traffic stream characteristics of highway lanes under mixed traffic environment. Int J Intell Transp Syst Res. https://doi.org/10.1007/s13177-021-00268-z
4. Singh S, Panda RK, Saw DK, Santhakumar SM (2020) Effect of heavy transport vehicles on speed-flow characteristics of mixed traffic on multi lane divided intercity highways, resilience and sustainable transportation systems. In: 13th Asia Pacific transportation development conference. American Society of Civil Engineers (ASCE), Shanghai, China, pp 176–185. https://doi.org/10.1061/9780784482902.021
5. Moridpour S, Mazloumi E, Mesbah E (2015) Impact of heavy vehicles on surrounding traffic characteristics. J Adv Transp 49:535–552

6. Bokare PS, Maurya AK (2014) Acceleration and deceleration behaviour of truck on indian highway. Indian Highways Indian Roads Congress 42(3)
7. Pokulwar SG, Dabhekar K, Khode B (2016) Heavy vehicle's impact on traffic flow at urban roads. Int J Sci Technol Eng 2
8. Gao C, Xu J, Jia X, Don Y, Ru H (2020) Influence of large vechicles on the speed of expressway traffic flow. Adv Civil Eng
9. Bains MS, Ponnu B, Arkatkar SS (2012) Modeling of traffic flow on indian expressways using simulation technique. In: 8th international conference on traffic and transportation studies, Changsha, China, pp 1–3
10. Patil V, Kurugod TP, Vinayaka B (2017) Modeling to traffic flow on Indian expressway and urban mid-block section using simulation technique. Int Res J Eng Technol (IRJET) 4(07)
11. Kumar M, Aggarwal P (2019) Traffic flow simulation using VISSIM software. J Civil Eng Environ Technol 6(4):241–251
12. Siddharth SMP, Ramadurai G (2013) Calibration of VISSIM for indian heterogeneous traffic conditions. In: 2nd conference of transportation research group of India (CTRG)
13. Singh S, Santhakumar SM (2021) Evaluation of lane-based traffic characteristics of highways under mixed traffic conditions by different methods. J Institut Eng (India): Ser A 102(3):719–735. https://doi.org/10.1007/s40030-021-00549-6
14. Singh S, Shukla BK, Santhakumar SM (2020) Infra-red sensor-based technology for collecting speed and headway data on highways under mixed traffic conditions. In: 2020 7th international conference on signal processing and integrated networks (SPIN). Institute of Electrical and Electronics Engineers (IEEE), Noida, India, pp 607–611. https://doi.org/10.1109/SPIN48934.2020.9070829
15. Singh S, Kumar A, Niyas M, Santhakumar SM (2020) Multivariate analysis of freeways speed and time headway under mixed traffic streams. In: 2020 international conference on communication systems and networks (COMSNETS). Institute of Electrical and Electronics Engineers (IEEE), Bengaluru, India, pp 116–121. https://doi.org/10.1109/COMSNETS48256.2020.9027497
16. PTV Vissim (2021) User Manual

Water Quality Index, Correlation and Regression Analysis in Temple Pond Water Study

P. Meenakshi and G. Sriram

Abstract This research article explains the prediction of parameters that mostly affect the water quality index by using correlation and regression analysis. This research work was carried out in January 2018 in 17 temple ponds of the holiest city Kanchipuram. The pond water samples were tested for 11 parameters: pH, dissolved oxygen, total hardness, calcium, magnesium, total dissolved solids, chloride, sulfate, total nitrogen, total phosphate, and iron. The calculated water quality index that varies from 202 to 387 indicates that the water is unfit for drinking purposes. This greater value is due to the total phosphate exceeding the limit. Correlation analysis indicates that WQI has a good correlation with total phosphate, total nitrate, and chloride (r = 0.956, 0.908, and 0.803). In regression analysis, WQI with total phosphate shows a greater R^2 value (0.914). The evaluation of experimental and expected values of the dissimilar water quality parameters reveals that the correlation and regression analysis are very useful for finding the parameter mostly affecting the water quality index.

Keywords Correlation · Regression · Water quality index · Pond water · Standards

1 Introduction

Water is the major resource for the nutrition of life. Freshwater will be an inadequate resource in the future. To assemble the water quality potential, surface water resources are also a requirement to keep groundwater [1]. The dissimilar resources of freshwater on earth are lakes, ponds, rivers, streams, runoff, snow, groundwater, and an underground stream. Freshwater is a significant ecological resource for which there is no alternative. In the total freshwater supply, the superior part of the freshwater is changed into the structure of ice and the remaining 90% is groundwater [2]. Water is an essentially expensive resource in the lifeline of all existing organisms. Ponds are a significant part of the earth's water cycle. Anthropogenic behavior such

P. Meenakshi (✉) · G. Sriram
Sri Chandrasekharendra Saraswathi Viswa Mahavidyalaya Enathur, Kanchipuram, Tamil Nadu 631 561, India
e-mail: meenathavamani82@gmail.com

L. Nandagiri et al. (eds.), *Recent Advances in Civil Engineering*, Lecture Notes in Civil Engineering 256, https://doi.org/10.1007/978-981-19-1862-9_23

as the release of domestic, engineering, and other main actions have caused major pollution harm to these rivers [3]. The chemical pollutants of industrial, domestic, and agricultural origin discover their way into ponds through surface runoff and precipitation and enlarge the stage of pollutants [4]. Quantitative estimation of water quality is one of the necessary aspects of efficient water source management. The water quality index value indicates the worth of water in terms of the index number for any proposed use. It is defined as a rating that indicates the composite power of different water quality parameters for the calculation of water quality index [5]. The water quality index value has been used in the assessment of potable water; analysis has shown very limited study has been passed out to evaluate the water for agriculture purpose [6]. The current research work is for the measurement of water quality parameters, finding the water quality index, and statistical analysis in the form of correlation and regression. The measurement components are obtained during the period January 2018 in temple ponds in Kanchipuram.

2 Materials and Methods

2.1 Study Area

This research work pays attention to temple ponds filled with water in Kanchipuram town. Kanchipuram city has a total area of 11.60 km square. The study area (temple ponds) has an elevation of 83.2 m (273 ft) above sea level. The land and temple ponds around Kanchipuram city are flat and slope towards the south and east. It is one of the prominent cities of temples in South India. Kanchipuram town is the northern segment of Tamil Nadu state. The temple pond location of the study area is shown in Fig. 1.

2.2 Source of Sample Water

The main source is precipitation; other sources are temple usage water. The pollution created in the pond is due to some anthropogenic activities like people washing clothes, bathing, taking a deep dip, washing their hands and legs, and disposing of limited household waste.

2.3 Sampling of Water

The sampling was done in January 2018. The pond water sample was collected in a clean polythene bottle (1 l capacity). It was rinsed with corresponding pond water

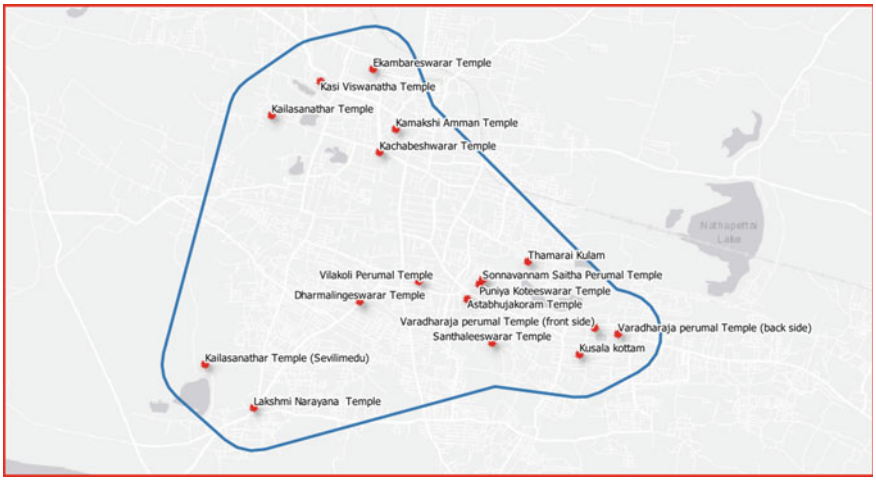

Fig. 1 Temple pond location of the study area

3–4 times, and the samples were collected by submerging the bottle half feet below the water surface. The water sample was collected fully in the bottle and tightly sealed with the cap. The collected water was identified as P1 to P17, and the sample water was sent for testing. The parameters pH, dissolved oxygen, total dissolved solids, chlorides, sulfate, total hardness, calcium, magnesium, total nitrogen, total phosphate, and iron were tested in the laboratory for 17 samples, and the measured water quality parameters were shown in Table 1.

3 Water Quality Index

The calculation of the water quality index is the most efficient tool to give information on the quality of water [7]. WQI is defined as a rating that reflects the complex influence of dissimilar water quality parameters [8, 9]. In the calculation of the water quality index in the present study, 11 parameters were considered. WQI—water quality index, WQP—water quality parameter.

There are three steps for calculating the WQI value:

1. The measured parameter was assigned a weight (wi) based on their effects on water, and the values are nearest to the WHO standard value. The assigned weight and standard value are shown in Table 2.

2. The parameters relative weight (Wi) is calculated by

$$Wi = \left[wi / \left(\sum_{n=1}^{n} wi \right) \right]$$

Table 1 Water quality parameter values of sample points

Sample point	Name of the temple	pH	DO mg/l	TDS mg/l	CL mg/l	SO_4 mg/l	TH mg/l	Ca mg/l	Mg mg/l	T N mg/l	TP mg/l	Fe mg/l
P1	Lakshmi Narayana Temple	7.03	6.8	159	56	22	106	21	13	8.9	5.6	0.07
P2	Kamakshi Amman Temple	7.32	6.5	744	84	53	172	42	16	9.7	4.8	0.09
P3	Kailasanathar Temple (Sevilimedu)	9.31	6.3	164	41	19	90	13	14	12.9	8.3	0.04
P4	Kasi Vishwanathar Temple	8.26	6.2	436	30	17	99	18	13	9.6	5.8	0.03
P5	Astabhujakoram Temple	7.91	6.2	148	28	16	122	32	10	9.5	5.7	0.08
P6	Puniya Koteeswarar Temple	7.68	6.4	183	35	13	133	40	8	8.7	5.7	0.03
P7	Kusala Kottam	8.04	7.6	744	158	94	203	43	23	13.4	8.6	0.08
P8	Kachabeeswarar Temple	6.86	6.8	114	32	17	85	24	6	11.6	7.3	0.02
P9	Vardharaja Temple (Front)	7.58	6.5	172	32	14	99	18	13	10.6	6.4	0.07
P10	Varadharaja Perumal Temple (Back)	7.62	7.5	740	130	67	261	56	29	11.9	6.7	0.07
P11	Sonnavanam saitha Perumal Temple	7.8	7.4	1146	312	138	221	45	26	12.7	7.2	0.03
P12	Dharmalingeshwarar Temple	8.86	6.2	1160	349	184	139	29	16	13.8	8.6	0.02

(continued)

Table 1 (continued)

Sample point	Name of the temple	pH	DO mg/l	TDS mg/l	CL mg/l	SO_4 mg/l	TH mg/l	Ca mg/l	Mg mg/l	T N mg/l	TP mg/l	Fe mg/l
P13	Ekambareswarar Temple	7.52	7.5	117	32	18	83	18	9	9.2	4.7	0.03
P14	Santhaleeswarar Temple	7.46	6.9	1076	206	148	310	69	33	12.8	7.4	0.05
P15	Vilaku Oli Perumal Temple	7.45	7.2	750	167	76	316	38	53	10.8	8.3	0.06
P16	Kailasanathar Temple	7.66	6.4	547	108	57	185	21	32	12.8	7.7	0.04
P17	Thamarai Kulam	7.42	7.8	1204	318	126	254	55	28	13.7	8.5	0.07

Table 2 WHO standards and relative weight

Chemical parameter	WHO standards	Weight	Relative weight
pH	6.5–8.5	1	0.034
DO	5	5	0.172
TDS	500	4	0.138
Cl	250	3	0.103
SO4	150	1	0.034
TH	300	2	0.069
Ca	75	1	0.034
Mg	50	1	0.034
TN	50	1	0.034
TP	0.5	5	0.172
Fe	0.3	5	0.172
		29	0.996

where *Wi* indicates the relative weight, *wi* indicates the weight of each measured parameter, and *n* is the number of parameters.

$$Qi = [(Ci/Si) \times 100]$$

where Qi = quality rating, Ci = concentration of each parameter in each water sample in mg/l, and Si = WHO water standard

$$SI = Wi\,Qi$$

$$WQI = \sum_{i=1}^{n} SI$$

where SI is the subindex of the *i*th parameter; Qi is the rating based on the concentration of *i*th parameter and n is the number of parameters. The calculated subindex and WQI values are shown in Table 3. The subindex values of total phosphate are greater than other parameters, which influence the higher value of the water quality index.

The calculated WQI values are classified into five categories: excellent to unsuitable for drinking purpose. WQI < 50 = Excellent, 50–100 = Good, 101–200 = Poor, 201–300 = Very poor, > 300 = Unsuitable.

Table 3 Subindex and water quality index values of sample points

S. no.	Sample point	SI = (pH)	SI = (DO)	SI = (TDS)	SI = (Cl)	SI = (SO4)	SI = (TH)	SI = (Ca)	SI = (Mg)	SI = (TN)	SI = (PO4)	SI = (Fe)	WQI
1	P1	3.68	23.39	4.39	2.31	0.50	2.44	0.95	0.88	0.61	192.64	4.01	235.80
2	P2	3.83	22.36	20.53	3.46	1.20	3.96	1.90	1.09	0.66	165.12	5.16	229.27
3	P3	4.87	21.67	4.53	1.69	0.43	2.07	0.59	0.95	0.88	285.52	2.29	320.62
4	P4	4.32	21.33	12.03	1.24	0.39	2.28	0.82	0.88	0.65	199.52	1.72	245.17
5	P5	4.14	21.33	4.08	1.15	0.36	2.81	1.45	0.68	0.65	196.08	4.59	237.32
6	P6	4.02	22.02	5.05	1.44	0.29	3.06	1.81	0.54	0.59	196.08	1.72	236.63
7	P7	4.21	26.14	20.53	6.51	2.13	4.67	1.95	1.56	0.91	295.84	4.59	369.04
8	P8	3.59	23.39	3.15	1.32	0.39	1.96	1.09	0.41	0.79	251.12	1.15	288.34
9	P9	3.96	22.36	4.75	1.32	0.32	2.28	0.82	0.88	0.72	220.16	4.01	261.58
10	P10	3.99	25.80	20.42	5.36	1.52	6.00	2.5	1.97	0.81	230.48	4.01	302.90
11	P11	4.08	25.46	31.63	12.85	3.13	5.08	2.04	1.77	0.86	247.68	1.72	336.30
12	P12	4.63	21.33	32.02	14.38	4.17	3.20	1.31	1.09	0.94	295.84	1.15	380.05
13	P13	3.93	25.80	3.23	1.32	0.41	1.91	0.82	0.61	0.63	161.68	1.72	202.05
14	P14	3.90	23.74	29.70	8.49	3.35	7.13	3.13	2.24	0.87	254.56	2.87	339.98
15	P15	3.90	24.77	20.70	6.88	1.72	7.27	1.72	3.60	0.73	285.52	3.44	360.26
16	P16	4.01	22.2	15.10	4.45	1.29	4.26	0.95	2.18	0.87	264.88	2.29	322.29
17	P17	3.88	26.83	33.23	13.10	2.86	5.84	2.49	1.90	0.93	292.4	4.01	387.49

4 Statistical Analysis

SPSS 18 software was used to carry out the statistical analysis in the study. Statistical parameters correlation coefficient and regression coefficient for physicochemical parameters are determined. Correlation analysis deals with the closeness of the relationship between measured variables [10, 11]. The coefficient values vary between 1 and –1, which show the great linear relationship between the two measured variables. To find out the closeness of the relationship among 11 tested water quality parameters and calculated WQI, Karl Pearson correlation matrix has been deployed. Correlation is the common relationship between the two variables. The correlation analysis explains if an increase or decrease in the value of one parameter is connected with a subsequent increase or decrease in the worth of other parameters [12]. In the current study, the arithmetical values of the correlation coefficient (r) for the 11 water quality parameters are tabulated in Table 4.

Correlation Coefficient (r):

Consider x and y are the two different variables having n pairs of calculated values and differ from 1, 2, 3, 4, 5, …, n. The correlation coefficient r is given by Eq. (1):

$$r = \frac{\left[n \sum x\, y - \sum x \sum y\right]}{\sqrt{\left[n \sum x^2 - \left(\sum x\right)^2\right] \times \left[n \sum y^2 - \left(\sum y\right)^2\right]}} \tag{1}$$

Multiple linear regression analysis is a statistical tool for understanding an outcome variable and several predictors (independent variables) that best represents the relationship in a population. The regression is given by Eq. (2). The regression equation and coefficient values are tabulated in Table 5.

Regression equation

Table 4 Correlation coefficient values for measured parameters

	pH	DO	TDS	Cl	SO4	TH	Ca	Mg	TN	TP	Fe	WQI
pH	1	−0.38	0.090	0.154	0.175	−0.209	−0.273	−0.106	0.366	0.371	−0.266	0.282
DO		1	0.398	0.405	0.328	0.534	0.513	0.424	0.294	0.224	0.222	0.354
TDS			1	0.932	0.941	0.752	0.706	0.612	0.677	0.529	0.063	0.749
Cl				1	0.960	0.610	0.560	0.508	0.725	0.624	−0.085	0.803
SO4					1	0.641	0.619	0.509	0.738	0.604	−0.080	0.786
TH						1	0.834	0.898	0.442	0.449	0.303	0.630
Ca							1	0.505	0.340	0.217	0.323	0.430
Mg								1	0.423	0.532	0.216	0.643
TN									1	0.882	−0.116	0.908
TP										1	−0.128	0.956
Fe											1	−0.049
WQI												1

Table 5 Regression study between WQI and WQP

Regression	R2	Regression Coefficient	Remarks
WQI = 0.002pH + 6.900	0.079	0.002	Positive
WQI = −0.003DO + 5.857	0.125	0.003	Positive
WQI = 5.141TDS−963.8	0.560	5.141	Positive
WQI = 1.489Cl−318.4	0.644	1.489	Positive
WQI = 0.731SO4-154.0	0.618	0.731	Positive
WQI = 0.831TH−77.84	0.396	0.831	Positive
WQI = 0.130Ca−18.69	0.413	0.130	Positive
WQI = 0.115 Mg−0.117	0.185	0.115	Positive
WQI = 0.027TN + 3.193	0.823	0.027	Positive
WQI = 0.021TP + 0.544	0.914	0.021	Positive
WQI = −2E.05×Fe + 0.057	0.002	−2E.05	Negative

$$y = ax + b \tag{2}$$

where y = dependent variable, x = independent variable, and a = regression coefficient.

The correlation and regression analysis was carried out using the software SPSS 18.

5 Results and Discussion

5.1 Water Quality Parameters

The pH is the hydrogen ion concentration that plays an important role in the biological processes of almost all aquatic living organisms. In the sampling points, measured pH values vary from 6.86 to 9.3, with pond water alkaline in nature [13]. P3 pond has a greater value of pH due to washing clothes and bathing. Dissolved oxygen represents how much quantity of oxygen is dissolved in a water medium [14]. A

DO value greater than 4 mg/l is essential, and for drinking purpose the value is 6 mg/l [15]. At sample points, the DO values vary between 6.2 mg/l and 7.8 mg/l. The total dissolved solids are the presence of different kinds of minerals in water and are denoted by total dissolved solids. TDS is directly connected with the purity of water. The sum of the cations and anions concentration is equal to TDS. As per IS:10500-2012 standards, the acceptable limit is 500 mg/l. In the present study, the TDS values vary from 114 mg/l to 1160 mg/l. P12 pond has the maximum value. The greater value of TDS is due to anthropogenic activities. Chloride is present in all types of natural waters, and the amount of chloride present is widely varying in concentration. When the mineral content in the water increases, the chloride content will automatically increase. Human activities will increase the concentration of chloride. As per IS:10500-2012, the acceptable limit of chloride is 250 mg/l. In the present study, the chloride content varies from 28 to 349 mg/l. P11, P12, and P17 are sample points having greater value, due to the leaching of deep sediments from the soil by rainwater. Sulfate is a naturally occurring mineral. Minerals dissolve for a long time for mixing into groundwater. The acceptable limit is 150 mg/l. In the present study, it varies from 13 to 184 mg/l. P12 pond has the greater value. Total hardness indicates the sum of calcium and magnesium hardness in mg/l[15]. The degree of hardness of clean water has been classified in terms of equivalent $CaCO_3$ concentration as follows: Soft nature: 0–60 mg/l, Medium: 60–120 mg/l, Hard nature: 120–180 mg/l, and terribly hard nature greater than 100–80 mg/l. In the present study, TH varies from 83 to 316 mg/l. Pond water is hard in nature. Calcium and magnesium are necessary nutrients required for an organism. A calcium value varies from 13 to 69 mg/l. A magnesium value varies from 6 to 53 mg/l. The acceptable limits for hardness in calcium and magnesium are 300, 75, and 50 mg/l. Total nitrogen is the combination of organic, inorganic nitrogen, and ammonia. It varies from 8.7 to 13.8 mg/l. Acceptable limit is 50 mg/l. Total phosphate is essential nutrition up to a standard limit. The acceptable limit is 0.5 mg/l. In the current study, it varies from 4.8 to 8.6 mg/l. The greater amount of phosphate is due to stormwater runoff and the decomposition of waste into the ponds. It creates water quality index of high value. Iron is an important nutrient element for humans. It is a significant mineral for the production of hemoglobin and myoglobin [16]. Iron is a significant water quality variable in aquaculture, and it is considered a necessary element for plants, bacteria, and animals. In the photosynthesis of plants, iron plays an important role. Iron is a dissolved nutrient essential in minor quantities by both aquatic plants and animals. Oxidation of ferrous iron into ferric iron often outcomes in reddish deposits of ferric hydroxide on pond bottoms. In many aquaculture systems, the presence of iron concentrations above 0.1 mg/l will damage the gills of the fish. The value of iron in the current study varies in the ranges from 0.02 to 0.09 mg/l.

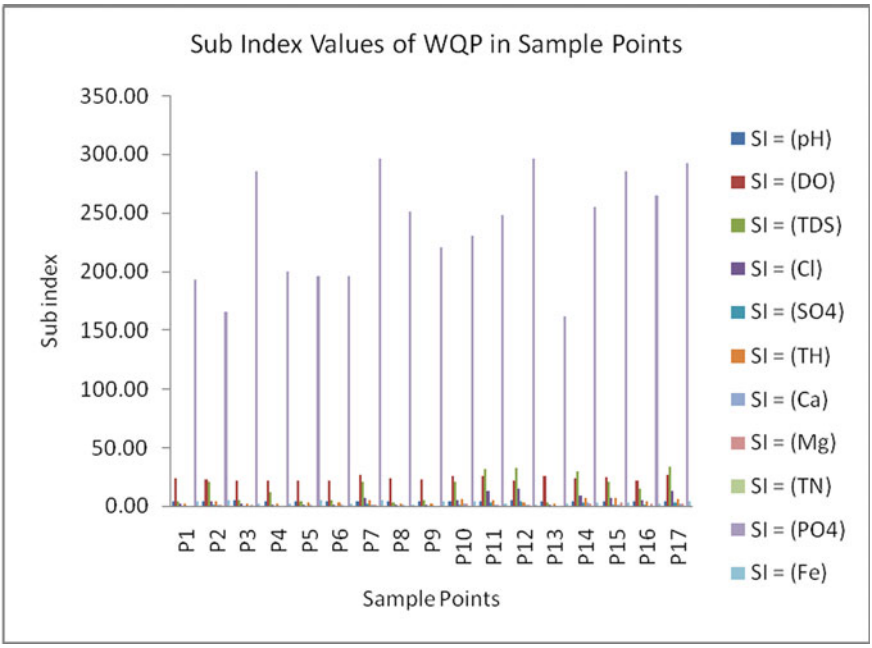

Fig. 2 Calculated subindex values of measured parameters

5.2 Water Quality Index

The subindex values of measured parameters and water quality index values for 17 sample points were calculated and tabulated in Table 3. The graphical representation of subindex values is shown in Fig. 2. The subindex values of total phosphate are majorly affecting the water quality index; it reflects in correlation and regression analysis. The sample points P3, P7, P10, P11, P12, P14, P15, P16, and P17 have a WQI value of 200–300. It shows the pond water is in very poor condition. The sample points P1, P2, P4, P5, P6, P8, P9, and P13 have a WQI value of greater than 300, so it is unsuitable for drinking purpose. The variation of water quality index values on the sample points is shown in Fig. 3. The higher value of WQI is due to the higher value of total phosphate.

5.3 Correlation and Regression Analysis

The correlation and regression model analysis is helping interpret pond water excellence numbers and relate them to definite hydro environmental processes [17, 18]. These model analyses are relatively useful in characterizing and getting first-hand matters of the pond water system than really departing through difficult methods [19,

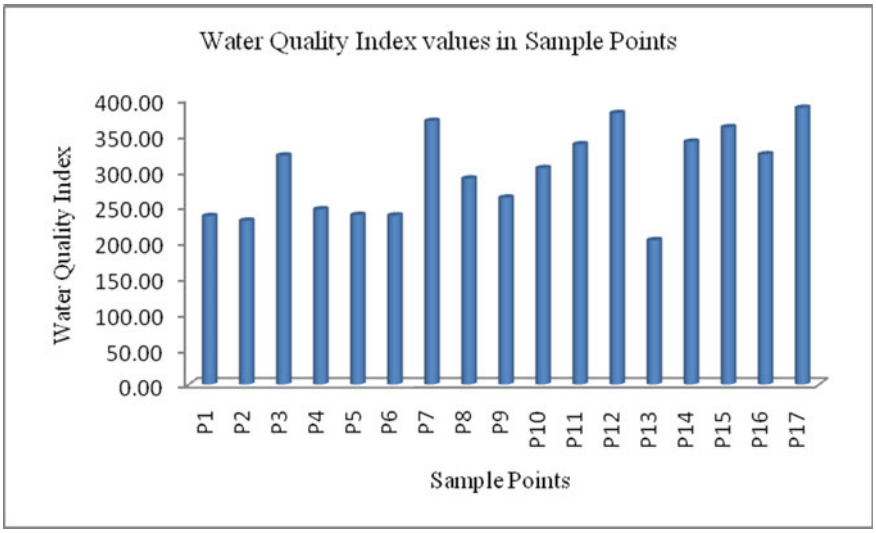

Fig. 3 Water quality index variation of sample points

20]. Correlation and regression analysis done with the SPSS software, the correlation coefficient values, and regression coefficient values were tabulated in Tables 5 and 6. WQI having a good positive correlation with TP, TN ($r = 0.956, 0.908$) and Cl, SO_4, TDS ($r = 0.803, 0.786, 0.749$). Good positive correlations TDS with SO_4, Cl, TDS, Ca ($r = 0.941, 0.932, 0.752, 0.706$). Cl with SO_4, TN ($r = 0.960, 0.725$). SO_4 with TN ($r = 0.738$). TH with Ca, Mg ($r = 0.834, 0.898$). TN with TP ($r = 0.882$). WQI moderate correlation with Mg, TH ($r = 0.643, 0.630$). WQI weak correlation with pH, DO, Ca ($r = 0.282, 0.354, 0.430$). WQI has a negative weak correlation with Fe ($r = -0.049$). From the result the greatest positive r value is WQI with TP ($r = 0.956$). This representation indicates a greater water quality index value due to total phosphate.

The significant effect of all the independent variables on the dependent variable has been identified by regression analysis. The effects of WQI with all measured parameters have been determined with ra egression plot. The graphical representation of the regression graph is shown for the following WQI with pH, DO in Fig. 4, WQI with TDS, Cl, SO_4 in Fig. 5, WQI with TH, Ca, Mg in Fig. 6, WQI with TN, TP in Fig. 7, and WQI with Fe in Fig. 8. The prediction of WQI with total phosphate is good. The multiple R^2 values (0.914) indicate that 91.4% of the variability in WQI might be recognized as the effect of total phosphate.

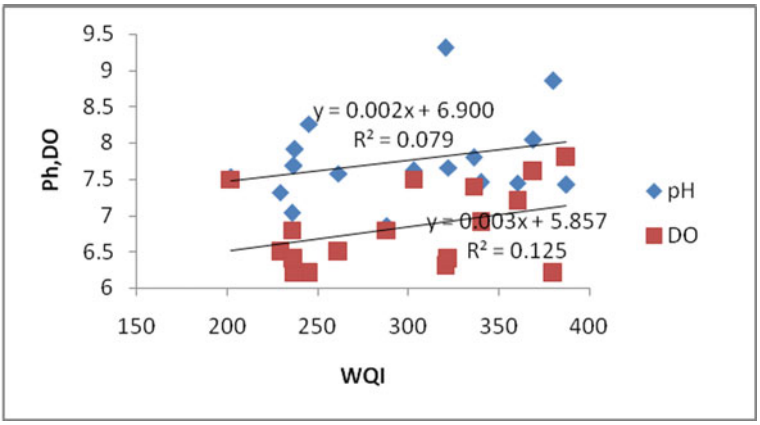

Fig. 4 Regression graph between WQI and pH, DO

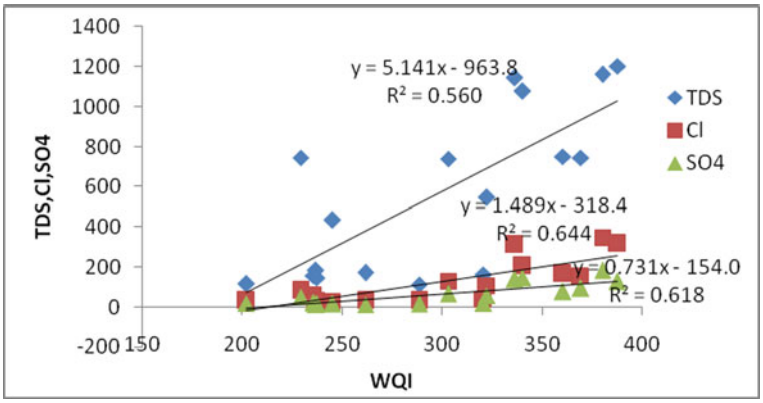

Fig. 5 Regression graph between WQI and TDS, Cl, SO_4

6 Conclusions

Maintaining the water quality of pond water at a good level is important to monitor regularly. Water quality monitoring study is useful for understanding the water quality and controlling the pollution effects. The variations have been noticed in definite pond water quality material among the sample water collected from various temple ponds and may be recognized to various anthropogenic activities, land utilization, and land coat factors. The calculated water quality value varies between very poor to unsuitable for drinking purposes. P17, P12, P7, and P3 ponds are unsuitable for drinking. These ponds need primary production in the form of fencing around the circumference. However, a significant correlation has been noticed between the water quality index and tested water quality parameters. There is a good positive correlation

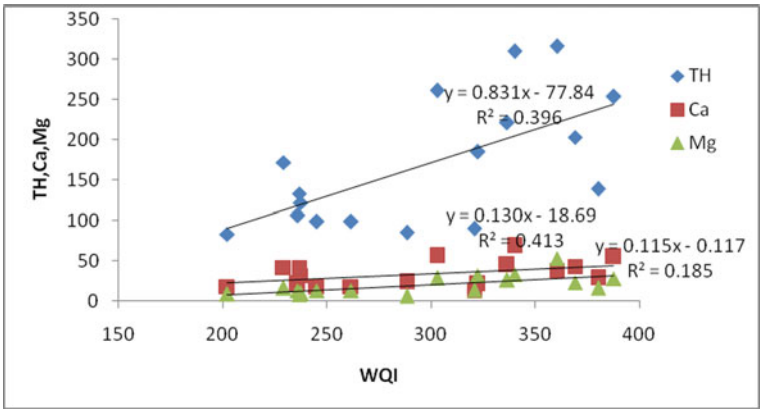

Fig. 6 Regression graph between WQI and TH, Ca, Mg

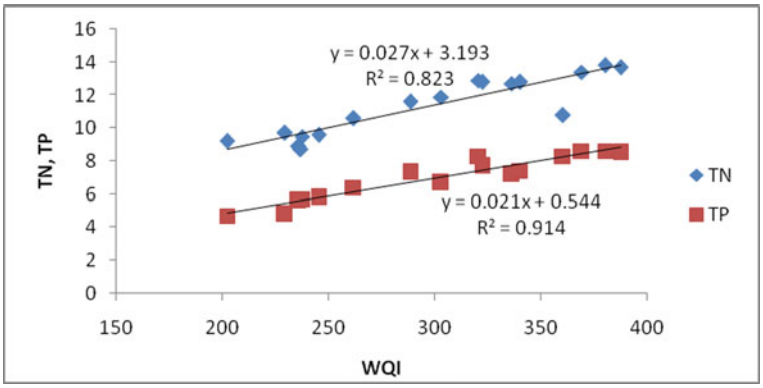

Fig. 7 Regression graph between WQI and TN, TP

that exists between WQI and water quality parameters (TP, TN, Cl, SO4, TDS). The significant effect between WQI and water quality parameters has been identified by regression analysis. The effect of total phosphate in WQI calculation is about 80%, which has more impact than other measured parameters. Total phosphate with WQI is a significantly positive correlation of 95.6%. The multiple regression model predicted WQI with total phosphate has 91.4% of R^2 value. This result indicated the presence of high total phosphate concentration and is the potential pressure for pollution of pond water. The correlation and regression model gives a good result for finding the most affected parameter in water quality. The above results have indicated a good relationship existing between water quality index and correlation, and regression analysis. It is recommended that the pond water conventional treatment followed by disinfection will give better results before drinking and potable uses. The present water is recommended for fish culture and temple usage.

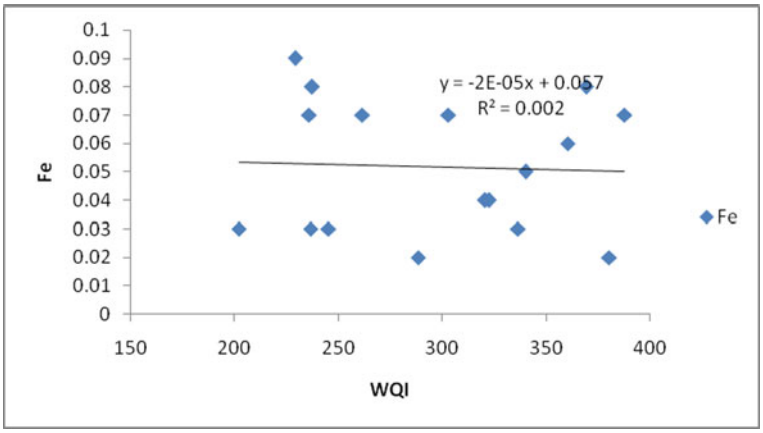

Fig. 8 Regression graph between WQI and Fe

References

1. Sukla SP, Agrawal V (2011) Water quality index of surface water in an industrial area in Kanpur City. J Instit Eng 92:1–5
2. Prashant Bhausaheb R, Jadhav MV (2016) The analysis of ground water quality status using linear regression method. Int J Eng Trends and Technol 38:23–228
3. Abhishek S, Khambete AK (2013) Statistical analysis to identify the main parameters to the astewater quality index of CETP : a case study at Vapi, Gujarat, India. J Environ Res Developm 7:1294–1304
4. AkshathaK N (2012) Assessment of water quality of a polluted pond at mysore using national sanitation foundation-water quality index (NSF-WQI). Nat Environ Pollut Technol 11:311–314
5. Puri PJ, Yenkie MKK, Rana DB, Meshram SU (2015) Application of water quality index (WQI) for the assessment of surface water quality (Ambazari Lake). European J Experim Biol 5:37–52
6. Ali Al-Dahhan NA, Hussein Al-Atwi AK, Murad.Al-Zubaidi MG (2019) Water quality index for surface water assessment by using remote sensing and GIS techniques, AL- Najaf, Al-Manathera district, Iraq. J Phys: Conf Ser 7:1–14
7. Krishnan S, Pushkaran P (2017) Water quality assessment and algal analysis of two temple ponds in the industrial area, Kollam District, Kerala. J Adv Biol Sci 4:68–71
8. Elayaraj B, Selvaraju M, Ajayan KV (2016) Assay on water quality variations of Pasupatheswarar Temple Pond, Annamalai Nagar, Tamil Nadu, India. J Int Acad Res Multidisciplinary 3:97–108
9. Bansal J, Dwivedi AK (2018) Assessment of ground water quality by using water quality index and physico chemical parameters: review paper. Int J Eng Sci Res Technol 7:170–174
10. Ambiga K, Annadurai R (2015) Development of water quality index and regression model for assessment of groundwater quality. Int J Adv Remote Sensing GIS 4:931–943
11. Saleem A, Dandigi MN, Vijay Kumar K (2012) Correlation-regression model for physico-chemical quality of groundwater in the South Indian City of Gulbarga. African J Environm Sci Technol 6:353–364
12. Chaubey S, Patil MK (2015) Correlation study and regression analysis of water quality assessment of Nagpur City, India. Int J Sci Res Publication 5:753–757
13. Chaudhary S, Kuniyal JC, Vaidya N, Puri S (2019) Water quality assessment in headwater of the Satluj Basin, Northwestern Himalaya, India. J Himalayan Ecol Sustain Develop14:19–33

14. Khatoon N, Khan AH, Rehman M, Pathak V (2013) Correlation study for the assessment of water quality and its parameters of Ganga River, Kanpur, Uttar Pradesh, India. J Appl Chem 5:80–90
15. Shrestha AK, Basnet N (2018) The correlation and regression analysis of physicochemical parameters of river water for the evaluation of percentage contribution to electrical conductivity. J Chem 1–9
16. Garg RK, Rao RJ, Uchchariya D, Shukla G, Saksena DN (2010) Seasonal variations in water quality and major threats to ramsagar reservoir, India. Afr J Environ Sci Technol 4:61–76
17. Rastogi GK, Sinha DK (2011) A novel approach to water quality management through correlation study. J Environm Res Developm 5:1029–1035
18. Shil S, Singh UK, Mehta P (2019) Water quality assessment of a tropical river using water quality index (WQI), multivariate statistical techniques and GIS. Appl Water Sci 9:1–21. https://doi.org/10.1007/S13201-019-1045-2
19. Harichandan PHS, Panda R, Sethy KM (2008) Water quality assessment of Bhubaneswar temple pond by using statistical method and water quality index. J Pollution Effect and Control 6:1–4
20. Nayak SK (2020) Assessment of water quality of brahmani river using correlation and regression analysis. 5:1–25

Strengthening of Axially Loaded Circular RC Column under Close-In and Contact Blasts: A Numerical Investigation

Rafat Tahzeeb, Mehtab Alam, and S. M. Muddassir

Abstract Damage to the structure and loss of life due to increasing unintentional and terrorist explosions are grabbing the attention of engineers, planners, and policymakers. The damage to certain key elements of the structure, such as column, is fatal and irreparable and may lead to the collapse of the structure. Following the validation of experimentally tested square RC column with seismic lateral reinforcement carrying axial load subjected to an explosive charge of 100 kg ANFO (82 kg-TNT equivalent) at a scaled distance of 1.00 m/kg$^{1/3}$ with 10 mm mesh size using ABAQUS/CAE software equipped with concrete damage plasticity model with strain rate effect, equivalent circular columns to the experimentally tested one having seismic circular transverse reinforcement carrying the same axial load under the blast are considered. With the aim of dissecting the impact of blast on the RC columns, a high-fidelity physics-based numerical model has been developed subjected to equal peak pressure of 8.71 MPa in close-in and contact blasts. To improve the response of the column, different types of retrofitting techniques, including UHPC and UHPFRP coating, and CFRP wrapping are considered. Blast performance in terms of maximum displacement, damage dissipation energy, and compressive stress in concrete are compared and discussed. The results indicated that the strengthening with UHPFRC is comparable to CFRP wrapping in the case of the close-in blast; however, CFRP wrapping is found to make the column give excellent performance in both close-in and contact explosion loadings.

Keywords Blast loading · RC columns · Carbon fiber-reinforced polymer (CFRP) · Ultra-high-performance concrete (UHPC) · Ultra-high-performance

R. Tahzeeb (✉) · S. M. Muddassir
Department of Civil Engineering, Faculty of Engineering and Technology, Jamia Millia Islamia, New Delhi, Delhi 110 025, India
e-mail: rafattahzeeb786@gmail.com

S. M. Muddassir
e-mail: smudassir@jmi.ac.in

M. Alam
Department of Civil Engineering, Netaji Subhas University of Technology, New Delhi, Delhi 110 073, India
e-mail: mehtab.alam@nsut.ac.in

L. Nandagiri et al. (eds.), *Recent Advances in Civil Engineering*, Lecture Notes in Civil Engineering 256, https://doi.org/10.1007/978-981-19-1862-9_24

fiber-reinforced concrete (UHPFRC) · Concrete damage plasticity model (CDP) · Damage dissipation energy (DDE)

1 Introduction

In recent years, the number of industrial, intentional, accidental, and unthought-of explosion-related devastating events is on the rise threatening the safety of structures which could result in huge property loss and casualties of the occupants, drawing increasing attention of structural designers and architects [1–8]. In a structure, failure of one or more load-carrying members may trigger cascading effects, leading to instability/collapse of the structure [1, 9]. Consequently, the safety of structures of higher importance such as buildings of government offices and institutions, bridges, railway stations, airports, offices, and heritage buildings are of significant concern against such impulsive blast loading [2, 10–15]. As per ASCE [16], an explosion in contact with the target surface is defined as a contact explosion, while an explosion with a scaled distance less than 1.2 m/kg$^{1/3}$ is defined as a close-in explosion. High strength materials like UHPC and UHPFRC are well known for their higher strength than normal concrete. UHPFRC with extraordinary ductility is found to be having higher blast resistance. UHPFRC is one such material known for its outstanding ductility, high strength, and durability too [17–19]. Its uniaxial compressive strength is up to 200 MPa with strain hardening characteristics and has flexural tensile strength as high as 40 MPa, enabling it to withstand fragmentation due to projectile invasion caused by the blast and prevent progressive kind of failure of the structure [19]. Fiber-reinforced polymer (FRP) wrappings on structural elements vulnerable to blast loading are advantageous because of their very high tensile strength and ductility. Carbon-FRP (CFRP) having the highest tensile strength than other FRPs such as aramid, basalt, and glass has been used in the form of wrapping in the present work [20–22].

Wu et al. [23] conducted a series of experiments to determine the blast resistance of slabs made of (1) normal strength concrete (NSC), (2) plain UHPC, and (3) UHPFRC; and the NSC slab strengthened with two layers of carbon fibre-reinforced polymer (FRP) plates in staggered manner, each of thickness 1.40 mm. Normal RC (NRC) slab was used as a reference specimen. It was found that the plain UHPC slab was having energy absorption capacity comparable to the reference one, but having higher cracking resistance. Performance of UHPFRC was superior with regards to damage and cracking. Roller [24] carried out a series of tests on the exposed hardened concrete surface to study the residual axial load-carrying capacity of the column under contact as well as close-in detonations. Performance of column constructed with normal strength concrete was compared with the column constructed with the advance material including polymer concrete, slurry infiltrated fiber concrete (SIFCON), ductile concrete (DUCON), and ultra-high-performance concrete (UHPC). It was found that the residual axial load-carrying capacity of the column can be increased by about 70% using the proposed retrofitting techniques.

Performance of column strengthened with 15 mm thick coating of SIFCON was found most superior under close-in blast loading, while the column with DUCON coating gave the best performance under contact blast. Jayasooriya et al. [25] carried out a numerical investigation on the concrete-steel composite (CSC) column to study the blast performance and residual axial load-carrying capacity of the column. By keeping the same dimension and steel ratio, the blast performance of the CSC column was compared with the RC column. The performance of the CSC column was found to be better than the RC column. Cui et al. [10] examined the effect of explosive mass on the validated model of 3600 mm long, 400 × 400 mm square axially loaded RC column using the LS-DYNA software program under close-in blast loading. It was observed that the blast performance of the column can be improved by applying a thinner concrete cover, a high stirrup ratio with lower stirrup spacing, and a larger cross-sectional area of the column. Xu et al. [26] conducted field test to determine the behaviour of ultra-high-performance fibre-reinforced concrete (UHPFRC) and high strength reinforced concrete (HSRC) column subjected to different explosive charges, at a standoff distance of 1.5 m in each case. It was observed that column with UHPFRC performed better than HSRC to tackle the losses due to blast loading. Kyei and Braimah [27] carried out experimental and numerical investigation on the square RC column with and without seismic reinforcement over confining region, and seismic reinforcement over confining and mid-region subjected to 82 kg and 123 kg TNT at a scaled distance varying from 0.25 to 0.85 m/kg$^{1/3}$. Performance of column with seismic reinforcement over confining as well as mid-height region was found to be superior. Wang et al. [28] numerically investigated the close-in blast performance of the hybrid fiber-reinforced polymer (FRP)-concrete-steel double-skin tubular (DSTC), concrete-filled steel tubes (CFST), and concrete-filled double-skin steel tubes (CFDST) columns using the LS-DYNA program. Performance of the CFDST column was reported to be superior with regards to displacement and damage. Li et al. [3] carried out experimental and numerical investigation to study the post-blast performance and residual axial capacity of CFDST column subjected to contact explosion. Blast resistance of the column was studied numerically using LD-DYNA, by the variation of parameters including charge weight, reinforcement ratio, boundary condition, and cross-sectional area. An empirical equation was developed for the rapid assessment of the damage to the column by varying the parameters. With the increase in reinforcement ratio and cross-sectional area, the blast resistance and post-blast axial residual capacity of the column increase. Dua et al. [1] performed experimental and numerical analysis to determine the response of rectangular RC column by varying width and compared with the results obtained by square cross-section RC column at constant depth subjected to contact explosion. Charge of mass 1, 0.5 and 0.115 kg was applied and placed on the ground adjacent to the tested columns. It was found that columns with 1 and 0.5 kg explosion charge had no residual axial capacity. The numerical study was conducted using high-fidelity LS-DYNA. On increasing the width of the RC column, axial residual capacity increases and also reduces the contact explosion effects. Hu et al. [29] conducted an RC column field test subjected to close-in and double-end-initiation blast test at a scaled distance of 0.67 m/kg$^{1/3}$ and charge of mass 11.1 kg TNT, with three retrofitting methods of

CFRP sheets. Later the numerical analysis was performed on LS-DYNA and the contribution of CFRP retrofitting on the blast loading was quantitatively evaluated. Different cases revealed the different levels of blast and damage resistance.

In this study, the 3000 mm long circular axially loaded RC columns of 350 mm diameter strengthened with (1) 15 mm thick coating of (a) UHPC and (b) UHPRFC, and (2) 2 mm thick CFRP wrapping have been analyzed under close-in as well as contact blast loadings using ABAQUS/CAE software. Maximum displacement, stresses, and damage have been evaluated and compared.

2 Numerical Modeling

With the help of FEM-based computer code, ABAQUS/CAE, RC circular column model has been developed and later these models have been subjected to blast loading under close-in and contact detonation. Nine models have been developed with the first model as a square RC column (C1) and the rest eight models as a circular RC column. The columns are subjected to peak pressure of 8.71 MPa in case of close-in and contact explosion. The charge is placed 1.50 m high from the ground surface [27].

2.1 Model Description

The first model, namely C1, is a 300 × 300 mm experimentally tested square concrete column under 82 kg TNT close-in load, carrying an axial working load of 950 kN, reinforced with 4 bars of 25 mm diameter of yield strength 500 MPa as longitudinal reinforcement and transverse reinforcement in the form of 10 mm diameter stirrups at 75 mm c/c over the seismic confining zones (600 mm, Fig. 2) [27]. The thickness of the concrete cover to the steel bars is 40 mm. The second model, namely "Close-in", is of an equivalent circular seismically confined RC column of diameter 350 mm reinforced with 6 longitudinal bars of 20 mm diameter and circular ties of 10 mm diameter having a spacing of 85 mm c/c over the confining zones and mid-height region, and 175 mm c/c over the remaining part, carrying the same axial load under close-in blast has been developed. The third model, named "Contact", with the same configuration as that of the second model "Close-in" is analyzed under contact blast loading. To investigate further, enhancement of blast resistance of the columns, namely "Close-in" and "Contact", and the next six models are obtained by applying (1) 15 mm thick coating of (a) UHPC and (b) UHPFRC, and (2) 2 mm thick CFRP wrapping under close-in and contact blast loadings (Fig. 2). Contact blast is considered with as much pressure as that of a close-in blast, i.e., 8.71 MPa. The columns are discretized with a 10 mm mesh size using the C3D8R explicit element [5, 30, 31]. The mechanical properties of the materials used in this study are tabulated in Table 1. CFRP wrapping has been modeled by using the experimental data of Phan-Vu

Table 1 Mechanical properties of the materials

Materials	ρ (kg/m^3)	f_c (MPa)	f_t (MPa)	E (MPa)	μ
NSC [27]	2500	30	3	26.6	0.2
UHPC [18]	2500	121.32	5.36	42.08	0.2
UHPFRC [18]	2500	150.56	9.07	45.55	0.2
Steel re-bar [27]	7850	500 (f_y)	545	210	0.3

* *Note* NSC = Normal strength concrete of grade M30; UHPC = Ultra-high-performance concrete; UHPFRC = Ultra-high-performance fiber-reinforced concrete; ρ = Density; f_c = Compressive strength; f_y = Yield strength; f_t = Tensile strength; E = Young's modulus; μ = Poisson's ratio of the material

et al. [32]. The re-bars are discretized with T3D2 truss explicit elements [30, 33]. The reinforcements are embedded in the column using the EMBEDDED_REGION constraint command [30, 34]. The wrapping is made in contact with the column surface using the TIE constraint command [30], while the UHPC and UHPFRC coating are attached to the concrete surface using the surface interactions command [17]. The axial load-carrying columns are modeled with no translational degree-of-freedom restraint in the direction of the applied load and the bottom of the columns is fully restrained [27].

2.2 Blast Loading

The pressure–time history generated as a result of the explosion is characterized by two phases (positive and negative, Fig. 1a) [4, 9, 31, 33–37]. Upon explosion, the surrounding air pressure is atmospheric till the arrival time of the pressure wave, t_A. This pressure instantaneously reaches its peak value, P_{OP} called peak overpressure, after a very infinitely small time interval, t_1 [4, 5, 37–39]. Due to the pressure difference between atmospheric pressure and overpressure, the blast wave travels back in the direction of the source and generates a negative pressure phase for a time duration of t' till it comes back at atmospheric pressure, P_o [5, 23, 31, 35–37, 39, 40] (Fig. 1a). Many approaches are available in the open literature to model the blast loading; however, the empirical model given by Wu and Hao [39] is adopted in the present study, defined in Eqs. (2), (3), (4), (5), and (6). The analyses are conducted with a peak pressure of 8.71 MPa for both close-in and contact blast loading cases. The stand-off distance in case of contact blast has been calculated using the empirical equation suggested by Mills [22].

$$P_{OP} = \frac{1.772}{z^3} - \frac{0.114}{z^2} + \frac{0.108}{z} \tag{1}$$

Pressure–time history in the case of the close-in blast was referred from the experiment conducted by Kyei and Braimah [27], while blast-pressure–time history in the

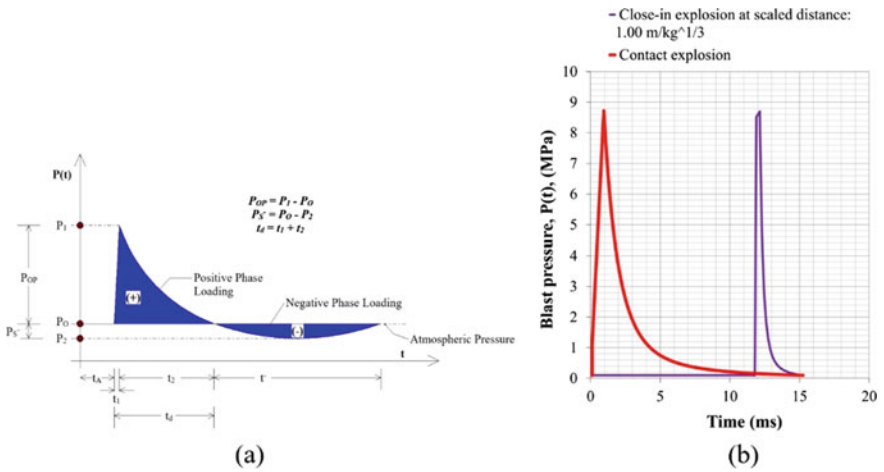

Fig. 1 **a** Idealized blast time history [39, 41] and **b** Pressure–time for $P_0 = 8.71$ MPa in close-in and contact detonation [27, 39]

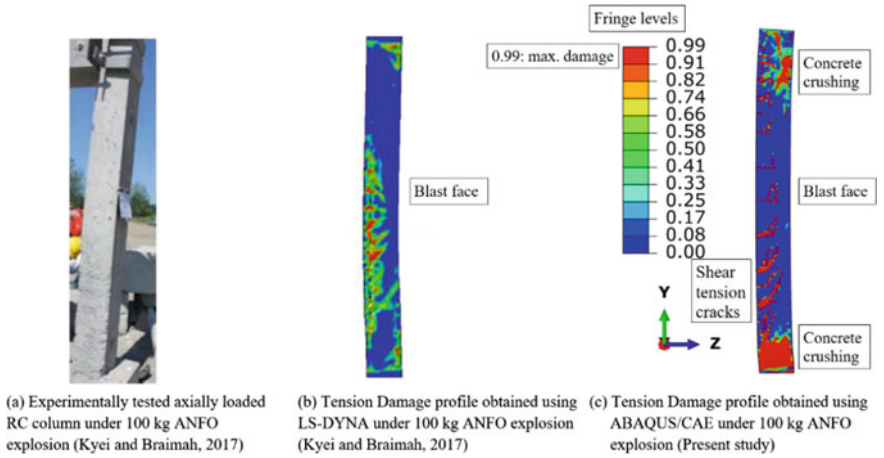

Fig. 2 Comparison of crack patterns of column C-1

case of contact detonation has been generated by assuming the same positive phase time duration as in the case of close-in blast, using the empirical equation proposed by Wu and Hao [39], where

$$t_A = 0.34R^{1.4}Q^{-0.2}/C_a \tag{2}$$

$$t_1 = 0.0019\left(\frac{R}{Q^{0.33}}\right)^{1.30} \tag{3}$$

$$t_2 = 0.0005 R^{0.72} Q^{0.16} \tag{4}$$

$$t_d = t_1 + t_2 \tag{5}$$

$$P(t) = \begin{cases} P_o, & (0 \le t < t_A) \\ P_o + P_{\mathrm{OP}}\left(\frac{t}{t_1}\right), & (t_A \le t \le t_1) \\ P_o + P_{\mathrm{OP}}\left(1 - \frac{t-t_1}{t_2}\right) \cdot \exp\left(-\frac{\xi(t-t_1)}{t_2}\right), & (t_1 \le t) \end{cases} \tag{6}$$

where t_a = arrival time (ms); t_1 = rising time (ms); t_2 = decreasing time (ms); and t_d = total positive phase duration (ms); Q = explosive charge (kg); R = detonation distance; C_a = speed of sound in the air = 340 m/s; $P(t)$ = blast pressure at time "t"; P_0 = 0.10 MPa (atmospheric pressure); P_{OP} = peak overpressure (MPa); Fig. 1a shows the idealized profile of the explosion loading. Following the current blast design guidelines, only the positive blast phase is modeled in the study [16, 35, 36, 42–45]. The blast load in the ABAQUS/CAE software is defined using the explicit solver technique [30, 46, 47]. Figure 1b represents the experimentally recorded and empirically generated blast history under close-in and contact explosion [27, 39].

2.3 Material Damage Modeling

The concrete damage plasticity (CDP) model is a plasticity-based constitutive model, which uses the plasticity limit to assess the damage and analyzes the failure of the concrete [36, 45, 48]. For the failure in the tension side of the concrete, the formation of tensile micro-cracks parameter after softening point is considered for the CDP model [38, 49, 50]. Previous research showed that the CDP model can simulate the cracking, crushing, and spalling of the concrete [20, 30, 51]. The damage plasticity model considers two types of failure mechanism, namely, tensile cracking and compressive crushing represented by two damage variables d_c and d_t, which are responsible for the reduction in stiffness [6, 7, 11–15, 38, 48, 50–52]. (Undamaged material)$d_c = 0$, and $d_t = 1$ (completely damaged material) [30, 38, 53]. The compressive and tensile behavior of concrete subjected to uniaxial compressive and tensile loadings are represented as [48, 53]

$$\sigma_t = (1 - d_t) E_0 \left(\varepsilon_t - \varepsilon_t^{pl,h}\right) \tag{7}$$

$$\sigma_c = (1 - d_c) E_0 \left(\varepsilon_c - \varepsilon_c^{pl,h}\right) \tag{8}$$

$$E_u = \left(1 - d_{i=c,t}\right) E_0 \tag{9}$$

Here, σ_t,σ_c = nominal tensile and nominal compressive stress, ε_t,ε_c = tensile and compressive strain, $\varepsilon_t = \varepsilon_t^{pl,h} + \varepsilon_t^{el}$, $\varepsilon_c = \varepsilon_c^{pl,h} + \varepsilon_c^{el}$,$\varepsilon_t^{pl,h}$, $\varepsilon_c^{pl,h}$ = plastic hardening tensile and compressive strain, ε_t^{el}, ε_c^{el} = elastic tensile and elastic compressive strain, E_0 = initial elastic modulus of concrete, E_u = reduced modulus of elasticity. To simulate the behavior of UHPC and UHPFRC, stress–strain data are incorporated in the CDP model of ABACUS/CAE, derived from the paper of Hassan et al. [18], and are converted into the required form with the help of equations provided by Hafezolghorani et al. [48]. The steel fiber content used in the case of UHPFRC is 2% by volume [18]. Experimental data obtained by Hafezolghorani et al. [48] is used to model the M30 concrete. The strain rate effect is incorporated by considering dynamic increase factors as given in reference [52]. The CFRP composite wrapping is modeled using the ABAQUS Hashin's damage model which predicts anisotropic damage mainly tension and compression damage in the fibers and matrix [30, 32, 39]. Hashin's damage parameters for the CFRP have been derived from Phan-Vu et al. [32].

3 Results and Discussions

Maximum transverse displacement and crack pattern of the square axially loaded RC column C1, i.e., the column with 4 bars of 25 mm diameter as longitudinal reinforcement and shear reinforcement in the form of 10 mm diameter stirrups at 75 mm c/c over the seismic confining zones, under 82 kg TNT blast loading are in close agreement with the maximum displacement and crack pattern obtained by Kyei and Braimah [27] with a percentage difference of 4% (Table 2 and Fig. 1). The top and bottom portions of the column are damaged with the concrete crushing of lengths 449 and 210 mm (Fig. 8), on the explosion face, while the tension face suffers from concrete spalling and flexure-shear cracks with a maximum depth of 190 mm (Fig. 9 and Table 3). The re-bars facing the explosion experience maximum principal compressive stress of 240.22 MPa at the mid-height of the column, while the re-bars on the rear side experience maximum tensile stress of 261.37 MPa (Fig. 7). The concrete on the blast face at the bottom and near the top of the column experiences maximum compressive stress of 33.92 MPa (>30 MPa) (Table 3 and Fig. 6).

Table 2 Comparison of maximum transverse mid-height displacement (mm) of column C-1

Experimental result (Kyei and Braimah [40])	ABAQUS/CAE result	% Age difference
36.00	34.57	4

Table 3 Summary of the responses obtained

Column description	Maximum transverse mid-height displacement (mm)	Maximum principal stresses in the longitudinal re-bars (MPa)	Maximum compressive stress in concrete (MPa)	DDE (J) at t = 15.25 ms	Average flexure crack depth (mm)
C1	34.57	+240.22; −261.37	+2.85; −33.92	600	190
Close-in	24.77	+231.56; −204.66	+2.81; −34.46	360	166
Contact	53.43	+247.34; −232.10	+2.49; −18.42	750	210
Close-in UHPC	17.60 ([a]29)	+207.71; −191.50	+2.87; −29.02	228	156
Contact UHPC	32.97 ([b]38)	+210.47; −208.80	+2.36; −30.54	509	200
Close-in UHPFRC	9.80 ([a]60)	+200.83; −165.69	+2.82; −42.56	48	125
Contact UHPFRC	28.63 ([b]46)	+202.96; −178.16	+2.36; −28.11	460	155
Close-in CFRP	6.26 ([a]75)	+101.64; −200.31	+2.78; −42.17	38	40
Contact CFRP	9.04 ([b]83)	+189.41; −168.31	+2.46; −98.41	51	75

Note C1 column: 300 mm × 300 mm; columns C2–C9 are circular RC columns of 350 mm diameter; + ve represents tensile stress and –ve represents compressive stress; DDE: damage dissipation energy; a = %age decrease with reference to "close-in" column, b = %age decrease with reference to "contact" column

3.1 Response of Equivalent Circular Column Under Close-In and Contact Explosions

The maximum transverse displacement in the case of "close-in" explosion is found to be 24.77 mm and the DDE is 360 J, (Table 3 and Figs. 3, 4 and 5). Reduction of the displacement is found to be 28%, and that in the damage is 40% with reference to column C1. The column undergoes higher displacement and suffers more damage under contact blast with the same pressure than in the case of a close-in blast. Maximum transverse displacement and DDE of the circular column under contact explosion are 53.43 mm and 750 J (Table 3 and Figs. 3 and 5).

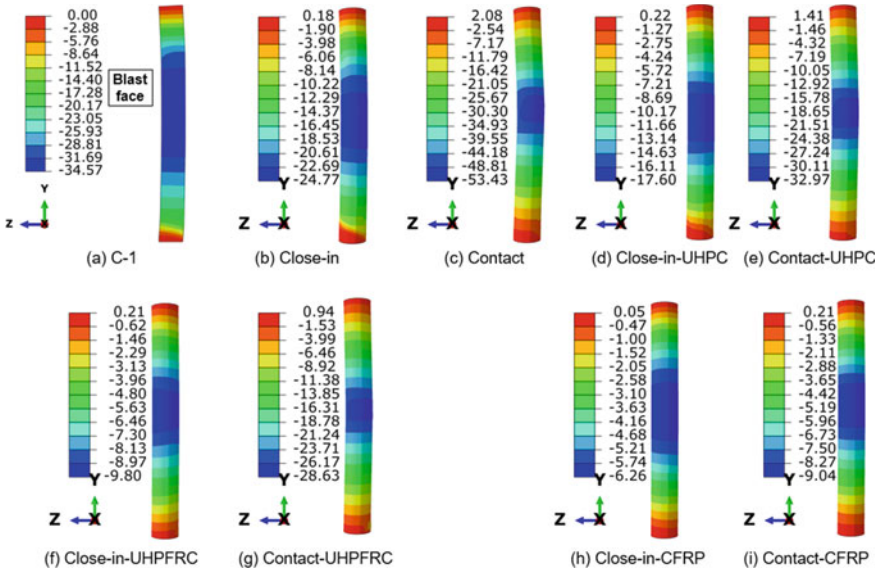

Fig. 3 Transverse displacements (mm) of different columns ($t = 15.25$ ms)

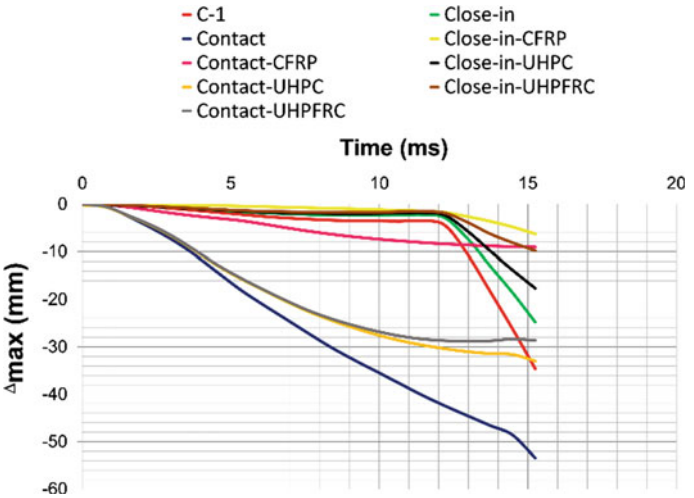

Fig. 4 Transverse displacement–time histories

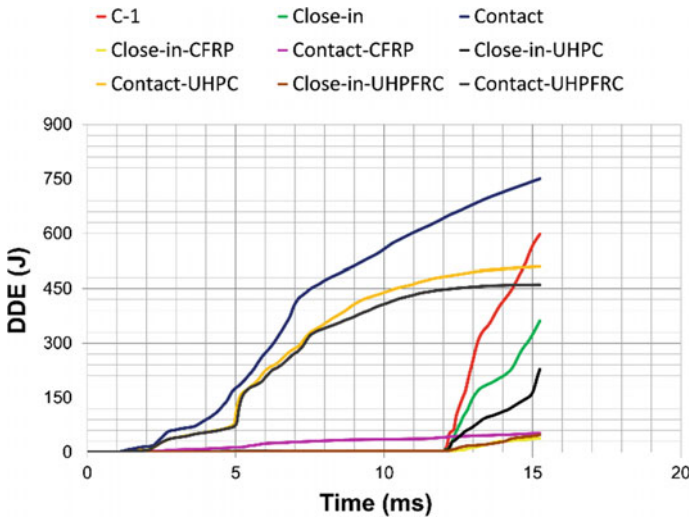

Fig. 5 Damage dissipation energy (DDE) of the columns

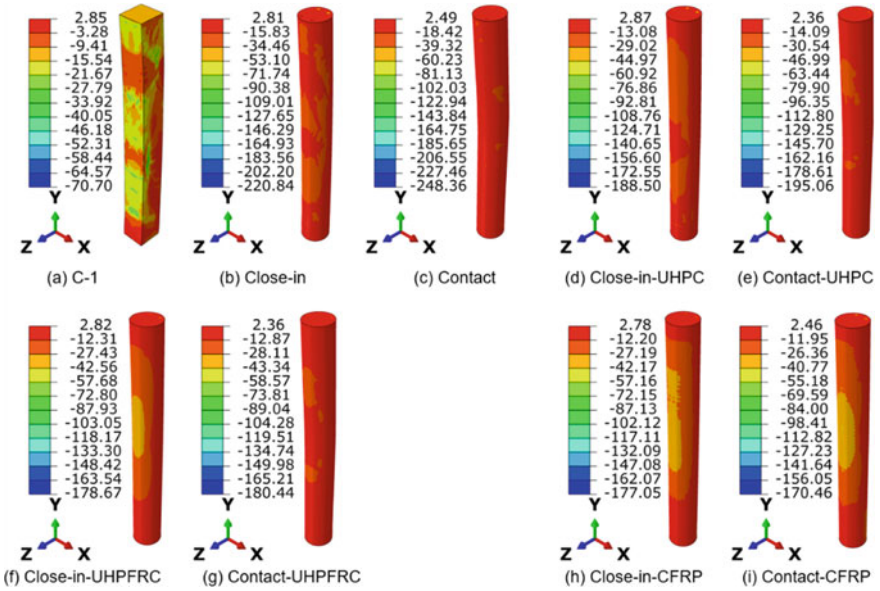

Fig. 6 Distribution of compressive stresses (MPa) in the concrete of the columns

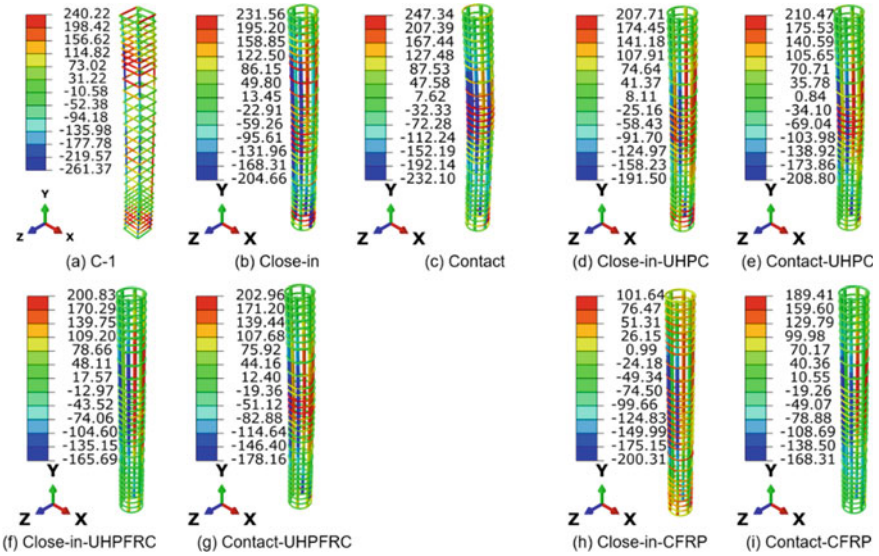

Fig. 7 Distribution of principal stresses (MPa) in the reinforcements of the columns

3.2 *Effect of UHPC Coating on the Circular Column Under Close-In and Contact Blast Loadings*

UHPC coating of 15 mm thickness on the circular RC column subjected to close-in blast improves the performance of the column. The maximum stress in the reinforcements and concrete of the column decrease, thereby reducing the maximum transverse displacement, DDE, and average flexural crack depth by 29, 37 and 6%, respectively, with respect to the corresponding response of the un-strengthened column (Table 3 and Figs. 3, 4 and 5). The percentage reductions of these parameters are 38, 32 and 5%, respectively, with respect to the corresponding response of the un-strengthened column under contact blast (Table 3 and Figs. 3, 4 and 5).

3.3 *Effect of UHPFRC Coating on the Circular Column Under Close-In and Contact Blast Loadings*

RC circular column with UHPFRC coating further excels the blast performance by reducing maximum transverse displacement, crack depth, and DDE by 60, 25, and 87%, respectively, under close-in blast, while the percentage reduction of these parameters under contact blast are 46, 30, and 26% with respect to their corresponding un-strengthened columns under close-in and contact blast (Table 3 and Figs. 3, 4 and 5). The UHPFRC of the strengthened column gets its maximum compressive stress

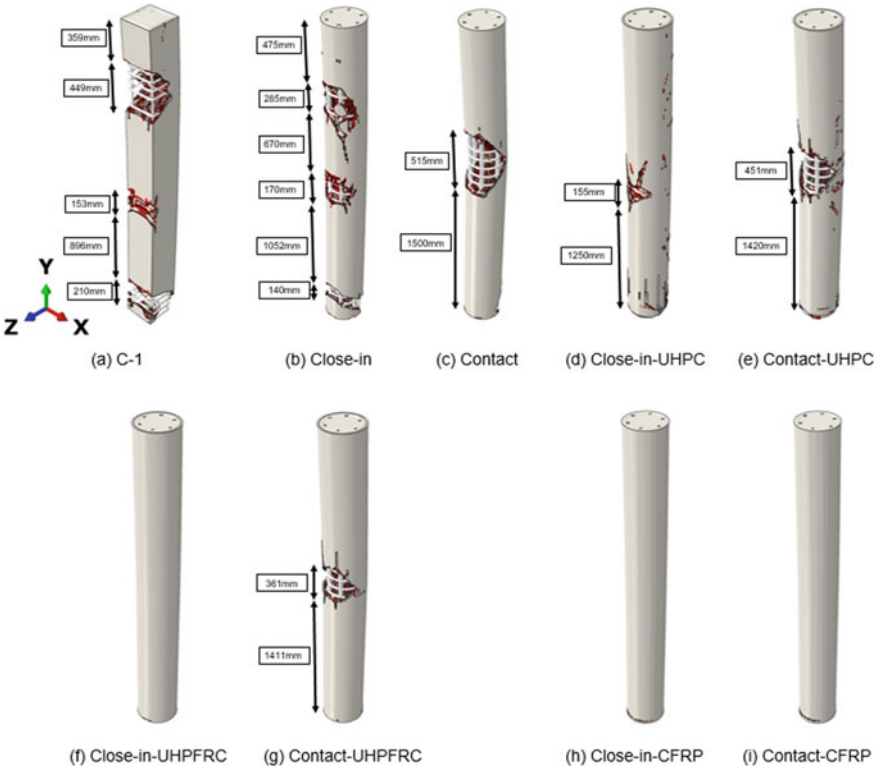

Fig. 8 Crushing of concrete of the columns [**Note* empty space in the figures shows the crushed concrete]

of 42.56 MPa and 28.11 MPa under column close-in and contact blast, respectively (Table 2 and Fig. 6). Comparing the blast performance of UHPFRC and UHPC strengthened columns; UHPFRC more significantly reduces the crushing of concrete under close-in blast but is not much significant in case of contact blast (Fig. 8). DDE of the column got reduced by 79% and crack depth reduces to 20% with respect to the close-in UHPC column (Table 3 and Fig. 5).

3.4 Effect of CFRP Composite Wrapping on the Circular Column Under Close-In and Contact Blast Loadings

The circular RC column strengthened with the CFRP composite wrapping gets minimum displacement, average flexural crack depth, and DDE by 75, 76, 89%, and 83, 64, 93%, respectively, with reference to the column under close-in and contact circular RC column (Table 3 and Figs. 3, 4 and 5). Almost negligible crushing and

Fig. 9 Concrete cracking and spalling of the columns

cracking are observed at the bottom of the column in both cases, proving to be the most superior among the strengthening techniques considered in this study (Figs. 9 and 10). Transverse displacement, average flexural crack depth, and DDE in case of CFRP decrease by 64, 74, 83% and 72, 62, 90%, with respect to UHPC close-in and contact, respectively. In comparing the CFRP-wrapped column with the UHPFRC-coated column, the transverse displacement, average flexural crack depth, and DDE decrease by 36, 68, 21% and 68, 51, 89%, with respect to UHPFRC close-in and contact, respectively (Table 3 and Figs. 3, 4 and 5). The performance of the column strengthened with the UHPFRC, and CFRP is comparable but the CFRP strengthened column is superior under the close-in explosion.

4 Conclusions

In this study, the following strengthening techniques have been considered to enhance the blast performance of the circular RC columns under (a) close-in and (b) contact blast, with the same peak pressure of 8.71 MPa, using ABAQUS/CAE software: (1)

15 mm thick coating of (i) UHPC and (ii) UHPRFC, and (2) 2 mm thick CFRP wrapping.

Analyses results from the numerical study conducted yield the following conclusions:

1. Un-strengthened circular column fails under (a) close-in blast due to (i) crushing of the concrete on the explosion face more at top and bottom than at mid-height region, and (ii) spalling of the concrete on tension side at bottom (b) contact blast due to (i) localized crushing of concrete at the mid-height region, and (ii) less severe spalling than in case of a close-in blast at the bottom but with additional spalling at mid-height region on tension face.
2. Localized severe crushing of concrete causes maximum stress in reinforcement increases over the smaller length of the reinforcement under contact explosion and this makes the maximum deflection more than two times that with a close-in explosion.
3. Application of UHPFRC and CFRP make the column give a comparable response but the CFRP makes the column perform better than UHPFRC under close-in explosion. UHPC does not significantly contribute to the blast performance of the column.
4. Under contact explosion the response of UHPC and UHPFRC is comparable but much inferior to CFRP. The application of CFRP superbly controls the damage and maximum deflection of the column in comparison to the concrete coatings.
5. Decision on application of coating or CFRP for strengthening of the column against blast loading may be taken depending upon size constraint on the columns and use of the structure.

References

1. Duaa A, Braimaha A, Kumar M (2020) Experimental and numerical investigation of rectangular reinforced concrete columns under contact explosion effect. Eng Struct Elsevier 205:1–19
2. Elsanadedy HM, Almusallam TH, Abbas H, Al-Salloum YA, Al-Salloum SH (2011) Effect of blast loading on CFRP-Retrofitted RC columns—a numerical study. Latin American J Solids Struct 8:55–81
3. Li M, Zong Z, Hao H, Zhang X, Lin J, Xie G (2019) Experimental and numerical study on the behaviour of CFDST columns subjected to close-in blast loading. Eng Struct Elsevier 185:203–220
4. Anas SM, Alam M, Umair M (2022) Influence of charge locations on close-in air blast response of pre-tensioned concrete U-girder. In: Kolathayar S et al. (eds) Resistant infrastructure, lecture notes in civil engineering. vol 202. Springer, Singapore. https://doi.org/10.1007/978-981-16-6978-1_40
5. Ahmadi E, Alam M, Anas SM (2022) Blast performance of RCC slab and influence of its design parameters. In: Kolathayar S et al. (ed) Resistant infrastructure, lecture notes in civil engineering, vol 202. Springer, Singapore. https://doi.org/10.1007/978-981-16-6978-1_31
6. Anas SM, Alam M (2022) Performance of simply supported concrete beams reinforced with high-strength polymer re-bars under blast-induced impulsive loading. Int J Struct Eng 12(1):62–76. https://www.inderscienceonline.com/doi/abs/10.1504/IJSTRUCTE.2022.119289

7. Anas SM, Alam M (2022) Performance of brick-filled reinforced concrete composite wall strengthened with C-FRP laminate(s) under blast loading. Mater Today: Proc. https://doi.org/10.1016/j.matpr.2022.03.162
8. Anas SM, Alam M, Umair M (2022) Effect of design strength parameters of conventional two-way singly reinforced concrete slab under concentric impact loading. Mater Today: Proc. https://doi.org/10.1016/j.matpr.2022.02.441
9. Anas SM, Alam M, Umair M (2022) Out-of plane response of clay brick unreinforced and strengthened Masonry walls under explosive-induced air-blast loading. In: Kolathayar S et al (eds) Resistant infrastructure, Lecture notes in civil enginering 2022, vol. 202. Springer, Singapore. https://doi.org/10.1007/978-981-16-6978-1_37
10. Cui J, Shi Y, Li Z-X, Chen L (2015) Failure analysis and damage assessment of RC columns under close-in explosions. Amer Soc Civil Eng 29:1–11
11. Shariq M, Alam M, Husain A, Anas SM (2022) Jacketing with steel angle sections and wide battens of RC column and its influence on blast performance. Asian J Civil Eng. Springer (Article in press)
12. Tahzeeb R, Alam M, Muddassir SM (2022) A comparative performance of columns: reinforced concrete composite and composite with partial C-FRP wrapping under contact blast. Mater Today: Proc. https://doi.org/10.1016/j.matpr.2022.03.367
13. Anas SM, Shariq M, Alam M, Umair M (2022) Evaluation of critical damage location of contact blast on conventionally reinforced one-way square concrete slab applying CEL-FEM blast modeling technique. Int J Protective Struct (Article in press)
14. Anas SM, Alam M, Umair M (2022) Performance based strengthening with concrete protective coatings on braced unreinforced masonry wall subjected to close-in explosion. Mater Today: Proc. Elsevier (Article in press)
15. Anas SM, Alam M, Shariq M, Umair M (2022) Damage response of conventionally reinforced two-way spanning concrete slab under eccentric impacting drop weight loading. Defence Technol (Article in press)
16. ASCE/SEI 59–11(2011) Blast protection of buildings, American Society of Civil Engineers, U.S.
17. Wua C, Oehlers DJ, Rebentrost M, Leach J, Whittaker AS (2009) Blast testing of ultra-high-performance fibre and FRP-retrofitted concrete slabs. Eng Struct J Elsevier 31:2060–2069
18. Hassan AMT, Jones SW, Mahmud GH (2012) Experimental test methods to determine the uniaxial tensile and compressive behaviour of ultra-high-performance fibre reinforced concrete (UHPFRC). Construct Build Mater Elsevier 37:874–882
19. Juechun X, Chengqing W, Hengbo X, Yu S, Zhong-Xian L, Qin F, Hong H, Zhongxian L, Yadong Z, Jun L (2016) Behaviour of ultra-high-performance fibre reinforced concrete columns subjected to blast loading
20. Abbood IS, Odaa SA, Hasan KF, Jasim MA (2021) (2021), Properties evaluation of fiber reinforced polymers and their constituent materials used in structures—a review. Mater Today Elsevier 43:1003–1008
21. Afifi MZ, Mohamed HM, Benmokrane B (2014) Strength and axial behavior of circular concrete columns reinforced with CFRP bars and spirals. J Composites for Construct ASCE 18:1–10
22. Mills CA (1987) The design of concrete structure to resist explosions and weapon effects. In: Proceedings of the first Int conference on concrete for hazard protections, Edinburgh, UK, pp 61–73
23. Anas SM, Alam M (2021) Response of free-standing (1) Unreinforced Brick Masonry wall, (2) cavity RC wall, (3) RC walls with (i) Bricks, (ii) Sand, in the cavity: A Macro-Modelling approach. In: Marano GC, Ray Chaudhary S, Unni Kartha G, Kavitha PE, Prasad R, Achison RJ (eds) Proceedings of SECON'21. SECON2021. lecture notes in civil engineering, vol 171. Springer, Cham, pp 921–930. https://doi.org/10.1007/978-3-030-80312-4_78
24. Roller C, Mayrhofer C, Riedel W, Thoma K (2012) Residual load capacity of exposed and hardened concrete columns under explosion loads. Eng Struct, Elsevier 1–7
25. Jayasooriya R, Thambiratnam DP, Perera NJ (2014) Blast response and safety evaluation of a composite column for use as key element in structural systems. Eng Struct Elsevier 61:31–43

26. Xu J, Wu C, Xiang H, Su Y, Li Z-X, Fang Q, Hao H (2016) Behaviour of ultra-high-performance fibre reinforced concrete columns subjected to blast loading. Eng Struct Elsevier 118:97–107
27. Kyei C, Braimah A (2017) Effects of transverse reinforcement spacing on the response of reinforced concrete columns subjected to blast loading. Eng Struct Elsevier 142:148–164
28. Wang W, Asce AM, Wu C, Li J (2018) Numerical simulation of hybrid FRP-concrete-steel double-skin tubular columns under close-range blast loading. ASCE J Compos Constr 22:1–15
29. Hu Y, Chen L, Fang Q, Kong X, Shi Y (2021) Study of CFRP retrofitted RC column under close-in explosion. EEng Struct Elsevier 27:1–23
30. ABAQUS/CAE FEA program (2017) Concrete-damaged plasticity model, explicit solver, three-dimensional solid element library. ABAQUS DS-SIMULIA User Manual
31. Ain Q, Ul, Alam M, Anas SM (2022) Behaviour of ordinary load bearing masonry structure under distant large explosion, Beirut Scenario. In: Kolathayar S et al (eds) Resistant infrastructure, lecture notes in civil enginering, vol 202. Springer, Singapore. https://doi.org/10.1007/978-981-16-6978-1_19
32. Phan-Vu P, Tran TD, Pham MT, Dang D T, Ngo-Huu C, Nguyen-Minh L (2021) Distinguished bond behaviour of CFRP sheets in unbonded post-tensioned reinforced concrete beams versus single-lap shear tests. Eng Struct Elsevier 234
33. Anas SM, Alam M, Umair M (2020) Performance of one-way composite reinforced concrete slabs under explosive-induced blast loading. In: 1st international conference on energetics, civil and agricultural engineering 2020, ICECAE 2020, Tashkent, Uzbekistan, vol 614. https://doi.org/10.1088/1755-1315/614/1/012094
34. Anas SM, Ansari MI, Alam M (2021) A study on existing masonry heritage building to explosive-induced blast loading and its response. Int J Struct Eng, 1(4): 387-412. https://www.inderscienceonline.com/doi/abs/10.1504/IJSTRUCTE.2021.118065
35. IS 4991(1968) Criteria for blast resistant design of structures for explosions above ground. Bureau of Indian Standards, New Delhi, India
36. TM 5–1300(1990) Structures to resist the effect of accidental explosions. Technical Manual, Joint Department of the Army, the Navy, and the Air Force, US.
37. Anas SM, Alam M (2021) Comparison of existing emperical equations for blast peak positive overpressure from spherical free air and hemisphere surface bursts. Iranian J Sci Technol Trans Civil Eng, 46: 965-984. https://doi.org/10.1007/s40996-021-00718-4
38. Anas SM, Alam M, Umair M (2021) Experimental and numerical investigations on performance of reinforced concrete slabs under explosive-induced air-blast loading: a state-of-the-art review. Struct Elsevier 31:428–461. https://doi.org/10.1016/j.istruc.2021.01.102
39. Wu C, Hao H (2005) Modeling of simultaneous ground shock and air-blast pressure on nearby structures from surface explosions. Int J Impact Eng Elsevier 31:699–717
40. Koccaz Z, Sutcu F, Torunbalci N (2008) Architectural and structural design for blast resistant buildings. 14 WCEE
41. Anas SM, Ansari MdI, Alam M (2020) Performance of masonry heritage building under air-blast pressure without and with ground shock. Aust J Struct Eng 21(4):329–344. https://doi.org/10.1080/13287982.2020.1842581
42. Alsendi A, Eamon CD (2020) Quantitative resistance assessment of SFRP-strengthened RC bridge columns subjected to blast loads. Amer Soc Civil Eng 34:1–9
43. IS 6922(1973) Criteria for safety and design of structures subject to underground blasts. Bureau of Indian Standards, New Delhi, India
44. UFC 3–340–02 (2008) Structures to resist the effects of accidental explosions. Department of Defence, U.S.
45. Anas SM, Alam M, Umair M (2021) Performance of on-ground double-roof RCC shelter with energy absorption layers under close-in air-blast loading. Asian J Civil Eng, 22: 1525-1549. https://doi.org/10.1007/s42107-021-00395-8
46. Hao H, Hao Y, Li J, Chen W (2016) Review of the current practices in blast-resistant analysis and design of concrete structures. Adv Struct Eng 2016:1–31
47. Anas SM, Alam M, Umair M (2021) Air-blast and ground shockwave parameters, shallow underground blasting, on the ground and buried shallow underground blast resistant shelters: a review. Int J Protect Struct, 13(1): 9-139. https://doi.org/10.1177/20414196211048910

48. Hafezolghorani M, Hejazi F, Vaghei R, Jaafar MSB, Karimzade K (2017) Simplified damage plasticity model for concrete milad. Struct Eng Int 27(1):68–78
49. Grassl P, Xenos D, Nyström U, Rempling R, Gylltoft K (2013) CDPM2: a damage-plasticity approach to modelling the failure of concrete. Int J Solids Struct Elsevier 50:3805–3816
50. Singh M, Sheikh AH, Ali MSM, Visintin P, Griffith MC (2017) Experimental and numerical study of the flexural behaviour of ultra-high-performance fibre reinforced concrete beams. Construct Build Mater Elsevier 138:12–25
51. Anas SM, Alam M, Umair M (2021) Performance of one-way concrete slabs reinforced with conventional and polymer re-bars under air-blast loading. In: Chandrasekaran S, Kumar S, Madhuri S (eds) Recent advances in structural engineering. lecture notes in civil engineering, April 2021, vol 135. pp 179–191. https://doi.org/10.1007/978-981-33-6389-2_18
52. Anas SM, Shariq M, Alam M (2022) Performance of axially loaded square RC columns with single/double confinement layer(s) and strengthened with C-FRP wrapping under close-in blast. Mater Today: Proc. https://doi.org/10.1016/j.matpr.2022.01.275
53. Farahmandpour C, Dartois S, Quiertant M, Berthaud Y, Dumontet H (2017) A concrete damage–plasticity model for FRP confined columns. Mater Struct RILEM 2017:14–20
54. Astarlioglu S, Krauthammer T, Morency D, Tran TP (2013) Behavior of reinforced concrete columns under combined effects of axial and blast-induced transverse loads. Eng Struct Elsevier 55:26–34
55. Li J, Wu C, Hao H, Liu Z (2017) Post-blast capacity of ultra-high performance concrete columns. Eng Struct Elsevier 134:289–302
56. Nasera MZ, Hawilehb RA, Abdalla JA (2019) Fiber-reinforced polymer composites in strengthening reinforced concrete structures: a critical review. Eng Struct Elsevier 198:1–20
57. Vojiadjis GZ, Taqieddin ZN, Kattan PI (2008) Anisotropic damage-plasticity model for concrete. Int J Plasticity 24(19):1–13
58. Wu C, Oehlers DJ, Rebentrost M, Leach J, Whittaker AS (2009) Blast testing of ultra-high-performance fibre and FRP-retrofitted concrete slabs. Eng Struct, Elsevier 31:2060–2069

Statistical Analysis on the Influence of Recycled Concrete Aggregate on the Concrete Properties

S. R. Shashikumara, R. Abhishek, S. Vivek, V. K. Nagaraj, and K. C. Sachin

Abstract The construction industry alone in India produces 10–15 million tonnes of waste annually. In new construction, usage of recycled concrete aggregate provides major benefits like reduction in environmental pollution and conservation of nature. In the present study, the different percentages of recycled concrete aggregate (0, 50, and 100%) are used as a replacement to natural coarse aggregate in concrete. The concretes are tested for workability and strength properties for the water to cement ratios: 0.40, 0.45, and 0.50. The experiment was designed using Minitab software. Taguchi method with L9 orthogonal array was selected for the variables: w/c, RCA content, mixing time, and curing period. The strengths were measured at 7, 28, and 56 days. *F*-value and *P*-value of ANOVA test were analyzed to understand the influence of variables on the concrete. Statistical analysis proved the negative impact of recycled concrete aggregate on workability. The strength test results indicated reduced strength for more than 50% replacement of recycled concrete aggregate.

Keywords ANOVA · Recycled aggregate concrete (RAC) · Recycled concrete Aggregate (RCA) · Regression equation · Residual plots · Taguchi method

1 Introduction

At present, the demand for the aggregates in the construction industry is more than 5.1 billion metric tons around the world. Because of this huge requirement, the natural sources such as stream, rivers, rocks, and quarried sand are getting depleted day by day. Scarcity of availability of aggregate has resulted in alternative sources.

S. R. Shashikumara (✉) · R. Abhishek · S. Vivek
JSS Academy of Technical Education, Bengaluru, Karnataka, India
e-mail: shashikumarsr@jssateb.ac.in

V. K. Nagaraj
Nagarjuna College of Engineering and Technology, Bengaluru, Karnataka, India

K. C. Sachin
R V College of Engineering, Bengaluru, Karnataka, India

L. Nandagiri et al. (eds.), *Recent Advances in Civil Engineering*, Lecture Notes in Civil Engineering 256, https://doi.org/10.1007/978-981-19-1862-9_25

The burden on the natural resources can be reduced by reusing construction demolition wastes as aggregate in concrete [1]. To overcome one of the crucial environmental issues, these waste material can be recycled to fabricate standard product such as structural or non-structural concrete. The recycled concrete aggregate (RCA) in concrete can be used economically and viable in environment. The aggregate obtained from crushing old concrete can be providing inconsistent properties like increased water-to-cement ratio and cement content in original concrete. In a concrete mixture, aggregates contribute about 50–55% of its volume. The RCA can be replaced totally or partially, i.e., 100% or <100% by natural aggregate. Due to the high water absorption and high cohesion of RCA, it is very difficult to control the quality of concrete [2]. Construction industry is the second largest industry after agriculture in India. Construction projects depend mainly upon the material. Twenty billion tonnes of aggregate, 1.52 billion tonnes of cement, and 820 million tonnes of water are used by construction industry. This contributes to about 5–7% of CO_2 emission. The characteristics of crushed RCA are almost similar to the natural aggregates and it is insignificantly impacted by grade or original concrete quality. Thus, by using the RCA in concrete, the consumption of natural resources can be reduced [3].

Design of experiment (DOE) is the widely implemented method for various mixture proportion studies. The time and cost are the two major problems arise in the experiment and complex calculations which are encountered by DOE practice. It employs an orthogonal array analysis which improves the efficiency and effectiveness by decreasing the time/cost of experiments with multiple responses [4]. In the significance of control factors identified for the DOE method, the significant control factor due to high contribution rate is water–cement ratio. The results obtained from mixture assessed from the full design are same as the mixture assessed from the reduced responses design. The interaction between the water–cement ratio and recycled concrete aggregate volume ratio is the most influential factor which gives the slump of 180 mm and compressive strength of 30.17 N/mm^2 [5].

At present, a good number of researches are focusing on the usage of construction demolition waste as aggregate replacement in concrete. Due to the problems associated with collection, transportation, crushing and segregation of recycled aggregate, its usage in concrete is still in developing stage. Difficulty in scientific segregation of construction demolition waste can be encountered by directly using the recycled concrete as coarse aggregate to reduce the time and cost. In this article, an effort was made to use the recycled concrete aggregate (RCA) at different replacement ratios. Natural coarse aggregates are replaced by RCA at the ratio of 0, 50, and 100% at the water to cement ratio (w/c) of 0.40, 0.45, and 0.50 to study the fresh and mechanical properties for concrete mixes at 7, 28, and 56 days of moist curing. Taguchi method was adopted with four variables and four responses to validate the experimental results.

Table 1 Ordinary Portland cement properties

Properties	Observed values
Specific gravity	3.15
Compressive strength (N/mm^2)	53
Fineness (m^2/kg)	225
Soundness (mm)	10
Initial setting time (min)	32
Final setting time (min)	567

2 Materials and Methods

2.1 Materials

Ordinary Portland cement (OPC) with properties tabulated in Table 1 was used in the present investigation. Manufactured sand (M-sand) used in the experiment as fine aggregate was in accordance with IS 383:1970 [6] (zone II). It had the specific gravity of 2.59, water absorption of 2.6%, fineness modulus of 4.92%, and density of 1500 kg/m^3. Coarse aggregate (CA) used in two size. First size was passing through 20 mm sieve and retaining on 16 mm sieve and the other one was passing through the 16 mm sieve and retaining on 12.5 mm sieve. Granite material having specific gravity of 2.62, water absorption of 2%, density of 1510 kg/m^3, impact value of 16%, abrasion value of 17%, and fineness modulus is 5.91% was used as natural coarse aggregate. The recycled concrete aggregate (RCA) was obtained from concrete blocks which were crushed mechanically and then sieved to obtain the similar size as that of natural coarse aggregate. RCA had specific gravity of 2.40, water absorption of 2.65%, impact value of 25.83%, abrasion value of 25.12%, density of 1392 kg/m^{3,} and fineness modulus of 5.91%. Potable quality water in line with IS 456: 2000 [7] requirements is used for concrete preparation.

2.2 Method

Three water-to-cement ratio (w/c): 0.40, 0.45, and 0.50, three recycled concrete aggregate content: 0, 50, and 100%, and three curing period of 7, 28, and 56 days were considered. Also, 30, 60, and 90 s of mixing time were considered to observed the influence on workability and mechanical properties. Concrete mixes considered for the experiments are depicted in Table 2.

Slump cone test and Vee-Bee Consistometer tests as shown in Fig. 1 were conducted as per IS 1199:1959 [8] to understand the effect of RCA, w/c and mixing time on workability of recycled aggregate concrete (RAC) and natural aggregate concrete (NC).

Table 2 Concrete mixes

Type of concrete	Mix code
Normal concrete (NC)	NC040
	NC045
	NC050
Recycled aggregate concrete (RAC)	RAC04050
	RAC04550
	RAC05050
	RAC040100
	RAC045100
	RAC050100

Fig. 1 Vee-Bee consistometer test setup

Compressive strength test as depicted in Fig. 2 was carried at 7, 28, and 56 days of moist curing as per the IS 516: 1959 [9] on the 150 × 150 × 150 mm cube specimens for both categories of concrete. Prism specimens of 150 × 150 × 750 mm casted and tested for flexural strength.

Experiment was designed on the licensed Minitab software to ascertain the set of experiments. Taguchi method with L9 orthogonal array was selected for the variables: w/c, RCA content, mixing time, and curing period. The set of experiments provided by software depicted in Table 3. Experiments were carried at the laboratory and the results were imported back to software. ANNOVA calculations were made to find the variance table and regression equation. Mix design of concrete was carried in accordance with IS 10262:2009 [10] and IS 456:2000 [7]. Proportion of concrete mixes are tabulated in Table 4.

Fig. 2 Compression test on cube specimen

Table 3 Set of experiment by Taguchi method

Mix code	Replacement of RCA ratio (%)	w/c	Mixing time (sec)	Curing period (days)
NC040	0	0.4	30	7
NC045	0	0.45	60	28
NC050	0	0.5	90	56
RAC04050	50	0.4	30	7
RAC04550	50	0.45	60	28
RAC05050	50	0.5	90	56
RAC040100	100	0.4	30	7
RAC045100	100	0.45	60	28
RAC050100	100	0.5	90	56

Table 4 Concrete mix proportion

Concrete type	Mix code	w/c	OPC (kg/m^3)	Fine aggregate (kg/m^3)	Natural coarse aggregate (kg/m^3)	Recycled concrete aggregate (kg/m^3)	Water (kg/m^3)
Natural concrete (NC)	NC040	0.40	493	738	950	0	197
	NC045	0.45	438	774	957	0	197
	NC050	0.50	394	808	960	0	197
Recycled aggregate concrete (RAC)	RAC04050	0.40	493	738	475	475	197
	RAC04550	0.45	438	774	478.50	478.50	197
	RAC05050	0.50	394	808	480	480	197
	RAC040100	0.40	493	738	0	950	197
	RAC045100	0.45	438	774	0	957	197
	RAC050100	0.50	394	808	0	960	197

3 Results and Discussion

3.1 Workability

Results displayed in Table 5 indicates that the highest slump obtained was 117 mm and the lowest slump achieved was 55 mm.

All mixes exhibited decreased workability with increased percentage of recycled concrete aggregate (RCA). This may be due to the rough surface texture and high absorption capacity of RCA [11]. When the natural aggregate (NA) is replaced by 50% RCA with the w/c ratio of 0.45 the slump value decreases by 14%. The slump value decreased by 24% with the replacement of NA by RCA completely with the water to cement ratio of 0.45. On the other hand, when the w/c increased to 0.50, the slump value increased by 42%.

Vee-Bee consistometer test results as shown in Fig. 3 indicated the maximum value of 34.2 s and the lowest value of 6.5 s. As the percentage of RCA increases, the

Table 5 Results of slump cone test

Mix code	Replacement of RCA ratio (%)	Slump (mm)
NC040	0	0
NC045	0	72
NC050	0	117
RAC04050	50	0
RAC04550	50	62
RAC05050	50	103
RAC040100	100	0
RAC045100	100	55
RAC050100	100	96

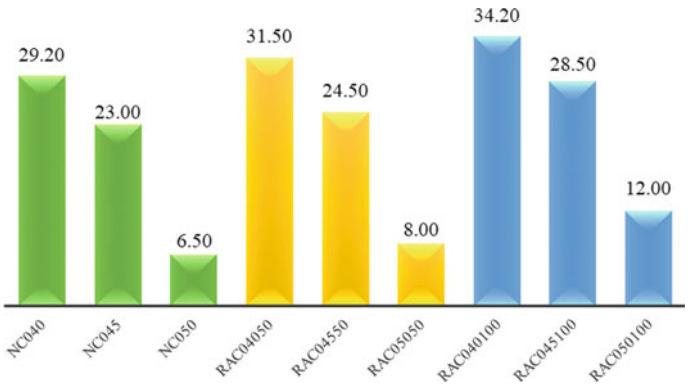

Fig. 3 Vee-Bee consistometer test results

Vee-Bee time increases due to porosity and water absorption [12]. At the same time with increase in w/c ratio, the Vee-Bee time decreases. The workability increases as the w/c ratio increases and due to the increase of RCA percentage the workability decreases. Due to more voids in RCA, the water absorption increases compared to NA; therefore, it leads to decrease in workability [13].

3.2 Mechanical Properties

RAC050100 shows compressive strength of 22.80 N/mm^2, whereas RAC05050 and NC050 displayed the strengths of 26.95–31.70 N/mm^{2,} respectively. Table 6 indicates after a 28 days of curing NC045 recorded a strength of 26.60 N/mm^2, whereas RAC04550 and RAC045100 shows a strength of 22.40–19.15 N/mm^2. This is due to increased water absorption by recycled concrete aggregates than the normal coarse aggregates [11, 14]. As the curing period increases from 7 to 56 days, the strength increases from 17.40 to 31.70 N/mm^2 in NC, whereas the strength increases from 14.70 to 26.95 N/mm^2 in RAC 50% replacement and from 12.53 to 22.82 N/mm^2 in RAC 100% replacement mixes.

Mixing is an important parameter for achieving workability and a desired target strength. The increase in compression strength is found with an increase in the mixing time. RCA compressive strength with 50% replacement is found to be 15% lesser and 28% lesser in 100% replacement compared to the natural aggregate concrete.

RAC045100 shows the flexural strength of 3.10 N/mm^2, whereas RAC04550 and NC045 recorded the strengths of 3.25–3.55 N/mm^{2,} respectively. NC050 displayed a strength of 4.00 N/mm^2 at the end of 28 days curing. But, RAC05050 and RAC050100 showed the strengths of 3.65–3.35 N/mm^2. This indicated the effect of free water absorption by recycled aggregate [15, 16]. As the curing period increases from 7 to 56 days, the strength increases from 3.15 to 4.00 N/mm^2 in NC, 3.00 to 3.65 N/mm^2 in

Table 6 Compressive strength test results

Type of concrete	Mix code	Replacement of RCA ratio (%)	w/c	Mixing time, (seconds)	Curing period (days)	Compressive strength (N/mm^2)
Natural concrete (NC)	NC040	0	0.40	30	7	17.40
	NC045	0	0.45	60	28	26.60
	NC050	0	0.50	90	56	31.70
Recycled aggregate concrete (RAC)	RAC04050	50	0.40	30	7	14.70
	RAC04550	50	0.45	60	28	22.40
	RAC05050	50	0.50	90	56	26.95
	RAC040100	100	0.40	30	7	12.55
	RAC045100	100	0.45	60	28	19.15
	RAC050100	100	0.50	90	56	22.80

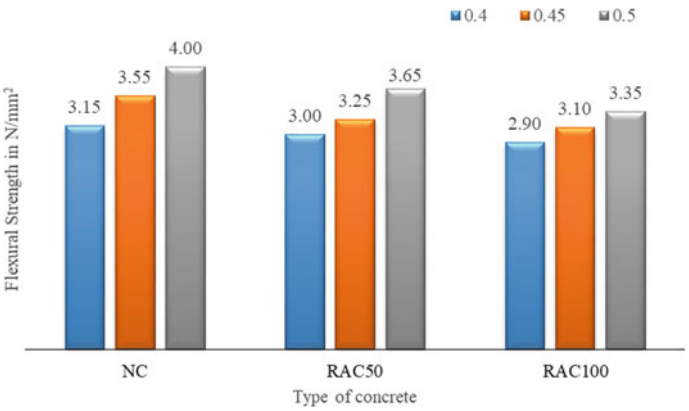

Fig. 4 Flexural strength test results

RAC50 replacement, and 2.90 to 3.35 N/mm^2 in RAC100. Average flexural strengths of RCA with 50% replacement is 6% lesser and RCA with 100% replacement is 12% lesser than the NC as displayed in Fig. 4.

4 Statistical Validation of Test Results

4.1 Workability Test Results

General linear model in ANOVA calculation was used to find the variance table and regression equation for slump test, Vee-Bee consistometer test, flexural strength, and compression strength.

The influence of variables: recycle concrete aggregate (RCA) replacement ratio, w/cm and mixing time on the responses: slump value, Vee-Bee time, compressive strength, and flexural strength were analyzed based on the *P*-value and *F*-value.

The *P*-value measures the probability evidence against null hypothesis. If *P*-value is less than 0.05, then that term is said to be more significant value and it is the test to determine variable association with the response. Higher *F*-value indicates that the term is significant. Tables 7 and 8 display the factorial information and analysis of variance for both slump value and Vee-Bee time, respectively.

Table 7 Factor information for workability tests

Factor	Levels	Values
RCA replacement ratio (%)	3	0, 50, 100
w/c	3	0.40, 0.45, 0.50
Mixing time (sec)	3	30, 60, 90

Table 8 Analysis of variance for workability tests

Source	Slump value		Vee-Bee time	
	F-value	*P*-value	*F*-value	*P*-value
RCA replacement ratio (%)	0.89	0.529	154.49	0.006
w/c	571.43	0.002	2901.56	0.000
Mixing time (sec)	2.73	0.268	1.00	0.500

Variance analysis indicated *P*-value of 0.002 for w/c ratio and *F*-value of 571.43. These values showed the evidence of w/c ratio influence on slump value [17]. *F*-value also evident the major effect of w/c ratio. Considerable effect of mixing time was evidenced with the *P*-value of 0.268 and *F*-value of 2.73. As per the variance analysis responses, the mixing time had minimal effect on the slump value. Same trend of influence was witnessed in the Vee-Bee time. *P*-value of 0.000 and *F*-value of 2901.56 supported the w/c influence. Among three factors and next to w/c, the effect of replacement ratio on the Vee-Bee time was proved with *P*-value of 0.006 and *F*-value of 154.49.

4.2 Mechanical Properties

The results of strength test were imported to Minitab software to identify the influence of factors on responses with the help of residual plots in Fig. 5, *P*- and *F*-values.

Table 9 provides the factor information and the *P*-value and *F*-value are tabulated in Table 10.

Curing period influence on compressive strength was evidenced [18] by *P* and *F*-value of 0.010 and 96.53. Curing period provided a strong evidence against null hypothesis. *F*-value of 17.36 indicated the RCA replacement ratio as the second most influencing factor. From the residual plots and variance analysis response, mixing time displayed least influence on the compressive strengths of RAC and NC.

Table 10 shows the factors: RCA replacement ratio, w/c, and curing period were significant in flexural strength as their *P*-values of 0.017, 0.033, and 0.002 less than 0.05 and provided strongest evidence against null hypothesis. According to the *F*-values, curing period with 399.57 value had key influence. The order of influence of the factor on flexural strength varies from curing period to w/c [19].

In overall, usage of RCA influences both workability and strength properties of concrete. Slump value and Vee-Bee time decreases by 24 and 46% due to complete replacement of natural coarse aggregate by RCA. Similar influence of RCA on strength properties was witnessed. Increase in the replacement % resulted in decreased strength properties of concrete. These behaviors necessitates the judicious use of RCA without compromising the workability and strength properties. Statistical validation of the experimental results clearly indicating the substantial

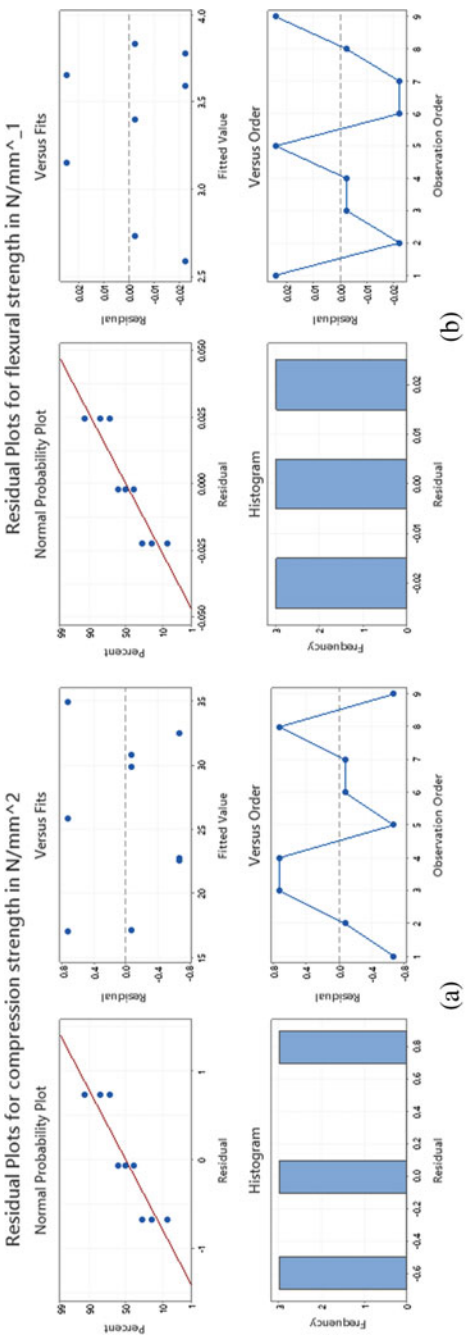

Fig. 5 Residual plots for **a** compressive strength, and **b** flexural strength test results

Table 9 Factor information for compressive and flexural strength tests

Factor	Levels	Values
RCA replacement ratio (%)	3	0, 50, 100
w/c	3	0.40, 0.45, 0.50
Curing period (days)	3	7, 28, 56

Table 10 Variance analysis of compressive and flexural strength tests

Source	Compressive strength		Flexural strength	
	F-value	*P*-value	*F*-value	*P*-value
RCA replacement ratio (%)	17.36	0.054	57.21	0.017
w/c	1.73	0.366	29.30	0.033
Curing period (days)	96.53	0.010	399.57	0.002

influence of considered variables: replacement ratio, w/c, mixing time, and curing period on the workability and strength properties of RAC.

5 Conclusions

Usage of RCA in concrete is a sustainable approach to reduce the environmental impact due to construction activity. Experimental test results indicate impact of RCA both on workability and strength. Although the RAC mixes displayed satisfactory workability, but it decreases with increase in RCA content. The w/c played a decisive role in achieving the satisfactory results. Reasonable slump value of 103 mm and Vee-Bee time of 8.00 s are notice with w/c of 0.50. This trend may indicate two possibilities: necessity of superplasticizer to get the required workability and restrict the RAC usage for lower grades. In comparison with NC mixes, both RAC mixes displayed lesser strength as the RCA content increases. The strength reduction shows the importance of treatment of RCA before its usage. The reduction is in concurrence with w/c from 0.40 to 0.50 and RCA content from 0 to 100%.

Mixed responses observed in the variance analysis for workability. But w/c influence on both slump value and Vee-Bee time was the strong evidence against the null hypothesis. Further, Vee-Bee time influence from w/c and RCA replacement ratio was witnessed with *P*-value of 0.000 and 0.006. In the workability test and statistical validation, Vee-Bee consistometer test provided conclusive response than slump test.

The compressive strength was decrease with addition of RCA both at 50 and 100% replacement. Among RACs, RAC05050 recorded the highest value of 26.95 N/mm^2 indicating RACs require longer duration of curing. ANOVA analysis also pointed the same with *P*- and *F*-values of 0.010 and 96.53, respectively, for curing period. In spite of reduction in flexural strengths, RAC50 mixes displayed good results indicating the 50% replacement of recycled concrete aggregate as optimum. Statistical validation

indicated the influence order of curing period, replacement ratio, and w/c on both compressive and flexural strengths.

The study opinioned, the mandatory usage of superplasticizer in RAC to achieve the satisfactory workability at lower w/c. Experimental studies required to ascertain the interaction between the superplasticizer and RCA. On the other hand, RAC requires suitable treatment to check the loss of free water due to absorption, which resulted in adopting the higher w/c and reduced strength.

References

1. Kumar R (2017) Influence of recycled coarse aggregate derived from construction and demolition waste (CDW) on abrasion resistance of pavement concrete. Constr Build Mater 142:248–255
2. Marinkovic SB, Malesev M, Ignjatovi I (2014) Life cycle assessment (LCA) of concrete made using recycled concrete or natural aggregates. In: Eco-efficient Construction and Building Materials. pp 239–266
3. Kubissaa W, Jaskulskia R, Kopera A, Szpetulskia J (2015) Properties of concretes with natural aggregate improved by RCA addition. Procedia Eng. 108:30–38
4. Chang CY, Huang R, Lee PC, Weng TL (2011) Application of a weighted grey-taguchi method for optimizing recycled. Cement Concr. Compos 33(10):1038–1049
5. Lin Y-H, Tyan Y-Y, Chang T-P, Chang C-Y (2004) An assessment of optimal mixture for concrete made with recycled concrete aggregates. Cem Concr Res 34(8):1373–1380
6. IS 383:1970 (1970) Specification for coarse and fine aggregate from natural sources for concrete. Bureau of Indian Standards
7. IS 456:2000 (2000) Plain and reinforced concrete—code of practice. Bureau of Indian Standards
8. IS 1199:1959 (1959) Methods of sampling and analysis of concrete. Bureau of Indian Standards
9. IS 516:1959 (1959) Methods of test for strength of concrete. Bureau of Indian Standards
10. IS 10262:2009 (2009) Concrete mix proportioning—guidelines. Bureau of Indian Standards
11. Adday FA, Awad A, Aleghnimat R, Bassam H, Khater A (2019) Fresh and hardened properties of recycled concrete aggregate modified by iron powder and silica. Int J Geomate 16(53):222–230
12. Sinha D (2014) Workability characteristic properties of concrete with varying percentages of steel fibre. Indian J Appl Res 4(7):230–233
13. Hadavand B, Imaninasab R (2019) Assessing the influence of construction and demolition wastematerials on workability and mechanical properties of concrete using statistical analysis. Innov Infrastruct Solutions 4:1–11
14. Mohammed MS, Mohamed SA, Johari MAM (2016) Influence of superplasticizer compatibility on the setting time, strength and stiffening characteristics of concrete. Adv Appl Sci 1(2):30–36
15. Wardeh G, Ghorbel E, Gomart H (2014) Mix design and properties of recycled aggregate concretes. Int J Concr Struct Mater 9(1):1–20
16. Evangelista L, de Brito J (2007) Mechanical behavior of concrete made with fine recycled concrete aggregates. Cem Concr Compos 29(5):397–401
17. Balaram Naik A, Reddy C (2018) Optimization of tensile strength in TIG welding using the taguchi method and analysis of variance (ANOVA). Therm Sci Eng Prog 8:327–339
18. El-Sinawi A, Al Ghailani L, Wanga Y (2019) ANOVA based pipeline scale formation detection using vibration estimates and minimum number of feedback sensors. Measurement 141:302–312
19. Hossaina MS, Rahim NA, Aman MM, Selvaraj J (2019) Application of ANOVA method to study solarenergy for hydrogen production. Int J Hydrogen Energy 44(29):14571–14579

Examining the Time Headway Distributions on Rural Highways Under Different Traffic Flow Conditions

Sandeep Singh, Vidya Rajesh, and S. Moses Santhakumar

Abstract The Time Headway (TH) between vehicles is one of the vital microscopic parameters in traffic engineering. It is influenced by the prevailing traffic flow characteristics of the highway segments. An accurate measure of TH is essential to deal effectively with any given traffic system. The selection of the suitable probability distribution function for a specific condition of traffic remained an open question. This research aims to evaluate the best-fitted TH probability distribution function for different traffic flow levels in multilane-divided rural highways under heterogeneous traffic conditions. The traffic-related data was obtained using a state-of-the-art, non-intrusive Infra-Red (IR) traffic detector system. The IR sensor system was used to collect the traffic data like vehicle class, traffic speed, traffic flow, and TH from the Chennai–Nagapattinam National Highways in India. To interpret and distinguish the driver behavior in maintaining different TH distributions at different traffic flow conditions, the Kolmogorov–Smirnov (K–S) test was used. The descriptive statistical results reveal that the mean TH values under different traffic flow conditions differ from each other, implying that the traffic flow conditions influence the TH distributions. Consequently, the research findings show significant variations in the TH following characteristics for the highway segment under various traffic flow conditions. The estimated TH distributions can be used to build the microscopic traffic simulation models.

Keywords Time headway · Probability distribution · Traffic flow · Rural highway · Heterogeneous traffic

S. Singh (✉) · S. Moses Santhakumar
Transportation Engineering and Management, Department of Civil Engineering, National Institute of Technology Tiruchirappalli, Tiruchirappalli, Tamil Nadu 620015, India
e-mail: sandeepsingh.nitt@gmail.com

V. Rajesh
School of Civil Engineering, Sastra Deemed University, Tanjore, Tamil Nadu 613401, India

L. Nandagiri et al. (eds.), *Recent Advances in Civil Engineering*, Lecture Notes in Civil Engineering 256, https://doi.org/10.1007/978-981-19-1862-9_26

1 Introduction

Time Headway (TH) is a microscopic traffic parameter that helps define the traffic condition [1]. "Headway or time headway is defined as the elapsed time between successive vehicles in traffic" [2]. The TH affects driving safety, capacity, and Level of Service (LoS) [3]. The TH is influenced by the prevailing characteristics of traffic flow in the highway section [4]. The TH maintained by the vehicles varies with respect to the flow levels. Higher is the flow; the lower is the TH and vice-versa [5]. Additionally, the TH distribution modeling is the basis for vehicle creation in traffic simulation models [6]. The central part of assessing a simulation model is the generation of vehicle arrival time [7].

Vehicles on highways interact with each other based on the headway maintained by the leader vehicles. Due to the presence of many heavy vehicles on the highway, the traffic speed gets reduced. This phenomenon leads to deterioration of mobility and maneuverability. Eventually, the dynamic passenger car unit (DPCU), capacity, and Level of Service (LoS) gets decreased. To effectively address any traffic problems, accurate vehicle metrics like TH are essential [8]. Hence, the method for TH measurement should be reliable and precise. This study analyzes the impact of the traffic flow rates on TH distributions of multilane-divided intercity highways.

2 Review of Literature

Many studies have modeled the theoretical TH distributions during past decades. Jang [2] modeled TH at different traffic flow levels using many other distributions. The TH characteristics of suburban traffic were analyzed using laser sensor data. Zhang et al. [3] also collected TH data using a loop analyzer from urban freeways. The author described the double displaced negative exponential distribution to better match the urban freeways. Jang et al. [4] collected TH data at three different flow rates. The researchers found that the Gamma distribution and Pearson VI distribution suited well, at low to moderate flow rates and at all flow rates, respectively. Recently, Kong and Guo [5] concluded that the traffic flow rate, and truck percentage, have a major effect on the TH. Nevertheless, these studies were conducted under homogeneous traffic conditions.

In the Indian context, Maurya et al. [8] and Singh and Santhakumar [9] determined the speed and TH characteristics at varying flow and density conditions for highway traffic. The studies emphasized the consideration of different traffic conditions for any traffic simulation modeling. The pieces of literature report that using the different probability distributions for TH at different traffic flow rates for heterogeneous traffic is limited because of the composite traffic condition prevailing in Indian highways. A deeper statistical analysis of TH on the divided roadways at different flow rates is needed. Therefore, the current study intends to examine the time headway variations using Probability Distribution Functions (PDFs) at different flow rates.

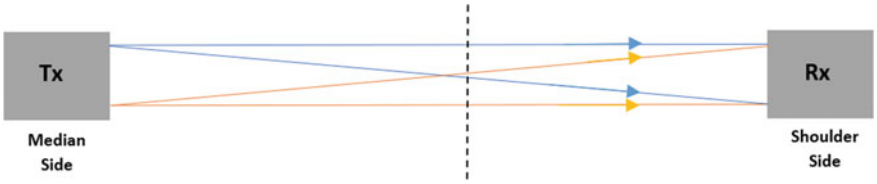

Fig. 1 Tx and Rx placement for vehicle detection

3 Data Collection

The Transportable Infra-Red Traffic Logger (TIRTL) is the IR sensor instrument used for collecting traffic data from the highways. It includes a transmitter (Tx) and receiver (Rx). It records traffic volume, speed, TH, and vehicle dimensions. The Tx is the basis for the IR beam generation. The Rx detects the disturbance in the IR beams due to the passing by vehicles. Two diagonal and two parallel beams transmit between Tx and Rx, as illustrated in Fig. 1.

A comparison between the TIRTL data with that of videotaped data for an hour showed 97% accuracy with regard to the vehicle classification, 95% accuracy with regard to vehicle speed, and 96% accuracy with regard to the TH. Another study by Minge et al. [10], which used the same TIRTL device, reported that the vehicle speed accuracy was up to 98% and vehicle volume accuracy was also up to 98%. A more detailed description of the working and accuracy of the TIRTL instrument is provided in the studies by Singh et al. [11–13]. Further, the Easy: Fit software was used to determine the best-fit distribution for the TH data. It ranked the best-fitted PDF based on a goodness-of-fit test called the Kolmogorov–Smirnov (K–S) test. The study explored the time headway distribution of heterogeneous traffic at different traffic flow levels viz 600–1200 DPCU/h, 1200–1800 DPCU/h, and 1800–2400 DPCU/h.

4 Study Site

The study site is located on the outskirts of Chennai city on the National Highway NH-32 (New) or NH-45 (Old). A google map showing the study location is illustrated in Fig. 2.

The intercity connects Chennai and Nagapattinam. The latitude and longitude of the location are 12.387602 and 79.797621, respectively. The highway has level terrain. It has two lanes (each 3.5 m in width) per direction and a shoulder lane (2.5 m in width). The median width is 5.0 m. The geometric layout of the highway is depicted in Fig. 3.

The traffic data is acquired using TIRTL for 12 h, covering peak hours and off-peak hours. This was done so to ensure that the complete traffic behavior is captured, considering day and night. The TIRTL instrument setup across the study site is

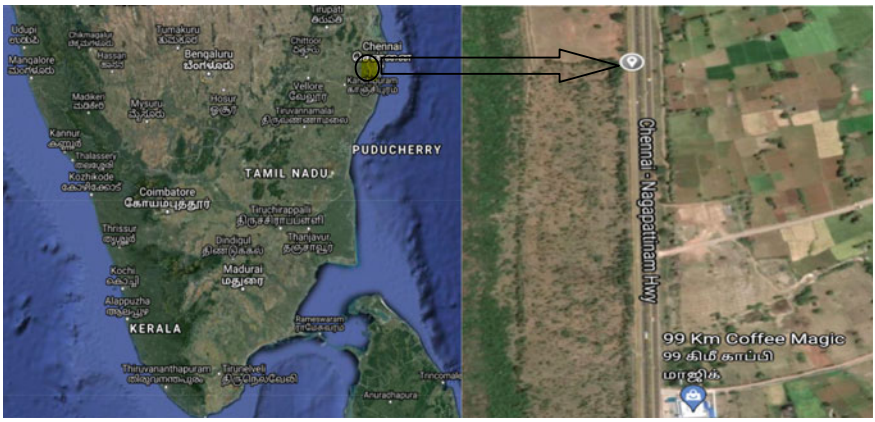

Fig. 2 Google Map showing the study location. *Source* Google Maps

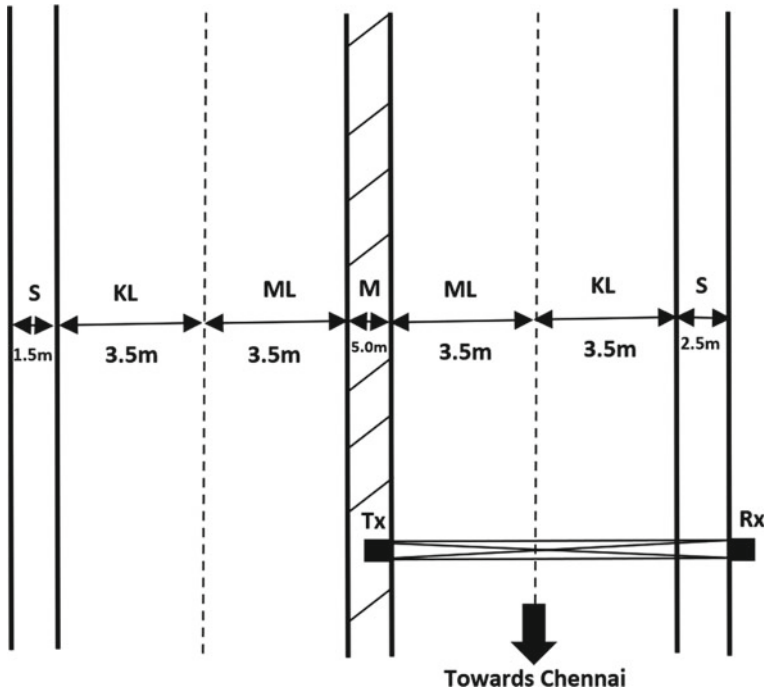

Fig. 3 Geometric layout of the highway

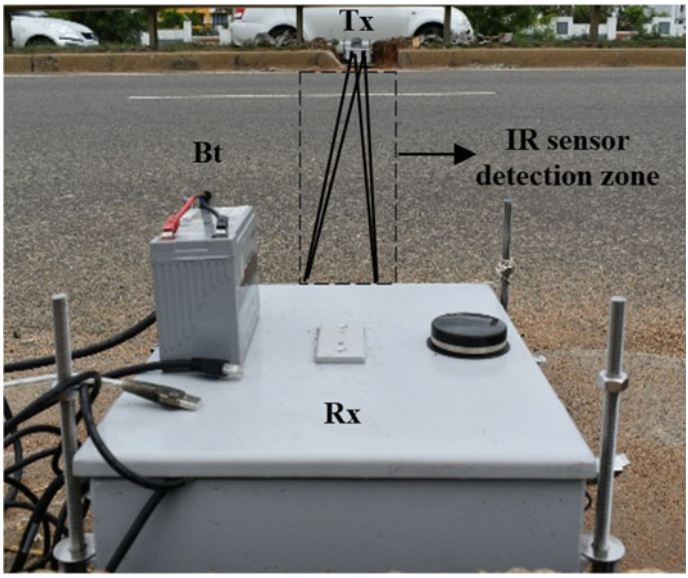

Fig. 4 Setup of the TIRTL instrument

depicted in Fig. 4. It shows the transmission of IR rays between Tx and Rx, which form the IR sensor detection zone. A 12.0 V battery (Bt) is connected to the Rx.

5 Traffic Characteristics of the Study Site

5.1 Traffic Composition and Volume

A total of 11,012 vehicles were recorded in 12 h data collection period. The vehicles composition constitutes two-Wheelers (2 W), three-Wheelers (3 W), Small Cars (SC), Big Cars (BC), Small Commercial Vehicle (SCV), Light Commercial Vehicle (LCV), Medium Commercial Vehicle (MCV), Heavy Commercial Vehicle (HCV), and Multi-Axle Vehicle (MAV). The SC and BC occupied the largest proportion of traffic composition with 48%, followed by 2 W with 20%, MCV with 18%, and so on, as illustrated in Fig. 5.

The peak hour traffic volume (vph) was observed as 1116 vehicles per hour between 18:00 and 19:00 h, as illustrated in Fig. 6.

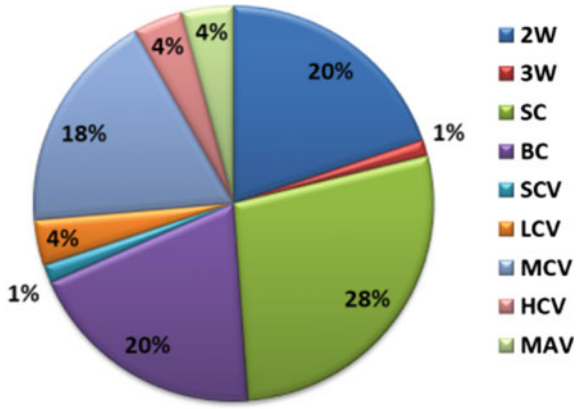

Fig. 5 Composition of traffic

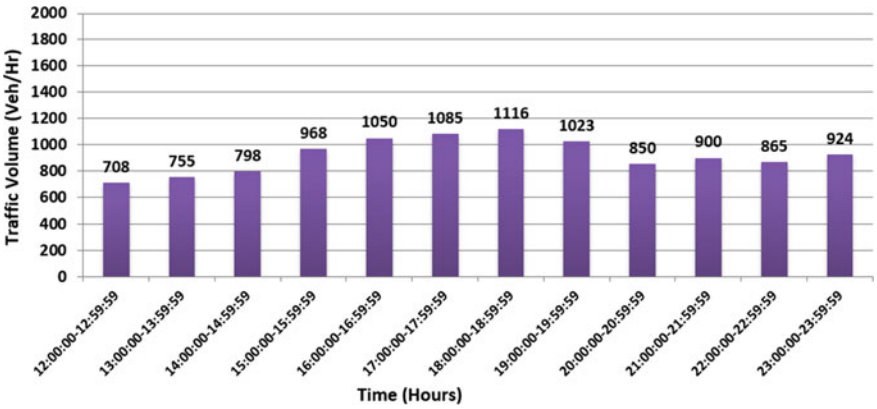

Fig. 6 Variation of traffic volume in vph

6 Determination of DPCU

The Indian Highway Capacity Manual [14] has suggested Eq. (1) to calculate the DPCU value of a vehicle type for Indian traffic. Therefore, this equation is used in this study for calculating the DPCU of individual vehicles.

$$\text{DPCU}_i = \frac{(V_c/V_i)}{(A_c/A_i)} \tag{1}$$

where

DPCU_i = DPCU for the vehicle type *i*.
V_c = speed of SC.
V_i = speed of the i^{th} type of vehicle.
A_c = area of SC.

A_i = area of the ith type of vehicle.

In DPCU estimation, SC was considered the base vehicle type due to its typical standard vehicular characteristics [14]. The speed ratio is the ratio of the speed of SC to the speed of the i^{th} type of vehicle, while the area ratio is the ratio of the area of SC to the area of the i^{th} type of vehicle. The calculated DPCU values of vehicles are shown in Table 1.

The peak hour traffic volume was observed as 2373 DPCU/hr between 23:00 h and 23:59 h, as illustrated in Fig. 7.

Table 1 Calculated DPCU values

Vehicles class	Vehicle speed (kmph)	Vehicle area (m^2)	Speed ratio	Area ratio	Estimated DPCU
2 W	68	1.19	1.12	4.33	0.26
3 W	44	2.81	1.73	1.83	0.95
SC	76	5.15	1.00	1.00	1.00
BC	80	7.69	0.95	0.67	1.42
SCV	51	5.00	1.49	1.03	1.45
LCV	65	7.60	1.17	0.68	1.72
MCV	47	12.01	1.62	0.43	3.77
HCV	41	13.00	1.85	0.40	4.63
MAV	36	16.56	2.11	0.31	6.81

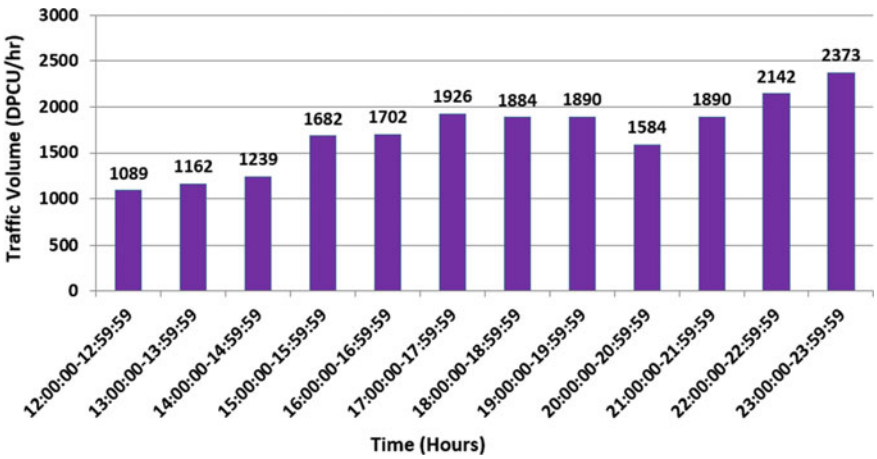

Fig. 7 Variation of traffic volume in DPCU per hour

Table 2 Summary of descriptive statistics of TH data

Statistical variable	Time headway (sec)		
	600–1200 DPCU/hr	1200–1800 DPCU/hr	1800–2400 DPCU/hr
Sample size	463	666	913
Minimum	0.62	0.55	0.49
Maximum	12.84	11.52	9.81
Mean	8.52	6.78	5.41
Median	8.38	6.45	5.33
Std. deviation	3.32	2.56	1.91
15^{th} percentile	1.85	1.62	1.38
85^{th} percentile	10.04	8.42	7.20

7 Time Headway Analysis

7.1 Descriptive Statistical Analysis

The speed and traffic flow are the fundamental traffic parameters used to measure operational efficiency [15]. The speed and TH are essential for microscopic traffic simulation model development and analysis [16, 17]. Hence, to find the TH distribution as a traffic flow rate function, the data were extracted for 10 DPCU/min (equivalent to 600 DPCU/hr), 20 DPCU/min (equivalent to 1200 DPCU/hr), 30 DPCU/min (equivalent to 1800 DPCU/hr), and 40 DPCU/min (equivalent to 2400 DPCU/hr). The summary of descriptive statistics of TH at varying flow levels is shown in Table 2.

Table 2 shows that with the increase in the traffic flow rate, the statistical parameters of TH decrease. Thus, indicating that the driver behavior of the vehicles in the traffic gets impacted due to the varying traffic flow conditions. The drivers tend to maintain higher TH values under relatively lower traffic flow conditions than higher traffic flow conditions.

7.2 TH Distributions at Different Flow Rates

The TH data is helpful in many aspects such as driver behavior analysis, traffic flow modeling, capacity assessment, and LoS evaluation. The K–S test was used to find the selected distributions' goodness-of-fit at a 5% significance level. The p-values and the K–S values rank the distributions for identifying the best-fitted distribution. The best-fit PDF and the statistical probability distribution parameters of the TH data for the three traffic flow rates, viz, 600–1200 DPCU/hr, 1200–1800 DPCU/hr, and 1800–2400 DPCU/hr, which are shown in Tables 3, 4 and 5, respectively.

Table 3 PDFs for TH at 600–1200 DPCU/hr flow rate

Distribution	Statistical parameters	*K–S* value (critical *K–S* Value = 0.4836)	*p*-value	Best-fitted distribution
Log-logistic	$\alpha = 1.42$ $\beta = 5.54$ $\gamma = 0.11$	0.1132	0.88	Log-pearson-III distribution
Log-pearson-III	$\alpha = 9.59$ $\beta = -0.31$ $\gamma = 5.26$	0.1075	0.95	
Burr	$k = 1.22E + 7$ $\alpha = 1.11$ $\beta = 7.99E + 7$ $\gamma = 0.23$	0.1283	0.74	
Weibull	$\alpha = 1.23$ $\beta = 9.55$	0.1187	0.79	
Log-normal	$\sigma = 0.88$ $\mu = 1.51$ $\gamma = -0.61$	0.1087	0.91	

Table 4 PDFs for TH at 1200–1800 DPCU/hr flow rate

Distribution	Statistical parameters	*K–S* value (critical *K–S* Value = 0.3621)	*p*-value	Best-fitted distribution
Log-logistic	$\alpha = 1.74$ $\beta = 1.96$ $\gamma = 0.05$	0.1617	0.87	Burr distribution
Log-pearson-III	$\alpha = 16.83$ $\beta = -0.28$ $\gamma = 6.09$	0.1567	0.91	
Burr	$\alpha = 0.48$ $\beta = 64.1$ $\gamma = 0.2$ $k = 12.6$	0.1378	0.98	
Weibull	$\alpha = 1.08$ $\beta = 9.15$	0.1476	0.94	
Lognormal	$\gamma = -0.77$ $\sigma = 0.81$ $\mu = 1.22$	0.1681	0.90	

The distributions with a *K–S* value lesser than the critical *K–S* value are considered. The *p*-value for the distributions indicates the threshold of the significance level. The distributions with *p*-values greater than this significance level will be accepted, while the other will be rejected. The higher the *p*-values, the better the model. Only the distributions with *p*-values greater than the critical *p*-value are presented here.

Table 5 PDFs for TH at 1800–2400 DPCU/hr flow rate

Distribution	Statistical parameters	*K–S* value (critical *K–S* value = 0.3244)	*p*-value	Best-fitted distribution
Log-logistic	$\alpha = 1.8$ $\beta = 1.8$ $\gamma = -5.5E-4$	0.1107	0.82	Log-logistic distribution
Log-pearson-III	$\alpha = 15.32$ $\beta = -0.27$ $\gamma = 5.94$	0.1812	0.74	
Burr	$\alpha = 3.24$ $\beta = 2.4$ $\gamma = -0.28$ $k = 0.77$	0.1156	0.80	
Weibull	$\alpha = 0.98$ $\beta = 17.09$	0.1245	0.77	
Lognormal	$\gamma = -0.21$ $\sigma = 0.71$ $\mu = 0.65$	0.1735	0.75	

With the variation in the flow, the statistical parameters of the distributions were found to be varying. This can be attributed to being due to the variability in the driver and traffic characteristics. The Log-Pearson-III distribution was estimated to be the best-fitted distribution when the traffic flow rate was between 600 DPCU/hr and 1200 DPCU/hr. The relatively lower values for shape parameter (α) and scale parameter (β) for this distribution denoted non-accumulation of shorter TH. These parametric values indicate that the vehicles at such flow rates are moving freely or are not much affected by the interacting traffic, which is logically possible and reasonable. Further, the location of the probability density function on the horizontal axis is determined by the local parameter (γ).

Under the Lognormal distribution, the shape parameter (σ) indicates the shape of the distribution. It also shows the degree of skewness. An increase in σ value will increase the degree of skewness. The scale parameter (μ) indicates peakedness and tailedness. The increase in μ value indicates the reduced peak and fatter tail. This indicates an increase in the TH value.

Meanwhile, Burr distribution was found to be the best-fitted distribution when the traffic flow rate was between 1200 DPCU/hr and 1800 DPCU/hr. The k in this distribution indicates the shape parameter, while the α is the scale parameter and the γ is the continuous location parameter. Finally, the Log-logistic distribution best fits the flow rate ranging from 1800 to 2400 DPCU/h. These results clarify that the traffic stream's behavior in maintaining a time headway depends on the prevailing traffic characteristics. Additionally, it can be interpreted that the PDF considerably differs as the traffic flow changes.

8 Conclusions

This study aimed to capture and identify the different TH PDFs of mixed vehicular traffic at various traffic flows. Subsequently, best-fit PDFs are estimated on the basis of *K–S* test using the Easy: Fit software. The critical observations of the study are discussed below.

- This study showed that the TH and its associated statistical parameters vary highly with the change in the traffic flow rate.
- The TH analysis provided unique insights into the behavioral characteristics of vehicles under different traffic flows.
- Subsequently, the TH distributions tend to change following the traffic interaction conditions, proving the assumption that using the same TH for varying flow rates is inaccurate.

Thus, the TH tends to change depending on the traffic conditions. The established relationship between TH and traffic flow explored the PDF's applicability to define the Indian traffic condition. The study results reveal variation in TH PDFs at various traffic flow rates. The TH distributions aid in interpreting the riders' risky driving behavior and the impact on traffic road safety. The present study's findings can be used to model microsimulation systems for analyzing car-following and lane-changing behavioral modeling of highway traffic. The developed TH distribution models allow transportation researchers, planners, and practitioners, to identify driver characteristics under different traffic flow rates. Nevertheless, like any other study, this study has certain limitations, which paves the way for further research. Further research may be conducted to determine the TH distributions for various vehicle-to-vehicle combinations.

References

1. Singh S, Santhakumar SM (2021) Empirical analysis of impact of multi-class commercial vehicles on multi-lane highway traffic characteristics under mixed traffic conditions. Int J Transp Sci Technol. https://doi.org/10.1016/j.ijtst.2021.07.005
2. Jang J (2012) Analysis of time headway distribution on suburban arterial. KSCE J Civ Eng 16:644
3. Zhang G, Wang Y, Wei H, Chen Y (2007) Examining headway distribution models with urban freeway loop event data. Transp Res Rec 1999:141–149
4. Jang J, Kim B, Choi N, Biak N (2011) Analysis of time headway distribution on Korean multilane highway using loop event data. J Eastern Asian Soc Transp Stud 9:1447–1457
5. Kong D, Guo X (2016) Analysis of vehicle headway distribution on multilane freeway considering car–truck interaction. Adv Mech Eng 8(4):1–12
6. Arasan V, Koshy R (2003) Headway distribution of heterogeneous traffic on urban arterials. J Instit Eng 84:210–215
7. Al-Ghamdi S (2001) Analysis of time headways on urban roads: case study from Riyadh. J Transp Eng 127:289–294
8. Maurya AK, Das S, Dey S, Nama S (2016) Study on speed and time-headway distributions on two-lane bidirectional road in heterogeneous traffic condition. Transp Res Procedia 17:428–437

9. Singh S, Santhakumar SM (2022) Assessing the impacts of heavy vehicles on traffic characteristics of highways under mixed traffic platooning conditions. European Transport\Trasporti Europei. https://doi.org/10.48295/ET.2022.86.3
10. Minge E, Kotzenmacher J, Peterson S (2010) Evaluation of non-intrusive technologies for traffic detection, Minnesota department of transportation, research services, office of the policy analysis research and innovation, Roseville, USA. MN/RC 2010–36. http://www.lrrb.org/PDF/201036.pdf. Accessed in July 2020
11. Singh S, Santhakumar SM (2021) Evaluation of lane-based traffic characteristics of highways under mixed traffic conditions by different methods. J Instit Eng (India): Series A 102(3):719–735. https://doi.org/10.1007/s40030-021-00549-6
12. Singh S, Vidya R, Santhakumar SM (2022) Effect of mixed traffic platooning by commercial vehicle types on traffic flow characteristics of highways. Periodica Polytechnica Transportation Engineering
13. Singh S, Santhakumar SM (2022) Platoon-based impact assessment of heavy-duty vehicles on traffic stream characteristics of highway lanes under mixed traffic environment. Int J Intell Transp Syst Res 20:29-45. https://doi.org/10.1007/s13177-021-00268-z
14. Indian Highway Capacity Manual (Indo-HCM) (2017) Central Road Research Institute, New Delhi, India
15. Singh S, Vidya R, Shukla BK, Santhakumar SM (2021) Analysis of traffic flow characteristics based on area-occupancy concept on urban arterial roads under heterogeneous traffic scenario—a case study of Tiruchirappalli city. In: Mehta YA et al (eds) Trends and recent advances in civil engineering (TRACE) 2020, Advances in water resources and transportation engineering, lecture notes in civil engineering, vol 149. Springer Nature, Singapore, pp 69–84. https://doi.org/10.1007/978-981-16-1303-6_6
16. Singh S, Santhakumar SM (2022) Influence of platooning of heavy transport vehicles operation on traffic flow mix of intercity highways. In: Maurya AK, Maitra B, Rastogi R, Das A (eds) Proceedings of the fifth international conference of transportation research group of India. Lecture notes in civil engineering, vol 219. Springer, Singapore. https://doi.org/10.1007/978-981-16-8259-9_29
17. Singh S, Barhmaiah B, Kodavanji A, Santhakumar SM (2020) Analysis of two-wheeler characteristics at signalised intersection under mixed traffic conditions: a case study of Tiruchirappalli city, Resilience and sustainable transportation systems, In: Proceedings of the 13th Asia Pacific transportation development conference, Shanghai, China, American Society of Civil Engineers (ASCE), pp 35–43. https://doi.org/10.1061/9780784482902.005

Adsorption Isotherm, Kinetic and Thermodynamic Studies of Nitrates and Nitrites onto Fish Scales

Veeravalli Preetham and Jagadish Vengala

Abstract One of the most important things that every human being on the planet must be aware of is sustainability. The term 'sustainability' refers to all aspects of the environment, including numerous characteristics such as the long-term viability of water bodies. Water pollution has been rapidly increasing over the last two decades for a variety of reasons. The significant development of industries is beneficial to the country's economy. Even though the wastes generated by these various industries and disposed of without proper treatment and practises have caused and continue to pollute the water bodies. Nitrates are one of the pollutants that can be found in most polluted river bodies. Nitrates can be found in river bodies from agricultural waste water due to pollutants released primarily from fertilizers used in excess amounts for agricultural practises. Adsorption proved to be the best solution for controlling the nitrate content in water. In this study, nitrates and nitrites are removed from adsorbent fish scales. The removal of fish scales as an adsorbent has been thoroughly researched. These studies involve different isotherm studies, kinetic studies as well as thermodynamic studies. Following the completion of the analysis, the results revealed that nitrates and nitrates can be effectively removed with fish scales, with the maximum percent biosorption found to be 97.96 and 99.72% at contact times of 140 min and 100 min, respectively, the pH is kept at 6, the temperature is kept at 303 degrees Celsius, and the adsorbent dosage is kept at 0.4 g for maximum adsorption. Thermodynamic studies has been also conducted where the results showed that the reaction is endothermic and spontaneous in nature based on the values of ΔS, ΔH and ΔG. In addition to the above analysis, isothermal and kinetic studies were performed, with the Langmuir isotherm studies fitting perfectly and the affinity between the pollutants and adsorbent indicating that second-order kinetic studies are best suited.

Keywords Adsorbent · Kinetic studies · Isotherm studies · Thermodynamic studies · Fish scales · Adsorption

V. Preetham (✉) · J. Vengala
Civil Engineering Department, PVP Siddhartha Institute of Technology, Vijayawada, Andhra Pradesh, India
e-mail: preethamveeravalli24@gmail.com

L. Nandagiri et al. (eds.), *Recent Advances in Civil Engineering*, Lecture Notes in Civil Engineering 256, https://doi.org/10.1007/978-981-19-1862-9_27

1 Introduction

Adsorption is one of the efficient approach for removing contaminants from wastewater. Water, particularly fresh water, has been polluted all throughout the planet, with only 3% of it being clean. In the majority of cases, human negligence is the primary source of water contamination. Even though India is surrounded on three sides by water, the amount of drinking water accessible is relatively limited, and it is contaminated due to the untreated release of pollutants into the water. Excess nitrate in water causes eutrophication, which causes oxygen levels in water to drop, resulting in water pollution. According to the Central Pollution Control Board (CPCB), the nitrate amount allowed in wastewater disposal is restricted to 10 parts per million (ppm), while the allowable level for nitrates in drinking water is 45 parts per million (ppm) (IS 10500)

Solid waste management has been tremendously increasing its importance because the solid waste which was generated from different sources has been causing lot of problems for so many years. The fish scales are solid waste material that generally being dumped in to the waste can be reduced by using it as an adsorbent. Different solid waste materials have been taken into consideration to check the suitability of material as a biosorbent for the nitrates removal from effluent. For example, the use of modified biochar made from sugarcane bagasse resulted in the maximum removal of nitrate with an adsorbent dosage of 2 g/l at a pH of 4.64 with 60 min contact time. The adsorption capacity (maximum) was found to be 28.21 mg/g [3].

Natural pumice was utilized as an adsorbent with a pH of 3 and dosage of 0.3 gm/L for the removal of nitrates in a similar way. The optimum nitrate removal was achieved with a contact time of 30 min. The elimination efficiency was 54.79%, while the nitrate uptake capacity was 164.37 mg/g. Among the isotherm tests conducted to determine the affinity of natural pumice for nitrate adsorption, the Freundlich isotherm proved to be the most suitable [6].

In general, kinetic studies, as well as isotherm and batch adsorption experiments, are required to demonstrate the effect of the adsorbent on the removal of contaminants. The use of onion peel dust for nitrate removal revealed that that the intra particle diffusion and first-order kinetics suited at most. The maximum adsorption capacity was 5.93 mg/g with an 85% pollutant removal. The Langumir isotherm was found to be an excellent fit for the study [11].

Several waste products have been employed to remove nitrates, including silica nanoparticles (SiNP) derived from rice husk ash. The data clearly show that SiNP has a high capacity for removing nitrate ions with a maximum adsorption capacity of around 14.22 mg/g at a dosage of 0.15 g/L. The optimum conditions maintained were pH value 6, contact period of 50 min [18].

The removal of nitrates using fish scales as an adsorbent has been studied in this study. Variations in contact time, adsorbent dosage and concentrations of contaminants (mg/l) are used to explore adsorption capabilities. The availability of biosorption capacity was further examined using thermodynamic studies in addition to

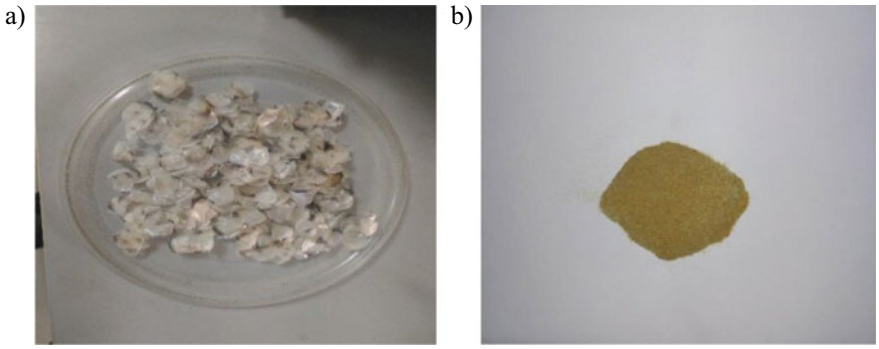

Fig. 1 a, b Fish scales and fish scale powder

kinetic models such as pseudo-first and second orders. The intensity of biosorption was assessed using various isotherm studies such as the Langmuir isotherm, the Freundlich isotherm and the Temkin isotherm.

2 Materials

2.1 Adsorbent

Fish scales: The fish scales were procured from local fish market in Kakinada, India. These were properly washed in distilled water to remove undesirable particles before being dried with a hot air oven at 110 °C. After drying, fish scales were crushed into a powdered form with a particle size of 0.85 mm, as shown in Fig. 1a, b [10]

2.2 Preparation of Adsorbate

In 1000 mL, 0.7218 g sodium nitrite salt (NaNO2) and potassium nitrate salt (KNO3) were added to make a 1000 mg/L nitrate and nitrite stock solution. Different standard solutions have been generated from the original stock solutions by serial dilution [1].

3 Experimental Procedure

The dosage of fish scales, which is an adsorbent, is 0.4 g in the beginning stages. The contents of nitrates and nitrites in the stock solution were kept constant at 50 mg/l. After that, the adsorbent and pollutant solution are combined and rotated at a

constant rpm of 165 rpm for 10 min to achieve the maximum adsorption capacity while keeping a steady pH and temperature. Various pollutants produced different outcomes, which were noted.

The concentration of contaminants was increased from 30 to 70 mg/l in the second stage, while the adsorbent dosage, i.e. fish scale powder remained constant at 0.4 g was utilised. In flasks containing the solution, the uptake of pollutants was examined for optimum contact duration, constant pH and constant temperature, and the results were recorded.

The amount of the adsorbent, i.e. fish scales, is changed in the third stage by varying the doses in three ways, i.e. 0.2, 0.4 and 0.6 g, and the findings obtained were reported correspondingly by keeping the remaining parameters constant. More research was carried out based on the findings, using other isotherm experiments. Similarly, a number of kinetic tests were investigated in order to ascertain the ultimate best parameters for use in a real-world setting. To assess whether an adsorbent's impact on a pollutant is endothermic or exothermic, thermodynamic studies are utilized.

4 Results and Discussion

4.1 Contact Time

Contact time variations were examined using 0.4 g of required adsorbent, i.e., fish scales powder in 200 ml of nitrate and nitrite stock solution concentrations of 50 ppm each. At a speed of 165 rpm, this procedure was performed for various time intervals such as 10, 20, 30, 40 and up to 140 min. The sample was examined after each time interval to determine the amount of nitrate and nitrite absorption. Percent biosorption capacities are shown in Fig. 2a, b at various time periods. On the fish scale as an adsorbent, nitrites have a higher adsorption percent, 99.70% at a contact time of 100 min, which is higher than nitrates' 97.96% with a contact time of 140 min. The removal of methylene blue from activated carbon by surfactant modelling exhibited similar findings as the time duration increased [8].

4.2 Dosage of Adsorbent

50 ppm standard solutions of each pollutants are taken in a standard volumetric flask with 200 ml each, with varying adsorbent dosages of 0.2, 0.4 and 0.6 g were considered. These were agitated for an equilibrium time at constant temperature with a constant agitation speed of 165 rpm. The HACH analyzer and spectrophotometer were used to determine the quantities of nitrate and nitrite in each individual sample. According to Fig. 3a, b, the capacity to remove nitrates increases from 96.62 to

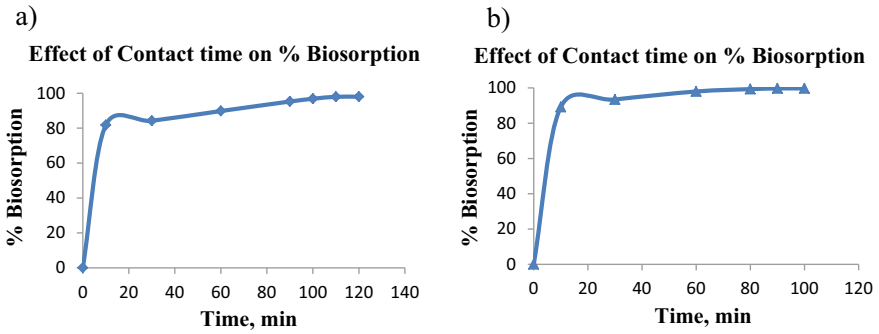

Fig. 2 **a, b** Nitrate and nitrite biosorption capacities at varying time intervals for adsorbents fish scales (initial concentration = 50 ppm, adsorbent dose = 0.4 gm/200 ml, temperature = 30 °C, pH = 6)

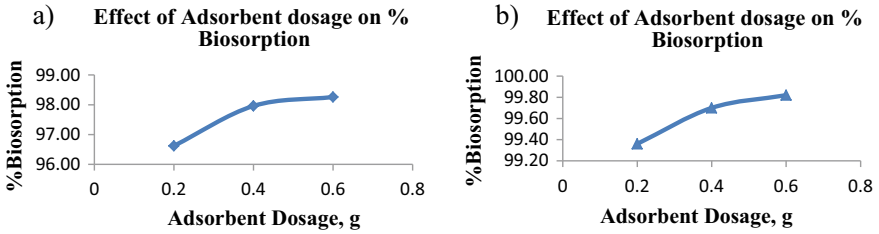

Fig. 3 **a, b** Nitrates and nitrites biosorption capacities at varying adsorbent dosages of fish scales (initial concentration = 50 ppm, temperature = 30 °C, pH = 6, orbital shaking speed = 165 rpm)

98.26% when the dose of fish scale adsorbent is increased from 0.2 to 0.6 g. Similarly, increasing the dose of fish scale adsorbent from 0.2 to 0.6 g increases the capacity for removing nitrites from 99.36 to 99.82%. According to the results, the percent removal of nitrites by fish scales as an adsorbent is greater than that of nitrates. Previous research has shown that increasing the adsorbent dosage can improve percentage adsorption; similar to how nitrate removal using coconut granular activated carbon (GAC) treated with zinc chloride (ZnCl2) has shown that percent bisorption can be improved with a constant increase in adsorbent dosage [1].

4.3 Initial Pollutant Concentration (Co)

The concentrations of pollutants has been varied from 30 to 70 ppm by considering each pollutant for a volume of 200 ml. Following that, 0.4 g of fish scale powder was added to each of the beakers. For the best contact time at room temperature, the beakers were rotated at 165 rpm. The nitrate and nitrite concentrations in the collected samples was determined by filtering them using filter paper. Figure 4a, b shows how

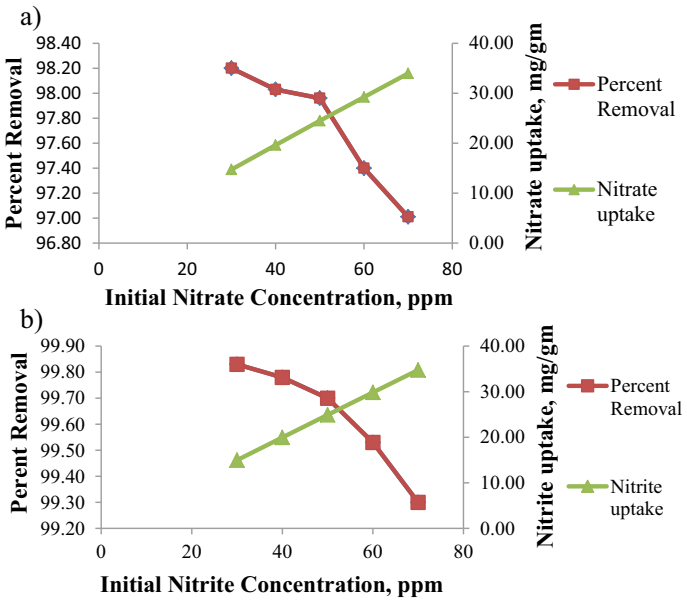

Fig. 4 **a, b** Nitrate and nitrite biosorption and uptake capacities at varying Initial pollutant concentration for adsorbent fish scales (adsorbent dose = 0.4 gm/200 ml pollutants solution, temperature = 30 °C, pH = 6)

the biosorption capacity decreases when the initial pollutants concentration varies for a fixed adsorbent dosage of 0.4 ppm. Similarly, as the pollutant concentration rises from 20 to 200 mg/l, the adsorption capacity reduced from 96.6 to 80.39 [19].

4.4 PH

The pollutant's surface charge and ionization degree are both affected by pH, which has a significant impact on biosorption, which is a key biosorption monitoring parameter [2]. In this investigation, data on the removal efficiency of nitrates and nitrites biosorption were collected in the pH range of 2–9, with an initial pollutant concentration of 50 mg/L and a constant adsorbent dosage of 0.4 g and Fig. 5 indicates the impact of pH on the percentage biosorption of nitrates and nitrites. As indicated in Fig. 5, the maximum percent biosorption capability of nitrates and nitrites was seen in the pH range of 5–7, which did not demonstrate maximum percent biosorption removal. This can be validated from the research paper done by Sayadi et al. [14] which shows that the best pH for COD, nitrate, and phosphate removal utilizing composite POFA was found to be pH 6, while the optimum pH for ammonia nitrogen removal was found to be pH 9.

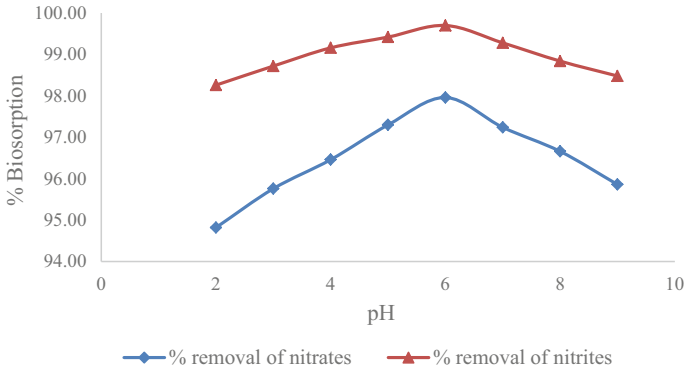

Fig. 5 Effect of pH on nitrates and nitrites (adsorbent dose = 0.4 gm/200 ml pollutants solution, Initial concentration = 50 ppm, temperature = 30 °C, orbital shaking speed = 165 rpm)

4.5 Effect of Temperature

The biosorption of nitrates and nitrites on to fish scales as adsorbent is demonstrated in Fig. 6 the effects of temperature changes on different pollutant uptake. The analysis shows that as the temperature was raised, the % biosorption increased [16]. To find the influence of temperature on pollutants, batch tests were conducted at five different temperatures: 298, 303, 308, 313 and 318 K [20]. The percent removal of nitrates and nitrites using fish scales as an adsorbent with pollutant concentrations of 50 mg/L increased from 96.94 to 98.64% as the temperature increased. Similarly, the % elimination of nitrites varies between 99.44 and 99.84%. Based on the analysis, results and activity of fish scales both with nitrates and nitrites, it is possible to conclude that the reaction is endothermic [7].

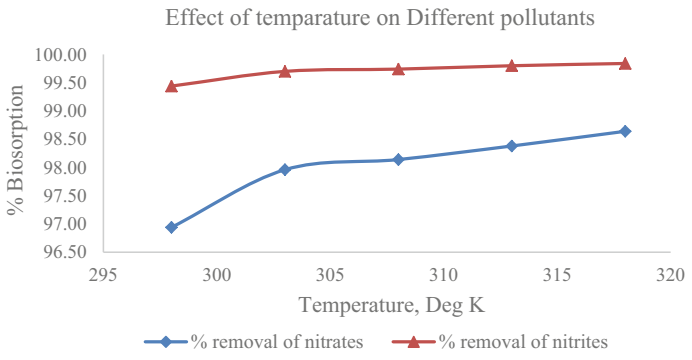

Fig. 6 Effect of temperature on nitrates and nitrites (0.4 gm/200 ml adsorbent, 50 ppm nitrates and nitrites, pH = 6, orbital agitation speed = 165 rpm)

4.6 Thermodynamic Studies

Experimental values such as enthalpy change (ΔH), Gibbs free energy (ΔG) and entropy change (ΔS) can be computed using the equation $\Delta G = \Delta H - \Delta S$ in adsorption thermodynamics. The slope and intercept of a plot of ln (K_L) against 1/T are used to compute the values of ΔH and ΔS [12]. K_L is given by $Q_{eq}/C_{eq,}$ where Q_{eq} pollutant adsorption capacity and C_{eq} represents pollution concentration in solution [18]. The graph of ln (K_L) against 1/T is shown in Fig. 7a, b. Table 1 illustrates the (G) readings for fish scale as an adsorbent at various temperatures. Negative values (ΔG) suggest that nitrates adsorption on fish scales powder is spontaneous and favourable [13], whereas the presence of positive values (ΔH) indicates that nitrate adsorption is endothermic [4]. The entropy change (S) result is as well positive, showing that nitrate particles are dispersed throughout the adsorbent surface at random [5]. Similarly, we may deduce that nitrite adsorption is endothermic in nature and that nitrite ions are randomly dispersed across the adsorbent surface based on the results [15].

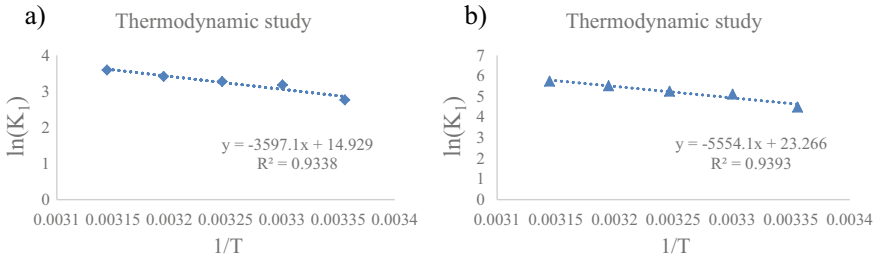

Fig. 7 **a, b** Plot between ln (K_L) vs 1/T for nitrates and nitrites (0.4 gm/200 ml adsorbent, 50 ppm nitrates and nitrites, pH = 6, orbital agitation speed = 165 rpm)

Table 1 Thermodynamic parameters of nitrates and nitrites on to fish scales

Pollutant type	Temperature (K)	K_L	ΔG (KJ mol^{-1})	ΔH (KJ mol^{-1})	ΔS (JK^{-1} mol^{-1})	R^2
Nitrate (NO_3^-)	298	15.84	−6.844	29.91	124.12	0.9338
	303	24.01	−8.006			
	308	26.39	−8.380			
	313	30.37	−8.882			
	318	36.26	−9.493			
Nitrite (NO_2^-)	298	88.76	−11.115	46.18	193.43	0.9393
	303	166.20	−12.881			
	308	191.85	−13.461			
	313	249.50	−14.363			
	318	312.00	−15.184			

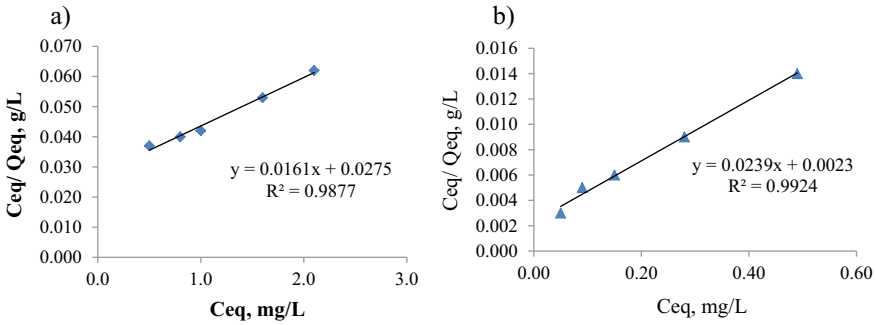

Fig. 8 **a, b** Langmuir isotherm representing % adsorption of nitrates and nitrites for fish scales

4.7 Adsorption Isotherms

4.7.1 Langmuir Isotherm

In general, the Langmuir isotherm is plotted between C_{eq} and C_{eq}/Q_{eq}, as shown in Fig. 8a and b, where Q_{eq} represents pollutant adsorption capacity and C_{eq} represents pollution concentration in solution, and maximum adsorption capacity (Q_{max}). Langmuir constant (b) values can be obtained from intercept and slope, respectively [5]. Table 2 shows the values of the Langmuir constant (b) for various pollutants, such as nitrates and nitrites. It can be seen in the Table 2 that the values of constant b for fish scales as adsorbent is higher for nitrites than for nitrates, implying that the effective bond for the removal of nitrites is greater than that of nitrates. There is also a little variance in R^2 values.

4.7.2 Freundlich Isotherm

Freundlich isotherm can be obtained by plotting the graph between log Q_{eq} and log C_{eq} which is represent below in Fig. 9a, b. The Freundlich constant (K_f) and M values are obtained from internet and slope [19]. Values of the Freundlich constant (K_f), which is used to determine whether an adsorbent is favourable for adsorption or not, in the instance of fish scales as an adsorbent. When comparing nitrates to nitrites, it can be seen that from Table 2 the K_f values for nitrates decreased. This means that the fish scales adsorption capacity is more for nitrites than for nitrates.

4.7.3 Temkin Isotherm

Temkin isotherm can be obtained by plotting the graph between Q_{eq} and ln (C_{eq}) [17]. Figure 10a and b illustrate the Temkin Isotherm parameters for various pollutants

Table 2 Comparison of different isotherm studies

Pollutant type	Langmuir isotherm and isotherm constants				Freundlich isotherm and isotherm constants				Temkin isotherm and isotherm constants			
	Isotherm equation	Q_{max} (mg/g)	b (L/mg)	R^2	Isotherm equation	K_f	M	R^2	Isotherm equation	A_T (L/mg)	b_T	R^2
Nitrate (NO_3^-)	$(C_{eq}/Q_{eq}) = 0.0161\ C_{eq} + 0.0275$	62.11	0.585	0.9877	$\log Q_{eq} = 0.5965 \log C_{eq} + 1.3581$	22.8	1.68	0.9845	$Q_{eq} = 0.3296 \ln C_{eq} - 1.5418$	0.808	7643	0.9907
Nitrite (NO_2^-)	$(C_{eq}/Q_{eq}) = 0.0239\ C_{eq} + 0.0023$	39.68	10.391	0.9924	$\log Q_{eq} = 0.3724 \log C_{eq} + 1.6799$	47.63	2.68	0.9762	$Q_{eq} = 0.57 \ln C_{eq}$ − 4.71	0.885	4372.8	0.9991

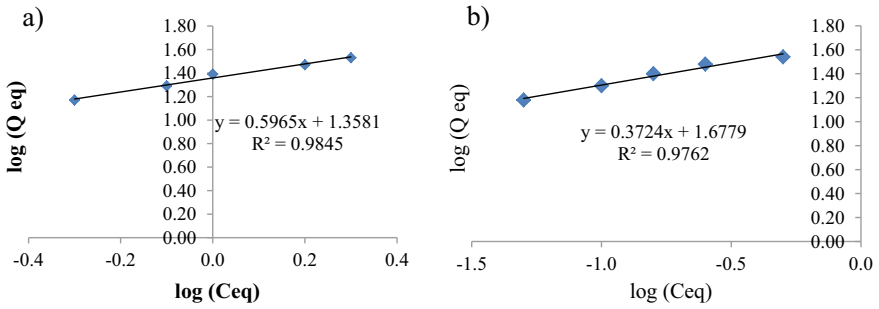

Fig. 9 **a, b** Freundlich isotherm representing % adsorption of nitrates and nitrites for fish scales

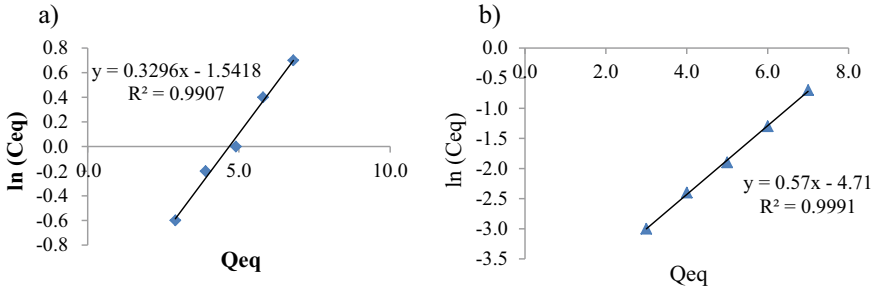

Fig. 10 **a, b** Temkin isotherm representing % adsorption of nitrates and nitrites for fish scales

such as nitrates and nitrites, while Table 2 shows the Temkin Constants A_T and B_T values.

The Langmuir model, based on isotherm studies and linear regression coefficient values, is more suitable for biosorption research for nitrate and nitrite contaminants.

4.8 Adsorption Kinetics

4.8.1 Kinetic Model (Pseudo-First Order)

The first- and second-order kinetics can be used to evaluate kinetic investigations. $(dq_t / dt) = k_1 (q_{eq} - q_t)$ is a pseudo-first-order kinetic equation [14] in which q_t is adsorption intensity at time t and q_{eq} is biosorption intensity at equilibrium time and k_1 represents first-order rate constant. In comparison to second-order kinetics results, first-order kinetics is not well suited for examining the appropriateness of using fish scale as an adsorbent for the removal of nitrates and nitrites as indicated in Table 3 and Fig. 11a, b.

Table 3 First-order kinetics

Kinetic model	Pollutant type	Kinetic model equation	R^2	First-order rate constant (K_1)
First order	Nitrate (NO_3^-)	Log ($Q_{eq} - Q_t$) = −0.0287 t −1.4814	0.6993	0.0661 min^{-1}
First order	Nitrite (NO_2^-)	Log ($Q_{eq} - Q_t$) = −0.036 t −1.2112	0.8497	0.0829 min^{-1}

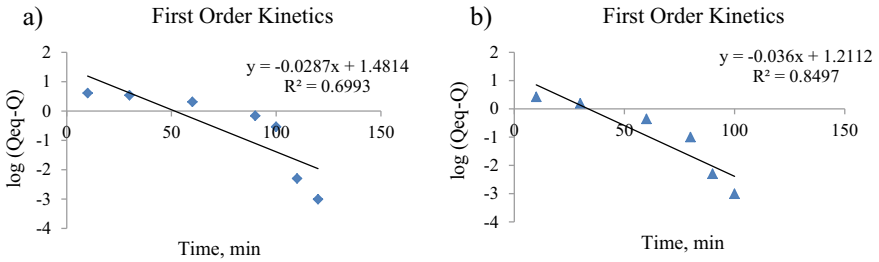

Fig. 11 **a, b** First-order kinetics for nitrates and nitrites

Table 4 Second-order kinetics

Kinetic model	Pollutant type	Kinetic mode equation	R^2	Second-order rate constant (K_2)
Second order	Nitrate (NO_3^-)	$t/Q_t = 0.0395\ t + 0.1948$	0.998	0.0080 gm./mg.min
Second order	Nitrite (NO_2^-)	$t/Q_t = 0.0393\ t + 0.0781$	0.999	0.0198 gm./mg.min

4.8.2 Kinetic Model (Pseudo-Second Order)

The kinetic equation (pseudo-second order) is simply $t/q_t = 1/q_{eq}\ (t) + 1/(K_2\ q_{eq}^2)$ [9], where qt is the biosorption intensity (at time t), q_{eq} is the biosorption intensity at equilibrium time, and K_2 is the second-order rate constant [12]. The value of constant K_2 increased for nitrites in comparison to nitrates, signifying that the percentage of pollutants eliminated increased as the K_2 value grew, based on the tabulated values of rate constant (K_2), as shown in Table 4 and Fig. 12.

5 Conclusions

Solid waste materials like fish scales were employed as adsorbents in this work to successfully remove two principal pollutants: nitrates and nitrites. Using fish scales

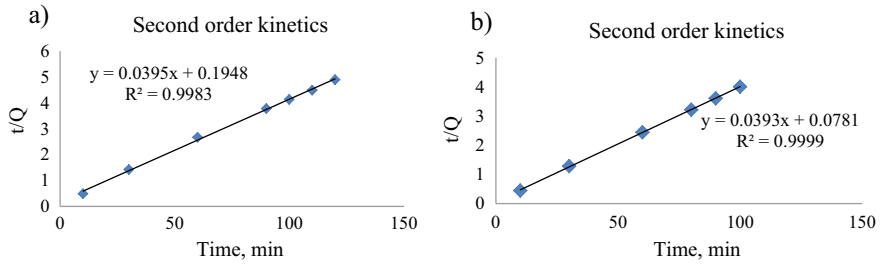

Fig. 12 **a, b** Second-order kinetics for nitrates and nitrites

as an adsorbent, around 96–99% of contaminants were removed over a broad range of pollutant concentrations. With an optimal contact period of 140 min for nitrates and 100 min for nitrites, the percent removal effectiveness was 97.96 and 99.70%, respectively. The maximum sorption capacity of fish scales as an adsorbent for nitrates is 24.49 mg/g at constant temperature 30 °C and pH 6, while the sorption capacity for nitrite is 24.93 mg/g. According to the thermodynamic analysis, the removal of nitrates and nitrites on fish scales is spontaneous and endothermic. Based on the results and R^2 values, we can conclude that the Langmuir model is more suitable for biosorption data for the various concentration ranges evaluated. Since the value of the second-order constant K_2 is much higher than the value of the first-order constant K_1, a pseudo-second-order kinetics equation would be the perfect fit for kinetic data. Furthermore, the values of constant K_2 for nitrites are higher than for nitrates when fish scales are used as an adsorbent. It may be inferred that when the K_2 value rises, the percentage of contaminants removed rises as well. Finally, based on the results of the aforementioned experiment, it can be concluded that fish scale is a possible adsorbent in the removal effectiveness of nitrates and nitrites, with the former, nitrates, being slightly less efficient than the latter, nitrites.

References

1. Bhatnagar A et al (2008) Removal of nitrate from water by adsorption onto zinc chloride treated activated carbon. Sepa Sci Technol 43(4):886–907. https://doi.org/10.1080/01496390701787461
2. Cengeloglu Y et al (2006) Removal of nitrate from aqueous solution by using red mud. Sep Purif Technol 51(3):374–78. https://doi.org/10.1016/j.seppur.2006.02.020
3. Divband Hafshejani L et al (2016) Removal of nitrate from aqueous solution by modified sugarcane bagasse biochar. Ecol Eng 95:101–110. https://doi.org/10.1016/j.ecoleng.2016.06.035
4. Doke KM, Khan EM (2013) Adsorption Thermodynamics to clean up wastewater; critical review. Rev Environ Sci Biotechnol 12(1):25–44. https://doi.org/10.1007/s11157-012-9273-z
5. El Hanache L et al (2019) Surfactant-modified MFI-type nanozeolites: super-adsorbents for nitrate removal from contaminated water. Micropor Mesoporous Mater 283:1–13. https://doi.org/10.1016/j.micromeso.2019.03.049

6. Helard D et al (2018) The adsorption and regeneration of natural pumice as low-cost adsorbent for nitrate removal from water. J Geosci Eng Environ Technol 3(2):86–93. https://doi.org/10.24273/jgeet.2018.3.2.1545.XXXX
7. Jiang LL, et al (2018) The effect of temperatures on the synergistic effect between a magnetic field and functionalized graphene oxide-carbon nanotube composite for Pb2+ and phenol adsorption. J Nanomater 2018. https://doi.org/10.1155/2018/9167938
8. Kuang Y et al (2020) Adsorption of methylene blue in water onto activated carbon by surfactant modification. Water (Switzerland) 12(2):587. https://doi.org/10.3390/w12020587
9. Liao J et al (2021) The synthesis of a novel titanium oxide aerogel with highly enhanced removal of uranium and evaluation of the adsorption mechanism. Dalton Trans 50(10):3616–3628. https://doi.org/10.1039/d0dt04320f
10. Mazarji M et al (2017) Removal of nitrate from aqueous solution using modified granular activated carbon. J Mol Liq 233:139–48. https://doi.org/10.1016/j.molliq.2017.03.004
11. Mondal NK et al (2019) Efficacy of onion peel towards removal of nitrate from aqueous solution and field samples. Environ Nanotechnol Monitor Manage 11:100222. https://doi.org/10.1016/j.enmm.2019.100222
12. Preetham V, Vengala J (2021) Removal of agricultural wastewater pollutants by integrating two waste materials fish scales and neem leaves as novel potential adsorbent. Water Sci Technol. https://doi.org/10.2166/WST.2021.294
13. Sanka PM et al (2020) Removal of selected heavy metal ions from industrial wastewater using rice and corn husk biochar. Water, Air, Soil Pollut 231(5):1–13. https://doi.org/10.1007/s11270-020-04624-9
14. Sayadi M et al (2020) Removal of nitrate, ammonium, and phosphate from water using conocarpus and paulownia plant biochar. Iranian J Chem Chem Eng 39(4):205–222. https://doi.org/10.30492/ijcce.2019.35183
15. Sharma A, Bhattacharyya KG (2005) Azadirachta indica (Neem) leaf powder as a biosorbent for removal of Cd(II) from aqueous medium. J Hazard Mater 125(1–3):102–112. https://doi.org/10.1016/j.jhazmat.2005.05.012
16. Song W et al (2016) Adsorption of nitrate from aqueous solution by magnetic amine-crosslinked biopolymer based corn stalk and its chemical regeneration property. J Hazard Mater 304:280–290. https://doi.org/10.1016/j.jhazmat.2015.10.073
17. Tan IAW et al (2009) Adsorption isotherms, kinetics, thermodynamics and desorption studies of 2,4,6-trichlorophenol on oil palm empty fruit bunch-based activated carbon. J Hazard Mater 164(2–3):473–82. https://doi.org/10.1016/J.JHAZMAT.2008.08.025
18. To PK, et al. (2020) Nitrate removal from waste-water using silica nanoparticles. J Chem vol 2020. https://doi.org/10.1155/2020/8861423
19. Xiaowen T et al (2017) Nitrate adsorption from aqueous solutions by calcined ternary Mg-Al-Fe hydrotalcite. Water Sci Technol 75(9):2194–2203. https://doi.org/10.2166/wst.2017.082
20. Zhang G et al (2009) removal of phosphate from water by a Fe-Mn binary oxide adsorbent. J Colloid Interface Sci 335(2):168–174. https://doi.org/10.1016/j.jcis.2009.03.019

Laboratory Evaluation of a Geosynthetic-Reinforced Pavement over Poor Subgrade

Gottumukkala Bharath, Amit Kumar Shaw, P. S. Prasad, and C. Kamaraj

Abstract Road construction and other infrastructure works have an ever-increasing demand for good quality construction materials. The availability of natural aggregates for such requirements are now becoming scarce due to the prevailing environmental constraints and the related need for socio-economic sustainability. As a result, recycling of used or waste materials has been gaining a dynamic momentum. One of such material is Reclaimed Asphalt Pavement (RAP) material obtained from the surface course of flexible (bituminous) pavements once the design life of pavement has exhausted. Though RAP material has got usage as partial replacement to the fresh bituminous mix, their performance as a fill material for the base layer of pavement is presented in this paper. To enhance the performance of RAP-filled base layers, it has been reinforced with different geosynthetic materials (geogrid, geocell) and their combination (geogrid plus geocell). For the need of clear distinction among the performance of different reinforcement cases, RAP-filled base layer was essentially prepared upon weak subgrade having low CBR value (black cotton soil). All studies were performed on laboratory-scale pavement model constructed inside an indigenously developed equipment named "Repeated Load Applicator for Pavement Performance". The RAP-filled base layer when reinforced with geocell and geogrid in single combination was found to perform better than the geocell confinement followed by the geogrid reinforcement. The performance of different reinforcement cases in comparison to the unreinforced case were evaluated in terms of Traffic Benefit Ratio (TBR) and Rut Depth Reduction factors (RDRF).

Keywords Geosynthetic reinforcement · Reclaimed asphalt pavement (RAP) material · Black cotton soil · Traffic benefit ratio · Rut depth reduction factor

G. Bharath (✉) · A. K. Shaw · P. S. Prasad · C. Kamaraj
CSIR-Central Road Research Institute, New Delhi 110025, India
e-mail: bharat.crri@nic.in

L. Nandagiri et al. (eds.), *Recent Advances in Civil Engineering*, Lecture Notes in Civil Engineering 256, https://doi.org/10.1007/978-981-19-1862-9_28

1 Introduction

In a bid towards more sustainable construction practices, there has been a gradual shift towards the reuse and recycling of the used and waste materials like concrete wastes from demolished buildings and rehabilitation works, fly ash, and other slag materials from refineries, reclaimed asphalt pavement (RAP) material, etc. In this study, we have considered RAP as one of the probable alternatives for the base layer material which generally requires good granular material. RAP is basically bitumen coated aggregates which has been milled off (reclaimed) from the top surface course of bituminous roads once the pavement design life has exhausted. Thus, the recycled use of the reclaimed bituminous mix not only helps reduce the amount of discarded waste but also facilitates cost savings in terms of reduced requirements for fresh aggregate material. However, it has been observed that RAP material does not possess a good strength of its own to be directly used as a fill material for the base layer of pavements [1, 2]. In such case, RAP material when placed as base layer needs to be strengthened or stabilized using a suitable method. Many researchers in their studies have tried to chemically stabilize the RAP material and some had proposed to partially replace the RAP content with fresh aggregates [3–8]. The noted methods of chemical stabilization and partial replacement technique though helps in reducing the required quantity of fresh aggregates, they may not be considered to be highly sustainable as partial replacement still requires some amount of fresh aggregates and use of chemical stabilizers may not always be environment-friendly [9]. To overcome these shortcomings, one of the recent studies has suggested the mechanical stabilization of RAP-filled base layers using cellular geosynthetic material called geocells [10].

Many types of geosynthetic materials like geogrid, geocell, geotextiles, etc., are being used for different types of ground improvement works for several decades [11]. The punching failure of subgrade can be altered towards general failure with inclusion of reinforcement [11]. The lateral spread of the confined layers is reduced with the inclusion of geogrids and geocell due to the confinement and tensioned-membrane effects [12]. The lateral restraint provided by geosynthetics is mainly responsible for the enhanced pavement performance of the reinforced sections [11]. The reinforcing effect due to geocell or geogrid tends to minimize the deterioration of granular layer material and can be beneficially used for low-to-moderate traffic volume conditions [12]. The elastic modulus of the reinforced layers increases significantly [12]. The geosynthetic-reinforced pavements exhibits lower surface rutting [12] and higher TBR values in comparison to the unreinforced case [13–16]. Thus, the geosynthetic-reinforced sections exhibits higher design life and helps reduce the required pavement thickness [11, 17]. Some of the previous studies on geosynthetic-reinforced pavements indicating the geosynthetic type, location, and the respective performance criterion, captured by other researchers are summarized below in Table 1.

Geosynthetic-reinforced pavements have been generally designed while considering conventionally used fresh aggregates. Nowadays, RAP material is gaining popularity as probable alternative to the conventionally required fresh aggregates for

Table 1 Summary for some of the earlier geosynthetic-based studies

Reference	Performance criterion	Geosynthetic type, structure	Geosynthetic location
Perkins [13]	Permanent sur-face deformation	Geogrid—punched, drawn, biaxial (polypropylene)	Base-subgrade interface and 100 mm above base–subgrade interface
		Geogrid—punched, drawn, woven (polypropylene)	Base–subgrade interface
		Geotextile	Base–subgrade interface
Leng and Gabr [15]	Vertical surface deformation	Geogrid—biaxial (polypropylene)	Base–subgrade interface
		Geonet with geotextile nonwoven	Base–subgrade interface
Tanyu et al. [18]	Rut depth	Geocell high-density polyethylene	Base–subgrade interface
Bhosale and Kambale [19]	Rut depth	Geotextile polypropylene multifilament woven	Base–subgrade interface
Abu-Farsakh and Chen [20]	Permanent deformation	Geogrid—biaxial & triaxial (polypropylene)	Upper one third of base course and middle of base layer
Qian and Han [16]	Permanent deformation	Geogrid—triaxial (polypropylene)	Base–subgrade interface

various construction and rehabilitation works of roads. In this study, we have analyzed the performance of RAP-filled base layers with different geosynthetic materials like geogrid, geocell, and combination of geogrid plus geocell. The results and analysis of the experimental studies presented in this paper provides a comparative assessment for different cases of geosynthetic reinforcements provided into base layers composed of RAP material.

2 Material Properties

This study involves two layers (subgrade and base layer) composed of distinct materials, constituting as a pavement model. The details of the pavement material and the geosynthetic reinforcements used in this study are summarized below.

2.1 Subgrade Layer

For subgrade layer, a highly expansive clayey soil called "black cotton soil" was used. The selection of this soil was based on the requirement of subgrade possessing low CBR value since the reinforcing effects are distinctly quantifiable in such cases [13, 21, 22]. The properties of the black cotton soil used in this study are given in Table 2. The grain size distribution of the black cotton soil and the RAP material (separated aggregates) used in base layer are shown in Table 3. The subgrade layer was compacted to 95% MDD (maximum dry density) at moisture content similar to its soaked CBR test condition. The thickness of the subgrade layer was kept as 500 mm (millimeter).

Table 2 Properties of subgrade soil

Material properties	Value	Test procedure
Soil classification	CH	IS 1498 [23]
Specific gravity	2.50	IS 2720-Part 3 [24]
Plasticity index	30	IS 2720-Part 5 [25]
Maximum dry density (g/cc)	1.77	IS 2720-Part 8 [26]
Optimum moisture content (%)	17	IS 2720-Part 8 [26]
CBR	2	IS 2720-Part 16 [27]
Moisture content at soaked CBR test condition	37	IS 2720-Part 2 [28]

Table 3 Grain size distribution curves for black cotton soil and RAP material

Sieve size (mm)	% passing	
	Black cotton soil	RAP material
26.5	100	100
19	100	100
13.2	100	87.15
9.5	99.1	71.69
6.3	–	63.83
4.75	96.3	41.50
2.36	93.1	29.64
1.18	89.3	13.90
0.600	87.0	8.29
0.425	85.4	5.06
0.300	85.1	3.92
0.150	82.9	1.22
0.075	81.4	0.32

2.2 Base Layer

Base layer was prepared using RAP (Reclaimed Asphalt Pavement) material which was compacted up to 95% of its maximum dry density (MDD = 2.03) at its optimum moisture content (OMC) of 4.8%. The collected RAP material was subjected to bitumen extraction process for separation of aggregates and binder. The standard specification of ASTM-D 2172M-11 [29] was followed for this binder extraction process. The aggregates gradation checked for the RAP material considering these separated aggregates are presented in Table 3. The thickness of the RAP-filled base layer was kept as 225 mm.

2.3 Geosynthetic Reinforcement Material

Two types of geosynthetic material have been used in this study. One of the materials is Geogrid which is basically planar in structure and having square openings on it; the other type of geosynthetic material used is Geocell which mainly consists of a three-dimensional cellular structure which helps confine the filled materials. The properties of Geogrid and Geocell used in this study are presented in Tables 4 and 5, respectively.

Table 4 Properties of geogrid*

Material properties	Values
Geogrid type	Biaxial
Material type	Polypropylene
Ultimate tensile strength	30 kN/m
Unit tension at 2.0% strain	11 kN/m
Unit tension at 5.0% strain	21.6 kN/m

*Properties as provided by the manufacturer

Table 5 Properties of Geocell*

Material properties	Values
Cell depth (mm)	150 (±3%)
Minimum thickness (mm)	1.52
Expanded cell area (cm^2)	290 (±3%)
Expanded cell dimension (mm)	259 × 224 (± 3%)
Specified seam strength (N per 150 mm)	2130
Weld spacing (mm)	356 (±3%)

*Properties as provided by the manufacturer

3 Experimental Work

Laboratory-scale pavement models were constructed inside an indigenously developed equipment named "Repeated Load Applicator for Pavement Performance" which consists of a large size tank (circular in shape, diameter, and height of one meter each) with arrangements for application of repeated cyclic loads. All tests related to the performance evaluation of the unreinforced and reinforced cases were performed using this large size tank. The material for different layers of the pavement were filled into the tank and compacted to the desired density and thickness. The different layers were compacted with a uniform lift of 7.5 cm each, thus maintaining a uniform level of compaction throughout the depth. After completing the layered construction of the pavement model, a circular loading plate (diameter 150 mm) for repeated cyclic loading is then lowered onto the top surface. The repeated cyclic load was then applied in "haversine pattern" (shown in Fig. 1) as it closely simulates the actual field traffic loading conditions. The maximum load intensity was kept as 10 kN to generate a contact pressure of 0.56 MPa with each cycle of 1.3 s duration and the total number of cycles for each test was restricted to 18,000 due to the prevailing technical limitations. After completing the designated number of load cycles, the acquired data for peak surface deformations (surface settlements) corresponding to each load cycle was then processed to have a cumulative settlement of the loaded surface. The photographs depicting each step of the test program as discussed above are presented in Fig. 2.

Thus, we had different plots for the varied reinforced cases, which were then used for their comparative performance assessment. The four types of pavement models which have been considered in this study are mentioned below and they have also been shown schematically in Fig. 3a–d. The respective test data for the cyclic plate

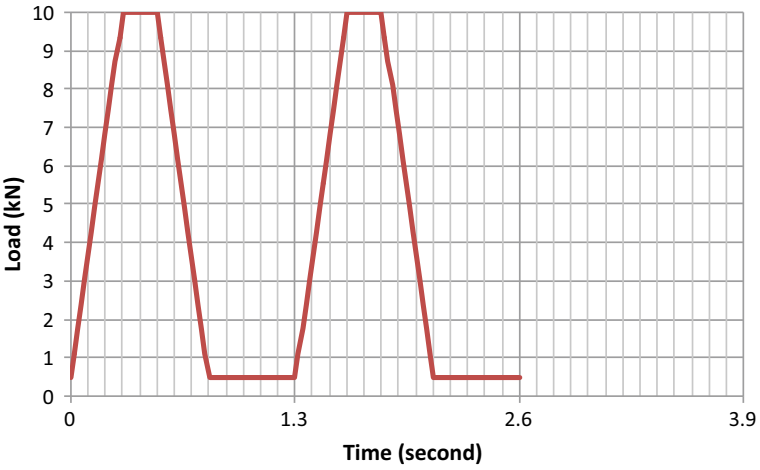

Fig. 1 Haversine loading pattern used in this study

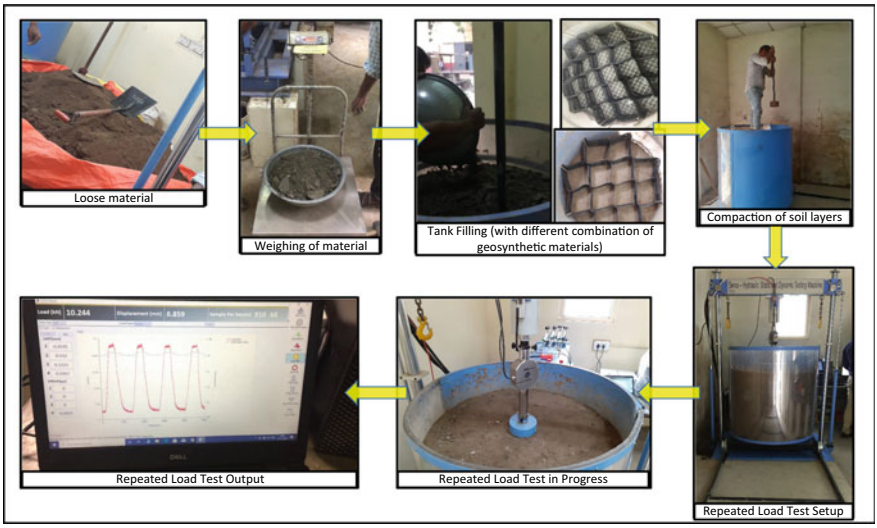

Fig. 2 Steps followed in test program

load tests performed for these reinforcement cases are shown graphically in Fig. 4.

(i) Unreinforced case
(ii) Reinforced with Geogrid (geogrid placed on top of subgrade)
(iii) Reinforced with Geocell (geocell fixed on top of subgrade)
(iv) Reinforced with Geogrid and Geocell (geogrid placed on subgrade, then geocell placed on geogrid)

4 Data Analysis

For each test performed on different reinforcement cases, we have test results in the form of cumulative surface settlement for the total number of loading cycles sustained by the test. These test results have further been used to calculate the two different performance parameters named TBR and RDRFs. The details for these two pavement performance parameters are discussed below.

4.1 Traffic Benefit Ratio (TBR)

It gives an indicative design life for the reinforced pavements in comparison to the unreinforced ones. The number of load cycles dissipated for the same value of surface settlement in the two comparative cases, gives the improvement in terms of a ratio called TBR. The mathematical equation used for the calculation of TBR is shown

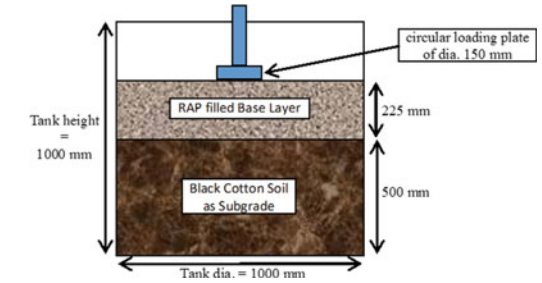

(a) Unreinforced case

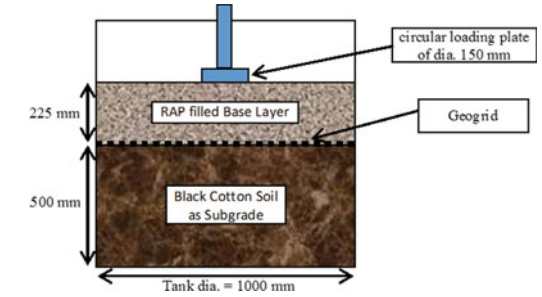

(b) Reinforced with Geogrid

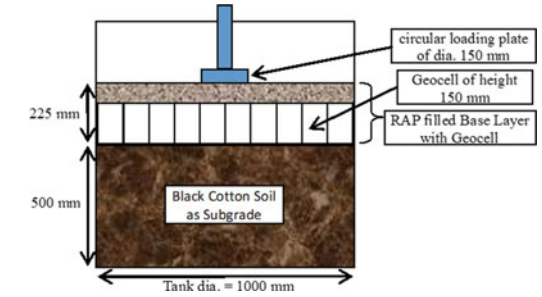

(c) Reinforced with Geocell

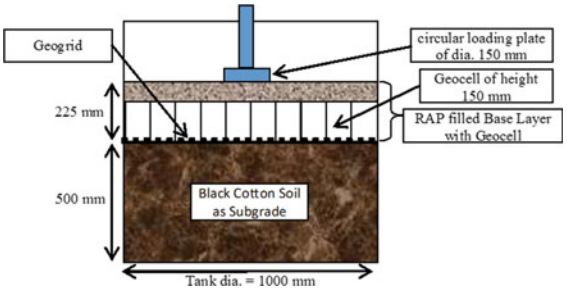

(d) Reinforced with Geogrid and Geocell

Fig. 3 **a** Unreinforced case. **b** Reinforced with geogrid. **c** Reinforced with geocell. **d** Reinforced with geogrid and geocell

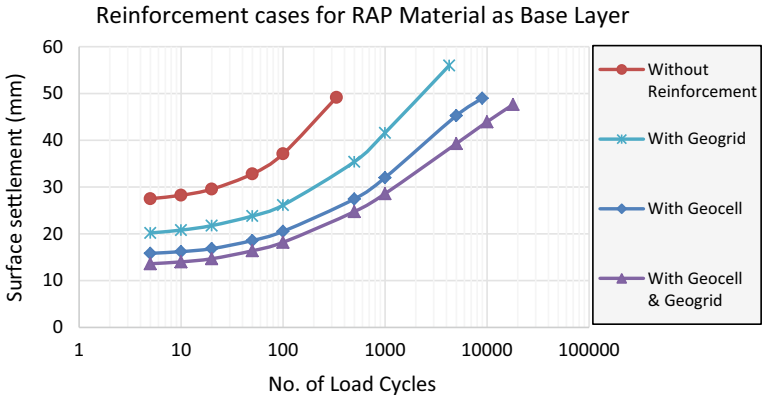

Fig. 4 Surface settlement for different cases of reinforcement

Table 6 TBR calculation for different reinforcement cases

Reinforcement type	Number of load cycles		TBR = (*b*)/(*a*)
	Unreinforced case (a)	Reinforced case (b)	
Reinforced with geogrid	24	225	9
Reinforced with geocell	24	749	31
Reinforced with geogrid plus geocell	24	1255	52

below in Eq. 1.

$$\text{TBR} = \frac{\text{Number of load cycles in reinforced case}}{\text{Number of load cycles in unreinforced case}} \quad (1)$$

From Fig. 4, it can be observed that the unreinforced case is showing high surface settlement behavior, accordingly the reference value of surface settlement for the calculation of TBR has been selected as 30 mm. The calculation of TBR value for all the reinforced cases are summarized in Table 6.

4.2 Rut Depth Reduction Factor (RDRF)

It gives a comparative idea for the pavement performance in terms of improvement in rutting behavior for a given number of load cycles. Mathematically, it is opposite to TBR and its calculation is shown below in Eq. 2.

$$\text{RDRF}\ (\%) = \frac{\text{Settlement in unreinforced case} - \text{Settlement in reinforced case}}{\text{Settlement in unreinforced case}} \times 100 \quad (2)$$

Table 7 Calculation of RDRF for different reinforcement cases

Reinforcement type	Surface settlement (mm)		RDRF = $[(a - b)/(a)]$ *100 (%)
	Unreinforced case (a)	Reinforced case (b)	
Reinforced with geogrid	37.104	26.13	30
Reinforced with geocell	37.104	20.527	45
Reinforced with geogrid plus geocell	37.104	18.183	51

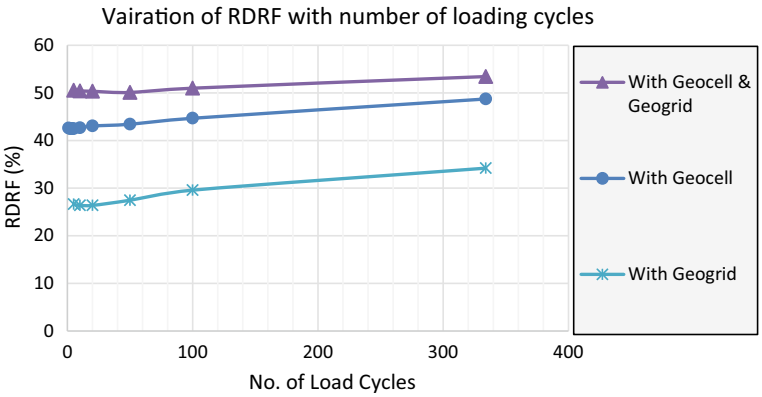

Fig. 5 RDRF for the three reinforcement cases

For the present study, 100 number of loading cycles have been considered as the reference criterion for computing the RDRF for different reinforcement cases. The calculation of RDRF is summarized below in Table 7. The graphical variation of the RDRF calculated up to 334 continuous cycles for each of the three reinforcement cases is shown in Fig. 5. The number of maximum cycles considered for calculation of RDRF is limited to 334, as it is the last possible loading cycle for the unreinforced case which acts as the reference for calculation of RDRF for the other reinforced cases.

5 Conclusions

This study is based on RAP-filled base layers on soft soil subgrades having low CBR. The test results for the laboratory scale pavement model studies were used to quantify the comparative improvement of the pavement performances for the case of reinforced sections in comparison to the unreinforced ones. The benefits of reinforcing the base layers were computed in terms of TBR and RDRF. The all three reinforcement cases namely (a) Geogrid on subgrade, (b) Geocell on subgrade, and

(c) combination of Geocell and Geogrid; considered in this study were found to considerably enhance the pavement performance. The following conclusions can be drawn from this study:

- The performance for the combined application of Geogrid and Geocell was found to be best among all three reinforcement cases, followed by the case of Geocell confinement and then the case of Geogrid reinforcement.
- The RDRFs for all the three reinforcement cases were found to continuously increase with the number of loading cycles.
- TBR values for the case of combined application of Geogrid and Geocell (TBR = 52), were found to be higher than the case of only Geocell (TBR = 31), followed by the case of only Geogrid (TBR = 9).
- The RDRF for the three reinforcement cases: (a) Geogrid reinforced base layers, (b) Geocell-confined base layers, and (c) combination application of Geogrid and Geocell on base layers were found to be 30, 45, and 51%, respectively.
- Geocell-confined base layer yields better performance than the Geogrid reinforced case. This can be related to the increased stiffness of the confined material under the action of lateral confinement and tension membrane effect offered by the geocell reinforcement.
- The improved performance of the geosynthetic-reinforced pavements (measured in terms of TBR & RDRF) can either be used for the reduction of base layer thickness (for a particular design life) or the thickness of base layer can be kept unaltered thus providing an increased design life to the pavement.

This study is limited to large-scale laboratory studies under repeated loading on single source of RAP material. This study further requires field implementation of geocell/geogrid reinforced sections under actual traffic loading to study long-term performance behavior.

Acknowledgements Authors are thankful to Director, CSIR—CRRI, New Delhi, for his kind permission to publish this paper. We thankfully acknowledge National Mission on Himalayan Studies, G.B. Pant National Institute of Himalayan Environment and Sustainable Development (GBPNHIESD) which gave us financial assistance for the project on "Sustainable Road pavements in high altitude regions using geosynthetics."

References

1. Kazmee H, Tutumluer E, Beshears S (2016) Using accelerated pavement testing to evaluate reclaimed asphalt pavement materials for pavement unbound granular layers. J Mater Civ Eng 29(2):1–13
2. Rana ASMA (2004) Evaluation of recycled material performance in highway applications and optimization of their use. Dissertation (PhD). Texas Tech University
3. Potturi AK (2006) Evaluation of resilient modulus of cement and cement fiber treated reclaimed asphalt pavement (RAP) aggregates using repeated load triaxial test. Thesis (MS). The University of Texas at Arlington

4. Deniz D, Tutumluer E, Popovics JS (2010) Evaluation of expensive characteristics of reclaimed asphalt pavement and virgin aggregate used as base materials. Transp Res Record: J Transp Res Board 2167:10–17
5. Puppala AJ, Hoyos LR, Potturi AK (2011) Resilient moduli response of moderately cement-treated reclaimed asphalt pavement aggregates. J Mater Civ Eng 23(7):990–998
6. Mohammadinia A et al (2014) Laboratory evaluation of the use of cement treated construction and demolition materials in pavement base and subbase applications. J Mater Civ Eng 28(7):899–1561
7. Avirneni D, Peddinti PRT, Saride S (2016) Durability and long term performance of geopolymer stabilized reclaimed asphalt pavement base courses. Constr Build Mater 121:198–209
8. Puppala AJ, Congress SSC, Bheemasetti TV et al (2018) Visualization of civil infrastructure emphasizing geomaterial characterization and performance. J Mater Civ Eng 30(10):04018236. https://doi.org/10.1061/(ASCE)MT.1943-5533.0002434
9. Sambodh A (2017) Mechanical properties of soil-RAP-geopolymer for the stabilization of road base/subbase. Thesis (MS). University of Louisiana at Lafayette
10. George AM, Banerjee A, Puppala AJ, Saladhi M (2021) Performance evaluation of geocell-reinforced reclaimed asphalt pavement (RAP) bases in flexible pavements. Int J Pavement Eng 22(2):181–191. https://doi.org/10.1080/10298436.2019.1587437
11. Zornberg JG (2011) Advances in the use of geosynthetics in pavement design. In: Proceedings of the second national conference on geosynthetics, geosynthetics India '11 Vol 1. India Institute of Technology Madras, Chennai, India, pp 3–21
12. Mamatha KH, Dinesh SV, Dattatreya JK (2017) Evaluation of flexural behaviour of geosynthetic-reinforced unbound granular material beams. Road Mater Pave Des. https://doi.org/10.1080/14680629.2017.1422790
13. Perkins SW (1999) Geosynthetic reinforcement of flexible pavements: laboratory based pavement test sections, final report: FHWA/MT-99–001/8138, State of Montana, Department of Transportation, Research, Development and Technology Transfer Program
14. Chen Q, Hanandeh S, Abu-Farsakh M, Mohammad L (2017) Performance evaluation of full-scale geosynthetic reinforced flexible pavement, Article in Geosynthetics International https://doi.org/10.1680/jgein.17.00031
15. Leng J, Gabr MA (2002) Characteristics of geogrid-reinforced aggregate under cyclic load. Transp Res Record 1786, Paper No. 02–4091
16. Qian Y, Han J, Pokharel SK, Parsons RL (2013) Performance of triangular aperture geogrid-reinforced base courses over weak subgrade under cyclic loading. Article J Mater Civ Eng. https://doi.org/10.1061/(ASCE)MT.1943-5533.0000577
17. Sun X, Han J, Corey R (2010) Equivalent modulus of geogrid-stabilized granular base back-calculated using permanent deformation. J Geotech Geoenviron Eng. https://doi.org/10.1061/(ASCE)GT.1943-5606.0001761
18. Tanyu BF, Kim WH, Edil TB, Benson CH (2003) Comparison of laboratory resilient moduli with back-calculated elastic moduli from large-scale model Experiments and FWD tests on granular materials, Resilient Modulus Testing for Pavement Components. In Durham GN, Marr AW, De Groff WL (eds) ASTM, West Conshohocken PA, USA, STP, vol 1437, pp 191–2080
19. Bhosale SS, Kambale BR (2008) Laboratory study for evaluation of membrane effect of geotextile in unpaved road. In: The12th international conference of international association for computer methods and advances in geomechanics (IACMA), Goa
20. Murad Abu-Farsakh Y, Chen Q (2012) Evaluation of the base/subgrade soil under repeated loading: Phase I–In-Box and ALF cyclic plate load tests. Final Report. No. FHWA/LA.09/450, Louisiana transportation research center, Baton Rouge, LA
21. Kiptoo D, Aschrafi J, Kalumba D, Lehn J, Moormann C, Zannoni E (2017) Laboratory investigation of a geosynthetic reinforced pavement under static and dynamic loading. J Test Eval 45(1):76–84. https://doi.org/10.1520/JTE20160170
22. Jeremy Robinson W, Mahaffay BJ, Howard IL, Norwood GJ (2019) Cyclic plate testing of geosynthetic reinforced airfield pavements. https://doi.org/10.1680/jgrim.18.00106

23. IS 1498: Classification and identification of soils for general engineering purposes. Bureau of Indian Standards, New Delhi
24. IS 2720-3-1 (1980) Methods of test for soils, Part 3: determination of specific gravity, Section 1: fine grained soils. Bureau of Indian Standards, New Delhi
25. IS 2720-5 (1985) Methods of test for soils, Part 5: determination of liquid and plastic limit [CED 43: soil and foundation engineering]. Bureau of Indian Standards, New Delhi
26. IS 2720-8 (1983) Methods of test for soils, Part 8: determination of water content-dry density relation using heavy compaction. Bureau of Indian Standards, New Delhi
27. IS 2720-16 (1987) Methods of test for soils, Part 16: laboratory determination of CBR. Bureau of Indian Standards, New Delhi
28. IS 2720-2 (1973): Methods of test for soils, Part 2: determination of water content [CED 43: Soil and Foundation Engineering]
29. ASTM-D2172M-11 (2011) Standard test methods for quantitative extraction of bitumen from bituminous paving mixtures. ASTM international, West Conshohocken, PA, United States, pp 19428–2959

A Study on Morphodynamic Nature of Muthalapozhi Fishery Harbour in Kerala Using Geospatial Approach

Kunhimammu Paravath, Ammu John, and T. Nasar

Abstract It is crucial to monitor the dynamics of any fragile coastal stretch on a regular basis. Shorelines on both sides of Muthalapozhi tidal inlet, which is located along Kerala coast in India, were modified after the construction of breakwaters for a fishing harbour. The fishing harbour work was initiated in 2002. Severe erosion at the immediate North of the breakwater and choking of harbour mouth due to spit formation was observed. The construction of modified breakwaters began in 2013, after resolving the deficiencies in the first phase. Coastal morphology needs to be further analysed to check the adequacy of the breakwaters. An attempt to study the dynamicity of coastal morphology of Muthalapozhi Harbour using geospatial approach is reported in this paper. In response to the breakwater construction, End Point Rate (EPR) and Linear Regression Rate (LRR) are calculated using Digital Shoreline Analysis System (DSAS) in ArcGIS software. The results indicate that high accretion with a maximum rate of 209 m/year in the year 2019 is observed on the immediate southern side of the south breakwater.

Keywords Muthalapozhi Harbour · Shoreline change · End point rate · Linear regression rate · Littoral drift

1 Introduction

A shoreline is a boundary between the land and the ocean, is prone to periodic changes on account of various dynamic factors such as wave characteristics, coastal orientation, currents and bathymetry [3]. As a result, shoreline location varies continuously with respect to time. Shoreline change is the direct consequence of coastal erosion and accretion, along with the effect of nearshore currents. Based on the sediment supply, shoreline can undergo three different conditions such as deficit, balance and surplus in sediment budget, which results in shoreline change for a short-term or long-term period [7, 9].

K. Paravath (✉) · A. John · T. Nasar
Department of Water Resources and Ocean Engineering, National Institute of Technology, Surathkal, Karnataka 575 025, India
e-mail: kunhimammup@gmail.com

L. Nandagiri et al. (eds.), *Recent Advances in Civil Engineering*, Lecture Notes in Civil Engineering 256, https://doi.org/10.1007/978-981-19-1862-9_29

Indian coastline of about 7516 km is under severe threat due to global warming and other human interventions [5]. The Western coastline of India has a large number of harbours and estuaries [15, 16]. The rapid growth in the socio-economic sector of this region demands a critical task of monitoring a coastal zone. Shoreline mapping and shoreline change detection are significant for coastal environmental protection, safe navigation, coastal resource management, sustainable development and planning of coastal zones [1, 2, 4]. Multi-year shoreline mapping is considered as a valuable part of coastal monitoring and assessment even though they remain difficult to undertake [14]. The advance and retreat of the shoreline position can be measured using the historical cartographic documents, providing useful results for the planning and management of the coastal zones [11, 12].

Rates of change of coastline can be predicted by using Digital Shoreline Analysis System (DSAS), which is an extension of Environmental Systems Research Institute (ESRI) ARCGIS software. The accuracy of the estimated shoreline change rate depends upon the availability of both historical and present shoreline data. It is essential to substantiate the rate of change of shoreline to formulate development activities in terms of both infrastructure and ecology [6]. The calculation of shoreline change rates is frequently used for summarizing historical shoreline movements and predicting the future shoreline positions through different modelling procedures [1]. Some of the techniques such as End Point Rate (EPR), Minimum Description Length (MDL), Average of Rates (AOR), Linear Regression Rate (LRR), Ordinary Least Squares (OLS) and Jack-knifing are being extensively used for the estimation and forecast of the rate of shoreline changes. Shoreline rate of change calculated by each method is based on measured differences between shoreline positions through time intervals. The estimation of EPR and LRR was expressed as metres of change along transects per year [10]. In the present study, the extracted shoreline data were fed into DSAS, and inter-annual variation and intra-annual variation of shoreline were estimated by calculating Linear Regression Rate (LRR) and End Point Rate (EPR) along transect lines placed at intervals.

2 Study Area

2.1 Muthalapozhi Harbour

The geographical location of the harbour is 8°37’53.14" N and 76°47’12.22" E, and it comes under the administration of Varkala Taluk, Trivandrum District, Kerala, India. It is situated at the mouth of Vamanapuram River and is bounded by the Arabian Sea on the West as shown in Fig. 1. The seasonal closure of the Muthalapozhi tidal inlet created many difficulties to the fishermen, including capsizing of vessels leading to loss of life and property. In order to make the river inlet perennial, a proposal was made to construct two breakwaters for training the river mouth.

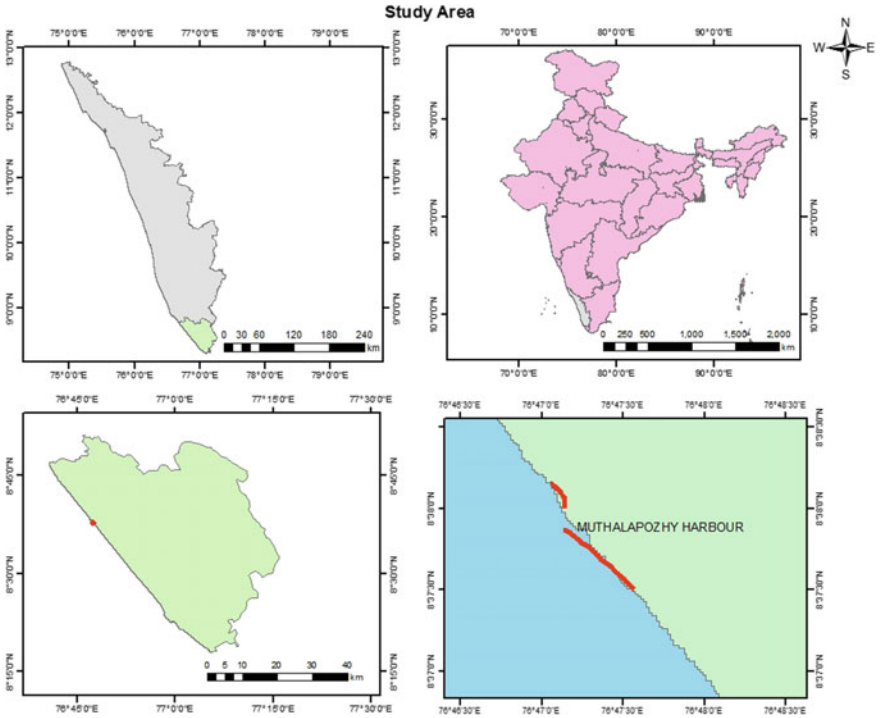

Fig. 1 Study area

In 2002, a breakwater construction was initiated for recommended breakwater configuration given by IIT Madras based on the model studies results. As per the studies, the net annual sediment transport is towards South. The recommended configuration was breakwaters with a length of 170 m on the Southern side and 480 m with an *L*-shape (280 m towards the West and an additional 200 m towards South) on the Northern side [13].

During construction, chocking of the mouth with sediment deposit and spit formation were observed which makes harbour non-functional. In order to overcome such problems, breakwater design was modified based on the expert advice of Central Water and Power Research Station (CWPRS), Pune. The extension of the North arm towards the South was limited to 130 m and the South arm was given an extension of 160 m towards South forming an *L*-shaped breakwater. Thus, the length of breakwaters was modified as 410 m (North arm) and 330 m (South arm) and the construction was completed in 2004.

As the problem persisted even after the construction of breakwater arms re-engineering studies were done. The net drift was observed towards the North which indicated a reversal of drift direction than predicted in the initial proposal during the year 2002. Based on the studies, it was decided to extend the straight portion of the Northern breakwater by 160 m and straight portion of the Southern breakwater by

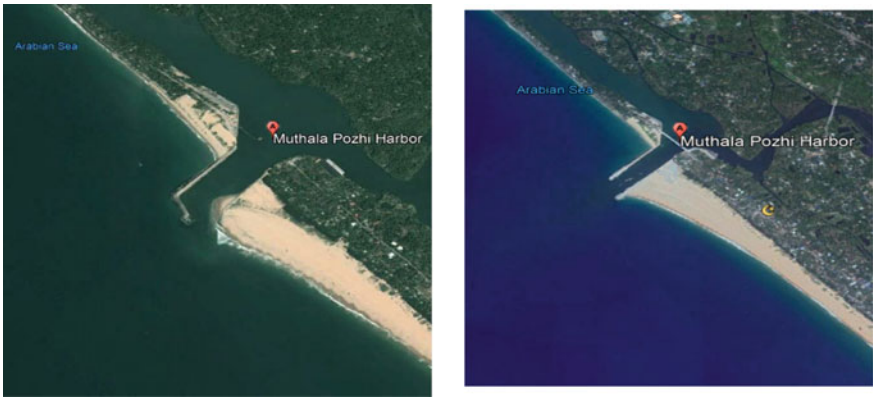

(a) (b)

Fig. 2 **a** Google Earth image of Muthalapozhi Harbour as on 21 January 2012**. b** Google Earth image of Muthalapozhi Harbour as on 25 November 2015

330 m, giving a combination of parallel breakwaters of length 440 m (North arm) and 500 m (South arm). This modification works were commenced in the year 2014, after which a considerable improvement in the tranquillity condition was observed. Over a period of 15–20 years, a bypassing of sand through the tip of the Southern breakwater was anticipated which require further studies [17]. The breakwaters before and after the modification are shown in Fig. 2.

3 Methodology

In the present study, the influence of a pair of breakwaters on the coast is studied using Digital Shoreline Analysis System (DSAS). DSAS calculates the rate of change of statistics from the historic shoreline vector data [11].

EPR is determined by dividing the total distance of shoreline movement with the time elapsed between the older most and the most recent shoreline. The ease of computation and the minimum requirement of only two shorelines are the major advantages of the EPR[8]. A least-squares regression line is fitted to all the shoreline points intersected by a particular transect to calculate the rate of change statistic, LRR. The following features are included in the method of linear regression: (i) irrespective of the changes in accuracy or trend, all the data are used, (ii) purely computational method and (iii) accepted statistical concepts are the basis of the calculation [18].

The shorelines along with suitable baseline are extracted from the field data and are appended to a single dataset. The shorelines and baselines are then exported to a personal geodatabase. The input from geodatabase is provided to the DSAS tool and transect lines of suitable lengths are obtained at suitable intervals in order to arrive

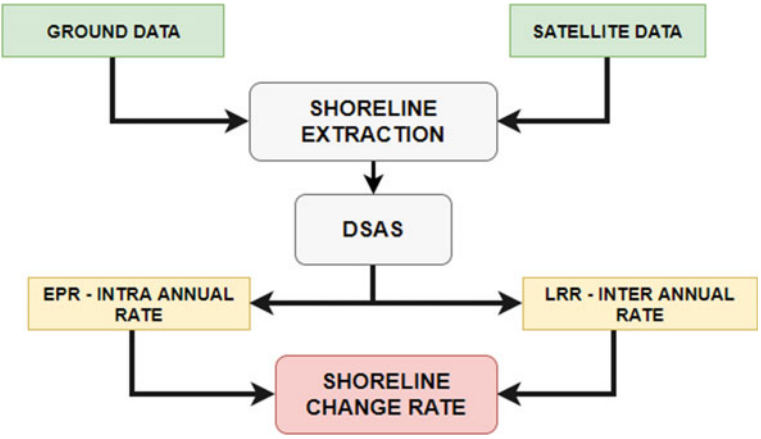

Fig. 3 Workflow to analyse the shoreline variation

the values of EPR and LRR. A flow chart representing the procedure involved in arriving shoreline variation is shown in Fig. 3.

4 Data Used

The shoreline data and LANDSAT-7 images are taken from the Department of Harbour Engineering of Kerala state, India and United States Geological Survey's Center for Earth Resources Observation and Science (USGS EROS), respectively, for the present work. Shorelines are extracted by the visual interpretation technique in ArcMAP 10.3. Shoreline (Vector format) data extracted from field survey for the period of 2002–2005, 2013–2017 and satellite data LANDSAT-7 for a period of 1999–2013, 2018–2019 were used to study shoreline change rate before and after the construction of training walls in Muthalapozhi Harbour.

5 Results and Discussion

The extracted shoreline was fed into DSAS and intra-annual variation of shoreline was estimated by calculating LRR and EPR. The data collected was divided into five categories based on the construction and modification periods of the breakwater which includes before construction (1999–2002), during construction (2003–2004), after construction (2005–2013), during modification (2014) and after modification (2015–2019). The computations were performed for these five phases along transect lines drawn at an interval of 20 m. The estimation of LRR is done for each year from 1999 to 2019. The shorelines are classified into three categories, viz, accretional,

Table 1 Coastal classification based on LRR criterion values

LRR value (m/year)	Coast type
<−2	Erosional
−2–2	Stable
>2	Accretional

stable and erosional based on sediment movement rate obtained through LRR criterion values which are mentioned in Table 1. The estimation of EPR is done for each month with shoreline data available from 1999 to 2019.

5.1 Pre-construction Shoreline Configuration Scenario

Extreme shoal formation was observed on both Northern and Southern sides of river inlet making the Arabian Sea inaccessible to the local fishermen. During the month of February 1999, it was observed that the inlet was completely closed by the spit formation. Whereas, in the month of September (year), the width of the river inlet was observed to be 77 m. The erosion was observed to be extreme on both the sides of the inlet during the years 1999–2001. The average rate of shoreline configuration dynamicity during the years 1999–2002 is given in Table 2. The negative and positive values in the tabulation indicate erosion and accretion pattern, respectively. The variation in LRR values for a distance of 4 km along the Northern shoreline and 6 km along the Southern shoreline is shown in Fig. 4.

The shoreline change rate during different months before the construction of the breakwaters can be understood from Table 3. During the pre-construction phase from 1999 to 2002, the maximum average shoreline change rates along the North and South were found to be −18.62 m/mo (metres per month) for the months March–May 2002 and 18.13 m/mo for the months November–December 2000, respectively.

5.2 During Breakwater Construction Scenario

The construction of breakwaters began in 2003 and lasted until late 2004. The average rate of shoreline configuration dynamicity during the years 2003 and 2004 is shown in Table 2. The variation in LRR values for a distance of 5 km each along the Northern and Southern shoreline is shown in Fig. 5. The average rates of shoreline configuration dynamicity for 2003 are 9.17 m/year (North side) and −39.52 m/year (South side) (Table 2). The Southern shoreline underwent accretion with average shoreline change rates of 12.85 m/mo during August–October and 11.13 m/mo during October–December of the year 2003 (Table 3). Along the pace of construction, chocking of the mouth with sediment deposit and spit formation was observed. To rectify the problem, breakwater design was modified to 410 m and 330 m. The average rate of

Table 2 LRR values before and during construction in m/year (1999–2004)

Shoreline phase	Year	Northern side			Southern side		
		Mean rate	Max. accretion	Max. erosion	Mean rate	Max. accretion	Max. erosion
Pre-construction	1999	−47.17	NIL	−63.92	−56.63	NIL	−159.51
	2000	−3.912	103.85	−41.85	−19.68	NIL	−82.84
	2001	−18.14	19.96	−89.03	−33.53	19.36	−76.77
	2002	−25.31	29.72	−74.83	17.29	41.41	−51.67
During construction	2003	9.17	52.52	−7.78	−39.52	NIL	−79.5
	2004	41.2	70.35	NIL	39.67	65.83	NIL
Post-construction	2005	−21.75	45.68	−46.51	−14.17	7.09	−36.58
	2006	−12.56	15.39	−41.96	−11.85	31.42	−68.92
	2007	−42.02	31.9	−65.51	−63.36	NIL	−178.52
	2008	−18.2	5.3	−41.4	−29.9	3.11	−134.5
	2009	−49.32	NIL	−138.5	−47.24	1.23	−75.49
	2011	41.1	81.59	NIL	2.84	47.08	−102.8
	2012	−16.01	NIL	−23.61	−22.95	NIL	−59.26
	2013	65.2	109.03	36.18	106.2	175.7	NIL
During modification	2014	5.86	9.56	−24.63	17.49	81.87	−21.12
Post-modification	2015	14.45	31.64	NIL	3.4	35.76	−19.88
	2016	65.64	108.06	−8.27	−95.77	NIL	−182.63
	2017	−33	NIL	−74.1	−23.62	33.82	−91.22
	2018	7.12	56.77	−51.03	−2.47	17.35	−130.4
	2019	24.88	65.49	−24.07	36	209	−37

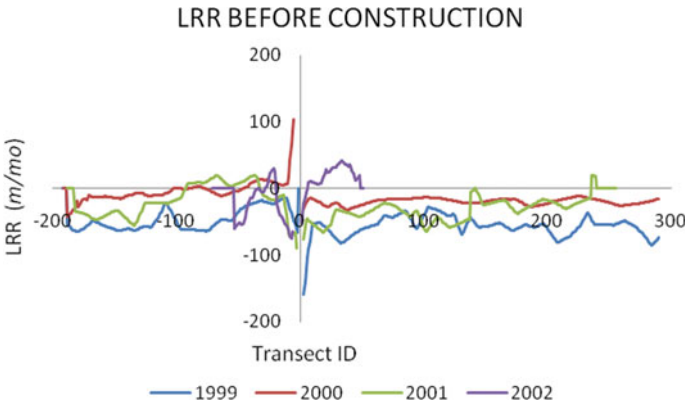

Fig. 4 LRR before construction (1999–2002)

Table 3 EPR before and during construction in m/mo (1999–2004)

Year	Month span	Northern side			Southern side		
		Mean rate	Max. accretion	Max. erosion	Mean rate	Max. accretion	Max erosion
1999	Feb–Sept	−5.14	NIL	−6.92	−6.41	NIL	−11.41
	Sept–Nov	6.38	29.44	−10.15	7.83	32.6	−13.59
2000	Jan–Aug	−2.8	16.16	−7.03	−6.49	NIL	−13.54
	Sept–Oct	9.06	34.81	−7.68	−1.54	18.55	−27.5
	Oct–Nov	13.02	46.1	−35.6	8.17	38.67	−4.2
	Nov–Dec	−3.73	15.41	−23.88	18.13	44.79	NIL
2001	Mar–May	−4.42	6.06	−29.48	−2.53	5.34	−15.58
	May–June	5.2	33	−13.7	2.89	23.15	−7.37
	June–Nov	−1.45	0.89	−3.86	−4.57	4.35	−9.75
2002	Mar–May	−18.62	−11.68	−38.91	−3.42	1.18	−11.16
	May–Sept	5.34	14.95	1.53	−3.3	2.53	−11.21
	Sept–Dec	−8.08	−4.03	−13.81	14.53	25.75	4.36
2003	Mar–May	−17.63	−10.42	−22.81	13.1	32.71	−8.43
	May–June	21.19	41.28	8.12	7.23	21.29	−8.05
	June–Aug	7.79	15.08	−16.15	−4.68	1.18	−19.62
	Aug–Oct	−2.36	5.52	−6.89	12.85	41.88	−4.09
	Oct–Dec	5.6	16.5	−9.19	11.13	24.41	1.19
2004	Jan–Feb	−6.22	5.42	−22.98	19	25.75	14.53
	Feb–Mar	−3.59	18.22	−14.11	3.04	22.6	−10.84
	Mar–May	−10.63	−4.52	−22.51	1.55	9.72	−7.91
	May–Nov	11.43	14.83	7.44	0.78	4.86	−3.96
	Nov–Dec	17.07	29.75	4.45	−2.42	10.22	−15.37

shoreline configuration dynamicity for the year 2004 is 41.20 m/year (North side) and 39.7 m/year (South side) (Table 2). From EPR criterion values given in Tables 3, it is inferred that, during the initial months of construction, Northern shoreline mostly underwent erosion, whereas the Southern side experienced accretion.

5.3 Post-construction of Breakwater Scenario

The required river inlet width of 220 m was gained due to the construction of breakwaters. As the natural sediment flow was interrupted, the stability of the adjacent shoreline was disrupted. The values of LRR obtained for the post-construction years from 2005 to 2013 are given in Table 2. The variation in LRR values for a distance of 5 km each along the Northern and Southern shoreline is shown in Fig. 6. From 2005

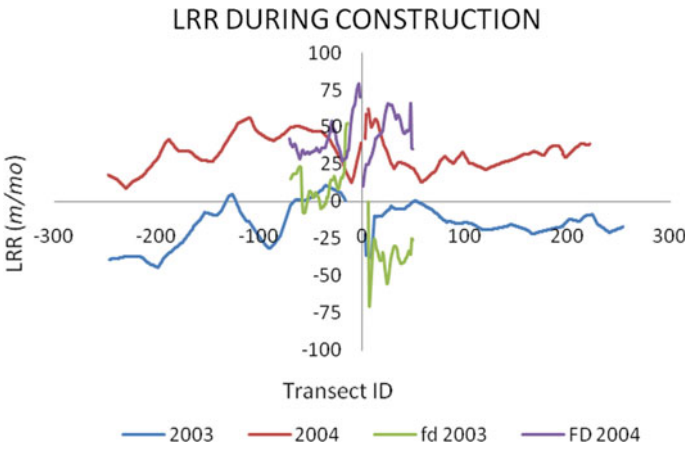

Fig. 5 LRR during construction (2003–2004)

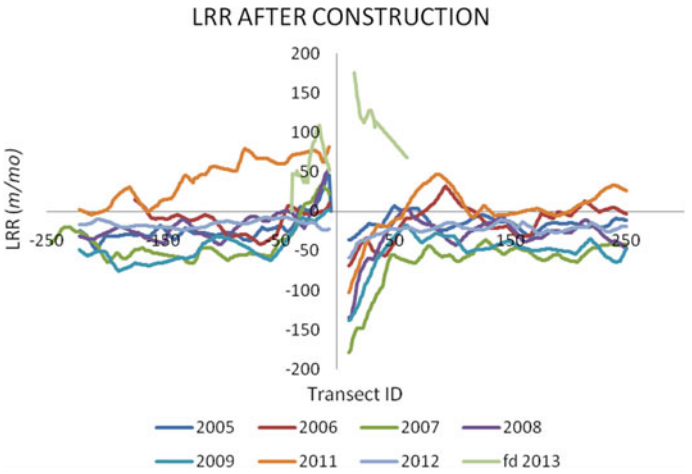

Fig. 6 LRR after construction (2005–2013)

to 2012, the shoreline at the immediate North and South of breakwaters underwent accretion and erosion, respectively. The erosion rate at the Southern side decreased during 2011–2012, but heavy accretion was observed during 2013. The inlet mouth got choked again, and the breakwaters no longer performed its intended function as the sediment transport direction changed. The inlet became shallow, and this situation demanded further modification in the breakwater design. From EPR criterion values given in Tables 4and 5, it is inferred that during the initial years, the shoreline was predominantly erosional. But, towards the end of 2013 heavy accretion was observed especially in the Northern side.

Table 4 EPR during post-construction phase in m/mo (2005–2010)

Year	Month span	Northern side			Southern side		
		Mean rate	Max. accretion	Max. erosion	Mean rate	Max. accretion	Max. erosion
2005	Jan–Feb	2.35	46.54	−20.64	−0.1	18.29	−13.74
	Feb–Mar	14.32	55.22	−49.4	4.93	31.73	−55.07
	Mar–Sept	−6.16	6.72	−9.65	−6.3	−3.68	−16.32
	Sept–Dec	2.19	9.83	−4.27	12.08	32.68	6.29
2006	Mar–Aug	9.05	16.37	−3.41	2.62	7.26	−16.08
	Aug–Nov	−6.06	4.7	−16.35	−7.6	−1.75	−34.24
2007	Jan–Feb	−8.72	22.26	−57.51	−19.13	9.23	−60.34
	Feb–Mar	0.93	16.18	−10.05	−0.72	45.47	−13.22
	Mar–Apr	−15.67	25.66	−39.04	2.12	50.96	−45.5
	Apr–Aug	−4.44	3.59	−8.67	−8.58	−1.53	−31.53
	Aug–Oct	9.3	23.37	−0.96	10.06	29.19	−5.1
2008	Jan–Feb	1.14	22.79	−30.78	4.79	80.75	−21.55
	Feb–Mar	5.5	51.38	−41.13	−19.78	30.8	−95.81
	Mar–Apr	−3.7	39.63	−51.71	13.36	68.6	−26.12
	Apr–Sept	−1.49	6.13	−5.57	−3.23	1.03	−10.59
2009	Jan–Feb	4.17	24.27	−21.33	7.03	47.35	−24.67
	Feb–Mar	−9.39	0.63	−21.26	−3.23	10.89	−24.86
	Mar–May	−3	7.48	−13.07	1.91	23.45	−11.79
	May–Oct	−2.9	4.22	−8.71	−6.95	−1.69	−26.2
2010	Jan–Feb	−4.64	8.85	−34.7	7.9	47.62	−2.14

5.4 During Breakwater Modification

The re-engineering studies were done in response to the inlet choking. Based on the studies, it was decided to extend the North breakwater by 160 m and South breakwater by 330 m, giving a combination of parallel breakwaters. The modification works were conducted in the year of 2014 during which the average rates of shoreline configuration dynamicity observed were −9.31 m/year (North side) and 16.92 m/year (South side) (Table 2). The estimation of LRR during the breakwater modification is depicted in Fig. 7. At a distance of 500 m on either side of the breakwater, a maximum rate of erosion of about −12.34 m/year and accretion of of about 81.55 m/year are observed on North and South sides of the breakwater, respectively, which is reflected in Fig. 7. The EPR values during the modification phase are given in Table 6. From EPR criterion values, it is inferred that during the initial months, accretion was more prominent while towards the end of the year it changed to erosion.

Table 5 EPR during post-construction phase in m/mo (2011–2013)

Year	Month span	Northern side			Southern side		
		Mean rate	Max. accretion	Max. erosion	Mean rate	Max. accretion	Max. erosion
2011	May–Aug	1.3	11.37	−5.49	−10.06	−1.69	−39.87
	Aug–Nov	7.05	19.38	−1.11	13.29	29.86	6.71
2012	Jan–Feb	−2.3	8.39	−13.7	5.01	36.5	−35.23
	Feb–Mar	−2.16	14.84	−47.94	−10.53	20.41	−35.65
	Mar–Apr	−9.51	15.93	−26.38	−10.17	29.22	−28.4
	Apr–Oct	−0.34	4.06	−2.34	−2.41	0.3	−13.63
	Oct–Nov	−3.37	17.65	−60.87	4.91	35.73	−17.62
	Nov–Dec	5.76	21.86	−13.7	46	87.94	−6.81
2013	July–Aug	26.64	45.69	2.24	9.433	22.411	−16.11
	Aug–Sept	3.94	6.65	0.56	−4.469	12.92	−23.05
	Sept–Oct	5.84	12.74	1.027	6.02	26.93	−14.13
	Oct–Nov	−3.17	9.51	−11.69	22.16	48.5	15.1
	Nov–Dec	3.02	13.86	−8.15	22.78	52.28	7.39

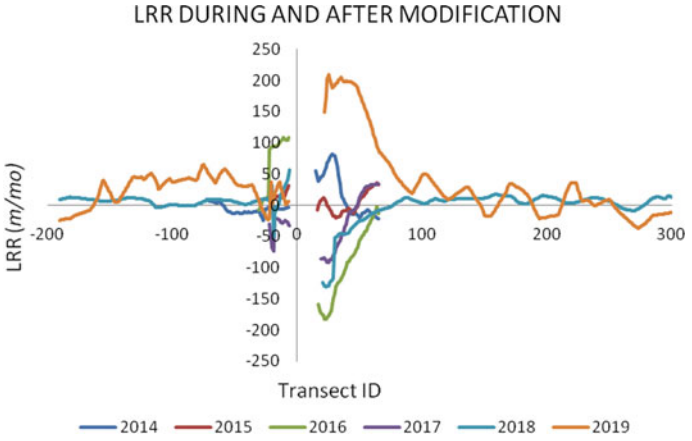

Fig. 7 LRR during and after modification (2014–2019)

5.5 After Breakwater Modification

After the modification, there was a considerable improvement in the harbour access and tranquillity condition. From Table 2, the average rates of shoreline configuration dynamicity on North for the years 2015, 2016, 2017, 2018 and 2019 are observed as 14.24 m/year, 67.11 m/year, −80.26 m/year, 7.12 m/year and 24.88 m/year, respectively. Similarly, the average rates of shoreline configuration dynamicity on South

Table 6 EPR during modification in m/mo (2014)

Year	Month span	Northern side			Southern side		
		Mean rate	Max. accretion	Max. erosion	Mean rate	Max. accretion	Max. erosion
2014	Jan–Feb	7.99	22.67	NIL	28.34	51.65	NIL
	Feb–Mar	7.29	30.93	−20.44	1.86	15.08	−12.65
	Mar–Apr	−4.66	9.81	−20.26	6.73	14.35	−0.38
	Apr–May	−0.55	1.03	−2.25	6.49	11.06	NIL
	May–June	4.54	5.74	NIL	12.24	48.1	NIL
	June–July	−9.67	2.73	−18.34	−3.05	8.35	−14.62
	July–Aug	0.13	0.21	NIL	−6.02	2.13	−14.47
	Aug–Sept	−0.21	NIL	−0.33	−2.88	10.12	−23.83
	Sept–Oct	9.01	22.2	NIL	−24.1	9.81	−48.47
	Oct–Nov	−7.89	NIL	−18.03	−8.92	9.23	−45.96
	Nov–Dec	−8.76	NIL	−12.47	24.44	54.4	NIL

for the years 2015, 2016, 2017, 2018 and 2019 are found to be 2.74 m/year, −91.82 m/year, −113.88 m/year, −2.47 m/year and 36 m/year, respectively. The estimation of LRR after the breakwater modification is shown in Fig. 7. For the year, 2015, the shoreline on the both sides are accretional with a maximum rate of 26.08 m/year at immediate North of the breakwater and 34.79 m/year at a distance of 1 km South of the breakwater. The Northern side of shoreline is accretional with a maximum rate of 120.14 m/year at a distance of 400 m North of the breakwater and while the Southern side was erosional with a maximum rate of −179.95 m/year at a distance of 200 m South of the breakwater during the year 2016. The shorelines on the both sides were found to be erosional for the year 2017 with a maximum rate of −92.46 m/year at a distance of 200 m North of the breakwater and −225.17 m/year at immediate South of the breakwater. Whereas the Northern side of shoreline was accretional with a maximum rate of 56.77 m/year at the immediate North of the breakwater while the Southern side was erosional with a maximum rate of −130.40 m/year at the immediate South of the breakwater for the year 2018. Similarly, for the year 2019, the shorelines on both sides were accretional with a maximum rate of 65.49 m/year at a distance of 1400 m North of the breakwater and 209 m/year at immediate South of the breakwater.

The values of EPR for different months during the post-modification period are given in the Tables 7 and 8. From EPR criterion values, it is inferred that the Northern coastline was generally erosional while the Southern coastline was accretional in 2015. Thus, it indicates a reversal of drift direction and confirms with the findings of re-engineering studies done by CWPRS, Pune. The erosion on the Northern side was high, so groins were constructed in 2016, which brought some stabilization to the Northern side. But, the deposition rate was found to be very high on the Southern

Table 7 EPR during post-modification phase in m/mo (2015–2016)

Year	Month span	Northern side			Southern side		
		Mean rate	Max. accretion	Max. erosion	Mean rate	Max. accretion	Max. erosion
2015	Jan–Feb	−5.61	NIL	−7.83	16.31	56.96	−14.05
	Feb–Mar	−5.76	NIL	−6.95	11.65	19.56	NIL
	Mar–Apr	5.33	9.1	NIL	24.45	48.63	NIL
	Apr–May	−8.42	NIL	−10.49	18.75	45.37	NIL
	May–June	−4.11	NIL	−7.86	−42.34	NIL	−62.47
	June–July	−3.87	NIL	−5.67	−33.51	NIL	−70.33
	July–Aug	22.61	29.61	NIL	12.41	36.5	−28.11
	Aug–Sept	5.65	13.56	NIL	32.82	61.49	−11.61
	Sept–Oct	−0.83	3.3	−4.84	3.66	38.89	−10.63
	Oct–Nov	20.2	4.74	−8.62	7.72	18.3	−6.93
	Nov–Dec	−9.27	NIL	−11.98	25.28	54.42	NIL
2016	Jan–Feb	−3.45	0.8	−9.13	−1.25	20.07	−30.77
	Feb–Mar	6.11	15.54	−0.29	13.16	18.9	NIL
	Mar–Apr	−11.13	NIL	−17.98	39.21	73.02	−12.71
	Apr–May	−6.42	NIL	−10.12	−53.15	NIL	−82.1
	May–June	−7.4	NIL	−8.73	−32.05	NIL	−65.15
	June–July	22.24	28.84	NIL	−51.91	NIL	−76.25
	July–Aug	33.55	47.77	NIL	1.6	16.21	−12.12
	Aug–Sept	28.35	49.24	NIL	5.4	31.41	−10.93
	Sept–Oct	9.31	24.63	−2.62	5.97	46.61	−6.53
	Oct–Nov	−3.13	NIL	−6.64	9.03	38.32	NIL
	Nov–Dec	−2.19	NIL	−6.24	47.51	83.52	NIL

side. During the initial months of 2019, an accretion rate of 209 m/year is observed at the immediate South of the Southern breakwater.

5.6 Morphodynamic Behaviour of the Coast

Initially, shoal formation was observed on both sides of the inlet making the harbour inaccessible. From 1999 to 2001 high erosion rates are observed on both sides of the inlet with the Southern shoreline being more erosional than the other. During the year 2002, heavy accretion was observed on the Northern side of the inlet. From EPR results, it is clear that the monthly sediment movement trends are different from the net yearly trend. In 2001 and 2002, the shoreline was erosional for the months March–May and accretional for the months May–June. During the construction phase of the

Table 8 EPR during post-modification phase in m/mo (2017–2019)

Year	Month span	Northern side			Southern side		
		Mean rate	Max. accretion	Max. erosion	Mean rate	Max. accretion	Max erosion
2017	Jan–Feb	5.53	9.91	NIL	9.02	12.3	NIL
	Feb–Mar	−3.4	NIL	−18.01	−19.14	25.74	−39.5
	Mar–Apr	4.22	14.92	−6.18	−0.21	6.36	−8.59
	Apr–May	−4.57	NIL	−6.93	5.37	8.17	NIL
	May–June	0.29.25	NIL	−38.36	6.28	36.72	−26.58
	June–July	−14.43	NIL	−21.06	−53.58	NIL	−74.78
	July–Aug	9.39	15.44	−2.73	−20.62	9.84	−60.24
	Aug–Sept	−4.8	NIL	−7.76	2.7	12.34	−10.58
	Sept–Dec	10.2	15.82	−3.15	25.99	37.58	NIL
2018	Jan–Feb	−5.16	5.35	−15.76	−4.31	13.21	−28.8
	Feb–Mar	−20.02	10.97	−13.84	7.98	39.45	−3.78
	Mar–Apr	−23.26	40.71	−96.6	−12.82	51.7	−53.61
	Apr–May	−3.02	9.09	−12.6	2.09	18.76	−11.57
	May–Aug	−0.69	14.39	−22.09	−11.39	0.15	−58.85
	Aug–Sept	55.9	145.49	−47.6	17.24	56	−49.84
	Sept–Nov	11.17	19.5	NIL	19.21	70.52	NIL
	Nov–Dec	−3.16	9.09	−11.96	1.75	21.55	−15.02
2019	Jan–Feb	2.89	27.43	−12.68	6.56	22.57	−9.31
	Feb–Mar	−0.66	19.49	−22.09	−29.63	NIL	−150.46
	Mar–May	3.12	16.12	−6.27	15.67	88.25	−6.32
	May–June	6.85	36.54	−36.11	−3.1	34.6	−44.74

breakwater, the North side was accretional with an average rate of 9.17 m/year in 2003 and 41.20 m/year in 2004. However, the South side experienced high erosion especially near the breakwater in 2003 and high accretion in 2004. The construction of the breakwaters disrupted the natural sediment flow. Towards the end of the breakwater construction, a maximum accretion rate of 65.85 m/year was observed on the Southern side. After the construction, during the years 2005–2009 there was a net erosion on both sides. During the years 2011 and 2013, the shoreline was accretional while the net trend was erosional in 2012. The year 2013 witnessed a heavy accretion rate of 175.7 m/year in the Southern side necessitating the need for a long discussed modification in the breakwater design. During the modification in 2014, the coast was slightly erosional in North and slightly accretional in South side. In 2015, the Northern side of the breakwater has undergone net accretion although heavy erosion occurred during the monsoon and towards the end of the year. This erosional trend continued till June 2016. From July, the shore underwent accretion compensating for the continuous erosion and stabilizing the coast on account of the construction

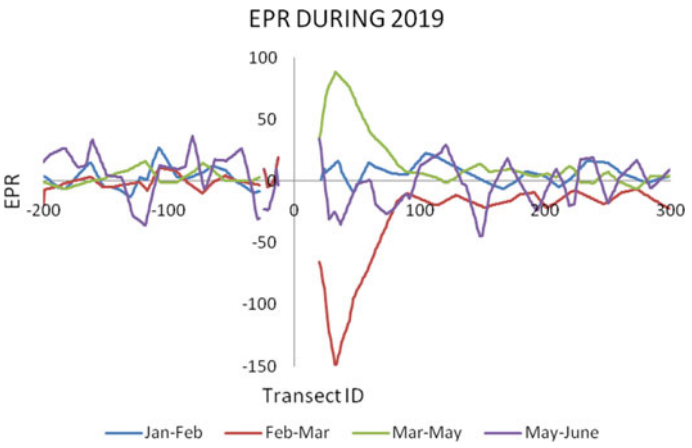

Fig. 8 EPR during the year 2019

of a groin at a distance of 600 m North of the Northern breakwater. There was a net accretion in 2016 and whereas in 2017, Northern shoreline has undergone a net erosion of −33.0 m/year. But, the trend again got reversed with the Northern side of the coastline which experienced an erosion of 7.12 m/year and 24.88 m/year for the year 2018 and 2019, respectively. In the Southern side of the coastline, the net accretion rate further decreased in 2015 and the shore became erosional in the years 2016 to 2018. However, till the month of June the Southern shoreline was accretional in nature with a net shoreline change rate of 36 m/year in the year 2019. The variation in EPR values during the year 2019 is shown in Fig. 8.

6 Conclusions

The study on analysing the coastal morphology of Muthalapozhi coast has paved a way to understand the morphodynamic behaviour of the considered coastal stretch and how a coast would react and stabilize to man-made interventions.

From 1999 to 2001, high erosion rates are observed on both sides of the inlet. However, a heavy accretion was observed on the Northern side and high accretion on the Southern side of the inlet in the year 2002. This indicates a net Southern littoral drift which conforms to the findings of the pre-construction studies done by IIT Madras. An *L*-shaped breakwater was constructed in response to the findings. During and after construction period of 2005–2009, the shoreline was more or less erosional. From 2011, an accretion in the Southern shoreline was observed in response to which a modification was done in 2014 by extending the breakwater mouth further into the sea to avoid its choking by longshore sediment transport. The Southern shoreline is observed to be highly erosional in the after modification period except during the

monsoon season. However, a net accretion is observed in Northern side and a net erosion is observed in the Southern side in the year 2018.

In 2019, till the month of June, the Southern side is observed to be highly accretional with a maximum rate of 209 m/year at the immediate South of the Southern breakwater. If this trend continues, it is expected that bypassing of sand across the breakwater tip will occur, causing the partial choking of the harbour. In that case, the breakwaters will not serve its purpose as safe navigation through the channel would not be possible. This necessitates the need for further studies to propose a more efficient breakwater arrangement.

References

1. Addo KA, Walkden M, Mills JT (2008) Detection, measurement and prediction of shoreline recession in Accra, Ghana. ISPRS J Photogramm Remote Sens 63(5):543–558
2. Ahmad SR, Lakhan VC (2012) GIS-based analysis and modeling of coastline advance and retreat along the coast of Guyana. Mar Geodesy 35(1):1–15
3. Avinash K, Deepika B, Jayappa KS (2013) Evolution of spit morphology: a case study using a remote sensing and statistical based approach. J Coast Conserv 17(3):327–337
4. Cracknell AP (1999) Remote sensing techniques in estuaries and coastal zones an update. Int J Remote Sens 20(3):485–496
5. Dwarakish GS, Nithyapriya B (2016) Application of soft computing techniques in coastal study—a review. J Ocean Eng Sci 1:247–255
6. Fedra K, Feoli E (1998) GIS technology and spatial analysis in coastal zone management. EEZ Technol 3:171–179
7. Hendriyono W, Wibowo M, Al Hakim B, Istiyanto DC (2015) Modeling of sediment transport affecting the coastline changes due to infrastructures in Batang-Central Java. Procedia Earth Planet Sci 14:166–178
8. Kaliraj S, Chandrasekar N, Magesh NS (2013) Impacts of wave energy and littoral currents on shoreline erosion/accretion along the South-west coast of Kanyakumari, Tamil Nadu using DSAS and geospatial technology. Environ Earth Sci 71(10):4523–4542
9. Kraus NC, Harikai S (1983) Numerical model of the shoreline change at Oarai Beach. Coast Eng 7(1):1–28
10. Moore LJ (2000) Shoreline mapping techniques. J Coast Res 16(1)
11. Murali RM, Dhiman R, Choudhary R, Seelam JK, Ilangovan D, Vethamony P (2015) Decadal shoreline assessment using remote sensing along the central Odisha coast, India. Environ Earth Sci 74(10):7201–7213
12. Natesan U, Parthasarathy A, Vishnunath R, Kumar GEB, Ferrer VA (2015) Monitoring longterm shoreline changes along Tamil Nadu, India using geospatial techniques. Aquatic Procedia 4:325–332
13. Noujas V, Thomas KV, Nair LS, Hameed TS, Badarees KO, Ajeesh NR (2014) Management of shoreline morphological changes consequent to breakwater construction. Indian J Geo-Mar Sci 43:54–61
14. Prabhakara Rao P, Nair MM, Raju DV (1985) Assessment of the role of remote sensing techniques in monitoring shoreline changes: a case study of the Kerala coast. Int J Remote Sens 6(3–4):549–558
15. Ranjan M, Chowdhury P (2017) Influence of large-scale variability in wave climate on long-term longshore sediment transport along regional coastlines. Progress Oceanogr
16. Rasuly A, Naghdifar R, Rasoli M (2010) Monitoring of Caspian sea coastline changes using object-oriented techniques. Procedia Environ Sci 2:416–426

17. Ravi G (2015) Hydrodynamic investigations on the shoreline changes due to construction of breakwaters at the Muthalapozhi Inlet of Kerala Coast. Int J Eng Res Technol 3(29)
18. Xu N (2018) Detecting coastline change with all available landsat data over 1986–2015: a case study for the state of Texas, USA. Atmosphere 9(3):107

Optimization Study on the Biosorption of Toxic Metals from Mining Wastewater Using *Carica Papaya* Stem Activated Carbons

Ezekiel A. Adetoro and Samson O. Ojoawo

Abstract Optimization studies enhanced the effectiveness of two *Carica Papaya* Stem Activated Carbons (CPSAC) in removing chosen harmful metals from mining wastewater and the associated problem of multivariate parameters in the process. Adsorbent dosage, stirring speed, contact time, particle size, pH, and temperature were used as independent variables in the experimental design. Batch adsorption experiments were carried out using the experimental design result, after which the collected experimental data was optimized with the Design-Expert program and the results were validated. CPSAC–NaOH had an adsorption optimization solution of 0.204 g adsorbent dosage, 149.887 rpm stirring speed, 52.79 min contact time, 1.999 mm particle size, pH 7, and 29.599 °C temperature, while CPSAC–H_3PO_4 had an adsorption optimization solution of 0.584 g adsorbent dosage, 147.426 rpm stirring speed, 53.303 min contact time, 2 mm particle size, pH 7, and 30 °C temperature, which results in 100% removal efficiencies for all selected toxic metals with a standard error of no more than 2.518%. Consequently, in adsorption investigations, the optimization method is a very valuable tool. It is strongly suggested for the biosorption of hazardous metals from mine wastewater with the adsorbent manufactured from the *Carica papaya* stem because it is cost-effective, energy-efficient, and time-saving.

Keywords Adsorbent · Adsorption · *Carica papaya* stem · Toxic metals · Optimization · Mining wastewater

E. A. Adetoro (✉) · S. O. Ojoawo
Department of Civil Engineering, Ladoke Akintola University of Technology, P.M.B. 4000, Ogbomoso, Nigeria
e-mail: yemmieadyt@yahoo.com

S. O. Ojoawo
e-mail: soojoawo@lautech.edu.ng

L. Nandagiri et al. (eds.), *Recent Advances in Civil Engineering*, Lecture Notes in Civil Engineering 256, https://doi.org/10.1007/978-981-19-1862-9_30

1 Introduction

The current necessity to remove harmful metals from wastewater and the environment has resulted in the development of biosorption, a practical and acceptable technology. It has gained popularity due to its effectiveness in removing harmful metals from wastewater at a low cost, with a simple operation, few chemicals, and enough room for adsorbent renewal and desorption. Biosorption is an ecosystem intimacy and metal absorption occurs through biological mediums that bind the metals by adsorption, ion exchange, and complexing using particular functional groups, such as alcohols, phenols, and other organic compounds [1, 2]. These biological media (adsorbents) have the ability to effectively and swiftly sequester poisonous metal ions from complex solutions, and can thus be utilized to lower dangerous metal ion concentrations in solution from parts per million (ppm) to parts per billion (ppb) [3].

The efficiency of low-cost adsorbents in removing hazardous metals from wastewater is being investigated in order to develop affordable natural adsorbents that are easily available and effective in removing dangerous compounds from mining wastewater. They have an excellent adsorption capability in general. These unconventional natural adsorbents offer benefits beyond those found in nature. Almost many of them are waste products from other industries and require little preparation. As a result, they can be used in place of more expensive adsorbents such as activated carbon, synthetic polymers, and so on [3, 4]. The utilization of agricultural biomaterials (e.g., leaves, seeds, and stems of Carica papaya) in the sequestration of hazardous metals from actual and synthetic sewage was previously demonstrated by [3, 5, 6].

Changing one independent variable (adsorbent dosage, stirring speed, contact time, particle size, pH, temperature, etc.) while keeping the others constant optimizes the biosorption of hazardous metals from wastewater. Response Surface Methodology (RSM) can be utilized under Design-Expert Software (statistical tool) for the optimization process to gain a better knowledge of the different phases of adsorption for these different factors. RSM is a useful experimental design tool for studying the interactions between independent and dependent variables and then predicting their reactions under certain situations [7, 8]. The goal of the optimization tool is to create a regression-based model and optimize an output variable called Response that is influenced by a number of independent input variables. To determine the cause of the change in the response variable, a series of experiments were carried out in which all of the input variables were changed.

The RSM tool is used in the optimization process to control the analysis and the numerical noise that comes with it. The RSM method saves time when evaluating all variables in the optimization process, making the laboratory test phase more efficient. It can also indicate the variables that have a significant impact on the model, allowing the researcher to focus on those variables for output acceptability [2, 9]. Earlier work by [2, 10–12] and others demonstrated the efficacy of the optimization approach in adsorption when other agricultural biomaterials were taken into account. This study focused on optimizing the biosorption of selected toxic metals from mining

wastewater (real-life wastewater) with *Carica papaya* stem activated carbon. The concentrations of the selected toxic metals in mining wastewater would be determined before and after treatment; determination and optimization of the efficiency of Carica papaya stem activated carbons in the remediation of the selected toxic metals from the mining wastewater (using H_3PO_4 and NaOH activating agents).

2 Materials and Methods

2.1 Wastewater Collection in the Mining Industry

The Morlap Marble Mining Site, 2 km along the Igbeti–Igboho Road, Igbeti, Oyo State, Nigeria, provided the study's mining wastewater sample. This was promptly sent for analysis to the Environmental Engineering Laboratory, Department of Civil Engineering, Ladoke Akintola University of Technology, Ogbomoso, Nigeria, in sterilized and sealed plastic containers.

2.2 Determination of Toxic Metal Concentrations in Mining Wastewater Prior to and After Treatment

For this experiment, three (3) hazardous metals (Co^{3+}, Fe^{2+}, and Pb^{2+}) were used. This was done using the modified method described in [3]. Before being evaluated by the Atomic Absorption Spectrophotometer (AAS) system, the mining wastewater sample and its complexity were broken down. A warming bottle was filled with 10 ml of the mining wastewater sample and another warming bottle with 10 ml of the blank sample. 15 mL of nitric acid (HNO3) was carefully added to the contents of the two warming bottles, covered and heated for 5 to 10 min before cooling and filtering into a volumetric flask using Whatman filter papers and funnels. 100 mL distilled water was used to make the filtrates. After that, the prepared filtrates were put into clear, tightly corked flasks in preparation for the AAS reading [3].

The hazardous metal ion concentration in the prepared digested and standard samples was measured using an AAS machine (PG 990 model), and the results were recorded. After that, the concentrations of hazardous metal ions were converted and calculated. Equation 1 is used to express concentration (in ppm).

$$\text{Concentration (ppm)} = \frac{R \times \text{FV} \times \text{DF}}{W} \tag{1}$$

where R denotes the machine reading, FV is the final volume after digestion, DF denotes the dilution factor, and W denotes the sample weight. The amounts of

Table 1 Variables in the experimental range of BBD

Factors	Code	Unit	Level	
			Low (−1)	*High* (+1)
Adsorbent dosage	A	g	0.2	1.0
Stirring speed	B	rpm	50	250
Contact time	C	minutes	20	120
Particle size	D	mm	0.075	2
pH	E		4	10
Temperature	F	°C	30	70

hazardous metal ions present in mining effluent before and after treatment were determined using this method.

2.3 Adsorbent Preparation

The *Carica papaya* stems were obtained locally from the Ladoke Akintola University of Technology (LAUTECH) Teaching and Research Farm in Ogbomoso, Nigeria. The adsorbents were made using modified techniques with H_3PO_4 and NaOH as activation agents [3].

2.4 Design of Experiments

The Box–Behnken Design (BBD) of the Response Surface Methodology (RSM) of the Design-Expert Software Version 13 (DOEv13) was used for the experimental design [8]. To produce a random number of experimental runs, six selected variables (as given in Table 1) were placed in the experimental range of BBD.

2.5 Adsorption Experiments in Batches

This study looked at the effects of adsorbent dosage, stirring speed, contact time, particle size, pH, and temperature on the biosorption of selected hazardous metals from mining effluent. According to [3], one-factor-at-a-time (OFAT) analyses are performed with the proposed test design of the BBD (as shown in Table 1).

2.6 Optimization Analysis

DOEv13 was used to analyze the experimental data, calculate the predicted response(s), and develop the factorial regression model to determine the optimal conditions and the optimization process. The optimal range conditions were estimated from regression analysis and three-dimensional (3D) response surface plots of the independent variables and each of the six dependent variables. The process has been optimized using model(s) previously developed in the area of response surfaces.

2.7 Validation of the Optimization

The batch adsorption studies of the determined optimal values were used to validate the optimization procedure.

3 Results and Discussions

3.1 Physical Characteristics of the Mining Wastewater Collected

At a temperature of 26 °C, the mining effluent was ash colored, had a foul odor, a bitter taste, and was murky with some finely split contaminants, lowering the purity of the water.

3.2 Toxic Metals Concentrations in the Mining Wastewater Sample Before and After Treatment

There is a chance of harmful metals in the mining effluent, as illustrated in Table 2. The hazardous metals' concentrations were measured in parts per million (ppm). Fe^{2+}, Pb^{2+}, and Co^{3+} equivalent values were in descending order: 756.5 > 45.8 > 9.6 ppm. The harmful metal concentrations were all higher above the [13] requirements. These findings demonstrated that mine wastewater damaged the environment. All hazardous elements were eliminated after treatment with optimal CPSAC–NaOH and H_3PO_4 concentrations (Table 2).

Table 2 Concentrations of the toxic metals in the sample before and after treatment

Toxic metal	Concentration (ppm)			
	Before treatment	After treatment		WHO (2011) Standards
	Mining wastewater	CPSAC–NaOH	CPSAC–H_3PO_4	
Cobalt	9.60 ± 0.05	ND	ND	–
Iron	756.50 ± 0.1	ND	ND	0.3
Lead	45.80 ± 0.06	ND	ND	0.01

* *ND*—Not Detected

3.3 Summary of the Design

A polynomial (fifth) design model was chosen with Removal Efficiencies (RE) as responses and no block. Using the range of values in Table 1 for the six specified adsorption variables, the design generated 54 runs. The RE's performance transformations were not performed, according to the results. Table 3 shows the design summary for both adsorbents (*Carica papaya* Stem Activated Carbon utilizing NaOH (CPSAC–NaOH) and H_3PO_4 (CPSAC–H_3PO_4)) for the 54 experimental runs for the selected hazardous metals.

3.4 Experimental Data Responses

Table 4 displays the experimental runs, related factors, and responses (removal efficiencies) for CPSAC–NaOH. The percentage of toxic metal removal efficiency for Co^{3+}, Fe^{2+}, and Pb^{2+}, respectively, ranged from 88.80 to 100.0, 99.69 to 100.0, and 95.63 to 100.0%. The best removal effectiveness for all selected hazardous metals was found in test 37, which used 0.2 g of adsorbent, 50 rpm stirring speed, 60 min contact time, 2.00 mm particle size, pH 7, and a temperature of 30 °C. While the adsorbent dosage was 0.2 g, the stirring speed was 150 rpm, the contact time was 120 min, the particle size was 2.00 mm, the pH was 7, and the temperature was 30 °C for worst removal efficiencies, which was obtained in tests 16 and 45.

Table 5 lists the H_3PO_4 adsorbent's experimental runs, relevant parameters, and reactions. The percentage of toxic metal removal efficiency ranged from 89.10 to 100.0% for Co^{3+}, 99.57 to 100.0% for Fe^{2+}, and 93.94 to 100.0% for Pb^{2+}, respectively. The maximum removal efficiency for all tested toxic metals was achieved in run 9, with an adsorbent dosage of 0.8 g, a stirring speed of 200 rpm, a contact period of 60 min, a particle size of 2.00 mm, a pH of 7, and a temperature of 30 °C. Experiment 1 had the lowest removal effectiveness, with 0.8 g of adsorbent, a stirring speed of 150 rpm, a contact period of 60 min, a particle size of 2.00 mm, a pH of 7, and a temperature of 30 °C. Table 6 summarizes the responses' high and low values, along with their respective runs for the adsorbents.

Table 3 Design summary for the selected toxic metals and adsorbents

Adsorbent	Response	Units	Analysis	Transform	Model	Adsorbent	Response	Units	Analysis	Transform	Model
CPSAC–NaOH	RE (Co^{3+})	%	Polynomial	None	Fifth	CPSAC–H_3PO_4	RE (Co^{3+})	%	Polynomial	None	Fifth
	RE (Fe^{2+})						RE (Fe^{2+})				
	RE (Pb^{2+})						RE (Zn^{2+})				

Table 4 Factors and responses for the experiment (CPSAC–NaOH)

RUN	Factors						Responses		
	A (g)	B (rpm)	C (mins.)	D (mm)	E	F (°C)	Co^{3+} (%)	Fe^{2+} (%)	Pb^{2+} (%)
1	0.2	150	60	2	7	50	93.09	99.96	98.94
2	0.4	150	60	2	7	30	95.67	99.89	99.09
3	0.6	150	60	2	7	30	94.31	99.81	98.99
4	0.8	150	60	2	7	30	97	99.88	98.74
5	1	150	60	2	7	30	98.34	99.81	98.59
6	0.2	50	60	2	7	30	99.92	99.98	100
7	0.2	100	60	2	7	30	93.51	100	100
8	0.2	150	60	0.125	7	30	99.33	99.78	96.97
9	0.2	200	60	2	7	30	95.31	100	100
10	0.2	250	60	2	7	30	99.35	100	100
11	0.2	150	20	2	7	30	95.81	99.91	99.45
12	0.2	150	40	2	7	30	93.48	99.94	99.45
13	0.2	150	60	0.425	7	30	97.41	99.75	96.97
14	0.2	150	80	2	7	30	92.31	99.93	99.53
15	0.2	150	100	2	7	30	91.15	99.95	99.56
16	0.2	150	120	2	7	30	**88.81**	**99.94**	**99.5**
17	0.2	150	60	0.075	7	30	97.41	99.77	96.97
18	0.2	150	60	0.125	7	30	99.33	99.78	96.97
19	0.2	150	60	0.25	7	30	99.95	99.76	96.56
20	0.2	150	60	0.425	7	30	97.41	99.75	96.97
21	0.2	150	60	1	7	30	99.33	99.71	96.56
22	0.2	150	60	2	7	30	100	99.69	96.56
23	0.2	150	60	2	4	30	89.68	99.95	99.87
24	0.2	150	60	2	6	30	96.67	99.91	99.87
25	0.2	150	60	2	7	30	92.97	99.93	95.63
26	0.2	150	60	2	8	30	99.33	99.96	99.5
27	0.2	150	60	2	10	30	97.41	99.94	99.17
28	0.2	150	60	2	6	30	96.67	99.91	99.87
29	0.2	150	60	2	7	40	95.3	99.89	98.94
30	0.2	150	60	2	7	50	93.09	99.96	98.94
31	0.2	150	60	2	7	60	92.65	99.94	98.94
32	0.2	150	60	2	7	70	90.43	99.94	98.83
33	0.4	150	60	2	7	30	95.67	99.89	99.09
34	0.6	150	60	2	7	30	94.31	99.81	98.99

(continued)

Table 4 (continued)

RUN	Factors						Responses		
	A (g)	B (rpm)	C (mins.)	D (mm)	E	F (°C)	Co^{3+} (%)	Fe^{2+} (%)	Pb^{2+} (%)
35	0.8	150	60	2	7	30	97	99.88	98.74
36	1	150	60	2	7	30	98.34	99.81	98.59
37	0.2	50	60	2	7	30	99.92	99.98	100
38	0.2	100	60	2	7	30	93.51	100	100
39	0.2	200	60	2	7	30	95.31	100	100
40	0.2	250	60	2	7	30	99.35	100	100
41	0.2	150	20	2	7	30	95.81	99.91	99.45
42	0.2	150	40	2	7	30	93.48	99.94	99.45
43	0.2	150	80	2	7	30	92.31	99.93	99.53
44	0.2	150	100	2	7	30	91.15	99.95	99.56
45	0.2	150	120	2	7	30	88.81	99.94	99.5
46	0.2	150	60	0.075	7	30	97.41	99.77	96.97
47	0.2	150	60	0.25	7	30	99.95	99.76	96.56
48	0.2	150	60	1	7	30	99.33	99.71	96.56
49	0.2	150	60	2	4	30	89.68	99.95	99.87
50	0.2	150	60	2	8	30	99.33	99.96	99.5
51	0.2	150	60	2	10	30	97.41	99.94	99.17
52	0.2	150	60	2	7	40	95.3	99.89	98.94
53	0.2	150	60	2	7	60	92.65	99.94	98.94
54	0.2	150	60	2	7	70	90.43	99.94	98.83

As indicated in Tables 4 and 5, A represents the adsorbent dosage (g), B represents the stirring speed (rpm), C represents the contact duration (minutes), D represents the particle size (mm), E represents the pH, and F represents the temperature (°C).

3.5 Model Summary and Adjustment Statistics

The model summary and adjustment data for the selected hazardous metals for the adsorbents are shown in Table 7. The standard deviation reflects how far the experimental values differ from the actual values (error). For CPSAC NaOH and CPSAC H_3PO_4, they ranged from 0.033 to 1.00 and 0.028 to 0.278, respectively. The corrected (R^2) and anticipated (r^2) values are the adjusted and predicted values, respectively, using DOEv13. The corrected (R^2) values for CPSAC NaOH and CPSAC H_3PO_4 were 0.839 to 0.908 and 0.965 to 0.993, respectively. The anticipated (r^2) values for CPSAC–NaOH and CPSAC–H_3PO_4 were 0.848 to 0.914 and 0.958 to 0.990,

Table 5 Factors and responses for the experiment (CPSAC–H_3PO_4)

RUN	Factors						Responses		
	A (g)	B (rpm)	C (mins.)	D (mm)	E	F (°C)	Co^{3+} (%)	Fe^{2+} (%)	Pb^{2+} (%)
1	0.8	150	60	2	7	50	**89.1**	**99.96**	**98.24**
2	0.4	150	60	2	7	30	99.68	99.64	98.99
3	0.6	150	60	2	7	30	100	99.64	99.17
4	0.2	150	60	2	7	30	99.68	99.73	98.74
5	1	150	60	2	7	30	100	99.68	99.22
6	0.8	50	60	2	7	30	98.91	99.98	100
7	0.8	100	60	2	7	30	94.64	100	99.4
8	0.2	150	60	0.125	7	30	100	99.69	99.17
9	0.8	200	60	2	7	30	**99.16**	**100**	**100**
10	0.8	250	60	2	7	30	96.06	100	93.94
11	0.8	150	20	2	7	30	94.4	99.8	99.56
12	0.8	150	40	2	7	30	97.9	99.71	99.13
13	0.2	150	60	0.425	7	30	99.68	99.73	98.74
14	0.8	150	80	2	7	30	100	99.65	99.13
15	0.8	150	100	2	7	30	100	99.66	99.53
16	0.8	150	120	2	7	30	100	99.66	99.53
17	0.8	150	60	0.075	7	30	99.33	99.93	99.5
18	0.8	150	60	0.125	7	30	96.04	99.94	99.5
19	0.8	150	60	0.25	7	30	96.73	99.9	99.17
20	0.8	150	60	0.425	7	30	96.73	99.91	99.5
21	0.8	150	60	1	7	30	98.71	99.92	99.5
22	0.2	150	60	2	7	30	98.06	99.91	98.12
23	0.8	150	60	2	4	30	97.04	99.63	99.87
24	0.8	150	60	2	6	30	96.26	99.57	99.4
25	0.6	150	60	2	7	30	100	99.64	99.17
26	0.8	150	60	2	8	30	99.33	99.98	99.5
27	0.8	150	60	2	10	30	99.33	99.95	99.81
28	0.8	150	60	2	6	30	92.86	99.96	98.41
29	0.8	150	60	2	7	40	91.31	99.95	98.24
30	0.8	150	60	2	7	50	89.73	99.96	98.24
31	0.8	150	60	2	7	60	89.73	99.96	98.06
32	0.8	150	60	2	7	70	91.89	99.96	97.66
33	0.4	150	60	2	7	30	99.68	99.64	98.99
34	0.6	150	60	2	7	30	100	99.64	99.17

(continued)

Table 5 (continued)

RUN	Factors						Responses		
	A (g)	B (rpm)	C (mins.)	D (mm)	E	F (°C)	Co^{3+} (%)	Fe^{2+} (%)	Pb^{2+} (%)
35	0.2	150	60	2	7	30	99.68	99.73	98.74
36	1	150	60	2	7	30	100	99.68	99.22
37	0.8	50	60	2	7	30	98.91	99.98	100
38	0.8	100	60	2	7	30	94.64	100	99.4
39	0.8	200	60	2	7	30	99.16	100	100
40	0.8	250	60	2	7	30	96.06	100	93.94
41	0.8	150	20	2	7	30	94.4	99.8	99.56
42	0.8	150	40	2	7	30	97.9	99.71	99.13
43	0.8	150	80	2	7	30	100	99.65	99.13
44	0.8	150	100	2	7	30	100	99.66	99.53
45	0.8	150	120	2	7	30	100	99.66	99.53
46	0.8	150	60	0.075	7	30	99.33	99.93	99.5
47	0.8	150	60	0.25	7	30	96.04	99.94	99.5
48	0.8	150	60	1	7	30	98.71	99.92	99.5
49	0.8	150	60	2	4	30	97.04	99.63	99.87
50	0.8	150	60	2	8	30	99.33	99.98	99.5
51	0.8	150	60	2	10	30	99.33	99.95	99.81
52	0.8	150	60	2	7	40	91.31	99.95	98.24
53	0.8	150	60	2	7	60	89.73	99.96	98.06
54	0.8	150	60	2	7	70	91.89	99.96	97.66

Table 6 Summary of the high and low values of the responses for the adsorbents

Adsorbent	High (%)	Run	Low (%)	Run
CPSAC–NaOH (RE)	99.92–100.00	37	88.81–99.50	16 and 45
CPSAC–H_3PO_4 (RE)	99.16–100.00	9	89.10–99.96	1

Table 7 Model summary and fit statistics for the selected toxic metals

Adsorbent	Toxic metal	Std. dev.	Adjusted R^2	Predicted r^2	Adequate precision	*F*-value	*p*-value	Comment
CPSAC–NaOH	Co^{3+}	1	0.908	0.914	15.998	11.245	<0.0001	Suggested
	Fe^{2+}	0.033	0.862	0.871	12.841	13.924	<0.0001	Suggested
	Pb^{2+}	0.487	0.839	0.848	10.171	19.205	<0.0001	Suggested
CPSAC–H_3PO_4	Co^{3+}	0.278	0.993	0.99	54.793	124.5	<0.0001	Suggested
	Fe^{2+}	0.028	0.965	0.958	22.193	43.57	<0.0001	Suggested
	Pb^{2+}	0.106	0.992	0.989	82.719	165.27	<0.0001	Suggested

* Significant at $p < 0.05$

respectively. As stated by [8], all anticipated (r^2) values agreed with corrected (R^2) values for all models because their differences were smaller than 0.2.

For CPSAC–NaOH and CPSAC–H_3PO_4, the tolerable accuracy that measures the signal-to-noise ratio has values that vary from 10.171 to 15.998 and 22.193 to 82.719, respectively. Because their reasonable precision values were larger than 4.0, all of the models for the dangerous metals considered had enough signals to navigate the design space. Because the *p*-values of all models were less than 0.05 and *F*-values as calculated by [8], this proved their significance and lack of neglect.

3.6 Variance Analysis (ANOVA)

Table 8 summarizes the findings of Analysis of Variance (ANOVA) for Co^{3+}, Fe^{2+}, and Pb^{2+} efficiency in toxic metal removal for CPSAC–NaOH using surface polynomial response models (fifth). The F-values for the Co^{3+}, Fe^{2+}, and Pb^{2+} models were 22.02, 14.27, and 12.01, respectively, indicating that the models were significant. Due to noise, such a high model *F*-value has a 0.01% probability of occurring. The model terms were extremely significant if the *P*-value was less than 0.05 (i.e., 95% confidence interval), whereas the models were not significant if the *P*-value was greater than 0.10. As the absolute *F*-value rises and the *P*-value falls, the model terms become more significant. The most relevant model terms in the Co^{3+} model in this example were C, D, E, A^2, D^2, E^2, E^3, A^4, B^4, D^4, E^4, and D^5. The Fe^{2+} model's most significant model terms were A, B, A^2, B^2, B^3, A^4, and B^4. The most critical model terms of the Pb^{2+} model were B, C, F, A^2, B^2, C^2, E^2, F^2, B^3, C^3, E^3, B^4, E^4, and C^5.

To support the hierarchy described in [8], the remaining model terms were required. Table 9 shows the ANOVA findings of the response surface polynomial models (fifth) of Co^{3+}, Fe^{2+}, and Pb^{2+} toxic metals removal efficiencies for CPSAC–H_3PO_4 for Co^{3+}, Fe^{2+}, and Pb^{2+} toxic metal removal efficiencies for CPSAC–H_3PO_4. The *F*-values of the Co^{3+}, Fe^{2+}, and Pb^{2+} models were 284.73, 59.64, and 257.47, respectively, indicating that they were significant. The primary model terms of the Co3 + model in this situation were A, B, E, C^2, F^2, B^3, D^3, F^3, C^4, and F^4. The major model terms of the Fe^{2+} model were A, B, C, E, F, A^2, B^2, E^2, F^2, A^3, B^3, C^3, E^3, B^4, E^4, and C^5, while the most important model terms of the Pb^{2+} model were B, F, B^2, C^2, E^2, A^3, B^3, F^3, B^4, E^4, and C^5. The remaining model terms were necessary to keep the hierarchy in place.

3.7 Equations for the Models

The regression equations used to predict RE (i.e., response) (final empirical models in the form of coded factors) for the selected toxic metals of the adsorbents are expressed in Eqs. (2)–(7). CPSAC–NaOH is represented by Eqs. (2)–(4), while CPSAC–H_3PO_4

Table 8 ANOVA of the selected toxic metals (CPSAC–NaOH)

Source	Co^{3+}				Fe^{2+}				Pb^{2+}			
	Sum of squares	Mean Square	*F*-value	*p*-value	Sum of squares	Mean square	*F*-value	*p*-value	Sum of squares	Mean square	*F*-value	*p*-value
Model	554.07	22.16	22.02	<0.0001*	0.3793	0.01517	14.2685	<0.0001*	71.208	2.84832	12.01284	<0.0001*
A	1.14	1.14	0.66	0.4209	8.01E-06	8.01E-06	0.9505	0.0039*	0.4461	0.4461	0.6927	0.4093
B	3.47	3.47	2.01	0.1625	4.93E-06	4.93E-06	0.9611	0.0024*	1.17E−12	1.17E−12	1.00E+00	<0.0001*
C	8.75	8.75	5.06	0.029*	0.0021	0.0021	1.03	0.3161	11.05	11.05	17.17	0.0001*
D	0.01	0.01	0.95	0.0042*	0.0003	0.0003	0.7041	0.146	0.1009	0.1009	0.694	0.1567
E	5.66	5.66	3.28	0.0764*	0.0025	0.0025	1.23	0.2736	0.1177	0.1177	0.6709	0.1827
F	4.47	4.47	2.59	0.114	0.0019	0.0019	0.9435	0.3362	0.0528	0.0528	0.7758	0.082*
A^2	7.71	7.71	4.46	0.0397*	0.0097	0.0097	4.72	0.0347*	9.21E−06	9.21E−06	0.997	0.0001*
B^2	1.03	1.03	0.59	0.4443	0.0302	0.0302	14.7	0.0004*	24.7	24.7	38.36	<0.0001*
C^2	2.93	2.93	1.69	0.1991	0.0022	0.0022	1.05	0.3113	3.29	3.29	5.11	0.0283*
D^2	0.06	0.06	0.86	0.0321*	0.0003	0.0003	0.7086	0.1414	0.0892	0.0892	0.7113	0.1386
E^2	33.57	33.57	19.44	<0.0001*	0.0049	0.0049	2.38	0.1291	21.49	21.49	33.36	<0.0001*
F^2	1.21	1.21	0.7	0.4065	0.0025	0.0025	1.2	0.2794	0.0061	0.0061	0.9231	0.0094*
A^3	0.32	0.32	0.67	0.1871	0.001	0.001	0.5089	0.479	1.72	1.72	2.67	0.1089
B^3	3.74	3.74	2.16	0.1477	0.0001	0.0001	0.8561	0.0332*	1.42E−14	1.42E−14	1.00E+00	<0.0001*
C^3	3.87	3.87	2.24	0.1411	0.0015	0.0015	0.736	0.3951	8.64	8.64	13.42	0.0006*
D^3	0.74	0.74	0.52	0.4274	0.0003	0.0003	0.714	0.1358	0.0485	0.0485	0.7849	0.0753
E^3	0.01	0.01	0.95	0.0044*	0.0026	0.0026	1.28	0.2631	0.0174	0.0174	0.87	0.0271*
F^3	0.25	0.25	0.71	0.1421	0.0007	0.0007	0.553	0.3568	0.7441	0.7441	1.16	0.2877
A^4	6	6	3.47	0.0683*	0.0097	0.0097	4.71	0.0348*	0.1395	0.1395	0.6437	0.2166

(continued)

Table 8 (continued)

Source	Co^{3+}				Fe^{2+}				Pb^{2+}			
	Sum of squares	Mean Square	*F*-value	*p*-value	Sum of squares	Mean square	*F*-value	*p*-value	Sum of squares	Mean square	*F*-value	*p*-value
B^4	7.37	7.37	4.27	0.0441*	0.0213	0.0213	10.37	0.0023*	16.66	16.66	25.87	<0.0001*
C^4	1.87	1.87	1.08	0.3037	0.0019	0.0019	0.9244	0.341	2.14	2.14	3.32	0.0747
D^4	0.05	0.05	0.87	0.0292*	0.0003	0.0003	0.1472	0.7029	0.0901	0.0901	0.7099	0.14
E^4	37.39	37.39	21.64	<0.0001*	0.004	0.004	1.95	0.1693	18.39	18.39	28.55	<0.0001*
F^4	1.91	1.91	1.1	0.2984	0.0019	0.0019	0.9492	0.3347	0.1238	0.1238	0.6629	0.1923
C^5	4.3	4.3	2.49	0.1212	0.0014	0.0014	0.6709	0.4167	7.45	7.45	11.57	0.0013*
D^5	0.15	0.15	0.77	0.0891*	0.0003	0.0003	0.7024	0.1477	0.0785	0.0785	0.7285	0.1219

* Significant at $p < 0.05$

Table 9 ANOVA of the selected toxic metals (CPSAC–H_3PO_4)

Source	Co^{3+}				Fe^{2+}					Pb^{2+}		
	Sum of squares	Mean square	*F*-value	*p*-value	Sum of squares	Mean square	*F*-value	*p*-value	Sum of squares	Mean square	*F*-value	*p*-value
Model	551.56	22.062	284.73	<0.0001*	1.174	0.047	59.64	<0.0001*	71.672	2.867	257.47	<0.0001*
A	5.91	5.91	2.84	0.0984*	0.048	0.048	15.15	0.0003*	0.0831	0.0831	1.81	0.1848
B	23.54	23.54	11.3	0.0015*	4.93E-06	4.93E-06	0.9687	0.0016*	1.82	1.82	39.57	<0.0001*
C	5.34	5.34	2.56	0.1158	0.0254	0.0254	8.01	0.0067*	0.097	0.097	2.11	0.1526
D	5.2	5.2	2.5	0.1206	0.0005	0.0005	0.6875	0.1637	0.0606	0.0606	1.32	0.2562
E	8.92	8.92	4.28	0.0438*	0.1572	0.1572	49.61	<0.0001*	0.0096	0.0096	0.6497	0.2089
F	3.42	3.42	1.64	0.2059	0.0003	0.0003	0.7756	0.0822*	0.0008	0.0008	0.897	0.0169*
A^2	2.97	2.97	1.43	0.2382	0.0103	0.0103	3.24	0.0781*	0.1274	0.1274	2.77	0.1022
B^2	4.39	4.39	2.11	0.153	0.1392	0.1392	43.94	<0.0001*	2.81	2.81	61.14	<0.0001*
C^2	0	0	0.9971	0	0.0028	0.0028	0.8896	0.3502	0.1915	0.1915	4.17	0.0466*
D^2	5.38	5.38	2.58	0.1145	0.0005	0.0005	0.1644	0.6869	0.0563	0.0563	1.22	0.2738
E^2	0.3333	0.3333	0.6909	0.16	0	0	0.9503	0.0039*	0.9889	0.9889	21.52	<0.0001*
F^2	0.1254	0.1254	0.8072	0.0602*	8.58E-06	8.58E-06	0.9587	0.0027*	0.012	0.012	0.6122	0.2603
A^3	5.01	5.01	2.41	0.1273	0.0465	0.0465	14.68	0.0004*	0.2339	0.2339	5.09	0.0286*
B^3	30.28	30.28	14.54	0.0004*	0.0001	0.0001	0.8839	0.0215*	11.27	11.27	245.35	<0.0001*
C^3	1.9	1.9	0.9105	0.3447	0.0166	0.0166	5.22	0.0267*	0.0149	0.0149	0.5715	0.3245
D^3	6.62	6.62	3.18	0.0808*	0.0005	0.0005	0.6942	0.1564	0.035	0.035	0.7625	0.3868
E^3	4.96	4.96	2.38	0.1291	0.084	0.084	26.5	<0.0001*	0.012	0.012	0.6116	0.2612
F^3	8.88	8.88	4.26	0.0443*	0.0062	0.0062	1.96	0.1682	0.1577	0.1577	3.43	0.07*
A^4	3.7	3.7	1.77	0.189	0.0088	0.0088	2.77	0.1022	0.1207	0.1207	2.63	0.1115

(continued)

Table 9 (continued)

Source	Co^{3+}				Fe^{2+}					Pb^{2+}		
	Sum of squares	Mean square	*F*-value	*p*-value	Sum of squares	Mean square	*F*-value	*p*-value	Sum of squares	Mean square	*F*-value	*p*-value
B^4	3.73	3.73	1.79	0.1868	0.0959	0.0959	30.27	<0.0001*	5.58	5.58	121.35	<0.0001*
C^4	0.1134	0.1134	0.8165	0.0544*	0.0037	0.0037	1.18	0.282	0.0679	0.0679	1.48	0.23
D^4	5.38	5.38	2.58	0.1145	0.0005	0.0005	0.6891	0.162	0.056	0.056	1.22	0.2751
E^4	0.3597	0.3597	0.6796	0.1726	0	0	0.9092	0.0131*	0.7129	0.7129	15.52	0.0003*
F^4	0.0342	0.0342	0.8986	0.0164*	0.0007	0.0007	0.6404	0.2209	0.0166	0.0166	0.5502	0.3619
C^5	1.69	1.69	0.8133	0.3716	0.0155	0.0155	4.9	0.0316*	0.0035	0.0035	0.7834	0.0764*
D^5	5.83	5.83	2.8	0.1008	0.0005	0.0005	0.6927	0.158	0.0495	0.0495	1.08	0.3044

* Significant at $p < 0.05$

is represented by Eqs. (5)–(7). A plus sign in front of the terms suggests a synergistic influence on the observed RE (i.e., response), whereas a minus sign indicates an antagonistic effect on the observed RE (i.e., response). As represented in Eqs. (2)–(7), A is the adsorbent dose (g), B is the stirring speed (rpm), C is the contact duration (min), D is the particle size (mm), E is the pH value, F is the temperature I, and RE is the removal rate.

$$\begin{aligned}&\text{Observed Removal Efficiency } (Cobalt, CPSAC - NaOH) = 96.05\\&+1.17A + 2.5B - 6.63C - 12.33D + 4.02E - 2.83F + 10.04A^2\\&-3.08B^2 - 5.24C^2 - 85.7D^2 + 33.77E^2 + 4.87F^2 + 0.6655A^3\\&-2.78B^3 + 18.59C^3 - 83.86D^3 - 0.1523E^3 + 0.7072F^3\\&-7.85A^4 + 8.03B^4 + 3.85C^4 + 82.77D^4 - 34.91E^4 - 5.42F^4\\&-15.46C^5 + 94.83D^5\end{aligned} \tag{2}$$

$$\begin{aligned}&\text{Observed Removal Efficiency}(Iron, CPSAC - NaOH)\\&= 99.62 - 0.0031A - 0.003B + 0.103C - 2.52D\\&+0.0847E + 0.059F + 0.3561A^2 + 0.5274B^2\\&+0.142C^2 - 6.2D^2 + 0.4077E^2 - 0.2196F^2\\&-0.0378A^3 + 0.0119B^3 - 0.3677C^3 + 1.63D^3\\&-0.897E^3 - 0.0386F^3 - 0.3152A^4 - 0.4315B^4\\&-0.1229C^4 + 6.41D^4 - 0.361E^4 + 0.1731F^4 + 0.2769C^5 + 4.21D^5\end{aligned} \tag{3}$$

$$\begin{aligned}&\text{Observed Removal Efficiency}(\text{Lead, CPSAC} - \text{NaOH}) = 99.95\\&-0.7307A + 0.0001B + 0.746C - 46.23D - 0.5791E\\&-0.3078F - 0.011A^2 + 15.09B^2 + 5.55C^2 - 108.65D^2\\&+27.01E^2 + 0.3449F^2 + 1.53A^3 - 27.8C^3 - 21.5D^3\\&+0.2309E^3 + 1.23F^3 - 1.2A^4 - 12.07B^4 - 4.12C^4\\&+110.7D^4 - 24.48E^4 - 1.38F^4 + 20.36C^5 + 67.73D(4)\end{aligned} \tag{4}$$

$$\begin{aligned}&\text{Observed Removal Efficiency}(\text{Cobalt, CPSAC} - \text{H3PO4}) = 100\\&-2.12A + 6.5B + 5.18C + 331.88D + 5.04E - 2.48F\\&-5.8A^2 - 6.36B^2 + 0.0163C^2 + 843.6D^2 - 3.36E^2 + 1.57F^2\\&+2.28A^3 - 7.93B^3 - 13.03C^3 + 251.18D^3 - 3.9E^3 - 4.25F^3\\&+5.64A^4 + 5.71B^4 - 0.9494C^4 - 855.24D^4 + 3.42E^4 + 0.7245F^4 + 9.71C^{5-583.66D^5}\end{aligned} \tag{5}$$

$$\begin{aligned}&\text{Observed Removal Efficiency(Iron, CPSAC} - \text{H3PO4}) = 99.79\\&+0.1909A - 0.003B - 0.3574C - 3.31D + 0.6694E\\&-0.0216F + 0.3407A^2 + 1.13B^2 - 0.1626C^2 + 8.3D^2\\&-0.0205E^2 + 0.013F^2 - 0.2197A^3 + 0.0119B^3 + 1.22C^3\\&-2.17D^3 - 0.5068E^3 + 0.1124F^3 - 0.2748A^4 - 0.9156B^4\\&+0.1726C^4 + 8.35D^4 + 0.0368E^4 - 0.1037F^4 - 0.9294C^5 + 5.41D^5\end{aligned} \tag{6}$$

$$\begin{aligned}&\text{Observed Removal Efficiency(Lead, CPSAC} - H3PO4) = 97.98\\&-2512A + 1.81B + 0.6987C - 35.84D + 0.1654E - 0.0374F\\&-1.2A^2 + 5.09B^2 + 1.34C^2 - 86.28D^2 + 5.8E^2\\&-0.4845F^2 + 0.4925A^3 - 4.84B^3 - 1.15C^3 - 18.27D^3\\&-0.1916E^3 - 0.5667F^3 + 1.02A^4 - 6.98B^4 - 0.7344C^4\\&+87.23D^4 - 4.82E^4 + 0.5056F^4 + 0.4418C^5 + 53.79D^5\end{aligned} \tag{7}$$

3.8 Model Plots

The graphs of predicted (expected) versus actual reactions for the adsorbents are shown in Fig. 1. For all of the hazardous elements studied, the experimental and predicted values were extremely close, with the greatest r^2 of 0.989. Most residual values were zero (i.e., the actual and predicted values were the same), but some were

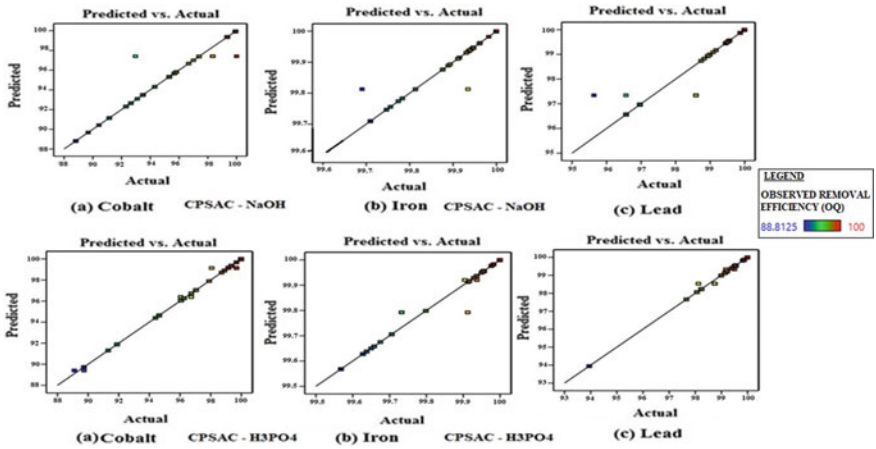

Fig. 1 Predicted against actual removal efficiency responses for the toxic metals (CPSAC–NaOH and H_3PO_4)

negative (i.e., the predicted values were bigger than the actual values) or positive (i.e., the actual values were greater than the expected values). The correlation between actual and predicted response values was consistent with the r^2 values in Table 7. As a result, all models were suitable for the hazardous metals specified in both adsorbents.

Figure 2 shows contour and 3D reaction area plots (removal efficiencies) for Co^{3+}, Fe^{2+}, and Pb^{2+} models of both adsorbents as functions of the six adsorption variables. The models were validated using the selected-response surface model predictions. All of the plots' projections fell within the hot (main) adsorption zone. The major adsorption zone in the figure is red, while the potential adsorption zone is green

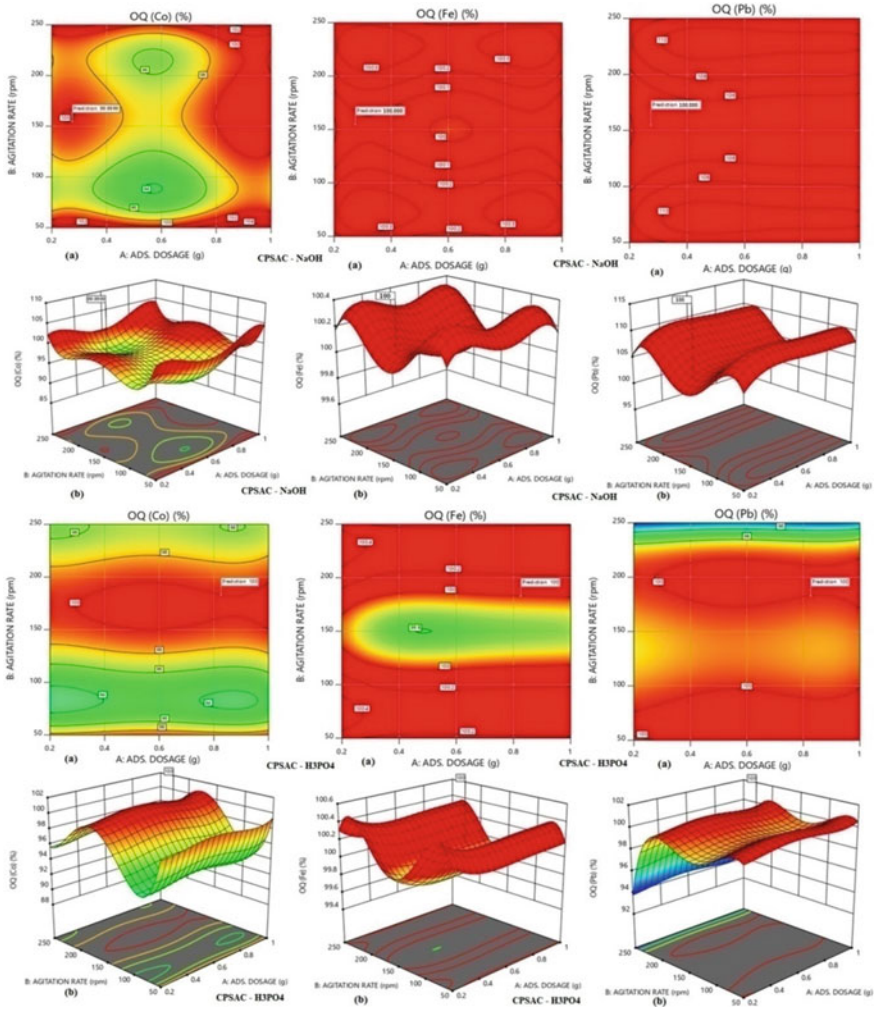

Fig. 2 **a** Contour and **b** 3D Response surface plots for CPSAC–NaOH, and H_3PO_4

(indicating that adsorption can occur in this zone even if it contains impurities), and the cold adsorption zone is blue (this means that in this zone adsorption is likely to occur, its probability is very small). The quartic natures of Co^{3+} and Fe^{2+} models show that six adsorption variables played a significant influence in the processes. Adsorption is strongly favored in this area, as evidenced by the high edges. Although all six adsorption factors were involved in the process, the saddle nature of the Pb^{2+} model indicated that two factors played a prominent role at the same time. The polynomial nature of the models was supported by the charts, as shown in Eqs. (2)–(7).

3.9 Optimization

Table 10 shows the constraints on the target variables of observed removal efficiencies (OQ) of the selected hazardous elements using both adsorbents. Table 11 shows optimized numerical solutions for the response surface models of both adsorbents. For CPSAC–NaOH, the chosen adsorption optimization solution was 0.204 g adsorbent dosage, 149.887 rpm stirring speed, 52.79 min contact time, 1.999 mm particle size, pH 7, and 29.599 °C temperature; for CPSAC H_3PO_4, the chosen adsorption optimization solution was 0.584 g adsorbent dosage, 147.426 rpm stirring speed, 53.303 min contact time, 2 mm particle size, pH 7, and 30 °C temperature. For all hazardous metals tested, these solutions resulted in 100% removal efficiency. The maximum standard error (Co^{3+}) is 2.518, which is acceptable. This yielded positive results, as the greatest value was less than 5%.

Table 10 Limitations for the targeted variables for both adsorbents

Name	Goal	Lower Limit	Upper Limit	Lower Weight	Upper Weight	Importance
A: Adsorbent dosage (g)	is in range	0.2	1.0	1	1	3
B: Stirring speed (rpm)	is in range	50	250	1	1	3
C: Contact time (min.)	is in range	20	120	1	1	3
D: Particle size (mm)	is in range	0.075	2.00	1	1	3
E: pH	is in range	4	10	1	1	3
F: Temperature (°C)	is in range	30	70	1	1	3
RE (percent)	is target = 100	99	100	1	1	3

Table 11 Optimized numerical solutions for the response surface models of both adsorbents

Adsorbent	No.	Adsorbent dosage (g)	Stirring speed (rpm)	Contact time (min.)	Particle size (mm)	pH	Temp. (°C)	OQ (Co^{3+}) (%)	Std. error (Co^{3+}) (%)	OQ (Fe^{2+}) (%)	Std. error (Fe^{2+}) (%)	OQ (Pb^{2+}) (%)	Std. error (Pb^{2+}) (%)
CPSAC–NaOH	**1***	**0.204**	**149.887**	**52.79**	**1.999**	**7**	**29.599**	**100**	**2.518**	**100**	**0.087**	**100**	**0.333**
	2	0.578	50.02	56.586	2	9.026	53.321	100	3.632	100	0.087	100	0.332
CPSAC–H_3PO_4	1*	**0.584**	**147.426**	**53.303**	**2**	**7**	**30**	**100**	**0.182**	**100**	**0.018**	**100**	**0.069**
	2	0.812	190.324	65.229	2	7.351	30.2	100	0.184	100	0.019	100	0.07

* Selected optimized numerical solution

3.10 Validation of the Optimization

The ideal accuracies for both adsorbents were validated by comparing the results of batch adsorption experiments with optimization solutions, as shown in Tables 11 and 12.

4 Conclusions

The optimization approach was found to be a useful tool in the study, and the *Carica papaya* stem is a good adsorbent for removing Co^{3+}, Fe^{2+}, and Pb^{2+} from mining effluent. The initial concentrations of the selected hazardous metals in mining effluent ranged from 9.6 to 94.1 ppm, with Co^{3+} having the lowest concentration. The optimization approach resulted in ideal adsorption dosages of 0.204 and 0.584 g for *Carica papaya* Stem Activated Carbon utilizing NaOH or H_3PO_4 with 100% removal efficiency. For *Carica papaya* Stem activated carbon utilizing NaOH, the best stirring speed, contact time, particle size, pH, and temperature were 149.887 rpm, 52.79 min, 1.999 mm, 7, and 29.599 °C, respectively. Furthermore, the stirring speed, contact time, particle size, pH, and temperature of Carica papaya Stem Activated Carbon with H_3PO_4 are 147.426 rpm, 53.303 min, 2 mm, 7, and 30 °C, respectively. In adsorption investigations, the optimization process has proven to be useful as a technique. It is strongly suggested for the biosorption of hazardous metals from mining effluent with the adsorbent manufactured from *Carica papaya* because it is cost-effective, energy-efficient, and time-saving.

Table 12 Results of validation through batch adsorption experiments for both adsorbents

Adsorbent	Number	Adsorbent dosage (g)	Stirring speed (rpm)	Contact time (min.)	Particle size (mm)	pH	Temp. (°C)	OQ (Co^{3+})(%)	OQ (Fe^{2+})(%)	OQ (Pb^{2+})(%)
CPSAC–NaOH	**1**	**0.20**	**150**	**53**	**2**	**7**	**30**	**100**	**100**	**100**
	2	0.58	50	57	2	9.00	53	95.66	100	98.01
CPSAC–H_3PO_4	1	**0.58**	**148**	**53**	**2**	**7**	**30**	**100**	**100**	**100**
	2	0.81	190	66	2	7.40	30	97.80	100	99.22

References

1. El–Moselhy KM, Abdel-Azzem M, Amer A, Al-Prol AE (2017) Adsorption of Cu(II) and Cd(II) from aqueous solution by using rice husk adsorbent. Phys Chem Ind J 12(2):109
2. Biswas S, Bal M, Behera SK, Sen TK, Meikap BC (2019) Process optimization study of zn^{2+} adsorption on biochar-alginate composite adsorbent by Response Surface Methodology (RSM).Water (MDPI) 11(325). https://doi.org/10.3390/w11020325
3. Adetoro EA, Ojoawo SO (2020b) Efficiency of *Carica papaya* stem activated with phosphoric acid and sodium hydroxide in mining wastewater treatment. In: Conference on civil engineering trends and challenges for sustainability (CTCS-2020) under international conference on emerging trends in engineering (ICETE-2020). Nnam Institute of Technology, Nitte, Karnataka, India on 22nd & 23rd of Dec (2020b)
4. Nguyen KM, Nguyen BQ, Nguyen HT, Nguyen HTH (2019) Adsorption of arsenic and heavy metals from solutions by unmodified iron-ore sludge. Appl Sci (MDPI) 9(619):1–14
5. Musa A, Wan Alwi SR, Ngadi N, Abbaszadeh S (2017) Effect of activating agents on the adsorption of ammoniacal nitrogen using activatedcarbon *papaya*peel. Chem Eng Trans 56:841–846
6. Idohou EA, Fatombi JK, Osseni SA, Agani I, Neumeyer D, Verelst M, Mauricot R, Aminou T (2020) Preparation of activated carbon/chitosan/*Carica papaya* seeds composite for efficient adsorption of cationic dye from aqueous solution. Surf Interfaces 21:1–13
7. Bai X, Wen S, Liu J, Lin Y (2018) Response surface methodology for optimization of copper leaching from refractory flotation tailings. Minerals 8(165):1–13
8. Stat-Ease. Design-expert software (Version 13). US, Minneapolis: Stat Ease Inc. http://www.statease.com. Last Accessed 09 Aug 2021
9. Mizhir H, Jawad K, Obaid ZH (2018) Analyzed statistically modelling and optimization of laser machining by response surface methodology. In: MATEC web of conferences, vol 153, pp 05005: 1–5
10. Deng S, Chen Y (2019) A study by response surface methodology (RSM) on optimization of phosphorous adsorption with nano spherical calcium carbonate derived from waste. Water Sci Technol 79(1):188–197
11. Anfar Z, Hassan AA, Zubair M, Abdallah A, Abdellah AF, Jada A (2021) Recent trends on numerical investigations of response surface methodology for pollutants adsorption onto activated carbon materials: a review. Critical Rev Environ Sci Technol. https://doi.org/10.1080/10643389.2019.1642835. Last Accessed 20 July 2021
12. Adetoro EA, Ojoawo SO (2020) Optimization study of biosorption of toxic metals from mining wastewater using *Azadirachta indica* bark. Water Sci Technol 82(5):887–904
13. World Health Organization (WHO) (2011) Guidelines for drinking-water quality.WHO, Geneva, Switzerland

Ezekiel A. Adetoro earned a B.Tech. (KWASU), Postgraduate Diploma from FUTA, an M.Sc. from University of Twente (Netherlands), and a Ph.D. from Lautech in Civil Engineering. He has many publications in respected journals and conference proceedings, and he has delivered scholarly papers at both worldwide and local conferences/workshops/seminars. He is a lecturer and a registered Civil Engineer.

Samson O. Ojoawo had a B.Tech. (LAUTECH), M.Sc. (Ibadan), and Ph.D. (Ibadan) in Civil Engineering, as well as a Postdoctoral Fellowship (India). He is currently a Professor of Civil Engineering (Water Resources and Environmental Engineering) at the Ladoke Akintola University of Technology in Ogbomoso, Nigeria's Faculty of Engineering and Technology. He has many publications in respected journals and conference proceedings, and he has delivered scholarly papers at both worldwide and local conferences/workshops/seminars. He is a licensed Civil Engineer as well as a public speaker.

Study of Characteristics of Alccofine-Based Coconut Shell Lightweight Concrete Beams Under Flexure

P. Bhuvaneshwari and L. J. Sanjeev Kumar

Abstract Globally, the role of lightweight concrete in reducing the self-weight of concrete structures is under research. The coconut shell could be used to replace the natural coarse aggregate to achieve lightweight concrete. The demerit of reduction in strength characteristics could be addressed to effectively utilize the waste coconut shell. The present study concentrated on the density and strength characteristics of Alccofine (ultrafine GGBFS)-based coconut shell lightweight concrete (30CS 6A, 30CS 8A, 30CS 10A, 30CS 12A) to arrive at an optimum mix. 30CS 8A (replacing 30% of natural aggregate with coconut shell aggregate and 8% of cement with Alccofine) has arrived as optimum. Beam specimens (100 × 150 × 1200 mm) were cast using control mix (CC_B) and optimum mix (30CS 8A_B) to analyse for the flexural characteristics. Parametric analysis was carried to compare the crack pattern, ultimate load, ultimate moment, stiffness, flexural toughness and ductility ratio. The comparison shows that the mix 30CS 8A could be effectively used to cast flexural components to achieve reduced self-weight, without compromising the flexural characteristics.

Keywords Coconut shell · Alccofine · Lightweight concrete · Density · Compressive strength · Flexural strength

1 Introduction

The usage of concrete in the construction industry is wide. The deadweight of the members plays a major role in contributing to the total load calculations. Lightweight concrete is a spearheading thought in bringing down the dead weight. Structural lightweight concrete has a density between 1440 and 1840 kg/m^3 depending on the type of aggregate substitution. Global contribution for coconut shell is from 80 nations. India plays a significant part in shredding coconut shells as waste. Because of the exhaustion of normal aggregates, the waste coconut shell might be considered for

P. Bhuvaneshwari (✉) · L. J. Sanjeev Kumar
School of Civil Engineering, SASTRA Deemed to be University, Thanjavur 613401, India
e-mail: bhuvaneswari@civil.sastra.edu

L. Nandagiri et al. (eds.), *Recent Advances in Civil Engineering*, Lecture Notes in Civil Engineering 256, https://doi.org/10.1007/978-981-19-1862-9_31

supplementing the traditional aggregates. Some of the actual qualities of the coconut shell which make it positive for coarse aggregate are high modulus properties, low cellulose content, and rough surface for bonding. Prior studies focussed on supplementing blue metal with coconut shell as a fractional substitution to accomplish acceptable strength. Olenipekan et al. [1] conducted both strength and cost analysis for Control Concrete (CC), Coconut Shell (CS) and Palm Kernel Shell (PKS) concrete by replacing coarse aggregate by 25, 50, 75, and 100%. It was found that CS concrete could be substituted for conventional concrete production. Lo et al. [2] found that the strength of lightweight concrete relies on the lightweight aggregate, hardened cement paste and interfacial zone. The increase in the number of pores in the above-mentioned region has brought down the strength. Gunasekaran et al. [3] experimented on the flexural strength, splitting tensile strengths and impact resistance of coconut shell concrete. It was proved that coconut shell fulfills the criteria for use as lightweight aggregate with enhanced impact and bond characteristics. Shannag [4] developed structural Lightweight Concrete (LWC) by replacing conventional aggregates with natural lightweight aggregates. It was found that the combination of 10% or more of silica fume, and 5% or more fly ash as a replacement for cement resulted in enhanced compressive characteristics and elastic modulus of LWC. Gunasekaran et al. [5] declared that coconut shell concrete is comparable to other types of lightweight concrete. The flexural behaviour was found to be well established by coconut shell concrete beams in terms of deflection, ultimate moment, bonding, ductility, crack width, stain capacity and end rotations. Bernardo et al. [6] experimented on the flexural ductility of lightweight aggregate concrete. It was found that for same grade of concrete, the increased longitudinal reinforcement ratio decreased the ductility. Compared to European codes, the ACI codes ensure more ductility for the tested beams.

Kanojia and Jain [7] experimented by replacing nominal coarse aggregate with coconut shells. It was reported that 40% replacement reduced the characteristic compressive strength by 22% and density by 7.5%. It was reported that even though the increase in cement content was about 22%, waste coconut shells could be effectively used in replacing the conventional aggregate in concrete. Nadir and Sujatha [8] concentrated on the durability characteristics of coconut shell concrete with and without mineral admixtures. It was noted that the addition of mineral admixtures improved the microstructure of CS concrete. Alhassan et al. [9] concentrated on the bending characteristics of lightweight concrete beam members. The influence of volume fraction of mixed fibres V_f and reinforcement ratio ρ was studied. It was concluded that cracking moment and nominal moment capacity were enhanced and service load deflection was decreased, with increased V_f and ρ. The values were also found to be in good agreement with ACI 318-14 [10].

Traore et al. [11] examined the effectiveness of different treatment methods on the mechanical characteristics of OPS and the properties of concrete cast with the similar aggregate. Different treatments involved lime (CH), sodium silicate (SS), polyvinyl alcohol (PVA), heat treatment (TH) and prewetting (SAT). Among the treatments used, the treatment with lime was reported as effective. It was suggested that the quantity of water for prewetting OPS should be determined precisely, to

avoid the increase in the water-to-cement (W/C) ratio of the mix. Bacinskas et al. [12] proposed a constitutive model of lightweight aggregate concrete and finite element-based numerical algorithms to improve the design codes. Since the density-dependent empirical coefficients do not capture the real behaviour of lightweight concrete, the constitutive model was applied for the same to extract reliable results. Wang et al. [13] studied the sustained flexural loading on 17 beams (one beam cast with normal weight concrete and 16 casts using lightweight aggregate concrete (LWAC)). Deflection, strain and crack width were noted from the experimental test and the values were compared to the theoretical values from US, European and Chinese codes for behaviour of concrete under sustained load. It was concluded LWAC has the similar serviceability characteristics as that of normal concrete. The presence of compression reinforcement or a wider compression flange was reported as to improve the structural characteristics.

The previous studies concluded that the substitution of coconut shells for natural aggregates has brought about a decrease in weight and strength characteristics. Prior research presumed that the impact of mineral admixture was found to enhance the strength attributes of ordinary concrete. In this way, the present work has been concentrated on improving the flexural characteristics of coconut shell lightweight concrete by partially replacing cement with Alccofine.

2 Experimental Study

2.1 Materials Used

Cement, Alccofine 1203, Fine aggregate, conventional coarse aggregate (CA) and broken coconut shell aggregates (CS) were utilized for delivering conventional and less dense concrete. The coconut shell is procured from an oil mill, Vallam Town, Thanjavur District, Tamil Nadu. Alccofine 1203 is a high glass content slag with high reactivity. It is prepared by granulation, and it was obtained from the local provider. The specific gravity was noted as 2.9 and bulk density 673 kg/m^3. The Marsh cone flow with a water/Alccofine ratio of 1.5 is 28. The chemical composition of 53-grade cement and Alccofine 1203 as per the supplier's manual are compared in Table1. The sieve analysis of aggregates was completed according to IS2386-1963 [14], and the gradation curves for CA and CS are compared (Fig. 1a, b). The physical properties of the materials are arranged in Table 2. The aggregates confirm with IS383-1970 [15].

Table 1 Chemical composition of binder materials

Materials	SiO_2	Al_2O_3	Fe_2O_3	CaO	SO_3	MgO	Na_2O	K_2O	TiO_2
Cement	22.5	4.78	2.1	62.5	0.16	0.8	0.58	0.15	2.2
Alccofine	35.6	20.8	1.28	34.0	0.11	6.2	0.43	0.56	2.38

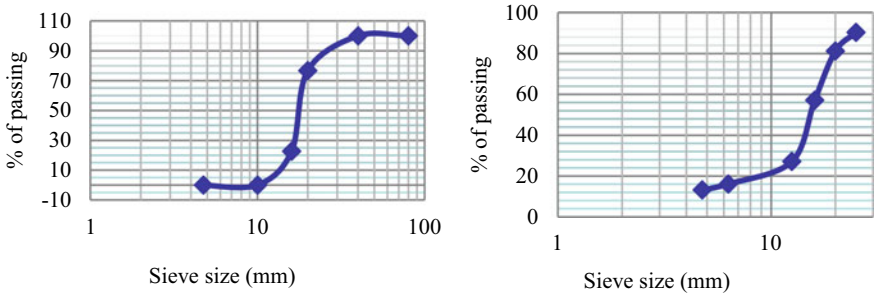

Fig. 1 Gradation curve for coarse aggregates

Table 2 Physical properties of materials

S. No.	Properties	Observed value			
		Cement (IS12269-2013) [16]	FA	CA	CS
			(IS2386-1963) [14]		
1	Setting time	32 min	–	–	–
2	Specific gravity	3.1	2.7	2.66	1.2
3	Consistency	33%	–	–	–
4	Fineness Modulus	–	3.35	8	6.4
5	Water Absorption	–	Nil	0.49%	20%
6	Crushing value	–	–	26.86%	23%
7	Impact value	–	–	22%	18%

2.2 Mix Proportion and Casting of Specimens

Mix design for concrete of grade M40 was carried out according to IS 10262-2019 [17]. The mix proportion determined was 1:1.21:2.2 with W/C ratio of 0.45. To produce the concrete with lower self-weight the conventional aggregate has been replaced by 30% of coconut shell for the nominal coarse aggregate.

Three cube specimens (100 × 100 × 100 mm) for both conventional concrete (CC) and coconut shell concrete (30CS) were cast for testing 7 days and 28 days strength, respectively. The cast cubes were demoulded after curing and surface dried before testing. Since the earlier studies reported a decrease in strength, when natural aggregate was replaced with lightweight aggregates, cement content in 30CS was replaced with Alccofine starting from 6, 8, 10 and 12% to check the optimum replacement level. The mix proportions for every one of the mixes and the details are displayed in Table 3.

Table 3 Mix proportions for the specimens (kg/m^3)

Mix	C	A	FA	CA	CS	Specimen details	Calculation (MPa) (IS516-1959) [18]
CC	493	–	598	1074	–	7 days-3 cubes 28 days-3 cubes (100 × 100 × 100 mm)	$\sigma c = \frac{P}{A}$
30CS	493	–	598	752	227		
30CS 6A	463	30	598	752	227	Three specimens for each Cube (100 × 100 × 100 mm)	Cube $\sigma c = \frac{P}{A}$
30CS 8A	453	39	598	752	227	Cylinder (200 × 100 mm)	Cylinder $\sigma t = \frac{2P}{\pi DL}$
30CS 10A	444	49	598	752	227	Prism (100 × 100 × 500 mm)	Prism $fb = \frac{3Pa}{bd^2}$
30CS 12A	434	59	598	752	227		

C—cement; A—Alccofine1203; *FA*—fine aggregate; *CA*—coarse aggregate; *CS*—coconut shell; σ_c—compressive strength; σ_t—tensile strength; fb—flexural strength; *P*—ultimate load (kN); *A*—area resisting the load (mm^2); *D*—diameter (mm); *L*—length (mm); *a*—distance between the crack point and closer support (cm); *b* —breadth of specimen (cm); *d* —depth at failure point (cm)

2.3 Testing of Specimens (IS516-1959) [18]

The specimens were surface dried before being tested. The cube specimens were compressed to failure in a compression testing machine (CTM) with a capacity of 3000 kN (Fig. 2a). Split tensile strength of cylinder specimens was carried out to confirm the tensile strength of concrete. Cylinders were arranged in CTM so that the load was applied in the longer length direction until the specimens get split into two halves (Fig. 2b). The prism specimens were subjected to bending in the flexure test instrument (Fig. 2c). Flexural strength is a measure of the bending tensile

(a)Compression test (b) Split tensile test (c) Flexure test

Fig. 2 Loading of specimens

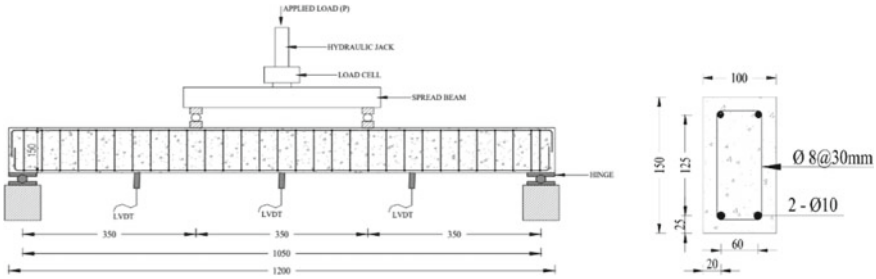

(a) Load setup for the beam (b) Cross-section

Fig. 3 Schematic sketch of the loaded beam

strength of the concrete mix. Flexural strength identifies the amount of bending stress that unreinforced concrete specimens can withstand such that they could resist any bending failure. It is also referred to as the modulus of rupture of concrete specimens.

Casting and testing of Reinforced Beam. Beam specimens (100 × 150 × 1200 mm) were designed as per IS456-2000 [19] as under reinforced section with $L/D = 10$. The provision of stirrups would restrict the shear failure. Both control and optimum mix were cast maintaining the cover as 20 mm. The percentage of steel $\rho st = Ast/bd$ was maintained as 1.256% for all the specimens. After a day duration, the specimens were demoulded and subjected to curing for 4 weeks. After curing, the beam specimens were surface dried and applied with four-point bending in a self-balancing loading frame of 1000 kN capacity. Figure 3a shows the schematic sketch of the loading setup. Linear variable differential transducer (LVDT) was fixed at the loading point and at one-third span to pick the deflection. Figure 3b shows the reinforcement detailing. The load was increased by 3 kN/minute until reversal of load. The applied load (kN) and deflection (mm) were recorded using an automated data acquisition system for further processing.

3 Results and Discussions

3.1 Density of Specimens

The density of the cube specimens for all the mixes is compared (Fig. 4). After curing, the Control Concrete (CC) without the addition of coconut shell showed the standard value for density.

After the replacement of 30 percent of natural aggregate with coconut shell (30CS), the density got reduced by 12.04%. A similar reduction in density was reported and portrayed that the decreased density was due to the less dense coconut shell aggregates by Kanojia and Jain [7]. The drop in the density values of the specimens was noticed up to 8% replacement of cement with Alccofine. The percentage

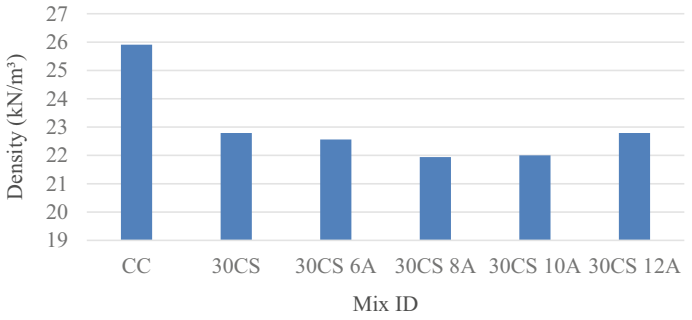

Fig. 4 Comparison of density of specimens

decreases were 12.93% and 15.32% for 30CS 6A and 30CS 8A, respectively. The additional replacement of cement with Alccofine resulted in less reduction in density for mixes 30CS 10A and 30CS 12A, respectively.

3.2 Compressive Strength of Cube Specimens

The compressive strength for all the mix proportions has been presented (Fig. 5). The control concrete (CC) yielded the characteristic compressive stress of 43.5 MPa.

The strength value got reduced by 29.38% by replacing 30% of the coarse aggregate with coconut shell (30CS), whereas the percentage reduction has been brought down to 21.22% and 7.95% by partially replacing 6% (30CS 6A) and 8% (30CS 8A) of cement with Alccofine. As per ASTM C330 standard [20], structural lightweight concrete would attain a characteristic compressive strength of 17 MPa. The range of cement content for the same is 480–510 kg/m^3. In the present study, due to partial replacement of cement with mineral admixture, the cement content was reduced to 454 kg/m^3, in mix 30CS 8A with encouraging results. The mineral admixture would have reacted with calcium hydroxide in presence of water to form additional

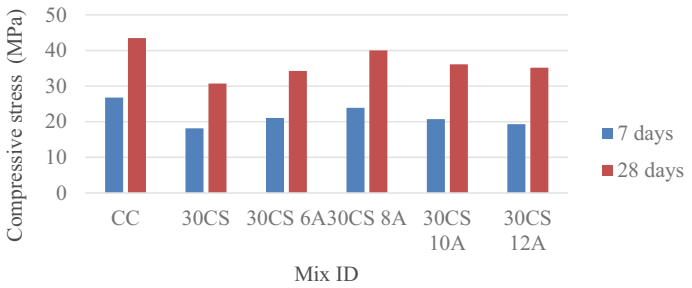

Fig. 5 Comparison of compressive strength of specimens

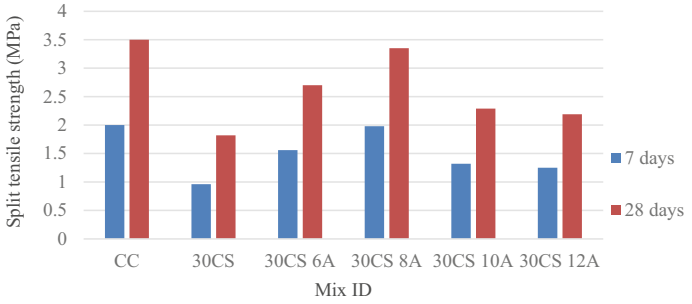

Fig. 6 Comparison of split tensile strength of the specimens

calcium silicate hydrate gel. Those secondary gel would have filled the voids, thus improved the matrix and enhanced the strength characteristics. Further replacement levels of cement with Alccofine (30CS 10A and 30CS 12A) did not show encouraging results. The additional percentage of mineral admixture beyond 8% would have been remained inert, thereby not showing any more enhancement in compressive strength.

3.3 Split Tensile Strength of Cylinder Specimens

The split tensile strengths of the specimens after 7 days and 28 days of curing are compared (Fig. 6). The splitting tensile strength of the control mix (CC) was observed to be 3.5 MPa.

The replacement of 30% of natural aggregate with coconut shell aggregate has brought down the value for 30CS to 1.82 MPa. The replacement of cement with 6% and 8% of Alccofine has enhanced the values of 30CS 6A and 30CS 8A as 2.7 MPa and 3.35 MPa, respectively. Similar values of split strength for coconut shell-based lightweight concrete were reported by Gunasekaran et al. [3]. The further increase in the percentage of Alccofine as 10% and 12% has increased the brittleness of the concrete and brought down the values to 2.29 MPa and 1.29 MPa for 30CS 10A and 30CS 12A, respectively.

3.4 Flexural Strength of Prism Specimens

The flexural strengths of the specimens after 7 days and 28 days of curing are compared in Fig. 7.

The flexural strength of the control mix (CC) was observed to be 4.75 MPa. The replacement of 30% of natural aggregate with coconut shell aggregate has brought down the value for 30CS to 2.5 MPa. The replacement of cement with 6% and 8% of Alccofine has enhanced the values of 30CS 6A and 30CS 8A as 3.5 MPa

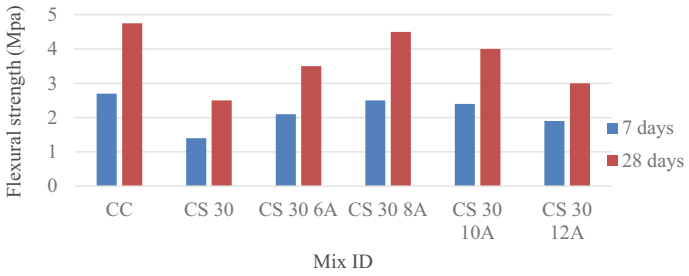

Fig. 7 Comparison of flexural strength of the specimens

and 4.5 MPa, respectively. The values were compared to that mentioned in IS 456-2000 as $0.7\sqrt{f_{ck}}$, f_{ck} being the characteristics compressive strength of concrete. The mix 30CS 8A yielded the required strength along with reduced cement content. Even though the coconut shell was brittle, the broken pieces of the reduced size of the shell as coarse aggregate resisted the applied load effectively as reported by Gunasekaran et al. [3]. The further increase in the percentage of Alccofine as 10% and 12% has brought down the flexure behaviour of the concrete and decreased the values to 4 MPa and 3 MPa for 30CS 10A and 30CS 12A, respectively.

3.5 Selection of Optimum Mix

Comparing the density, compressive strength, split tensile strength and flexural strength of all the mixes, 30CS 8A has been arrived as an optimum mix to achieve lightweight concrete.

3.6 Flexural Behaviour of Reinforced Concrete Beams

The load–deflection behaviour of beam members CC_B and 30CS 8A_B were compared and the parametric analysis like ultimate load, stiffness, ductility ratio, crack pattern, and energy absorption was carried out.

Crack pattern. The crack pattern in the loaded CC and 30CS 8A beams are presented (Fig. 8a, b). In both the specimens, the initial cracks started from the middle third span where the bending moment was maximum. The propagation of these flexural cracks was in the vertical direction. On either side of the middle third span, flexural-shear cracks initiated in the vertical direction after that they deflected by 45°. Since the beam specimens were designed as under reinforced sections, the yielding of longitudinal reinforcements has resulted in ductile failure. Since the percentage of reinforcement provided in the beams was less than that for the balanced

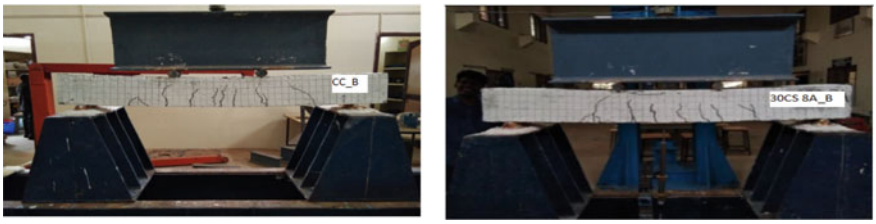

(a) Flexural cracks in CC (b) Flexural cracks 30CS 8A

Fig. 8 Four-point bending in beams

section, the steel in the tension zone yields before failure. The similar crack pattern in the deflected beams was reported by Alhassan et al. [9].

Load-deflection behaviour. The average values of load-deflection values for beams cast using control concrete (CC_B) and optimized mix (30CS 8A_B) are displayed (Fig. 9a, b), respectively. Both types of beams have failed under flexure through the yielding of steel reinforcements.

The pattern of load-deformation curves indicates that the curve follows a straight line up to the initiation of cracks. After the initiation of cracks, the slope of the plot had a different value indicating that the stiffness of the beam was reduced. The reduction in stiffness was due to the yielding of the steel in the tension zone. After yielding of steel, the specimens showed an increase in strength followed by a drop in strength. The ultimate moment for the CC_B was found to be 29.5 kNm, while for the beam 30CS 8A_B the ultimate moment was 24.9 kNm. The behaviour of beams under flexure was found to be similar without showing much difference in the moment capacity. The beam CC_B has undergone an ultimate deflection of 13.9 mm. A similar amount of maximum deflection of 11.2 mm was noticed in 30CS 8A_B.

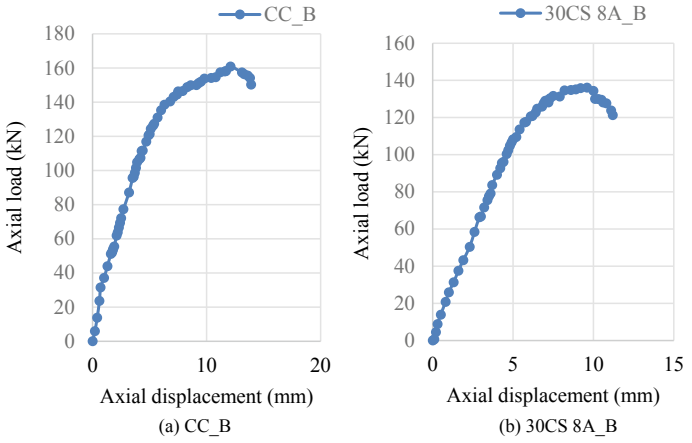

(a) CC_B (b) 30CS 8A_B

Fig. 9 Load-deflection behaviour of beam specimens

Table 4 Flexure behaviour of beam specimens

Flexural characteristics	CC_B	30CS 8A _B
Ultimate load (kN)	160.9	136.1
Ultimate moment (kNm) (experimental)	28	24.96
Ultimate moment (kNm) (theoretical)	27.9	23.8
Flexural toughness (kNm)	1.67	1.07
Crack pattern	Steel yielding-Flexure	Steel yielding-Flexure
Initial stiffness (kN/mm)	9.3	9.9
Ductility ratio	3.16	2.59

Equation (1) as per ACI 318-14 was used to calculate the theoretical maximum mid-span deflection. The values calculated were compatible with the experimental results. The various parameters are displayed in Table 4.

$$\delta \max = \frac{\mathrm{Ma}}{24\mathrm{EcI}}\left(3L^2 - 4a^2\right) \tag{1}$$

where Ma—ultimate moment (Nmm); L—the span of the beam (mm); a—shear span of the beam (mm); Ec—elastic modulus for normal concrete (N/mm^2); Ec—$w^{1.5}0.043\sqrt{}$fc' for lightweight concrete (N/mm^2); w—the unit weight of lightweight concrete (kN/m^3); I—moment of inertia of gross concrete section (mm^4).

Ultimate moment. The ultimate moment obtained from the experimental data for beam specimens CC_B and 30CS 8A_B were 28 kNm and 24.96 kNm, respectively. The experimental values were validated with theoretical values calculated based on the expression provided in ACI 318-14. Equation (2) gives the expression for the calculation of theoretical cracking moment (Mcr):

$$\mathrm{Mcr} = \frac{\lambda \mathrm{frIg}}{\mathrm{yt}} \tag{2}$$

where λ is the reduction coefficient to be utilized for lightweight concrete. The value recommended for λ is 0.85; fr = $0.62\sqrt{}$fc' is the modulus of rupture (N/mm^2); fc'—characteristic compressive strength (N/mm^2); Ig—gross moment of inertia of concrete section (mm^4); yt—neutral axis depth (mm). The theoretical cracking moment values were 27.9 kNm and 23.8 kNm for CC_B and 30CS 8A_B, respectively.

Stiffness. The slope of the load-deflection curve at the initial linear portion before the formation of flexure cracks was calculated for initial stiffness. Equation (3) is used to calculate the stiffness K:

$$K = \frac{\Delta y}{\Delta x} \tag{3}$$

where Δy—the difference in coordinates in the vertical direction (mm); Δx—the difference in coordinates in the horizontal direction (mm). Both control and lightweight concrete beams were found to have a similar stiffness of about 9.5 kN/m. Alhassan et al. [9] reported similar results for initial stiffness from the load-deflection curve for lightweight concrete beams. Thus, lightweight concrete could be effectively used as structural beams without any degradation in stiffness characteristics.

Flexural Toughness. The flexural toughness is an important parameter to be verified to ensure that the beam specimens maintained sufficient strength without compromising the ductility. The parameter is calculated as the area under the load-deflection curve of the specimens. The value obtained for 30CS 8A beam specimens shows that flexural strength was retained along with ductile behaviour.

Ductility ratio. Ductility is the preferable structural property that would ensure the capability for a structural member to undergo large deformations before failure. Equation (4) is used to calculate the ductility ratio (δ):

$$\delta = \frac{\delta u}{\delta y} \tag{4}$$

where δu—the deflection corresponding to ultimate load (mm); δy—the deflection corresponding to yield load (mm). The ductility ratios for CC_B and 30CS 8A_B were 3.16 and 2.59, respectively. The lightweight concrete shows sufficient ductility due to the shock-absorbing nature of coconut shell aggregates as mentioned by Gunasekaran et al. [5]. The lightweight concrete beams have thus ensured ductile behaviour under flexure.

4 Conclusions

The following conclusions were arrived at based on the study carried out:

- Preliminary investigations such as crushing value and impact value for coconut shell aggregates have given very good results with 23% and 18%, respectively, confirming extremely strong aggregates.
- The percentage reduction in compressive strength for the 30CS cubes was 29.38%, compared to that of CC cubes.
- The partial replacement of cement with the Alccofine (ultrafine GGBFS) in mix 30CS (30CS 8A) has gained the characteristic compressive strength.

- The maximum reduction in density of about 15.32% was achieved for lightweight concrete 30CS 8A, compared to control concrete.
- The ultimate load for 30CS 8A_B beam was comparable to the control beam CC_B.
- The ultimate moments obtained from the experimental data for beam specimens CC_B and 30CS 8A_B were 28 kNm and 24.96 kNm, respectively. Similar values have arrived from theoretical calculations.
- The control beam CC_B has undergone an ultimate deflection of 13.9 mm. A similar amount of maximum deflection of 11.2 mm was noticed in 30CS 8A_B. The experimental deflections were comparable with the theoretical values.
- The flexural toughness obtained for 30CS 8A_B specimens was comparable to that of CC_B. The flexural strength was retained in the specimens along with the ductile behaviour.
- Both CC_B and 30CS 8A_B beams were found to have similar stiffness. Thus, lightweight concrete could be effectively used as structural beams without any degradation in stiffness characteristics.
- The ductility ratios for CC_B and 30CS 8A_B were 3.16 and 2.59, respectively. The lightweight concrete beams have thus ensured ductile behaviour under flexure.
- It could be concluded that the flexural members cast using lightweight concrete mix 30CS 8A would result in less dense components without compromising the flexural characteristics.

Acknowledgements The authors extend their sincere thanks to School of Civil engineering, SASTRA Deemed to be University for extending the facilities to complete the work successfully.

References

1. Olanipekun EA, Olusola KO, Ata O (2006) A comparative study of concrete properties using coconut shell and palm kernel shell as coarse aggregates. Build Environ 41:297–301
2. Lo TY, Tang WC, Cui HZ (2007) The effect of aggregate properties on lightweight concrete. Build Environ 42(8):3025–3029
3. Gunasekaran K, Kumar PS, Lakshmipathy M (2011) Mechanical and bond properties of coconut shell concrete. Constr Build Mater 25(1):92–98
4. Shannag MJ (2011) Characteristics of lightweight concrete containing mineral admixtures. Constr Build Mater 25(2):658–662
5. Gunasekaran K, Annadurai R, Kumar PS (2013) Study on reinforced lightweight coconut shell concrete beam behavior under flexure. Mater Des 46:157–167
6. Bernardo LFA, Nepomuceno MCS, Pinto HAS (2016) Flexural ductility of lightweight-aggregate concrete beams. J Civil Eng Manage 22(5):622–633
7. Kanojia A, Jain SK (2017) Performance of coconut shell as coarse aggregate in concrete. Constr Build Mater 140:150–156
8. Nadir Y, Sujatha A (2018) Durability properties of coconut shell aggregate concrete. KSCE J Civil Eng 22:1920–1926
9. Alhassan M, Al-Rousan RZ, Ababneh AN (2017) Flexural behavior of lightweight concrete beams encompassing various dosages of macro synthetic fibers and steel ratios. Case Stud Constr Mater 7:280–293

10. ACI committee 318-14 (2014) Building code requirements for structural concrete (ACI 318M-14). American Concrete Institute, Michigan (USA)
11. Traore YB, Messan A, Hannawi K, Gerard J, Prince W, Tsobnang F (2018) Effect of oil palm shell treatment on the physical and mechanical properties of lightweight concrete. Constr Build Mater 161:452–460
12. Bacinskas D, Rumsys D, Sokolov A, Kaklauskas G (2019) Deformation analysis of reinforced beams made of lightweight aggregate concrete. Materials 13:1–12
13. Wang Z, Li X, Jiang L, Wang M, Xu Q, Harries K (2020) Long-term performance of lightweight aggregate reinforced concrete beams. Constr Build Mater 264:120231
14. IS2386 (Part I)-1963: Indian standard methods of test for aggregates for concrete, part I particle size and shape. Bureau of Indian Standards (BIS), New Delhi
15. IS383-1970: Indian standard specification for coarse and fine aggregates from natural sources for concrete. (Second Revision) Bureau of Indian Standards (BIS), New Delhi
16. IS12269-2013: Ordinary Portland cement–specification. Bureau of Indian Standards (BIS), New Delhi
17. IS10262-2019: Indian standard concrete mix proportioning-guidelines. Bureau of Indian Standards (BIS), New Delhi
18. IS516-1959: Indian standard methods of tests for strength of concrete. Bureau of Indian Standards (BIS), New Delhi
19. IS456-2000: Indian standard plain and reinforced concrete-code of practice. Bureau of Indian Standards (BIS), New Delhi
20. ASTM C330: Standard specification for lightweight aggregates for structural concrete. Annual Book of ASTM Standards

Performance Evaluation of Copper and German Silver Electrodes During Electrochemical Oxidation of Ametryn in Water

Basavaraju Manu, Sanjeev Sangami, Viplav Gritlahre, and Yash Malviya

Abstract The comparative electrocoagulation treatment was studied for the degradation and mineralization of ametryn in water using copper (CE) and German silver (GE) electrodes both in batch and continuous modes of operation. The operating variables such as the number of electrodes (2, 4), voltage (6, 12 V), current density (4–15 A/m^2), initial concentration of ametryn (15, 20, 25 ppm), reaction time (0–120 min) and flow rate (0.5, 1, 1.5 Lph) were varied without changing the actual pH of the aqueous solution. The maximum removal of 80–85% of ametryn was achieved with a combination of 2 electrodes, 6 V, 1 Lph of flow rate and 80 min of reaction time. The copper electrode shows better performance than German silver electrodes, with less power consumption. The removal efficiency was decreased with increasing the initial concentration of ametryn and pH was gradually increased from 7–9.5. As the reaction proceeds, the pH was slowly increased in GE electrodes (7–9.6), which is more than in CE electrodes (7.8.6). The overall results revealed that CE and GE electrodes proved to be an alternative for other electrodes such as aluminum, iron and platinum.

Keywords Ametryn · Copper electrodes · German silver electrodes · Continuous process · Electrocoagulation

B. Manu
Department of Civil Engineering, National Institute of Technology Karnataka, Surathkal, India
e-mail: bmanu@nitk.ac.in

S. Sangami (✉)
Department of Civil Engineering, Jain College of Engineering, Belagavi, India
e-mail: sanjeevenv08@gmail.com

V. Gritlahre
Public Health Engineering, Department, Raipur, Chhattisgarh, India

Y. Malviya
Department of Civil Engineering, National Institute of Technology Karnataka, P.O. Srinivasnagar, Surathkal, India

L. Nandagiri et al. (eds.), *Recent Advances in Civil Engineering*, Lecture Notes in Civil Engineering 256, https://doi.org/10.1007/978-981-19-1862-9_32

1 Introduction

Ametryn(2-ethylamino-4-(isopropylamino)-6-(methylthio)-s-triazine)is used to destroy the unwanted plants from the agricultural field and other specific surfaces such as industrial and home gardens [1]. Though this is more efficient in the removal of all kinds of weeds, the residue present in soil and water [2] creates a harmful effect on the human beings, other beneficial plants and organisms such as crustaceans and mollusks [3, 4], and therefore, toxicity levels in drinking water are limited to $1.4-14\ \mu g{\cdot}L^{-1}$ [5]. The direct discharge of agricultural runoff water containing this herbicide into the municipal sewage plants and drinking water sources such as rivers and other streams makes the treatment system more difficult. For the degradation of this herbicide, many methods were applied such as Cl_2 [6] and membrane process [7]. However, all these processes have the limitations like maintenance of filters due to their clogging effect and chlorine is not a suitable method for the actual agricultural run of water, where the formation of halomethanes was observed. Electrocoagulation method shows a great interest due to its advantages such as no use of chemicals, economical, minimal sludge, faster reaction kinetics, production of insitu coagulants, requires less space and no secondary pollutants where the complete mineralization of compounds was observed [8]. Electrocoagulation starts with anode dissolution of both electrodes when proper DC current is supplied and at the cathode, generation of hydrogen gas and hydroxide ions was observed and later metal hydroxide complexes were formed (pH > 8). In general, these reactions are given below (Eqs.1–3), where M = Copper and German silver electrodes, z = valency and x and y = number of moles of water and H_2

$$\text{Anode: } M_{(S)} \Leftrightarrow {M_{(aq)}}^{z+} + ze \tag{1}$$

$$\text{Cathde: } xH_2O_{(l)} + ze^- \Leftrightarrow {yH_{2(g)}}^{z+} + zOH^-{}_{(aq)} \tag{2}$$

$$\text{Insitu - coagulents: } M^{z+} + zOH^- \Leftrightarrow M(OH)_z \tag{3}$$

To the best of the author's knowledge, no studies were reported on the electrochemical oxidation of ametryn with both copper and German silver electrodes. Hence, the research has been conducted to degrade the ametryn using electrocoagulation in both batch and continuous modes of operation.

Table 1 Reactor Specifications

Reactor	Specifications	Electrodes	Specifications
Shape	Rectangle	Dimensions	67 × 92 mm
Capacity	1 L	Thickness	1 mm
Size and thickness	9.21 × 9.21 × 14.3 cm and 6 mm	Arrangement	Monopolar

2 Materials and Methods

2.1 Materials

The ametryn (Sigma Aldrich) and other chemicals such as FAS (ferrous ammonium sulfate), NaOH, $HgSO_4$, potassium dichromate, $AgSO_4$, HPLC solvents such as methanol and water were obtained from Merck manufactured in India. The reactor, copper and German silver electrodes were procured from the local metal industry and their details are given in Table 1.

2.2 Experimental Setup

In this electrocoagulation process, the performance of the electrodes was studied in both batch and continuous processes with monopolar-parallel configuration. The electrodes were connected to the cathode and anode of the DC power supply unit. Batch experiments were performed by varying the voltages for different plates, which are submerged in ametryn solution. The inlet and outlet are closed in the batch process, and in the continuous process, it is vice versa. In this process, the overflow end is connected to the filter bed, so that the floating particles are removed from the treatment system. The magnetic stirrer was used for uniform mixing and the magnetic bead was used in the reactor for stirring and a sufficient gap was provided between the electrodes. The setup was given in Fig. 1.

2.3 Experimental Procedure

The HPLC calibration curve was prepared from the standard solutions of 5–20 ppm of ametryn (stock solution = 100 ppm). The Electrocoagulation (EC) was initiated for three concentrations such as 15, 20 and 25 ppm. In batch mode, all experiments were conducted at a room temperature of about 25 °C with a total reaction time of 120 min, and after that, the samples were dispensed to the filter paper every 20 times. All experiments were performed with 6–12 V and 2–4 electrodes, and after

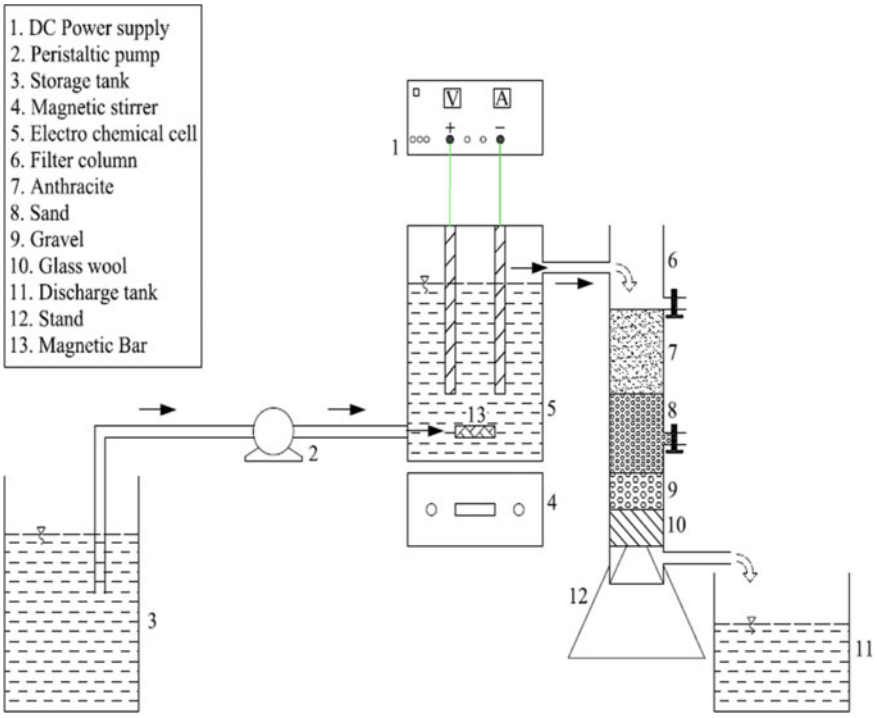

Fig. 1 Experimental setup of continuous Electrocoagulation Process

completion of each set of the experiment, the electrodes were washed with 20% of HCl (30%) for further use.

For all the samples, pH, turbidity and conductivity were analyzed. Finally, the filtered sample was analyzed in HPLC for the residual ametryn with the help of a calibration curve ($R^2 = 0.99$) and the operating parameters (Number of electrodes, voltage and reaction time) were optimized. In continuous mode, the experiments were conducted at optimum conditions using a peristaltic pump for different flow rates (0.5, 1, 1.5 Lph) with a reaction time of 2 h. The outlet end was connected to the filter bed, where three types of filter materials (sand, gravel and anthracite) were used. Anthracite acts as a multi-media source for the filter, which is durable with a wide range of temperature susceptibility. The filter sand and gravel support each other along with anthracite with varying sizes of 25–250 mm, which helps in mechanical sterilization and sedimentation of the particles thereby improving the overall removal efficiency. Here also, residual ametryn and pH were analyzed by taking the sample from the filter outlet at regular intervals of time. To understand the extent of mineralization of ametryn, all the samples were analyzed for COD (chemical oxygen demand) [9].

2.4 Analytical Procedure

The residual ametryn was measured with HPLC (Agilent 1260), which consists of Zorbax-RP-C18 column (100*4.6 mm, 3.5 μ pore size), diode array detector (DAD), column temperature = 25 °C, binary pump flow rate = 1 ml/min, solvents: methanol: water (58: 42), elution time = 8.8 min. The pH and λ_{max}(223 nm) were measured with a Systronics pH meter and UV-Vis double beam spectrophotometer. The mineralization process was measured as COD using the titration method [9].

3 Results and Discussion

3.1 Batch Process

The mineralization (% COD removal) and degradation (% removal) of ametryn were studied by varying the number of electrodes (2, 4) and voltages (6 V and 12 V) for copper(CE) and German silver(GE) electrodes with a reaction time of 120 min shown in Fig. 2a (CE-2electrodes), Fig. 2b (CE-4 electrodes) and Fig. 3a (GE-2electrodes), Fig. 3b (GE-4 electrodes), respectively. Along with removal efficiency, the corresponding power consumption and current densities were also evaluated (Fig. 4). The highest removal efficiency of 85% (copper electrodes) and 80% (German silver electrodes) was observed with a current density of 4–15 (A/m^2) and power consumption of 1.5–7.8 Wh. The reaction was faster at the initial stages (till 60 min) with a removal efficiency of >50, and after that, it decreased. It may be due to the increase in the production rate of hydroxide complexes till 60 min, and after that, there is no generation of actives coagulants[10]. The COD removal of <70% was observed for both

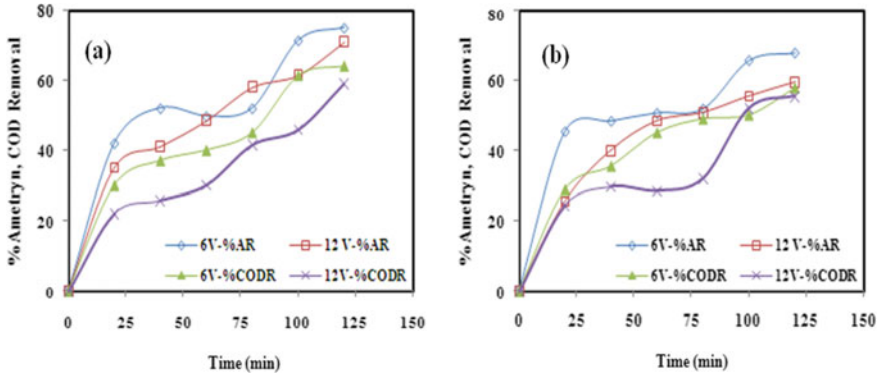

Fig. 2 Plot of % ametryn removal (%AR), COD removal (CODR) versus Time for the Copper electrodes **a** 2 Electrodes **b** 4 Electrodes, Initial pH = 7 and Initial ametryn concentration = 15 ppm

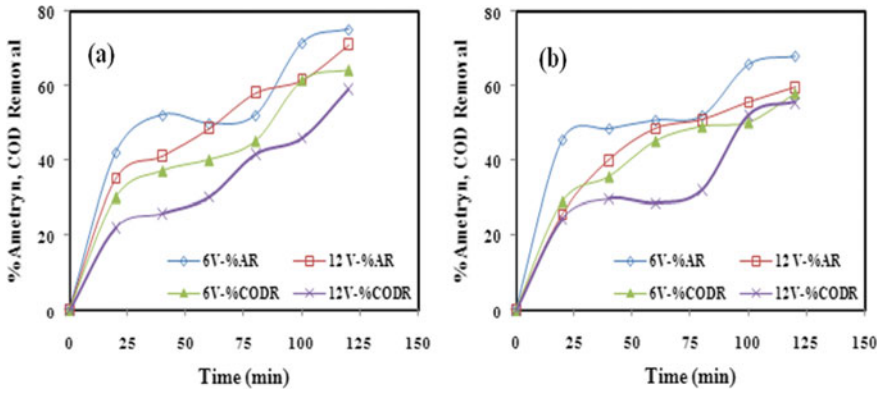

Fig. 3 Plot of % ametryn removal (%AR), COD removal (CODR) versus Time for the German silver electrodes **a** 2 Electrodes **b** 4 Electrodes; Initial pH = 7; Initial ametryn concentration = 15 ppm

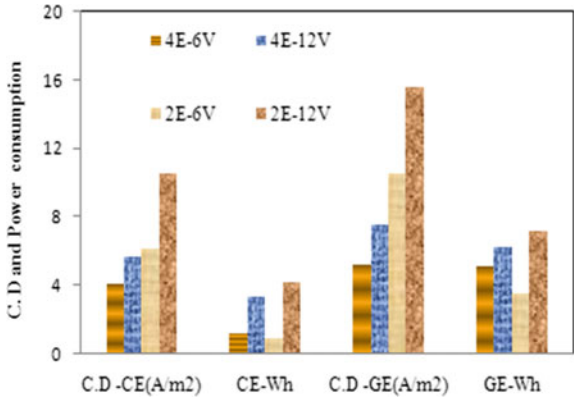

Fig. 4 Plot of current density (C.D in A/m^2) and power consumption (Wh = Watt hour) versus both electrodes and voltage, 4E-6 V = 4 electrodes-6 voltage, CE = copper electrodes and GE-German silver Electrodes

types of electrodes, which is lesser than the degradation process. It clearly indicates that the formation of mineral acids, CO_2 and H_2O was slower than the transformation of ametryn to some other compounds. Finally, active coagulants combine with released (adsorption of pollutants on sludge) ions and settle as a sludge at the bottom of the reactor. The removal efficiency was slightly higher for 12 V (5–8%) than the 6 V, and for 2 electrodes than the 4 electrodes.

Hence, 2 plates and 6 V were considered optimum. Also, an increase in the current density (4–8.5 A/m^2 for CE and 5–15 A/m^2 for GE) increased the degradation process, and the more the surface area of electrodes released the lesser active coagulants. The power consumption for the treatment process was calculated according to the literature [11] and it is seen that the treatment cost using German silver electrodes is more than copper electrodes. This may be due to the light brown precipitate formed for the copper electrodes during the EC process is more reactive than green sludge

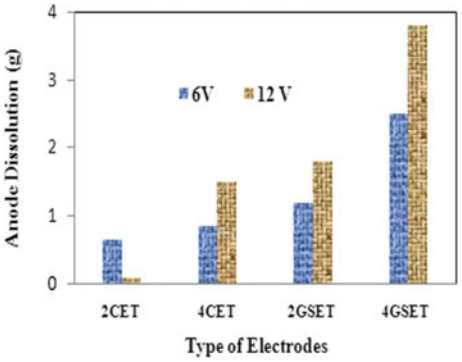

Fig. 5 Anode dissolution in grams (g) versus different types of electrodes with different voltages, 2CET = 2 copper Electrodes and 2GSET = 2 German silver Electrodes

formed for the German silver electrodes [12]. Anode dissolution (0.5–5 g) was also monitored throughout the batch treatment process (Fig. 5) and the highest dissolution was observed for the 4 electrodes than 2 electrodes. It means that more numbers of less active coagulants are released during EC (Electrocoagulation) process thereby hindering the degradation process. The current density is also directly related to the amount of sludge produced according to Faraday's law [13], and according to this, the more the current density more the anode dissolved and it is true in the present study also. During electrocoagulation as the current density is increased, the small bubbles were released and it clearly indicates that the mechanism of floatation was favored by the production of hydrogen gas, which helps in the mineralization of ametryn. Therefore, a 6 V and 2 electrode combination is finally considered as a optimum value.

3.2 Effect of pH

In the present study, the experiments were conducted at near to the neutral pH (7–7.3) and later variation was measured at every time interval. Many literature say that the EC process has many disadvantages in the acidic (pH = 5–7) and alkaline range (7–9.5) [14, 15], and in this study, the pH variation was not performed. After treatment, the pH slowly increased from 7–8.6 for copper electrodes and for German silver electrodes 7–9.5 as the time progresses, and also slowly the removal efficiency was increased till 120 min (Fig. 6a-CE electrodes, Fig. 6b)-GE electrodes). However, the highest removal efficiency (50–65%) was observed within 60 min and later gradually increased. The pH increase in GE electrodes may be due to the production of more number of less quality hydroxides, and hence, the removal efficiency is less in GE electrodes than in CE electrodes. It was seen that at acidic pH copper electrodes combine with H^+ ions, forming the many hydroxide complexes with more amount of anode dissolution at pH = 5 [16] (Eqs. 4–5) such as $Cu(OH)_2^+$, $Cu(H_2O)_2^+$ and

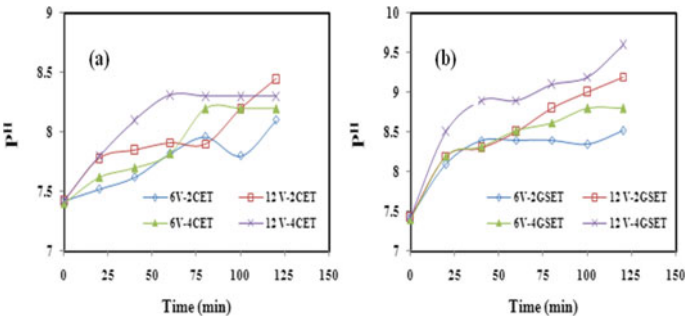

Fig. 6 Variation of pH versus time for different electrodes, 6 V-2CET = 6 voltage-2 copper electrode, 6 V-2GSET = 6 voltage-2 German silver electrode **a** Copper electrodes **b** German silver electrodes

$Cu(H_2O)_5OH_2^+$, and these hydroxide complexes entrap the degraded or mineralized products [17] and finally settle as sludge at the bottom of the reactor.

However, in the present study, the pH was not reduced to the acidic range, because of the highest anode dissolution and production of the less active coagulants with less removal efficiency and it also depends on the interactions between the type of the compounds and type of the electrodes during EC process. The experiments were conducted for three ametryn concentrations such as 15, 20 and 25 ppm for different electrodes (2, 4) and different voltages (6, 12 V) shown in Fig. 7a, b. It is clear that the pH was gradually increased from 7 to 9.5 by increasing the initial concentration and also slightly increasing the pH for the 12 V than 6 V. This is due to the more OH ions produced at 12 V with less active site for degradation process. Hence, it is finally concluded that 2 electrodes and 6 V combination is considered as optimum without varying aqueous solution pH and these conditions were adopted in the continuous treatment process.

$$\text{Anode: } 2Cu_{(S)} + 4H^+ \rightarrow 2Cu^{2+} + 2H_{2(g)} \tag{4}$$

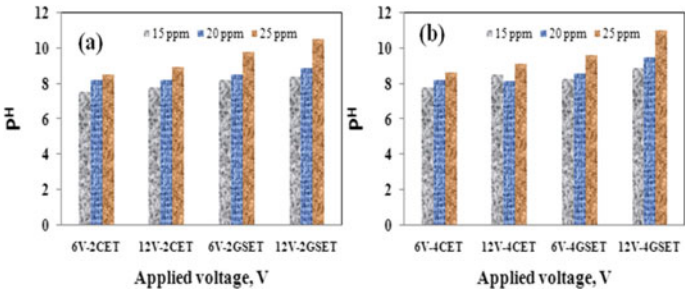

Fig. 7 Variation of pH versus voltage with different electrodes for different initial concentrations of ametryn 6 V-2CET = 6 voltage-2 copper electrode, 6 V-2GSET = voltage-2 German silver electrode **a** 2 plates **b** 4 plates

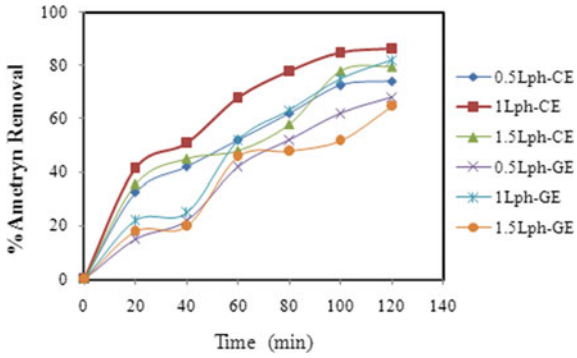

Fig. 8 Effect of flow rate on the removal efficiency of ametryn; 0.5Lph-CE = 0.5 L per hour-copper electrodes; 0.5Lph-GE = 0.5 L per hour-German silver electrodes; Initial ametryn concentration = 15 ppm; Initial pH = 7; Number of electrodes = 2; voltage = 6 V

$$\text{Cathde: } 4H_2O_{(l)} + 4e^- \rightarrow 2H_{2(g)}{}^{z+} + 4OH^-{}_{(aq)} \quad (5)$$

4 Continuous Processes

The continuous treatment was performed for different flow rates, i.e. 0.5, 1, 1.5 Lph shown in Fig. 8. The sample was collected at every regular interval of time (every 20 min) from the filter bed outlet (Fig. 1). It was observed that the highest removal of 86% was achieved at 1 Lph with optimum experimental conditions of 2 electrodes and 6 V. Here also, it is confirmed that the degradation efficiency of copper electrodes is more than the German silver electrodes.

5 Conclusions

Based on both batch and continuous experiments, the following conclusions were drawn.

1. The maximum degradation (80–85%) and mineralization (70–75%) were achieved with 2 electrodes and 6 V in parallel for both types of electrodes, and in the continuous process, 1 Lph is considered to be an optimum flow rate.
2. The less power consumption was observed for copper electrodes (CE) than German silver electrodes (GE) and the removal efficiency was more in CE than the GE electrodes.
3. Increase in the current density (4–15 A/m^2 for GE) enhanced the degradation process and the more the surface area of electrodes released the lesser active coagulants.
4. The pH was slowly increased from 7–9.5 as the initial concentration of ametryn was increased from 15–25 ppm and also slightly increased the pH for the 12 V

than 6 V. As the reaction proceeds, the pH increase was comparatively more in GE electrodes (7–9.6) than CE electrodes (7–8.6). Hence, the EC process using CE electrodes and GE electrodes proved to be efficient for the removal of ametryn from water and an alternative to the other type of electrodes such as Al, Fe and Pt.

References

1. Jiang L, Huang J, Liang L, Zheng YP, Yang H (2008) Mobility of prometryne in soil as affected by dissolved organic matter. J Agric Food Chem 56:11933–11940
2. Catalkaya EC, Kargi F (2009) Degradation and mineralization of simazine in aqueous solution by ozone/hydrogen peroxide advanced oxidation. J Environ Eng 135:1357–1364
3. Kolpin DW, Thurman EM, Linhart SM (1998) The environmental occurrence of herbicides: the importance of degradates in ground water. Arch Environ Contam Toxicol 35:385–390
4. Briggs SA (1992) Basic guide to pesticides: their characteristics and hazards. Hemisphere Publishing, Washington, DC
5. EPA (2010) Reregistration eligibility decision (RED) for Ametryn. https://archive.epa.gov/pesticides/reregistration/web/pdf/ametryn_red.pdf. Accessed on 07 May 2017
6. Xu B, Gao N, Cheng H, Hu CY, Xia SJ, Sun XF, Wang X, Yang S (2009) Ametryn degradation by aqueous chlorine: kinetics and reaction influences. J Hazar Mat 169:586–592
7. Shurvel T, Keir G, Jegatheesan V, Shu L, Farago L (2014) Removal of ametryn through nanofiltration and reverse osmosis. Desalin Water Treat 52:643–649
8. Chen G (2004) Electrochemical technologies in wastewater treatment. Sep Purif Technol 38(1):11–41
9. APHA, AWWA, WPCF (eds) (2005) Standard methods for the examination of water and wastewater. Washington DC
10. Kobya M, Gengec E, Demirbas E (2016) Operating parameters and costs assessments of a real dyehouse wastewater effluent treated by a continuous electrocoagulation process. Chem Eng Process 101:87–100
11. Sridhar R, Sivakumar V, Immanuel VP, Maran JP (2011) Treatment of pulp and paper industry bleaching effluent by electrocoagulant process. J Hazard Mater 186(2):1495–1502
12. Asselin M, Drogui P, Brar SK, Benmoussa H, Blais JF (2008) Organics removal in oily bilgewater by electrocoagulation process. J Hazard Mater 151(2):446–455
13. Mollah MYA, Schennach R, Parga JR, Cocke DL (2001) Electrocoagulation (EC)—science and applications. J Hazard Mater 84(1):29–41
14. Prajapati AK, Chaudhari PK (2014) Electrochemical treatment of rice grain-based distillery effluent: chemical oxygen demand and colourremoval. Environ Technol 35(2):242–249
15. Golder AK, Samanta AN, Ray S (2007) Removal of trivalent chromium by electrocoagulation. Sep Purif Technol 53(1):33–41
16. Prajapati AK, Chaudhari PK, Pal D, Chandrakar A, Choudhary R (2016) Electrocoagulation treatment of rice grain based distillery effluent using copper electrode. J Water Process Eng 11:1–7
17. Sahu O, Mazumdar B, Chaudhari PK (2014) Treatment of wastewater by electrocoagulation: a review. Environ Sci Pollut Res 21(4):2397–2413

Behavior of Cable-Stayed Bridge Due to Different Cases of Cable Loss

Aarsha Degvekar and Purnanand Savoikar

Abstract The study of cable behavior is vital in cable-stayed bridges as they are known to carry load from the deck/girder to the pylon. However, the cables are exposed to atmospheric corrosion (humidity, etc.) and metal corrosion which causes them grave damage. Further, it is observed that fatigue failure due to variation in load causes microfractures in the stay cables. Due to the above facts, maintenance of cables is imperative and mandatory monitoring should be observed. A simple model of cable-stayed bridge is designed and analyzed using MIDAS Civil. Unknown Load Factor method, which is the optimization method, is used to determine the cable forces. A cable-stayed bridge is modeled and analyzed using MIDAS Civil. Seven different cases of cable loss are considered for the study undergoing static forces only (dead load cases), and for each case, the results for cable forces, beam stresses, beam moments, support reactions and deformed shapes are carefully studied. The results obtained reveal the effect of cable loss on the structure. It was observed that the loss of outermost cable/s affects the most. This study can be highly useful as a reference, to different cable-stayed bridge models, and further, the behavior of the structures can be examined.

Keywords Cable stay · Pylon · Loss of cables · Cable forces · Beam stresses

1 Introduction

In most cable-stayed structures around the world, the cables used are made up of a group of wires laid in parallel, and each strand is made up of wires twisted together. Cables are the main element in the maintenance of cable-stayed bridges. The stay cables are subjected to repeated loading with force variation due to which fatigue action takes place and minor cracks occur on the cables. In addition, the stay cables are exposed to harsh environmental conditions, which cause them to rust and thus reduce the bearing capacity of the cables. Extreme events are such as lightning

A. Degvekar · P. Savoikar (✉)
Goa College of Engineering, Farmagudi, Ponda, Goa, India
e-mail: psavoikar@gmail.com; pps@gec.ac.in

L. Nandagiri et al. (eds.), *Recent Advances in Civil Engineering*, Lecture Notes in Civil Engineering 256, https://doi.org/10.1007/978-981-19-1862-9_33

strikes, high winds, earthquakes, vehicle fires and shock/blast waves. Stay cables are mainly damaged due to varying fatigue actions during the structure lifetime, as they are subjected to repeated loading with force variations and millions of load cycles. Moreover, stay cables are exposed to harsh environmental conditions which results in rusting of stay cables reducing the bearing capacity of cables. Also, stay cables might be exposed to extreme events like exposure to vehicle fires, blast waves, lightning strikes, strong winds, earthquakes, etc.

It is mainly due to long-term corrosion that leads to damage to the cable and premature failure due to different fatigue effects, which affects the service life of the cable and causes the collapse of the structure. It is essential to protect the cables from corrosion. To protect the cable from corrosion, a high-density polyethylene jacket filled with cement grout is used. When the cable reaches the end of its useful life or its integrity is compromised due to extreme events, it is necessary to replace the stay cable.

2 Literature Review

Previous studies describe the need to replace cables, the methods used during the replacement of cables and the solutions developed for removing existing cables and installing and tensioning new cables.

Mehrabi et al. [1] conducted a detailed study in phases for assessing the condition of the stay cables of Hale Boggs Bridge in Luling, Louisiana. In Phase I, the cable condition was evaluated and it was found that cables possessed low damping capability. In Phase II, Non-Destructive tests were carried out and flaws in the materials were detected. Based on the inspection carried out, five plans were presented for correcting defects in the cables. It was decided to replace all the stay cables of the bridge in accordance with the economic efficiency theory. The entire structure was analyzed for change in the force which was caused while installing temporary cables, removing existing cables and stressing replacement cables.

Pipinato et al. [2] performed an analysis with FEM software MIDASoft (2000) on a typical cable-stayed bridge model. Different cable arrangement pattern types were analyzed, i.e., semi-harp and fan-type arrangements. Two boundary conditions of deck of the central span were considered; first, two decks connected by a hinge and second was continuous deck. Spacing between the stands was varied and the different cases were compared. Static analysis shows that fan-shaped patterns are more detrimental in external elements, whereas the situation is unfavorable for the semi-harp pattern corresponding to the internal cables. Reducing the gap between strands or changing the boundary conditions, the improvement achieved by a semi-harp rather than by a fan configuration remains almost unchanged.

Lavery et al. [3] outlined the need for cable replacement at Ewijk Bridge. The design approach adopted during cable replacement and the solutions developed to enable the existing cables to be removed and new cables installed and tensioned were discussed. Replacing the damaged cables of Ewijk Bridge was done by de-tensioning

one cable set entirely by jacking down the cable saddle, followed by replacement of that set of cables with new cables, and then jacking of the cable saddle support beams to apply the required tension force in the cables. Replacing the cables prolongs the service life of the bridge.

Yamamoto et al. [4] described the rehabilitation works carried out on the "Binh Bridge" in Vietnam, especially the main girder repair and stay cable replacement. A temporary hanger system using a pulley which was able to move along a cable was used in order to replace some of the cables and was, thus, able to replace cables in a safe and accurate manner. Their investigation confirmed that the wires had corroded due to the rupture of the cover. It was concluded that the cover of a stay cable was damaged and it was very important to repair it so as to prevent water intrusion.

Dao and Nguyen [5] carried out an analysis of cable-stayed replacing solutions for in-service cable-stayed bridge in Vietnam. Two parallel wire systems and steel girder of the bridge were damaged due to impact from large 3 vessels. Due to this impact, the stay cables were replaced. Before replacement, modeling and structural analysis of the bridge were carried out by the software Midas/Civil 7.01.

Fu et al. [6] performed modeling and structural analysis of a long-span cable-stayed bridge where the method of using temporary cable is not feasible to replace the stay cable. In the analysis, it was concluded that while removing the shortest cable in a side span, the largest peak value of cable force increment appeared. During the removal of the longest cables, the cable-stayed bridge had the greatest deflection of both beam and top tower. The replacement sequence of short to long was recommended based on the result of the bending strain energy analysis.

Ali et al. [7] carried out a parametric study on the safety of stay cables of cable-stayed bridges considering the factors affecting their ultimate and fatigue strengths. Through this study, it was concluded that to satisfy the requirements of ultimate and fatigue limit states, a safety factor in the range of 2.3–2.5 is essential under normal situations. A minimum safety factor of 2.4 is compulsory in a situation like single cable loss is considered in the design procedure and a safety factor of 2.5 is appropriate in case of multiple loss scenarios. However, this study was limited as the above results were based on only one model of a cable-stayed bridge.

Hongjiang [8] studied the details of cable replacement in the Yonghe Bridge in Tianjin, China. The study concluded that for a concrete cable-stayed bridge with a long service life, after renovation, the structural condition before replacement of the cable is generally uncertain, so the design pretension in the cable is also difficult to determine. Considering that the structural conditions tend to stabilize over time, the current measured cable force can be used as an effective reference for the target pre-tensioning force of the alternative cable. After the replacement of the whole cable is completed, the new cable can be adjusted appropriately to improve the overall structural condition, depending on the actual situation of the bridge.

The above studies show that the maintenance of the stay cables is very important in order to extend the service life of cable-stayed bridges. Sometimes, there is no direct arrangement to replace the cable, since during that time the need to replace the cable was not considered. The use of software for structural modeling and analysis is important to calculate cable tension at each stage in order to compare and evaluate the

effectiveness of application solutions. Some studies also concluded that retrofitting of the cables is not always possible and sometimes the cable is in a critical condition and needs to be replaced. However, the correct cable replacement procedure must be followed to avoid disturbing the rest of the structure. The above literature suggest developing stay cables from materials that can bear the ultimate load and also resist corrosion and fatigue. Local structural damage like the loss of a cable in cable-stayed bridge can lead to the breakdown of a major portion of the structural system. Furthermore, it can result in the collapse of the whole structure. In this study, a simple model of cable-stayed bridge is considered. The cable-stayed bridge is modeled and analyzed using MIDAS Civil software. Different cases of cable loss are analyzed and discussed in the following section. The results obtained show that, as the maximum load is carried by the outermost/longest cables, designing the longest cables carefully is most the important factor to increase the service life of the bridge.

3 Analysis of Cable-Stayed Bridge for Loss of Cables

A three-dimensional finite element model of cable-stayed bridge is developed and analyzed by using "MIDAS CIVIL" software. The model is symmetric along its Z-axis. Stay cables are modeled as truss elements (80 cables). Seven cases of cable loss are considered for this study. All the parameters like cable stresses, beam stresses, beam forces, reaction forces at the support and deformed shapes will be compared. The results of the analysis are tabulated to give us a brief idea about the analysis. The total length and height of the bridge are 420 m and 90 m, respectively. The bridge has 3 continuous spans and has a width of 15.6 m. All the supports are considered as fixed during the analysis.

3.1 Bridge Details

The bridge consists of 3 continuous spans with a total length of 420 m. The midspan is of 220 m and the side span is of 100 m each. The width of the bridge is 15.6 m which has 2 lanes. Figure 1 shows the typical details of the bridge. The cases of cable loss are considered as follows:

Case 1: General case, without loss of cables.
Case 2: Innermost cable loss on both the pylons.
Case 3: Innermost cable loss on the left pylon.
Case 4: Innermost cable loss on the right pylon.
Case 5: Outermost cable on both the pylons.
Case 6: Outermost cable on the left pylon.
Case 7: Outermost cable on the right pylon.

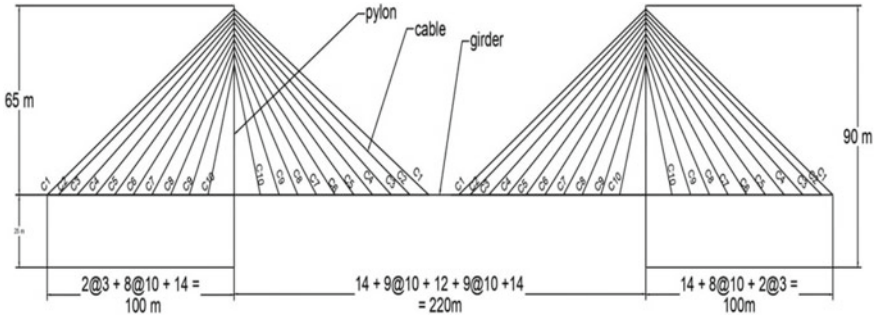

Fig. 1 Model of bridge used for analysis

3.2 Loading Conditions

The self-weight of the structural components and the additional dead load like crash barrier, etc., acting on the structure is considered for the analysis. The analysis is performed only considering the dead load. It is assumed that no live load will be acting on the structure after failure or loss of stay cable as vehicular traffic will not be allowed on the structure. The overall structure is analyzed using MIDAS Civil software. The software uses the optimization technique of Unknown Load Factor to calculate the initial prestress in the cable, i.e., the tension in the cable without loss of cables. Subsequently, the stresses in the cables are analyzed on a similar line due to various cable loss cases. Figure 2 shows the model of the cable-stayed bridge used for analyses. The parameters of the model used in the present analysis are given in Table 1.

The static load is considered for the study in order to obtain the results. The dynamic loads like wind and earthquake are not considered for the study.

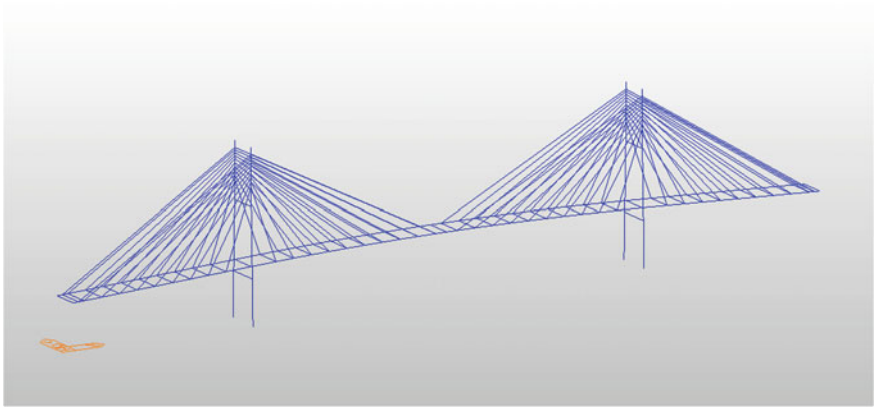

Fig. 2 Model of bridge using MIDAS Civil

Table 1 Parameters for the bridge model

S. No.	Component	Modulus elasticity kN/m^2	Poisson's ratio	Weight density kN/m^3	Area m^2	I_{xx} m^4
1	Cable	1.9613×10^8	0.3	77.09	0.0052	0.00
2	Girder	1.9995×10^8	0.3	77.09	0.3092	0.007
3	Pylon	2.78×10^7	0.2	23.56	9.200	19.51
4	Cbeam girder	1.9613×10^8	0.3	77.09	0.0499	0.0031
5	Cbeam pylon	2.78×10^7	0.2	23.56	7.2	15.79

4 Results and Discussions

4.1 Influence of Cable Loss on Forces in Cables

The analysis of forces in cables due to loss of cable was calculated for each of the above 7 cases. Results showing cable forces for Case 1 to Case 7 are shown in Table 2. Figure 3a and b shows the typical comparison of cable forces on left-hand side for the left and right pylon, respectively.

It was observed that the load on the outermost cables of both the pylons in the general case was 689.85 kN. Similarly, the load on the inner side of both the pylons was 750.53 kN for the General case. Not much variation in load in the outermost cables was observed during the loss of innermost cables. In the case where there was a loss of the outermost cable on the left side of the pylon, an increase in the load of the outermost cable on the right pylon was observed. Similarly, due to the loss of the outermost cable on the right side of the pylon, the load on the outermost cable on the left side was increased. If the innermost cables on both sides of the pylon are damaged, then the load is distributed on the other cables on the same side of the pylon. The loss of outermost cables causes major damage to the other cables as an increase in load on the remaining cables is observed.

4.2 Influence of Cable Loss on Beam Stresses

The beam stresses are evaluated for seven cases of cable loss and results are presented. Figures 4 and 5 show the beam stresses for Case 1 (general case, without loss of cable) and Case 6 (loss of left side cable on left pylon). Table 3 shows the maximum values of beam stresses observed in particular elements.

Table 2 Results for cable forces for Case 1 to Case 7

S. No.	Cable No.	Case 1				Case 2			
		Left pylon		Right pylon		Left pylon		Right pylon	
		Left side kN	Right side kN	Right side kN	Left side kN	Left side kN	Right side kN	Left side kN	Right side kN
1	C1	689.85	750.53	750.53	689.85	693.32	749.10	752.36	689.23
2	C2	695.90	853.14	853.14	695.90	698.62	852.48	854.24	695.72
3	C3	732.93	896.16	896.16	732.93	733.10	896.24	896.58	733.90
4	C4	757.09	886.32	886.32	757.09	755.69	887.04	886.24	758.59
5	C5	760.27	834.38	834.38	760.27	759.34	835.45	834.21	761.76
6	C6	738.48	751.92	751.92	738.48	742.27	752.47	752.64	739.47
7	C7	695.25	649.13	649.13	695.25	711.54	647.48	652.54	695.25
8	C8	627.17	518.17	518.17	627.17	668.58	510.94	527.36	625.38
9	C9	517.74	331.55	331.55	517.74	597.03	313.49	349.86	513.02
10	C10	324.22	66.13	66.13	324.22	–	35.68	–	316.36
S. No.	Cable No.	Case 3				Case 4			
		Left pylon		Right pylon		Left pylon		Right pylon	
		Left side kN	Right side kN	Left side kN	Right side kN	Left side kN	Right side kN	Left side kN	Right side kN
1	C1	693.63	749.76	752.08	690.57	689.53	749.89	750.81	688.53
2	C2	698.99	852.96	854.28	696.91	695.53	852.67	853.10	694.73
3	C3	733.57	896.53	896.91	734.55	732.47	895.87	895.83	732.29
4	C4	756.13	887.19	886.75	758.78	756.67	886.18	885.82	756.90
5	C5	759.68	835.49	834.57	761.65	759.94	834.34	834.03	760.36

(continued)

Table 2 (continued)

S. No.	Cable No.	Case 3				Case 4			
		Left pylon		Right pylon		Left pylon		Right pylon	
		Left side kN	Right side kN	Left side kN	Right side kN	Left side kN	Right side kN	Left side kN	Right side kN
6	C6	742.46	752.46	752.02	739.37	738.28	751.93	752.52	738.58
7	C7	711.58	647.48	649.30	695.58	695.19	649.13	652.30	694.93
8	C8	668.46	511.01	518.62	626.88	627.24	518.11	526.70	625.71
9	C9	596.73	313.70	332.58	516.73	517.95	331.37	348.40	514.13
10	C10	–	36.04	67.80	322.55	324.56	65.81	–	318.18
S. No.	Cable No	Case 5				Case 6			
		Left pylon		Right pylon		Left pylon		Right pylon	
		Left side kN	Right side kN	Left side kN	Right side kN	Left side kN	Right side kN	Left side kN	Right side kN
1	C1	–	728.25	728.25	–	–	674.36	805.39	720.52
2	C2	920.59	844.09	844.09	920.59	882.13	804.43	893.19	724.54
3	C3	899.41	896.51	896.51	899.41	870.88	871.89	920.76	754.19
4	C4	860.85	892.02	892.02	860.85	843.04	880.48	897.62	770.37
5	C5	809.34	841.81	841.81	809.34	800.90	839.86	836.00	766.57
6	C6	748.41	758.23	758.23	748.41	746.66	761.97	747.91	739.79
7	C7	685.03	651.39	651.39	685.03	686.68	657.54	642.88	694.05
8	C8	615.45	512.73	512.73	615.45	617.23	519.42	511.71	625.90
9	C9	520.10	313.76	313.76	520.10	519.24	320.84	325.25	518.50
10	C10	347.38	35.07	35.07	347.38	342.75	42.93	59.64	327.84

(continued)

Table 2 (continued)

S. No.	Cable No.	Case 7			
		Left pylon		Right pylon	
		Left side kN	Right side kN	Left side kN	Right side kN
1	C1	745.17	811.93	–	599.55
2	C2	747.37	914.29	1041.76	610.96
3	C3	770.53	946.60	1040.69	667.98
4	C4	780.10	921.23	979.83	715.06
5	C5	770.76	853.43	881.45	738.97
6	C6	740.27	757.85	764.31	732.75
7	C7	692.89	646.04	641.98	698.24
8	C8	625.21	509.69	505.86	632.12
9	C9	520.17	319.59	324.87	519.25
10	C10	332.51	52.07	69.76	319.92

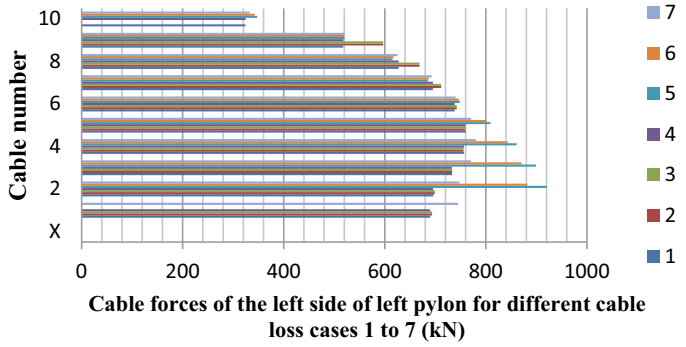

(a)

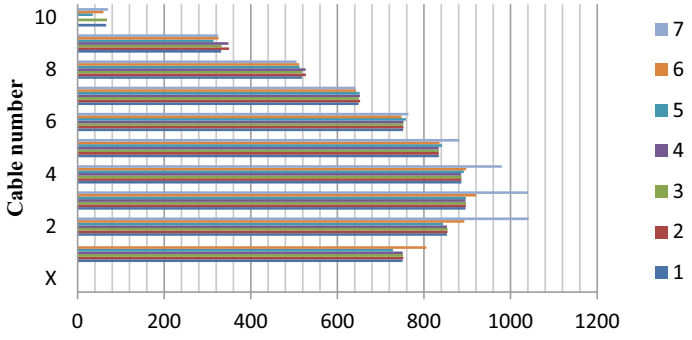

(b)

Fig. 3 Comparison of cable forces on **a** left side of the left pylon,and **b** left side of the right pylon

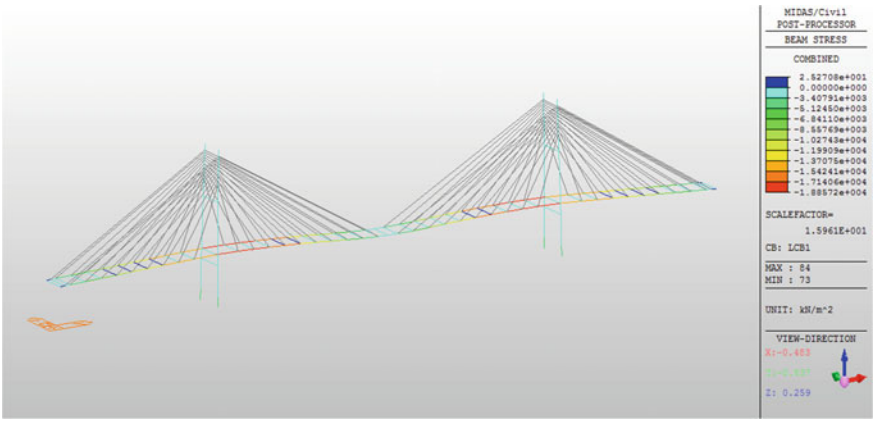

Fig. 4 Beam stresses for Case 1 (general case, no loss of cables)

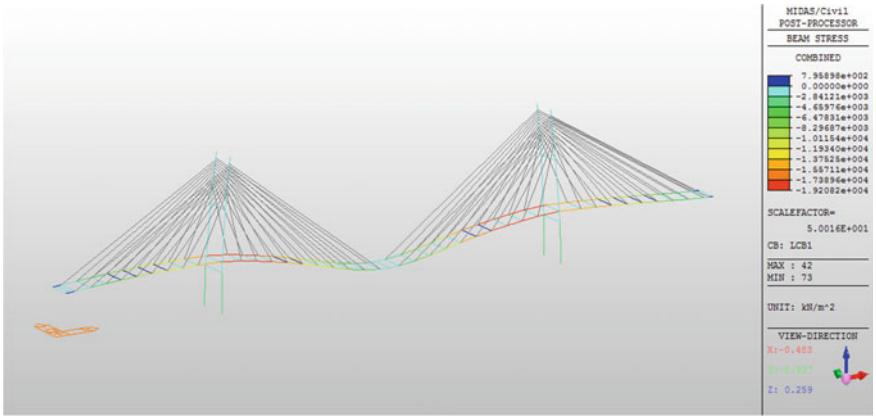

Fig. 5 Beam stresses for Case 6 (loss of left side cable for left pylon)

Table 3 Maximum values of beam stresses observed in particular elements

Element No.	Case 1 kN/m^2	Case 2 kN/m^2	Case 3 kN/m^2	Case 4 kN/m^2	Case 5 kN/m^2	Case 6 kN/m^2	Case 7 kN/m^2
52	-1.88×10^4	-1.86×10^4	-1.86×10^4	-1.88×10^4	-1.88×10^4	–	-1.95×10^4
53	-1.86×10^4	–	–	-1.87×10^4	-1.86×10^4	–	-1.94×10^4
72	-1.86×10^4	-1.86×10^4	-1.85×10^4	-1.87×10^4	-1.86×10^4	-1.90×10^4	–
73	-1.87×10^4	-1.87×10^4	-1.87×10^4	-1.87×10^4	-1.88×10^4	-1.92×10^4	–
162	-1.88×10^4	-1.86×10^4	-1.86×10^4	-1.88×10^4	-1.88×10^4	–	-1.95×10^4
163	-1.86×10^4	–	–	-1.87×10^4	-1.86×10^4	–	-1.94×10^4
182	-1.86×10^4	-1.86×10^4	-1.85×10^4	-1.87×10^4	-1.86×10^4	-1.90×10^4	–
183	-1.87×10^4	-1.87×10^4	-1.87×10^4	-1.87×10^4	-1.88×10^4	-1.92×10^4	–

The maximum value of the beam stress is observed in the inner elements of the bridge. The girders on the inner side near to pylon are subjected to maximum stresses. A similar pattern is observed in Cases 1, 2, 3, 4 and 5. However, in Case 6, the maximum stress is observed at the inner side of the right pylon for the loss of outermost on the left side of the pylon. Similarly, in Case 7, the maximum stress is observed at the inner side of the left pylon for the loss of outermost on the right side of the pylon. The maximum value of beam stress is observed for Case 7, i.e., 1.95×10^4 kN/m^2. It can be observed that, if the outermost cable of the cable-stayed bridge

is damaged on either one of the pylon, the maximum beam stresses are induced in the girder opposite to the pylon where the cable is damaged. Further, it is also observed that there is no significant increase in beam stresses in the girder due to the loss of the innermost cables.

4.3 Influence of Cable Loss on Beam Forces/Moments

The beam moments are calculated for seven cases of cable loss and the results are presented. Figures 6 and 7 show the beam moments for Case 1 (general case, without loss of cable) and Case 6 (loss of left side cable on left pylon). Table 4 shows values

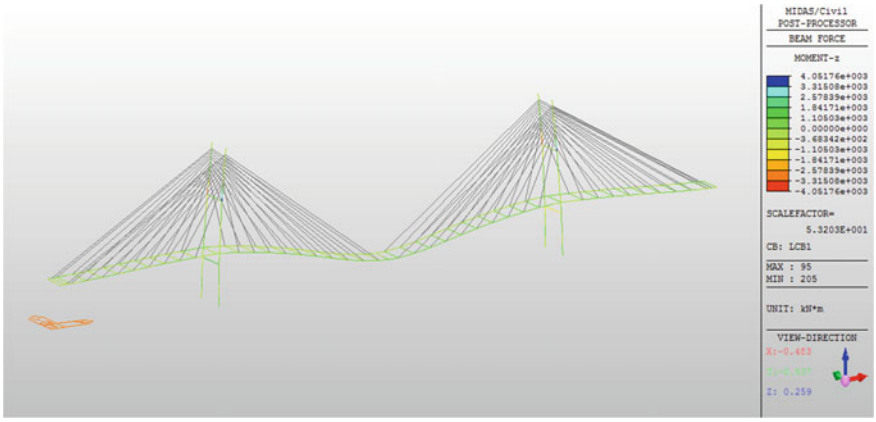

Fig. 6 Beam moments for Case 1 (general case, no loss of cables)

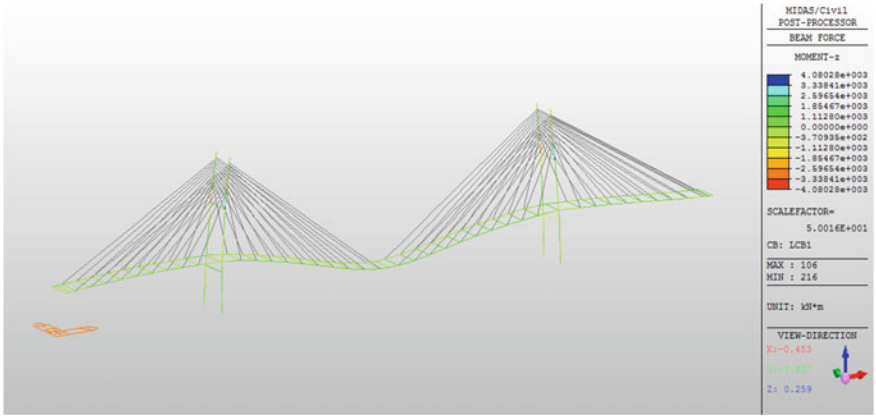

Fig. 7 Beam moments for Case 6 (loss of left side cable for left pylon)

Table 4 Maximum bending moments in the beam for various cases of loss of cable

S. No.	Case	Left pylon Mz (kN-m)	Right pylon Mz (kN-m)
1	Case 1	4.05×10^3	4.05×10^3
2	Case 2	3.97×10^3	4.03×10^3
3	Case 3	3.97×10^3	4.05×10^3
4	Case 4	4.05×10^3	4.03×10^3
5	Case 5	4.01×10^3	4.01×10^3
6	Case 6	–	4.08×10^3
7	Case 7	4.10×10^3	–

of maximum bending moments in beam for all the 7 cases.

The maximum moment in the z-direction is observed in the pylons on the modeled bridge. The maximum value of the moment is observed in the left pylon for Case 7, i.e., 4.10×10^3 kN-m. Not much difference in the values of the moment of the left and right pylon is seen in Cases 1, 2, 3, 4 and 5. However, in Case 6, the maximum value of the moment occurs only in the right pylon due to the loss of the outermost cable of the left side of the pylon. Similarly, in Case 7, the maximum value of the moment occurs only in the left pylon due to the loss of the outermost cable of the right side of the pylon.

4.4 Influence of Cable Loss on Support Reactions

The support reactions were also calculated for seven cases of cable loss and the results are presented. Figures 8 and 9 show the support reactions for Case 1 (general

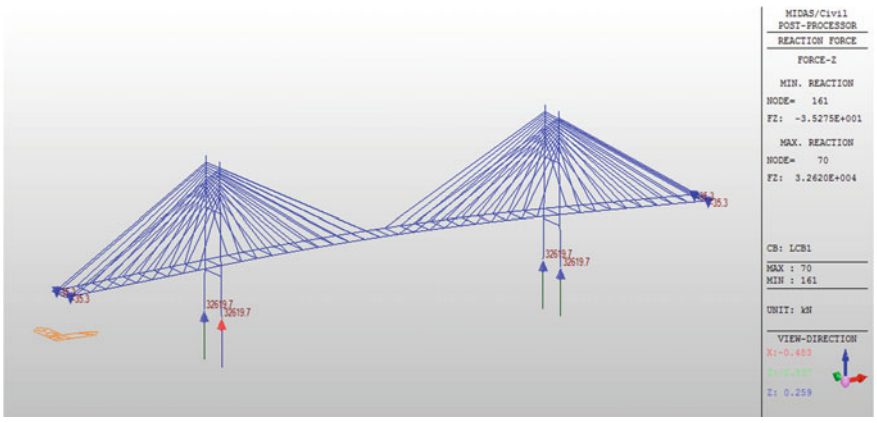

Fig. 8 Support reactions for Case 1 (general case, no loss of cables)

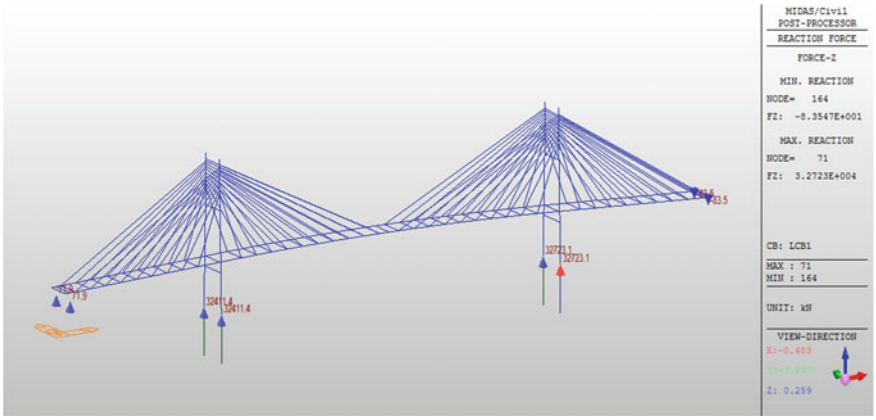

Fig. 9 Support reactions for Case 6 (loss of left side cable for left pylon)

Table 5 Maximum support bending moments and reactions

S. No.	Case	Maximum support reaction, Fz (kN)	Maximum support moment, Mz (kN-m)
1	Case 1	3.26×10^4	114.74
2	Case 2	3.26×10^4	136.68
3	Case 3	3.26×10^4	138.81
4	Case 4	3.26×10^4	112.64
5	Case 5	3.25×10^4	119.38
6	Case 6	3.27×10^4	122.11
7	Case 7	3.28×10^4	109.21

case, without loss of cable) and Case 6 (loss of left side cable on left pylon). When the structure was analyzed for support reaction, not much difference was found due to various cable loss cases. Table 5 shows the maximum support bending moments and reactions. From the above analysis, it was observed that there is no difference or variation in the reaction at the support due to various cable loss cases. The reaction at the support is 3.28×10^4 kN for all the cases. The moment at the support varies for each case. The maximum moment at the support occurs due to Case 3. It may be concluded that there is not much effect on the support reaction due to cable loss. However, the moment may vary for the same.

4.5 Influence of Cable Loss on Deformed Shape

The deformed shape was obtained for all seven cases of cable loss and the maximum values of deflection are presented in Table 6. Figures 10 and 11 show the maximum

Table 6 Maximum defection

S. No.	Case	Maximum deformation (m)
1	Case 1	−0.391
2	Case 2	−0.395
3	Case 3	−0.395
4	Case 4	−0.394
5	Case 5	−0.447
6	Case 6	−0.420
7	Case 7	−0.425

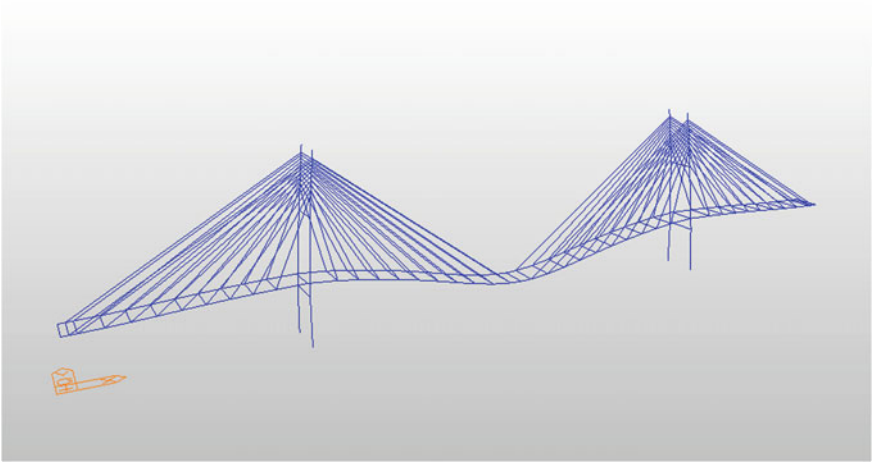

Fig. 10 Deformed shape of the bridge due to Case 1

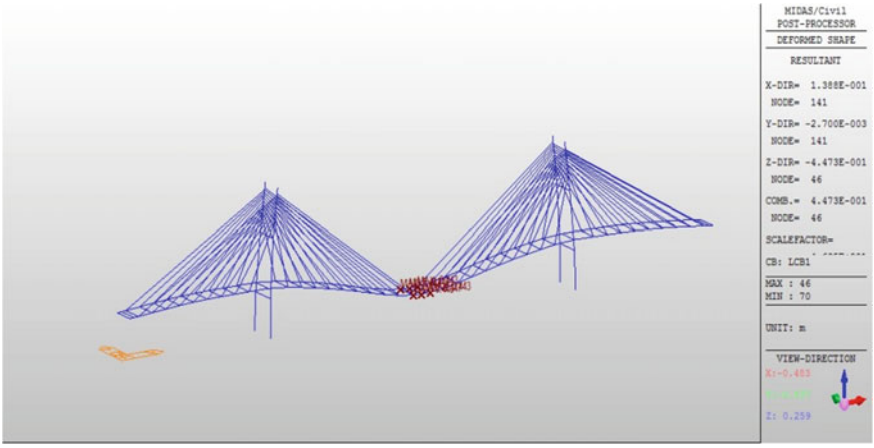

Fig. 11 Deformed shape of the bridge due to Case 5

deflection for Case 1 (general case, without loss of cable) and Case 5 (loss of outermost cable on both pylons). It can be seen that the maximum deflection was observed for Case 5.

From Figs. 10 and 11 and Table 6, the following observations are made:

In the analysis of cable-stayed bridge, the maximum deformation was 0.447 m. The maximum deformation was observed for Case 5, i.e., outermost cable loss of the structure on both the pylons. The least deformation was for Case 1, i.e., when all the cables were intact. The maximum deformation in the structure is noticed when the outermost cables are damaged. The loss of innermost cables had minimum effect on the bridge in terms of deflection. It may be concluded that, if the outermost cable is damaged, it will have an adverse effect on the cable-stayed bridge with respect to deflection. For all the cases, the maximum deformation occurred at the center of the bridge.

It is observed that the deformation at the midspan of the structure is increased up to 14.32% due to the loss of the outermost cables. However, there was not much difference in deformation due to the loss of the innermost cable. The failure of outermost cables also induces more stress in the structure than the loss of innermost cables. The structure is more affected due to the loss of the outermost cables than the loss of any innermost cables. There was not much effect on the support reaction observed due to the loss of cables.

5 Conclusions

In this analysis of the cable-stayed bridge, the cable forces, beam stresses, beam moments, support reactions and deformed shape are studied for different cases of cable loss. This analysis gives a brief idea about the effect of cable loss on the cable-stayed bridge. The following conclusions are drawn from the present study on the influence of loss of cables on cable forces, moments, stresses and deflection:

1. The loss of any of the outermost cables or either of the outermost cable of the pylon can lead to major structural deformation of the bridge or even the collapse of the bridge. Also, the stresses induced in the structure because of the failure of the outermost cable are more compared to the loss of innermost cables.
2. The deformation increased up to 14.32% due to the loss of the outermost cable. Due to the loss of innermost cables, the maximum deformation increased to 1.02%.
3. It can be concluded that the most of structural damage to the Cable-Stayed Bridge can be caused because of loss of outermost cables.
4. The maintenance of the cables is important and regular inspection will allow us to know the behavior of the cables against the load and other environmental factors.
5. Appropriate protective coating is a must for the cables during installation. The coating can decrease the damage to the cables and prolong their serviceable life.

6. Replacement of cables needs to be done very precisely and an accurate method has to be adopted so that the remaining structure is not harmed. Studies also show that short cables need to be replaced first in case of damage.
7. It can be concluded that a particular type of cable can be developed to take care of the ultimate capacity and also the damage caused by fatigue and corrosion. The carbon fiber-reinforced polymer (CFRP) cables or a composite of CFRP and steel for stays cables as a replacement to high tensile steel cables are commonly used nowadays as it has high tensile strength than steel and it resists corrosion.

References

1. Mehrabi A, Ligozio C, Ciolko A, Wyatt S (2010) Evaluation, rehabilitation planning, and stay-cable replacement design for the Hale Boggs Bridge in Luling Louisiana. J Bridge Eng 15(4):364–372
2. Pipinato A, Pellegrino C, Fregno G, Modena C (2012) Influence of fatigue on cable arrangement in cable-stayed bridges. Int J Steel Struct 12(1):107–123
3. Lavery C, Moore P, Vonk E, Nagtegaal G (2013) Replacement of the cable stays at Ewijk Bridge, The Netherlands. In: IABSE symposium report, vol 99, no 5, pp 1776–1783
4. Yamamoto Y, Kaifuku S, Kawabata S, Tokuchi T, Idani T (2014) Report on rehabilitation project of the "Binh Bridge" in Vietnam. IHI Eng Rev 46(2):42–51
5. Dao D, Nguyen V (2015) Analysis of stayed-cable replacing solution for in-service cable stayed bridge in Vietnam. In: International conference innovations in construction, CIGOS Paris 2015
6. Fu Z, Ji B, Yang M, Sun H, Maeno H (2015) Cable replacement method for cable-stayed bridges based on sensitivity analysis. J Perform Constructed Facil 29(3)
7. Ali K, Katsuchi H, Yamada H (2018) Parametric study on cable safety of cable-stayed bridge considering ultimate and fatigue limit states. J Struct Eng 64A:99–108
8. Hongjiang L (2020) Replacement of cable stays in Yonghe Bridge in Tianjin, China. Adv Civil Eng 6650393

Analysis of Alkali Activated Concrete Pavement Using Kenpave Software for Low Volume Roads

Shriram Marathe, I. R. Mithanthaya, and J. Ashwin

Abstract In the present study, an attempt was made to analyze the concrete pavement developed using alkali activated concrete (AAC) mixes. Finite element method (FEM)-based software package called KENSLAB (constituent of KENPAVE software) has been used for this study. In the study, the pavements were modeled for single wheel load applications and standard wheel load applications, obtained as per the IRC standards. The combined wheel load and temperature flexural stresses at interior, edge, and corner region were analyzed and the obtained results were compared with the models of various trial thicknesses ranging from 150 to 400 mm. The results indicate that for all the loading positions, as the thickness of the concrete increases, the combined temperature and wheel load flexural stress decreases. The values are in the range of 1.0–4.75 MPa for the wheel load application; and the range of 0.795–7.05 MPa for standard axle load applications. Most of the values are less than the 28 day flexural strength of the reference and optimum AAC mixes, making it suitable for pavement applications.

Keywords KENPAVE · Alkali activated concrete · Pavement · KENSLAB · Flexural stresses

S. Marathe (✉) · I. R. Mithanthaya · J. Ashwin
Department of Civil Engineering, NMAM Institute of Technology, NITTE, Karkala, Karnataka, India
e-mail: ram.nmamit@gmail.com

I. R. Mithanthaya
e-mail: irmithanthaya@nitte.edu.in

J. Ashwin
e-mail: jashwin2000@gmail.com

L. Nandagiri et al. (eds.), *Recent Advances in Civil Engineering*, Lecture Notes in Civil Engineering 256, https://doi.org/10.1007/978-981-19-1862-9_34

1 Introduction

1.1 General

With the extensive growth of traffic, it becomes necessary to design the pavement more effectively to function for a longer design life. For this purpose, the necessity arises to determine the design parameters such as stresses, thickness, deflections, etc., at edge, corner and interior of the concrete pavement slab. Numerical and Analytical methods can't be utilized for the above-mentioned purpose easily without giving chance to the errors due to manual computations. This indicated the necessity of Finite element methods (FEMs). As the name says, FEM means the division of a structure into a number of finite elements. It has its own credit in the field of engineering. Due to its extensive features utilization of FEM has been extended in the area of pavement analysis and design. Many software packages have been developed exclusively for the analysis of pavements. At present, FEM has embedded its root in the field of highway engineering [3].

The utility of FEM in pavement design dates back to 1960s. Finite element method for analyzing slabs on elastic foundations of both liquid and solid types was developed. Later, the method was applied to jointed slabs. The theory was also extended for solving layered foundation. The other software packages based on finite element method for designing pavements are: KENPAVE developed by Huang, Y. H (1974), ILLI-SLAB developed by Tabatabaie and Barenberg [9], WESLIQUID and WESLAYER developed by Chou and Huang (1981), FEACONS developed by Tia, M (1987), EVERFE developed by Davids et al. [2], ILSL2 developed by Khazanovich and Yu (1998), ISLAB2000 developed by Khazanovich (1999), ABAQUS developed by Hibbitt, Karlsson and Sorensen (2002) [2, 8–10]. Stresses induced by wheel loads are playing an important role in the life of rigid pavements. Most of the literature provides information regarding stress calculation using a solution based on Westergaard's equation. Using these equations, attempts were made to develop FEM packages. The effectiveness of this software in identifying the correct location of critical stresses is yet to be explored [1]. In view of this, a sincere attempt has been made to study the location of critical stresses in rigid pavement slabs under axle load using available software. The width (single lane) has been kept constant and the trial thicknesses are varied to find the stresses due to wheel load and temperature variations.

The present work consists of analyzing various concrete slabs using KENSLB package of KENPAVE software. Further stresses at different locations are analyzed with this package and the results were compared.

1.2 FEM in Pavement Analysis and Design

As known, rigid pavement has been limited to two layers (mostly) which are the subgrade and concrete slab which is rigid in nature and offers a harder surface. Rigid pavements are analyzed by plate theory using FEM. PLATE THEORY is a simplified version of the layered theory that assumes concrete slab to be a medium thick plate with a plane before bending, which remains a plane after bending. If the wheel load is applied in the interior of the slab, either plate or layered theory can be used and both should yield nearly the same stress or strain.

If the wheel load is applied near to the slab edge, say less than 2 feet from the edge, only the plate theory can be used for rigid pavements. More clearly, if we consider the finite element grid, the grid will be along the size of pavement while analyzing rigid pavements and along the depth of the pavement while analyzing flexible pavements. Figure 1 shows the 2D model of rigid pavements divided into a number of finite elements. Finite elements are divided along the plan in case of rigid pavements. The small rectangles on plan of the rigid pavement indicate the wheel loads. FEM can be effectively used to analyze the rigid pavement subjected to both wheel load and temperature stresses with utmost accuracy, even for multi-slab systems.

KENPAVE, is an FEM package developed by Huang, Y. H is specifically used for the design of both rigid and flexible pavements. It is quite simple, easy to understand and operate. Also, it offers extensive features that can be used to analyze the pavement subjected to different conditions based on stiffness matrix method.

This package can be used to analyze both rigid as well as flexible pavements considering different loading conditions. Now-a-days it is being widely used, and it was found that the results obtained from KENPAVE are compared with other conventional methods.

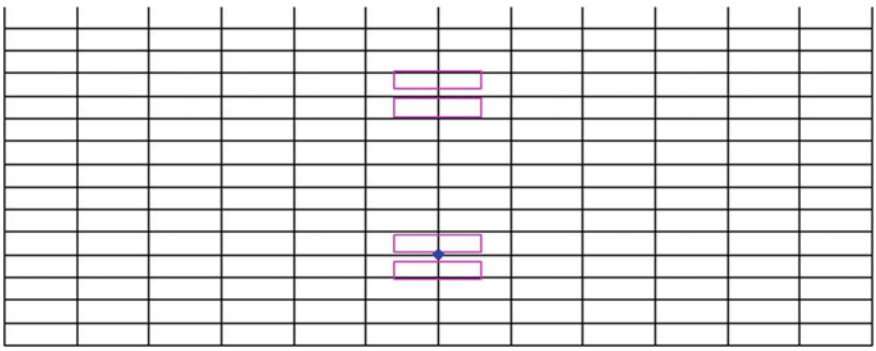

Fig. 1 2D Model of rigid pavement in FEM

2 Details on Present Analysis

In the present study, the rigid pavement for highway pavement subjected to single wheel load and single standard axle load with varying thickness is studied. Following are the few assumptions made in this present analysis: (i) Slab and sub-grade are in full contact; (ii) Pavement slab is symmetrical about both along X and Y directions; (iii) Pavement slab are homogeneous and isotropic; (iv) The thickness of the slab is uniform throughout; (v) The Temperature stresses are considered.

Different cases of loading points are considered over entire slab and stresses at these points are calculated and compared. The maximum stresses developed in the slab due to different loading patterns are analyzed using KENPAVE software. The slab dimension that is considered for this analysis is 4.50 m × 3.75 m.

The analysis for the above-mentioned slab was performed by considering different slab thickness viz. 150, 200, 250, 300, 350, and 400 mm, and three standard loading conditions. The soil support below the slab is assumed to be Winkler foundation (Dense-Liquid). The different cases of loading considered for the KENPAVE analysis are as follows: Loading at Interior, Loading at Corner, and Loading at Edge.

The following are the input parameters used for the study, which are obtained from the literatures, i.e., the published sources by the author (alkali activated concrete properties) and from the IRC guidelines [4, 6, 7]: Design Wheel Load = 51 kN; Standard Axle load = 102 kN; Modulus of Elasticity of concrete (E) = 34.2 GPa; Poisson's ratio of concrete (μ) = 0.15; Density of Alkali Activated concrete (γ) = 24.15 kN/m^3; Coefficient of Thermal Expansion (α) = 10 × 10^{-6}/°C; Temperature differential = 20 °C; Modulus of subgrade reaction (k) = 80 MN/m^3; Tyre Pressure = 0.8 MPa.

In this study, the analysis of the pavement is done for two conditions, i.e., for the application of single wheel load and standard axle load at interior, edge and corner region are studied. In this analysis, the standard axle load (i.e., single axle containing 2 wheels on either side of axle) is considered for the investigation. Two more types of axles called tandem axle, and tridem axle assembly is also in use for heavy vehicles in India. The legal axle load limit in India has been fixed as 102 kN, 180 kN, and 240 kN for single axles, tandem, and tridem axles, respectively [5]. But the studies reveal that the destruction caused (with respect to the stresses induced) by standard axle load is more than that of the tandem and tridem axle loads, due to less contact surface. Figure 2 shows the actual wheel dimensions (tyre imprints) of standard axle truck which is considered for this analysis.

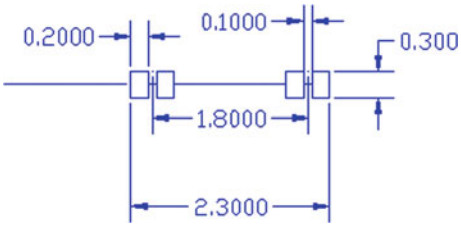

Fig. 2 Wheel configuration of standard axle (All dimensions are in m)

3 Results of KENPAVE Analysis

3.1 Stresses Due to Application of Single Wheel Load

The single wheel load application at interior, edge and corner regions for the alkali activated concrete pavement slab of dimension 4.50 m × 3.75 m modeled using KENPAVE software are presented here. The coordinates of the loading are presented in Table 1. XL1, XL2, YL1, and YL2 are the coordinates to be put as inputs in KENSLAB application; where XL1 and XL2 represent lower and upper limit of loading in *X*-axis; and, YL1 and YL2 represent lower and upper limit of loading in *Y*-axis. Typical Output images from KENPAVE analysis for interior, edge and corner loading are respectively presented in Figs. 3, 4, and 5. The results shown in these images are for 150 mm thick pavement slab. On similar lines, the results were

Table 1 Inputs for the KENPAVE for wheel load application

Region	*X*-coordinate (cm)	*Y*-coordinate (cm)	XL1 (cm)	XL2 (cm)	YL1 (cm)	YL2 (cm)
Interior loading	225	187.5	210	240	177.5	197.5
Edge loading	0	187.5	0	15	177.5	197.5
Corner loading	0	0	0	30	0	20

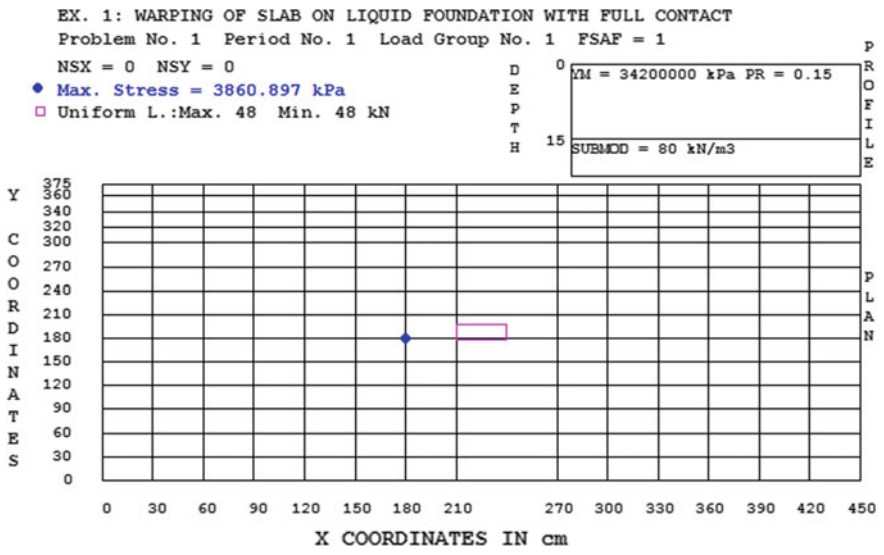

Fig. 3 Typical output for interior wheel loading for 15 cm pavement

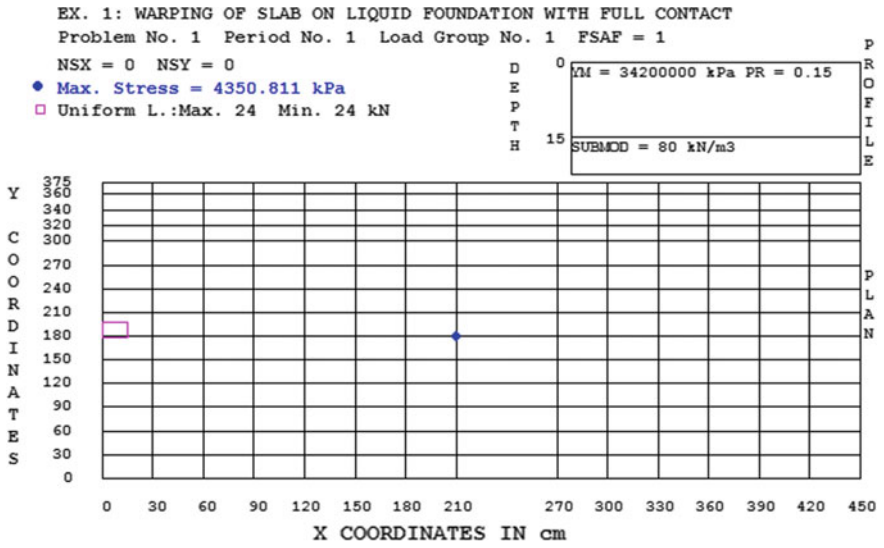

Fig. 4 Typical output for edge wheel loading for 15 cm pavement

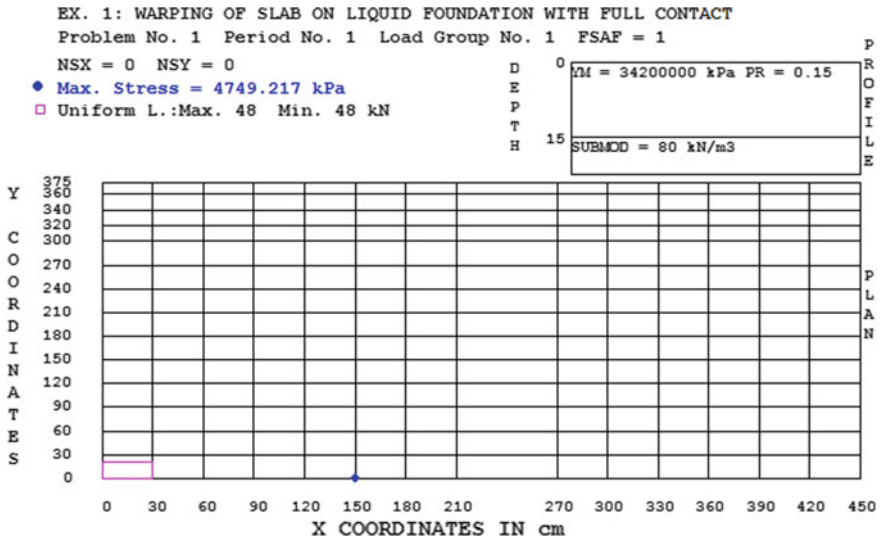

Fig. 5 Typical output for corner wheel loading for 15 cm pavement

obtained for the other trial thicknesses and the maximum stress generated due to the combined wheel load and temperature warping is presented in chart format. The results are presented in Fig. 6.

From Fig. 6, the analysis indicates that for the given conditions, the combined temperature and wheel load stress are in the range of 1.0–4.75 MPa. The maximum

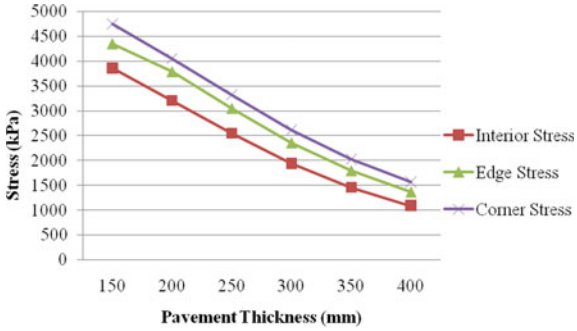

Fig. 6 Maximum stress results from KENPAVE analysis for wheel loading

values are obtained for 15 cm thick pavement slab. The interior stresses are least and the corner stresses are greater than the edge stresses in all the cases. General observation is that, as the thickness of the alkali activated pavement increases, the stress developed in the pavement decreases. The flexural strength of the optimum alkali activated concrete mix at 28 days of air curing is 5.94 MPa [6], which is far greater than the maximum tensile stress developed in the pavement slab (i.e., 4.75 MPa, for 15 cm thick pavement from Fig. 6). Thus, the alkali activated concrete is a well-suited eco-friendly alternative for the construction of concrete pavement instead of using conventional OPC-based concrete in pavement construction.

3.2 Stresses Due to Application of Standard Axle Load

Similar to the wheel load analysis, the standard axle load application at interior, edge and corner regions for the alkali activated concrete pavement slab of dimension 4.50 m × 3.75 m is carried out. The results of the analysis are presented in this section. The coordinates of the loading provided as the input in KENPAVE analysis are presented in Table 2. The coordinates of the loading XL1, XL2, YL1, and YL2 are the coordinates to be put as inputs in KENSLAB application; where XL1 and XL2 represent lower and upper limit of loading in *X*-axis; and, YL1 and YL2 represent lower and upper limit of loading in *Y*-axis. Typical Output images generated from KENPAVE analysis for interior, edge, and corner loading are respectively presented in Figs. 7, 8, and 9. The results shown in these images are for 150 mm thick pavement slab. On similar lines, the results were obtained for the other trial thicknesses and the maximum stress generated due to the combined wheel load and temperature warping is presented in chart format. The combined stress results for all the trial thicknesses are presented in Fig. 10.

The analysis indicated in Fig. 10 that for the given conditions, the combined temperature and wheel load stress are in the range of 0.795–7.05 MPa. The maximum values are obtained for 15 cm thick pavement slab. The interior stresses are least and the corner stresses are greater than the edge stresses in all the cases.

Table 2 Inputs for the KENPAVE for standard axle load application

Region	*X*-coordinate (cm)	*Y*-coordinate (cm)	XL1 (cm)	XL2 (cm)	YL1 (cm)	YL2 (cm)
Interior loading	225	187.5	210	240	72.5	92.5
			210	240	102.5	122.5
			210	240	252.5	272.5
			210	240	282.5	302.5
Edge loading	0	187.5	0	15	72.5	92.5
			0	15	102.5	122.5
			0	15	252.5	272.5
			0	15	282.5	302.5
Corner loading	0	0	0	30	0	20
			0	30	30	50
			0	30	180	200
			0	30	210	230

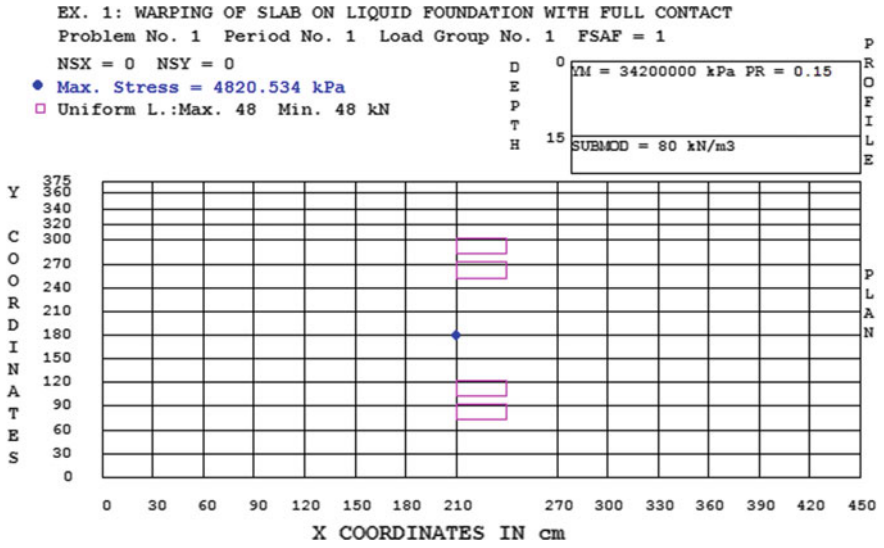

Fig. 7 Typical output for interior standard axle loading for 15 cm pavement

General observation from the results obtained is that, as the thickness of the alkali activated pavement increases, the stress developed in the pavement decreases. This observation is in line with that of the OPC-based concrete pavements from IRC: 58 [5]. The flexural strength of the optimum alkali activated concrete mix (i.e., M-15) at 28 days of air curing is 5.94 MPa (from literature [6]), which is far greater than the maximum tensile stress developed in the pavement slab (i.e., 5.25 MPa,

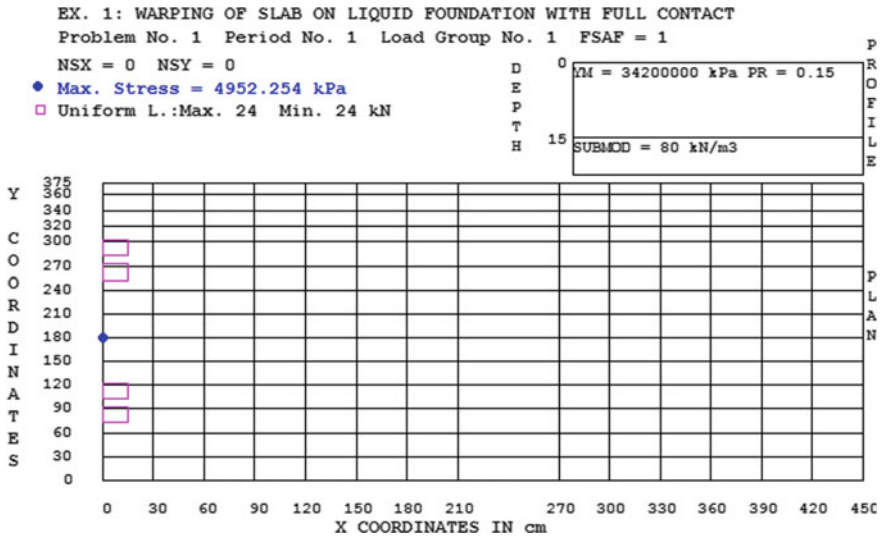

Fig. 8 Typical output for edge standard axle loading for 15 cm pavement

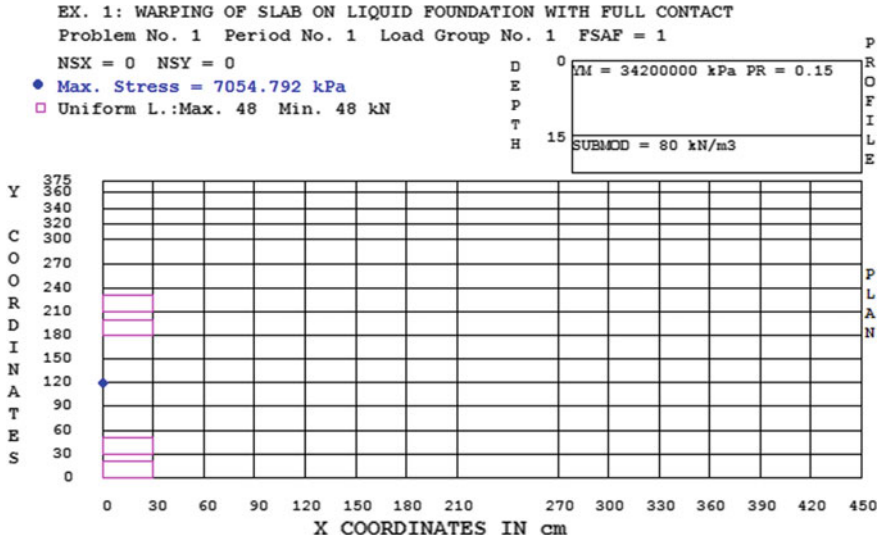

Fig. 9 Typical output for corner standard axle loading for 15 cm pavement

for 20 cm thick pavement from the Fig. 10). Thus, the developed slag-fly-ash-glass powder-based alkali activated concrete is a well-suited eco-friendly alternative for the construction of concrete pavement instead of using conventional OPC-based concrete in pavement construction if the concrete slab is of thickness greater than 200 mm. However for the concrete slab of 150 mm has shown higher value of flexural

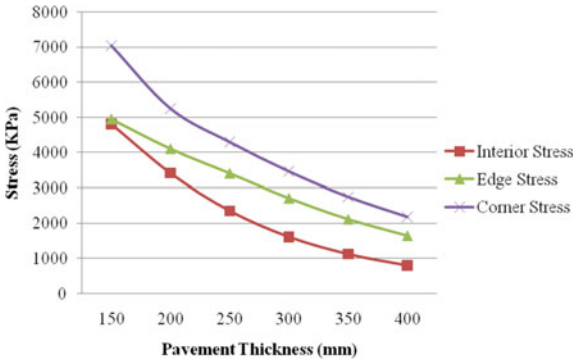

Fig. 10 Maximum stress results from KENPAVE analysis for standard axle loading

stress than the flexural strength of optimum AAC mix, which indicates that for the standard axle considerations, a slab thickness of greater than or equal to 200 mm is warranted to avoid pavement failure.

4 Conclusions

In this study, detailed investigations were carried out on the analysis of stresses for concrete pavement slab modeled using KENPAVE software using the developed alkali activated concrete for both the single wheel load application and standard axle load application at interior, edge and corner region for the concrete slab. The trial thicknesses adopted for the analysis were ranging between 150 and 400 mm, increased at an increment of 50 mm. The results indicate that for all the loading positions, as the thickness of the concrete increases, the combined temperature and wheel load flexural stress decreases. The values are in the range of 1.0–4.75 MPa for the wheel load application; and the range of 0.795–7.05 MPa for standard axle load applications. Most of the values are less than the 28 day flexural strength of the reference and optimum AAC mixes, making it suitable for pavement applications.

These results can be utilized to design the concrete pavement for the low volume roads; however, for the high volume roads the design method suggested by IRC: 58 can be adopted, which can be considered as a future scope for extended research.

References

1. Abhilash BR (2009) Analysis of rigid pavements using KENPAVE and EverFE software. National institute of technology, Surathkal, Mangalore
2. Davids WG et al (1998) EverFE rigid pavement three-dimensional finite element analysis tool. Transp Res Rec 1629:41–49. https://doi.org/10.3141/1629-06
3. Huang YH (2004) Pavement analysis and design. Pearso education Inc., New Jersey, USA
4. IRC:15-2011: Standard specifications and code of practice for construction of concrete roads. Bureau of indian standards, New Delhi (2011)
5. IRC:58-2015: Guidelines for the design of plain jointed rigid pavements design highways. Bureau of indian standards, New Delhi (2015)
6. Marathe S et al (2021) Durability and microstructure studies on slag-fly ash-glass powder based alkali activated pavement quality concrete mixes. Constr Build Mater 287(123047):1–19. https://doi.org/10.1016/j.conbuildmat.2021.123047
7. Marathe S et al (2020) Performance of slag-fly ash based alkali activated concrete for paver applications utilizing powdered waste glass as a binding ingredient. Int J Pavement Res Technol. https://doi.org/10.1007/s42947-020-0173-2
8. Shoukry SN, William GW (2015) Evaluation of load transfer efficiency measurement. Morgantown
9. Tabatabaie AM, Barenberg EJ (1978) Finite-element analysis of jointed or cracked concrete pavements. Transp Res Rec 671:11–19
10. Yanov DV, Zelepugin SA (2019) Road pavement design using the finite element method. J Phys: Conf Ser 1–8. https://doi.org/10.1088/1742-6596/1214/1/012024

Red Mud-Based Geopolymeric Clay Brick

Smita S. Borchate, Nayana P. Hoolikantimath, Basavaraj Katageri, and Praveen A. Ghorpade

Abstract In earlier works, the successful fabrication of clay bricks using geopolymeric constitutes was done. In the present study, considering the increasing demand for sustainable and environmentally friendly construction materials, the red mud-based geopolymeric clay bricks were cast by utilizing the red mud as fresh caustic, since red mud has bound caustic which participates in the reaction and is used in bulk quantity. The objective of the present study is to utilize Bayer's processed red mud from the alumina manufacturing process in clay bricks using geopolymeric approach. The production of geopolymeric bricks is considered to be one of the solutions to the ever-increasing red mud disposal problems. The geopolymeric bricks with alkali liquid to binder ratio 0.4 and sodium silicate to sodium hydroxide ratio 2.5 were studied. These bricks were optimized by varying the molarity of NaOH, along with the replacement of clay in clay bricks with varying percentages of fly ash, red mud, and curing conditions. The casted bricks were characterized by X-ray diffraction (XRD). The compressive strengths and water absorption of optimized red mud-based geopolymeric bricks were compared with conventional brunt clay bricks. The compressive strength of casted bricks was comparable to conventional clay bricks were as water absorption was less than 1.70%.

Keywords Red mud · Bayers process · Geopolymerization · Clay bricks

1 Introduction

Red mud is the solid waste remains of the digestion of bauxite ores with caustic soda for alumina (Al_2O_3) production by Bayer's process is very alkaline having pH 10 to 12.5, high solids content (15–30%), and has main constituents Fe_2O_3 (20–60%),

S. S. Borchate
Kolhapur Institute of Technology's College of Engineering (Autonomous), Kolhapur, India

N. P. Hoolikantimath · B. Katageri · P. A. Ghorpade (✉)
KLE, Dr. M.S. Sheshgiri College of Engineering and Technology, Belagavi, India
e-mail: praveenghorpade1@gmail.com

L. Nandagiri et al. (eds.), *Recent Advances in Civil Engineering*, Lecture Notes in Civil Engineering 256, https://doi.org/10.1007/978-981-19-1862-9_35

Al_2O_3 (10–30%), SiO_2 (2–20%), Na_2O (2–10%), CaO (2–8%), TiO_2 and other oxides up to 28% [1].

The research has been done on the utilization of treated red mud as a raw material for capping municipal landfills, in the construction of roads, acid land reclamation, balancing the fertility of agricultural land, scrubbing of flue gas, adsorbent to remove H_2S from industrial sludge, raw material in buildings, a catalyst for eliminating toxic elements from wastewater, amendment for remediation of contaminated soil and preparation of anti-corrosive material [2].

The previous study shows its utilization as a raw material for the production of various building products as they used red mud in bricks, concrete blocks, lightweight aggregates, roofing tiles, glass ceramics, cement industry as cement and special cement, concrete industry, and iron recovery [3, 4].

For sustainable development and conservation of natural resources, while manufacturing the clay bricks, previous studies show a flay ash-based geopolymer approach [5]. Since the main problem associated with the manufacturing of clay bricks using the calcination (firing) process is the pollution of the environment as it releases a substantial quantity of greenhouse gases, as the kilns are built in a large open area, due to its high temperature the surrounding area is making unfit for uses in the agricultural activities. The cost of the brick is also high due to the calcination process [6].

To avoid such problems associated with conventional clay brick various researchers' utilized industrial solid waste such as fly ash, waste foundry sand in clay brick as a replacement for clay to save energy and the environment. Fly ash (F-class) can be used as pozzolanic material by using high alkaline solutions through a chemical reaction that processes aluminosilicate polymers which are known as geopolymers. Geopolymer is an inorganic, amorphous alumina-silicate cementations material, and it can be synthesized by polycondensation reaction of polymeric precursor and alkali polysilicates known as geopolymerization process. Production of fly ash-based geopolymeric clay brick not only reduces the cost of conventional brick but also utilized waste generated by the industries [7, 8].

For the production of fly-based geopolymeric clay bricks, most of the researchers used sodium hydroxide and sodium silicate as an activator. These studies show that they used alkalinity from sodium hydroxide (NaOH) (as fresh caustic).

As the red mud is alkaline due to bound caustic associated with it. In the present study red mud is used as a source of caustic in the manufacturing of geopolymeric clay bricks along with other geoploymeric constituents. The main aim of the current study is to use the red mud in bulk quantity in clay bricks using geopolymeric approach and to study its physic-chemical properties to check the feasibility of its utilization compared to conventional clay bricks.

Many works through the literature, presented different techniques of optimizing different aspects of the geopolymer formulation, from material composition to uses of recycled waste Nivetha et al. have studied the utilization of red mud for partial replacement of clay in clay bricks for 5, 10, 15, 20 and 25% replace with red mud and its effect on water absorption, effloresces and compressive strength with conventional clay bricks [9]. Arjundas et al. have studied partial replacement of soil by red mud in

clay bricks. he prepared three mixed compositions for his work. The mix composition on are mix-I, mix-II, mix-III, and mix-IV are 100:0 (red mud: soil), 75:25, 50:50, and 75:25 (red mud: fly ash) with the addition of 5% and 8% of hydrated lime. He investigated the effect of red mud replacement on the compressive strength of brick. He fined the maximum wet compressive strength of 3.73 MN/m^2 with 5% lime and 4.22 MN/m^2 with 8% lime is obtained after 28 days of casting and humid curing [10]. Apithanyasai et al. [11] studied how geopolymeric bricks are safe for the environment when compared to concrete bricks. Firstly they set the compositions of materials used in the brick and then the testing was done for compressive strength. The mixed ratio used in the study are of 70:30:0, 60:30:10, 50:30:20, and 40:30:30 with 8 M sodium hydroxide (NaOH) and 98% purity sodium silicate (Na_2SiO_3) with a ratio of 2.5 [11]. Li et al., paper prepared red mud-based geopolymer materials from Municipal Solid Waste Incineration Fly Ash and red mud [12].

2 Materials and Method

2.1 Material and Chemical

In the present work, the materials used for manufacturing of red mud-based geopolymeric clay bricks were red mud obtained from local alumina refinery plant in Belagavi (unit of HindalcoIndustries Pvt. limited, located in Karnataka.), Desur clay obtained from local brick manufacturer, Belagavi, (F-class) fly ash from the Jindal South West energy, Jaigad and waste foundry as raw materials. The activator used was a combination of sodium silicate solution and sodium hydroxide solution. The Sodium silicate (Na_2SiO_3) solution was supplied by SunchemChemicals, Belagavi. The chemical composition of the Na_2SiO_3solution was Na_2O = 16.25%, SiO_2 = 34.25%, wt. ratio = 1:2.1 and water = 49.50%. Sodium hydroxide pellets (NaOH, Qualigens fine chemicals grade, 97.9% assay), sulphuric acid (H_2SO_4, s fine chemicals limited, LR grade, 38–38% assay), demineralized water (conductivity less than 10 μS/cm)), phenolphthalein and methyl orange solution (union drug and chemical company LR grade, 1%purity) and filter paper (Ashless, 125 mmϕ, Cat No 1440125).

2.2 Chemical Composition of Solid Materials Used

In the present study red mud was obtained from a local alumina refinery. It has a higher pH of 10.6, red due to the presence of ferric oxide (Fe_2O_3) and is very fine (<2.36 mm) in nature. Red mud was collected from the red mud disposal site from the alumina industry and was screened (passing through a 75 mm sieve) and used without any treatment in the present study. The red mud chemical composition is given in Table 1.

Table 1 Chemical compositions of red mud

Chemical constituents	% (w/w)
Al_2O_3	20.80
CaO	3.23
Fe_2O_3	39.99
Na_2O	5.89
SiO_2	10.84
TiO_2	6.90
P_2O_5	0.318
V_2O_5	0.25
Moist	21.40
LOM	10.60

The clay utilized in the study is composed of 50% of agricultural soil and 50% of Kaolin clay. The pH of Desur clay was 8.6. The clay exhibited the following geotechnical properties: (i) specific gravity (2.21), (ii) liquid limit (46.61%), and (iii) plastic limit (29%). The available Kaolin clay has a low shrink-swell capacity and low cations exchange capacity. The chemical composition of clay is present in Table 2.

WFS used were obtained from the local foundry which contained high silica (87.91%) and bentonite clay. The pH of foundry sand was 10.67. The other physical properties of WFS are water absorption (0.42%), specific gravity (2.18), fineness modules (1.89), and moisture content (0.11%). Waste foundry sand chemical composition is shown in Table 3.

Table 2 Chemical composition of clay

Chemical constituents	% w/w
SiO_2	90.47
Fe_2O_3	3.61
Al_2O_3	2.92
MgO	0.70
CaO	0.56
K_2O	0.24
Na_2O	0.12
P	0.09
N	0.08
LOI	1.01

Table 3 Chemical compositions of WFS

Chemical constituents	% w/w
SiO_2	87.91
Al_2O_3	4.70
Fe_2O_3	0.94
CaO	0.14
MgO	0.30
SO_3	0.09
Na_2O	0.19
K_2O	0.25
TiO_2	0.15
Mn_2O_3	0.02
LOI	5.15

2.3 Mineralogical Characteristics of Material Used

2.3.1 Red Mud

Mineralogical Characterization of red mud was carried with the finely powdered red mud passing 75 μm was analyzed for XRD in X-Ray Diffractometer (Rigaku smart lab) and values were plotted with 2θ angle varying between 10° and 90°at the scanning speed of 1°/min. XRD analysis was representing in Fig. 1 (Table 4).

The 2θ value 13.97 was matched with the standard card of silicon oxide for JCPDS card no. 871592 and 862363 with high intensity 779. The 2θ value 25.33 was matched with the standard card of aluminum oxide for JCPDS card no. 110517 and 100414 with high intensity 799. The 2θ value 18.31 was matched with the standard card of Aluminium hydroxide for standard JCPDS card no. 741775 with intensity

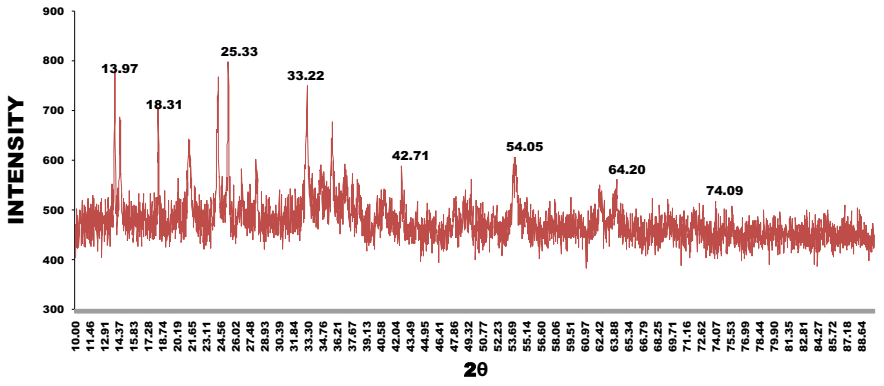

Fig. 1 XRD Analysis of red mud

Table 4 Mineralogical characterization of red mud

2ϴ	Intensity	JCPDS card no.	JCPDS card value	Composition
25.3321	799	110517; 100414	25.228,25.391	Al_2O_3
13.97	799	871592; 862363	13.989,13.956	SiO_2
33.2197	750	790007	33.225	Fe_2O_3
18.31	707	741775	18.311	$Al(OH)_3$
64.2	562	741877	64.224	FeO(OH)
54.05	606	821691	54.076	CaO
74.09	518	770444	74.01	TiO_2
42.71	589	261327	42.754	K_2O

707, 2ϴ value 64.2 was matched standard card of Iron (III) oxide-hydroxide for standard JCPDS card no. 741877 with intensity 562, 2ϴ value 54.05 was matches standard JCPDS card of calcium oxide for standard JCPDS card no. 821691 with intensity 606,2ϴ value 74.09 was matches standard card of Titanium dioxide for standard JCPDS card no. 770444 with high intensity 779,2ϴ value 42.71 was matches standard JCPDS card of Potassium oxide for slandered JCPDS card no. 261327 with high intensity 589.

2.3.2 Fly Ash

Mineralogical Characterization of fly ash was carried with the finely powdered passing 75 μm was analyzed for XRD in X-Ray Diffractometer (Rigaku smart lab) and values were plotted with 2ϴ angle varying between 10° and 90° at the scanning speed of 1°/min. XRD analysis was represented in Fig. 2 (Table 5).

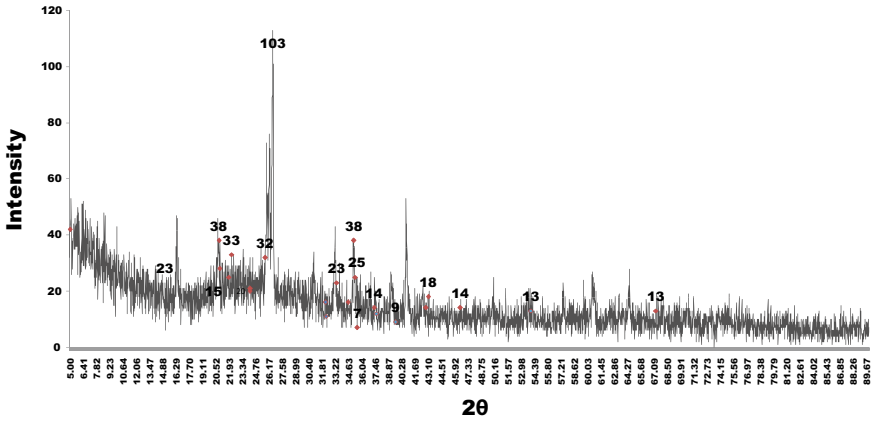

Fig. 2 XRD Analysis of fly ash

Table 5 Mineralogical characterization of fly ash

2ϴ	Intensity	JCPDS card no.	JCPDS Card value	Composition
34.736	14	880107	34.733	Al_2O_3
15.1642,20.874	23,38	840384, 821570	15.166,20.874	SiO_2
33.4066	23	840310	33.401	Fe_2O_3
20.9314, 35.5949	28,7	170912, 170912	20.934, 35.597	CaO
25.7784	32	770211	25.779	K_2O
45.0638	7	50428	45.067	SO_3
43.0144	18	751525	43.145	MgO

The 2ϴ values 15.1642, 19.9702, 26.8623, 27.0259, and 20.874 were matched with the standard card of silicon oxide for JCPDS card no. 840384, 821572, 832467, 861561 and 821570 with high intensity 23, 15, 15, 16 and 38. The 2ϴ values 34.736,35.736,35.3086 and 35.329 were matched with the standard card of aluminum oxide for JCPDS card no. 880107, 880107, 711127, and 750784. The 2ϴ value 43.0144, 42.8551, and 42.9164 was matched with the standard card of magnesium oxide for standard JCPDS card no.751525,711176 and 870652 with intensity 18, 14, and 16, 2ϴ value 33.4066, 35.6358 and 33.3862 was matches standard card of Iron (III) oxide-hydroxide for standard JCPDS card no. 840310 with intensity 23, 2ϴ value 20.9314, 35.5949, 24.1627, 32.2, and 40.64 was matches standard JCPDS card of calcium oxide standard JCPDS card no.170912, 170912, 280775, 481467 and 31123 with intensity 28, 7, 21, 16 and 40, 2ϴ value 45.0638 was matched standard card of sulfur trioxide for standard JCPDS card no. 050428 with high intensity 7, 2ϴ value 25.7784 was matched standard JCPDS card of Potassium oxide for slandered JCPDS card no. 770211 with high intensity 32.

2.3.3 Desure Clay

Mineralogical Characterization of desure clay was carried with the finely powdered passing 75 μm was analyzed for XRD in X-Ray Diffractometer (Rigaku smart lab) and values were plotted with 2ϴ angle varying between 10° and 90° at the scanning speed of 1°/min. XRD analysis was represented in Fig. 3.

The 2ϴ values 26.63, 26.68, and 26.95 were matched with the standard card of silicon oxide for JCPDS card no. 861630, 861560, 861629, 861628, and 832,469.The 2ϴ values 34.73, 35.44, and 34.43 were matched with the standard card of aluminum silicate for JCPDS card no. 880107, 750786, and 711684. The 2ϴ values 43.0378, 42.9154, and 42.9052 were matched with the standard card of magnesium oxide for standard JCPDS card no. 870653, 870652, and 780430, 2ϴ values 33.1642, 33.2152, and 33.446 were matched with the standard card of Iron (III) oxide-hydroxide for standard JCPDS card no. 860550, 850987, and 840311, 2ϴ values 37.4686, 37.4074, and 37.489 were matches standard JCPDS card of calcium oxide standard JCPDS card no. 821691, 821690, and 780649, 2ϴ values 29.3086 were matched with the

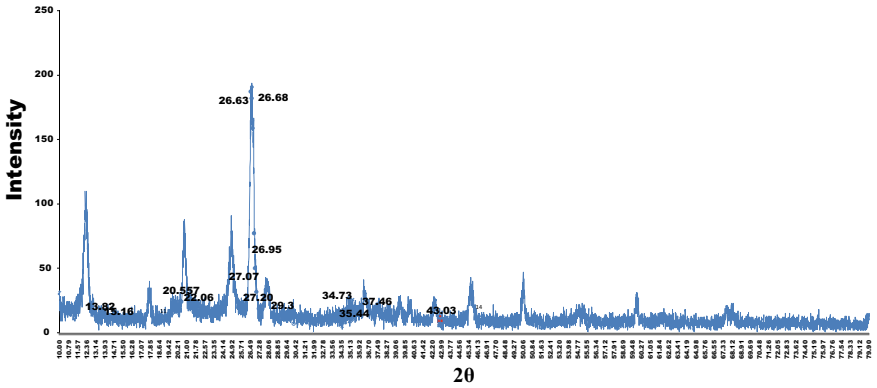

Fig. 3 XRD Analysis of desure clay

standard card of potassium oxide for standard JCPDS card no. 77476, 2ɵ values 46.2712, 33.766, and 32.7766 were matched with the standard JCPDS card of Potassium oxide for slandered JCPDS card no. 772148, 770209, and 740899. 2ɵ 35.5102, 35.398, and 35.31 were matched with the standard JCPDS card of Phosphorous for slandered JCPDS card no. 761967, 761964, and 761962, 2ɵ 32.5592, 27.34, and 27.3196 were matched with the standard JCPDS card of Phosphorous for slandered JCPDS card no. 762379, 742138, and 741457.

2.4 Alkaline Activators

The present study involves the preparation of an activator using sodium hydroxide (NaOH) and sodium silicate (Na_2SiO_3) with a ratio of $Na_2SiO_3/NaOH = 2.5$ [13]. The composition of the activator contains 0.35% Sodium hydroxide solution, 0.87%. Sodium silicate solution and 570 ml of water.

2.5 Experimental Methods

Red mud-based geoploymeric clay bricks were cast by using the wooden brick mold of size 230*110*90. To have homogeneous mixer desure clay, waste foundry sand, fly ash, and red mud were mixed in a dry state and then the activator and water are added. To avoid caustic leaching from casted bricks, the part of fresh caustic was replaced by red mud. The concentration of caustic present in red mud is depending upon the Na_2O percentage, for that XRF of red mud was carried out. From the XRF report, we know that the Na_2O percentage is 5.89%. In the present work, two sets of red mud-based geopolymeric 5 M clay bricks were cast. The first SET I was cast by

Table 6 Composition of bricks

Set No.	Compositions for brick				Solution			
	Fly ash (%)	WFS (%)	Desur clay (%)	Red mud (%)	Molarity of NaOH from red mud (25%)	Molarity of NaOH from fresh caustic (75%)	Total molarity of NaOH	Water in mL
I	30	22.85	35.36	11.78	1.25	3.75	5	150
II	40	22.85	27.86	9.28	1.25	3.75	5	150
III	30	22.85	28.3	18.79	0.62	1.87	2.5	150

using 30% fly ash, 22.85% waste foundry sand, 35.36 desur clay, and 11.78% red mud (of bound caustic of 3.75 M out of 5 M). The second SET II bricks were cast by 40% fly ash, 22.85%waste foundry sand, 27.86% desur clay, and 9.28% red mud (bound caustic of 3.75 M). And 2.5 M SET III bricks were prepared by 30% fly ash, 22.85%waste foundry sand, 28.3% desur clay, and 18.79% red mud (bound caustic of 0.625 M) (Table 6).

2.6 Curing Method Adopted

For all sets of bricks, casted bricks were allowed to be set at room temperature for 24 h. The bricks were then wrapped in wet clothes for 6 days and then kept in an oven for 24 h at 80 °C to activate geopolymeric reactions.

3 Analytical Tools

Digital pH meter (TOSHANIWAL CAT no. L.54)was used to analyze pH and it was calibrated with pH 4, 7, and 9.2 solutions (prepared by using pH capsules of 4, 7, and 9.2); Conductivity was checked using digital auto-ranging conductivity meter with a magnetic stirrer (EQUIPTRONICS, EQ.6644) and it was calibrated using 0.1 M potassium chloride (KCL) solution. A flame photometer (Systronics, 128 μc) was used for sodium analysis and it was calibrated using 20, 40, 60, 100 mg/L NaCl solutions. Universal Testing Machine (UTM) (AIMIL, Least Count 5 KN) was used for compressive strength, to weigh balance (PHOENIX, NITIRJ ENGINEERS PVT LTD. IS09001 COMPONY) was used to weigh the chemical, The finely powdered representative sample of brick was analyzed for XRD in X-Ray Diffractometer and values were plotted with 2ϴ angle varying between 100° and 900° at the scanning speed of 1°/min.

4 Results and Discussion

Compressive strength test is tested according to IS 3495 (Part 1): 1992. The classes of common burnt bricks are classified under clause 4.1 (IS 1077: 1992) which is based on the compressive strength of bricks. The class of bricks is designated as class "35" to class "3.5" whose compression strength varies from 35 N/mm^2 to 3.5 N/mm^2. The water absorption of the brick should not exceed more than 20% by weight up to class 12.5 and 15% by weight for higher classes (IS 3495 (Part 2): 1992) [14].

The compressive strength of Set I and II 5 M red mud-based geopolymeric clay brick was 2.78 N/mm2 and 1.58 N/mm^2, respectively as shown in Fig. 4. For SetIII 2.5 M, it was 1.49 N/mm^2.The testing of bricks was done for four and the average of it was taken.

The Set I and II combination brick gave desired strength when compared to Set III due to less caustic content.

Since there was poor intermolecular bonding between the materials for red mud-based geopolymeric bricks due to increased red mud content. All these red mud-based geopolymeric bricks gave less strength compared to conventional brunt clay bricks. The classes of common burnt bricks are classified under clause 4.1 (IS 1077: 1992) [15] which is based on the compressive strength of bricks. The class of bricks is designated as class "35" to class "3.5" whose compression strength varies from 35 N/mm^2 to 3.5 N/mm^2. As compressive strength is less than 3.5 N/mm^2 it will not use for load-bearing. But it can be used as a partition wall or compound wall.

Table 7 and Fig. 5 show that the water absorption was very less in red mud-based geopolymeric bricks. As the geopolymeric bricks avoid burning and the voids present in the bricks are filled by fly ash which is very fine the geopolymeric brick showed the highest resistance toward water absorption.

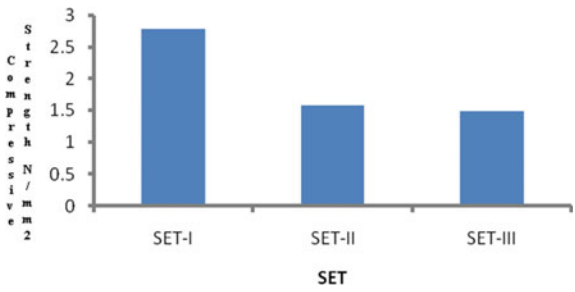

Fig. 4 Compressive strength of bricks

Table 7 Compressive strength and water absorption

Set No.	Average compressive strength in (N/mm^2)	Water absorption in (%)
I	2.786	1.79
II	1.575	1.04
III	1.486	0.668

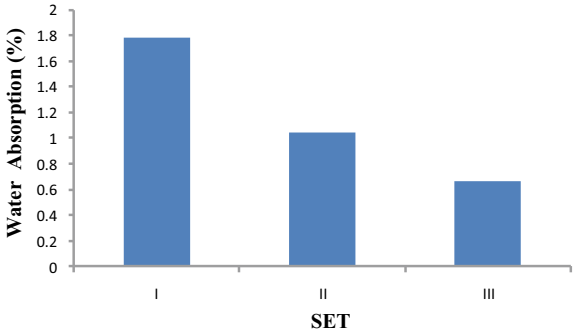

Fig. 5 Water absorption of bricks

5 Conclusions

1. The clay bricks were casted using industrial wastes such as desure clay, red mud, waste foundry sand, and fly ash. The casted bricks could successfully partially replace the natural clay by adopting geopolymeric approach.
2. The bricks casted with optimum concentration of 5 M caustic, 30% fly ash, 11.78% red mud, 35.36% desure clay, and 22.85% waste foundry sand gave the best compressive strength of 2.78 N/mm^2 with 1.79% water absorption.
3. These bricks were cured at room temperature for 6 days followed by calcination at 80 °C for one day by avoiding conventional calcination process. The present work shows that red mud can be utilized to make clay bricks without any pretreatment and caustic associated with red mud can be used in the strength reaction.
4. In three sets of bricks, SET I, SET II, AND SET III brick gave compressive strength of test 2.786, 1.575, and 1.486 N/mm^2, respectively as compared to conventional clay brick.
5. It was observed that with reduced concentration of sodium hydroxide (2.5 M), results in the reduction of compressive strength.

References

1. Luukkonen T (2017) Cem Concr Res. https://doi.org/10.1016/j.cemconres.2017.10.001
2. Peddireddy S, Narala G,Vesna Z (2020) Properties and assessment of applications of red mud (bauxiteresidue): current status and research needs. J Waste Biomass Valorization. https://doi.org/10.1007/s12649-020-01089-z19May2020
3. Wanchao L, Jiakuan Y, Bo X (2009) Application of Bayer red mud for iron recovery and building material production from alumosilicate residues. J Hazard Mater 161:474–478
4. Wan MW, Kamarudin H, Mohd MA, Aeslina K, Mohammed B (2015) A review of fly ash-based geopolymer lightweight bricks. Appl Mech Mater 754–755:452–456
5. Subramani T, Sakthivel P (2016) Experimental investigation on flyash based geopolymer bricks. Int J Appl Innov Eng Manag (IJAIEM). 5 ISSN 2319-4847

6. Shakir A, Mohammed A (2013) Manufacturing of bricks in the past, in the present and in the future: a state of the art review. IJAAS 2:145–156
7. Abdullah M, Ibrahim W, Tahir M (2015) The properties and durability of fly ash-based geopolymeric masonry bricks. J Eco-efficient Masonry Bricks and Blocks. https://doi.org/10.1016/B978-1-78242-305-8.00012-7. Copyright©2015ElsevierLtd.,Allrightsreserved
8. Sutar H, Mishra S, Sahoo S, Chakraverty A, Maharana H (2014) Progress of red mud utilization: an overview. Am Chem Sci J 4(3):255–279
9. Nivetha C (2017) Study on strength and behavior of red mud bricks. Int J Ind Pollut Control. ISSN 1227-1230
10. Das A, Malhotra S (1990) Lime stabilized red mud bricks. Int J Mater Struct. ISSN 252-255
11. Apithanyasai S, Supakata N, Papong S (2020) The potential of industrial waste: using foundry sand with fly ash and electric arc furnace slag for geopolymer brick production. Heliyon 6:1–11
12. Li Y, Min X, Ke Y, Liu D, Tang C (2019) Preparation of red mud-based geopolymer materials from MSWI fly ash and red mud by mechanical activation. J Waste Manag 83:202–208
13. Wan MW, Kamarudin H, Mohd MA, Aeslina K, Mohammed B (2014) Processing and characterization of fly ash-based geopolymer bricks. Rev Chim (Bucharest). 65(11)

Performance of Bacteria-Based Non-encapsulated Self-healing Concrete

G. Vigneswaran, K. Poonguzhali, D. Gowdhaman, A. Sumathi, and A. Rajesh

Abstract This study focuses on the mechanical performance of non-encapsulated self-healing concrete using bacteria by direct application. The influence of *Bacillus subtilus* bacteria on crack healing, compressive strength regains, sorptivity, water absorption, impact strength, and concrete microstructures was examined in this study. M30 grade concrete with a water-cement ratio of 0.45 was used for control specimens. For bacteria incorporated specimens, water content was fully replaced with three different percentage of healing agent. The healing agent comprises of 10, 20, 30% bacterial solution (BS) and 90, 80, 70% nutrient solution (NS) was directly mixed with concrete mixtures with bacillus subtilis bacterial concentration of 10^5 cells/ml and the mixtures were designated as BC 1, BC 2, and BC 3. The concrete specimens were subsequently cured by two methods; wet-dry cycle and full-wet and the results were compared with the control. The cast specimens were immersed in water for 24 h, then held at room temperature for another 24 h in the wet-dry cycle, which was repeated for 28 days. Specimens were immersed in water for 28 days during full-wet curing. However, the curing water was changed every 24 h to ensure that the bacteria had enough oxygen to precipitate calcium carbonate. Results show that the addition of bacteria enhances the mechanical properties compared with control concrete. SEM and XRD results show the micro-structural morphology and the calcium carbonate precipitation.

Keywords Self-healing concrete · Crack healing · Compressive strength · Split tensile strength · Impact strength · *Bacillus subtilus*

G. Vigneswaran · K. Poonguzhali · A. Sumathi (✉) · A. Rajesh
School of Civil Engineering, SASTRA Deemed to be University, Thanjavur, India
e-mail: sumathi@civil.sastra.edu

D. Gowdhaman
School of Chemical and Biotechnology, SASTRA Deemed to be University, Thanjavur 613401, India
e-mail: gowdhaman@biotech.sastra.edu

L. Nandagiri et al. (eds.), *Recent Advances in Civil Engineering*, Lecture Notes in Civil Engineering 256, https://doi.org/10.1007/978-981-19-1862-9_36

1 Introduction

Self-healing concrete or microbial concrete are other names for bacterial concrete. It's a sort of concrete that can create limestone organically to fill in fractures on the surface of any concrete construction. Bacteria that can continuously precipitate calcite can be embedded in concrete to create "Bacterial concrete". A healing agent that works by converting nutrients into limestone by microorganisms implanted in concrete. Concrete wakes up when it is cracked or deconstructed and comes into contact with water and oxygen. With the help of nutrients, the bacteria will multiply and start to produce Calcium carbonate which helps in filling the cracks. The limestone solidifies on the cracked surface. Preparation of bacteria is of three types, i.e., Direct application, encapsulation, and immobilization. CEMI and CEMIII with 60% Ground Granulated Blast Furnace Slag (GGBS) with and without non-encapsulated iron aerobic respiration bacteria, according to [1]. The water absorption velocity was dramatically reduced when a micro agent was added to CEMI and CEMIII concrete samples. When microbial is introduced to concrete in the form of CEMIII, water absorption is reduced by at least 25% [2] represents the research was conducted out with 6 different microbial concentration levels in concrete water mixtures. Concrete specimens were cured for 7, 14, and 28 days. In the samples with a microbial concentration of 10^5 cells/ml of water, a highest of 32% rise in compressive strength, 14% growth in split tensile strength, and 29% enhancement in flexural strength were reported. Kunal et al. [3] identified in their study that after 91 curing days, utilizing 10% bacterial-treated in concrete resulted in 26.6% increases in strength as compared to the control (CC) treatment. Water absorption (64%) and porosity (53%) both decreased significantly, whereas chloride permeability decreased by 22%. According to Luo et al. (2016), adding the Type 1 ingredient to cementitious material reduced compressive strength by roughly 14.7%, 6.8%, and 0.1% after 3,7, and 28 days of curing, respectively. Type 2 admixture causes a compressive strength loss of roughly 1.6 and 2.2% after 3 and 7 days of curing, respectively, and an 8.1% rise after 28 days of curing. After three days, the carbonation depths of control samples for Type 1 and 2 specimens were 6.6 mm, 7.0 mm, and 6.5 mm, respectively. Reference [4] studied the present investigation looked at how Bacillus sp. CT-5, isolated from cement, affected strength as well as durability. Also, in relation to bacterial cells, the compressive strength of cement mortar boosted by 36%. As a consequence of bacterial calcite deposition, treated cubes consumed 6 times less moisture than control cubes. Pachaivannan et al. [5], The strength viz., compressive, split tension, and flexure of 14 days old bacterial concrete was higher than that of CC on the 7th, 14th, and 28th day. Ureolysis of *Bacillus Subtilis* in yeast extract and peptone medium results in $CaCO_3$ precipitation, according to Nguyen et al. [6]. The addition of a microbial adjuvant resulted in a large reduction in permeability of gas of around 70% after 210 days. After 44 days of water immersion, the 400 m fissures in the bacterial concrete were fully closed. De Belie et al. (2015) studied the mechanical properties like compressive and tensile properties of three flexure beams (40 mm × 10 mm × 160 mm) by encapsulating, Bacillus sphaericus in Modified Alginate hydrogel. On addition of 0.5 and

1% of Modified Alginate hydrogel tensile strength was reduced by 15.6 and 30%; compressive strength was reduced by 16.2 and 23.4%. Hence higher dose addition of Modified Alginate hydrogel reduces the mechanical properties. Navneet [7] evaluated the effect of Sporosarcina pasteurii bacteria in silica fume added concrete. Mechanical properties like compressive strength, water absorption and rapid chloride permeability test was conducted. Results indicate that addition of Sporosarcina pasteurii in concrete, Compressive strength was increased by 38.2 MPa for 28 days and 44 MPa for 91 days. Meanwhile, porosity and water absorption capacity are reduced. Nidhi [8] conducted compressive strength and tensile strength for 150 mm × 150 mm × 150 mm cube and 150 mm dia with 300 mm height cylinder specimens. *Bacillus subtilis*, Bacillus megaterium and consortia bacteria were added in concrete specimens. Results concluded that compared to conventional concrete, compressive strength was increased by 14.36, 22.58, and 15.86% and split tensile strength was increased by 25.3, 18.29, and 19.51%. According to Shanmuga Priya et al. [9] by replacing cement with Micronized Biomass Silica (MBS) at 4%, 8%, and 12% and bacteria addition, strength, and durable properties were compared. With 20 ml bacterial solution and cementitious addition of 8% compressive strength was increased by 13.53%, splitting tensile strength increased by 16.38% and flexural strength increased by 13.32%. M. [10] Bacillus paralicheniformis was extracted bacteria from concrete made of Portland pozzolanic cement containing all composites. 28-day Compressive strength of bacteria added Portland pozzolanic cement concrete is 2.8% which is lower than conventional concrete and bacteria added Portland cement type 2 is 1.96% lower than conventional concrete. Water absorption percentage of the two types of cement concrete is 0.07 and 0.19, respectively. Salman Rais et al. [11] used gram-positive aerobic bacteria, Bacillus megaterium in recycled aggregate concrete with supplementary cementitious additions of silica fume and metakaolin. With micro silica and metakaolin additions, 28-day compressive strength ranged from 73 to 93% but for 120 days the compressive strength tends to decrease from 57 to 85%. Ratio of permeability coefficient. For 28 days ranged from 143 to 173% but for 120 days it increased from 163 to 181%. The aim of the current study is to enhance the mechanical performance of bacteria-based non-encapsulated self-healing concrete by direct application adopting two curing stages. The water has been completely replaced by the healing agent. The healing agent constituted 10%, 20%, 30% of *Bacillus subtilus* bacterial solution (BS) and 90%, 80%, 70% of nutrient solution (NS), respectively and specimens were cast and the bacteria concrete results were compared with the CC.

2 Experimental Programme

2.1 Materials and Methods

Ordinary Portland cement (OPC) 53 grade, with a specific gravity (SG) of 3.15 and a fineness modulus of 6.95%, was used confirming IS 12269 [12]. Fine aggregate (FA) river sand was used with a maximum size of 4.75 mm and a SG of 2.65 according to IS 383 [13]. Crushed gravel with a SG of 2.74 was used with sizes 12.5 and 20 mm. ***Bacillus subtilis*** was initially cultured and inoculated in the nutrient medium and Nutrient solution is prepared with Calcium nitrate, urea, and yeast extract concentrations was 5 g/l, 5 g/l, and 3 g/l by cement mass, respectively. Figure 1 shows the bacteria which is prepared in the petri dish. *Bacillus subtilus* properties are shown in Table 1.

Fig. 1 Bacillus subtilus in petri dish

Table 1 Morphological and biochemical characteristics

S. No.	Test	Observation
1	Configuration	Circular lobate
2	Elevation	Flat
3	Pigmented	White
4	Gram reaction	Gram positive
5	Shape of isolate	Rod in chains
6	Margin	Irregular
7	Endospore staining	Central spore

2.2 Preparation of Bacterial Cell Solution

To prepare the media and reagent preparation, 200 ml distilled water is taken in 250 ml conical flask and Luria broth(25g/l) is added to it and autoclave at 121 °C for 20 mins, cool it down for 20mins in Fig. 2. Then 50ml distilled water is taken in 100 ml conical flask, LB Agar(15g/l) is added to it and autoclaved then pour the medium into a sterile petri dish and cool it to solidify as shown in Fig. 3. To prepare the pure culture, pick a single colony from the old culture and do a quadrant streak and incubate the plate at 37 °C for 24 h as shown in Fig. 4. The methodology is that the broth culture is prepared by inoculating the medium conical flask with bacteria and kept in incubator for 24 h and the bacterial solution is prepared in cultured medium in falcon tubes, which are spun in centrifuge machine for about 10 min. The supernatant and pellets were resuspended in saline solution, i.e., NaCl solution

Fig. 2 Broth medium preparation

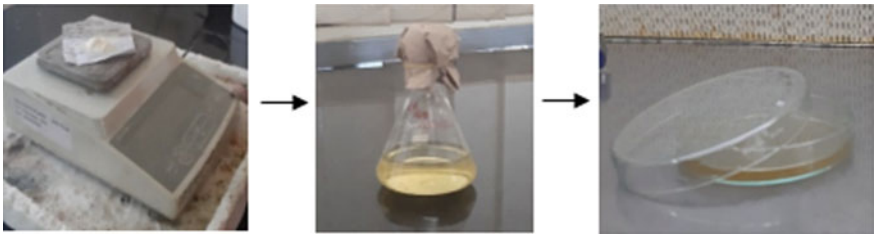

Fig. 3 Reagent preparation

Fig. 4 Pure culture preparation

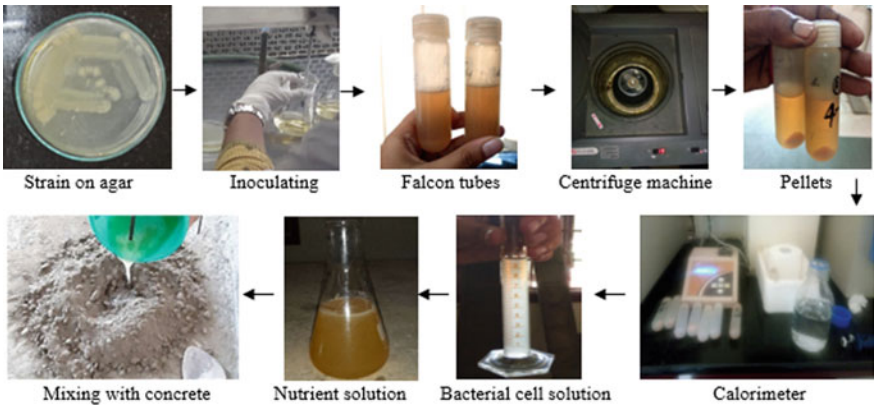

Fig. 5 Preparation of bacterial cell solution

(9g/l). Now, cell concentration is adjusted to 10^7 cells/ml in calorimeter to get the bacterial cell solution as shown in Fig. 5.

2.3 Mix Details and Cast Specimens

Mix design ratio for M30 grade of concrete was obtained as 1:1.70:2.33 as per IS 10262-2019 [14] with fixed water-cement ratio 0.45. In this work, mixes were prepared for different percentage of bacterial solution (BS) of 10%, 20%, and 30% and nutrient solution (NS) of 90%, 80% and 70% respectively. For each mix thespecimens were cast and cured under two different curing methods and the mix proportions details are shown in Table 2. Four different mixes were prepared i.e., Control concrete (CC) which is prepared with ordinary water, Bacterial concrete 10% (BC1), Bacterial concrete 20% (BC2), Bacterial concrete 30% (BC3) is prepared with healing agents by adopting two curing stages i.e., Wet-Dry (WD), Full-Wet (FW). Compressive strength (CS) was determined using 100 mm cube samples, according to IS: 516-1959 [15]. Cylinders of 100 mm diameter and 200 mm height were used for split

Table 2 Mix proportions (kg/m^3)

Mix	Cement	FA	CA	Water (0.45)	
				BS	NS
CC	437.77	811.1	1111.7	196.99	
BC 1	437.77	811.1	1111.7	19.7	177.29
BC 2	437.77	811.1	1111.7	39.4	157.59
BC 3	437.77	811.1	1111.7	59.1	137.89

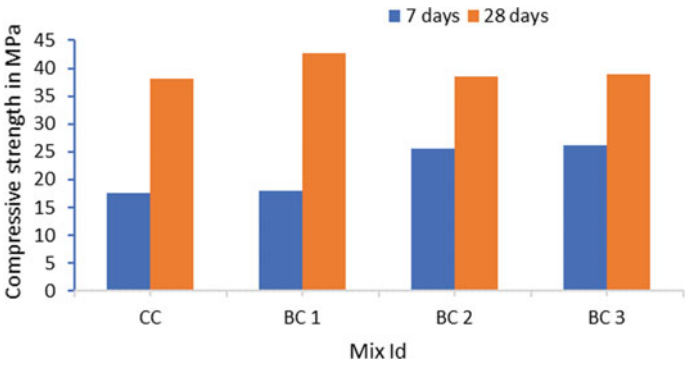

Fig. 6 Compressive strength results for 7 and 28 days

tensile strength (STS). To calculate the impact energy specimens of 150 mm in diameter and 64 mm in height were used in accordance with ACI 544 [16]. Sorptivity test was performed on cylindrical samples measuring 100 mm in diameter and 50 mm in height in accordance with ASTM C1585 [17]. Water absorption was measured using 100 mm cube specimens in accordance with ASTM C642 [18].

3 Results and Discussion

3.1 Compressive Strength (CS)

Figure 6 depicts the CS of cubes after 7 and 28 days. The CS of the BC is higher than the CC under full-wet curing due to the presence of bacteria. The CS of BC is higher than CC after 7 days and 28 days of curing. The increase in CS of BC 1 using *B. Subtilus* for 7 days is 2.43% and for 28 days is 12.12% higher than CC. The percentage increase in CS of BC 2 using *B. Subtilus* for 7 days is 44.55% and for 28 days is 1.23% higher than CC. The percentage increase in CS of BC 3 using *B. Subtilus* for 7 days is 48.52% and for 28 days is 2.52% higher than CC.

3.2 Regained Compressive Strength

Figure 7 shows regained CS of pre-cracked specimen on each mix After the bacterial specimens (BC 1, BC 2, BC 3) were pre-cracked at the age of 3 days under full-wet curing, the bacterial samples are cured under both the curing condition, i.e., Full-Wet and Wet-Dry conditions. After 25 days of curing process, the samples are tested in compression machine until the peak load. The regained CS of BC 1 in FW curing at 25th day was increased by 75.23% and in WD curing at 25th day was

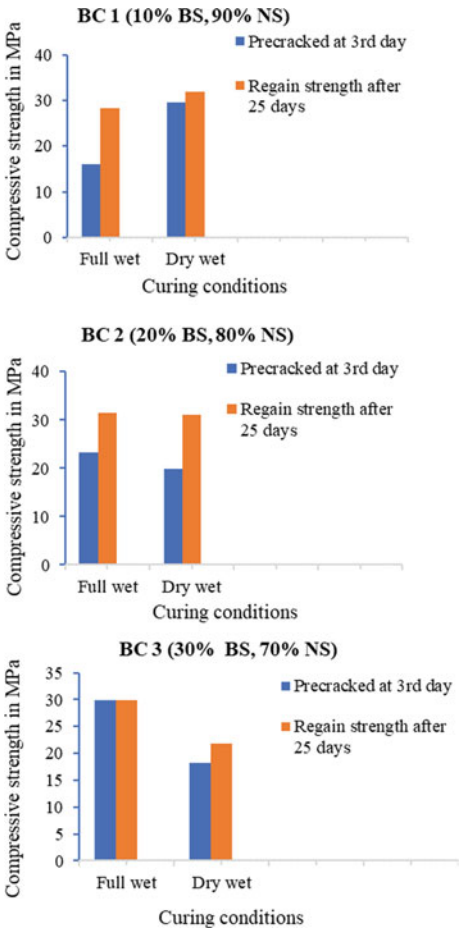

Fig. 7 Regained compressive strength on both curing conditions

increased by 8.31% when especially in comparison to the third day's pre-cracked strength properties. The regained compressive strength of BC 2 in FW curing at 25th day was increased by 35.43% and in WD curing at 25th day increased by 56.81% compared to the 3rd day pre-cracked strength. The CS of BC 3 in FW curing at 25th day was increased by 0.33% and in WD curing at 25th day was increased by 19.58% compared to the 3rd day pre-cracked CS.

3.3 Split Tensile Strength (STS)

The STS is performed after 28 days of full-wet curing and the results are shown in Fig. 8. Due to the addition of bacteria, the tensile strength of (BC) is generally higher than CC. The increase in the tensile strength of BC 1 is 12.13 % higher than

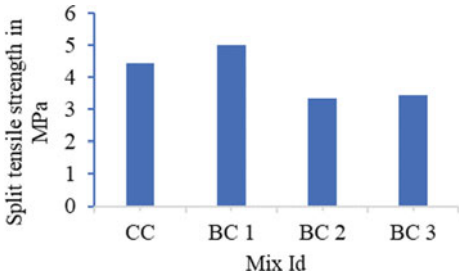

Fig. 8 Split tensile strength for 28 days

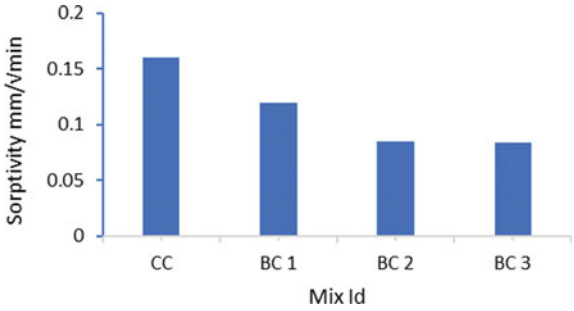

Fig. 9 Sorption coefficient results

the CC. BC samples containing 20 and 30% of bacteria show lesser tensile strength compared to the CC and the BC containing 10% of bacteria.

3.4 Sorptivity

Sorptivity results for CC and BC after 28 days of curing are shown in Fig. 9. The samples without microbes, i.e., CC, clearly demonstrated greater sorptivity than that of the samples with microbes. Sorptivity tends to decrease as microbes are added to the mix, and the setup becomes denser. Because of the enhanced filling potential of the capillaries and gaps, the sorptivity value reduced significantly to much more calcium silicate hydrate powder and excessive curing effectiveness in the mixture [3, 19, 20]. Percentage of sorptivity in BC 1, BC 2, BC 3 was 33.33%, 88.23%, 90.47% compared to the CC.

3.5 Water Absorption

The water absorption percentage of each mix is calculated for full-wet curing method at 28 days. The water absorption percentage gets decreased for the BC compared

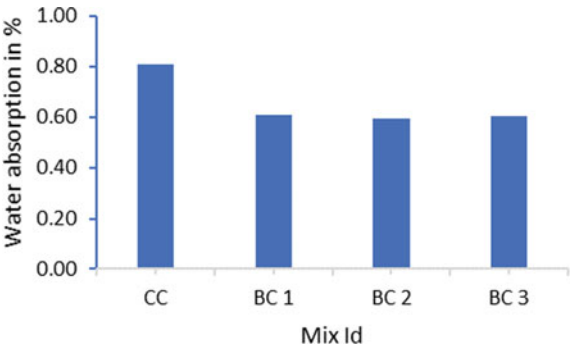

Fig. 10 Water absorption results

to the CC as shown in Fig. 10, presence of bacteria resulting in the filling of tiny capillaries and gaps than CC.

3.6 Impact Strength Test

To identify the impact strength of the concrete according to ACI 544. Impact energy is calculated for the interval of 28 days after full-wet curing. Figure 11 shows the crack pattern which appears on the bacterial and CC specimens. The impact energy was calculated for CC and bacterial specimens (BC 1, BC 2, BC 3) at first crack and final failure, and the results are shown in Fig. 12. Due to the addition of bacteria in the bacterial specimens which has higher number of blows and impact energy compared to the CC at first crack and final failure. The bacterial specimens (BC 3) show higher impact energy compared to Bacterial specimen (BC 2, BC 3). The figure shows the impact energy on each mix and number of blows on each mix. Thus, it concluded that the addition of bacterial spore in the concrete will give maximum strength.

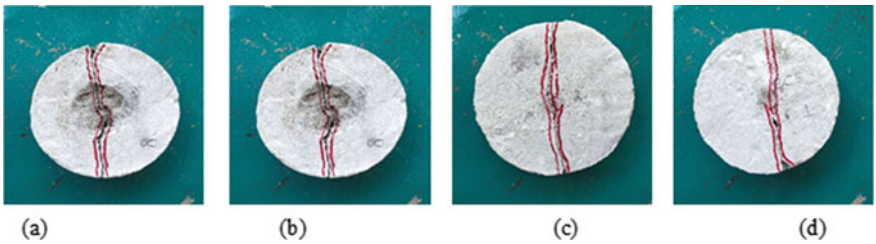

Fig. 11 Crack formation pattern **a** CC, **b** BC 1, **c** BC 2, **d** BC 3

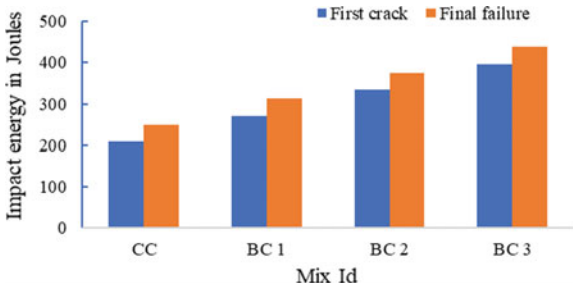

Fig.12 Impact strength test for 28 days

3.7 Visual Observation and Microscopic Observation of Bacterial Concrete

The crack healing efficiency was examined at intervals of 0, 7, 14 days under wet-dry and full-wet conditions for BC 1, BC 2, BC 3. After 28 days of healing period, the samples BC 1, BC 2, BC 3 were gathered in order to visualize the self-healing efficiency shown in Figs. 13, 14, 15, respectively, and microscopic view is shown in Fig. 16.

Table 3 shows the width of the cracks which is before healing and after healing of WD and FW. The crack healing percentage was examined in BC 1 (WD) is about 19% at 7 days, 39% at 14th day, and 84% at 28th day where in BC 2 (WD) is about 21% at 7th day, 44% at 14 days and 94% at 28 days and in BC 3 (WD) was 23% at 7 days, 47% at 14 days and 95% in 28 days, this ensures that cracks are healed fully at 28 days and it was not able to view. Crack healing percentage was examined in BC 1 (FW) is about 19% at 7 days, 39% at 14 days, and 84% at 28 days where in BC 2 (FW) is about 21% at 7 days, 43% at 14 days and 93% at 28 days and in BC 3 (FW) was 22% at 7 days, 46% at 14 days and 94% in 28 days (Table 4).

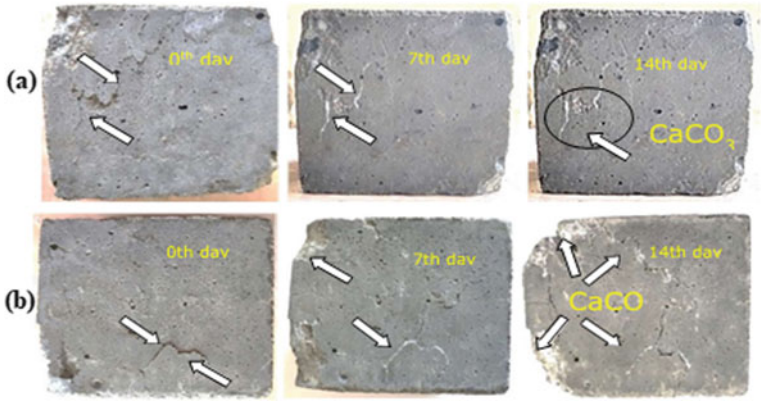

Fig. 13 Visual observations of BC 1 (**a**) cracks under FW and (**b**) cracks under WD

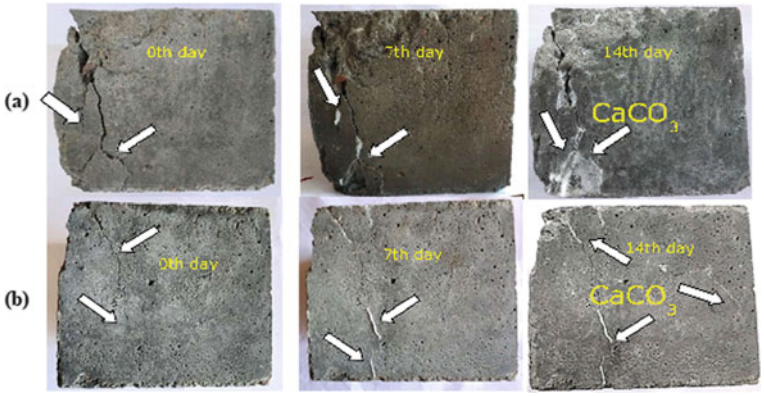

Fig. 14 Visual observations of BC 2 (**a**) cracks under FW and (**b**) cracks under WD

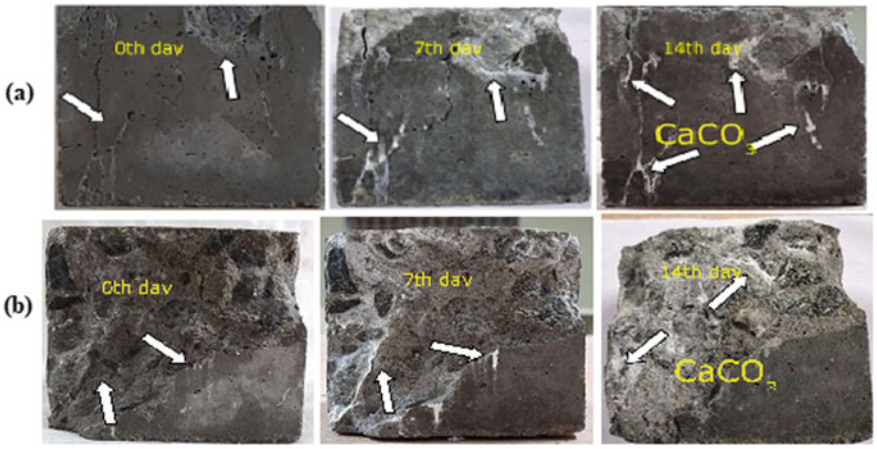

Fig. 15 Visual observations of BC 3 (**a**) cracks under FW and (**b**) cracks under WD

3.8 Scanning Electron Microscope (SEM)

Initially, the fracture was examined microscopically with a compact microscope. SEM analysis has been used to examine the morphology of the crushed test sample after 28 days and define the quality of material precipitated (i.e., calcium carbonate) to even further enhance the structural morphology of its particles [3, 6, 19–23]. To make a comparison of the microstructures of the BC 1, BC 2, BC 3, and CC samples, specimens were tested from the control specimen and the specimens containing bacteria. The SEM images are shown in Fig. 17.

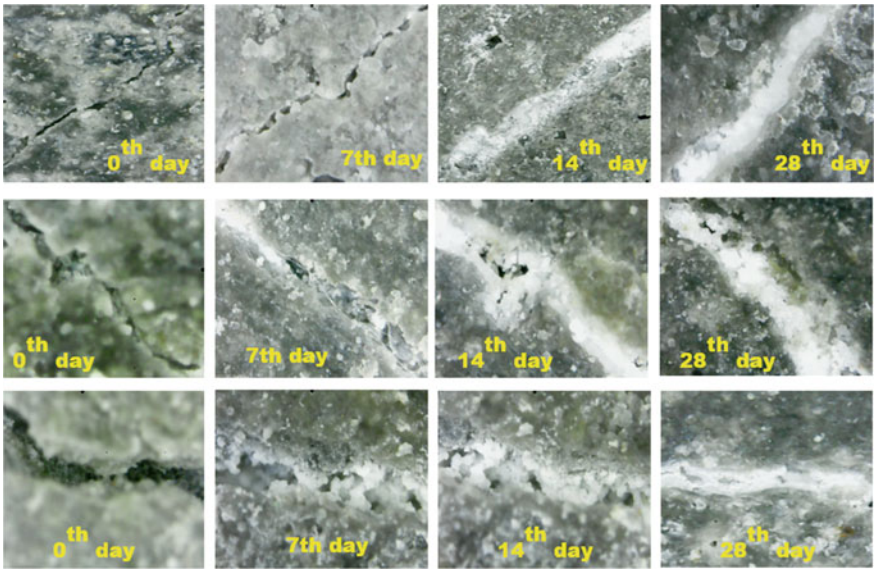

Fig. 16 Microscopic observations of cracks BC 1, BC 2, BC 3

Table 3 Crack width before and after healing of WD

Mix id (WD)	Initial crack width (mm)	Crack healed size (mm)			Crack healing percentage		
		7 Days	14 Days	28 Days	7 Days	14 Days	28 Days
BC 1	0.39	0.315	0.234	0.055	19	39	84
BC 2	0.37	0.295	0.214	0.035	21	44	94
BC 3	0.35	0.275	0.194	0.018	23	47	95

Table 4 Crack width before and after healing of FW

Mix id (FW)	Initial crack width (mm)	Crack healed size (mm)			Crack healing percentage		
		7 Days	14 Days	28 Days	7 Days	14 Days	28 Days
BC 1	0.40	0.325	0.244	0.065	19	39	84
BC 2	0.36	0.285	0.204	0.025	21	43	93
BC 3	0.34	0.265	0.184	0.020	22	46	94

3.9 X-Ray Diffraction (XRD)

XRD findings show a combination of precipitation of nutrients produced by bacteria, which include calcite (Ca), aragonite (AR), and vaterite (Va). Fig. 18 shows the

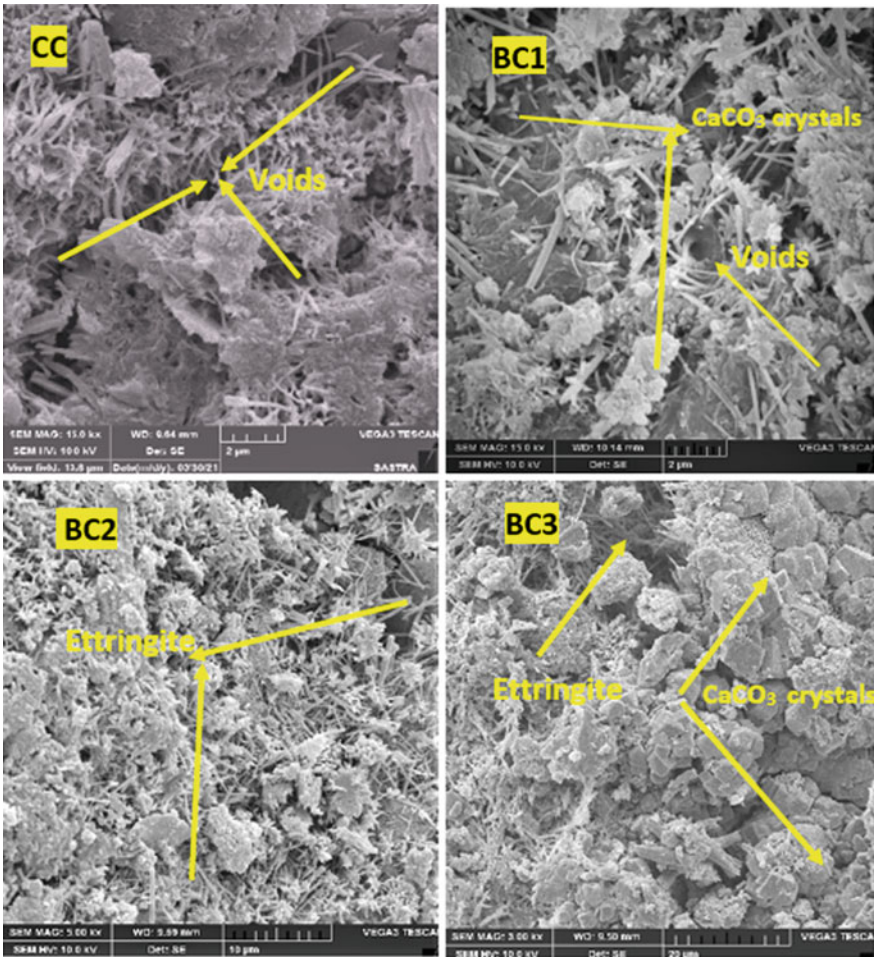

Fig. 17 SEM images

28 days samples of XRD results. In XRD analysis the peak value was obtained for the compound aragonite which is a polymorph of calcium carbonate. This confirms that the precipitated mineral was calcium carbonate-based [16].

4 Conclusions

The current study explores the use of *Bacillus subtilus* and compares the strength, compressive strength regain, crack healing efficiency, and durability of concrete

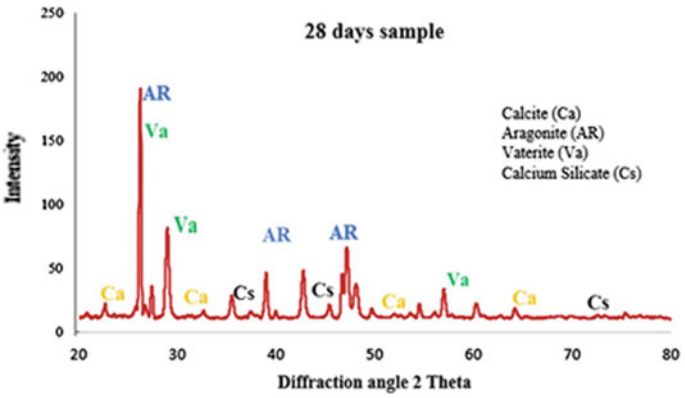

Fig. 18 XRD results

under wet-dry and full-wet curing conditions were studied. The experimental results were analyzed and interpreted, resulting in the following conclusions.

1. The compressive strength and tensile strength of bacterial concrete were much higher than the control concrete. This factor occurs as a result of the development of calcium silicate hydrate inside the pores of concrete, which contributes to increased strength and durability properties.
2. The pre-compressed concrete specimens regained compressive strength at 25 days after being pre-cracked on the third day, which was nearly equal to the characteristic compressive strength. This means that the precipitation of calcium carbonate in fracture areas not only enhances the concrete matrix but also allows it to regain its original strength after failure.
3. Impact energy is calculated for both the normal concrete and bacterial concrete. 30% bacterial concrete and 70% of nutrient solution show higher impact energy compared to other bacterial concrete and normal concrete. As addition of bacteria which increases the impact energy due to $CaCO_3$ precipitation improves the packing of concrete and it delays the propagation of cracks at initial and final stages.
4. At 28 days, exterior repair was observed in the Full-Wet and Wet-Dry pre-cracked samples at approximately 90% and 88%, respectively. Calcium carbonate precipitation in the concrete matrix was caused by bacterial activity that aids in internal curing and it improves the mechanical performance of the concrete.
5. The samples with larger precipitation had reduced water absorption rates, implying that precipitation caused by microbial activity hardens the pores in the concrete matrix, minimizing the volume of water uptake significantly.
6. SEM and XRD analysis confirms the bacteria show different morphological crystals in concrete and the peak value in XRD analysis was obtained for the compound aragonite, which is a polymorph of $CaCO_3$. This demonstrates that the precipitated mineral was composed of calcium carbonate. The influence of

$CaCO_3$ used as a calcium source for this current research may have resulted in a polymorph of calcium carbonate.

Scope of Future Work

The development of bacterial concrete by directly applying, encapsulating, and immobilizing a combination of different types of bacteria to improve the regained strength, crack healing efficiency, and durability properties of concrete with various fibers (steel, basalt, polypropylene, glass) could be the focus of future research.

References

1. Mohammed H, Ortoneda-Pedrola M, Nakouti I, Bras A (2020) Experimental characterization of non-encapsulated bio-based concrete with self-healing capacity. Constr Build Proc 256. 0950-0618
2. Jena S, Basa B, Panda KC, Sahoo NK (2020) Impact of *Bacillus Subtilis* bacterium on the properties of concrete. Mater Today: Proc 129. 2214-7853
3. Kunal, Siddique R, Rajor A, Singh M (2016) Influence of bacterial-treated cement kiln dust on strength and permeability of concrete. Am Soc Civ Eng 28(10):04016088
4. Achal V, Mukherjee A, Sudhakarareddy M (2011) Microbial concrete: way to enhance the durability of building structures. Am Soc Civ Eng 23:730–734
5. Pachaivannan P, Hariharasudhan C, Mohanasundaram M, Anithabhavani M (2020) Experimental analysis of self-healing properties of bacterial concrete. Mater Today: Proc 782. 2214-7853
6. Nguyen TH, Ghorbel E, Fares H, Cousture A (2019) Bacterial self-healing of concrete and durability assessment. Cem Concr Compos 104. 0958-9465
7. Chahal N, Siddique R, Rajor A (2012) Influence of bacteria on the compressive strength, water absorption and rapid chloride permeability of concrete incorporating silica fume. Constr Build Mater 37:645–651
8. Nain N, Surabhi R, Yathish NV, Krishnamurthy V, Deepa T, Tharannum S (2019) Enhancement in strength parameters of concrete by application of Bacillus bacteria. Constr Build Mater 202:904–908
9. Shanmuga Priya T, Ramesh N, Agarwal A, Bhusnur S, Chaudhary K (2019) Strength and durability characteristics of concrete made by micronized biomass silica and Bacteria-Bacillus sphaericus. Constr Build Mater 226:827–838
10. Pourfallahi M, Nohegoo-Shahvari A, Salimizadeh M (2020) Effect of direct addition of two different bacteria in concrete as self-healing agent. Structures 28:2646–2660
11. Rais MS, Khan RA (2021) Experimental investigation on the strength and durability properties of bacterial self-healing recycled aggregate concrete with mineral admixtures. Constr Build Mater 306:124901
12. IS: 12269 (2013) Specification for 53 grade ordinary Portland cement
13. IS 383 (2016) Coarse and fine aggregate for concrete—specification
14. IS 10262 (2019) Recommended guidelines for concrete mix design. Bureau of Indian Standards, New Delhi
15. IS: 516-1959 (2004) Method of tests for strength of concrete. Bureau of Indian Standards, New Delhi, India
16. ACI committee 544.2R-89. Measurement of properties of fiber reinforced concrete
17. American Society for Testing and Materials (ASTM) (2013) Standard test method for measurement of rate of absorption of water by hydraulic-cement concretes. ASTM C1585, ASTM International, West Conshohocken, Pennsylvania

18. ASTM C642-13 (2013) Standard test method for density, absorption, and voids in hardened concrete. ASTM International, West Conshohocken, PA
19. Sumathi A, Murali G, Gowdhaman D, Amran M, Fediuk R, Vatin NI, Laxme RD, Gowsika TS (2020) Development of bacterium for crack healing and improving properties of concrete under wet–dry and full-wet curing. Sustainability 12(24):1–20
20. Madhu Sudana Reddy B, Revathi D (2019) An experimental study on effect of Bacillus sphaericus bacteria in crack filling and strength enhancement of concrete. Mater Today: Proc 135. 2214-7853
21. Krishnapriya S, Venkatesh Babu DL, Prince Arulraj G (2015) Isolation and identification of bacteria to improve the strength of concrete. Microbiol Res 174:48–55
22. Padichetty M, Sreekrishna RV, Chinthakunta H, Deepalakshmi R, Sumathi A (2021) A study on the strength of bacteria-based cementitious mortar. Lect Notes Civ Eng 124:543–552
23. Khaliq W, Ehsan MB (2016) Crack healing in concrete using various bio influenced self-healing techniques. Constr Build Mater 102:349–357

Grid Level Analysis of the Performance of Artificial Neural Network Classifier on the Classification of Multispectral RS Data: A Case Study

B. R. Shivakumar and B. G. Nagaraja

Abstract Remote sensing data has found its use in a variety of social applications such as change detection, mapping, vegetation analysis, and land cover detection. The classification outcomes vary depending on the algorithms employed, the type of the classifier, and the data complexity. In this paper, we use an artificial neural network (ANN) classifier for mapping two Landsat-8 images of different complexity. The data are analyzed for LULC class separation in spatial space using Jeffries-Matusita and transformed divergence metrics. Further, we analyze the performance of ANN by studying the impact of three network generalization parameters; the number of hidden layers, number of training iterations, and training rate on the classification outputs. Accuracy assessment is carried out to verify the correctness of the output thematic maps using 1000 ground truth points. The study presents a detailed analysis of the classification performance by considering Anderson's level 1 and level 2 classes. Lastly, we compare the classification performance of ANN with other well-known classifiers commonly employed in remote sensing.

Keywords Artificial neural network · Classification · Remote sensing · Land cover mapping · Image classification

1 Introduction

Remote sensing (RS) technology has enabled the study and analysis of objects of varying sizes and types from a remote distance. The RS technology has significantly improved the cost and time requirements compared to conventional field survey techniques [1]. One of the basic tasks employed in remote sensing studies is image classification. Image classification is the means of assigning a class label to objects present in the image. This is achieved traditionally by employing one of the two

B. R. Shivakumar (✉)
NMAM Institute of Technology, Nitte 574110, India
e-mail: shivkumarbr@nitte.edu.in; shivkumarbr@gmail.com

B. G. Nagaraja
KLE Institute of Technology, Hubli 580027, India

L. Nandagiri et al. (eds.), *Recent Advances in Civil Engineering*, Lecture Notes in Civil Engineering 256, https://doi.org/10.1007/978-981-19-1862-9_37

conventional methods; unsupervised or supervised classification. The unsupervised classification is machine-dependent and may require only minimal inputs from the analyst. Supervised classification, on the other hand, requires analyst's intervention at multiple levels and the quality of the output relies on the attributes of the training data fed to the system by the analyst [2].

Traditionally, a large number of classification techniques are introduced in history, such as probability-based techniques (maximum likelihood classifier, Bayes' classifier), distance-based techniques (minimum distance classifier, Mahalanobis distance classifier), spectral classifiers (spectral information divergence, spectral correlation mapper, spectral angle mapper), parallelepiped classifier, and k-nearest neighbor classifier. However, lately, classifiers such as expert systems, support vector machines (SVM), decision trees, fuzzy-based classifiers, and neural networks have been extensively used for RS classification studies.

The task of image classification, from a remote sensing perspective, is challenging due to factors such as data heterogeneity, high inter-class variance, exceedingly high spectral bands, mixed pixels, and the limited number of training sites [3]. Choosing a classification algorithm is pivotal in these scenarios considering the spectral, spatial, radiometric, and temporal resolutions of the data. With recent advancements in space science, analysts can lay hands on the latest data sets, keeping the field open even today.

Several authors [4, 5] have discussed the classification of RS data using different classification techniques. Literature [6] presents a review on RS data classification using ANN. In the past few decades, ANN is extensively used in several RS applications. Zhang et al. [7] have used ANN for estimating impervious surfaces using optical as well as synthetic aperture radar (SAR) RS images. Syifa et al. have used ANN for classifying RS imagery for disease detection in trees [8] and flood mapping [9]. Zhai et al. [10] have used ANN for soil texture classification using RS imagery. Literature [11] has employed ANN classification for mapping urban impervious surfaces. Literature [12] presents the use of ANN for object-based classification of high-resolution RS imagery. Literature [13] employs ANN for leaf area index detection using RS imagery. Literature [14] employs ANN for tracing suspended matter over Tiab estuary using RS imagery. Literature [15] employs ANN for extracting leaf area index of crops from hyperspectral imagery obtained from unmanned aerial vehicles. Literature [16] employs ANN for soil salinity assessment using multi-source RS data. Literature [17] employs ANN for crop biophysical parameters from Sentinel-2 RS imagery.

Many researchers [10, 13] have used ANN classifiers with a fixed input set parameter and have not analyzed the impact of network parameters on the overall classification performance. In this paper, we address this issue. This paper has a two-fold objective; i. To classify the Landsat 8 data with different complexity using ANN classifier, and ii. to study and analyze the effects of three network generalization parameters: the number of nodes, training iterations, and training rate on the classification performance of ANN. The study considers two Landsat8 data for performing

the classification. The land cover classes in the considered study areas are thoroughly analyzed for their spatial and spectral distribution, spectral overlapping, and intraclass variability.

The rest of the paper is organized as follows. In Sect. 2, we present the neural network classifier and the network generalization parameters. Section 3 discusses the methodology employed in this study. Section 4 presents the study areas, classification results, and their analysis. Lastly, conclusions drawn from the results obtained are presented in Sect. 5.

2 Neural Network Classifier

A neural network (NN) is a connection of neurons or nodes. A NN is broadly classified into two types; biological or artificial. A biological NN, as its name suggests, is a connection of biological neurons. On the other hand, an ANN is a connection of artificial neurons built for solving artificial intelligence problems. In a biological NN, the neuron connections are modeled as weights. A positive weight emulates a simulative connection, while a negative weight emulates a repressive connection. Thus, the NN weights are modified and summed. This activity is referred to as a linear combination [18].

For thematic mapping applications, ANN can be employed as a nonparametric classification technique [19]. The decision boundaries created by NN are not fixed but are divided iteratively by minimizing an error criterion. A similar approximation is also used in clustering techniques.

In general, a NN is formed of three layers; input layer, output layer, and hidden layer. The input layer nodes are representatives of the input data and do not perform any operations. Generally, the training data vectors are used to form input layers [20]. The nodes at the hidden layers transform the input test pattern into an output pattern. Both hidden and output layer nodes are the processing elements of the network.

Consider the NN indicated in Fig. 1. Every node at the output and hidden layer performs a summation and transformation operation. A node j in the hidden layer performs an operation on the input pattern P_i to create an output, h_j, as per Eq. (1).

$$S_j = \sum_i w_{ij} P_i \quad \text{and } h_j = f\left(S_j\right) \tag{1}$$

where, S_j represents the summation operation and $f(.)$ represents the transformation operation performed at hidden layer j. The output h_j is then sent to each output node, k, which once again performs a similar operation to produce an output, o_k.

$$S_k = \sum_i w_{kj} h_j \quad \text{and } o_k = f(S_k) \tag{2}$$

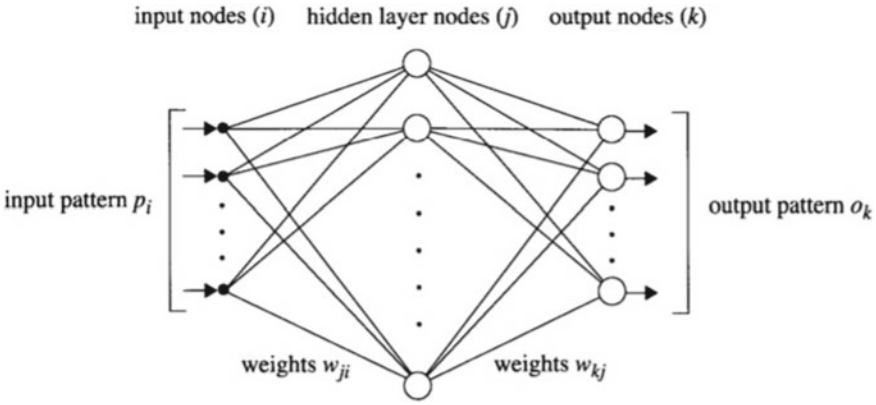

Fig. 1 Structure of a three-layered NN [21]

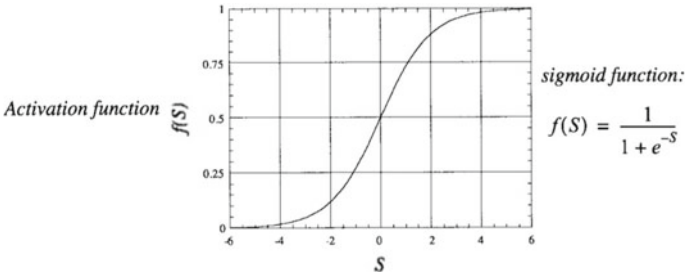

Fig. 2 Sigmoid activation function [21]

where, S_k represents the summation operation.

Sigmoid function, as shown in Fig. 2, is the most commonly used transformation function, and is defined as,

$$f(S) = \frac{1}{1+e^{-S}} \tag{3}$$

Other transformation functions such as hard threshold with no gradient are also available however, these transformation functions are scarcely used due to the network sensitivity issues [21].

2.1 Back-Propagation Algorithm

The ability of the ANN to discriminate and then assign a test pixel to one of the LULC classes is contained in its weights. The network weights are continuously modified

during training so that the network achieves the ability to distinguish the test patterns. One of the most commonly used criteria for modifying the weights is to minimize the squared error over all patterns at the network output. Generally, this scheme is implemented by using the back-propagation algorithm, and it was the very first of the approaches employed for training the network. The backpropagation algorithm is an iterative or gradient descent algorithm. Detailed mathematical analysis on the back-propagation algorithm can be found in [21].

The errors are propagated back through the network to adjust the network weights. For the three-layered fully connected network shown in Fig. 1, let B denote the number of input spectral bands or features, H denotes the number of nodes in the hidden layer, and C denotes the number of LULC classes. The total number of free parameters or weights of the network is then given by [22],

$$N_{\text{ANN}} = H(B + C) \tag{4}$$

If values for B and C are known, then for a fully connected network, the number of hidden layer nodes can be found as [22],

$$\text{Number of hidden layer nodes} = H = \frac{N_{ANN}}{B + C} \tag{5}$$

2.2 Back-Propagation Algorithm

Generalization can be thought of as a process in which the NN can interpolate and extrapolate to data that is not included in the training. The performance of the NN depends on the way in which the network generalizes to new inputs. Several factors affect this procedure, and a few of them are discussed in the following sections.

Number of Nodes and Architecture: The mathematical structure of the NN can be made very flexible by using a large number of nodes. This enables the use of NN for a large number of applications. However, this is not always necessary. Yahn and Simpson [23] have demonstrated that simple NN with a small number of data points can still generalize. In general, the literature suggests that when the number of nodes in the hidden layers is high, NN can better represent the data, but this comes at the cost of generalization capacity [24].

Training Iterations: Since almost all NN perform forward and backward passes during training to produce network weights, the number of times these passes are made (iterations) put a great impact on generalizing the network. By a general rule of thumb, the higher the number of iterations during training, the better the generalization achieved.

Training Rate: The learning rate or training rate is a parameter that governs the changes in the model with respect to the estimated error, whenever the network weights are updated. A smaller value may take a long time for training, sometimes

causing the network to get stuck. On the other hand, a large value may speed up the training but the network weights will become unstable. Therefore, the analyst should choose the training rate value while having an intuition on the model behavior.

3 Methodology

Figure 3 shows the block diagram of the methodology used for this study. The blocks of the methodology diagram are briefly explained in this section.

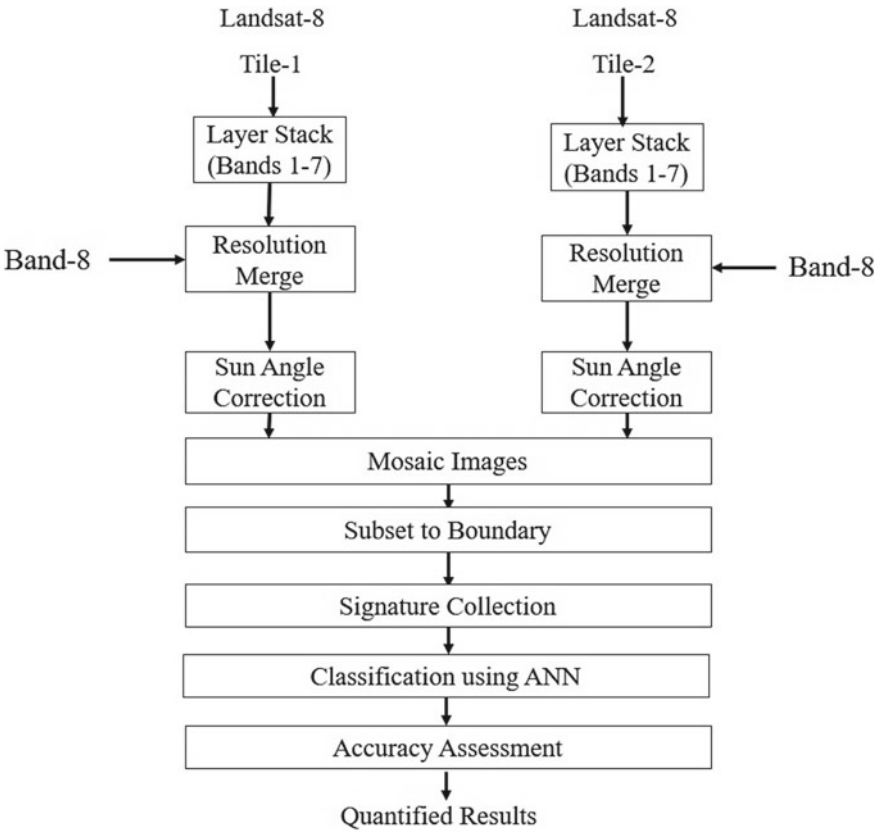

Fig. 3 Methodology of the work

Table 1 Signature/training data size

Area	Signature/training size in pixels study						
	Evergreen forest	Deciduous forest	Scrub land	Water body	Kharif	Double crop	Built up
North Canara	28,192	35,906	25,310	14,927	14,339	6652	2714
Kumta	2059	450	1571	3413	730	561	136

3.1 Preprocessing

The Landsat 8 data collected from earthexplorer website [25] is applied to four preprocessing procedures: layer stacking, resolution merge, mosaicking, and subset to boundary. We have used the first 8 bands of the Landsat 8 data set for this study.

The North Canara district boundary spans more than one tile of Landsat-8 image and hence two images acquired on the same date were collected. In each data, the first seven bands of the data are applied to layer stacking operation to create a 30 m spatial resolution image. This image is then applied to resolution merge technique, along with the 15 m spatial resolution panchromatic band 8 to create a 15 m multispectral data. The two images are then subjected to sun-angle correction and mosaicked to create a single data tile. This multispectral image is then applied to subset operation to extract the North Canara and Kumta study area imagery.

By rigorous inspection of the study areas using Google maps [26], Wikimapia maps [27], cross-referring to previous studies [28], and using government census documents [29], seven spectral classes were recognized in each study area. These classes are; built up (BU), water body (WB), evergreen forest (EGF), Kharif (KH), deciduous forests (DF), scrubland (SL), double-crop (DC). By employing an on-screen selection of lines, points, and polygons, signature/training information was collected for each LULC class, and this is indicated in Table 1. It's worth noting that the primary study area's training data size is higher than the secondary study area's. To better understand the spectral relativeness of the LULC classes, we measured the class separability between each class pair by calculating Jeffries-Matusita (JM) and Transformed Divergence (TD) metrics. Class pairs with severe spectral overlapping are given in Table 2 for both study areas.

3.2 Post-processing

The thematic maps created by the classification process are subjected to accuracy assessment process to produce quantitative analysis of the classification performance. A total of 1000 ground truth (validation) points were selected by using stratified random approach. The accuracy assessment procedure provides a quantitative approximation of the classification performance in terms of performance metrics.

Table 2 Pair-wise class separability in spectral space measured in Jeffries-Matusita distance and Transformed Divergence

Class-pair	North Canara			Kumta	
	JM[a]	TD[b]	Class-pair	JM[a]	TD[b]
DF-SL	1.29381150	1.62976945	EGF-DCP	1.46683581	1.95754919
BU-KH	1.45675134	1.60031081	KH-BU	1.90907271	2.00000000
EGF-DCP	1.47137640	1.64988537	SL-DF	1.98816550	2.00000000
KH-SL	1.73930315	1.87348605	SL-BU	1.99885822	2.00000000
BU-SL	1.91547945	1.97042385	EGF-DF	1.99982318	1.99999994
KH-DF	1.94612265	1.99999037	SL-KH	1.99994694	2.00000000
EGF-DF	1.98664047	1.99999998	WB-BU	1.99999962	2.00000000
EGF-SL	1.99332146	1.99998332	EGF-SL	1.99999991	2.00000000

[a]JM—Jeffries-Matusita distance
[b]TD—transformed divergence

In this study, we have used three classification performance metrics for result analysis; overall classification accuracy (OCA), overall Kappa value (OKV), and user's accuracy (UA).

The OCA is the ratio of number of correctly classified validation points to the total number of validation points. OCA only accounts for the number of validation points considered and does not imply anything on the remaining pixels on the data. To obtain knowledge on the classification performance of all pixels on the data set, we use OKV metric. OKV metric ranges between 0 and 1. An OKV value of 0 indicates no agreement between the reference image and classification image. On the other hand, an OKV value of 1 indicates full similarity between reference image and classified image. Therefore, a higher value of OKV indicates higher classification performance. Lastly, UA is the ratio of total number of correctly classified pixels of a class to the total number of validation pixels assigned to that class. For 95% confidence with ±4% error margin, the estimated range of classification accuracy for the primary study area is 77.520% to 82.486%, and for the secondary study area is 78.240% to 81.760% [30]. More information on accuracy assessment and its metrics can be found in [31].

$$\text{OCA} = \frac{\text{Number of correctly classified ground} - \text{truth pixels}}{\text{Total number of ground} - \text{truth pixels}} \tag{6}$$

$$\text{OKV} = \frac{\text{Observed accuracy} - \text{chance agreement}}{1 - \text{chance agreement}} \tag{7}$$

$$\text{UA} = \frac{\text{Number of correctly classifier pixels of a class}}{\text{Total number of pixels assigned to that class}} \tag{8}$$

4 Results and Discussions

This section provides a brief introduction to the two study areas considered for the experimentation. Also, the section provides a detailed analysis of the classification results of the ANN classifier for different network parameter combinations.

4.1 Study Areas

For experimentation, we acquired Landsat-8 OLI/TIRS data from the Earthexplorer.com website [32]. Further, considering the data complexity, we selected two study areas of similar characteristics. The North Canara district boundary in Karnataka, India is selected as the primary study area, and the Kumta Taluka boundary in Karnataka, India is selected as the secondary study area. These study areas are indicated in Figs. 4 and 5, respectively. It is worth noting that the secondary study area is a subset of the primary study area, and hence, acquires spatial and spectral characteristics from the primary study area.

Both study areas exhibit a wide canopy of thick vegetation, which is a fragment of the Western Ghats of India. The thick vegetation is a combination of Evergreen forests and moist deciduous forests. Scrublands are found distributed all over the study areas. The agricultural fields are categorized into two parts, namely, Kharif and double-crop, based on the cultivation method. Double crop class is found mostly towards the western boundary of the study areas while Kharif is found mainly towards the eastern boundary. Several water bodies are found throughout the study areas in various forms such as rivers, reservoirs, estuaries, and ponds. They are all combined to form a single water body class. The Built Up class is made up of urban settlements.

4.2 ANN Results

We used ENVI v4.8® RS and GIS software for conducting ANN classification of the study areas. To explore the effects of generalization parameters discussed previously, we tested the classifier for different values of training rates, hidden layers, and training iterations. The input parameters to the ANN classification module are; activation function: logistic, training threshold contribution: 0.9, training momentum: 0.9, and training RMS exit criteria: 0.1.

Case 1: Impact of Number of Hidden Layers: The study areas were classified using two values for the number of hidden layers: 1 and 2. This has been done to see if the number of hidden layers affected overall classification performance. The ANN did not generalize well for other values of the number of hidden layers and is therefore not discussed further. The training rate and training iterations for this study were set to 0.2 and 1000, respectively.

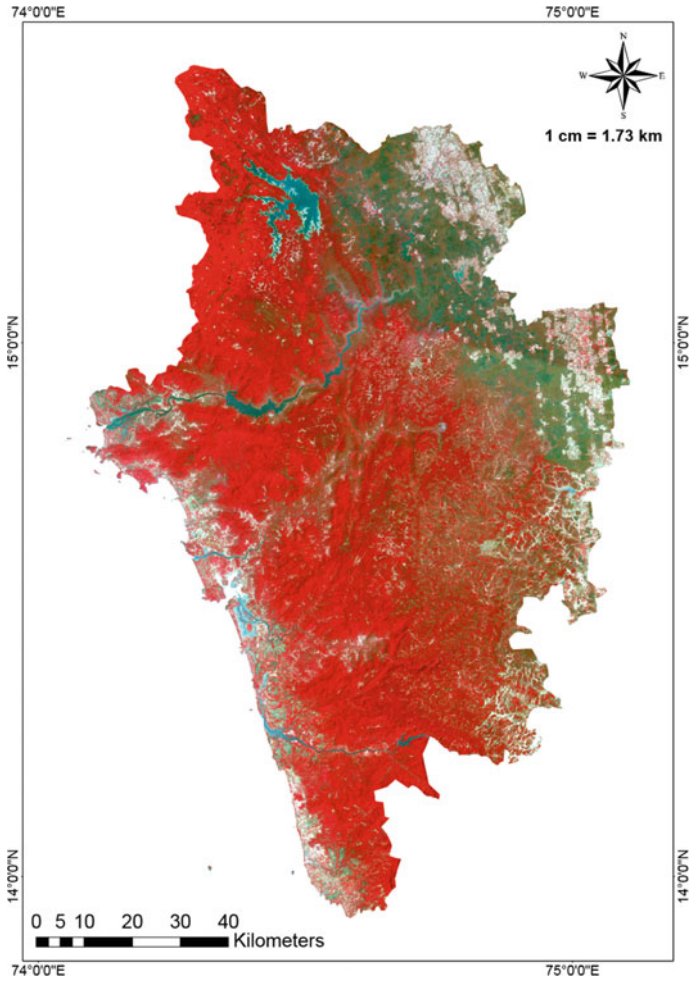

Fig. 4 Map composition for the North Canara District boundary (primary study area)

When the study areas were classified using an NN classifier with 1 hidden layer, the OCA of the primary study area was 72.50% and that of the secondary study area is 72.80%. When the number of hidden layers is increased to 2, the NN did not generalize well for the primary study area and the classifier failed to separate the LULC classes. On the contrary, the NN generalized well for the secondary study area and produced an improved OCA of 75.10%.

For one hidden layer, the NN classifier created the spectrally dominant classes expertly. Evergreen forest and water body classes, for example, were recovered with $\geq$85% user's accuracy (UA). The NN classifier successfully separated some of the spectral class-pairs (for example, evergreen forest and double-crop class-pair) with high efficiency. However, when the spectral overlapping spans more than two classes

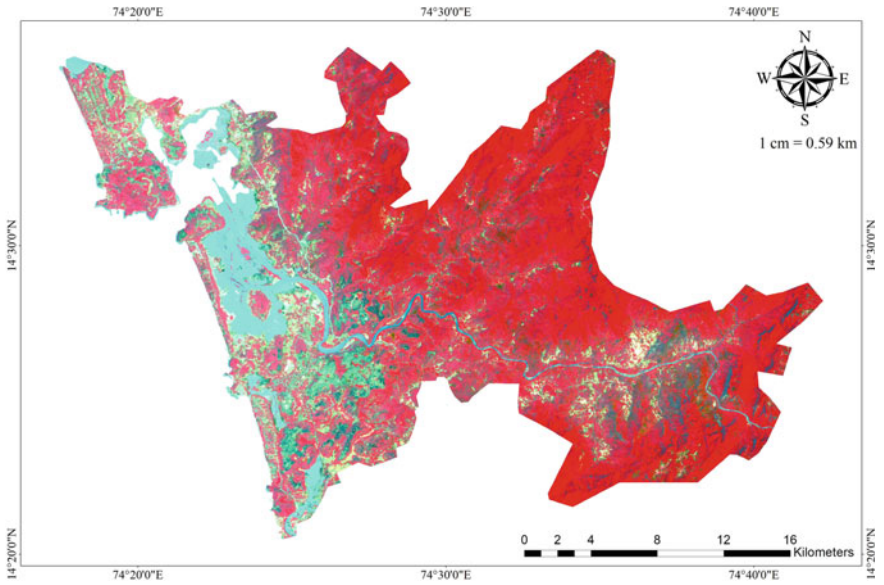

Fig. 5 Map composition for the Kumta Taluk boundary (secondary study area)

(for example, deciduous forest, scrubland, and Kharif classes), the classifier showed bias towards the spatially dominant classes of the overlapping class. LULC classes that are both spatially and spectrally subservient are extracted with the lowest user's accuracies. When the number of hidden layers was increased to 2, the NN classifier extracted the spectrally dominant classes with even higher user's accuracies, whereas, user's accuracies of spectrally subservient classes were further reduced. However, as the OCA has increased, the classification performance can also be said to be increased. Table 3 indicates the classification statistics for all the experiments in Case 1.

Case 2: Impact of Number of Training Iterations: To analyze the effect of the number of training iterations on the NN classifier, the study areas were classified with several training iterations values spanning from 1000 to 10,000, at different intervals. For this experiment, the value of the training rate was set to 0.2. As per the results in Sect. 4.2.1, the primary study area was classified with 1 hidden layer, whereas the secondary study area was classified with 2 hidden layers in the ANN.

For the primary study area, the classification performance increased with an increase in the number of training iterations, with the best value of OCA attained at the training rate value of 10,000. On the contrary, for the secondary study area, the NN classifier produced the best results at the training iterations value of 1000. The classification performance was reduced with an increase in training iterations.

The NN classifier retrieved the spectrally dominant classes brilliantly when the number of training iterations was 1000, while the spectrally subservient classes were poorly extracted. The NN classifier separated the spectral class-airs exceptionally

Table 3 Classification statistics for Case 1

No. of hidden layers	Evergreen forest	Deciduous forest	Water body	Scrub land	Kharif	Double crop	Built up	OCA[a]	OKV[b]
North Canara									
1	84.10%	63.91%	100.00%	29.56%	87.67%	83.33%	–	72.50%	0.5838
Kumta									
1	82.82%	22.22%	96.00%	75.47%	63.16%	77.78%	17.86%	72.80%	0.5372
2	89.93%	19.17%	97.30%	69.23%	66.67%	70.69%	13.95%	75.10%	0.5963

[a]OCA—Overall classification accuracy
[b]OKV—overall Kappa value

well for the primary study area. As the number of training iterations was increased, the NN classifier separated the spectrally overlapping class pairs even better and hence the classification performance has linearly increased. The NN classifier failed to recover the built up class completely throughout the experimentation in this case. Table 4 indicates the classification results for the primary study area for case 2.

The NN classifier performed admirably in extracting the spectrally dominating classes in the secondary study area. The spectrally subservient classes, on the other hand, were poorly extracted. As the number of training iterations increased, the overall classification performance deteriorated. Throughout the experiment, the classifier failed to successfully extract the built up class. Table 5 indicates the classification results for the secondary study area for case 2.

Case 3: Impact of Training Rate: To study the impact of training rate on the NN classifier, we classified the study areas using different training rate values. During

Table 4 Classification statistics for case 2 for primary study area

Class	Number of training iterations					
	1000	2000	3000	4000	5000	1000
Evergreen forest	84.10%	90.64%	88.87%	87.63%	86.96%	86.08%
Deciduous forest	63.91%	55.75%	61.54%	61.13%	61.16%	64.80%
Water body	100.00%	100.00%	100.00%	90.91%	100.00%	100.00%
Scrub land	29.56%	37.25%	36.44%	34.92%	37.50%	41.57%
Kharif	87.67%	88.89%	85.23%	88.41%	89.74%	85.56%
Double crop	83.33%	91.67%	81.25%	100.00%	100.00%	100.00%
Built up	–	–	–	–	–	–
OCA[a]	72.50%	75.50%	75.59%	74.50%	76.05%	76.87%
OKV[b]	0.5838	0.6347	0.6372	0.6172	0.6363	0.6501

OCA[a]: overall classification accuracy, OKV[b]: overall Kappa value

Table 5 Classification statistics for case 2 for secondary study area

Class	Number of training iterations					
	1000	2000	3000	4000	5000	10,000
Evergreen forest	89.93%	83.51%	84.50%	88.21%	84.62%	84.73%
Deciduous forest	19.17%	23.33%	17.36%	19.17%	17.74%	17.80%
Water body	97.30%	100.00%	100.00%	97.30%	97.22%	100.00%
Scrub land	69.23%	77.19%	61.90%	78.00%	74.51%	58.90%
Kharif	66.67%	66.15%	70.13%	70.83%	71.01%	70.59%
Double crop	70.69%	78.95%	–	73.33%	–	–
Built up	–	–	–	–	–	–
OCA[a]	75.10%	74.50%	74.90%	76.90%	74.50%	74.40%
OKV[b]	0.5963	0.5689	0.5639	0.6174	0.5615	0.5565

this experimentation, we set the number of training iterations to 1000. Further, we set the number of hidden layers for the primary study area to 1, whereas for the secondary study area, it was set to 2.

Both study areas were classified with the best OCA when the training rate was minimal. As the training rate was increased, the classification performance degraded gradually. The NN generalized well only for two values of training rate; 0.1 and 0.2. for higher values of training rate, the NN classifier failed to extract most of the LULC classes. The individual class accuracies were also seen to degrade with the increase in training rate. particularly, at higher training rates, the NN classifier extracted only the dominant classes of the spectral class pairs. Tables 6 and 7 indicate the classification

Table 6 Classification statistics for case 3 for primary study area

Class	Number of training iterations				
	0.1	0.2	0.3	0.4	0.5
Evergreen forest	90.89%	84.10%	85.48%	85.26%	80.96%
Deciduous forest	61.11%	83.33%	00.00%	–	–
Water body	91.67%	100.00%	84.00%	95.65%	–
Scrub land	60.08%	63.91%	57.22%	60.80%	–
Kharif	29.69%	29.56%	25.21%	24.66%	–
Double crop	84.34%	87.67%	91.38%	81.93%	91.89%
Built up	–	–	00.00%	–	01.32%
OCA[a]	72.40%	72.50%	68.12%	69.22%	54.28%
OKV[b]	0.5969	0.5838	0.5236	0.5406	0.3533

[a]OCA—Overall classification accuracy
[b]OKV—overall Kappa value

Table 7 Classification statistics for case 3 for secondary study area

Class	Number of training iterations				
	0.1	0.2	0.3	0.4	0.5
Evergreen forest	83.43%	89.93%	94.65%	95.64%	–
Deciduous forest	32.43%	19.17%	–	–	–
Water body	97.30%	97.30%	95.71%	94.37%	100.00%
Scrub land	66.67%	69.23%	42.78%	38.04%	–
Kharif	70.69%	66.67%	64.18%	–	–
Double crop	84.62%	70.69%	–	–	–
Built up	22.22%	13.95%	–	–	–
OCA[a]	77.40%	75.10%	73.50%	71.20%	07.90%
OKV[b]	0.6040	0.5963	0.5421	0.5025	0.0000

[a]OCA—Overall classification accuracy
[b]OKV—overall Kappa value

Table 8 Thematic map accuracies for some commonly employed supervised classifiers [30]

Classifier	North Canara		Kumta	
	OCA[a]	OKV[b]	OCA[a]	OKV[b]
Maximum likelihood	78.23%	0.6811	75.40%	0.5733
Minimum distance	58.20%	0.4428	54.20%	0.3856
Mahalanobis distance	64.12%	0.5165	58.40%	0.4302
Support vector machines	78.20%	0.6275	78.10%	0.6230
Fuzzy-based maximum likelihood	86.20%	0.7870	77.00%	0.6069
Fuzzy-based minimum distance	69.58%	0.5482	70.40%	0.5496
Fuzzy-based Mahalanobis distance	70.58%	0.5552	68.80%	0.5198

[a]OCA—Overall classification accuracy
[b]OKV—overall Kappa value

statistics for primary and secondary study areas, respectively, for case 3.

Table 8 shows the classification results of some common supervised classifiers for the same input and training conditions as ANN. Comparing the OCA and OKV values of ANN with other classifiers as shown in Table 8 we find that, ANN results are better than distance/Fuzzy-based distance classifies, comparable to maximum likelihood and support vector machines, and is only inferior to the Fuzzy-based maximum likelihood classifier. Further, ANN classified the secondary study area more efficiently, which is more heterogeneous than the primary study area. This is not seen in any other classifiers shown in Table 8 (except for the Fuzzy-based minimum distance classifier, which only has $\cong 0.5\%$ improvement). This indicates that ANN has a better ability to separate overlapping classes.

4.3 Observations

By analyzing the results of the ANN classifier for a different set of input conditions, we make the following observations;

- This study has tested the ANN classifier by providing an exhaustive training set for the spatially dominant classes on the data for which the classifier has generalized excellently. For other classes, the spatially subservient ones, the network did not generalize effectively due to the training set size and hence has produced average results.
- The ANN classifier has very efficiently separated the spectrally overlapping classes making it a good choice for classifying heterogeneous data sets.
- The number of hidden layers affects the generalization of the network and is dependent on the data size. In our experimentation, for large data, the NN classifier did not generalize efficiently at a higher number of hidden layers. On the contrary, for smaller data, the ANN did generalize efficiently at a higher number of hidden

layers. It is believed that the number of hidden layers should be selected depending upon the complexity of the data.
– It is observed that classification performance improves upon increasing the training iterations. However, there exists an upper limit for training iterations above which the classification performance decreases. In our study, larger data (North Canara) had higher upper limit than smaller data (Kumta). This upper limit on training iterations can be found by rigorous testing.

The training rate can be introduced as a solution to the large training times consumed by the ANN. However, this study shows that the ANN best generalizes at lower training rates but consumes a very large time for training.

5 Conclusion

ANN classifiers have great capacity in applications such as image classification provided the training data is true and exhaustive. In this study, however, their potential is challenged by the type of data rather than the correctness of the training set. This paper presented a grid-level analysis of the ANN classifier for identifying Anderson's level-1 and level-2 classes on two RS imagery. The study has accomplished its objectives and the thematic maps indicate a close match to the estimated accuracy values with 95% confidence with $\pm 4\%$ error margin. The observations made from the results obtained provide useful suggestions while employing ANN on RS data. As a future scope, we plan to employ an ANN classifier for classifying hyperspectral imagery.

Acknowledgements This work was supported by N.M.A.M. Institute of Technology, Nitte, Karnataka, India and K.L.E. Institute of Technology, Hubli, Karnataka, India.

References

1. Yuan Q, Shen H, Li T, Li Z, Li S, Jiang Y, Xu H, Tan W, Yang Q, Wang J et al (2020) Deep learning in environmental remote sensing: achievements and challenges. Remote Sens Environ 241:111716
2. Jensen JR (2015) Introductory digital image processing: a remote sensing perspective. Prentice Hall Press
3. Carranza-Garcia M, Garcia-Gutierrez J, Riquelme JC (2019) A framework for evaluating land use and land cover classification using convolutional neural networks. Remote Sens 11(3):274
4. Lu D, Weng Q (2007) A survey of image classification methods and techniques for improving classification performance. Int J Remote Sens 28(5):823–870
5. Ayhan E, Kansu O (2012) Analysis of image classification methods for remote sensing. Exp Tech 36(1):18–25
6. Mahmon NA, Ya'acob N (2014) A review on classification of satellite image using artificial neural network (ann). In: 2014 IEEE 5th control and system graduate research colloquium. IEEE, pp 153–157

7. Zhang H, Zhang Y, Lin H (2012) A comparison study of impervious surfaces estimation using optical and sar remote sensing images. Int J Appl Earth Obs Geoinf 18:148–156
8. Syifa M, Park S-J, Lee C-W (2020) Detection of the pine wilt disease tree candidates for drone remote sensing using artificial intelligence techniques. Engineering 6(8):919–926
9. Syifa M, Park SJ, Achmad AR, Lee C-W, Eom J (2019) Flood mapping using remote sensing imagery and artificial intelligence techniques: a case study in Brumadinho, Brazil. J Coast Res 90(SI):197–204
10. Zhai Y, Thomasson JA, Boggess JE III, Sui R (2006) Soil texture classification with artificial neural networks operating on remote sensing data. Comput Electron Agric 54(2):53–68
11. Xiong Y, Zhang Z, Chen F (2020) Comparison of artificial neural network and support vector machine methods for urban land use/cover classifications from remote sensing images a case study of guangzhou, south china. In: 2010 International conference on computer application and system modeling (ICCASM 2010), vol 13. IEEE, pp V13–V52
12. Buddhiraju KM, Rizvi IA (2010) Comparison of cbf, ann and svm classifiers for object based classification of high resolution satellite images. In: 2010 IEEE international geoscience and remote sensing symposium. IEEE, pp 40–43
13. Jensen R, Binford M (2004) Measurement and comparison of leaf area index estimators derived from satellite remote sensing techniques. Int J Remote Sens 25(20):4251–4265
14. Ghaderi D, Rahbani M (2021) Tracing suspended matter in tiab estuary applying ann and remote sensing. Reg Stud Mar Sci 44:101788
15. Yuan H, Yang G, Li C, Wang Y, Liu J, Yu H, Feng H, Xu B, Zhao X, Yang X (2017) Retrieving soybean leaf area index from unmanned aerial vehicle hyperspectral remote sensing: analysis of rf, ann, and svm regression models. Remote Sens 9(4):309
16. Jiang H, Rusuli Y, Amuti T, He Q (2019) Quantitative assessment of soil salinity using multi-source remote sensing data based on the support vector machine and artificial neural network. Int J Remote Sens 40(1):284–306
17. Xie Q, Dash J, Huete A, Jiang A, Yin G, Ding Y, Peng D, Hall CC, Brown L, Shi Y et al (2019) Retrieval of crop biophysical parameters from sentinel-2 remote sensing imagery. Int J Appl Earth Obs Geoinf 80:187–195
18. Kepuska VZ, Mason SO (1995) A hierarchical neural network system for signalized point recognition in aerial photographs. Photogramm Eng Remote Sens 61(7):917–925
19. Foody G (2004) Supervised image classification by mlp and rbf neural networks with and without an exhaustively defined set of classes. Int J Remote Sens 25(15):3091–3104
20. Paola JD, Schowengerdt RA (1995) A detailed comparison of backpropagation neural network and maximum-likelihood classifiers for urban land use classification. IEEE Trans Geosci Remote Sens 33(4):981–996
21. Schowengerdt RA (2006) Remote sensing: models and methods for image processing. Elsevier
22. Paola JD, Schowengerdt RA (1997) The effects of neural-network structure on a multispectral land-use/land-cover classification. In: Photogrammetric engineering and remote sensing (USA)
23. Yhann SR, Simpson JJ (1995) Application of neural networks to avhrr cloud segmentation. IEEE Trans Geosci Remote Sens 33(3):590–604
24. Atkinson PM, Tatnall AR (1997) Introduction neural networks in remote sensing. Int J Remote Sens 18(4):699–709
25. USGS EarthExplorer, Us department of the interior. US Geological Survey. Available: http://earthexplorer.usgs.gov
26. Google, Google maps. Available: https://www.google.com/maps/
27. Wikimapia, Wikimapia maps. Available: https://wikimapia.org/
28. Ramachandra T, Setturu B, Chandran S (2016) Geospatial analysis of forest fragmentation in Uttara Kannada district, India. Forest Ecosyst 3(1):10
29. "District census handbook uttara kannada," in Census of India, 2014

30. Shivakumar BR (2020) Study and analysis of pixel-based classification of remotely sensed data using different classifiers. Ph.D. thesis, Visvesvaraya Technological University, Belagavi
31. Richards JA (2013) Remote sensing digital image analysis, vol 5. Springer
32. U. EarthExplorer, Us department of the interior. US Geological Survey. http://earthexplorer.usgs.gov

An Assessment of Groundwater Quality of Ilkal Taluk, Bagalkot District, Karnataka, India Using GIS and CCME WQI

Madhumati Dhaduti, Anand Hunashyal, and K. Sujay

Abstract Groundwater (GW) quality in Ilkal Taluk of Bagalkot district, Karnataka, India needs special attention as it is a significant alternate source of potable water, domestic needs and industrial applications for the people residing in this area. From the geological features of the area, it is evident that the region is comprised of granite and gneiss metasediments whose significant composition is the fluorite mineral. In this study, Spatial Distribution Maps (SDM) were prepared for the water quality parameters analyzed for the GW samples from 32 different locations of Ilkal taluk using Inverse Distance Weighting (IDW) technique of Arc GIS. From the SDM of Ilkal taluk it is observed that concentration of fluoride in all the samples was more than the BIS maximum allowable value of 1.5 mg/l, pH in all the samples was found well within the range, total dissolved solids exceeded the acceptable value in an area covering 638.09 km^2 and permissible value in an area of 2.34 km^2 and hardness exceeded the permissible value in an area covering 473.87 km^2, Nitrate exceeded the acceptable value in an area of 78.89 km^2 and Total alkalinity exceeded the acceptable value of 200 mg/l in an area of 649.53 km^2. GW quality assessment was done using Canadian Council of Ministers of the Environment Water Quality Index (CCME WQI) which resulted in poor ranking. Hence, continuous monitoring and appropriate treatment of the GW to make it fit for drinking and to protect the health of the people residing in this area is a prime necessity.

Keywords Groundwater · Fluoride · Spatial distribution map · Canadian Council of Ministers of the Environment Water Quality Index

M. Dhaduti (✉) · K. Sujay
Department of Civil Engineering, K.L.E. Institute of Technology, Hubballi, India
e-mail: madhumatisdhaduti@gmail.com

A. Hunashyal
School of Civil Engineering, KLE Technological University, Hubballi, India

L. Nandagiri et al. (eds.), *Recent Advances in Civil Engineering*, Lecture Notes in Civil Engineering 256, https://doi.org/10.1007/978-981-19-1862-9_38

1 Introduction

Water is the most exquisite endowment of nature, the most pivotal for supporting life and all anthropogenic activities—for drinking, municipal use, agriculture and industries. Due to rapid growth in population and exponential anthropogenic activities the surface water is getting highly contaminated and groundwater is extensively used for various activities. In both urban and rural area, groundwater has become one of the major sources. Therefore the management and assessment of groundwater becomes very important in the current scenario [1]. The quality of groundwater is potentially affected by the presence of nitrate and fluoride. The fluoride in Ilkal taluk is very significant because of its geological formation. Fluorine occurs in various forms and types naturally [2]. Presence of fluoride is significantly due to filtrate of fluoride-rich minerals, because natural hard rock areas and deeper geological formations are found to have high fluoride concentration [3]. The fluoride levels in groundwater increase during the monsoon season and also due to disintegration of rocks [4]. The sources of fluoride are fluorite, fluorspar and fluorapatite, these are found in granite, granite gneisses and pegmatite [5]. Fluoride is a micronutrient essential for human body. Fluoride concentration ranging between 0.5 and 1.5 mg/L is considered to be a potable value and appropriate for drinking purpose. Whereas high fluoride intake is hazardous leading to several health issues [6]. According to BIS 1.0 mg/L of fluoride is a desirable value, which is permissible up to 1.5 mg/L if no other source is available [7].

An investigation and assessment of groundwater for Ilkal taluk of Bagalkot District, Karnataka, India is done using Arc GIS and CCME WQI. The water quality index describes the groundwater quality and its suitability for the purpose of portability in accordance with drinking water standards [8]. The geospatial information of groundwater quality helps in effective surveil of groundwater resources of an area [9–11].

1.1 Study Area

Geographical area of Ilkal taluk as shown in Fig. 1 is about 651.28 km^2. It is situated in a valley that lies in south-east corner of Bagalkot district and is very near the boundaries of Kushtagi taluk of the Koppal area and is situated between longitudes 75° 50′ 00″–76°25′00″ E and scopes 15°45′ 00″–16° 15′ 00″ N. As per the 2011 Indian Census, Ilkal had a populace of 60,242 among which males and females percentage is 51% and 49%, respectively [12]. The rainfall pattern of Ilkal taluk of Bagalkot district as per Karnataka State Natural Disaster Monitoring Centre report of 2020 is:

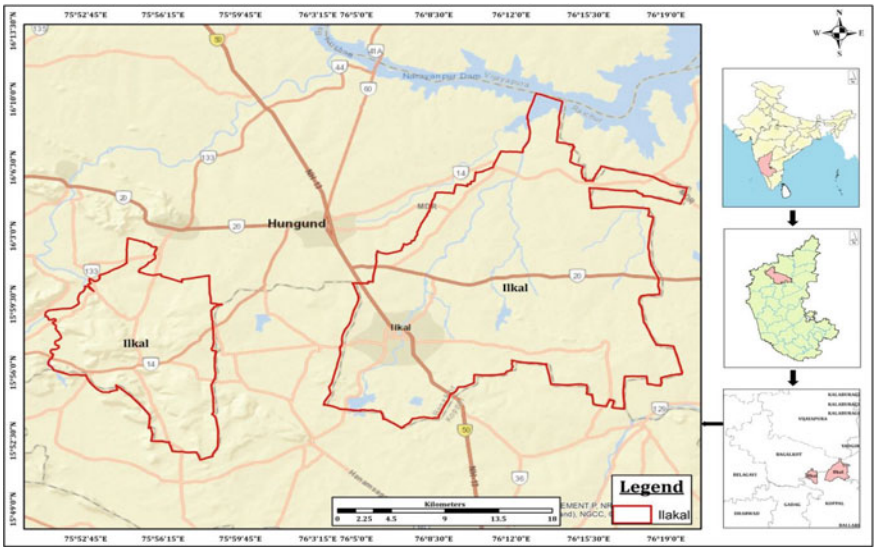

Fig. 1 Ilkal taluk map, Bagalkot district, Karnataka, India

(a) Pre-monsoon (1st January to 31st May 2020), actual rainfall is 94 mm with − 10% departure.
(b) South West monsoon (1st June to 30th September 2020), actual rainfall is 570 mm with 42% departure.
(c) North East monsoon (1st October to 31st December 2020), actual rainfall is 182 mm with 25% departure.

Actual Annual Rainfall Pattern of Ilkal taluk for the year 2020 (1st January to 31st December) is 846 mm with 30% departure.

1.2 Geological Features

The intrinsic layers of the study area mainly constitute of crystalline formations which have formed during different ages of evolution of earth. The earliest of the geologic age formations include granites, gneisses at northern and eastern part of Ilkal Taluk. Metamorphic rocks of sedimentary origin of Dharwar super Group are found in the central part and granite is predominant with small traces of sandstone in southern region. In western region of Ilkal taluk are found the sandstones with different grains overlaid with gneiss and granite along with shale and limestone. The occurrence of laterites and river alluvium are negligible. Ilkal taluk has a leveled surface and, in some directions, it is surrounded by hillocks consisting of plentiful granite stones enriched with minerals. Ilkal taluk is well known for its World-class I pink granites and high-quality deposits of limestone. Granite is found to be comprised

of minerals such as feldspar, quartz and fluorite and gneiss comprises of K-feldspar, hornblend, quartz fluorite and biotite. The color of the soil in this region is found to be grayish to pink and is of sandy-loam nature. The soil is less permeable, moderately fertile and has good water retention capacity. The occurrence of groundwater in these geological formations is usually found trapped in porous sites such as joints, cracks and interstices of unweathered parts of rocks [13].

1.3 Preliminary Study of Ilkal Taluk

The residents of Ilkal taluk were interviewed to collect information through datasheets comprising of the following details: Name, age, village, period since when they are residing in the area, source of water, whether the water that is consumed is treated or not, since when they are dependent on the same source and any health issues if they have.

From the interview, it was found that 95% of the interviewed population depended on the groundwater for their daily water requirement and people who have resided in the area for more than 20 years have health issues like joint pains, deformation of bones and discoloration of teeth because of consumption of groundwater containing high amount of fluoride.

2 Methods

The groundwater samples collected across the study area were analyzed. The samples were named as station 1 to station 32. The names of the stations are depicted in Table 1. Polyethylene bottles were used for collecting samples and were analyzed for various parameters in accordance with standard procedures.

2.1 Preparation of Spatial Distribution Maps

Ilkal is a newly formed Taluk of Bagalkot District. Earlier it was located in Hungund taluk of Bagalkot district. Ilkal started functioning as a separate taluk since 1st January 2018. In the present study, the taluk boundary map has been extracted from Karnataka State Remote Sensing Application Centre (KSRSAC) website [14]. Spatial Distribution Maps of the parameters related to groundwater quality are prepared using Arc GIS. The laboratory data was integrated with the geographical data and was evaluated by Inverse Distance Weighting (IDW) spatial interpolation technique. Presently GIS has become a significant tool for assessment in various sectors [15].

Table 1 Groundwater quality parameters

S. No.	Village	Samples	pH	EC (mS/cm)	TDS (ppm)	F^- (mg/L)	Hardness (mg/L)	Ca (mg/l)	Mg (mg/l)	NO_3^- (mg/l)	Alkalinity (mg/l)
1	Gorabala	S-1	7.18	2.9	1856	2.15	143	103.0	39.6	40	794.0
2	Ingalagi	S-2	7.17	1.5	960	2.20	476	320.0	156.0	48	568.0
3	Jambaladinni	S-3	7.22	3.6	2304	2.15	932	780.0	152.0	52	856.0
4	Anakuntti	S-4	7.97	2	1280	2.05	808	398.0	410.0	32	640.0
5	Tariwala	S-5	7.53	3.1	1984	2.40	1400	516.0	884.0	48	476.0
6	Budhihala SK	S-6	7.56	0.6	384	2.12	188	120.0	68.0	38	158.0
7	Karadi	S-7	7.11	2.5	1600	2.25	986	576.0	410.0	52	550.0
8	Koovivala	S-8	7.81	0.8	512	2.02	468	308.0	160.0	47.4	350.0
9	Harinapur	S-9	7.71	2.0	1280	2.01	770	440.0	330.0	32	528.0
10	Nandawadagi	S-10	7.25	1.7	1088	2.10	872	492.0	380.0	49	480.0
11	Kandagall	S-11	7.26	2.2	1408	2.05	1026	508.0	518.0	22	432.0
12	Gonal SK	S-12	7.03	2.1	1344	2.15	1678	704.0	974.0	40	486.0
13	Krishnapura	S-13	7.46	1.0	640	2.10	522	296.0	226.0	38	456.0
14	Hiresinganagutti	S-14	7.27	1.6	1024	3.20	810	396.0	414.0	48.8	522.0
15	Hireotageri	S-15	7.54	1.2	768	2.79	796	436.0	360.0	49.2	428.0
16	Vajjal	S-16	7.12	2	1280	3.03	744	506.0	238.0	32	504.0
17	Edageri	S-17	7.22	0.5	320	2.85	470	266.0	204.0	19.4	170.0
18	Ilal	S-18	6.93	1.3	832	2.12	962	580.0	382.0	22	402.0
19	Gudur	S-19	7.09	1.4	896	2.98	816	388.0	428.0	12	494.0
20	Kelur	S-20	7.34	1.2	768	2.15	978	528.0	450.0	18	390.0
21	Tallikeri	S-21	7.45	1.0	640	2.05	650	362.0	288.0	38	284.0

(continued)

Table 1 (continued)

S. No.	Village	Samples	pH	EC (mS/cm)	TDS (ppm)	F^- (mg/L)	Hardness (mg/L)	Ca (mg/l)	Mg (mg/l)	NO_3^- (mg/l)	Alkalinity (mg/l)
22	Chikanal	S-22	7.03	0.9	576	2.43	584	420.0	164.0	44	338.0
23	Bhimangada	S-23	7.35	0.8	512	2.35	402	368.0	34.0	40	394.0
24	Dairy Muradi	S-24	7.98	0.6	384	2.54	462	390.0	72.0	42	292.0
25	Muradi	S-25	6.87	1.4	896	2.45	990	720.0	270.0	38	332.0
26	Hosur	S-26	7.13	0.8	512	2.85	602	464.0	138.0	43	234.0
27	Balkundi	S-27	7.59	0.7	448	2.60	392	312.0	80.0	36	390.0
28	Sanklapur	S-28	7.72	0.8	512	2.40	578	348.0	230.0	28	514.0
29	Chikkodagali	S-29	7.45	0.9	576	2.11	550	430.0	120.0	38	390.0
30	Hirekodagali Tanda	S-30	7.55	0.7	448	2.15	498	390.0	108.0	21	282.0
31	Hirekodagali	S-31	7.67	1.1	704	2.10	290	240.0	50.0	42	414.0
32	Vadageri	S-32	7.20	0.8	512	2.00	340	250.0	90.0	41	385.0

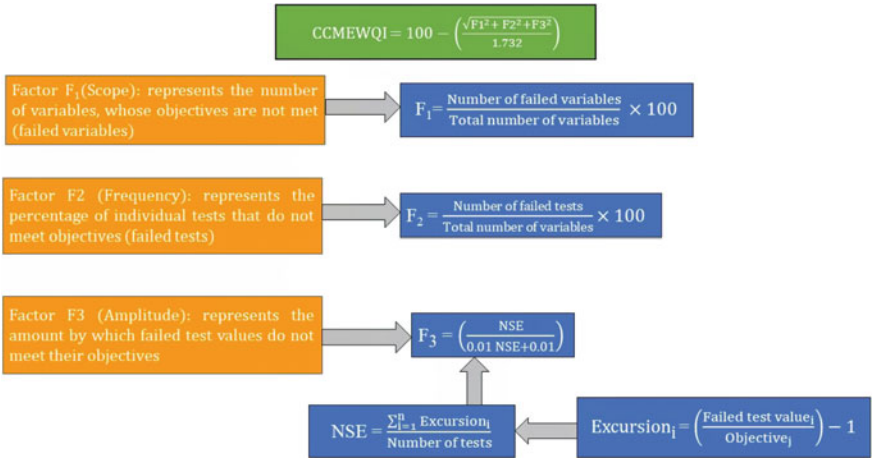

Fig. 2 Mathematical representation of CCMEWQI [18–21]

2.2 Calculation of Water Quality Index (WQI)

A few strategies have been presented previously to create an appropriate WQI technique. Every strategy had a few benefits and a few detriments too [16]. CCME WQI (Canadian Council of Ministers of the Environment Water Quality Index) gives a predictable technique, which can be applied by many water organizations in different nations with slight change [17]. To calculate WQI, three unique estimations of water quality: scope (F1), frequency (F2), and amplitude (F3) are evaluated and the index is obtained by using mathematical formulation and is graded using the ranking scale as depicted in Figs. 2 and 3 respectively.

3 Results and Discussion

The GW samples analyzed for various parameters from 32 different locations of Ilkal region are depicted in Table 1.

3.1 pH

As per the BIS the pH ranges from 6.5 to 8.5. The SDM of pH values of samples is depicted in Fig. 4a. The pH varies from 6.87 in (S-25) to 7.98 in (S-24). The pH of all the samples is in accordance with acceptable range of 6.5–8.5 as laid by BIS. Higher pH values effect the microbial life and alkalinity of soil [22].

Fig. 3 CCME water quality index grading scale

3.2 Electrical Conductivity (EC)

The dispersal of EC of Ilkal is indicated in Fig. 4b. The electrical conductivity values vary from a value as low as 0.5 mS/cm in (S-17) to a high value of 1.7 mS/cm in (S-10). The measure for the presence of salinity and total dissolved solids that affects the palatability of drinking water is the electrical conductance. The temperature, ionic mobility and valence also effects the electrical conductivity [23].

3.3 Total Dissolved Solids (TDS)

TDS of water signifies the presence of different kind of minerals, purity and quality of water. The total of cations and anions concentration is equal to the water TDS [24]. TDS is measured using TDS meter or from the EC value as:

$$\text{TDS(ppm)} = \text{EC(mS/cm)} \times 640, \text{ for EC between 0.1 and 5.0 mS/cm}$$

$$\text{TDS(ppm)} = \text{EC(mS/cm)} \times 800, \text{ for EC greater than 5.0 mS/cm}$$

The acceptable value of TDS is 500 mg/l whereas, 2000 mg/l is the maximum allowable value as per BIS [7]. The samples exhibit TDS values varying from 320

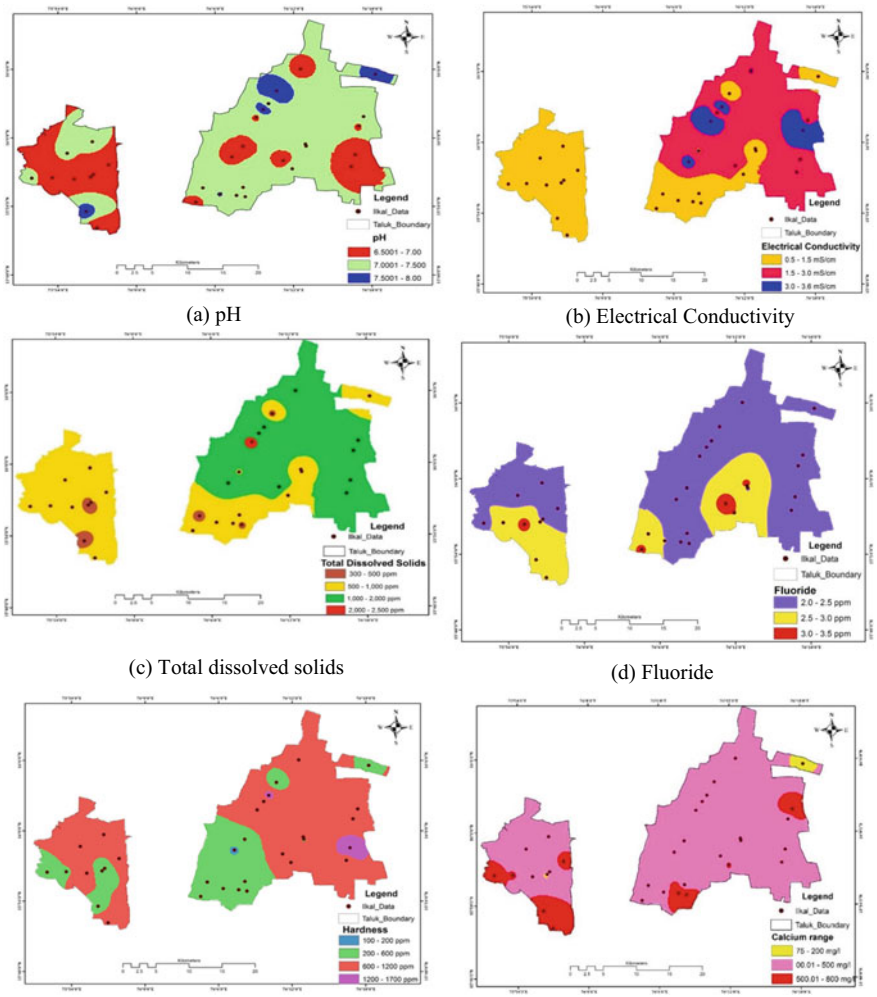

(a) pH (b) Electrical Conductivity

(c) Total dissolved solids (d) Fluoride

(e) Hardness (f) Calcium

Fig. 4 **a–i** Spatial distribution maps of water quality parameters

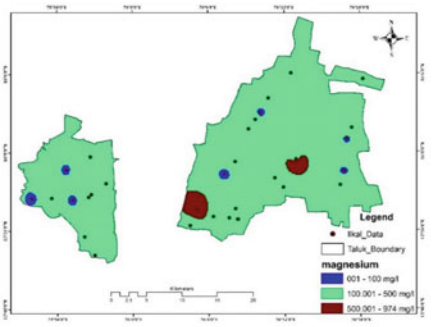

(g) Magnesium

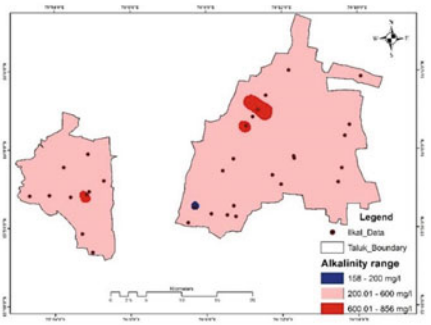

(h) Alkalinity

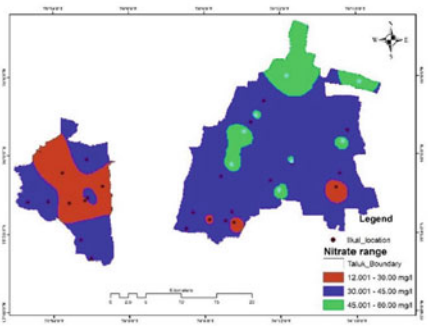

(i) Nitrate

Fig. 4 (continued)

to 2304 ppm in the sample stations (S-17) and (S-3) respectively. Figure 4c indicates the variation in spatial distribution of the TDS values. The sampling stations except Budhihala SK, Edageri, Balkundi and Hirekodagali Tanda have high TDS values greater than the acceptable value and are considered to have less saline water. The sample station Jambaladinni has a value higher than the permissible value and is considered to be consisting of highly saline water. Total dissolved solids have exceeded the acceptable value in an area covering 638.09 km^2 and permissible value in area of 2.34 km^2.

3.4 Fluoride

Fluoride (F^-) is a double-edged sword as it can either be detrimental or beneficial to human health based on its intake. It is one of the micronutrients required for teeth enamel and bone development in human beings. Fluoride value of (0.4–1.0 mg/L) helps in the calcinations of bones and promotes good teeth health. Skeletal fluorosis and discoloration of teeth are caused if the fluoride value is in excess (more than 1.5 mg/L). Hence the fluoride levels in water beyond the standard values are

considered to be a serious environmental and health jeopardy worldwide [25]. The acceptable limit of fluoride concentration suggested by WHO is between 0.5 and 1.5 mg/L. Whereas, BIS suggests the acceptable value of fluoride in the range 1.0 to 1.5 mg/l. In all the samples the fluoride levels were found to exceed the permissible value of BIS and WHO. Figure 4d depicts the spatial distribution of the fluoride. From the map it is found that 545.78 km^2 area has fluoride ranging from 2 to 2.5 mg/l, 2.5 to 3 ppm is found in 104.19 km^2 area and from 3 to 3.5 mg/l is found in 0.653 km^2 area.

3.5 Hardness

The sum of concentration of alkaline cations Calcium Ca^{++} and Magnesium Mg^{++} is expressed as hardness in water. Hardness of water is always expressed as its $CaCO_3$ equivalent [26]. Temporary hardness and permanent hardness together form total hardness. As per the BIS, the Total hardness of water as $CaCO_3$ equivalent is 200 mg/L, which is an acceptable value and 600 mg/L is the maximum allowable value. Beyond this concentration, the water may cause encrustation in pipeline and scaling in boilers. The hardness in the samples collected and analyzed for the stations (S-1) and (S-6) only have the hardness values well within the acceptable range with area covering 1.36 km^2. Sample stations (S-5), (S-11) and (S-12) exhibited a very high value of hardness covering an area of 14.35 km^2. The Fig. 4e indicates the spatial distribution variation mapping of the hardness data of Ilkal area.

3.6 Calcium

It is one of the supplementary element required for good bone health but consumption of calcium in higher amount through water may lead to abdominal diseases and it may also cause encrustation [27]. As per BIS, the acceptable and permissible values are 75 mg/l and 200 mg/l, respectively. From Fig. 4f it is observed that an area of 7.12 km^2 is having the Calcium concentration ranging between 75 and 200 mg/L, area of 483.84 km^2 has 200–500 mg/l of calcium and an area of 68.10 km^2 has a concentration ranging between 500 and 800 mg/l.

3.7 Magnesium

Magnesium (Mg) in water is principally because of the deterioration of gypsum, dolomite and magnesium calcite present in the bedrock [28]. Magnesium when present in the form of oxides imparts dark brown or black color to the water which causes stains on the clothes and utensils [29]. Acceptable and permissible values

of magnesium as per BIS are 30 mg/l and 100 mg/l, respectively. From Fig. 4g it is observed that an area of 9.31 km^2 is having concentration values ranging from 0 to 100 mg/l, area of 622.95 km^2 is having a concentration ranging between 100 and 500 mg/l and an area of 18.36 km^2 is having magnesium concentration ranging between 500 and 1000 mg/l.

3.8 Total Alkalinity

Total alkalinity of water is the sum total of alkaline components which increase the pH such as against a standard acid titrant and is expressed as mg/l of $CaCO_3$. Bedrock-containing limestone deposits are good contributors of carbonates in groundwater [30]. Bureau of Indian standards recommends total alkalinity of 200 mg/l as the minimum and 600 mg/l as the maximum value. From SDM of total alkalinity as shown in Fig. 4h alkalinity concentration in an area of 1.09 km^2 is ranging between 158 and 200 mg/l, in an area of 636.74 km^2 is ranging from 200 to 600 mg/l and in an area of 12.79 km^2 is ranging from 600 to 856 mg/l.

3.9 Nitrate

Nitrate is a polyatomic ion NO_3^-. If this ion is present in any of the salts they are called nitrates. Basically, the fertilizers, engine emissions and domestic effluents contain nitrate in them. It is basically, produced and discharged into the nature through various anthropogenic activities such as agriculture, fertilizer industries, sewage, etc. BIS recommends a maximum desirable nitrate value of 45 mg/l [30]. Nitrate concentration greater than 45 mg/l in water causes methemoglobinemia in infants below the age of 6 months [28]. From the SDM of nitrate shown in Fig. 4i it is observed that an area of 571.72 km^2 is having nitrate value of 0–45 mg/l and an area of 78.89 km^2 is having nitrate value from 45 to 60 mg/l.

3.10 Canadian Council of Ministers of the Environmental Water Quality Index (CCME WQI)

WQI of Ilkal taluk groundwater was calculated using the CCME WQI classification. MS Excel platform is adopted and the parameters obtained are tabulated as indicated in Table 2 for the calculation of CCME WQI.

The CCME WQI for the groundwater of Ilkal taluk is 20.770 which attains a "poor" rank as it falls in the range of 0–44 of the CCME WQI as shown in Fig. 3.

Table 2 Results of CCME WQI for analyzed groundwater parameters of Ilkal taluk

Description	Code	CCME data
Number of failed variables (parameters)	X	8
Total number of variables (parameters studied)	Y	9
Total number of tests	Z	288
Total number of failed tests (all parameters exceeding)	E	225
Factor 1	F1	88.889
Factor 2	F2	78.125
Normalised sum excursion	NSE	2.275
Factor 3	F3	69.470
CCME WQI		20.770

4 Conclusion

The Ilkal Taluk of Bagalkot district, Karnataka, India was selected for the investigation and assessment of groundwater. Total of 32 groundwater samples covering the entire Ilkal taluk was tested in the laboratory for various water quality parameters using standard procedures. From the analysis results, it is observed that the potability of water is effected due to TDS exceeding its maximum limit in S-3, Hardness in S-3, S-4, S-5, S-7, S-9, S-10, S-11, S-12, S-14, S-15, S-16, S-18, S-19, S-20, S-21, S-25 and S-26, Nitrate in S-2, S-3, S-5, S-7, S-8, S-10, S-14 and S-15 and total alkalinity was found to exceed in S-1, S-3 and S-4.

From the spatial distribution map, it is very clear that all the water samples tested for pH were well within the range of drinking water as suggested by BIS. Total dissolved solids have exceeded the acceptable value in an area covering 638.09 km^2 and permissible value in area of 2.34 km^2. Hardness is also under permissible value in an area covering 1.36 km^2 and has crossed the permissible value in an area covering 473.87 km^2. The entire area is having Fluoride concentration greater than 1.5 mg/l, Calcium concentration has been found to be exceeding its acceptable value for the entire area and an area of 551.94 km^2 is having Calcium exceeding its maximum acceptable value of 200 mg/l. Magnesium concentration is found to be exceeding its maximum value of 100 mg/l in an area of 631.31 km^2. An area of 1.09 km^2 is having total alkalinity value in its acceptable range of 200 mg/l and an area of 12.79 km^2 is found to have total alkalinity above the permissible value of 600 mg/l. An area of 571.72 km^2 is having the nitrate concentration well within the acceptable value and an area of 78.89 km^2 is having the nitrate value above the acceptable limit.

Based on CCME WQI calculation, the groundwater WQI of Ilkal taluk ranked poor, which is an indication that water quality is almost always threatened or impaired; condition usually departs from natural or desirable levels. Among the tested parameters, EC, TDS, total alkalinity, total hardness, calcium, magnesium and fluoride contributed for the poor WQI value. The summed up complex water quality information obtained by the combination of GIS and WQI can be handily perceived

and this data can be of extraordinary incentive for water consumers (public), regional governing bodies and researchers for managing and monitoring the groundwater resources of Ilkal taluk. From the groundwater quality experimental analysis results, spatial distribution maps and CCME WQI it can be concluded that the Ilkal taluk groundwater has to be continuously monitored and treated to make it potable and also to protect the health of the people residing in this area, as the entire population depends on the groundwater as their major source of water supply.

References

1. Patil SB, Bisanal MG (2012) Geochemical analysis of fluoride in ground water using GIS 8(2):7
2. Singh SK, Srivastava PK, Pandey AC (2013) Fluoride contamination mapping of groundwater in Northern India integrated with geochemical indicators and GIS. Water Supply 13(6):1513–1523. https://doi.org/10.2166/ws.2013.160
3. Naika K, Ravikumar P, Prakash KL (2020) An investigation of fluoride contamination in groundwater of Yadgir district, Karnataka p 8
4. Gaonkar SM, Karabasannavar SS, Patil VBB, Kalashetty MB, Kalashetty BM (2019) Studies on toxicity of fluoride and impact of endemic fluorosis from groundwater resources of Bagalkot district, Karnataka—geospatial information system approach. J Geol Soc India 93(1):109–112. https://doi.org/10.1007/s12594-019-1129-5
5. Rai A (2020) Fluoride contamination issues of groundwater in Rajasthan: a review. https://www.semanticscholar.org/paper/FLUORIDE-CONTAMINATION-ISSUES-OF-GROUNDWATER-IN-A-Rai/496c15b94e347844d37fa2d7a6de6f962017b512. Accessed 01 July 2021
6. Jagtap S, Yenkie MK, Labhsetwar N, Rayalu S (2012) Fluoride in drinking water and defluoridation of water. Chem Rev 112(4):2454–2466. https://doi.org/10.1021/cr2002855
7. IS 10500 (2012) Drinking water, p 16
8. Pande CB, Moharir KN, Singh SK, Dzwairo B (2020) Groundwater evaluation for drinking purposes using statistical index: study of Akola and Buldhana districts of Maharashtra, India. Environ Dev Sustain 22(8):7453–7471. https://doi.org/10.1007/s10668-019-00531-0
9. Bera A, Mukhopadhyay BP, Barua S (2020) Delineation of groundwater potential zones in Karha river basin, Maharashtra, India, using AHP and geospatial techniques. Arab J Geosci 13(15):693. https://doi.org/10.1007/s12517-020-05702-2
10. Rezaei H, Bozorg-Haddad O, Demirel MC (2021) Remote sensing application in water resources planning. In: Bozorg-Haddad O (ed) Essential tools for water resources analysis, planning, and management. Springer, Singapore, pp 101–124. https://doi.org/10.1007/978-981-33-4295-8_5
11. Pande CB, Khadri SFR, Moharir KN, Patode RS (2018) Assessment of groundwater potential zonation of Mahesh River basin Akola and Buldhana districts, Maharashtra, India using remote sensing and GIS techniques. Sustain Water Resour Manag 4(4):965–979. https://doi.org/10.1007/s40899-017-0193-5
12. "Ilkal City Municipal Council City Population Census 2011–2021 Karnataka." https://www.census2011.co.in/data/town/803050-ilkal-karnataka.html. Accessed 01 July 2021
13. Tirumalesh K, Shivanna K, Jalihal AA (2007) Isotope hydrochemical approach to understand fluoride release into groundwaters of Ilkal area, Bagalkot District, Karnataka, India. Hydrogeol J 15(3):589–598. https://doi.org/10.1007/s10040-006-0107-3
14. "KSRSAC" https://ksrsac.karnataka.gov.in/map.aspx. Accessed 07 July 2021

15. Sharma A, Kumar M, Hasteer N (2020) Applications of GIS in management of water resources to attain zero hunger. In: AlKhaddar R, Singh RK, Dutta S, Kumari M (eds) Advances in water resources engineering and management, vol 39. Springer Singapore, pp 211–218. https://doi.org/10.1007/978-981-13-8181-2_16
16. Sinha K, Das (Saha) P (2015) Assessment of water quality index using cluster analysis and artificial neural network modeling: a case study of the Hooghly River basin, West Bengal, India. Desalination Water Treat 54(1), 28–36. https://doi.org/10.1080/19443994.2014.880379
17. Tyagi S, Sharma B, Singh P, Dobhal R (2020) Water quality assessment in terms of qater quality index. Am J Water Resour 1(3):34–38. https://doi.org/10.12691/ajwr-1-3-3
18. Lumb A, Halliwell D, Sharma T (2006) Application of CCME water quality index to monitor water quality: a case study of the Mackenzie River Basin, Canada. Environ Monit Assess 113(1):411–429. https://doi.org/10.1007/s10661-005-9092-6
19. Mahagamage Y, Manage Y (2014) Water quality index (CCME-WQI) based assessment study of water quality in Kelani river basin, Sri Lanka
20. Haldar D, Halder S, Das P, Halder G (2014) Assessment of water quality of Damodar River in South Bengal region of India by Canadian Council of Ministers of Environment (CCME) water quality index: a case study. Desalin Water Treat, pp 1–14. https://doi.org/10.1080/19443994.2014.987168
21. Sharma D, Kansal A (2011) Water quality analysis of River Yamuna using water quality index in the national capital territory, India (2000–2009). Appl Water Sci 1(3):147–157. https://doi.org/10.1007/s13201-011-0011-4
22. Awoyemi OM, Achudume AC, Okoya AA (2014) The physicochemical quality of groundwater in relation to surface water pollution in Majidun Area of Ikorodu, Lagos State, Nigeria. Am J Water Resour 2(5):126–133. https://doi.org/10.12691/ajwr-2-5-4
23. Hanipha M, Hussain Z (2017) Seasonal variations of groundwater quality in and around Dindigul Town, Tamilnadu, India. Chem Sin 8(2). Accessed 05 July 2021. [Online]. Available: https://www.imedpub.com/abstract/seasonal-variations-of-groundwater-quality-in-and-aroundrndindigul-town-tamilnadu-india-18887.html
24. Bansal J (2018) Assessment of ground water quality by using water quality index and physico chemical parameters: review paper. https://doi.org/10.5281/ZENODO.1165780
25. Borgohain X, Boruah A, Sarma GK, Rashid MdH (2020) Rapid and extremely high adsorption performance of porous MgO nanostructures for fluoride removal from water. J Mol Liq 305:112799. https://doi.org/10.1016/j.molliq.2020.112799
26. Kugali NM, Yadawe MS (2013) Physicochemical analysis of water of Bagalkot district, Karnataka in India. Int Res J Pharm 4(8):202–204. https://doi.org/10.7897/2230-8407.04839
27. Kumar Subbiah K, Ashokkumar L, Godson P, Chandrasekar N (2014) Hydro-geochemistry and application of water quality index (WQI) for groundwater quality assessment, Anna Nagar, part of Chennai City, Tamil Nadu, India. Appl Water Sci 5. https://doi.org/10.1007/s13201-014-0196-4
28. Jebastina N, Arulraj PG (2017) GIS based assessment of groundwater quality in Coimbatore district, India. J Environ Anal Toxicol 07(03). https://doi.org/10.4172/2161-0525.1000454
29. Pandey HK, Tiwari V, Kumar S, Yadav A, Srivastava SK (2020) Groundwater quality assessment of Allahabad smart city using GIS and water quality index. Sustain Water Resour Manag 6(2):28. https://doi.org/10.1007/s40899-020-00375-x
30. Dohare D, Deshpande S, Kotiya A Analysis of ground water quality parameters: a review 3:6

Exclusion of Non-value Efforts in Construction Projects

M. S. Deepak, G. Beulah Gnana Ananthi, Anupkumar G. Ekbote, and Rithika Raj

Abstract An effort that adds non-value (ENV) could be saved if the project had been better planned, conducted, monitored, and regulated. To recognize and reduce ENV in micro-level analysis such as sampling of works and balance charts explaining the balance of the asset is used broadly. These methods are particularly successful when analyzing operations with modest performance variance in each cycle and can discover redundant stages in highly repetitive building activity. Data is gathered through literature reviews and site visits. The main aim of this study is to construct a dynamic tool that can detect and enumerate ENV, and changes can be done in the design. This proposed model was then used in two case studies, it was discovered that errors and changes caused 18.61% ENV and if the project is delayed, there will be a delay of 128 days in the case of project I and 72 days in case project II. Furthermore, productivity loss and Interruption (RFIR) form the major part of ENV, causing delays in both the case studies. Based on the findings, this research stated that this proposed tool could be used as a device to improve ENV comprehension in projects, resulting in a more significant reduction in ENV.

Keywords ENV · Time overrun · Cost overrun · Rework · Delay

1 Introduction

In India, construction projects have high cost and time overruns, resulting in increasing consumer dissatisfaction. Reducing waste or non-value-adding activities is a viable solution to the Indian construction industry's difficulties. The effort that adds non-value in a design and construction project is time and money that could be

M. S. Deepak · A. G. Ekbote · R. Raj
Department of Civil Engineering, BMS Institute of Technology and Management, Bengaluru, India

G. Beulah Gnana Ananthi (✉)
Division of Structural Engineering, Anna University, Chennai, India
e-mail: beulah28@annauniv.edu

L. Nandagiri et al. (eds.), *Recent Advances in Civil Engineering*, Lecture Notes in Civil Engineering 256, https://doi.org/10.1007/978-981-19-1862-9_39

saved and planned better. This waste of time and money has been identified as a significant source of design and construction project delays in schedule and cost overruns. According to research undertaken by ASCE and CII, rework costs directly account for around 5% of the total building cost (CII 2005). Design or scope changes, which account for most rework in the construction sector, cause high cost and schedule overruns. The industrialized countries are conducting research and investigations to determine the causes of ENV and to develop models that can detect ENV early on and decrease its impact. In India, a study on this subject is still in its infancy, and construction professionals have yet to grasp the magnitude of the waste's impact on the project. The main objective of this study is to identify the factors causing ENV and develop a Dynamic Model, using the interrelation between those critical factors to Calculate the ENV caused due to errors and design changes.

Horman et al. [1] found that 49.6% of the operating time in their case projects is squandered without generating value. This conclusion suggests that a reduction in unnecessary effort is linked to the efficiency of a design and construction project. As a result, one of the key study concerns in the construction management field has been how to reduce ENV. Lopez et al. [2], Many catastrophic catastrophes have occurred due to design flaws; as a result, workers and members of the public have died or been injured. In building and engineering projects, he investigated and classified the nature of error and design error causation. According to an assessment of the normative literature, design flaws are generated by various factors that might interact. A generic framework for classifying design errors according to people, organization, and the project is discussed. His findings imply that people, rather than organizational or project management systems, have the most incredible proclivity for reducing errors through situated knowledge and learning. It is mainly due to the character and ability of individuals to do jobs is influenced by the working environment provided by an organization and the methods utilized to deliver construction and engineering projects.

Park et al. [3], RMC vendors have had difficulty delivering ready mixed concrete (RMC) quickly and cost-effectively. He used system dynamics to create a dynamic simulation model. The model illustrates the generic RMC operating process and may be customized for different operational settings by changing its structure and parameters. According to the findings, the model-generated information aids in establishing a cost-effective RMC supply by keeping the number of queuing truck mixers at an acceptable level while meeting the contractor's requirements. They concluded that the dynamic model could be used as an automated tool to help RMC suppliers plan their supply. Love et al. [4] looked at rework caused by design errors. Around 70% of the total rework in projects was due to design errors. Owner pressure and time constraints are the primary causes of these blunders. Figure 1 depicts the several factors that agitate the designer and increase his chances of making mistakes. Due to time constraints, incomplete designs are frequently handed over to contractors on public projects. Design audits and bringing inexperienced people to the design team are good places to start when it comes to reducing errors.

Hwang et al. [5] looked at 359 construction projects from the Construction Industry Institute (CII) database to link project groups to rework sources. The Total

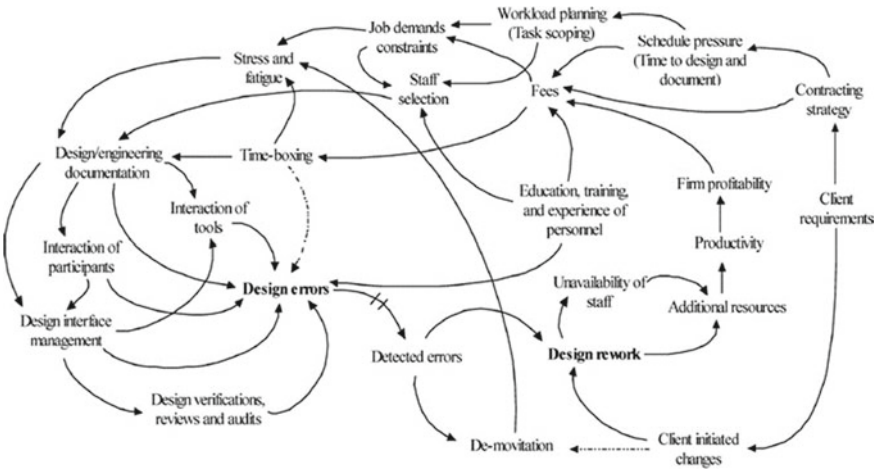

Fig. 1 Influence diagram of design error induced rework

Field Rework Factor (TFRF), developed by CII, is a statistic used to evaluate the influence of rework on construction costs. Rework on modernization projects cost twice as much as add-on projects. The two variables that resulted in the most significant rework expenses were owner changes and design faults. Forcada et al. [6] researched problems that arise after delivery. Because the problems occurred during the defect responsibility period, the contractor was responsible for rectifying them. According to a Chi-square (2) test of independence, the defect type and element had a strong association. The most prevalent problems discovered by clients upon handover were incorrect positioning of toilet fittings and missing tile grouts. Taggart et al. [7] investigated the role of the supplier chain in rework in building projects in Ireland. The research reveals management's limitations in collecting and documenting rework data. The main reason for not stopping the constant occurrence of rework is a lack of standard methods for repairing the recognized rework area. The study found that enhancing supply chain coordination and collaboration would result in significant cost reductions for the project. The use of a collaborative IT system can help to reduce rework [8–13]. The ENV studies are done based on the following phases:

- In the first phase, a detailed review of ENV kinds of literature is done. The primary causes for ENV were eminent in the literature and conversations with construction professionals. The literature was also examined to see how wastage, such as rework, could be caught on the job site and what methods could be used to reduce it.
- In the second phase, the classification of ENV, factors causing ENV, and their interrelations are dealt with thoroughly. Then, based on their generating patterns and recurrence times, ENV generated by mistakes and changes are divided into three categories.

- The third phase was creating a Qualitative model from critical factors attributing to ENV, which detects fundamental connections among mistakes and ENV.
- A quantitative model is offered that can quantify the influence of errors and changes on project performance in the fourth phase, based on the understanding gained from the qualitative model. Finally, a relational equation is formulated to calculate ENV, derived from those two models.
- Site visits are undertaken in the fifth phase to identify regions where ENV is most likely to occur and to identify root causes of ENV through observation and expert interviews.
- In the sixth phase, the developed model is validated by feeding the data gathered from site visits, and ENV should be calculated using the derived equation for each project activity.
- At last, the results obtained from the data analysis are discussed, and the impact of ENV on the project schedule is projected.

Depending on the generation patterns and timings of occurrence, ENV generated by mistakes and changes is split into three categories:

1. Before the execution: Intermission
2. During the process of execution: Other sources of productivity loss
3. Following the execution: Revise.

One may argue that calculating the negative consequences of ENV on the outcome of the project is as simple as comparing the allotted effort to the created value. However, control steps to limit ENV can differ contingent on the prevailing kind of ENV. Therefore the patterns must still be identified. On the other hand, quality improvement and scope freezing may be more appropriate if the revision of the work constitutes the mainstream of ENV. In addition, each ENV pattern demands a different amount of extra work to recompense the detrimental effect. For example, ENV caused by a loss of production necessitates a compensating effort equivalent to the loss in the effort. The three patterns (interruptions, additional productivity losses, and rework) all have something in common. Each pattern wastes a portion of the given effort, necessitating more effort to compensate for the initial effort.

2 Value Addition Rate

A statistic known as the value addition rate (VAR) represents the fraction of VAE per unit and calculates the amount of time and effort wasted and compensating effort. The VAR measure is generally in the range of 0–100%. However, it can be outside of this range. As a result, the VAR measure can be more significant than 100% for some time if highly motivated, and skilled workers execute an activity at a higher than nominal output rate. The VAR measure might also be 0% or negative. However, this is uncommon. The VAR measure is 0% for the period allotted on the effort is worthless, such as creating building components that have no contribution to

the project. Furthermore, the VAR measure can be harmful if these poorly designed components of the building depreciate previously manufactured components or entail destruction or redoing of unnecessary effort.

2.1 Qualitative Model

The overall linkage among essential variables is established through a rigorous analysis of existing research, specifically relevant to errors and changes to understand better. Then, as shown in Fig. 2, a qualitative fundamental loop diagram was created to explain how errors and modifications result in ENV. VAE and ENV make up construction activity. VAE and ENV sum equal the total effort expended in an activity (Points 1 and 2 in Fig. 2). When faults are discovered during inspection, they must be reworked, which may increase the quantity of ENV (Points 3 and 4 in Fig. 2). Although rework frequently requires the demolition of what has already been built, construction managers change their plans and specifications to avoid rework for challenging activities. (point 5 in Fig. 2).

Late design modifications and faults are damaging since they can obviate the requirement for rework, which is already built components (Fig. 8 in Fig. 2). In addition, design adjustments frequently result in a rise in the scope of work and requirements for the VAE (Points 9 and 10 in Fig. 2), increasing the project's necessary effort and duration. Errors and alterations can cause significant productivity loss in addition to rework and interruption (Points 11, 12, and 13 in Fig. 2). As a result,

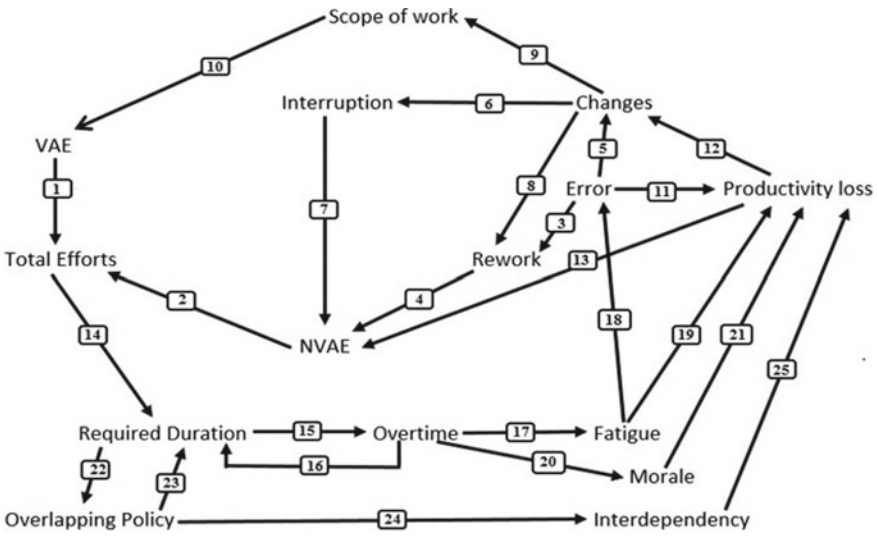

Fig. 2 Qualitative model—feedback mechanism model

ENV necessitates additional effort as compensation, increasing the project's overall effort and time (points 2 and 14 in Fig. 2).

When real progress falls behind schedule, the construction manager takes corrective action to keep the project on track. (Points 15 and 16 in Fig. 2). On the other hand, time-off policies may cause additional issues like weariness, leading to more errors and a decrease in productivity. (points 17, 18, and 19 in Fig. 2). Furthermore, working long hours diminishes employee morale and, as a result, productivity (points 20 and 21 in Fig. 2). Another extensively used strategy for timetable acceleration is an overlapping policy. (points 22 and 23 in Fig. 2). However, while overlapping policies do not cause weariness, they tend to create interdependency with other processes, leading to a drop in productivity due to additional coordination and space constraints. (points 24 and 25 in Fig. 2).

2.2 Quantitative Model

A quantitative simulation model is constructed based on fundamental interdependencies linked to errors, changes, and ENV determined through a qualitative model. The dynamic model may effectively capture the dynamics of errors and changes, illustrating how they affect project performance. Any activity can be in one of six states in the general work execution module. These are *Activity to be Completed* (ATC), *Activity Listed for Checking* (ALC), *Activity Completed* (AC), *Activity Halted for Additional Information* (AHFAI), *Activity Waiting for Predecessor Correction* (AWPC) and *Activity Undergone Design Change* (AUDC). In addition, the general work execution module is introduced to accessible activities at a particular moment through an Activity Introduction Rate (AIR) physical constraints, and imposed precedence relationships is determined.

The activity that is introduced is then saved in ATC. Work Rate (WR), determined by the number of resources assigned and the productivity of those resources, is used to perform activities in ATC and then transfer them to ALC (i.e., effort). Activities in ALC are examined, and only those that are appropriately executed are moved to AC. At the same time, those that have been wrongly executed are returned to ATC. Activities in ATC are not always ready to be carried out. The Dynamic model used to find out the ENV is shown in Fig. 3. The model is developed to represent the basic construction process focusing on iterative cycles during the actual execution. It is based on the existing system dynamics project model, which many researchers and practitioners have developed.

Activities in AHFAI have three ways to flow out. The first option is going back to ATC because it may accommodate the change made in the predecessor activity. If not, the successor activity can request the correction of the change. Therefore, the associated task accumulates in AWPC. It will be back to ATC and performed after correction in the predecessor activity is completed. Back to AHFAI, the last option is to flow into the stock of AUDC. If it is revealed as a latent change in the predecessor

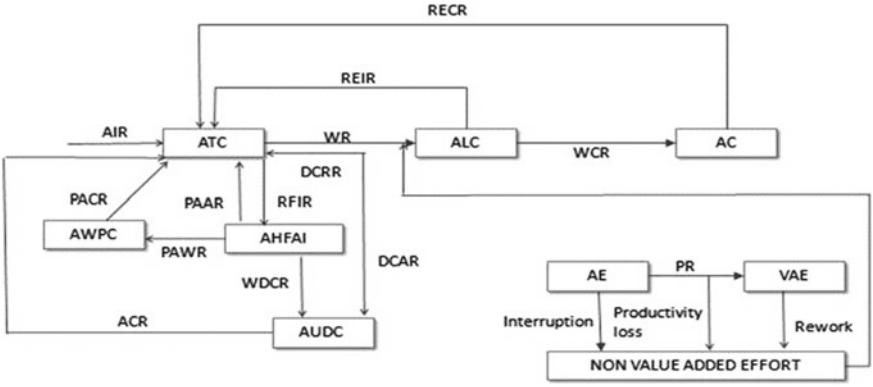

Fig. 3 Dynamic model to calculate non-value added effort

activity, the manager may request the decision to the claim and change group. In short, AUDC has two inflows, one from AHFAI and one from ATC.

Late change orders can prevent some ATC activities from performing, even if there are no quality issues or conflicts between project papers and site conditions. In this instance, some activities are temporarily housed in AUDC until all modification orders have been reviewed and authorized. As a result, during the project implementation phase, the standard work module records the life cycle of activities, and the quantity of activities in a given status at any given time is mathematically determined. For instance, at the *j*th activity, ATC (i.e., the number of accessible activities for execution) is calculated as follows:

$$\frac{\mathrm{d}}{\mathrm{d}t}(\mathrm{ATC}_j) = \mathrm{AIR}_j + \mathrm{REIR}_j - \mathrm{WR}_j - \mathrm{DCAR}_j + \mathrm{DCRR}_j + \mathrm{RECR}_j + \sum_{j=1}^{n}(\mathrm{PARR}_{(j,k)}) - \sum_{j=1}^{n}(\mathrm{RFIR}_{(j,k)}) + \sum_{j=1}^{n}(\mathrm{PACR}_{(j,k)}) \quad (1)$$

To accurately quantity and reduce ENV, it must first be recognized. As previously stated, ENV manifests itself in three ways: interruption, additional output loss, and rework. This categorization will be followed; the time spent on both are recorded in the effort module, Design Change Approved Rate (DCAR; change order-driven ENV creation) and RFI Rate (RFIR; RFI ENV generation). Then, productivity loss is estimated by comparing the work rate to the nominal work rate (NWR) obtained from the resource module. Re-Execution of Incomplete Activity Rate (REIR; ENV dealt with during the inspection phase) and Re-Execution of Completed Activity Rate (RECR; ENV addressed during the inspection process) are also quantified in the model (RECR; ENV discovered through succeeding activities). Finally, the total amount of ENV is calculated by combining the time wasted due to interruptions, other productivity losses, and rework. The following is a numerical representation of this concept:

$$\frac{\mathrm{d}}{\mathrm{d}t}(\mathrm{NVAE}_j) = \mathrm{DCAR}_j + \mathrm{NWR}_j - \mathrm{WR}_j + \mathrm{REIR}_j + \mathrm{RECR}_j + \sum_{j=1}^{n} (\mathrm{RFIR}_{(j,k)}) \quad (2)$$

As indicated in the introduction, the purpose of this approach is to find and measure ENV caused by mistakes and alterations by which the designed model can be tested to see if it is accurate.

2.3 Data Collection

Two case studies of an industrial project and a road project are carried out for testing the model. Site visits and expert interviews are carried to record the factors causing ENV. To obtain accurate facts about the source of wasted effort, relevant project papers such as a daily log, non-conformance report, RFIs, and change order logs are analyzed.

3 Data Analysis and Discussion

Data collected from the site visits have been incorporated into the developed model as per the research methodology discussed in the previous chapter. The analysis includes calculations of ENV, delays, percentage of VAE for every activity using the formulated equation. Two case studies are considered for analyzing the ENV involved in the construction projects. This chapter includes the quantification of ENV using the model for the projects under consideration and interpretation of the results after analysis.

3.1 Case Study I

Project Details:

Project consultant	Jones Lang Lasalle (JLL)
Client	Hexaware
Main contractor	Shapoorji Palonji
Built-up area	43,000 ft^2
Place	Sipcot–Siruseri (Chennai)

ENV Calculation

Table 1 gives the detailed calculation of ENV using various measures of wasted effort like REIR, RECR, DCAR, RFIR and Productivity loss. Also, it calculates the delay due to ENV for each of the project activities using Eq. 2.

A sample calculation of ENV for footing by using the model has shown below.

$$\frac{\mathrm{d}}{\mathrm{d}t}(\mathrm{NVAE}_j) = \mathrm{DCAR}_j + \mathrm{NWR}_j - \mathrm{WR}_j + \mathrm{REIR}_j + \mathrm{RECR}_j + \sum_{j=1}^{n} (\mathrm{RFIR}_{(j,k)})$$

$$\frac{\mathrm{d}}{\mathrm{d}t}(\mathrm{NVAE}_j) = 0.5\% + 12.26\% - 2.26\% + 2.00\% + 1.20\% + 4.00\% = 17.70\%$$

3.2 Case Study II

Project Details:

Project consultant	Jones Lang Lasalle (JLL)
Main contractor	McNally Bharat
Built-up area	15,000 ft^2
Place	Navalur (Chennai)

ENV calculation

Table 2 gives the detailed calculation of ENV using various measures of wasted effort like REIR, RECR, DCAR, RFIR and Productivity loss. Also, it calculates the delay due to ENV for each of the project activities. In this project, the quantification of ENV will be very helpful for effective project management because of the repetition of activities.

3.3 Results Interpretation

The results obtained from quantifying all the three categories of ENV, i.e., Rework, Interruption and Productivity loss, are interpreted. Figure 4 shows the Actual duration of all the activities under consideration, highlighting the delay in each activity—the actual duration of Milestone activities after incorporating the delay obtained from quantification of ENV in MS PROJECT. Fig. 4 clearly shows that the productivity loss contributes to the majority of ENV involved in the project. Therefore, all the

Table 1 ENV calculation for Case Study I

Activity	Task	Activity duration (days)	Wasted effort(% of total effort)				Productivity loss	ENV	Delay (days)	Variation	Delayed time (days)
			Rework		Interruption						
			REIR	RECR	DCAR	RFIR					
Construction drawings—main factory building	Footings	93	2.00%	1.20%	0.50%	4.00%	10.00%	17.70%	16.461	82.30%	109
	Pedestal Including Bolt Fixing	80	0.00%	0.00%	0.50%	1.00%	2.00%	3.50%	2.8	96.50%	83
	Plinth Beam	78	0.00%	0.00%	0.00%	2.00%	4.50%	6.50%	5.07	93.50%	83
	Masonry up to FFL (if any)	60	0.00%	0.00%	0.25%	1.50%	3.00%	4.75%	2.85	95.25%	63
	Back Filling, Crushed Stone Filling & Compaction for Erection of PEB Structure	30	0.00%	0.00%	0.00%	0.25%	0.50%	0.75%	0.225	99.25%	30
	Hand over to PEB Vendor for Erection	1	0.00%	0.00%	0.00%	0.00%	0.00%	0.00%	0	100%	1
Other works above FFL	Block work till lintel level	75	0.00%	1.00%	1.00%	2.00%	4.00%	8.00%	6	92.00%	81

(continued)

Table 1 (continued)

Activity	Task	Activity duration (days)	Wasted effort(% of total effort)				Productivity loss	ENV	Delay (days)	Variation	Delayed time (days)
			Rework		Interruption						
			REIR	RECR	DCAR	RFIR					
	Casting of column	44	1.00%	3.00%	5.00%	8.00%	15.00%	32.00%	14.08	68.00%	58
	Lintel and sunshade	34	0.00%	0.25%	0.00%	4.00%	10.00%	14.25%	4.845	85.75%	39
	Block work above lintel	26	0.00%	0.00%	0.00%	1.00%	5.00%	6.00%	1.56	94.00%	28
	Plastering works	76	0.75%	0.50%	0.00%	2.00%	8.00%	11.25%	8.55	88.75%	85
	Plastering	45	0.75%	0.50%	0.00%	2.00%	7.00%	10.25%	4.6125	89.75%	50
	Tiling	60	2.00%	2.50%	0.00%	4.20%	10.75%	19.45%	11.67	80.55%	72
Flooring works	PCC	30	1.50%	1.75%	0.25%	4.00%	8.00%	15.50%	4.65	84.50%	35
	Rebar	27	0.50%	0.50%	1.00%	1.50%	4.00%	7.50%	2.025	92.50%	29
	Concrete	33	3.00%	2.80%	0.75%	6.20%	13.00%	25.75%	8.4975	74.25%	41
Mezzanine floor work	Concreting works	34	1.20%	1.89%	0.30%	7.90%	14.30%	25.59%	8.7006	74.41%	43
	Epoxy painting	20	0.10%	15.00%	0.00%	0.50%	2.00%	17.60%	3.52	82.40%	24
Painting works	Painting works	60	0.00%	0.00%	0.00%	0.35%	2.00%	2.35%	1.41	97.65%	61
Utility Block 1	Setting out	25	0.00%	0.00%	0.00%	0.00%	1.50%	1.50%	0.37	98.50%	25

(continued)

Table 1 (continued)

Activity	Task	Activity duration (days)	Wasted effort(% of total effort)				Productivity loss	ENV	Delay (days)	Variation	Delayed time (days)
			Rework		Interruption						
			REIR	RECR	DCAR	RFIR					
Sub electrical room	Earth works	7	0.00%	0.00%	0.00%	1.20%	2.00%	3.20%	0.224	96.80%	7
	Foundation works	15	0.50%	0.50%	0.00%	2.00%	6.00%	9.00%	1.35	91.00%	16
	Structural works (GF, FF, SF & Terrace)	145	2.50%	0.75%	1.00%	2.90%	8.50%	15.65%	22.69	84.35%	168
	Water Proofing works	17	0.15%	1.00%	0.00%	2.40%	4.00%	7.55%	1.28	92.45%	18
	Block work	20	0.00%	0.00%	0.00%	0.65%	2.00%	2.65%	0.53	97.35%	21
	Plastering	25	0.75%	0.00%	0.00%	2.00%	6.00%	8.75%	2.18	91.25%	27
	Joinery/Façade	7	1.00%	0.00%	1.00%	2.00%	6.00%	10.00%	0.70	90.00%	8
	Tiling	10	2.00%	1.50%	0.00%	3.00%	7.00%	13.50%	1.35	86.50%	11
	Painting works	37	1.00%	1.50%	0.00%	2.00%	8.00%	12.50%	4.62	87.50%	42
Electrical Panel room	Earth works	7	0.00%	0.00%	0.00%	4.00%	17.00%	21.00%	1.47	79.00%	8
	Foundation works	5	1.00%	0.50%	0.00%	3.00%	12.00%	16.50%	0.82	83.50%	6
	Structural works including VDF	79	1.00%	1.15%	0.40%	5.00%	20.00%	27.55%	21.76	72.45%	101

(continued)

Table 1 (continued)

Activity	Task	Activity duration (days)	Wasted effort(% of total effort)				Productivity loss	ENV	Delay (days)	Variation	Delayed time (days)
			Rework		Interruption						
			REIR	RECR	DCAR	RFIR					
	Block work	15	0.00%	0.00%	0.00%	2.00%	9.00%	11.00%	1.65	89.00%	17
	Plastering	10	1.00%	0.75%	0.00%	3.00%	13.00%	17.75%	1.77	82.25%	12
	Joinery/Façade	7	1.00%	1.20%	0.00%	5.00%	13.00%	20.20%	1.41	79.80%	8
	Painting works	24	1.00%	3.00%	0.00%	4.00%	17.00%	25.00%	6.00	75.00%	30
UTILITY BLOCK 2—chemical storage and scrap store	Earth works	7	0.50%	0.75%	0.00%	1.00%	9.00%	11.25%	0.78	88.75%	8
	Foundation works	5	0.00%	0.35%	0.00%	2.00%	7.00%	9.35%	0.46	90.65%	5
	Structural works machine foundation	14	1.00%	1.75%	1.50%	5.00%	16.00%	25.25%	3.53	74.75%	18
	Block work	15	0.00%	0.50%	0.00%	2.00%	10.00%	12.50%	1.875	87.50%	17
	Plastering	10	1.00%	0.50%	0.00%	3.00%	8.00%	12.50%	1.25	87.50%	11
	Joinery/Façade	7	1.00%	2.00%	0.00%	1.50%	14.00%	18.50%	1.29	81.50%	8
	Painting works	33	0.75%	0.50%	0.00%	5.00%	10.00%	16.25%	5.36	83.75%	38
DG room & transformer yard	Earth works	7	0.00%	0.00%	0.00%	6.00%	18.00%	24.00%	1.68	76.00%	9

(continued)

Table 1 (continued)

Activity	Task	Activity duration (days)	Wasted effort(% of total effort)				Productivity loss	ENV	Delay (days)	Variation	Delayed time (days)
			Rework		Interruption						
			REIR	RECR	DCAR	RFIR					
	Foundation Works	5	0.75%	0.00%	0.00%	5.00%	19.00%	24.75%	1.23	75.25%	6
	Structural works & Machine foundation	14	1.75%	2.00%	0.00%	12.00%	25.00%	40.75%	5.70	59.25%	20
	Block work	15	0.75%	0.50%	0.00%	4.00%	15.00%	20.25%	3.03	79.75%	18
	Plastering	10	0.50%	1.00%	0.00%	7.00%	8.00%	16.50%	1.65	83.50%	12
	Joinery/Façade	7	0.50%	0.35%	0.00%	9.00%	18.00%	27.85%	1.94	72.15%	9
	Painting works	45	1.50%	3.00%	0.00%	12.00%	22.00%	38.50%	17.32	61.50%	62
Other buildings-UG tanks and pump room	Earth works	7	0.50%	0.25%	0.00%	6.00%	13.00%	19.75%	1.38	80.25%	8
	Bottom slab	5	1.60%	2.00%	0.00%	9.00%	19.00%	31.60%	1.58	68.40%	7
	Side wall & columns for pump room	96	0.50%	0.75%	0.00%	7.00%	15.00%	23.25%	22.32	76.75%	118
	Top slab	17	0.25%	0.00%	0.00%	8.00%	20.00%	28.25%	4.80	71.75%	22

(continued)

Table 1 (continued)

Activity	Task	Activity duration (days)	Wasted effort(% of total effort)				Productivity loss	ENV	Delay (days)	Variation	Delayed time (days)
			Rework		Interruption						
			REIR	RECR	DCAR	RFIR					
	Water proofing	87	1.00%	0.75%	0.00%	12.00%	17.00%	30.75%	26.75	69.25%	114
	Backfilling	35	0.00%	0.00%	0.00%	8.00%	20.00%	28.00%	9.80	72.00%	45
Pump room and security	Structural works	80	1.90%	1.50%	0.00%	7.00%	18.00%	28.40%	22.72	71.60%	103
	Block work	15	0.90%	0.50%	0.00%	5.00%	11.00%	17.40%	2.61	82.60%	18
	Plastering	10	0.00%	0.00%	0.00%	5.00%	13.00%	18.00%	1.80	82.00%	12
	Flooring	10	0.75%	1.00%	0.00%	8.00%	17.00%	26.75%	2.67	73.25%	13
	Joinery/Façade	80	1.00%	1.50%	0.00%	8.00%	16.00%	26.50%	21.20	73.50%	101
	Painting works	48	1.00%	0.75%	0.00%	5.00%	15.00%	21.75%	10.44	78.25%	58
Security building	Earth works	7	0.00%	0.00%	0.00%	5.00%	9.00%	14.00%	0.98	86.00%	8
	Foundation works	15	0.00%	0.00%	0.00%	2.00%	15.00%	17.00%	2.55	83.00%	18
	Structural works (GF, FF, and Terrace)	140	1.80%	3.50%	0.00%	12.00%	18.00%	35.30%	49.42	64.70%	189
	Water Proofing works	17	0.00%	0.75%	0.00%	8.00%	15.00%	23.75%	4.0375	76.25%	21
	Block work	20	0.00%	0.00%	0.00%	7.00%	12.00%	19.00%	3.8	81.00%	24

(continued)

Table 1 (continued)

Activity	Task	Activity duration (days)	Wasted effort(% of total effort)				Productivity loss	ENV	Delay (days)	Variation	Delayed time (days)
			Rework		Interruption						
			REIR	RECR	DCAR	RFIR					
	Plastering	25	1.00%	1.50%	0.00%	7.00%	11.00%	20.50%	5.125	79.50%	30
	Joinery/Façade	7	0.75%	0.50%	0.00%	9.00%	12.00%	22.25%	1.5575	77.75%	9
	Tiling	10	1.00%	2.50%	0.00%	6.00%	10.00%	19.50%	1.95	80.50%	12
	Painting works	35	1.00%	3.00%	0.00%	13.00%	16.00%	33.00%	11.55	67.00%	47
Other security rooms (2 Nos)	Earth works	7	0.50%	0.00%	0.00%	7.00%	15.00%	22.50%	1.575	77.50%	9
	Foundation works	15	0.75%	0.00%	0.00%	8.00%	15.00%	23.75%	3.5625	76.25%	19
	Structural Works	20	1.20%	1.50%	0.00%	7.00%	18.00%	27.70%	5.54	72.30%	26
	Water Proofing works	15	1.00%	1.50%	0.00%	8.00%	18.00%	28.50%	4.27	71.50%	19
	Block work	15	0.00%	0.00%	0.00%	7.00%	15.00%	22.00%	3.30	78.00%	18
	Plastering	15	0.30%	0.50%	0.00%	2.50%	4.00%	7.30%	1.09	92.70%	16
	Joinery/Façade	82	4.00%	7.00%	1.75%	6.00%	23.00%	41.75%	34.23	58.25%	116
	Tiling	10	1.00%	2.00%	0.00%	5.50%	7.90%	16.40%	1.64	83.60%	12
	Painting works	20	1.00%	1.00%	0.00%	5.00%	17.00%	24.00%	4.80	76.00%	25
External works	Setting out	10	0.50%	0.25%	0.00%	2.00%	9.00%	11.75%	1.175	88.25%	11
	Rain water harvesting tank	22	3.00%	1.30%	0.00%	8.00%	14.00%	26.30%	5.78	73.70%	28

(continued)

Table 1 (continued)

Activity	Task	Activity duration (days)	Wasted effort(% of total effort)				Productivity loss	ENV	Delay (days)	Variation	Delayed time (days)
			Rework		Interruption						
			REIR	RECR	DCAR	RFIR					
	Storm water drain	90	2.00%	2.00%	0.60%	4.00%	15.00%	23.60%	21.24	76.40%	111
	Road and culvert works	40	2.00%	2.50%	0.00%	5.00%	15.00%	24.50%	9.80	75.50%	50
	Car parking and two	20	0.50%	0.75%	0.00%	7.00%	16.00%	24.25%	4.85	75.75%	25
	Walk ways	25	0.00%	0.50%	0.00%	2.00%	8.00%	10.50%	2.62	89.50%	28
	Snagging and hand over	25	2.75%	4.00%	3.00%	15.00%	18.00%	42.75%	10.68	57.25%	36
			0.81%	1.15%	0.21%	4.87%	11.57%		Total Var	81.39%	

Table 2 ENV calculation for Case Study II

Activity	Task	Activity duration (days)	Wasted effort(% of total effort)				Productivity loss	ENV	Delay (days)	Variation	Delayed time (days)
			Rework		Rework						
			REIR	RECR	DCAR	RFIR					
Foundation work	Foundation marking	35	1.70	1.50	0.40	3.00	7.50	14.10	4.93	85.90	39.93
	Excavation (foundation footing)	78	1.00	3.00	5.00	8.00	15.00	32.00	24.96	68.00	102.96
	PCC for footing	20	0.00	0.25	0.00	4.00	10.00	14.25	2.85	85.75	22.85
	Footing reinforcement work	65	0.00	0.00	0.00	1.00	5.00	6.00	3.90	94.00	68.90
	Footing concrete	26	0.75	0.50	0.00	2.00	8.00	11.25	2.92	88.75	28.92
	Plinth beam concrete	30	0.00	0.00	0.00	1.50	4.00	5.50	1.65	94.50	31.65
	Column raising	41	0.75	0.50	0.00	2.00	7.00	10.25	4.20	89.75	45.20
	Basement brick work	58	2.00	2.50	0.00	4.20	10.75	19.45	11.28	80.55	69.28
	Backfilling foundation	7	1.50	1.75	0.25	4.00	8.00	15.50	1.08	84.50	8.08
	Soil consolidation	26	0.50	0.50	1.00	1.50	4.00	7.50	1.95	92.50	27.95
Ground floor	Staircase shuttering	28	0.00	0.00	2.00	0.35	2.00	4.35	1.12	95.65	29.12

(continued)

Table 2 (continued)

Activity	Task	Activity duration (days)	Wasted effort(% of total effort)				Productivity loss	ENV	Delay (days)	Variation	Delayed time (days)
			Rework		Rework						
			REIR	RECR	DCAR	RFIR					
	Staircase bar bending	39	0.00	0.00	0.00	2.00	1.50	3.50	1.36	96.50	40.36
	Staircase waist slab concrete	23	0.00	1.00	1.00	1.20	2.00	5.20	1.19	94.80	24.19
	Column raising upto roof level	27	0.50	0.50	0.00	2.00	6.00	9.00	2.43	91.00	29.43
	Roof shuttering	19	2.50	0.75	1.00	2.90	8.50	15.65	2.97	84.35	21.97
	Roof bar bending	48	0.15	1.00	0.00	2.40	4.00	7.55	3.62	92.45	51.62
	Roof concreting	21	0.00	0.00	2.00	1.65	2.00	5.65	1.18	94.35	22.18
	Deshuttering	3	0.00	0.00	0.00	0.00	0.00	0.00	0.00	100.00	3.00
	Ceiling plastering	40	1.00	0.00	1.00	2.00	6.00	10.00	4.00	90.00	44.00
	Brickwork upto lintel level	22	2.00	1.50	0.00	3.00	7.00	13.50	2.97	86.50	24.97

(continued)

Table 2 (continued)

Activity	Task	Activity duration (days)	Wasted effort(% of total effort)				Productivity loss	ENV	Delay (days)	Variation	Delayed time (days)
			Rework		Rework						
			REIR	RECR	DCAR	RFIR					
	Lintel & sunshade shuttering work	7	1.00	1.50	0.00	2.00	8.00	12.50	0.87	87.50	7.87
	Lintel & sunshade concrete	9	0.00	0.00	0.00	0.35	2.00	2.35	2.11	97.65	11.11
	Brick work up to roof level	53	0.00	0.00	0.00	0.00	1.50	1.50	7.95	98.50	60.95
	Door and window frame fixing work	34	0.00	0.00	0.00	1.20	2.00	3.20	10.88	96.80	44.88
	Wall plastering	59	0.50	0.50	0.00	2.00	6.00	9.00	5.31	91.00	64.31
	Painting work	105	2.50	0.75	1.00	2.90	8.50	15.65	16.43	84.35	121.43
	Floor tile laying	96	0.15	1.00	0.00	2.40	4.00	7.55	7.24	92.45	103.24
	Door and window shutter fixing work	34	0.00	0.00	0.00	0.65	2.00	2.65	0.90	97.35	34.90

(continued)

Table 2 (continued)

Activity	Task	Activity duration (days)	Wasted effort(% of total effort)				Productivity loss	ENV	Delay (days)	Variation	Delayed time (days)
			Rework		Rework						
			REIR	RECR	DCAR	RFIR					
	Cleaning and handing over	24	0.75	0.00	0.00	2.00	6.00	8.75	2.10	91.25	26.10
	Column raising up to roof level	36	1.00	0.00	1.00	2.00	6.00	10.00	3.60	90.00	39.60
	Staircase shuttering	26	2.00	1.50	0.00	3.00	7.00	13.50	3.51	86.50	29.51
	Staircase bar bending	39	1.00	1.50	0.00	2.00	8.00	12.50	4.87	87.50	43.87
	Staircase waist slab concrete	21	0.00	0.00	0.00	4.00	17.00	21.00	4.41	79.00	25.41
	Roof shuttering	26	1.00	0.75	0.00	5.00	15.00	21.75	5.65	78.25	31.65
	Roof bar bending	58	0.00	0.00	0.00	5.00	9.00	14.00	8.12	86.00	66.12
	Roof concrete	29	0.00	0.00	0.00	2.00	15.00	17.00	4.93	83.00	33.93
	Deshuttering	7	1.80	3.50	0.00	12.00	18.00	35.30	2.47	64.70	9.47
	Ceiling plastering	63	0.00	0.75	0.00	8.00	15.00	23.75	14.96	76.25	77.96

(continued)

Table 2 (continued)

Activity	Task	Activity duration (days)	Wasted effort(% of total effort)				Productivity loss	ENV	Delay (days)	Variation	Delayed time (days)
			Rework		Rework						
			REIR	RECR	DCAR	RFIR					
	Brickwork upto lintel level	72	0.00	0.00	0.00	7.00	12.00	19.00	13.68	81.00	85.68
	Lintel & sunshade shuttering	18	1.00	1.50	0.00	7.00	11.00	20.50	3.69	79.50	21.69
	Lintel & sunshade bar bending	26	0.75	0.50	0.00	9.00	12.00	22.25	5.78	77.75	31.78
	Lintel & sunshade concrete	11	1.00	2.50	0.00	6.00	10.00	19.50	2.14	80.50	13.14
	brickwork up to roof level	32	1.00	3.00	0.00	13.00	16.00	33.00	10.56	67.00	42.56
	Door and window frame fixing work	37	0.50	0.00	0.00	7.00	15.00	22.50	8.32	77.50	45.32
	Wall plastering	91	0.75	0.00	0.00	8.00	15.00	23.75	21.61	76.25	112.61
	Painting work	112	1.20	1.50	0.00	7.00	18.00	27.70	31.02	72.30	143.02

(continued)

Table 2 (continued)

Activity	Task	Activity duration (days)	Wasted effort(% of total effort)				Productivity loss	ENV	Delay (days)	Variation	Delayed time (days)
			Rework		Rework						
			REIR	RECR	DCAR	RFIR					
	Floor tile laying	104	1.00	1.50	0.00	8.00	18.00	28.50	29.64	71.50	133.64
	Door and window shutter fixing work	42	0.00	0.00	0.00	7.00	15.00	22.00	9.24	78.00	51.24
	Cleaning and handing over	31	0.30	0.50	0.00	2.50	4.00	7.30	2.26	92.70	33.26
Second floor	Column raising up to roof level	71	4.00	7.00	1.75	6.00	23.00	41.75	29.64	58.25	100.64
	Staircase shuttering	35	1.00	2.00	0.00	5.50	7.90	16.40	5.74	83.60	40.74
	Staircase bar bending	23	1.00	1.00	0.00	5.00	17.00	24.00	5.52	76.00	28.52
	Staircase waist slab concrete	20	0.50	0.25	0.00	2.00	9.00	11.75	2.35	88.25	22.35
	Roof shuttering	27	3.00	1.30	0.00	8.00	14.00	26.30	7.10	73.70	34.10
	Roof bar bending	42	2.00	2.00	0.60	4.00	15.00	23.60	9.91	76.40	51.91

(continued)

Table 2 (continued)

Activity	Task	Activity duration (days)	Wasted effort(% of total effort)				Productivity loss	ENV	Delay (days)	Variation	Delayed time (days)
			Rework		Rework						
			REIR	RECR	DCAR	RFIR					
	Roof concrete	31	2.00	2.50	0.00	5.00	15.00	24.50	7.59	75.50	38.59
	Deshuttering	11	0.50	0.75	0.00	7.00	16.00	24.25	2.66	75.75	13.66
	Ceiling plastering	74	0.30	0.50	2.00	5.00	4.00	11.80	8.73	88.20	82.73
	Brickwork up to lintel level	47	1.00	1.75	1.50	5.00	6.50	15.75	7.40	84.20	54.40
	Lintel & sunshade shuttering	14	0.00	0.00	1.30	2.00	0.50	3.80	0.53	84.25	14.53
	Lintel & sunshade bar bending	20	1.40	0.50	0.60	3.20	5.00	10.70	2.14	96.20	22.14
	Lintel & sunshade concrete	21	1.00	2.00	2.00	1.50	14.00	20.50	4.30	79.50	25.30
	brickwork up to roof level	45	3.00	1.20	2.00	3.30	7.50	17.00	7.65	83.00	52.65

(continued)

Table 2 (continued)

Activity	Task	Activity duration (days)	Wasted effort(% of total effort)				Productivity loss	ENV	Delay (days)	Variation	Delayed time (days)
			Rework		Rework						
			REIR	RECR	DCAR	RFIR					
	Door and window frame fixing work	24	0.50	0.75	3.00	1.10	2.50	7.85	1.88	92.15	25.88
	Wall plastering	83	0.20	0.00	3.00	1.40	3.00	7.60	6.30	92.40	89.30
	Painting work	117	0.50	0.75	1.20	4.00	6.00	12.45	14.56	87.55	131.56
	Floor tile laying	127	0.25	1.20	3.80	4.00	11.00	20.25	25.71	79.75	152.71
	Door and window shutter fixing work	46	1.00	0.75	1.00	0.00	0.75	3.50	1.61	96.50	47.61
	Cleaning and handing over	26	0.00	0.00	1.20	2.00	0.50	3.70	0.96	96.30	26.96
Pump room and security	Earth works	18	4.50	3.00	7.00	5.00	4.00	23.50	4.23	76.50	22.23
	Bottom slab	7	2.50	1.40	2.30	3.00	0.50	9.70	0.67	90.30	7.67
	Top slab	11	3.00	4.20	7.00	3.30	15.00	32.50	3.57	67.50	14.57
	Side wall including	21	0.15	1.00	0.00	2.40	3.00	6.55	1.37	93.45	22.37
	Water proofing	15	2.00	1.50	6.20	5.00	7.00	21.70	3.25	78.30	18.25

(continued)

Table 2 (continued)

Activity	Task	Activity duration (days)	Wasted effort(% of total effort)				Productivity loss	ENV	Delay (days)	Variation	Delayed time (days)
			Rework		Rework						
			REIR	RECR	DCAR	RFIR					
	Backfilling	8	1.00	1.50	3.50	7.00	3.50	16.50	1.32	83.50	9.32
	Structural works	17	1.00	0.00	0.75	2.00	5.00	8.75	1.48	91.25	18.48
	Block work	37	1.40	0.50	0.60	3.20	5.00	10.70	3.95	89.30	40.95
	Plastering	24	1.00	2.00	2.00	1.50	4.00	10.50	2.52	89.50	26.52
	Flooring	11	1.10	2.00	0.30	2.00	6.20	11.60	1.27	88.40	12.27
Electrical room	Foundation works	9	1.00	1.50	3.50	7.00	3.50	16.50	1.48	83.50	10.48
	Structural works	18	1.00	0.00	0.75	2.00	5.00	8.75	1.57	91.25	19.57
	Block work	24	1.00	1.15	2.00	0.40	3.00	7.55	1.81	92.45	25.81
	Plastering	15	1.00	0.00	2.30	3.00	1.00	7.30	1.09	92.70	16.09
	Painting works	22	1.20	0.25	0.00	4.00	10.00	15.45	3.40	84.55	25.40
			0.01	0.02	0.01	0.03	0.06	0.14	Total variance	0.86	72.45

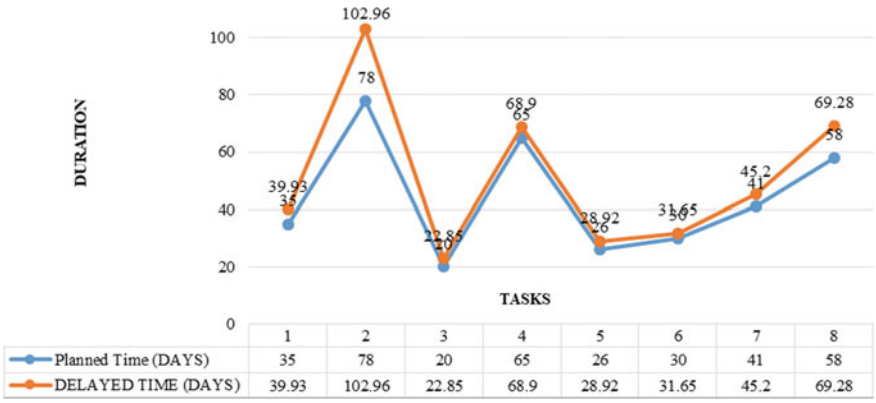

Fig. 4 Planned versus actual schedule

types of ENV have to some extent, influence over the project, which can be seen in the Figure.

4 Conclusion

Projects involving design in any construction sector, ENV is a primary cause of schedule delays and expense overruns. By adopting this model, which can pinpoint the location and time, construction managers can improve project performance by properly scheduling, planning, and directing resources. In addition, construction managers can reduce ENV with personnel deployed where a significant degree of disruption is foreseen. The main aim of this study is to construct a dynamic tool that can detect and enumerate ENV, and changes can be done in the design. This proposed model was then used in two case studies, it was discovered that errors and changes caused 18.61% ENV and if the project is delayed, there will be a delay of 128 days in case of project I and 72 days in case project II. Productivity loss and Interruption (RFIR) form the central part of ENV, causing delays in both the case studies. In the case of repetitive projects, identifying the percentage of ENV in the initial stage can be helpful in proper planning and monitoring to avoid the repetition of delays in the successive stages.

References

1. Horman MJ, Kenley R (2005) Quantifying levels of wasted time in construction with meta-analysis. J Constr Eng Manag 131(1):52–61
2. Lopez R, Love PED, Edwards J, Davis PR (2010) Design error classification, causation, and prevention in construction engineering. J Perform Constructed Facil
3. Park M, Kim W, Lee H, Han S (2011) Supply chain management model for ready mixed concrete. Autom Constr (20)1:44–55
4. Love PED, Edwards DJ, Irani Z (2008) Forensic project management: an exploratory examination of the causal behaviour of design-induced rework. IEEE Trans Eng Manage 55:234–247
5. Hwang BG, Thomas SR, Haas CT, Caldas CH (2009) Measuring the impact of rework on construction cost performance. J Constr Eng Manag ASCE 135(3):187–198
6. Forcada N, Macarulla M, Love PED (2013) Assessment of residential defects at post-handover. J Constr Eng Manag, ASCE 139(4):372–378
7. Taggart M, Koskella L, Rooke J (2013) The role of supply chain in the elimination and reduction of construction rework and defects: an action research approach. In Proceedings of 29th annual ARCOM conference. Association of Researchers in Construction Management, Reading, UK, pp 503–512
8. Alwi S, Hampson K, Mohammed S (2002) Non value-adding activities: a comparative study of Indonesian and Australian construction projects. In Proceedings of 10th international group of lean construction conference, Brazil, pp 627–638
9. Hanna AS, Taylor CS, Sullivan KT (2005) Impact of extended overtime on construction labor productivity. J Constr Eng Manag 131(6):734–739
10. Kothari CR (2006) Research methodology. New Age International (P) Ltd. Publishers, New Delhi
11. Love PED, Li H (2000) Quantifying the causes and costs of rework in construction. Constr Manag Econ 18(4):479–490
12. Love PED, Wang X, Sing C, Tiong RLK (2013) Determining the probability of project cost overruns. J Constr Eng Manag, ASCE 139(3):321–330
13. Report on Study on project schedule and cost overruns, KPMG in India-PMI Survey on Cost and Schedule Overrun (2012)

Production of High Strength Eco-Concrete Incorporating Alccofine and Basalt Fiber

H. N. Rajakumara and M. Pradeep

Abstract The goal of this investigation is to find the significance of the alccofine and basalt fiber in fly ash-based high strength concrete. Usage of supplemental cementitious materials in concrete manufacture is thought to provide economical, technical, and environmental benefits Alccofine is a new generation of ultrafine ground matter that is utilized to make high-strength concrete and has a substantial impact on workability and strength. Alccofine 1203 was used as a partial replacement (0, 4, 8, 12 and 14% by weight) as substitute to cement with varying volume fractions of chopped basalt fiber (0, 0.2, 0.3, and 0.4% by total mix volume). Fly ash is used at the constant percentage of 25% by weight as substitute to cement. The combined impact of the 12 mm long basalt fiber and the alccofine 1203 on the mechanical characteristics of fresh and hardened concrete was studied. The outcomes showed noteworthy improvement in HSC mechanical characteristics.

Keywords High strength concrete · Alccofine · Basalt fibers · Fly ash · Supplementary cementitious materials

1 Introduction

Concrete is the world's most commonly used material [1]. The concrete industry must be made sustainable in the present world to minimize the negative influence on the environment [2]. Concrete with a characteristic strength ranging between 40 N/mm^2 and 100 N/mm^2 is referred to as high strength concrete (HSC). Construction of bridges, skyscrapers, megaprojects, and other structures that need HSC. The present surge in demand for big structures has pushed the usage of HSC in construction to reduce concrete structure C/S & self-weight [3]. Even though the initial cost of HSC

H. N. Rajakumara
BMS Institute of Technology and Management, Bangalore, Karnataka, India
e-mail: drhnrajkumara@bmsit.in

M. Pradeep (✉)
Madanapalle Institute of Technology and Science, Madanapalle, Andhra Pradesh, India
e-mail: pradeepm@mits.ac.in

L. Nandagiri et al. (eds.), *Recent Advances in Civil Engineering*, Lecture Notes in Civil Engineering 256, https://doi.org/10.1007/978-981-19-1862-9_40

is higher than that of ordinary concrete, it might be more cost-effective. This is due to the fact that using HSC will result in a structure that is lighter, more durable, and has a longer service life. The primary need for HSC is a low water-cement ratio [4].

Low W/C proportion is necessary for low solid porousness, which is fundamental for high durability. The usage of supplemental cementitious materials (SCM) is gradually growing due to technological, economic, and environmental benefits [5]. Pour filling action of fine pozzalonic increases also aids impermeability. The use of low water-cement proportions and various cementitious materials necessitates the use of superplasticizers. HSC exceeds normal concrete in terms of structural performance and durability by a significant margin. HSC without fibers is relatively brittle and fails suddenly when compared with HSC with different types of fibers.

Fibers can efficiently prevent the start and spread of cracks in concrete, lowering its brittleness and increasing its toughness [6]. HSC is characterized by its brittleness. As a result, one of the most pressing problems of HSC is the need to find strategies to change its brittle behavior to ductile behavior [7]. Fibers can impact cracking behavior, control the fracture process and offer strength and toughness after cracking [8]. One of the key benefits of mineral compounds in HSC is to reduce OPC content, which not only offers economic and environmental benefits but also improves compression strength by decreasing temperature growth. Cement demand is rising globally, with about 4.3 billion tonnes consumed each year [9]. SCM materials lead to a technical revolution for civil works and become popular in the building industry [10]. Alccofine (an ultra-fine type of slag) is a steel industry by-product with cementitious characteristics and may be used to SCM, which pollutes the environment [3]. Alccofine1203 is one with low silicates of calcium; Alccofine 1101 is one with high silicates of calcium [10].

AF is a slag-based substance with a high percentage of glass and a great reactivity [11]. AF can be utilized for flow-improving enhanced functionality to boost compressive quality. AF is a pozzalonic material with ultrafine particles that improve workability, strength, and cost-effectiveness. AF is a new micro-fine substance that may be used in concrete as a partial replacement for OPC [12]. The underlying rate of solidification of AF concrete is equivalent or increased to that of silica fume, and AF, like pozzalans, burns down $Ca(OH)_2$ from concrete hydration to generate more CSH gel. The ultrafine particle of AF produces a more even and smooth surface finish. The increased specific surface area of AF particles has a bigger influence on the performance of concrete for both the fresh & hardened stages [13, 14]. Addition of AF as a mineral admixture with recycled aggregate in concrete with the underlying expectation that the mechanical property of finished concrete will be enhanced [15]. AF has the ability to extend the life of concrete by its packing effect [16]. AF manufacturing is more ecologically friendly than OPC production [17]. It has been observed that adding AF to concrete improves its workability and fluidity in addition to its compressive strength [18].

Cement is expensive and emits CO_2, hence cement may be replaced by SCM like fly ash and AF, which cut CO_2 emissions by 40% [3]. Fly ash granules have a spherical form and are used to make concrete more workable. It also increases and strength of hardened concrete [19]. In the presence of water and chloride ions, use of fly

ash inside the formation of concrete can significantly reduce concrete permeability [20]. Using fly ash as a low cost component in concrete instead of discarding it offers major commercial and environmental benefits [21]. The combination of AF and fly ash appears to be beneficial in the formation of HSC [22]. To cut costs and CO_2 emissions, SCM like fly ash and GGBS are commonly used to substitute portions of OPC [23]. By adding BF to concrete, there will be a slow down of plastic deformation process and enhances the bending strength of the material [24]. BF has gained appeal as a reinforcement in building and polymer blends because of its eco-friendliness, ease of manufacturing, nontoxicity, and lower cost than other fibers [25]. BF are having good thermal range (259–960 °C), high tensile strength (approximately 2100 MPa) [26].

Compared to Plain concrete, the splitting tensile, compressive, and bending strengths of concrete reinforced with 12 mm BF improve by 14.08–24.34%, 0.18–4.68%, and 6.30–9.58%, respectively [27]. When compared to other sources of fibers, the manufacturing methods of BF use less energy. Other benefits, such as its low cost, low cost and outstanding resilience to high temperature exposure and chemical assault, among other advantages [28].

The addition of chopped BF to concrete had minimal influence on its compressive strength, but it considerably improved its flexural modulus [29]. Steel and polyvinyl alcohol fibers are difficult to handle and so form balls, whereas BFs simply disseminate in the concrete mix without losing their shape due to its flexible nature [30].

The cost of incorporating BF in concrete has been determined to be less expensive than steel fiber, s-glass, and carbon fibers [31]. BF is a suitable building material with outstanding thermal and mechanical properties [32]. Apart from possessing an elastic structure, BF is highly heat resistant and has insulating properties [33]. One Kg of BF replaces 9.6 kg steel fiber. The advantage of BF as compared to steel fiber is its low weight, high hardness, which has a significant impact on the improvement in concrete abrasion resistance. BF can be offered as a potential strengthening material in concrete composite. BF increases flexural strength even at low concentrations [31].

Concrete can benefit from BF in terms of mechanical characteristics, corrosion resistance, and chemical stability [34]. BF has the capacity to chemically bind with cement it can reduce the amount of pores in concrete thereby enhancing permeability [35]. Despite the fact that the manufacturing methods for basalt and glass fibers are identical, BF requires less energy and no additives [36]. BF are considered non-hazardous and environment acceptable materials [37]. BF can be added to concrete to help develop a strong spatial network structure to improve a variety of concrete properties [38]. The addition of a particular percentage of BF to concrete increases its toughness, preventing cracking and brittle behavior [39]. Concrete mechanical characteristics can be greatly enhanced by adding a tiny amount of short BF [40].

The current research reports on an experimental study M80 grade of fly ash-based HSC incorporating AF and BF. Compressive, tensile, and flexural strength of proposed mixtures developed in the experimental study were tested at 7 and 28 days.

Table 1 Chemical compositions of OPC, Alccofine and Fly ash [10, 12]

Constituents (%)	Cement	Alccofine 1203	Fly ash
CaO	62.58	33.92	2.35
SiO_2	20.24	34.82	61.55
Al_2O_3	5.32	21.43	28.15
Fe_2O_3	4.05	1.40	4.22
MgO	2.81	6.82	1.02
SO_3	2.72	0.010	0.25
Loss of ignition (LOI)	0.76	0.59	3.5

2 Materials

2.1 Cement

OPC of 53-Grade made by the Gujarat-based Ultratech cement business was used in the research work. The specific gravity of the OPC examined was 3.16, and the normal consistency was 29 percent, which satisfied Indian standards (IS 12269: 2013). The OPC initial and final settings time took 35 min and 520 min respectively. The OPC tested had a fineness of 98%. The measured compressive strength of OPC was 61 MPa after 28 days, according to (IS 4031:1988), with particle sizes ranging from 7.5 to 31 μm. Table 1 shows the chemical constituents of OPC.

2.2 Alccofine

AF was purchased from Ambuja Cement Ltd, Goa, and was utilized throughout the investigation in compliance with ASTM C989-1999. Table 1 shows the chemical composition of AF. Table 2 shows the physical properties of AF. Mixes are made by changing the AF from 0%, 8%, 10%, 12%, and 14% by weight of binder.

Table 2 Physical properties of alccofine 1203

Specific gravity		2.9
Fineness (cm^2/gm)		> 12,000
Bulk density (kg/m^3)		700–900
Particle size distribution (μ)	D 10	1.5
	D 50	5
	D 90	9

Table 3 Physical properties of fine aggregate and coarse aggregate

	Fine aggregate	Coarse aggregate
Particle size (mm) down	4.75	20 down
Fineness modulus	2.92	6.77
Specific gravity	2.65	2.74
Water absorption (%)	1.50%	0.80
Bulk density (kg/m^3)	1640	1560

2.3 Fly Ash

Class F fly ash that conforms with IS: 3812-Part-I is utilized to replace 25% of the OPC weight. The Ultratech Ready Mix Concrete facility provides fly ash. Bulk density and specific gravity are respectively 0.88 g/cm^3 and 1.95 g/cm^3. Table 1 shows the chemical composition of fly ash.

2.4 Aggregates

Crushed stone aggregates with a down size of 20 mm from a local source that met IS: 383-1970 criteria were utilized. M-sand that passed through a 4.75 mm IS sieve according to IS: 383-1970 grading zone-II was utilized. Table 3 lists the physical characteristics of aggregates.

2.5 Basalt Fiber

Nickunj Eximp Enterprise Private Limited provided the chopped BF. In the concrete matrix, the BF was spread evenly and randomly. Mixes are made by changing the volume fraction by the entire mix volume from (0%, 0.2%, 0.3%, and 0.4%). Table 4 lists the physical and chemical properties of basalt fiber, respectively.

2.6 Water

Portable water was utilized to make concrete and cure it in accordance with IS: 456-2009.

Table 4 Chemical composition and physical properties of Basalt fibers [27, 40]

Chemical composition		Physical properties	
Constituents	Composition [%]	Physical property	Results
SiO_2	51.5–57.6	Diameter (μm)	17
Al_2O_3	16.8–18.1	Length (mm)	12
CaO	5.3–7.7	Density (g/cm^3)	2.64
MgO	1.2–3.6	Tensile strength (MPa)	4150–4750
Na_2O	2.4–6.3	Modulus of elastic (GPa)	94–110
K_2O	0.9–4.6	Elongation at break (%)	3.1–3.2
Fe_2O_3	4–9.4	Water absorption (%)	< 0.5
		Aspect ratio (L/D)	705

2.7 Super Plasticizer

Adhere mix 700, a naphthalene-based superplasticizer with a specific gravity of 1.1 and a cement weight of 1%, was used in all mixes in line with IS: 9103-1999. It was available locally and matched the chemical properties of the Poly carboxyl ether. It assists in the improvement of concrete workability without raising the water ratio [11].

3 Methodology

Table 5 shows the mix proportions for M80 grade HSC based on the IS: 10262-2019 guideline of 0.24 W/C ratio. Mix proportions are designated from CM to $MA_{14}B_{0.4}$ where M stands for mix, A for Alccofine 1203, and B for Basalt fiber. Because AF contains a significant amount of $Ca(OH)_2$ and Al_2O_3, utilizing it alone in the production of HSC may result in undesired outcomes [22]. To minimize undesirable features and increase HSC performance, a 25% substitution of class F fly ash was used in the control mix and all AF-based mixes. The control mix (CM), is made up of 75% cement, 25% fly ash, and 0% AF, whereas the other nineteen mixes are made up of partial replacement of OPC by AF and varying volume fractions of BF.

The dose of superplasticizer is 1% of the total weight of the binder ingredients. Different amounts of BF (0%, 0.2%, 0.3%, and 0.4% by total mix volume) and AF (0%, 8%, 10%, 12%, and 14% by weight) were added to the HSC mix as a cement alternative. Dry aggregates were first mixed uniformly for 1 min in a concrete mixer, and then binders and BF were added and blended for 2 min. After that, 90% of the mixing water was added, then the remaining 10% water and adhere mix 700 being mixed for 3 min to make the concrete homogenous as wet. ACI 544 was followed while adding BFs to the concrete mix. After the inclusion of BF to concrete mixes, no balling impact was observed. On a vibrating platform, specimens were vibrated

Table 5 Mix proportion

Mix	OPC (kg/m^3)	Fly ash (kg/m^3)	AF (kg/m^3)	Water (kg/m^3)	FA (kg/m^3)	CA (kg/m^3)	Adhere mix 700 (kg/m^3)	Slump (mm)
CM	447	149	0	159	597	1096	5.96	135
$MA_0B_{0.2}$	447	149	0	159	597	1096	5.96	130
$MA_0B_{0.3}$	447	149	0	159	597	1096	5.96	126
$MA_0B_{0.4}$	447	149	0	159	597	1096	5.96	120
MA_8B_0	399.4	149	47.6	159	597	1096	5.96	153
$MA_8B_{0.2}$	399.4	149	47.6	159	597	1096	5.96	148
$MA_8B_{0.3}$	399.4	149	47.6	159	597	1096	5.96	141
$MA_8B_{0.4}$	399.4	149	47.6	159	597	1096	5.96	138
$MA_{10}B_0$	387.4	149	59.6	159	597	1096	5.96	167
$MA_{10}B_{0.2}$	387.4	149	59.6	159	597	1096	5.96	159
$MA_{10}B_{0.3}$	387.4	149	59.6	159	597	1096	5.96	151
$MA_{10}B_{0.4}$	387.4	149	59.6	159	597	1096	5.96	142
$MA_{12}B_0$	375.5	149	71.5	159	597	1096	5.96	152
$MA_{12}B_{0.2}$	375.5	149	71.5	159	597	1096	5.96	145
$MA_{12}B_{0.3}$	375.5	149	71.5	159	597	1096	5.96	137
$MA_{12}B_{0.4}$	375.5	149	71.5	159	597	1096	5.96	124
$MA_{14}B_0$	363.6	149	83.4	159	597	1096	5.96	136
$MA_{14}B_{0.2}$	363.6	149	83.4	159	597	1096	5.96	131
$MA_{14}B_{0.3}$	363.6	149	83.4	159	597	1096	5.96	126
$MA_{14}B_{0.4}$	363.6	149	83.4	159	597	1096	5.96	121

at 150 Hz to eliminate any trapped air. To research the impact of AF and BF on compressive strength (conforming to IS 516-1959), split tensile strength (conforming to IS 5816-1959), and flexural strength (conforming to IS 516-1959) of HSC, cubes (150 × 150 × 150 mm), cylinders (150 × 300 mm), and prisms (150 × 150 × 700 mm) are casted. The demolding of specimens was done after 24 h.

For each combination, six specimens were used in all of the experiments in which 3 specimens for 7 day and 3 specimens for 28 days strength. For the compressive tests 120 cubes, for splitting tensile tests 120 cylinders and for flexural test 120 prisms were used. Samples were demoulded from the moulds the next day after casting and stored in curing tanks until they were removed for further testing.

4 Results and Discussion

4.1 Workability

The slump cone test, as defined by IS 1199-1959, was used to determine the workability of fresh HSC shortly after mixing. The slump of HSC is greatly improved when cement is replaced with AF. The CM HSC has a slump of 135 mm and maximum slump of 167 mm was observed in $MA_{10}B_0$. As can be observed in Table 5, the slump was reduced to some extent as a result of the BF addition. It may be established that incorporating BF into the HSC may result in a reduction in slump. The reason for this is that the dispersed BF in the HSC will form a network structure, which prevents the mixture from segregating and flowing.

4.2 Compressive Strength

Compression testing on HSC cubes was done according to IS 516-1959 at a load speed of 0.5 mm/min with Universal Test Machine. Figure 1 demonstrates a 7 and 28 days variation of compressive strength with different contents of BF and AF material cured under normal conditions. On average, three samples were reported with each compressive strength result. Figure 1 depicts $MA_{10}B_{0.3}$ for 7 days at 65.7 MPa, and 90.6 MPa for 28 days for compressive maximum strength. Tiny particle size of AF

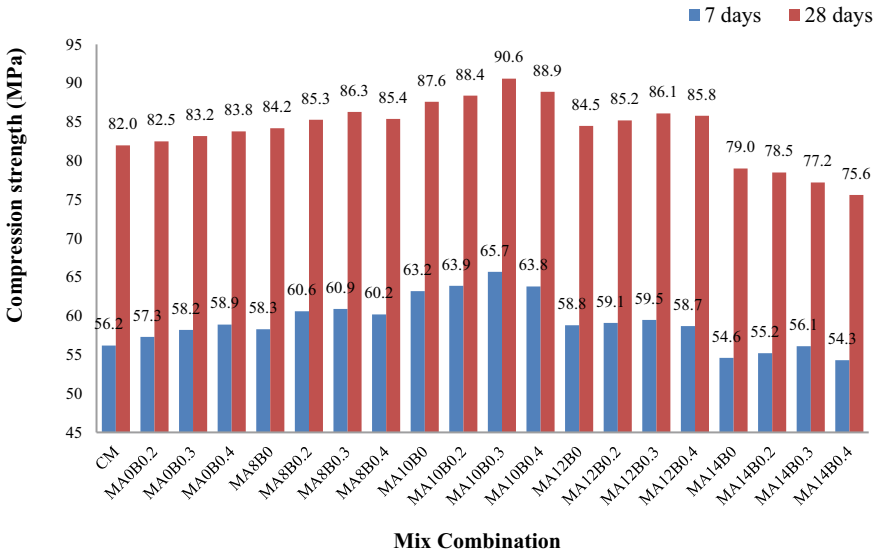

Fig. 1 Compressive strength of HSC cube

will fill those vacuum areas and serves as a hydration activator. The higher CaO content of 33.9% in AF (Table 1) leads to the generation of greater CSH gel. AF was beneficial up to a replacement level of 10%, above which there was a noticeable drop in strength due to AF being much fine than cement, it raises the water requirements for workable mix. The decrease in compressive strength with the addition of AF in cases of 12 and 14% replacement could be attributed to the binder's unsoundness as a result of a rise in free lime CaO, MgO, and Al_2O_3, which hydration resulted in abrupt rises and the emergence of micro-cracks, thereby loosening the matrix of the specimens. The test findings also demonstrate that 0, 0.2%, 0.3%, and 0.4% of BF had minimal effect on the compressive strength HSC mixtures. Table 6 shows the % increase in compressive strength–effectiveness of AF-based mixtures over CM. These findings are in accordance with that of Srinivas et al. [10], who obtained 56.66 MPa at 10% AF substitution for M50 grade.

Table 6 Increase in % of strength of alccofine-based mixes compared to CM

Mix designation	Compressive strength		Split tensile strength		Flexural strength	
	7 days	28 days	7 days	28 days	7 days	28 days
CM	–	–	–	–	–	–
$MA_0B_{0.2}$	1.96	0.61	6.34	2.39	2.17	2.06
$MA_0B_{0.3}$	3.56	1.46	11.96	4.38	3.99	4.01
$MA_0B_{0.4}$	4.80	2.20	4.71	2.00	1.82	1.82
MA_8B_0	3.74	2.68	10.87	4.61	4.19	5.44
$MA_8B_{0.2}$	7.83	4.02	16.12	9.70	8.83	7.00
$MA_8B_{0.3}$	8.36	5.24	19.02	10.37	9.44	8.43
$MA_8B_{0.4}$	7.12	4.15	13.77	8.82	8.03	7.15
$MA_{10}B_0$	12.46	6.83	20.11	15.47	14.08	10.29
$MA_{10}B_{0.2}$	13.70	7.80	23.01	17.02	15.49	11.43
$MA_{10}B_{0.3}$	16.90	10.49	26.99	21.01	19.13	14.56
$MA_{10}B_{0.4}$	13.52	8.41	22.10	16.80	15.29	12.14
$MA_{12}B_0$	4.63	3.05	10.33	5.71	5.20	5.86
$MA_{12}B_{0.2}$	5.16	3.90	13.22	6.38	5.81	6.86
$MA_{12}B_{0.3}$	5.87	5.00	15.58	7.27	6.61	8.15
$MA_{12}B_{0.4}$	4.45	4.63	11.59	5.49	5.00	7.72
$MA_{14}B_0$	−2.85	−3.66	0.36	−3.60	−3.27	−1.98
$MA_{14}B_{0.2}$	−1.78	−4.27	4.53	−2.27	−2.06	0.48
$MA_{14}B_{0.3}$	−0.18	−5.85	7.07	−0.27	−0.25	3.38
$MA_{14}B_{0.4}$	−3.38	−7.80	1.99	−4.26	−3.88	−6.83

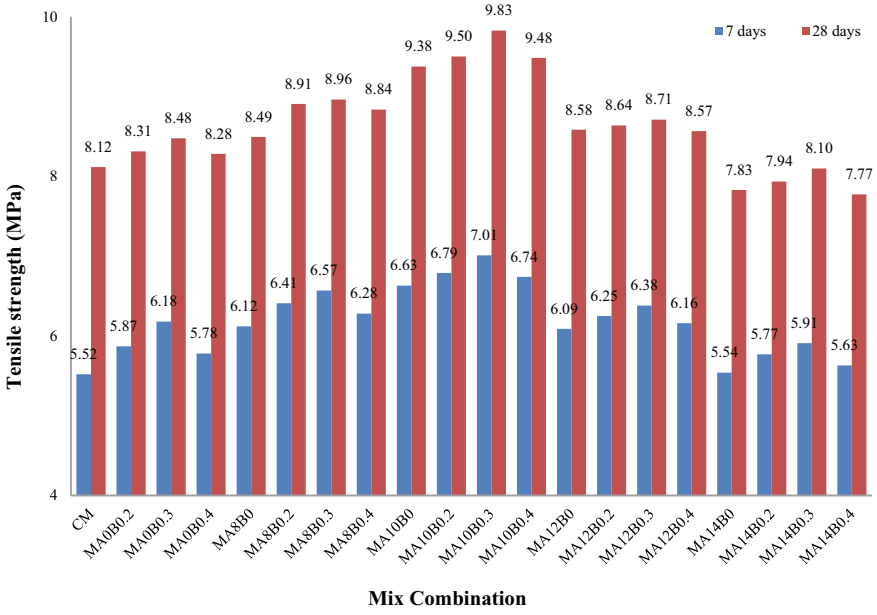

Fig. 2 Tensile strength of cylinder

4.3 Split Tensile Strength

The splitting tensile strength of cylindrical specimens in UTM was performed at 7 and 28 days of normal curing in compliance with IS 5816-1959. Figure 2 depicts the fluctuation in tensile strength of specimens of 7 and 28 days strength with varying BF and AF concentrations. The splitting tensile strength was calculated by averaging the failure loads of the three specimens. Splitting tensile strength was found maximum when we used 0.3% v/v of BF and 10% of AF by weight of cement ($MA_{10}B_{0.3}$). Table 6 tabulates the % increase in splitting tensile strength–effectiveness of AF-based mixes over CM. These findings are consistent with those of Bode Venkata Kavyateja et al. [13], who improved split tensile strength by 39.25% using 10% AF and 25% fly ash substitution for OPC in M25 grade.

4.4 Flexural Strength of Concrete

Figure 3 exhibits the variability of flexural strength of HSC prisms of 7 and 28 days strength with varying BF and AF material compositions. Applying the failure load in UTM under 4-point loading to assess the flexural strength of HSC prisms. The maximum flexural strength of HSC was found in $MA_{10}B_{0.3}$. This is due to BF

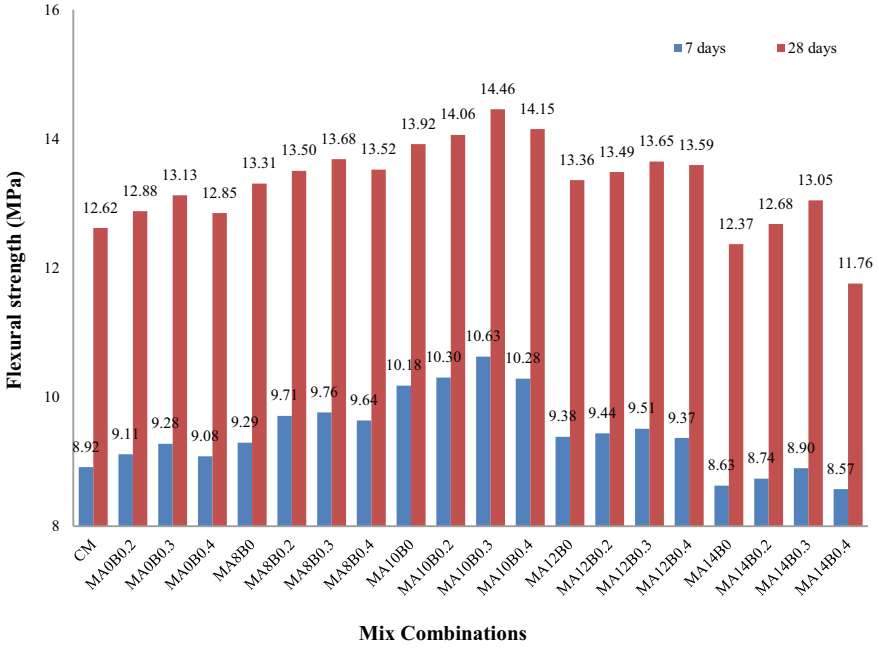

Fig. 3 Flexural strength of prism

inhibiting micro-cracks. It was also discovered that the initial crack in the BF reinforced HSC appeared approximately around the maximum value and was located near the prism's mid-span. Table 6 shows the % improvement in flexural strength–effectiveness of AF-based mixtures over CM. Sagar et al. [22] reported a flexural strength of 6.22 MPa for OPC in M60 grade with 10% AF and 25% fly ash substitution.

5 Conclusions

Following conclusions are drawn on the experimental studies carried out on fly ash-based HSC incorporating AF and BF.

1. The workability of concrete is greatly improved when OPC is 10% replaced with AF.
2. According to Figs. 1, 2 and 3, OPC with 10% AF and 25% fly ash replacement has higher strength due to the greater surface area and high pozzalonic interaction nature of AF and fly ash.
3. Above 10% AF concentration, the concrete's strength features decrease owing to a greater amount of AF particles in the hydration process than liberated lime quantity.

4. The use of AF and fly ash as a cement counterpart results in environmentally friendly and long-lasting concrete and also helps to solve the problem of industrial waste disposal while also producing eco-concrete that is stronger.

References

1. Latawiec R, Woyciechowski P, Kowalski KJ (2018) Sustainable concrete performance—CO_2-emission. Environ MDPI 5:1–14. https://doi.org/10.3390/environments5020027
2. Narender Reddy AN, Meena T (2018) A study on compressive behavior of ternary blended concrete incorporating alccofine. Mater Today Proc 5:11356–11363. https://doi.org/10.1016/j.matpr.2018.02.102
3. Reddy PN, Kavyateja BV (2020) Durability performance of high strength concrete incorporating supplementary cementitious materials. Mater Today Proc 33:66–72. https://doi.org/10.1016/j.matpr.2020.03.149
4. Nor NM, Ghazali MAA, Ahmad MZ, Yusof MA, Vikneswaran M, Yahya MA (2018) Revisiting high strength concrete using common admixtures. J Fundam Appl Sci 9:546. https://doi.org/10.4314/jfas.v9i3s.42
5. Biswas R, Rai B (2019) Efficiency concepts and models that evaluates the strength of concretes containing different supplementary cementitious materials. Civ Eng J 5:18. https://doi.org/10.28991/cej-2019-03091222
6. Fu Q, Xu W, Li D, Li N, Niu D, Zhang L, Guo B, Zhang Y (2021) Dynamic compressive behaviour of hybrid basalt-polypropylene fiber-reinforced concrete under confining pressure: experimental characterisation and strength criterion. Cem Concr Compos 118:103954. https://doi.org/10.1016/j.cemconcomp.2021.103954
7. Jang SJ, Do Yun H (2018) Combined effects of steel fiber and coarse aggregate size on the compressive and flexural toughness of high-strength concrete. Compos Struct 185:203–211. https://doi.org/10.1016/j.compstruct.2017.11.009
8. Larsen IL, Thorstensen RT (2020) The influence of steel fibers on compressive and tensile strength of ultra high performance concrete: a review. Constr Build Mater 256:119459. https://doi.org/10.1016/j.conbuildmat.2020.119459
9. Narasimha Reddy P, Ahmed Naqash J (2019) Effect of alccofine on mechanical and durability index properties of green concrete. Int J Eng Trans B Appl 32:813–819. https://doi.org/10.5829/ije.2019.32.06c.03
10. Srinivas K, Sankar LP, Swamy CK (2021) Experimental investigation on rapid strength gain by adding alccofine in high strength concrete. Mater Today Proc 46:925–929. https://doi.org/10.1016/j.matpr.2021.01.068
11. Reddy GGK, Ramadoss P (2020) Influence of alccofine incorporation on the mechanical behavior of ultrahigh performance concrete (UHPC). Mater Today Proc 33:789–797. https://doi.org/10.1016/j.matpr.2020.06.180
12. Srinath BLNS, Patnaikuni CK, Balaji KVGD, Kumar BS, Manjunatha M (2021) A prospective review of alccofine as supplementary cementitious material. Mater Today Proc. https://doi.org/10.1016/j.matpr.2021.03.719
13. Kavyateja BV, Guru Jawahar J, Sashidhar C (2020) Effectiveness of alccofine and fly ash on mechanical properties of ternary blended self compacting concrete. Mater Today Proc 33:73–79. https://doi.org/10.1016/j.matpr.2020.03.152
14. Parveen, Singhal D, Junaid MT, indal BB, Mehta A (2018) Mechanical and microstructural properties of fly ash based geopolymer concrete incorporating alccofine at ambient curing. Constr Build Mater 180:298–307. https://doi.org/10.1016/j.conbuildmat.2018.05.286
15. Jasani KS, Manivel S, Kumar GS (2018) An experimental investigation on strength properties of alccofine 1203 along with recycle aggregate in concrete. Int J Civ Eng Technol 9:138–148

16. Balamuralikrishnan R, Saravanan J (2019) Study on bond strength of alccofine based normal and high strength concrete. Civ Eng J 5:679. https://doi.org/10.28991/cej-2019-03091278
17. Reddy PN, Naqash JA (2019) Development of high early strength in concrete incorporating alccofine and non-chloride accelerator. SN Appl Sci 1:1–11. https://doi.org/10.1007/s42452-019-0790-z
18. Rajesh Kumar S, Samanta AK, Roy DKS (2015) An experimental study on the mechanical properties of alccofine based high grade concrete. Int J Multidiscip Res Dev 2:218–224. http://www.scientific.net/AMR.941-944.2611
19. Phul AA, Memon MJ, Shah SNR, Sandhu AR (2019) GGBS and Fly ash effects on compressive strength by partial replacement of cement concrete. Civ Eng J 5:913–921. https://doi.org/10.28991/cej-2019-03091299
20. Kubissa W, Simon T, Jaskulski R, Reiterman P, Supera M (2017) Ecological high performance concrete. Procedia Eng 172:595–603. https://doi.org/10.1016/j.proeng.2017.02.186
21. Huda S, Ahmad A, Ahmad SA, Khan ZR (2017) An experimental study of fly ash concrete with steel fiber hooked ends to obtain strength of M30 grade. Int J Civ Eng Technol 8:282–291
22. Sagar B, Sivakumar MVN (2020) An experimental and analytical study on alccofine based high strength concrete. Int J Eng Trans A Basics 33:530–538. https://doi.org/10.5829/IJE.2020.33.04A.03
23. Wu B, Ye G (2017) Development of porosity of cement paste blended with supplementary cementitious materials after carbonation. Constr Build Mater 145:52–61. https://doi.org/10.1016/j.conbuildmat.2017.03.176
24. Zhao YR, Wang L, Lei ZK, Han XF, Shi JN (2018) Study on bending damage and failure of basalt fiber reinforced concrete under freeze-thaw cycles. Constr Build Mater 163:460–470. https://doi.org/10.1016/j.conbuildmat.2017.12.096
25. Khandelwal S, Rhee KY (2020) Recent advances in basalt-fiber-reinforced composites: tailoring the fiber-matrix interface. Compos Part B Eng 192:108011. https://doi.org/10.1016/j.compositesb.2020.108011
26. Banibayat P, Patnaik A (2014) Variability of mechanical properties of basalt fiber reinforced polymer bars manufactured by wet-layup method. Mater Des 56:898–906. https://doi.org/10.1016/j.matdes.2013.11.081
27. Jiang C, Fan K, Wu F, Chen D (2014) Experimental study on the mechanical properties and microstructure of chopped basalt fiber reinforced concrete. Mater Des 58:187–193. https://doi.org/10.1016/j.matdes.2014.01.056
28. Smarzewski P (2019) Influence of basalt-polypropylene fibers on fracture properties of high performance concrete. Compos Struct 209:23–33. https://doi.org/10.1016/j.compstruct.2018.10.070
29. High C, Seliem HM, El-Safty A, Rizkalla SH (2015) Use of basalt fibers for concrete structures. Constr Build Mater 96:37–46. https://doi.org/10.1016/j.conbuildmat.2015.07.138
30. Ayub T, Shafiq N, Nuruddin MF (2014) Mechanical properties of high-performance concrete reinforced with basalt fibers. Procedia Eng 77:131–139. https://doi.org/10.1016/j.proeng.2014.07.029
31. Zorla E, Ipbuker C, Gulik V, Kovaljov S, Kiisa M, Biland A, Tkaczyk AH (2016) Optimization of basalt fiber in concrete composite for industrial application in Estonia. Fresenius Environ Bull 25:355–364
32. Kirthika SK, Singh SK (2018) Experimental investigations on basalt fiber-reinforced concrete. J Inst Eng Ser A 99:661–670. https://doi.org/10.1007/s40030-018-0325-4
33. Biradar SV, Dileep MS, Vijaya Gowri T (2020) Studies of concrete mechanical properties with basalt fibers. In: IOP conference series: materials science and engineering, vol 1006. https://doi.org/10.1088/1757-899X/1006/1/012031
34. Wang Z, Zhao K, Li Z, Ma H (2017) Experimental study on durability and mechanical properties of basalt fiber reinforced concrete under sodium sulfate erosion. Chem Eng Trans 62:961–966. https://doi.org/10.3303/CET1762161
35. Elshafie S, Whittleston G (2015) Review of the effect of basalt fiber lengths and proportions on the mechanical properties of concrete. Int J Res Eng Technol 4:458–465. https://doi.org/10.15623/ijret.2015.0401069

36. Algin Z, Mermerdas K, Khalid LW (2020) Mechanical performance of basalt fiber reinforced concretes. J Inst Sci Technol 10:1093–1106. https://doi.org/10.21597/jist.626757
37. Fiore V, Scalici T, Di Bella G, Valenza A (2015) A review on basalt fiber and its composites. Compos Part B Eng 74:74–94. https://doi.org/10.1016/j.compositesb.2014.12.034
38. Gong Y, Song J, Lin S, Yang J, He Y, Tan G (2020) Design optimization of rubber-basalt fiber-modified concrete mix ratios based on a response surface method. Appl Sci 10:1–14. https://doi.org/10.3390/app10196753
39. Manibalan P, Baskar R (2020) Experimental research on mechanical properties of basalt fiber reinforced concrete. J Crit Rev 7:353–357. https://doi.org/10.31838/jcr.07.13.61
40. Wang X, He J, Mosallam AS, Li C, Xin H (2019) The effects of fiber length and volume on material properties and crack resistance of basalt fiber reinforced concrete (BFRC). Adv Mater Sci Eng. https://doi.org/10.1155/2019/7520549

Development of Trip Attraction Models for the Core Area of Thiruvananthapuram City

A. Nanditha and V. S. Sanjay Kumar

Abstract Infrastructure developments and increased employment opportunities in an area lead to increase in travel demand consequently causing traffic and transportation problems. This can be overcome by proper transportation planning, which includes identifying the travel demand and implementing plans accordingly, thereby maintaining a balanced urban transportation system. Therefore, it is highly warranted to study the trip generation pattern of an area. The present paper attempts to identify the factors that influence the trip attraction potential of the core area of Thiruvananthapuram, the capital of Kerala, India. The attraction characteristics of various establishment types, purposes, and zones are determined followed by the development of trip attraction models. The significant variables identified for the trip attraction were the number of employees, floor area, seating capacity, and available parking space.

Keywords Travel demand · Trip attraction · Establishment · Employment · Thiruvananthapuram

1 Introduction

Transportation plays a paramount role in the growth and economy of a nation. In view of the growth in population, and the all-round development of the country, it is essential to provide a reliable transport system. To examine the influence of developments, it is required to develop models that can estimate travel demand with higher accuracy. The traditional method for urban transportation planning is the classical four-step travel demand modeling which consists of trip generation, trip distribution, mode split and trip assignment. The trip generation aims to forecast the number of trips that will commence from or end at each travel analysis zone in the study area under consideration. The trip generation is composed of trip production and

A. Nanditha (✉)
JEC, Thrissur, India
e-mail: nandithaa97@gmail.com

V. S. Sanjay Kumar
NATPAC, Thiruvananthapuram, India

L. Nandagiri et al. (eds.), *Recent Advances in Civil Engineering*, Lecture Notes in Civil Engineering 256, https://doi.org/10.1007/978-981-19-1862-9_41

trip attraction. Trip production mainly refers to trips originating from predominantly residential zones. Trip attraction models are utilized to describe trips engendered by activities at the non-home end influenced by employment, retail trade, and so on, and focus on predicting the total number of trips attracted to each spatial unit of the study area.

Trip attraction modeling plays a pivotal role in the overall spatial planning of a region. Any over-prediction or under-prediction of trip attraction rates can cause a major quandary in the entire transportation planning process. Therefore, determining trip attraction rate is significant in considering the impact of the new establishment such as workplaces, shopping places, and residential development to the traffic engineers and urban planners. The number of trips attracted to shopping places will be more compared to other workplaces as these trips are the desiderata of the economy.

Previous research provides details on the existence of a strong link between trip attraction, the type of land use, and the intensity of activities. The factors such as, the extent of land use, floor area, number of employees in commercial areas (or employment opportunities), number of shopping centres in commercial areas, number of offices in the commercial areas, number of schools and enrolment, volume of retail sale, number of vehicles parked in the areas, and the accessibility to the areas are considered to influence the trip attractions [1–4].

Thiruvananthapuram Corporation is the most sizably voluminous city corporation in the state of Kerala, India by area and population and administrates Thiruvananthapuram, the capital of Kerala. As the city develops at a rapid pace, the number of daily trips attracted to it increases. Formulating trip attraction models avails in presaging the number of trips attracted to the study area and thereby helping in opportune land use orchestrating to minimize congestions and other urban transportation quandaries.

2 Scope and Objectives

The scope of the study is confined to the development of trip attraction models for the core region of Thiruvananthapuram Corporation. The objectives are

- To identify the factors that influence the trip attraction potential of various establishment types.
- To develop trip attraction models for the various establishment types.
- To develop trip attraction models for various trip purposes.
- To develop zonal level trip attraction model.

3 Literature Review

Anderson and Olander [5] investigated the feasibility of generating production and attraction values for traffic analysis zones in small urban community travel models utilizing a single internal trip purpose. The study fixated on the truncation of data

requisites and simplified the trip generation computation. A multi-purpose modeling approach was adopted for modeling smaller-urban communities. They concluded that trip production and trip attraction remained virtually the same for traffic analysis zones and there is no significant advantage in adopting a multi-purpose modeling approach.

Soltani and Esmaeili Ivaki [6] examined the relationship between urban form and personal daily trips between urban zones across Metropolitan Shiraz, Iran. The variables considered were physical characteristics of the metropolitan and socio-economic characteristics of trip makers. The study found that sub-urbanization and distance from public transport facilities were negatively associated with trip generation. Other factors like land use mix and network connectivity were found to influence inter-zone trip generation.

Bashirul Haque et al. [7] examined the relative importance of socio-economic and land use factors on household travel behavior factors on household daily trips generation rate and kilometers traveled in Sylhet City Corporation area of Bangladesh. Socio-economic parameters considered were household size, household income, and auto ownership which were collected through a household survey. Land use parameters like accessibility and entropy were considered. Linear regression models have been developed. In the case of trip attraction model, independent variables considered are accessibility, retail floor area, and employment opportunity. It was found that land use parameters have a significant contribution to trip production, trip attraction, and household kilometers traveled along with the socio-economic characteristics. The developed models could be serviceable to ensure urban planning balance utilization of spaces where an individual can meet their demands from the proximate distance. It can reduce the commuter trip length, the total number of person trips and is useful for other cities in Bangladesh as well as other developing countries for formulating comprehensive transport and land use policy.

George et al. [4] developed a trip attraction model that can predict the trip attracted to commercial nodes in the medium-sized towns in Kerala, India. Socio-economic and commercial land use characteristics variables were considered. They carried out a combination of analytical and descriptive methods. The higher correlation was given by the number of employees and percentage of offices in the commercial node which gives a better estimation of trip attraction and other factors like total commercial area, the number of commercial establishments, percentage of shops where food items are sold, percentage of office and shop in the commercial node and percentage of commercial establishment with the year of operation between 5 and 10 years. The developed models could be useful for estimating the trips attracted to new or existing commercial centers and to assess the traffic impact of the commercial center on the geometric design of roadways in the surrounding area.

Sasidhar et al. [8] analyzed the trip attraction rates in different cities of Telangana and Andhra Pradesh states of India. Trip attraction rates of commercial land use were determined. The variables considered were floor area, parking space, number of employees and the number of stores. By observing overall statistics, it was found that weekend trip attraction rates of shopping areas are more than the weekday trip

attraction rates. Further, male trip rates are more when compared to female and children on both weekdays and weekends.

Al Razib and Ibn Rahman [9] estimated trip attraction rates of the shopping centers at Uttara Road of Dhaka city using the trip rate analysis method. Few behaviors were considered such as shopping, fitness centers, and other services for the people and vehicles attracted to the shopping centers when they visit the particular building. The surveyed data deals with the relationship between trip attraction rates of the shopping center holistically. The study identified that a maximum and a minimum number of people and cars enter the shopping centers during the peak hour. The main demerit of the study was a limited number of data and they considered only physical features of tip attraction rate of shopping centers. It will engender complications if two shopping centers with different compositions of stores exist with similarities in physical features.

Agustin and Waloeya [1] developed a trip attraction model of land use for industrial areas in Malang city. The study aimed to determine the effect of industrial vehicle movement on the road's level of service in an industrial area. The variables considered include the number of movements, building area, number of employees, number of shifts, frequency of delivery, and visitor counts. The sampling technique adopted was stratified arbitrary sampling. They carried out multiple linear analysis and found that the number of employees and the delivery frequency influences the industrial vehicle movement.

The change in land use plays an important role in changing trip attractions. Variation in trip attraction before and after construction processes of a market area was studied by Agustini et al. [3]. Modeling technique adopted for the trip attraction of visitors to the market was multiple linear regression analysis with a stepwise method. The predictor variables in the form of total traffic flow from the observed zone to the observed destination zone give the estimated number of trips from and to destination generated by the characteristics of the socio-economic zone for zone-based travel. Analysis carried out found that trip attraction of visitors was more influenced by factors like profession, transportation mode, and retail item and significant change in trip attraction rate was observed after the construction processes.

Basuki et al. [10] developed a trip attraction model in small-scale commercial and service areas in the road corridor in, Banyumanik, Sukun Road in Semarang City. The data was collected from considered areas along 200 m in 50 outlets. The modeling technique carried out for trip attraction was using multiple linear regression with the backward method. Variables considered were number of visitors attracted by outlet, number of store employees, area of the shop floor, storehouse parking area, sales income which were accumulated through interviews with store managers on outlets commercial and services. The travel attraction in the small-scale trading area and services was found influenced by socio-economic character, namely sales income in the total attraction of the visitor's car and motorbike and store areas, parking areas, sales income. The developed models could be useful for planning and structuring trade areas and small-scale services to foresee transportation problems because they contribute to the flow of traffic.

Yulianto et al. [2] determined standard trip attraction models for various land uses which include hotels and minimarkets in Surakarta City. The extent of traffic impact that occurred due to the building construction is affected by the amount of trip generation and attraction made by the building activities. The data were collected on the vehicle volume in and out of land use which is considered as the dependent variable. The independent variables on land use parameters such as the number of rooms for hotels and size of building floor area for minimarket were collected for modeling purposes. It was found that regression trip attraction models of 3-star hotels, 4 and 5-star hotels, and minimarket are valid models that give linear regression equations with a sufficient coefficient of correlation and coefficient of determination.

4 Methodology

The study is divided into five phases. The first phase of this study involved understanding the concept of trip generation, trip attraction and the procedure that needs to be adopted for attaining the framed objectives. Earlier studies on similar area were explored and reviewed. The delineation of the study area is the second phase of the study. The study area was fixed after identifying the wards that house major establishments. Based on these criteria, 18 wards were selected.

The third phase of the study involved data collection, data compilation, and analysis. The data collection was accomplished through a questionnaire survey and the minimum sample size was determined using Cochran formula. The survey was done based on the questionnaire designed in which details regarding spatial resources like floor area, rent, etc., data on employment opportunities and travel patterns like the number of visitors, employees, parking availability, etc. were requested from the respondents. The data compilation and preliminary analysis were done to get the initial information regarding the obtained data.

Modeling is the fourth phase of the study. To identify the significant variables, the correlation analysis was carried out before modeling. Using these identified variables the best fit regression models for various establishment types, purposes and zonal levels were developed for the core region of the city. Then validation of models is done to check whether the model is acceptable or not based on the root mean square error value (RMSE).

5 Study Area

Thiruvananthapuram corporation stretches over an area of 214.36 km^2. It is the most populous city in Kerala with a population of 957,730 as per the 2011 Census. The city consists of 100 electoral wards. The present study includes 18 wards selected from CBD area of the city which houses many Central and State government offices,

Fig. 1 Study area map

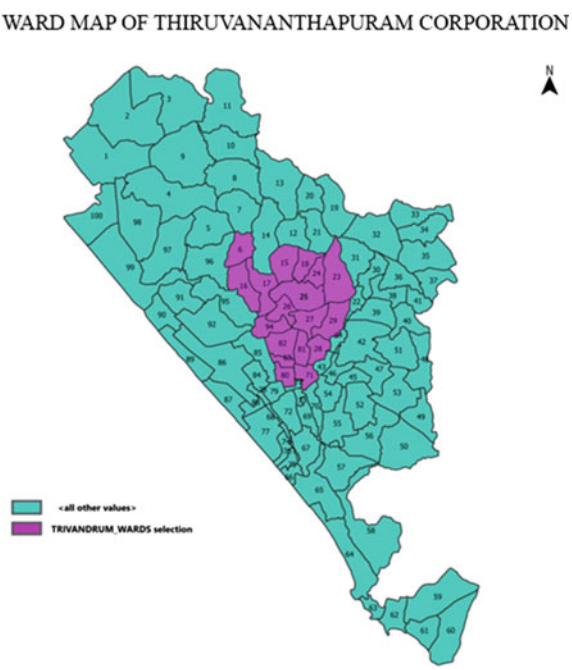

organizations, private sector companies, educational institutions, and research institutions and forms the core region of the city. Figure 1 shows the study area map and the details regarding the selected wards are listed in Table 1.

6 Methods of Data Collection

The data collection was classified into two namely, secondary data collection and establishment survey. The area, population, road length, and the total number of establishments were the secondary data collected. The primary data collection was accomplished through a questionnaire survey and the minimum sample size was determined using Cochran formula. According to the formula, the minimum number of sample size obtained was 360. Thereafter survey was done based on the questionnaire designed in which details regarding the spatial resources like floor area, rent, etc., data on employment opportunities and travel patterns like the number of visitors, employees, parking availability, etc. were requested from the respondents. The establishment survey was carried out in various establishments types like textiles, footwear and bag shops, medical shops, fancy shops, grocery stores, jewelery, electronic shops, furniture shops, restaurants, bakeries, financial institutions, offices, and other shops. 860 samples were collected from the establishments of selected wards.

Table 1 General details of study area

Sl. No.	Ward No	Ward name	Area (km^2)	Population (2011 census)	No. of establishments
1	6	Ulloor	1.17	9376	244
2	15	Kesavadasapuram	1.46	10,153	260
3	16	Medical college	2.01	10,845	430
4	17	Pattom	1.76	10,863	383
5	18	Muttada	1.03	10,322	168
6	23	Kowdiar	2.14	10,372	431
7	24	Kuravankonam	1.21	10,136	383
8	25	Nanthancodu	2.18	9798	328
9	26	Kunnukuzhy	1.13	9799	148
10	27	Palayam	1.31	10,055	599
11	28	Thycaud	1.01	10,712	598
12	29	Vazhuthacaud	1.59	9967	588
13	71	Chalai	0.93	8954	649
14	80	Fort	0.74	9156	480
15	81	Thampanoor	0.79	9461	616
16	82	Vanchiyoor	1.46	9784	770
17	83	Sreekanteswaram	0.46	9967	397
18	94	Kannamoola	1.15	10,250	231

7 Preliminary Analysis and Results

Before the development of trip attraction models the preliminary analysis of collected data is carried out. Table 2 shows the distribution of various parameters. To understand the relationship between the dependent variable and independent variables the scatter plots were plotted for various establishment types and zonal level. The dependent variable considered is number of trips attracted and independent variables include the number of employees, floor area, parking space, seating capacity, area, population, road length and the total number of establishments. The scatter plots showed the trip attraction has a positive linear relationship with the number of employees, floor area, parking space, seating capacity and the total number of establishments.

8 Development of Trip Attraction Models

Trip attraction models were developed using multiple linear regression method after correlation analysis. The correlation analysis done for the variables showed that the

Table 2 Distribution of various parameters

Sl. No.	Parameter	Value	Proportion (%)
1	Number of employees	1	23.74
		2	28.53
		3	16.53
		4 and above	31.20
2	Floor area (sqft)	50–150	23.98
		151–251	24.21
		252–352	17.12
		353–453	11.64
		454–554	6.75
		555 and above	16.30
3	Parking space (ECS)	0–1.0	79.39
		1.1–2.0	5.47
		2.1–3.0	4.20
		3.1–4.0	3.61
		4.1 and above	7.33
4	Seating capacity	0–10	51.85
		11–21	22.22
		22–32	10.37
		33–43	8.15
		44–54	2.22
		55 and above	5.19

trip attraction is positively correlated with number of employees, floor area in sq. ft, seating capacity, and parking space in Equivalent Car Space.

Models were developed for various establishment types, purposes like shopping and work trips, and zonal level by taking 80% of data. The remaining 20% was used for model validation. Validation of model involves comparison of observed trips and predicted trips and based on root mean squared error. Several trials were performed and the most significant one is only presented. The trip attraction models developed for various establishments, purposes and zonal level are tabulated and their corresponding R^2, t statistics and RMSE values are given in Tables 3, 4 and 5.

where,

T_E is the number of trips attracted to electronic shops
T_{FA} is the number of trips attracted to fancy shops
T_G is the number of trips attracted to grocery stores
T_T is the number of trips attracted to textiles
T_{FB} is the number of trips attracted to footwear and bag shops
T_F is the number of trips attracted to furniture shops
T_J is the number of trips attracted to jewelery

Table 3 Trip attraction models developed for various establishment types

Establishment types	Model	R^2	*t*-values	RMSE
Electronic shops	$T_E = 2.138 + 9.416E + 0.041FA + 2.743PS$	0.621	0.452, 7.445, 2.733, 2.517	9.744
Fancy shops	$T_{FA} = 14.596 + 12.145E + 8.918PS$	0.743	2.945, 6.830, 5.484	11.451
Grocery stores	$T_G = 11.309 + 8.560E + 0.071FA + 14.773PS$	0.766	2.128, 5.017, 3.703, 7.453	9.402
Textiles	$T_T = 11.156 + 3.473E + 0.095FA + 7.665PS$	0.773	2.623, 3.021, 9.569, 5.055	9.370
Footwear and bag shops	$T_{FB} = 7.379 + 11.744E + 0.053FA + 14.792PS$	0.736	0.947, 3.644, 3.832, 2.572	5.586
Furniture shops	$T_F = 13.920 + 4.623E + 4.353PS$	0.746	2.334, 2.813, 2.602	6.197
Jewelery	$T_J = 9.461 + 10.876E + 0.057FA$	0.685	1.117, 4.449, 2.822	6.980
Medical shops	$T_M = 5.043 + 12.703E + 0.136FA$	0.590	0.455, 4.187, 4.627	10.493
Bakery	$T_B = 18.463 + 13.699E + 12.089PS$	0.558	3.797, 6.164, 4.412	10.010
Restaurants/hotels	$T_R = 31.307 + 5.170PS + 2.399S$	0.741	3.514, 2.860, 7.303	11.927
Other shops	$T_{OT} = 7.007 + 5.139E + 0.059FA + 4.770PS$	0.754	2.537, 6.384, 8.315, 4.995	8.594
Offices	$T_{OF} = 22.791 + 2.317E + 0.017FA$	0.613	6.319, 2.975, 3.714	8.702
Financial institution	$T_{FI} = 17.082 + 7.220E$	0.731	2.067, 7.178	9.793

Table 4 Trip attraction models for various purposes

Purpose types	Model	R^2	*t*-values	RMSE
Shopping trips	$T_S = 17.872 + 7.317E + 0.046FA + 6.252PS$	0.580	8.752,13.96, 9.037,9.295	15.892
Work trips	$T_W = 16.809 + 6.546E$	0.671	3.945, 10.088	10.772

Table 5 Zonal level trip attraction model

Type	Model	R^2	*t*-values	RMSE
Zonal level trips	$T_Z = 853.012 + 16.211E$	0.996	2.675, 53.784	11.755

T_M is the number of trips attracted to medical shops
T_B is the number of trips attracted to bakery
T_R is the number of trips attracted to restaurants
T_{OT} is the number of trips attracted to other shops

T_{OF} is the number of trips attracted to offices
T_{FI} is the number of trips attracted to financial institution
E is the number of employees
FA is the floor area
PS is the parking space
S is the seating capacity.

For various establishment types, the trip attraction is found to increase with the increase in number of employees, floor area, parking space, and seating capacity. The first term in the models is a constant that represents the predicted criterion value when both predictors equal zero. The trip attraction is found to be positively influenced by the number of employees, parking space, and floor area in electronic shops, grocery stores textiles, footwear and bag shops, and other shops. In the above equations for fancy shops, furniture shops, and bakery the trip attraction was found to increase with the increase in the number of employees and parking space. Restaurants are also found to be positively influenced by parking space and seating capacity. The trip attraction is found to be positively influenced by the number of employees and floor area in jewelery, medical shops, and offices. In case of the financial institutions, the trip attraction was found to increase as the number of employees increased. For these models, the coefficient of determination or R^2 obtained varied from 0.558 to 0.773. The t-values of the independent variables are also found to be significant which ranged between 2.517 and 9.569. From the above equation, the root mean square error (RMSE) for various establishment types was found to be minimum.

where,

T_S is the number of trips attracted to shopping places
T_W is the number of trips attracted to workplaces.

The models developed for various purposes include shopping trips and work trips. The shopping trips were found to be positively influenced by the number of employees, floor area, and parking space. The work trips were found to increase as the number of employees increased. For these models, the coefficient of determination obtained for shopping trip is 0.580 and for work trips is 0.671. The t-values of the independent variables are also found to be significant that varied from 3.945 to 13.96. The RMSE value obtained for shopping trips and work trips is found to be minimum.

where,

T_Z is the number of trips attracted to zonal level.

The first term in the zonal level trip attraction model (853.012) is a constant that represents the predicted criterion value when both predictors equal zero. The regression coefficient of the number of employees is represented by the value of 16.211. The coefficient of determination for this model is 0.996, indicating that 99.6% of the variation in the trips is explained by the variation in number of employees. In the models developed for the zonal level, the error was found to be minimum.

9 Conclusions

Urban centers play a significant role in attracting various trips. As the trip attraction rate increases, it results in urban transportation problems which can be rectified with the help of the trip attraction model. Using multiple linear regression analysis, this study developed trip attraction models for various establishment types, purposes, and zonal level. The study found that for various establishment types and purposes, the trip attraction is positively correlated with variables such as the number of employees, parking space, floor area, and seating capacity. In case of zonal level model, the number of employees was found to influence the trip attraction.

The models developed can be of effective use for land use planning to reduce congestion and other urban transportation problems.

References

1. Agustin I, Waloejo B (2017) Trip Attraction model of land use for industrial area. IPTEK J Proc Ser 3. https://doi.org/10.12962/j23546026.y2017i6.3262
2. Yulianto B, Setiono S, Sugiyarto S, Purnomo S, Prasetyo RA (2020) Study of standard trip attraction models of various land use in the Surakarta City. J Phys Conf Ser 1625(1)
3. Agustini M, Buchari E, Agustien M (2019) Analysis of trip attraction as land use development effect in palembang: case study on Cinde traditional market. J Phys Conf Ser 1198
4. George P, Kattor GJ, Malik KV (2013) Prediction of trip attraction based on commercial land use characteristics. Int J Innov Res Sci Eng Technol 2:352–359
5. Anderson MD, Olander JP (2002) Evaluation of two trip generation techniques for small area travel models. J Urban Plann Dev 128(2):77–88
6. Soltani A, Esmaeili Ivaki Y (2011) The influence of urban physical form on trip generation, evidence from metropolitan Shiraz, Iran. Indian J Sci Technol 4(9): 1168–1174
7. Bashirul Haque M, Rahman M, Abu Sayed Khan M, Nahid Parvez M (2013) Impact of land use parameters on household travel behavior. Am J Civ Eng Architect 1(4):70–74
8. Sasidhar K, Vineeth Y, Subbarao SSV (2016) Trip attraction rates of commercial land use: a case study. Indian J Sci Technol 9
9. Al Razib S, Rahman FI (2017) Determination of trip attraction rates of shopping centers in Uttara Area, Dhaka. Am J Manag Sci Eng 2(5):150–155
10. Basuki Y, Rahayu S, Rahmawati NW (2020) Analysis of backward methods for determining trip attraction model on commercial and service area in Sukun Raya Road, Banyumanik, Semarang. In: IOP conference series: earth and environmental science, vol 409, issue no 1

Study of Mechanical Characteristics of Concrete with Shredded Rubber Tire Aggregate

Sooraj Kumar and Aishwarya Lakshmi

Abstract The unending human needs have given rise to the development of innovative methods in the field of construction. There is the parallel raise in the population and demand and here supply fails to meet the needs. This creates an imbalance. The possibility of using tire aggregates as replacement was ensured based on the scanning electron microscope (SEM) images obtained. The amount of waste shredded rubber tire aggregate (WSRT) which can be implemented in concrete for satisfactory gain in strength is studied here. W/C ratio was kept constant and 2.5, 5, 7.5, and 10% of sand was replaced to check the efficiency of WSRT by conducting study on microstructure and it was found that 5% replacement provided better result.

Keywords Waste shredded rubber tyre aggregate · Concrete · SEM analysis

1 Introduction

Due to increase in the population, there is rapid lift up in the demand for infrastructural facilities which will be safe and aesthetic. There exists a conflict when this criteria of demand and supply is applied into the construction field. When environmental health and safety is considered, it becomes an inevitable fact we are prey of the world of desires we have created. Natural resources when used in excess will lead to hindering of the quality of source and also the quality causing imbalance in the nature. There is huge fuss regarding dumping of the tires. The refining of the tires provides byproducts by using one among them the tires are manufactured. On burning of the tires, toxic gases get liberated into the environment which when inhaled by living beings can be harmful [1]. The gases prove to be fatal when they are dissolved in the water and also affects the aquatic life [2]. The universal disposal of tires is always questionable. The composition of typical tire materials is mentioned in Fig. 1.

S. Kumar (✉)
Shri Madhwa Vadiraja Institute of Technology and Management, Bantakal, Udupi, India
e-mail: sooraj.civil@sode-edu.in

A. Lakshmi
Manipal Institute of Technology, MAHE, Manipal, India

L. Nandagiri et al. (eds.), *Recent Advances in Civil Engineering*, Lecture Notes in Civil Engineering 256, https://doi.org/10.1007/978-981-19-1862-9_42

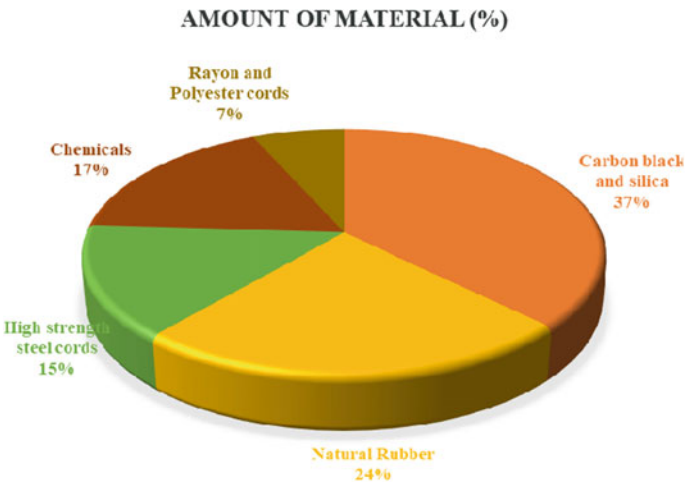

Fig. 1 Composition of tire [1]

Tire is actually an elastomer which has got strength against fatigue failure. Hence, it can be used in concrete to bear the loads. Many research works is done in order to use the rubber aggregates Strength study is done and satisfactory results are also obtained. Surface treatment is employed to modify the bonding properties [3] for 0.45 ratio of rubber to cement. They observed negligible difference in strength value [2]. Various fields of construction are trying to incorporate waste tires in different forms so that it can be efficiently used with less part going to the dumping zone. Hence, this study is using WSRTA whose physical feature resembles that of sand. Few works have been conducted where these aggregates have been used as coarse aggregates [4]. The alternate ways of utilizing this waste material are as follows:

- Incinerating waste tires as a source of alternative fuel
- As aesthetic materials to improve the decorative looks
- As construction substitutes or inclusions.

The following study attempt has been made to utilize the shredded waste tire aggregates as replacement to fine aggregates in the production of concrete for which basic tests and treatments on this is done to check the suitability of WSRTA. The main criteria used for the acceptance of these aggregates is the study of results obtained from microstructural study of concrete prepared using WSRTA.

Throughout the world, the disposal of old tires is posing the problem as degradation period is long, Risk of fire hazards is high, leachate is toxic and contains heavy metals. Since 90s, the waste rubber tire crumbs are utilized as fillers. This has helped in reduction of pollution to certain extent. Meanwhile, this has also bridged the structural requirements of infrastructure. This study particularly aims at identifying the reason for structural property contribution of rubber aggregates.

In recent years, the usage of WSRT is finding prominence and they are mostly used as fillers in the concrete. But no relation was given regarding strength and matrix of cement paste. Many research works are done in order to use the rubber aggregates. Few researchers have used this as aggregates and some have utilized as reinforcements, but no sufficient data is provided for the basis of choosing the optimum dosage. Works have been conducted on the filler property [5], damping nature [6], sound absorption [7], thermal property [8], and strength properties [9] of this material is done and satisfactory result is obtained but nobody tried to explain the reason behind the development of strength in the concrete due to its addition. Therefore, the following study aims at studying the microstructure of the specimens in order to provide proof for this phenomenon.

2 Materials and Methodology

Quantitative methodology is chosen with experimental strategy implemented.

Raw materials used in present study are as follows:

Cement: OPC 53 Grade.

Fine Aggregate: River Sand, confirming IS 383 – 1970 [10].

Coarse Aggregates: Crushed rock (20 mm down size) confirming IS 383 – 1970.

Waste shredded rubber tire aggregates.

2.1 Surface Treatment of Shredded Rubber

The shredded rubber was surface treated with NaOH before usage [11]. The reason was to improve the surface property, after immersing the sample in NaOH solution for 24 h. It is thoroughly washed with water thrice. It was observed that the surface seemed to develop latex finish type surface, so that it adheres well with the concrete mix. As a further step to improve the surface roughness, sand paper rubbing was carried out. The specific gravity of the shredded rubber in Fig. 2 was found to be 0.55. Treatment with sodium hydroxide cleansed the surface of WSRTA [12–14] and sandpaper rubbing prepared the surface of to blend well with cement paste.

2.2 Experimental Procedure

Basic tests on cement and aggregates were carried out along with sieve analysis for WSRTA. Fresh concrete was tested for slump to observe the slump variations with varying dosage of WSRTA replacements. Two set of specimens were casted one

Fig. 2 Waste shredded rubber tire aggregate (WSRTA)

set of conventional concrete being control group $C_{R(0)}$ and concrete made with fine aggregate partially replaced with WSRTA being test group $C_{R(2.5)}$, $C_{R(5)}$, $C_{R(7.5)}$, and $C_{R(10)}$. Impact resistances of the specimens were studied by drop hammer testing. SEM analysis was carried out to evaluate the microstructure and corelate the same with strength property. The methodology is mentioned in Fig. 3.

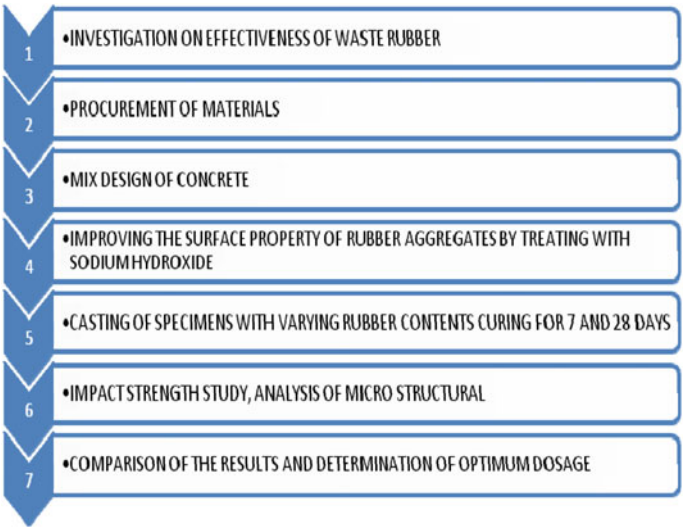

Fig. 3 Flow chart of methodology

3 Results and Discussion

3.1 Mix Design

The mix ratio was calculated [15]and final mix proportion of 1:1.6:2.3 was obtained. Castings were carried out as per the guidelines [16].

Grade of concrete:	M30
Target strength:	$f_{ck} + 1.65(s) = 35$ Mpa
Cement content:	456.57 kg/m^3
Water/cement:	0.30
Water content:	165.53 kg/m^3
Fine aggregate:	763.60 kg/m^3
Coarse aggregate:	1115.99 kg/m^3
Final mix proportion:	1:1.6:2.3.

3.2 Grain Size Distribution of WSRTA

Sieve analysis results:

The gradation test was carried for WSRTA after they were immersed in 1 molar NaOH solution for 24 h, oven dried and finally rubbed with sand paper. Graph is plotted in Fig. 4 for results in Table 1 and following inference was drawn based on results.

Coefficient of uniformity: 3 (CU > 4 or 6).

Coefficient of curvature: 1.40 (1 < CC < 4).

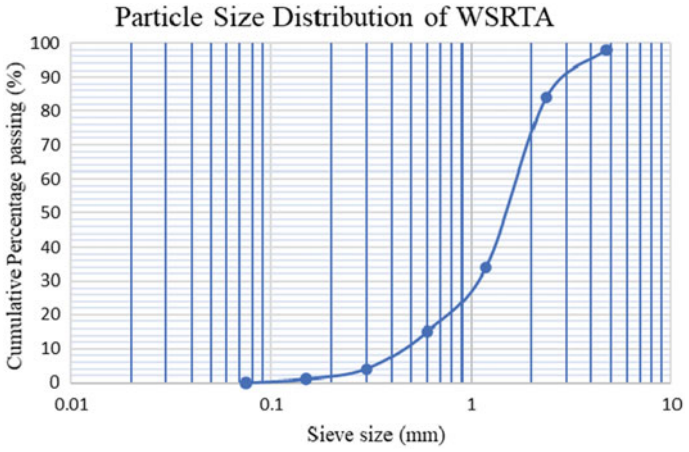

Fig. 4 Gradation curve for WSRTA

Table 1 Grain size distribution

Sieve size	Weight retained (g)	%Weight retained	Cumulative % weight retained (X)	Cumulative % weight passing (100-X)
4.75 mm	4	2	2	98
2.36 mm	18	13	15	84
1.18 mm	68	49	65	34
600 micron	26	18	84	15
300 micron	216	11	95	4
150 micron	4	2	98	1
75 micron	2	1	100	0
Total = 435				

This shows that CC is within limits and CU does not satisfy the condition. Hence, these aggregates can be considered as uniformly graded, i.e., it contains particles of similar sizes, distribution of particles is not uniform.

$$\begin{aligned}\text{Fineness Modulus} &= (\text{Cumulative Percentage weight retained})/100\\ &= 435/100\\ &= 4.35\end{aligned}$$

3.3 Slump Test

Gradation of WSRTA affects the workability of concrete. In the present work workability decreased with increase in replacement percentage similar to the trend observed in [1].

The expected slump in this study is 100 mm as per design of desired mix.

The sample of freshly mixed concrete (1:1.6:2.3) was prepared for the water to cement ratio of 0.30 and 0.8% of super plasticizer. The slump was obtained in the range of values as mentioned in Table 2 and graph is plotted Fig. 5.

3.4 Impact Resistance Study

Normally, aggregates of rubber have the shock absorbing nature[1]. In this study, WSRTA concrete was impact loaded, in order to determine the dynamic nature of concrete.

Table 2 Slump characteristics

Replacement (%)	Slump value (mm)
0.00	99
2.50	102
5.00	104
7.50	107
10.00	109

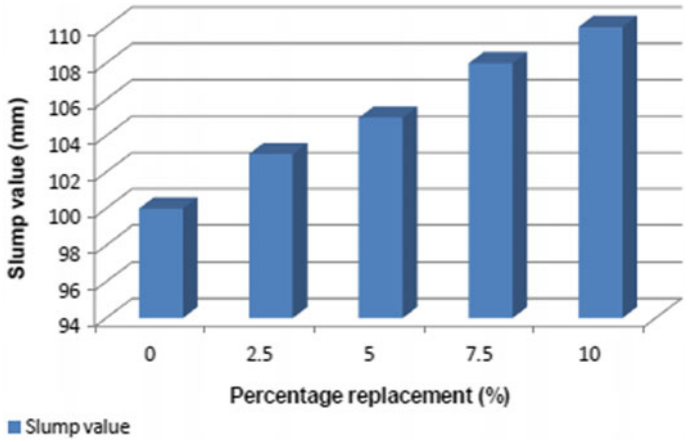

Fig. 5 Variation of slump for different percentages

Weights of 1, 2, and 5 kg were dropped on concrete specimen by maintaining height of 1 m. Samples with (0, 2.5, 5, 7.5, and 10%) were tested after the gain of strength.

The dropping cycle was 5 with 10 dropping per cycle. The test results are provided in Fig. 6.

From this test, it was found that with the increase of replacement cracks also increased ending up with chipping off. It is seen that for lower weight values, all the samples proved to be successful in bearing the impact. The spread of cracks was speed in the case of WSRTA implemented concrete.

3.5 Micro Structural Property

SEM study was conducted to analyze the micro structural property of specimens made with WSRTA. The quality of the transition zone was analyzed in this study to explain the reason behind strength factors. The texture of the specimen in its microstructural level was observed. The orientation of materials and adhesiveness between the components can be identified easily by the 2D image obtained. Inclusion

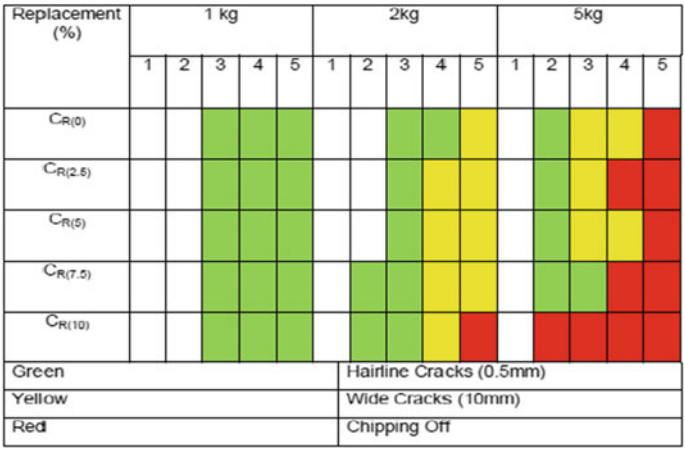

Fig. 6 Impact resistance study results

of surface treated WSRTA with their increased dosage showed variation in transition zone characteristics which supports the findings of [3]. Figure 7 represents the SEM image of control specimen.

R 2.5%

For this amount of replacement transition zone is semiporous in nature and main reason behind decreased strength was this nature of semiporosity between aggregate and cement paste (Fig. 8).

R 5%

For this amount of replacement, compactness of transition zone is present. This compact nature is reason for the good strength of the cubes (Fig. 9).

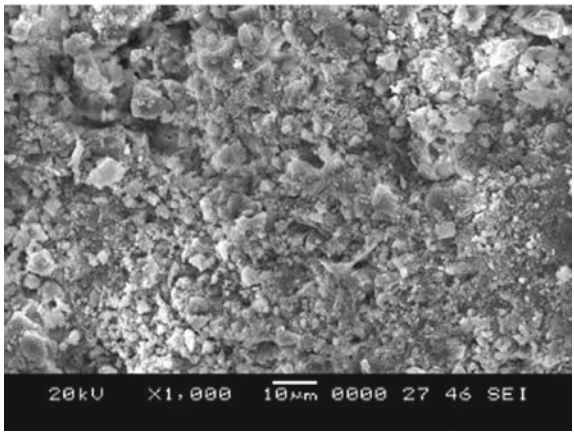

Fig. 7 SEM image specimen image with 0% replacement

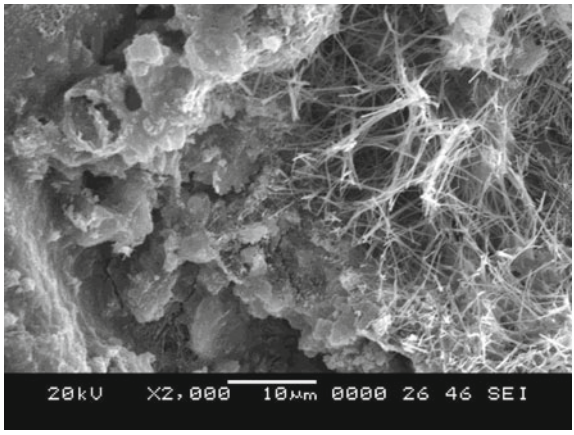

Fig. 8 SEM image specimen image with 2.5% replacement

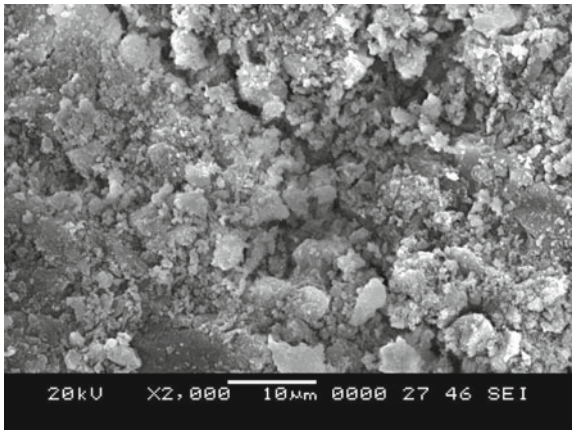

Fig. 9 SEM image specimen image with 5% replacement

R 7.5%

For this amount of replacement, the transition zone is lightly porous. This nature is responsible was the slightly decreased strength of cubes (Fig. 10).

R 10%

For this amount of replacement, the transition zone is densely porous due to which, there is sudden drop in the strength of cubes (Fig. 11).

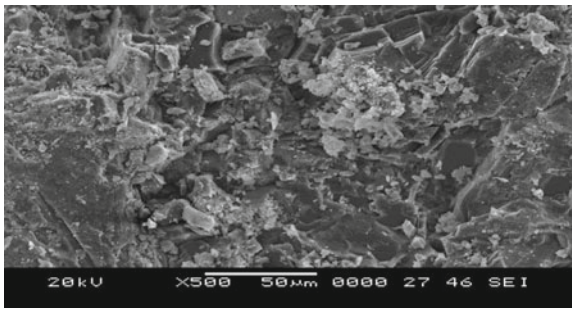

Fig. 10 SEM image specimen image with 7.5% replacement

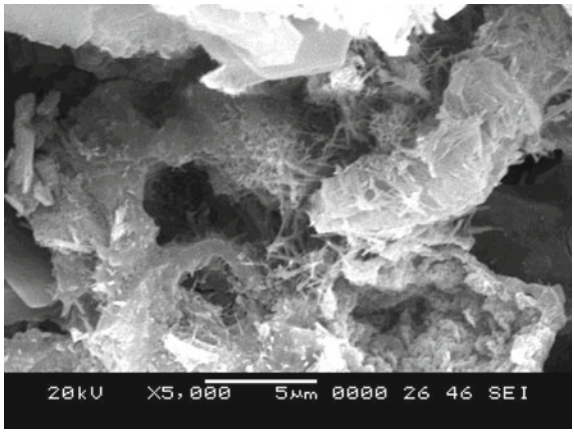

Fig. 11 SEM image specimen image with 10% replacement

4 Conclusion

Based on the works carried out during the test period, it is clearly depicted that WSRTA can be efficiently used as a replacement of sand in the manufacture of concrete. Even though the strength obtained was lower than that of conventional concrete, the results were satisfactory.

- From the works carried out, it was found that as the dosage of WSRTA (waste shredded rubber tire aggregates) increased the workability of the mix showed an increase. This shows that for obtaining of consistent mix WSRTA can be used.
- The impact test followed is nonconventional in nature but it clearly depicted the comparison between $C_{R(0)}$ and $C_{R(5)}$ by showing better results for the latter.
- The SEM analysis clearly showed that compactness in the transition zone of $C_{R(5)}$ is the reason for satisfactory results obtained for compressive and impact strength.
- Based on this study, it can be conclude that 5% replacement of fine aggregates by WARTA is optimum to gain usable concrete.

References

1. Hamdi A, Abdelaziz G, Farhan KZ (2020) Scope of reusing waste shredded tires in concrete and cementitious composite materials: a review. J Build Eng 102014
2. Fattuhi NI, Clark LA (1996) Cement-based materials containing shredded scrap truck tyre rubber. Constr Build Mater 10(4):229–236
3. Liu R, Zhang L (2015) Utilization of waste tire rubber powder in concrete. Compos Interfaces 22(9):823–835
4. Corinaldesi V, Mazzoli A, Moriconi G (2011) Mechanical behaviour and thermal conductivity of mortars containing waste rubber particles. Mater Des 32:1646–1650
5. Gupta T, Chaudhary S, Sharma RK (2014) Assessment of mechanical and durability properties of concrete containing waste rubber tire as fine aggregate. Constr Build Mater 73:562–574
6. Liu F, Chen G, Li L, Guo Y (2012) Study of impact performance of rubber reinforced concrete. Constr Build Mater 36:604–616
7. Ghizdaveț Z, Ștefan B-M, Nastac D, Vasile O, Bratu M (2016) Sound absorbing materials made by embedding crumb rubber waste in a concrete matrix. Constr Build Mater 124:755–763
8. Sukontasukkul P (2009) Use of crumb rubber to improve thermal and sound properties of pre-cast concrete panel. Constr Build Mater 23:1084–1092
9. Lv j, Zhou T, Du Q, Wu H (2015) Effects of rubber particles on mechanical properties of lightweight aggregate concrete. Constru Build Mater 91:145–149
10. IS 383:2016. Coarse and fine aggregate for concrete specification. Bureau of Indian Standards, New Delhi
11. Guo S, Dai Q, Si R, Sun X, Lu C (2017) Evaluation of properties and performance of rubber-modified concrete for recycling of waste scrap tire. J Cleaner Product 148:681–689
12. Huynh H, Raghavan D (1997) Durability of simulated shredded rubber tire in highly alkaline environments. Department of Chemistry, Howard University, Washington, pp 138–143
13. Segre N, Joekes I (2000) Use of tire rubber particles as addition to cement paste. Cem Concr Res 30:1421–1425
14. Albano C, Camacho N, Reyes J, Feliu JL, Hernandez M (2005) Influence of scrap rubber addition to Portland I concrete composites: destructive and non-destructive testing. Compos Struct 71:439–446
15. IS 456:2000. Plane and reinforced concrete-code of practice. Bureau of Indian Standards, New Delhi
16. IS 10262: 2019. Recommended guidelines for concrete mix design. Bureau of Indian Standards, New Delhi

Domestic Wastewater Treatment Using Areca Husk

T. S. Umesha, H. Devasharma, S. Manjushree, K. Muskan, Mohamed Arshad, and K. Monisha

Abstract Numerous domestic and municipal wastewater treatment systems have been developed to improve effluent water quality, but most of them require consideration of economic aspects. This study was carried out to investigate the applications of Areca husk filtration as an efficient method to economically remove BOD, COD, chlorides, sulphates and nitrates by the principle of trickling filter. Biofiltration was carried out to study the performance and treatment efficiency of Areca husk as filter media in treating domestic wastewater at different contact periods (48, 72 and 96 h). Due to higher specific surface area, fibrous materials are often considered as a better choice for increased microbial support and treatment efficiency. When Areca husk was used as a filter bed, considerable reduction in BOD, COD and nutrients such as chlorides, sulphates and nitrates were observed. BOD was reduced by 53.9% and COD by 55.7% after four days treatment, respectively. The pH was found to be almost constant throughout the contact period of 96 h. The treated wastewater can be used for various domestic purposes like cleaning, washing and gardening and the spent fibres will have a high fertilizer value and can be used for agricultural purpose.

Keywords Areca husk · Biochemical oxygen demand (BOD) · Chemical oxygen demand (COD) · Fibrous materials

1 Introduction

Water is required for sustaining life. Water covers 71% of the earth's surface mostly in seas and oceans, however, the availability of water for human utilization and consumption is very less. It is used in many anthropogenic activities such as agriculture, washing and industries. Globally, 80% of water flows back into the ecosystem as wastewater being untreated and reused. Domestic wastewater is defined as the wastewater produced due to human activities in household, i.e. water generated from kitchen, bathrooms including washbasins, shower, toilet, laundry, etc.

T. S. Umesha (✉) · H. Devasharma · S. Manjushree · K. Muskan · M. Arshad · K. Monisha
Siddaganga Institute of Technology, Tumakuru, Karnataka, India
e-mail: tsumesha@sit.ac.in

L. Nandagiri et al. (eds.), *Recent Advances in Civil Engineering*, Lecture Notes in Civil Engineering 256, https://doi.org/10.1007/978-981-19-1862-9_43

The use of water source which is not well treated will cause waterborne diseases. Waterborne diseases can be reduced by proper water treatment. Wastewater treatment is a process of removal of contaminants from wastewater and converting it into an effluent that can be returned to the environment with minimum impact. Its treatment aims at reducing the contaminants to acceptable levels to make the water safe so that it can be discharged back into the environment. In developed countries and major cities, water supplies are primarily managed by centralized water treatment systems. Conventional centralized water treatment systems consist of essential processes for the removal of harmful microorganisms. Treated water is then distributed to households through extensive piping systems. However, in developing countries and in rural areas, the upfront cost of a centralized water treatment and distribution system, due to the low density of houses, hindered its installation.

Conventional treatment of wastewater is proven to be costly and not efficiently working. The design and operation of activated sludge reactor requires experts and skilled supervision for watching out mechanical failures. The mechanical parts like rotars and aerators of activated process consume electricity for operation. Considering all these aspects, the method adopted here, wastewater treatment using natural fibres is simple. Among all the natural fibre materials, Areca husk appears to be a promising material because of its abundant availability, low cost and a really high potential perennial crop. The disposal of Areca nut in its own form is a challenging one and requires lot of time for decomposition. Alternatively, this can be used in the treatment of wastewater.

The strength of domestic wastewater is reduced using natural fibrous bed materials as filter media. The use of natural fibres as filtration media is gaining more attention. This is due to its acceptable density range, high sorption capacity, easy availability and feasibility and environmentally friendly characteristic. Natural fibres are among the alternatives for oily wastewater treatment for their simplicity, excellent oil removal properties, environmentally friendly characteristic and easy availability and feasibility [1]. Riahi et al. [2] studied the application of date-palm fibres (surface fibres) filters as porous medium for the tertiary domestic wastewater treatment. The result indicated that the diameter of the fibres had the most significant factor affecting the treatment. Etim et al. [3] investigated the efficiency of raw coconut coir dust (without physical/chemical modificativon or activation) as a low-cost adsorbent for the removal of methylene blue from aqueous solution. The coconut coir has good adsorption capacity for methylene blue and showed strong adsorption as the initial concentration of the dye was more. Suhartini et al. [4] conducted an experiment on wastewater from tapioca starch industry, particularly in Indonesia, which contains high organic matters, high biochemical oxygen demand (BOD) and chemical oxygen demand (COD) value using Moringa oleifera seeds and natural filter media as sand and coconut coir and the result showed improvement in appearance and quality of final effluent, with higher reduction of BOD, COD, TSS and stability in pH value. Low et al. [5] conducted experiments to determine the pollutants removal efficiency of coconut coir for river water and the results showed that the coconut coir in the fabricated column model along with circulating water showed biodegradability to be more effective and efficient. Natural fibres can also be used as adsorbents for wastewater

treatment and removal of oil, dyes, heavy metals, ionic compounds [6]. Different modification types are used to enhance the fibres and mechanism for removal of adsorbents. It was observed that none of these modified fibres could remove more than one type of contaminant at a time, as far as industrial and domestic relevant pollutants are concerned. Coir fibres on grafting with butyl acrylate gives oil absorption of 13.45 g/g which is significantly higher (275% increase) than that of unmodified coir fibre (3.58 g/g) [7]. The fibres can be reused for at least three times before disposing them. The results of the experiments illustrate that oil sorption capacity decreases during repeated use of the sorbent. Gondhar and Shukla [8] intended to highlight the performance of fixed-bed columns arranged in series using oxidised coconut coir (OCC) as a cheap and renewable biosorbent for removal and recovery of Cd(II) ions from aqueous solution. The experimental results showed that the flow rate has greater influence on Cd(II) uptake by oxidised coir. The increase in flow rate resulted in decreased metal uptake, due to insufficient residence time of solute in the column.

2 Materials

In this present study, Areca husk was used as filter media for domestic wastewater treatment. Wastewater quality analysis has been conducted in laboratory for the sample collected from SIT Campus sewage treatment plant for various parameters such as BOD, COD, pH, chlorides, sulphates and nitrates. Among all the natural fibre materials, Areca husk appears to be a promising material because of its abundant availability, low cost and a really high potential perennial crop. Areca husk fibre is a versatile natural fibre extracted from mesocarp tissue or husk of the areca fruit. It belongs to the species areca catechu L., under the family palmecea and originated in Malaya Peninsular, east India. The husk of Areca is a hard fibrous portion covering the endosperm. It constitutes 3o–45% of the total volume of the fruit. Most part of the Areca husk fibres are composed of hemicellulose and not of cellulose. Areca fibres contain l3–24.6% of lignin, 35–64.8% of hemicelluloses, 4.4% of ash content and remaining 8–25% of water content. The portions of the middle layer contain soft fibres and the fibres adjoining the inner layer are irregularly lignified group of cells called hard fibres. Areca husk was brought from local rural areas. It was cleaned and washed to remove dust and other particles and allowed to dry (Fig. 1). This method of treatment adopted using Areca husk as a filter media follows the principle of trickling filter in which wastewater is made to trickle over a filter media containing seeding agent, due to biological action, the organic compounds present in wastewater gets decomposed resulting in the reduction of strength (BOD) in the wastewater.

Fig. 1 Cleaning of Areca husk

3 Experimental Procedure

The sample used was SIT Campus sewage water (Fig. 2). 20L of raw wastewater was collected from the campus sewage treatment plant. Wastewater samples were analysed for various physical and chemical parameters like pH, BOD, COD, chlorides, sulphates and nitrates.

Experimental set-up consists of 50L plastic circular water container of diameter 30 cm and height 60 cm (Figs. 3 and 4). Meshes of sizes 25 mm and 2.36 mm were placed at a depth of 5 cm from the bottom surface. A tap was fitted at the bottom for the outlet of treated water. Areca husk was cleaned and washed to remove dust and other particles. It was placed evenly with slight compaction to a depth of 10 cm

Fig. 2 Collection of wastewater sample

Fig. 3 Plastic drum used for treatment

Fig. 4 Mesh used as filter

above the mesh (Figs. 5 and 6). Cow dung was mixed with wastewater and added to filter bed for seeding and this set-up was left for 7 days for acclimatization and development of biomass. Wastewater was fed into a container for treatment. Treated wastewater was then analysed for various physical and chemical parameters after 2, 3 and 4 days. Results were recorded and removal efficiency was calculated.

Fig. 5 Raw Areca husk

Fig. 6 Arecahusk mixed with cow dung

4 Results and Discussions

Table 1 represents the initial values of BOD, COD, chlorides, sulphate, nitrate and pH as 852 mg/L, 900 mg/L, 259.91 mg/L, 45 mg/L, 1.6 mg/L and 7.41, respectively. After 48 h of contact period, there was a decrease in the values of BOD, COD, chlorides, sulphates and nitrates and were recorded as 538.46, 657, 156.97, 18 and 1.11 mg/L, respectively. The removal efficiencies were calculated, BOD was found to

Table 1 Initial tests conducted on wastewater sample

Parameters	Initial
BOD (mg/L)	852
COD (mg/L)	900
Chlorides (mg/L)	259.91
Sulphates (mg/L)	45
Nitrates (mg/L)	1.6
pH	7.41 @ 29.2 °C

be 36.8%, COD 27%, chlorides 39.6%, sulphates 60% and nitrates 30.4%. Similarly, after 72 h, the removal efficiency was observed to be 44%, 42.5%, 45.4%, 69% and 45.7%, respectively (Table 2), and at the end of 96 h, it was found to be 53.9%, 55.7%, 49.3%, 75% and 52.8%, respectively (Table 3). The pH was found to be almost constant throughout the contact period of 96 h.

Figure 7 represents the removal efficiency of BOD after 2, 3 and 4 days as 36.8%, 44% and 53.9%, respectively. Figure 8 represents the removal efficiency of COD after 2, 3 and 4 days as 27%, 42.5% and 55.7%, respectively. Figure 9 represents the removal efficiency of chlorides after 2, 3 and 4 days as 39.6%, 45.4% and 49.3%, respectively. Figure 10 represents the removal efficiency of sulphates after 2, 3 and 4 days as 60%, 69% and 75%, respectively. Figure 11 represents the removal efficiency of nitrates after 2, 3 and 4 days as 30.4%, 45.7% and 52.8%, respectively.

Table 2 Results after two days treatment using Areca husk—10 cm depth

Parameters	Initial	After 2 days	Removal efficiency (%)
BOD (mg/L)	852	538.46	36.8
COD (mg/L)	900	657	27
Chlorides (mg/L)	259.91	156.97	39.6
Sulphates (mg/L)	45	18	60
Nitrates (mg/L)	1.6	1.11	30.4
pH	7.41	7.46	–

Table 3 Results after three days treatment using Areca husk—10 cm depth

Parameters	Initial	After 3 days	Removal efficiency (%)
BOD (mg/L)	852	477.12	44
COD (mg/L)	900	517.5	42.5
Chlorides(mg/L)	259.91	141.90	45.4
Sulphates(mg/L)	45	13.95	69
Nitrates(mg/L)	1.6	0.87	45.7
pH	7.41	7.5	–

Table 4 Results after four days treatment using Areca husk—10 cm depth

Parameters	Initial	After 4 days	Removal efficiency (%)
BOD (mg/L)	852	392.77	53.9
COD (mg/L)	900	398.7	55.7
Chlorides (mg/L)	259.91	13.76	49.3
Sulphates (mg/L)	45	11.25	75
Nitrates (mg/L)	1.6	0.75	52.8
pH	7.41	7.48	–

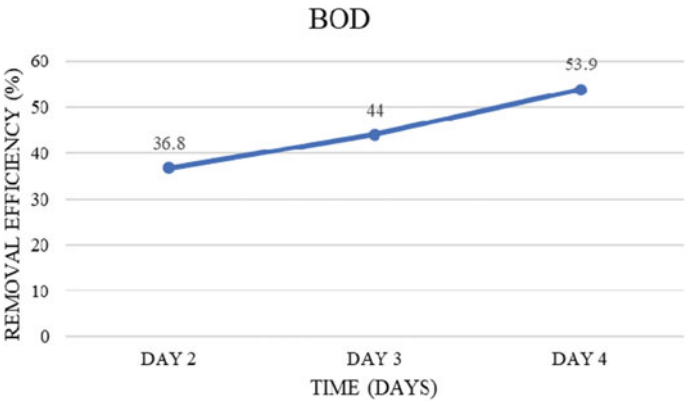

Fig. 7 BOD removal efficiency using 10 cm Areca husk filter bed

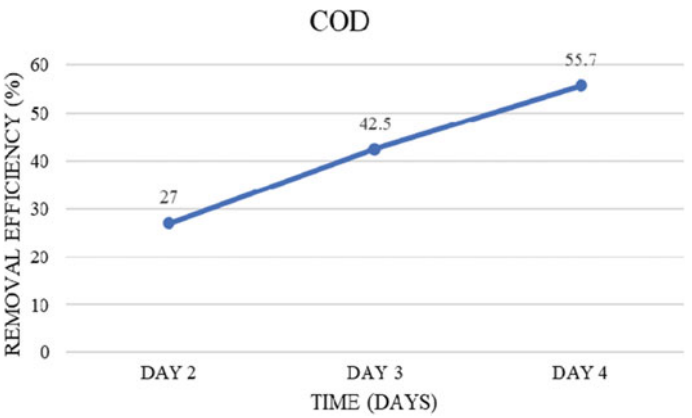

Fig. 8 COD removal efficiency using 10 cm Areca husk filter bed

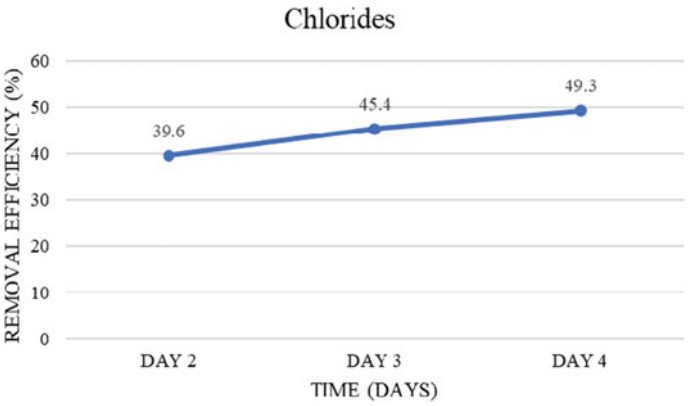

Fig. 9 Chlorides removal efficiency using 10 cm Areca husk filter bed

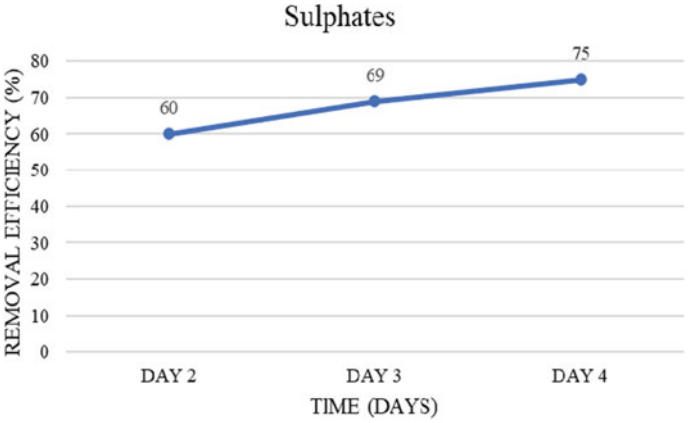

Fig. 10 Sulphates removal efficiency using 10 cm Areca husk filter bed

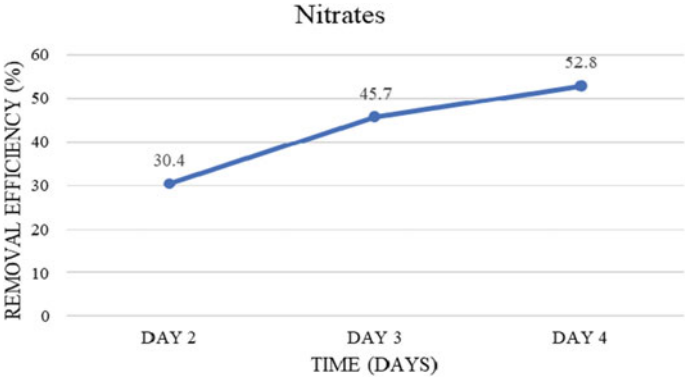

Fig. 11 Nitrates removal efficiency using 10 cm Areca husk filter bed

5 Conclusions

When Areca husk was used as a filter bed, considerable reduction in BOD, COD and nutrients such as chlorides, sulphates and nitrates were observed. BOD was reduced by 36.8% after 2 days, 44% after 3 days, 53.9% after 4 days of treatment and COD by 27%, 42.5% and 55.7% after 2, 3 and 4 days treatment, respectively. The treated wastewater can be used for various domestic purposes like cleaning, washing and gardening and the spent fibres will have a high fertilizer value and can be used for agricultural purposes.

References

1. Wahi R, Chuah LA, Choong TSY, Ngaini Z, Nourouzi MM (2013) Oil removal from aqueous state by natural fibrous sorbent: an overview. Sep Purif Technol 113:51–63
2. Riahi K, Mammou AB, Thayer BB (2009) Date-palm fibers media filters as a potential technology for tertiary domestic wastewater treatment. J Hazard Mater 161:608–613
3. Etim UJ, Umoren SA, Eduok UM (2016) Coconut coir dust as a low cost adsorbent for the removal of cationic dye from aqueous solution. J Saudi Chem Soc 20:67–76
4. Suhartini S, Hidayat N, Rosaliana E (2013) Influence of powdered Moringa oleifera seeds and natural filter media on the characteristics of tapioca starch wastewater. Int J Recycling Organ Waste Agric 2:12
5. Low W-P, Md Din MF, Ponraj M, Fulazzaky MA, Iwao K, Songip AR, Chelliapan S (2013) Application of low-cost fabricated column model for the adsorption analysis of pollutants from river water using coconut coir. Desalination Water Treatment 53(5):1342–1351
6. Abd Rahman NS, Yhaya MF, Azahari B, Ismail WR (2018) Utilisation of natural cellulose fibres in wastewater Treatment. Cellulose 9
7. Teli MD, Valia SP Mifta J (2016) Application of functionalized coir fibre as eco-friendly oil sorbent. J. Textile Inst
8. Gondhar SC, Rleka Shukla S (2019) Enhanced adsorption performance of oxidised coconut coir for removal of Cd(II) ions by multi-column arrangement in series. Environ Sci Pollut Res 26:28022–28030

Local Scour Around Non-uniform Bridge Piers: Vortex Power Concept

G. Veerappadevaru, M. A. Nagesh, and H. Devasharma

Abstract The prediction of equilibrium scour depth is carried out by tweaking the power of the vortex that crops up in front of non-uniform piers. This modification is based on replacing the width of uniform pier with equivalent width for a non-uniform pier. The ratio of the projected area of the components of pier to the depth, $Y_{\min}$ constitutes equivalent width. Minimum scour depth occurs for type-I piers and to a depth $Y_{\max}$ at which maximum scour depth occurs for type-II piers. The vortex power concept is based on equivalent width and is tested using author's experimental data relative to data available in literature. It is found that the prediction accuracy in both cases is substantially accurate.

Keywords River engineering · Non-uniform piers · Local scour depth · Vortex power · Equivalent width

Notations

A	Width of deep scour hole at the ridge level (m)
B	Vertical width of the deep scour hole (m)
B	Flume width (m)
d_{50}	Median grain size (m)
d	Diameter of piles (m)
D	Diameter of the cylindrical pier (m)
D_c	Diameter of caisson pier (m)
D_v	Size of vortex (m)
D_e	Equivalent diameter of the pier (m)

G. Veerappadevaru (✉) · H. Devasharma
Department of Civil Engineering, Siddaganga Institute of Technology, B. H. Road, Tumakuru, Karnataka 572103, India
e-mail: gvd@sit.ac.in

M. A. Nagesh
School of Civil Engineering, REVA University, Yelahanka, Bengaluru, Karnataka 560064, India

L. Nandagiri et al. (eds.), *Recent Advances in Civil Engineering*, Lecture Notes in Civil Engineering 256, https://doi.org/10.1007/978-981-19-1862-9_44

D_p Diameter or width of pile cap (m)
F_{Dc} Flow parameter based caisson width (−)
F_{De} Flow parameter based equivalent width (−)
P_c Power consumed in dislodging the sediment from its position (W)
P_v Power available in vortex (W)
G Acceleration due to gravity (m/s^2)
h Depth of flow for the upstream of pier (m)
h_s Scour depth (m)
L Length of oblong pier (m)
L_C Length of oblong caisson pier (m)
m Number of piles exposed to flow (−)
N Vortex rotation (rps)
n Number of pile provided (−)
T Thickness of pile cap (m)
V_{*c} Critical shear velocity of the sediment grain
Y Vertical depth measured with respect to bed level; (−ve) below bed level and (+ve) above bed level (m)
PC Pile cap top level (m)
CT Caisson top (m)
SL Scour level (m)

1 Introduction

River bridge piers are built over the foundation structure. This may be of caisson well type or an array of piles with their protruding pile cap. The stability of the bridge piers against flood flow depends on foundation depth. The design of foundation depth consists of the prediction of local scour depth. The knowledge of the maximum scour depth for uniform piers is available. The scour depth information on piers like cylindrical piers built on cylindrical caisson foundation was carried out through experiments by Melville and Raudkivi [4] and Parola et al. [6]. Experiments to predict scour depth for piers built on pile caps supported by an array of piles are carried out by Coleman [2] and Seshagiri Rao et al. [8]. The empirical approach was adopted in the above cases to predict the maximum scour depth. In this paper, an attempt has been made to predict the maximum scour depth based on the power available in the primary vortex for different positions of non-uniform piers with respect to bed level by adopting the equivalent width concept. The equivalent width is considered because the width of a non-uniform pier varies abruptly from pier to caisson and pier to pile cap supported by piles. Uniform piers built on caisson foundation are designated as type-I non-uniform piers. Type-II piers refer to non-uniform piers found on pile caps supported by a cluster of piles.

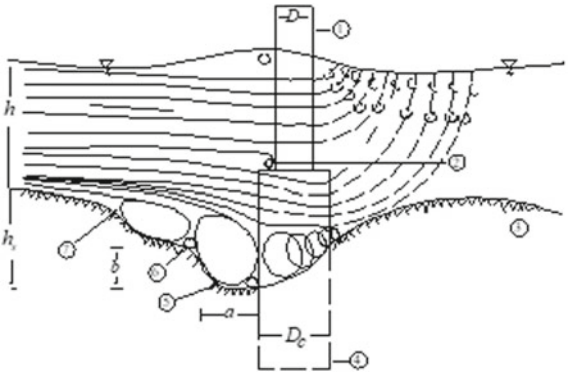

Fig. 1 Details of vortex zones and ridge for flow around bridge pier with caisson (1) Cylindrical pier (2) Vortex at the junction of pier and caisson (3) Sandbed (4) Caisson (5) Primary vortex (6) Ridge (7) Secondary vortex (Ref. Veerappadevaru et al. [9, 10])

1.1 Vortex Participation in Scour Process

It is well known that the corner of the pier attached to the river bed will be subjected to critical flow separation. The vortices of the sediment laden with huge mass of sediment grain along with downstream velocity are the main reasons for the local scour. It is also stated that secondary vortex together with primary vortex always exist in pairs. While primary vortex is generated at the front of the pier surface, behind the piers acts the secondary vortex. This conjointly dislodges the sediment there by causing a local bowl in front of the pier. The ridgeline is formed whenever primary vortex and secondary vortex separates from each other. The downstream flow and incoming curved flow will just confluence into the bowl caused by the scour and further aggravates the situation. Added to this, the caisson top or pile cap obstructs certain portion of downward flow causing restricted movement of water and thus increasing velocity of flow. The formation of both primary and secondary vortex is indicated in Fig. 1.

1.2 Power Concept for Local Scour

Power P_v is given by (Veerappadevaru et al.):

$$P_{\mathrm{v}} = \rho\pi^2 D_{\mathrm{v}}^2 N D_{\mathrm{c}} V^2 \tag{1}$$

where ρ is the water density, D_v is the vortex size, N is the rotational speed of vortex, D_c is the width of pier or caisson at primary vortex level and velocity of flow is designated as V and it is at the primary vortex level. When the scouring process reaches equilibrium, the power available in the primary vortex is utilized to overcome the resistance offered by sediment grains in the scour hole surface. The power consumed P_c by the sediment grains in the scour hole was estimated by Veerappadevaru et al. [9, 10] as:

$$P_c = 2/3\pi D_v D_c(\rho_s - \rho)(gd_{50})V_{*c} \tag{2}$$

where ρ_s is the sediment density, g is m/s^2, d_{50} is the median size of sediment and V_{*c} is the critical shear velocity for the grain of the sediment to be obtained by Shield's criteria related to critical shear stress. D_c is the width of caisson when its top level coincides with the general bed level. For equilibrium state of scour

$$P_v = P_c \tag{3}$$

Rearranging the terms, one gets

$$F_{Dc} \infty (h + h_s)/D_c \tag{4}$$

where F_{Dc} is the vortex flow parameter defined as:

$$F_{Dc}^3 = q^3/\left[\left[\left(D_c^2 h\right)((\rho_s - \rho)/\rho)\right)(gd_{50})^{1.5}\left(V_{*c}/\sqrt{(gd_{50})}\right)\right] \tag{5}$$

where q quantum of incoming flow's discharge. Using the data available in the literature and their own data, Veerappadevaru et al. [9, 10] proposed the constant of proportionality 0.48 as:

$$(h + h_s)/D_c \approx 0.48 F_{Dc} \tag{6}$$

The scour level is measured with respect to the free surface and not with respect to the general bed level. Equation (6) was developed for the case when caisson top is located at bed level before the start of the scouring process. The variation of caisson top for type-I non-uniform pier or pile cap level for type-II non-uniform pier with respect to bed level needs to be considered in the scour depth prediction for non-uniform piers [3] and Veerappadevaru et al. [9, 10] proposed the depth parameter as $(D_c^2\ h)^{1/3}$ in estimating the scour depth. This parameter is modified as $(D_e^2\ h)^{1/3}$ by replacing D_c by D_e in the present work. The notation 'D_e' that indicates equivalent width is the ratio of the projected area (frontal) to appropriate depth from free surface to the position of minimum scour level Y_{min} for caisson type piers type-I non-uniform pier and maximum scour level Y_{max} for piers founded on cluster of piles. The equivalent width concept presented in this paper is supported by experimental work and also verified from the data available in the literature.

2 Experimental Methodology

In an experimental study, 5.5 m length flume of trapezoidal cross-section was developed. The depth was 0.30 m and the width of the bed was set to 1.0 m. It was so developed in such a way to possess rigid banks and mobile sand beds. The rigidity was obtained by smearing rich cement mortar slurry. The sand median size d_{50} was

found to be 0.52 mm with standard deviation σ_g at 1.912 (geometric). An overhead tank was used to generate the flow in the channel. A screen of stone of 20 cm wide is provided to achieve this. It extends the entire flume and also covers the entire height from the bed level to the top of the sandbank was also provided. Apart from this, a pebble mat was placed along with a stone screen to obviate possible erosion. At the downstream end of the flume, a trap for sediment is also placed. The discharge was meticulously measured using 90° V-notch which was placed at the tail end of the flume. The overall experimental set-up is showcased in Fig. 2.

The pier models were made of wood and were painted to avoid warping. Figure 3 shows the shapes of the piers used for experiments, they include, pier with piles, cylindrical pier with caisson, cylindrical pier, uniform oblong pier, caisson type oblong pier, and oblong pier with pile cap. All of them being supported on a sequence of piles.

Experiments were conducted for maintaining a critical state of sand bed in the flume bed at depth of flow h was 8 cm. The bed shear velocity V_{*c} was 0.00763 m/s. The pier models were placed at the centre of the flume at a distance of 4.1 m from the upstream side and 1.4 m from the sediment trap. Bed is levelled and flow is

Fig. 2 The front view of river flume

Fig. 3 Pier models with piles and pile cap, with caisson and cylindrical pier

Table 1 Variation of scour depth across pile cap

Y (mm)	100	75	50	25	0	−25	−50	−75	−100
h_s (mm)	8.3	6.7	6.9	21.8	17.8	14.5	32.2	35.4	32.6

Table 2 One typical value of scour depth and completed equivalent diameter

Caisson top or pile cap top position (mm)	−120	−90	−60	−30	0	30	60	90	120
Scour depth h_s (mm)	16	14	12	10	7.6	11	21	26	33
Equivalent diameter D_e (mm)	75	63.75	52.5	41.25	30	30	30	30	30

allowed to reach a fairly uniform state. The piers are inserted into the sediment bed at the test section by stopping the flow. The flow is resumed by gradual opening of the valves to maintain predetermined depth of flow. The scour level in front of the pier surface is measured at regular intervals of time from the start up to 10 h of flow duration. At the end of 10 h, the scour hole geometry like depth and width, scour hole surface dimensions along the front and sides of piers, primary vortex size associated with ridge dimensions are measured. A vertical point gauge having 0.1 mm precision on the Vernier scale was used to measure the depths. The scour depth data was collected after 10 h of flow duration. This data is used along with similar data available in the literature for the framing of a formulation for computing depth of scour for non-uniform piers. The experimental duration was restricted to 10 h due to power availability.

Table 1 For caisson piers, $D = 5$ cm; $D_c = 10.8$ cm; $d_{50} = 0.52$ mm; $h = 8$ cm; $q = 0.0154$ m^2/s; $Y_{\min} = 75$ mm at $h_s = 6.7$ mm.

Table 2 For cylindrical pier with an array of pile caps, $D = 5$ cm; $D_p = 10$ cm; $d_{50} = 0.52$ mm; $d = 1$ cm; $n = 4$; $h = 8$ cm; $q = 0.0154$ m^2/s; $Y_{\max} = 100$ mm; $h_s = 26.7$ mm.

2.1 Location of Scour Level for Different Positions of Non-uniform Piers

Experiments to find the location of minimum scour for type-I piers (uniform pier supported on caisson type with the same shape) and location of maximum scour for type-II piers (uniform pier supported on a pile of the same shape of pier and supported by a group of piles) is carried out first. The scour depth level against caisson top level is plotted in Fig. 4 in the present study data.

Table 3 shows the final scour depths at the end of 10 h for oblong caisson piers, $D = 3$ cm; $D_c = 6$ cm; $L = 12$ cm; $L_C = 16$ cm; and $q = 0.0154$ m^2/s. $h = 8$ cm.

Final scour depths at the end of 10 h of flow are indicated in Table 4. This pertains to oblong piers with pile caps propped by a group of piles. Here, $D = 5$ cm; $D_p = 10$ cm; $d = 1$ cm; $n = 8$; and $q = 0.0154$ m^2/s, $h = 8$ cm.

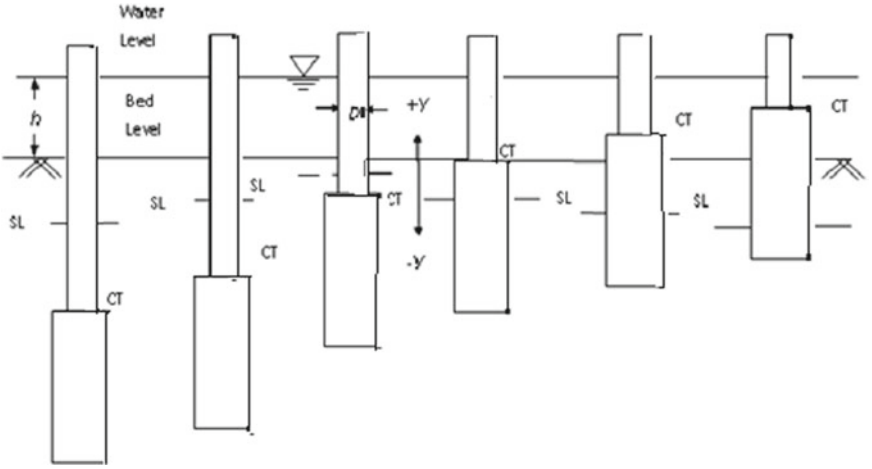

Fig. 4 Scour depth level (SL) variation for different locations of caisson top

Table 3 The scour depth value for different '*y*' positions for type-II piers

Y (mm)	100	80	60	40	20	0	−20	−40	−60	−80	−100
h_s (mm)	26.7	25.3	24.8	20	17.6	14.1	14	7.6	5	3.3	1.9

Table 4 The scour depth value and computed value of equivalent diameter 'D_e' for different positions of '*y*' for type-II piers

Caisson top or pile cap top position (mm)	Scour depth h_s (mm)	Equivalent diameter D_e (mm)
−120	1.4	106.13
−90	3.8	115.48
−60	5	96.77
−30	6.6	87.42
0	10.3	78.06
30	21.2	68.71
60	26.6	59.35
90	18.6	50
120	**11.7**	50

The position of the top of the caisson with reference to bed level along with the position of the scour level reached at the end of 10 h is shown in Fig. 4. Table 1 shows the magnitude Y with scour depth for type-I pier. Figure 4 indicates that the scour depth decreases as caisson top level lowers down from free surface (Fig. 4d, f) and reaches a minimum when the caisson top (CT) is below bed level at $Y = Y_{min}$ (Fig. 4c). Scour depth increases further lowering of caisson top as shown in Fig. 4a, b. This reduction in scour depth is result of reduction in the surface area of

caisson exposed to flow which results in the reduction in the magnitude of downflow. The projected surface width '*b*' between caisson and pier acts as an obstruction to the downflow causes the formation of the vortex in the corner. Formation of vortex in the corner utilizes most of the downflow effect. The reduction in the portion of downflow along the caisson surface due to formation of vortex in the corner of the pier and caisson top may result in the reduction in scour depth caused in front of caisson. As caisson top level further lowers below the $Y_{\min}$ level (Fig. 4a, b), there is a marginal increase in scour depth. This is mainly due to formation of downflow due to pier surface not having the caisson top level. This variation in the magnitude of scour depth was observed for all caisson pier scour data given by Melville and Raudkivi [4]. Similar trend was observed in scour data of Seshagiri Rao et al. [8] and Parola et al. [6] and also in the present study. The above observation revealed that there may be a relation between the $Y_{\min}$ and width of projection '*b*' between the caisson edge and pier surface. Using the depth parameter $(D_c{}^2h)^{1/3}$ suggested by Unger and Hager [3] and also derived by Veerappadevaru et al. [9, 10], the plot of $b/(D_c{}^2h)^{1/3}$ against $Y_{\min}/(D_c{}^2h)^{1/3}$ is made in Fig. 5. The variation of $b/(D_c{}^2h)^{1/3}$ decreases as $Y_{\min}/(D_c{}^2h)^{1/3}$ increases. An expression based on statistical regression analysis indicates:

$$b/(D_c^2h)^{1/3} = 0.387\mathrm{e}^{(-1.667Y_{\min}/(D_c2h)1/3}$$

with $R^2 = 0.86$. The value of $Y_{\min}$ is the vertical distance measured from top to the bed level for the case when the scour depth is minimum.

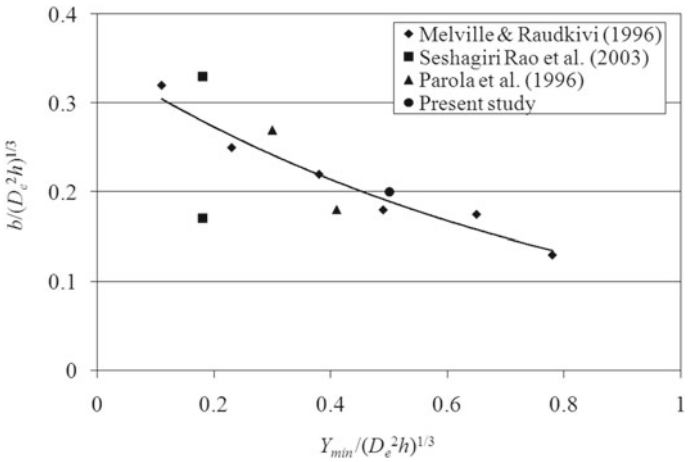

Fig. 5 The relation between $Y_{\min}$ with caisson top projection '*b*'

2.2 Computation of Equivalent Diameter (D_e) for Non-uniform Pier with Caisson Type-I

Melville and Raudkivi [4] proposed the equivalent diameter for caisson type pier as projected area divided by depth equal to $(h + h_s)$. This appears to be not possible because h_s is unknown and to be predicted. In the present analysis h_s is replaced by Y_{min} and equivalent width D_e is computed for different cases of caisson top (CT) location as indicated in Fig. 6.

Case 1: When CT is at bed level: $D_e = (Dh + D_c Y_{min})/(h + Y_{min})$.

Case 2: When CT is above bed level: $D_e = [D(h - z) + D_c(Y_{min} + z)]/(h + Y_{min})$.

Case 3: When CT is below Y_{min} level: $D_e = D(h + Y_{min})/(h + Y_{min})$.

Case 4: When CT is above water level: $D_e = (D_c(h + Y_{min}))/(h + Y_{min})$

Computed values of equivalent diameter for different positions of caisson top are listed in Table 2. This equivalent width D_e is used later to show the validity of scour depth prediction in Fig. 10.

3 Scour Depth Prediction for Non-uniform Piers (Type-II)

In many situations, due to physical conditions of river bed and economical consideration of bridge piers are built over pile caps where piles are supported by a group of piles. Usually pile cap top is located at or below river bed level. Due to aggradations and degradations caused by flood flows, the river bed level may be elevated or lowered down with respect to pile cap level, respectively.

The prediction of scour depth for a pier with pile cap supported by an array of pile is attempted by Melville and Coleman [5], Coleman [2] and Richardson and

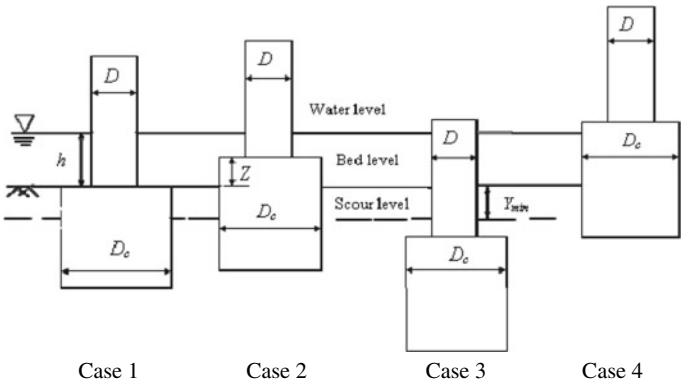

Fig. 6 Different positions of caisson top for computation of equivalent diameter (Case 1–4)

Davis [7]. Richardson and Davis [7] developed a method to predict scour depth in the US-HEC 18 programme. Melville and Coleman [5] observed that HEC-18 uses the superposition of scour depths based on conceptual separation of the pier, pile cap and pile group. They inferred this approach is more complicated and suffers from conceptual practical limitations. Melville and Coleman [5] adopted the approach similar to Richardson and Davis [7]. They suggested the expression as: $h_s = K_{yb}\, K_f\, K_D\, K_s\, K_\theta\, K_t$.

Where h_s is scour depth measured below bed level, K_{yb} parameter representing flow depth-pier size factor, K_f as flow intensity factor, K_D is the foundation alignment factor, K_s is foundation shape factor, K_θ is pier alignment factor and K_t time factor. The result predicted by this equation agrees fairly well with their laboratory results N_{Z1} and N_{Z2} and also US data of Coleman [2].

The way to predict the scour depth for non-uniform pier type-II is based similar to the method adopted in type-I pier. Here, D_p is the pile cap variation of $b/(D_c{}^2 h)^{1/3}$ which increases with increase in $(Y + T)/(D_p{}^2 h)^{1/3}$. The cap level Y measured from bed level below is denoted as (+ve) Y and above as (-ve) Y. The scour depth level is maximum in Fig. 7c for the pile cap level $Y = Y_{max}$ measured from bed surface level. As the position of pile cap lowers as indicated in Fig. 7a, b and when pile cap level rises as shown in Fig. 7d–g, the scour depth will be lower than in Fig. 7c. This variation in scour level is opposite to that of pier with caisson (Type-I). The reason is mainly due to the shape of the lower portion of pile cap. In type-I pier, caisson surface will be uniform till to the foundation level where as in type-II pier, pile cap has certain thickness 'T', below it pile cap is supported by an array of piles. There is a passage available for flow to take place below the pile cap and in between the piles as can be seen in Fig. 7d–g. Flow over these passages possesses less obstruction width of piles, which results in less scour.

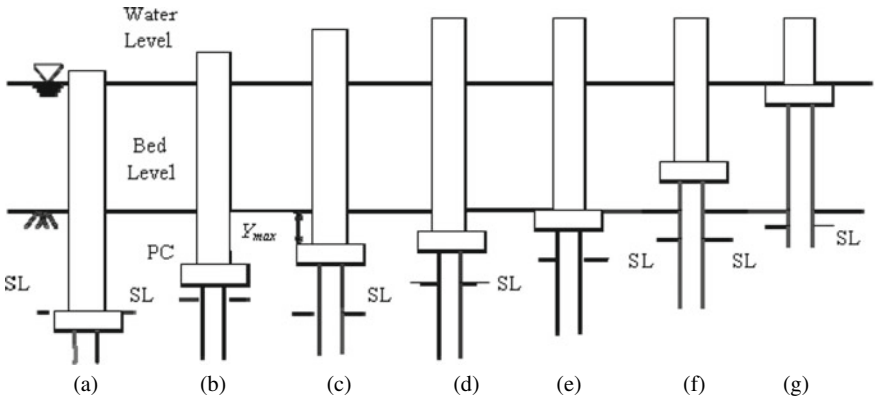

Fig. 7 The scour depth variation for different locations of pile cap with respect to bed level (SL = Scour Level, PC = Pile cap top level)

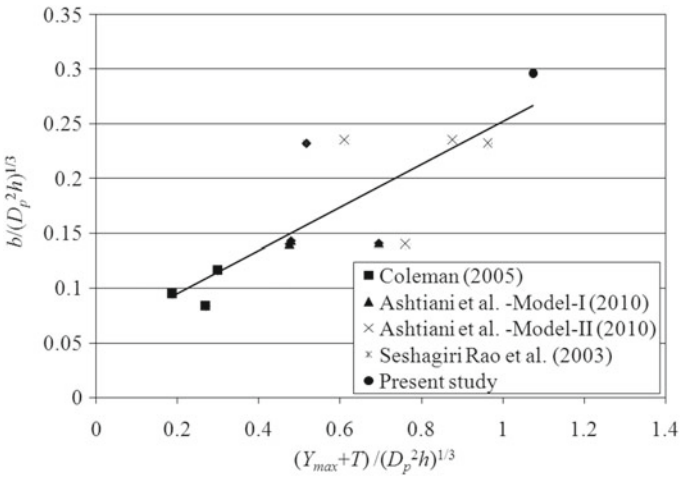

Fig. 8 Shows the relation between the position of pile cap top and pile cap thickness ($Y_{\max} + T$) with projection width 'b'

3.1 *Relation of Y_{max} with Projection Width 'b' and Pile Cap Thickness 'T'*

The magnitude of $Y_{\max}$ is computed from the data of Coleman [2], Seshagiri Rao et al. [8] and the present data of experimental investigation. These values are used in the development of the relation between $Y_{\max}$ with 'b' the projected width between pier and pile cap edge and pile cap thickness 'T'.

Using computed value of $Y_{\max}$ from the experimental data of Coleman [2], Ataie-Ashtiani et al. [1], Seshagiri Rao et al. Seshagiri [8] and the present investigation a relation between $b/(D_c{}^2h)^{1/3}$ and $(Y_{\max} + T)/(D_p{}^2h)^{1/3}$ is plotted in Fig. 8. The statistical relation between them may be written as:

$$b/\left(D_c^2h\right)^{1/3} = 0.2041(Y_{\max} + T)/(D_p^2h)^{1/3} + 0.0446 \tag{8}$$

with correlation coefficient $R^2 = 0.754$. The position of $Y_{\max}$ may be computed for given 'b' and 'T' values using Eq. (8).

3.2 *Computation of Equivalent Width 'D$_e$' for Non-uniform Piers Type-II*

Based on the concept of equivalent diameter defined for caisson pier type-I, the D_e for pier on pile cap propped by an array of piles is computed similarly taking into account

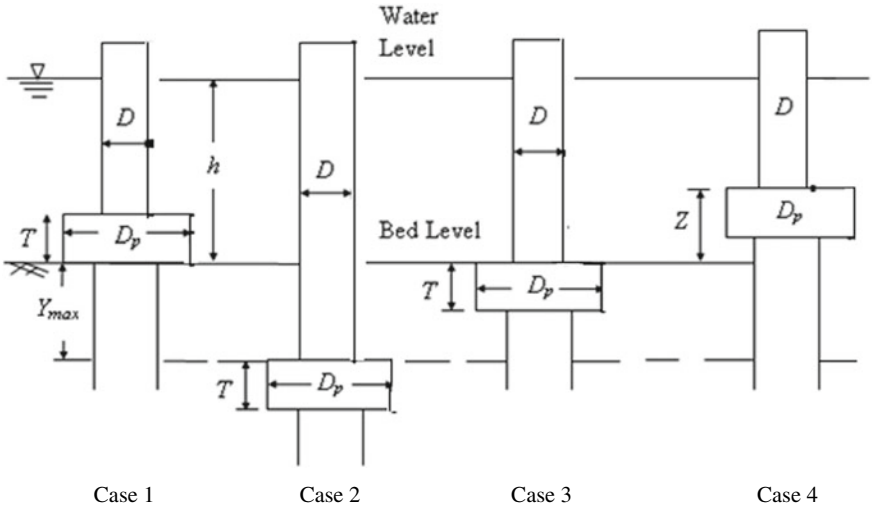

Fig. 9 Different positions of pile cap for computation of equivalent dia (Case 1–4)

the facade area being exposed to the flow. Four number of piles having a diameter of 1.0 cm were used for the experiments. The equivalent diameter is calculated for a few cases as follows:

Referring to Fig. 9, computation of D_e is illustrated below

Case 1: When lower surface of pile cap is at bed level:

$$D_e = \left[\left((h - T)D + T\,D_p + Y_{max}md\right)/(h + Y_{max})\right]$$

Case 2: When upper surface of pile cap is below Y_{max}:

$$D_e = (h + Y_{max})\mathrm{D}/\,(h + Y_{max})$$

Case 3: When upper surface of pile cap top is just below bed level:

$$D_e = \left[\left(hD + T\,D_p\right) + (Y_{max} - T) + (md)\right]/(h + Y_{max})$$

Case 4: When lower surface of pile cap is above bed level:

$$D_e = \left[(h - Z)D + (T)D_p + (Y_{max} + (Z - T))\,(md)\right]/(h + Y_{max})$$

(Case 1–4 as shown in Fig. 9).

Table 4 shows the computed value of equivalent diameters for type-II piers for different positions of Y values.

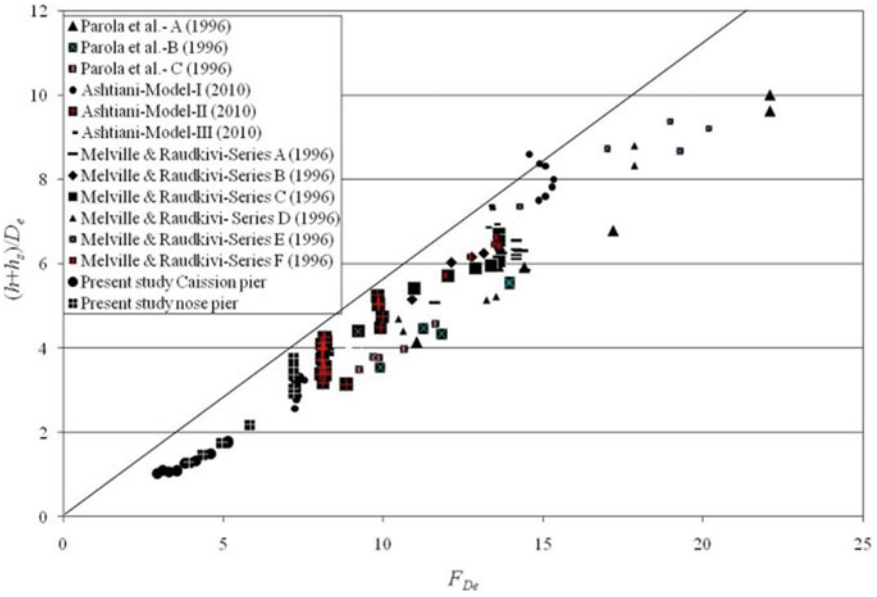

Fig. 10 Relation between $(h + h_s)/D_e$ and F_{De} [(Parola et al. [6]—A to C—Type-I pier), (Ataie-Ashtiani et al. [1]—Model-I to III and Melville and Raudkivi [4]—series A to F—Type-II pier]

Here, 'm' is the number of piles exposed to the incoming flow. In the case of cylindrical pier with pile cap supported by a number of piles exposed to flow $m = 2$ is used. Similarly, in the case of pier that is oblong and having the pile cap. The number of piles exposed to flow, m = 3 is used, as there were three piles that are exposed to incoming flow.

4 Equilibrium Scour Depth for Non-uniform Piers

Melville and Raudkivi [4] used equivalent diameter for Caisson piers based on ratio of projected area concept. Here an attempt is made to predict scour depth using equivalent width based on the location of maximum scour depth for type-II pier with respect to bed level. Equation (5) is used for computation of flow parameter F_{De} and scour depth parameter $((h + h_s)/D_e)$. The data of present work along with the data available in literature are used to compute F_{De} and $((h + h_s)/D_e)$ are plotted in Fig. 10.

4.1 Computation of Scour Depth Around Non-uniform Piers Type-I and Type-II

The power concept proposed by Veerappadevaru et al. Veerappadevaru et al. [9, 10] is modified by replacing caisson width (D_c) in type-I and pile cap width (D_p) in type-II by equivalent width (D_e). The flow parameter F_{De} is defined as:

$$F_{De}^3 = q^3/\left[\left(D_e^2 h\right)((\rho_s - \rho)/\rho)(g d_{50})^{1.5}\left(V_{*c}/\sqrt{(g d_{50})}\right)\right] \tag{9}$$

The magnitudes of F_{De} and $(h + h_s)/D_e$ are computed from data of Melville and Raudkivi [4], Coleman [2], Parola et al. [6] and Seshagiri Rao et al. (1993) and present study data. These data points are plotted in Fig. 10. A fairly linear relationship is observed between the variables. An enveloping line is drawn for data points as shown in Fig. 10 for both pier type-I and pier type-II. The relationship for this enveloping line may be written as:

$$(h + h_s)/D_e = 0.575 F_{De} \tag{10}$$

The proportionality constant is modified to 0.575 from 0.48 and used in Eq. (10). The data of Melville and Raudkivi [4] follows a straight line as indicated in Fig. 10. The present study fall below the enveloping line. This is due to the duration of flow being much shorter than the equilibrium duration and hence equilibrium state of scour depth is not adequately represented. The data of Parola et al. [6] also falls below the enveloping line.

5 Discussion and Conclusions

Non-uniformity in pier width is introduced by building piers on caisson-type foundation and pier mounted on pile caps. This non-uniformity in pier surfaces modifies the scouring processes. The scouring process in front of pier depends on strength of vortex formed at the junction of pier with sediment bed in river flows. The strength of vortex depends on the nature of flow down the frontal face of pier. Also the curving of flow into the scour hole. The projection width provided at the junction of pier with caisson or pile cap results partly in arresting the downflow by forming the vortex at their corner on a hard surface. The change in magnitude of frontal surface area due to non-uniformity in width of pier will result in the modification of the width of the pier active in scouring action.

Further, change in river bed level due to aggradations and degradations result in change in the exposure of non-uniform pier surface to the downflow and curving of flow in to scour hole. These situations occurring in the scouring vortex formation needed to be considered in the prediction of scour depths. The vortex power concept for non-uniform piers developed by Veerappadevaru et al. [9, 10] is modified by

introducing equivalent width 'D_e'. The concept of 'D_e' was proposed by Melville and Raudkivi [4]. The modification in the computation of equivalent width 'D_e' is carried up to specified depth Y_{min} for type-I pier and Y_{max} for type-II piers. The specified depths Y_{min} and Y_{max} are functions of projected width between pier and caisson for type-I pier and pier end pile cap for type-II pier and are observed to exist in similar experimental investigations carried out by other investigators as cited already.

The vortex power concept modified using equivalent width results in a linear relationship between the scour depths measured from free surface to the vortex flow parameter as can be seen in Fig. 10. The closeness of the experimental results of various investigators indicates the validity of the vortex power concept.

References

1. Ataie-Ashtiani B, Baratian-Ghorghi Z, Behesti AA (2010) Experimental investigation of clear-water local scour of compound piers. J Hydraulic Eng ASCE 136(6):343–351
2. Coleman SE (2005) Clear-water local scour at complex piers. J Hydraulic Eng 131(4):330–334
3. Unger J, Hager WH (2007) Down-flow and horseshoe vortex characteristics of sediment embedded bridge piers. Exp Fluids 42(1):1–19
4. Melville BW, Raudkivi AJ (1996) Effects of foundation geometry on bridge pier scour. J Hydraulic Eng 122(4):203–209
5. Melville BW, Coleman SE (2000) Bridge scour. Water Resources Publications, Colo
6. Parola AC, Mahavadi SK, Brown BM, Khoury AE (1996) Effects of rectangular foundation geometry on local pier scour. J Hydraulic Eng 122(1):35–40
7. Richardson EV, Davis SR (2001) Evaluating scour at bridges. In: Hydraulic engineering circular no. 18, (HEC-18), 4th edn. Report No. FHWA NHI 01–001. Federal Highway Administration, Washington, DC
8. Seshagiri Rao R, Gangadharaiah T, Gupta AK, Setia B, Srinivas N, Kapil M (2003) Research report on scour protection around bridge piers and abutments. In: Indian National Committee on hydraulic research. Central Water Commission Ministry of water resources, Govt. of India, New Delhi, pp 1–145
9. Veerappadevaru G, Gangadharaiah T, Jagadeesh TR (2011) Vortex scouring process around bridge pier with a caisson. J Hydraulic Res 49(3):378–383
10. Veerappadevaru G, Gangadharaiah T, Jagadeesh TR (2011) Grip length for bridge piers. J Hydraulic Eng (ISH) 17(2):1–15

Static Behavior of Damaged Composite Conoidal Shells Using Finite Element Method

Suman Pandey and Tanmoy Chakraborty

Abstract An extensive survey of past research work reflects that the static behavior of damaged composite conoidal shells has received very limited attention. Hence in the present work, static characteristics of composite conoidal shells with central delamination has been examined. Point loaded conoidal shells with simply supported and clamped boundary conditions are taken up. A finite element computer code using eight noded isoparametric elements has been developed and results are compared with those available from previous research. Further, more works have been done taking variation in boundary condition, aspect ratio, stacking sequences. Final conclusions have been drawn with help of extracted results and its meticulous investigation.

Keywords Aspect ratio · Clamped · Composite · Conoidal shell · Delamination · Finite element method · Point load · Simply supported

Notations

w'	Non dimensional transverse deflection (wh^3E_{22}/q_0a^4)
q_0	Transverse load
a	Length of shell in plan
b	Width of shell in plan
c	Length of delaminated area in plan
d	Width of delaminated area in plan

S. Pandey (✉) · T. Chakraborty
Techno India University (W.B), Saltlake, Kolkata, India
e-mail: suman.p@technoindiaeducation.com

L. Nandagiri et al. (eds.), *Recent Advances in Civil Engineering*, Lecture Notes in Civil Engineering 256, https://doi.org/10.1007/978-981-19-1862-9_45

1 Introduction

Laminated composites in form of plates and shells have started gaining popularity since the second half of the last century due to presence of various superior characteristics [1]. Among laminated composite shells, conoidal shells have a special position in the various field of engineering. Being doubly curved anticlastic shell forms, these roof structures are very easy to fabricate and looks aesthetically beautiful. Often these shell forms are used for providing large column-free area and for allowing north light, particularly in medical, chemical, and food processing industries where entry of north light is desirable [2].

As these shell forms are industrially important**,** various researchers like [3–5] have studied and provided a significant contribution regarding static behavior of conoidal shells using variational method and finite element method, respectively. With increase in the demand in form of cantilevered roof covering for stadiums, for factories or industries where more ventilation and illumination is required, these roof shells are becoming more and more fashionable. Many times laminated composite shells are subjected to hidden damage which is not visible outside. Hence, it can be very dangerous if left unattained. Delamination is a form of critical type of defect which can be caused due to manufacturing defect, impact load, or air entrapment between layers. Separation of layers may cause loss in stiffness thereby causing overall failure of structures. Hence comprehensive investigation on this type of hidden defect is very essential.

In the past, Acharyya et al. [6] have worked on damaged cylindrical shells using FEM. Nanda [7] studied delaminated composite shell panels using layer-wise theory. Dey and Karmakar [8] investigated delaminated composite conical shells under low velocity impact. In some of the very latest research works delaminated conical shells have been studied by Kamaloo et al. [9]. In this work, nonlinear free vibration characteristics throughout circumferential delaminated shells have been focused. However, this indicates the fact that mostly these research works are associated with cylindrical shells or conical shell forms with damage. Behavioral changes of composite conoidal shells with damage have not been covered up widely. Hence, in this paper, a detailed study on static analysis of laminated composite conoidal shells with delamination has been done under point load.

2 Derivation of Mathematical Equations

To derive important mathematical equations for the current research work, the following parameters for the composite conoidal shells have been considered.

1. Total thickness of shell $= h$. However, it can be comprised of any number of thin laminae keeping the total thickness of shell constant. (Refer Fig. 1)
2. Radius of curvature along Y direction $= R_y$ (see Fig. 5)
3. Radius of cross curvature $= R_{xy}$.

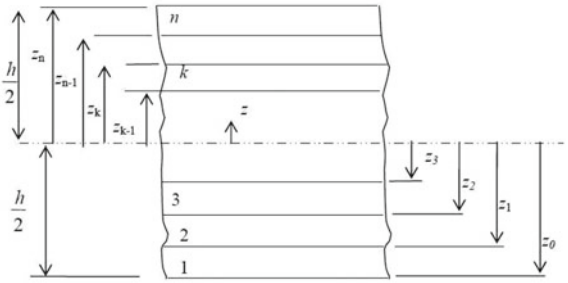

Fig. 1 Typical shell section showing "*n*" number of laminates

4. θ is the orientation angle of each laminate with respect to *x*-axis (Refer Fig. 2).
5. Shell thickness may have '*n*' number of laminates and '*p*' number of multiple delamination. However, in this case, single delamination situated at the center of mid-plane has been considered (see Fig. 3).
6. Figure 4 shows the inner view of a usual delamination crack tip. At this crack tip, element number 1 without damage and element number 2 and 3 with delamination are meeting together to form a common node "O."
7. Figure 5 shows the delaminated zone along with centrally applied point load.

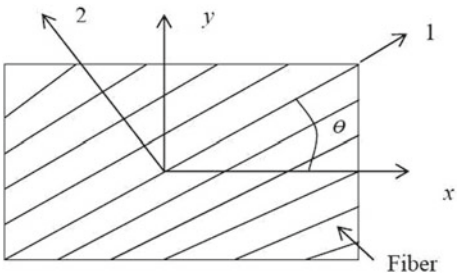

Fig. 2 Orientation of fiber

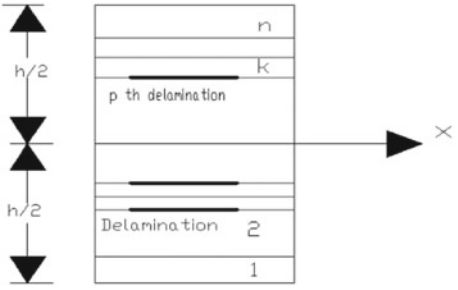

Fig. 3 Shell thickness showing multiple delamination Kumari et al. [10]

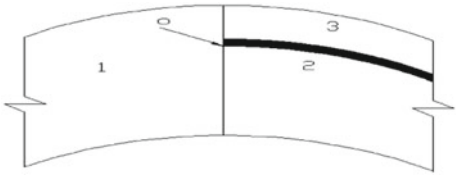

Fig. 4 Common crack tip of delaminated shell Kumari et al. [10]

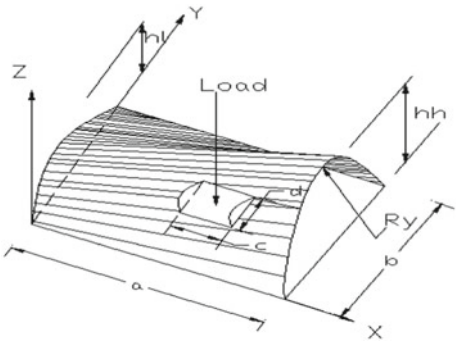

Fig. 5 Conoidal shell with central delamination and centrally applied point load Kumari et. al. [10]

2.1 Undelaminated Segment Formulation

Refering to Fig. 4, undelaminated segment of delaminated shell marked as 1 can be formulated as

$$\{F\} = [D]\{\varepsilon\} \tag{1}$$

Here,
$[D]$ is elasticity matrix of undelaminated shell segment
$\{\varepsilon\}$ is strain displacement matrix.

2.2 Delaminated Segment Formulation

In a thin conical shell with partial damage, in-plane strain and curvature, for the undamaged portion 1 (refer Fig. 4) can be related as:

$$\{\varepsilon\}_1 = \left\{\varepsilon^0\right\}_1 + z\{k\}_1 \tag{2}$$

Point "O" is a crack tip which is located on the boundary line of the delaminated area. Segments 2 and 3 are delaminated portions (refer Fig. 4). For these segments, in-plane strains, curvatures, and transverse shear strains are identical at the crack tip (i.e., point "O" of Fig. 4) as suggested by Gim [11]. Hence, in-plane strain vectors

at the mid surface of delaminated segment can be given as:

$$\left\{\varepsilon^0\right\}_L = \left\{\varepsilon^0\right\}_1 + z_L^0\{k\}_1 \tag{3}$$

In the above equation, suffix "*L*" has been used to indicate delaminated segment and suffix "*1*" has been used to present undelaminated segment.

Again, in Eq. (3)

$\left\{\varepsilon^0\right\}$ is the mid-surface in-plane strain vectors

$\{k\}$ is mid-surface curvature vectors

z_L^0 is the mid surface distance along transverse direction between undelaminated and delaminated segments.

Finally, Eq. (1) becomes,

$$\{F\}_L = [D]_L\left\{\varepsilon^*\right\}_1 \tag{4}$$

where, $\{\varepsilon^*\}$ are the generalized strain vectors.

2.3 Finite Element Formulation

For the development of computer code, an isoparametric shell element with eight nodes and five degrees of freedom per node (i.e., u, v, w, α, β) is used in finite element formulation.

The displacement field of any arbitrary point can be expressed as:

$$\begin{aligned} u(x, y, z) &= u^0(x, y) - z\alpha(x, y) \\ v(x, y, z) &= v^0(x, y) - z\beta(x, y) \\ w(x, y, z) &= w^0(x, y) \end{aligned} \tag{5}$$

where, u^0, v^0, w^0 are the mid-plane translational displacement components along the local coordinate axes x, y, z, respectively, and α, β are the mid-plane rotational displacements components along y and x axes, respectively (Reddy [12]).

At the end, the static equilibrium problem takes the following shape:

$$\left[K_g\right]\left\{\delta_g\right\} = \left\{P_g\right\} \tag{6}$$

Here, $\left[K_g\right]$ = global stiffness matrix
$\left\{\delta_g\right\}$ = global displacement vector, and
$\left\{P_g\right\}$ = global load vector.

Table 1 Comparison of maximum nondimensional downward deflection ($w' \times 10^2$) of composite plate of square shape with point load

Stacking sequence	Reddy [12]	Present study
(0/90)	4.666	4.697
(90/0)	4.666	4.679
$(0/90)_2$	2.210	2.228

3 Validation Problem

3.1 Validation of Model for Point Load Formulation

In order to validate the present approach, the outcome of developed computer code and that of Reddy[12] are compared for square form composite plate with simply supported boundary conditions and reflected in Table 1. In order to solve plate problems, authors have assigned very high value to R_{xy} and R_y.

Results of Table 1 exhibit correctness of present formulation done for point load and its modeling as a computer code using finite element approach.

3.2 Validation of Delamination Formulation

To check the correct implementation of mathematical formulation for delaminated conoidal shells, the result of current computer code are compared with those of Kumari et al. [10]. These values are reflected in Table 2, which proves that the mathematical incorporation of delamination in laminated composite conoidal shells under point load has been done correctly.

4 Results and Discussion

Close agreement of values of maximum critical deflection of composite plates shown in Table 1 and that of damaged composite conoidal shells with clamped edges

Table 2 Comparison of maximum downward deflection ($w' \times 10^2$) of clamped conoidal shell roof subjected to point load for different stacking sequence

Stacking sequence	Delamination ratio (c/a)	Kumari et al. [10]	Present study
$(0°/90°)_2$	0.25	0.399	0.399
	0.50	0.537	0.537
$(45°/-45°)_2$	0.25	0.393	0.393
	0.5	0.459	0.459

(refer Table 2) ensure correctness of bending formulation for delaminated composite conoidal shells subjected to point load in the present computer code.

Apart from validation problems, the current code is further used to analyze static behavior of simply supported and clamped boundary condition shells under effect of centrally applied point load.

Following common points have been considered and followed throughout this study:

1. Thin shells ($a/h = 100$), with square plan form ($a = b$) are considered.
2. Material properties of graphite–epoxy composite conoidal shells considered in present research work is $E_{11} = 25E_{22}$, $\nu_{12} = 0.25$, $G_{12} = G_{13} = 0.25E_{22}$, $G_{23} = 0.2E_{22}$.
3. In all the cases mid surface damage has been considered which varies as $c/a = 0, 0.25, 0.5, 0.75$. Delamination is of rectangular shape, single and central.
4. Four-layered laminations, both cross-ply and angle-ply patterns are studied.
5. Variation in aspect ratio $a/b = 0.5$–2.0 is done for present study purpose.
6. Simply supported and clamped boundary condition have been considered for all the cases of laminated shells taken up here.

4.1 Effect of Aspect Ratio on Deflection Behavior

It is very clear from the results of Tables 3 and 4 that as aspect ratio of conoidal shells increases from 0.5 to 2.0, the value of maximum downward deflection increases too. This is true for both undamaged and damaged shells. It is also important to note that few cases of conoidal shells are exhibiting different behavior than the common trend. For example among $(0°/90°)_S$ shells with $a/b = 1$ and damage ratio $c/a = 0.25, 0.5$ maximum value of downward deflection can be noted. This observation is true for both types of boundary conditions.

4.2 Effect of Damaged Area on Deflection Behavior

When results of Tables 3 and 4 are studied, it is found that critical deflection value increases with increase in damaged area. This fact is correct for almost all the cases of conoidal shells taken up here. There are few exceptions like $(0°/90°)_S$ with $c/a = 0.5$ and aspect ratio $a/b = 2.0$, where critical deflection value has decreased. This observation stands correct for both the boundary conditions. In these cases, as the area of delamination increases, the entire deflected surface also changes, and it acquires a basin-like shape. Due to this change in deflected shape, maximum transverse deflection decreases, whereas the mean deflection of the delaminated area actually increases.

Table 3 Non-dimensional deflection ($w' \times 10^3$) for different aspect ratios and delamination areas of simply supported shells subjected to point load

Stacking sequence	*c*/*a*	Aspect ratio (*a*/*b*)				
		0.5	0.75	1.0	1.5	2.0
$(0°/90°)_2$	0	1.856	2.247	2.566	3.096	3.612
	0.25	3.618	4.626	5.376	6.171	6.654
	0.5	5.225	6.208	7.007	7.937	8.454
	0.75	6.379	7.592	8.483	9.510	10.05
$(0°/90°)_S$	0	1.730	2.015	2.251	2.700	3.146
	0.25	2.095	1.112	13.18	4.373	4.404
	0.5	4.248	4.612	6.249	4.381	3.069
	0.75	3.727	2.428	5.876	4.557	4.533
$(+45°/-45°)_2$	0	1.415	1.626	1.771	2.200	2.975
	0.25	3.184	4.008	4.456	5.084	5.842
	0.5	4.208	4.896	5.437	6.671	7.876
	0.75	4.804	5.628	6.458	8.234	9.541
$(+45°/-45°)_S$	0	1.494	1.689	1.819	2.232	2.993
	0.25	2.865	3.388	3.619	4.036	4.736
	0.5	4.911	4.951	5.174	5.791	6.512
	0.75	1.592	15.56	7.828	8.418	8.601

4.3 Effect of Boundary Condition on Deflection Behavior

On comparing outcome of computer code for simply supported (Table 3) and clamped boundary condition (Table 4), it is observed that clamped shells are better performer in almost all the cases taken as numerical example considered here. However, for few conoids with clamped edge condition like $(0°/90°)_s$ with $c/a = 0.5$ and $a/b = 0.75$, this trend does not holds good. Some more example with this context is lamination $(45°/-45°)_s$ with $c/a = 0.75$ and $a/b = 0.5, 0.75$. For these typical cases detail investigation is required.

4.4 Comparison of Symmetric and Anti-Symmetric Sequences

Anti-symmetric and symmetric stacking sequences are also compared according to different boundary condition groups. It has been observed that symmetric sequences are the best performer among cross-ply shells for both the boundary conditions. Again, among angle-ply conoids anti-symmetric sequences exhibit less deflection as compared to symmetric sequences for undamaged shells, while for damaged

Table 4 Non-dimensional deflection ($w' \times 10^3$) for different aspect ratios and delamination areas of clamped conoidal shells subjected to point load

Stacking sequence	*c*/*a*	Aspect ratio (*a*/*b*)				
		0.5	0.75	1.0	1.5	2.0
$(0°/90°)_2$	0	1.255	1.407	1.440	1.439	1.432
	0.25	2.796	3.571	3.997	4.131	3.933
	0.5	4.032	4.874	5.371	5.672	5.577
	0.75	4.582	5.395	5.836	6.116	6.068
$(0°/90°)_S$	0	1.175	1.189	1.183	1.172	1.163
	0.25	1.337	0.502	11.52	2.585	2.048
	0.5	3.478	3.551	12.74	2.467	0.413
	0.75	1.166	3.624	0.754	4.828	1.657
$(+45°/-45°)_2$	0	1.071	1.322	1.444	1.533	1.550
	0.25	2.632	3.495	3.938	4.149	4.048
	0.5	3.440	4.124	4.597	5.196	5.484
	0.75	3.740	4.415	4.926	5.617	5.969
$(+45°/-45°)_S$	0	1.121	1.374	1.486	1.548	1.541
	0.25	2.291	2.887	3.112	3.120	2.964
	0.5	3.800	4.014	4.281	4.336	4.229
	0.75	9.637	6.024	5.438	5.234	4.955

shells behavior of anti-symmetric and symmetric laminates are mixed on ground of maximum downward deflection.

4.5 Comparison of Cross-Ply and Angle-Ply Shells

From results of Table 3, it is very clear that, angle-ply conoids are better than the cross-ply ones among anti-symmetric sequences. However, for symmetric laminates this observation is just reverse and cross-ply laminates are found to be better than the angle-ply ones.

From comparison of angle-ply and cross-ply shells, it is noticed that under clamped edge category angle-ply shells are mostly better operators. This fact stands correct among antisymmetric sequences but among symmetric sequences the case is just reverse.

5 Conclusions

From the present research work, authors have casted some pinpoint conclusions:

1. Increase in damaged area, measured as *a*/*c* ratio results in increase in maximum downward deflection.
2. Increased value of aspect ratio has also adverse effect on critical deflection of conoidal shells for both the types of boundary conditions. Hence, it is better to use smaller units as conoidal shell roofing sheds.
3. Among simply supported boundary conditions and clamped edge conditions, the latter are better performers under damaged conditions.
4. Among all the laminated composite conoids, taken up in the present study, anti-symmetric cross-ply shells are best for simply supported boundary condition as well as for clamped edge condition.
5. Maximum deflection value is usually less among angle-plies and that too with clamped edges. However, it will be further advisable to check symmetricity of shells while selecting for roofing units.

References

1. Bakshi K, Chakravorty D (2013) Static and dynamic characteristics of composite conoidal shell roofs. In: Advances in acoustics and vibrations, vol 2013. Article ID: 539817. Hindwai Publications
2. Sahoo S (2013) Dynamic characters of stiffened composite conoidal shell roofs with cutouts: design aids and selection guidelines. J Eng 2013(Article ID 230120) (Hindwai Publications)
3. Hadid HA (1964) An analytical and experimental investigation into the bending theory of elastic conoidal shells. Ph.D. thesis, University of Southampton
4. Choi CK (1984) A conoidal shell analysis by modified isoparametric element. Comput Struct 18(5):921–924
5. Dey A, Bandyopadhyay JN, Sinha PK (1992) Finite element analysis of laminated composite conoidal shell structures. Comput Struct 43(3):469–476
6. Achryya AK, Chakravorty D, Karmakar A (2009) Bending characteristics of delaminated composite cylindrical shells—A finite element approach. J Reinf Plast Compos 28(8):965–978
7. Nanda N (2014) Static analysis of delaminated composite shell panels using layerwise theory. Acta Mechanica 225(10):2893–2901
8. Dey S, Karmakar A (2013) Dynamic analysis of delaminated composite conical shells under low velocity impact. J Reinforced Plast Compos 32(6):380–392
9. Kamaloo A, Jabbari M, Tooski MY, Javadi M (2020) Nonlinear free vibrations analysis of delaminated composite conical shells. Int J Struct Stab Dyn 20(1)
10. Kumari S, Chakravorty D (2010) Finite element bending behavior of discretely delaminated composite conoidal shell roofs under concentrated load. Int J Eng Sci Technol 2(4):54–70
11. Gim CK (1994) Plate finite element modeling of laminated plates. Comput Struct 2(1):157–168
12. Reddy JN (1997) Mechanics of laminated composite plates-theory and analysis. CRC Press

A Comparative Study on the Single Degree of Freedom System

Thushar S. Shetty, Manikandan, and Pradeep Karanth

Abstract This research looks into an investigation on the innovative optimum design of single degree of freedom system with and without viscous fluid damper. This kind of damper dissipates the mechanical energy of the building into heat energy. The majority of structures are susceptible to varying loads throughout time, resulting in vibration. This vibration in structural system may result from a wide variety of sources such as wind and seismic waves. The effect of vibration on a Single Degree of Freedom System (SDOF) is investigated in this study using simulation software in accordance with codal provisions.

Keywords Single degree of freedom system · Response spectrum analysis · Viscous fluid damper · Damping ratio · Vibration control · Sensor

1 Introduction

1.1 General

Earthquake is considered to be one of the most devastating natural phenomena on the planet. Seismic waves are produced as a result of unexpected release of energy in the crust of the earth. When seismic waves reach the structure's foundation level, it experiences horizontal and vertical movement at ground level [1]. There are various design philosophies in earthquake engineering now in use, all of which use experimental data, computer simulations, information, and observations gained from the earlier earthquakes to provide the requisite performance for the seismic threat at the location of interest. These include everything from properly sizing the structure to ensure it is durable and ductile enough to withstand the earthquake with minimal damage, to installing base isolation or employing structural vibration control technologies

T. S. Shetty (✉) · Manikandan · P. Karanth
Department of Civil Engineering, NMAM Institute of Technology, Nitte, Udupi, India
e-mail: shettythushar@nitte.edu.in

P. Karanth
e-mail: pradeepkaranth@nitte.edu.in

L. Nandagiri et al. (eds.), *Recent Advances in Civil Engineering*, Lecture Notes in Civil Engineering 256, https://doi.org/10.1007/978-981-19-1862-9_46

to reduce any stresses and deformations. While most earthquake-resistant structures employ the former method, significant facilities, landmarks, and cultural heritage structures use the more sophisticated (and expensive) isolation or control techniques to survive severe earthquakes with minimal damage [2].

Accelerograms, which provide detailed information on ground acceleration during earthquakes, became more widely available in the 1960s. The development of advanced computer-based analytical tools and the introduction of strength design philosophies permitted a much closer analysis of the seismic response of multi-degree of freedom structures [3]. It soon became evident that seismic design to existing lateral forces indicated in the codes was often inadequate to assure that the structural strength specified was not exceeded by the requirements of strong earthquake motion. On the other hand, observations of structural responses in severe earthquakes demonstrated that this lack of strength did not always result in failure, or even in severe damage. The structures could survive the earthquake if the structural strength could be maintained without significant degradation when inelastic deformations developed, and they could often be repaired economically. However, severe damage or collapse was common when inelastic deformation resulted in a large decrease in strength, as often occurs in conjunction with shear failure of concrete or masonry elements. With a growing understanding that excessive strength is really not necessary or even desired, the focus in design has made the switch from resisting significant earthquake forces to the evasion of these forces. Inelastic structural response has evolved from the darkness of speculations, to become a vital factor in the evaluation of seismic design of structures. It is now well accepted that not all inelastic modes of deformation are equally viable. As previously said, some cause failure while others provide ductility, which is an essential trait for preserving structural strength when the system is subjected to reversals of inelastic deformations during seismic response.

Passive fluid viscous damping systems are generally well suited to vibration control of civil structures subjected to seismic excitation [4]. In particular, fluid viscous dampers that work on the concept of fluid orificing exhibit extraordinarily high levels of energy dissipation density. Using steady-state cycle data, the dynamic behavior of a fluid orificing damper is investigated. The cyclic test data is used to generate mathematical models of the damper, which are then applied to provide analytical evaluations of the seismic response of a scale-model building structure subjected to earthquake ground acceleration. A generalized mathematical model for understanding both linear and nonlinear fluid viscous damper behavior is considered as part of the discussion on fluid orificing dampers. The energy dissipation characteristics of generalized fluid viscous dampers are then examined with reference to the performance of an idealized single-story structure.

Pythagoras initiated the vibration theory in the fifth century BC. He quantified the theory of acoustics by developing a systematic way of measuring sound frequencies. With his hammer experiments, he proved that natural frequencies are system properties that are independent of the magnitude of excitation. In the seventh century, Galileo also experimented with pendulums. He observed that the relationship between sound and vibration of mechanical systems had long been understood, but Galileo was the first to prove that pitch is influenced by the frequency of vibration.

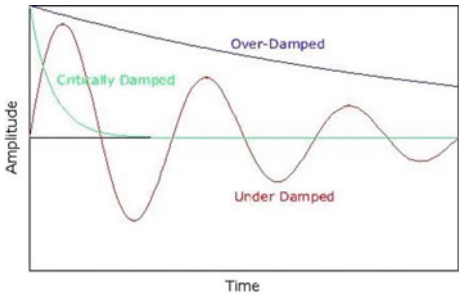

Fig. 1 Classification of damping based on damping ratio

Vibrations have advanced so rapidly in the previous few decades that the introduction of the computer resulted in a revolution in this, as well as many other fields. Vibration of any structure may cause a change in the position and orientation of the structure with respect to its initial position [5]. As a result, the simplest approach to describe a vibratory system is as a degree of freedom (DOF). The number of degrees of freedom refers to the number of independent coordinates required to specify the arrangement or position of a system at any time. It also denotes the least number of independent coordinate systems required to denote the location of the mass at any point in time. A single degree of freedom system (SDOF) is one that needs just one coordinate to describe its position at any given time. System with more than one degree of freedom is termed as multi-degree of freedom system (MDOF).

The damping parameters of structures are another essential consideration in seismic-resistant design. Damping is a phenomenon that causes any vibrating structure's amplitude of motion to gradually decrease due to energy dissipation through numerous mechanisms [6]. The damping is classified based on Vibration (ξ), if $\xi = 1$, Critically, damping condition, if $\xi < 1$, underdamping condition, if $\xi > 1$, overdamping condition. Generally, the buildings are designed under damping conditions, where the system oscillates at reduced frequency with amplitude gradually decreasing to zero (Fig. 1).

2 Importance

To study the behavior of structure by the installation of damper and to know the responses of single degree of freedom structure.

3 Literature Review

3.1 General

The following researches were studies prior to setting objectives for the present study.

Dicleli et al. [7], conducted a comparative study on the seismic behavior of chevron braced frames (CBF) with and without viscous fluid dampers (VFD) as a function of ground motion and damper properties. The VFD dissipates the structural base shear as well as deflection. The VFD reduces the story drift by 30–70% as well as story shear force of 40–70%. Also, it prevents the compression failure due to the axial loads. The deformation of the frame will decrease as the damping ratio increases. The practical implication of using VFD shows that the maximum deformation of four-story CBF without VFD produces 30% damping and with VFD 50% damping so there will be the dissipation of energy occurs.

Garrido et al. [8], worked on improving a tuned mass damper using rotational inertia through a tuned viscous mass damper. The study involved the rotational inertia double-tuned mass damper (RIDTMD) for an SDOF. system. The RIDTMD is a combination of rotational inertia viscous damper (RIVD) and tuned viscous mass damper (TVMD) both which will dissipate the displacement of motion into rotational motion. So, on applying the De-Alembert's principle, the damping parameters are to determined such as natural frequency and mode shape. In order to determine the response of RIDTMD three main parameters are to be considered such as tuned mass damper, structural displacement, and mass. To represent the structural response in frequency, domain dynamic magnification factor (DMF) is used. The DMF provided with frequency ratio ranging from 0.5 to 1.5 for RIDTMD and TMD has been compared. It can be noticed that the structure provided with RIDTMD has lower DMF than the structure with TMD due to a flatter in frequency response curve.

Mevada et al. [9], has made a study on the experimental determination of structural damping for various materials. It deals with the experimental method to investigate the behavior of structural components due to harmonic vibration. Dynamic analysis was used to find the natural frequency of the beam and its damping ratio. In dynamic analysis, vibration is more significant than the deflection control in designing buildings. It effectively necessitates two sets of calculations, such as the natural frequency of the beam and the peak acceleration caused due to dynamic loading, which is approximated by determining the effective mass of the system and then computing the peak acceleration. By the experimental set-up, beams are fixed at one end and due to the external force, the beam will oscillate and it is sensed by the accelerometer. In this case, beam is made up of aluminium, brass, steel, and the obtained result is validated with lab view software.

Chaitra et al. [10] have carried out a study on the performance of regular and vertically irregular structures with damper, shear wall, and infill wall. The model is studied using equivalent static analysis and time history analysis after the damper, shear wall, and infill wall are installed. It can be seen from this research that the storey displacement of the model with an infill wall is lower than the model with

shear wall and damper. The stiffness of infill structure was also found to be higher than that of the structure with shear wall and damper.

Javidialesaadi et al. [11] have worked on the transfer of energy and passive control of single degree of freedom structure using one-directional inertia viscous damper. In this work, it was proposed to control the structural vibration by means of one-directional rotational inertia viscous damper (ODRIVD). The traditional method of controlling the structural motion into the rotational vibration is known as rotational inertia viscous damper (RIVD). RIVD is one of the inerter-based device having large inertial mass for the passive control device. Due to the inertial mass, there may be a possibility of reduction in the natural frequency of system as well as the position and orientation of structure may differ. Therefore, a new technique of RIVD was developed, known as the ODRIVD. In this case, the maximum dissipation of energy takes place and the amplitude of vibration reduces.

Wang et al. [12], conducted a study on inerter-based tuned liquid column damper for seismic vibration control of a single degree of freedom system (SDOF). This work deals with the optimal installation of a tuned liquid column damper inerter (TLCDI) for the SDOF structure to control the base excitation of the structure by reducing the response of structure. Also, the effectiveness of TLCDI has been investigated with respect to the varying frequency ratio. The behavior of the TLCDI is carried out for 44 actual induced earthquakes and which reduces 77–81% of displacement of the structure.

4 Objectives

The key objectives of this work are:

1. To measure the damping factor for designed damper.
2. To compare the response SDOF system with damper and validate same using finite element software.

5 Methodology

5.1 Design of SDOF Model

The model used in this study is constructed using standard metals. The geometry of the model is being selected based on the literature review. The selected model is designed as a single degree of freedom (SDOF) system by considering the entire mass of the structure lumped into a single point that is at slab level and the slab is considered to be 100% rigid. The columns and beams are rigidly connected to the system with stiffness value of 4EI/L. The material and its specifications used for modelling SDOF system are, base plate is made up of wood having dimensions

(30 × 15) cm and thickness is about 1.25 cm, column is made up of aluminum and dimensions (2.5 × 15) cm and height 40 cm, slab is also made up of aluminum and dimensions (30 × 15) cm and thickness is about 1.25 cm. The aluminum used in this study has a Young's Modulus of 69 GPa.

5.2 Frame Structure Detail

The earthquake response of the structures that are asymmetric in plan is characterized by coupling between translation and torsional degrees of freedom. The imbalance might be caused by an asymmetrical distribution of mass, damping, stiffness, and strength characteristic. When exposed to horizontal support motions, such structures exhibit not only bending oscillations, but also torsional vibrations. The structure under this investigation is a single-story building frame model made out of a comparatively rigid rectangular aluminium frame with four aluminium columns supporting it at the corners. Apart from the stiffness distribution, the mass and damping properties of aluminium columns would also contribute to the structure's planar asymmetry. Since the slab is significantly stiffer than the columns, it is logical to predict that the slab would move in its own plane under the action of dynamic base motions. For the purpose of an experimental arrangement, the frame is positioned on the table which is powered by an electric motor.

5.3 Design of Dampers

Viscous fluid dampers are installed to the system which dissipates the mechanical energy into heat energy. These dampers are placed diagonally in between the columns in the direction opposite to the vibration.

5.4 Measurement of Vibration

For that system, the excitation force will be applied by using DC motor. This excitation force will be measured by using "Tilt sensor." A tilt sensor monitors the tilting position in relation to gravity and allows for easy orientation and vibration detection. The amplitude will be measured for the applied excitation force to the SDOF structure in presence and absence of damper. The damping ratio of an underdamped system in the time domain is determined by logarithmic decrement, which is used to compute the successive amplitudes. The measured amplitude of SDOF structure will be validated using any one of the finite element software such as ETABS, SAP. Finally, the result will be interpreted.

5.5 Shake Table

The shake table is an essential instrument used for evaluating the behavior of structural components, the entire system simulates a similar effect as induced in real earthquakes. It is used to investigate the dynamic impacts on the performance of specimens. The horizontal shake table is used for horizontal vibration, allowing it to induce harmonic motions of various amplitudes. The frequency of the base motion can be altered by varying the speed of the motor.

5.6 Tilt Sensor

A tilt sensor is a device that measures the tilt of a reference plane along multiple axes. These are used in a variety of applications to measure the tilting position in relation to gravity. In addition, it also provides easy detection of inclination and orientation. Depending on the environment, this sensor will respond to various parameters such as light, heat, motion, pressure, temperature, and moisture. Using sensors, currents, and voltages can be controlled. In every sensor, there exists three terminals namely; Voltage Common Collector (VCC), Ground (GND) and Output. The activation of the sensor is done by VCC, while GND is being used to establish a stable negative reference, and the sensor's output is received in analogue form.

5.7 Working Principle of Tilt Sensor

These tilt sensors are made up of a rotating ball with a conductor plate underneath it. As soon as the power is received by the sensor, the rotating ball falls to the sensor's bottom, forming an electrical connection. Whenever the sensor is tilted, the rotating ball does not fall to the bottom, preventing the current from flowing between the terminals of the sensor.

6 Modeling and Analysis

6.1 SDOF System Without Dampers

1. The analysis of SDOF system is based on the following assumptions:
2. The entire mass is concentrated at the slab level.
3. Beams and slabs are 100% rigid. Flexibility and stiffness are taken by column.
4. Joints between the column and beam and beam and slab are rigid.

Table 1 Selection of geometry and material property

SDOF system element	Material	Dimension (mm)
Base plate	Steel	300 × 150 × 10
Column	Steel	300 × 25 × 3
Slab	Steel	300 × 25 × 3

Table 2 Modal period and frequency

Case	Mode	Period (s)	Frequency (rad/s)	CircFreq. (rad/s)	Eigen value (rad^2/s^2)
Modal	1	0.146	6.862	43.1132	1858.7471

Table 3 Modal period and frequency

Case	Mode	Period (s)	Frequency (rad/s)	CircFreq. (rad/s)	Eigen value (rad^2/s^2)
Modal	1	0.898	1.113	6.9949	48.9287

The selection of the geometry and the material properties of the SDOF system is carried out by the reference of Indian Institute of Science Bangalore (IISC). The SDOF. system mainly consists of base plate, column, and slab portion. Also, the modeling of SDOF system is accomplished by using ETABS software (Tables 1 and 2).

6.2 SDOF System with Damper

An SDOF system with viscous fluid damper is used, which works under the principle of dissipation of energy. By the use of dampers, the amplitude of vibration is minimized and deformation of the structure is nullified (Table 3).

6.3 Story Displacement and Drift

From the Figs. 2, 3, 5, and 6, it is noted that the story displacement and drift are maximum with the absence of viscous fluid damper (VFD). When external forces where applied, the models with VFD assisted in lowering the amplitude of vibration to a maximum extent, minimizing the deformation of SDOF system (Fig. 7).

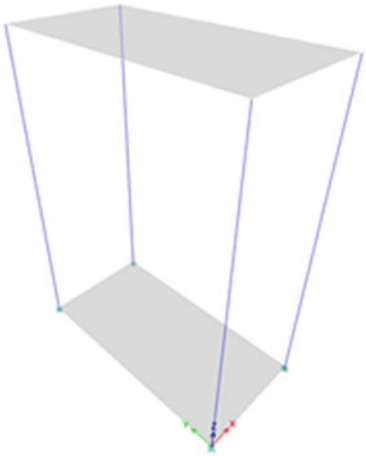

Fig. 2 SDOF system without damper

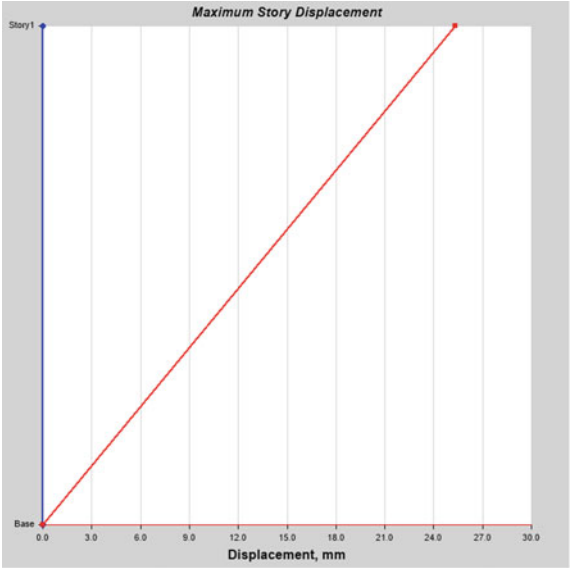

Fig. 3 Story response versus story displacement

6.4 Analysis

The analysis of SDOF system is determined with the help of Response Spectrum Analysis (RSA). It is the representation of maximum of damped SDOF system of different natural periods but having the same damping under the application of earthquake ground motion at their base (Tables 4, 5, 6, 7, 8, and 9).

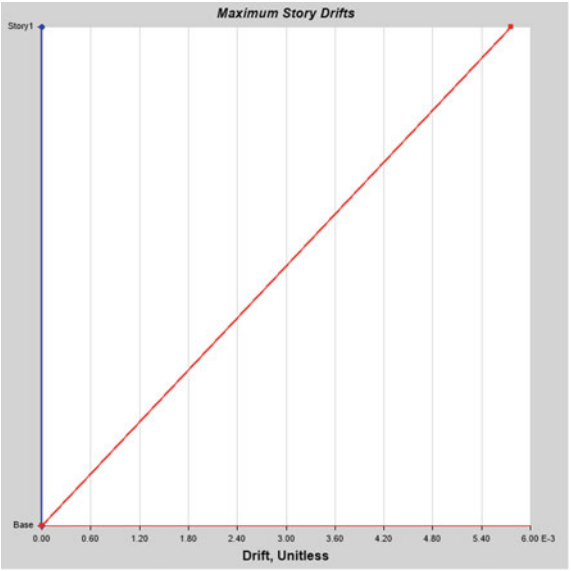

Fig. 4 Story response versus story drift

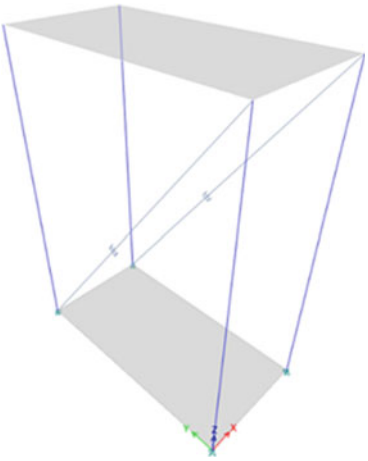

Fig. 5 SDOF system with damper

7 Conclusions

This study explains the behavior of SDOF system under the performance of dynamic load with and without viscous fluid damper based on that following conclusion can be made.

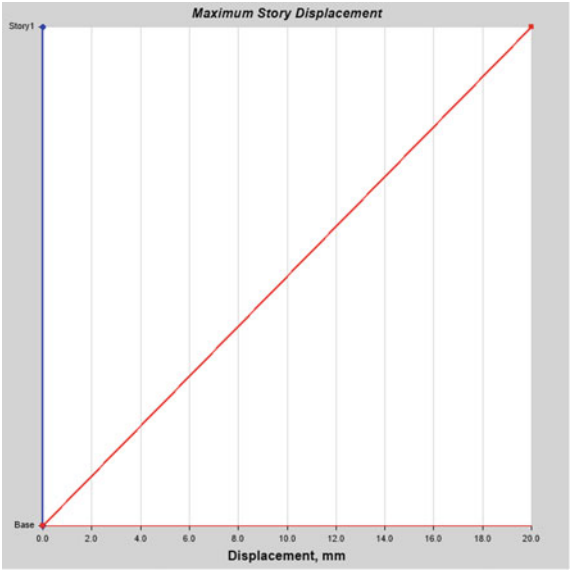

Fig. 6 Story response versus story displacement under damping condition

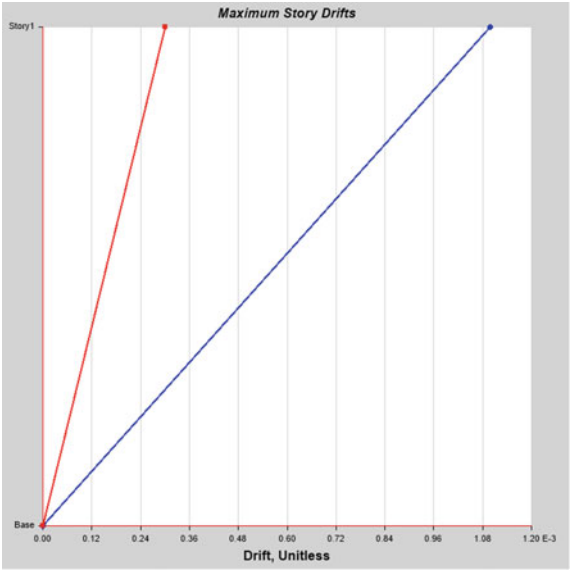

Fig. 7 Story response versus story drift under damping condition

1. The analysis shows that the time period of structure increases when VFD are mounted because this frequency of the structure decreases and the dynamic effect on building also reduces.
2. The amplitude of vibration is obtained from the mode shape of an SDOF system.

Table 4 Loading cases

Name of the load	Category
Dead	Linear static analysis
Live	Linear static analysis
Modal	Modal—Eigen
RP-X	Response spectrum analysis
RP-Y	Response spectrum analysis

Table 5 Response Spectrum—IS 1893-2016

Name	T (s)	Value	Seismic zone	I	Soil type	R	Damping ratio
IS 1893-2016H	0	0.036	V	1	II	5	0.1
IS 1893-2016H	0.1	0.09					
IS 1893-2016H	0.55	0.09					
IS 1893-2016H	0.8	0.061					
IS 1893-2016H	1	0.048					
IS 1893-2016H	1.2	0.040					
IS 1893-2016H	1.4	0.034					
IS 1893-2016H	1.6	0.030					
IS 1893-2016H	1.8	0.027					
IS 1893-2016H	2	0.024					
IS 1893-2016H	2.5	0.019					
IS 1893-2016H	3	0.016					
IS 1893-2016H	3.5	0.013					
IS 1893-2016H	4	0.012					
IS 1893-2016H	4.5	0.012					
IS 1893-2016H	5	0.012					
IS 1893-2016H	5.5	0.012					
IS 1893-2016H	6	0.012					
IS 1893-2016H	6.5	0.012					
IS 1893-2016H	7	0.012					
IS 1893-2016H	7.5	0.012					
IS 1893-2016H	8	0.012					
IS 1893-2016H	8.5	0.012					
IS 1893-2016H	9	0.012					
IS 1893-2016H	9.5	0.012					

Table 6 Modal participating mass ratios with damper

Case	Mode	Period (s)	U_x	U_y	U_z	ΣU_x	ΣU_y	ΣU_z	R_x	R_y	R_z	ΣR_x
Modal	1	0.898	0	0.516	0	0	0.516	0	0.516	0	0.1032	0.516

Table 7 Modal participating mass ratios without damper

Case	Mode	Period (s)	U_x'	U_y'	U_z'	$\Sigma\ U_x'$	$\Sigma\ U_y'$	$\Sigma\ U_z'$	R_x	R_y	R_z	$\Sigma\ R_x$
Modal	1	0.146	0	1	0	0	1	0	0.6257	0	0	0.6257

Table 8 Modal load participation ratios with damper

Case	Type	Element	Static percentage	Dynamic percentage
Modal	Acceleration	U_x'	0	0
Modal	Acceleration	U_y'	51.6	51.6
Modal	Acceleration	U_z'	0	0

Table 9 Modal load participation ratios without damper

Case	Type	Element	Static percentage	Dynamic percentage
Modal	Acceleration	U_x'	0	0
Modal	Acceleration	U_y'	100	100
Modal	Acceleration	U_z'	0	0

References

1. Thorne L, Terry CW (1990) Modern Global Seismology. Academic Press, USA
2. Andre F (2013) Elements of earthquake engineering and structural dynamics, 3rd edn. Presses Internationales Polytechnique, Canada (2013)
3. Roberto V (2009) Fundamental concepts of earthquake engineering. CPC Press, First Edition, Boca Raton
4. Reza SK, Payam T (2021) Effects of using different arrangements and types of viscous dampers on seismic performance of intermediate steel moment frames in comparison with different passive dampers. Structures 33:3382–3396
5. Madhujit M (2021) Structural dynamics vibrations and systems. Springer
6. Curadelli RO, Riera JD, Ambrosini D, Amani MG (2008) Damage detection by means of structural damping identification. Eng Struct 30(12):3497–3504
7. Dicleli M, Mehta A (2007) Seismic performance of chevron braced steel frames with and without viscous fluid dampers as a function of ground motion and damper characteristics. 63(8):1102–1115. https://doi.org/10.1016/j.jcsr.2006.09.005
8. Garrido H, Curadelli O, Ambrosini D (2013) Improvement of tuned mass damper by using rotational inertia through tuned viscous mass damper 56:2149–2153. https://doi.org/10.1016/j.engstruct.2013.08.044
9. Mevada H, Patel D (2016) Experimental determination of structural damping of different materials. Procedia Eng 144:110–115. https://doi.org/10.1016/j.proeng.2016.05.013
10. Chaitra HN, Swamy BS (2016) Study on performance of regular and vertically irregular structure with dampers, shear wall and infill wall. Int Res J Eng Technol (IRJET) 592–596
11. Javidialesaadi A, Wierschem NE (2019) Energy transfer and passive control of single-degree-of-freedom structures using a one-directional rotational inertia viscous damper. Eng Struct 196:109339. https://doi.org/10.1016/j.engstruct.2019.109339

12. Wang Q, Deep N, Qiao H, Wang Q (2020) Inerter-based tuned liquid column damper for seismic vibration control of a single-degree-of-freedom structure. Int J Mech Sci 184:105840. https://doi.org/10.1016/j.ijmecsci.2020.105840
13. Narkhede DI, Sinha R (2014) Behavior of nonlinear fluid viscous dampers for control of shock vibrations. J Sound Vib 333(1):80–98. https://doi.org/10.1016/j.jsv.2013.08.041
14. Patwa R, Maru S (2018) Comparative Study of Seismic Analysis of Dampers in Asymmetrical R. C. Frame Building. International Journal for Research in Applied Science & Engineering Technology (IJRASET) 6(8):648–656
15. Tagawa H, Yamanishi T, Takaki A, Chan RWK (2016) Cyclic behavior of seesaw energy dissipation system with steel slit dampers. J Constr Steel Res 117:24–34. https://doi.org/10.1016/j.jcsr.2015.09.014
16. Tsuji M, Nagano Y, Ohsaki M, Uetani K. Optimum design method for high-rise building frame with viscous dampers. 1–8
17. Caldero C (2016) Experimental evaluation of viscous damping coefficient in the fractional underdamped oscillator. Adv Mech Eng 8(4):1–12. https://doi.org/10.1177/1687814016643068

Global Buckling of CFS Complex Angle Columns

K. S. Vivek and R. Baskar

Abstract The global buckling behaviour of cold-formed steel complex angle sections subjected to axial compression is investigated. The length of the columns is considered to be 1 m upon preliminary analysis using CUFSM such that global buckling governs. Linear and non-linear finite element buckling analyses are carried out using commercial finite element software ABAQUS. Fixed boundary condition is assumed throughout the study. The column strengths and post-buckling capacities of the considered sections are presented. Influence of stiffener type on axial load capacity of the angle sections is discussed. The obtained numerical column strengths are compared with the Direct Strength Method (DSM) design strength equations of global buckling mode available in AISI-S100 and literature. On comparison, it is observed that the design equations in the available literature either underestimate or overpredict the capacity of complex-shaped angle members subjected to global buckling under axial compression.

Keywords Axial compression · Complex angles · Direct strength method · Global buckling · Light gauge steel framing · Post-buckling

1 Introduction

Cold-formed steel (CFS) construction is becoming popular in recent years due to advantages such as light-weight, versatility of shape, ease of manufacturing and transport [1]. Since the CFS sections are manufactured by rolling or press-braking *thin* sheets into required shapes, they are subjected to complex instability such as local, distortional and global (flexural/flexural–torsional) buckling or interaction of

K. S. Vivek (✉)
Department of Civil Engineering, VVIT, Nambur, Andhra Pradesh 522508, India
e-mail: saivivek@vvit.net

R. Baskar
Department of Civil and Structural Engineering, Annamalai University, Chidambaram 608002, India

L. Nandagiri et al. (eds.), *Recent Advances in Civil Engineering*, Lecture Notes in Civil Engineering 256, https://doi.org/10.1007/978-981-19-1862-9_47

these when subjected to compression [2]. CFS angle sections are most commonly used in light gauge steel-framed (LGSF) buildings and trusses.

Significant research was conducted on plain and lipped angle sections subjected to compression for both simply supported and fixed boundary conditions [3–9]. The effect of post-buckling reserve strength, warping restrains and end boundary conditions in global buckling mode was studied by Shifferaw and Schafer [10]. It was reported that columns with fixed ends exhibit significant post-buckling strength which was not considered in the Direct Strength Method (DSM) provisions of AISI-S100 [11]. New procedure of design was proposed to account for the post-buckling capacity and warping restrain effect for plain and lipped angles with fixed ends. Two different methods were suggested, i.e. using 'local DSM' curve or 'Distortional DSM'. Extensive numerical analysis was carried out by Silvestre et al. [12] and design procedures for fixed–fixed and pinned–pinned columns were presented. Ananthi et al. [13] studied the behaviour of single angles and star angles with ball end support and bolted end connections. It was reported that the predicted loads were reduced by 2% and 18% for bolted end single and star angles, respectively.

Narayanan and Mahendran [14] carried out experimental and numerical investigation on behaviour of innovative and complex sections. It was reported that residual stresses had a negligible effect on the ultimate strength. The distortional behaviour of web stiffened intermediate length channel sections with various edge stiffeners was analysed by Manikandan et al. [15]. Based on the obtained results, modification to existing DSM provisions of AISI was proposed. Aruna et al. [16] carried out experimental study on built-up square sections. Stiffened angle sections were used to form the built-up box sections. Mahar et al. [17] performed finite element analysis of lipped angle and lipped channel sections subjected to axial compression in order to evaluate the design recommendations of European and Indian codes of practice (EN: 1993-1-3, AISI: S100-07 and IS 801: 1975 respectively). It was reported that compression members subjected to flexural–torsional buckling possessed post-buckling strength. DSM provisions were found to be slightly unconservative. Studies on sigma sections and complex channel sections were also carried out, respectively [18, 19].

From the available literature, the global buckling of stiffened/complex angle sections under axial compression is not available to the best knowledge of the authors and hence is investigated in the present study by adopting non-linear finite element (numerical) analysis with the help of ABAQUS software. The scope of the study is limited to analysis of fixed-end members only. Also, nominal column strengths based on DSM [10, 20] alone are presented as the Effective Width Method (EWM) adopted in IS 801:1975 and EN:1993-1-3 is difficult to be applied for intermediate stiffened sections.

2 Validation Study

Lipped angle sections with fixed ends subjected to axial compression previously analyzed by Shifferaw and Schafer [10] were reanalyzed using finite element software

Table 1 Validation study

Specimen	$P/P_{cr,e}$		
	Previous study+[10]	Present study	Difference (%)
L1.5L1500	2.06	2.083	1.12
L1.5L2000	2.90	2.94	1.38
L1.5L2500	3.48	3.58	2.87

+Approximate

ABAQUS. However, S4R element is adopted in the present study instead of S9R5 element. Initially, a linear buckling analysis was carried out to find the elastic critical buckling loads ($P_{cr,e}$).

Then, non-linear finite element analysis including imperfections was carried out to obtain the ultimate loads (P). The obtained values of $P/P_{cr,e}$ are presented in Table 1 along with those of the previous study. The $P/P_{cr,e}$ versus axial displacement plot was depicted in Fig. 1 which is similar to Fig. 8 of the previous study [10]. Good agreement is observed between the results of previous and present studies. Negligible average difference of 1.79% was observed. This negligible difference is due to the different types of elements adopted [21].

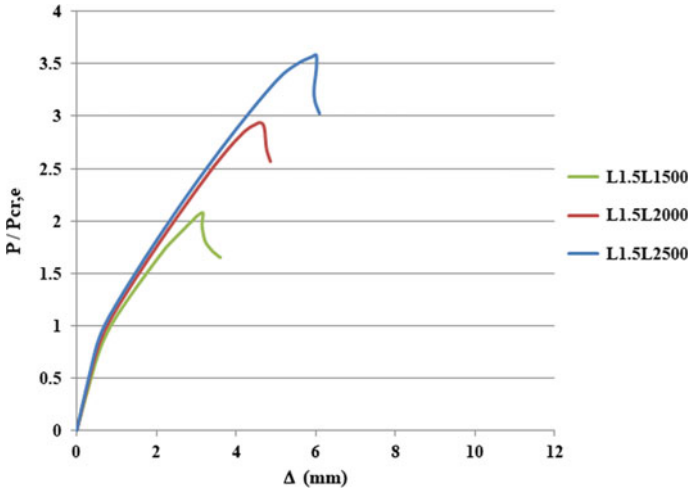

Fig. 1 $P/P_{cr,e}$ versus axial displacement (Δ)

3 Analysis of Complex Angle Columns

3.1 Section Definition and Preliminary Analysis

The complex angle sections depicted in Fig. 2 are considered for analysis in the present study. The thickness (t) of all the sections is assumed as 2.0 mm. The dimensions of the cross-section assumed to satisfy the limits specified in Table B4.1–1 of AISI-S100-16 [22]. The stability of the considered sections is analyzed by observing the obtained 'signature curve' using CUFSM software [20] which is based on the finite strip method. The obtained 'signature curve' for Section 1 is represented in Fig. 3. It is observed that at a length of 1000 mm, the section is subjected to global buckling predominantly (i.e. 99.9%) upon performing the buckling mode classification. Similarly, all the remaining sections are modelled and analysed. All the sections considered in this study are subjected to global buckling predominantly for a length of 1000 mm. Hence, the length of the complex angle sections is assumed as 1000 mm for the entire study.

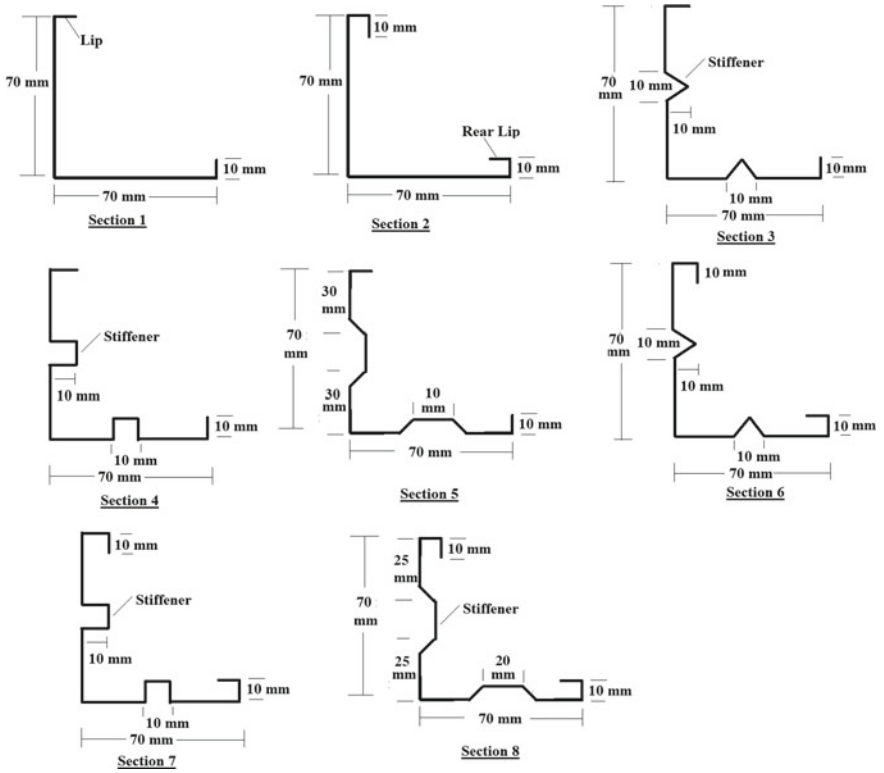

Fig. 2 Complex angle sections (thickness, $t = 2$ mm)

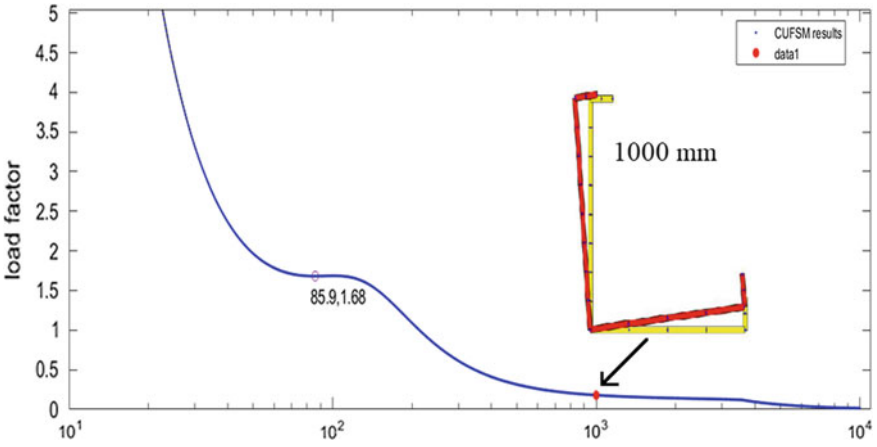

Fig. 3 Signature curve for Section 1

3.2 Linear Elastic Finite Element Analysis

The considered angle sections of length 1000 mm are analyzed using finite element software ABAQUS. Corners of the sections are modelled as sharp corners. The Modulus of Elasticity (E) of the material is taken as 200 GPa and Poisson's ratio (v) as 0.3. S4R element—a four-noded shell element with 6° of freedom at each node is considered for meshing. A mesh size of 10 is considered after repeated trials. Fixed boundary condition is assigned at ends by using MPC constraint. At loaded end, all degrees of freedom are restrained except translation along the direction of application of load whereas at the other end all the degrees of freedom are restrained. A compressive force of 1 N is applied and linear buckling analysis is carried out. The elastic critical buckling loads are noted. The primary mode of buckling for all the sections is found to be global (Torsion dominant-Flexural buckling) buckling as represented in Fig. 4.

3.3 Non-linear Finite Element Analysis

In order to obtain the column strengths/ultimate load-carrying capacity (P) and account for the post-buckling strength, Geometric and Material Non-linear Imperfection Analysis (GMNIA) is carried out. Elastic-perfectly plastic stress–strain curve was considered in the study with yield stress (f_y) of 350 MPa to include material non-linearity.

As all the sections are observed to undergo global buckling predominantly from previous analyses, the imperfection was included by scaling the primary mode shape of buckling (obtained from linear-finite element analysis) by L/1000 [17]. Rik's

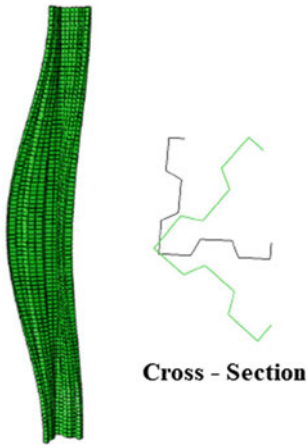

Fig. 4 Primary buckling mode (linear-elastic analysis)

method was selected as the solution method and initial arc length is assumed as 0.1. Residual stresses have negligible effect on ultimate strength and are hence not included in the models [14, 23]. The Von-Mises stress contour and deformed shape of the Section 6 are represented in Fig. 5.

4 Direct Strength Method (DSM) Design

4.1 AISI-S100-16 Design Provisions [22]

For sections which undergo yielding and global buckling (torsional/torsional-flexural buckling), the nominal column strength (in terms of stress) can be calculated as follows.

$$\text{For } \lambda_c \leq 1.5 \quad F_n = (0.658^{\lambda c^2}) F_y \tag{1}$$

$$\text{For } \lambda_c > 1.5 \quad F_n = \left(\frac{0.877}{c^2}\right) F_y \tag{2}$$

$$P_{ne} = A_g F_n \tag{3}$$

where $\lambda_c = \sqrt{\frac{F_y}{F_{cr,e}}}$.

$F_{cr,e}$ Critical buckling stress, N/mm^2 (as per section E2.1 of code).
F_y Yield stress, N/mm^2.
F_n Compressive stress, N/mm^2.

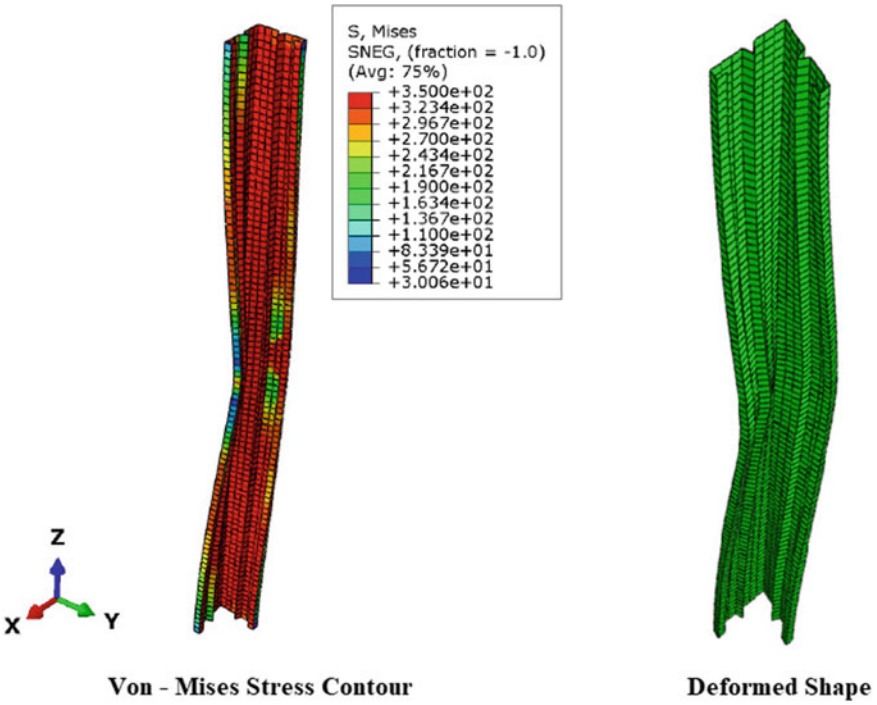

Fig. 5 Von-Mises stress contour and deformed shape

A_g Gross area, mm^2.
P_{ne} Nominal axial strength, N or kN.

The equations do not consider the post-buckling capacity.

4.1.1 Design Equations Proposed by Schifferaw and Schafer [10]

From the study conducted by the authors, it was reported that significant post-buckling strength was possessed by the lipped angles with fixed ends which when unconsidered results in a very unconservative design. Therefore three options for considering the post-buckling strength were proposed. In the present study the second option i.e., use of 'local DSM' post-buckling curve with transition for P_{ne} is considered. The design equations (in terms of stress) are as follows:

$$\text{For } \lambda_c \leq 1.446 \quad F_{ne,l} = (0.82^{\lambda c^2})\, F_y \tag{4}$$

$$\text{For } \lambda_c > 1.446 \quad F_{ne,l} = \left(1 - 0.15\left(\frac{F_{cre,FT}}{F_y}\right)^{0.4}\right)\left(\frac{F_{cre,FT}}{F_y}\right)^{0.4} F_y \tag{5}$$

where $F_{cre,FT}$ = critical elastic flexural-torsional buckling stress
$P_{cre,FT} = F_{cre,FT} A_g = P_{cr,e\_FEA}$ in present study

$$\text{Nominal strenth } P_{ne} = F_{ne,l} A_g \tag{6}$$

5 Results and Discussion

The obtained elastic critical loads (P_{cr,e_FEA}) and ultimate loads ($P_{u,FEA}$) of the various complex angle sections considered are presented in Table 2 along with the design strengths $P_{ne,\,AISI}$ [22] and P_{ne}, [10] obtained from 'Eqs. (3) and (6)', respectively. The plot of axial load vs axial displacement for the considered complex angle sections is depicted in Fig. 3. The axial load capacity and normalized load capacity ($P_{u\_FEA}/P_{cr,e\_FEA}$) for the considered sections are presented in Figs. 4 and 5, respectively. From observing Table 2 and Figs. 6, 7 and 8, the following inferences are made.

(1) Providing stiffeners enhances the ultimate load-carrying capacity (P_u). The ultimate loads of angle sections with stiffeners (Sections 3–8) are greater than that of the lipped angle sections (Sections 1 and 2) due to the reason that the cross-section area increases and lesser unstiffened width to thickness ratio.
(2) In comparison to Section 1, the increase in ultimate load of Sections 2, 3, 4, 5, 6, 7 and 8 are 19.22%, 21.95%, 35.44%, 32.65%, 37.71%, 56.77% and 54.22% respectively.
(3) Though the highest ultimate load of 92.76 kN is obtained for Section 7 with an area of 440 mm^2, an ultimate load of 91.25 kN is obtained for Section 8 which has a relatively much lesser area of 409.44 mm^2. Interestingly Section 6 which is also of area 409.44 mm^2 is found to have a much lower ultimate load of 81.48 kN. Hence, Section 8 may be regarded as a preferable section shape considering the ultimate load as the only criteria.
(4) The ratio of ($P_{u\_FEA}/P_{cr,e\_FEA}$) which is called normalized load capacity, represents the post-buckling capacity [11]. The ratio is highest for Section 1 with 2.08 and least for Section 8 with 0.92. Also, on comparing Section 1 with other sections, it can observed that providing rear lip and/intermediate stiffeners reduces the post-buckling capacity irrespective of the increase in area.
(5) Among the Sections 3, 4 and 5 (sections with no rear lips) which are provided with triangular, square and sigma type stiffeners respectively, Section 4 which has greater area of cross-section possessed higher ultimate load and normalized load carrying capacity (or) post-buckling strength.
(6) Considering Sections 1 and 2, providing rear lip resulted in increase of ultimate load by 19.22% but decrease in normalized load capacity by 14.29%. Similar behaviour is noticed between Sections 4 and 7 and Sections 5 and 8, however

Table 2 Column strength

Specimen	A (mm^2)	P_{cr,e_FEA} (kN)	P_{u_FEA} (kN)	P_{ne_AISI}, [22] (kN)	P_{ne}, [10] (kN)	$P_{u\_FEA}/P_{cr,e\_FEA}$	P_{u_FEA}/P_{ne}, [10]
1	320	28.38	59.17	21.47	59.07	2.08	1.00
2	360	38.69	70.54	32.24	71.22	1.82	0.99
3	369.44	67.96	72.16	59.6	88.64	1.06	0.81
4	400	58.42	80.14	51.34	88.26	1.37	0.91
5	369.44	73.03	78.49	64.05	90.99	1.07	0.86
6	409.44	74.81	81.48	65.61	97.97	1.09	0.83
7	440	91.45	92.76	80.2	110.25	1.01	0.84
8	409.44	99.13	91.25	86.94	107.56	0.92	0.85

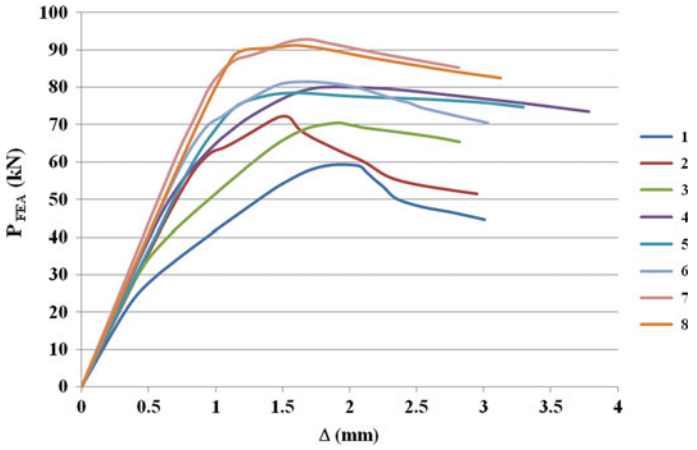

Fig. 6 Axial load (P_{FEA}) versus axial displacement (Δ)

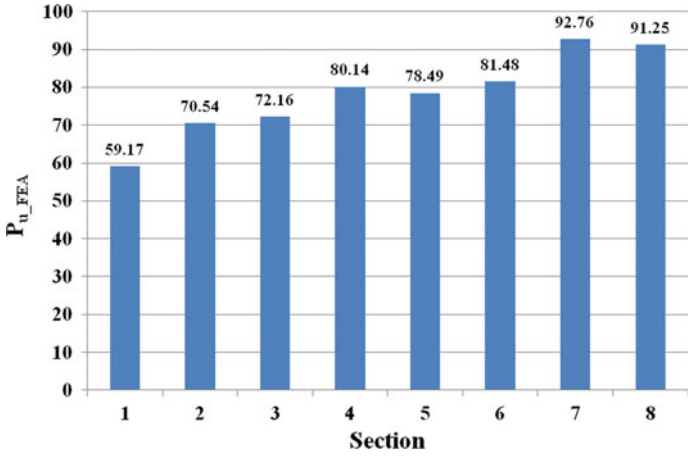

Fig. 7 Axial load of various sections

with the exception of Sections 3 and 7 for which the normalized load capacity also increased.

(7) The design provisions of AISI S-100-16 [22] resulted in under-estimate of ultimate load capacity of the angle sections. The reason is that the design provisions do not consider the post-buckling capacity under fixed boundary conditions.

(8) The design equations proposed in the previous study [10] over-predict the ultimate capacity of complex angle sections which are provided with intermediate stiffeners and/rear lips.

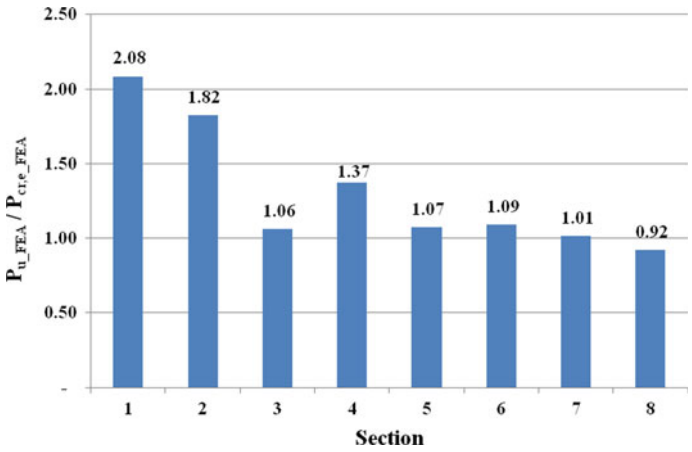

Fig. 8 Normalized load capacity of various sections

6 Conclusions

A simple numerical and theoretical study on the global buckling behaviour and design of complex angle sections is presented. Complex angle sections, i.e. angle sections provided with rear lip and/stiffeners of 1 m length are considered upon preliminary analysis of cross-section stability using CUFSM. The sections are modelled in ABAQUS and linear-elastic finite element analysis is performed to find the primary elastic critical load and buckling mode (global) shape. Then the analysis is extended to Geometric and Material Non-linear Imperfection Analysis (GMNIA) to find the ultimate load capacity of the sections considered in the study. Based upon the obtained results of the study, the following conclusions are stated.

(1) Providing rear lips and/intermediate stiffeners increases the ultimate load-carrying capacity but decreases the post-buckling capacity.
(2) Angle sections (with/without rear lip) with intermediate square type stiffener (Sections 4 and 7, respectively) possessed maximum increase in ultimate loads in comparison with lipped angle section (Section 1).
(3) Angle sections of sigma type intermediate stiffener (Sections 5 and 8) resulted in the least post-buckling capacity either in the case of with or without rear lips.
(4) Lipped angle section without rear lip and intermediate stiffeners (Section 1) possessed maximum post-buckling capacity.
(5) The design provisions available in literature [10, 22] lead to inaccurate prediction of ultimate loads incase of complex angle sections.

References

1. Yu WW, LaBoube RA, Chen H (2020) Cold-formed steel design 5. Wiley, USA
2. Schafer BW (2002) Local, distortional, and euler buckling of thin-walled columns. J Struct Eng ASCE 128(3):289–299
3. Popovic D, Hancock GJ, Rasmussen KJR (1999) Axial compression tests of cold-formed angles. J Struct Eng ASCE 125(5):515–523
4. Young B (2004) Tests and design of fixed-ended cold-formed steel plain angle columns. J Struct Eng ASCE 130(12):1931–1940
5. Ellobody E, Young B (2005) Behaviour of cold-formed steel plain angle columns. J Struct Eng ASCE 131(3):457–466
6. Young B (2005) Experimental investigation of cold-formed steel lipped angle concentrically loaded compression members. J Struct Eng ASCE 131(9):1390–1396
7. Young B, Ellobody B (2005) Buckling analysis of cold-formed steel lipped angle columns. J Struct Eng ASCE 131(10):1570–1579
8. Young B, Ellobody B (2007) Design of cold-formed steel unequal angle compression members. Thin-Walled Struct 45(3):330–338
9. Young B, Chen J (2008) Column tests of cold-formed steel non-symmetric lipped angle sections. J Constr Steel Res 64(7):808–815
10. Schifferaw Y, Schafer BW (2014) Cold-formed steel lipped and plain angle columns with fixed ends. Thin-Walled Struct 80:142–152
11. AISI-S100 (2007) North American specification for the design of cold-formed steel structural members. American Iron and Steel Institute. AISI
12. Silvestre N, Dinnis PB, Camotim D (2013) Developments in the design of cold-formed steel angles J Struct Eng ASCE 139(5):680–694
13. Beulah Gnana Ananthi G, Vishnuvardhan S, Samuel Knight GM (2015) Experimental and numerical investigation on thin-walled single and starred angle sections under compression. Arab J Sci Eng 40:3417–3427
14. Narayanan S, Mahendran M (2003) Ultimate capacity of innovative cold-formed steel columns. J Constr Steel Res 59:489–508
15. Manikandan P, Sukumar S, Kannan K (2018) Distortional buckling behaviour of intermediate cold-formed steel lipped channel section with various edge stiffeners under compression. Int J Struct Eng 10:189–198
16. Aruna G, Sukumar S, Karthika V (2015) Study on cold-formed steel built-up square sections with intermediate flange and web stiffeners. Asian J Civ Eng BHRC 16(7):919–931
17. Mahar AM, Anil Kumar MV, Jaychandran AS (2018) Evaluation of design equations for globally buckling cold-formed steel compression members. In: Proceedings of the 11th structural engineering convention. SEC-18, Jadavpur Univeristy, Kolkata, India, pp 2–7
18. Aghoury MA, El Hanna MT, Amoush EA (2017) Experimental and theoretical investigation of cold-formed single lipped sigma columns. Thin-Walled Struct 111:80–92
19. Xiang Y, Zhou X, Shi Y, Xu L, Xu Y (2020) Experimental investigation and finite element analysis of cold-formed steel channel columns with complex edge stiffeners. Thin-Walled Struct 152:1–19
20. Schafer BW, Adany S (2006) Buckling analysis of cold-formed steel members using CUFSM: conventional and constrained finite strip methods. In proceedings of Eighteenth international speciality conference on cold-formed steel structures, pp. 39–54
21. Schafer BW, Li Z, Moen CD (2010) Computational modeling of cold-formed steel. Thin-Walled Struct 48:752–762
22. AISI-S100 (2016) North American specification for the design of cold-formed steel structural members. American Iron and Steel Institute. AISI
23. Schafer BW, Pekoz T (1998) Computational modelling of cold-formed steel: characterizing geometric imperfections and residual stresses. J Constr Steel Res 47:193–210

Analysis and Design Approaches of Cold-Formed Steel Members—A Review

H. Hema and H. G. Nahushananda Chakravarthy

Abstract In present times, the utilization of cold formed steel (CFS) members in building industry is rapidly growing on account of its higher strength-to-weight ratio and the significant flexibility of shapes and size accessible to the structural steel engineer. Beside these advantages, it has also some desirable properties which create more challenges during its use in construction. As the thickness is very small it can easily get affected by different types of buckling, torsional failure, web crippling, and have low resistance to fire. The key focus of this study is to represent the CFS members by reviewing its properties, classification, buckling modes, etc. The paper discusses the codes and guidelines available for cold-formed steel sections and different analysis methods carried out by many researchers. At present time, the application of modernized finite element method in CFS will permit the development of creative and structured building products. The selection of the best section is a great challenge and also expensive, the use of artificial neural network will predict the strength of the sections. In this review paper CFS sections design, analysis, and use of artificial neural network are discussed.

Keywords Cold-formed steel · Codes and specifications · Buckling · Finite element method · Artificial neural network

1 Introduction

In steel structures two classes of steel sections are used, they are hot formed and CFS [1]. Hot-rolled products are produced at high temperatures and CFS members are manufactured at ambient room temperatures. The CFS members are made from carbon or low alloy steel sheet, flat bar, or strip plate in cold rolling machines or by bending or press brake operations [2]. Cold rolling method is used for large volume production and press breaking method is used for low volume production. The thickness of these members normally ranges from 0.8 mm to 3 mm [3].

H. Hema · H. G. Nahushananda Chakravarthy (✉)
Department of Civil Engineering, Siddaganga Institute of Technology, Tumakuru 572103, Karnataka, India
e-mail: Chakravarthyn@sit.ac.in

L. Nandagiri et al. (eds.), *Recent Advances in Civil Engineering*, Lecture Notes in Civil Engineering 256, https://doi.org/10.1007/978-981-19-1862-9_48

There are various forms of CFS shapes available as structural components, they are: single sections for, e.g., Z, C, and hat sections and built-up sections which are formed by connecting two or more CFS members together such as box sections, I sections, etc. [4].

The usage of CFS sections in construction of buildings began in nineteenth century in both Great Britain and US. The very first specification for CFS construction was formed in USA around mid-twentieth century [5], the original UK codal provision was formed in 1961 [6]. Europe saw much attention in this field in the 1970s and new European recommendations and UK codes for designing the CFS members were formed and also new American code in 1980s.

CFS sections can result in economic design than the hot-formed steel members due to properties like higher strength to weight ratio, which facilitates in fabrication during construction [7]. The members offer very flexible design using different cross-sectional shapes but can more demands on the designer because elastic local and buckling phenomena need to be taken into account practically in all designs [8].

CFS sections are generally used in structural building construction as primary structural components such as beams, columns, frames, etc., also as a secondary structural element such as roof purlins [9]. CFS members can be used for complete buildings and for wall and floor systems, and also it can be used as separate framing elements, like joists, truss, and stud members [10].

2 Literature Gap Analysis

Many researches and reviews have been carried out to understand the behavior, properties, and application of CFS. These researches include both experimental and numerical investigation. The numerical analyses like finite strip and generalized beam method have been outdated. In the present times, the finite element method has become a powerful tool to analyze the CFS.

The use of artificial intelligence in the field of civil engineering applications is increasing day to day. There are very limited numbers of studies available in machine learning technique on CFS. Hence, the present study focuses on the application of neural network to forecast the behavior of CFS.

3 CFS Columns

In contrast to the conventional structural behavior of hot-rolled columns, the prominent role of instabilities complicates the design and also the behavior of CFS columns. The members are prone to instability in different types of modes that can be generally termed as,

- Local buckling,
- Distortional buckling,
- Global buckling.

3.1 Local Buckling

This is specifically common and is characterized by comparatively shortwave buckling of single plate elements [7]. The plate elements are thin plates with higher slenderness ratio and therefore buckle locally prior to yield stress is achieved. Support conditions and geometry of the sections impact the local buckling mode of cold formed members. However this doesn't result in the failure of the section [8]. Extra load can be bared by members in its post buckling behavior prior to failure takes place.

3.2 Distortional Buckling

In this buckling the corners of the members are not in exact position and flanges allowed to rotate. It occurs as a result of distortion of the cross section and is distinguish the comparative change of fold elements. The buckling wavelength is commonly in between the local buckling and global buckling [8]. It is also termed as local torsional buckling or stiffener buckling. It is described by revolving of flange at the flange web junction in the members with edge stiffened fold lines [7]. For the sections with intermediate stiffened elements, the buckling is distinguished by the movement of the intermediate stiffener perpendicular to the element plane.

3.3 Global Buckling

It involves elastic Euler buckling and torsional flexural buckling in columns [7]. Concentrically loaded columns of angle sections can buckle in any of the given three modes [8]: Flexural buckling, characterized by bending along weaker principal axis or torsional buckling which is characterized by twisting about shear center and torsional flexural buckling by both bending and twisting at the same time. Axially loaded single equal leg angles fail by flexural buckling along the asymmetric minor principal axis or together by bending and twisting about symmetric major principal axis depending upon the length, cross section dimensions and support conditions of member, whereas concentrically loaded single unequal leg angles always fail by torsional flexural buckling. Concentrically loaded compound angles, with one axis of symmetry fail either by flexural buckling along the asymmetric axis or by torsional flexural buckling along the symmetric axis. Concentrically loaded compound angles

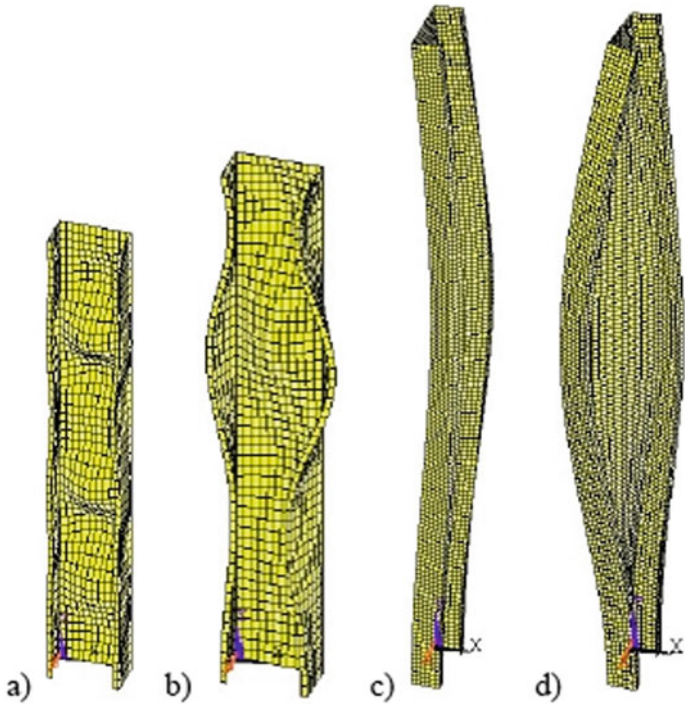

Fig. 1 Modes of buckling in CFS members [11]

with two axes of symmetry either by flexural buckling along weak symmetric axis or by torsional buckling about the shear center. Figure 1 shows the different failure modes in CFS columns

4 CFS Beams

Generally, local Buckling and distortional buckling occurs in CFS beams same as in CFS columns. There are many other different types of buckling that takes place in beams and are briefly explained here,

4.1 Shear Buckling

It usually occurs in the web of the beam having much larger h/t ratio or it can be deep beams [9]. In short beams, although this phenomenon is substantially stable it can be neglected. The beam webs are susceptible to bucking under shear loading this is termed as shear buckling.

4.2 Web Crippling

Web Crippling is similar to a buckling; it occurs at the web of the beam, subjected to compression under the action of concentrated loads. It is often occur at the supports of the beam, when the bottom flange is placed on the support and the top flange is bearing up the load [10]. It is also called as web buckling or web crushing.

4.3 Lateral Torsional Buckling

This is same as the torsional flexural buckling in columns. It occurs in open sections when beam is subjected to bending load, half of it experiences compression while the other is in tension. If that compression flange has no lateral support then the beam will not only experience large lateral deflection but also twist [12].

5 Interaction of Buckling Modes

Concurrently, the local, distortional and global buckling loads lead to a nonlinear interaction between the buckling modes [8]. Interaction between shorter wavelength and longer wavelength buckling modes has been shown the effect on the post buckling behavior. Additionally, the uncontrolled imperfections may remarkably reduce the load carrying strength of CFS beams. The buckling interaction is studied either by the evaluation of the stiffness of the locally buckled member or it is on the General Koiter theory [13]. The idea of effective width method is applied to find out the post buckling strength of locally buckled plate element.

5.1 Local and Overall Buckling

A Local buckling not only reduces the effective cross-sectional properties, but also shifts the centroid about the axis of symmetry [14]. Therefore, a concentrically loaded column becomes beam-column. The testing of those columns for an axial load i.e., exactly eccentric throughout its load history is very difficult. Moreover, such kind of columns not at all exists, as most of the columns with no clear end moments applied can in fact be, beam columns [12]. The generally used method for interaction between these two buckling modes is based on effective cross section that depends on local buckling behavior of individual plate members [15].

5.2 Local and Distortional Buckling

Here, interaction of these buckling modes has fairly unrevealed effects. The normally used explanation of the local buckling behavior of cross section is preferably incorrect. Moreover the post buckling capacity of distortional buckling modes is inconsistent and in many cases it is unpredictable [16]. Since the number of feasible cross sections and feasible types of failure modes is very huge and the study is restricted to the particular CFS cross sections. Fig 2. Shows the types of interaction of buckling modes.

6 CFS Panels

The CFS members are commonly used for wall panels, roof decks, bridge form and sliding material [5]. Decks and steel panels are useful to provide the strength required to carry the loads and the surface for roofing, flooring and to fill the concrete. Also, the provisions for electrical conduits, which can be penetrated and integrated with audio absorbing medium to form an audio conditioned roof ceiling [13, 17]. The panels can be used as ducts for air conditioning and heating. Steel roof decks are

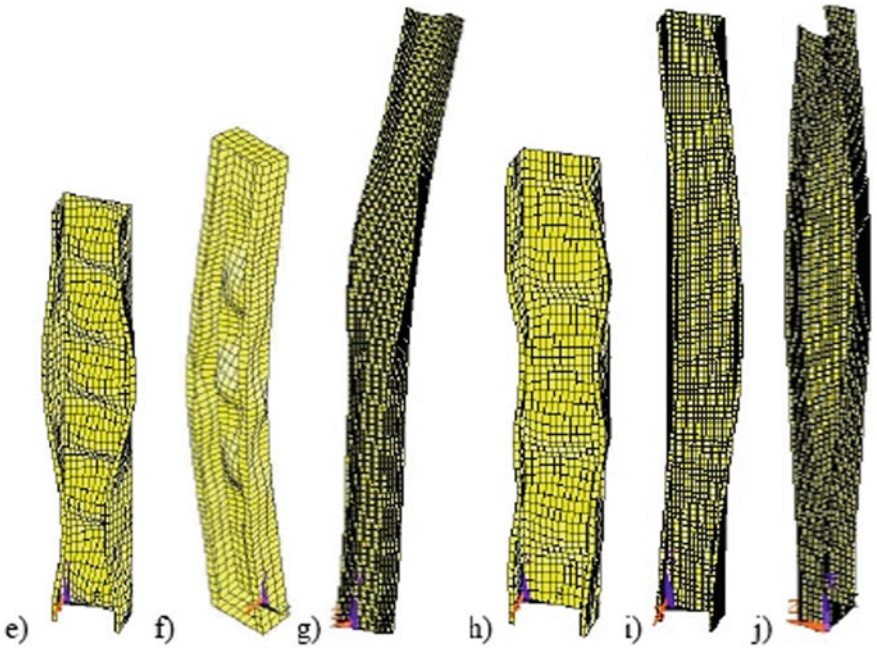

Fig. 2 Interaction of buckling modes [11]

used in hyperbolic paraboloid roof construction. Roof decks are bend to suit the shape of an arched roof very easily. Over the last few decades, CFS decks are being extensively used in formwork and also for reinforcement of composite concrete roof and floor slabs. Corrugated sheets are frequently used as panels for roofs or walls, exterior curtain wall panels, arched roofs of drainage structures and underground shelters.

7 Codal Provisions

There are many guidelines and specifications available in different codes of CFS members that makes easy for the application of CFS members in construction. The AISI Specification named, North American specification is intentional to use throughout United States, Mexico and Canada. This specification gives a consolidated therapy of Allowable strength design (ASD), Load and resistance factor design (LRFD) and limit state design (LSD). It is adopted by using suitable resistance factors for the LRFD and LSD and suitable safety factors for ASD [18]. The limit state method of Australian/New Zealand standard (AS/NZS) for CFS structural design was originally produced in 1996. At present, two basic design methods are accessible in the code they are Effective Width Method (EWM) and Direct strength method (DSM). DSM has been significantly revised to consider combined bending and compression, shear, holes in sections, and inelastic reserve capacity [19]. British Standard (BS) are produced by BSI groups which is officially named as National Standard Body of the United Kingdom (UK). Code of practice for design of cold formed steel for design of cold formed thin gauge sections BS 5950-5:1998 gives recommendation for the design of structural steelwork in buildings and associated structures by using CFS members. This is basically considered for the thickness of steel up to 8mm. The sections can be of both open and closed, made of flat elements and can be bounded by bends or free edges. Their angles should not exceed 1358 and internal radius should not exceed 5 times the thickness [20]. The Indian Standard (IS) was adopted by the Indian standard institutions, mainly based on "Specification for the design of cold formed structural steel members" by AISI New York. It can also use for the structures apart from the buildings for which the allowances are available for dynamic effects [21]. The European Standard EN 1993-1-3, Eurocode 3 has been produced by Technical committee CEN/TC250. It gives the design conditions for CFS members and sheeting. It is applicable to the CFS products which may be coated or uncoated, hot-rolled or cold rolled sheet or strips which are produced press breaking or cold rolled forming. It can also applicable for the design of steel sheeting for concrete slabs and composite steel which is at the stage of construction [22].

8 Connections

Connection is described as a mechanical component that physically connects the structural members to transfer the force and moment to supporting elements [2]. Many different types of connections available for CFS structures they are, bolted, screw, welded and storage rack connections. Screw connection is the most regular type of connection which is used in the CFS. Because of less thickness of CFS the provision of connection with screw gives easy design and quick installation [23, 24]. Storage racks are particularly created by CFS members. As the storage rack structures are same as that of light gauge steel frames the variables which included in design are mostly identical [3]. Welded connections provides hard joint between CFS members. The welding procedure requires expert labors and extra care compared to other connections. Laser beam welding is extensively applied in automobile field but it is yet a modern technique in CFS construction. The Laser beam welding method is exactly welded at the joints which reduces the inaccuracy and thereby increasing the protection of the connections. Bolted connection, a frequent method of connection that can be used for both hot formed and CFS. Bolt configuration and edge distance are the two main variables that influence the net section rupture of the bolted connection.

9 Design of CFS Members

9.1 Direct Strength Method (DSM)

This method includes the estimation of ultimate strength of CFS section by considering the Euler buckling capacities in local, distortional and global modes [8]. It provides a constant approach in determining member compression and flexural strengths without considering the cross sections the member. The DSM readily considers the distortional buckling, which is important for the members whose strength is managed by distortional buckling [25]. It is used to calculate the capacity of members with optimized cross sections. DSM design approach mainly focuses on buckling modes which helps to know the behavior of CFS sections by increasing the strength of the section or member reinforcing in retrofitting. Since DSM predicts strength by considering the buckling loads, if the section includes only slender elements, the elastic buckling load might be very low which may be overly conservative. The Direct strength method doesn't allow the provisions for web, crippling, shear, members with holes etc., the existing provisions can be used.

9.2 Effective Width Method (EWM)

This method considers the, results of local buckling, in reduction of effective cross section of the member. Reducing cross-sectional area from gross to the effective cross section is the main basic for the use of the EWM. An effective width method gives an exact model for positions in cross sections where the member is incapable of bearing the load, it leads to the idea of shifting of the neutral axis because of local buckling and it provides a clear means to include interaction of local-global buckling where reduction in cross section properties influences global buckling [8]. However, an effective width method ignores the compatibility and equilibrium between elements while determining the buckling behavior and creates more complications to determine the effective cross section so as to make the section more optimize [26]. This method is similar to traditional elastic stability and the design methodology is different compared to that of hot-rolled steel sections.

9.3 Finite Strip Method

It is a general method used in the design of CFS to predict elastic buckling [8]. The traditional, semi numerical finite strip analysis provides the widest approach to investigate the unreliability in CFS section due to longitudinal stress. Basically, the finite element strip is an alternative of the FE method [27]. A member cross-section is split into a number of vertical strips which is very similar to finite element discretization. For every strip, the elastic stiffness matrix is calculated based on the assumption of plane stress and Kirchoff plate theory. After the transformation of local coordinates to global coordinates according to the orientation of the strip and the assembly of overall strips, the global elastic and also the stiffness matrices can be derived.

9.4 Generalized Beam Theory

Generalized beam theory is used as a substitute for finite strip method. GBT analysis involves solving equilibrium equations that include displacement and deformation modes [28]. Thus, the analysis of buckling behavior of the given section must be preceded by a set of cross-sectional analysis which are aimed at recognizing the corresponding buckling modes and determining the combined mechanical properties. Once all the buckling modes and their mechanical properties are known, the member eigenvalue buckling can be formulated and is explained by the GBT equilibrium equation.

10 Recent Approaches of CFS Design

10.1 Finite Element Method

FEM is an exact and reliable technique to predict the behavior of the structure under different loading types. FEA is now a commonly used design process to carry out new concepts before prototypes are made and tested. The software packages such as ABAQUS [29] and ANSYS [30] can be used for finite element analysis. The analysis includes three stages preprocessing, simulation and post-processing. Nonlinearity in terms of material and geometry, boundary conditions, and contact properties between elements has to be considered in the analysis. The meshing is done by considering suitable mesh size and mesh shape so as to get accurate results. Post-processing includes result files with requested outputs. The behavior of CFS in terms of ultimate strength under compression, buckling modes, web crippling of flexural members, etc., can be known by finite element analysis.

10.2 Artificial Neural Networks

ANN is a modeling approach influenced by the human nervous system that enables learning by example from data set describing a decision process. A distinguishing characteristic is their ability to form empirical relationships between variables, as well as take out precise data and complicated knowledge from data sets.

ANNs are made up of a layer of input neurons and a layer of output neurons that are linked by several layers of hidden units. Input layer units transmit information to the hidden layer with some activation function. The weights are applied to the findings in the hidden layers, and when a value of a specific node in the hidden layer reaches a certain threshold, a value is passed to the output layer.

These are the algorithms of artificial intelligence in logical tasks like optimization and learning [31]. The neural networks are especially used in the circumstances when the rules are neither unknown nor difficult to find, i.e., when there is no possibility to use conventional mathematical models [1]. Before using a neural network, it is trained adequately with a selected set of data. A result from the trained neural network is comparatively faster than finite element models and design codes [32]. Development of neural dynamics models helps in optimization problems highly nonlinear and complicated constraints [4]. Many design curves are available to predict the optimum value of depth of the web to thickness ratio, width of the flange to thickness ratio, and thickness for I-shaped beams [33], hat-shaped beams [34], and z-shaped beams [35].

11 Conclusions

The development in structural application of CFS across the world shows the importance of CFS members with respect to engineering applications. Hence, the number of research has been conducted to understand the CFS behavior, manufacturing, applications, and design methods. Based on these reviews, the following conclusions are drawn.

- Light gauge members are prone to buckling, hence it is necessary to strengthen the members with suitable strengthening materials.
- There are many guidelines and specifications available in various codes of CFS structures that will provide economical and safe design methods.
- Finite element technique can be widely applicable to analyze the behavior of CFS members.
- Finite element methods can be considered as an efficient method, because it reduces the experimental expenditures.
- Artificial Intelligence can assist inexpert users to solve engineers' problems and can also help knowledgeable users to upgrade their work efficiency.
- Artificial neural network helps to predict the best efficient section that can be used in the new applications.

Acknowledgements The work is based on the reviews by the authors mentioned in the references. We would like to acknowledge them for their useful information which helped in the present work.

References

1. El-Kassas EMA, Mackie RI, El-Sheikh AI (2002) Using Neural networks to predict the design load of cold- formed steel compression members. Adv Eng Softw 33:713–719
2. Lee YH, Tan CS, Mohammad S, Tahir MM, Shek PN (2014) Review on cold formed steel connections. Sci World J Volume, Article ID 951216:11
3. Bucmys Z, Sauciuvenas G (2013) The behaviour of cold formed steel structure connections. Eng Struct Technol 5(3):113–122
4. Adeli H, Karim A (1997) Neural network model for optimization of cold formed steel beams. J Struct Eng 123:1535–1543
5. Halabi Y, Alhabad W (2002) Manufacturing, applications, analysis and design of cold formed steel in engineering structures: a review. Int J Adv Eng Res Sci (IJAERS) 7(2):ISSN: 2349–6495(P) | 2456–1908(O)
6. Kankanamge ND, Mahendran M (2011) Mechanical properties of cold formed steel at elevated temperatures. Thin-Walled Struct 49(1):26–44
7. Schafer BW (2002) Local, distortional, and Euler buckling of thin-walled columns. J Struct Eng 128(3):289–299
8. Macdonald M, Heiyantuduwa MA, Rhodes J (2008) Recent developments in the design of cold formed steel members and structures. Thin Walled Struct 46:1047–1053

9. Keerthan P, Mahendran M (2011) Shear buckling characteristics of cold formed steel channel beams. J Struct Eng 137(12)
10. Janarthan B, Sundarajah L, Mahendran M (2019) Web crippling behaviour and design of cold formed steel sections. Thin-Walled Struct 140:387–403
11. Dubina D, Ungureanu V, Landolfo R (2014) Design of cold formed steel structures. Eurocode 3: Design of steel structures. Part 1–3: Design of cold formed steel structures, ECCS Eurocode design manuals
12. Kankanamge ND, Mahendran M (2012) Behaviour and design of cold-formed steel beams subject to lateral–torsional buckling. Thin-Walled Struct 51:25–38
13. Ye J, Mojtabaei SM, Hajirasouliha I (2018) Local-flexural interactive buckling of standard and optimised cold formed steel columns. J Construct Steel Res 144:106–118
14. Robert S, Glauz PE (2016) Lateral torsional buckling of general cold formed steel beams. In: Yu WW (ed) International specialty conference on cold-formed steel structures, Baltimore, Maryland, USA
15. Pi YL, Put BM, Trahair NS (1998) Lateral buckling strengths of cold-formed channel section beams. JStruct Eng 124(10):1182–1191
16. Matsubara GY, Batista de EM, Salles GC (2019) Lipped channel cold formed steel columns under local-distortional buckling mode interaction. Thin-Walled Struct 137:251–270
17. Baran E, Alica C (2012) Behaviour of cold formed steel wall panels under monotonic horizontal loading. J Constr Steel Res 79:1–8
18. AISI Manual (2016) Cold formed steel design, American iron and steel institute
19. AS/NZS: 4600 (2018) Cold formed steel structures, Australia/New Zealand Standard
20. BS 5950–5:1998 Part-5 code of practice for design of cold formed thin gauge sections, British Standard
21. IS 801 (1975) Code of practice for use of cold formed light gauge steel structural members in general building construction, Indian Standard
22. EN 1993–1–3 (2006) Eurocode-3 design of steel structures, part 1–3 general rules—supplementary rules for cold formed members and sheeting
23. Naganathan S, Chakravarthy HGN, Anaur NA, Kavalagunta S, Mustapha KNB (2020) Behaviour of Cold formed steel Built-up channel columns strengthened using CFRP. Int J Steel Struct 20:415–424
24. Chakravarthy N, Naganathan S, Beddu S, Akmal MH, Kavalagunta S, Mustapha KNB, Phalguna HG (2017) Load carrying capacity of CFRP strengthened cold formed steel builtup box sections. Int J Adv Appl Sci 4(10):175–218
25. Schafer BW (2008) Review: the direct strength method of cold formed steel member design. J Construct Steel Res 64(7–8):766–778
26. Cheng Y, Yan W (2011) Effective width method for determining distortional buckling strength of cold formed steel flexural C and Z sections. Thin-Walled Struct 49(2):233–238
27. Li Z, Schafer BW (2010) Application of the finite strip method in cold formed steel member design. J Construct Steel Res 66(8–9):971–998
28. Silvestre N, Camotim D (2003) Nonlinear generalised beam theory for cold formed steel members. Int J Struct Stability Dyn 03(04):461–490
29. Roy K, Mohammadjani C, Lim JBP (2019) Experimental and numerical investigation into the behaviour of face to face builtup cold formed steel channel sections under compression. Thin-Walled Struct 134:291 309
30. Manikandan P, Arun N (2016) Numerical investigation on cold formed steel lipped columns with intermediate web stiffeners. J Inst Eng (India): Seriws A 97(1):1–7
31. El Kassas EMA, Mackie RI, El-Sheikh AI (2001) Using neural networks in cold formed steel design. In: ICAAICSE '01: proceedings of the sixth international conference on application of artificial intelligence to civil and structural engineering, pp 43–44
32. Guzelbey IH, Cevik A, Erklig A (2006) Prediction of web crippling strength of cold formed steel sheetings using neural networks. J Construct Steel Res 62(10):962–973

33. Karim A, Adeli H (2000) Global optimum design of cold-formed steel i-shape beams. Pract Period Struct Des Constr 5:78–81
34. Karim A, Adeli H (1999) Global optimum design of cold formed steel hat shaped beams. Thin-Walled Struct 35:275–288
35. Karim A, Adeli H (1999) Global optimum design of cold formed steel z shaped beams. Practice periodical on structural design and construction

Bulk Utilization of WRP Slag for Geotechnical Characterization: An Experimental Study

Jancy Mathew, Mohini Patel, and P. S. Prasad

Abstract Environmental restrictions imposed on mining natural aggregates, for use in construction activities, necessitated the use of industrial byproducts as a substitute. In the present study, the Waste Recycled Product (WRP) slag has been characterized primarily for its usage in different geotechnical engineering applications such as embankment construction, reinforced earth construction, and filling of low-lying areas. California Bearing Ratio (CBR) and angle of shearing resistance (φ') of WRP slag compacted under varying relative compactions (RC) have been determined. Correlations have been developed between California Bearing Ratio (CBR), angle of shearing resistance (φ'), and relative compactions (RC). It was concluded that WRP slag being a cohesionless material, with low compressibility, high CBR value, high φ', is amenable to utilization in various geotechnical applications such as embankment and road construction. Stability analysis of Dykes constructed using WRP slag has been carried out using limit equilibrium method using GEO5 software to demonstrate the efficacy of the obtained properties and similarly, a pavement composition has been designed using IRC 37–2018 and its analysis has been carried out using linear elastic layered theory using IITPAVE software.

Keywords WRP slag · Relative compaction · CBR · Angle of shearing resistance · Utilization · Industrial waste · Dykes · Embankment · Subgrade

J. Mathew
Construction Skill Development Council of India, Gurgaon, Haryana, India

M. Patel (✉)
Pandit Deendayal Energy University, Gandhinagar, Gujarat, India
e-mail: mohinipatel16198@gmail.com

P. S. Prasad
CSIR-Central Road Research Institute, New Delhi, India

L. Nandagiri et al. (eds.), *Recent Advances in Civil Engineering*, Lecture Notes in Civil Engineering 256, https://doi.org/10.1007/978-981-19-1862-9_49

1 Introduction

Detailed geotechnical and chemical tests were carried out on the WRP slag, produced at TISCO manufacturing unit, Jamshedpur, India, to assess its potential as a construction material, as an alternate to aggregates in: road embankments, pavement construction, and as a fill material in reinforced earth applications. Fig. 1 shows the WRP slag considered for the current study.

Slag is a spinoff spawned during industrial of pig iron and steel. Steel slag generation is circa 20% by mass, of the rudimentary steel output. China's yearly slag generation is more than 100 million tons (MT) and its ingesting rate is only 29.5% [1]. The steel industry in India is engendering about 24 MT of BF slag and 12 MT of steel slag per annum [2]. In Japan, annual steel slag production is around 13–15 MT, out of which 98.4% is utilized in different engineering applications such as road construction, cement industry, soil improvement, landfill and other civil engineering applications [1, 4].

Iron slag from BF slag may be anticipated to be 25–30% of rudimentary iron production and steel furnace slag may be gauged to be 10–15% of raw steel production [3]. Malaysia produces 2.5–5.0 MT of steel yearly and producing 0.20–0.60 MT of steel slag, as of 2020 [5]. Slags (BF slag, BOF slag, and EAF slag) generated from steel and iron production are most commonly used in the manufacture of aggregates, mostly in concrete and road construction [6].

Several efforts were made in the past to utilize steel slag as a landfill cover material [29, 31], aggregate for road construction [10–14, 18–23], as a fine aggregate in the concrete [15–17, 25–27] and geotechnical applications like replacement in sand drain, surcharge material for soil improvement and fill material for cell revetment, etc [30]. Environmental impact assessment was performed on steel slag and concluded that steel slag is a non-hazardous material and can be used in place of natural aggregates [10, 28, 32, 33].

The present paper is aimed at the geotechnical characterization of industrial solid waste products from steel industry, i.e., WRP slag and feasibility of its utilization in geotechnical applications. Stability analysis of embankment/dyke constructed with

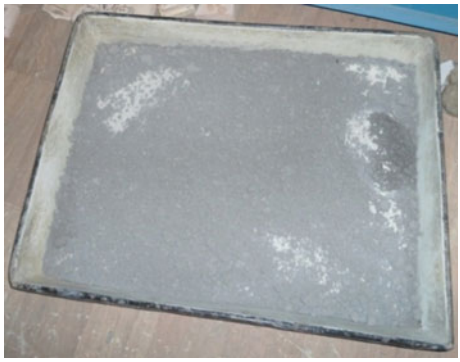

Fig. 1 WRP Slag for the present study

Table 1 Chemical composition of steel slag reported in literature compared with WRP slag

References	[11]	[34]	[17]	[35]	[36]	Present study (WRP slag)
Cao (%)	33.2	47.9	50–57	41.3	35–40	46.23
Fe_2O_3 (%)	29.6	26.3	10–13	31.2	–	25.06
SiO_2 (%)	10.1	12.2	9–11	12.5	15–25	12.65
Mgo (%)	13.1	0.82	1–2	4.3	6–13	1.76
Al_2O_3 (%)	1.66	1.22	1.4–0.7	2.4	3–7	1.16
MnO (%)	6.18	0.28	4–5	6.1	0.5–3	0.45
Na_2O (%)	0.02	0.04	0.02–0.04	–	–	–
K_2O (%)	0.06	0.07	0.04–0.01	–	–	–
P_2O_5	–	3.33	2.3–3.2	1.1	0–1	–
S	–	0.28	0.12–0.1	–	<0.4	0.3
LOI	–	7.54	–	–	–	

WRP slag was carried out using limit equilibrium method. A road pavement was designed and analyzed using linear elastic layered theory.

2 Chemical Properties

Steel slag consists of silicates and oxides. Table 1 presents the comparison of the chemical composition of steel slags from literature and WRP slag.

3 Physical Properties

3.1 Specific Gravity

The specific gravity value of WRP slag (3.16) is considerably higher than natural soils (2.64–2.67). The high value for the WRP slag is due to higher percentage of Fe_2O_3. The specific gravity of materials from the literature and WRP slag are shown in Table 2.

3.2 Particle Size Distribution

The particle size distribution curve of WRP slag and other steel slags from the literature is shown in Fig. 2. Table 3 presents the gradation characteristics of WRP

Table 2 Specific gravity from literature and present study

Specific Gravity	Remarks
3.16	Present study
2.75	[42]
3.2–3.6	[43, 44]
2.9	[34]
2.99–3.38	[48]
3.51	[16]
3.69	[39]

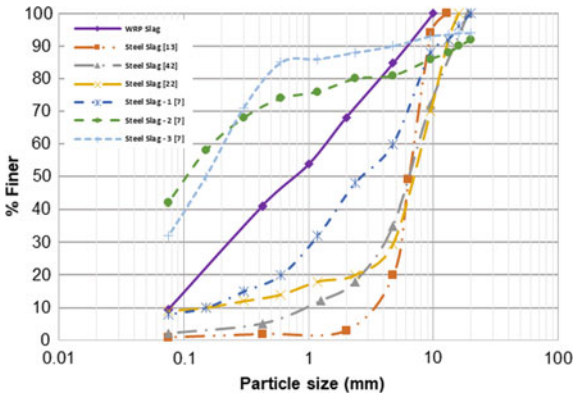

Fig. 2 Particle size distribution cures of WRP slag (present study) and steel slags (Literature)

Table 3 Gradation characteristics of WRP slag

Properties	WRP slag
Gravel size (%)	15.3
Coarse and medium sand size (%)	43.6
Fine sand size (%)	31.7
Silt size (%)	9.5
Clay size (%)	0
Uniformity coefficient, C_u	17.5
Coefficient of curvature, C_c	0.6
D_{10} size, mm	0.075
D_{30} size, mm	0.26
D_{60} size, mm	1.4

slag. From the grain size analysis, it was observed that WRP slag contains coarse-grained material with little fines; major portion is of sand-size particles with particle size varying from 0.075 mm to 10 mm which is fine to coarse sand and gravel. As per Unified Soil Classification System, WRP slag sample was classified as SW-SP.

3.3 Atterberg's Limit

Atterberg's limit (LL and PL) of the WRP slag sample could not be determined as it did not show any plasticity with addition of water. WRP slag contains 75% of sand-size particles. WRP slag sample is almost similar to sands indicating that it is non-plastic.

4 Geotechnical Properties of WRP Slag

4.1 Compaction Characteristics

The compaction characteristics of WRP slag used in the current study and other steel slags reported in the literature are tabulated in Table 4. The value of maximum dry density (MDD) of compacted WRP slag is higher compared to sand, which is in the range of 16.8–18.5 kN/m^3 [49]. The compaction curve of WRP slag and Badarpur sand are shown in Fig. 3. The higher value of MDD is due to high iron content and well-graded fractions within available coarse-grained particles of WRP slag. As

Table 4 Compaction characteristics of WRP slag

Modified proctor		References
$\gamma_d$max (kN/m^3)	OMC (%)	
24	9	Present study
23.5	8	[42]
23–24	8–12	[46]
26	6	[29]
18.7–23.9	–	[30]
17–26	19 – 9	[47]

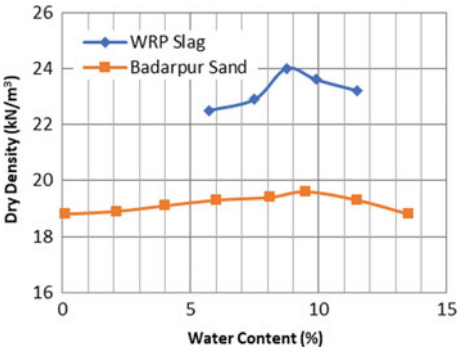

Fig. 3 Compaction curve of WRP slag and Badarpur Sand

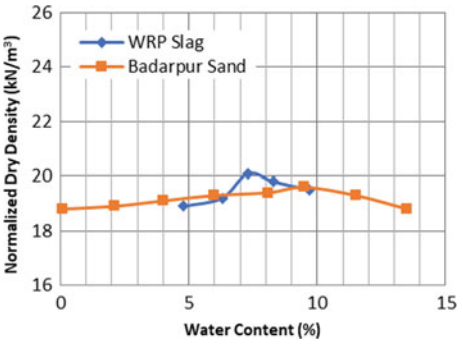

Fig. 4 Normalized compaction curve of WRP slag and Badarpur Sand

mentioned earlier, the variations in specific gravity of slag are larger (2.75–3.6); the dry density and corresponding water contents of a WRP slag is normalized with a standard specific gravity (2.65). The normalized compaction curve of WRP slag and Badarpur sand is shown in Fig. 4. Normalized dry density and compaction curve of WRP slag is almost comparable to Badarpur sand. Compacted dry densities are insensitive to moisture content during compaction. In the field, WRP slag doesn't necessitate considerable compaction control.

4.2 California Bearing Ratio (CBR)

WRP slag being cohesionless material, CBR tests [45] were carried out for different relative compactions. Figure 5 shows the relative compaction (RC) versus CBR value for WRP slag. The following correlations are proposed for the WRP slag to determine the CBR value in the field with the help of RC (Eq. 1).

$$\mathrm{CBR} = -0.051\mathrm{RC}^2 + 10.94\mathrm{RC} - 548.8 \tag{1}$$

where RC = Relative compaction in % (percentage).

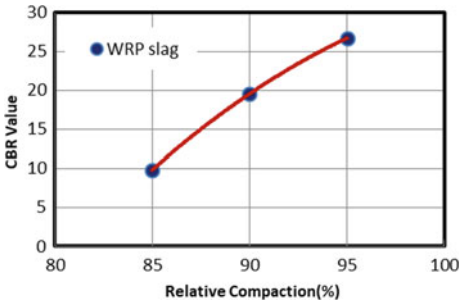

Fig. 5 Relative compaction versus CBR

The soaked CBR value of WRP slag varied from 8.82 to 26.71 with RC being varied from 85 to 95%, respectively. The higher CBR value of WRP slag is mainly attributed to its high density, well-graded and coarser particle size. The high value of CBR for WRP slag makes them seemly for its usage as subgrade material in the construction of roads.

4.3 Shear Strength Characteristics

For checking the stability of embankments/dykes, the angle of internal friction is the most important parameter. To examine the strength behavior of WRP slag in loose, medium, and dense states, direct shear tests [49] were conducted at different relative compactions, i.e., 75%, 80%, 85%, 90%, and 95% respectively. Figure 6 presents the shear strength properties of WRP slag under different states of relative compaction. The effective angle of shearing resistance (φ') of WRP slag increases with an increase in RC. WRP slag being cohesionless, non-plastic material, owes all it's shear strength from frictional cog. The angle of shearing resistance of WRP slag varies from 32^0 to 46^0 under increasing relative compactions, i.e., 75% to 95%, respectively. The result obtained shows a good correlation between φ' and RC which is as given below.

$$\varphi' = 0.04(\mathrm{RC})^2 - 6.170(\mathrm{RC}) + 268.6 \tag{2}$$

where

φ' = effective angle of internal friction.
RC = Relative compaction (%).

Eq. (2) is very much useful for finding the φ' with respect to varying compaction (RC) in the field.

The φ' of steel slag varies from 40^0 to 50^0 [29, 39]. The higher φ' value (40^0–45^0) provides higher stability to embankments [37]. WRP slag exhibits very good shear strength properties. Very high shear strength parameters of WRP slag both in the low

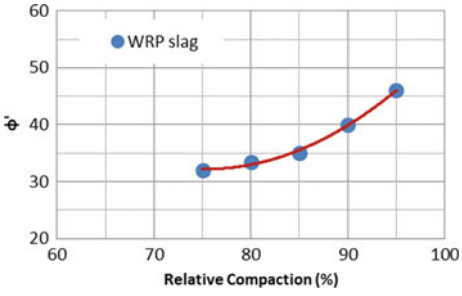

Fig. 6 Angle of internal friction for WRP slag under different relative compaction

Table 5 Consolidation characteristics of WRP slag

Parameters	WRP slag
Initial void ratio (e_0)	0.580
c_c	0.098
m_v	5.59×10^{-5} (m^2/kN)
c_v	1.79×10^{-3} (m^2/sec)

density (75% RC) and high density (95% RC) under saturated conditions favor their use in the geotechnical applications like construction of embankments, as a subgrade material and structural fill for retaining walls.

4.4 Consolidation Characteristics

To estimate the settlement of structures placed on WRP slag embankments, fills and as a subbase material, compressibility characteristics are important. Table 5 presents the consolidation characteristics of WRP slag. The e –log (σ') curve of WRP slag is similar to sand, pond ash, and other granular materials. It is very difficult to note the initial time—compression readings during the consolidation test, which is most important to determine the coefficient of consolidation (c_v). Hence the c_v value is calculated from Eq. (3) from permeability (k) and coefficient of volume change (m_v) values measured from consolidation test.

$$c_v = k/(m_v \gamma_w) \tag{3}$$

Consolidation test results reveal that WRP slag has a low initial void ratio and low compression index with high coefficient of consolidation. The low compression index and high rate of consolidation of WRP slag is favorable for its use as an embankment material and reclamation fills.

4.5 Permeability

The permeability values reported in literature and present study are presented in Table 6. The WRP slag being coarse-grained and devoid of fines have a high coefficient of permeability compared to steel slag available in the literature. The high k-value of WRP slag indicated that it is an appropriate material for the construction of subgrade and embankment.

Table 6 Permeability values of WRP slag and steel slag

Permeability k (cm/sec.)	References
1.0×10^{-4}	Present study
10^{-3}	[29]
$1–10^{-2}$	[30]
10^{-4}	[43]
3×10^{-3}	[42]
$7 \times 10^{-6}–10^{-10}$	[9]
$1.4 \times 10^{-6}–4.5 \times 10^{-9}$	[7]
$<10^{-9}$	[8]
10^{-8}	[47]

5 Utilization of WRP Slag for Embankment and Dyke Construction

The existing study aims to perceive the impact of relative compaction on stability of dykes. The waste material is dumped in the disposal area by trucks. These materials are spread in uniform layers through scrapers. The materials will be compacted to maximum density through vibratory rollers. To optimize the cost of construction of dykes the effect of relative compaction on stability is studied. The slope stability analysis was carried out with the help of GEO5 software. The following parameters are considered for the design of dykes. Table 7 presents the subsoil property and layer thickness considered for analysis.

5.1 Problem Variables

Following are the variables used in various cases of analysis:

a. Construction materials
   Materials considered for the construction of dykes is WRP slag.
b. Slope
   Embankment with side slopes 1H: 1.5V and 1H: 2V, respectively
c. Berm width and height of dyke
   Berm widths 3m and 4.5m were used for analysis and the maximum height of dyke considered was 54m.

Table 7 Subsoil profile of the WRP slag embankment under the current study

Type of soil	Thickness (m)	γ_b (kN/m^3)	c' (kPa)	Φ' (degrees)
Sandy soil	10	18	0	30

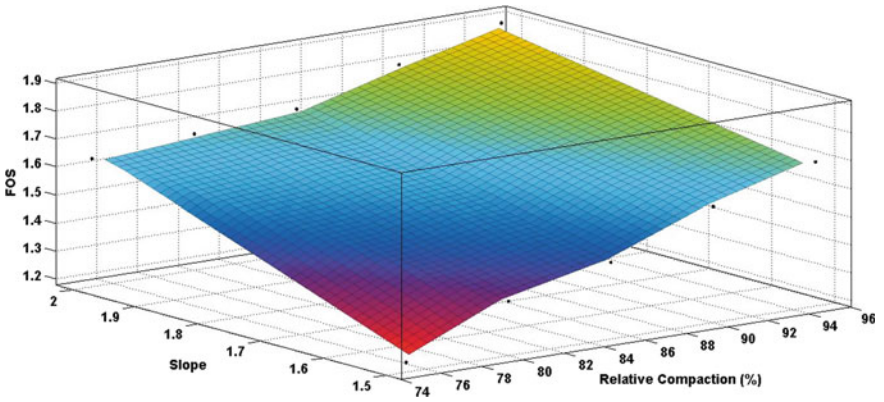

Fig. 7 Response Surface of FOS under the influence of Slope and RC -3D

d. Effect of phreatic line

To evaluate the effect of position of phreatic line on the stability of raised dyke's analysis is carried out under the following assumed conditions.

- Water table at existing ground level
- Water table 2.0 m above ground level.

Figure 7 shows the FOS of the dyke with respect to side slopes and relative compaction. The minimum factor of safety of the dyke at 75% relative compaction is 1.21 and 1.63 with the side slopes of the embankment are 1H: 1.5 V and 1H: 2 V, respectively. WRP slag being cohesionless material, it is easily eroded by wind and water. The embankment/dyke should be covered with soil of 1 m to 1.5 m thickness and the final sloping surface should be treated with turfing.

6 Pavement Composition and Its Analysis with IITPAVE

From the obtained values of soaked CBR of WRP slag, which varied from 8.82 to 26.71 with Relative Compaction being varied from 85 to 95% respectively, the composition of flexible pavement consisting of subgrade, granular layers, and bituminous layers was designed with WRP slag as a subgrade material using IRC 37–2018 guidelines for traffic level of 50 msa. The pavement composition was analyzed for tensile and compressive strains as well as for deflections at critical points in a pavement structure with vehicular loads (LL) by linear elastic layered theory using IITPAVE software. Thickness of each layer of designed pavement for both the cases of Relative compaction are presented in Table 8.

According to CBR and design traffic values, thickness of each layer was estimated from the graphs provided in IRC 37–2018. The M_R value (Resilient modulus) of WMM, GSB, and subgrade was derived from the equations given in IRC [50]. For

Table 8 Pavement composition with WRP slag as a subgrade material

Type of layer	Thickness of layer for subgrade compacted at 85% RC (mm)	Thickness of layer for subgrade compacted at 95% RC (mm)
Granular subbase (GSB)	200	200
Granular base (WMM)	250	200
Base/binder course (DBM)	110	65
Surface course (BC)	40	40

roads, design traffic between 20 and 50 msa, VG40 bitumen as a BC layer is recommended as per IRC guidelines. DBM with VG40 bitumen was used for base/binder course confirming IRC specifications. As per Indian conditions, an average annual pavement temperature of 35 C is considered for the present study, therefore indicative value of M_R value of bituminous mix was taken from the table given in IRC specifications for BC and DBM with VG40 bitumen. Allowable Vertical Compressive Strains (ε_v) and Allowable Horizontal Tensile Strains (ε_t) were calculated from the equations given in IRC 37–2018.

The value of Poisson's ratio for bituminous, granular (WMM and GSB), and subgrade layers was taken from IRC specifications for the inputs of IITPAVE and 80 kN standard axle load (wheel load) of vehicle and 0.56 MPa tyre pressure was assumed as per IRC [50].

The results obtained from IITPAVE software are presented in Table 9, which shows that $\varepsilon_{t\text{-actual}}$ at the base of BC layer and $\varepsilon_{v\text{-actual}}$ at the upper surface of subgrade layer are reduced with increase in CBR value of WRP slag resulted from increased relative compaction. These strains are within the allowable limits calculated using IRC guidelines. Figure 8a, b shows the Pavement Composition for subgrade compacted at 85% RC and 95% RC, respectively.

In the present study, WRP slag has only been used as a subgrade material to design a pavement composition, though it can be used for a granular base and subbase layer with cementitious materials and suitable stabilizers. For which, further research is under progress.

7 Conclusions

The high shear strength, high CBR values, and good drainage characteristics of WRP slag favor its utilization in various geotechnical engineering practices such as, as a fill material in embankment, structural fill material for retaining walls, dykes, and pavement material for subgrade. Due to its high permeability and well-graded, WRP slag can be used as a fill material behind retaining walls. Dykes constructed with WRP slag give a good factor of safety even at a medium compacted state. The low compression index and high rate of consolidation of WRP slag is favorable for its usage in embankment construction and in reclamation fills. WRP slag being

Table 9 Allowable and actual strains

Relative compaction (%)	$\varepsilon_{v\text{—allowable}}$(micro-strain)	$\varepsilon_{v\text{-actual}}$(micro-strain)	$\varepsilon_{t\text{- allowable}}$ (micro-strain)	$\varepsilon_{t\text{-actual}}$ (micro-strain)
85	472	289	239	177
95	472	232	239	165

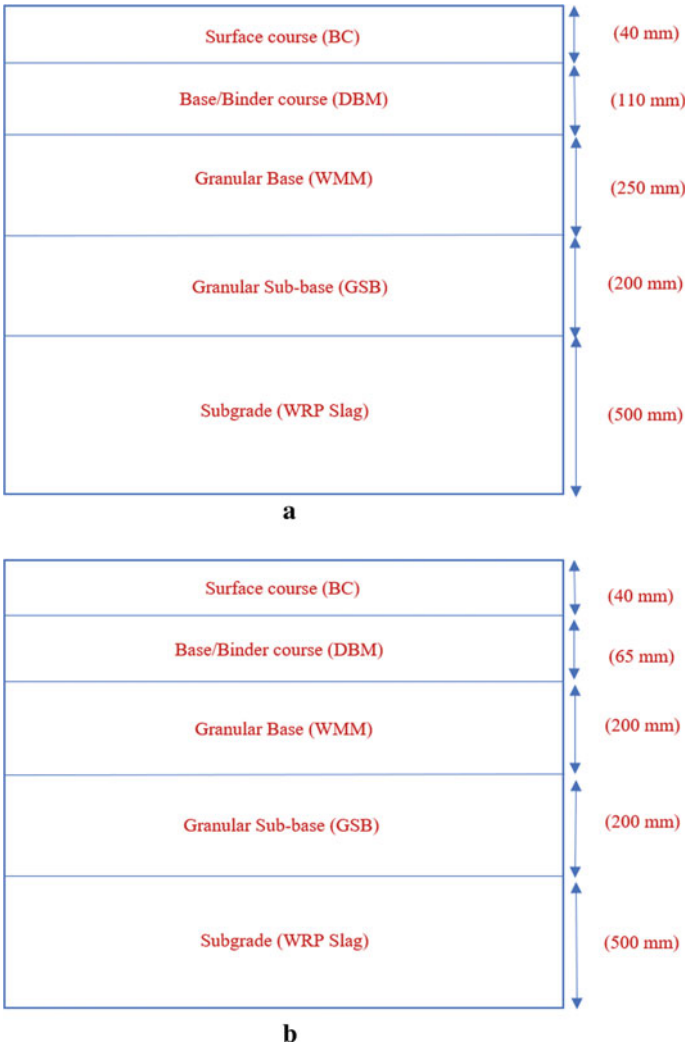

Fig. 8 **a**. Pavement composition for subgrade (WRP slag) compacted at 85% RC. **b**. Pavement composition for subgrade (WRP slag) compacted at 95% RC

cohesionless material, the side slopes of the embankment should be covered with local soil and turfing should be done to prevent erosion due to wind and rain runoff. Correlations have been developed between CBR versus RC and φ versus RC. Based on field density, these correlations can be effectively utilized to find the CBR and φ. Road Pavement constructed with WRP slag as a subgrade material assists in reducing thickness of upper layers of the pavement and thereby helps in reducing depletion of natural resources.

References

1. Jianlong G, Yanping B, Min W (2018) Steel slag in China: treatment, recycling, and management Beijing, China. Waste Manage 78(2018):318–330
2. Ministry of Steel, India (2018) National Institution for Transforming India (NITI Aayog), Strategy Paper on Resource Efficiency in Steel Sector through Recycling of Scrap and Slag; FinalR4
3. U.S. Geological Survey (USGS) (2021) Mineral Commodity Summaries, Iron and Steel slag, mcs-2021
4. Nippon Slag Association: Iron and Steel slag statistics, Production and Uses of Steel Slag in Japan; (2017 FY)
5. Ter Teo P et al (2020) Assessment of electric arc furnace (EAF) steel slag waste's recycling options into value added green products: a review, Multidisciplinary Digital Publishing Institute (MDPI), Metals 2020, 10:1347
6. Hosseini S, Soltani SM, Fennell PS, Choong TSY, Aroua MK (2016) Production and applications of electric-arc-furnace slag as solid waste in environmental technologies: a review. Environ Technol Rev, Taylor & Francis 2016. https://doi.org/10.1080/21622515.2016.1147615
7. Andreas L, Herrmann I, Lidstrom- Larsson M, Lagerkvist L (2005) Physical properties of steel slag to be reused in a landfill cover, in: Tenth international waste management and landfill symposium, Cagliari, Italy, pp 1–7
8. Herrmann I, Anfreas L, Diener S, Lind L (2010) Steel slag used in landfill cover liners laboratory and field tests. Waste Manage Res 28(12):1114–1121
9. Diener S, Andreas L, Herrmann I, Lagerkvist A (2007) Slag used as landfill cover liner material. In: Proceedings Sardina, eleventh international waste management and landfill symposium, Cagliari, Italy, pp 1–5
10. Motz H, Geiseler J (2001) Products of steel slags an opportunity to save natural resources. Waste Manage 21(3):285–293
11. Sofilic T, Maldenovic A, Sofilic U (2010) Characterization of the EAF steel slag as aggregate for use in road construction. Chem Eng Trans 19:117–123
12. Sofilic T, Sofilic U, Brnardic I (2012) The significance of iron and steel slag and by-product for utilization in road construction. In: 12th international foundrymen conference, Opatija, Croatia, pp 419–436
13. Hunt L, Boyle GE (2000) Steel slag in hot mix asphalt concrete final report, research project no. 511, Oregon Department of Transportation, Oregon
14. Ye G, Burstrom E, Fallman AM (1995) Utilization and stabilization of steelmaking slags. Survey, AFR-Report 57, Stockholm
15. Omer O, Isa Y, Ozgur M (2007) Strength properties of concrete incorporating coal bottom ash and granulated blast furnace slag. JWaste Manage 27(2):161–167
16. Maslehuddin M, Sharif AM, Shameem M, Ibrahim M, Barry MS (2003) Comparison of properties of steel slag and crushed lime stone aggregate concretes. Constr Build Mater 17:105–112
17. Ameri M, Shahabishahmiri H, Kazemzadehazad S (2012) Evaluation of the use of steel slag in concrete. In: 25th ARRB conference—shaping the future: linking policy, research and outcomes, Perth, Australia, pp 1 – 9
18. Emery JJ (1982) Slag utilization in pavement construction. extending aggregate resources ASTM, STP 774 American society for testing and materials, pp 95–118
19. Motz H (2008) Utilization of steel slag in Germany – Technical and environmental aspects, II Workshop "Sustainability of Steel Sector" – Case Studies: By-product Management, Sao Paulo, Brasil
20. Nicolae M, Vilciu I, Zaman F (2007) X-ray diffraction analysis of steel slag and blast furnace slag viewing their use for road construction, UPB Svi Bull Series B 9(2):99–108
21. Wu S, Xue Y, Chen QY (2007) Utilization of steel slag as aggregates for stone mastic asphalt (SMA) mixtures. Build Environ 42:2580–2585

22. Xue Y, Wu S, Hou H, Zha J (2006) Experimental investigation of basic oxygen furnace slag used as aggregate in asphalt mixture. J Hazard Mater B138 :261–268
23. Ahmedzade P, Sengoz B (2009) Evaluation of steel slag coarse aggregate in hot mix asphalt concrete. J Hazard Mater 165(1–3):300–305
24. B Farrand J Emery 1995 Recent improvements in the quality of steel slag aggregate Transp Res Rec 1468 137 141
25. Kamon M, Katsumi T (1994) Civil engineering use of industrial waste in Japan, in Balasubramaniam AS et al. (eds) Development in geotechnical engineering, Balkema, Rotterdam, pp 265–278
26. Shi C (2004) Steel slag—its production, processing, characteristics, and cementitious properties. ASCE J Mater Civ Eng 16(3):230–236
27. Shen W, Zhou M, Ma W, Hu J, Cai Z (2009) Investigation on the application of steel slag-fly ash phosphor gypsum solidified material as road base material. J Hazard Mater 164(1):99–104
28. Proctor DM, Fehling KA, Shay EC, Wittenborn JL, Avent C, Bigham RD, Connolly M, Lee B, Shepker TO, Zak MA (2000) Physical and chemical characteristics of blast furnace, basic oxygen furnace, and electric arc furnace steel industry slag, Environ Sci Technol 1576–1582
29. Ghionna VN, Pedroni S, Tenani P, Vegg S (1996) Geotechnical investigation on steel slags mixtures for landfills embankments. Environmental Geotechnics, Balkema, Rotterdam, pp 709–714
30. Takahasi K, Komuro T, Horinouchi Y (1996) Properties and usage of iron and steel slag. Environmental Geotechnics, Balkema, Rotterdam; 915–920
31. Sloot Van der HA (1996) Developments in evaluating environmental impact from utilization of bulk inert wastes using laboratory leaching tests and field verification. Waste Manage 16:65–81
32. Fallman AM, Hartlen J (1996) Utilization of electric furnace steel slag in road construction. Environmental geotechnics, Balkema, Rotterdam; 703–708
33. Milacic R, Zuliani T, Oblak T, Mladenovic A, Ancar J (2011) Environmental impacts of asphalt mixes with electric arc furnace steel slag. J Environ Qual 40(4):1153–1161
34. Das B, Prakash S, Reddy PSR, Misra VN (2007) An over view of utilization of slag and sludge from steel industries. Resour Conserv Recycl 50(1):40–57
35. Chaurand P, Rose J, Briois V, Olivi l, Hazemann, JL, Proux O, Domas J, Botterro JY (2007) Environmental impacts of steel slag reused in road construction: a crystallographic and molecular (XANES) approach. J. Hazardous Mater 139(3):537–542
36. Chang-long W, Yan-Ming QI, Jin-Yun H (2008) Experimental study on steel slag and slag replacing sand in concrete. International Workshop on Modeling Simulation and Optimization, IEEE Computer Society, pp 451–455
37. Barisic I, Dimter S, Netinger I (2010) Possibilities of application of slag in road construction. Technical Gazette 17(4):523–528
38. Ziemkiewicz P (1998) Steel slag: applications for AMD control, in: Proceedings of the conference on Hazardous Waste Research, pp 44–62
39. Khan ZA, Malkawi RH, Al-Ofi KA, Khan N (2002) Review of steel slag utilization in Saudi Arabia. In: 6th Saudi engineering conference KFUPM, Dhahran 3:369–381
40. FHWA – NHI – 00 – 043 (2001) Mechanically stabilized earth walls and reinforced soil slopes design and construction guidelines, U.S. Department of Transportation Federal Highway Administration
41. BS 8006 – 1 (2010) Code of practice for strengthened/reinforced soils and other fills. British Standards
42. Havanagi VG, Sinha AK, Arora VK, Mathur S (2012) Waste materials for construction of road embankment and pavement layers. Int J Environ Eng Res 1(2):51–59
43. Federal Highway Administration: User guidelines waste and byproduct materials in pavement construction, Publication No: FHWA- RD-97–148
44. Emery J (1984) Steel slag utilization in asphalt mixes. In: Proceedings of Canadian technical asphalt association, Ontario L6T 4Vi, Canada
45. ASTM D 1883: Standard test method for CBR (California Bearing Ratio) of laboratory compacted soils. ASTM International, USA

46. www.asa-inc.org.au. A guide to the use of iron and steel slag in roads
47. Joshi VK, Arenicz RM Use of slag—a direct benefit to our environment, National slag association. MF 203 – 11, pp 1–11
48. George W, Thompson T (2011) Slag use in highway construction—the philosophy and technology of its utilization. Int J Pavement Res Technol 4(2):93–103
49. ASTM D 3080: Standard test method for Direct shear test of soils under consolidated drained conditions. ASTM International, USA
50. IRC:37–2018: Guidelines for the Design of Flexible Pavements, (Fourth Revision); Indian Roads Congress, India; (November, 2018)

Review of Literature on Design of Rubble Mound Breakwaters

P. K. Akarsh and Babloo Chaudhary

Abstract Breakwaters are offshore structures constructed to protect the coastal and port structures from uncertain and extreme wave conditions. It creates tranquility in and around the harbor side for smooth transactions of ships. Depending upon the availability of rocks, depth of water, geotechnical nature of the sea bed, and its functional requirement, breakwaters are classified as rubble mound breakwaters, caisson type, and composite breakwaters. Rubble mound is a flexible, heterogeneous, trapezoidal structure consisting of quarried rocks in the core and artificial armor as a protection cover. Armor units at the outer layer absorb most of the energy and underlayers prevent transmission of the wave energy. The main advantage of the rubble mound is its failure is not immediate and can be repaired by adding the stones in the flushed-out part. More than 50% of breakwaters constructed around the world are of rubble mounds. Looking at its importance for coastal structures, this paper gives an overview of the basic aspects of rubble mound breakwaters, design considerations, and its failure conditions. The design of rubble mound breakwaters include hydraulic stability of it against wave actions, structural components design, and geotechnical considerations. The common modes of rubble mound failure are hydraulic damage, erosion of subsoil, slope failures, toe erosion, overtopping, liquefaction of subsoil, crest erosion, and leeside damage. The failure of rubble mound breakwater at Ergil fishery port, Turkey due to Kocaeli earthquake of 1999 has been explained to support this part.

Keywords Breakwater · Rubble mound breakwaters · Concrete armor units · Wave action · Liquefaction

P. K. Akarsh (✉) · B. Chaudhary
Department of Civil Engineering, National Institute of Technology, Surathkal, Karnataka, India
e-mail: akarshpk00784@gmail.com

B. Chaudhary
e-mail: babloo@nitk.edu.in

L. Nandagiri et al. (eds.), *Recent Advances in Civil Engineering*, Lecture Notes in Civil Engineering 256, https://doi.org/10.1007/978-981-19-1862-9_50

1 Introduction

Due to the effect of the wind, waves are generated in the mid-sea and traveled toward the coast. The waves traveling toward the coast carry an enormous amount of energy and dissipate partly by action of wave breaking, current and tides generation, changes in the water level, turbulence, etc., and the rest of the wave energy is neutralized by hitting against coastal shore area [31]. The coastal structures like ports/harbors are subjected to vigilant wave actions throughout the year and need to be designed to dissipate these forces. They are meant to protect the ships from tides, currents, and waves, for loading and unloading of cargo goods, for mooring and berthing activities of ships. To have smooth transactions of ships and to protect the ports from these wave actions, a structure called breakwater is constructed.

An offshore structure should be designed to minimize both the excitation forces associated with the wind, wave, current, seismic, and the response of the structure to these excitation forces [8]. A breakwater is an offshore structure constructed to have tranquil conditions in and around the harbor location. Breakwaters are either completely offshore (detached breakwaters) or it may be extending into the water to protect the ports, anchorages, shore areas from the devastating waves, currents, and tsunamis. Breakwaters are constructed in pairs and there will be opening in between for vessels' movement. They are usually parallel to the shore and perpendicular to the waves, thus helping in absorbing the wave energy before it reaches to the shoreline [12, 25]. For ex, Fig. 1 shows the longest breakwater in the world measuring 14.523 km in length constructed at Al-Faw Grand Port in Iraq and Fig. 2 shows the breakwater at Alexandroupoli port, Greece.

The breakwaters are to be designed to withstand critical random loads. They should be stiff enough to keep lateral displacements, overturning moments, vertical

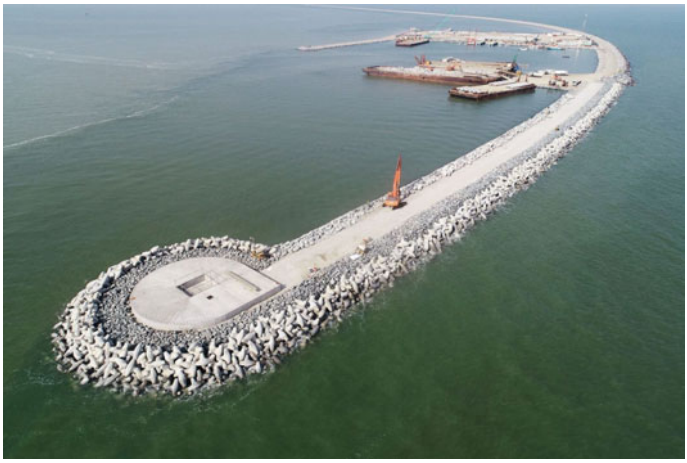

Fig. 1 Breakwater at Al-Faw grand port in Iraq-longest breakwater in the World [1]

Fig. 2 Breakwater constructed at Alexandroupoli port, Greece [2]

settlement within the prescribed limits given by relevant codes of practice. Depending upon the availability of rocks, depth of water, geotechnical nature of sea bed and functions, breakwaters are mainly classified into three types, (1) Rubble mound breakwaters, (2) Vertical/wall type/caisson breakwater and (3) Vertical wall on rubble base or composite breakwaters. Occasionally floating breakwaters can also be provided as per the design requirement. The rubble mound breakwaters consist of granular material in their core and are protected by armor units. The vertical breakwaters consist of masonry concrete/concrete/sheet steel plate filled with gravel laid on rip rap rocks as toe protection. The composite breakwaters are combinations of both rubble mound and caisson type used in extreme conditions and are costly in nature. Breakwater usage depends on many conditions, forex, if the natural rocks are available within 30–60 km, rubble mound breakwaters are preferred rather than other types. Likewise, in deep waters (depth greater than 15 m), it's advisable to use composite breakwaters to save the material rather than rubble mound alone. In soft foundations and likely to settle conditions, rubble mound is recommended [6, 39].

2 Rubble Mound Breakwaters

Rubble mound is a flexible heterogeneous assemblage structure of natural rubble consisting of quarried rocks in the core and natural or artificial armor as a protection cover. The word rubble means riprap and rock armor. It's generally trapezoidal in shape with flatter slopes on its seaside and steeper slopes on the harbor side with slope 1:1.33–1:2 [6]. In any plan, rubble mound breakwaters consist of two sections, trunk, and head sections. The head section is more flat than the trunk section with slopes 1:3–1:5. Generally, the rubble mound consists of protective armor units, crest

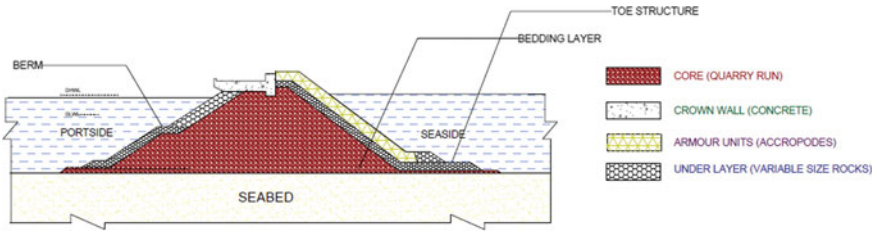

Fig. 3 Typical cross-section of Rubble mound breakwater provided with berm

provided with concrete crown wall, one or two under layers made up of granular material, berms, and wide -graded core as superstructure and Toe and bedding layer as foundation structures. The typical cross-section of rubble mound breakwaters is shown in Fig. 3.

The superstructure depends on wave properties and the foundation depends on sea bed properties. To provide geotechnical stability against rolling down of armor units and scouring protection, toe structures are needed to be provided. To increase the stability of wave energy dissipation and for the usage of smaller gradation stones, berms are generally provided. Depending on the sea bed conditions, geotextiles are used in rubble bound to decrease the vertical settlements and to prevent the erosion of core materials. The different forms of rubble mound breakwaters as per CIRIA C683 [6] have shown in Fig. 4. In India, rubble mound breakwaters are commonly used due to its easier construction, the requirement of smaller construction equipment, availability of materials, and its maintenance. These are economic if the depth of water is shallow and costly in deep waters due to the requirement of construction material. The main advantage of rubble mound is the failure is not sudden and can be repaired by adding the stones in the flushed-out part.

Rubble mound dissipates the wave energy mostly by absorbing (about 60–70%) and partly by reflecting (about 30–40%) in contrast with other types. Armor units at the outer layer absorb most of the energy and inner underlayers prevents transmission of the wave energy. The wave energy generated will be dissipated through the voids of these breakwaters and there might be wave run-up by partial reflection [36]. These rubble mounds are similar to earthen dams (e.g., estimation of hydrodynamic pressure on the embankment slopes) and yet there are some differences. In many of the situations, breakwaters are placed on the wet, permeable, and soft foundations, whereas dams are constructed on dry, impermeable, and firm foundations. Dams hold water on only one side, but these breakwaters are on both sides. Breakwaters can allow limited transmissions, whereas dams are restricted to allow any of the transmissions. In rubble mound breakwaters, approx. 4–5% damage/failure is allowed due to waves and wind load but for dams, failure is not allowed. The granular core materials used for the breakwaters are also different from the dams [14, 15, 26]. According to the International breakwater directory maintained by the Delft University of technology and H. R. Wallingford, the rubble mound breakwaters constitute approximately, 57% of total breakwaters constructed as shown in Fig. 5. However, the numbers are

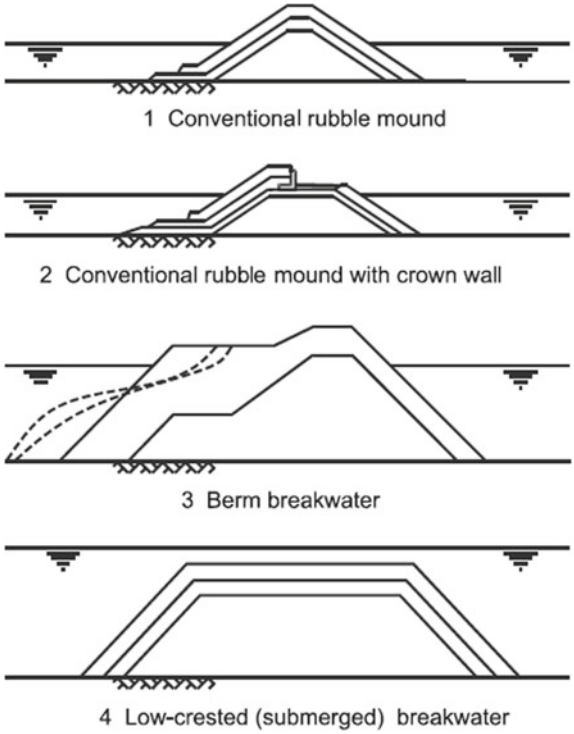

Fig. 4 Forms of rubble mound breakwaters [6]

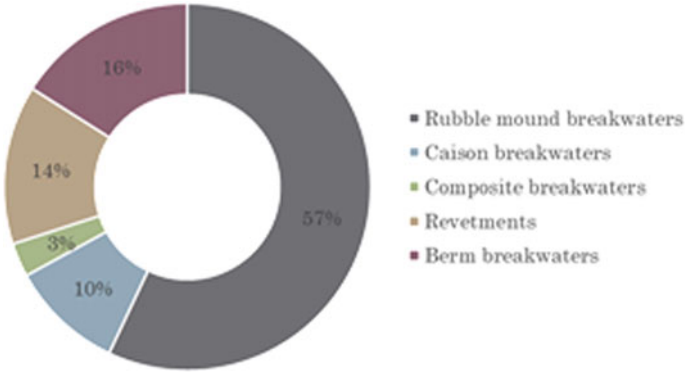

Fig.5 Breakwater proportion around the world as per international breakwater directory [3]

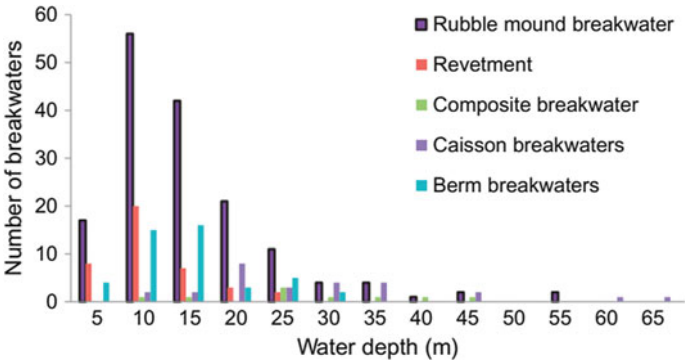

Fig. 6 Number of breakwater for various water depth as per International breakwater directory [3]

likely to be more than this and mostly not reported. From Fig. 6, about 70% of the breakwaters constructed are rubble mounds of heights ranging from 6 to 20 m.

3 Design Considerations

The design of rubble mound generally requires hydraulic considerations, structural parameters, and geotechnical aspects. The rubble mound shall be designed well enough to perform in its ultimate limit state or exceedance of serviceability. While designing, loads like dead load (weight of armor, core, under layers, etc.), live load (due to movement of vehicles), hydrodynamic loads (waves and currents with different amplitude, wavelength, frequency, and wave height), seismic forces, frictional resistance between the members, buoyancy force, impact loads, loads causing settlement, etc., shall be considered for the longevity performance of breakwaters.

3.1 Wave Action Study

The wave generated by the wind is characterized by the wave height, length or period, maximum water levels due to tides or storm surges, predicted sea level rises, wave-induced currents. The waves which are away from the generation point are called swell or long-crested waves and waves which are influenced by the wind are called irregular or short waves. As the waves approach the shore, the speed and length decrease but the height increases due to energy conservation. This is called "Wave Shoaling" as shown in Fig. 7. Also, waves travel slower in shallow water comparable to deep water causing "Wave bending" [30].

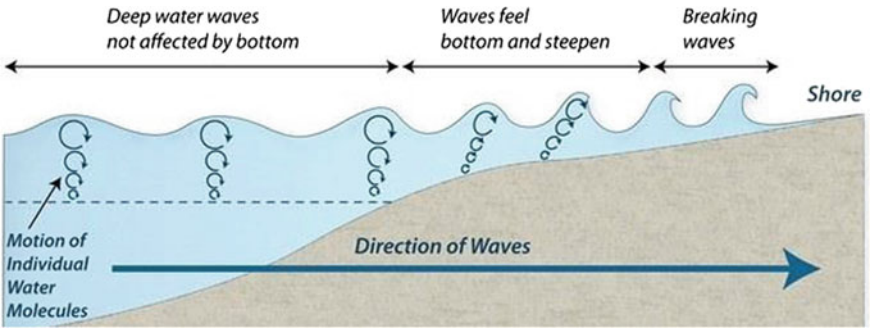

Fig. 7 Wave Shoaling [30]

1. **Wave height**

While deciding the wave height, it's necessary to consider whether the wave is breaking at the structure or before it reaches the structure. If the water depth at the level of toe is sufficient for the design wave to sustain, its non-breaking wave condition. If the waves are breaking at the toe, the armor shall have the stability to withstand the breaking wave condition. The breaking of waves depends on the depth of water and wave steepness. If the steepness index, H/L_o is greater than 1/7, the breaking wave takes place in case of deep sea. Where, H is design wave height and L_o is wavelength. The breaking wave height or maximum wave height can be calculated by using eq. (1). The design height of wave is significant wave height instead of maximum wave height for rip rap rubble mound. The significant wave height (H_s) is the one-third of the highest waves ($H_{1/3}$) and can be calculated by using eq. (2). In some cases, the avg. of highest of 10% of all the waves (H_{10} =1.27 H_s) can also be used as conservative wave height [24]. These wave heights are useful in finding the weight of the armor. The significant wave period, T_s is another parameter that would be 5–20 s.

$$H_{\max} \text{ or } H_b = 0.78\, d_s \tag{1}$$

where, 0.78= breaking wave coefficient
d_s= depth of water at the structure.

$$H_s = H_{\max}/1.6 \text{ to } 1.8 \tag{2}$$

A parameter called the surf similarity factor ξ_m, which is linked to wave steepness can be found by using Eq. (3). To distinguish the surging and plunging wave, Vander Meer [43] has given the threshold critical value given in Eq. (4)

$$\xi_m = \tan\theta/\sqrt{s_m} \tag{3}$$

where, wave steepness, $s_m = 2\pi.H_s / gT_s^2$

T_s= significant wave period.

$$\xi_m = \left(6.2P_b^{0.31}\sqrt{\tan\theta}\right)^{\frac{1}{(P_b+0.5)}} \tag{4}$$

where, P_b= Overall porosity of breakwater

2. **Wave run-up and overtopping**

The wave action on the rubble mound causes the wave to move in the vertical range usually more than the incident wave height. The upper extreme level gives the wave run-up and it's comparable with the static water level. It's generally used to fix the crest level, can be taken as the upper limit for overtopping criteria or to design other structural components. The increase in sea level, increases wave run-up. Thus all the dependent parameters for the design [17]. The run-up value according to Van der Meer [46], for surf similarity parameter, ξ_p<2, given in Eq. (6) and for ξ_p>=2 given in Eq. (5).

$$R_{2\%} = 1.5\, H_s r_f \xi_p \tag{5}$$

$$R_{2\%} = 3\, H_s r_f \tag{6}$$

[46] where,

$R_{2\%}$= run-up exceeded by 2% of the wave

r_f = friction factor

When the waves are in extreme condition, it overpasses or overtops the crest level. Usually, breakwaters are designed to have some amount of overtopping discharge during storm conditions. It's defined by the dimensionless parameter, Q using overtopping discharge (q) and it's given by Eq. (7). The overtopping also depends on the slope angle and wave steepness.

$$Q = q/\left(\sqrt{gH_s^3}\right) \tag{7}$$

3.2 Armor Unit Stability and Thickness

Armor units are used in outer layers and on slopes of rubble mound breakwaters. To control the damage or failure of rubble mound from the wave forces, the interlocking packing of armor units is very important. Up to 5 m water depth natural stones are beneficial as they are cheaper, but above 5 m water depth, the artificial concrete armor units are more advantageous in dissipating the wave energy. The stability of rubble

mound components mainly depends on the stability of the armor units placed on the seaside. In order to have sufficient stability to withstand the wave action, armor should have minimum weights prescribed by codes of practice to account for the uncertainty of wave forces coming on the individual armor unit. To determine the weight of the armor, the empirical formula given by Iribarren [23], Hudson's [22], and Van der Meer's [41, 46] can be used. Generally, Hudson's formula is widely used by Engineers. Hudson et al. conducted many experiments at the US army corps of Engineers and obtained an Eq. (8) shown below. In his experiment, he considered non-breaking and non-overtopping monochromatic waves. He has not considered the incident wave period, duration of the storm, permeability, and allowable damage level of armor.

$$W = \frac{wH^3}{K_D(S_r - 1)^3 \mathrm{Cot}\theta} \tag{8}$$

where

W = weight of the armor units in kg.
w = unit weight of armor in (kq/m^3).
H_s = Design wave height (m).
Sr = specific gravity of armor (2.65-quarry stones and 2.4-concrete).
Θ = Slope angle of the breakwater.
K_D = Stability Co-efficient.

Nowadays, Van der Meer's formula [41, 42] is getting attention from the researcher as he considers significant wave height. He used two different equations based on the plunging and surging breakers to define the stability number (N_s) shown in Eqs. (9) and (10) respectively.

For plunging breakers,

$$N_s = (H_S/\Delta_a D_a) = C_s . P_b^{0.18} \left(S_a/\sqrt{N_w}\right)^{0.2} \xi_m^{-0.5} \tag{9}$$

For surging breakers,

$$N_s = (H_S/\Delta_a D_a) = C_s . P_b^{-0.13} \left(S_a/\sqrt{N_w}\right)^{0.2} \sqrt{\cot\theta} . \xi_m^{P} \quad {}_b \tag{10}$$

where

C_s, C_p = Surging and plunging water co-efficient depends on depth of water resp.
Δ_a = relative underwater density of armor.
N_w = Number of waves acting on the breakwater.
D_a = Nominal diameter of armor in meters.
S_a = Armor damage.

Table 1 Armor type, shape and its contribution

Placement pattern	Number of layers	Shape	Main contribution		
			Self-weight	Interlocking	Friction
Random	Double layer	Simple	Cube, Modified cube, Antifer	–	–
			Tetrapod, tripod		–
		Complex	–	Dolos	–
	Single layer	Simple	Cube	–	Cube
		Complex	–	Accropode, Core-Loc, X-bloc	–
Uniform	Single layer	Simple	Haro	–	Seebee, Haro
		Complex	–	–	Cob, Tribar, diode

Weight of the armor unit (W) depends on the significant wave height (H_s) and weight of the other layers depends on the W. Here stability coefficient, K_D depends on the type of armor unit, interlocking ability, roughness, shape, etc., e.g., the K_D value for tetrapod and rough angular stone has 8 and 4, respectively, when it's subjected to non-breaking waves [38]. The thickness of the armor unit and packing density (no. of armors required for the unit surface area) are shown in Eqs. (11) and (12) ,respectively. The thickness of the armor shall be a minimum of 300–500 mm. If the porosity is less, the waves will be reflected. So, it's adjusted between 35 and 55%.

$$T = n.K_{\Delta}(W/w)^{2/3} \tag{11}$$

$$(N/A) = n.K_{\Delta}(W/w)^{2/3}(1 - P) \tag{12}$$

where,

n= No. of armor unit layers
K_{Δ} = Layer coefficient to take care the interlocking errors.
W = Weight of armor in kg.
w = unit weight of armor in kg/m^3.
A = Surface area.
N = Number of units.
P = Avg. porosity of armor layer in percentages.

Different artificial concrete armor units like tetrapod (France, 1950), dolos (South Africa, 1963), accropode (France, 1980), core-loc (USA, 1996), cubipod (Spain, 2006) etc., have shown in Fig. 8, placement and contribution have shown Table 1 and the parameters considered for their design is shown in Table 2. In India and most of the countries, tetrapods are commonly used. Recently, accropodes are getting

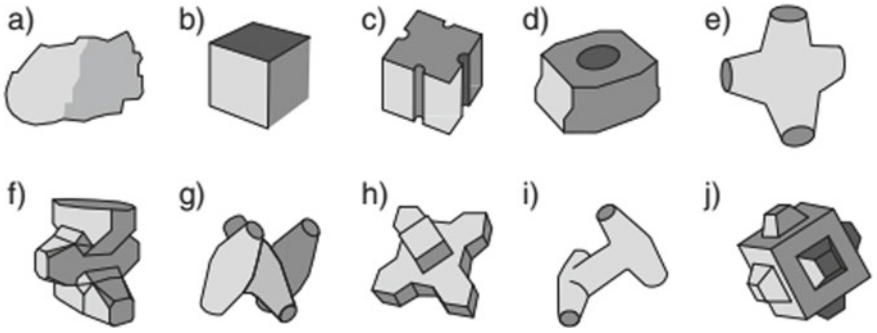

Fig. 8 Concrete armor units: **a** Rock, **b** Cube, **c** Antifer, **d** Haro, **e** Tetrapod, **f** Accropode, **g** Core-loc, **h** X-bloc, **i** Dolos and **j** Cubipod (after Molines and Medina [27])

Table 2 Comparison of design parameters of different armor units [43, 44]

Parameters	Accropodes	Core-Loc	Tetrapod	Cube	Cube
Number of layers	1	1	2	2	1
K_D for breaking waves	12	16	7	7	7
Slope	1:1.33	1:1.33	1:1.5	1:1.5	1:1.5
Stability number, $\mathrm{Hs}/\Delta D_n = N_s$	2.5	2.8	2.2	2.2	2.2
Damage initiation N_{od}	0	0	0.5	0.5	0
Damage %	0	0	5	5	0
Packing density, ϕ	0.61	0.56	1.04	1.17	0.70
Concrete/m^2 on slope	0.182 $\mathrm{H_s}$	0.148 $\mathrm{H_s}$	0.350 $\mathrm{H_s}$	0.370 $\mathrm{H_s}$	0. 236$\mathrm{H_s}$

attention in India as they save the overall cost of construction, require only single layer placement, and provide maximum interlocking [7]. Many researchers worked on stability of different armors like Suh and Kang [32], Çelikoğlu and Engin [9] worked on stability of tetrapods, Bakker et al. [4] worked on the hydraulic performance of X-bloc armors, Holtzhausen and Zwamborn [21] compared the stability of accropode with dolosse, Cevic et al. [10], Simpalean [30] used core-locs to check the stability given by them for structures, Martín and Medina [19] worked on heterogeneous packing and hydraulic stability of Cube and Cubipod armor units and many more. According to Van der Meer [40, 43], the armor damage is defined by factor S_a, related to erosion area (A_e) and nominal armor diameter (D_a) given by Eq. (13). He recommends S_a shall be a minimum of 2 for zero damage.

$$S_a = A_e / D_a^2 \tag{13}$$

3.3 Crest Width and Crest Elevation

The crest elevation depends on the high water level criteria, wave transmission, and return period. If this structure is constructed by the land equipments, at least the height of the crest should be 1 m above design high water level. The crest width depends on the allowable overtopping and construction requirement. The crest width and crest elevation are properly fixed, so that the overtopping and wave run-up shall not cause any damage on the harbor side. Its calculated based on Eq. (14). The crest width shall be a minimum width of three to four armor stones. A crown wall of minimum of 2–4 m is provided on the crest if pedestrians or vehicles need an access. The provision of crown wall is logically correct, as it reduces the amount of armor unit, it gives access for repair and maintenance, and supports berthing. According to Palmer and Christian [29], the crown wall shall not extend above the level of armor to subside the force on superstructure and cut-off wall shall be plunged into the core.

$$B = n.K_{\Delta}(W/w)^{1/3} \tag{14}$$

where,

$n =$ No of stones at the top layer (min, $n = 3$).
$B =$ width of crest in m.

3.4 Under Layers

The underlayers which are made up of granular material provide stability outer armor layer and prevent the migration of core material through voids of armor units. The underlayers may be laid in one or more layers depending on the surrounding conditions. The underlayer increases the wave dissipation capacity of breakwaters. The under layer is designed with a rule, D_{15} of armor is less than five times the D_{85} of under layer. The thickness of the under is determined with $n = 2$ in Eq. (11).

3.5 Core and the Bedding Layer Properties

The core is the central and inner most part of rubble mound consists variable sizes of quarry rocks, so that sediments shall not pass through the voids of the structure. The permeability of the core is lesser than the outer layers because of wide graded stones. The weight of the individual stones varied from 50 to 125 kg. The bedding material or filter units made up of granular materials provided to avoid settlement of core material and washing out of finer material. The stones used in filter may have 1–50 kg and size not less than 100 mm. According to Terzaghi and Perk [35], the design of filter shall follow the criteria like,

$$D_{15\text{filter}}/\,D_{85\text{base}} \leq 5$$
$$D_{15\text{filter}}/\,D_{50\text{base}} < 25$$
$$4 < D_{15\text{filter}}/\,D_{15\text{base}} < 5$$

where, D_{15}= diameter exceeded by 85% of layer material

According to U.S. Army Corps of Engineers [37], the grain size distribution for filters to avoid scouring follows,

$$D_{15\text{filter}}/D_{85\text{base}} \leq 5$$
$$D_{50\text{filter}}/D_{50\text{base}} \leq 25$$
$$5 \leq D_{15\text{filter}}/D_{15\text{base}} \leq 20$$

The hydraulic boundary conditions need to be checked if these geometrical criteria doesn't fulfill, i.e., critical hydraulic gradient conditions. The maximum gradient is an important factor to assess the reliability of filters [20]. As core and filter rubbles are light in nature, they shall be constructed in calm weather and narrowly graded filters are used instead of broadly graded in order to avoid segregation and "reverse filter" condition. Another thing, whenever the breakwater is placed on clay or loose sand, the use of geotextile filter is essential to avoid the settlement.

3.6 Toe Mound and Berm Structures

Toe mound is one of the important structures of breakwater provided for scour protection, to prevent undermining, resistance against the armor sliding, and structural stability against the slip or circular failure (ref. Figure 9). The depth of water at the toe shall be at least H_s to $1.5H_s$ on the seaside and at the harbor side, it depends on the wave attack (usually 3 m). The minimum toe weight shall be calculated by Eq. (15) given by Tanimoto et al. [34]. Generally, the weight of the granular material used in

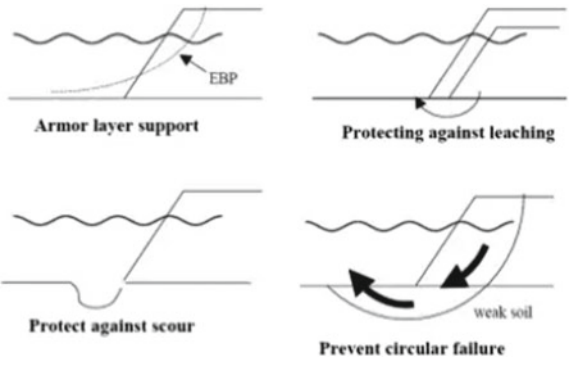

Fig. 9 Toe protection [6]

Table 3 Weight ratios for different components

Layer	Weight ratio
Armor	W
First under layer and Toe berm	W/10 (if K_D <=10) to W/15 (if (K_D > 10)
Second under layer	W/200
Core and bedding layer	W/100–W/4000

the toe shall be between 150 and 500 kg, respectively.

$$\text{Weight of toe stone} = \frac{wH^3}{N_s^3\left(S_g - 1\right)} \tag{15}$$

where,

N_s = stability number and a maximum of
$N_s = 1.3\ [(1\text{-K})/\text{K}^{1/3}]\ (\text{h}_\text{b}/\text{H}_\text{s}) + 1.8\ \exp[(-1.5(1\text{-K})^2.\text{h}_\text{b})/\ (\text{K}^{1/3}.\text{H}_\text{s})]$ or 1.8

$$D_{50} = (W/w)^{1/3} \tag{16}$$

The width of toe mound shall be the maximum of twice of wave height and 0.4 times the wave depth or three stone width. The height of it may be taken as 0.5 times the width. The nominal diameter D_{50} is given by Eq. (16). If toe protection is not used, the armor layer should extend below the maximum scouring depth and the slope is adjusted to have minimum scour. In deep waters and sandy conditions, the smaller size of the rocks could be used to support the armor. Sometimes, gabions are used to minimize the scouring depth.

The thumb rule for calculating the weight of the component is shown in Table 3.

3.7 Geotechnical Considerations

It generally deals with the mechanical behavior of the foundation and rock body subjected to seepage forces, pore pressures, and accelerations produced by waves and tremors. The geotechnical failures are probabilistic by nature and are third in rank after armor instability and breakage.

The stability of granular slopes depends on the internal resistance to shear deformation. The inter-granular points show non-linear internal friction due to crushing and yielding due to erosion and the interfaces between consecutive layers are likely to slip if different materials are used due to decreased interlocking. The internal friction for rubble mound can be expressed by Eq. (17).

$$\Phi = \Phi_o + R\ \log\left(S/\sigma'\right) \tag{17}$$

where,

Φ_o = Basic friction angle.
R = roughness corresponding to rock and porosity.
$\sigma^{'}$ = Actual stress level corresponding to particle size and strength.
S = Equivalent stress.

The stability of slopes in rubble mound is usually analyzed by the Bishops method by considering the nonlinear friction as the possibility of generation of shallow slip surfaces are less. For the rock fill subjected to waves, the local field flow shall be considered and determined based on the wave pressure, non-linear water table, and internal water table. The instability of the structure depends on the wave-induced pore pressure and it will be predominant if the drainage capacity is insufficient, and thus, it will directly decrease the slope stability. The weight of the structure needs to be considered in the slope stability analysis if dynamic pressure is acting on te breakwater slope and the weight should be submerged rather than saturated due to the nonappearance of pertinent drag forces. This approach of consideration provides a positive effect on slope stability factors [45]. The gravitational settlement of rubble mound and the compressible layers present in the foundation can be estimated by the standard formulae and by site investigation. The multiphase system (soil–water–air) plays an important role in poro-hydrodynamics. Experimental results given by the Costa [47] show that permeability plays important role in the dynamic deformation of breakwaters (ref. Figure 10).

The water which plunges or overtops on striking to surface induces impact forces and acts as shock waves. The shock waves can create horizontal accelerations in core and slope to a scale of 0.1 g, affecting the slope stability of the system. These shock waves are compressive in nature and upon reflection create tensile forces at the leeside causing dynamic piping and lifting of particles. The intensity of shockwaves

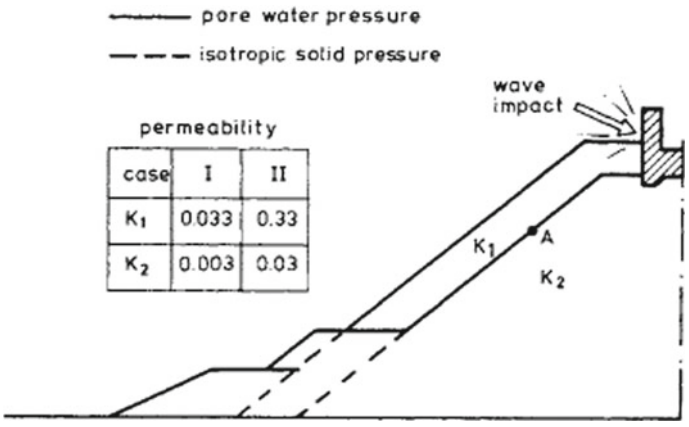

Fig. 10 Effect of permeability of breakwater on the wave impact [47]

would decrease drastically in semi-saturated breakwaters due to internal damping and relative interphase friction.

The stability of surface particles would be altered by the up and down rush drag forces carried by protruding particles of outflow. A group of coherent particles in the granular compacted core would be loosened first, giving way for the outflow (similar behavior observed in sand). The core particles possess better self-healing potential comparable to armor units in outflow considerations.

Pore pressure generates by loading or storage and dissipates by porous flow. Due to dynamic loading, the granular material deforms by creating volumetric strain and thus, excess porous pressure. The porous flow created by excess pressure could affects the shear resistance by reducing slope stability. With the help of dissipation period, one can assess excess pressure. In rubble mound, the drainage capacity is sufficient to rapidly dissipate the excess pore pressure. There are four processes involved in cyclic dissipation and buildup of excess pore pressure namely, (1) wave-induced internal setup, (2) field storage, (3) liquefaction, and (4) dynamic deformation. The granular material experiences the concept of dilatancy due to shear deformation. If the top bed is of saturated granular soil, the tendency for the reduction in shear strength is high due to development of excess pore pressure by dynamic waves until the soil liquefies. The liquefaction potential of soil bed could be determined by the site investigation, soil characterization, and porosity of collected sample. Along with this, the critical porosity at zero dilatancy and cyclic mobility determined in laboratory and considering the drainage condition and relevant stress level in simulation model would help to create and assess the actual condition [5].

4 Failure Modes of Rubble Mound Breakwaters

In its lifetime, rubble mounds are mostly subjected to wave actions rather than seismic actions and rarely both. Many disastrous earthquake-like Chile earthquake in 2010, Sanriku-haruka-oki (Japan) in 1994, Kobe (Japan) in 1995, Kocaeli (Turkey) in 1995, Sumatra (Indonesia) in 2003 affected marine structures. Hattaro Breakwater in Hachinohe Port, the breakwater at Onagawa Port, Miyagi Prefecture Aomori Prefecture; Ryujin-zaki breakwater at Miyako Port, Iwate Prefecture were collapsed due to foundation failure during the Tohoku earthquake in 2011. According to CIRIA C683 [6], the rubble mound may either fail by wave actions or geotechnical instability as shown in Fig. 11. The failure in toe structure, slope instability, hydraulic damage, internal erosion, overtopping, crest damage, and port side erosion are common modes of damage. The possibility of damage at the round head portion will be higher than the longer trunk.

According to PIANC [28], due to seismic actions, there would be differential settlement causing crest lowering, lateral spreading, and failure of superstructures due to liquefaction of subsoil. When foundations of the breakwaters are subjected to earthquake, there will be excessive pore water pressure in the soil and shear strain in the structure leading to deformation or settlement of the breakwater. Sever

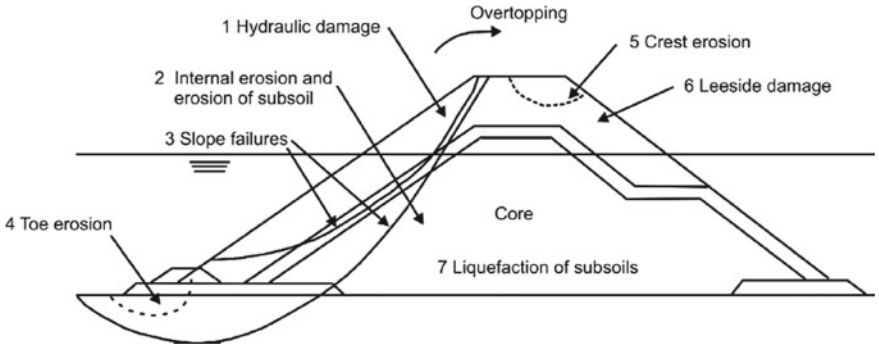

Fig.11 Failure modes of rubble mound considering all the aspects [6]

tremors creates liquefaction condition. Due to this earth vibration, there will be a subsequent tsunami approaching toward the breakwaters. The coming tsunami will be having wave height greater than the design high water level and induce excess pore water pressure, seepage, and scouring action. The excess pore water pressure may also create piping condition and vertical settlement. Ultimately, due to the effect of liquefaction and piping, the bearing capacity of the soil decreases, and breakwater will collapse inevitably Chaudhary et al. [11, 13]. The tranquil condition in and around the coast and port structures will be vanished.

After the great eastern Japan Earthquake and Tsunami of 2011, the Japanese coastal Engineering community has classified the different levels of Tsunami, level 1-Tsunami with return period of several decades to 100 years with relatively low height of 7–10 m and level 2-Tsunami with return period between 100 and few 1000 years with 20–30 m height. Thus, 2011 Japan's earthquake and tsunami at Tohoku and 2004 Indian Ocean tsunami attack would fall in this criteria. According to Esteban et al. [16], the Hudson's formula for the weight of the armor stone was modified. For level 1 and the level 2 tsunamis, the use of Eq. (18) and Eq. (19) is recommended.

$$W = \frac{w H_{\text{tsunami}}^3}{K_D \left(S_g - 1\right)^3 \text{Cos}\theta} \tag{18}$$

$$W = 0.25 \frac{w H_{\text{tsunami}}^3}{K_D \left(S_g - 1\right)^3 \text{Cos}\theta} \tag{19}$$

where, H_{tsunami} is the height of the tsunami in meters and rest parameters are the same.

The physical model or scale-down studies are useful to know the cause for the failure of any breakwaters and to analyze case studies by considering similar boundary conditions. For instance, Yuksel et al. [48] studied seismically induced deformation, ground motions, and seismic-induced liquefaction at Ergil Fishery Port

breakwaters along the southern coast of Izmit bay after Kocaeli earthquake, Turkey 1999. Izmit bay was dynamically affected due to interaction of North Anatolian Fault zone and Marmara Graben system with earthquake magnitude of $M_w = 7.4$ The breakwater was about 210 m long and depth of -3.50 m relative to still water level and consists of quarry stones (armor and core). From the field observation, they noticed larger settlements of 1.5 m on the seaside in the form of flattening and sliding of slope and lower side of rubble mound intruded into the loose sand at sea bed (ref. Figure 12). They did SPT boring studies to know the subsurface condition (Rubble mound— > thick silty sand layer— > thick sand—> stiff clay). In order to know the ground deformations, they used finite element application called Plaxis 7.2 (ref. Figure 13) and to know static stability, limit equilibrium analysis was done. From analysis, they found that, the maximum deformation was predicted to be at crest (40 mm), the breakwater was statically stable and settlement due to self-weight

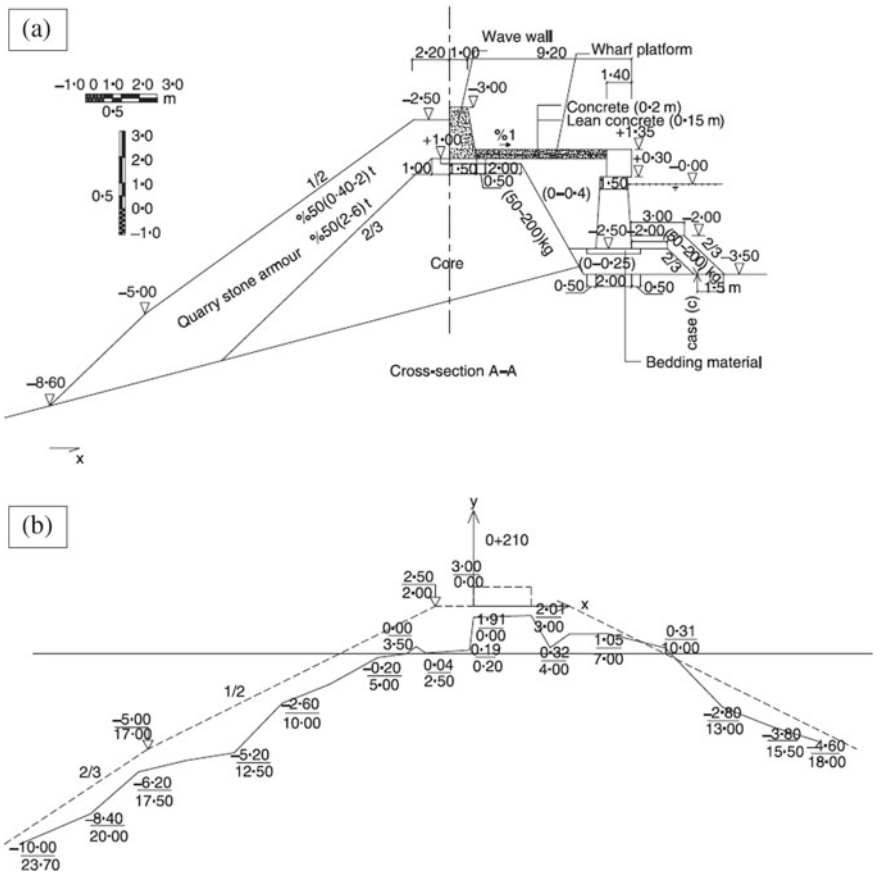

Fig. 12 Cross -ection of Ergil fishery port breakwater **a** before and **b** after Kocaeli earthquake, 1999 (after Yuksel et al. [48])

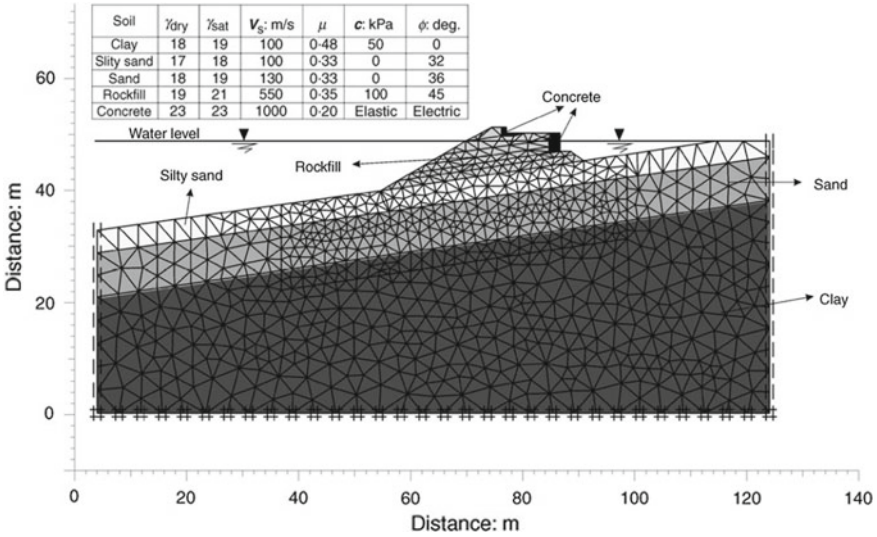

Fig.13 Finite element model used by Yuksel et al. [48]

was very small. From the dynamic numerical analysis (FLAC software) and pseudo-static limit equilibrium analysis, the breakwater was marginally stable with FOS of 0.93–1.01 considering horizontal acceleration as 0.35 g (pore water pressure was neglected here). To assess the stability triggering potential of liquefaction on performance of slope, they used cyclic stress ratio and to assess the liquefaction resistance, SPT-based cyclic resistance ratio was used. The silty sand layer was susceptible to liquefaction with residual friction of 7° and deformation was mainly due to the passage of shallower potential failure plane through silty sand layer. Some of the other rubble mound structures damaged due to Kocaeli earthquake of 1999 have shown in Table 4.

Table 4 Breakwater failures due to Kocaeli earthquake of 1999 [18, 48, 49]

Presence of breakwater	Cause for damage of breakwater and effects
Eskihisar fishing harbor	Slight damage as it was found on the sandy gravel base and there was no sign of liquefaction
Karamursel-eregli fishing harbor	Observations like flattening on cross-sections, sliding of slope, there was a settlement of breakwater of about 1.5 m along its axis, differential movement of about 10 cm between wave walls, cracks were found between crown wall and backfill (30 cm). The cause for the failure is liquefaction of subsoil
Cinarcik fishing harbor	Crown wall cracked with width of 30 cm, concrete slabs were detached (15 to 20 cm apart) by sinking and swelling action
Esenkoy fishing harbor	Minor damage (Cracks along the crown wall)

5 Conclusion

This paper explains, the basic features of rubble mound breakwaters, functions of different parts, and reviews the work done on "Rubble mound breakwaters, design considerations, and its failure modes." The rubble mound breakwaters usually fail due to hydraulic instability or by following improper geotechnical guidelines. The larger settlements of 1.5 m on the seaside in the form of flattening, sliding of slope and the lower side of rubble mound intruded into the loose sand at sea bed were observed at the Ergil Fishery Port breakwaters along the southern coast of Izmit bay due to Kocaeli earthquake (1999). The failure was mainly due to the liquefaction of the underlying silty sand layer. The literature review carried out suggests that the uncertainties in wave forces and ground motions need to be considered in the design of breakwaters. The methods described in this paper can be used effectively in overall breakwaters design systems. It's possible to create suitable countermeasures to minimize the damage imposed by uncertainties. By using suitable design considerations, improvisation of materials, implementing the modern techniques described, the uncertainties could be encountered. The ultimate goal of the designer is to design the breakwater to be resilient to Tsunami or earthquake even after it's partially damaged and yet it performs its functions.

References

1. https://www.concretelayer.com/en/news/al-faw-grand-port-technologie-core-loctm
2. https://www.hradf.com/en/portfolio/view/167/organismos-limenos-aleksandroypolhs-a-e-ola-a-e
3. Allsop NWH, Cork RS, Verhagen HJ (2009) A database of major breakwaters around the world, In: Proceedings of coasts, marine structures and breakwaters, Edinburgh, UK
4. Bakker P, Klabbers M, Muttray M, Van den Berge A (2005) Hydraulic performance of Xbloc® armour units. In: 1st International conference on coastal zone management and engineering in the middle East. Dubai
5. Barends FBJ (1986) Geotechnical aspects of rubble mound breakwaters, Developments in breakwaters. Thomas Telford Ltd, London
6. CIRIA; CUR; CETMEF (2007) The rock manual. The use of rock in hydraulic engineering, 2nd ed, C683, CIRIA, London, UK
7. Campos A, Castillo C, Molina-Sanche R (2020) Damage in rubble mound breakwaters part i: historical review of damage models. J Mar Sci Eng 8:317s
8. Capanoglu C (2005) Novel and marginal field offshore structures in handbook of offshore engineering, in Chakrabarti SK (ed), Elsevier
9. Çelikoğlu Y, Engin D (2017) Placement effect on the stability of tetrapod armor unit on breakwaters in irregular waves China Ocean Eng 31(6):747–753
10. Cevik E, Cihan K, Yüksel Y (2005) Stability for structures armored with core-loc™ Turk J Eng Environ Sci 29:225–233
11. Chaudhary B, Hazarika H, Pasha SMK (2017) Countermeasures for breakwater foundation subjected to foreshocks and main shock of earthquake loading Taylor and Francis Marine Georesources and Geotechnology

12. Chaudharya B, Hazarikab H, Nishimurab K (2017) Effects of duration and acceleration level of earthquake ground motion on the behavior of unreinforced and reinforced breakwater foundation Soil Dyn Earthq Eng 98:24–37
13. Chaudharya B, Hazarikab H, Murakami A, Fujisawa K (2019) Development of resilient breakwater against earthquake and tsunami. Int J Geomech ASCE 19(1)
14. Cihan K, Yuksel Y (2011) Deformation of rubble-mound breakwaters under cyclic loads. Coast Eng 58:528–539
15. Cihan K, Yuksel Y, Berilgen M, Cevik EO (2012) Behavior of homogenous rubble mound breakwaters materials under cyclic loads. Soil Dyn Earthq Eng 34:1–10
16. Esteban M, Morikubo I, Shibayama T, Aranguiz R, Mikami Muñoz T, Thao ND, Ohira K, Ohtani A (2012) Stability of rubble mound breakwaters against solitary waves. Coast Eng 2012:1–13
17. Esteban M, Takagi H, Thao ND, Yamamoto L (2015) Stability of shallow rubble mound breakwaters under climate change induced sea level rise, Chapter 31 Elsevier handbook of coastal disaster mitigation for engineers and planners
18. Gunbak AR, Muyesser O, Yuksel Y (2000) Damages recorded at the coastal and port structures around Izmit Bay under the August 17, 1999 Earthquake. PIANC Buenos Aires Conf, 1–19
19. Gómez-Martín ME, Medina JR (2014) Heterogeneous packing and hydraulic stability of cube and cubipod armor units. J Waterway Port Coastal Ocean Eng 140:100–108
20. Heibaum MH (2004) Geotechnical filters—the important link in scour protection. Federal Waterways Engineering and Research Institute, Kussmaulstr. 17–76187, pp 1–16
21. Holtzhausen AH, Zwamborn JA (1991) Stability of accropode® and comparison with dolosse. Coast Eng 15(1–2):59–86
22. Hudson RY (1959) Laboratory investigations of rubble mound breakwaters. In: Proceedings of the American society of civil engineers, ASCE, waterways and harbours division, vol 85, No. WW3, Paper No. 2171
23. Iribarren CR (1938) A formula for the calculation of rock-fill dikes. Revista de Obras Publicas, (Translation in The Bulletine of the Beach Erosion Board, vol 3(1), Jan. 1949)
24. Kudale MD, Bhalerao AR (2015) Equivalent Monochromatic Wave Height for the Design of Coastal Rubble mound structures. Proceedings of International conference on water resources, coastal and ocean engineering, Elsevier, Aquatic Procedia, 4:264–273
25. Kudale MD Overview of Coastal protection in India andInnovative methods of protection. Training Course on Coastal engineering and coastal zone management, CWPRS, Pune
26. Memos CD (2000) Experimental investigation of the seismic response of rubble-mound breakwaters. Maritime Engineering and Ports II, Brebbia CA, Olivella J (eds), WIT Press
27. Molines J, Medina JR (2015) Calibration of overtopping roughness factors for concrete armor units in non-breaking conditions using the CLASH database. Coast Eng 96:62–70
28. PIANC (2001) Seismic design guidelines for port structures, Balkema
29. Palmer GW, Christian CD (1998) Design and construction of rubble mound breakwaters. IPENZ Trans 25(1/CE)
30. Simpalean AR (2019) Experimental investigations of core-loc armour units. Master of Applied Science in Civil Engineering thesis, University of Ottawa, Canada
31. Status Report on Coastal Protection & Development in India, Central water commission, December 2016.
32. Suh KD, Kang JS (2012) Stability formula for tetrapods. J Waterway Port, Coastal and Ocean Engineering, ASCE 138(3)
33. Sumer BM, Ansal A, Cetin KO, Damgaard J, Riza Gunbak A, Hansen NO, Sawicki A, Synolaki CE (2007) Earthquake-induced liquefaction around marine structures. J Waterway Port Coastal Ocean Eng ASCE 133(1):55–82
34. Tanimoto K, Yagyu T, Goda Y (1982) Irregular wave tests for composite breakwater foundation. Proceedings 18th conference coastal engineering, Capetown, ASCE, 2144–2163
35. Terzaghi K, Peck R (1948) Soil mechanics in engineering practice Wiley New York
36. Tulsi KR (2016) Three dimensional method for monitoring damage to dolos breakwaters. Master of Science thesis, Stellenbosch University

37. US Army Corps of Engineers (1953) Waterways experiment station: filter experiments and design criteria. Techn Memo Vicksburg
38. US Army Waterways Experiment Station, Corps of Engineer (1984) Shore protection manual. US Government Printing Office, Washington DC
39. US Army Corp of Engineers (1995) Design of coastal revetments, seawalls and bulkheads—engineering and design, Washington, DC
40. Van der Meer J (1987) Stability of breakwater armour layers—design formulae. Coast Eng 11:219–239
41. Van der Meer (1988) Rock slopes and gravel beaches under wave attack, Ph.D. Thesis, Delft University of Technology, Delft, The Netherlands
42. Van der Meer J (1992) Conceptual design of rubble mound breakwaters. In: York AN (ed) Proceedings of a short course on the design and reliability of coastal structures, 23rd conference coastal engineering Venice, 447–510
43. Van der Meer JW (1995) Conceptual design of rubble mound breakwaters. Adv Coastal Ocean Eng 221–315
44. Van der Meer JW (1999) Design of concrete armor layers. Proceedings of the coastal structures
45. Van Seters AJ (1984) Earthquake analysis of rubble mound breakwaters—a case study of sines west breakwater. Int Conf Ocean Struct Dynamics, Houston
46. Van der Meer JW (1993) Conceptual design of rubble mound breakwaters. Delft Hydraulics Publication number 483
47. Vasco Costa F (1984) The modelling of non-uniform and unsteady flow, symp scale effects in modelling. Hydr Struct Esslingen am Neckar
48. Yuksel Y, Cetin KO, Ozguven O, Isik NS, Cevik E, Sumer BM (2004) Seismic response of a rubble mound breakwater in Turkey. Proceedings of the institution of civil engineers, Maritime Engineering 157, 151–161
49. Yüksel Y et al (2000) Effects of the Eastern Marmara Earthquake on the marine structures and coastal areas, report-1. AFP No. 99–05–01–01, Yildiz Technical Univ., Yildiz, Turkey

Parametric Study Using FE Analysis of Cantilever Retaining Wall with Pressure Relieving Shelves

Smita Aldonkar and Purnanand Savoikar

Abstract Retaining wall is a necessity in today's infrastructure development projects. The construction works at hill sites or when there is difference in elevation of soil exists, earth retaining structures like cantilever retaining walls are required which often has limitation on height retained due to increase in soil pressure on the wall. For reducing the earth pressure on stem relieving shelves are provided. There are many research studies reported in literature for optimal location and designing shelves. Most of such analytical studies reported in literature have utilized FEM analysis using 2D elements. Also, there are reports of failures of retaining walls with shelves. Investigating causes of such failure needs proper forensic analysis and study simulating actual site condition in 3D domain. There is a need for analysis of Retaining wall considering the soil behaviour effect in all three dimensions. In the present study, the finite element analysis for cantilever retaining wall of 10 m high with relieving shelves, is performed by using 3D elements by varying number of shelves for different soil parameters. It was observed that the top displacement and the soil pressure acting on stem reduced with increase in number of shelves. A parametric study is performed using Midas GTS NX software using 3D elements which reveals the effect of number of shelves, on variation of unit weight and friction angle on deflection and earth pressure acting on the stem.

Keywords Retaining wall · FEM analysis · Soil pressure · Pressure relieving shelves · 3D elements · Friction angle · Stem displacement

1 Introduction

Retaining walls are used to retain or maintain earth at different levels on its either sides and also to prevent the earth from moving downhill. Retaining wall resist lateral

S. Aldonkar
Goa Engineering College, Farmagudi, Ponda, Goa 403401, India

P. Savoikar (✉)
Department of Civil Engineering, Goa Engineering College, Farmagudi, Ponda, Goa, India
e-mail: psavoikar@gmail.com; pps@gec.ac.in

L. Nandagiri et al. (eds.), *Recent Advances in Civil Engineering*, Lecture Notes in Civil Engineering 256, https://doi.org/10.1007/978-981-19-1862-9_51

forces with help of gravity or cantilever action. Retaining walls can also provide usable land. Reinforced concrete cantilever retaining walls are used in a variety of engineering constructions such as roads, dams, tunnels, mines and construction of building complexes on sloping terrain.

A retaining wall is a structure, which is designed and constructed to resist the lateral pressure of soil and to support vertical or near vertical backfills. There are situations where high retaining walls are to be built for resisting lateral earth pressure. In such cases providing cantilever retaining wall would become uneconomical owing to abnormal sizing of stem for counter resisting high bending moments at the base of the stem. Lateral thrust on the wall can be reduced by providing shelves in the stem, which reduces the sectional dimensions of the wall and cost of the project. If the shelves are extended up to rupture surface, the effective lateral earth pressure on the wall decreases considerably, comparing to retaining wall without shelves [1]. In case of counterfort retaining walls, the relief shelves are provided along the length of counterfort retaining structure and the soil beneath the relieving shelves needs to be well compacted to provide support to shelves [2].

2 Retaining Walls with Shelves

The reinforced cement concrete cantilever retaining walls usually prove to be uneconomical for retained heights of above 6 m. To support more height of earth mass, studies are done in cantilever retaining wall by adding relief shelf perpendicular stem along the height of wall. Due to provision of relief shelf the soil pressure on the stem of retaining wall is reduced resulting in economy in stem design and improvement in stability of retaining wall. Relief shelves are thin horizontal cantilever platforms which extend into the backfill along the length of the retaining wall. The shelves are constructed monolithically with the stem of the retaining wall. This technique though proposed much earlier, due to limited theoretical studies without systematic analysis and proper validation, has not become popular. It results in reduced lateral earth pressure on the stem and at the same time results in better stability of the retaining wall [3]. Providing relief shelves on the back fill side of retaining wall reduces the earth pressure on the wall. This results in thinner sections of the wall and reduces construction cost [4].

The complex behaviour of shelves was studied on a 6 m high retaining wall with 2 relief shelves having varying width of relief shelves ranging 0.5–0.8 m to understand the influence of width of relief shelves, surface profile settlement of backfill, deflection of relief [5]. The study reported that retaining walls with relief shelves can considerably reduce the lateral thrust on wall in the range of 10.56–12.5%. Effectiveness of the shelves, number of shelves, height, width, thickness of shelves on wall deformation and earth pressure distribution was studied using 31 models of cantilever retaining walls with shelves using PLAXIS 2D-AE.01 [6]. It was observed that the retaining wall exhibited lower earth pressure and less bending moment. The shelves decreased the bending moment and the top movement of the

wall. A parametric study was performed on retaining wall with shelves using STAAD Pro Vi8 to understand the effectiveness of shelf to reduce earth pressure, for retaining wall with no shelf, one, two, three and four shelves [7].

A study on retaining wall with shelves, in the presence of shelves reported a reduced lateral thrust by 43–48% as compared to retaining walls without relieving shelves [8]. Such walls are constructed across the world but the behaviour was not standardized.

From the extensive literature review, it is observed that the shelves on the retaining wall reduces the lateral earth pressure on the wall and increases the stability retaining wall. Recently the finite element methods are being employed to study effect of backfill soils. Finite Element Analysis using PLAXIS-2D AE/FLAC and parametric studies have been conducted on retaining walls with shelves to investigate the effect of shelf position, length and stiffness of the shelves on lateral earth pressure distribution. Retaining wall with shelves was analysed using FE Analysis employing 2D approach. It has been noticed that there are merely any analysis of retaining wall in 3D domain. The actual field problems are always in 3D domain, the 2D simplification isn't enough for modelling actual field problems. In the case of retaining wall with pressure relieving shelves, a 2D model cannot catch the actual behaviour of retaining wall and soil between the shelves. The only way to solve the problem is to make a Finite element analysis employing 3D modelling approach. In this study FEM analysis of the cantilever retaining wall is conducted by modelling retaining wall and retained soil using 3D elements to simulate the actual in-situ field condition. The procedures for 3D modelling and 3D analysis are reported. Retaining wall and soil behaviour for different types of soil are investigated using 3D Finite Element Analysis.

3 FE Analysis Methodology

The main aim of the FE analysis in this study is to simulate actual site condition of in-situ behaviour of wall acted upon by soil mass. In most of the studies reported in literature, earth pressure is calculated and applied on wall. In this study Retaining wall along with soil mass is modeled using 3D finite elements. The actual site conditions are simulated using appropriate boundary condition. The retaining wall is proportioned based upon moment equilibrium. The FEM is used for liner static analysis of the retaining wall (with and without shelf) to determine its behaviour.

3.1 Proportioning of Retaining Wall

The shelves in the retaining wall are acted upon by weight of the earth retained above it. If shelves are constructed monolithically with stem, the portion of the retaining wall stem and shelves act as one unit in resisting moments generated by

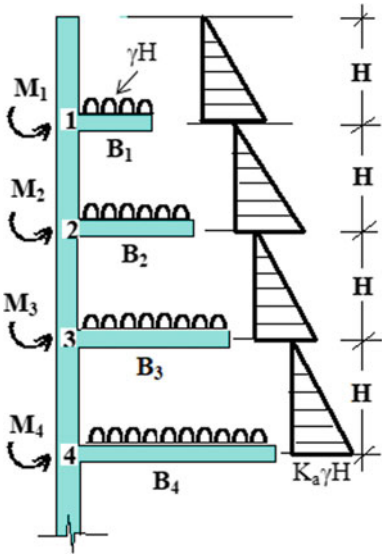

Fig. 1 Retaining wall with varying shelf length

lateral earth pressure and weight of soil. The weight of soil on shelves creates clockwise moment at the shelves and stem junction, whereas the lateral earth pressure on stem creates anticlockwise moment at the junction. The basic principle adopted here is to proportion shelves width based on its location along the height of stem, to make moment equilibrium at junction. Expressions were developed for calculating length of shelves so that moment equilibrium is attained at junction. The expressions consider the number of shelves to be provided and their location along the height for calculating the length of shelves. Figure 1 shows the relief shelves of widths B_1, B_2, B_3…..B_n. Considering the moment equilibrium condition $\Sigma M = 0$ at junction, if this moment increases, the retaining wall is pushed into the backfill causing the lateral pressure to be more than at the rest condition. Considering the moment equilibrium at each junction and keeping height of each segment same, the expressions are developed for the widths of shelf as shown below using Eq. 1–5 [8]:

$$B_1 = H.\sqrt{k/3} \tag{1}$$

$$B_2 = H.\sqrt{5k/6} \tag{2}$$

$$B_3 = H.\sqrt{5k/3} \tag{3}$$

$$-M + B_4^2.\gamma.H/2 + 3.\gamma.H.(B_4 - B_3).\left(\frac{B_4 + B_3}{2}\right) - \frac{k.\gamma.H^2}{2}\left(\frac{H}{3} + H + 2H + 3H\right) = 0 \tag{4}$$

$$B_4 = H.\sqrt{17k/6} \tag{5}$$

where B_1 to B_4 are the width of shelves, M is the bending moment at stem and shelf junction, H is the equal height in to which the shelves divide the height of stem and k is the earth pressure coefficient. The whole method of proportioning retaining wall with shelves was automated using spreadsheet so that quickly the shelf lengths can be arrived for particular soil parameters. The spread sheet developed requires input parameters like height of retaining wall and numbers shelves to be provided. It calculates the earth pressure coefficients using soil properties and computes widths of shelves for zero moment at the stem-shelf junction. The width of shelf so obtained is used in modeling retaining wall for FE analysis.

3.2 Assumptions Made in Analysis

Following assumptions are made in the FEM analysis.

1. Junction of relief shelf and wall is rigid and remains 90° unchanged even when the wall movement happens
2. Retaining wall is fixed at the bottom.
3. Cohesion-less backfill is assumed.

3.3 Parameters Used in the FE Analysis

To achieve objectives of determining wall behaviour to different soil parameters, total 27 different cases were considered with different soil parameters and were analysed using Finite Element Method. The industry standard software MIDAS GTS NX is employed to model and analyse the retaining wall. The typical Retaining wall model consists of a retaining wall having wall height of 10.0 m and width of base slab 6.0 m. The base slab length is calculated from the basic design principles. The length of base slab is 0.6H and heel length is 0.2 H, where H is height of the wall. The width of shelves is derived using spreadsheet as explained earlier using Bowles' moment equilibrium condition. The thickness of the shelf is considered as 0.4 m. Total 27 analyses were performed considering unit weight of soil (γ) as 16, 18 and 20kN/m^3 with different Soil friction angle $\phi = 25^\circ, 30^\circ, 35^\circ$.

4 FE Modeling of Retaining Wall

The retaining walls are modelled in MIDAS GTS Nx software using 3D elements. The software has the option of implementing different soil models to simulate actual site condition including computing earth pressure. Figure 2 shows the step by step method of modelling retaining wall along with foundation soil, retained and back fill soil.

The cross-sectional geometry of the retaining wall along with shelves is formed using create surface option in the software. The surface is extruded to the required length to create the 3D space geometry. The create surface option is used again to model foundation soil, retained soil and backfill soil and surface is extruded as mentioned earlier to generate model as shown in Fig. 2. The whole unit of retaining wall and soil mass is discretized using 3D elements.

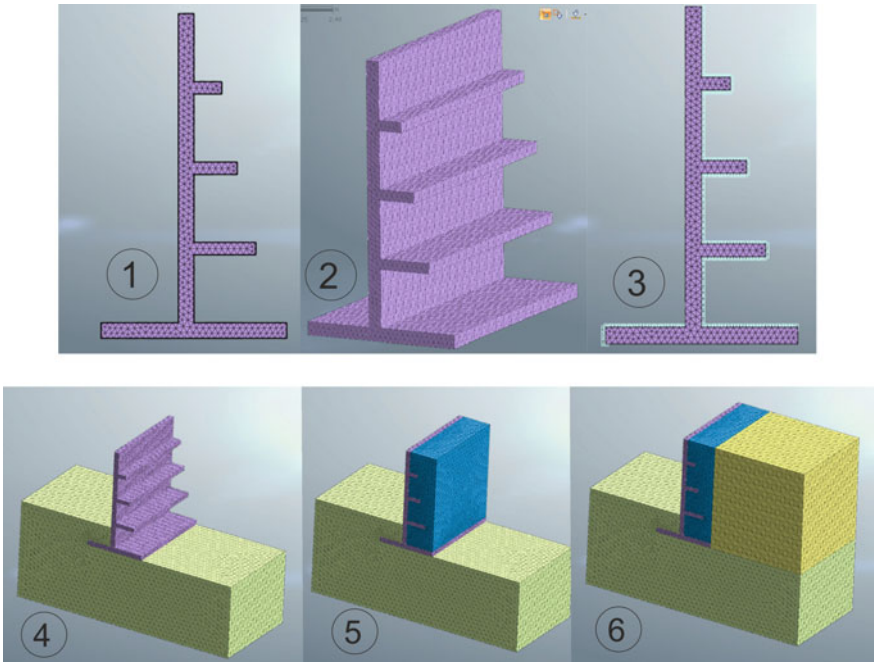

Fig. 2 Retaining wall modeling steps in MIDAS GTS NX

4.1 Geometry Modeling

Retaining wall geometry is created in 3D space with geometry for each part of the system of retaining wall, foundation soil, back fill and retained soil. These geometries are auto connected to remove any break between each unit so that whole system acts as one unit. The material properties viz. elastic modulus, Poisson's ratio, unit weight, damping ratio are added for simulating behaviour of elastic materials like concrete and steel. The foundation soil, retained soil and back fill soil is simulated using Mohr–Coulomb soil model. For modeling soil behaviour the additional material properties like friction angle, anisotropy, permeability coefficients, drained and undrained conditions, dilatancy angle, and tensile strength parameters were added in the software.

5 FE Analysis

In this study, the retaining wall, foundation soil, back fill and retained soil are modelled in 3D space using 3D elements. The meshing has been carried out such that each node points are connected at interface between different units of retaining wall and soil mass. The Mohr–Coulomb theory is adopted to model the behaviour of soil in foundation soil, back fill and retained soil. Anisotropy property of soil is incorporated to calculate earth pressure in all three directions. The fully drained condition of back fill soil is simulated by using appropriate options available in the software. The typical FE model with three shelves is shown in Fig. 3. Total of 30 m retained soil in the perpendicular direction to the longitudinal axis is considered.

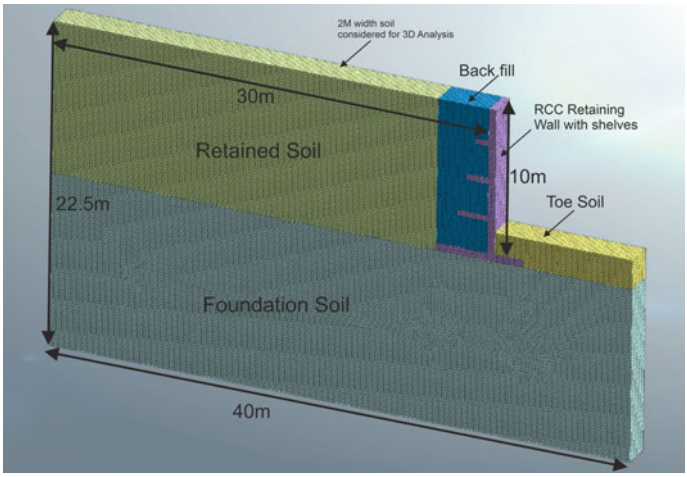

Fig. 3 FEM model of retaining wall with pressure reliving shelves

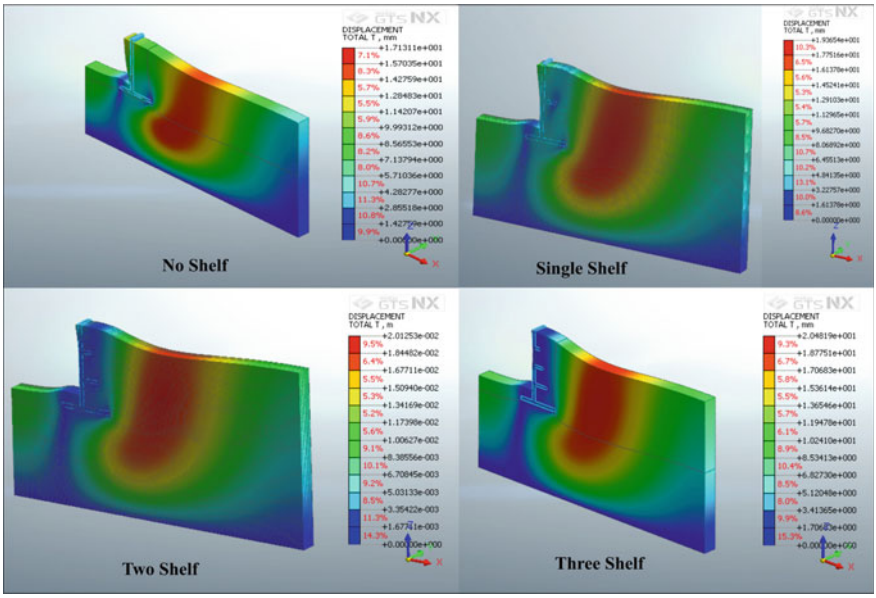

Fig. 4 Displacement/Stress in retaining wall and soil mass for typical cases of no shelves, one shelf, two shelves and three shelves

To simulate 3D effect, the 2 m length of wall is considered along the longitudinal direction of retaining wall.

The linear static analysis is conducted without applying any additional surcharge load to understand the in-situ behaviour of retaining wall and retained soil due to self-weight of wall and self-weight of soil mass. The typical model consists of a retaining wall with a height of 10 m and base slab width equal to 6.0 m. The wall and base slab thickness are 0.5 m. As mentioned earlier, total 27 different cases were analysed using MIDAS GTS NX. For each case, the retaining wall displacement pattern and soil settlement pattern were recorded along with the displaced pattern of retained soil mass. The typical results for one of case considered are presented here. Stem Displacement pattern for a typical case of backfill with unit weight 16 kN/m^3 and friction angle 25° is shown in Fig. 4.

6 Result and Discussion

The linear static analysis was conducted as described in the above section. In all the 27 cases, it is observed that the horizontal earth pressure is reduced to minimum below each shelf. This directly justifies the assumptions that pressure just below the shelf is minimum as assumed in the study while deciding shelf length. The pressure and displacement pattern of retaining wall and soil mass for the typical cases (no

shelf, one shelf, two shelves and three shelves) is shown in Fig. 4. Such shelf pressure reduction and variations are observed in all cases considered. However, reporting all such cases in this report graphically is beyond the scope of this study, and hence typical cases are presented.

It is clearly observed that the stem displacement reduces as more number of shelves are provided. Figure 5 shows comparison of retaining wall top free displacement reduction in wall having one, two, three shelves cases with no shelves. It is observed that the stem top deflection reduces by 24.05%, 64.77% and 82.77% respectively for single, two and three shelves respectively as compared to retaining wall without shelf. Shelves act as hold-back ties which reduces the deflection of stem top. It is also seen that because of provision of shelves, the horizontal earth pressure is getting reduced to minimum at the bottom of each shelf.

Earth pressure reduction at the locations of shelf can be seen in the graph shown in Figs. 6 and 7, for different soil parameters. The earth pressure reductions on stem at places where shelves are provided are clearly observed in each type of retaining wall.

A detailed parametric study using FE analysis was conducted to verify the behaviour of retaining wall with different number of shelf to varying site conditions. Three different cases of soil unit weight 16, 18 and 20 kN/m^3 have been considered. The parametric study was conducted to study how the friction angle variation affects behaviour of retaining wall. Three cases of soil friction angle 25°, 30° and 35° were considered for parametric study. In all the cases of parametric studies, the proportion of the retaining wall for each case and each type is done using spreadsheet developed earlier. The results of parametric study are presented in graphs shown in Figs.8 and 9. In all the cases, it is observed that shelves are effective in reducing earth pressure on retaining wall. The effect of friction angle on stem displacement was studied in detail. All the retaining walls having one shelf, two shelf and three shelves show decreased stem displacement as friction angle increases. Figure 8 shows displacement pattern of retaining walls to soils having different friction angle.

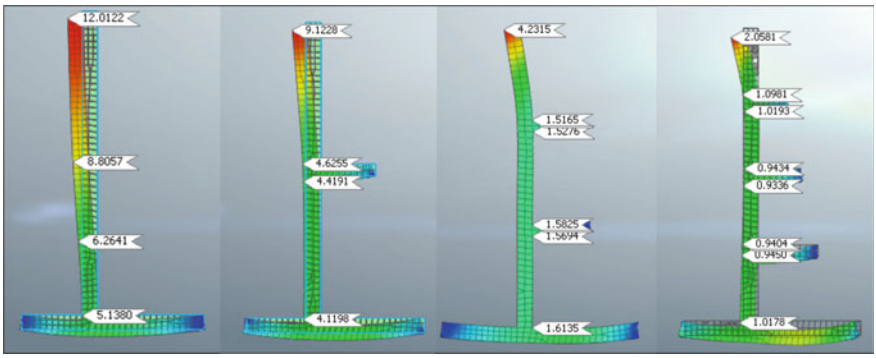

Fig. 5 Displacement in retaining wall for typical cases of no shelf, one shelf, two shelves and three shelves

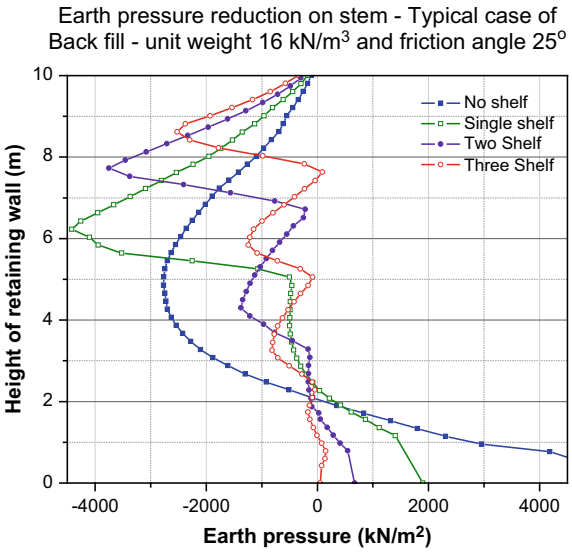

Fig. 6 Earth pressure reduction on stem for typical cases of no shelf, one shelves, two shelves and three shelves

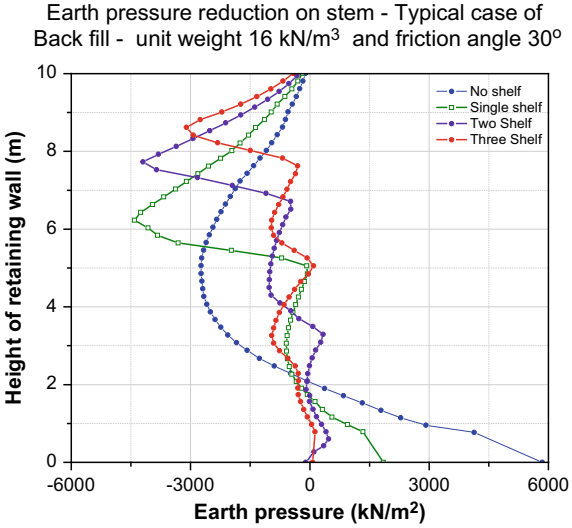

Fig. 7 Earth pressure reduction on stem for typical cases of no shelf, one shelf, two shelves and three shelves

7 Conclusions

The FE analysis of retaining wall using 3D elements has been performed using MIDAS GTS NX. The retaining wall and retained soil mass modeled using 3d elements are effective in clearly depicting displacement and stress patterns in 3D domain. The 3D analysis clearly shows variation of stress patterns which is useful for designers in detailing reinforcements in shelfs and retaining walls. Parametric

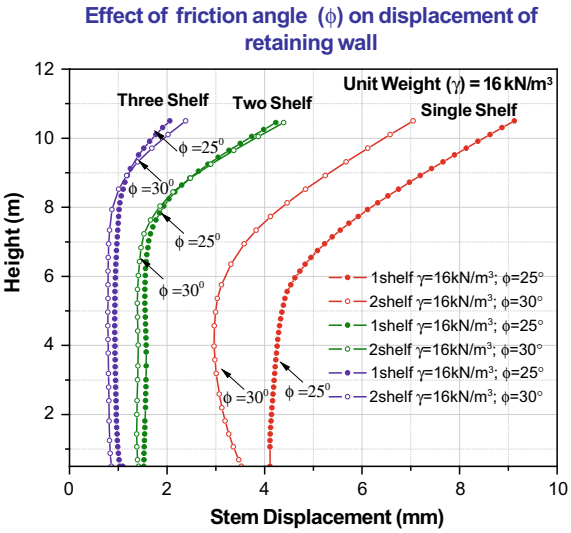

Fig. 8 Stem displacement comparison for different values of friction angle of soil fill

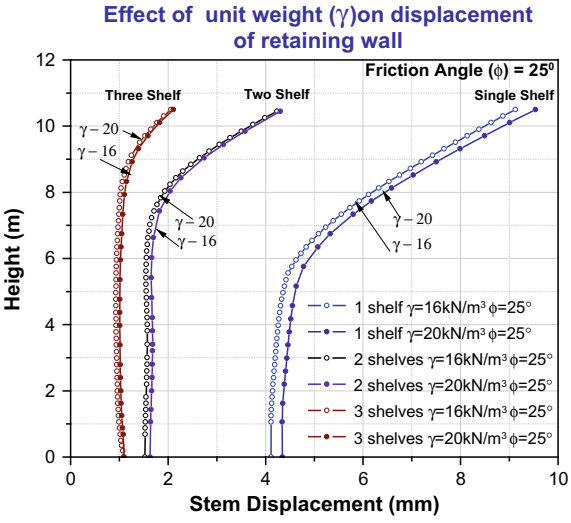

Fig. 9 Stem displacement comparison for different values of unit weight of soil fill

study considering the shelves at equal heights along the cantilever retaining wall, reduces the stem displacement by 24.05–82.87% and so also the lateral earth pressure. Maximum reduction in the stem top displacement and the lateral earth pressure is observed by increasing the number of shelves. Analysis with three shelves resulted in least stem top displacement and maximum reduction of wall pressure. The stem displacement and earth pressure decreases as the density of soil is low and friction angle increases. The earth pressure profile below each shelf is similar and is varying approximately in parabolic shape.

References

1. Bowles JE (1997) Foundation analysis and design, 5th edn. McGraw-Hill, Singapore
2. Jumikis AR (1967) Introduction to soil mechanics. Van Nostrand Reinhold Inc. US
3. Raychaudhuri R, Garg AK (1973) Design of retaining walls with relieving shelves. IRC J 35:289–325
4. Padhye RD, Ullagaddi PB (2011) Analysis of retaining wall with pressure relief shelf by Coulomb's method. In: Indian geotechnical conference proceedings. Kochi, pp 671–673
5. Chauhan VB, Dasaka SM (2016) Reduction of lateral earth pressure acting on non-yielding retaining wall using relief shelves. In: International geotechnical engineering conference on sustainability in geotechnical engineering practices related urban issues proceedings, Mumbai, India
6. Farouk HS (2016) Retaining wall with relief shelves. Innovative Infrastruct Solutions 1(4):1–13
7. Faldesai M, Savoikar P (2019) Comparative analysis and behaviour of cantilever retaining wall with and without relief shelves. In: International association for computer methods and advances in geomechanics proceedings, IIT Gandhinagar, India
8. Chauhan VB, Dasaka SM, Khan R (2016) Numerical study on the behaviour of rigid retaining wall with relief shelves. In: Indian geotechnical conference IGC2016 proceedings, Pune

Study on Processed Granulated Blast Furnace Slag as a Replacement for Fine Aggregates for the Greener Global Construction

D. Arpitha, C. Rajasekaran, and Pramodkumar Kappadi

Abstract As innovation in concrete technology advances and the environment weakens, it is currently evident that the boundless utilization of construction materials and its initial expense being the common determination model has become a routine with regard to the past. Since there is great interest for raw materials and natural resources are rare, it is expected to utilize a high volume of alternative materials in concrete that would be monetarily beneficial like crushed sand, blast furnace slag, etc. An experimental investigation was carried out to examine the behaviour of mortars incorporating partial volumes of secondary material to fine aggregates. Processed granulated blast furnace slag (PGBS), newly processed slag which had overcome the limitations of granulated blast furnace slag obtained as a by-product during the extraction of steel was tested for fine aggregate (FA) replacement. Several combinations of mortar mixes were prepared using Lignosulfonate (LS), Sulphonated Naphthalene Formaldehyde (SNF) and Polycarboxylate Ether (PCE)-based superplasticizers (SP) for 0 and 50% replacement levels of FA by PGBS to recognize the feasible optimum dosage of SP required to achieve desired flow characteristics of mortars. Based on the optimum dosage of SP and w/c obtained, mortar cubes were prepared and cured for 3, 7, and 28 days. These cubes were tested for compressive strength periodically, the results revealed that PCE-based SP exhibited better performance concerning flow behaviour and strength gain parameters along with the effective reduction in w/c for both 0 and 50% FA replaced mixes. PGBS exhibited higher strength when compared to 0% replaced mixes though there was a slight increase in water content required for the cohesive mix.

Keywords Mortars · Superplasticizers · Flow behaviour · Fine aggregates · Processed granulated blast furnace slag

D. Arpitha (✉) · C. Rajasekaran
Department of Civil Engineering, National Institute of Technology, Surathkal, Mangalore, Karnataka 575025, India
e-mail: arpitha.5790@gmail.com

P. Kappadi
Department of Civil Engineering, Dayananda Sagar College of Engineering, Bangalore 560078, India

L. Nandagiri et al. (eds.), *Recent Advances in Civil Engineering*, Lecture Notes in Civil Engineering 256, https://doi.org/10.1007/978-981-19-1862-9_52

1 Introduction

Broad utilization of alternative materials as aggregates in concrete was hindered, principally because modest, great quality common aggregates were promptly accessible in many places of the world, yet additionally because broad research in regards to the properties of concrete with alternative aggregates is required [1].

Since there is an incredible interest in raw materials and natural assets are rare, it is predictable that the utilization of alternative materials in bulk in the cement and concrete industry would be financially favourable. As concrete innovation advances and the environment decays, it is currently evident that the boundless utilization of construction materials, with the initial expense being the predominant choice. Ecological concerns communicated by new legislation and business patterns have pushed the concrete industry towards limiting its environmental effect, for the most part by lessening CO_2 emissions and towards utilization of natural resources [2, 3]. Research demonstrates that there is overall low revenue for conventional aggregate substitution, either because of the absence of budgetary motivations or lacking regulations [4]. Likewise, the ecological improvement from utilizing alternative aggregates is constrained, contingent upon transport distances [5]. All together for the construction industry to go for creating such concrete, the ecological and monetary benefits must be clear and the technical advancements must be accessible.

The effective incorporation of granulated blast furnace slag in the form of fine aggregates as a construction constituent involves the reflection of certain problems. Primarily, this slag as an industrial by-product till recent times was disposed of in landfills. The query is, can it be an alternative suitable material in the construction sector? Then the technical features of the product are studied because of its physic-ochemical properties as steel slag involves special care, nevertheless can also afford maximum worth if utilized for specific requests. It is a co-product of steel obtained during steel extraction from iron and steel industries. The work carried out defined at this point, forms the part of an investigation program on the usage of alternative materials in advance concrete construction where greater strengths can be achieved by overcoming the compatibility-related issues. PGBS was produced to be used as a 100% replacement to river sand, for construction purposes by a new processing technique. The quality, strength, and durability of the concrete prepared with PGBS were found to satisfy the guideline prerequisites of the cube tests. This creative slag sand is a financially practical and ecologically adequate alternative material for supplanting conventional FA having a huge monetary effect, protection of natural assets, and profitable re-cycling co-products [6].

Firstly, the physical and chemical properties of the materials were evaluated through standardized tests to understand the above aspects. The research queries which instigate conducting this work are: How to resolve the workability issues by decreasing the water content to achieve higher flow properties for the selected new alternative material (PGBS)? How does PGBS will show its effect on the compressive strength of mortars? How much optimum percentage of slag is to be used? Does

the variation of percentage of slag affect the strength parameters? Does the optimum amount of slag fulfil the minimum engineering properties needed for construction?

An effort is made to understand the compatibility issues between ordinary Portland cement (OPC) and different types of SP with the incorporation of PGBS as a partial replacement for FA. This aids in understanding the ideal dosage required and w/c required to accomplish attractive advisable flow for mortars. Likewise, these features examine the properties of the green and seasoned condition of cement mortars. Flow table tests for various w/c, for diversified types and dosages of SP, were investigated in the present work. A trial program was completed to research the likelihood of producing cement mortars replacing the partial volume of secondary materials produced as by-products by industries. The alternative material tested was PGBS in contrast to FA.

Studies concentrated on the compressive quality of cement mortars which contain 0 and 50% substitution of PGBS for FA that led to comprehending the mechanical properties. Mortar mixes were prepared to recognize the achievability of producing mortars with the most extreme utilization of alternative materials. At varied ages, these mixtures were subjected to tests to determine their mechanical strength.

2 Materials Used for the Present Study

2.1 Binder

In the present work, OPC 53 grade conforming to IS: 12269-1987 has been used. The physical properties of OPC have been shown in Table 1.

Table 1 Physical properties of OPC

S. No.	Properties	Obtained values	Requirements as per IS: 12269-1987
1	Fineness	2.5%	Not more than 10%
2	Soundness	1 mm	Not more than 10 mm
3	Setting time Initial Final	170 min 380 min	Not less than 30 min Not more than 600 min
4	Compressive strength (As provided by manufacturer) 3 days 7 days 28 days	29.5 N/mm2 41 N/mm2 60 N/mm2	Not less than 27 N/mm2 Not less than 37 N/mm2 Not less than 53 N/mm2
5	Standard consistency	31%	–
6	Specific gravity	3.10	–

2.2 Fine Aggregates (FA)

Locally accessible river sand was sourced from Gurupura River Bed, Dakshina Kannada, India was used as FA. FA confirms to zone II of IS: 383-2016. FA supplied had a specific gravity of 2.6 with a water absorption capacity of 0.2% and fineness modulus of 3.59.

2.3 Processed Granulated Blast Furnace Slag (PGBS)

PGBS was supplied from M/s JSW Ltd., Bellary, India. Sieve analysis of FA and PGBS is shown in Fig. 1 which satisfies the requirement of IS codal provision. PGBS has a specific gravity of 2.55, a water absorption capacity of 1.4% with a fineness modulus of 2.34, and a bulk density of 1.44 g/cc. The results obtained from sieve analysis of PGBS aggregate are shown in Fig. 1. PGBS was similar to the true river sand. The size distribution of the processed granulated slag was also identical to river sand. The PGBS matched the required physical properties of fine aggregate to be used in concrete.

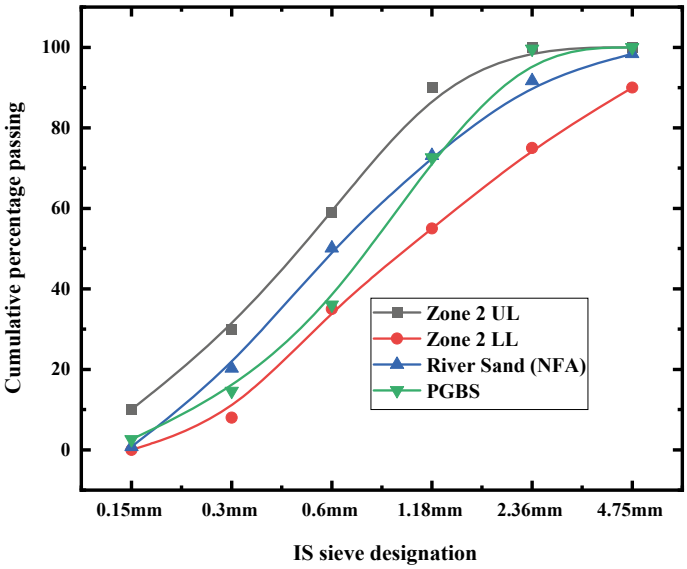

Fig. 1 Sieve analysis

2.4 Superplasticizers

Three different types of chemical admixtures were considered.

Lingo Sulfonate-Based SP: Pozzolith 102. A liquid form odourless dark brown superplasticizer with pH value ranging between 6 and 11 and the density will vary from 1.125 to 1.155 g/cm3 which is soluble in water and other solvents. This is a non-chloride extra set retarder and water reducer SP which controls the setting time on the variation of the dosage. This SP meets ASTM C494 requirements for type D water-reducing and retarding admixtures.

Naphtha-Based SP: Rheobuild 1125. Master Rheobuild 1125 is composed of Sulphonated Naphthalene Formaldehyde-based SP which is a dark brown free flow liquid having 1.24 density and $\geq$ 6 pH. Master Rheobuild 1125 is the preferred admixture for triple blend binder system-based high-performance concrete This SP conforms to ASTM C494 Type En934-2 T11.1/11.2G IS: 9103.

Poly Carboxylate Ether (PCE)-based SP: Master Glenium SKY 8233. Master-Glenium SKY 8233 is an admixture of a new generation based on modified polycarboxylic ether. MasterGlenium SKY 8233 is a reddish-brown liquid having a pH of $\geq$ 6 and a density of 1.08. It conforms to ASTM C494 Type F En934-2 T3.1/3.2, IS: 9103-1999, IS2645-2003.

3 Experimental Investigations

The experimental investigation was carried out to understand the feasibility of PGBS as a replacement for FA. The physical properties of the aggregates used in the mix proportion decide the quality of the mix. Therefore, it becomes important to understand the behavior of the aggregates in both fresh and hardened states.

3.1 Flow Table Test

The mortar mixtures were prepared per ASTM C109 using a Horbat blender. Flow test was conducted for all three types of SP and variation was done concerning the dosages of SP for every w/c from 0.4 to 0.5. Mortar mix was prepared for cement: sand of 1:3 by weight for 0 and 50% replacement of FA by PGBS. With this test, a truncated cone was loaded up with mortar samples and spot at the focal point of the flow table. The truncated cone was expelled leaving the mortar sample which was dropped consistently 25 times.

Graphs were plotted for the flow percentage versus dosages of chemical admixture. The curves at the dosage value beyond which the super-plasticizer would not build the flow with an increment in the dose of SP and the flow is resolved.

3.2 Compressive Strength of Cement Mortars

The cubes of mortar samples were cast in 7.07 × 7.07 × 7.07 cm moulds as per IS code 4031-1988 (Part VI). Cube specimens were cast for each mixture. After 24 h of curing under water, the mortar specimens were removed and subjected to Compressive strength, which was determined on a normal of three mortar samples for each combination were cured for 3, 7, and 28 days as per ASTM C109.

4 Results and Discussion

4.1 Performance of Flow for Mortar Mixes

Performance of flow for mortar mixes concerning w/c ratio without the addition of SP is depicted in Figs. 2 and 3. Sustaining sufficient workability of the green mortar mix without the addition of SP is a challenging issue. Because of this reason flow of cement mortar varies for the mix with and without SP. In Fig. 2 it is observed that the w/c demand is less compared to w/c obtained from Fig. 3. It is noted that partially replaced FA absorbs more water to achieve the desired flow. This may affect the strength parameters as water content increases though the required workability obtained is for less w/c in the case of Fig. 3.

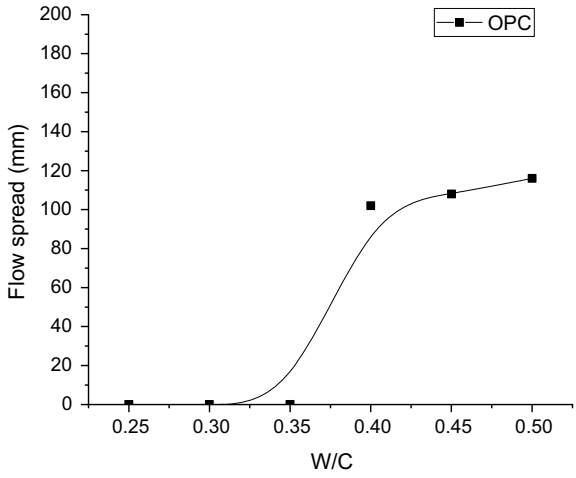

Fig. 2 0% replacement of FA

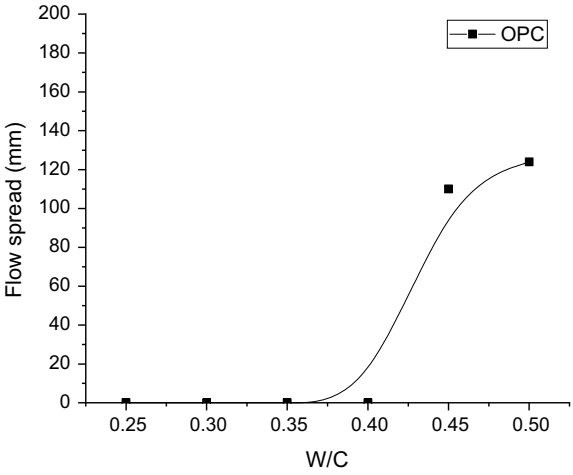

Fig. 3 50% replacement of PGBS for FA

4.2 Performance of Mortar Flow with Partial Replacements of FA

Fractional Substitution of FA by PGBS for 0.4 w/c

The quality and spread of the mortar depends on w/c. In this case, w/c of 0.4 is fixed and the dosage is varied for all types of SP along with the variation of FA partially by PGBS. It is observed that the amount of dosage of PCE required is less when compared to SNF-based and LS-based SP in both Figs. 4 and 5. The difference is in flow percentage, though not much variation is seen in the case of

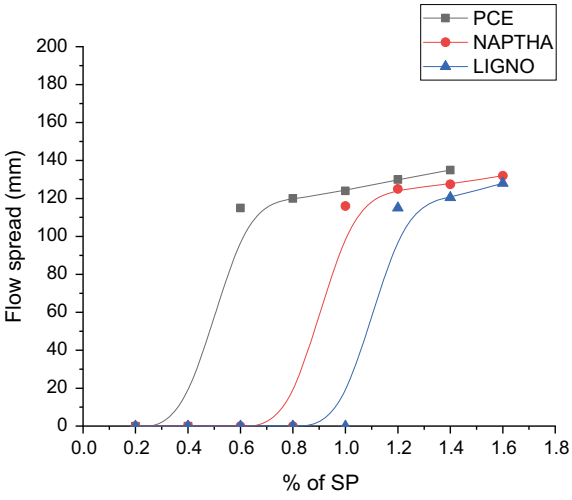

Fig. 4 0% replacement of FA

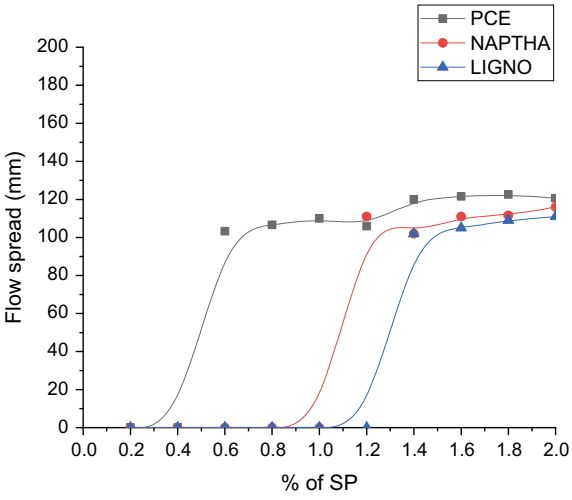

Fig. 5 50% replacement of FA by PGBS

the optimum percentage of SP adsorbed in the case of PCE in both the graphs. For the mix with SNF-based SP, the flow is appreciable in case of 0% replacement but variation happens when the shape and surface features of the aggregate change which demands more water content. But the chemistry of the mechanism has played a vital role when the same mix was made to flow by adding PCE. Thus, the optimum dosage of PCE required for both the mixes after partial replacement of FA has shown better flow which is remarkable.

Fractional Substitution of FA by PGBS for 0.45 w/c

As w/c decreases the amount of SP to reach the required flow increases. In Figs. 6 and 7 even though there is an increase in w/c there is only a slight consistent variation in dosage of the SP when compared to flow characteristics in case w/c 0.4. In this condition, the mix obtained had improved its cohesiveness. In the case of 50% replaced FA by PGBS, the optimum dosage obtained for all types of SP is almost equal to the optimum dosage of SP in the case of 0.4 w/c mixes. This shows that better flow is obtained without much increment in dosage of SP for the mix having PGBS by balancing water content in the mix.

Fractional Substitution of FA by PGBS for 0.5 w/c

As per the observation noted from 4.2. flows attained remained within the recommended limits stated by ASTM C1437as shown in Figs. 8 and 9 The outcomes with 50% partial replacement of the flow test demonstrate the slag sand mortar with PGBS slag. It is observed that the flow value has not shown much variation with the replacement of FA by PGBS and the w/c.

When the water-binder ratio is 0.4 and the PGBS slag replaces 0 and 50% of the FA, the flow values have tried to exhibit the minimum w/c required to get better workability. In the case of 0.45 w/c, the flow has revealed better quality in case of the

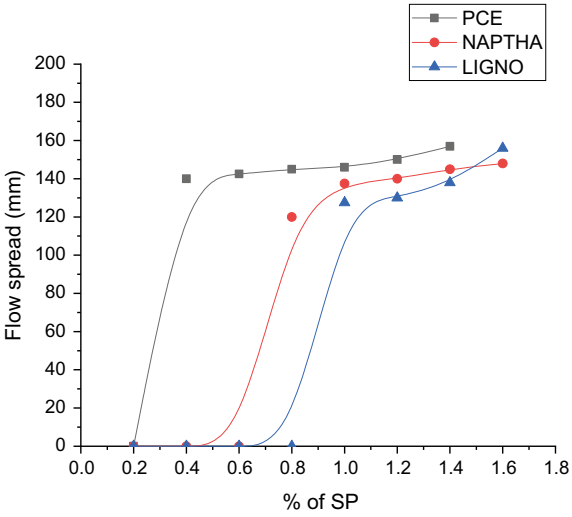

Fig. 6 0% replacement of FA

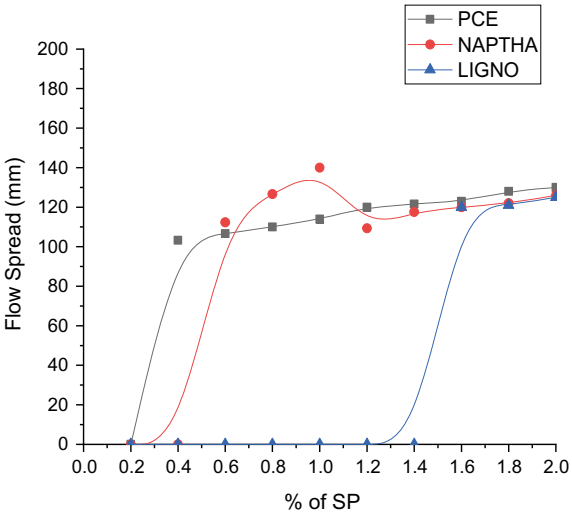

Fig. 7 50% replacement of FA by PGBS

texture of the mix, and the additional spread of the mortar was noted while related to the other w/c without any appearance of segregation or bleeding.

For the w/c ratio of 0.5, the mortar flow value intensifies with the intake of water. The small particle pore size of the PGBS slag absorbs water which results in more than water after the pores get filled though particle size is similar when linked with that of FA, the flow value increases. Therefore, the greater the PGBS replacement, the better is the workability.

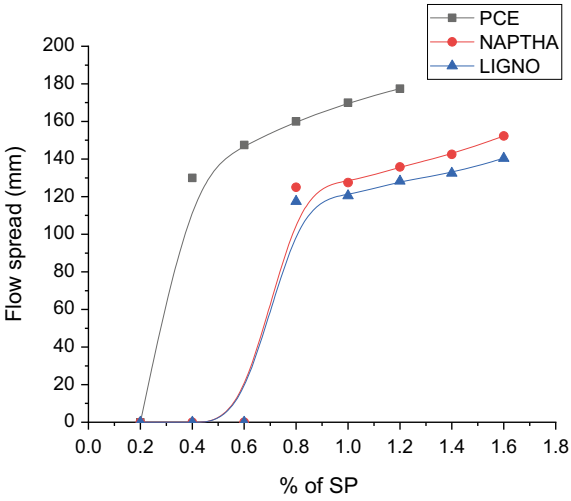

Fig. 8 0% replacement of FA

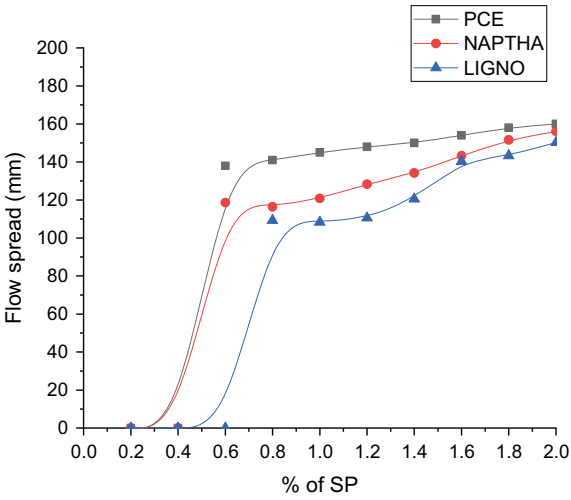

Fig. 9 50% replacement of FA by PGBS

4.3 Ideal Dosage of PCE, SNF, and LS to Decide Ideal W/C

In Fig. 10, the even distribution of cement granules can be observed along with the particles of PGBS. Results obtained from the above graphs show the optimum dosage of SP required for the mixes. But w/c optimization is also important to make sure for what percentage of SP dosage is it possible to achieve the same flow by optimizing the w/c. This helps to understand the requirements to get better workability, cohesiveness, and consistency in the mix that can be achieved which helps to produce better quality mortars. Figures 11 and 12 provide the values about the perfect combination of dosage

Fig. 10 Mortar with 50% PGBS and PCE

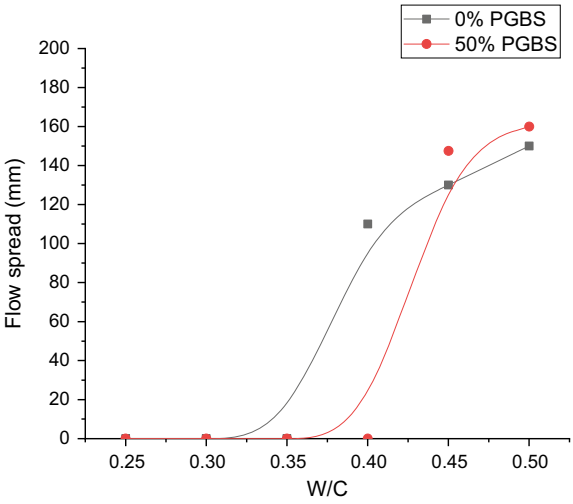

Fig. 11 W/c ratio for optimum dosages of PCE

of SP and optimized w/c. Also, the incorporation of PGBS partially for FA has proved that a good spread of mortars can be attained with a reduction in w/c and with less percentage of SP for the mix and not much variation is observed when compared with a mix of 0% replaced FA. With this indication, mortar cubes were cast for the optimized results.

From the results, a clear indication could be drained that PCE-based SP had performed better as it differed from all types of traditional SP and it was an innovative one as the distinctive mechanism of action significantly progressed the efficiency of scattering the cement particles. The negative charge of the cement grain surface gets intensified by the sulphonic groups of the polymer chains and scatter the particles

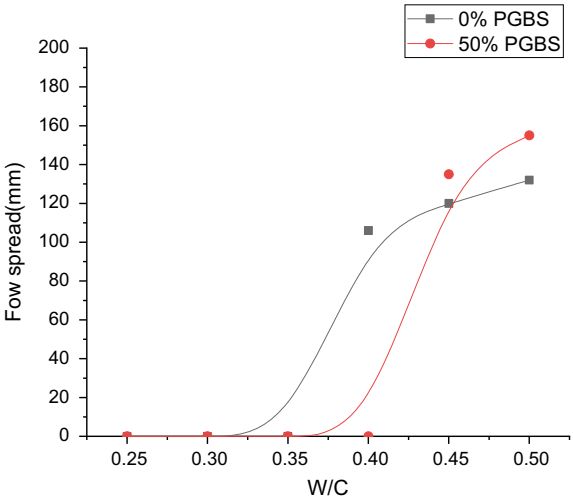

Fig. 12 W/c ratio for optimum dosages of SNF

of cement by electrical repulsion. Polymers get captivated by the cement particles in the case of SNF at a very initial phase of the mixing process as they cover around the grain surface areas [7].

The different chemical structure of PCE, when compared to other SP, involves the carboxylic ether polymer which has long side chains that initiate the similar electrostatic dispersion mechanism like traditional SP, but the side chains connected to the polymer backbone create a steric hindrance which significantly makes the cement particles stable and capable to discrete and scatters. Steric hindrance offers a physical barricade (alongside the electrostatic barrier) among the cement particles. As a result concrete flow increases with a great reduction in water content. When water is added to the mixture the distance between the cement granules increases and viscosity decreases. The static workability of the mix is influenced by w/c. This static flowability was not seen though there was an increment in SP dosages for w/c 0.35 until there was a disturbance created by dropping the tabletop 25 times after which a dynamic flow was observed along with the increase in w/c. Flow value increased with an increase in dosage of SP and the optimum dosage was noted after which there was only a slight increase in the flow which resulted in bleeding with the increase in SP dosage.

The point at which a slight movement of the mix was observed was considered as the initial point for further investigation from which the critical behaviour of every mix was drawn till it reached the saturation point. There was a difference in the optimum dosages obtained which was pure because of different chemical structures present in different brands of SP. Based on these factors the better percentage dosage of SP required for the specific mix was estimated.

4.4 *Impact of Fractional Substitution of FA by PCBS on Compressive Strength of Mortars*

The lesser bulk density found with the usage of granulated blast furnace slag when compared to FA had resulted in the reduction of the strength of concrete. Decrease in specific gravity with increase water absorption added to lower the properties of the mix. Microstructural studies had shown the presence of vesicular structure along with micropores existing in the slag particles. PGBS was produced by improving the physical characteristics of the slag to overcome these problems which satisfied all requirements required to produce good concrete when replaced up to 100% replacement [8].

It is observed that as PGBS content increases the amount of SP correspondingly increases to meet the desired flow properties. The PCE polymer was voluntarily and permanently adsorbed by some clay fines that were present in aggregates. PCEs were moderately unaffected from, the time of adding, permitting for better flexibility in mixes. The saturation dosage obtained for all types of SP was considered to cast the mortar cubes for the optimum w/c noted from Figs. 11, 12, and 13. The compressive strength results for 0% FA and 50% replaced FA by PGBS increased due to the positive effect of PCE which increased the workability and scattering of cement grains (Figs. 14 and 15).

As predicted, strength improved with the curing period. The results also show that FA replaced mortar cubes gained maximum strength at every phase of curing. This specified that 50% replacement was a better suitable substitute for FA. This tendency could be due to the angular shape of slag particles. The bonding with cement paste and magnitude of surface area increases as the amount of these type of particles intensifies. Also, this decreases the huge stress concentrations caused internally important for

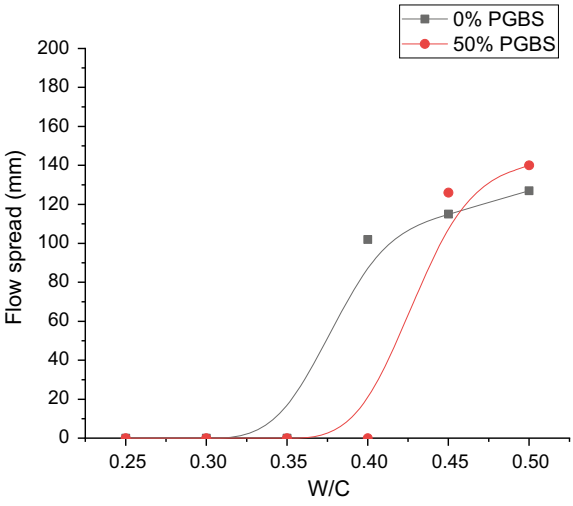

Fig. 13 W/c ratio for optimum dosages of LS

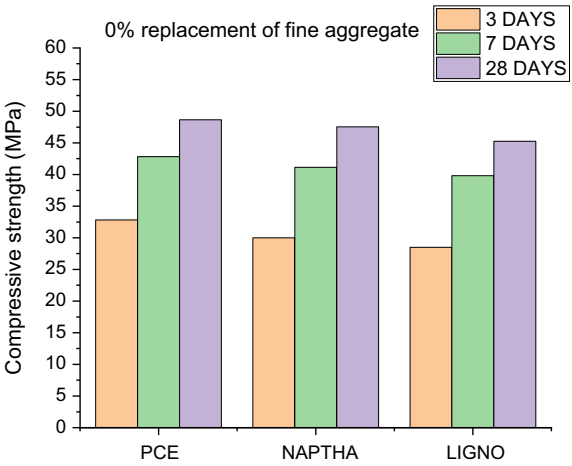

Fig. 14 Compressive strength of mortars for 0% replacement of FA

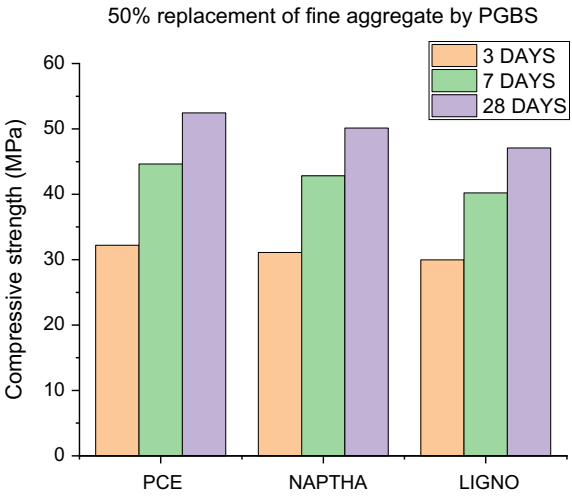

Fig. 15 Compressive strength of mortar for 50% replacement of FA by PGBS

higher strength values and no expansion was observed unlike when other slags when replaced for FA. For mortars with PCE, the compressive strength got increased as interparticle in cement particles got reduced and even dispersion of particles in the mix with reduced w/c. SNF and LS belong to polyelectrolytes and sulphonated groups are attached to their main polymer chains. The negative charges are produced when it adsorbs on the surface of cement particles that cause scattering of particles by electrostatic repulsion between cement granules. Super retarding setting of the paste or the paste will never set is the general problem faced by LS-based SP.

LS which are formed by phenylpropane units that are connected by ether non-regular and latter is found between aromatic rings. This differed with age-old certainty that previous generation polymers perform uniquely by electrostatic repulsion. The

setting of cement gets delayed with LS. The molecular weight also affected the performance of LS. The higher molecular weight fractions of LS exhibited better plasticizing properties [9]. But the cementitious system having high ionic strength gradually reduces the electrostatic repulsion [10].

5 Conclusions

1. On no account noteworthy variation in the behaviour of mortars was observed for mortars with and without replacement of FA by PGBS.
2. The pattern of flow behaviour was almost similar though there were variations in absolute values obtained.
3. PGBS demanded more w/c compared to FA but the bleeding was observed for 0.5 w/c. This shows that cohesive mix and better flow can be achieved for lesser w/c but a minimum of 0.4 w/c is required for the mortars for both 0 and 50% replaced FA.
4. SP having PCE are formulated with a defoamer which controls the air entrainment in-built with the PCE polymer. This creates a demand in concrete applications as effective management of air contents can be done with proper selection of PCE-based SP.
5. The significant strength variance, attained by just altering the SP type from LS, SNF to PCE, was beneficial in dipping cement contents despite the fact which met the strength conditions. Remarkably, the strength alteration may not appear to be related to improved heat of hydration. PCE-based SP has calcium-based accelerating or corrosion-inhibiting content that might have resulted to produce denser microstructure which may be the reason for strength gain.
6. However, SNF-based SP has also tried to provide good results but performance-wise when compared to PCE-based SP it has decreased due to differences in chemical structures.
7. The performance of PGBS was proved to be better in concern to basic properties of the material, flow properties, and hardened state of mortars when compared to FA.
8. Reduction in cost makes this material more viable and a permanent solution for the disposal of this industrial waste by effective utilization adds to the list of available eco-friendly material.
9. This contributes to the sustainable green building construction with the probable improvement in durability properties.

References

1. Saak AW, Jennin HM, Shah SP (2004) A generalized approach for the determination of yield stress by slump and slump flow. Cem Concr Res 34(3):363–371
2. Mroueh U, Eskola P, Laine-Ylijoki J (2001) Life-cycle impacts of the use of industrial by-products in road and earth construction. Waste Manage 21:271–277
3. Rao A, Jha KN, Misra S (2007) Use of aggregates from recycled construction and demolition waste in concrete. Resour Conserv Recycl 50(1):71–81
4. Golaszewski J, Szwabowski J (2004) Influence of superplasticizers on rheological behaviour of fresh cement mortars. Cem Concr Res 34:235–248
5. Motz H, Geiseler J (2001) Products of steel slags an opportunity to save natural resources. Waste Manage 21:285–293
6. Satish Kumar D, Kumar P, Sah R, Kaza M, Prasad SMR (2016) Converting granulated blast furnace slag as fine aggregate. Int J Civ Eng Res 7:91–103
7. Flatt RJ, Bowen P (2004) Electrostatic repulsion between particles in cement suspensions: domain of validity of linearized Poisson–Boltzmann equation for nonideal electrolytes. Cem Concr Res 33:781–794
8. Reknes K, Petersen BG (2003) Novel: Lignosulfonate with superplasticizer performance. In: Malhotra VM (ed) Proceedings 7th CANMET/ACI International conference on superplasticizers and other chemical admixtures in concrete. Berlin ACI, Supplementary Papers, pp 285–299
9. Setién J, Polanco JA, Alaejos P, Sánchez de Juan M (2013) Durability of recycled aggregate concrete. Constr Build Mater 40:1054–1065
10. Giaccio G, Zerbino R (2002) Optimum super-plasticizer dosage for systems with different cementitious materials. Indian Concr J 76:553–566

Effect of Binder Type on the Properties of Dry Lean Concrete Mixes

Somanath Khot, Nitendra Palankar, Archana N. Shagoti, and B. M. Mithun

Abstract The present study concentrates on evaluating the mechanical and durability properties of Dry Lean Concrete (DLC) manufactured with Ordinary Portland Cement (OPC) and Portland Pozzolana Cement (PPC) based on mix design and IRC: SP:49–2014 guidelines. In the present investigation, the OPC mixes are prepared for binder contents of 160, 173 and 186 kg/m^3 and PPC mixes are prepared for 178, 197 and 215 kg/m^3 binder contents to identify the optimal mixes for moisture contents. The prepared DLC mixes for both OPC and PPC were evaluated for the mechanical properties and durability properties. From the comparative evaluation of compressive strengths of the prepared mixes, it is evident that the OPC containing 186 kg/m^3 and PPC mix having binder content of 215 kg/m^3 yielded targeted strength. The suitable moisture content for DLC mixes observed irrespective of the type of the cement was in the range of 6.02–6.52%.

Keywords Dry lean concrete · Eco-friendly materials · Mechanical property · Durability

1 Introduction

Cement concrete is the most versatile and famous construction material from past few decades. The consumption of cement in construction industry is increasing day by day, especially in countries like China and India. India has produced around 340

S. Khot · N. Palankar (✉) · A. N. Shagoti
Department of Civil Engineering, KLS Gogte Institute of Technology, Belagavi, India
e-mail: nnpalankar@git.edu

S. Khot
e-mail: smkhot@git.edu

A. N. Shagoti
e-mail: anshagoti@git.edu

B. M. Mithun
Department of Civil Egineering, NMAM Institute of Technology, Karkala, Udupi, India
e-mail: mithunbm@nitte.edu.in

L. Nandagiri et al. (eds.), *Recent Advances in Civil Engineering*, Lecture Notes in Civil Engineering 256, https://doi.org/10.1007/978-981-19-1862-9_53

million metric tonnes of cement in the year 2020, standing 2nd to China, which has produced 2.20 billion metric tonnes of cement in 2020 [1]. The major drawback of cement production industry is emission of greenhouse gases and thus leading to global warming and climate change globally. In view of this, uses of industrial waste products having pozzolanic properties are being used in cement manufacturing process to produce blended cements.

The performance of blended cements is at par with Ordinary Portland cement and by effective usage of industrial wastes in construction, the theme of sustainability in construction is attained. Portland Pozzolana cement and Portland Slag cements are widely used in construction industry in India. The highway infrastructure is one such area where cement concrete is widely used in construction of rigid pavements. In India, only 3.5% of roads are made up of rigid pavements and 58.8% is made with bituminous material. With increase in population and economy, the commercial traffic is growing at a rate of 7–8% annually. Hence, Ministry of Road Transport and Highways [MORTH] is initiating the construction of new expressways and national highways across the country, which are being constructed with rigid concrete pavement for its high durability and lesser maintenance. Most of the time, rigid concrete pavements comprise of pavement quality concrete (PQC) functioning as a wearing course followed by DLC functioning as base layer or sub-base layer and will be resting on prepared subgrade soil. The type of base course provided for PQC greatly influences the mechanical and durability properties of rigid pavements. In India, DLC is widely used as base course/sub-base course layer for the PQC. Dry lean concrete (DLC) is basically consisting of high aggregate to cement ratio and does not have any slump value. The minimum cement quantity required to prepare DLC is about 140 kg/m^3 [2]. DLC not only provides the firm supporting layer for PQC, but it also acts as a drainage layer due to its high aggregate to cement ratio and making it a suitable material for base course/sub-base course. As per IRC: SP: 49-2014, the DLC can be prepared with OPC, PPC and PSC. The minimum compressive strength required for DLC to be used as a base course or sub-base course layer after 7-days water curing for OPC is 10 MPa for 140 kg/m^3 [2]. However, there is no clear mentioning of amount of binder content, cement to aggregate ratio, moisture contents to be used if DLC is manufactured with PPC and PSC. For Expressways, National highways and State highways 150 mm thick DLC layer is recommended, however, actual thickness is directed based on design requirements. The use of DLC as base course can reduce mud pumping, firm support for formwork for laying PQC and laying dowel bars, evenly distributing the loads to subsequent layers and it was evident that on properly designed and constructed DLC layer, the designer can reduce the thickness PQC layer on account of axle load distribution. For the purpose of sub-base course, 100 mm thick DLC layer is sufficient. If the width of DLC as base course/sub-base course is extended beyond pavement edges up to 500 mm or so, there is an improvement in the flexural strength characteristics of PQC and it also helps in mobilizing the construction equipment [3]. To attain sustainability in construction materials, IRC: SP:49-2014 promotes the use of Fly ash (FA) and Ground Granulated Blast Furnace Slag (GGBFS) in preparation of DLC at specified range of 15–30% and 25–30% respectively by total weight of binder content [2].

Although, the DLC beings a significant layer in concrete pavement, no satisfactory research data is available on DLC. S. Suryateja evaluated the effect of extended DLC base layer on flexural strength properties of PQC using FEM Analysis and found that there is a reduction of stresses on PQC and also the PQC layer can be curtailed [3].

From the long-term studies, it was evident that the water absorption and effective porosity were least for PSC than PPC and OPC in order. The corrosion resistance properties were found to be better in case of PSC samples than PPC and OPC [4]. Fly ash is used in many civil engineering constructions mainly in construction of embankments. Copper slag and Stone dust blended together for fine aggregates replacement in the proportions of 20, 40, 60 and 80% to manufacture DLC and it was concluded that up to 40% use of copper slag as blending material has resulted in required mechanical properties [5]. Along with industrial by-products usage in DLC preparation, studies have been carried out to the feasibility of using Reclaimed Asphalt Pavement (RAP) aggregates, Copper slag, etc., in manufacturing of DLC. From the studies, results were evident that RAP aggregates extracted from 3.0 years aged asphalt pavements nearly 75% of aggregates can be used as coarse aggregates and up to 50% can be replaced as fine aggregates [6]. Kumar performed a study on DLC manufactured with OPC versus PPC and he concluded that the amount of PPC required to gain the required strength after 7-days curing would be 10–15% higher than the OPC content and required moisture content is also on higher side than required for OPC [7].

In construction practices, often DLC is manufactured as sub-base layer and serving as drainage layer too. The strength requirements after 7-days water curing would be 10 MPa. As per standard instructions from code, moisture contents should be in the range of 5, 5.5, 6, 6.5 and 7% by weight of the total mixture for OPC consisting minimum of 140 kg/m^3 and 1:14 cement to aggregate ratio. If PPC is used for manufacturing of DLC, then the cement to aggregate ratio is kept up to 1:12 [2].

2 Experimental Analysis

2.1 Ingredients

In the present investigation, DLC mixes are manufactured with OPC-43 [8] and PPC confirming to IS 1489-2005 [9]. The binder properties were assessed according to standard procedures. The coarse aggregates were procured locally and the engineering properties assessed as per standard specifications of BIS [10], so as to use in the manufacturing of DLC. In Table 1, the engineering properties of the ingredients are presented.

The gradation of the aggregates used is as instructed in guidelines [2]. The coarse aggregates used were restricted to maximum of 26.5 mm. The fine aggregates used were found to be in Zone II gradation and the evaluations were done as per standard

Table 1 Engineering properties of the ingredients

Basic property	Natural coarse aggregates	Natural fine aggregates	Binder	
			OPC	PPC
Specific gravity	2.72	2.67	3.15	3.15
Crushing value (%)	28.81	–	–	–
Abrasion value (%)	16.62	–	–	–
Impact value (%)	11.28	–	–	–
Water absorption (%)	0.38	1.13	–	–
Blaine's fineness (m^2/kg)	–	–	325	342
3-days compressive strength (MPa)	–	–	26	23
7-days compressive strength (MPa)	–	–	33	31
Normal consistency (%)	–	–	32	35
Initial setting time (min)	–	–	94	120
Final setting time (min)	–	–	330	350

specifications [2]. The potable water is used for preparation of specimen and as well as for curing.

2.2 Mix Design

An attempt is made to compare the DLC mixes prepared with OPC and PPC using new mix design approach which considers volumetric calculation [11].

For the defined moisture contents, the mix design was prepared. A flexibility is offered to the designers in IRC: SP: 49-2014, so that the cement content can be varied to arrive at the cement and aggregate ratio. A minimum of 140 kg/m^3 cement content and maximum aggregate ratio to be 1:14 is recommended for OPC mixes and maximum aggregate ration of 1:12 is mentioned for the use of PPC. However, there is no specific mention of minimum cement content to be used for DLC mixes when PPC/PSC is used [2]. By mix design approach, the minimum required mechanical and durability properties of DLC manufactured with OPC can be attained as mentioned in IRC: SP: 49-2014 [11].

The mix design for both OPC and PPC was carried out by estimating the volume of each ingredient by limiting the ratio of the materials as guided in the standard specifications [2]. The water content is fixed so as to reach the recommended moisture contents of 5.49, 6.02, 6.52 and 7.02% for both OPC and PPC mixes. The different

cement contents of 160, 173 and 186 kg/m^3 for OPC and 178, 197 and 215 kg/m^3 for PPC are considered. After doing the calculations of individual volumes of ingredients in the mix, the amounts of binder and coarse aggregate were tuned to be in the 1:14 for OPC mixes and 1:12 for PPC mixes as per guidelines [2].

2.3 Methodology

In this study, the binder contents for both OPC and PPC were arrived based on design calculations. The tilted drum mixer is used for mixing of the ingredients and for the manufacturing of specimen. The Vibrating Jack Hammer [7] is used for compaction of the cube specimens of size 15 × 15 × 15 cm. The specimens were water cured for 7-days. In Table 2, the details of the mix proportions of the ingredients used in preparation of OPC and PPC specimens are presented. The prepared mixes were assessed for their mechanical properties. The durability aspects like water absorption, Volume of Permeable Voids (VPV) and Ultra-Sonic Pulse Velocity (UPV) were assessed for OPC and PPC mixes. Vee-Bee Consistometer is used to evaluate the consistency of freshly prepared DLC mixes. The prepared specimens were cured for 7-days in water and tested for both compressive and flexure strength characteristics [5]. The durability properties like UPV test and VPV test were performed as mentioned in the guidelines of ASTM C 597-09.

3 Results and Discussions

3.1 Compressive Strength

The compressive strength of OPC and PPC DLC mixes are presented in Fig. 1 and Fig. 2 respectively. The DLC mixes were water cured for 7 days and tested for compressive strength. From the figure, it was observed that the strength for DLC mixes for OPC and PPC were in between 10.22 MPa to 14.26 MPa and 9.86 MPa to 13.87 MPa respectively. The results indicate that for OPC mix of O11 for 6.52% moisture content attained 14.26 MPa strength, which highest than any other combinations for OPC mixes. On the other hand, from Fig. 2 PPC mix P10 yielded strength of 13.98 MPa for 6.02% moisture content. From Figs. 1 and 2 it was evident that, there exist a direct proportion to binder content and strength of the DLC till moisture content reaches 6.52% and beyond the 6.52% moisture content, it was observed that there is a slight downward trend in the compressive strength for both OPC and PPC mixes. It was observed that the strength of OPC mixes yielded higher values than that of PPC mixes for same moisture contents. The reason for increased PPC content in the present study was to attain the same amount of compressive strength

Table 2 Ingredients quantities for different binder contents

OPC				
Binder content of 160 kg/m^3				
Moisture content (%)	5.49	6.02	6.52	7.03
Water content (kg)	135	147	158	169
Mix No.	O1	O2	O3	O4
Cement to aggregate ratio	1:13.54	1:13.34	1:13.15	1:12.97
Fresh density (kg/m^3)	2460	2440	2422	2404
Binder content of 173 kg/m^3				
Mix No.	O5	O6	O7	O8
Cement to aggregate ratio	1:12.46	1:12.27	1:12.10	1:11.93
Fresh density (kg/m^3)	2462	2443	2425	2406
Binder content of 186 kg/m^3				
Mix No.	O9	O10	O11	O12
Cement to aggregate ratio	1:11.53	1:11.35	1:11.20	1:11.04
Fresh density (kg/m^3)	2465	2445	2427	2408
PPC				
Binder content of 178 kg/m^3				
Mix No.	P1	P2	P3	P4
Cement to aggregate ratio	1:12.08	1:11.90	1:11.74	1:11.57
Fresh density (kg/m^3)	2463	2443	2426	2407
Binder content of 197 kg/m^3				
Mix No.	P5	P6	P7	P8
Cement to aggregate ratio	1:10.84	1:10.67	1:10.58	1:10.38
Fresh density (kg/m^3)	2466	2447	2428	2410
Binder content of 215 kg/m^3				
Mix No.	P9	P10	P11	P12
Cement to aggregate ratio	1:9.86	1:9.71	1:9.57	1:9.48
Fresh density (kg/m^3)	2469	2449	2431	2413

as compared to OPC mixes and hence 10–15% higher PPC content should be considered [7]. Higher binder content and increased moisture contents for both OPC and PPC have increased the compressive strength for all mixes, which is due to increased movement of ingredients in the mixes. For the lesser binder contents, the mixes were found to be too dry and harsh and there is no considerable amount of compressive strength was noticed [11]. From the results, it is noticed that for OPC and PPC mixes, the ideal moisture content suitable for the manufacturing of DLC would lies in between 6.02–6.52%. However, the cement content for OPC would be 15–18% lesser than that required for PPC mixes. The initial strength of PPC mixes was on lower side as compared to OPC and the long-term strength gain of PPC mixes is at

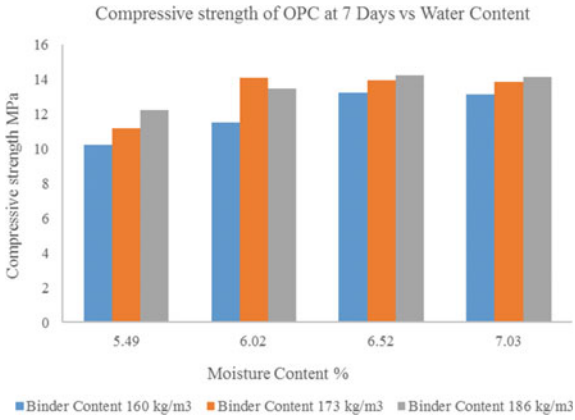

Fig. 1 Compressive strength of OPC

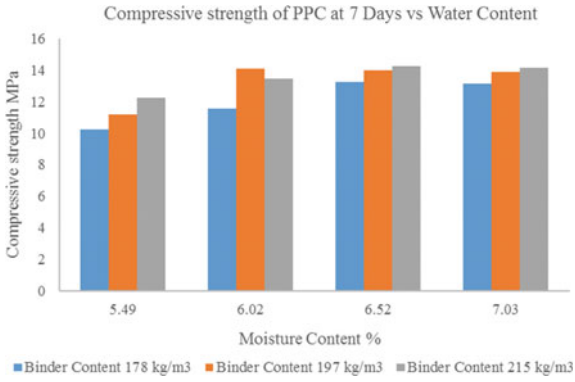

Fig. 2 Compressive strength of PPC

par with the requirements [5, 7]. From the application side of DLC mixes, the binder content of 186 kg/m^3 of OPC and 215 kg/m^3 of PPC would be ideal for the moisture content in the range of 6.02–6.52%.

3.2 Flexure Strength

The flexure strength of DLC is important in reducing the overall stresses on subsequent layers as well as for PQC [3]. The two-point loading conditions were applied for prepared DLC mixes for OPC and PPC specimen [12]. The flexural strengths of OPC and PPC mixes were presented in Fig. 3 and Fig. 4, respectively. From the results, it was observed that the amount of binder in the mixes directly affects the strength, both for OPC and PPC mixes. The mixes O1 to O4 and P1 to P4 with lesser binder contents than other mixes have shown less flexural strengths. As the moisture content increased, good consistency is attained and leading to noticeable increase in

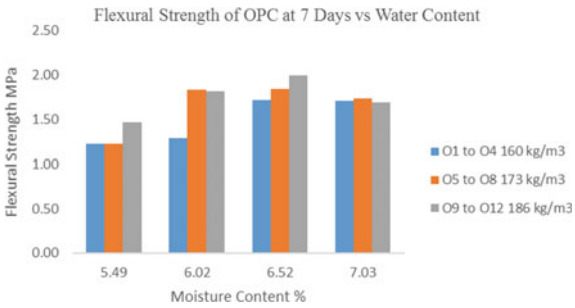

Fig. 3 Flexural strength of OPC

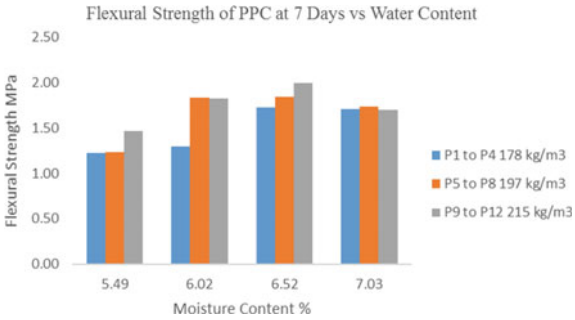

Fig. 4 Flexural strength of PPC

the strength for both OPC and PPC mixes. OPC mix O11 and PPC mix P10 have attained maximum flexure strengths than any other trials. The ideal moisture content would be 6.02–6.52% for both OPC and PPC-based DLC mixes.

3.3 Water Absorption and VPV

The DLC specimens were tested for Water absorption and VPV after curing period of 7 days as per ASTM C 642-06 guidelines and the results are tabulated in Table 3. The OPC specimens O1 to O12 have displayed slightly higher values as compared to DLC specimens prepared with PPC. The higher binder contents for PPC mixes could be the reason for lesser values of water absorption and VPV as compared to OPC. The binder to aggregate ratio for PPC mixes was kept within 1:12 as compared to 1:14 for OPC mixes [2]. Higher binder to aggregate ratio has slightly increased the VPV values in OPC-based DLC mixes as compared to PPC-based DLC mixes.

Table 3 Durability test results on OPC and PPC specimens

DLC mixes manufactured with OPC				
Mix ID	Water absorption (%)	VPV (%)	UPV (km/s)	Vee-Bee consistency (s)
O1	6.51	16.29	3.82	18.50
O2	5.78	15.87	3.94	17.88
O3	4.72	14.92	4.08	16.87
O4	4.23	13.75	4.11	14.35
O5	6.22	15.94	4.18	17.47
O6	5.66	15.24	4.22	16.98
O7	4.62	14.52	4.31	15.54
O8	4.12	13.81	4.28	13.62
O9	6.10	15.26	4.22	16.88
O10	5.41	14.21	4.28	15.28
O11	4.51	13.78	4.38	14.64
O12	4.1	13.41	4.30	13.24
DLC mixes manufactured with PPC				
P1	6.38	15.87	3.90	17.86
P2	5.62	15.49	4.10	17.23
P3	4.66	14.52	4.08	15.54
P4	4.13	13.71	4.14	14.21
P5	6.10	15.54	4.11	17.19
P6	5.54	15.37	4.19	16.52
P7	4.48	14.21	4.28	14.80
P8	4.10	13.54	4.28	13.42
P9	5.86	15.10	4.34	15.59
P10	5.41	14.12	4.37	15.19
P11	4.40	13.57	4.40	14.12
P12	3.98	13.21	4.47	12.94

3.4 Ultra-Sonic Pulse Velocity Test

The analysis of the test results for present comparative study were presented in Table 3. The results indicate that the OPC mixes have recorded lower UPV values than PPC mixes. The PPC mixes were having 10–15% higher binder content than OPC mixes and lesser binder to aggregate ratio [2]. This shall be related to the higher VPV values in OPC specimens and lower UPV values and vice-versa for PPC specimens. Even in OPC mixes, increased UPV values are noticed as binder and moisture contents increased, this could be because increased binder content leading to increased mobility and better compaction in the mixes. The UPV values for OPC

specimens lie in between 3.82–4.38 km/s and for PPC in between 3.90–4.47 km/s, which were within the range of specified values to be ranked as good quality concrete.

3.5 Vee-Bee Consistometer Test

In this investigation, the consistency of OPC and PPC were evaluated by conducting the Vee-Bee Consistometer test and the results are presented in Table 3. With high binder to aggregate ratio, DLC mixes are harsh mixes [13]. The results indicate that the DLC mixes based on OPC displayed slightly higher Vee-Bee seconds than the PPC mixes. This may be attributed due to increased binder content of PPC than OPC mixes [7]. The binder to aggregate ratio is also higher for OPC mixes than PPC mixes, hence PPC mixes attained better constancy and slightly lesser Vee-Bee seconds. It may be noted that, as moisture content increased, irrespective of type of binder viz. OPC or PPC, the Vee-Bee consistency displayed lower time. Similar trends of lower Vee-Bee seconds were observed for both the mixes prepared with OPC and PPC.

4 Conclusions

The conclusions for the present comparative study were summarized as below.

1. From the obtained results it is evident that, the amount of binder is directly proportional to the consistency and nature of compaction of DLC mixes both for OPC and PPC-based mixes. The ideal moisture content for both OPC and PPC mixes were found to be in the range of 6.02–6.52% irrespective of the type of cement. The binder content of OPC mix 186 and 215 kg/m^3 have recorded the minimum targeted compressive strength and flexure strength. The strength values of OPC mixes were comparatively higher than PPC mixes. To attain similar strength characteristics of OPC, 10–15% additional PPC should be considered. However, the PPC mixes attain better compressive strength in long term.
2. Volume of Permeable Voids and Water absorption values found to be slightly higher for OPC-based DLC mixes than PPC-based DLC mixes. The higher binder to aggregate ratio in OPC mixes has resulted in minimal increase in the VPV values.
3. The PPC-based DLC mixes displayed comparatively better UPV values than OPC-based DLC mixes. The higher binder content of PPC mixes attained better compaction and consistency. The UPV values for OPC mixes lie in between 3.82–4.38 km/s and for PPC mixes 3.90–4.47 km/s, which were within the range of specified values to be ranked as good quality concrete.
4. Increase in the moisture contents in DLC mixes, irrespective of the type of binder has resulted in the lower Vee-Bee time.

5. It may be summarized that the use of PPC-based DLC mixes would yield similar mechanical and durability characteristics for the same moisture contents. The use of PPC can be an effort to attain the sustainable approach in construction of DLC layers for rigid pavements.

References

1. Ministry of Road Transport and Highways [MORTH] (2016–2017) Basic Road Statics of India
2. IRC (2014) Guidelines for the use of dry lean concrete as sub-base for rigid pavement. New Delhi
3. Suryateja S, Reddy MA, Pandey BB (2018) Effect of extended dry lean concrete base on flexural stresses in concrete pavements. J Indian Roads Congr 79(2)
4. Saraswathy V, Karthick S, Lee HS, Kwon SJ, Yang HM (2017) Comparative study of strength and corrosion resistant properties of plain and blended cement concrete types. In: Advances in materials science and engineering
5. Kumar B (2013) Properties of pavement quality concrete and dry lean concrete with copper slag as fine aggregate. Int J Pavement Eng 14:746–751
6. Singh S, Ransinchung GD, Monu K (2019) Sustainable lean concrete mixes containing wastes originating from roads and industries. Constr Build Mater 209:619–630
7. Kumar R (2016) A comparative study on dry lean concrete manufactured with OPC vis-a-vis PPC to be used for the construction of concrete roads. Indian Concr J 70–76
8. Bureau of Indian Standard (BIS) (2013) IS:8112–1989, Specification for 43 grade Ordinary Portland cement. Bureau of Indian Standard, Delhi, p 17
9. Bureau of Indian Standard(BIS) (2005) IS:1489(Part 1)—1991(Reaffirmed 2005), Portland Pozzolana cement specification fly ash based. Bureau of Indian Standard, Delhi
10. Bureau of Indian Standard (BIS) (1970) IS 383:1970 Specification for coarse and fine aggregates from natural sources for concrete. Indian Standard, pp 1–24
11. Khot S, Mithun BM, Shagoti AN, Palanakar N (2022) Studies on dry lean concrete with new mix design approach. In Sustainability trends and challenges in civil engineering. Springer, Singapore, pp 917–926
12. IS 516:2014 (2004) Method of tests for strength of concrete. IS 516-1959 (Reaffirmed 2004). New Delhi, India
13. Chandrashekhar SY, Madhu KA, Anil Kumar MS, Rajakumara HN (2019) Production of dry lean concrete by sustainable materials to use in road sub-base layer for rigid pavement. Int J Recent Technol Eng **8**:750–757

Visualize the 3D Virtual Model Through Augmented Reality (AR) Using Mobile Platforms

Janakaraj Murthy, Raksha Rajani Dsouza, and A. R. Lavanya

Abstract The Architecture, Engineering, and Construction (AEC) industry is amongst the oldest. Developments to transform the virtual models and visualize them in the real world are the ongoing innovations. The AEC industry often faces problems in communicating ideas, which may look vague or cannot come up with the words to describe them between the client and the work executers; errors during construction due to lack of imagination; improper planning and execution; and wastage of resources. To address the lack of imagination or visualization of elements in architecture, an effort has been made by creating virtual 3D models like chairs, tables, office cabins, and furnished house structures. The elements are exported to a game environment to create an application that can be used on the Android platform. This in turn helps the user to visualize the 3D model with details and proactively rectify the errors. The app development kit includes Unity 3D and Vuforia. This paper focuses on the development of an application for the visualization of virtual 3D models augmented on the Android mobile platform.

Keywords Augmented reality · 3D model · AEC industry · Mobile augmentation · Android

1 Introduction

1.1 General

Augmented Reality transforms the surroundings into a digital interface by inserting virtual items into the actual world, in actual time [1] Unlike virtual reality, which creates a fictitious environment, augmented reality uses the existing environment and overlays new data on top of it.

In the architecture, engineering, and construction industries, a few issues are looked at because of inappropriate communication between the customer and the

J. Murthy (✉) · R. R. Dsouza · A. R. Lavanya
Department of Civil Engineering, NMAM Institute of Technology, Nitte, India
e-mail: janakaraj@nitte.edu.in

L. Nandagiri et al. (eds.), *Recent Advances in Civil Engineering*, Lecture Notes in Civil Engineering 256, https://doi.org/10.1007/978-981-19-1862-9_54

work executers; mistakes during development because of improper visualizations; blunders because of improper planning that prompts improper execution of undertakings; and wastage of time, cash, and different assets. These issues will be overcome by increased reality, where one will be able to perceive what's happening in real time. A blend of advanced innovation, virtual data, and mobile technology makes it simpler to imagine the 3D model in genuine condition.

1.2 Background

See Table 1.

1.3 Augmented Reality Concepts

Each time when an augmented reality application is developed, the common processes that take place at every stage are:

a. The real world's current state must be determined by the application.
b. The virtual objects current state must be determined.
c. The augmentation of virtual object's with respect to the real world should be in such a way that the user should feel that those virtual objects are present in the real world itself, then again move to step a, as it is a continuous process.

The augmented reality system should mainly consist of camera, sensors, processor and display.

1.4 Mobile Augmented Technology

In day to day life, mobile has become a very common device which a person carries, and which is easily carryable. Nowadays, the advancements of hardware platforms in mobile phones have enabled the augmentation with various components and sensors such as camera, Global Positioning System. Cells phones are very less expensive when compared to other electronic devices through which augmentation is possible.

One must know that there is difference between portable augmented reality and mobile augmented reality. A desk-PC, Laptop is used as portable augmenting devices whereas smartphones, smart tablets are used for mobile augmentation.

Table 1 Some of the important works [2]

Year	Work conducted	Work by	Description
1968	The Sword of Damocles	Ivan Sutherland and Bob Sproull	a. Head-mounted display b. Operator experiences computer graphics which them feel as they were in alternate reality
1974	VideoPlace	Myron Krueger	c. The mix of a projection system and video recording systems that are displayed on the screen
1990	"Augmented Reality"	Tom Caudell	d. Term Coined
1992	Virtual Fixtures	Louis Rosenburg, USAF Armstrong's Research Laboratory	e. Placement of labours work data in an Automatic framework environment
1994	Moving in Cyberspace	Julie Martin	f. Augmented reality in theatre g. Dance of acrobat artists in and around the virtual objects
1998	1st and Ten graphic system	Sportsvision and PVI Virtual Media Services	h. Showcase virtual yellow first down marker during live NFL game
1999	Hybrid synthetic vision system	NASA	i. Used in test flights of spacecraft X-38 to improve navigation
2000	ARToolkit	Hiroka Zukato	j. Captures real-world action and combines with interations of virtual object
2009	AR in print media	Esquire magazine with Robert Downey Jr. Collaboration	k. Computer scans the barcode present in the magazine by which customer can experience AR
2011	Niztendo NDS	Niantic	l. Augmented Reality handheld game console
2013	MARTA App	Volkswagen	m. Augmented Reality in their car manuals n. Showing internal working of vehicles
2014	Google glass	Google	o. Wearable Augmented reality gadget p. Helps working through daily tasks to be more productive and efficient
2016	HoloLens	Microsoft	q. Wearable augmented reality gadget
2016	Pokemon Go	Niantic	r. Augmented Reality mobile Game

1.5 Unity 3D

Unity 3D is a cross-stage composed of 3D software for the advancement of games made by Unity Technologies Co., Ltd. The application usage of Unity is made available free for development and prototyping [3, 4] to educators, students, and developers. It can put virtual things or scenes into reality and recognizes human-PC correspondence with some AR headway apparatuses. It licenses Vuforia Software Development Kit (SDK) extension modules to differentiate and follow the corresponding ports, and it creates AR applications and games. It gives abundant progression box abilities to make games and other instinctive 3D content. Unity 3D can connect sunlight, fog, wind, skybox, water, and other physical materials to the virtual scene, enveloping sound and vivifying video. In the meantime, you can examine, test, and modify 3D application circumstances. Moreover, it is open to discharge to the necessary stages, for instance, Windows, iOS, Android, etc. [5].

1.6 Vuforia

Qualcomm's Vuforia SDK is an AR software development kit for mobile phones. Vuforia developer licenses are available with 1000 seats/month. This consists of advanced camera, external camera, model targets, and watermark. It uses PC vision innovation to perceive and catch planar pictures or 3D objects progressively and grants engineers the ability to put virtual articles through the viewfinder of the camera and change the situation of items on the foundation of the camera. The Vuforia SDK underpins all kinds of 2D and 3D objects, including different target setups, pictures with fewer images, and casing labels. There is an additional capacity in the SDK. It exploits virtual catches to identify restricted impediments. In addition, it can choose and reconfigure the target picture continuously and make a target set by the plan. Cell phones can hold onto pictures of each casing in the current genuine scene through the camera and afterward coordinate recognizable proof items in the database, as indicated by the pixel group transformation. From that point forward, it includes present virtual items, for example, 3D models, activities, or videos of genuine scenes. It can likewise communicate with these virtual items, rendering and yielding data at portable terminals [5].

1.7 About the Work Carried Out

This paper projects the work that has been carried out while developing an augmented reality android application for visualizing 3D models such as houses, office cabins, chairs, tables, etc. in the real world. A total of eight android applications were developed for augmenting eleven 3D virtual models with the help of a marker/target using

Unity and Vuforia software, and observations were made after using those applications. The main objectives of the work are to develop an application to display virtual 3D models in the real world and to view the models through mobile augmentation and check for uncertainties and their behaviour.

2 Literature Review

2.1 General

Wang [6] has explored the possibilities and difficulties of augmented reality in engineering and planning. This paper presents the idea and related empowering advances of AR and, furthermore, presents a study of its current applications in the zone of engineering and structure. Another focal point of the paper is to talk about how the distinguished key specialized issues might be tended to with regard to engineering and planning applications. This survey on input device tracking systems and output devices is carried out. The author has classified input devices based on their input mechanisms, i.e., 2D input devices, 2D limited controller devices, Spatial Input Devices, Gesture Input Devices, Tangible Input Devices, Body-centred Input Devices, where they write about their descriptions and beneficial usages. It also describes various tracking systems, their advantages, disadvantages, and some usage suggestions for them. Tracking systems such as magnetic, mechanical, acoustic, inertial, optical, and GPS are discussed. The different displays, such as hand-held monitors, video-based head mounted displays, optical-based head mounted displays, screen-based, transparent projection screens, head-mounted projectors, and spatially augmented reality displays, have been discussed with their centricity, advantages and disadvantages, and some usage suggestions. also discussed three problems faced by developers in the architecture and design fields. The problem of getting the data is that all the data will be present in 2D form, but for AR it is required to be in 3D format. While preparing and importing virtual models, there may be problems arising in the rendered scenes and the complexity of the 3D models of buildings creates off-line augmentation. It was also discussed the methods of creating models, such as creating a model using already present information and the other being manually determining the data by taking measurements or so. The rendering of virtual objects is very problematic. If the model is poorly rendered, then the feeling of augmentation by the user may be of very bad quality. Technological limitations are another problem faced as it requires highly accurate tracking and sensing devices. If these are not accurate and of poor quality, then it negatively impacts the user's augmentation experience.

2.2 Marker-Based Tracking

Adiyodi et al. [7] have investigated Interior Design utilizing Augmented Reality Environments. The application of augmented reality is based upon the type of object to be placed on the marker, where the object is scaled down proportionately. The item size is totally dependent on the size of the marker and the camera separation. Everything is connected with a marker. When the AR camera is impelled, it perceives the features of the marker and the related thing is delivered. The client could control the things and spot them, as demonstrated by the scene. Pulling the thing will change the circumstances of the article. The thing can be turned, and the plane of transformation is basic for the client to fathom, as it might be found progressively.

Jani et al. [8] have taken a shot at Interior Design in an Augmented Reality Environment. A strategy for applying AR innovation to inside structure work was made, where a client can see virtual furnishings and speak with 3D virtual furniture information utilizing a dynamic and adaptable UI. Furthermore, all of the virtual furniture's properties can be balanced by employing an impediment-based collaboration strategy for Tangible Augmented Reality.

2.3 CAD System

Janusz [9] has gone a step further in his investigation of the New Mixed Reality Environment for Interior Design. The paper presents a PC-supported structure (CAD) framework for inside engineering configurations called Design3R. The fundamental premise of this undertaking is the usage of the accomplishments from the fields of augmented reality (AR) and virtual reality (VR) so as to insert the structure procedure into the principal individual point of view and perceptual scale. It enables working with furniture and other interior components in their true size, legitimately in a reasonable perspective on the designed interior. The creator of the paper created Design3R as cross-stage programming and, moreover, as participation in the field of innovative work with the 3R Studio Mobile organization. The Design3R venture is expected to exploit the potential outcomes offered by HTC Vive and Google Tango to create a plan domain in which the genuine space of the building inside and the developing inside structure are totally coordinated. The paper guarantees that the introduced strategies bolster the plan procedure and create another, more instinctive point of view on the impression of the task.

2.4 AR Application

Kivrak [10] has learned about an augmented reality framework being created for encouraging building site exercises. The framework enables directors, specialists,

and development workers to track each stage of the development activities for which they are responsible. Clients can get access to information on preparing materials and development techniques identified in the exercises. Hence, the danger of committing errors in site exercises will be limited. Utilizing savvy glasses, the framework is tried for steel fixing and block divider development. The created framework can possibly improve the quality and profitability of building site exercises and, in this way, give critical commitments to the development business.

Alsafouri and Ayer [11] has investigated portable augmented reality to impact structure and constructability audit meetings. This exploration contemplated the utilization of AR through an organized plan audit action, including current industry specialists in structure and constructability survey meetings, and tried to determine whether the virtual–physical nature of AR encourages similar activities and results as recommended by earlier work that utilized virtual reality-based models or physical models. Likewise, this examination distinguished and broke down different activities into different categories, for example, dynamic, critical thinking, and planning choices that happen as clients cooperate with AR on various portable PCs. This examination gives a better understanding of how unique portable PCs, for example, wearables and handheld gadgets demonstrating a similar specialized AR condition, can prompt various activities among clients. This exploration found that AR can encourage a portion of the activities of virtual reality and physical models in plan and constructability survey meetings, including dynamic, structural choices, and clear, explanative, and critical thinking activities. What's more, unique portable PCs prompted diverse watch activities during the plan survey meetings. For instance, handheld gadgets between 15.24 cm (6 in.) and 25.5 cm (10 in.) enabled more dynamic activities than some other gadgets tried. As extra testing is finished, future discoveries might be contrasted with those introduced in this work to decide the activities that are reliably observed with AR in structure and constructability audit meetings. In the end, this may provide a significant device to permit future specialists and experts to deliberately get ready for AR innovation utilization dependent on what explicit human activities are attractive for a given application.

Zaher et al. [12] have concentrated on mobile augmented reality applications for development ventures. The reason for this examination is to pave the way towards observing development ventures. Great practice for development progress following depends on paper reports, which involve a genuine measure of manual information assortment just as much as the exertion of envisioning the real advancement from desk work. This work presents another system for observing development progress utilizing advanced mobile phones. This is done by proposing another framework comprising of a recently evolved application named "BIM-U" and a versatile augmented reality (AR) channel named "BIM-Phase." "BIM-U" is an Android application that permits the end-client to refresh the advancement of exercises nearby. This information is utilized to refresh the task's 4D model with various cost boundaries, for example, earned worth, real expense, and arranged worth. The "BIM-Phase" application is a portable augmented reality channel that is utilized during the development stage through the actualization of a 4D "as-arranged" staged model incorporated with an augmented video indicating genuine or arranged advancement. The

outcomes from the task are then examined and evaluated to envision the capability of these and comparative strategies for subsequent time and cost on development ventures. The proposed framework through "BIM-U" and "BIM-Phase" misuses the capability of versatile applications and augmented reality in development using handheld cell phones to offer additional opportunities for estimating and observing work progress utilizing building information modelling.

Hemamalini et al. [13] have directed a study of versatile utilization of augmented reality. They fundamentally offered significance to the utilization of portable applications for augmented reality and assortment of instruments utilized and the favourable circumstances and disservices of versatile increase. The versatile expansion is utilized in fields, for example, instruction, notice and promoting, the travel industry, language translation, gaming, and so forth. By leading this review, the focal points they watched were by utilizing versatile innovation area based enlargement can be watched, they are extremely minimal effort when contrasted with different gadgets utilized for augmented reality. The inconveniences watched were constrained assets are accessible on versatile which execution of augmented reality mind-boggling and restricted memory of portable restrains the use of utilization. They have presumed that as portable innovation is getting more proficient as days passes by it makes engineers work simpler, they tend to make rich and vivid encountering stage. This makes more noteworthy extent of augmented reality for instruction, games, sports, designing, medication, and so forth.

Akdag et al. [14] has led to a concentration on the assessment of augmented reality in engineering through example applications. This investigation looks at the properties of augmented reality and its suggestions to the field of planning through example applications. To the extent of the examination, five diverse augmented reality applications that serve various purposes in engineering have been inspected and assessed. It has been seen that, through the applications analysed, augmented reality innovation can give critical commitments to a wide range of zones of engineering and give a great number of offices to originators. It is also a result of the research that new introduction procedures that cannot be delivered by the strategies used for augmented reality innovation can be developed. Also, it's expressed that there are a wide range of augmented reality applications that serve the structure field that have substance and explicit highlights for sub-disciplines like inside planning, urban structure, archaeology, rebuilding, etc. Although augmented reality applications at present utilized can't create powerful and timely victories, all things considered, augmented reality will be changed into an innovation that architects can utilize all the more effectively with new programming and equipment that will create innovation. It is natural for people to notice the augmented reality (AR) and engineering and add to future works as a result of the work.

Jadeja et al. [15] have directed an investigation called "New Era of Teaching and Learning: 3D Marker Based Augmented Reality." The fundamental target of this examination is to give lucidity of ideas to the understudies in a genuine like condition through 3D (3 Dimensional) visual guides that might be utilized to explain or improve comprehension of an idea or procedure. This paper centres around including the kids in comprehension of the ideas in 3D (3 Dimensional) condition. The conventional

technique incorporates idea of redemption not founded on visual guides. Presently the advanced encouraging philosophy incorporates visual guides, for example, projector, straightforward slides, and models in 2D (2 Dimensional) condition. On the off chance that visual guides are changed over from 2D (2 Dimensional) to 3D (3 Dimensional) condition, the client will have a live situation to comprehend the ideas. Visual guides apparatuses are accessible to client to include reality, lucidity, and assortment to the drill which is essential for client at the previous phases of language learning.

Oh et al. [16] have concentrated on productive 3D configuration drawing perception dependent on portable augmented reality. In this examination, a proficient 3D configuration drawing perception method dependent on versatile augmented reality is proposed. The proposed strategy initially perceives the configuration drawing area, and just performs picture following in its district. Through execution examination, it could be seen that in the method being recommended in this paper, drawing acknowledgement time was diminished by 4–33%, drawing coordinating acknowledgement rate was expanded by 5–15%, and the number of yield lines every second was expanded by 7–8 edges for each second.

Phan et al. [17] investigated inside structure in augmented reality settings. This research analysed virtual furnishings and modification work to make another plan strategy utilizing Augmented Reality innovation for Interior Design training. This investigation proposes a strategy for applying augmented reality innovation to inside planning work, where a client can see virtual furnishings and speak with 3D virtual furniture information utilizing a dynamic and adaptable UI. Furthermore, all of the virtual furniture's properties can be balanced by utilizing an impediment-based connection technique for Tangible Augmented Reality.

Wang [18] has concentrated on utilizing Augmented Reality to plan virtual construction sites. This examination is connected to augmented reality work and issues in development and portrays the idea and model of an augmented reality-based development arranging apparatus, AR Planner, with virtual component sets and substantial interface. The purpose of this paper is to distinguish and incorporate worksite organizing rules into the AR organizer with the end goal of cleverly avoiding potential arranging blunders and procedure wastefulness and, as a result, expanding overall efficiency. The effectiveness of the framework for the latter half depends upon the amount and nature of development parts accessible within the virtual element sets. The execution of arranging rules helps the client and forestalls potential blunders that typically happen during the arranging stages.

[19] P. Anders et al. (2005) have concentrated on Ambiviewer: an instrument for making architectural blended reality. This examination presents another blended reality framework for architecture, Ambiviewer. The framework utilizes advanced video, on-board modeling, and worldwide positioning to blend physical and mimicked elements on the screen. The framework is used to show what extends nearby, and takes into consideration the undertaking environs. The examination also talks about the utilization of Ambiviewer in making half breeds, arrangements of virtual and material reality. The paper finishes up with a portrayal of a little task embraced with Ambiviewer and its suggestions for half and half architecture.

Thomas et al. [20] have conducted research on utilizing Augmented Reality to Visualize Architecture Designs in an Outdoor Environment. This paper presents the utilization of a wearable PC framework to picture open air architectural highlights utilizing augmented reality. The paper inspects the inquiry: how can one picture a plan for a structure, an adjustment to a structure, or augmentation to a current structure in comparison with its physical environmental factors? The solution introduced to this issue is to utilize a portable augmented reality stage to picture the plan in the spatial setting of its last physical environmental factors. The paper depicts the versatile augmented reality stage TINMITH2 utilized in the examination. The activity of the framework is portrayed through a point by point case study of the framework in activity. The framework was used to visualize a simple addition to a structure on one of the University of South Australia's campuses.

3 Methodology

See Fig. 1.

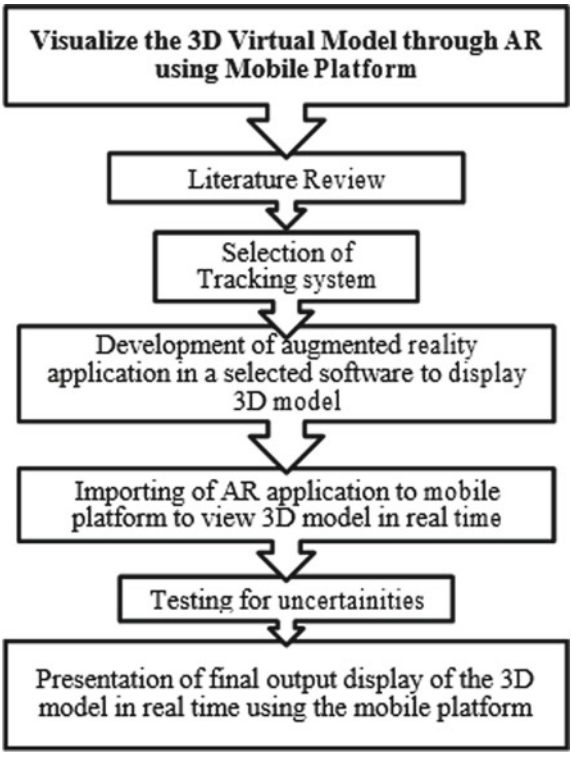

Fig. 1 Methodology [7, 8]

4 Work Carried Out

4.1 Tracking System Selection

A marker-based system is selected as the tracking system. As in the marker system, a trigger photo is used by a person that can be scanned using a mobile via an augmented reality application. The mobile scan triggers the 3D content which is prepared in advance on the top view of the marker.

Marker recognition can be local or cloud based. The image of the marker should be unique. If the marker image is prepared correctly, marker-based augmented reality content provides a quality-based experience and stable tracking. It will be easy to use as first-time users will not need any detailed information regarding its usage instructions.

An augmented reality object disappears if the scanner is moved away from the marker. So keep the mobile camera focussed on the marker to have an augmented reality experience. In augmented reality, objects disappear even when the marker reflects the light. If possible, markers should have contrast black and white colours and borders should be darker colours. A marker should not contain repetitive patterns as hopping of the augmented object can be observed if so.

4.2 Development of Augmented Reality Application

It mainly involves three main stages; those are:

a. Environment for the development of applications
b. Working in Unity 3D software
c. Usage of the android application on the cell phone.

The tools required for the development of AR apps are Unity 3D, Vuforia plugins, Android Development Kit, Microsoft Visual Studio, Android Studio. The Vuforia extensions package and its licenses can be made available by registering in the developer portal.

Once the licenses are obtained, the target images are checked for the rating through the Vuforia portal.

Working in Unity 3D software mainly includes three stages: creating a main scene, creating a menu scene, and building an android application. In Unity software, the required asset package for tracker can be imported. In the Vuforia package, AR cameras and image target prefabs are used. The AR camera can be configured by adding the license obtained from the Vuforia portal. The 3D model with an .obj file is placed above the image target database priorly. The main scene is made functional through the C # script.

An Android application is built by editing build settings and player settings. The developed application will be in the .apk file format. The file is later downloaded to

the cell phone and installed by giving the required permissions. Open the application and click on Scan. The result can be viewed by placing the augmented 3D models on their respective markers.

4.3 Visual Experience of Developed AR Application in Mobile Platform

A total of eight trials were conducted as a result of which eight augmented reality applications were developed using Unity 3D and Vuforia software. Models are created using Revit and 3Ds Max. Some models were created using data taken from manually taped measurements of the real objects.

Table 2 shows the data of the model and tracker used while developing the augmented reality android application. Figures 2, 3, 4, 5, 6, 7, 8, 9, 10, 11, 12,

Table 2 Data for application development

Trial No.	Data						
	3D Virtual object	Target type	Target augmentable status in Vuforia	Number of targets/Markers	Number of 3D virtual models	Virtual model texture applied	Scale of virtual model
1	House	Predefined	4 star	1	1	No	In appropriate
2	Table and chair	Predefined	3 star	1	1	Yes	1:1
3	Chair	Predefined	3 star	1	1	Yes	1:1
4	Table	Predefined	5 star	1	1	Yes	1:1
5	Office Cabin	Predefined	3 star	1	1	Yes	1:1
6	House (Exterior, fully furnished house, interior of house)	Predefined	5 star	3	3	Yes	1:27
7	House (Exterior, fully furnished house, interior of house)	Predefined	5 star	3	3	Yes	1:16

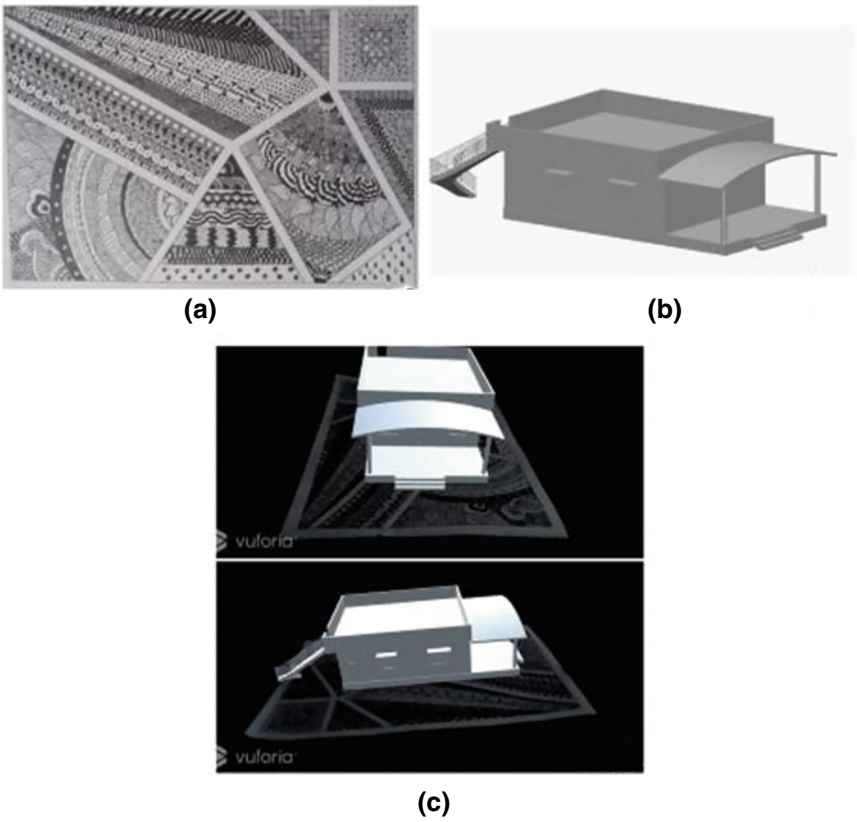

Fig. 2 Trial 1 **a** Marker/tracker used in augmentation of the model; **b** virtual 3D model of house; **c** view of virtual 3D house model on marker/tracker through augmented reality using mobile platform via android application

13, 14 and 15 shows the maker and 3D virtual model used in development of application and how the augmented model looks on the display of the cell phone. Table 3 shows observation made while visualizing the models of all these eight applications.

5 Outcome

Some of outcomes obtained are as follows:

1. *Development of application to have an augmented reality display for virtual 3D model in the real time*:

   A total of seven trials were conducted as a result of which seven different augmented reality applications were developed in Trial 1 The application

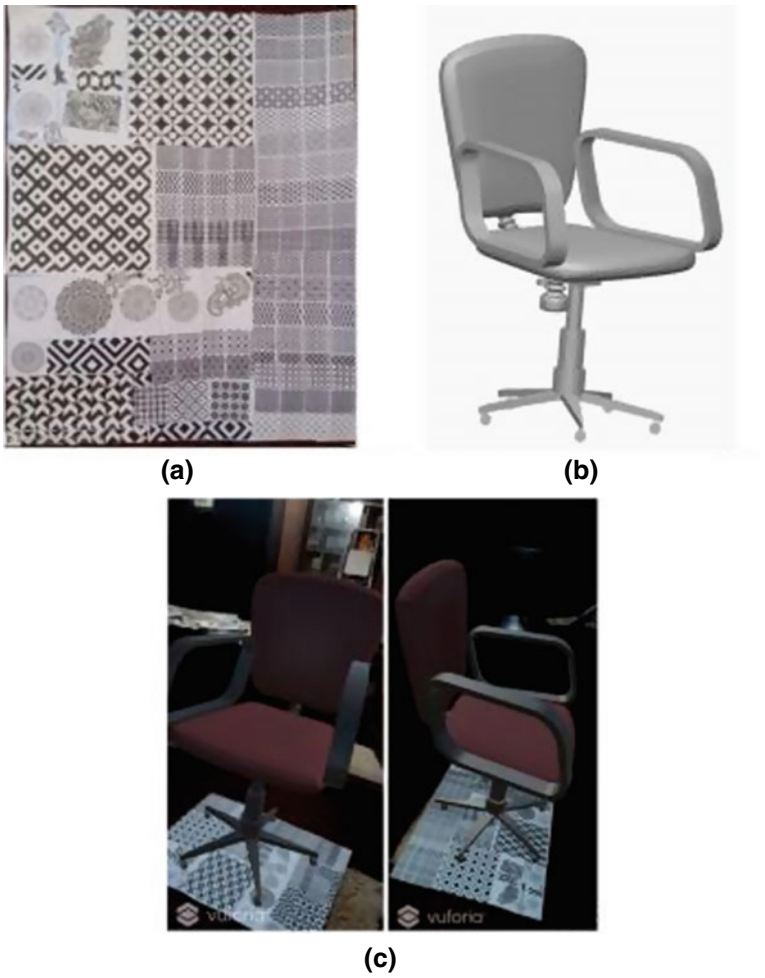

Fig. 3 Trial 2 **a** Marker/tracker used in augmentation of the model; **b** virtual 3D model of table and chair; **c** view of virtual 3D table-chair model on marker/tracker through augmented reality using mobile platform via android application

contains the 3D model of a house, Trial 2 application includes 3D models of a chair and a table; Trial 3 application includes a 3D model of a chair; Trial 4 application includes a 3D model of a table; Trial 5 application includes a 3D model of an office cabin; and Trials 6 and 7 applications include an exterior, interior, and complete model of a 1 BHK house. The Trial 8 application contains all the markers and virtual 3D models from trial 1 to trial 7.

2. *Visualization of developed app for the virtual 3d model in mobile augmentation and checking for uncertainties:*

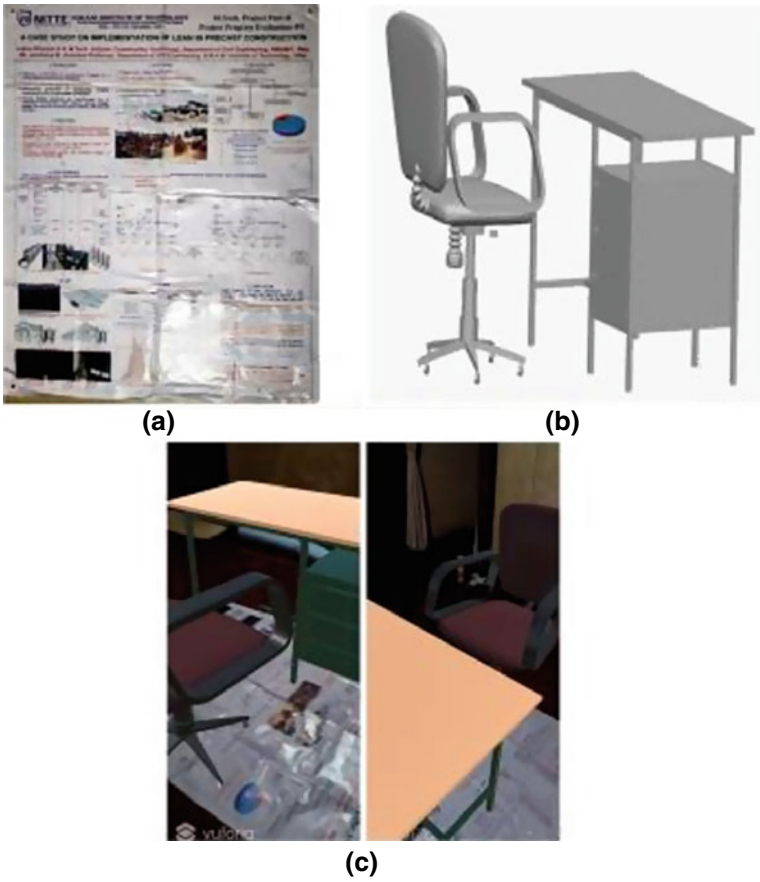

Fig. 4 Trial 3 **a** Marker/tracker used in augmentation of the model; **b** virtual 3D model of the chair; **c** view of virtual 3D chair model on marker/tracker through augmented reality using mobile platform via android application

The augmented models were initially tested for visibility in horizontally 360° and vertically 180°, and the models displayed were normal in texture, size, and clarity.

a. The texture was visible in all the trial models except in trial 1.
b. The clarity of the models from trials 1, 3, 4, 6, and 7 was good. However, trials 2 and 5 lacked the rendering clarity.
c. Secondarily, the number of targets was varied, the model trails from 1 to 5 were seated on only one marker, whereas trials 6 and 7 were seated on three different markers.

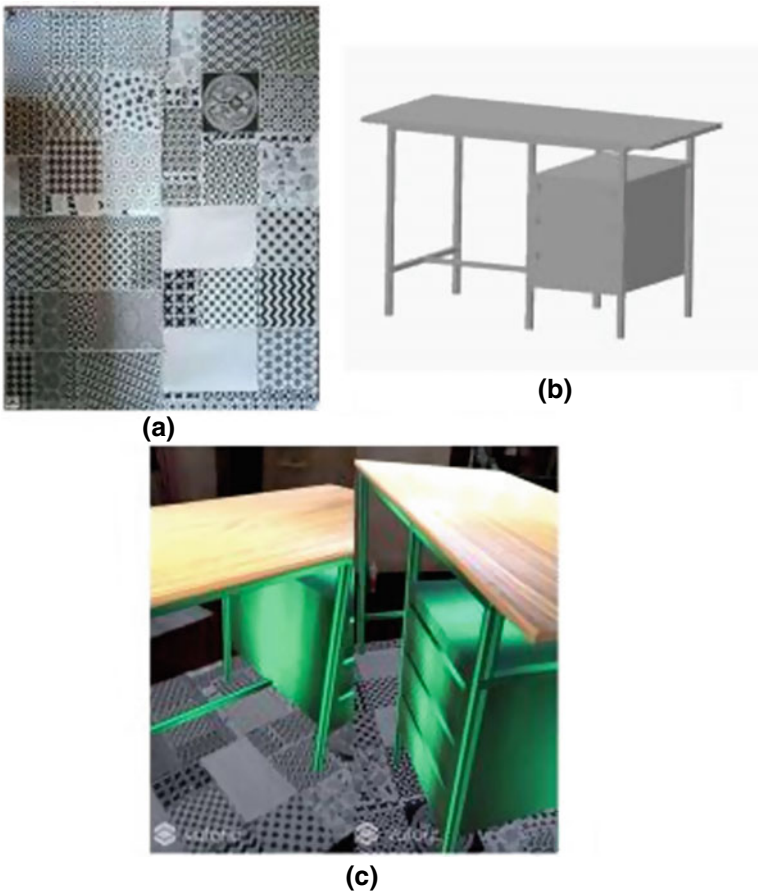

Fig. 5 Trial 4 **a** Marker/tracker used in augmentation of the model **b** virtual 3D model of the table **c** view of virtual 3D table model on marker/tracker through augmented reality using mobile platform via android application

6 Conclusion

Some of the conclusion drawn from the project work are as follows:

a. The marker-based augmented reality is feasible for small elements of interiors. The creation of virtual 3D model over a marker seems to be difficult, as the dimensions and the uncertainties are directly proportional.
b. The application developed will be independent of a predefined marker and model.
c. The viewability of the model over a mobile screen can be increased with the depth sensor in the camera, using AI- and AR-enabled mobile phones.

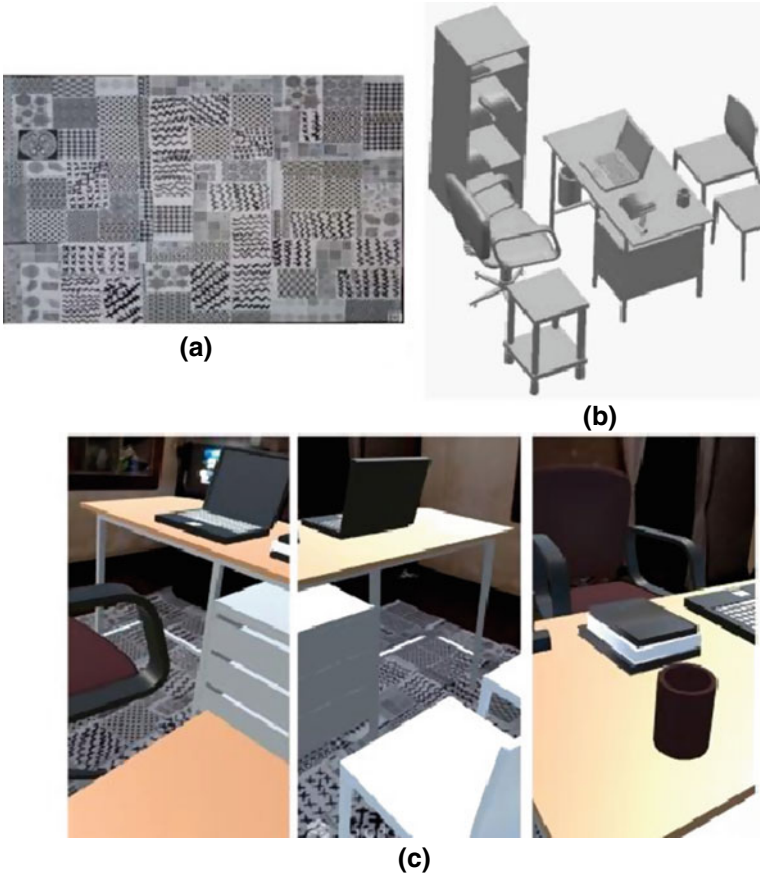

Fig. 6 Trial 5 **a** Marker/tracker used in augmentation of the model; **b** virtual 3D model of the office cabin; **c** view of virtual 3D office cabin model on marker/tracker through augmented reality using mobile platform via android application

d. Basic knowledge of C # scripting is essential to advance the visual experience using this application.

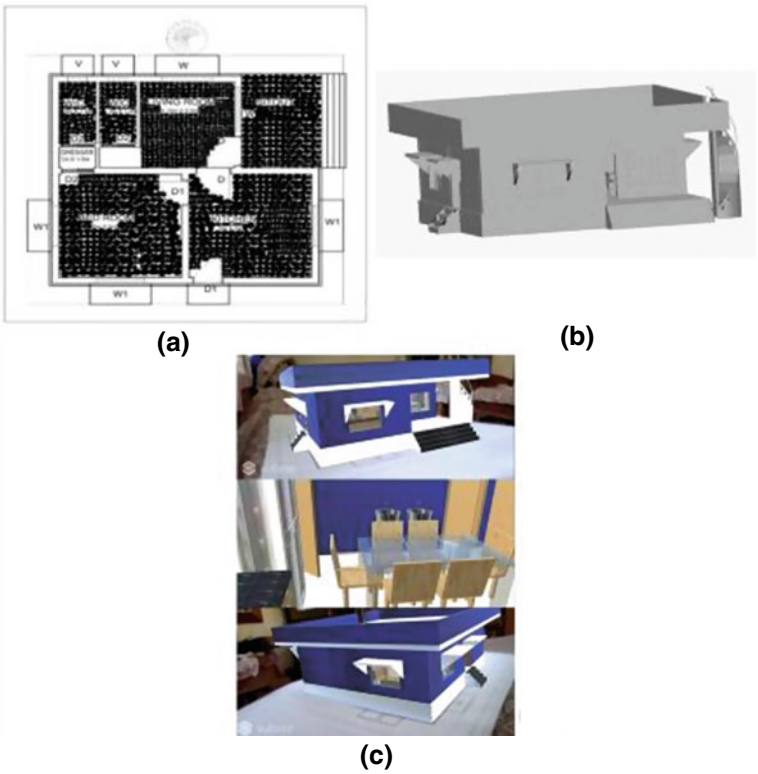

Fig. 7 Trial 6 **a** Marker/tracker used in augmentation of the model; **b** virtual 3D model of the fully furnished house; **c** view of virtual 3D fully furnished house model on marker/tracker through augmented reality using mobile platform via android application

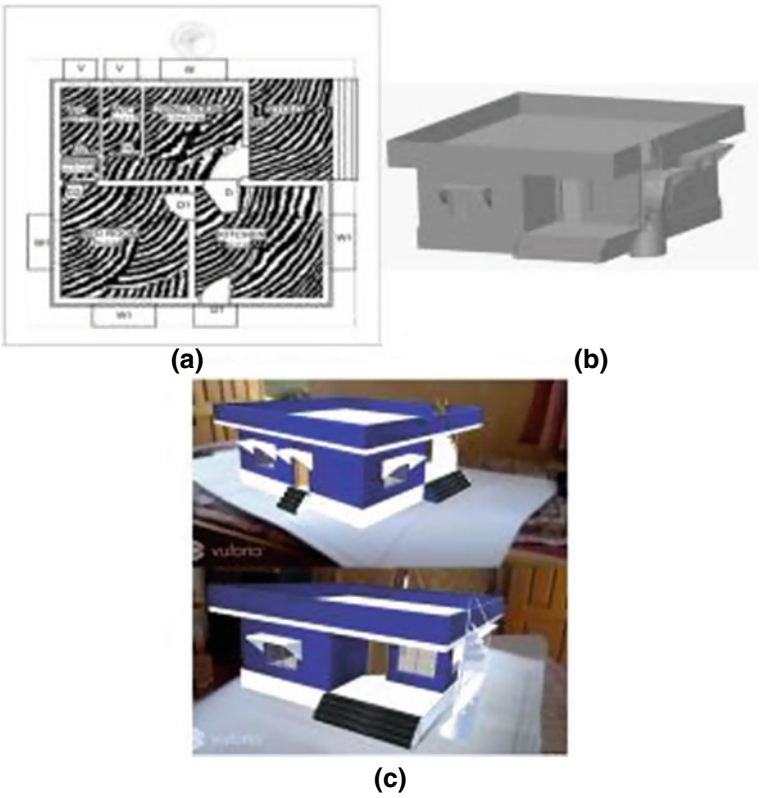

Fig. 8 Trial 6 **a** Marker/tracker used in augmentation of the model; **b** virtual 3D model of the exterior of house; **c** view of virtual 3D exterior of house model on marker/tracker through augmented reality using mobile platform via android application

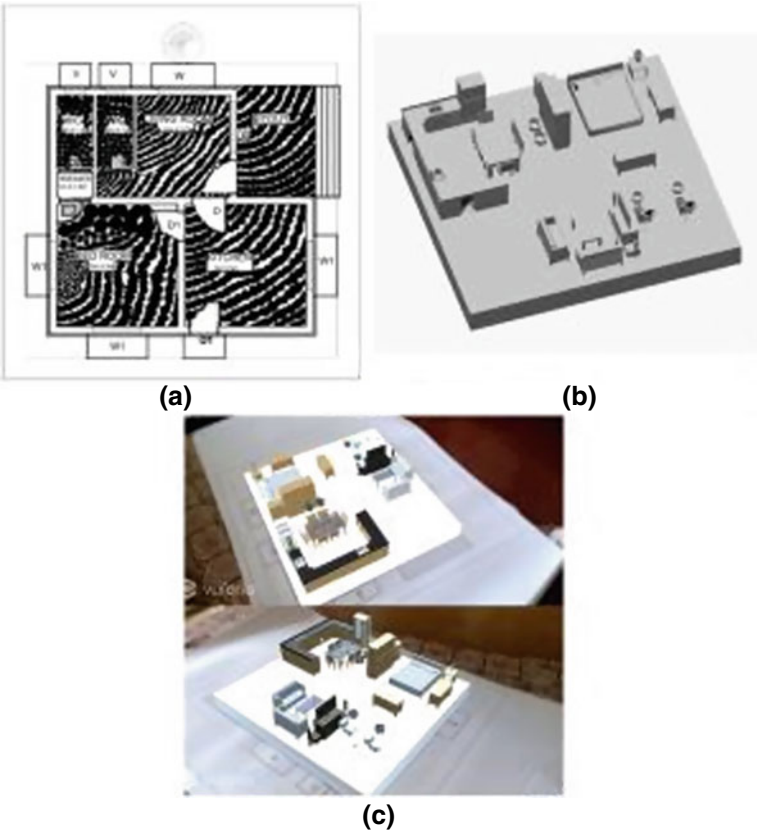

Fig. 9 Trial 6 **a** Marker/tracker used in augmentation of the model; **b** virtual 3D model of the interior of house; **c** view of virtual 3D interior model of house on marker/tracker through augmented reality using mobile platform via android application

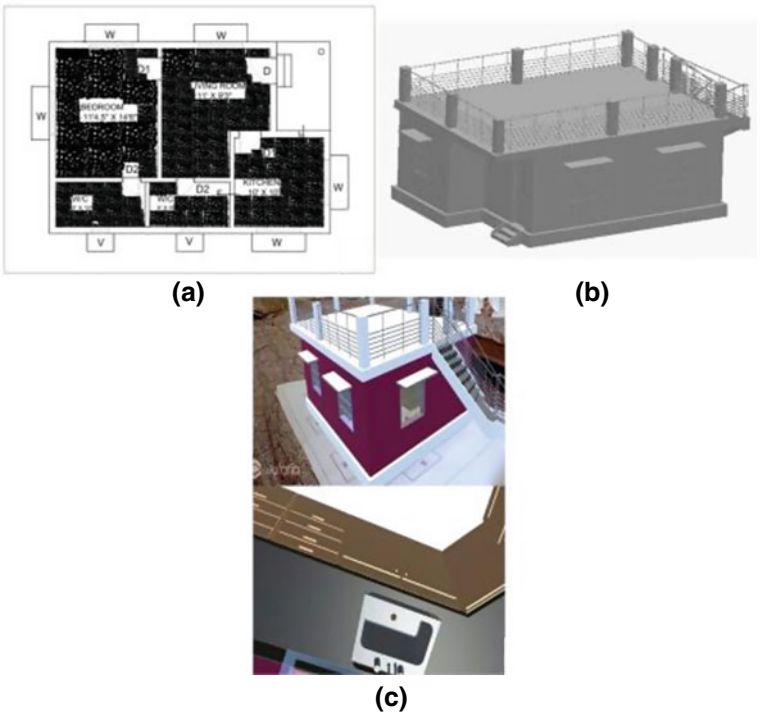

Fig. 10 Trial 7 **a** Marker/tracker used in augmentation of the model; **b** virtual 3D model of the fully furnished house; **c** view of virtual 3D fully furnished house model on marker/tracker through augmented reality using mobile platform via android application

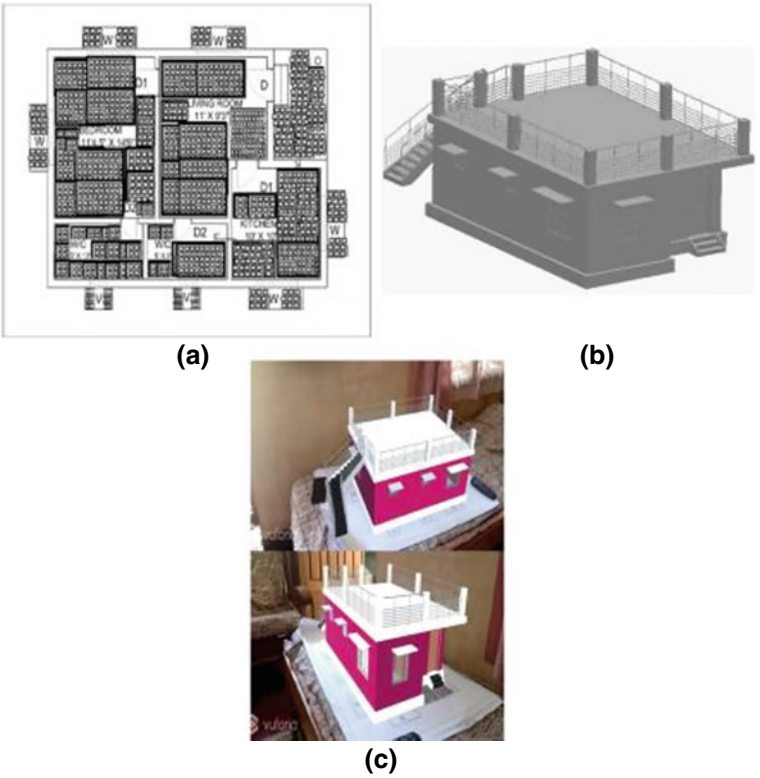

Fig. 11 Trial 7 **a** Marker/tracker used in augmentation of the model; **b** virtual 3D model of exterior of house; **c** view of virtual 3D exterior of house model on marker/tracker through augmented reality using mobile platform via android application

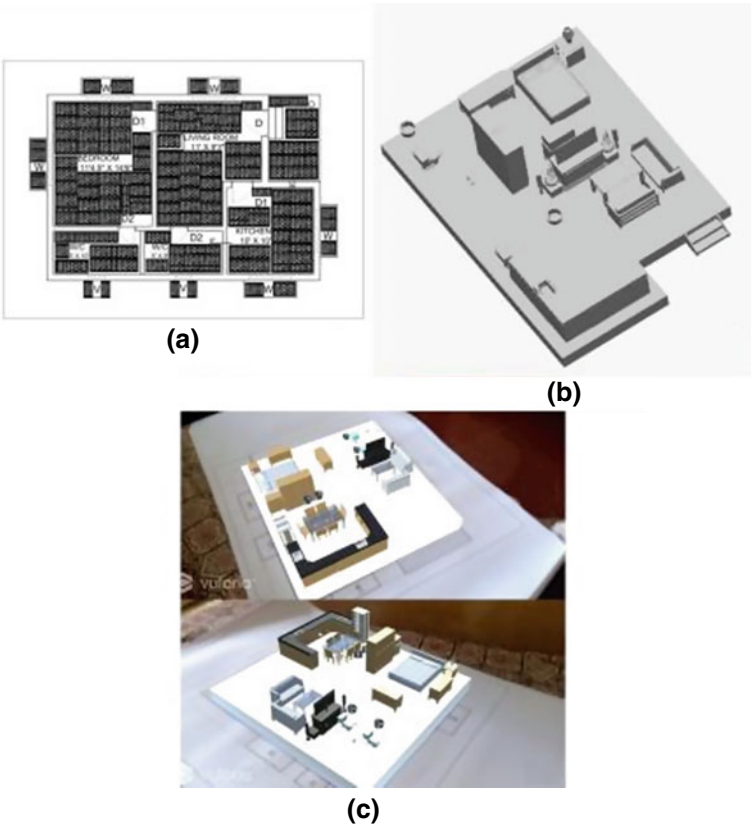

Fig. 12 Trial 7 **a** Marker/tracker used in augmentation of the model; **b** virtual 3D model of the interior of house; **c** view of virtual 3D interior model of house on marker/tracker through augmented reality using mobile platform via android application

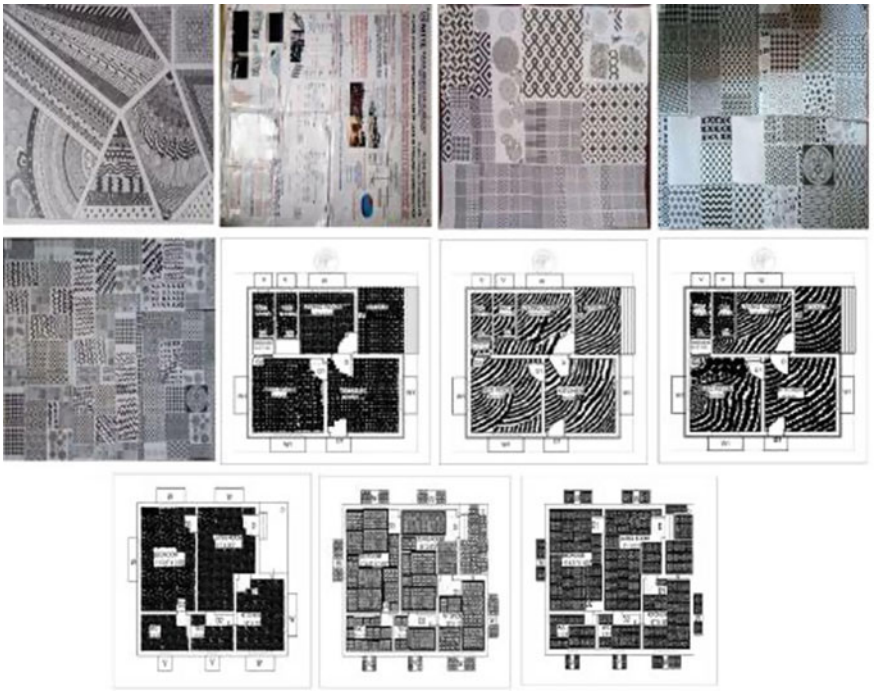

Fig. 13 Markers/trackers used in augmentation of the model for trial 8

Fig. 14 3D virtual models used in the application for trial 8

Fig. 15 View of augmented 3D models in the real world as seen on the cell phone display

Table 3 Observation made during augmenting 3D models in developed augmented reality android application

Trial No.		Observation				
	3D Virtual object seen	Size/scale of 3D virtual object	Virtual model texture present	Stability	Visibility	Other
1	House	Inappropriate	No	Stable	All parts visible	–
2	Table and chair	Same as real objects	Yes	Stable	Some parts visible	–
3	Chair	Same as real objects	Yes	Stable	All parts visible	–
4	Table	Same as real objects	Yes	Stable	All parts visible	–
5	Office Cabin	Same as real objects	Yes	Stable	Some parts visible	Some flashes on the material are observed because very less thickness of material

(continued)

Table 3 (continued)

Trial No.		Observation				
	3D Virtual object seen	Size/scale of 3D virtual object	Virtual model texture present	Stability	Visibility	Other
6	House (Exterior, fully furnished house, only interior furniture)	Same as that of plan as it is exactly situated over it	Yes	Stable	All parts visible	–
7	House (Exterior, fully furnished house, only interior furniture)	Same as that of plan as it is exactly situated over it	Yes	Stable	All parts visible	–
8	From trial 1 to trial 7	Same as that of plan as it is exactly situated over it	Trial 1 Model no, other models yes	Stable	As in trial 1 to trial 7	–

Acknowledgements We would like to express our gratitude to all our fellow workers who helped in completing the work. Many thanks to the Unity hub team and Vuforia team for addressing the queries during work.

References

1. https://www.augment.com/how-augmented-reality-works/
2. https://www.colocationamerica.com/blog/history-of-augmented-reality
3. https://unity3d.com/unity/activation/personal
4. https://www.ptc.com/en/products/vuforia/vuforia-engine/pricing
5. Liu X, Sohn Y-H, Park D-W (2018) Application development with augmented reality technique using Unity 3D and Vuforia. Int J Appl Eng Res 13(21):15068–15071
6. Wang X (2009) Augmented reality in architecture and design: potentials and challenges for application. Int J Archit Comput 07(2):309–329
7. Adiyodi A, Agrahara M, Gamnani P, Pampattiwar K (2016) Interior design using augmented reality environment. Int J Innov Res Sci, Eng Technol 5(4):6104–6110
8. Jani BY, Dahale P, Nagane A, Sathe B, Wadghule N (2015) Interior design in augmented reality envi ronment. Int J Adv Res Comput Commun Eng 4(3):286–288
9. Janusz J (2019) Toward the new mixed reality environment for interior design. IOP Conf Ser: Mater Sci Eng 471. Session 9

10. Kivrak S, Arslan G (2019) Using augmented reality to facilitate construction site activities. In: Advances in informatics and computing in civil and construction engineering, Springer, pp 215–221
11. Alsafouri S, Ayer SK (2019) Mobile augmented reality to influence design and constructability review sessions. J Archit Eng, ASCE 25(3)
12. Zaher M, Greenwood D, Marzouk M (2018) Mobile augmented reality applications for construction projects. Constr Innov, Emerald Insight 18(2):152–166
13. Hemamalini S, Hema Priya K, Vinston Raja R, Poonkuzhali SM (2017) A survey of mobile application using augmented reality. Int J Pure Appl Math 117(22):209–213
14. Akdag F, Baydogan MC (2017) Evaluation of augmented reality in architecture through sample applications. Eurasian J Civ Eng Archit 1(1):42–52
15. Jadeja A, Mehta R, Sharma D (2016) New era of teaching learning: 3D marker based augmented reality. Int J Inf Sci Tech (IJIST) 6(1–2):81–88
16. Oh Y-J, Park K-W, Kim E-K (2015) Efficient 3D design drawing visualization based on mobile augmented reality. J ICACT Trans Adv Commun Technol (TACT) 4(1):568–573
17. Phan VT, Choo SY (2010) Interior design in augmented reality environment. Int J Comput Appl 5(5):16–21
18. Wang X (2007) Using augmented reality to plan virtual construction worksite. Int J Adv Robot Syst 4(4):501–512
19. Anders P, Lonsing W (2005) AmbiViewer: a tool for creating architectural mixed reality. In: Smart architecture: integrati on of digital and building technologies, proceedings of the 2005 annual conference of the association for computer aided design in architecture, pp 104–113
20. Thomas B, Piekarski W, Gunther B (2001) Using augmented reality to visualise architecture designs in an outdoor environment. In: Proceedings of the design computing on the net

Assessment on Suitability of CD Waste as Infill for Construction of Slopes

M. N. Asha and J. Jubin

Abstract Alternative materials and methods for improving the ground have always been a subject of study. The viability of construction and demolition waste (CD waste) as slope infill is examined in this research. To investigate its suitability for construction of slopes, a three-layered slope infill is considered. Parameters studied in the present study include thickness of CD waste layer and slope angles. CD waste is used in the middle layer and its thickness is varied from 0 to 7 m in increments of 1 m. The bottom layer thickness is kept constant at 7 m, whereas the top layer depth is varied such that the total height of embankment is 17 m. The SLOPE/W module of GEOSTUDIO is used to perform a slope stability analysis, and the factor of safety is calculated for various embankment sections. Limit equilibrium analysis is carried out for three different slope angles; viz., 30°, 45° and 60°. From the analysis, it is observed that angle of friction of infill is critical as far as stability of slope is considered. According to study, 17–25% of the thickness of an embankment can be replaced with cohesionless CD waste without compromising on factor of safety.

Keywords CD waste · Slope stability · Infill thickness · Factor of safety · Slope angle

1 Introduction

Infrastructure development is an important parameter as far as economy of a country is concerned. Availability of strong foundation soil is necessity for any structure. Scarcity of natural soil is a challenge and hence this has led to the development of different ground improvement techniques. However, industrial and human activities have led to the accumulation of waste materials and owed to the good shear properties of these materials, they have been extensively used for construction. Based on the availability and properties, some of these materials have been used as a partial or full replacement in concrete or soil. Some of the materials that have found its application

M. N. Asha (✉) · J. Jubin
CMR Institute of Technology, AECS Layout, ITPL Main Road, Kundalahalli, Bengaluru, Karnataka 560037, India
e-mail: asha.n@cmrit.ac.in

L. Nandagiri et al. (eds.), *Recent Advances in Civil Engineering*, Lecture Notes in Civil Engineering 256, https://doi.org/10.1007/978-981-19-1862-9_55

in geotechnical engineering are fly ash [1], lime [2], Ground granulated blast furnace slag (GGBS) [3], construction and demolition waste [4], tyre shreds [5], mine tailing wastes, plastic waste [6] and so on. Majority of the studies focus on its suitability with respect to foundation or embankments. Also, with the advent of geosynthetics even researchers have tried to explore the suitability of reinforcement mechanisms on different types of infills.

Slopes or embankments are some of the common geotechnical applications wherein suitability of different infills are studied. Types of slope failure include toe failure, base failure, slope failure and so on. Model tests [7–9], simulation studies [10, 11] are extensively used to study the suitability of different materials for construction of embankments. Some of the commonly used softwaree for the simulation studies are PLAXIS 2D and 3D [12, 13], FLAC 2D and 3D [14], ROC FALL [15] and so on. However, few of the researchers used analytical methods for the analysis [16].

In many cases, the alternative materials may or may not be a full replacement of the model section. Though many research activities have been carried out to explore the suitability of different materials for geotechnical applications, partial replacement of thickness with the sustainable waste materials is not studied by many. Factor of safety forms quickest and easiest mode of assessment of stability of slopes.

Lacuna of space and boom in construction are the major reasons for the accumulation of construction and demolition waste in the country. According to the reports given by Centre for Science and Environment, 2020, only 1% of CD waste is recycled. This is because in our country only limited recycling facilities are available. Hence, it's the need of the hour to identify alternative uses for CD waste. Major challenge associated with this waste material is its diverse nature. Components like steel, wood, etc., can be easily retrieved from the waste. Properties of demolition waste depend upon its constituents [17, 18]. For proper management of CD waste, it is essential to identify applications that enable its maximum use. The use of demolition wastes for various infrastructure applications such as building, roadways, embankments, and slopes offers a possible solution to the problem. It is reported that porosity and strength of concrete increases when CD waste is used as aggregates. CD waste is used to stabilize clay as well as to make mud blocks because of its low plasticity and increased drainage properties [19]. The present study explores the feasibility of using varying thickness of CD waste layer while constructing slopes. The feasibility is estimated in terms of assessment of factor of safety of the slope. Accordingly, the following objectives are identified in the present study:

- Analyze the suitability of CD waste as infill in construction of slopes with respect to its shear properties.
- Identify an optimum thickness of CD waste so as to maximize Factor of safety of the embankment section.
- Compare the effectiveness of CD waste as an infill for different slope angles.

2 Materials and Methodology

2.1 Materials

In the present study, construction and demolition waste is used as the infill. However, properties of CD waste vary based on the source. For the study, cohesionless waste comprising of plaster waste is used. The construction waste used has an average size of 1.5 mm with angle of internal friction of 45.4° and cohesion of 1.8 kPa. However, in literature, researchers have examined frictional properties of clay mixed with CD waste. To make comparison with the waste material used in the study, a mix proportion (comprising of 92% clay and 8% CD waste) as given in the literature is also used [20]. The objective of this comparison is to investigate majorly the effect of shear properties on slope stability. Properties of the infill used for the study is presented in Table 1.

The proposed waste material is used as a part of three-layered embankment. Infill properties are adopted from the literature [20] and are tabulated in Table 2. The embankment has a total height of 17 m and the thickness of bottom layer is maintained at 7 m throughout, in all studies. The thickness of the top layer and middle layer (comprising of CD waste) is varied such its total thickness is 10 m. The cross-section of the embankment used in the study [10] is shown in Fig. 1. To simulate the worst condition, phreatic line is assumed to pass through the cross-section.

Table 1 Properties of waste material used in the study

Particulars	Present study (plaster waste)	Literature [20] (92% clay mixed with 8% CD waste)
Designation	IF1	IF2
% of clay	0	92
% of CD waste	100	8
Classification	SW	CI
c (kPa)	1.8	14.7
ϕ (°)	45.4	16.9

Table 2 Properties of infill used for the stability analysis

Infill type	Designation	Unit weight (kN/m^3)	c (kPa)	ϕ (°)
Present study (plaster waste)	IF1	16.9	1.8	45.4
Literature [20] (92% clay mixed with 8% CD waste)	IF2	20.2	14.7	16.9
Properties of top layer	TL	17	15	25
Properties of bottom layer	BL	15	20	30

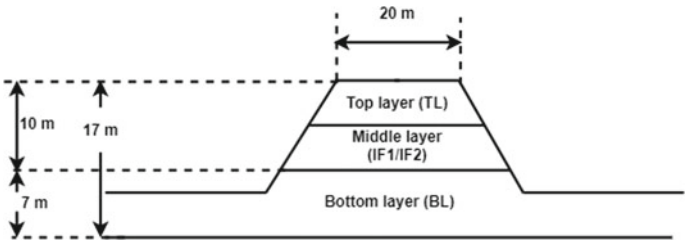

Fig. 1 Cross section of embankment used in the study

2.2 Methodology

To investigate the stability of the embankment, SLOPE/W module of GeoStudio software is used. For the simulation studies, Mohr–Coulomb failure model is assumed and limit equilibrium analysis is performed on the embankment section. Step by step procedure involved in the analysis include:

1. Domain/workspace creation—here the reference axis and units of measurement are defined. Definition of failure model is also made in this stage.
2. Use of CAD drawing to import domain regions—in this stage, half section of the embankment is generated. While generating domain, the thickness of each layer is also defined.
3. Material attributes description and definition of phreatic line—here the properties of different materials is specified. The properties considered for the analysis are its density and shear properties. Phreatic line indicates the water table of the infill. Presence of water will weaken the infill.
4. Definition of entry and exit regions—here the zone of failure of the slope is defined. Entry and exit regions are identified along the sides of the slope.
5. Analysis and estimation of Factor of Safety—after defining the zone of failure, the section is analyzed and its factor of safety is estimated.

The axis symmetric cross section of embankment used for the analysis is presented in Fig. 2.

3 Analysis of Results

The simulation results are analyzed systematically to investigate the effect of infill properties on slope stability. The influence of thickness of CD waste infill on slope angle is also studied.

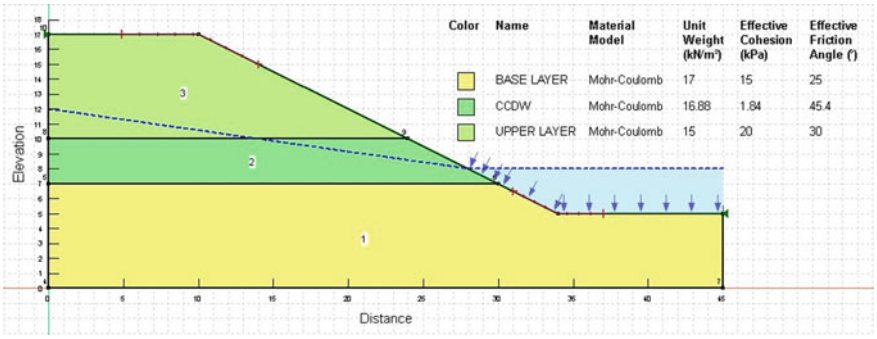

Fig. 2 Axis symmetric cross section of the embankment used for analysis

3.1 Effect of Type of Infill on Factor of Safety

To determine the effect of angle of internal friction on slope stability, two waste materials as explained in Subsection on Materials, i.e., IF1 and IF2 are considered. IF1 is a cohesionless infill with a high angle of friction whereas IF2 has higher cohesion in comparison to angle of friction. Nevertheless, both these infills are investigated for its suitability for geotechnical application. The trial slip surfaces as obtained from the analysis are presented in Fig. 3. From this, the Factor of Safety corresponding to critical surface is estimated and is tabulated in Table 3. Table 3 compares the Factor of Safety obtained on analyzing the slope for different thickness of infills.

A comparison of the results reveals that FoS is dependent upon friction angle of the infill and higher the angle of internal friction, higher is the FoS. Also, the variation of Factor of Safety with the thickness of different infills is presented in Fig. 4.

It is observed that the inclusion of even a small thickness of infill with less interfacial friction does not contribute to the stability of embankment dams. On the contrary,

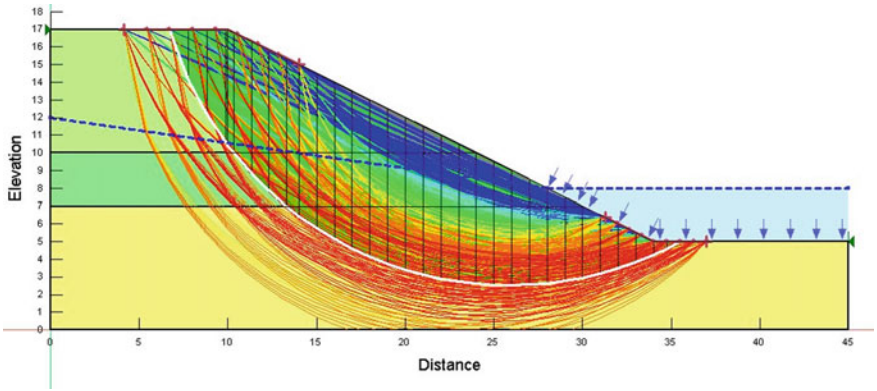

Fig. 3 Computed slip surfaces in color map

Table 3 Variation of factor of safety with type of infill

S. No.	Thickness of BL (m)	Thickness of TL (m)	Thickness of IF1/IF2 (m)	IF1 FoS	IF2 FoS
1	7	10	0	1.798	1.798
2	7	9	1	1.814	1.764
3	7	8	2	1.821	1.719
4	7	7	3	1.823	1.665
5	7	6	4	1.818	1.610
6	7	5	5	1.808	1.547
7	7	4	6	1.792	1.488
8	7	3	7	1.773	1.439

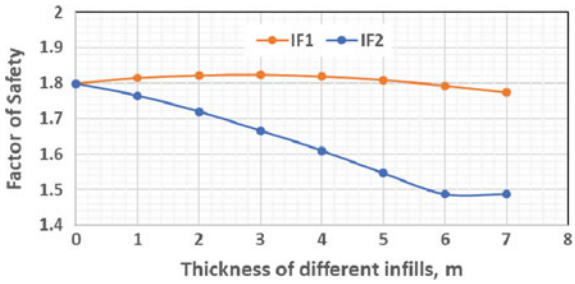

Fig. 4 Variation of friction angle with respect to type of infill

if the infill has higher friction resistance, 3–4 m thickness of the material can enhance the stability of slopes.

3.2 Effect of Slope Angle on Factor of Safety

To investigate the effect of infill thickness on slope angles three different slope angles are considered. The angles considered are 30°, 45° and 60°. The cross-section of the different slope sections along with the phreatic line is presented in Fig. 5. For the different slope angles, thickness of infill is varied and accordingly the FoS of the critical surface is estimated from SLOPE/W analysis. FoS of the critical surface is plotted with respect to the thickness of infill and is presented in Fig. 6.

From the analysis its observed that irrespective of the slope angle, CD waste is a suitable infill material for construction of embankments. Optimum thickness of infill was estimated as 3 m for slope angle of 30° and 45°. As expected for a given thickness of different layers, FoS decreases with slope angle. For 60° slope, highest FoS is obtained for 4 m thickness of CD infill. To estimate the effectiveness of CD infill in enhancing the stability of embankment, percentage increase in Factor of Safety is determined as follows:

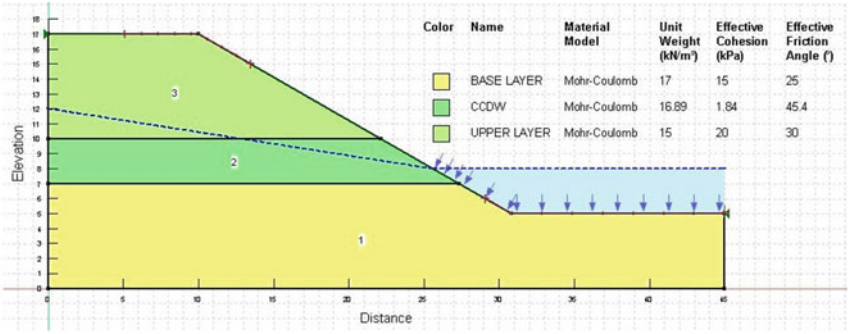

a

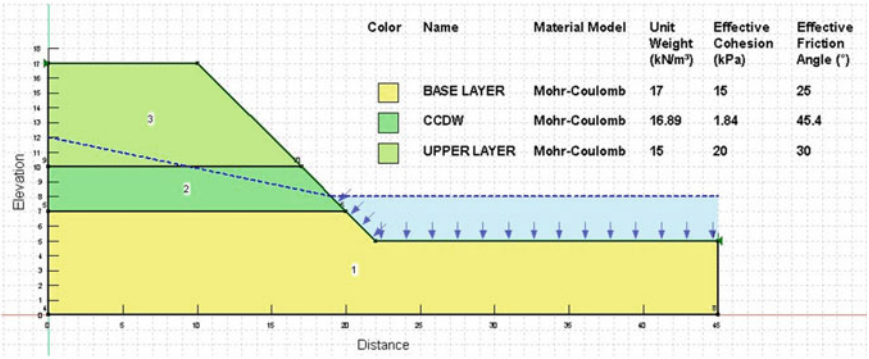

b

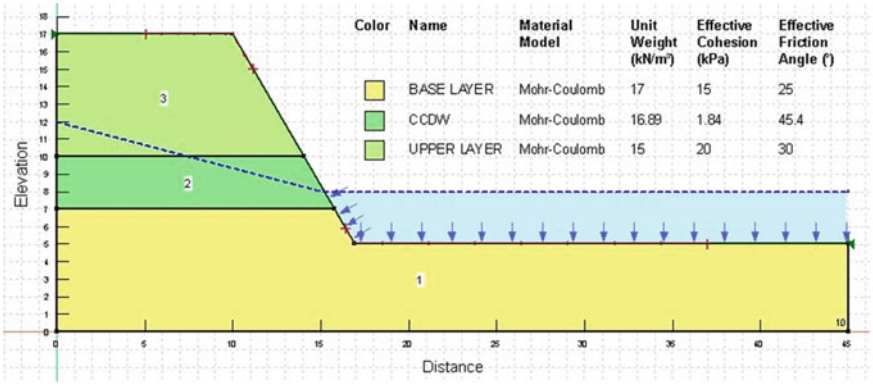

c

Fig. 5 Embankment sections of slope angle: **a** 30°, **b** 45° and **c** 60°

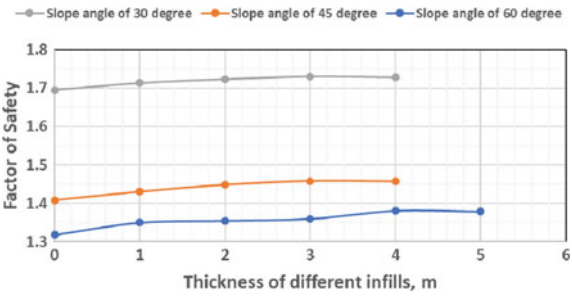

Fig. 6 Variation of FoS with respect to different slope angle

Table 4 Percentage increase in Factor of Safety with respect to slope angle

Slope angle (°)	FoS max	FoS_i	% increase in FoS
30	1.73	1.695	2.06
45	1.458	1.408	3.55
60	1.381	1.318	4.78

$$\text{Percentage increase in FoS} = [(FoS_{max} - FoS_i)/FoS_i] \times 100 \quad (1)$$

Here, FoS_{max} is the FoS of the critical surface having optimum thickness of CD infill and FoS_i is the safety factor for a two-layered slope (no CD infill). The results are summarized in Table 4.

Although FoS decreases as slope angle increases, the percentage increase in FoS with the addition of CD waste is directly proportional to slope angle, as seen in the table. This infers that the shear properties of the infill especially angle of internal friction, plays a crucial role as far as stability of slope is considered.

4 Discussion of Results

Though construction and demolition waste is used for improving hydraulic and strength properties of concrete and clay, its application with respect to slope stability has not been explored by researchers. The present study investigated the suitability of this waste material in construction of slopes with reference to three different aspects viz., type of infill, thickness of infill, slope of infill. The appropriateness of these parameters are assessed with reference to factor of safety of the slope. From the analysis, it is observed that cohesionless CD waste is a preferred material since it enhances strength and hydraulic properties of the infill. The effectiveness of these cohesionless infill is high for steep slopes which infers that angle of internal friction is a critical parameter as far as stability of slope is concerned. The observed results are in agreement with the literature though the applications are different [20, 21].

5 Conclusions

The present study summarizes the suitability of CD waste as infill for construction of embankments. the parameters estimated include properties of CD infill, thickness of infill and slope angle. From the results the following conclusions can be made:

- For construction of slopes, angle of internal friction is critical as far as its stability is concerned.
- 17–24% of the height of embankment can be replaced with CD infill without compromising on Factor of Safety.
- Effectiveness of CD waste as infill increases with slope angle.

The current study presents a static approach to analyze the stability of the embankments. From the investigations, it is observed that demolition wastes is a good infill as far as construction of slopes is concerned. The CD waste considered in the present study is a cohesionless infill. Keeping in mind the limited recycling facilities of CD waste, it is essential to segregate the waste at its source itself so that with minimum processing the material will be made available for any application. However, the analysis can be expanded by applying dynamic loads to simulate real-time situations which can be considered as a scope for future study. The simulated results can also be validated through experimental studies to investigate the failure patterns.

References

1. Pandian NS (2004) Fly ash characterization with reference to geotechnical applications. J Indian Inst Sci 84:189–216
2. Kenai S (2010) Effect of curing time on shear strength of cohesive soils stabilized with combination of lime and natural pozzolana. Int J Civ Eng 9
3. Kumar Sharma A, Sivapullaiah PV (2012) Improvement of strength of expansive soil with waste granulated blast furnace slag In GeoCongress 2012 State Art Practice Geotechnology Engineering. ASCE, 3199-208
4. Tavakoli Mehrjardi G, Azizi A, Haji-Azizi A, Asdollafardi G (2020) Evaluating and improving the construction and demolition waste technical properties to use in road construction. Transp Geotech 23:100349
5. Reddy SB, Krishna AM (2017) Tyre chips as compressible inclusions in earth-retaining walls. Proc Inst Civ Eng Gr Improv 170:137–148
6. Sivakumar Babu GL, Chouksey SK (2012) Analytical model for stress-strain response of plastic waste mixed soil. J Hazard Toxic Radioact Waste 16:219–228
7. Kolathayar S, Suja P, Nair V, Krishna S, Tamilarasi G (2019) Performance evaluation of seashell and sand as infill materials in HDPE and coir geocells. Innov Infrastruct Solut 4:1–8
8. Lal D, Sankar N, Chandrakaran S (2017) Effect of reinforcement form on the behaviour of coir geotextile reinforced sand beds. Soils Found 57:227–236
9. Dutta S, Mandal JN (2017) Model studies on encased fly ash column–geocell composite systems in soft clay. J Hazard Toxic Radioact Waste 21:04017001
10. Rouaiguia A, Dahim MA (2013) Numerical modeling of slope stability analysis. Int J Eng Sci Innov Technol 2:533–542
11. Hegde A (2017) Geocell reinforced foundation beds-past findings, present trends and future prospects: a state-of-the-art review. Constr Build Mater 154:658–674

12. Georgiannou VN, Serafis A, Pavlopoulou EM (2017) Analysis of a vertical segmental shaft using 2D & 3D finite element codes. Int J Geomate 13:138–146
13. Sobhey M, Shahien M, El Sawwaf M, Farouk A (2021) Analysis of clay slopes with piles using 2D and 3D FEM. Geotech Geol Eng 39:2623–2631
14. Khosravifar A, Elgamal A, Lu J, Li J (2018) A 3D model for earthquake-induced liquefaction triggering and post-liquefaction response. Soil Dyn Earthq Eng 110:43–52
15. Vishal V, Siddique T, Purohit R, Phophliya MK, Pradhan SP (2017) Hazard assessment in rockfall-prone Himalayan slopes along National Highway-58, India: rating and simulation. Nat Hazards 85:487–503
16. Grund S, Lüdtke O, Robitzsch A (2016) Multiple imputation of missing covariate values in multilevel models with random slopes: a cautionary note. Behav Res Methods 48:640–649
17. Jain S, Singhal S, Pandey S (2020) Environmental life cycle assessment of construction and demolition waste recycling: a case of urban India. Resour Conserv Recycl 155:104642
18. Ng S, Engelsen CJ (2018) Construction and demolition wastes. Elsevier
19. Joshi AM, Basutkar SM, Ahmed MI, Keshava M, Seshagiri Rao R, Kaup SJ (2019) Performance of stabilized adobe blocks prepared using construction and demolition waste. J Build Pathol Rehabil 4:1–14
20. Sharma A, Sharma RK (2019) Effect of addition of construction–demolition waste on strength characteristics of high plastic clays. Innov Infrastruct Solut 4:1–11
21. Ibrahim HA, Goh Y, Ng ZA, Yap SP, Mo KH, Yuen CW, Abutaha F (2020) Hydraulic and strength characteristics of pervious concrete containing a high volume of construction and demolition waste as aggregates. Constr Build Mater 253:119251

Improved Single-Sensor-Based Modal Identification Using Singular Spectrum Analysis

Basuraj Bhowmik

Abstract The present study aims to demonstrate the capabilities of singular spectrum analysis (SSA) as a filter bank that could potentially be integrated into a modal identification framework using single-sensor output information. SSA reconstructs the original time series using principal components from the signal subspace—thereby eliminating noise components altogether—and yields a filtered signal that finds its use in modal identification. Using time-domain decomposition and least-squares technique, the modal response generated using SSA is fit with a free-decay signal from which the estimates of natural frequencies and damping ratios are carried out. The paper attempts to investigate a simple model of a dynamical system and analyzes it using the proposed approach to provide a comparison with traditional operational modal analysis techniques. The results demonstrate that SSA can be used as a powerful tool for the analysis of vibratory behavior for structures exhibiting well-separated spectral components. Inherent filtering embedded within its framework and its seamless integration into a modal identification framework hold strong promise for application inbuilt infrastructure systems.

Keywords Filtering · Singular spectrum analysis · Modal identification · Damping ratios · Natural frequencies

1 Introduction

A representative class of methods based on statistical signal processing—known as blind source separation (BSS)—dealing with the recovery of modes from response-only data, has gained significant pre-eminence in recent times [1, 2]. Despite its progress in terms of accuracy and robustness in mode separation, single-sensor-based modal identification for built infrastructures poses a significant challenge [3]. Although traditional BSS-based modal analysis utilizes a full set of system responses to identify modal parameters (natural frequencies, mode shapes, and damping ratios),

B. Bhowmik (✉)
Department of Civil Engineering, GITAM University, Bengaluru, India
e-mail: bbhowmik@gitam.edu

L. Nandagiri et al. (eds.), *Recent Advances in Civil Engineering*, Lecture Notes in Civil Engineering 256, https://doi.org/10.1007/978-981-19-1862-9_56

the analysis becomes more complicated when a subset of sensors is instrumented. A complete modal identification becomes more involved if only a single sensor is placed to monitor the system health and its properties—particularly evident during cost constraints, improper accessibility—that require changes in the algorithmic structure and mathematical formulations to extract such modal parameters [3, 4]. In this paper, a new approach employing singular spectrum analysis (SSA) as a filter bank is resorted to identify modal parameters using the response obtained from a single sensor.

A simpler alternative to traditional operational modal analysis (OMA) is offered by BSS toward separating individual modes. However, successful implementation of BSS is warranted by second-order blind identification (SOBI) that relies on joint diagonalization approaches [2]. Owing to computational complexities—especially while dealing with multiple lagged covariance matrices—becomes a challenge, when attempted to perform using single-sensor information. The provision of creating Hankel matrices from the set of responses eases the construct of the formulation; thereby providing a consistent mathematical formulation, leading to an automatic noise removal paradigm embedded within the auspices of modal identification. SSA is an emerging signal processing technique that has been applied for real-time structural health monitoring and damage detection studies. The use of recursive principal component analysis (PCA) for real-time damage detection [5, 6] suggested the application of SSA in single-sensor monitoring, particularly considering the rigorous analysis brought about by the decomposition and the reconstruction of the signal. Accommodating bidirectional capabilities for monitoring can be considered a direct application of multichannel singular spectrum analysis (MSSA).

The premise of extracting proper orthogonal modes (POMs) is numerically consistent with identifying the linear normal modes (LNMs) of a system—both offline and in real time [7]. To achieve this realization within a gamut of structural dynamics problems, algorithms such as PCA, independent component analysis (ICA), canonical correlation analysis (CCA)—and their real-time counterparts—have shown success with a fair amount of errors [7–9]. In this context, the selective hypothesis of singular value decomposition (SVD) of a Hankelized covariance matrix provides information pertaining to the spectral content of the noise-free bands that are eventually processed with modal extraction tools, leading to the identification of natural frequencies, mode shapes, and damping ratios. While these modal properties provide straightforward interpretation of the condition of a monitored system, traditional identification techniques are computationally intensive, constrained by limitations on assumptions, and in a lot of cases—fail to accurately identify distortions within a sparse network of sensors. Figure 1 shows a schematic approach to the proposed approach that not only accommodates single-sensor modal identification for a possible subset of modes, but also clearly demonstrates the potential to be applied to a mobile decentralized topology for complete identification, with the removal of noise components from the signal.

Accordingly, this work is motivated by the potential application of SSA as a filter bank that effectively removes the noise components and reconstructs the signal from the noise-free subspace. This study aims at demonstrating the capabilities of SSA as

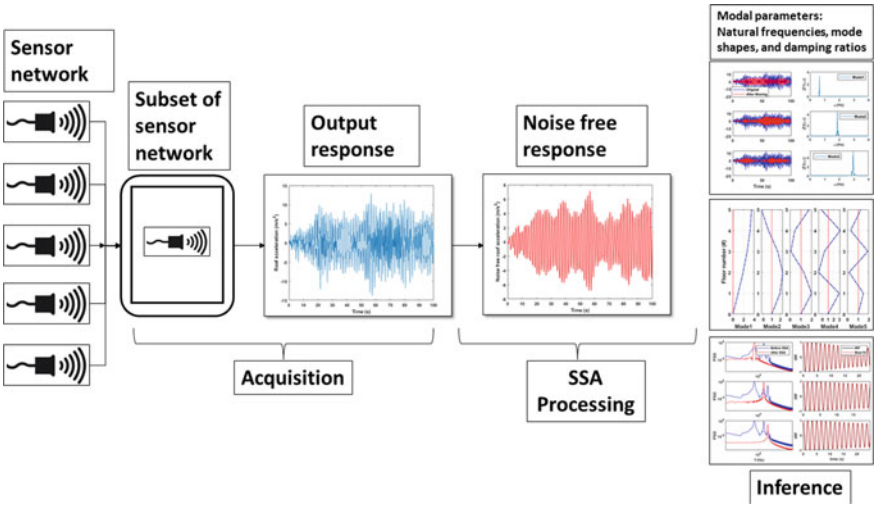

Fig. 1 Schematic of the proposed SSA-based single-sensor modal identification technique

a tool for modal analysis—especially when spectral and modal decomposition techniques are rendered ineffective due to periodic-nonharmonic signal components—in interpreting the useful components from a signal. An automated algorithm to first filter the noise components of a signal and identify the modal properties of a linear five degrees of freedom (5 DOF) system is introduced in the following sections. The proposed procedure complements the traditional identification strategy and a steady comparison between the methods are sought.

The remainder of the paper is organized as follows: Sect. 2 provides the detailed methodology of implementing SSA as a filter bank. The subsequent section discusses a case study on a simulated linear 5 DOF system, where filtering and reconstruction of the signal are performed. The comparison against the traditional algorithm is presented next. Finally, the application of the proposed approach toward estimating natural frequencies and damping ratios of the system concludes the work.

2 Methodology—SSA as a Filter Bank

For any seemingly complicated time series, SSA demonstrates the potential to uncover its structure—be it for structural damage assessment or climatological studies—to a fundamental stratum. A key feature of SSA is the nonparametric constitution of the algorithm that makes it a preferred choice for source identification and simultaneous reconstruction without the need for a dynamic system model or information pertaining to its parameters. The signal processing algorithm uses the output from a single sensor to create a Hankel covariance matrix that essentially identifies

the *trend component of the signal* in order to *remove the components from the noise subspace*. This inherent filtering property of SSA is automatically embedded in a pre-processing stage to remove any outliers and low-energy noise components arising during acquisition, monitoring, or even human errors. The *frequencies* of the diversified periodic *components of different spectral bands* can be extracted along with the corresponding *cycles*. Finally, SSA aims to eliminate the unwanted components of the signal and *reconstructs it using principal components of the noise-free subspace*. Recovering the structure of the signal can be particularly useful in identifying any existing harmonics that might reduce the efficacy of the filter bank.

2.1 SSA—Summary of Key Steps

The fundamental concept behind SSA is seemingly intuitive and simple. SSA can be considered a fundamental extension of PCA. Like all PCA methods, SSA projects a signal into a transformed space bearing a lower dimension. Even while retaining most of the variance, the new signal contains all of the important information which is a comprehensive aggregate of lagged signal components in the time domain. While in PCA, SVD is implemented on spatiotemporal datasets, SSA utilizes a single-channel response (usually vibratory—displacement or acceleration) and creates a Hankel covariance matrix. Simply put, SSA provides information purely on a temporal signal much like the seminal investigation on Fourier decomposition.

With two major steps, SSA is implemented to perform decomposition, reconstruction, and prediction. In the first stage, SSA aims to decompose the original signal into several independent components that are interpretable among themselves. The method initiates "*embedding"* by producing a Hankel covariance matrix from the single-channel time series by sliding a window that is essentially shorter in length than the original signal. Next, this matrix is decomposed into several elementary matrices of decreasing variance contribution using SVD. These components usually form a part of either or all of the slowly varying trends, oscillatory constituents, and unwanted low-frequency noise. In the next stage, reconstruction of the original signal using the selected principal components from the noise-free subspace is ensured that contains the most important *signal information*. This is the stage where the trend, oscillatory, and noise components are completely eliminated, discarded from the reconstruction, and removed altogether to create a *noise-devoid* signal in the transformed lower dimensional space. Finally, in the "*grouping"* stage, the time series is generated using the diagonal averaging technique representing a smoothened, filtered version of the original series.

2.2 SSA—Detailed Steps for Filter-Bank Approach

Stage 1: Decomposition

Each of the steps for embedding and singular value decomposition is discussed below.

Embedding: The process of embedding maps a one-dimensional time series $Y_T = (y_1, \ldots y_T)$ into a multidimensional series $X_1, \ldots X_k$ with vectors

$$X_i = (y_1, \ldots y_{i-L+1}) \in \mathrm{R}_L, \text{ where } K = T - L + 1. \quad (1)$$

For the purpose of single-channel modal identification, the acceleration signal acquired at this stage is mapped onto K lagged vectors X_i, with an individual window length L; $\forall 2 \leq L \leq T$. Embedding produces the trajectory matrix given by

$$\mathrm{X} = [X_1, \ldots, X_k], \; i, j = 1, \ldots, L, K \quad (2)$$

The structure of the above trajectory matrix is essentially a Hankel matrix with the elements along the diagonal $i + j = \text{const}$ equal. For the purposes of this study, Fig. 2 illustrates the Hankel matrix corresponding to the output signal obtained from the roof floor of the linear 5 DOF system. For filter-bank applications in vibration analysis, if a phenomenon corresponding to frequency f is desired, the minimum window length should be set at $L \geq f_s/f$, with f_s being the sampling frequency of the signal.

Singular Value Decomposition (SVD)

A representative summation set of rank-one bi-orthogonal elementary matrices is produced through this step. SVD on the Hankel covariance matrix $\mathrm{C}_H = \frac{1}{N-1}\mathrm{X}\mathrm{X}^T$

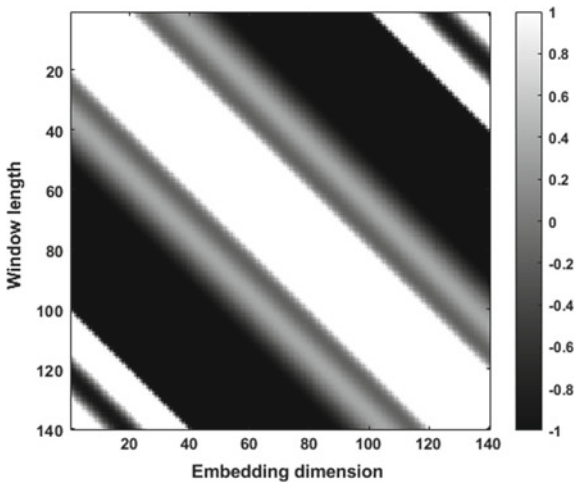

Fig. 2 Hankel covariance matrix obtained for SSA filter-bank application on the linear 5 DOF system

yields eigenvalues in decreasing order of their contribution to the variance. Denoted by $\lambda_1, \ldots, \lambda_L$; $\lambda_1 \geq \ldots \geq \lambda_L$ the eigenvalues are accompanied by a set of corresponding orthonormal eigenvectors $\mathrm{U}_1, \ldots, \mathrm{U}_L$ with $\mathrm{U}_i, \mathrm{U}_j = 0$, for $i = j$ (orthogonality property) and $\|\mathrm{U}_i\| = 1$(unit norm property). Denoting $\mathrm{V}_i = \mathrm{X}^T \mathrm{U}_i / \sqrt{\lambda_i}$, the SVD of the trajectory matrix is given by

$$X = X_1 + \ldots + X_d \tag{3}$$

where $\mathrm{X}_i = \sqrt{\lambda_i} \mathrm{U}_i \mathrm{V}_i^T$ for $i = 1, \ldots, d$. The contribution of the matrix X_i to the expansion of X is given by the ratio $\lambda_i / \sum_{i=1}^{d} \lambda_i$.

Stage 2: Reconstruction

This stage concerns the mathematical expressions for grouping and diagonal averaging.

Grouping: Indexed within the matrix is a set of several groups of elementary matrices that are first split and then summed up corresponding to each matrix band. Choosing the groups $X_{I_1}, X_{I_2}, \ldots, X_{I_m}$ is known as Eigen triple grouping which creates the trajectory matrix through the equation.

$$X = X_{I_1} + X_{I_2} + \ldots + X_{I_m} \tag{4}$$

with indices $I = \{i_1, i_2, \ldots, i_k\}$.

Diagonal Averaging: In this step, each k^{th} element of each of the matrices X_i of the time series is obtained by averaging over the ensemble of i and j such that $i + j = k + 2$. This yields Hankelization of the matrix $\mathbf{Z}$ to H_Z corresponding to the series obtained through diagonal averaging. Referring to Eq. (4), the equivalent decomposition of the initial signal $Y_T = (y_1, \ldots y_T)$ results in a sum of m signals:

$$y_t = \sum_{k=1}^{m} y_t^{(k)} \tag{5}$$

2.3 SSA—Application to Vibrating Signals for Filtering

After acquiring the signal from an instrumented DOF, it is passed through an SSA filter in order to remove the noise components from the signal. The inherent filtering property not only allows working with a noise-devoid signal at a subsequent stage, but also transforms the signal to a lower dimension—thereby enabling easier computation. The key steps of the process are enumerated as follows:

(1) The temporal coordinates of the measured acceleration signal are embedded into a sequence of simultaneously lagged multidimensional acceleration vectors.
(2) Using SVD, the orthogonal basis vector is estimated in the next stage.
(3) The lagged vectors obtained from step 1 are projected to the new basis vectors. This ensures a lower dimensional transformation.
(4) Noise components from the subspace are automatically removed by selecting relevant principal components that contribute to most of the variance.
(5) The next step is to recover the Hankel structure of the trajectory matrix which is carried out through diagonal averaging.
(6) Finally, the reconstructed signal is created by resorting to embedding once again that provides an approximation of the original time series.

3 Filter Bank and Single-Sensor Modal Identification—A Case Study

For the purpose of this work, a linear 5 DOF system is considered to have the following properties. On each floor, the centered mass is considered to be 10 kg with individual stiffness as 2 kN/m. As accurate modeling of the spectral components of the acceleration response is crucial to investigate the performance of the algorithm, realistic interpretation of damping ratios ranges from 3% (moderate damping) to 7% (very high damping). The situation described here is fundamentally different and more accurate from most research work where the damping ratio is usually considered to be on the lower to moderate side of the critical damping. With a sampling interval of 0.01 s, a synthetic Gaussian white noise with zero mean and unit variance is used as an input excitation to the system. Typical acceleration plots of the system are shown in Fig. 3 that indicate the response—theoretically obtained—from all the floor levels.

From a statistical perspective, it is important to ensure the dependence of one physical response on another. Correlation between physical responses (both positive and negative) indicates the coupled nature of the time series. A useful representation for observations evolving from a linear dynamical system is captured in Fig. 4. The correlation patterns between various responses in the physical domain attest to the fact that the response is coupled, which ensures a mix of spectral band representation in the frequency domain. One of the key advantages of using SSA lies in the automatic removal of mode mixing, thereby potentially providing a noise-free "single-degree of freedom (SDOF)-like" response, which will be discussed in the later stages of the manuscript.

Before proceeding to identify modal parameters of the system using the proposed SSA-based single-sensor approach, it is important to understand the theoretical behavior of the vibratory modes. Using fundamental modal analysis techniques, the dynamical linear 5 DOF system exhibits the following vibratory characteristics for each of its modes. It can be seen from Fig. 5 that the modes are well-behaved and do not provide an indication of permutation ambiguity—the details of which can be accessed elsewhere [10].

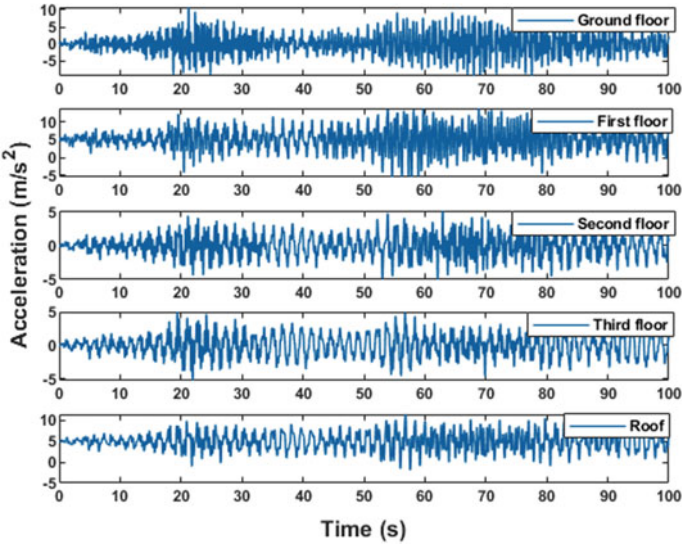

Fig. 3 Acceleration plots for the linear 5 DOF system

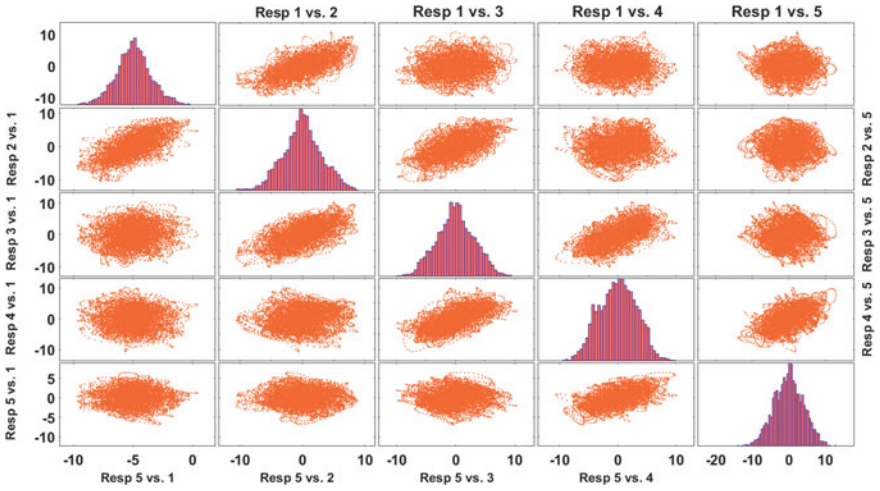

Fig. 4 Scatter plots indicating the correlation between the physical responses of the linear 5 DOF system

3.1 Application to Filtering and Reconstruction

SSA—like any other filter—provides a semblance of the original signal with an aim of preserving most of the signal constituents that contribute to the variance. At each step of SSA, the original signal is restructured into some form or the other—a Hankelized

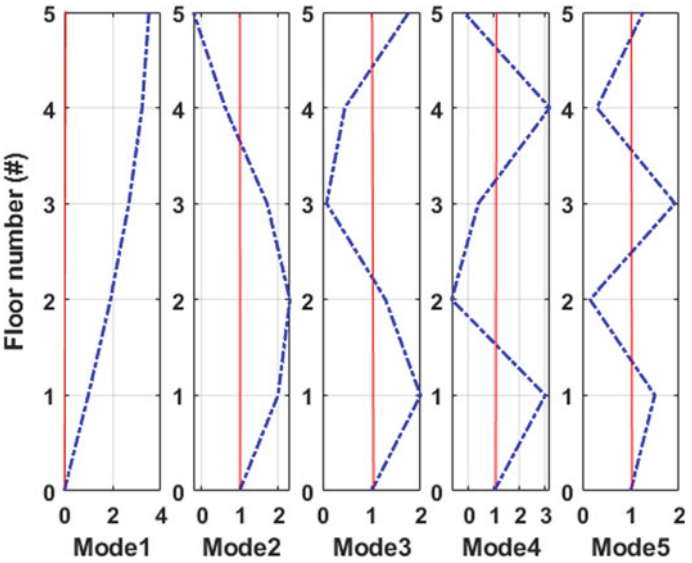

Fig. 5 Vibratory mode representation for the linear 5 DOF system

version, a lower dimensional transformation, or even a filtered variation—finally culminating in the reconstructed component that resembles the original time series.

For the present case study, the acceleration response of the roof is considered to be the single-sensor input for the SSA module. As the vibration modes are well-behaved and sufficiently separated, the resonant response of each Eigen frequency can be isolated. After embedding, the SVD on the covariance matrix produces singular vectors that approximately correspond to the natural frequencies of the system. In the grouping stage, an automated investigation on the choice of principal components (PCs) is carried out that corresponds to a 95% variance contribution for the system. In doing so, the low-energy principal components—arising from the noise subspace—are automatically eliminated, resulting in a noise-free subspace. A graphical representation of the principal components is provided in Fig. 6. The figure shows the evolution of the PCs over time, which indicates that 5 PCs can sufficiently determine most of the variance of the system.

Once the number of PCs is selected, the remaining are discarded that essentially form low spectral bands in the noise subspace. Automated elimination of the PCs ensures that the filtering technique contributes to lower computational expense for further processing. In doing so, the reconstructed components (RCs) that are selected have low to almost zero noise components, the evidence of which is shown in Fig. 7.

Evident from the figure, the evolution of the RCs over time indicates a "beat-phenomenon" type progression that statistically implies the devoid of noise components in the new time series. To supplement the findings, Fig. 8 provides better clarity on the investigation by identifying the vibratory modes corresponding to the 5 DOF system.

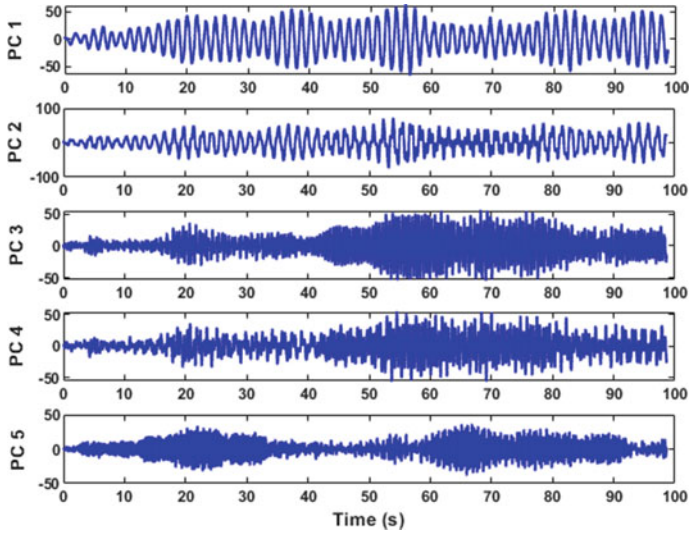

Fig. 6 Principal components based on 95% variance contribution for the system

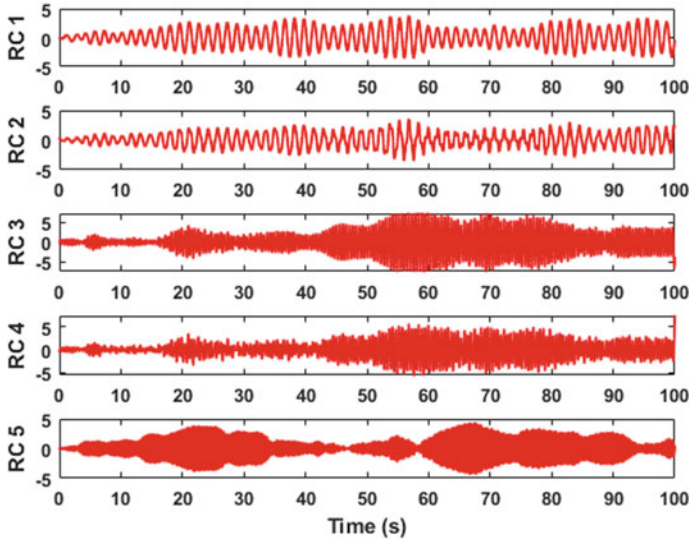

Fig. 7 Evolution of the reconstructed components corresponding to the PCs

With an increased number of DOF for a monitored system, the optimal placement of sensors becomes crucial. It becomes more involved and seemingly complicated when only a single sensor is instrumented at a strategic DOF. For the present case study, as the 5 DOF system is monitored using the acceleration response from the

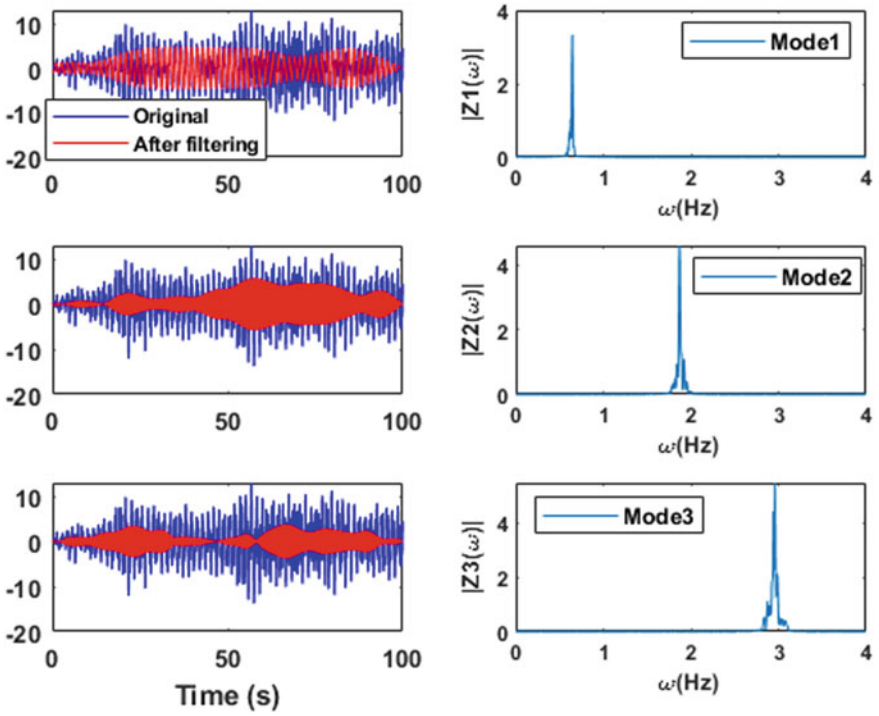

Fig. 8 Reconstructed signal and mode recovery for the first three modes of the 5 DOF system

roof, it becomes challenging to identify all the five vibratory modes of the system at one pass. This exact complexity attributes to the identification of only the first three modes (out of the five) as shown in Fig. 8. Each of the frequency plots shown here corresponds to the vibratory modes of the system—resembling an "SDOF system behavior"—that demonstrates the decoupling, modal recovery, and extraction of meaningful information regarding the health of the system.

For advanced analysis, a possible workaround for the investigation would involve the setting up a mobile decentralized framework. Using this approach, even though researchers have intended to extract a complete set of modal responses and mode recovery [11], most of these works are heavily reliant on multi-sensor technologies. In a first-of-its-kind, SSA in conjunction with a modal identification approach could cater not only to lower computational expense, but additionally provide embedded filtering strategy that is generally not available in the existing literature.

3.2 Comparison Against Traditional OMA Methods

It is important to critically review the performance of the proposed approach against its traditional counterparts. Traditional operational modal analysis has been at the forefront of research in this genre for the past few decades. Methods such as operational modal analysis (OMA), frequency domain decomposition (FDD), and stochastic subspace identification (SSI)—to name a few—have been integrated both into research and industrial domains, respectively [12–14]. In this context, the performance of the proposed SSA-based single-sensor modal identification is reviewed.

Conforming to the notion of partial modal recovery, an OMA analysis based on the 5 DOF system is carried out. With similar inputs from the roof acceleration, the SSA-based filtering stage is omitted—as prevalent for the OMA module—leading to certain inconsistencies in the identified modes. To ensure uniformity in comparison, the principal components that correspond to more than 95% of the variance are considered and the spectral decomposition is carried out. Evident from Fig. 9, each of the recovered modes shown on the right-hand plot contains traces of mode mixing—that are obvious from the distortions in the spectral bands—leading to frequency leakage, information loss, and lower accuracy of mode recovery.

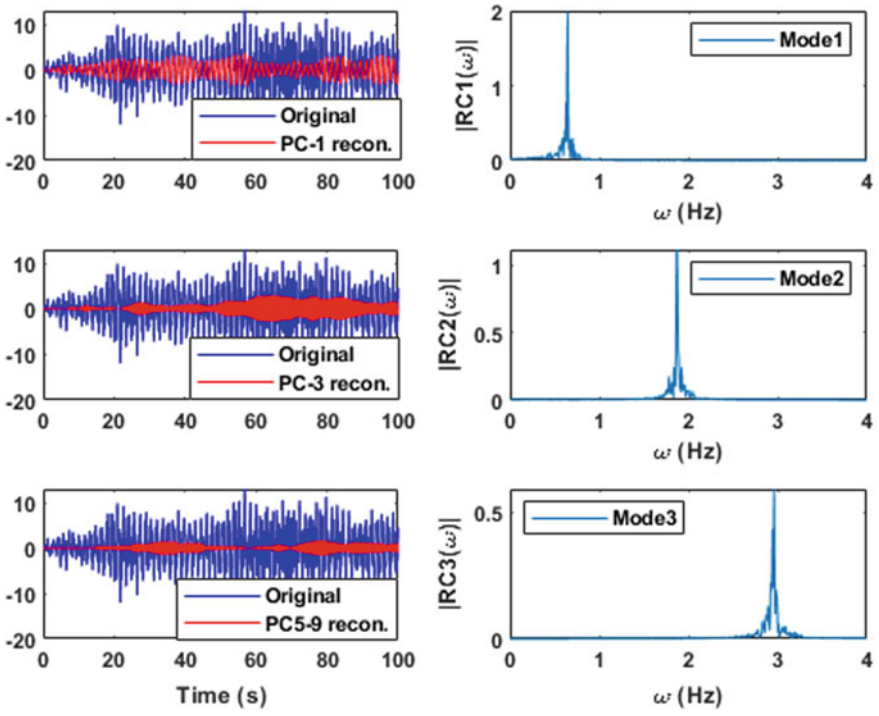

Fig. 9 Mode extraction using traditional OMA indicating inaccurate recovery

3.3 Application to Structural Damping Estimation

Spectral decomposition and extraction of modes for the linear 5 DOF system ensure that the vibration modes are sufficiently separated which enables smooth isolation of the resonant response for each Eigen frequency. The damping ratio is estimated using a least-squares fitting of an SDOF system response corresponding to the modal acceleration free-decay response of the output signal. Without performing forced resonance tests, the proposed approach provides an easy estimation of the damping ratios that are in general challenging for built infrastructure systems.

In this investigation, the key concept is to explore free-decay signals for each mode of the system and estimate the damping. However, the accuracy can sometimes be compromised due to the presence of a damage in the system—which is controlled in the present case of the linear 5 DOF structure—that can be alleviated using local damage detection strategies employing Eigen perturbation analysis [6]. The ambient excitation is utilized in the same way as an impulse load or an imposed displacement—for initial conditions—adopted for free vibration tests.

To estimate the damping ratios, a few additional steps are implemented: the modal accelerations are first computed using time-domain decomposition (TDD) [15]. Then, an exponentially damped cosine function is fit to each of the corresponding signals obtained from the analysis that provides an estimation of both the natural frequencies and the damping ratios corresponding to each mode.

Starting with the acceleration response, the proposed approach uses SSA as a filter bank and transforms the original time series into modal responses. As a low signal-to-noise ratio tends to flatten the peak—resulting in frequency leakage—free-decay tails have the potential to artificially alter the modal recovery, and therefore, the damping estimation, in turn [16, 17]. The system can be considered as a linear viscous model for which the free-decay response of an SDOF low to moderately damped is given as

$$z(t) = Ae^{-\omega_n \xi t} \cos(\omega_D t + \phi) \tag{6}$$

where $z(t)$ is the target decay signal, corresponding to the peak amplitude A. The nth circular Eigen frequency ω_n, and the damped Eigen frequency ω_D are related using the damping ratio ξ as$\omega_D = \omega_n\sqrt{1-\xi^2}$. With ϕ as the phase angle at time t, the vertical modal peaks are displaced due to the lagged covariance structure. Further, with the possibility of "beating" phenomena—evident from Fig. 7—decay signals that exhibit substantial occurrence are automatically discarded prior to the fitting procedure. Using Hilbert transform, the local decay signal envelopes can be estimated. Selected as the representative amplitude value, Eq. (6) is fit to the normalized modal displacement decay that provides the natural frequency ω_n and the damping ratio ξ. Using the proposed method, the results obtained are shown in Fig. 10.

Based on the above procedure, the following estimates of natural frequencies and damping ratios can be observed:

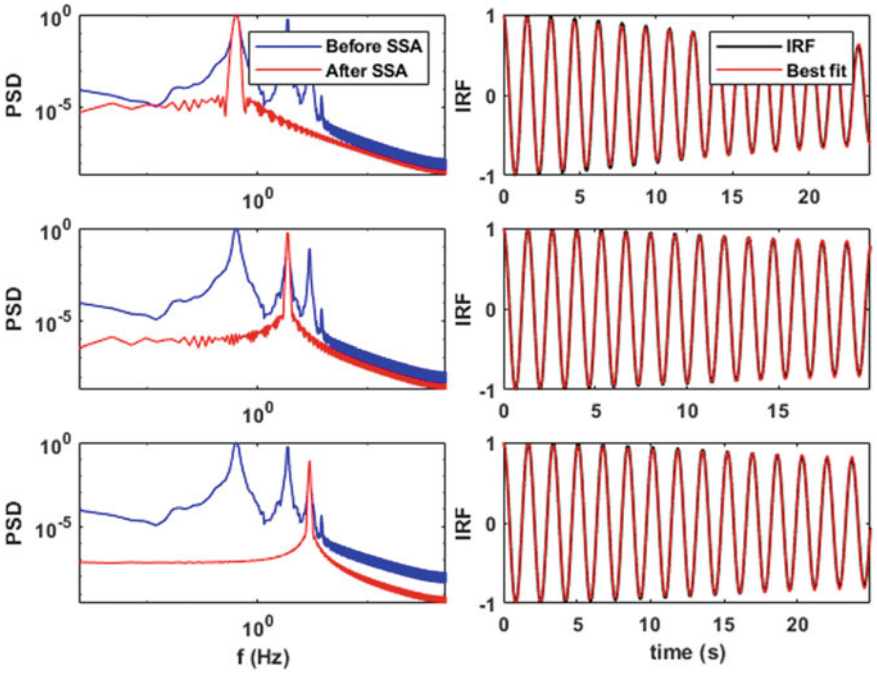

Fig. 10 Spectral representation of the modal response and the corresponding SDOF system fit

From the estimates in Table 1, it is evident that the proposed approach caters to accurate modal recovery for a linear dynamical system. Corresponding percentage errors of natural frequencies indicate the separability of modes. An interesting point to note here is that while the error percentage in estimating damping ratios looks staggered (more evident from Fig. 11), the numerical value corresponding to the ratios is almost similar. Due to higher precision in representation, the errors are exaggerated. Graphically, Fig. 11 provides the error percentage in the estimates of both natural frequencies and damping ratios corresponding to the first three modes of the considered linear 5 DOF system.

Table 1 Estimates of natural frequencies and damping ratios using the proposed approach

Natural frequencies (Hz)			Damping ratios		
Target	Estimate	|% error|	Target	Estimate	|% error|
0.641	0.642	0.156	0.03	0.031	3.330
1.870	1.871	0.053	0.04	0.039	2.500
2.948	2.953	0.170	0.05	0.051	2.000

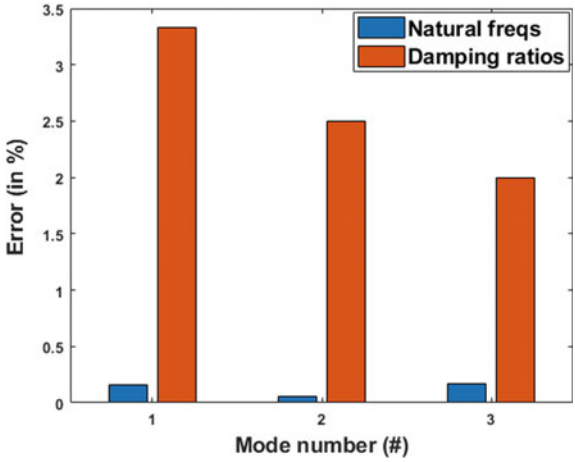

Fig. 11 Percentage errors in the estimation of natural frequencies and damping ratios

4 Conclusions

The goal of this work is to demonstrate the filter-bank capabilities of SSA and its integration toward the identification of modal parameters for a linear dynamical system. With the above aim, this study analyzes the response of a simulated linear 5 DOF system. The response obtained from a single sensor is considered for further investigation. In the first stage, SSA decomposes the signal into its fundamental constituents and reconstructs the signal by considering the principal components from the noise-free subspace. With an automated noise removal, filtering of the signal allows preserving of key information that is vital for the subsequent modal identification. Using time-domain decomposition, free-decay responses are fit from which natural frequencies and mode shapes have been identified. The discrepancies in the estimation of these modal parameters form the key findings of this research work. Improvements in the application of SSA towards modal identification for a decentralized mobile topology is an exciting work to be addressed in the future.

References

1. Zhou W, Chelidze D (2007) Blind source separation based vibration mode identification. Mech Syst Signal Process 21(8):3072–3087
2. Hazra B, Sadhu A, Roffel AJ, Narasimhan S (2012) Hybrid time-frequency blind source separation towards ambient system identification of structures. Comput-Aided Civ Infrastruct Eng 27(5):314–332
3. Li J, Zhu X, Law SS, Samali B (2019) Drive-by blind modal identification with singular spectrum analysis. J Aerosp Eng 32(4):04019050
4. Bhowmik B, Krishnan M, Hazra B, Pakrashi V (2019) Real-time unified single-and multi-channel structural damage detection using recursive singular spectrum analysis. Struct Health Monit 18(2):563–589

5. Krishnan M, Bhowmik B, Hazra B, Pakrashi V (2018) Real time damage detection using recursive principal components and time varying auto-regressive modeling. Mech Syst Signal Process 101:549–574
6. Bhowmik B (2018) Online structural damage detection using first order Eigen perturbation techniques. Doctoral Dissertation
7. Bhowmik B, Tripura T, Hazra B, Pakrashi V (2019) First-order Eigen-perturbation techniques for real-time damage detection of vibrating systems: theory and applications. Appl Mech Rev 71(6)
8. Yang Y, Nagarajaiah S (2013) Time-frequency blind source separation using independent component analysis for output-only modal identification of highly damped structures. J Struct Eng 139(10):1780–1793
9. Bhowmik B, Tripura T, Hazra B, Pakrashi V (2020) Real time structural modal identification using recursive canonical correlation analysis and application towards online structural damage detection. J Sound Vib 468:115101
10. Bhowmik B, Tripura T, Hazra B, Pakrashi V (2020) Robust linear and nonlinear structural damage detection using recursive canonical correlation analysis. Mech Syst Signal Process 136:106499
11. Sadhu A, Hazra B, Narasimhan S (2013) Decentralized modal identification of structures using parallel factor decomposition and sparse blind source separation. Mech Syst Signal Process 41(1–2):396–419
12. Zhang L, Brincker R (2005) An overview of operational modal analysis: major development and issues. In: Proceedings of the 1st International operational modal analysis conference, April 26–27, 2005, Copenhagen, Denmark. Aalborg Universitet, pp 179–190
13. Brincker R, Zhang L, Andersen P (2001) Modal identification of output-only systems using frequency domain decomposition. Smart Mater Struct 10(3):441
14. Peeters B, De Roeck G (1999) Reference-based stochastic subspace identification for output-only modal analysis. Mech Syst Signal Process 13(6):855–878
15. Kim BH, Stubbs N, Park T (2005) A new method to extract modal parameters using output-only responses. J Sound Vib 282(1–2):215–230
16. Cheynet E, Daniotti N, Jakobsen JB, Snæbjörnsson J (2020) Improved long-span bridge modeling using data-driven identification of vehicle-induced vibrations. Struct Control Health Monit 27(9):e2574
17. Bhowmik B, Panda S, Hazra B, Pakrashi V (2021) Feedback-driven error-corrected single-sensor analytics for real-time condition monitoring. Int J Mech Sci 106898

An Appraisal of the Characteristics of Road Crashes Involving Vulnerable Road Users

V. S. Sanjay Kumar, K. R. Jinumol, and Ebin Sam

Abstract Road users that are vulnerable to road crashes are primarily those who are unprotected by a protective outer shield, such as pedestrians, cyclists, and motorcyclists of all ages and abilities, such as children, the elderly, and people who have disabilities (physically or mentally). The present paper aims at a review to provide an investigation of the crashes involving vulnerable road users reported in the state of Kerala from the year 2018 to 2020. It consists of crash data analysis concerning age group and collision type and vehicle type. It was found that the highest percentage of vulnerable road users involved in the crashes are from the two-wheeler category (59.11%), followed by pedestrians (20.35%). The highest percentage of crashes for pedestrians and cyclists are due to collisions with two-wheelers. The most susceptible groups for pedestrians and cyclists are those aged 41–60 years, while those aged 26–40 years are more vulnerable to two-wheeler crashes.

Keywords Road crash · Vulnerable road users · Collision · Age group

1 Introduction

As per the Global Status report on Road Safety 2018, road crashes are the eighth leading cause of death worldwide, claiming the lives of more than 1.35 million people annually, with 90% of these fatalities occurring in developing countries. The World Health Organization reports that road crashes are the leading cause of death among children and adults from 5 to 29 years old. Around the world, 54% of all traffic fatalities involve pedestrians, cyclists, or motorcyclists. This causes substantial economic losses not only to individuals and their families, but also to the country as a whole [14].

In India, there were 449,002 crashes in 2019, resulting in 151,113 deaths and 451,361 injuries. As reported in the World Road Statistics, 2018, India ranked first among 199 countries in the number of persons killed on roads. The number of persons

V. S. Sanjay Kumar (✉) · K. R. Jinumol · E. Sam
KSCSTE—NATPAC, Thiruvananthapuram, Kerala, India
e-mail: sanjay.natpac@gmail.com

L. Nandagiri et al. (eds.), *Recent Advances in Civil Engineering*, Lecture Notes in Civil Engineering 256, https://doi.org/10.1007/978-981-19-1862-9_57

injured in India ranks third after that of the United States and Japan. During the year 2019, 4440 deaths and 46,055 injuries were reported from 41,111 road crashes in Kerala. In terms of the overall number of crashes and deaths in crashes, Kerala ranked fourth and 16th among Indian states, respectively. The fatalities of pedestrian and bicycles were 28.3%, 2.2% of total crash fatalities. The total number of pedestrians and bicycle victims in total crashes was 10,385 and 1,046 respectively, in the year 2019 [5].

This pandemic is regarded as the greatest health challenge that the whole world has ever faced. Many types of research have been carried out to understand the effect of lockdown in road crashes [10–11].

A term used to describe those who are most at risk from road crashes is "vulnerable road users". So, vulnerable users of the road are mainly those without an outer shield, such as pedestrians or bicyclists, as they are susceptible to suffering injuries in collisions with vehicles, and therefore need to be protected from such collisions. In contrast, pedestrians and cyclists are the most unlikely to injure other road users, while motorized two-wheelers pose a higher risk because of their heavier machines and higher speeds [6]. At present, car manufacturers, government agencies, and researchers have made many efforts to improve the protection performance of vehicles against VRUs [3, 4].

2 Literature Review

The ability to move from one place to another using one or more modes of transportation to meet daily needs is what we call mobility. Road crashes can lead to injury or death for anyone using the roads. The term Vulnerable Road Users (VRU) refers to those road users who are more vulnerable than others. Various definitions of the term have been given: World Health Organization in 2013 considered VRUs to be "pedestrians, cyclists, and motorcyclists". US Department of Transportation National Strategy on Highway Safety has a more complex definition: "road users who are most at risk for serious injury or fatality when they are involved in a motor-vehicle-related collision. These include pedestrians of all ages, types and abilities, particularly older pedestrians and people with disabilities. VRU's also include bicyclists and motorcyclists. Older drivers may also be considered to fit into this same user group". European Union's Intelligent Transport System Directive refers to "non-motorized road users, such as pedestrians and cyclists as well as motor-cyclists and persons with disabilities or reduced mobility and orientation" [8].

Nearly half of all traffic deaths involve vulnerable road users, including pedestrians, cyclists, and motorcyclists. The number of pedestrians and cyclists killed worldwide in 2014 was 26%, while motorized vehicles with two and three wheels accounted for 28% of deaths. 29% of deaths were caused by car occupants. Two-wheelers are the most common cause of death in Southeast Asia and the Western Pacific. Three- and two-wheeled motor vehicles account for 43% and 36% of all deaths, respectively [14].

The number of pedestrians killed in India accounts for 17%t, two-wheelers for 37%, and cars, jeeps, and taxis for 16%. Pedestrians and two-wheelers account for 54% of crashes-related deaths worldwide, and these two categories are the most vulnerable in light of global trends [5].

COVID-19 pandemic caught the world by surprise with its vicious ability to affect the daily life of people. To contain the spread of the pandemic, the Kerala government announced a state-wide lockdown from March 23, 2020 to May 31, 2020 in stages with a difference in the level of restriction at each stage. During the COVID-19 lockdown period from March 23, 2020 to May 31, 2020, the total number of crashes fell by 80% compared to the same period in the years 2018 and 2019. Even though the absolute number of crashes decreased, the fatality rate (fatalities per 100 crashes) was found to be increased to 13.82 (about a 17% increase) during the lockdown period compared to the corresponding period of previous years, viz., 11.57 in 2018 and 11.98 in 2019 [11].

Although traffic safety has greatly improved over the past few decades, the progress in ensuring safe mobility for vulnerable road users (VRUs), particularly two-wheelers, has been less substantial [1, 12]. In order to reduce the deaths of VRUs, extensive research has been carried out to identify the causes and prevention of vulnerable road user crashes [2, 6, 7, 13, 15].

3 Scope and Objective

The scope of the study is limited to road crashes reported from the year 2018 to 2020 in the state of Kerala, India. The objective of the study is to investigate the crash characteristics of various vulnerable road users.

4 Data and Methodology

Crash data pertaining to the year 2018, 2019, and 2020 were collected from Kerala State Crime Records Bureau (SCRB). The selected vulnerable road users are pedestrians, cyclists, and two-wheelers. The selected VRUs were analyzed concerning age group and cross-tabulation. Age groups selected for analysis are under 18 years, 18–25 years, 26–40 years, 41–60 years, and over 60 years. Cross-tabulation of vulnerable road users was done with vehicle types such as two-wheelers, car/jeep, pedestrian, single (road user alone), three-wheelers, lorry/trucks, and buses.

Table 1 Types of crashes in Kerala State (2018–20)

Type of crash	2018	2019	2020	Total
Fatal crashes	4069	4183	2745	10,997
Grievous injury crashes	28,714	29,569	19,817	78,100
Minor injury crashes	5971	6043	3729	15,743
Non-injury crashes	1427	1316	823	3566
Total crashes	40,181	41,111	27,114	108,406

Table 2 Severity of the victims

Severity of victims	2018	2019	2020	Total
Fatalities	4303	4440	2898	11,641
Grievous injuries	31,672	32,570	21,592	85,834
Minor injuries	13,786	13,485	8100	35,371
Total victims	49,761	50,495	32,590	132,846

5 Results and Discussion

5.1 Road Crashes

A total of 1,08,406 crashes occurred in Kerala during the three calendar years from 2018 to 2020, including 10,997 fatal crashes, 78,100 grievous injury crashes, and 15,743 minor injury crashes. Details of the type of crashes during 2018–2020 in the state are listed in Table 1. Travel restrictions imposed to slow the spread of the COVID-19 pandemic resulted in a decrease in the absolute number of crashes in 2020.

5.2 Severity of Victims Involved

During the past three calendar years, 11,641 people died, 85,834 people were grievously injured and 35,371 people suffered minor injuries in road crashes in the state. Details of the severity of crash victims in the state are listed in Table 2.

5.3 Vulnerable Road Users

The vulnerable road users constitute 89.42% of out of the total 1,32,811 victims. From Fig. 1, it is clear that the highest percentages of crashes are associated with

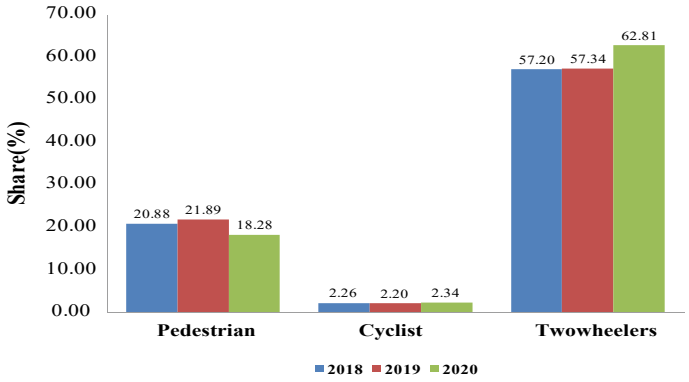

Fig. 1 Share of different road user categories involved in the crashes from 2018 to 2020

two-wheelers. The share of two-wheelers involved in road crashes increased from 57.2 to 62.8% from 2018 to 2020. The second-highest share of the road user category was from the pedestrian category. The share of the pedestrian in the road crashes has not changed much in these three years. However, the share of the pedestrians involved in road crashes decreased from 20.9 to 18.3% from 2018 to 2020. The share of the cyclist increased from 2.3 to 2.3%. Except for pedestrians, the shares of both categories are still high in 2020, despite the lockdown.

The percentage of fatalities of vulnerable road users was graphically represented in Fig. 2. It is clearly understood that the trend of pedestrian fatality has decreased (29.1–28.8%) from 2018 to 2020. However, it increased for cyclists and two-wheelers. The percentage of two-wheelers involved in the crashes has been approximately the same in 2018 and 2019. The fatality rate of two-wheelers has decreased (53.3%) in the year 2019 and again increased in 2020 (57.3%).

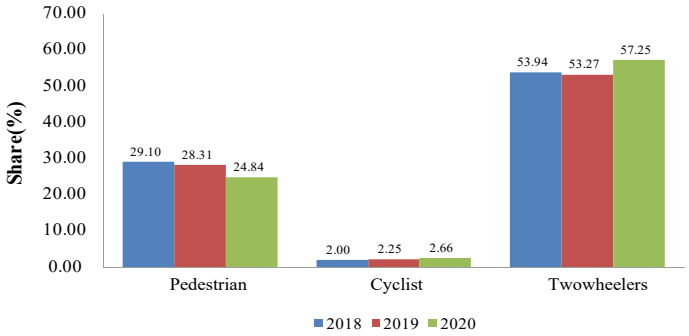

Fig. 2 Percentage of fatalities of vulnerable road users from 2018 to 2020

5.4 Age Group

From Fig. 3, the highest percentage of pedestrians involved in road crashes from 2018 to 2020 is those aged 41–60 years (39.3%), followed by those over 60 years (32.3%). The percentage of pedestrians in the age group 41–60 years was 39.2%, 38.5%, and 40.1% from 2018 to 2020. Therefore, there has been no significant change in pedestrians in this category. The share of pedestrians aged 26–40 years is reported less than the other two age groups.

When analyzed by cyclists, it can be understood that the share remains the same for cyclists under 18 years. In 2019, their percentage was lesser when compared to the other two years, which is represented in Fig. 4. The share of involvement of pedestrians and cyclists whose age was above 60 years was highest observed compared to other age groups except for 26–40 years.

The highest shares of crashes associated with two-wheelers fall under the age group of 26–40 years. The second-highest share has been contributed from the 18–25 and 41–60 year age groups. For those under 18–25 years, the share has decreased from 28.7 to 22.5%. However, it has increased from 25 to 32.6% for those aged 41–60 years, as shown in Fig. 5.

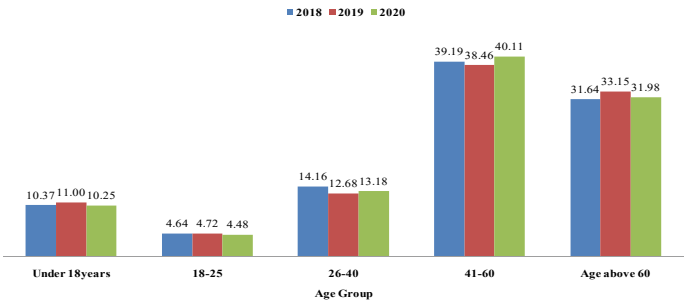

Fig. 3 Share of pedestrian involved in the crashes based on age group

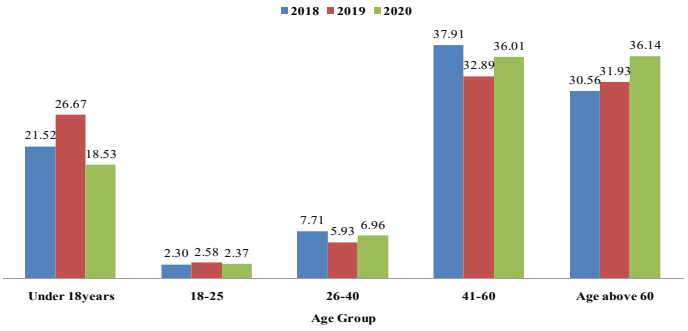

Fig. 4 Share of cyclists involved in the crashes based on age group

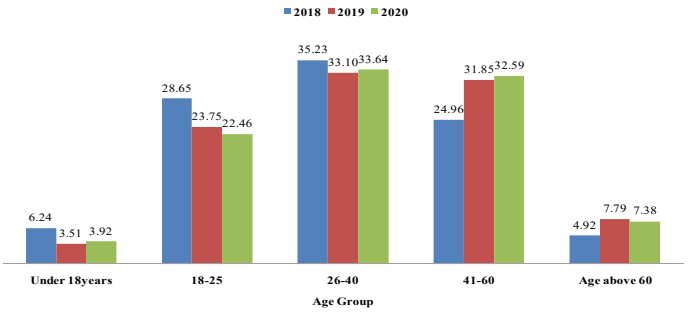

Fig. 5 Share of Two-wheelers involved in the crashes based on age group

Table 3 Share of vulnerable road users with respect to collision

VRUs (No)	Collision with						
	Two-wheelers	Cars/jeep	Pedestrian	Single	Three-wheelers	Lorry/trucks	Buses
Two wheeler	38,457	18,739	15,016	9008	5779	3290	3132
Cyclists	51	22	–	–	–	–	–
Pedestrians	15,388	6268	–	–	1788	714	1114

5.5 *Cross-Tabulation of VRUs*

A road crash can include collisions between vehicles or pedestrians or animals or fixed obstacles. There can be single-vehicle crashes, in which one vehicle alone is involved. Table 3 represents the number of vulnerable road users involved in road crashes (2018–2020) with respect to other road users.

Considering the pedestrian category, the highest share of involvement in the road crashes is from the collision with two-wheelers (60.9%) followed by the car/jeep category (24.8%). The highest share of cyclists is also the same as that of pedestrians, two-wheelers (69.9%) followed by car/jeep (30.1%). Considering the share of involvement of two-wheelers, collisions between two-wheelers to two-wheelers were found to be highest (41.2%), followed by car/jeep (20.1%) and pedestrian (16.1%). The two-wheelers are alone, accounting for crashes due to skidding, which is 9.6% of the total two-wheelers involved in the crashes. The share of cross-tabulation of vulnerable users is represented in Fig. 6.

5.6 *Discussion*

The analysis of the crash data from 2018 to 2020 revealed that pedestrians, cyclists, and two-wheelers are the most vulnerable road users. The highest number of persons

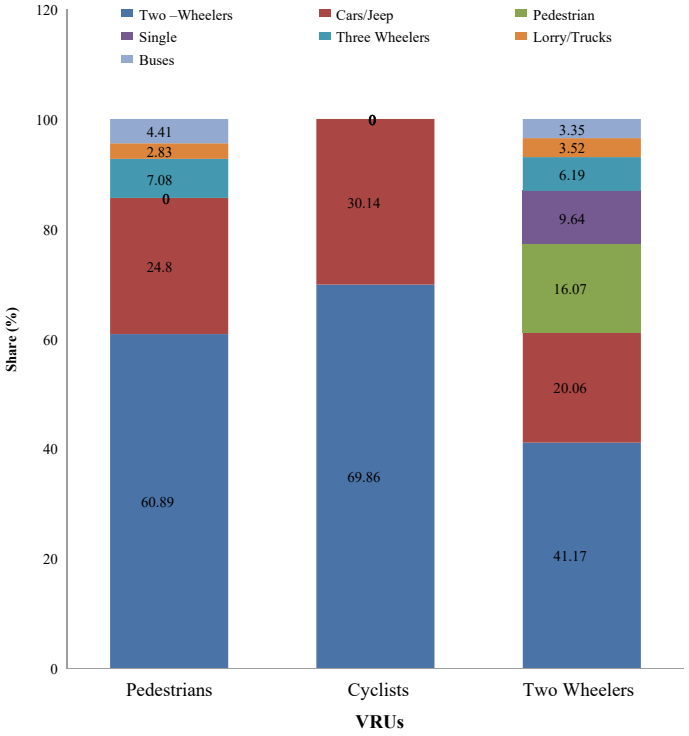

Fig. 6 Cross-tabulation of VRUs

involved in road crashes are aged 41–60 years (39.3%) followed by age above 60 years (32.3%) in the pedestrian category. The share of involvement of pedestrians and cyclists with ages above 60 years was the highest, as compared to other age groups, except for the 26–40 age groups. The highest share of crashes associated with two-wheelers falls in the age group of 26–40 years. Considering the pedestrian category, the highest share of involvement in road crashes is from the collision with two-wheelers (60.9%) followed by the car/jeep category (24.8%). 9.6% of the two-wheelers crashes are attributed to skidding, contributing to the highest share of two-wheeler crashes.

The study can be further extended to the identification of crash-prone locations involving VRUs, investigating the cause of crash occurrence, and formulating appropriate remedial measures.

6 Conclusion

- A total of 1,08,406 crashes occurred in Kerala during the three calendar years from 2018 to 2020, including 10,997 fatal crashes, 78,100 grievous injury crashes, and 15,743 minor injury crashes.
- Road crashes in Kerala resulted in 11,641 deaths, 85,834 grievous injuries, and 35,371 minor injuries over the past three years.
- The highest percentage of vulnerable road users involved in the crashes was from the two-wheeler category from the year 2018 to 2019, approximately an average of 59.1%, followed by pedestrians (20.4%).
- Road crashes are more likely to occur among cyclists and pedestrians aged 41–60 years. However, analyzing two-wheelers, the most vulnerable are those aged 26–40 years.
- The share of involvement of pedestrians and cyclists whose age was above 60 years was highest observed compared to other age groups except for 26–40 years.
- The highest percentage of pedestrians and cyclists involved in road crashes are due to collisions with two-wheelers.

Acknowledgements The authors wholeheartedly acknowledge the efforts taken by Kerala Police in collecting the crash data and sharing the same for the study purpose.

References

1. Anaya JJ, Merdrignac P, Shagdar O, Nashashibi F, Naranjo JE (2014) Vehicle to pedestrian communications for protection of vulnerable road users. In: IEEE intelligent vehicles symposium, proceedings, (IV), Dearborn, Michigan, USA, pp 1037–1042
2. Fredriksson R, Dahlgren M, van Schijndel M, de Hair S, Van MS (2014) A real-life based evaluation method of deployable vulnerable road user protection systems. Traffic Inj Prev 15:S183–S189
3. Honda (2005) Motorcycle airbag system. https://global.honda/innovation/technology/motorcycle/Airbagpicturebook.html. Last accessed 15 June 2021
4. MORTH (2018) Central Motor Vehicle Rules, Technical Standing Committee Set-Up
5. MORTH (2019) Road accidents in India
6. OCDE/OECD (1998) Safety of vulnerable road users. DSTI/DOT/RTR/RS7(98)1/Final
7. Olszewski P, Szagała P, Rabczenko D, Zielińska A (2019) Investigating safety of vulnerable road users in selected EU countries. J Safety Res 68:49–57
8. PIARC: Road safety Homepage. https://rno-its.piarc.org/en/network-operations-its-road-safety/vulnerable-road-users. Last accessed 14 June 2021
9. Qureshi AI, Huang W, Khan S, Lobanova I, Siddiq F, Gomez CR, Suri MFK (2020) Mandated societal lockdown and road traffic accidents. Accident Anal Prevent 146(2020):105747
10. Saladie O, Bustamante E, Gutierrez A (2020) COVID-19 lockdown and reduction of traffic accidents in Tarragona province, Spain. Transp Res Interdiscip Perspect 8:100218
11. Sam E, Mathew AM, Kumar VSS (2020) Macroscopic assessment of road safety scenario in Kerala during Covid-19 lockdown. In: 7th conference on transportation systems engineering and management, proceedings, pp 85–89

12. Sewalkar P, Seitz J (2019) Vehicle-to-pedestrian communication for vulnerable road users: survey, design considerations, and challenges. Sensors (Switzerland) 19(2):1–18
13. Stigson H, Rizzi M, Ydenius A, Engstrom E, Kullgren A (2017) Consumer testing of bicycle helmets. IRCOBI Conference 17–30:173–181
14. WHO (2018) Global status report on Road Safety 2018
15. Zegeer CV, Bushell M (2012) Pedestrian crash trends and potential countermeasures from around the world. Accid Anal Prev 44(1):3–11

Numerical Evaluation on Improvement of Bearing Capacity of Sand Beds Using 2D and 3D Pipe Geogrid and Its Comparative Study

N. Avinash, Saqlain Sayeedahmed Momin, and S. Gangadhara

Abstract A 3D pipe geogrid is a geogrid that contains an extruded circular pipe around the aperture of the geogrid. This type of geogrid is newly invented to study its performance and the position it holds in terms of increasing the bearing pressure when compared to that of 2D reinforced and unreinforced sand beds. In this present research work, attempts are made to find out the influence of the 2D geogrid and 3D pipe geogrid on the bearing capacity of the square surface footing overlying sand beds, and a comparative study is made between them. The *S*/*B* ratios, i.e., the ratio of spacing of the reinforcements (*S*) to the width of the footing (*B*), The relative density of the sand beds, and the height of the pipe in 3D pipe geogrid are the variables set in this study to determine the optimum values of those parameters. A finite element analysis package Abaqus is used for modeling the problem. The soil hardening Drucker–Prager model is used as the constitutive modeling of the sand beds to simulate the sand behavior. A Hooke's model (linear-elastic) is used to simulate the 2D and 3D reinforcements. To validate the result of the finite element analysis the experimental program is set out for unreinforced, 2D reinforced, and 3D reinforced sand beds for one case and the results are validated.

Keywords 3D pipe geogrid · Square surface footing · Sandbeds · Abaqus · Reinforcement

1 Introduction

Soil reinforcement is used to increase the soil's bearing capacity. 2D reinforcements are introduced to increase the bearing capacity to a considerable limit, if the demand is very high then the spacing of the geogrids is reduced or the strength of the geogrids is increased which will result in a considerable increase in the cost of the project.

N. Avinash (✉)
Civil Engineering Department, PESCE Mandya, Mandya, Karnataka, India
e-mail: avinashn@pesce.ac.in

S. S. Momin · S. Gangadhara
Civil Engineering Department, UVCE Bangalore, Bangalore, Karnataka, India

L. Nandagiri et al. (eds.), *Recent Advances in Civil Engineering*, Lecture Notes in Civil Engineering 256, https://doi.org/10.1007/978-981-19-1862-9_58

So, to meet the demand and be cost-effective a unique type of geogrid is been used called 3D pipe geogrid. A 3D pipe geogrid is a normal geogrid having a circular pipe extruded around the aperture of the geogrid. The pattern of the pipes can be changed based on the requirement.

To evaluate the performance of this unique geogrid, numerical analysis is been carried out in the Abaqus software. Unreinforced sandbeds, sandbeds with 2D reinforcement, and sandbeds with 3D pipe geogrids are analyzed in the software and the results are compared. Based on the results the optimum variables such as the relative density of sand, the spacing of the reinforcement, height of the pipe are determined. The optimum spacing of the first layer (U) is 0.3 times the width (B) of the footing, Avinash et al. [5] so (U/B) is fixed as 0.3 throughout the study, also the number of geogrids is set to 3 as it is the optimum number [5]. Hexagonal biaxial types of geogrids are used in the analysis. The comparative study is made between the sand beds with 2D reinforcement and sand beds with 3D pipe geogrids. Various works such as Saha et al. [4], Kazi et al. [8], Mosadegh et al. [9], El-Soud et al. [10], Belal et al. [2], Aminaton Marto et al. [3], have carried out the work on improvement of bearing capacity using 2D geogrids, but the study on 3D pipe geogrids is limited. In this present research work, an attempt has been made to investigate the performance of surface footing lying on 2D and 3D pipe geogrid reinforced sand beds and a detailed comparative study has been made. All the work is been carried out using FEM Abaqus [1].

2 Statement of the Problem

The study consists of the modeling of the square surface footing of size 100 mm × 100 mm × 4 mm in the finite element package Abaqus. The soil dimension is taken as 500 mm × 500 mm × 390 mm, and only a quarter of the soil has been modeled as the problem is symmetric along both the X- and Y-axis. As the hexagonal geogrid and a 3D pipe geogrid have a complex shape it is been modeled in the AutoCAD 3D and then it is imported into Abaqus software in the IGES file format. The plan dimension of the reinforcement is 250 mm × 250 mm and has a thickness of 3 mm. The soil densities are varied and kept to 20% and 36% relative density, which is about 14.85 kN/m^3 and 15.37 kN/m^3, respectively. Figure 1 Shows the soil and the footing model modeled in the finite element package Abaqus. The parameters that have been varied during the analysis in order to compute the optimum of those parameters are given below.

1. The spacing of the reinforcement is varied as 0.3, 0.4, and 0.5 times the footing's breadth.
2. In 3D pipe geogrid, the height of the pipe is varied as 20 mm, 30 mm, 40 mm, and 50 mm.

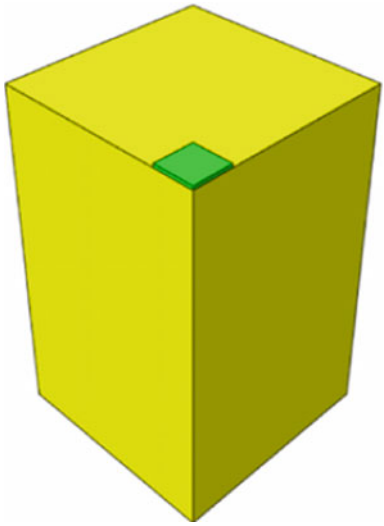

Fig. 1 Soil model and a square footing in Abaqus

3 Assumptions

All the cases are analyzed in a finite element package Abaqus, and certain assumptions are made to make the analysis simple and behave the same as that of the natural conditions. The assumption made in the analysis is listed below.

1. The soil is been constituted as elasto-plastic, and to make a model of the soil's behavior Drucker–Prager soil model is used in the analysis.
2. Linearly elastic material modeling is been done for both 2D reinforcement and 3D pipe geogrid.
3. The boundary conditions are been assumed, the middle side faces of the soil are been given symmetric boundary conditions, while the other two faces of the soil are been restricted to translate in the axis perpendicular to the plane. The bottom of the soil is kept fixed.

4 Materials

Properties of 2D reinforcement and 3D pipe geogrid are the same as mentioned in the above table. The difference between them is that 2D geogrid is a biaxial hexagonal grid whereas the 3D pipe geogrid contains an extra pipe extruded around the aperture of the geogrid. Figure 2 shows the plan view of the hexagonal 2D geogrid and Fig. 3 shows the isometric view of the 3D pipe geogrids that has been newly invented and used in the present research work.

Fig. 2 2D reinforcement

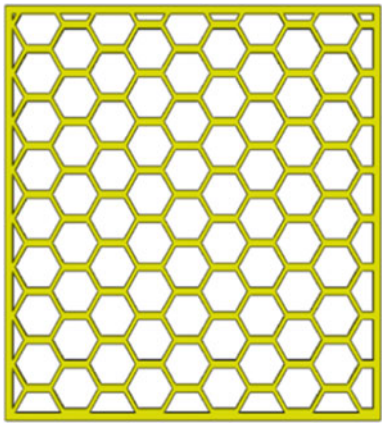

Fig. 3 3D pipe geogrid

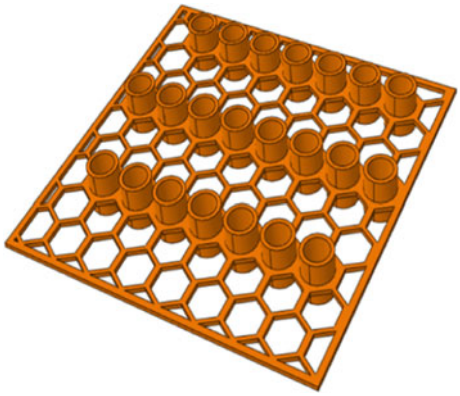

5 Numerical Analysis

The numerical analysis is carried out in the Abaqus FEM package. The static general analysis is performed on unreinforced, 2D reinforced, and 3D reinforced sand beds. The soil is modeled as the rectangle box, hexagonal geogrids, and 3D pipe geogrids are modeled in such a way that exactly simulates the original geometry. In the analysis, a sequence of sophisticated steps is followed, which are given below.

5.1 Loading

In the load module of the Abaqus analysis, two steps are set. The first one is the initial step wherein the program executes all the boundary conditions given to the model. The second step is a static general step in which the loading is been assigned, the

Table 1 Properties of sand

S. No.	Property	Test result	
1	Clay and silt (%)	0.2	
2	Sand (%)	99.8	
3	Gravel (%)	0	
4	Coefficient of uniformity (C_u)	3.03	
5	Coefficient of curvature (C_c)	1.65	
6	Specific gravity (G)	2.68	
7	Effective particle size (D_{10})	0.33 mm	
8	Maximum dry density (kN/m^3)	17.98	
9	Minimum dry density (kN/m^3)	14.17	
10	Maximum voids ratio (e_{max})	0.85	
11	Minimum voids ratio (e_{min})	0.46	
12	Soil classification	Poorly graded Sand SP	
13	Relative density (%)	20	36
12	Dry density (kN/m^3)	14.85	15.37
15	Angle of internal friction (°)	33	34.6
16	Young's modulus (MPa)	37.1	41.28
17	Poisson ratio	0.3	0.3

Table 2 Properties of geogrid

S. No.	Property	Value
1	Structure	Biaxial hexagonal
2	Rib thickness	3 mm
3	Joint thickness	5 mm
4	Aperture size horizontal	25.4 mm
5	Aperture size vertical	31.8 mm
6	Density of geogrid	1.40 g/cm^3
7	Water absorption	0%
8	Pipe inside diameter	21.4 mm
9	Pipe outside diameter	25.4 mm
10	Thickness of geogrid	3 mm
11	Modulus of elasticity	1480 MPa

time of this step is kept as one second. And the displacement of 25 mm is given to the footing in the downward direction. To avoid the abrupt displacement of the footing and the Abaqus encountering an error, the analysis increment is fixed at 0.025 as the initial increment and 0.1 as the maximum increase.

5.2 Interactions

In this module of the model, the interaction between the soil, 2D and 3D reinforcements have been set to penalty. Various contact surfaces have been defined and the interactions between them are set to penalty to simulate the ground conditions. Penalty defines the frictional property of the surfaces. The penalty behavior denotes that there is a finite coefficient of friction value between the surfaces and no slip will occur along the surfaces. The sliding along the surfaces is considered finite sliding.

5.3 Meshing Criteria

In this analysis, the mesh size is considered by several trial analyses. The mesh size of the reinforcement layer has been chosen finer than the mesh size of the sand profile to get more realistic and closer to the desired result. In this problem for both sand and reinforcement, 3D stress element has been chosen and C3D8R:8-node linear brick, reduced integration, hourglass control is used.

6 Validation of Result

The results obtained from the Abaqus are compared to that of the experimental results to validate. The experimental setup was established and the experiment was conducted for sand beds that are unreinforced, 2D reinforced, or 3D reinforced. During the experimental procedure, the relative densities of sand were maintained by the rainfall method and the loading on the footing was applied with the help of the loading frame. The load is recorded with the help of a proving ring and the settlement was recorded by the linear variable differential transformer (LVDT), and the plots of bearing capacity versus settlement were plotted. The results of the finite element analysis are then compared to the findings of the experimental results, it has been seen that the results match perfectly. Figure 4 shows the results of bearing pressure versus settlement of the surface footing resting on the unreinforced sand beds obtained from experimental and numerical analysis, it also shows the bearing pressure calculated using the theory proposed by Tezarghis [6, 7]. The magnitude of bearing pressure obtained from both Experimental and FEM at 25 mm Settlement is below the bearing pressure computed from Tezarghis theory. Figure 5 shows the bearing pressure versus the settlement of the square surface footing lying on the 2D and 3D reinforced sand beds obtained from the experimental setup and numerical analysis. In both Figs. 4 and 5, the results are matching and trace a similar pattern.

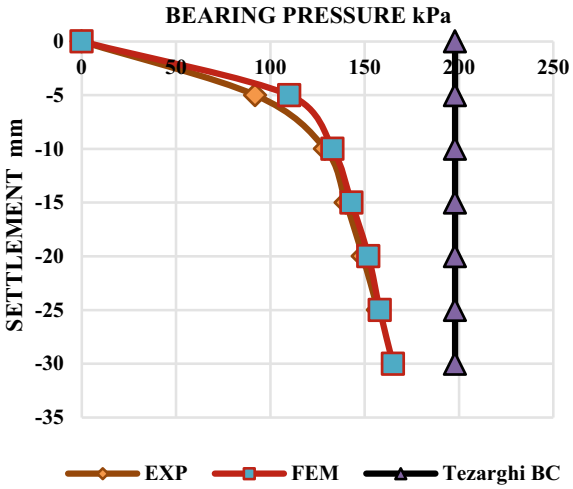

Fig. 4 Bearing pressure versus settlement curves for unreinforced sand beds obtained from experimental and FEM

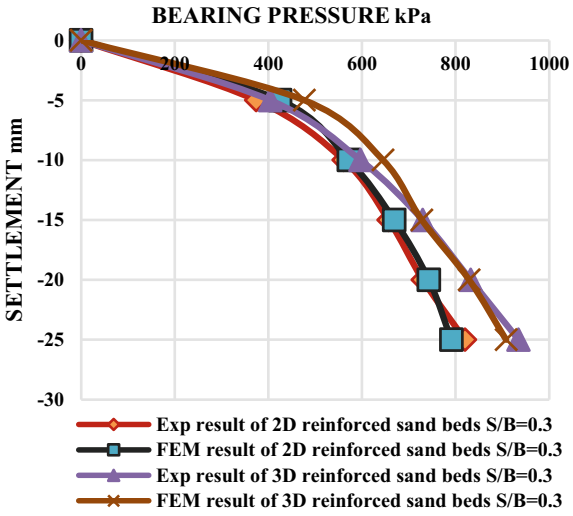

Fig. 5 Bearing pressure versus settlement curves for 2D and 3D reinforced sand beds obtained from experimental and FEM

7 Results and Discussion

In total, 26 cases were modeled in Abaqus which includes unreinforced, 2D reinforced, and 3D reinforced sand beds. The parameters that are kept as variables are the relative density of sand, analysis was made for the relative density of 20% and 36%. The reinforcement's vertical spacing and the reinforcements spacing were kept as 0.3, 0.4, and 0.5 times the breadth of the footing for both 2D and 3D reinforcement. The height of the pipe in 3D reinforcement was also varied and kept as 20 mm, 30 mm, 40 mm, and 50 mm. Figure 6 indicates the results of the settlement of surface

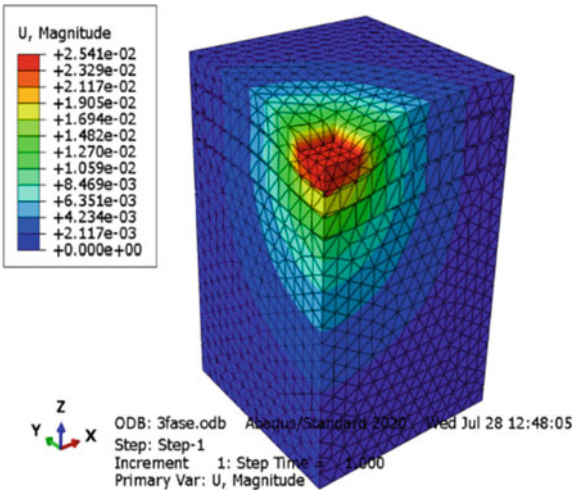

Fig. 6 Settlement of a footing resting on 3d pipe geogrid reinforced sand beds, $H = 20$ mm, $S/B = 0.3$

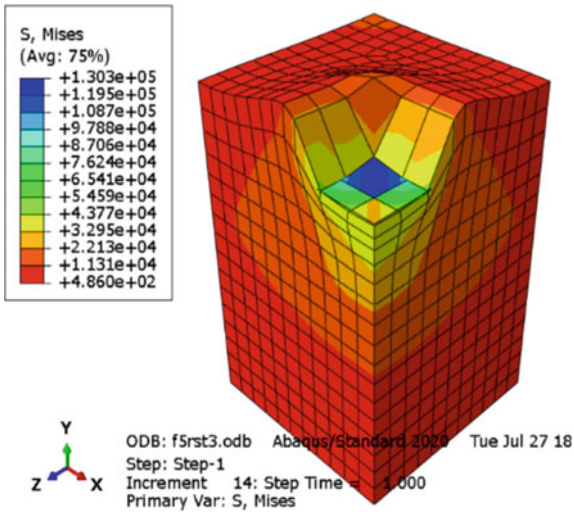

Fig. 7 S Mises stresses distribution of an unreinforced sand beds

footing rested on the 3D pipe geogrids with a height of the pipe of 20 mm and an S/B ratio of 0.3.

Figure 7 shows the distribution of the S Mises stress across the surface of the footing and throughout the depth of the soil, the stresses so generated in this Fig. 7 are due to the settlement of 25 mm of the surface footing resting on the unreinforced sand beds. When the load is applied on the footing, the footing starts settling and the reinforcement provided gets activated, i.e., it starts taking loads. Figures 8 and 9 display the stress distribution across the geogrids and the deformation that is taken

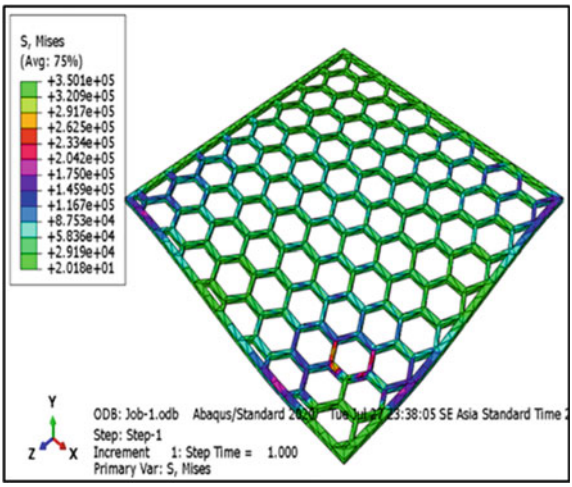

Fig. 8 S Mises stress distribution across the 2D geogrid

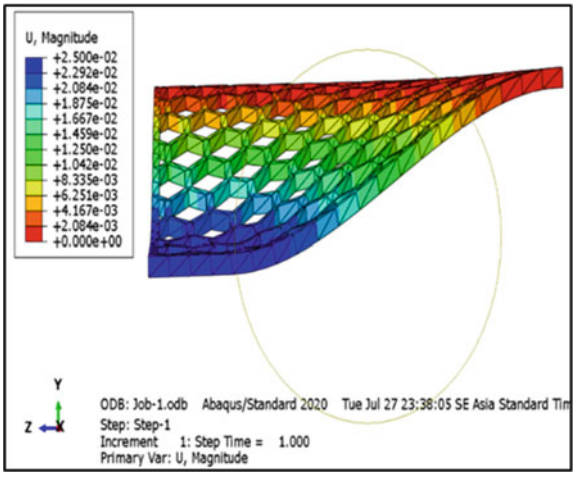

Fig. 9 Deformation of a 2D geogrid

placed within the geogrid, respectively. Figures 10 and 11 show the deformation of the 3D pipe geogrid and Settlement of the pipes, respectively.

Ultimate Bearing Capacity (UBC)

Ultimate bearing capacity of the sand beds is defined as the ultimate stress that the sand beds can carry without undergoing any shear failure and excessive settlement. The UBC is used to compare the results of the reinforced sand beds with that of unreinforced sand beds.

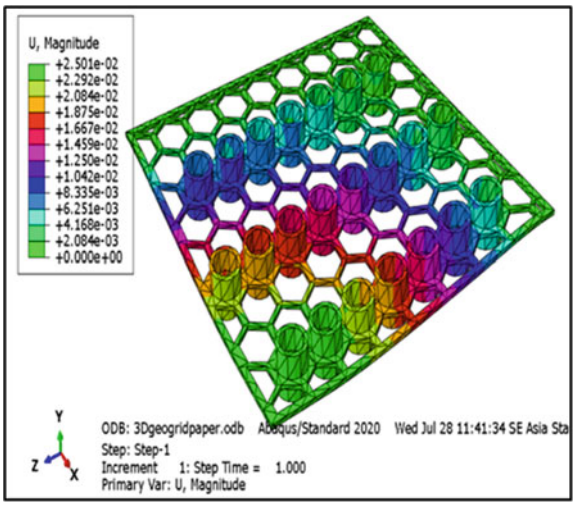

Fig. 10 Deformation of a 3D pipe Geogrid

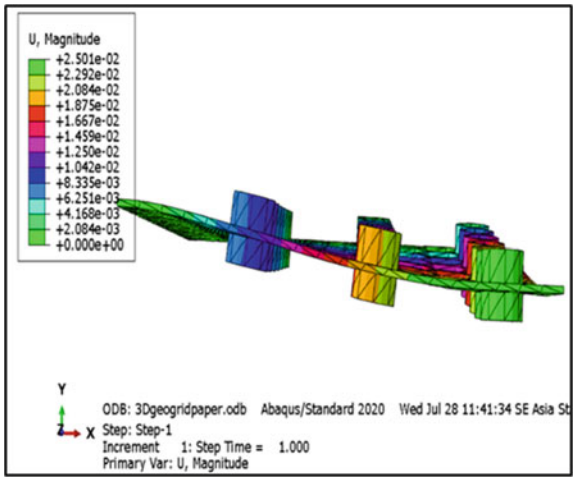

Fig. 11 Settlement of pipes in a 3D pipe geogrid

7.1 Unreinforced Sand Beds

Numerical modeling shows that the UBC of the unreinforced sand beds for the surface footing is 158 kPa at 20% relative density. According to the experimental procedure, the UBC is 157 kPa which is very well tracing the path of numerical analysis. The UBC calculated for unreinforced sand beds by the Terzaghi bearing capacity equation comes out to be 197.9 kPa. The UBC at 36% relative density is 174 kPa. The average increase in the UBC of the sand beds when the relative density of the sand is increased from 20 to 36% is about 15.28%.

7.2 2D Reinforced Sand Beds

When the 2D reinforcement was introduced in the sand beds, the bearing capacity was considerably increased, and was optimum for the *S*/*B* ratio of 0.3 The UBC of 2D reinforced sand beds at 20% relative density with an *S*/*B* ratio of 0.3*B* is 791 kPa, which is almost five times the UBC of unreinforced sand beds. Further, if the vertical spacing of the reinforcement was increased to 0.1 times the footing breadth. The UBC was decreased to about an average of 13.5% for 20% relative density and 11% for 36% relative density. For all cases of the 2D reinforcement, the UBC at 36% relative density performed better than the 20% relative density. The average difference in the UBC at 20% and 36% relative density is about 5.5%. Figures 12 and 13 show the change of bearing pressure versus settlement for various S/B ratios, for 2D reinforced sand beds with a relative density of 20% and 36%, respectively.

Bearing Capacity Ratio

For the purpose of comparison of the load-bearing capacity of the sand beds which are reinforced with that of unreinforced one, a non-dimensional factor has been introduced called bearing capacity ratio (BCR). BCR is the ratio of the bearing pressure of the reinforced sand beds to the bearing pressure of the unreinforced sand beds at the same settlement. Greater the BCR greater will be the bearing capacity of sand beds and vice versa.

$$\text{BCR} = \frac{\text{At a particular settlement, the bearing pressure of reinforced sand beds.}}{\text{At the same settlement, the bearing pressure of unreinforced sand beds.}}.$$

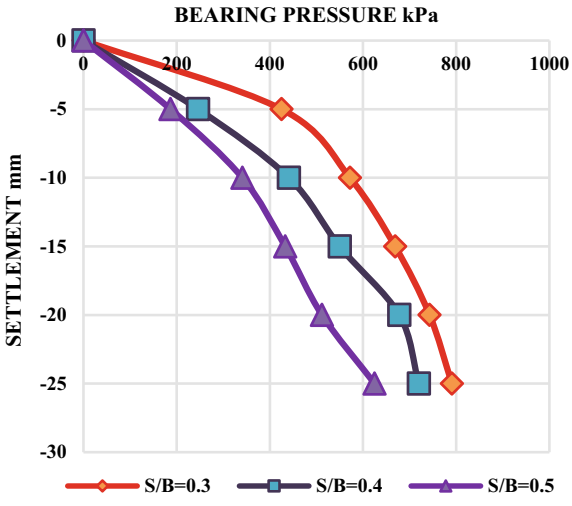

Fig. 12 Pressure versus settlement curves for 2D reinforced sand beds at 20% relative density

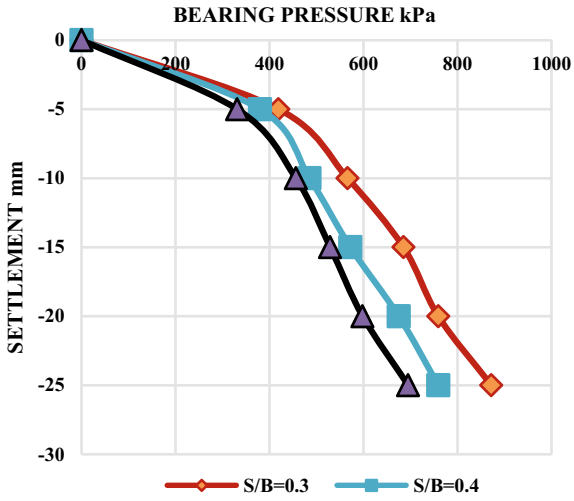

Fig. 13 Pressure versus settlement curves for 2D reinforced sand beds at 36% relative density

Figure 14 shows the BCR for 2D reinforced sand beds with the relative density of 20% and 36%, from this figure it is seen that the BCR for 2D reinforced sand beds is inversely proportional to the spacing of the reinforcement.

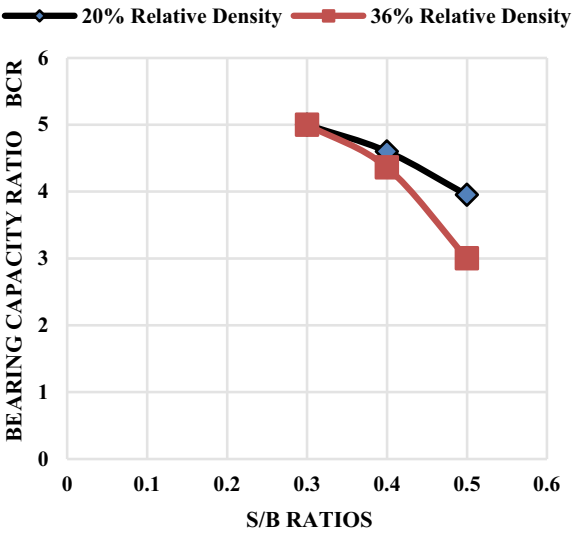

Fig. 14 Bearing capacity ratio curves for 2D reinforced sand beds

7.3 3D Reinforced Sand Beds

The UBC of sand beds with 3D reinforcement ($H = 20$ mm) for an S/B ratio of 0.3 at 20% relative density is 908 kPa, which is almost 5.8 times the UBC of unreinforced sand beds and 1.2 times the 2D reinforced sand beds. Further, when the spacing of the reinforcement is increased to 0.1 times the footing breadth, the UBC also increases to an average of 15.5% for 20% relative density and 13.8% for 36% relative density and becomes optimum at the spacing of 0.4 times the footing breadth. Increasing the amount of reinforcement spacing results in a decrease of the UBC to an average of 5%. The height of the pipe also plays a very important role in improving the UBC. When the height of the pipe was 20 mm and the S/B ratio is $0.4B$ the UBC at 20% relative density is 1085 kPa and when it is increased to an increment of 10 mm the UBC also increased to an average of 24.6% and becomes optimum at the pipe height of 40 mm. Further increase in the height of the pipe will reduce the UBC. For all the cases of the 3D reinforcement, 36% relative density sand performed well. The average increase in the UBC when the relative density was changed from 20 to 36% was about 13.5%. Figure 15 shows the bearing pressure variation versus the settlement of the footing for various S/B ratios for 3D reinforced sand beds at 20% relative density and the 3D geogrid has a pipe height of 30 mm. Figure 16 displays the contrast of the bearing pressure with respect to the settlement for different pipe height of 3D geogrids at a relative density of 20% and S/B ratio of 0.3. In order to get a clear picture of the height of the pipe affecting the bearing pressure Fig. 17

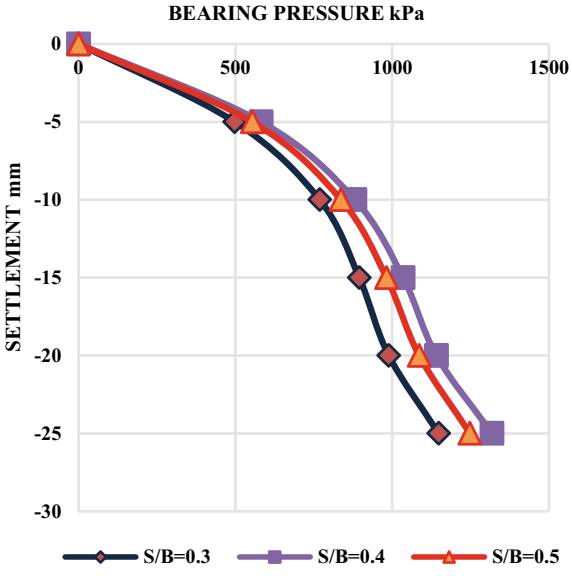

Fig. 15 Bearing pressure versus settlement curves for 3D reinforced sand beds at 20% relative density and 30 mm height of the pipe

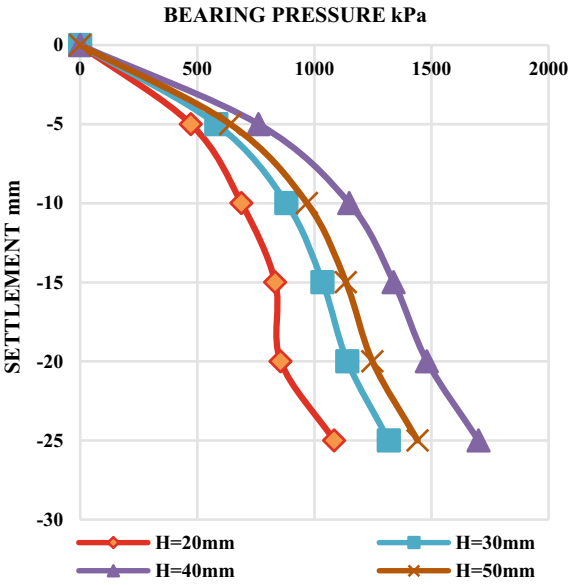

Fig. 16 Pressure versus settlement curves for 3D reinforced sand beds at 20% relative density and *S*/*B* ratio of 0.4

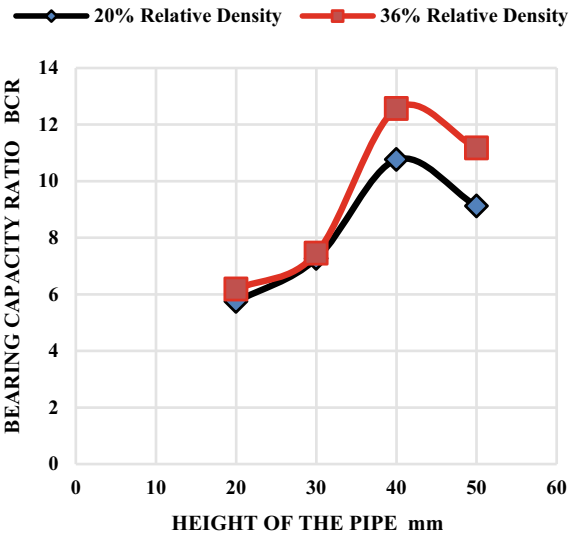

Fig. 17 Bearing capacity ratio curves for 3D reinforced sand beds

is plotted which shows the BCR versus the height of the pipe. From the graph, it is seen that the optimum height of the pipe at which the bearing pressure is maximum is 40 mm.

8 Conclusions

A series of the different cases were modeled and analyzed in the Abaqus. Unreinforced, 2D reinforced, and 3D reinforced sand beds were analyzed with different variables such as the relative density of sand, spacing of the reinforcement, and the height of the pipe in 3D pipe geogrid. And the results aimed to compute the optimum of those parameters. The following conclusions have been formed based on the numerical modeling test results.

1. When the numerical modeling tests results were compared to that of the experimental result, an acceptable performance was depicted for the behavior of the soil and the reinforcements both 2D and 3D. The stresses and the displacement of the surface footing drawn from numerical modeling followed a similar pattern of experimental results.
2. The bearing capacity of the sand beds was considerably increased when the reinforcement was placed, the average increment in the bearing capacity with 2D reinforcement was 4.54 times the bearing capacity of unreinforced sand beds. And the average increment in bearing capacity with 3D reinforcement was about 8.6 times the bearing capacity of sand beds which are unreinforced and 2.12 times the bearing capacity with 2D reinforcement.
3. The bearing capacity in all the cases of unreinforced, 2D reinforced, and 3D reinforced sand beds was found to be higher at 36% relative density of sand. The average difference between the bearing capacities at 20% and 36% relative densities is 11.16%.
4. The optimum 2D reinforcement's vertical spacing that gives the maximum UBC of sand beds was discovered to be 0.3 times the footing breadth and for every 0.1 increase in the vertical spacing of the 2D reinforcement, there will be an average decrease in bearing capacity of about 13.5% at 20% relative density and 11% at 36% relative density.
5. The optimum 3D reinforcement's vertical spacing that gives the maximum UBC of sand beds was discovered to be 0.4 times the footing breadth. And for every 0.1 increment in the vertical spacing of the 3D reinforcement, there will be an average decrease in bearing capacity of about 5% at 20% relative density and 5.8% at 36% relative density.
6. The optimum height of the pipe in 3D reinforcement which gives the maximum ultimate bearing capacity of the sand beds is 40 mm. As the U/B ratio is the same for all the cases the optimum height can be generalized to 1.33 times the spacing of the first reinforcement layer from the lower level of the footing.

References

1. ABAQUS user manual version 6.8. Hibbitt, Karlson and Sorensen, Inc., Pawtucket, RI (2008)
2. Nagy ABN, Elshesheny E (2015) Numerical evaluation of bearing capacity of square footing on geosynthetic reinforced sand. In: Proceedings of the international conference on civil, structural and transportation engineering, Ottawa, Ontario, Canada, 4–5 May 2015
3. Aminaton Marto A, Oghabi M, Yunus NZM (2015) Bearing capacity of circular footing on sand deposit. Appl Mech Mater, 1518–1523
4. Saha A, Patra S, Das A, Bera AK (2018) Bearing capacity of footing on sand overlay by soft soil using Abaqus: a numerical based study. Indian Geotech J
5. Avinash N, Gangadhara S, Malashree (2021) A study on the performance of surface footings on 3D Geogrid reinforced sand beds. Int J Eng Res Technol
6. Bowles JE (1996) Foundation analysis and design, 5th edn. Wiley
7. Terzaghi K (1943) Theoretical soil mechanics. Wiley, New York, p 510
8. Kazi M, Shukla SK, Habibi D (2014) An improved method to increase the load-bearing capacity of strip footing resting on geotextile-reinforced sand bed. Indian Geotech J
9. Mosadegh A, Nikraz H (2015) Bearing capacity evaluation of footing on a layered-soil using ABAQUS. J Earth Sci Clim Change
10. El-Soud SA, Belal AM (2019) Numerical modeling of rigid strip shallow foundations overlaying geosynthetics-reinforced loose fine sand deposits. Arab J Geosci

Pavement Design Using TerraZyme Stabilized Soil

A. S. Chandana, Shriram Marathe, and B. V. Kiran Kumar

Abstract Pavement is a structure, which is laid to support the wheel load and to spread the load stress to a wider area on the top of soil subgrade. The process of changing the physical, chemical, and biological property of a natural soil, in order to improve their tensile strength, bearing capacity and overall performance, by using controlled compaction, proportioning, in addition of suitable stabilizer and admixture, is known as stabilization of soil. The major application of soil stabilization is in the field of pavement set up over a weak subgrade soil. It is very much essential to improve its strength, bearing capacity, and performance to a level higher than the existing condition. By modifying the subgrade soil properties, economy can be achieved in pavement construction by having reduced upper crust thickness. The main objective of this work is to have an economical pavement design. In this study, the type of soil used is silty sand (SM), and for stabilization of soil, TerraZyme was used. After stabilizing the soil by using TerraZyme, there was a marked improvement in compaction property, California bearing ratio (CBR) value, unconfined compressive strength (UCS) value, cohesion value, and angle of intersection. The pavement thickness was designed by using IRC:37-2012, after stabilization of soil the thickness of the pavement was reduced.

Keywords Subgrade · Stabilization · TerraZyme · California bearing ratio · Unconfined compressive strength

A. S. Chandana (✉)
WSP Consultant Pvt. Ltd., Manyata Embassy Business Park, Bengaluru, India
e-mail: chandanaarunkumar22@gmail.com

S. Marathe
Department of Civil Engineering, NMAM Institute of Technology, Nitte, India

B. V. Kiran Kumar
Department of Civil Engineering, Govt. SKSJTI Engineering College, Bangalore, India

L. Nandagiri et al. (eds.), *Recent Advances in Civil Engineering*, Lecture Notes in Civil Engineering 256, https://doi.org/10.1007/978-981-19-1862-9_59

1 Introduction

1.1 General

Pavement is a surface material that is laid to support the wheel load and to spread the load stress to a wider area on the top of the soil subgrade. The pavement is also called a road surface. This may be constructed over an embankment or at the ground level itself depending upon the site condition, environmental condition, and vertical alignment. It is always advantageous to construct the pavement well above the maximum water table to keep the subgrade soil relatively dry.

According to structural behavior, a pavement is classified as flexible pavement, rigid pavement, semi-rigid or composite pavement, and interlocking cement concrete pavement. Flexible pavements are those, which has less or negligible flexural strength and are relatively flexible when they are subjected to loads. The pavement layers will show the non-recoverable and recoverable deformations of the lower layers together with the subgrade. The rigid pavements are those that have greater flexural strength compared to flexible ones. These pavements are generally constructed using cement concrete and are thus called CC pavement. Semi-rigid pavements are a special type of pavements, which are constructed using a semi-rigid base layer (usually, a cement-treated base or cement-stabilized soil base), overlaid with the asphalt mixture at the top. Interlocking cement concrete pavement is a pavement in which the concrete blocks are made from small paving units embedded and joined in the sand.

The different layers of pavement are surface course, subsurface course, base course, sub-base course, and subgrade course. The uppermost layer of the road pavement that is directly exposed to the traffic is called the wearing course or surface course. There may be more than one layer in the case of flexible pavement. A good wearing course should be impenetrable, withstand changes in weather, and should also not be affected by the abrasive action of the traffic. Sometimes, in addition to the surface course, one or more layers of sub-surface (i.e., binder) course can be provided which will further help in distributing the stresses to a greater area beneath the base course. The binder course makes use of aggregates with less binder and doesn't need high quality as that required for the surface course. Thus, introducing the binder course beneath the wearing course helps the pavement to reach a more economical design. The base layer could be in a single layer or a double layer. This is supplied above the sub-base course, or sometimes provided straight away over the road formation based on the design requirements. This course is considered to be the most important and a major component of the road pavement structure. It is because this course can tolerate the impact of traffic wheel load as transferred through the wearing course. In the case of a rocky subgrade, this layer is not necessary. The finished and compacted surface of earthwork on which a road pavement rests is called subgrade or formation. The subgrade of a road pavement may be provided in embankment, in cutting, and at existing ground level depending upon the topography and finished formation level. Subgrade is compacted to its optimum density and moisture conditions, finished with proper camber and gradient. The thickness

and the type of pavement are directly proportional to the strength of the subgrade because the entire load of traffic and that of pavement is ultimately taken up by the subgrade (Khanna et al. [10]).

The process of changing the physical, chemical, and biological properties of natural soil, in order to improve its tensile strength, bearing capacity, and overall performance, with the use of proportioning and by addition of suitable admixtures (or stabilizers) followed by controlled heavy compaction is known as stabilization of soil. Stabilization of soil is very much essential to increase the strength, thereby improving the bearing capacity and overall performance of soil. In soil stabilization, various techniques are used. These include mixing different materials, applying cementing agent, water-proofing agents, chemical stabilization, and heat treatment (Jeb Tingle et al. [5]).

TerraZyme is an enzyme solution that helps improve the mechanical and chemical characteristics of the soil. It helps to produce a more stable and compact soil with enhanced engineering qualities. TerraZyme is a proven cost-saving technology that allows the use of alternative construction methods for road subgrade construction. This eliminates the need for costlier traditional methods of stabilized subgrade construction. The previous studies have proven that up to 40% of savings in total cost and about 75% savings in maintenance cost can be achieved through the usage of this stabilization method. TerraZyme can be used anywhere where GSB and WMM are used in construction as it replaces them, for example in the construction of highways, all-weather rural roads, internal roads in townships, service roads, factory roads, parking lots and yard area, sealing of ponds, landfills, temporary access roads, subgrade improvement, floor bases, road shoulders, construction roads, etc. Sravan et al. [1], Ravi et al. [2], Li et al. [3], Tanveer et al. [4]

The specific objectives of the current study involve the following:

1. To study the index property of soil that is locally available;
2. To obtain the optimum dosage of TerraZyme required for stabilization of soil;
3. To determine the California bearing ratio (CBR) of soil samples with and without TerraZyme;
4. To establish the unconfined compressive strength (UCS) of soil samples with and without TerraZyme;
5. To design the pavement as per IRC:37-2012.

2 Literature Review

Sahoo et al. conducted a comparison study on three soil samples, i.e., with two different dosages of TerraZyme stabilizer and the soil samples without TerraZyme. Results show that the TerraZyme can be successfully used to stabilize the soil, and improvement was found in both soaked CBR and UCC. It was concluded that the TerraZyme can be used as a stabilizing agent for clayey soils and to reduce the construction cost of roads [9].

Venkatesh et al. related the use of TerraZyme a bio-enzyme for stabilization of soil. Various dosage of TerraZyme, i.e., 0%, 1%, 2%, 3%, and 4% was mixed with the soil and CBR test for both soaked and unsoaked conditions was done. The test result shows that with the increase in the percentage of TerraZyme and curing period the shear strength of soil increased from 10.8 to 49.05 kPa for 4-day curing period [12].

Athira et al. deal with the study of the effect of laterite soil collected from Aduvassery of Ernakulam district, which was mixed with different dosages of TerraZyme for different curing periods. The tests result shows that with time the TerraZyme has an effect on improving the unconfined compressive Strength (UCS) and California Bearing Ratio (CBR) values of the soil [6].

Saini et al. made use of bio-enzyme, an eco-friendly chemical, which is also economical in order to improve the properties of soil. In this study, the virgin soil was mixed with different dosages of TerraZyme. This was intended to improve the index properties of soil (that is, specific gravity, OMC, MOD, CBR (soaked and unsoaked)) with different durations the various dosages were 3.0 m^3/200 ml, 25 m^3/200 ml, 2.0 m^3/200 ml, and 1.5 m^3/200 ml. It was concluded that the use of TerraZyme eliminates the use of granular sub-base and subgrade course. The test results also showed that the third dosage of TerraZyme was the optimum dosage. This reduced the consistency limits and increased the soaked CBR after 2 weeks of the curing period [11].

Sen et al. conducted a test on various index properties of black cotton soil for the stabilization process. Various doses of bio-enzymes (3 m^3/200 ml, 25 m^3/200 ml, 1.5 m^3/200 ml) were mixed with black cotton soil, and the strength of this stabilized soil was evaluated after 0 days, 14 days, 21 days, and 28 days of curing periods. The test result shows that the use of bio-enzymes improves the strength of black cotton soil, i.e., bearing capacity and resistance to deformation increases [7].

3 Study Area, Materials Used, Methodology, and Essential Properties of the Normal and Modified Soil

The present study was conducted on silty sand (SM), which comes under alluvial soil with a poorly graded sand silt mixture, which is of low plasticity. TerraZyme is used for soil stabilization of subgrade, for this study the dosage of TerraZyme used is 200 ml for 2.2 m^3 of soil (Table 1).

Alluvial soil having fines of 35%, laboratory investigation such as specific gravity, Atterberg's limits, and indices test. Sieve analysis was conducted as per the relevant Indian Standard code IS:2386. The soil classification was done as per IS:1498-1970. In order to study the compaction characteristic of the soil, a modified proctor test was carried out. Based on the observed test results of the modified proctor test, the CBR and UCS tests were conducted to determine the stiffness characteristics and

Table 1 Geotechnical properties of soil used

Specific gravity	2.5
Atterberg's limit	
Liquid limit (%)	28.8
Plastic limit (%)	26
Plasticity index (%)	2.8
Gravel (%)	3
Sand (%)	88
Silt and Clay (%)	9
Soil classification as per BIS	SM

Table 2 Strength and stiffness properties of soil used

IS light compaction	
MDD	1.96 g/cm^3
OMC	10%
CBR Test Soaked	8%
UCS Test	
UCS value	280 kN/m^2
C-value	140 kN/m^2
Ø-value	45°

strength. The test results are tabulated in Table 2 and it indicates the average of four test results.

In this work, an attempt was made to use the results of the modified proctor (IS light compaction) test as per IS:2780-1983 (PART-8) in order to obtain an optimum dosage of TerraZyme. To determine the strength using UCS and penetration resistance in terms of CBR, optimum dosage was selected based on the dosage of TerraZyme corresponding to the highest value of maximum dry density (MDD). The water content used for CBR and UCS test with TerraZyme is 9% (Figs. 1, 2, and 3; Table 3).

4 Design of Pavement Thickness as Per IRC:37-2012 [8]

IRC 37 is a guideline on flexible pavement which was previously based on CBR of subgrade and traffic with respect to the number of commercial vehicles more (than 3 tons laden weight). These guidelines were, respectively, revised in 1984, 2001, 2012, and 2018. Under the scope of IRC:37-2012, six cross-sections were considered according to which the pavement is designed [8].

In this present study, the pavement was designed for 5000 commercial vehicles per day (CVPD) in two directions, traffic growth rate of 6%, design life of road for 20 years, vehicle damage factor (VDF) of 5.20, lane distribution factor (LDF) of

Fig. 1 California bearing ratio

Fig. 2 TerraZyme

0.75, initial traffic assuming 50% in each direction 2500, soil CBR 8%, Soil CBR after stabilization 13%.

The design traffic (N) is calculated as per IRC 37-2012. For design calculated design traffic (N) is 131 msa.

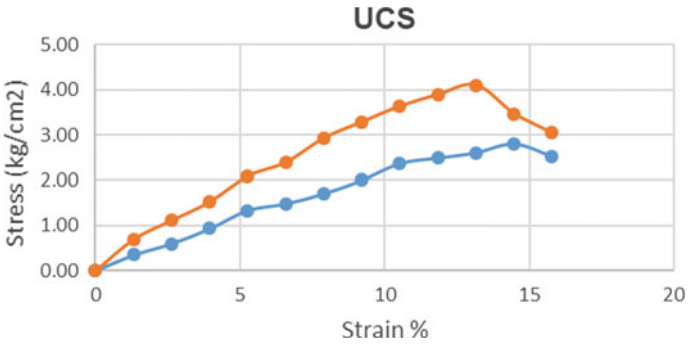

Fig. 3 Unconfined compressive strength

Table 3 Strength and stiffness properties of soil used

IS light compaction	
MDD	1.96 g/cm^3
OMC	9%
CBR Test with TerraZyme soaked	13%
UCS Test with TerraZyme	
UCS value	410 kN/m^2
C-value	205 kN/m^2
Ø-value	25°

For Cross-section 1

The total thickness of pavement for CBR 8% is 650 mm, and the total thickness of pavement for CBR 13% is 625 mm.

For soil CBR, 8% the thickness of pavement is as follows (Fig. 4 and Table 4):

For soil CBR 13%, the thickness of pavement is as follows (Fig. 5 and Table 5):

As the CBR increases, the thickness of the pavement decreases. Therefore, in the present study, as the CBR increased from 8 to 13%, the thickness of pavement decreased from 650 to 625 mm. The total reduction in pavement thickness after stabilization of soil is 25 mm.

For Cross-section 2

The total thickness of pavement for CBR 8% is 575 mm, and the total thickness of pavement for CBR 13% is 550 mm.

For Soil CBR 8% the thickness of pavement is as follows (Fig. 6 and Table 6):

For soil CBR 13%, the thickness of pavement is as follows (Fig. 7 and Table 7):

In the present study as the CBR increased from 8 to 13%, the thickness of pavement decreased from 575 to 550 mm. The total reduction in pavement thickness after stabilization of soil is 25 mm.

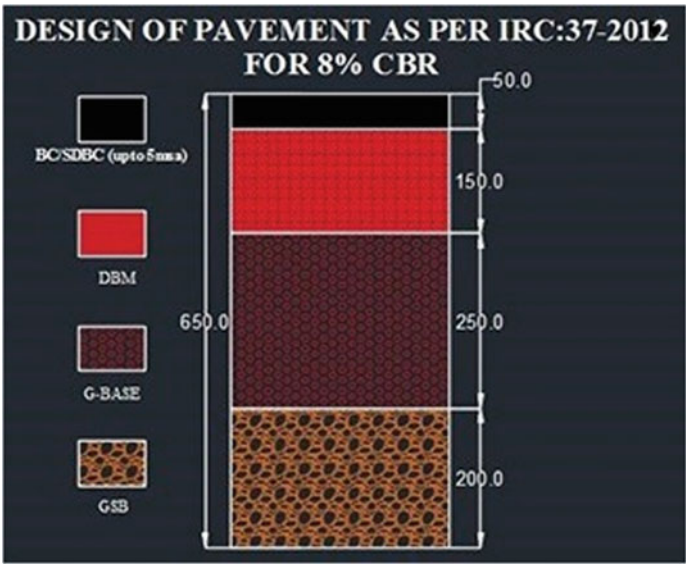

Fig. 4 Design of pavement Cross-section 1 as per IRC:37-2012 for 8% CBR in mm

Table 4 Thickness of pavement for 8% CBR

Design crust details	Thickness of pavement as per IRC 37-2012 in mm
GSB	200
WMM	250
DBM	150
BC/SDBC	50
Total thickness	650

For Cross-section 3

The total thickness of pavement for CBR 8% is 525 mm, and the total thickness of pavement for CBR 13% is 500 mm.

For Soil CBR 8%, the thickness of pavement is as follows (Fig. 8 and Table 8).

For soil CBR 13%, the thickness of pavement is as follows (Fig. 9 and Table 9):

The thickness of pavement decreased from 525 to 500 mm. When the CBR changed from 8 to 13%. The total reduction in pavement thickness after stabilization of soil is 25 mm.

For Cross-section 4

The total thickness of pavement for CBR 8% is 525 mm, and the total thickness of pavement for CBR 13% is 500 mm.

For soil CBR 8%, the thickness of pavement is as follows (Fig. 10 and Table 10).

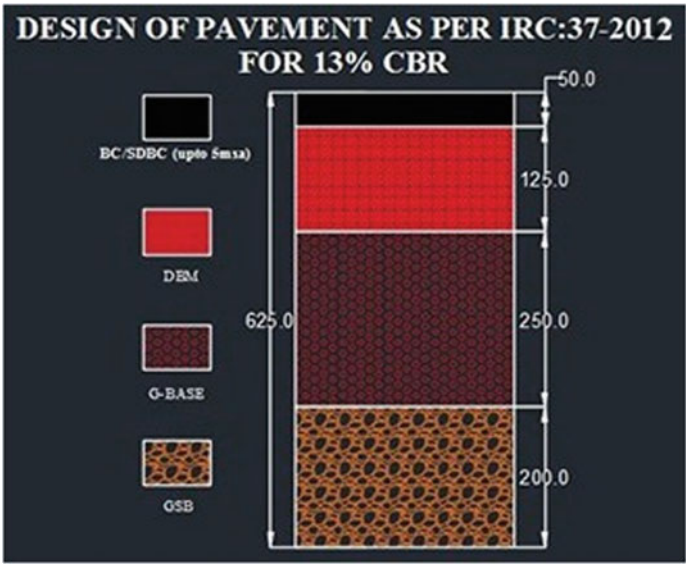

Fig. 5 Design of pavement Cross-section 1 as per IRC:37-2012 for 13% CBR in mm

Table 5 Thickness of pavement for 13% CBR

Design crust details	Thickness of pavement as per IRC 37-2012 in mm
GSB	200
WMM	250
DBM	125
BC/SDBC	50
Total thickness	625

For soil CBR 13% the thickness of pavement is as follows (Fig. 11 and Table 11).

The total reduction of pavement thickness is 25 mm after soil stabilization. As the CBR increased from 8 to 13%, the thickness of pavement decreased from 525 to 500 mm.

For Cross-section 5

The total thickness of pavement for CBR 8% is 650 mm, and the total thickness of pavement for CBR 13% is 625 mm.

For soil CBR 8%, the thickness of pavement is as follows (Fig. 12 and Table 12).

For soil CBR 13%, the thickness of pavement is as follows (Fig. 13 and Table 13).

The pavement thickness decreased from 650 to 625 mm after the stabilization of soil, i.e., there was a total reduction of 25 mm in thickness of the pavement, has the CBR increased from 8 to 13%.

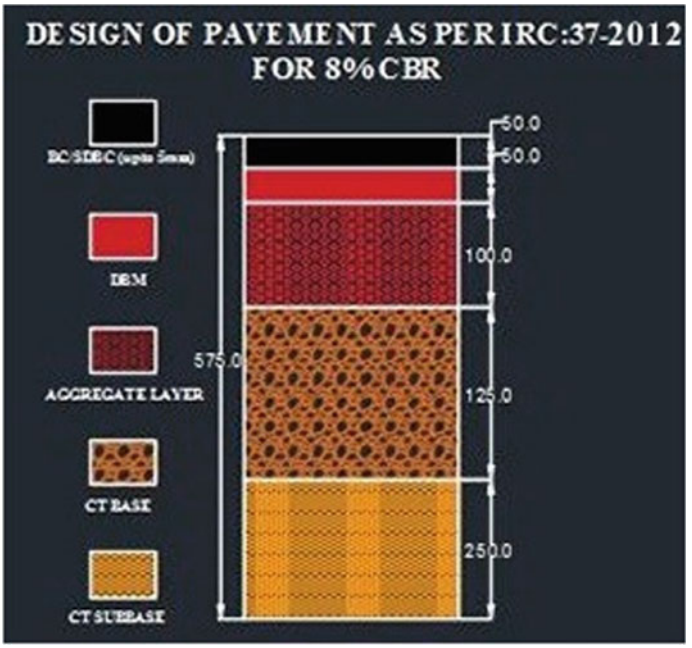

Fig. 6 Design of pavement Cross-section 2 as per IRC:37-2012 for 8% CBR in mm

Table 6 Thickness of pavement for 8% CBR

Design crust details	Thickness of pavement as per IRC 37-2012 in mm
CT sub-base	250
CT base	125
Aggregate layer	100
DBM	50
BC/SDBC	50
Total thickness	575

5 Quantity and Cost Calculation of TerraZyme

In the present study, the quantity of TerraZyme required is calculated for a 1 m^2 area and a depth of 0.5 m. The overall volume of cross-section is 0.5 m^3. The standard ratio of TerraZyme taken is 200 ml for 2.2 m^3. Therefore, the optimum dosage of TerraZyme to be used is 45.45 ml, i.e., 45.5 ml for 0.5 m^3. The cost of TerraZyme is Rs. 6000/- per liter. For 45.5 ml, the cost of TerraZyme is Rs. 273/- approximately Rs. 275/-.

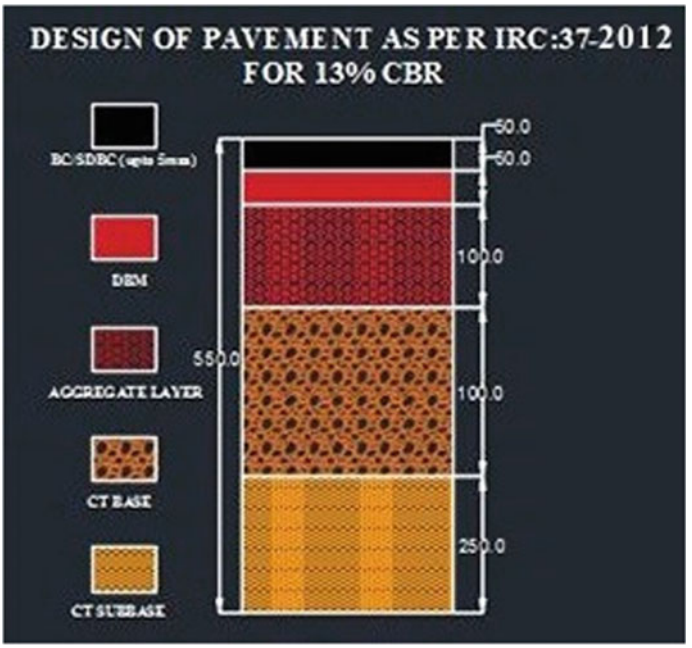

Fig. 7 Design of pavement Cross-section 2 as per IRC:37-2012 for 13% CBR in mm

Table 7 Thickness of pavement for 13% CBR

Design crust details	Thickness of pavement as per IRC 37-2012 in mm
CT sub-base	250
CT base	100
Aggregate layer	100
DBM	50
BC/SDBC	50
Total thickness	550

6 Conclusion

For the pavement to be economically viable, it should have a strong and durable subgrade. To achieve this, it is very much essential to modify the existing weak mechanical properties of the soil. Therefore, in the current study, by using TerraZyme for the stabilization of soil, the CBR of soil increased from 8 to 13%. Also, UCS of soil increased from 280 to 410 kN/m^2. The thickness of pavement also reduced as the CBR increased. Moreover, the use of TerraZyme for soil stabilization is cost-effective.

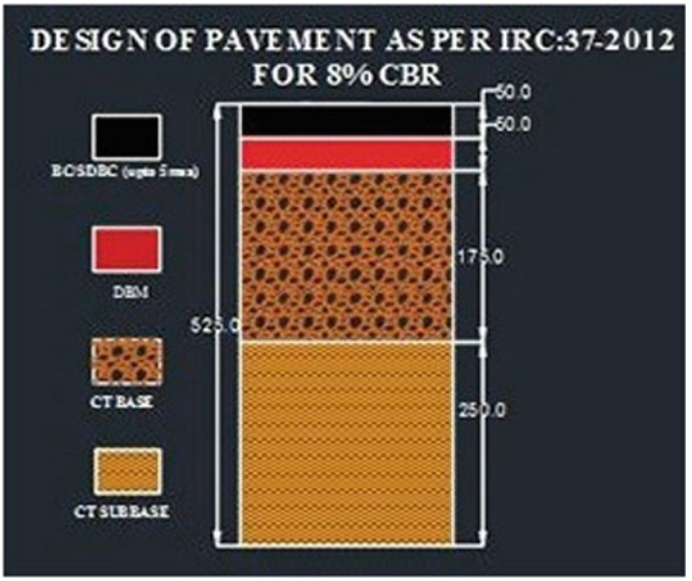

Fig. 8 Design of pavement Cross-section 3 as per IRC:37-2012 for 8% CBR in mm

Table 8 Thickness of pavement for 8% CBR

Design crust details	Thickness of pavement as per IRC 37-2012 in mm
CT sub-base	250
CT base	175
DBM	50
BC/SDBC	50
Total thickness	525

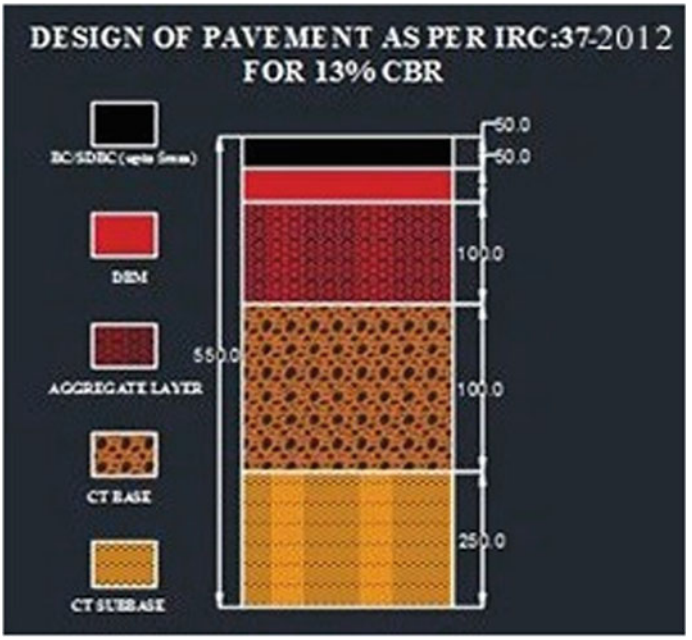

Fig. 9 Design of pavement Cross-section 3 as per IRC:37-2012 for 13% CBR in mm

Table 9 Thickness of pavement for 13% CBR

Design crust details	Thickness of pavement as per IRC 37-2012 in mm
CT sub-base	250
CT base	150
DBM	50
BC/SDBC	50
Total thickness	500

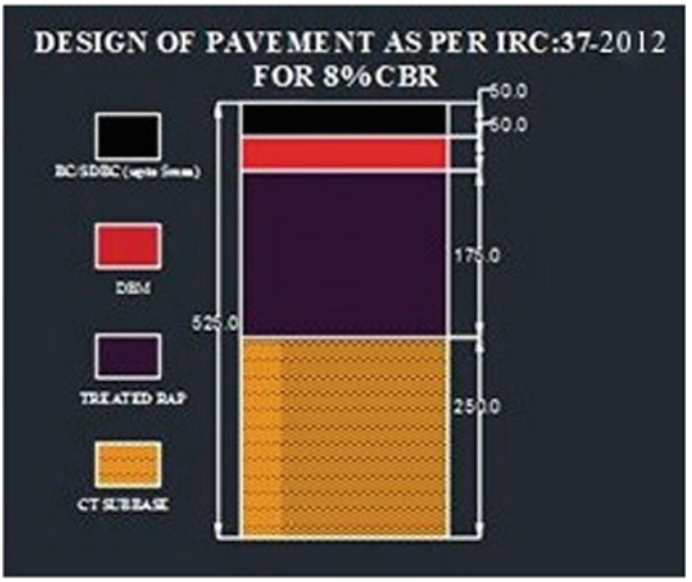

Fig. 10 Design of pavement Cross-section 4 as per IRC:37-2012 for 8% CBR in mm

Table 10 Thickness of pavement for 8% CBR

Design crust details	Thickness of pavement as per IRC 37-2012 in mm
CT sub-base	250
Treated rap	175
DBM	50
BC/SDBC	50
Total thickness	525

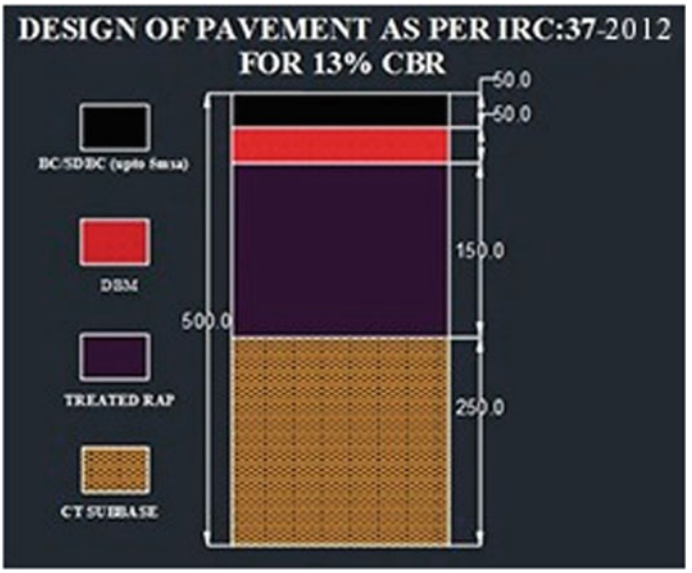

Fig. 11 Design of pavement Cross-section 4 as per IRC:37-2012 for 13% CBR in mm

Table 11 Thickness of pavement for 13% CBR

Design crust details	Thickness of pavement as per IRC 37-2012 in mm
CT sub-base	250
CT base	150
DBM	50
BC/SDBC	50
Total thickness	500

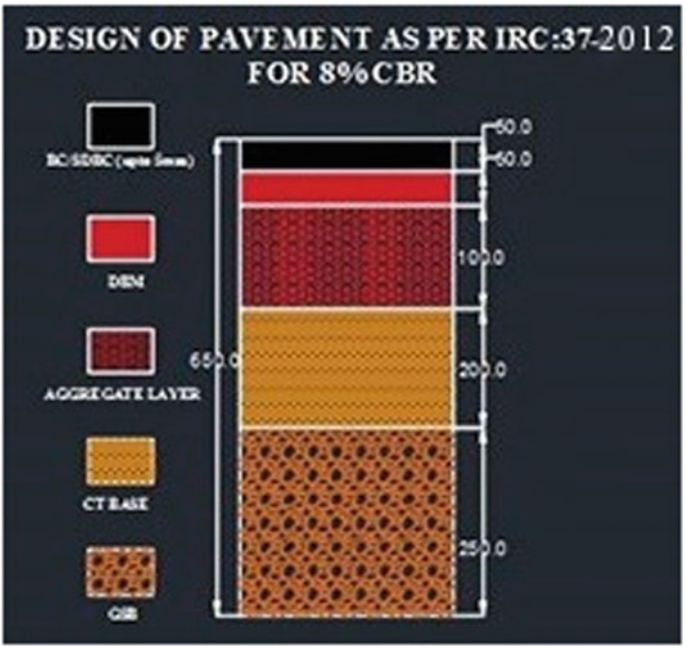

Fig. 12 Design of pavement Cross-section 5 as per IRC:37-2012 for 8% CBR in mm

Table 12 Thickness of pavement for 8% CBR

Design crust details	Thickness of pavement as per IRC 37-2012 in mm
GSB	250
CT base	200
Aggregate layer	100
DBM	50
BC/SDBC	50
Total thickness	650

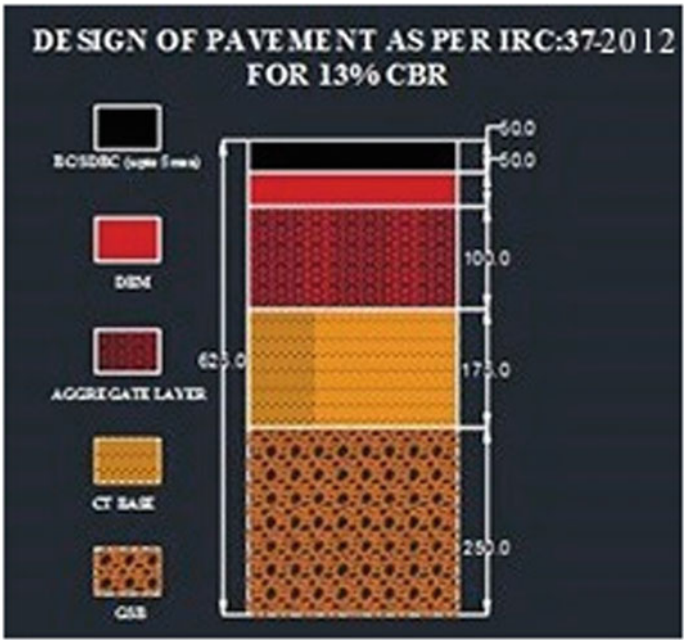

Fig. 13 Design of pavement Cross-section 5 as per IRC:37-2012 for 13% CBR in mm

Table 13 Thickness of pavement for 13% CBR

Design crust details	Thickness of pavement as per IRC 37–2012 in mm
GSB	250
CT Base	175
Aggregate layer	100
DBM	50
BC/SDBC	50
Total thickness	625

References

1. Muguda S, and Nagaraj HB (2019) Effect of enzymes on plasticity and strength characteristics of an earthen construction material. Int J Geo-Eng 10(2):1–14
2. Ravi Shankar AU, Mithanthaya I (2009) Bio-enzyme stabilized lateritic Soil as a highway material. J Indian Road Congress, 143–151
3. Li Y-j, Li L, Dan H-c (2011) Study on application of TerraZyme in road base course of road. Appl Mech Mater 97–98:1098–1108
4. Khan TA, Taha MR (2015) Effect of three bioenzymes on compaction, consistency limits, and strength characteristics of a sedimentary residual soil. Hindawi Publication, pp 1–9
5. Jeb Tingle S, Kent Newman J, Steve Larson L, Charles Weiss A, John Rushing F (1989) Stabilization mechanisms of non-traditional additives. Transp Res Record, 59–67

6. Athira S, Safana BK, Sabu K (2017) Soil stabilization using TerraZyme for road construction. Int J Eng Res Technol (IJERT) 6(03):547–549
7. Sen J, Sing JP (2015) Stabilization of black cotton soil using bio enzyme for highway material. Int J Innov Res Sci Eng Technol 04(12):12453–12459
8. IRC:37-2012 third revision December (2012) Guidelines for the design of flexible pavements. Indian Roads Congress Publication
9. Sahoo S, Sridevi, G (2018) Soil stabilization using bio enzyme. Int J Pure Appl Math
10. Khanna SK, Justo CEG, Veraragavan A (2015) Highway engineering, vol 10. New Chand and Bross Publication
11. Saini V, Vaishnava P (2015) Soil stabilization using TerraZyme. Int J Adv Eng Technol (IJAET) 8(4):556–573
12. Venkatesh A, Srinivas Reddy G (2017) Study of BC soil used as subgrade and treated with TerraZyme—a bio-enzyme. Int Res J Eng Technol 04(January):615–619

Development of Carbon Dioxide Absorbing Concrete for Urban Pavements—An Experimental Study

S. Rahul Raj, N. Anirudh, Chetan Jorapur, R. Babitha, Ankit Singh, Nayana N. Patil, Jayateerth Ramachandra Mudakavi, and T. Niranjana Prabhu

Abstract Academic researchers, policymakers, and other professionals are paying increasing attention to climate change, which is one of the world's greatest challenges. Global climate change has been attributed primarily to carbon dioxide emissions. In this context, carbon emission monitoring has been recognized through reference to carbon mitigation strategies and policies at different levels (product, organization, city, and national). Consequently, researchers have begun calculating global carbon emissions based on this increasing attention. It has been found that avoiding high amounts of CO_2 emission from construction will probably reduce the overall CO_2 emission. We have investigated the utilization of zeolite as a substitute for cement that will consequently absorb CO_2. This will reduce the amount of CO_2 in the environment without hampering the characteristic properties of concrete. In this study, the addition of zeolite-blended concrete has been applied to rigid pavement blocks to test the various properties for heavy traffic load.

Keywords CO_2 emissions · Zeolite · Roads · Urban area · Greenhouse gases · Carbon dioxide absorption

1 Introduction

Sustainable concrete refers to concrete that combines materials and technologies in an optimal way, including economic, technical, and environmental aspects [1]. In comparison with steel, wood, and concrete structures with similar, optimized designs, the concrete structures produce the most greenhouse gas emissions [2]. Concrete has the highest CO_2-equivalent emission per unit of mass compared to steel and wood, but only by a few percent. Researchers have attempted to reduce the "emission" of concrete because of the huge consumption of concrete worldwide. Concrete's emission of greenhouse gases is a misnomer since concrete doesn't emit carbon

S. Rahul Raj · N. Anirudh · C. Jorapur · R. Babitha · A. Singh · N. N. Patil (✉) · J. R. Mudakavi · T. N. Prabhu
Ramaiah University of Applied Sciences, University House, New BEL Rd, M S R Nagar, Mathikere, Bengaluru, Karnataka 560054, India
e-mail: Nayanapatil.ce.et@msruas.ac.in

L. Nandagiri et al. (eds.), *Recent Advances in Civil Engineering*, Lecture Notes in Civil Engineering 256, https://doi.org/10.1007/978-981-19-1862-9_60

dioxide. For concrete, "emission" refers to the entire life cycle, but mainly to the extraction of the raw materials, the component production, the build-up process, and it also represents the total greenhouse gas emissions expressed in CO_2 equivalents. When it comes to concrete, cement production is the main source of high greenhouse gas emissions.

A reinforcing rod and section steel are among the seven major building materials accounting for more than 90% of building greenhouse gas (GHG) emissions. Concrete generates 70% of all these major building materials' CO_2 emissions [3]. Depending on the structure, type, and region of a building, concrete can be designed differently (mix design, strength). Construction sites are applying high-strength concrete, and processes have been developed for procuring low-CO_2-emission materials [4]. A quantitative assessment method of CO_2 emissions from concrete production to site procurement is needed as part of such research, as well as a proposal to reduce CO_2 emissions at construction sites using such methods.

2 Literature Review

There are many potential sources of uncertainty in previous studies on construction emissions, including geographic representativeness and measurements at origin plants [5]. A series of emissions calculations—cradle to grave, cradle to gate, or cradle to cradle—is shown in [6]. The discount rate for electricity and fuel may vary based on the location [7]. In [8], concrete compressive strength was used as a basis for the calculation of CO_2-equivalent emissions. A comparison of the environmental impact of ultrahigh performance concrete (UHPC) and ordinary concrete by Stengel and Schießl [9] found that the latter's impact is up to 2.4-fold higher. Uncertainty is primarily caused by a variety of impacts due to the correlation of production plants (mainly energy mixes) [10]. In "[11]", zeolite and meta-kaolin were combined in concrete to increase compressive strength, tensile strength, and flexibility and improved strength results with the addition of micro–nano-bubbles of water, which significantly increased all of these properties. A study of CO_2 absorbing concrete was conducted by Adil et al. [12]. We must drastically reduce CO_2 emissions by the end of the century in order to combat global climate change. The strength parameters (compressive strength) of concrete have been investigated. The replacement method for control concrete incorporates a mix design based on the IS standard of M30. A comparison of replacement levels of 10%, 20%, and 30% was conducted. A study on the uptake of carbon dioxide by cement-based materials was carried out [13].

Estimating net CO_2 emissions was the primary objective of the re-carbonation project. The annual carbon dioxide uptake (ACDU) values are related to the reported calcination CO_2 emission. Carbon dioxide absorption attributed to the Spanish cements produced from 2005 to 2015 was estimated at 31,290,753 tons when using the simplified methodology, i.e., applying a factor of 0.20 during the service life and 0.03 for the end-of-life and secondary use. Subramani and Karthickrajan [14]

have studied about the partial replacement of cement with 25% of zeolite for the absorption of carbon dioxide by M30 concrete. According to this author, concrete can be strengthened by adding zeolite up to 25%. Subash et al. [15] have studied about the partial replacement of zeolite with cement. Zeolite mixed concrete gives the grade of M_{30} concrete mix in both substitutions of 10% and 30% of zeolite in concrete that brings similar compressive strength. He observed that there are no changes in compressive strength and minimal use of zeolite reduces the construction cost. Krishna Lekha and Vanreyk [16] have studied zeolite addition. Concrete obtained using natural zeolite has a porous structure with a porosity of 54.7%. The pore volume is increased and there will be the finer porous present in the zeolite. The use of this zeolite concrete will reduce the global warming index compared to conventional concrete, which indicates the effectiveness of the consumption of the zeolite in concrete to make concrete more environmentally friendly. Cirajudeen and Prakash [17] have investigated the effect of partial replacement of zeolite and observed the workability of concrete goes on to decrease as the replacement of cement by zeolite increases. Higher compressive strength, higher flexural strength, higher shear strength for concrete may be obtained by replacing 5% cement with zeolite. Kwon and Wang [18] used silica fume as a mix design aid in achieving low CO_2, high-strength concrete, and studies have shown that there is no simultaneous possibility of achieving the lowest CO_2 emission and lowest cost.

The main objectives of this study are to evaluate the amount of absorption of CO_2 by the cubes when introduced to dry ice in the carbonation chamber for a specified time and perform a carbonation test and also evaluate the maximum level of saturation of absorption of CO_2 and also to evaluate the amount of absorption of CO_2 in the normal traffic condition and calculate the cost estimation for 1 m^3 of concrete and compare the estimation between conventional concrete and concrete added with zeolite.

3 Methodology

3.1 Materials and Testing

In the present experimental work, studies are conducted on compressive and tensile strength, flexural strength, and absorption of CO_2 properties of conventional and using zeolite-added concrete with varying percentages of zeolite for a concrete mix of M_{30}. For this experimental study, the ingredients we used are cement—OPC 43, fine aggregate (M-Sand), coarse aggregate (20 mm and 10 mm), water, and zeolite.

3.2 Characteristics of Zeolite

- Degree of hydration is very high.
- Density is low as well as it produces more void volume when it is hydrated.
- Dehydration stability of crystals.
- Cation exchange properties.
- Dehydrated crystals with molecularly sized channels.
- Absorbent ability Catalytic properties.

Casting of cubes and beams of M30 mix without CO_2 exposure was done. For this, standard 150 mm^3 blocks were cast and tested for compressive strength at 14 days and 28 days of ambient curing and in the case of casting for CO_2 test, 150 mm^3 cubes, are cast for testing the strength, CO_2 absorption, and for carrying out carbonation test of concrete. Beams of 500 * 100 * 100 mm for CO_2 absorption in natural traffic conditions was used to understand the development of carbon dioxide absorbing properties of concrete used for roads. Results are observed and compared with standard parameters to arrive at a conclusion.

4 Results and Discussion

4.1 Mechanical Properties of Concrete with Addition of Varying Percentage of Zeolite

4.1.1 Mechanical Properties

i. Compressive Strength:
   The compressive strengths of conventional concrete and concrete with the addition of zeolite with varying percentages of 11%, 22%, and 33% when tested for 28 days water cured specimen and results shown in Fig. 1 was obtained.
ii. Split-Tensile Strength:
   The split-tensile strengths of conventional concrete and concrete specimen with the addition of zeolite with varying percentages of 11%, 22%, and 33% were tested for 28 days water cured specimen, and results were obtained as shown in Fig. 2.
iii. Flexural Strength:
   The flexural strengths of the concrete specimen with varying percentages of zeolite, i.e., 0%, 11%, 22%, and 33% were tested and results, as shown in Fig. 3, was obtained.

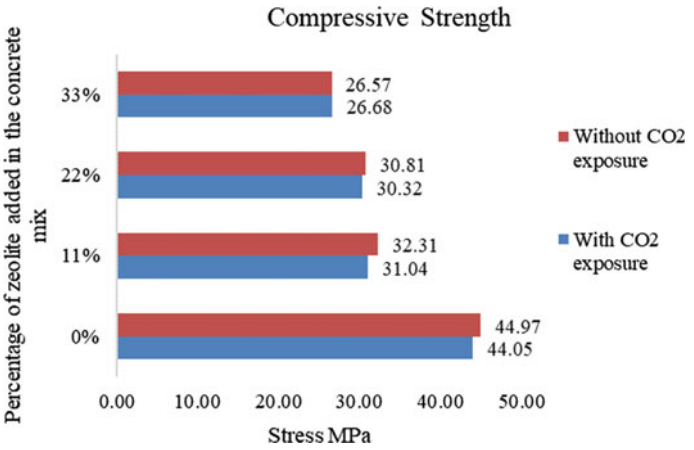

Fig. 1 Compressive strength of 28 days water-cured specimen

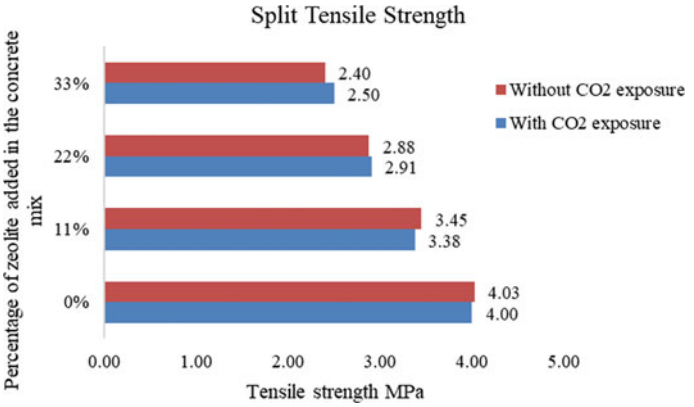

Fig. 2 Split tensile strength of 28 days water-cured specimen

4.2 Carbon Dioxide Absorption–Absorption of Carbon Dioxide in an Artificial Environment (CO_2 Chamber) and Natural Traffic Conditions

4.2.1 Carbon Dioxide Absorption Test

The concrete specimens are cast in molds of dimensions 150 mm × 150 mm × 150 mm and 500 mm × 100 mm × 100 mm and demolded and cured in water for 14 and 28 days, respectively. The specimen is then exposed to the atmosphere for carbon dioxide absorption near the Nelamangala toll plaza for 7 and 14 days, respectively. A few samples were exposed to the controlled carbon dioxide chamber for 2 days.

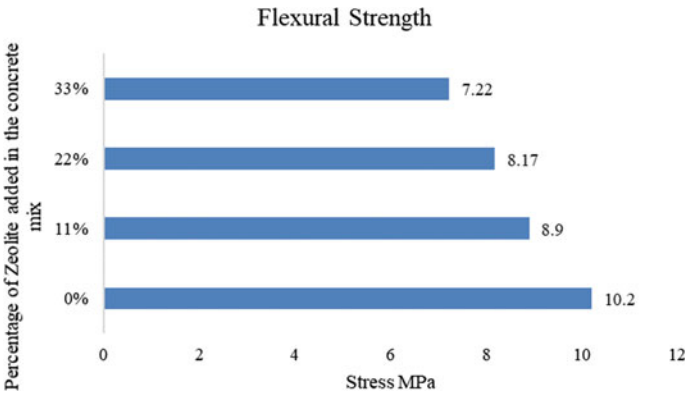

Fig. 3 Flexural strength of 28 days water-cured specimen

The specimen is then weighed to know the amount of carbon dioxide absorbed. The amount of carbon dioxide absorption is expressed in moles.

Carbon dioxide absorption of concrete for all mixes are presented in Table 1. In comparison with conventional concrete, the amount of carbon dioxide absorption is more in case of zeolite added concrete.

It was observed that when compared to conventional concrete, zeolite-added concrete blocks absorbed more carbon dioxide. Within the different percentages of zeolite added, the 33% addition of zeolite concrete absorbed more carbon dioxide. The absorption of carbon dioxide is more for 14 days of curing of water than 28 days of curing of water as shown in Fig. 4.

4.2.2 Absorption of Carbon Dioxide in the Natural Environment

The results and observations of the carbon dioxide absorption of the concrete for all mixes are recorded in Table 2. In comparison with conventional concrete, the amount of carbon dioxide absorption is more in case of zeolite added concrete (Table 3).

It was observed that when compared to conventional concrete the zeolite-added concrete absorbed more carbon dioxide. Within the different percentages of zeolite added, the 33% addition of zeolite concrete absorbed more carbon dioxide for 14 days of exposure. The comparison of amount of carbon dioxide absorption for 7 days and 14 days of exposure in the natural environment is shown in Fig. 5 (Figs. 6 and 7; Table 4).

4.2.3 Carbon Dioxide Absorption for 1 km of Road Made of Concrete

Let us consider a road of length 1 km (1000 m) and width of 100 feet (30.48 m) with a thickness of 0.15 m made of concrete. As we all know the whole volume of

Table 1 Carbon dioxide absorption in a CO_2 chamber

Specimen type	Area (cm^2)	Test days	Weight before CO_2 introduction (kg)	Weight after CO_2 introduction (kg)	Absorption of CO_2 (moles)
Plain concrete	225	14	7.992	8.003	0.249
	225	14	7.795	7.802	0.159
	225	14	8.103	8.113	0.227
	225	28	8.290	8.304	0.318
	225	28	8.200	8.209	0.204
	225	28	8.010	8.017	0.159
11% zeolite addition	225	14	7.872	7.898	0.590
	225	14	7.573	7.589	0.363
	225	14	7.573	7.597	0.545
	225	28	7.790	7.801	0.249
	225	28	7.870	7.883	0.295
	225	28	7.670	7.686	0.363
22% zeolite addition	225	14	7.687	7.909	0.499
	225	14	7.449	7.468	0.431
	225	14	7.557	7.569	0.272
	225	28	7.400	7.413	0.295
	225	28	7.460	7.472	0.272
	225	28	7.410	7.419	0.204
33% zeolite addition	225	14	7.580	7.598	0.408
	225	14	7.557	7.585	0.636
	225	14	7.742	7.765	0.522
	225	28	7.800	7.817	0.386
	225	28	7.720	7.734	0.304
	225	28	7.880	7.893	0.295

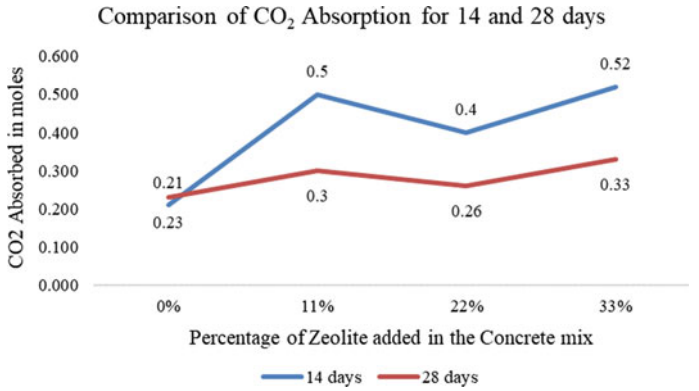

Fig. 4 Comparison of carbon dioxide absorption for 14 days and 28 days curing of water

Table 2 Amount of carbon dioxide absorption (toll)

Specimen type	Area (cm^2)	Test days	Before CO_2 introduction (kg)	After CO_2 introduction (kg)	Absorption of CO_2 (moles)
Plain concrete	100	7	11.899	11.900	0.023
	100	7	11.970	11.970	0
	100	7	11.921	11.920	0.023
	100	14	11.899	11.900	0.023
	100	14	11.970	11.971	0.023
	100	14	11.921	11.923	0.045
11% zeolite addition	100	7	11.420	11.420	0
	100	7	11.118	11.120	0.045
	100	7	11.607	11.610	0.068
	100	14	11.420	11.422	0.045
	100	14	11.118	11.121	0.068
	100	14	11.607	11.612	0.114
	100	7	11.489	11.490	0.023
22% zeolite addition	100	7	11.188	11.190	0.045
	100	7	11.380	11.380	0
	100	14	11.489	11.492	0.068
	100	14	11.188	11.194	0.136
	100	14	11.380	11.381	0.023
33% zeolite addition	100	7	11.028	11.028	0
	100	7	11.482	11.482	0
	100	7	11.381	11.381	0
	100	14	11.028	11.029	0.023
	100	14	11.482	11.487	0.114
	100	14	11.381	11.386	0.114

Table 3 Average percentage of carbon dioxide absorption (toll)

Specimen	Area (cm^2)	Percentage increase in CO_2 absorption	
		7 days exposure (%)	14 days exposure (%)
Plain Concrete	100	58	23.3
11% zeolite addition	100	47.5	11.6
22% zeolite addition	100	59.6	30.3
33% zeolite addition	100	8.46	7.97

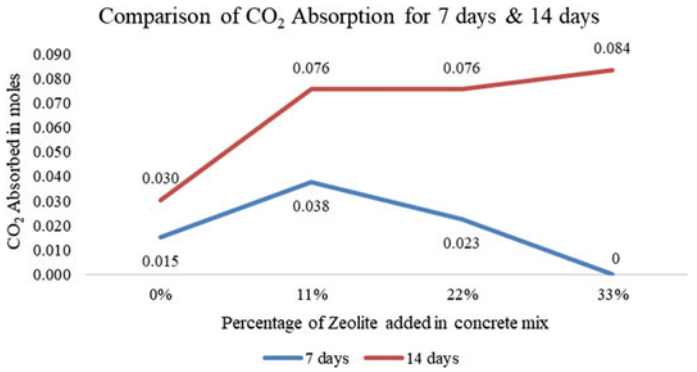

Fig. 5 Comparison of carbon dioxide absorption for 7 days and 14 days

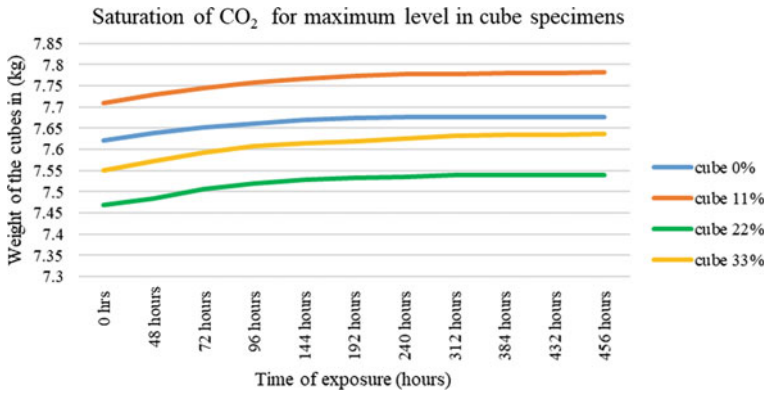

Fig. 6 Saturation of CO_2 absorption level of cube specimens

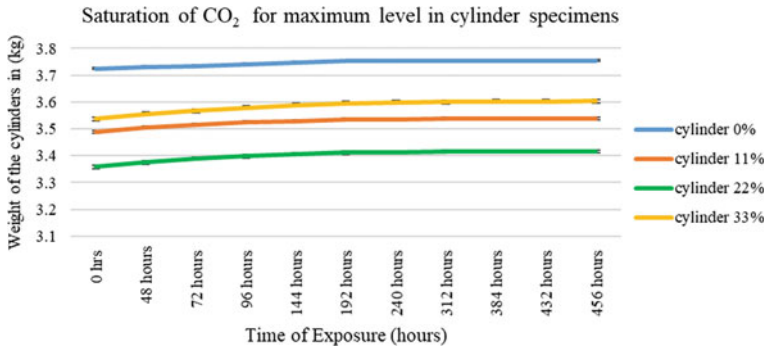

Fig. 7 Saturation of CO_2 absorption level of cube specimens

Table 4 Saturation of CO_2 absorption level of performance

Date		June 28	June 30	July 1	July 3	July 5	July 7	July 9	July 12	July 15	July 17	July 19
Hours (h)		0	48	72	96	144	192	240	312	384	432	456
Percentage	Cube 0%	7.622	7.639	7.652	7.661	7.67	7.673	7.676	7.677	7.677	7.677	7.677
	Cube 11%	7.71	7.729	7.745	7.758	7.767	7.774	7.778	7.778	7.78	7.78	7.781
	Cube 22%	7.468	7.484	7.506	7.519	7.528	7.533	7.536	7.539	7.54	7.54	7.54
	Cube 33%	7.551	7.573	7.592	7.608	7.614	7.62	7.625	7.632	7.635	7.635	7.636
	Cylinder 0%	3.725	3.731	3.735	3.741	3.748	3.752	3.754	3.754	3.755	3.755	3.755
	Cylinder 11%	3.489	3.505	3.516	3.525	3.529	3.534	3.536	3.537	3.537	3.538	3.538
	Cylinder 22%	3.358	3.375	3.389	3.398	3.405	3.411	3.413	3.415	3.415	3.415	3.415
	Cylinder 33%	3.538	3.556	3.567	3.579	3.588	3.596	3.599	3.601	3.602	3.602	3.603

concrete will not be considered for CO_2 absorption as they are not exposed to the outside atmosphere.

So, considering only the surface area which is subjected to the exposure of the atmosphere and is intended to absorb the CO_2 from the polluted air in the surrounding to a very small extent. From the experiments conducted near the toll roads using specimens of concrete beams for 2 weeks, we have concluded that there is some minor increase in the weight of specimens which in turn indicates absorption of CO_2.

The varying percentages of zeolites added in concrete specimens showed varied percentages of absorption of CO_2, as the percentages increased when the CO_2 absorption also increased.

Based on the above tests conducted, on a practical note, we can calculate the absorption level of CO_2 for varying percentages of zeolite in concrete specimens.

For 1 km Length of Road

As we know, the outer surface area of the beam specimen is $= (0.5 \times 0.1)4 + (0.1 \times 0.1)2$.

$= 0.2 + 0.2$
$= 0.22\ m^2$.

The total surface area of 1 km road $= 1000 \times 30.48 =$ **30,480 m².**
Without zeolite, the absorption of CO_2 is, (for a size of 0.22 m²)

For 7 days $= 11.930666 - 11.930 = 6.66 \times 10^{-4}$ g.
For 14 days $= 11.9313 - 11.930 = 1.33 \times 10^{-3}$ g.

With respect to the above values calculating for 1 km road, i.e., (30,480 m^2).
Let x be the value of absorption for a 1 km road.
For 7 days,

30,480 $m^2 \times 6.66 \times 10^{-4} = 0.22 \times X$.
$20.29 = 0.22x$.
$X =$ **92.27 g.**

For 14 days,

30,480 $m^2 \times 1.33 \times 10^{-3} = 0.22 \times X$.
$X =$ **184.26 g** $\rightarrow$ for 14 days.

Similarly, for 11% addition of zeolite, the absorption of CO_2 observed was (for a surface area of 0.22 m²).

11% zeolite addition		
For 7 days	$11.3833 - 11.3816 = 1.7 \times 10^{-3}$ g	$30{,}480 \times 1.7 \times 10^{-3} = 0.22 \times X1$ $X1 =$ **235.527 g**

(continued)

(continued)

14 days	$1.385 - 11.3816 = 3.4 \times 10^{-3}$ g	$30{,}480 \times 3.4 \times 10^{-3} = 0.22 \times X1$ $X1 =$ **471.05 g**
22% zeolite addition		
7 days	$11.3833 - 11.3816 = 1.7 \times 10^{-3}$ g	$30{,}480 \times 1.7 \times 10^{-3} = 0.22 \times X1$ X1 = **235.527 g**
14 days	$1.385 - 11.3816 = 3.4 \times 10^{-3}$ g	$30{,}480 \times 3.4 \times 10^{-3} = 0.22 \times X1$ $X1 =$ **471.05 g**
33% zeolite addition		
7 days	$11.297 - 11.2943 = 2.7 \times 10^{-3}$ g	$30{,}480 \times 1 \times 10^{-3} = 0.22 \times X^2$ X2 = **138.545 g**
14 days	$11.3006 - 11.2943 = 6.36 \times 10^{-3}$ g	$30{,}480 \times 6.36 \times 10–3 = 0.22 \times X^3$ $X3 =$ **881.149 g**

Note There may be some factors that influence the increase in weight of concrete like the following:

1. Dust
2. Rains
3. Traffic conditions
4. Level of pollution
5. Contents of particles in air, etc.

4.3 Cost Estimation for 1 m³ of Concrete

For 0% Addition of zeolite:

- Cement quantity required is 450 kg,
- Cost per 50 kg bag of cement = 375 (Adithya Birla 43 grade OPC), and
- Total cost of cement = (450/ 50) × 375 = Rs. 3375.

Cost of aggregates:

Fine Aggregate

- Quantity required = 644.34 kg,
- Cost per ton of M-sand grade I = Rs.7 50, and
- Total cost of sand = (644.34/1000) × 750 = Rs. 483.255.

Coarse Aggregate:

- Quantity required = 1122.8 kg,
- Cost of CA per ton = Rs. 750,
- Total cost of CA = (1122.8/1000) × 750 = Rs. 842.1. Total cost of 1 m^3 of concrete is 3375 + 484 + 842 = **Rs. 4699/.**

Similarly for 11% addition of zeolite:

The total cement quantity required will be 400.5 kg and the cost of cement will be Rs. 3003.75, while the zeolite quantity required will be 99 kg costing Rs. 750 per 100 kg. Thus, the total cost of zeolite will be Rs. 742.5.

When the cost of aggregates is considered, the overall cost of fine aggregate will be Rs. 483.255/ ton and the cost of coarse aggregate will be Rs. 842.1 per ton. Thus, the overall cost of the concrete mix will be Rs. 4702/-.

For 22% addition of zeolite:

The total cement quantity required will be 351 kg and the cost of cement will be Rs.2632.5, while the zeolite quantity required will be 49.5 kg costing Rs. 750 per 100 kg. Thus, the total cost of zeolite will be Rs. 371.25.

The total quantity required will be 644.34 kg and the cost per ton of M-sand grade I = Rs.750. Thus, the total cost of sand = (644.34/1000) × 750 = Rs. 483.255. Also, the quantity of coarse aggregate required will be 1122.8 kg while the cost of CA per ton = Rs. 750. Thus, the total cost of CA will be Rs. 842.1. So, the overall cost of concrete mix will be Rs. 4702/-.

For 33% addition of zeolite:

The total cement quantity required will be 301.5 kg and the cost of cement will be Rs. 2261.25, while the zeolite quantity required will be 148.5 kg costing Rs. 750 per 100 kg. Thus, the total cost of zeolite will be Rs. 1113.75.

The total quantity required will be 644.34 kg and the cost per ton of M-sand grade is I = Rs. 750. Thus, the total cost of sand = (644.34/1000) × 750 = Rs. 483.255. Also, the quantity of coarse aggregate required will be 1122.8 kg while the cost of CA per ton = Rs. 750. Thus, the total cost of CA will be Rs. 842.1. So, the overall cost of concrete mix will be Rs. 4702/-.

5 Overall Findings

By conducting the tests for the mechanical properties, we could observe that there was a considerable decrement in the compressive strength due to the addition of zeolite, i.e., for varying contents of 11%, 22%, and 33%, there were about 28.2%, 31.5%, and 40.9% decreases for 28 days water-cured specimens compared to the conventional concrete mix. Also, there was a considerable decrement in the split tensile strength due to the addition of zeolite, i.e., for varying contents of 11%, 22%, and 33%, there were about 15.5%, 27.3%, and 37.5% decreases for 28 days water cured as compared to the conventional concrete mix. Last but not least, we also see there was a considerable decrement in the flexural strength due to the addition of zeolite, i.e., for varying contents 11%, 22%, and 33%, there were about 12.7%, 19.9%, and 29.2% decreases for 28 days compared to the conventional concrete mix. These results may differ by the type of zeolite used in the concrete mix.

The addition of zeolite in the concrete increases the carbon dioxide absorption capacity of concrete. The carbon dioxide absorption for 14 days of water + 48 h dry ice cured concrete specimen was observed to be 0.211 mol, 0.499 mol, 0.400 mol, and 0.522 mol for replacement of 0%, 11%, 22%, and 33% of cement with zeolite in the mix. When the ultimate saturation of the CO_2 level in the specimen test was carried out, it showed a significant result till it is 18 to 20 days of pure CO_2 curing after which the rate became static and had absorbed a maximum of 20 to 25 g of CO_2. The cost comparison for the normal conventional concrete and zeolite added concrete was carried out, which shows the cost for construction per cubic meter of concrete was approximately the same which was around Rs. 4700/-.

A calculation for CO_2 absorption by a 1 km road of 100 ft wide was also carried out. It shows that there was an absorption of 92.279 to 374.07 g for 7 days and 184.2 to 881.14 g for 14 days exposure to the atmosphere with respect to a varied amount of addition of zeolite.

CO_2 increases zeolite weight, and the thickness of the block prepared with zeolite sand and powder as a substitute is not affected by gas [19]. In the buildings, this can, therefore, be used without any difficulty. As well as in the pavements of roads, chimneys of factories, and the building's faces, zeolite blocks can also be used for this purpose. Only a small substitution with zeolite would make it affordable for society [20]. Zeolite can be found in abundance. It is also possible to manufacture this. There are too many problems caused by CO_2 which causes environmental imbalances, greenhouse effect, and many other harmful pollutants [21]. There is a major role of CO_2 in this process. The amount of carbon dioxide in the atmosphere should be reduced as much as possible. Due to CO_2's gaseous form, it directly touches the constructions built around [22]. Construction is another major contributor to CO_2 emissions, contributing to 70%. When cement is manufactured, and when the structure is cured, it becomes a part of the atmosphere. Reduced emissions are therefore very important [23]. There will definitely be a reduction in emissions from this material. Therefore, the construction must use it.

6 Conclusions

As a result of recent technological advances, pollution has increased substantially. As a result, we need time to reduce pollution, otherwise, adverse effects will occur. CO_2 is absorbed by concrete made with zeolite but isn't emitted. Other than that, general concrete emits huge amounts of CO_2. In this way, it cleans the air by absorbing pollutants from the environment. Concrete made with Portland cement has greater durability as well as great performance. The strength of concrete is increased when olivine is present. As a result of adding zeolite, cement gains strength and CO_2 emissions are reduced.

7 Future Scope of the Study

Experimental studies could be carried out on the behavior and characteristics of zeolite-added concrete when subjected to steel reinforcement. A study on strength of zeolite added concrete when subjected to the addition of admixture and plasticizers can be carried out. Experimental studies on the maintenance, reusability, and recyclability of zeolite concrete can be carried out. Also, a study of the characteristics of concrete at the cold joints seen in the pavement can be carried out.

References

1. Czarnecki L, Justnes H (2012) Sustainable durable concrete. Cem Lime Concr 6:341–362
2. Maas GP (2011) Comparison of quay wall designs in concrete, steel, wood and composites with regard to the co-emission and the life cycle analysis. Master's Thesis, Delft University of Technology, Delft, The Netherlands, 18 February 2011
3. Roh SJ, Tae SH, Shin SW, Woo JH (2013) A study on the comparison of characterization of environmental impact of major building material for building life cycle assessment. Archit Inst Korea 29:93–100
4. Lee SH, Park WJ, Lee HS (2013) Life cycle CO_2 assessment method for concrete using CO_2 balance and suggestion to decrease LC CO_2 of concrete in South-Korean apartment. Energy Build 58:93–102
5. Hong J, Shen QG, Peng Y, Feng Y, Mao C (2016) Uncertainty analysis for measuring greenhouse gas emissions in the building construction phase: a case study in China. J Clean Prod 129:183–195
6. Załegowski K, Jackiewicz-Rek W, Garbacz A, Courard L (2013) Carbon footprint of concrete (in Polish). Mater Bud 12:34–36
7. Hasanbeigi A, Menke C, Therdyothin A (2011) Technical and cost assessment of energy efficiency improvement and greenhouse gas emission reduction potentials in Thai cement industry. Energy Efficiency 4:93–113
8. Kim T, Chae C, Kim G, Jang H (2016) Analysis of CO_2 emission characteristics of concrete used at construction sites. Sustainability 8:348
9. Stengel T, Schießl P (2014) Life cycle assessment (LCA) of ultra high-performance concrete (UHPC) structures. In: Eco-efficient construction and building materials, vol 22. Woodhead Publishing, Cambridge, UK, pp 528–564. ISBN 978-0-85709-045-4
10. Zastrow P, Molina-Moreno F, García-Segura T, Martí JV, Yepes V (2017) Life cycle assessment of cost-optimized buttress earth-retaining walls: a parametric study. J Clean Prod 140:1037–1048
11. Zadeh PM, Saghravani SF, Asadollahfardi G (2018) Mechanical and durability properties of concrete containing zeolite mixed with meta-kaolin and micro-nano bubbles of water. Retrieved from: https://onlinelibrary.wiley.com/doi/abs/10.1002/suco.201800030
12. Adil SE, Vasudev A, Vinay Kumar P, Santhosh Reddy A (2017) Study on carbon dioxide absorbing concrete block. Int J Civil Eng Technol (IJCIET) 8(4):1778–1784
13. Sanjuán MÁ et al (2020) Carbon dioxide uptake by cement-based materials: A Spanish case study. Appl Sci 10(1):339
14. Subramani T, Karthickrajan J (2016) Experimental study on absorption of carbon dioxide by M30 concrete as a partial replacement of cement by 25% of zeolite. Int J Appl Innov Eng Manage (IJAIEM) 5(5)
15. Subash S, Sasikumar G, Praveenkumar V, Karthikeyan VR, Jegan Mohan K (2016) Partial replacement of zeolite with cement. Imperial J Interdiscip Res (IJIR) 2(5)

16. Krishna Lekha RT, Vanreyk AJ (2017) Zeolite addition on concrete sustainability—a review. Int J Adv Res Innov Ideas Educ 3(2)
17. Cirajudeen AH, Prakash KB (2017) An investigation on the effect of partial replacement of cement by zeolite on the properties of concrete. Int Res J Eng Technol (IRJET) 04(07)
18. Kwon S-J, Wang X-Y (2019) Optimization of the mixture design of low-CO_2 high-strength concrete containing silica fume. Hindawi Adv Civil Eng 2019, Article ID 7168703
19. Chenarboni HA et al (2021) The effect of zeolite and cement stabilization on the mechanical behavior of expansive soils. Constr Build Mater 272:121630
20. Rożek P, Król M, Mozgawa W (2019) Geopolymer-zeolite composites: a review. J Clean Prod 230:557579
21. Kushnir ARL et al (2021) The fire resistance of high-strength concrete containing natural zeolites. Cement Concr Compos 116:103897
22. Yoshioka K et al (2013) New ecological concrete that reduces CO_2 emissions below zero level new method for CO_2 capture and storage. Energy Procedia 37:6018–6025
23. Kjellsen KO, Guimaraes M, Nilsson A (2005) The CO_2 balance of concrete in a life cycle perspective. Danish Technological-DTI

Performance Analysis of Resistive Based Environmental Sensors on Air Pollution Monitoring: A Brief Review

K. Deekshitha, Thanushree A. Hegde, P. Saranya, and R. Thangamani

Abstract Increased pollution levels in both indoor and outdoor areas have resulted from the rise of industry and many other undesirable human activities. These contaminants are harmful to both humans and the environment. The constant release of numerous chemical pollutants into the environment, such as NO_x, NH_3, C_2H_5OH, CO and fluorocarbons, from industry emissions, automobile exhaust, and home trash, causes a slew of issues. This review study focuses primarily on the numerous methodologies and fabrication technologies utilised in the production of environmental sensors, as well as key sensor performance characteristics. This paper describes the current status of different materials which are used in the development of resistive based sensor devices to detect major gases such as Carbon monoxide, Ammonia etc. and their status of sensitivity, selectivity, response time, recovery time etc. we also reviewed different methods of growth techniques of Two dimensional thin films and also the sensing mechanism of resistive based environmental sensors.

Keywords Gas sensor · Environmental pollution · Pollutants · REDOX reaction · Sensors · Particulate matter

1 Introduction

In recent years, environmental pollution has emerged as a major issue, with serious toxicological effects for both human health and the ecology. Pollution comes from a variety of sources, including cigarettes, natural sources, and enormous emissions and releases of hazardous substances from automobile engines and industrial activities [1, 2]. Long-term and short term exposure to air toxicants has a different toxicological effects on humans, including cardiovascular disease and respiratory problems [3], eye irritation [4], neuro-psychiatric problems [5], skin diseases [6] and chronic diseases such as cancer [7, 8]. The industrial sectors such as thermal power, transportation, coal consumption residential are the major sources of pollutants [9]. Furthermore,

K. Deekshitha (✉) · T. A. Hegde · P. Saranya · R. Thangamani
Department of Civil Engineering, N.M.A.M. Institute of Technology, NITTE, Udupi 574110, India
e-mail: deekshitha.k@nitte.edu.in

L. Nandagiri et al. (eds.), *Recent Advances in Civil Engineering*, Lecture Notes in Civil Engineering 256, https://doi.org/10.1007/978-981-19-1862-9_61

some incidences of severe air pollution have been observed in numerous semi-urban regions, most likely as a result of mining and related operations [10, 11]. Increased levels of particulate matters, air pollutants, were the result of these activities and/or factors [12–15].

As a result, the Indian government has recently taken a number of steps, including conducting rigorous and planned monitoring of both traditional and emergent air pollutants in order to establish a practical approach for improving air quality in Indian cities [16–20]. Despite the many precautions taken, there is still a high necessity for more systematic investigations to understand the quality of our breathing air and major sources of air pollution in the world. It's also critical to comprehend the contributions of various air pollution sources, as this allows us to investigate appropriate control approaches via targeted emission and reduction tactics [21]. One of the most important strategies that emerged was to identify probable causes of atmospheric pollution, establish a relationship between activity and cause, and devise long and short-term action plans to reduce upcoming air pollution occurrences. The Not-to-Exceed technique is the regulatory methodology used in the United States for assessing in-use. Initially, an air pump and a platinum-based (Pt) oxidation catalyst were used to convert HCs and CO in the exhaust gas to less harmful CO_2 and H_2O [22]. Ammonia (NH_3), being one of the most common contaminants and harmful gases, can irritate the eyes, skin, throat, and respiratory system, among other things. Hydrogen sulphide (H_2S), which is fatal at high doses, is another dangerous gases for animals and human health (more than 100 ppm) [23, 24]. Hot springs, Crude oil, and the breakdown of human and animal waste from bacteria are all natural sources of H_2S [25]. H_2S has already been connected to numerous accidents in most of the industries [26]. As a result, the quality, measurement performance, and accuracy of H_2S gas detection devices are critical characteristics for saving lives [27].

A gas sensor is only functional in practice if it can identify the active component in the presence of non-interfering background constituents. To put it another way, the sensor must be selective and operate within acceptable and controllable sensitivity and detectability limits. Precise pollutant measurement utilising a resistive-based sensor will be a significant contribution to society. Toxic gas detection and analysis has traditionally relied on mass spectrometers [28], gas chromatographs [29], Flame ionisation detectors [30], and Fourier transform infrared spectrometers [31]. These analytical machines are typically large and expensive, and they frequently necessitate the use of skilled operators. As a result, they're used in labs for certain functions. Furthermore, because to their size, they cannot be utilised for onsite measurements, restricting their range of uses. Gas sensors, unlike bulky analytical instruments, are usually compact and do not require sample preparation. A instrument that converts information in the chemical form into an analytically usable signal is referred to as a gas sensor, which is a subclass of chemical sensors [32, 33]. Different types of gas sensors, like acoustic surface wave gas sensors [34], quartzcrystal optical gas sensors [35], electrochemical-gas sensors microbalance-gas sensors [36], gasochromicgas sensors, catalytic-gas sensors [37], cataluminescence sensors, thermal-conductivity type of gas sensors [38], and resistive-based gas sensors [39], havebeen developed and studied. Sensors based on nano-structured thin films of metal semiconducting oxides

having been used extensively in automotive and safety applications as and reliable devices for detecting hazardous, flammable, and toxic vapours and gases. Small size, simple operation, great sensitivity, and relatively simple accompanying circuitry have made resistive-based semiconductor chemical sensors popular. However, the majority of them still have nonselectivity. In addition, they have a short shelf life and are less stable at higher temperatures. The current status of various materials used in the development of resistive-based sensor devices to detect important pollutants such as Carbon monoxide, NO_x, ammonia, SO_x, as well as their selectivity, response time, sensitivity, andrecovery time, is described in this paper.

2 Materials Used in Environmental Sensors

Carbon monoxide and hydrocarbons could be oxidised while NO_x was reduced alltogether on a single "three-way catalyst" containing Pt–Rh by the early 1980s [40]. The standard fourcontact vanderPauw method for assessing the resistivity can also be used to detect NO gas [41, 42]. Many chemical compounds, including ammonia, are expelled from the lungs in human breath. Low levels of ammonia in the breath suggest that the person is in good health. Breath analysis can be used to evaluate the quantities of gases such as ammonia as biomarkers, which can be useful in the early detection of diseases [43]. Breath analysis being non-invasive NH_3 detection via breath analysis has become more significant. Hence, knowledge of existing sensors and their working mechanisms is required to fabricate new sensors. Chemiresistive sensors based on various metal-oxide semiconductors are often utilised ammonia gas detection technologies [44, 45], such as ZnO [46, 47], In_2O_3 [48, 49], ZrO_2 [50], WO_3 [51], carbon nanotubes [52, 53], Fe_2O_3 [54], Co_3O_4 [55] and V_2O_5 [56].

3 Mechanisms of Resistive Based Sensors

In the gas detection sector, nano-structured thin films of metal oxides are recognised as a viable option. Organic and physical qualities, synthesis techniques, measurement conditions, and the type of vapours all influence the sensor properties of [57]. In the majority of metal-oxiderelated sensors, the chemi-resistance property implies the resistance of the detecting layerchanges in proportion to that specific pollutant concentration. In other words, when the gas interacts with metal-oxides on the surface of thin films, it either acts as a charge carrier acceptor/donor or changes the resistivity of the metal oxide. The property of gas molecules in ambient air and the nature of charge carrier in a semiconductor-thin-film determine the increase/decrease in resistivity of metal oxide films. The conductivity of thin films is reduced in p-type materials by the donor, while in n-type materials by the acceptor. The receptor function, in combination with the transduction function, describes the chemi-resistive property of semiconductor metal oxide gas sensors. Metal oxide sensors come in a

variety of shapes and sizes, including thick and thin films and sintered pellets. Interconnectivity among crystallites of the materials generated, as well as the geometry of the crystallites, are both important factors in determining the receptor and transduction functions. At least one electron is transferred from one molecule to another in a redox reaction. Reducers are compounds that are capable of transferring electrons and are therefore considered to be reductant. Oxidizers are compounds that are capable of removing an electron and hence are considered to be oxidative. They have low sensitivity and selectivity, which serves as a major impetus for the development of novel materials and methods for detecting gases. The change in sensor signal in a metal oxide resistive-based sensor is caused by ionosorption and can be explained by the transfer of free charge carriers from the sensing layer to adsorbed surface species. The adsorption process and, as a result, the sensing signal are hugely affected by pre-adsorbed species. In the influence of humidity, air, and residual gases, a metal oxide-based sensor is commonly used. Numerous oxygen species, water, and carbon dioxide-related species can be observed on the metal oxide's surface at standard working temperatures (200–400 °C). Some species exchange electrical charge to form a bond with specific surface sites (surface atoms) and may create dipoles that have no impact on the concentration of free charge-carriers or the resistance of the sensitive layer [58, 59]. A porous semiconductor layer, such as WO_3, SnO_2, TiO_2, ZnO, and others, is used in resistive gas sensors to increase sensitivity at higher temperatures. This means indicates that the sensors may be used to measure even exhaust gases by utilising more energy for heating. As a result, it's critical to find appropriate materials capable of increasing the sensor's gas sensing capabilities [60].

4 Performance of Different Resistive Based Gas Sensors

Any gas sensor's performance can be evaluated using the following criteria: (1) sensitivity, (2) response time, (3) selectivity, (4) operating temperature, and detection limit. The response (R) of a gas-sensor for target-gas is the very important metric. A gas-sensor that is unable to detect a target gas cannot be employed in practiseThe gas response of semiconductor-based gas-sensors may be defined in a number of different ways. The response is typically expressed as a resistance-variation-ratio [22]. It is not appropriate to use the words sensitivity (S) and reaction (R) interchangeably. The ratio of measured resistance (R) to analyte concentration (c), or the slopes of a calibration graph, is defined as—$S = R/c$. The response, on the-other-hand, is the sensor resistance ratio mentioned earlier. Because some target gases are highly toxic or explosive, a fast response, recovery time are always-preferred in all actual application of a gas sensor. The response-time (R_{resp}) is the time it takes for a gas-sensor to alter resistance by 90% with the presence of the target-gas, and the recovery-time is the time taken for the resistance of a gas-sensor to restore to 90% of its original baselinevalue once the target gas is removed [61]. Another important feature of a gas sensor is selectivity. It describes a sensor's ability to distinguish a specific target gas from other interfering gases. When compared to response to interfering type of

gases, a gas sensor with high selectivity has a stronger response to the target gas [62]. Gas sensors are typically sensitive to multiple gases and have cross-sensitivity. As a result, It's difficult to get a gas sensor with a high selectivity which is limiting gas sensor uses. The sensitivity of a gas-sensor is found by its operating temperature. Because gas-sensing phenomena are temperature-dependent and are linked to target gas diffusion and reaction, As the sense temperature rises, the response of gas sensing increases. Metal-oxide-gas-sensors typically operate at temperatures in the range 25–500 °C. Chemical reaction speeds at low temperatures and the diffusion rate of gas-molecules at high temperatures defines the response. The rates of adsorption–desorption become equal at intermediate temperatures, producing the best response. The ideal sensing temperature for any gas sensor is determined by the target gas, chemical composition, and shape [63]. Lower sensing temperatures are preferable from an energy standpoint since they need less power and allow the gas sensor to be used in more remote locations. However, high-temperature gas sensors are necessary for specific applications, such as ammonia manufacturing, which happens at temperatures above 450 °C [64]. At a given temperature, the detection-limit is the lowest gas-concentration that can be detected. Table 1 shows performance parameters of gas-sensors depending on different types of materials.

Table 1 shows that barium-substituted p-type bismuth-ferrite [67] has a long response time when compared to the other materials. The increased gas-sensing performance of barium-substituted bismuth ferrite p-type sensor is linked to increased oxygen-vacancy-concentration caused by the addition of Bi^{3+} ion by Ba^{2+} ion at the A-site of the perovskite structure. Furthermore, the ZnO nanorod-bundle thin film sensor [82] has a fast recovery period. ZnO nanorod-bundle thin films were also shown to have a higher sensitivity to alcohol (100 ppm) than ZnO-nanoparticle thin-films. This is due to the fact that the triblock copolymer surfactants were able to successfully adjust the morphologies and aspectratios of nano-ZnO, thus increasing its gas-sensing characteristics..

As shown in Table 2, the sensor responds significantly faster than a 0.1% RGO-SnO_2-based sensor when compared to all other ammonia sensors. The response time for NH_3 [89], which is approximately 14 s, which is quite short when compared to other sensors.

Different NO_2 sensors and their performance properties are shown in Table 3. Compared all other materials RGO–MWCNTs–WO_3 is better material for NO_2-sensing. The developed sensor has a good NO_2 sensing performance, with a maximum-response-of-17% to 5 ppm, a 1 ppm limit of detection and a response/recovery time of 7/15 min. As a result, the proposed WO3NPs–MWCNTs–RGO hybrid sensor could be used to build high-performance, flexible NO_2 sensors.

Table 4 shows other important gas sensors and their sensing parameters. RGO–CNT–TiO_2 is found to be a better toluene sensor. The sensing criteria of 3D-titaniumdioxide/graphene-carbon nanotube due to the formation of Schottky-metal–semiconductor [111]. Further, low level humidity detection is possible through polyelectrolyte/graphene bilayer humidity sensorsQC-P4VP and RGO thin films were sequentially deposited on interdigitated gold electrodes to create these bilayer-structured humidity sensors [112].

Table 1 Ethanol sensing ability of different sensing materials

Sensing material	Response time (s)	Recovery time (s)	Conc. range (ppm)	Response (%)	Operating temperature	Reference
SnO_2:Sb nanowires	~9	~44	40	1.13	RT	[65]
1 wt% Ag/SnO_2	52	53	200	1.24	RT	[66]
SnO_2	55	85	200	1.48	RT	[66]
Ag@SnO_2	34	68	200	2.24	RT	[66]
p-type barium-substituted bismuth ferrite	~3	~10	100	4	310 °C	[67]
Hexagonal indium oxide nanorods (H-In_2O_3)	6	11	50	11.5	330 °C	[68]
Back-gated graphene FET	NA	NA	–	17	–	[69]
ZnO–SnO_2 nanofiber	5	6	100	18	300 °C	[70]
$LaNiO_3$	~5	NA	200	20	400 °C	[71]
Aloe-like SnO_2	1.2	76	50	23	285 °C	[72]
ZnONanorods[	NA	NA	100	29.7	300 °C	[73]
MWNTs/ZnO	4	20	50	46	260 °C	[74]
SnO_2 Doped Poly-Diallyl dimethyl ammonium Chloride	88	NA	150	71.6	RT	[75]
ZnO Nanorods	14	70	1530	94	200 °C	[76]
Nano Fe_2O_3	7	32	25 0	180	350 °C	[77]
Zinc-oxide porous-shell hollow spheres (ZnO-PHS)	~5–12	~8–13	300	~80	350 °C	[78]
In_2O_3 nanowire	6	11	5	~1.84	330 °C	[68]
ZnO nanorods	NA	NA	1	~10	300 °C	[79]
In_2O nanowires	10	~20	100	~2	370 °C	[80]
TiO2 Nanoparticles	3	15	20	~2.5 × 10^5	600 °C	[81]
ZnO nanorods	10	5	100	~20	325 °C	[82]
MgO/In_2O_3 + 17%SnO_2	160	260	200–2500	~1.7	378 °C	[83]
p-TiO_2	39	15	100	~146	150 °C	[84]
Vanadium oxide thin film	~16 min	~20 min	1000	2000	300 °C	[85]
ZnO	~200	~220	100	60	RT	[86]
SnO_2-reduced graphene oxide (SnO_2-rGO)	5	9	1.12 × 10^{-6}	–	RT	[80]
Silicon nanoporous pillar array((Si-NPA)	15	30	50 ppm	7	RT	[87]
ZnO	4	108	50	–	RT	[88]

Table 2 Ammonia sensing ability of different sensing materials

Sensing material	Response time (s)	Recovery time	Conc. Range (ppm)	Response	Operating temperature	References
GO–ZnO–PANI	30 s	–	100	38.31%	RT	[90]
indium trioxide and stanous oxide(90:10)	30–40	60–80	10–150	–	RT	[91]
Nanoporous Alumina films	24	169	13.6–48	–	23 °C	[92]
Polypyrrole thin film	27–36	4–10	4–80	–	RT	[93]
Graphene/Polyaniline	20 min after exposure	10 min	1–6400	–	RT	[94]
polyaniline nanoparticles	4		40 to 2993	–	500 °C	[95]
MoO_3	50	350	–	–	500 °C	[96]
MoS_2–Co3O4	105	136	0.1–5	10–60%	RT	[97]
MoS_2	650–700	750–1400	50–480	10–70% (125 °C)	75–150 °C	[98, 99]
RGO–TiO_2	Not reported		1–50	1–4.9% (RT)	RT–100 °C	[100]
Chemically Exfoliated SnS_2	Not reported		50–800	2.04–6.5 times	RT	[101]
Graphene–Ag	120	72 s	1000–12,500	26–77.8%	RT	[102]
WS_2	252	648 (for 10 ppm)	5–60	4.5–12 times	RT	[103]
GO	30	100	2–100	6–30%	RT	[104]
RGO–SnO_2	8	14 s	100–2000	$Rair/RNH_3$ = 1.014–11.79	RT	[89]

Table 3 NO_2 sensing ability of different sensing materials

Sensing material	Response time (s)	Recovery time (s)	Conc. range (ppm)	Response	Operating temperature	References
MoS_2 (UV activated)	29	Not reported	5–100	~15–30%	RT	[105]
SnS_2–SnO_2	159	297 s (for 8 ppm)	1–8	1.5–5.3 times	80 °C	[106]
Epitaxial graphene	10–3000	Not reported	1–50	1–17%	RT	[107]
ZnO–RGO	75	132	1–10	119–400%	RT	[108]
S-RGOH	11	12 s	0.2–2	6.1–22.5%	RT	[109]
RGO–MWCNTs–WO_3	7	15 min	1–5	9–17%	RT	[110]
Crumpled RGO	8	53 min	1–10	1.5–3.8	RT	[105]

Table 4 Other important environmental Room Temperature sensing materials and their sensing ability

Sensing material	Target gas (es)	Response time (s)	Recovery time (s)	Conc. range (ppm)	Response	References
Multistep reduced GO	SO_2	122	145	5–50	5.93–47.44%	[113]
Pd–TiO_2–MoS_2	Toluene			100 ppb–100 ppm	–	[114]
RGO–CNT–TiO_2	Toluene	9	11 s(500 ppm)	50–500	42.9% (500 ppm)	[111]
CuO–RGO	CO	70–76 s	147–232	0.25–1000	1.06–6.61%	[115]
RGO–MoS_2	Formaldehyde	-		2.5–15	1.5–6.5%	[116]
Graphene–Pd	H_2	40	490	10,000	30%	[117]
WS_2–WSe_2	Humidity	45	65 (for 60%RH)	40–80%RH	15.4–57 times	[118]
Graphene–Polyelectrolyte	Humidity	21	78	10–90% RH	300–1000%	[112]
MoS2–GO	Humidity	90	110 s (for 71.8%RH)	35–85%RH	3–1600 times	[119]
Li–GO B–GO	Humidity	4/25	40/50	11–97% RH	GO (17.13–3038.16%), B–GO (6.95–631.10%	[120]

5 Conclusion

Strict emission laws and heightened environmental consciousness have prompted engine manufacturers and research institutes to do extensive research into emissions reduction. NOx detection is becoming a critical feature in these settings, and numerous sensing and transduction strategies have been studied in recent literature. In conclusion, the surface reactions are intimately linked to the gas sensing mechanism. The response activation of different metaloxide-based compounds to the target gases varies. If the catalytic actions of the components complement each other, composite metal oxides usually have a better gas response than single components. We studied and compared the many types of environmental gas sensors, classifying them according to the approaches utilised for air pollution detection. It has been observed that while various technologies are capable of meeting the requirements, no single technology can be regarded the ideal candidate. The development of a critical sensitive and selective room temperature ethanol sensor is still proving tough. Our review consists of performances of different sensing materials for different environmental pollutants. More focused research into developing gas sensors based on novel 2D materials is expected to lead to the development of much more efficient environmental pollutant sensing systems, which could help to reduce the 7 million deaths per year linked to poor air quality and improve well-being in less polluted areas. From this review it is clear that most of the oxide semiconductors are better sensing materials. Further, the sensing properties can be tuned by optimising the grain size surface structure by choosing appropriate growth technique, sensing material and by fixing the operating temperature. As per this review, materials response time is high for ethanol in p-type barium-substituted bismuth ferrite rGO-SnO_2-based sensor has response time of 14 s for NH_3 and RGO–MWCNTs–WO_3 found to be a better material for NO_2 sensing. On the other hand, RGO–CNT–TiO_2 is found to be a better toluene sensor. Further, low level humidity detection is possible through polyelectrolyte/graphene bilayer humidity sensors.

References

1. Manisalidis I, Stavropoulou E, Stavropoulos A, Bezirtzoglou E (2020) Environmental and health impacts of air pollution: a review. Front Public Heal 8
2. Habre R, Coull B, Moshier E et al (2014) Sources of indoor air pollution in New York City residences of asthmatic children. J Expo Sci Environ Epidemiol 24. https://doi.org/10.1038/jes.2013.74
3. Tajudin MABA, Khan MF, Mahiyuddin WRW et al (2019) Risk of concentrations of major air pollutants on the prevalence of cardiovascular and respiratory diseases in urbanized area of Kuala Lumpur, Malaysia. Ecotoxicol Environ Saf 171. https://doi.org/10.1016/j.ecoenv.2018.12.057
4. Chang CJ, Yang HH (2020) Impact on eye health regarding gaseous and particulate pollutants. Aerosol Air Qual Res 20

5. Hahad O, Lelieveld J, Birklein F et al (2020) Ambient air pollution increases the risk of cerebrovascular and neuropsychiatric disorders through induction of inflammation and oxidative stress. Int J Mol Sci 21
6. Abolhasani R, Araghi F, Tabary M et al (2021) The impact of air pollution on skin and related disorders: a comprehensive review. Dermatol Ther 34
7. Kim HB, Shim JY, Park B, Lee YJ (2018) Long-term exposure to air pollutants and cancer mortality: a meta-analysis of cohort studies. Int J Environ Res Public Health 15. https://doi.org/10.3390/ijerph15112608
8. Khorrami Z, Pourkhosravani M, Rezapour M et al (2021) Multiple air pollutant exposure and lung cancer in Tehran, Iran. Sci Rep 11. https://doi.org/10.1038/s41598-021-88643-4
9. Yadav M, Soni K, Soni BK et al (2019) Source apportionment of particulate matter, gaseous pollutants, and volatile organic compounds in a future smart city of India. Urban Clim 28. https://doi.org/10.1016/j.uclim.2019.100470
10. Nagar PK, Singh D, Sharma M et al (2017) Characterization of PM2.5 in Delhi: role and impact of secondary aerosol, burning of biomass, and municipal solid waste and crustal matter. Environ Sci Pollut Res 24. https://doi.org/10.1007/s11356-017-0171-3
11. Yadav M, Sahu SP, Singh NK (2019) Multivariate statistical assessment of ambient air pollution in two coalfields having different coal transportation strategy: a comparative study in Eastern India. J Clean Prod 207. https://doi.org/10.1016/j.jclepro.2018.09.254
12. Gautam S, Yadav A, Tsai CJ, Kumar P (2016) A review on recent progress in observations, sources, classification and regulations of PM2.5 in Asian environments. Environ Sci Pollut Res 23. https://doi.org/10.1007/s11356-016-7515-2
13. Pekey H, Pekey B, Arslanbaş D et al (2013) Source apportionment of personal exposure to fine particulate matter and volatile organic compounds using positive matrix factorization. Water Air Soil Pollut 224. https://doi.org/10.1007/s11270-012-1403-2
14. Prakash J, Lohia T, Mandariya AK et al (2018) Chemical characterization and quantitativ e assessment of source-specific health risk of trace metals in PM1.0 at a road site of Delhi, India. Environ Sci Pollut Res 25. https://doi.org/10.1007/s11356-017-1174-9
15. Sharma A, Massey DD, Taneja A (2018) A study of horizontal distribution pattern of particulate and gaseous pollutants based on ambient monitoring near a busy highway. Urban Clim 24. https://doi.org/10.1016/j.uclim.2017.08.003
16. Sarkar C, Chatterjee A, Majumdar D et al (2017) How the atmosphere over eastern Himalaya, India is polluted with carbonyl compounds? Temporal variability and identification of sources. Aerosol Air Qual Res 17. https://doi.org/10.4209/aaqr.2017.01.0048
17. Tiwari S, Dumka UC, Gautam AS et al (2017) Assessment of PM2.5 and PM10 over Guwahati in Brahmaputra River Valley: temporal evolution, source apportionment and meteorological dependence. Atmos Pollut Res 8. https://doi.org/10.1016/j.apr.2016.07.008
18. Jain S, Sharma SK, Mandal TK, Saxena M (2018) Source apportionment of PM10 in Delhi, India using PCA/APCS, UNMIX and PMF. Particuology 37. https://doi.org/10.1016/j.partic.2017.05.009
19. Jain S, Sharma SK, Srivastava MK et al (2021) Chemical characterization, source apportionment and transport pathways of PM2.5 and PM10 over Indo Gangetic Plain of India. Urban Clim 36. https://doi.org/10.1016/j.uclim.2021.100805
20. Mukherjee A, Agrawal M (2018) Air pollutant levels are 12 times higher than guidelines in Varanasi, India. Sources and transfer. Environ Chem Lett 16. https://doi.org/10.1007/s10311-018-0706-y
21. Ghosh S, Rabha R, Chowdhury M, Padhy PK (2018) Source and chemical species characterization of PM10 and human health risk assessment of semi-urban, urban and industrial areas of West Bengal, India. Chemosphere 207. https://doi.org/10.1016/j.chemosphere.2018.05.133
22. Ménil F, Coillard V, Lucat C (2000) Critical review of nitrogen monoxide sensors for exhaust gases of lean burn engines. Sens Actuat B Chem. 67
23. Kim KH, Jeon EC, Choi YJ, Koo YS (2006) The emission characteristics and the related malodor intensities of gaseous reduced sulfur compounds (RSC) in a large industrial complex. Atmos Environ 40. https://doi.org/10.1016/j.atmosenv.2006.04.026

24. Kim KH, Choi Y, Jeon E, Sunwoo Y (2005) Characterization of malodorous sulfur compounds in landfill gas. Atmos Environ 39. https://doi.org/10.1016/j.atmosenv.2004.09.083
25. Kimura H (2011) Hydrogen sulfide: Its production and functions. Exp Physiol 96
26. Hughes MN, Centelles MN, Moore KP (2009) Making and working with hydrogen sulfide. The chemistry and generation of hydrogen sulfide in vitro and its measurement in vivo: a review. Free Radic Biol Med 47
27. Ayesh AI, Abu-Hani AFS, Mahmoud ST, Haik Y (2016) Selective H_2S sensor based on CuO nanoparticles embedded in organic membranes. Sensors Actuators, B Chem 231. https://doi.org/10.1016/j.snb.2016.03.078
28. Bu Y, Er S, Niemantsverdriet JW (Hans), Fredriksson HOA (2018) Preferential oxidation of CO in H_2 on Cu and Cu/CeO_x catalysts studied by in situ UV–Vis and mass spectrometry and DFT. J Catal 357. https://doi.org/10.1016/j.jcat.2017.11.014
29. Moriaux AL, Vallon R, Parvitte B et al (2018) Monitoring gas-phase CO_2 in the headspace of champagne glasses through combined diode laser spectrometry and micro-gas chromatography analysis. Food Chem 264. https://doi.org/10.1016/j.foodchem.2018.04.094
30. Becker C, Jochmann MA, Schmidt TC (2019) An overview of approaches in liquid chromatography flame ionization detection. TrAC—Trends Anal Chem 110
31. Souza MCMM, Grieco A, Frateschi NC, Fainman Y (2018) Fourier transform spectrometer on silicon with thermo-optic non-linearity and dispersion correction. Nat Commun 9. https://doi.org/10.1038/s41467-018-03004-6
32. Simon I, Bârsan N, Bauer M, Weimar U (2001) Micromachined metal oxide gas sensors: Opportunities to improve sensor performance. Sensors Actuators, B Chem 73
33. Hulanicki A, Glab S, Ingman F (1991) Chemical sensors definitions and classification. Pure Appl Chem 63. https://doi.org/10.1351/pac199163091247
34. Liu B, Chen X, Cai H et al (2016) Surface acoustic wave devices for sensor applications. J Semicond 37
35. Wu Y, Yao B, Yu C, Rao Y (2018) Optical graphene gas sensors based on microfibers: a review. Sensors (Switzerland) 18
36. Addabbo T, Fort A, Mugnaini M et al (2018) Quartz-crystal microbalance gas sensors based on TiO_2 nanoparticles. IEEE Trans Instrum Meas 67. https://doi.org/10.1109/TIM.2017.2785118
37. Harley-Trochimczyk A, Pham T, Chang J et al (2016) Platinum nanoparticle loading of boron nitride aerogel and its use as a novel material for low-power catalytic gas sensing. Adv Funct Mater 26. https://doi.org/10.1002/adfm.201503605
38. Tardy P, Coulon JR, Lucat C, Menil F (2004) Dynamic thermal conductivity sensor for gas detection. Sensors Actuators, B Chem 98. https://doi.org/10.1016/j.snb.2003.09.019
39. Mirzaei A, Neri G (2016) Microwave-assisted synthesis of metal oxide nanostructures for gas sensing application: a review. Sensors Actuators, B Chem 237:749–775
40. Fleming WJ (2001) Overview of automotive sensors. IEEE Sens J 1. https://doi.org/10.1109/7361.983469
41. Garcia MA, Losurdo M, Wolter SD et al (2007) Functionalization and characterization of InAs and InP surfaces with hemin. J Vac Sci Technol B Microelectron Nanom Struct 25. https://doi.org/10.1116/1.2746337
42. Uhlrich J, Garcia M, Wolter S et al (2007) Interfacial chemistry and energy band line-up of pentacene with the GaN (0 0 0 1) surface. J Cryst Growth 300. https://doi.org/10.1016/j.jcrysgro.2006.11.035
43. Mathew T, Pownraj P, Abdulla S, Pullithadathil B (2015) Technologies for clinical diagnosis using expired human breath analysis. Diagnostics 5. https://doi.org/10.3390/diagnostics5010027
44. Kim ID, Rothschild A, Tuller HL (2013) Advances and new directions in gas-sensing devices. Acta Mater 61. https://doi.org/10.1016/j.actamat.2012.10.041
45. Comini E, Baratto C, Concina I et al (2013) Metal oxide nanoscience and nanotechnology for chemical sensors. Sensors Actuators, B Chem 179. https://doi.org/10.1016/j.snb.2012.10.027

46. Dar GN, Umar A, Zaidi SA et al (2012) Ultra-high sensitive ammonia chemical sensor based on ZnO nanopencils. Talanta 89. https://doi.org/10.1016/j.talanta.2011.12.006
47. Zeng Y, Lou Z, Wang L et al (2011) Enhanced ammonia sensing performances of Pd-sensitized flowerlike ZnO nanostructure. Sensors Actuators, B Chem 156. https://doi.org/10.1016/j.snb.2011.04.064
48. Li C, Zhang D, Lei B et al (2003) Surface treatment and doping dependence of In_2O_3 nanowires as ammonia sensors. J Phys Chem B 107. https://doi.org/10.1021/jp0361531
49. Guo P, Pan H (2006) Selectivity of Ti-doped In_2O_3 ceramics as an ammonia sensor. Sensors Actuators, B Chem 114. https://doi.org/10.1016/j.snb.2005.07.040
50. Satsuma A, Shimizu K, Hattori T et al (2007) Polytungstate clusters on zirconia as a sensing material for a selective ammonia gas sensor. Sensors Actuators, B Chem 123. https://doi.org/10.1016/j.snb.2006.10.011
51. Xu CN, Miura N, Ishida Y et al (2000) Selective detection of NH_3 over NO in combustion exhausts by using Au and MoO_3 doubly promoted WO_3 element. Sensors Actuators, B Chem 65. https://doi.org/10.1016/S0925-4005(99)00413-X
52. Huang J, Wang J, Gu C et al (2009) A novel highly sensitive gas ionization sensor for ammonia detection. Sensors Actuators, A Phys 150. https://doi.org/10.1016/j.sna.2009.01.008
53. Bekyarova E, Davis M, Burch T et al (2004) Chemically functionalized single-walled carbon nanotubes as ammonia sensors. J Phys Chem B 108. https://doi.org/10.1021/jp0471857
54. Abaker M, Umar A, Baskoutas S et al (2011) A highly sensitive ammonia chemical sensor based on α-Fe_2O_3 nanoellipsoids. J Phys D Appl Phys 44. https://doi.org/10.1088/0022-3727/44/42/425401
55. Deng J, Zhang R, Wang L et al (2015) Enhanced sensing performance of the Co_3O_4 hierarchical nanorods to NH_3 gas. Sensors Actuators, B Chem 209. https://doi.org/10.1016/j.snb.2014.11.141
56. Modafferi V, Panzera G, Donato A et al (2012) Highly sensitive ammonia resistive sensor based on electrospun V_2O_5 fibers. Sensors Actuators, B Chem 163. https://doi.org/10.1016/j.snb.2012.01.007
57. Wang C, Yin L, Zhang L et al (2010) Metal oxide gas sensors: sensitivity and influencing factors. Sensors 10
58. Barsan N, Koziej D, Weimar U (2007) Metal oxide-based gas sensor research: How to? Sensors Actuators, B Chem 121. https://doi.org/10.1016/j.snb.2006.09.047
59. Mirzaei A, Lee JH, Majhi SM et al (2019) Resistive gas sensors based on metal-oxide nanowires. J Appl Phys 126
60. Wagner T, Haffer S, Weinberger C et al (2013) Mesoporous materials as gas sensors. Chem Soc Rev 42. https://doi.org/10.1039/c2cs35379b
61. Ma H, Yu L, Yuan X et al (2019) Room temperature photoelectric NO_2 gas sensor based on direct growth of walnut-like In_2O_3 nanostructures. J Alloys Compd 782. https://doi.org/10.1016/j.jallcom.2018.12.180
62. Korotcenkov G, Cho BK (2017) Metal oxide composites in conductometric gas sensors: Achievements and challenges. Sensors Actuators, B Chem 244
63. Gadkari AB, Shinde TJ, Vasambekar PN (2011) Ferrite gas sensors. IEEE Sens J 11. https://doi.org/10.1109/JSEN.2010.2068285
64. Wu N, Wang B, Han C et al (2019) Pt-decorated hierarchical SiC nanofibers constructed by intertwined SiC nanorods for high-temperature ammonia gas sensing. J Mater Chem C 7. https://doi.org/10.1039/c9tc01330j
65. Wu JM (2010) A room temperature ethanol sensor made from p-type Sb-doped SnO_2 nanowires. Nanotechnology 21. https://doi.org/10.1088/0957-4484/21/23/235501
66. Wu RJ, Lin DJ, Yu MR et al (2013) Ag@SnO_2 core-shell material for use in fast-response ethanol sensor at room operating temperature. Sensors Actuators, B Chem 178. https://doi.org/10.1016/j.snb.2012.12.052
67. Dong G, Fan H, Tian H et al (2015) Gas-sensing and electrical properties of perovskite structure p-type barium-substituted bismuth ferrite. RSC Adv 5. https://doi.org/10.1039/c5ra01869b

68. Xu J, Chen Y, Shen J (2008) Ethanol sensor based on hexagonal indium oxide nanorods prepared by solvothermal methods. Mater Lett 62. https://doi.org/10.1016/j.matlet.2007.08.054
69. Chen B, Liu H, Li X et al (2012) Fabrication of a graphene field effect transistor array on microchannels for ethanol sensing. Appl Surf Sci 258. https://doi.org/10.1016/j.apsusc.2011.05.101
70. Song X, Liu L (2009) Characterization of electrospun ZnO-SnO_2 nanofibers for ethanol sensor. Sensors Actuators, A Phys 154. https://doi.org/10.1016/j.sna.2009.06.010
71. Obayashi H, Sakurai Y, Gejo T (1976) Perovskite-type oxides as ethanol sensors. J Solid State Chem 17. https://doi.org/10.1016/0022-4596(76)90135-3
72. Mei L, Deng J, Yin X et al (2012) Ultrasensitive ethanol sensor based on 3D aloe-like SnO_2. Sensors Actuators, B Chem 166–167. https://doi.org/10.1016/j.snb.2011.06.054
73. Li CC, Du ZF, Li LM et al (2007) Surface-depletion controlled gas sensing of ZnO nanorods grown at room temperature. Appl Phys Lett 91. https://doi.org/10.1063/1.2752541
74. Shan H, Liu C, Liu L et al (2014) Excellent ethanol sensor based on multiwalled carbon nanotube-doped ZnO. Chinese Sci Bull 59. https://doi.org/10.1007/s11434-013-0034-3
75. Zhan S, Li D, Liang S et al (2013) A novel flexible room temperature ethanol gas sensor based on SnO_2 doped poly-diallyldimethylammonium chloride. Sensors (Switzerland) 13. https://doi.org/10.3390/s130404378
76. Roy S, Banerjee N, Sarkar CK, Bhattacharyya P (2013) Development of an ethanol sensor based on CBD grown ZnO nanorods. Solid State Electron 87. https://doi.org/10.1016/j.sse.2013.05.003
77. Pawar NK, Kajale DD, Patil GE et al (2012) Nanostructured Fe_2O_3 thick film as an ethanol sensor. Int J Smart Sens Intell Syst 5. https://doi.org/10.21307/ijssis-2017-489
78. Wang LL, Wang HY, Wang YQ, Li XJ (2012) Highly sensitive and selective ethanol sensor based on micron-sized zinc oxide porous-shell hollow spheres. Mater Res Bull 47. https://doi.org/10.1016/j.materresbull.2012.06.007
79. Yang Z, Li LM, Wan Q et al (2008) High-performance ethanol sensing based on an aligned assembly of ZnO nanorods. Sensors Actuators, B Chem 135. https://doi.org/10.1016/j.snb.2008.07.016
80. Chang Y, Yao Y, Wang B et al (2013) Reduced graphene oxide mediated SnO_2 nanocrystals for enhanced gas-sensing properties. J Mater Sci Technol 29. https://doi.org/10.1016/j.jmst.2012.11.007
81. Arafat MM, Haseeb ASMA, Akbar SA (2014) A selective ultrahigh responding high temperature ethanol sensor using TiO_2 nanoparticles. Sensors (Switzerland) 14. https://doi.org/10.3390/s140813613
82. Ge C, Bai Z, Hu M et al (2008) Preparation and gas-sensing property of ZnO nanorod-bundle thin films. Mater Lett 62. https://doi.org/10.1016/j.matlet.2007.11.073
83. Vaishnav VS, Patel PD, Patel NG (2005) Indium tin oxide thin film gas sensors for detection of ethanol vapours. In: Thin solid films
84. Hazra A, Dutta K, Bhowmik B, Bhattacharyya P (2015) Highly repeatable low-ppm ethanol sensing characteristics of p-TiO_2-based resistive devices. IEEE Sens J 15. https://doi.org/10.1109/JSEN.2014.2345575
85. Micocci G, Serra A, Tepore A et al (1997) Properties of vanadium oxide thin films for ethanol sensor. J Vac Sci Technol A Vacuum, Surfaces, Film 15. https://doi.org/10.1116/1.580471
86. Beniwal A, Sahu PK, Sharma S (2018) Sol–gel spin coating assisted room temperature operated nanostructured ZnO ethanol sensor with behavior transformation. J Sol-Gel Sci Technol 88. https://doi.org/10.1007/s10971-018-4841-5
87. Li XJ, Chen SJ, Feng CY (2007) Characterization of silicon nanoporous pillar array as room-temperature capacitive ethanol gas sensor. Sensors Actuators, B Chem 123. https://doi.org/10.1016/j.snb.2006.09.021
88. Parthasarathy S, Nandhini V, Prakalya D, Jeyaprakash BG (2015) Light-assisted ethanol sensor at ambient temperature using spray deposited ZnO thin films. Int J ChemTech Res 7

89. Feng Q, Li X, Wang J (2017) Percolation effect of reduced graphene oxide (rGO) on ammonia sensing of rGO-SnO_2 composite based sensor. Sensors Actuators, B Chem 243. https://doi.org/10.1016/j.snb.2016.12.075
90. Andre RS, Shimizu FM, Miyazaki CM et al (2017) Hybrid layer-by-layer (LbL) films of polyaniline, graphene oxide and zinc oxide to detect ammonia. Sensors Actuators, B Chem 238. https://doi.org/10.1016/j.snb.2016.07.099
91. Mishra SK, Kumari D, Gupta BD (2012) Surface plasmon resonance based fiber optic ammonia gas sensor using ITO and polyaniline. Sensors Actuators, B Chem 171–172. https://doi.org/10.1016/j.snb.2012.06.013
92. Varghese OK, Gong D, Dreschel WR et al (2003) Ammonia detection using nanoporous alumina resistive and surface acoustic wave sensors. Sensors Actuators, B Chem 94. https://doi.org/10.1016/S0925-4005(03)00252-1
93. Joshi A, Gangal SA, Gupta SK (2011) Ammonia sensing properties of polypyrrole thin films at room temperature. Sensors Actuators, B Chem 156. https://doi.org/10.1016/j.snb.2011.03.009
94. Wu Z, Chen X, Zhu S et al (2013) Enhanced sensitivity of ammonia sensor using graphene/polyaniline nanocomposite. Sensors Actuators, B Chem 178. https://doi.org/10.1016/j.snb.2013.01.014
95. Hibbard T, Crowley K, Kelly F et al (2013) Point of care monitoring of hemodialysis patients with a breath ammonia measurement device based on printed polyaniline nanoparticle sensors. Anal Chem 85. https://doi.org/10.1021/ac403472d
96. Prasad AK, Kubinski DJ, Gouma PI (2003) Comparison of sol-gel and ion beam deposited MoO_3 thin film gas sensors for selective ammonia detection. Sensors and Actuators, B: Chem
97. Zhang D, Jiang C, Li P, Sun Y (2017) Layer-by-Layer Self-assembly of Co_3O_4 Nanorod-decorated MoS_2 nanosheet-based nanocomposite toward high-performance ammonia detection. ACS Appl Mater Interfaces 9. https://doi.org/10.1021/acsami.6b15669
98. Burman D, Ghosh R, Santra S et al (2017) Role of vacancy sites and UV-ozone treatment on few layered MoS_2 nanoflakes for toxic gas detection. Nanotechnology 28. https://doi.org/10.1088/1361-6528/aa87cd
99. Xiangfeng C, Caihong W, Dongli J, Chenmou Z (2004) Ethanol sensor based on indium oxide nanowires prepared by carbothermal reduction reaction. Chem Phys Lett 399. https://doi.org/10.1016/j.cplett.2004.10.053
100. Li X, Zhao Y, Wang X et al (2016) Reduced graphene oxide (rGO) decorated TiO_2 microspheres for selective room-temperature gas sensors. Sensors Actuators, B Chem 230. https://doi.org/10.1016/j.snb.2016.02.069
101. Wang H, Xu K, Zeng D (2015) Room temperature sensing performance of graphene-like SnS_2 towards ammonia. In: 2015 IEEE sensors—proceedings
102. Song H, Li X, Cui P et al (2017) Morphology optimization of CVD graphene decorated with Ag nanoparticles as ammonia sensor. Sensors Actuators, B Chem 244. https://doi.org/10.1016/j.snb.2016.12.133
103. Gu D, Li X, Wang H et al (2018) Light enhanced VOCs sensing of WS_2 microflakes based chemiresistive sensors powered by triboelectronic nangenerators. Sensors Actuators, B Chem 256. https://doi.org/10.1016/j.snb.2017.10.045
104. Zhu S, Sun H, Liu X et al (2017) Room-Temperature NH_3 sensing of graphene oxide film and its enhanced response on the laser-Textured silicon. Sci Rep 7. https://doi.org/10.1038/s41598-017-15270-3
105. Chen Z, Wang J, Umar A et al (2017) Three-dimensional crumpled graphene-based nanosheets with ultrahigh NO_2 gas sensibility. ACS Appl Mater Interfaces 9. https://doi.org/10.1021/acsami.7b01229
106. Gu D, Li X, Zhao Y, Wang J (2017) Enhanced NO_2 sensing of SnO_2/SnS_2 heterojunction based sensor. Sensors Actuators, B Chem 244:67–76. https://doi.org/10.1016/j.snb.2016.12.125
107. Novikov S, Lebedeva N, Satrapinski A et al (2016) Graphene based sensor for environmental monitoring of NO_2. Sensors Actuators, B Chem 236. https://doi.org/10.1016/j.snb.2016.05.114

108. Xia Y, Wang J, Xu JL et al (2016) Confined formation of ultrathin ZnO nanorods/reduced graphene oxide mesoporous nanocomposites for high-performance room-temperature NO_2 sensors. ACS Appl Mater Interfaces 8. https://doi.org/10.1021/acsami.6b12501
109. Wu J, Tao K, Guo YY et al (2017) A 3D chemically modified graphene hydrogel for fast, highly sensitive, and selective gas sensor. Adv Sci 4. https://doi.org/10.1002/advs.201600319
110. Yaqoob U, Uddin ASMI, Chung GS (2016) A high-performance flexible NO_2 sensor based on WO_3 NPs decorated on MWCNTs and RGO hybrids on PI/PET substrates. Sensors Actuators, B Chem 224. https://doi.org/10.1016/j.snb.2015.10.088
111. Seekaew Y, Wisitsoraat A, Phokharatkul D, Wongchoosuk C (2019) Room temperature toluene gas sensor based on TiO_2 nanoparticles decorated 3D graphene-carbon nanotube nanostructures. Sensors Actuators, B Chem 279. https://doi.org/10.1016/j.snb.2018.09.095
112. Li Y, Fan K, Ban H, Yang M (2016) Detection of very low humidity using polyelectrolyte/graphene bilayer humidity sensors. Sensors Actuators, B Chem 222. https://doi.org/10.1016/j.snb.2015.08.052
113. Kumar R, Avasthi DK, Kaur A (2017) Fabrication of chemiresistive gas sensors based on multistep reduced graphene oxide for low parts per million monitoring of sulfur dioxide at room temperature. Sensors Actuators, B Chem 242. https://doi.org/10.1016/j.snb.2016.11.018
114. Zhang D, Jiang C, Zhou X (2018) Fabrication of Pd-decorated TiO_2/MoS_2 ternary nanocomposite for enhanced benzene gas sensing performance at room temperature. Talanta 182. https://doi.org/10.1016/j.talanta.2018.01.064
115. Zhang D, Jiang C, Liu J, Cao Y (2017) Carbon monoxide gas sensing at room temperature using copper oxide-decorated graphene hybrid nanocomposite prepared by layer-by-layer self-assembly. Sensors Actuators, B Chem 247. https://doi.org/10.1016/j.snb.2017.03.108
116. Li X, Wang J, Xie D et al (2017) Flexible room-temperature formaldehyde sensors based on rGO film and rGo/MoS_2 hybrid film. Nanotechnology 28. https://doi.org/10.1088/1361-6528/aa79e6
117. Alfano B, Polichetti T, Miglietta ML et al (2017) Fully eco-friendly H_2 sensing device based on Pd-decorated graphene. Sensors Actuators, B Chem 239. https://doi.org/10.1016/j.snb.2016.08.039
118. Jha RK, Guha PK (2018) Humidity sensing properties of coexfoliated heterogeneous WS_2/WSe_2 nanohybrids. IEEE Trans Nanotechnol 17. https://doi.org/10.1109/TNANO.2018.2827056
119. Burman D, Ghosh R, Santra S, Guha PK (2016) Highly proton conducting MoS_2/graphene oxide nanocomposite based chemoresistive humidity sensor. RSC Adv 6. https://doi.org/10.1039/c6ra11961a
120. Rathi K, Pal K (2017) Impact of doping on GO: fast response-recovery humidity sensor. ACS Omega 2. https://doi.org/10.1021/acsomega.6b00399

Development of Arduino Prototype for the Detection of Fire, Smoke, and Carbon Monoxide from Open Waste Burning

Nalini Rebello, Aleema Safa, Arpitha Y. Pujar, Blesson Joseph, and V. C. Deekshith

Abstract The open burning of solid wastes has been frequently observed in developing countries like India that emits harmful gases into the environment which causes air pollution. Open waste burning leads to poor air quality, thus resulting in significant health problems. Therefore, frequent supervision of burning events must be imposed by the government authorities. This may be readily accomplished by using an Arduino-based detection system to monitor the required location. This paper presents monitoring of open waste burning and its detection using a set of sensors that is Arduino based. It comprises of a sensor node that is low-cost and easy to be installed in any required place. The sensor node consists of various sensors, which detect open waste burning by detecting the fire and smoke being emitted due to burning. It also gives the air quality with respect to carbon monoxide (CO) concentration of the particular area. The sensor node is able to transfer the sensor data to the host wherein the data is being processed for detection of open waste burning. The prototype of the detection system was put to test in order to check if it could detect the burning and give the level of CO concentration in PPM. It was tested for different cases of burning, such as burning of candle, incense stick, paper waste, cloth waste, plastic waste, and also outdoor burning of wastes.

Keywords Open waste burning · Detection system · Arduino · Air quality

1 Introduction

Open burning of waste is defined as the burning of solid waste materials in an open area without the presence of a chimney or stack. Open waste burning can emit toxic pollutants that can cause severe harm to the environment and contributes to

N. Rebello · A. Safa (✉) · A. Y. Pujar · B. Joseph · V. C. Deekshith
Department of Civil Engineering, Sahyadri College of Engineering and Management, Adyar, Mangaluru, India
e-mail: aleemasafa8105@gmail.com

N. Rebello
e-mail: nalini.civil@sahyadri.edu.in

L. Nandagiri et al. (eds.), *Recent Advances in Civil Engineering*, Lecture Notes in Civil Engineering 256, https://doi.org/10.1007/978-981-19-1862-9_62

air pollution. This is frequently observed in a developing country like India [1]. The National Green Tribunal (NGT) had imposed a ban on burning of waste in open places since 2016. Despite the ban, many still continue to light fire to plastic and other waste materials in different parts, posing health hazards. Even those aware of the consequences continue to burn waste out of habit or because other disposal options are not readily available. Open waste burning leads to poor air quality, thus causing serious health issues. Therefore, regular inspection of burning events must be enforced.

Several researchers have carried out studies on air quality monitoring using different techniques. A wireless sensor network system was developed by Sudhir G Nikhade using Raspberry Pi and ZigBee for a wide variety of applications related to environmental monitoring [2]. Rohi et al. investigated large-scale air pollution elimination to remove pollutants that are already in existence in the environment. This method involves the use of environmental drones (E-drones) to autonomously monitor the air quality at a specific location [3]. Ibrahim et al. used a temperature sensor known as a flame sensor with an Arduino device to detect fire outbreaks and to measure the amount of heat intensity generated by a fire outbreak or in a specific location in our house, offices, and other places [4].

In this paper, monitoring of open waste burning and its detection is carried out using a set of Arduino-based sensors. The Arduino consists of a sensor node that is low-cost and easy to be installed in any specific location. The sensor node consists of various sensors, which detect open waste burning by detecting the fire and smoke being emitted due to burning. It also gives the air quality with respect to carbon monoxide (CO) concentration in a particular area. The sensor node transfers the sensor data to the host and the data needs to be further processed for detection of open waste burning.

The main objective of the prototype is to monitor open waste burning and detect the fire, smoke, and level of carbon monoxide in PPM using various sensors. This is achieved by building a sensor node using Arduino that consists of various sensors in order to detect open waste burning and by building a wireless communication using transceiver modules for transferring data from the sensor.

2 Methodology

In this article, we mainly concentrate on building an Arduino-based module consisting of a transmitter and a receiver. The detection system using sensors detects the burning by detecting the fire and the smoke being emitted. The sensor node also determines the air quality with respect to CO concentration of the particular area. The sensor node sends the data to the host through transceiver modules, thus, ensuring wireless communication. The sensor node acts as a transmitter and the host end acts as a receiver.

2.1 The Transmitter

The transmitter consists of an Arduino nano microcontroller that controls the transmitter. A 5 V power supply is provided to the Arduino using a type B cable. It consists of an Nrf24l01 module for radio communication between the transmitter and the receiver. It consists of 3 sensors: an IR Flame sensor for detecting fire, an MQ2 sensor for detecting smoke, and an MQ135 sensor for determining the quality of the air. Figure 1 shows the block diagram of the transmitter and Fig. 2 shows the prototype of the transmitter.

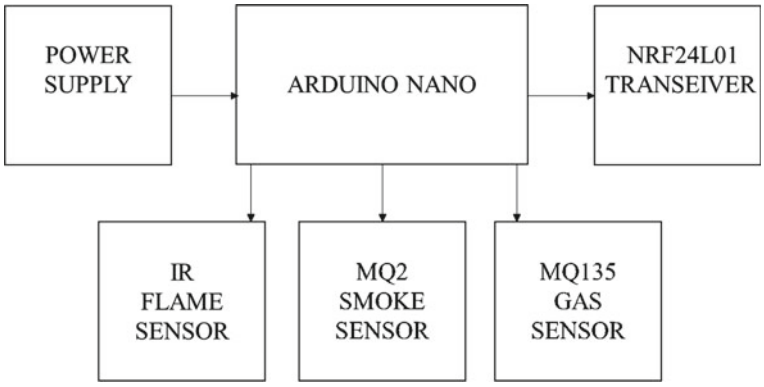

Fig. 1 Block diagram of the transmitter

Fig. 2 Prototype of the transmitter

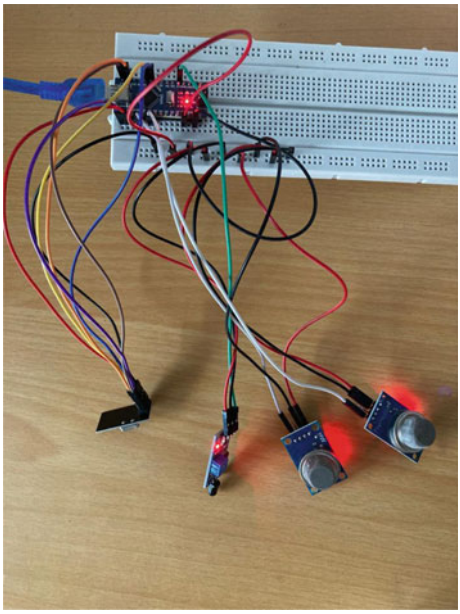

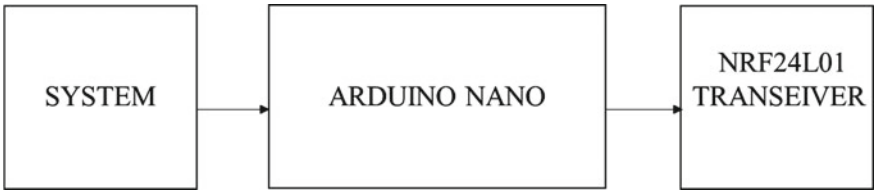

Fig. 3 Block diagram of the receiver

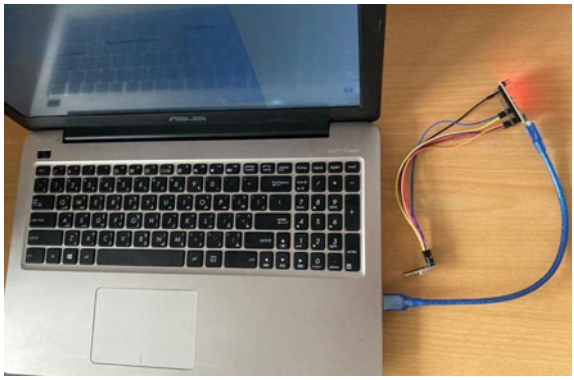

Fig. 4 Prototype of the receiver

2.2 Block Diagram of the Receiver

The receiver consists of an Arduino Nano microcontroller that controls the receiver. A 5 V power supply is provided to the Arduino using a type B cable which is connected to the computer for displaying the output. It consists of an Nrf24l01 module for radio communication between the transmitter and the receiver. Figure 3 shows the block diagram of the receiver and Fig. 4 indicates the block diagram of the receiver.

2.3 Working Flow

The IR flame sensor used in the prototype gives a digital output, either 0 or 1. Here, 0 means the fire has not been detected and 1 means the fire has been detected. The MQ2 flame sensor used is an Analog sensor that gives a value based on the output voltage of the sensor. Its value varies between 0 and 1000. Several readings were taken in the fresh environment and also in the presence of smoke to decide a threshold value which came to be around 250. This means any value below 250 indicates that there is no presence of smoke and a value above 250 would indicate the presence of smoke. The MQ135 sensor used is an analog sensor that gives a value based on the output voltage of the sensor. Its value varies between 0 and 1000. The output value

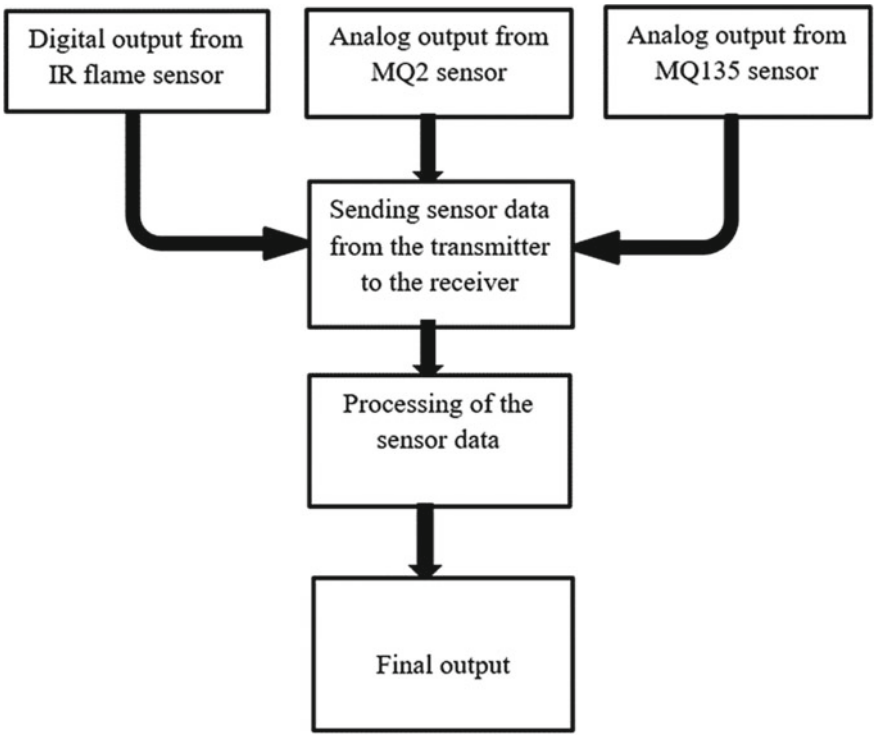

Fig. 5 Flowchart representing the working flow

has been converted to give the CO value in PPM. The conversion has been done by calibrating it with reference to the value of the MQ135 sensor in fresh air [5].

The output from the sensors, i.e., the digital output from the IR flame sensor, analog output from the MQ2 sensor, and MQ135 sensor is sent to the receiver from the transmitter through the transceiver modules. The sensor data received at the receiver end is then being processed by the Arduino for detection of open waste burning. The final output will be displayed in the serial monitor of the Arduino software. The working flow of the prototype is as shown in Fig. 5.

3 Results and Discussions

The prototype of the detection system was tested for the different cases of burning, such as burning of candle, incense stick, paper waste, cloth waste, plastic waste, and also outdoor burning of wastes. During the burning of candle, it was observed that fire was detected and the smoke was not detected, as candle burning did not emit heavy smoke. During incense stick burning, the fire was not detected but it

Table 1 Results obtained on the burning of candle

Trial No.	Fire detection	Smoke detection	Carbon monoxide (ppm)
1	Detected	Not detected	7.02
2	Detected	Not detected	7.24
3	Detected	Not detected	7.72
4	Detected	Not detected	7.48
5	Detected	Not detected	7.72
Average			7.44

Table 2 Results obtained on the burning of an incense stick

Trial No.	Fire detection	Smoke detection	Carbon monoxide (ppm)
1	Not detected	Detected	165.61
2	Not detected	Detected	190.75
3	Not detected	Detected	222.91
4	Not detected	Detected	215.38
5	Not detected	Detected	190.75
Average			197.08

emitted a heavy amount of gases. During paper, cloth, plastic and outdoor burning, both fire and smoke were detected, and also air quality (in PPM) for all the events was recorded. Air quality contamination recorded during outdoor burning was the highest. The results obtained on various burning events are as mentioned in the tables below.

Table 1 shows that the burning of a candle produces fewer smoke, but the sensor detects the fire. Since the least amount of smoke is produced while burning a candle, the air quality (in ppm) remains the least (7–8 ppm).

Table 2 shows that the burning of an incense stick produces considerable smoke but the sensor does not detect the fire. Since a considerable amount of smoke is produced while burning a candle the air quality (in ppm) varies from least to moderate (160–225 ppm).

Table 3 shows that the burning of paper waste produces smoke and detects fire. Since the least amount of smoke is produced while burning paper waste the air quality (in ppm) remains low (60–90 ppm).

Table 4 shows that the burning of cloth waste produces smoke and detects fire. Since the least amount of smoke is produced while burning cloth waste the air quality (in ppm) remains low (30–50 ppm).

Table 5 shows that the burning of plastic waste produces smoke and detects fire. Since the least amount of smoke is produced while burning plastic waste the air quality (in ppm) remains low (50–80 ppm).

Table 6 shows that outdoor waste burning contaminates the most. It produces a

Table 3 Results obtained on the burning of paper waste

Trial No.	Fire detection	Smoke detection	Carbon monoxide (ppm)
1	Detected	Detected	64.83
2	Detected	Detected	84.3
3	Detected	Detected	66.18
4	Detected	Detected	79.42
5	Detected	Detected	71.82
Average			73.31

Table 4 Results obtained on the burning of cloth waste

Trial No.	Fire detection	Smoke detection	Carbon monoxide (ppm)
1	Detected	Detected	32.86
2	Detected	Detected	48.18
3	Detected	Detected	36.88
4	Detected	Detected	38.59
5	Detected	Detected	49.24
Average			41.15

Table 5 Results obtained on the burning of plastic waste

Trial No.	Fire detection	Smoke detection	Carbon monoxide (ppm)
1	Detected	Detected	63.50
2	Detected	Detected	66.18
3	Detected	Detected	53.66
4	Detected	Detected	70.37
5	Detected	Detected	45.12
Average			59.77

Table 6 Results obtained on outdoor burning of waste

Trial No.	Fire detection	Smoke detection	Carbon monoxide (ppm)
1	Detected	Detected	383.25
2	Detected	Detected	497.47
3	Detected	Detected	533.85
4	Detected	Detected	487.65
5	Detected	Detected	477.32
Average			475.91

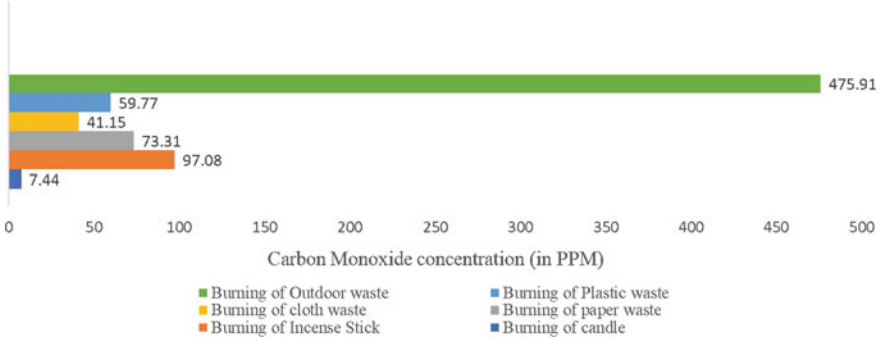

Fig. 6 Comparison of the level of carbon monoxide (in PPM) for various tests conducted

large amount of smoke and detects fire. Since a large amount of smoke is produced while burning waste outdoors the air quality (in ppm) goes up (350–600 ppm) (Fig. 6).

According to the graph, outdoor waste burning produces most of the pollution. However, in the other cases, complete combustion was happening due to the material. But in the case of outdoor waste burning since the waste is not sorted and due to the presence of different materials, complete combustion of those materials was not possible, due to which a large amount of smoke was produced as a result. The experimental studies show the amount of suspended particles present in the atmosphere due to the unscientific method of burning that causes most pollution in the atmosphere of that region.

4 Conclusion

The sensor module which has been developed successfully detects the fire and smoke produced in the atmosphere. The prototype built is user-friendly, easy to access, inexpensive, does not require Internet, and yet successfully monitors the area and detects open waste burning by detecting the fire and the smoke in the surrounding area. The sensor node has been made remotely accessible for convenient monitoring although it has a certain range limit. The radio communication between transmitter and receiver works decently for smaller distances, which are better for using the module in drones. Although for longer ranges, better communication has to be used. Thus, the prototype built detects fire, smoke, and CO concentration due to open waste burning.

References

1. Cogut A (2016) Open burning of waste: a global health disaster. R20 regions of climate action

2. Nikhade SG (2015) Wireless sensor network system using Raspberry Pi and zigbee for environmental monitoring applications. In: 2015 international conference on smart technologies and management for computing, communication, controls, energy and materials (ICSTM). IEEE
3. Rohi G, Godswill O (2020) Autonomous monitoring, analysis, and countering of air pollution using environmental drones. Heliyon 6(1):e03252
4. Khalaf OI, Abdulsahib GM, Zghair NAK (2019) IOT fire detection system using sensor with Arduino. AUS 26:74–78
5. https://jayconsystems.com/blog/understanding-a-gas-sensor

Post-disaster Climate Responsive Indigenous and Local Construction Systems of North Gujarat, India

Nikhil Sanjay Shah, Shoumik Desai, and Soumya Hosamani

Abstract This study explores the sustainable indigenous and local construction systems and practices of the North Gujarat region of Kutch, which have emerged post-earthquake as a result of collaborative participatory processes between local communities, master artisans, and community-centric developmental organizations. It engages with diverse geographical settings and the critical regional architectural and construction systems which have evolved with the local materials resulting in minimal ecological impact. This entails detailed analytical narratives of Pakkha dwellings, Bhungas, and Gujarati Stone house. It reflects upon the construction systems at multiple scales from building elements to the details as evolved by the communities. There is a high degree of emphasis on the reuse and recycling of the construction materials making it an exemplary model for ecological sensitivity of the highest order in an ontological manner. This would also narrate the unique 'ways of living', world-views, and the synthesis of form as a deep culturally embedded and rooted process in a continuous dialogue with the geographical context. At the functional scale, this study describes unique construction elements like shallow domes as a roofing system, debris block as walling system for the informal marginalized settlements, mud rolls, and fly ash lime rolls as a roof insulation system. This study would conclude with the manner in which sustainable living systems, local construction technology, and building materials support the ecosystem of a place and result in diverse contextual morphological responses.

Keywords Sustainable construction · Earth architecture · Local knowledge systems · Critical regionalism and community participation

1 Introduction

India currently ranks at number three after China and the USA in recording the highest number of natural disasters over the past 20 years (2000–2019), which implies that

N. S. Shah · S. Desai (✉) · S. Hosamani
Nitte Institute of Architecture (NITTE DU), Mangaluru, Karnataka 575018, India
e-mail: shoumik.desai@gmail.com

L. Nandagiri et al. (eds.), *Recent Advances in Civil Engineering*, Lecture Notes in Civil Engineering 256, https://doi.org/10.1007/978-981-19-1862-9_63

there are a huge economic implications and loss of life. One such natural disaster earthquake of 7.7 Richter scale occurred in the Kutch region of Gujarat in the year 2001, which devastated the region enormously and displaced communities to a large extent. It is estimated that approximately 14,000–20,000 people lost their lives with nearly 200,000 people injured along with an overall economic loss of 500 Crores INR. Recently, in July 2021, a tremor of 3.9 magnitude hit the Kutch region, which makes the region vulnerable in the future as well. The main reason behind this recurring earthquake is because of the region's proximity to the Eurasian plate and Indian plate, which is currently undergoing a drift because of its natural course which results in the development of new low-angle thrust faults in the Kutch region. Hence, this scenario requires engaging with the diverse climatic, geographical, and socioecological contexts of the Kutch region and informing the construction systems in a responsive manner with the locally available materials and resources.

Post the 2001 earthquake, there was a need for widespread reconstruction of dwellings in the urban and rural settings all across the region. While there were interim and temporary shelters constructed as a measure of rehabilitation, there was a need to address human habitation through long-term sustainable practices in order to strengthen the resilience and disaster preparedness of the communities. This observed emergence of a complex participatory process of reconstruction of habitation where the communities, artisans, and community-centric developmental organizations came together to discover the potentials of the local construction techniques, local materials, and the manner in which dwelling types have evolved with time and sustained over many centuries. This was coupled with the evolution of form, refinement of construction systems, and improvisation of material composition and details as a learning from the past series of catastrophic events.

This paper investigates varied geographical conditions across the region of Kutch and the construction systems which have evolved in a responsive manner post-earthquake. It entails analytical narratives on the dwellings in the region of Dhragawandh, Banni, Reha, Anjar, Bhujodi, and Bhuj. It would also reflect upon the construction details evolved in the city of Bhuj by Hunnarshala Foundation for varied building components as a cross-learning between similar geographic settings globally.

2 Research Context

After the freedom from colonial rule in the year 1947 AD., Jawaharlal Nehru was elected as the first prime minister of Independent India. The then prime minister envisioned that the dawn of newly found national freedom should evolve from the after effects of colonial rule and partition and establish a liberated, forward-looking state that was truly modern. The journey began with Jawaharlal Nehru entrusting Swiss–French modernist icon Le Corbusier to design the master plans for the city of Chandigarh and briefed in 1950 AD that "Let this be a new town, symbolic of freedom

of India unfettered by the traditions of the past… an expression of the nation's faith in the future" [2].

This modernist architecture and style became a preferred mode of urbanism, style of architecture, and people's lifestyle [5, 10]. The utopian ideals of modernism provided India with a belief and hope to overcome its issues of caste divide and social inequality through the newly found space design approach [3]. However, in the subsequent decades, modernist architecture altered into a design practice that was heavily imitated and imported from Western architectural ideas. As a result of this, India in subsequent years witnessed heavily transplanted, and featureless building blocks which have failed to respond to site, sociocultural and ecological context, and human comfort conditions [11].

Indian architects struggled to get modernist architectural practice to be recognized in the popular imagination because they could not adequately address complex contextual ecological and sociocultural problems in their designs [7]. In the 1970s and 1980s, Revathi Kamath, Laurie Baker, Balkrishna Doshi, Charles Correa, Raj Reval, Achyut Kanvinde, and other Indian architects started integrating ideas of significant regionalism, using local materials, and other design features to combat the rising misinterpretation of the modernist architecture [6, 9]. Their architectural space design and construction practice were evolved from the in-depth understanding of the local context, by making use of regional building construction materials, employing indigenous construction techniques, and spatially configuring their built architecture in built forms in a method that was analogous to the traditional architecture of respective regions. Regional assertions in Indian architecture peaked in the year 1980s when various building typologies like cultural institutions, educational institutions, public housing, office buildings, and high-rise buildings were evolving. These evolving space typologies also started integrating the critical regional approach in their designs [1]. Furthermore, the introduction of liberalization policy in the Indian economy in the 1990s brought along a dramatic change in the office typology buildings, which were characterized by comfortable and luxurious office spaces along with the air-conditioned curtain glass building [1]. However, in the subsequent years, the lack of design sensitivity, ecological concerns, human comfort, humanity, and urban sensitivity represented by this "Universal" architectural design approach has stimulated a strong reaction among certain Indian architects in favor of critical regionalism [8]. As India advances toward a bright future in the twenty-first century, regionalist practitioners continue to culturally enrich contemporary Indian society with a potent new architecture [4].

This study focuses on the current construction practices which are built in the region of Kutch after the 2001 earthquake. The study focuses on the collaborations, dynamics, and associations that helped the region to capacitate local communities for the reconstruction of their habitat. In the aftermath of the post-quake reconstruction, the building construction practices focused largely on the regional and indigenous construction methods. This included earth construction, use of local materials, and reuse of debris from the earthquake. These practices were later realized to be invaluable not only for the reconstruction process but also for enduring sustainable development and ecological systems. Integration of modern building science, indigenous

construction practices, regional craftsmanship, and traditional wisdom emerged to deliver a quality building, infrastructure, and reclaimed shared spaces.

3 Methodology

This research aims to give a comprehensive understanding of the steps involved in understanding the post-disaster climate-responsive indigenous and local construction systems of North Gujarat. The methodology is based on the hands-on collaborative training along with community participation.

The process involves collecting data through semi-structured interview, further based on which the prototypes are developed, tested, evaluated, and then executed. Following are the process steps.

1. Discussions with artisans, craftspersons, and the local community were conducted in a semi-structured manner. These discussions were aimed at understanding their method of construction, working knowledge about the local materials as practiced by them, and their knowledge systems. Additionally, the rationale behind their construction techniques and vernacular wisdom was unraveled to learn from the existing buildings constructed by these communities. Outcomes of these discussions were documented through photographs and drawings.
2. Mapping of the construction process and details was done through on-site photographic documentation, semi-structured discussions, hands-on experiments, sketches, and generation of drawings.
3. Generation of prototypes based on the above steps was evaluated. Furthermore, based on the evaluation of the prototype, required changes were incorporated in the design.
4. Working drawing details were made and documented with the working prototype.
5. Execution of the details was done with the help of the local community, artisans, expert craftsmen, and local materials.

4 Discussions and Findings

This section has been divided into three parts which are as follows:

- Indigenous dwelling construction systems—This subsection talks about the findings from the discussions with artisans, craftsperson, and local community that were conducted in a semi-structured manner. Outcomes of these discussions were documented through photographs and drawings.
- Local construction systems of Bhuj—This subsection discusses the local construction techniques that evolved in a participatory manner in the city of Bhuj while working with the local communities, inhabiting the slums.

- Unique Construction Systems and Elements—This subsection discusses the shallow dome construction system, debris block and mud, and fly ash roles.

4.1 Indigenous Dwelling Construction Systems

In the region of Dhragawandh, we observe a unique building typology of Pakkha homes, which are inhabited by the nomadic tribe identified as the Fakirani Jatt community (Fig. 1). These communities migrated from the region of Iraq centuries ago along the trade routes and settled in the ecologically sensitive zones comprising sand dunes. These communities believe in the 'way of living' of continuously moving and never settling down in a particular setting. There are anecdotes and oral traditions which suggest that the day the community settles down permanently in a particular location it will be a doomsday for them. Subsequently, the notions of sustainability are informed by the way the built form is envisaged and also the construction process. The communities keep shifting their locations such that they let the ecosystem of a particular place rejuvenate to its natural condition. With the virtue of the form, these homes can be dismantled with great ease, compacted, and carried over by camels to be shifted to another location and erected there. This as a result aligns with the natural ecological cycles and rhythms making it sustainable to the highest order, where sustainability is realized to its true meaning as being interspecies and intergenerational equity of natural resources. This also makes it a living system which is a closed-loop energy system.

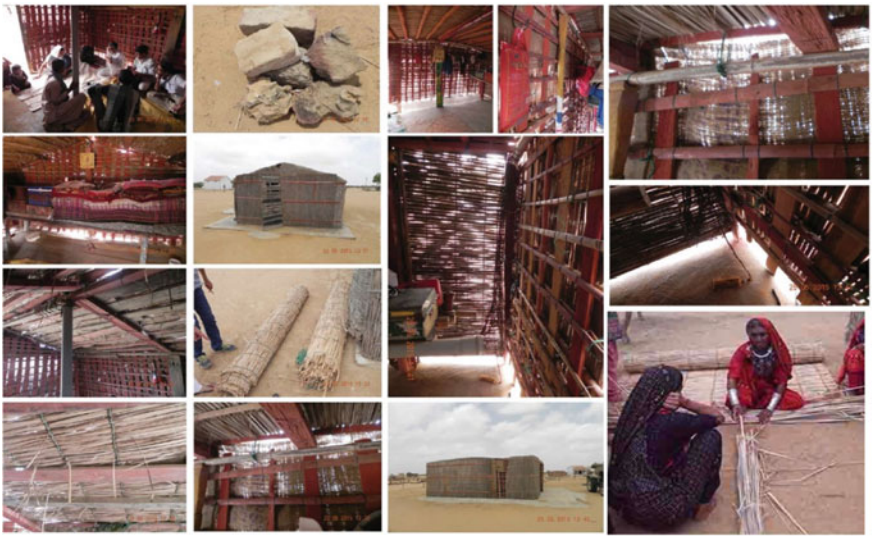

Fig. 1 Pakkha dwellings, Dhragawandh, Kutch (Documented by First Author)

The form of the dwelling is informed in the way whereby it is oriented such that the shorter side (wall) of the home in the plan faces the predominant wind direction. The longer facade is made up of inclined braces of varied types which support the lateral load of the wind on the shorter façade. The pitch of the roof also has an inclination of around 8–15°, which makes them sustain the wind through an aerodynamic geometry. There are openings on the leeward side that are covered with the mats vertically and can be rolled up according to the indoor comfort of the inhabitants.

The Pakkha homes have a masculine part in their making and a feminine part as recognized by the community. This makes for a smart way of incorporating gender equity in the process of making which also is reflected in the aesthetics of the home. The masculine part of the home comprises of wooden posts which are procured from abandoned ships which make that wood most appropriate for this particular region because the wood is highly seasoned and can acclimatize to the shifting weather conditions with regards to humidity, wind, airborne salinity, and sun. The posts are erected within a shallow pit and the foundation base is made strong with the local stone rubble. The wooden posts are also painted with local motifs, which also become an identity of their homes and as they are painted using bright colors they form a contrast with the natural colors of the arid landscape around. The plinth level of the home comprises of shallow stone bed with a layer of PCC (plain cement concrete). This makes it like a floating base that acts similarly in terms of morphology a camels' foot, mimicking the functional attributes. The feminine part of the home comprises of grass mats, which are made up of the local reed known as Kall. These mats are usually woven by women and they use the local fishing net threads to maintain the strength of the mats. This weaving of mats is part of the festivities, which also translates to the celebration of their dwelling and expressing gratitude toward Gaia. The mats act as an external skin to the home mounted over split bamboo which is in turn mounted onto the wooden posts. The climatic response of these mats becomes operational through the optimal light and wind conditions, which it lets inside the home. The majority of light inside the home enters from the base where there is a gap between the mat and datum. There is a small level difference, which makes the sand settle down, accumulate and not enter inside the home. It also becomes instrumental in breaking the sand dunes and inhibits the sand from entering the living spaces. The mats are rolled over the external skin with horizontal as well as vertical striations which makes it highly responsive to the locational setting and offers the inhabitants flexibility to transform the home to the diurnal cycles and shifts. It also acts as an opening on the leeward side, where the grass mat striations are horizon-tally done and the mats can be rolled and adjusted along the vertical surface of the home. Finally, a participatory design process was undertaken with the communities and typologies were evolved as a prototypical system (Fig. 2).

The Banni grasslands observe a unique dwelling form which is known as Bhunga and is inhabited by the Pastoralist Maldhari communities. This building form is unique as it is shaped circular in the plan form, which makes it responsive to the high winds through its aerodynamic design. Post-earthquake reconstruction of these Bhunga homes observed opposite evolution of the materials, which could function more efficiently in an earthquake condition and details which would strengthen the

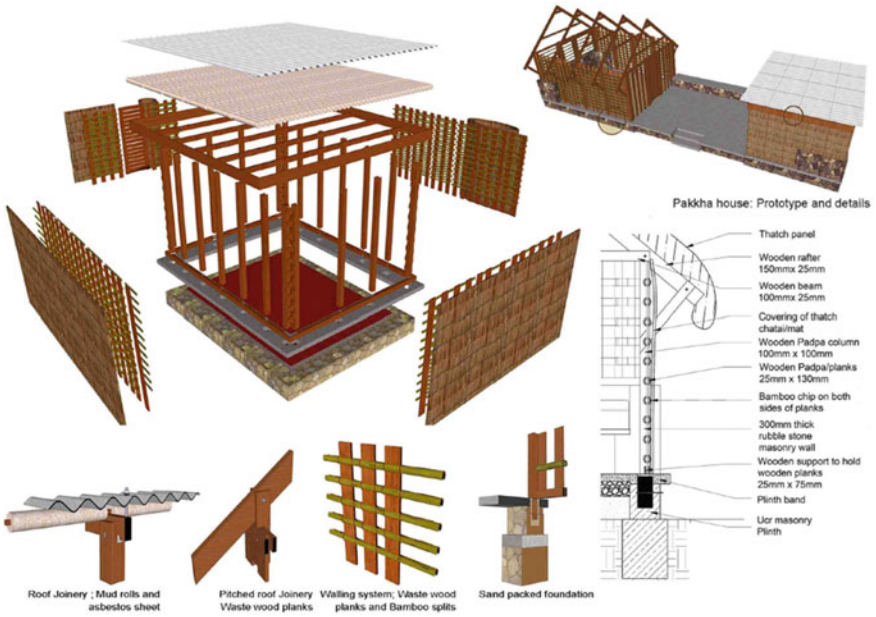

Fig. 2 Participatory design Pakkha dwellings details, Dhragawandh, Kutch (Documented by First Author)

form as a whole. The local communities believed in the notion that the earthquake as a natural phenomenon doesn't necessarily become life-threatening; however, the use of heavy building materials can account for injuries and can cause damage in case of failure. This resulted in deeper participatory processes, where the materials and form were evolved through the incorporation of the indigenous wisdom of the communities and the master artisans and the built environment professionals working in the domain of built environment. In the village of Rudramata, the Bhunga dwellings which were constructed post-earthquake observed many technological interventions. The primary shift in the walling system was made with the use of CSEB blocks (compressed stabilized earth blocks), the proportions of which were determined on the basis of soil testing and the load compressive strength conditions, which were unique to each dwelling cluster. There was also experimentation with the use of the rammed earth technique, which made the process of construction faster as compared to then CSEB blocks; however, it was viable only for mass housing and had limitations of customization in accordance to the inhabitants' needs as the formwork cost was expensive for construction of an individual unit and became viable only when it could be executed in large numbers (Fig. 3).

The roofing structure was evolved to a hexagonal pyramidal form in continuation of the conical roof made of grass. The corner joiner details fixing the roof with the wall were developed to create a triangular chair-like formation fastened using bolts. There were cyclone hooks made using GI wires, which would also hold the roof in

place when exposed to lateral forces. A thick lintel band, plinth band, and sill band were also introduced which strengthened its load carrying capacity and also acted as a tie member in case of a lateral load. The central finial of the home was topped with an inverted Matka (earthen pot), which prevented the water from seepage when lined with cement.

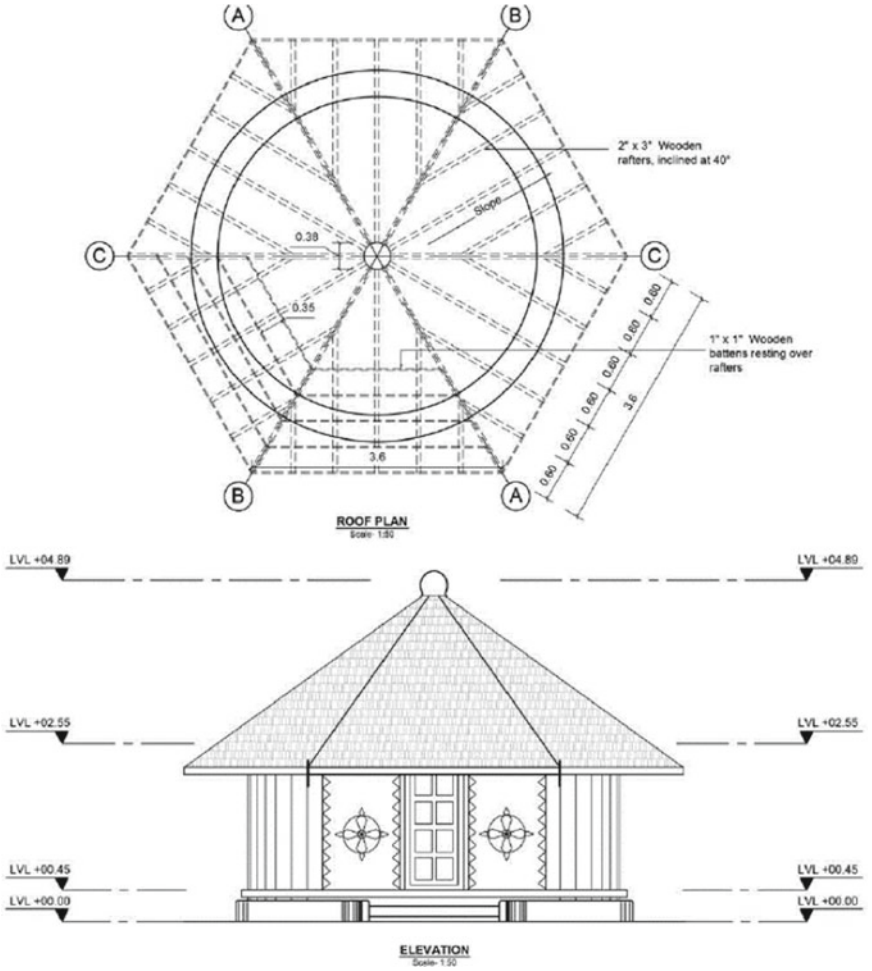

Fig. 3 Bhunga dwellings, Banni, Kutch (Drawn and drafted by First Author)

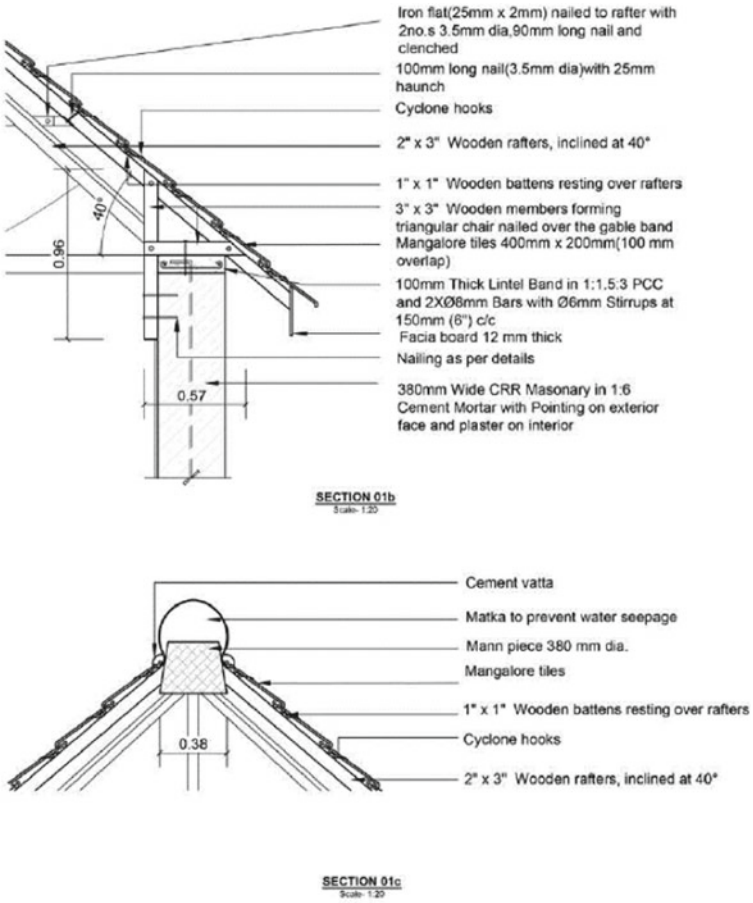

Fig. 3 (continued)

4.2 Local Construction Systems of Bhuj

There were many innovations that emerged as a result of the participatory process addressing the housing for the informal marginalized communities. The traditional Gujarati stone house typology from Reha, Bhujodi was explored in order to retain the ways of living, whereas new spatial configurations emerged as a response to the shift in occupational structures and gender roles. There was a possibility of the unit expanding incrementally; horizontally forming community spaces, workspaces, and vertically, which the inhabitants could add as the family expanded or if there was economic growth. There was the use of reinforced masonry edges, which acted as a composite construction system. The pardi stone which was used as a load-carrying wall masonry had tethered edges at the corner and instead of using four reinforcement bars as used in the conventional frame structures a single bar of heavier

Fig. 4 Gujarati stone house details, Bhuj, Kutch (Documented by First Author)

grade usually 16 mm was used. This reduced the quantity of steel and cement required in the construction process, simultaneously it also drastically reduced the cost of construction making it financially viable for the marginalized and economically poor communities (Fig. 4).

4.3 Unique Construction Elements and Systems

In terms of construction elements, there was significant exploration with regards to walling materials, roofing system, and roof insulation system. Post-earthquake, there was a massive quantity of debris which got accumulated in the natural water systems as a discard and waste. As a response, there was a strategy at the local area level to clear up these lakes, water channels, and streams and use the debris to create debris block, which could be used as a walling material as a building block or as part of the rammed earth system where the aggregates comprised of the debris. Within both of these systems, it is critical to know the composition of debris and use it appropriately with the technical expertise and experience of the master artisans (Fig. 5).

The other system which emerged as a unique roofing technology was the shallow brick domes. This technique has been traditionally common in Uttar Pradesh region of India. However, with the artisans taking the skill forward diminishing in numbers, this technique is dying. During the post-riot rehabilitation work, which was undertaken in the town of Muzaffarnagar, this technique was revived and artisans were

Fig. 5 Debris block details (Documented by First Author)

trained through the process of making their own dwellings. This technique can be instrumental in reducing the quantity of steel and cement drastically making it more economically viable and simultaneously with a lesser ecological footprint. This roofing system comprises of a brick dome, which has a rise of 8–10 in. in the center. This technique can be used for shelters with spans ranging from 3.5 to 7 m. After the shuttering is laid to construct the roof a mud mound is created which becomes the underside of the dome. Then a center is marked and a star pattern is created which is an 8-to-12-pointed star depending on the span of the roof. Then the half-cut CSEB blocks or bricks (Barange) are laid in concentric circles. Subsequently, cement mortar is used to level the upper surface. After the dome roof gains substantial strength after almost 21 days the mud formwork is removed. This technique can be employed in low-cost housing and also can be potentially used in the multistoried construction of homes up to 11 stories (Fig. 6).

As a roof insulation system, there was a construction detail evolved in the form of mud and fly ash roles. This comprised of wooden battens covered with a layer of dried local grass wrapped with mud-soaked gunny bags. After drying and gaining appropriate strength, it is used over the pitched roof with a layer of country tiles. This works as a heat insulation layer for lightweight construction (Fig. 7).

Fig. 6 Shallow brick dome construction process (Documented by First Author)

5 Conclusion

India is a land of diverse culture, language, identity, and comprises varieties of topographical conditions, climate conditions, and enormous micro-contextual histories. Building and expressing this regional identity in architecture is very critical as it helps to construct with traditional wisdom, which in turn ensures human comfort and balanced sustainable development. Additionally, regional construction practices can help counter the homogeneity inherent in "global" architecture language making it truly modern and holistic decolonial development.

This research focuses on the sustainable indigenous and local construction systems and practices of the North Gujarat region of Kutch, which have emerged post-earthquake as a result of collaborative participatory processes between local communities, master artisans, and community-centric developmental organizations.

Based on the studies, the paper can be concluded with three main aspects/learnings.

Fig. 7 Mud and fly ash roles construction process (Documented by First Author)

1. *Understanding of the local building practices*
   It can be inferred from the aforementioned study that there are various ways of engaging with the built form. This engagement could be done by integrating local traditions, artisans, craftsmen, and local communities. This mode of engagement brings out an overall development that focuses on all the aspects of the built environment from designing, detailing, and execution to celebrating life itself. It can be understood from the local construction systems and practices of the North Gujarat region of Kutch that focus on structure, use of local materials, designing as per traditional living patterns can help the occupants achieve a good quality of life as well as overall comfort. This suggests that vernacular building practices should be encouraged in all regions. Disseminating these local practices will provide scientific footing and rationale making them more widely acceptable. There needs to be in-depth research into the design principles and driving forces that produce the traditional architectural forms of a particular region. Furthermore, this disseminated knowledge also needs to be taught to the architectural design students as it will help students to develop a deeper understanding of the traditional and regional architecture of the place.
2. *Building material*
   Building material plays a major role in defining the built environment of the place. Its thermophysical properties help the occupants to stay comfortable indoors regardless of the outdoor weather condition. In the past decade, the construction industry had to evolve with the building construction details, materials, and techniques to meet the rising built space demand. Owing to this the

stakeholders are using the latest building technology in architecture, which helps expedite the construction. While this is a much-needed development and adaptation, we need to be cautious against the use of these modern materials which are solely used to cut down the construction time and add to the aesthetics rather than the functionality of the building. Materials such as glass, concrete, and steel should be used only as suited to a building program and site but not for the bias toward material and greater profit margins. This can be achieved by an appropriate understanding of the materials, their hygro-thermal properties, embodied energy associated with it, and the degree of human comfort that they can offer. Additionally, the first cost and the operational cost also need to be taken into consideration.

3. *Focus on built forms and urban planning*
   While situating their designs in the urban milieu, built forms must be carefully planned in harmony with the ecological settings as it helps to achieve sustainability and environmental balance. Currently, the contemporary approach to the built environment is generating stand-alone buildings, which are largely neglecting the relationship between a building, its immediate environment, and the regional context. This in turn hampers the ecological balance of the region. Furthermore, existing planning norms in the country are derivatives of the modernist principles that dampen a harmonious relationship between built forms and their surrounding site context. This is a very pressing issue and it needs to be addressed through the national and regional policy framework.

To conclude, the authors recognize the difficulties and challenges that are faced by the architects and designers in building while keeping regional architecture in mind. However, as per the study mentioned and explained in this paper, it lays paths for building with regional architecture which is expected to gain importance in the future owing to its overall balanced and sustainable methods of building. It can be safely reckoned that although greater technological progressions will emerge in the future, the intricacies of different cultures and regions would continue to exist and we would need to integrate that into architecture not just to retain regional cultural identity but also to achieve balanced overall development.

References

1. Bahga S, Raheja G (2018) An account of critical regionalism in diverse building types in postcolonial Indian architecture. Front Archit Res 7(4):473–496. https://doi.org/10.1016/j.foar.2018.09.001
2. Frederick N (2017) Chandigarh: India's modern dream—studio Nicholson. Retrieved 10 Sept 2021, from https://www.studionicholson.com/blogs/features/chandigarh-india-s-modern-dream
3. Gupta S, Kalamdani K (1998) Architecture: India 50 years of independence 1947–97: status, growth & development. B R Publishing. Retrieved from https://scholar.google.com/scholar?q=Architecture: India 50 Years of Independence 1947–97: Status, Growth Development

4. Jain U (2000) Regionalism-what regionalism? Architecture design. Retrieved from https://www.proquest.com/openview/24d719a3eb3cf45917e373b78ec658bc/1?cbl=1816889&pq-origsite=gscholar
5. Kassim SJ, Nawawi NM, Ibrahim M (2018) Modernity, nation and urban-architectural form: The dynamics and dialectics of national identity vs regionalism in a tropical city. Modernity, nation and urban-architectural form: the dynamics and dialectics of national identity versus regionalism in a tropical city, (May 2019), 1–264. https://doi.org/10.1007/978-3-319-66131-5
6. Lang J (2002) A concise history of modern architecture in India. Permanent black. Retrieved from https://books.google.co.in/books?hl=en&lr=&id=gxyGbhlKQXQC&oi=fnd&pg=PP12&ots=ijKZP52H_g&sig=Je0w4MF4G_TdX5wNrManHK2BX_k&redir_esc=y#v=onepage&q&f=false
7. Mehrotra R (2011) Mehrotra: architecture in India: Since 1990. Pictor Bombay. Retrieved from https://scholar.google.com/scholar_lookup?title=Architecture in India since 1990&publication_year=2011&author=R. Mehrotra
8. Menon AGK (2000) Interrogating modern Indian architecture. Archit Plus Des. Retrieved from https://www.proquest.com/openview/a8c8e438b7562b4832a4a04bbe8927c1/1?pq-origsite=gscholar&cbl=1816889
9. Misra S, Chakraborty M, Mandal NR (2018) Critical regionalism in the post-colonial architecture of the Indian subcontinent. J Archit Urban 42(2):103–111. https://doi.org/10.3846/jau.2018.6140
10. Prakash G (2010) Contributors: In: Prakash G (ed) Noir urbanisms: dystopic images of the modern city. Princeton University Press, pp 261–264. https://doi.org/10.1515/9781400836628.261
11. Shah J (2008) Contemporary Indian architecture. Lustre Press, Roli Books. Retrieved from https://scholar.google.com/scholar_lookup?title=ContemporaryIndianArchitecture&publication_year=2008&author=J.Shah

A Study of the Impact of Soil–Structure Interaction on Multi-storey Structure with Varying Hill Slopes

Thushar S. Shetty and Vasudeva Kamath

Abstract The primary goal of this study is to examine the structures built on sloping terrain, which are especially sensitive to earthquakes owing to their irregular design and elevation. Soil–structure interaction (SSI) is often overlooked while studying structures under seismic loads. A summary of the research on the seismic behavior of buildings resting on the sloping ground has been presented. The seismic behavior of structures on sloping terrain is observed to be different from that of other buildings. The influence of slope angle variations for buildings erected on hilly terrain has been investigated in this study, in which both fixed and flexible structure bases (SSI) are taken into account. The findings from this work suggest the criticality related to increasing slope angle, both with and without considering SSI. The significance of taking SSI into account when performing seismic analysis has also been justified.

Keywords Slope angle variation · Soil–structure interaction · Response spectrum analysis · Hilly terrain · Storey displacement · Storey drift · Base shear

1 Introduction

1.1 General

The interaction between soil (ground) and a structure erected on it is recognized as soil–structure interaction (SSI). It is essentially a mutual stress exchange, in which the type of ground as well as the kind of construction both influence the development of the ground-structure framework. This is especially true in seismically active places. Different soil and structural combinations can either enhance or reduce development and the associated harm. In general, a structure built on solid ground rather than malleable ground will suffer more significant damage [1].

Strong earthquakes hit diverse parts of the planet, obliterating life and all kinds of structures. Structures with anomalies are the most sensitive to earthquake loading,

T. S. Shetty (✉) · V. Kamath
Department of Civil Engineering, NMAM Institute of Technology, Nitte, Karnataka, India
e-mail: shettythushar@nitte.edu.in

L. Nandagiri et al. (eds.), *Recent Advances in Civil Engineering*, Lecture Notes in Civil Engineering 256, https://doi.org/10.1007/978-981-19-1862-9_64

despite the fact that all structures are vulnerable. Construction on the slopes is necessary due to the shortage of flat ground in the hilly terrain [2]. Earth excavation is a costly and time-consuming method of preparing plain areas for development; yet, it damages the natural beauty of environments. Because of the land improvement, financial growth and rapid urbanization have been energized in these inclining places. As a result, there has been a rise in population density dramatically, and the hilly regions have an imbalanced land accessibility-to-land-need ratio. As a result, the construction of multi-storey structures on slope slants has become well-known. When planning, it should be seen that constructions on slants are not the same as those on flat terrain, in that they are very eccentric and unsymmetrical in both the horizontal and vertical planes. Consequently, the centers of mass and rigidity on different levels do not coincide since the mass and stiffness of such structures vary in vertical and horizontal planes, and the structures twist. Evaluate the behavior of these structures in order to make them earthquake resistant and preventing their downfall, in order to limit the number of people killed and property lost. Because of the incompatibility of mountainous slopes, the influence of slope variation on earthquake-prone constructions should be investigated. The foundations of constructions are frequently assumed to be fixed. It is presumed that the bases are indefinitely stiff. And that is incorrect since the ground beneath the building is pliable; therefore, SSI should be included to obtain the structure's appropriate reaction [3].

In a seismic study, providing one of the most significant options is a bracing system for ensuring that the structure is strong and stiff enough to withstand lateral stresses. The most efficient bracing systems in terms of SSI impact stability must be assessed because the distinctive configuration of various braces modifies the reaction of buildings [4, 5]. Scarfone et al. [6] quantified SSI consequences for a 20-storey structure using time–space 3D nonlinear dynamic studies and an elastoplastic nonlinear constitutive model for the soil. According to their findings, an upsurge in deformability of the foundation causes a reduction in the extreme base shear strength. Mohasseb et al. [7] investigated the impact of soil pile–structure interaction (SPSI) pressures on the seismic response of two giant, enormous structures. They came to the conclusion that the enhanced cone model might be used to analyze foundation vibration and dynamic soil–structure interactions in the actual world advances in engineering since it is advantageous, rapid, and precise. Ghosh and Debbarma [8] performed a study on the effect of inclination angle variation on structures that rest on sloping terrain. They came to the conclusion that increasing the slope angle has a negative influence on structures sitting on sloping land, and that special thought should be given to the construction of columns on the upper levels of the gradient of structures. Akhtarpour and Mortezaee [9] studied the solidifying soil models having small strain stiffness (HS-small) utilized to dissect a 17-storey structure situated close to a deep unearthing using three methodologies: utilizing a fixed base construction model, utilizing soil–structure interaction model, and utilizing a soil–structure excavation interaction model. Based on seismic examination data, they suggested that base shears in two interaction models are less than the fixed-based model's base shear. Hassan and Pal [10] performed nonlinear time history and response spectrum analysis using ETABS software to consider the impact of soil form underneath the detached base.

They discovered that a design's ghostly reaction is linked to soil conditions. They assumed that the hard and medium soils were assessed to be appropriate for base detachment construction.

From a thorough review of the above literature, it can be found that while analyzing a structure, the SSI effect plays an important role, especially in structures located in hilly terrain. Also, the slope angles and soil types contribute to the stability of the structure. Hence in this work, an effort has been made to address these issues and the same has been stated in the objectives.

2 Objectives

This work has the following objectives:

1. Study the seismic behavior of the structures located on flat terrain and structures located in hilly terrain with and without SSI consideration.
2. Investigation of the impact of varying slope angles on structures resting on sloping terrain.
3. Stability checks of the structure on the different soil types in hilly region.
4. Performance study of the bracing system in the structures on hill slopes.

3 Methodology

3.1 General

The following step-by-step procedures have been used to accomplish the stated objectives:

- A thorough literature review was conducted in order to identify the objectives of the current work.
- Understanding the soil–structure interaction on plain terrain and hilly terrain.
- Analyzying of all models with response spectrum analysis using ETABS software by applying design loads as per IS 875 was carried out.
- Evaluating the results of the above said analysis and investigating the necessity of the geometrical restrictions (Fig. 1).

3.2 Selection of Parameters for Modeling

For modeling the structures, various parameters such as number of bays, column sizes, beam sizes, and loads have been considered based on the literature reviews.

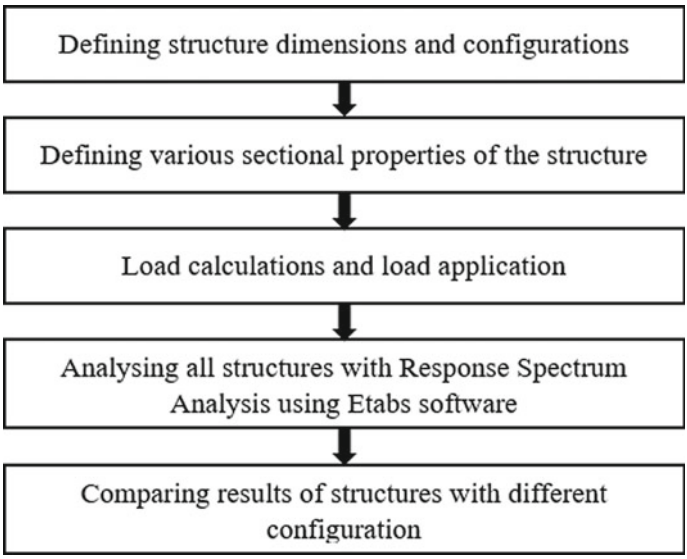

Fig. 1 Flowchart

For the purpose of this study, a $G + 15$ storey RC structure with 7 bays in longitudinal and 5 bays in transverse directions has been considered.

3.3 Sectional Properties

The sectional properties for the analysis of RC framed structure in this study were considered by the trial-and-error method. The column size of 600 mm × 600 mm has been used from base to storey 5, column size of 500 mm × 500 mm from storey 6 to storey 10, and the column size of 400 mm × 400 mm has been assigned from storey 11 to storey 15. The beam size of 300 mm × 400 mm and 150-mm-thick slab has been considered for the entire structure.

3.4 Loads

The load assigned for the structure is shown in Table 1. The seismic loads are applied as per IS 1893–2016. As this study is on a structure on hilly terrain, zone-V is considered which is the most seismic active region covering the northeastern regions of India. As per this zone, the seismic zone factor is considered 0.36 and the importance factor is 1.5, which is mentioned in Table 6 of IS 1893-2016. The response reduction factor has been considered as 5.

Table 1 Loads assigned to the structure

Type of load	Value
Dead load on the walls	$19.1 \times 0.23 \times (3 - 0.4) = 11.42$ kN/m
Dead load on the slab	$(0.15 \times 25) + 1$ kN/m^2 $= 4.75$ kN/m^2
Live load	3 kN/m^2

Table 2 Details of soil parameters (obtained from IBC Code 2006)

Description	Hard soil	Medium soil	Soft soil
Mass density of soil, ρ (kN/m^3)	18	16	15.5
Shear wave velocity, Vs (m/s)	520	240	120
Poisson's ratio, μ	0.25	0.35	0.45
Shear modulus, G (kN/m^2)	4867.2×10^3	921.6×10^3	223.2×10^3

3.5 Soil Characteristics

The response of the structure is influenced by the dynamic analysis of the structure and its interaction with the material (foundation soil) beneath it. The foundation–soil interaction is determined by the elastic features of the foundation soil and the foundation dimensions. The analysis considers foundation flexibility by replacing the foundation with statically equivalent springs. The details of the soil parameters have been tabulated in Table 2.

The shear modulus (G) in Table 2 has been determined using the formula shown in Eq. (1).

$$G = V_s^2 \times \rho \tag{1}$$

3.6 Foundation Characteristics

The modeling of foundation soil has been done using spring constants, as shown in Table 3, in accordance with George Gazetas' equations (1991).

In Table 3, B is the half-width and L is the half-length of a rectangular foundation. The terms I_{bx}, $I_{by,}$ and I_{bz} are the moment of inertia of the foundation area with respect to the longitudinal, lateral, and vertical axis, respectively, and A_b is the area of the foundation (Table 4).

Table 3 Stiffness and co-efficient for randomly shaped foundations on the surface of homogeneous half-space equations

Mode of vibration	Stiffness (K)
Horizontal (K_x) (longitudinal direction)	$K_x = \frac{2GL}{(2-\mu)}\left(2 + 2.5x^{0.85}\right) - \left[\frac{0.2}{(0.75-\mu)}\right]GL\left(1 - \frac{B}{L}\right)$
Horizontal (K_y) (lateral direction)	$K_y = \frac{2GL}{(2-\mu)}\left(2 + 2.5x^{0.85}\right)$
Vertical (K_z)	$k_z = \frac{2GL}{(1-\mu)}\left[0.73 + 1.54x^{0.75}\right]$
Rocking (K_{rx}) (about longitudinal, x-axis)	$K_{rx} = \left[\frac{3G}{(1-\mu)}\right]I_{bx}^{0.75}\left(\frac{L}{B}\right)^{0.25}\left[2.4 + 0.5\left(\frac{B}{L}\right)\right]$
Rocking (K_{ry}) (about lateral, y-axis)	$K_{ry} = \left[\frac{3G}{(1-\mu)}\right]I_{by}^{0.75}\left(\frac{L}{B}\right)^{0.15}$
Rotation (K_t)	$K_t = 3.5GI_{bz}^{0.75}\left(\frac{B}{L}\right)^{0.4}\left(\frac{I_{bz}}{B^4}\right)^{0.2}$
Area (x)	$x = \frac{A_b}{4L^2}$

Table 4 Soil spring stiffness (kN/m)

Type of soil	Hard soil	Medium soil	Soft soil
Horizontal (K_x) (longitudinal direction)	264.0×10^5	499.88×10^4	121.06×10^4
Horizontal (K_y) (lateral direction)	264.0×10^5	499.88×10^4	121.06×10^4
Vertical (K_z)	334.85×10^5	634.04×10^4	153.55×10^4
Rocking (K_{rx}) (about longitudinal, x-axis)	368.05×10^4	696.91×10^3	168.78×10^3
Rocking (K_{ry}) (about lateral, y-axis)	173.71×10^5	328.92×10^4	796.62×10^3
Rotation (K_t)	128.23×10^5	242.81×10^4	588.07×10^3

3.7 Footing

The footing of the structure considered in this study has a length (L) of 2.2 m and width (B) of 2.2 m. The depth of footing (d) is taken as 0.8 m with the depth of foundation from ground level (D) as 1.5 m. The depth of centroid of effective sidewall contact (h) is taken as 1.1 m.

3.8 Modeling

The structure has been modeled using ETABS software and the above-mentioned loads and parameters were assigned (Figs. 2, 3, 4, 5, and 6; Table 5).

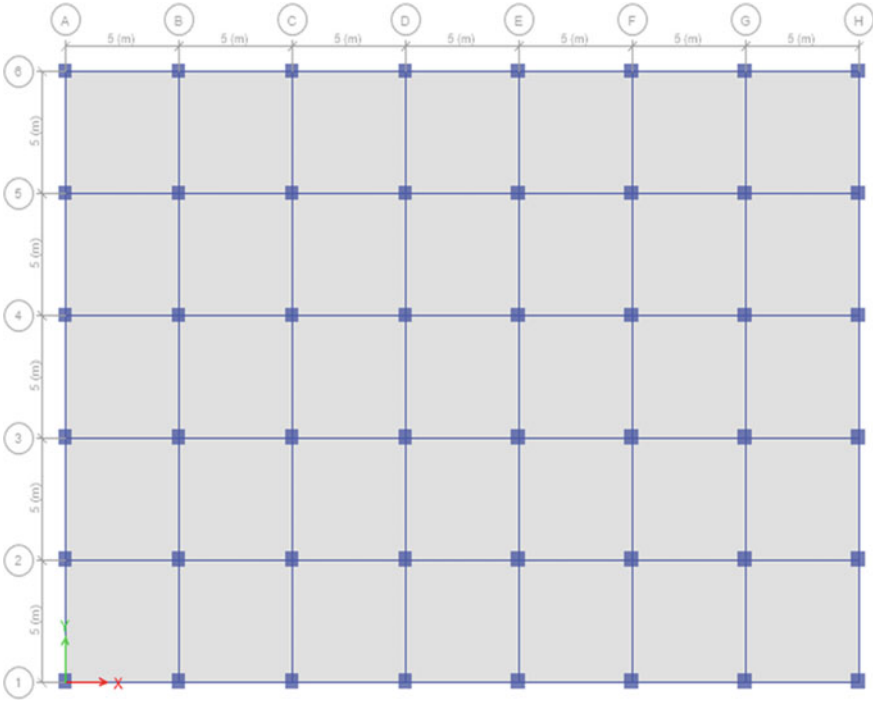

Fig. 2 Column positions in the ETABS model

Fig. 3 3D view of the ETABS model

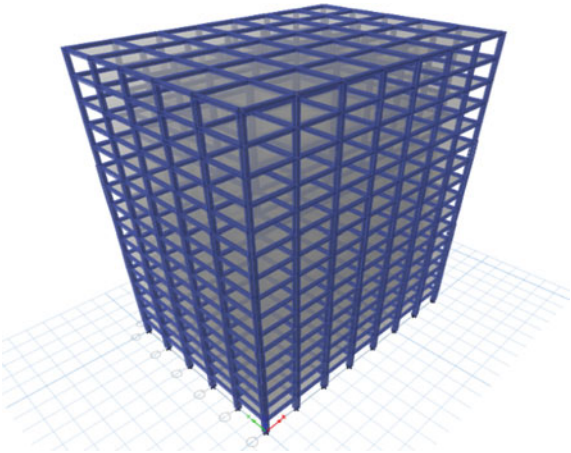

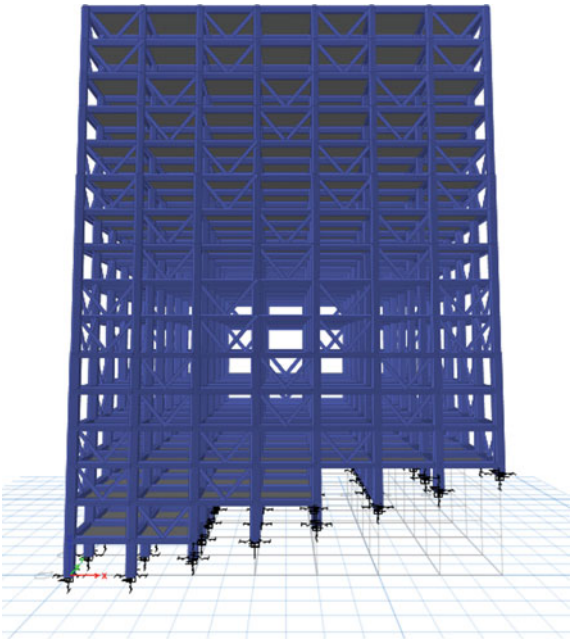

Fig. 4 3D view of 15° model with SSI

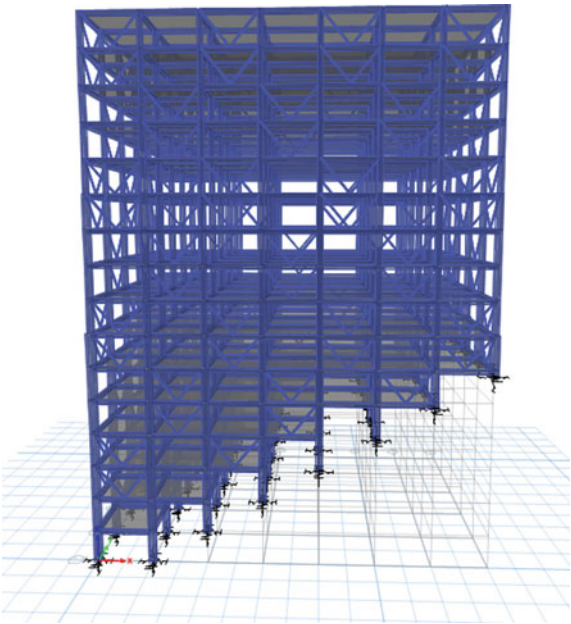

Fig. 5 3D view of 30° model with SSI

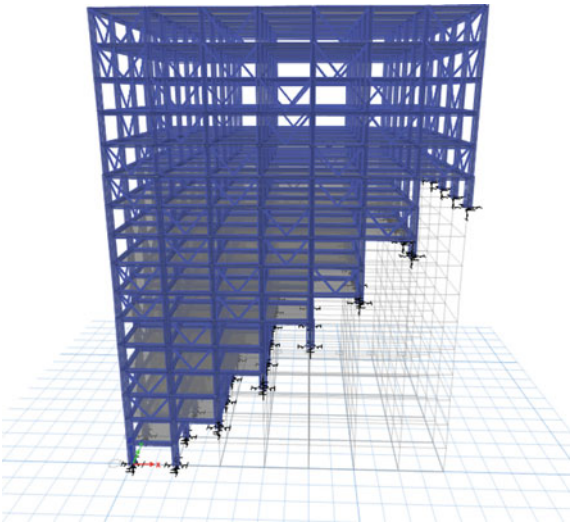

Fig. 6 3D view of 45° model with SSI

Table 5 Description of the models prepared

Model No.	Description
Model-I	Structure with fixed base in 0° slope
Model-II	Structure with fixed base in 15° slope
Model-III	Structure with fixed base in 30° slope
Model-IV	Structure with fixed base in 45° slope
Model-V	Structure with SSI at base in 0° slope
Model-VI	Structure with SSI at base in 15° slope
Model-VII	Structure with SSI at base in 30° slope
Model-VIII	Structure with SSI at base in 45° slope

4 Results and Discussion

Once the modeling was complete, the model was checked and analyzed. The various parameters that included maximum storey displacements, storey drift, and base shear values were extracted from the software.

4.1 Maximum Storey Displacements

The overall displacement of the top storey from the base is referred to as maximum storey displacement. The following graphs show the comparison of various parameters between the models considered in this study (Figs. 7, 8, 9, 10, 11, 12, 13 and 14).

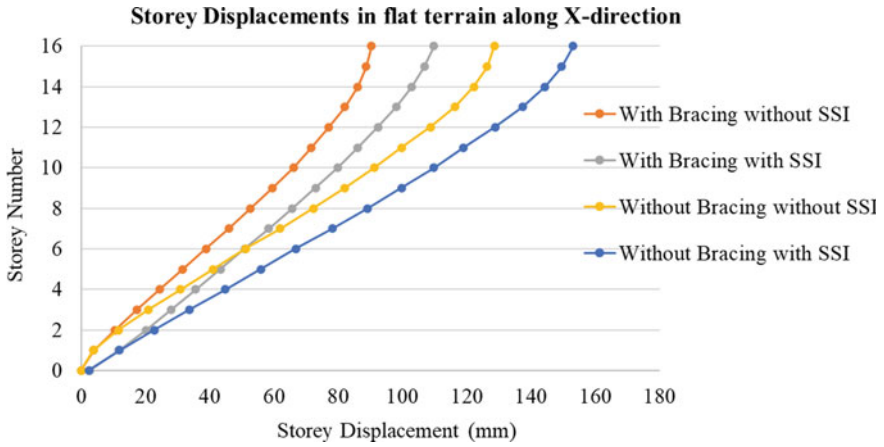

Fig. 7 Displacements in flat terrain along the *x*-direction

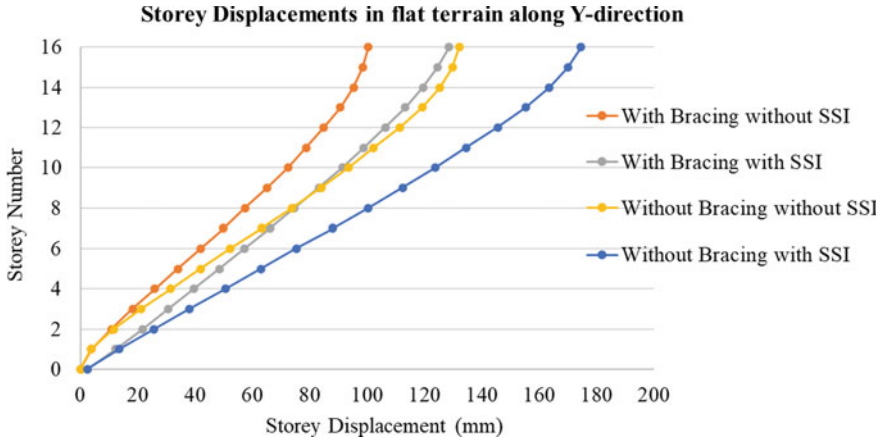

Fig. 8 Displacements in flat terrain along the *y*-direction

4.2 Comparison of Maximum Storey Displacement

See Figs. 15, 16, and 17.

4.3 Storey Drifts

See Figs. 18, 19, 20, 21, 22, 23, 24, and 25.

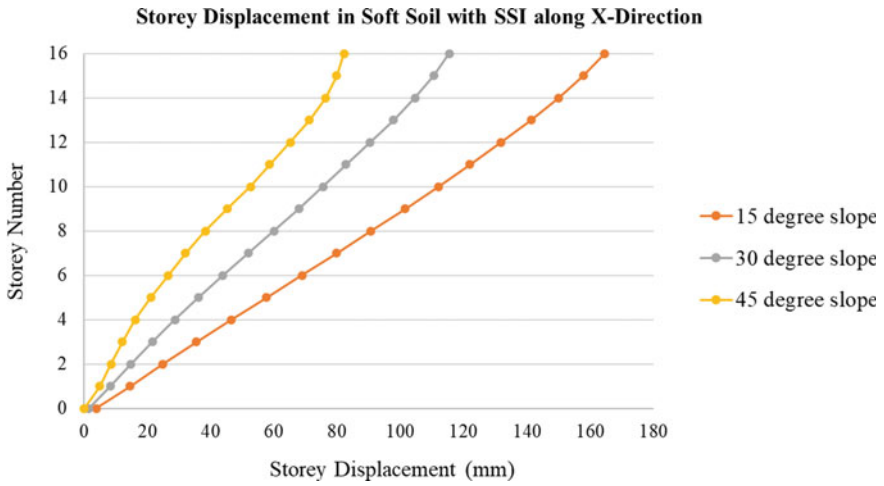

Fig. 9 Displacements in soft soil along the *x*-direction

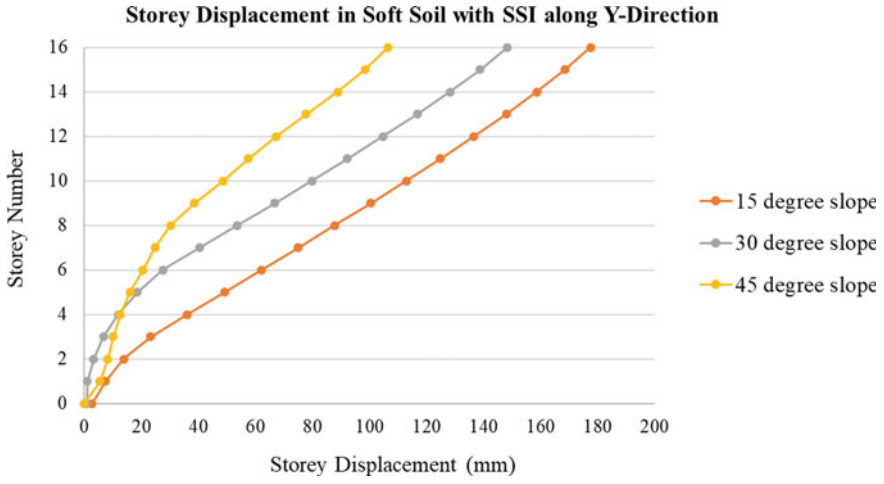

Fig. 10 Displacements in soft soil along the *y*-direction

4.4 Comparison of Maximum Storey Drift

See Figs. 26, 27, and 28.

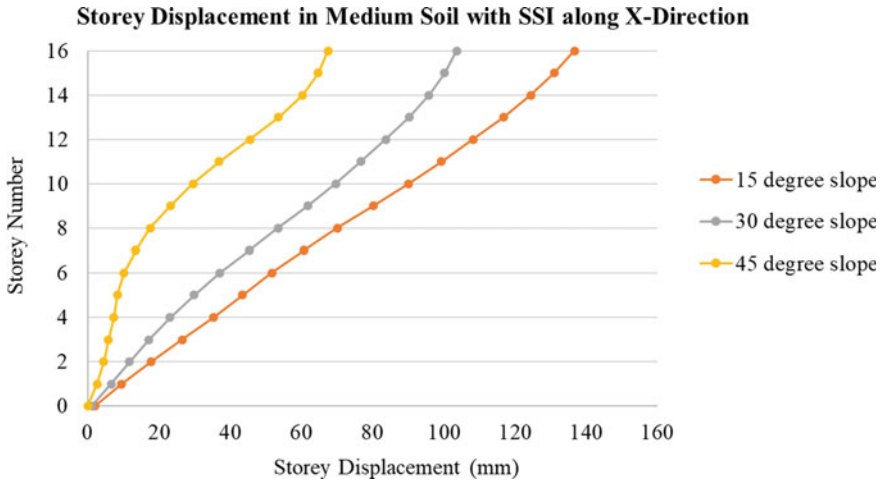

Fig. 11 Displacements in medium soil along the *x*-direction

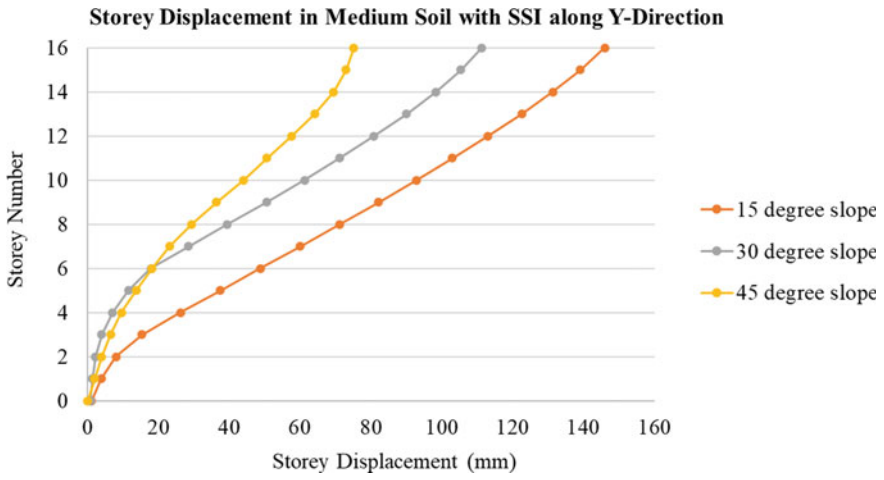

Fig. 12 Displacements in medium soil along the *y*-direction

4.5 Natural Time Period

The structure is evaluated using modal analysis as a continuous model with a determinate quantity of natural frequencies and degrees of freedom. There are several key elements that impact the structure's seismic behavior, among them, one of the significant factors is the natural time period of the building. Hence, this study has been carried out which shows the results that demonstrate the fundamental time period for structures resting on various slopes and soil profiles (Figs. 29, 30, 31, 32).

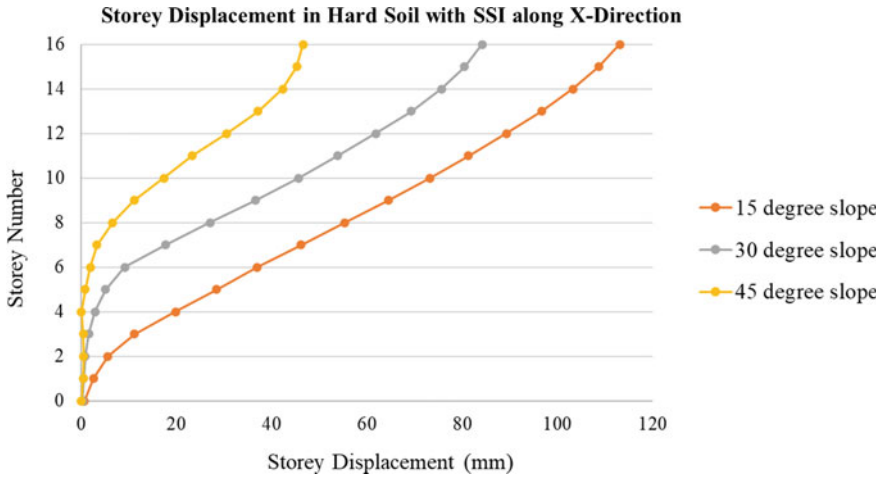

Fig. 13 Displacements in hard soil along the *x*-direction

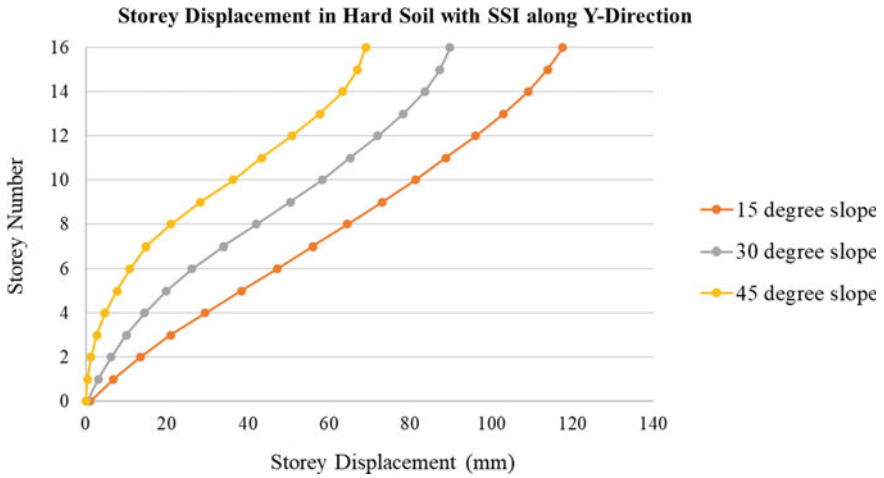

Fig. 14 Displacements in hard soil along the *y*-direction

4.6 Seismic Base Shear

One of the primary factors for seismic design is the seismic base shear, which particularly reflects lateral weakness. The variation in base shear for structures resting on different slopes and soil profile is shown below. The decrease in base shear is mainly due to the displacement of the foundation on flexible soil (Figs. 33, 34, 35, 36).

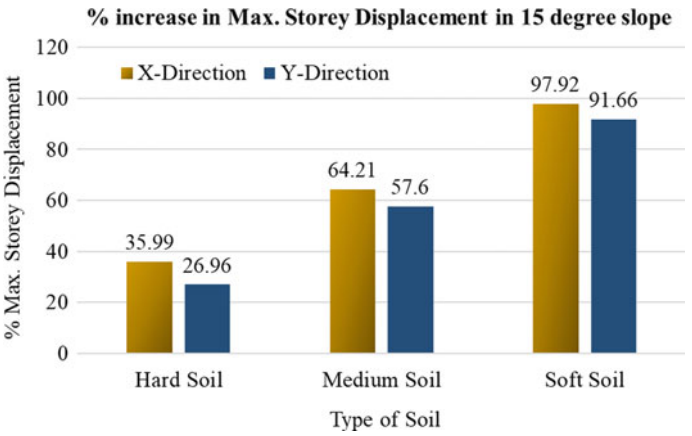

Fig. 15 Percentage increase in maximum storey displacement in 15° slope

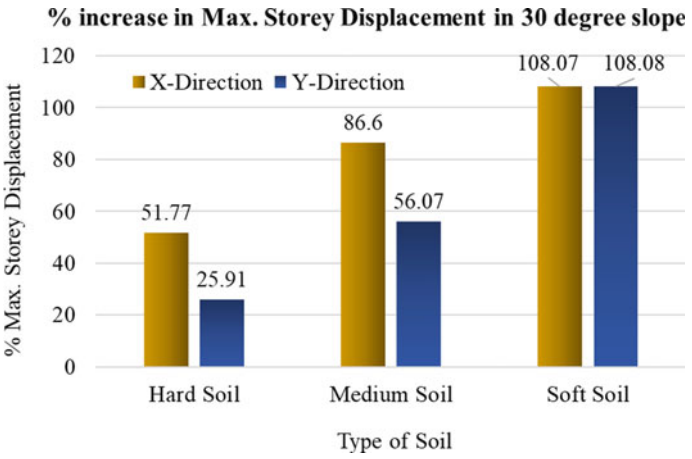

Fig. 16 Percentage increase in maximum storey displacement in 30° slope

5 Conclusion

In this present work, RC building of $G + 15$ storeys with different slope angles have been investigated with and without incorporating SSI. Soil springs have been used to incorporate SSI. The seismic performance of a flexible base is compared with that of a fixed base in terms of storey displacement, storey drift, time period, as well as base shear.

The following conclusions may be drawn from the results given in relation to the structural models considered:

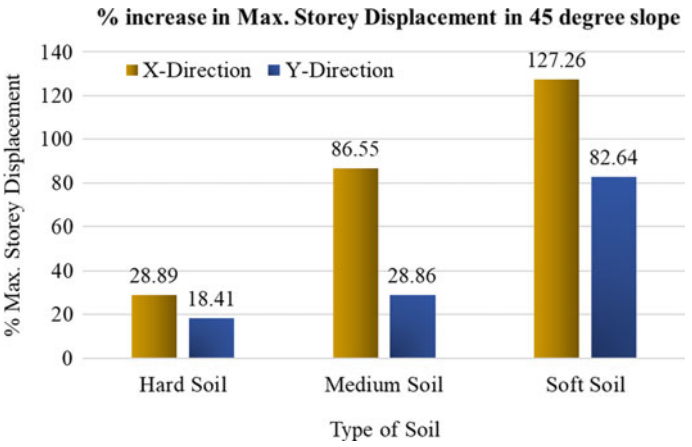

Fig. 17 Percentage increase in maximum storey displacement in 45° slope

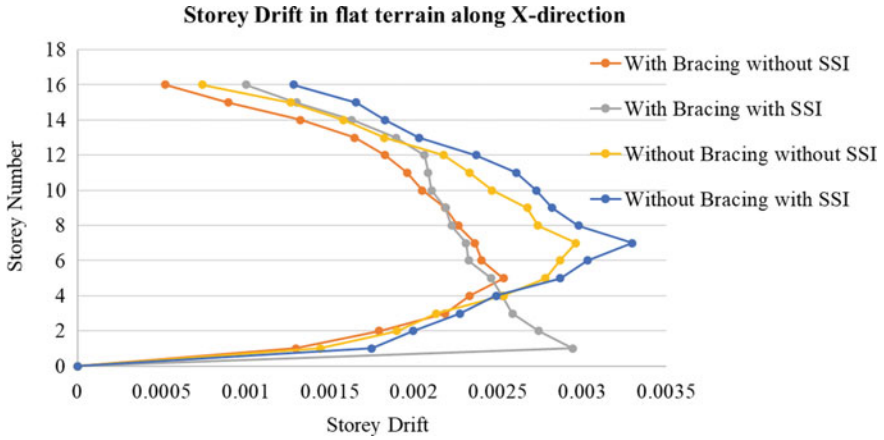

Fig. 18 Storey drift in flat terrain along the *x*-direction

- The effect of SSI on storey displacement of $G + 15$ storey structure is evaluated. According to the findings, displacement intensifies in models with SSI.
- The values of storey displacement, storey drift, and time period are magnified due to the effect of SSI. These reaction characteristics are greatest in soft soil.
- Soil–structure Interaction effect leads to the reduction of base shear of the building.
- Soft soil shows a greater reduction of base shear as compared to hard soils. That is, 21.79 and 18.29% reduction in *x*- and *y*-directions in 15° models, 17.48 and 19.17% reduction in *x*- and *y*-directions in 30° models, 15.83 and 19.58 reduction in *x*- and *y*-directions in 45° models).

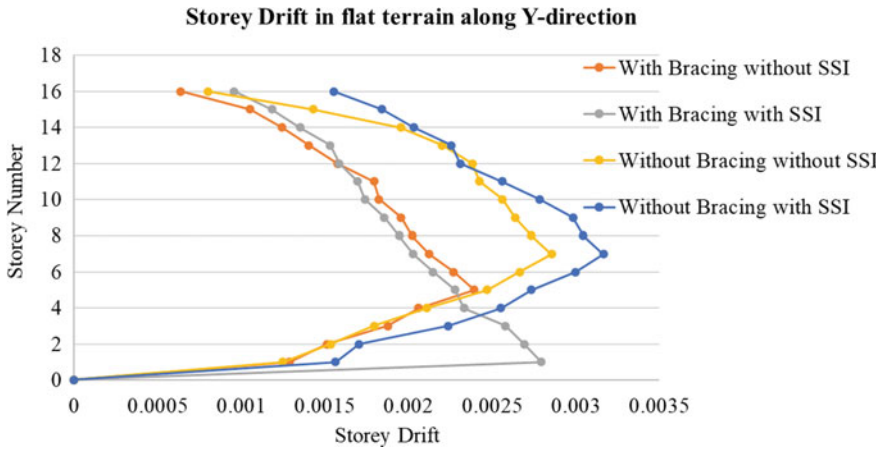

Fig. 19 Storey drift in flat terrain along the *y*-direction

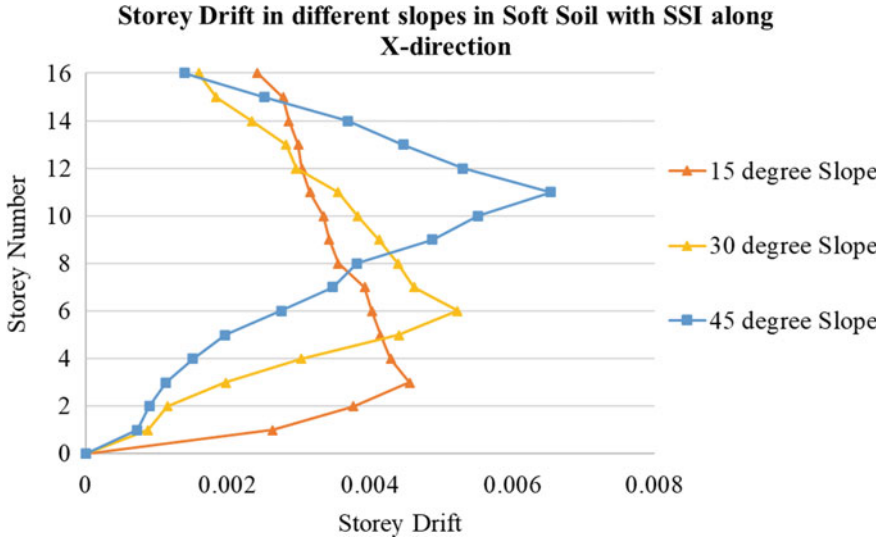

Fig. 20 Storey drift in soft soil with SSI along the *x*-direction

- Increase in slope angle results in a decrease of maximum storey displacement. That is, 50.09% reduction in the *x*-direction and 39.99% reduction in the *y*-direction in 45° models when compared with 15° models.
- As slope angle is increased, storey drift also increased enormously. Storey drift is increased by 14.83% and 19.56% in *x*- and *y*-directions in 30° models when compared with 15° models, 43.77 and 43.71% increase in *x*- and *y*-directions in 45° models when compared with 15° models.

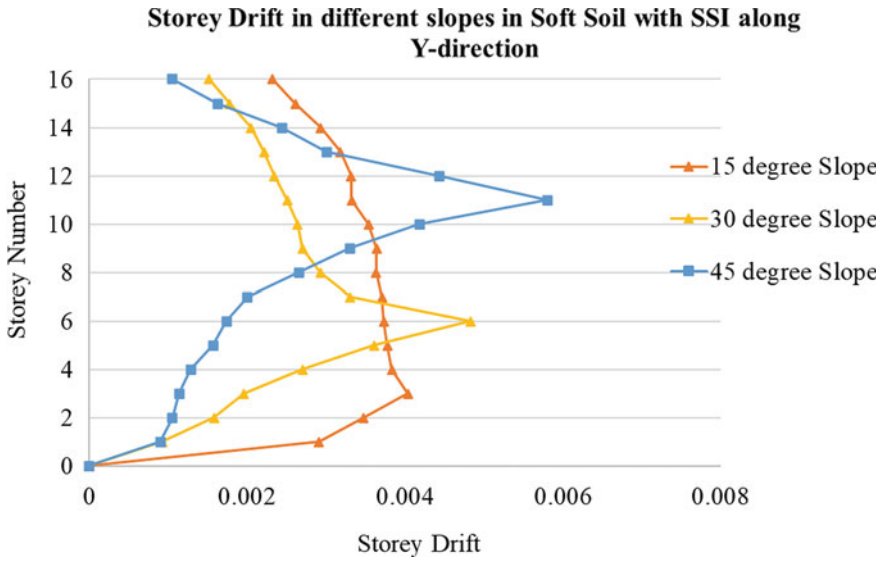

Fig. 21 Storey drift in soft soil with SSI along the *y*-direction

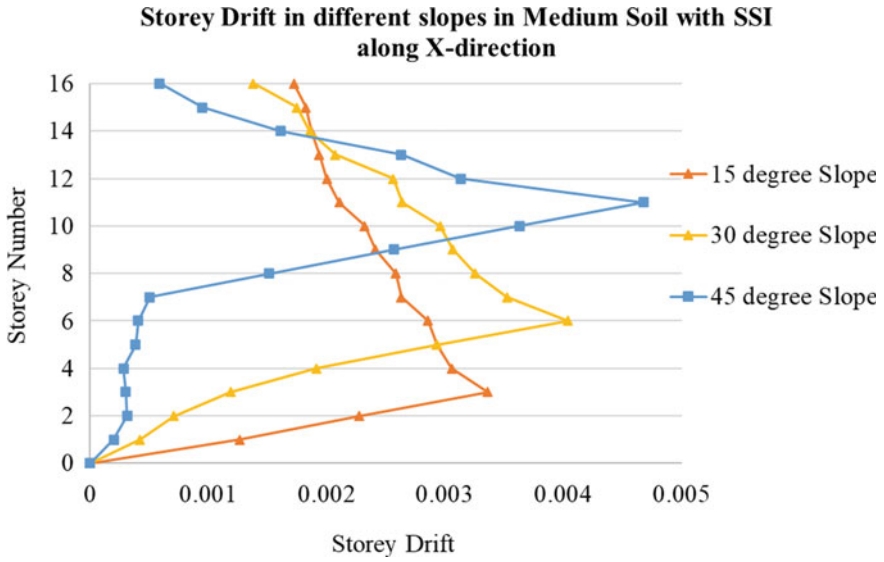

Fig. 22 Storey drift in medium soil with SSI along the *x*-direction

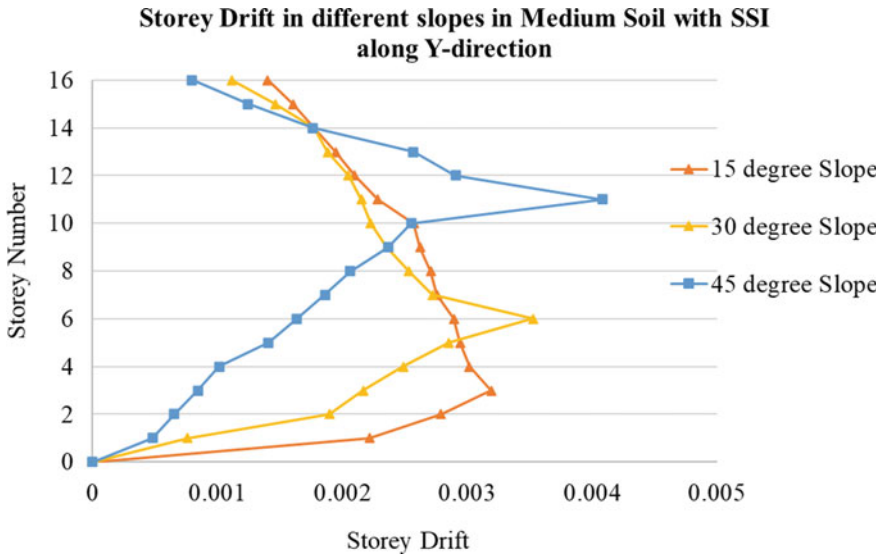

Fig. 23 Storey drift in medium soil with SSI along the *y*-direction

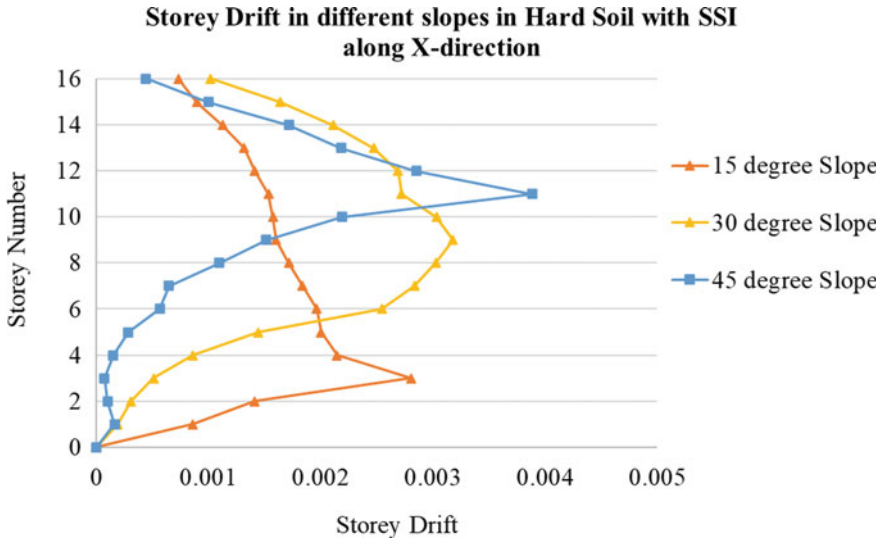

Fig. 24 Storey drift in hard soil with SSI along the *x*-direction

- As the slope angle increases, base shear was also increased. In 30° models, 12.75% increment in *x*-direction and 13.63% increment in *y*-direction were found when compared with 15° models, in 45° models 22.80% increment in the *x*-direction

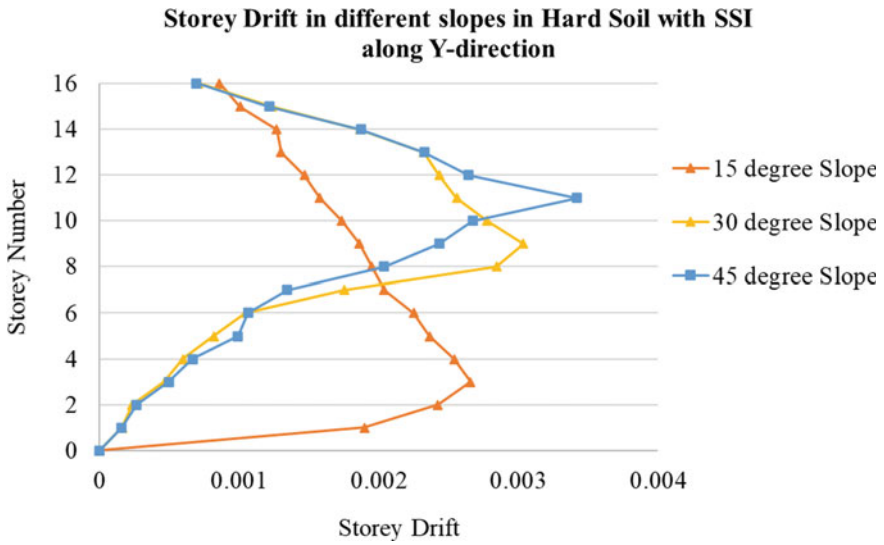

Fig. 25 Storey drift in hard soil with SSI along the *y*-direction

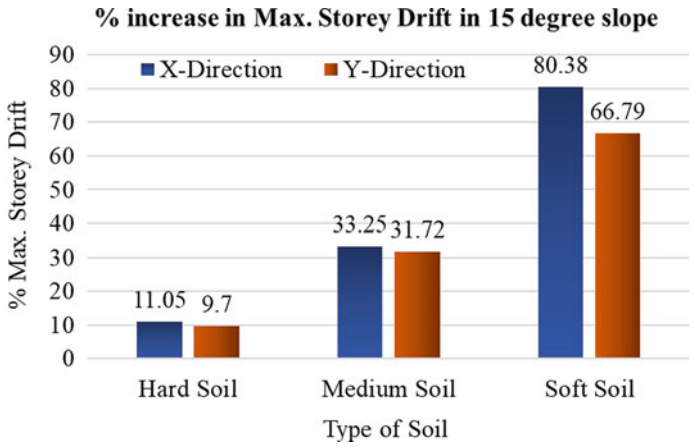

Fig. 26 Percentage increase in maximum storey drift in 15° slope

and 27.75% increment in the *y*-direction was found when compared with 15° models.

- The natural time period was found less in the fixed base as compared with the flexible base (SSI) condition. The reduction in natural time period was found when the slope angle increased. The minimum time period of 1.373 s was found in fixed base of the 45° model and the maximum time period of 4.269 was found in the soft soil of the 15° model.

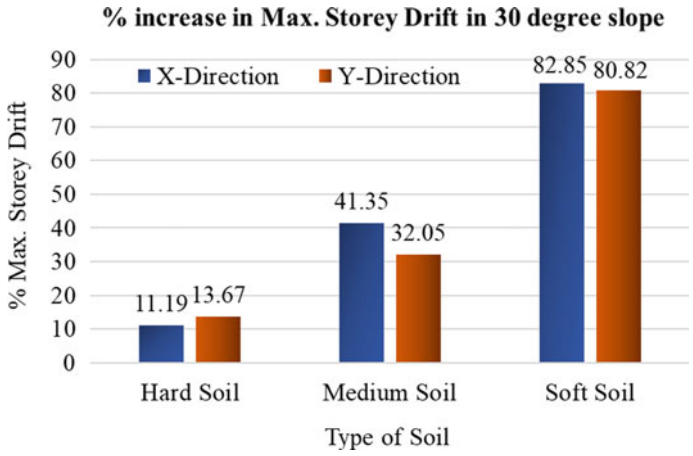

Fig. 27 Percentage increase in maximum storey drift in 30° slope

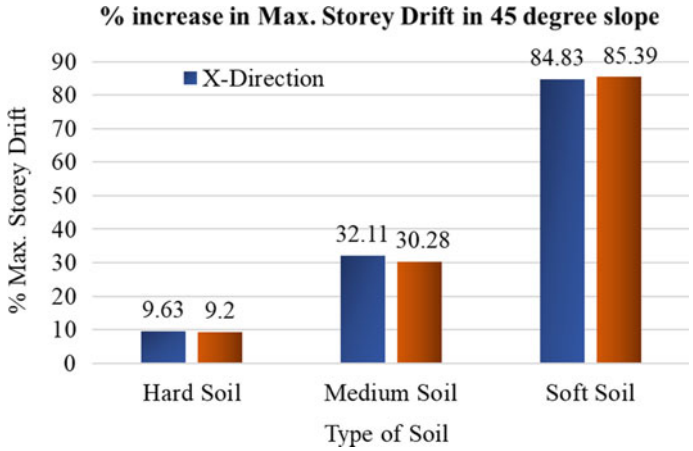

Fig. 28 Percentage increase in maximum storey drift in 45° slope

- From the results, the storey displacement and storey drift of the building decrease after the application of the bracing system. It also reduces natural time period, bending moments, and shear forces in the structural members.
- When compared to the traditional approach of presuming a fixed base, the responsiveness of RC structures using SSI has shown a substantial increase.

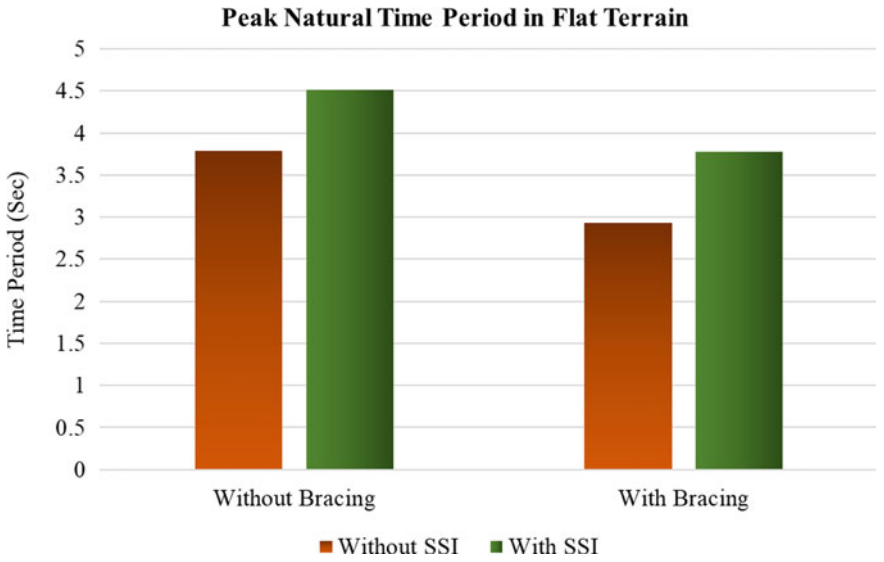

Fig. 29 Peak natural time period in flat terrain

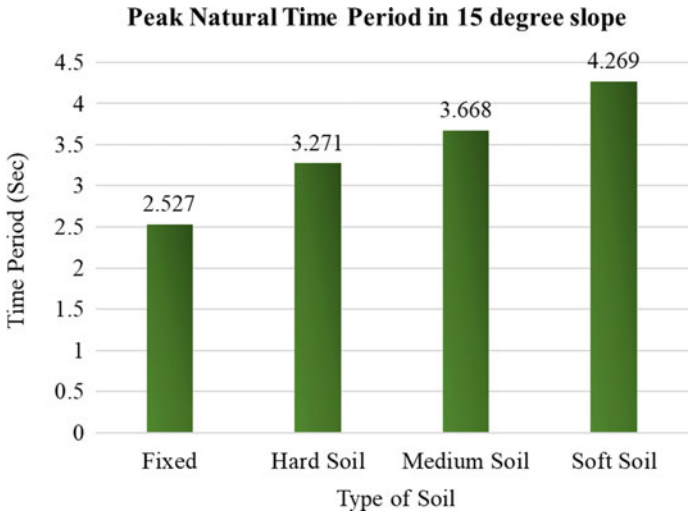

Fig. 30 Peak natural time period in 15° slope

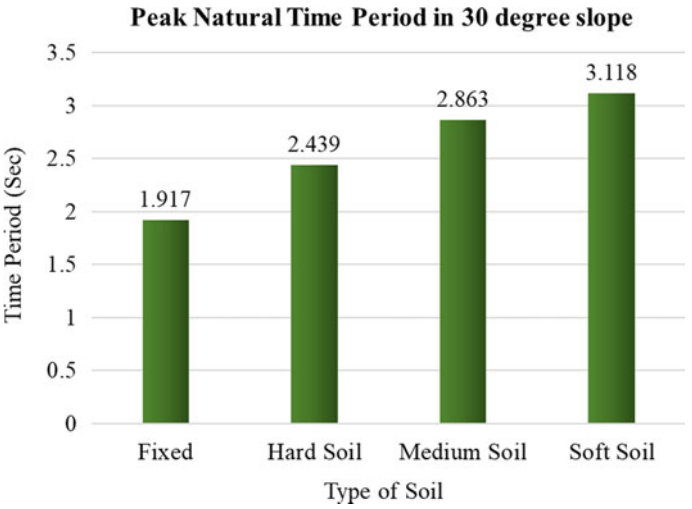

Fig. 31 Peak natural time period in 30° slope

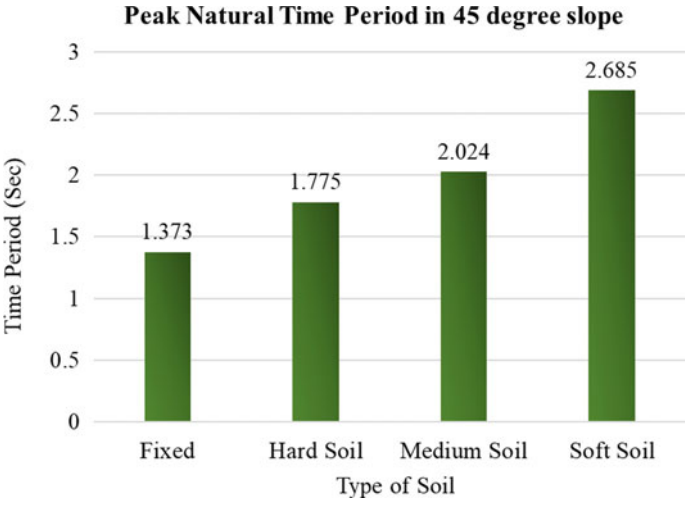

Fig. 32 Peak natural time period in 45° slope

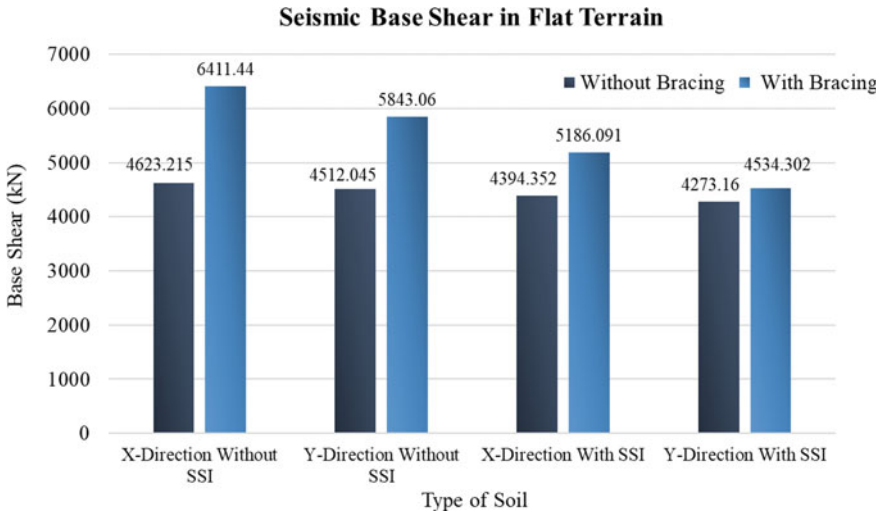

Fig. 33 Seismic base shear in flat terrain

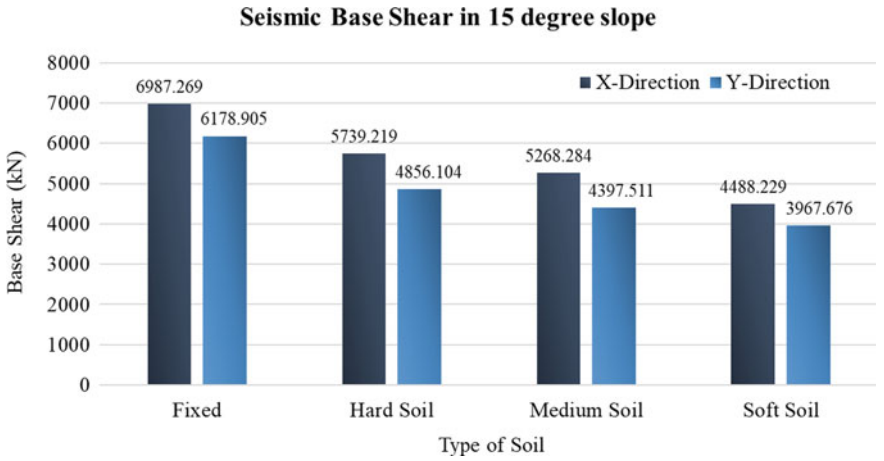

Fig. 34 Seismic base shear in 15° slope

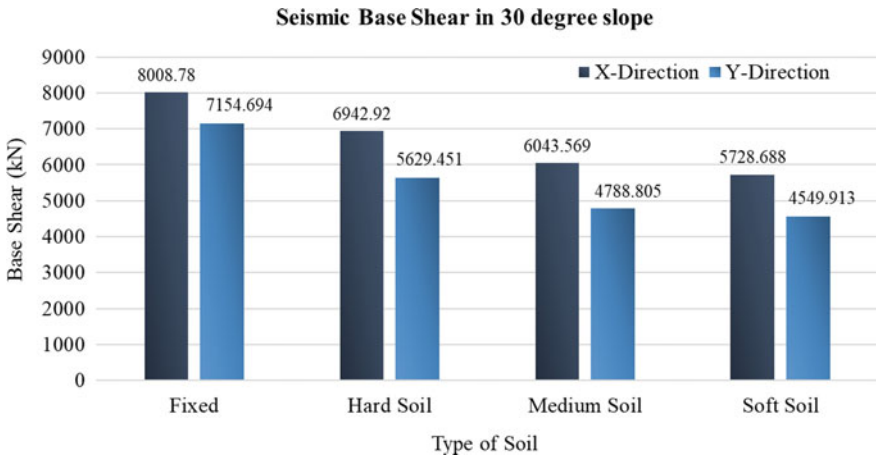

Fig. 35 Seismic base shear in 30° slope

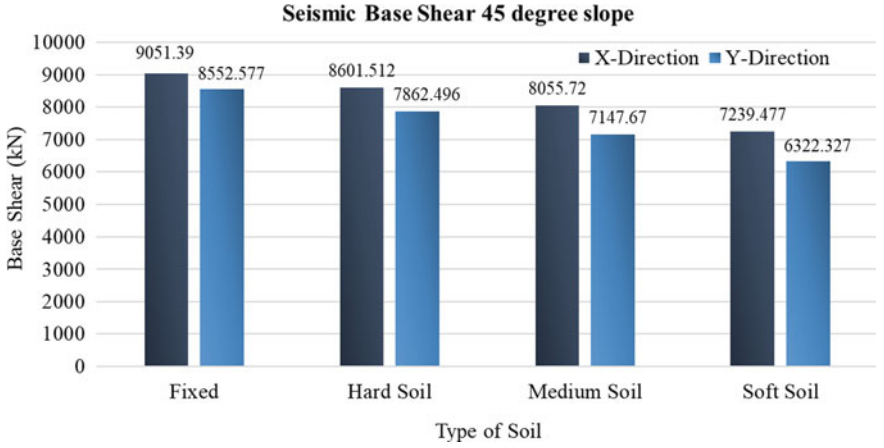

Fig. 36 Seismic base shear in 45° slope

References

1. Ismail S, Kaddah F, Raphael W (2018) Seismic soil structure interaction of a midrise frame structure. In: Advanced research on shallow foundations, Lebanon. pp 73–88
2. Chore HS, Sawant VA (2016) Soil-structure interaction of space frame supported on pile foundation embedded in cohesionless soil. Ind Geotech J 46:415–424 (Mumbai)
3. Jayalekshmi BR, Chinmayi HK (2018) Non-linear soil-structure interaction analysis of multi-storey shear wall buildings with site specific ground response. Facing the challenges in structural engineering. Surathkal, pp 73–88
4. Hirave V, Kalyanshetti M (2018) Seismic response of steel braced building frame considering soil structure interaction (SSI): an experimental study. J Inst Eng (India): Ser A 99:113–122 (Solapur, India)

5. Rajak P, Debbarma R (2017) Effect of soil structure interaction on RC building under earthquake load. Int J Adv Mech Civil Eng 4:82–87 (India)
6. Scarfonea R, Morigib M, Contic R (2020) Assessment of dynamic soil-structure interaction effects for tall buildings: A 3D numerical approach. Soil Dyn Earthquake Eng 128 (Italy)
7. Mohasseb S, Ghazanfari N, Rostami M, Rostami S (2019) Effect of soil–pile–structure interaction on seismic design of tall and massive buildings through case studies. Transport Infrastruct Geotech (Switzerland).
8. Ghosh R, Debbarma R (2019) Effect of slope angle variation on the structures resting on hilly region considering soil–structure interaction. Int J Adv Struct Eng 11: 67–77
9. Akhtarpour A, Mortezaee M (2018) Dynamic response of a tall building next to deep excavation considering soil–structure interaction. Asian J Civil Eng 20:479–502 (Iran)
10. Hassan A, Pal S (2018) Effect of soil condition on seismic response of isolated base buildings. Int J Adv Struct Eng 10:249–261

Fatigue Characteristics of Bituminous Concrete Mixtures Utilizing Copper Slag

Chavan Ravishankar, M. S. Nagakumar, and B. G. Shivaprakasha

Abstract India has a large number of copper production plants. All of its by-products, copper slag, are deposited in open places at random, causing serious several environmental hazards. The purpose of this research is to investigate the efficacy of utilizing copper slag (a combination of fine aggregate and mineral filler) in enhancing the engineering features, particularly the fatigue life of bituminous concrete grading 2 mixtures (BC-2) prepared with copper slag. The investigation began with an examination of the copper slag's morphology (SEM—Scanning Electron Microscope) and chemical characteristics (EDXA—Energy Dispersive X-ray Analyzer). Then, five different copper-slag-containing mixtures were investigated. The copper slag's efficacy was determined by the improvement in Marshall stability, split tensile strength ratio (TSR), modulus of resilience, and fatigue life of bituminous concrete grading-2 Marshall cylindrical specimens. It was observed that the bituminous concrete grading-2 mixture with CSFAMF (Copper Slag as Fine Aggregate and Mineral Filler) showed higher efficiency to repeated load than the mixture with traditional materials.

Keywords Copper slag · SEM · EDXA · Split tensile strength · Modulus of resilient · Fatigue life

1 Introduction

Because of the modernization of the construction sector, the utilization of waste products is an appealing trend with great potential for many transportation researchers, with the primary goal of environmentally friendly practices and profitable development. For these professionals, the primary goal of their work is to assure that roads are economically, safely, smoothly, and sustainably designed to bear the projected loads. Under these conditions, there has been a surge in interest in the development of road materials that can decrease structural deterioration and improve the performance [1]

C. Ravishankar (✉) · M. S. Nagakumar · B. G. Shivaprakasha
RV College of Engineering, Bengaluru, Karnataka 560059, India
e-mail: hobicons@gmail.com

L. Nandagiri et al. (eds.), *Recent Advances in Civil Engineering*, Lecture Notes in Civil Engineering 256, https://doi.org/10.1007/978-981-19-1862-9_65

of bituminous pavements. A ton of copper produces about 2.2–3 tons of copper slag. Copper slag is manufactured in India at a rate of roughly 0.4 million tons/year, in Japan at an average of nearly 2 million tons/year [2], and in Iran, Brazil, and Oman at an average of approximately 360,000, 244,000, and 60,000 tons, respectively [3–5]. Khanzadi and Behnood [6] mentioned the utilization of copper slag (CS) as a coarse aggregate (CA) in the concrete mixture that meets the ASTM C 33 grading standards for aggregates size of passing 12.5 to retained on 4.75 mm. According to Wu et al. [7], copper slag (CS) can be used as a fine aggregate (FA) in cement concrete. The density of the copper slag used in this study was 3660 kg/m^3, which was higher than the density of fine aggregate, which was 2640 kg/m^3. Al-Jabri et al. [8] determined the strength parameters of cement mortar and cement concrete using copper slag (CS) as a fine aggregate and found that the cement mortar and cement concrete with copper slag had a high compressive strength value compared to traditional materials in cement mortar and cement concrete. Until using the copper slag, it was ground down in the research lab to the desired size. Brinda et al. [9] utilized copper slag as a partial substitute for fine aggregate and cement in the concrete mix.

In view of the enormous potential of industrial by-products for the construction of flexible pavements in India, the present research study was undertaken to analyze the factors that affect the decision on the maximum industrial by-product (copper slag) content that can be used in bituminous concrete mixtures. The selection of the industrial by-product content of the bituminous concrete grade-2 mixtures [10] is investigated in this research corresponding to the mid-limit aggregate gradation, and the performance of the bituminous concrete mixture, in particular against water resistivity and fatigue cracking. The present research work, which was carried out without anti-stripping agents, was able to recognize the maximum potential industrial by-product content from different criteria.

2 Objectives and Methodology

The primary goal of this research is to explore the properties of CSFAMF-added bituminous concrete mixtures. The copper slag material brought from the industrial plant was subjected to a grain size distribution test, and findings show that a large percentage of the particles passed the 4.75 mm IS Sieves. A considerable quantity of 1.18 mm downsize was observed among them. Therefore, in this research work, 1.18 mm downsize traditional materials were replaced with copper slag. Standard experiments [11] were used for this research, including the Marshall test (ASTM-D 1559 -89), split tensile strength [12] test (ASTM-D 6931-12), water resistivity test [13], fatigue test (repeated load indirect tensile test), morphology of materials (SEM), and elemental composition analyzer (EDXA). Split tensile strength and fatigue tests are carried out at temperatures ranging from 25 °C to 45 °C to 65 °C, respectively.

3 Experimental Program

3.1 Materials

The aggregate gradation in our research study is shown in Table 1.

In this investigation, the VG-30-viscosity grade from the MRPL (Mangalore Refinery and Petrochemicals Limited) oil refinery was used [14]. The properties of bitumen are summarized in Table 2.

The grain size distribution (GSD) of industrial by-products is shown in Fig. 1.

Table 1 Aggregate gradation for CSFAMF-added BC2 mixtures

IS Sieve size (mm)	Range of gradation	Cumulative percentage passing on sieve sizes (Mid limit)	Percent of CSFAMF content
19	100	10.5	
13.2	79-100	10.5	
9.5	70-88	17	
4.75	53-71	12	
2.36	42-58	9	
1.18	34-48	9	0, 25, 50, 75 & 100
0.6	26-38	9	
0.3	18-28	7	
0.15	12-20	9	
0.075	4-10	7	

Table 2 Properties of VG-30

Description of tests	Test procedure code	Results	Requirements (IS 73—2006)
Penetration value at 25 °C, 0.1 mm	IS 1203 1978	68.33	50–70
Softening point (°C)	IS 1205 1978	51.75	>47 °C
Ductility value, 27 °C, cm	IS 1208 1978	82.5	–
Specific gravity (Sp.gr) at 27 °C	IS 1202 1978	1.00	–
Flash Point (°C)	IS 1448 1969	260	220 °C
Viscosity test at 135 °C, cst	IS 1206 1978	390	>350 cst

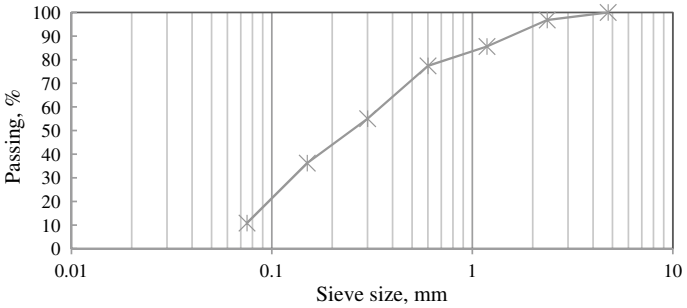

Fig. 1 Grain size distribution for copper slag materials

Table 3 Properties of quarry stone materials

Description of tests	Test procedure code	Test results	Requirements of MoRT&H 500–17
Combine Index (%)	IS-2386 part 1	30.10	≤30
Loss angles abrasion value (%)	IS-2386 part 4	26.01	≤30
Aggregate impact value (%)	IS-2386 part 4	22.00	≤24
Water absorption (%)	IS-2386 part 3	0.3	≤2
Stripping (%)	IS-6241	98	≥95
Sp.gr of stone CA	IS-2386 part 3	2.67	–
Sp.gr of stone FA	IS-2720 part 3 1980	2.65	–
Sp.gr of stone MF	IS-2720 part 3 1980	2.68	–

Table 4 Physical properties of industrial by-products

Test	Test procedure code	Test results
Sp.Gr. of CSMF	IS-2720 part 3 1980	2.85
Sp.Gr. of CSFA	IS-2720 part 3 1980	3.09
Specific surface area of CSMF (cm^2/gm)	IS-8425 1977	2649
Specific surface area of Cement (cm^2/gm)	IS 4031(part 2): 1999	3181

3.2 Fatigue Test

Repeated load tests on cylindrical specimens were carried out using ITFT (Indirect tensile fatigue testing) equipment (Marshall specimens). The performance of the BC-2 mixes containing 0, 25, 50, 75, and 100% CSFAMF was tested under repeated loads at 25, 45, and 65 °C and 20% stress levels, respectively. Fatigue testing on cylindrical specimens (diametrical loading) was carried out at 1 Hz using a sinusoidal

waveform. Figures 6 and 7 show the fatigue testing results of BC-2 mixes having 0, 25, 50, 75, and 100% CSFAMF content at temperatures of 25 °C, 45 °C, and 65 °C, respectively. Equations 1, 2, and3 are used to determine the tensile stress, tensile strain, and resilient modulus of bituminous concrete mixture with or without industrial by-product content, respectively.

$$\sigma = \frac{2 \times P}{\pi \times d \times H} \tag{1}$$

where

σ Tensile stress, Mpa,
P Applied load, *N,*
D dia. of Marshall specimen, mm, and
H Average thickness of the specimen, mm.

$$MR = \frac{P \times (0.27 + \mu)}{H_r \times H} \tag{2}$$

where

M Resilient modulus, Mpa,
P Applied load, *N,*
μ Poisson's ratio, and
H Average thickness of the specimen, mm.

$$\varepsilon_t = (1 + 3\mu) \times \frac{\sigma}{MR} \tag{3}$$

where;

ε_t Tensile strain,
σ Tensile stress, Mpa,
μ Poisson's ratio, and
MR Resilient modulus, Mpa.

4 Results and Discussion

As illustrated in Table 6, the OBC of a BC2 mixture replaced with CSFAMF decreases significantly from CSFAMF25 to CSFAMF75%; however, the drop in optimum bitumen content becomes minor after CSFAMF75% replacement. Bulk density values at optimal bitumen percentage in bituminous mixes for CSFAMF0,

Table 5 Elemental composition of CS material

Element line	Weight (%)	Atom (%)
C K	2.72	5.02
O K	30.77	42.57
F K	1.19	1.39
Na K	2.45	2.36
Al K	10.66	8.74
Si K	46.75	36.84
K K	5.45	3.08
Total	100	100

CSFAMF25, CSFAMF50, CSFAMF75, and CSFAMF100% replacement are shown to increase with percentage of CSFAMF replacement. Also from the Marshall test results, it is observed that the high percentage of silica content and angular shape (Figs. 2 and 3) of the fine aggregate of copper slag material has enhanced the stability value of CSFAMF-added bituminous concrete mixture (Table 6) compare to traditional (CSFAMF0) bituminous mixtures. From split tensile strength test results (Table 7), it is observed that the rough texture and angular shape property of copper slag enhanced the resistance to tensile load and eventually the CSFAMF added BC2 mixture had higher split tensile strength values compared to traditional bituminous mixtures. From fatigue test results, it is observed that the bituminous concrete mixture with CSFAMF showed low initial tensile strain values at 25, 45, and 65 °C temperatures compare to traditional material. This may be due to the rough texture and irregular shape of copper slag fine aggregate and mineral filler particle has enhanced the resistance to horizontal deformation of the mixture and eventually it has increased the fatigue life and resilient modulus (Figs. 5, 6, and 7) values. The water resistance test is used to assess the influence of CS material on moisture resistivity (Tables 8 and 9) of bituminous concrete mixes. The obtained outcomes are presented in Tables 8 and 9. Section 500 Tables 517 and 519 of the MoRT&H 4th revision specifications are fulfilled by CSFAMF-replaced mixtures (MoRT&H 2001). The quantitative elemental composition of copper slag (Fig. 4 and Table 5) showed a high percentage of weight and atoms of silica in copper slag when compared to conventional materials (cement and stone dust).

5 Conclusion

The primary goal of this study is to evaluate the performance of CSFAMF-added bituminous concrete mixes, with an emphasis on the amount of industrial by-products that can be utilized for target gradation (BC-2) and target binder (VG-30). Water-resistance testing of bituminous concrete mixes at 25, 45, and 65 °C showed that the split tensile strength ratio of all mixtures satisfies the required minimum value.

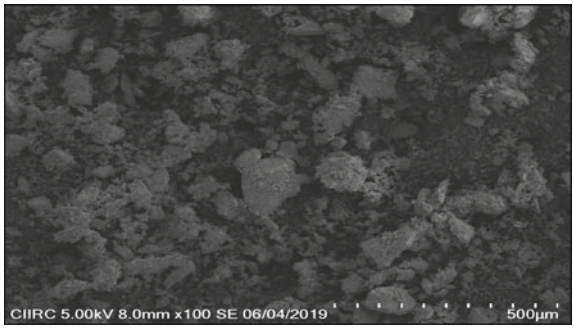

Fig. 2 SEM micrographs of CSFA <1.18 mm

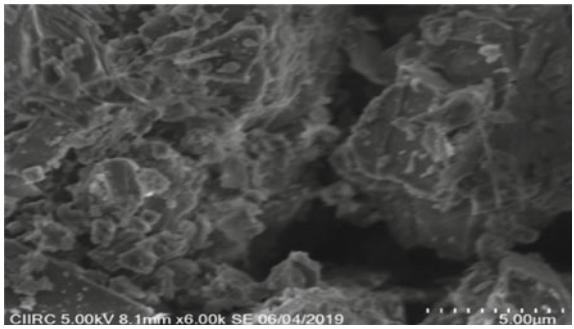

Fig. 3 SEM micrographs of CSMF

Table 6 Marshall mixture design properties of BC2 mixtures with CSFAMF content

CS FAMF content	Stability (Kg)	Flow (mm)	Total air voids (Vv) (%)	Bulk Density (Gb) (g/cc)	VMA (%)	VFB (%)	OBC (%)
CSFAMF0%	2316	3.63	4.16	2.37	17.18	75.78	5.48
CSFAMF25%	2481	3.53	4.13	2.37	16.67	75.21	5.28
CSFAMF50%	2742	3.47	4.04	2.39	16.60	75.65	5.25
CSFAMF75%	2833	3.40	4.03	2.40	16.56	75.69	5.22
CSFAMF100%	2888	3.07	3.91	2.44	16.64	76.48	5.22

Table 7 Split tensile strength value (MPa) of BC2 mixtures with CSFAMF content

Temperature (°C)	CSFAMF0%	CSFAMF25%	CSFAMF50%	CSFAMF75%	CSFAMF100%
25	0.904	0.979	1.065	1.085	1.146
45	0.394	0.470	0.480	0.540	0.576
65	0.217	0.232	0.257	0.288	0.318

Table 8 TSR of BC2 conventional mixtures

Temperature (°C)	IBPFAMF 0% (conventional mixtures)
25	0.857
45	0.861
65	0.852

Table 9 TSR of BC2 mixtures with CSFAMF

Temperature (°C)	CSFAMF25%	CSFAMF50%	CSFAMF75%	CSFAMF100%
25	0.857	0.852	0.851	0.852
45	0.855	0.862	0.853	0.865
65	0.867	0.871	0.865	0.867

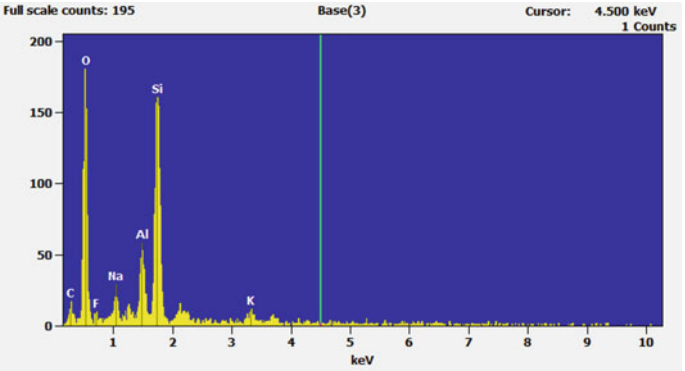

Fig. 4 EDX spectrum of CS material

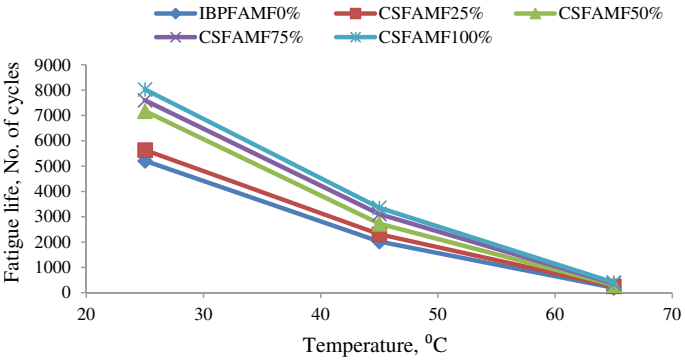

Fig. 5 Fatigue life versus temperature

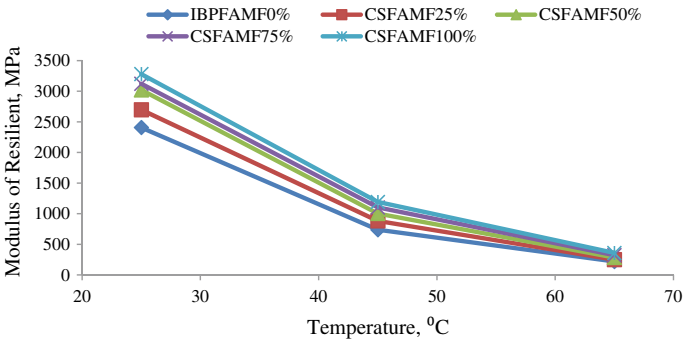

Fig. 6 Modulus of resilient versus temperature

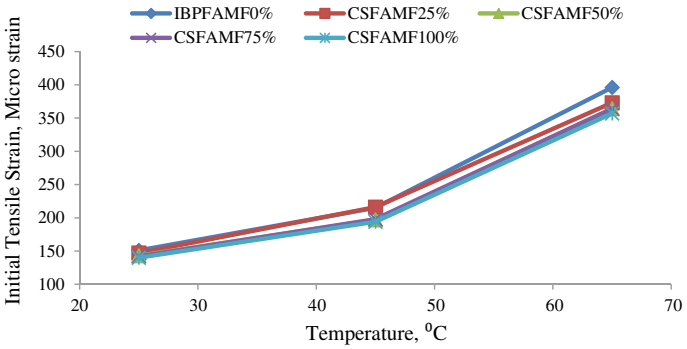

Fig. 7 Initial tensile strain versus temperature

The addition of CSFAMF to a grade-2 bituminous concrete mixture considerably enhanced water resistance when compared to conventional mixes (IBP-FAMF0). The CSFAMF100 added bituminous concrete mixture had the highest conditioned split tensile strength values of all mixers. In comparison to the mixture with traditional material, the bituminous concrete mixture with CSFAMF has a higher resistance to repeated load. Fatigue test findings for bituminous concrete grading-2 mixes using CSFAMF materials exhibited a greater modulus of resilience (MR) and reduced initial tensile strain than traditional BC-2 mixtures.

References

1. Chandra S, Choudhary R (2013) Performance characteristics of bituminous concrete with

industrial wastes as filler. J Mat Civ Eng 25:1666–1673. https://doi.org/10.1061/(ASCE)MT.1943-5533.0000730
2. Ayano T, Sakata K (2000) Durability of concrete with copper slag fine aggregate. In: Fifth CANMET/ACI international conference on durability of concrete, SP 192. American Concrete Institute. Farmington Hills, pp 141–158
3. Behnood A (2005) Effects of high-temperatures on high strength concrete incorporating copper slag aggregates. In: 7th international symposium on high performance concrete, SP 228—66. Washington, USA, pp 1063–1075
4. Moura W, Masuero A, Dal Molin D, Vilela A (1999) Concrete performance with admixtures of electrical steel slag and copper concerning mechanical properties. In: Second CANMET/ACI international conference on high performance concrete, SP—186 American Concrete Institute. Farmington Hills, MI, pp 81–100
5. Taeb A, Faghihi S (2002) Utilization of copper slag in the cement industry. ZKG Int 55(4):98–100
6. Khanzadi M, Behnood A (2009) Mechanical properties of high-strength concrete incorporating copper-slag as coarse aggregate. Constr Build Mater 23(6):2183–2188
7. Wu W, Zhang W, Ma G (2009) Optimum content of copper slag as a fine aggregate in high strength concrete. Mater Des 31(6):2878–2883
8. Al-Jabri KS, Al-Saidy AH, Taha R (2011) Effect of copper slag as a fine aggregate on the properties of cement mortars and concrete. Constr Build Mater 25(2):933–938
9. Brinda D, Baskaran T, Nagan S (2010) Assessment of corrosion and durability characteristics of copper slag admixed concrete. Int. Jour. Civil. Struct. Eng. 1(2):192–211
10. Specifications for road and bridge works (4th Revision) Ministry of Road Transport and Highways, Government of India, IRC, New Delhi (2001)
11. ASTM D-1559 (1979) Test method for resistance of plastic flow of bituminous mixtures using marshall apparatus, ASTM-International, West Conshohocken, PA, USA
12. ASTM D-6931–12 (2012) Standard test-method for indirect tensile (IDT) strength of bituminous mixtures. ASTM-International, West Conshohocken, PA, USA
13. AASHTO-T 283 (2014) Standard method of test for resistance of compacted asphalt mixtures to moisture induced damage. AASHTO. Washington, DC, USA
14. Bureau of Indian standards for Paving bitumen—specification 4th-Revision IS-73:2013, BIS, New Delhi (2013)

Comparative Study on Design of Water Supply Distribution Network Using LOOP and WaterGEMS Software: A Case Study

Abhishek Nalatawada, Sanjeev Sangami, and Chidanand Patil

Abstract A growing population country like India needs a sufficient amount of resources. Nowadays, most of our rural areas are not having a sufficient quantity of potable drinking water facilities, so the main objective of this study is to provide an efficient and optimal water distribution network design using LOOP and WaterGEMS software by satisfying CPHEEO norms and Jal Jeevan Mission guidelines. The project is carried on Awaradi village in Gokak taluk, Belagavi district. This project is carried out the designing rural drinking water with 55 LPCD. The population is forecasted for a design period of 30 years (2051) from 2021. The survey is carried out in the proposed village to collect ground data and area topographical profile. Then further hydraulic calculations are made with the use of LOOP 5.0 software and WaterGEMS Software. The velocity and head losses are high in the LOOP software design as compared with the WaterGEMS software. The pressure values are slightly more in the WaterGEMS software, but both the software results are meeting the CPHEEO norms as well as Jal Jeevan Mission guidelines with a pressure head of 7 m.

Keywords FHTC · Extended period simulation · Graphical interface · LOOP · WaterGEMS · Raw water demand

1 Introduction

Potable drinking water is necessary for human beings. India has 18% of the world's population and 20% of the world's livestock population. It has only 2.3% land and 4% of global potable water sources in the world [1]. There is growth in demand for freshwater, whereas the source of water is limited. To satisfy water demand with a

A. Nalatawada (✉) · S. Sangami
Department of Civil Engineering, Jain College of Engineering Belagavi, Belagavi, Karnataka 590014, India
e-mail: abhisheksn321@gmail.com

C. Patil
Department of Civil Engineering, KLE DR MSSCET Belagavi, Belagavi, Karnataka 590008, India

L. Nandagiri et al. (eds.), *Recent Advances in Civil Engineering*, Lecture Notes in Civil Engineering 256, https://doi.org/10.1007/978-981-19-1862-9_66

limited source of freshwater is a complex issue, and also to remove the gap between service levels in rural and urban areas. 60–70% of the total population of India lives in rural areas so to provide water distribution network facilities for villagers.

The design of a water supply distribution network system for rural areas is to provide an adequate quantity of potable drinking water to the villages by efficient design of water distribution using the software. This study refers to the comparative design of water distribution networks using LOOP and WaterGEMS software. The main objective is to satisfy the functional needs at design standards with minimum cost because 65.07% of the population of India lives in rural areas [2]. The government of India has decided to give functional household tap connection to each household in rural India through the "Jal Jeevan Mission" Scheme. In the water distribution system, 50–70% of the total cost of water supply is consumed for the water supply network [3], so the optimal design of the water distribution network is necessary. Here we are going to study the network analysis and design between LOOP and WaterGEMS software to get a safe, adequate, optimal, and efficient water distribution network.

About Loop Software

LOOP Software: LOOP software is based on the Hardy–Cross principle. Loop calculates the hydraulic properties of a loop network for a water distribution network. The network is formed by pipes and nodes [4]. Data is required for the elements of the network such as pipe lengths, diameters, friction coefficients, nodal demands and ground elevation, and data describing the geometry of the network [4]. The program outputs include hydraulic gradient levels, flows, and pressures at each node [5].

About WaterGEMS Software

WaterGEMS is a software that performs extended period simulation of hydraulic and water quality behavior within interconnected pipe networks. A network consists of pipes, nodes, pumps, valves, and storage tanks or reservoirs. "Water Gems shows the flow and velocity of water in each pipe, the pressure at each node and the height of each tank" [6].

2 Methodology

Initially, collection of data for design is carried out from field surveying and data sources and then those data are converted and calculated as software input, hydraulic analysis was done using software, those results are distinguished from each other and then concluded that which software is giving better results (Fig. 1).

Study Area and Data Collection

Avaradi is a village is located in Gokak Taluk in Belgaum District of Karnataka State, India. It has a population of 3404 with 671 households. Avaradi village comes under Belagavi division. The details about the study area are listed (Fig. 2 and Table 1).

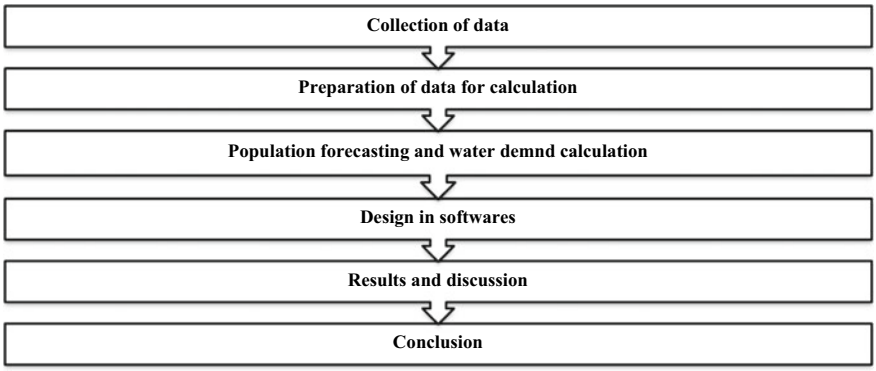

Fig. 1 Methodology

Fig. 2 Village map

Preparation of Data for Calculation

See Table 2.

Population Forecasting and Water Demand

See Table 3.

Design Using Loop Software

In LOOP design, 76 pipes are interconnected to each other for the loop network to validate the Hardy–cross principle, each junction is considered as node points that are 67 in number (including overhead tank) for PVC pipe considering HWC as 145 for hydraulic design. In this design, above-mentioned data are entered into the LOOP software and then outputs are obtained for the velocity of water in each pipe, head loss in each pipe, HGL at every node point, pressure head at each node, and flow. In this design, 7 m is the minimum pressure head for the water distribution network (Table 4; Fig. 3).

Table 1 Village details

Sl. No.	Description	Details
1	*Village details*	
	District	Belagavi
	Taluka	Gokak
	Village	Awaradi
2	*Population details*	
	Total population	3404
	Taluka growth rate	18.81%
3	*FHTC details*	
	Total FHTCs	671
	New connection	378
4	*Water demand*	55 LPCD
5	*Design period*	30 Years (2050)
6	*Hydraulic details*	
	Peak factor	4
	Minimum residual pressure head	7 m

Design Using WaterGEMS Software

WaterGEMS software designs the water distribution network by using layout maps, starting with placing overhead tank with their capacity and elevation in the layout, then connecting node points with pipes (with the suitable diameter and PVC as pipe material), for PVC pipe considering 145 as HWC, the elevation of each junction points are assigned. After all data entry is completed, water demand is entered at each node point. Then the design for the proposed distribution network is computed and those results are the velocity of water flow in the pipe network, hydraulic gradient level, and pressure head at each node point (in m) (Table 5 and Fig. 4).

3 Results and Discussion

The LOOP software considers every pipe in the network to be straight, bends in the network are neglected or it assumes there are no bends, so there is no reduction of flow due to bends and the velocity of water flow in the network is more. The WaterGEMS software considers each and every minute detail because the software has a graphical interface every data is collected while drawing the network layout so the velocity values are comparatively less than the LOOP software (Fig. 5).

The pressure in the water distribution network mainly depends upon the head of the water. The WaterGEMS software requires water tank details such as base elevation, the initial water level in the water tank, minimum water level, and maximum water level in the water tank. So that the pressure value is comparatively higher whereas

Table 2 Details for software input

Avaradi pipe distribution details								
Pipe number	From node	To node	Pipe length (M)	Houses per pipe	Population in pipe	Total demand/day	Pipe DIA (MM)	Flow in L/S
1	200	1	27.12	1	8	433.40	160	0.01
2	1	2	28.78	2	16	866.80	140	0.01
3	2	3	50.83	5	39	2167.00	110	0.03
4	3	4	31.8	6	47	2600.40	90	0.03
5	3	5	62.27	8	63	3467.20	90	0.04
6	5	6	27.42	2	16	866.80	90	0.01
7	6	7	9.77	1	8	433.40	63	0.01
8	7	8	31.79	8	63	3467.20	63	0.04
9	7	9	48.88	6	47	2600.40	63	0.03
10	7	10	674.2	15	118	6501.00	63	0.08
11	6	11	161.6	10	79	4334.00	75	0.05
12	5	11	95.8	8	63	3467.20	90	0.04
13	11	12	30.77	3	24	1300.20	90	0.02
14	12	33	22.58	4	32	1733.60	90	0.02
15	33	34	16.5	2	16	866.80	63	0.01
16	12	13	94.9	13	102	5634.20	75	0.07
17	13	14	50.1	7	55	3033.80	63	0.04
18	13	15	23.6	4	32	1733.60	75	0.02
19	15	16	22.9	4	32	1733.60	63	0.02
20	16	17	29.9	6	47	2600.40	63	0.03
21	16	18	12.8	2	16	866.80	63	0.01
22	18	19	26.6	5	39	2167.00	63	0.03
23	18	20	42.5	8	63	3467.20	63	0.04
24	15	21	15.8	3	24	1300.20	75	0.02
25	21	22	22.1	6	47	2600.40	63	0.03
26	21	23	17.45	3	24	1300.20	75	0.02
27	23	24	8	2	16	866.80	63	0.01
28	23	25	21.7	4	32	1733.60	75	0.02
29	25	26	2.6	0	0	0.00	75	0.00
30	26	27	15.4	3	24	1300.20	63	0.02
31	26	28	59.2	9	71	3900.60	75	0.05
32	28	29	44.9	5	39	2167.00	90	0.03
33	29	30	58.3	7	55	3033.80	75	0.04
34	29	2	56.8	3	24	1300.20	110	0.02

(continued)

Table 2 (continued)

Avaradi pipe distribution details								
Pipe number	From node	To node	Pipe length (M)	Houses per pipe	Population in pipe	Total demand/day	Pipe DIA (MM)	Flow in L/S
35	28	31	16.8	2	16	866.80	90	0.01
36	31	32	62.6	10	79	4334.00	75	0.05
37	32	26	14.1	2	16	866.80	63	0.01
38	33	35	53.9	7	55	3033.80	90	0.04
39	35	36	82.9	11	87	4767.40	63	0.06
40	36	37	30.8	6	47	2600.40	63	0.03
41	37	38	3.02	1	8	433.40	63	0.01
42	38	39	43.6	6	47	2600.40	63	0.03
43	37	40	33.3	7	55	3033.80	63	0.04
44	36	40	59.5	10	79	4334.00	63	0.05
45	40	41	52	6	47	2600.40	63	0.03
46	41	32	26.4	4	32	1733.60	63	0.02
47	41	42	22.5	3	24	1300.20	63	0.02
48	42	51	43.5	6	47	2600.40	63	0.03
49	42	43	65.4	11	87	4767.40	63	0.06
50	43	44	8.6	1	8	433.40	63	0.01
51	44	45	6.8	1	8	433.40	63	0.01
52	44	50	28.1	3	24	1300.20	63	0.02
53	43	46	40.9	6	47	2600.40	63	0.03
54	38	46	45.9	7	55	3033.80	63	0.04
55	46	49	19.2	3	24	1300.20	63	0.02
56	47	49	34.3	5	39	2167.00	90	0.03
57	47	48	27.9	4	32	1733.60	63	0.02
58	35	47	56.3	8	63	3467.20	63	0.04
59	49	50	49.2	3	24	1300.20	90	0.02
60	50	51	79.5	10	79	4334.00	90	0.05
61	51	52	44.5	7	55	3033.80	90	0.04
62	52	53	22.3	3	24	1300.20	90	0.02
63	53	54	52.3	8	63	3467.20	63	0.04
64	31	53	57.7	2	16	866.80	90	0.01
65	52	55	156.3	3	24	1300.20	90	0.02
66	55	56	13	0	0	0.00	63	0.00
67	56	57	28.5	1	8	433.40	63	0.01

(continued)

Table 2 (continued)

Avaradi pipe distribution details								
Pipe number	From node	To node	Pipe length (M)	Houses per pipe	Population in pipe	Total demand/day	Pipe DIA (MM)	Flow in L/S
68	56	58	239.9	0	0	0.00	63	0.00
69	58	59	18.8	4	32	1733.60	63	0.02
70	58	60	13.5	4	32	1733.60	63	0.02
71	55	61	1212.2	9	71	3900.60	63	0.05
72	1	62	85.9	3	24	1300.20	110	0.02
73	62	63	91.6	5	39	2167.00	90	0.03
74	62	64	32.5	2	16	866.80	90	0.01
75	64	65	152.7	4	32	1733.60	75	0.02
76	64	66	218.5	2	16	866.80	90	0.01
77	200	66	35.6	1	8	433.40	160	0.01
78	66	67	47.1	1	8	433.40	140	0.01
79	67	68	27.3	2	16	866.80	110	0.01
80	68	69	31.7	3	24	1300.20	110	0.02
81	69	70	30.6	2	16	866.80	110	0.01
82	70	71	63.6	4	32	1733.60	110	0.02
83	70	72	114.6	8	63	3467.20	75	0.04
84	72	73	5.5	2	16	866.80	75	0.01
85	72	74	37.6	3	24	1300.20	75	0.02
86	69	74	103.7	7	55	3033.80	75	0.04
87	74	75	31.2	3	24	1300.20	75	0.02
88	68	75	98.2	6	47	2600.40	75	0.03
89	75	76	27.3	2	16	866.80	75	0.01
90	67	68	96.6	5	39	2167.00	90	0.03
91	76	77	812.7	1	8	433.40	90	0.01
92	77	78	81.8	0	0	0.00	63	0.00
93	78	79	7.5	0	0	0.00	63	0.00
94	78	80	150.14	9	71	3900.60	63	0.05
95	80	81	15.1	2	16	866.80	63	0.01
96	80	83	198.7	7	55	3033.80	63	0.04
97	83	82	86.5	3	24	1300.20	63	0.02
98	83	84	75.5	3	24	1300.20	63	0.02
99	84	85	40.7	2	16	866.80	63	0.01
100	84	86	160.9	1	8	433.40	63	0.01

(continued)

Table 2 (continued)

Avaradi pipe distribution details								
Pipe number	From node	To node	Pipe length (M)	Houses per pipe	Population in pipe	Total demand/day	Pipe DIA (MM)	Flow in L/S
101	86	87	13.3	0	0	0.00	63	0.00
102	86	88	399.9	6	47	2600.40	75	0.03
103	88	89	63.4	4	32	1733.60	63	0.02
104	82	88	79.2	3	24	1300.20	75	0.02
105	77	82	299	6	47	2600.40	90	0.03

Table 3 Population forecasting

Avaradi village rural population as per census 2001							2443		
Avaradi village rural population as per census 2011							2656		
Difference							213		
Percentage of decadal growth							18.81%		
Village name	Projected population						LPCD	Water demand in liter/day		Raw water demand in 2051 including losses of 20%
	2011	2021	2031	2035	2041	2051		2041	2051	
Avaradi	2656	2888	3141	3248	3415	3714	55	187,827	204,243	245,092.1

LOOP software only considers the bottom elevation water level in the overhead tank. So that the pressure value is comparatively less than WaterGEMS software.

The head losses are depending upon the size of the pipe, bends involved in the water distribution network, and size reduction in the pipe network, so that the LOOP software assumes that each pipe in the network is straight, here head losses in bends are neglected and it also having that concept that each junction meets at right angles to each other head losses in right-angle bends is more because of fluid friction in junctions so that head loss values are comparatively higher than the WaterGEMS software.

For this study area (i.e., Avaradi village of Gokak taluk of Belagavi district, Karnataka), the software Loop 5.0 and WaterGEMS v8i have been used for the design and analysis of the water distribution system. They are first of all applied to determine the minimum pressure head in a distribution network. Results obtained for the minimum pressure head at each node through both software are varying as shown in Fig. 6, it may be due to a change in the design control parameters of the respective software. It may be summarized that the designed pressure heads through both the software satisfy the requirements of 7 m pressure head (Fig. 7).

Table 4 LOOP software output

TITLE : AVARADI
NO. OF PIPE : 76
NO. NODES : 67
PEAK FACTOR : 4
MAX HEADLOSS/Km : 30
MAX UNBAL(LPS) : 0.006

PIPE NO.	FROM Node	TO Node	LENGTH (M)	DIA (MM)	HWC	FLOW (LPS)	VELOCITY (MPS)	HEADLOSS (M/KM)	HEADLOSS (M)
1	100	1	27.12	160	145	8.40	0.42	1.16	0.03
2	1	2	28.78	140	145	7.96	0.52	2.01	0.06
3	2	3	50.83	110	145	3.46	0.36	1.40	0.07
4	3	4	31.80	90	145	0.12	0.02LO	0.01	0.00
5	3	5	62.27	90	145	3.22	0.51	3.25	0.20
6	5	6	27.42	90	145	1.38	0.22LO	0.67	0.02
7	6	7	9.77	63	145	0.64	0.21LO	0.93	0.01
8	7	8	31.79	63	145	0.16	0.05LO	0.07	0.00
9	7	9	48.88	63	145	0.12	0.04LO	0.04	0.00
10	7	10	674.20	63	145	0.32	0.10LO	0.26	0.17
11	6	11	161.60	75	145	0.70	0.16LO	0.47	0.08
12	5	11	95.80	90	145	1.69	0.27LO	0.98	0.09
13	11	12	30.77	90	145	2.02	0.32	1.37	0.04
14	12	33	22.58	90	145	1.30	0.20LO	0.60	0.01
15	33	34	16.50	63	145	0.04	0.01LO	0.01	0.00
16	12	13	94.90	75	145	0.65	0.15LO	0.40	0.04
17	13	14	50.10	63	145	0.16	0.05LO	0.07	0.00
18	13	15	23.60	75	145	0.21	0.05LO	0.05	0.00
19	15	16	22.90	63	145	0.52	0.17LO	0.63	0.01
20	16	17	29.90	63	145	0.12	0.04LO	0.04	0.00
21	16	18	12.80	63	145	0.32	0.10LO	0.26	0.00
22	18	19	26.60	63	145	0.12	0.04LO	0.04	0.00
23	18	20	42.50	63	145	0.16	0.05LO	0.07	0.00
24	21	15	15.80	75	145	0.39	0.09LO	0.16	0.00
25	21	22	22.10	63	145	0.12	0.04LO	0.04	0.00
26	23	21	17.00	75	145	0.59	0.13LO	0.35	0.01
27	23	24	8.00	63	145	0.04	0.01LO	0.01	0.00
28	25	23	21.70	75	145	0.71	0.16LO	0.49	0.01
29	26	25	2.60	75	145	0.79	0.18LO	0.59	0.00
30	26	27	15.40	63	145	0.08	0.03LO	0.02	0.00
31	28	26	59.20	75	145	1.22	0.28LO	1.30	0.08
32	29	28	44.90	90	145	4.10	0.64	5.06	0.23
33	29	30	58.30	75	145	0.16	0.04LO	0.03	0.00
34	2	29	56.80	110	145	4.38	0.46	2.15	0.12
35	28	31	16.80	90	145	2.68	0.42	2.31	0.04
36	31	32	62.60	75	145	0.84	0.19LO	0.66	0.04
37	26	32	14.10	63	145	0.30	0.10LO	0.23	0.00
38	33	35	53.90	90	145	1.18	0.19LO	0.51	0.03
39	35	36	82.90	63	145	0.46	0.15LO	0.51	0.04
40	36	37	30.80	63	145	0.15	0.05LO	0.06	0.00
41	37	38	3.02	63	145	0.12	0.04LO	0.04	0.00
42	38	39	43.60	63	145	0.12	0.04LO	0.04	0.00
43	40	37	33.30	63	145	0.09	0.03LO	0.02	0.00
44	36	40	59.50	63	145	0.07	0.02LO	0.02	0.00
45	41	40	52.00	63	145	0.37	0.12LO	0.34	0.02
46	32	41	26.40	63	145	0.86	0.28LO	1.61	0.04
47	41	42	22.50	63	145	0.37	0.28LO	0.33	0.01
48	42	51	43.50	63	145	0.05	0.12LO	0.01	0.00
49	42	43	65.40	63	145	0.24	0.02LO	0.15	0.01
50	44	43	8.60	63	145	0.09	0.08LO	0.02	0.00
51	44	45	6.80	63	145	0.04	0.03LO	0.01	0.00
52	50	44	28.10	63	145	0.17	0.01LO	0.08	0.00
53	43	46	40.90	63	145	0.08	0.05LO	0.02	0.00
54	46	38	45.90	63	145	0.04	0.03LO	0.01	0.00
55	49	46	19.20	63	145	0.24	0.01LO	0.15	0.00

(continued)

Table 4 (continued)

56	47	49	34.30	90	145	0.32	0.05LO	0.04	0.00
57	47	48	29.90	63	145	0.08	0.03LO	0.02	0.00
58	35	47	56.30	63	145	0.56	0.18LO	0.71	0.04
59	50	49	49.20	90	145	0.12	0.02LO	0.01	0.00
60	51	50	79.50	90	145	0.45	0.07LO	0.09	0.01
61	52	51	44.50	90	145	0.72	0.11LO	0.20	0.01
62	53	52	22.30	90	145	1.52	0.24LO	0.81	0.02
63	53	54	52.30	63	145	0.16	0.05LO	0.07	0.00
64	31	53	57.70	90	145	1.80	0.28LO	1.11	0.06
65	52	55	156.30	90	145	0.64	0.10LO	0.16	0.03
66	55	56	13.00	63	145	0.36	0.12LO	0.32	0.00
67	56	57	28.50	63	145	0.04	0.01LO	0.01	0.00
68	56	58	239.90	63	145	0.24	0.08LO	0.15	0.04
69	58	59	18.80	63	145	0.08	0.03LO	0.02	0.00
70	58	60	13.50	63	145	0.08	0.03LO	0.02	0.00
71	55	61	1212.20	63	145	0.20	0.06LO	0.11	0.13
72	1	62	85.90	110	145	0.40	0.04LO	0.03	0.00
73	62	63	91.60	90	145	0.12	0.02LO	0.01	0.00
74	62	64	32.50	90	145	0.20	0.03LO	0.02	0.00
75	64	65	152.70	75	145	0.08	0.02LO	0.01	0.00
76	64	66	218.50	90	145	0.08	0.01LO	0.00	0.00

NODE NO.	FLOW (LPS)	ELEVATION (M)	H G L (M)	PRESSURE (M)
100 R	8.400	555.36	555.36	0.00
1	-0.040	546.26	555.33	9.07
2	-0.120	545.46	555.27	9.80
3	-0.120	544.91	555.20	10.29
4	-0.120	545.35	555.20	9.84
5	-0.160	542.95	554.99	12.05
6	-0.040	543.55	554.98	11.42
7	-0.040	543.75	554.97	11.22
8	-0.160	544.38	554.96	10.58
9	-0.120	543.58	554.96	11.39
10	-0.320	539.31	554.79	15.48
11	-0.360	539.77	554.90	15.13
12	-0.080	538.61	554.86	16.24
13	-0.280	542.15	554.82	12.67
14	-0.160	542.16	554.82	12.66
15	-0.080	542.91	554.82	11.91
16	-0.080	543.16	554.82	11.64
17	-0.120	543.10	554.80	11.70
18	-0.040	543.45	554.80	11.35
19	-0.120	544.57	554.80	10.23
20	-0.160	544.47	554.80	10.33
21	-0.080	543.49	554.80	11.34
22	-0.120	544.11	554.82	10.71
23	-0.080	544.23	554.83	10.60
24	-0.040	544.04	554.83	10.79
25	-0.080	544.05	554.84	10.79
26	-0.040	544.31	554.84	10.53
27	-0.080	544.29	554.84	10.55
28	-0.200	544.10	554.92	10.81
29	-0.120	544.77	555.15	10.38
30	-0.160	545.14	555.14	10.01
31	-0.040	543.89	554.88	10.99
32	-0.280	544.86	554.84	9.97
33	-0.080	540.29	554.84	14.56
34	-0.040	540.29	554.84	14.55
35	-0.160	540.42	554.82	14.40

(continued)

Table 4 (continued)

36	-0.240	542.56	554.77	12.22
37	-0.120	542.56	554.78	12.21
38	-0.040	542.66	554.78	12.11
39	-0.120	542.57	554.77	12.20
40	-0.360	544.05	554.78	10.73
41	-0.120	544.14	554.80	10.66
42	-0.080	542.23	554.79	12.55
43	-0.240	541.88	554.78	12.90
44	-0.040	541.49	554.78	13.29
45	-0.040	540.86	554.78	13.25
46	-0.280	540.66	554.78	13.93
47	-0.160	538.33	554.78	14.12
48	-0.080	540.86	554.78	16.45
49	-0.200	541.67	554.78	13.92
50	-0.160	542.19	554.79	13.11
51	-0.320	542.52	554.80	12.59
52	-0.160	543.33	554.82	12.28
53	-0.120	541.12	554.81	11.49
54	-0.160	537.97	554.77	13.69
55	-0.080	537.97	554.77	16.80
56	-0.080	537.94	554.77	16.83
57	-0.040	537.69	554.77	17.07
58	-0.080	536.50	554.73	18.23
59	-0.080	536.50	554.73	18.24
60	-0.080	536.32	554.73	18.41
61	-0.200	535.52	554.64	19.12
62	-0.080	545.96	555.32	9.37
63	-0.120	545.11	555.32	10.21
64	-0.040	545.99	555.32	9.33
65	-0.080	544.87	555.32	10.45
66	-0.080	541.84	555.32	13.48

Fig. 3 Avaradi village layout design in LOOP software

Table 5 WaterGEMS software output

Flex table: pipe table							
Label	Length (Scaled) (m)	Start node	Stop node	Diameter (mm)	Material	Hazen–Williams C	Velocity (m/s)
P-1	17	T-1	J-1	160.0	PVC	145.0	0.10
P-2	29	J-1	J-2	140.0	PVC	145.0	0.13
P-3	52	J-2	J-3	110.0	PVC	145.0	0.09
P-4	32	J-3	J-4	90.0	PVC	145.0	0.00
P-5	63	J-3	J-5	90.0	PVC	145.0	0.13
P-6	28	J-5	J-6	90.0	PVC	145.0	0.05
P-7	10	J-6	J-7	63.0	PVC	145.0	0.05
P-8	33	J-7	J-8	63.0	PVC	145.0	0.01
P-9	48	J-7	J-9	63.0	PVC	145.0	0.01
P-10	675	J-7	J-10	63.0	PVC	145.0	0.03
P-11	161	J-6	J-11	75.0	PVC	145.0	0.04
P-12	30	J-11	J-12	90.0	PVC	145.0	0.08
P-13	96	J-11	J-5	90.0	PVC	145.0	0.07
P-14	23	J-12	J-13	90.0	PVC	145.0	0.06
P-15	17	J-13	J-14	63.0	PVC	145.0	0.01
P-16	94	J-12	J-15	75.0	PVC	145.0	0.02
P-17	50	J-15	J-16	63.0	PVC	145.0	0.01
P-18	25	J-15	J-17	75.0	PVC	145.0	0.02
P-19	23	J-17	J-18	63.0	PVC	145.0	0.04
P-20	30	J-18	J-19	63.0	PVC	145.0	0.01
P-21	13	J-18	J-20	63.0	PVC	145.0	0.03
P-22	26	J-20	J-21	63.0	PVC	145.0	0.01
P-23	42	J-20	J-22	63.0	PVC	145.0	0.01
P-24	16	J-17	J-23	75.0	PVC	145.0	0.02
P-25	22	J-23	J-24	63.0	PVC	145.0	0.00
P-26	17	J-23	J-25	75.0	PVC	145.0	0.03
P-27	8	J-25	J-26	63.0	PVC	145.0	0.00
P-28	22	J-25	J-27	75.0	PVC	145.0	0.03
P-29	2	J-27	J-28	75.0	PVC	145.0	0.05
P-30	15	J-28	J-29	63.0	PVC	145.0	0.01
P-31	59	J-28	J-30	75.0	PVC	145.0	0.07
P-32	44	J-30	J-31	90.0	PVC	145.0	0.16
P-33	59	J-31	J-32	75.0	PVC	145.0	0.02
P-34	57	J-31	J-2	110.0	PVC	145.0	0.12

(continued)

Table 5 (continued)

Flex table: pipe table							
Label	Length (Scaled) (m)	Start node	Stop node	Diameter (mm)	Material	Hazen–Williams C	Velocity (m/s)
P-35	17	J-30	J-33	90.0	PVC	145.0	0.11
P-36	62	J-33	J-34	75.0	PVC	145.0	0.04
P-37	14	J-34	J-27	63.0	PVC	145.0	0.01
P-38	54	J-13	J-35	90.0	PVC	145.0	0.04
P-39	83	J-35	J-36	63.0	PVC	145.0	0.03
P-40	31	J-36	J-37	63.0	PVC	145.0	0.01
P-41	2	J-37	J-38	63.0	PVC	145.0	0.01
P-42	44	J-38	J-39	63.0	PVC	145.0	0.01
P-43	34	J-37	J-40	63.0	PVC	145.0	0.01
P-44	58	J-40	J-36	63.0	PVC	145.0	0.00
P-45	51	J-40	J-41	63.0	PVC	145.0	0.03
P-46	26	J-41	J-34	63.0	PVC	145.0	0.07
P-47	23	J-41	J-42	63.0	PVC	145.0	0.03
P-48	43	J-42	J-43	63.0	PVC	145.0	0.00
P-49	66	J-42	J-44	63.0	PVC	145.0	0.02
P-50	8	J-44	J-45	63.0	PVC	145.0	0.01
P-51	7	J-45	J-46	63.0	PVC	145.0	0.02
P-52	28	J-45	J-47	63.0	PVC	145.0	0.01
P-53	41	J-44	J-48	63.0	PVC	145.0	0.01
P-54	42	J-48	J-38	63.0	PVC	145.0	0.00
P-55	20	J-48	J-49	63.0	PVC	145.0	0.01
P-56	35	J-49	J-50	90.0	PVC	145.0	0.00
P-57	28	J-50	J-51	63.0	PVC	145.0	0.03
P-58	56	J-50	J-35	63.0	PVC	145.0	0.04
P-59	49	J-49	J-47	90.0	PVC	145.0	0.01
P-60	79	J-47	J-43	90.0	PVC	145.0	0.02
P-61	45	J-43	J-52	90.0	PVC	145.0	0.03
P-62	23	J-52	J-53	90.0	PVC	145.0	0.06
P-63	52	J-53	J-54	63.0	PVC	145.0	0.01
P-64	58	J-53	J-33	90.0	PVC	145.0	0.07
P-65	157	J-52	J-55	90.0	PVC	145.0	0.03
P-66	12	J-55	J-56	63.0	PVC	145.0	0.03
P-67	28	J-56	J-57	63.0	PVC	145.0	0.00

(continued)

Table 5 (continued)

Flex table: pipe table

Label	Length (Scaled) (m)	Start node	Stop node	Diameter (mm)	Material	Hazen–Williams C	Velocity (m/s)
P-68	260	J-56	J-58	63.0	PVC	145.0	0.02
P-69	20	J-58	J-59	63.0	PVC	145.0	0.01
P-70	13	J-58	J-60	63.0	PVC	145.0	0.01
P-71	1212	J-55	J-61	63.0	PVC	145.0	0.02
P-72	86	J-1	J-62	110.0	PVC	145.0	0.01
P-73	92	J-62	J-63	90.0	PVC	145.0	0.00
P-74	33	J-62	J-64	90.0	PVC	145.0	0.01
P-75	153	J-64	J-65	75.0	PVC	145.0	0.00
P-76	218	J-64	J-66	90.0	PVC	145.0	0.00

Flex table: junction table

Label	Elevation (m)	Hydraulic grade (m)	Pressure head (m)
J-1	546.36	556.36	10.00
J-2	546.26	556.35	10.09
J-3	545.46	556.35	10.89
J-4	544.91	556.35	11.44
J-5	545.35	556.33	10.98
J-6	542.95	556.33	13.38
J-7	543.55	556.33	12.78
J-8	543.75	556.33	12.58
J-9	544.38	556.33	11.95
J-10	543.58	556.32	12.74
J-11	539.31	556.33	17.02
J-12	539.77	556.32	16.55
J-13	538.61	556.32	17.71
J-14	542.15	556.32	14.17
J-15	542.16	556.32	14.16
J-16	542.91	556.32	13.41
J-17	543.16	556.32	13.16
J-18	543.10	556.32	13.22
J-19	543.45	556.32	12.87
J-20	544.57	556.32	11.75
J-21	544.47	556.32	11.85
J-22	543.49	556.32	12.83

(continued)

Table 5 (continued)

Flex table: junction table

Label	Elevation (m)	Hydraulic grade (m)	Pressure head (m)
J-23	544.11	556.32	12.21
J-24	544.23	556.32	12.09
J-25	544.04	556.32	12.28
J-26	544.05	556.32	12.27
J-27	544.31	556.32	12.01
J-28	544.29	556.32	12.03
J-29	544.10	556.32	12.22
J-30	544.77	556.33	11.56
J-31	545.14	556.34	11.20
J-32	543.89	556.34	12.45
J-33	544.86	556.33	11.47
J-34	540.29	556.32	16.03
J-35	540.29	556.32	16.03
J-36	540.42	556.32	15.90
J-37	542.56	556.32	13.76
J-38	542.56	556.32	13.76
J-39	542.66	556.32	13.66
J-40	542.57	556.32	13.75
J-41	544.05	556.32	12.27
J-42	544.14	556.32	12.18
J-43	542.23	556.32	14.09
J-44	541.88	556.32	14.44
J-45	541.49	556.32	14.83
J-46	540.86	556.32	15.46
J-47	540.66	556.32	15.66
J-48	538.33	556.32	17.99
J-49	540.86	556.32	15.46
J-50	541.67	556.32	14.65
J-51	542.19	556.32	14.13
J-52	542.52	556.32	13.80
J-53	543.33	556.32	12.99
J-54	541.12	556.32	15.20
J-55	537.97	556.32	18.35

(continued)

Table 5 (continued)

Flex table: junction table			
Label	Elevation (m)	Hydraulic grade (m)	Pressure head (m)
J-56	537.97	556.32	18.35
J-57	537.94	556.32	18.38
J-58	537.69	556.31	18.62
J-59	536.50	556.31	19.81
J-60	536.50	556.31	19.81
J-61	536.32	556.31	19.99
J-62	535.52	556.36	20.84
J-63	545.96	556.36	10.40
J-64	545.11	556.36	11.25
J-65	545.99	556.36	10.37
J-66	544.87	556.36	11.49

Fig. 4 Avaradi village layout design in WaterGEMS software

4 Conclusion

The LOOP software does not consist of a graphical interface for water distribution network design. LOOP software has a lengthy process to operate and consumes

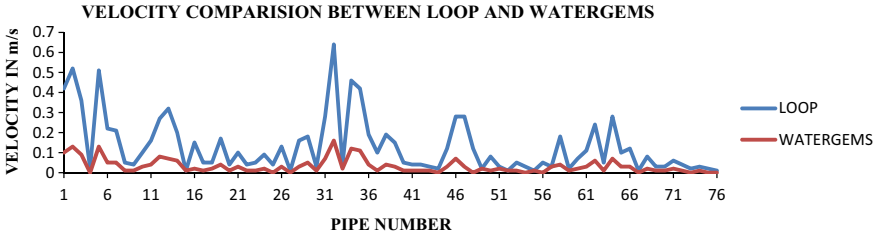

Fig. 5 Velocity comparison graph

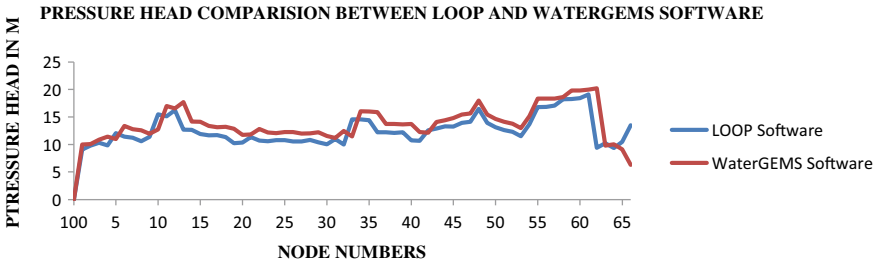

Fig. 6 Pressure comparison graph

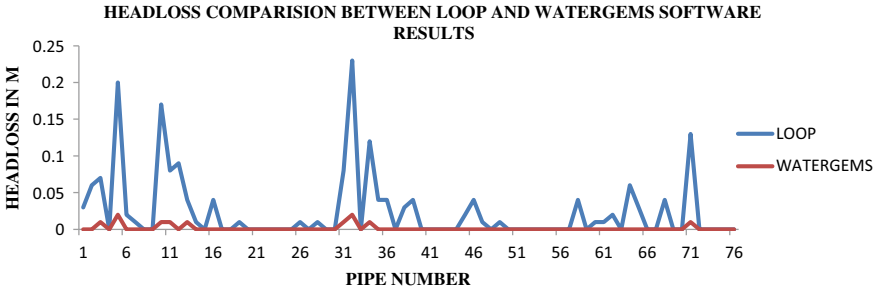

Fig. 7 Head loss comparison graph

more time for manual entry of data into the software, most of the calculations are done before the entry into the software. Designing a water supply network with this software is a more tedious job. This software is limited to 500 pipe and 400 node points if a larger area is to be designed that can be a break into small zones then designing is carried out.

The WaterGEMS software is more user-friendly software in analysis and design for the water distribution networks. It enters every detail in easier steps and has a graphical representation interface so that any modifications are done easily and here less calculation is required before entry into the software. WaterGEMS software

gives a direct-designed layout as output. This software has no limits for the design of the layout.

The results from each software are almost the same but some results differ due to limitations and assumptions adopted in both software. The conclusion is that WaterGEMS is user-friendly, quick, and easy to operate for designing an optimal water distribution network.

References

1. Mehta VN, Joshi GS (2019) Design and analysis of rural water supply system using loop 4.0 and water gems V8i for Nava Shihora zone 1. Int J Eng Adv Technol 9(1):2258–66
2. Government of India Ministry of Jal Shakti Department of drinking water and sanitation national Jal Jeevan Mission New Delhi 110 003 December, 2019 " Jal Jeevan Mission Guidelines"
3. Mehta VN, Design and analysis of rural water supply system using loop 4.0 and water gems V8i for Nava Shihora Zone 1
4. Zolapara B, Joshi M, Designing water supply distribution network using loop software for zone-I of Village Kerala
5. Sumithra RP, Amaranath J (2013) Feasibility analysis and design of water distribution system for Tirunelveli corporation using loop and water gems software. Int J Appl Bioeng 7(1)
6. Schmid R (2002) Review of modeling software for piped distribution networks. Water Supply Environ Sanitation

Fire Resistance of RCC T-beam Under Cyclic Load: A Numerical Study

Dibya Jyoti Basu, Devjit Acharjee, and Debasish Bandyopadhyay

Abstract Fire hazards of RCC bridges and their failures in recent years have warned to check the effect of fire on the structural members, which is very often overlooked in popular design codes. Bridge fire occurring below the superstructure can severely hamper its strength, durability, and further stability. Hence, it is very essential to study the fire resistance of the RCC structural members of bridge-like lifeline structures. This present study aims to develop a thermomechanical model of a simply supported RCC T-beam representing real-life bridge girders. The model is based on a transient heat-transfer analysis and a coupled temperature–displacement analysis. The cross-sectional temperature of the RCC T-beam is determined following the heat transfer analysis. Higher temperature changes inside structures demonstrate stress redistribution; leading to a rapid deterioration in strength, stiffness, and service life. The second part of this paper aims to analyze the variations in stress on the material fibers due to fire exposure. The changing nonlinear cross-sectional temperature distribution of a bridge girder during the fire exposure may cause it to experience distress in form of thermal cracks. This study also includes the effects of repetitive loading on the T-beam subjected to concrete damage adopting the Concrete Damaged Plasticity (CDP) model for illustration of flexural damage pattern. The entire Finite Element Analysis (FEA) has been carried out using the commercial FEA package ABAQUS. The present study assumes importance as one of the first attempts made to assess the fire resistance of RCC bridge girders.

Keywords ABAQUS · Coupled temperature–displacement analysis · Finite element analysis · Heat transfer analysis · RCC T-beam

1 Introduction

Strategic bridges are designed to withstand the continuous loadings of varying amplitudes [8]. These structures are susceptible to facing fire events. Many of the popular

D. J. Basu · D. Acharjee (✉) · D. Bandyopadhyay
Jadavpur University, Kolkata, India
e-mail: devjitacharjee1996@gmail.com; devjita.construction.rs@jadavpuruniversity.in

L. Nandagiri et al. (eds.), *Recent Advances in Civil Engineering*, Lecture Notes in Civil Engineering 256, https://doi.org/10.1007/978-981-19-1862-9_67

Fig. 1 Different reasons behind bridge fire events

design codes often ignore the high-cost problems such as fire events, which can result in the catastrophic failure of the structure. The main reasons for the frequent fire events that occurred under bridges were studied by Joo et al. [7]. Among these, some were mainly linked to the inflammable articles placed under the bridges. Figure 1 represents such real-life observations. The vulnerability of bridge fires was discussed by Giuliani et al. [6] in their study. RCC structures exhibit an in-built efficiency of withstanding higher temperature zones. Concrete mixes have a low thermal conductivity at ambient temperature and it decreases over time with changing temperature. During a fire attack, the temperature increases rapidly inside steel and concrete components. The resultant thermal expansion produces nonlinear temperature fields, which can generate thermal stress and cause structural components to deteriorate in terms of their strength, flexural rigidity, and service life. Although the fire resistance of RCC structures is very important, there are various ways of assessing this issue. The influence of temperature fields on fire-free surfaces of RC beams was examined by Fu et al. [5]. The shear tests were conducted by Liao et al., and a FE formulation for predicting the shear flexural capacity of post-fire RCC beams was proposed [12]. The mechanical behavior of post-fire RCC beams in the shear zone may be evaluated using the method of the test by Hawary et al. [3]. Shi et al. have investigated RCC beams in high-temperature zones, defining the temperature distribution of beam sections and developing a temperature–stress constitutive equation [13]. But most of these experiments are very time-consuming, cumbersome, and costly. Kodur et al. proposed a computer program for evaluating the fire resistance of RCC columns [10]. The cross-sectional temperature method proposed by Wickstrom [15] is a widely accepted method for predicting fire resistance of engineering structures. This approach is widely used for its simplicity and computational efficiency. The cross-sectional temperature after a fire hazard depends primarily on the structural dimensions and thermal properties of the materials used. In a study made by Kodur et al. [9], the feasibility of a cross-sectional temperature approach toward the determination of fire resistance of a structure was discussed. A finite element or finite difference analysis can be conducted for determining the temperature fields in the cross-section of the structure [11].

Nonlinear temperature change in the cross-section causes stress redistribution inside the structure. It was studied by Kodur et al. [8] and the effect of fire-induced degradations on RCC beams was discussed. Stress developed only by temperature can be termed as self-equilibrating stress. Whereas the stress generated due to both incident loading and fire attack can be termed as total stress. El-Tayeb et al. have studied the variations of true stress, continuity stress, and total stress on the structure after fire exposure [4]. In another study made by Cai et al., the residual flexural capacity of RCC beams on fire exposure was discussed [2]. Song et al. conducted experimental works to investigate the fire resistance of simply supported RCC beams with changing reinforcement configurations [14].

The present study focuses on assessing the fire resistance of a simply supported RCC T-beam under repetitive cyclic load. The RCC beam resembles a real-life bridge girder. The entire study is divided into two parts. The first part of the study incorporates a transient heat transfer analysis to visualize the cross-sectional temperature distribution of the beam cross-section under fire exposure. And the second part consists of a fully coupled temperature–displacement analysis to record the effect of fire load on the structure. The analysis is carried out by employing a constant amplitude and frequency loading along with temperature boundary conditions to investigate the variations of stresses on the material fibers of the beam after a fire attack. The typical flexural damage pattern of the beam is established with a tensile damage contour adopting the popular CDP model. A higher magnitude of heat-induced stress is observed for rebars than for concrete. The entire FEM study is conducted using the commercial FEM package ABAQUS. The present study assumes its significance in the context of assessing the fire resistance of RCC flexural members like bridge girders.

2 Heat Transfer Analysis

The transient heat transfer analysis is carried out to find out the temperature field of the RCC T-beam. For the FEM simulations, the mode of heat transfers or the interactions adopted for the fire exposed surfaces is considered to be surface film condition and surface radiation. Here the surface film condition interaction is made on the basis of film coefficient or the coefficient of heat conduction and sink temperature. The surface radiation interaction is made on the basis of the emissivity of concrete and sink temperature. The heat conduction and surface radiation equations for concrete are given below.

$$q_k = \alpha_k\left(\theta_s - \theta_f\right) \tag{1}$$

$$q_r = \Phi\varepsilon_s\varepsilon_f\sigma_{S-B}\left(\left(\theta_f + 273\right)^4 - \left(\theta_s + 273\right)^4\right) \tag{2}$$

q_k is the heat flux generated due to heat conduction, α_k is the convection coefficient of fire, θ_s and θ_f are the surface temperature and temperature of fire exposure in degree centigrade, q_r is the generated heat flux from surface radiation in W mm^{-2}, Φ is the radiation view factor, ε_s and ε_f are the emissivity of concrete surface and emissivity of fire, σ_{S-B} is referred to as the Stephan–Boltzmann constant, which is considered as 5.68×10^{-8} W mm^{-2} K^{-4}. The material properties are initiated and simply supported boundary conditions are initialized and the analysis is performed. The ISO 384 temperature–time curve is considered for the heat transfer analysis, the ambient temperature is kept to be 27 °C. The heating curve is a linear logarithmic relationship between temperature and time which is as follows:

$$T = T_0 + 345\ln(8t + 1) \tag{3}$$

Here, T_0 and T are the ambient temperature and temperature achieved after time t.

3 Coupled Temperature–Displacement Analysis

For obtaining the post-fire mechanical properties of the RCC T-beam a fully coupled thermomechanical analysis is performed. Nonlinear temperature change induces higher stresses on flexural members because any fiber attached to other fibers cannot undergo free expansion with temperature change. Thermal stress developed in the structure can be referred to as self-equilibrating stress. The stress values can be calculated following the equations below.

$$\varepsilon_f = \alpha_t \Delta T \tag{4}$$

$$\sigma_{\text{restrained}} = -E\varepsilon_f \tag{5}$$

$$\Delta N = \int \sigma_{\text{restrained}} \mathrm{d}A \tag{6}$$

$$\Delta M = \int \sigma_{\text{restrained}} y \mathrm{d}A \tag{7}$$

$$\Delta\varepsilon_0 = \frac{1}{E}\left(-\frac{\Delta N}{A}\right) \tag{8}$$

$$\Delta\Psi = \frac{1}{E}\left(-\frac{\Delta M}{I}\right) \tag{9}$$

$$\sigma = E\left[-\varepsilon_f + \Delta\varepsilon_0 + \Delta\Psi y\right] \tag{10}$$

Here ε_f is the strain at the centroid of the section due to change in temperature, $\sigma_{\text{restrained}}$ is the normal stress in MPa if the beam is restrained from expanding, E is the modulus of elasticity, ΔN and ΔM are the respective reaction forces and bending moment. The moment of inertia and the area of the cross-sections, respectively, are I and A. $\Delta\varepsilon_0$ is the additional uniform strain, $\Delta\Psi$ is the radius of curvature, σ is the developed thermal stress in MPa.

The model considers the coupled temperature–displacement step using a direct solver approach. The analysis step performed here is a nonlinear estimation in which the displacements and temperature are solved in a simultaneous manner. Here the influence of temperature on displacements is calculated through thermal expansion and the effect of continuity stress is also measured and its variation with time is shown. A relative comparison between the self-equilibrating stress, continuity stress, and thermal stress is made to the depth of the beam. The interactions made in the previous step are followed in this step and no further changes are made. A constant amplitude and frequency periodic loading are applied to the model. The thermal boundary conditions are initiated in this analysis step.

4 Numerical Modeling

The fire resistance of the RCC T-beam is assessed using nonlinear FEA using the commercial software package ABAQUS. Three-dimensional brick elements and two-dimensional truss elements are used for discretizing the beams. Figure 2 describes the FE assembly of the T-beam considered for the analysis. The basic numerical model is based on the properties of M 25 grade of concrete and FE 500 grade steel. A periodic loading of 48 KN/mm^2 with a constant amplitude and a constant frequency of 0.5 Hz is applied over a region of 250 mm × 260 mm on the flange of the simply supported T-beam (shown in Fig. 3). The sectional dimensions are also provided in the same figure. The first part is based on a transient heat transfer analysis, which is essential to analyze the cross-sectional temperature fields inside the flexural member due to a fire attack. The concrete member is discretized using heat transfer and coupled temperature–displacement three-dimensional brick elements, while the reinforcing steel

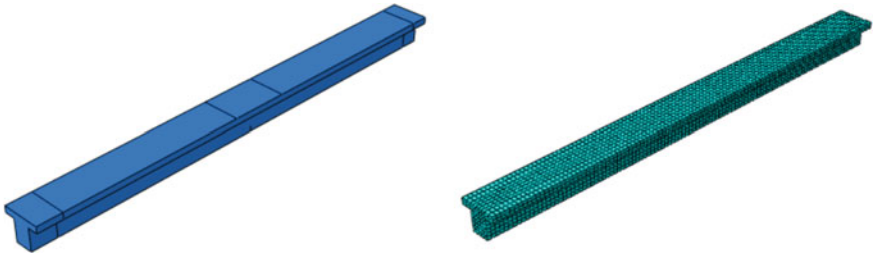

Fig. 2 FE assembly and discretization of the RCC T-beam

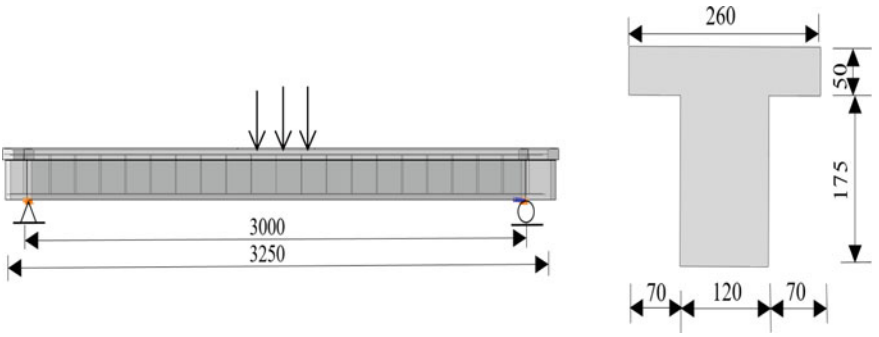

Fig. 3 Geometry and sectional dimensions of the T-beam with loading arrangements

members are discretized using two-dimensional heat transfer and coupled temperature–displacement truss elements. The popular CDP model in ABAQUS is adopted to illustrate the typical tensile damage and crack pattern of the RCC T-beam. Some additional material properties are taken under consideration which include the concrete compression damage parameters and concrete tension damage parameters. All these data have been collected from existing literature. The crack formed in concrete further induces very higher stresses in the rebars. The amount of damage is expressed by a tensile damage index and its relation with time is discussed. The next part of the study deals with a fully coupled thermal–displacement analysis. This particular analysis scheme has the potential to record the thermal effect inside the structure due to fire attacks along with the effect of live loading. The variations of self-equilibrating stress, continuity stress, and total stress are discussed following the results obtained from the analysis. The simply supported boundary conditions are initiated and loadings are kept the same as before. Few modifications to the initial material properties are made from before. Table 1 constitutes the material properties considered for the construction of the present thermomechanical model. Finally, the results obtained from the nonlinear FEA are discussed in the Result and Discussions section.

Table 1 Materials properties considered for the thermomechanical model

Material properties	Concrete	Steel
Mass density (kg/m^2)	2400	7879
Young's modulus	25,000 MPa	200 GPa
Poisson's ratio	0.2	0.3
Thermal expansion coefficient	1.2×10^{-5}	1.08×10^{-5}
Thermal conductivity (W/m.°C)	1.2	60
Specific heat (J/kg.°C)	1000	500

5 Results and Discussions

To obtain the temperature fields and nodal temperatures of the RCC T-beam, a transient heat transfer analysis is carried out using ABAQUS/CAE. Thermal boundary conditions are initiated on the surfaces exposed to fire in the transient heat transfer analysis step. Mechanical boundary conditions are applied in the initial step of the analysis. The field output and history output are kept as default.

Figure 4 illustrates the nodal temperature contour of the entire beam after fire exposure. Figure 5 describes the temperature field contour of the T-beam with the nodal temperatures at the cross-section of the beam. The maximum temperature regime is given by a red contour. Three different nodes are chosen on the cross-section at different heights to show the variation of temperature with time. It can

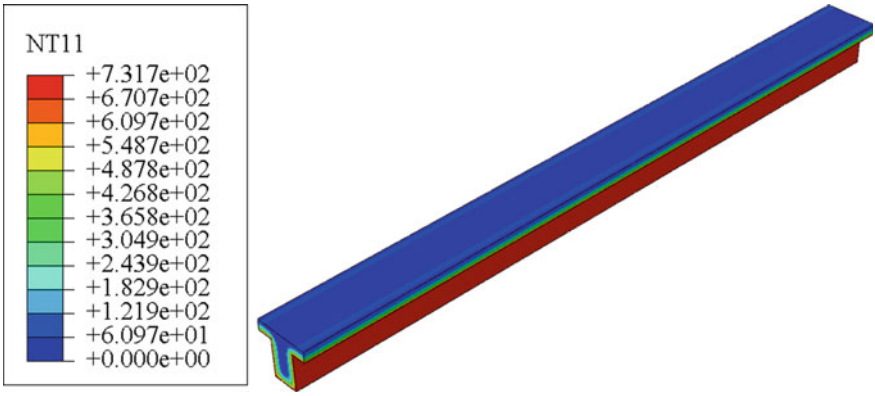

Fig. 4 Nodal temperature contour of the RCC T-beam

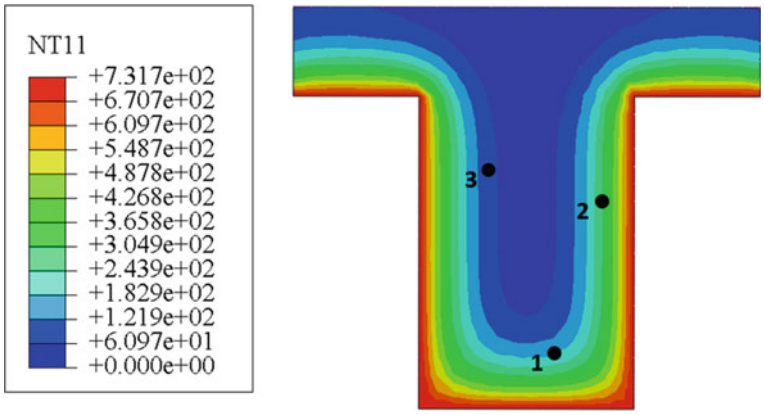

Fig. 5 Temperature field contour of the RCC T-beam cross-section post-analysis

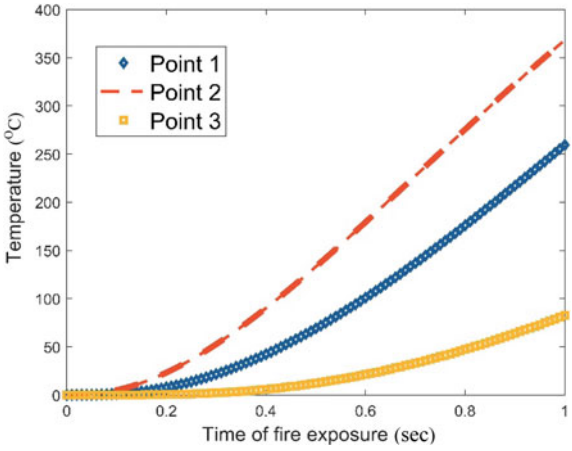

Fig. 6 Nonlinear temperature variation with time of fire exposure post analysis

be seen that the variation of temperature is nonlinear for this case leading to stress redistribution and finally stiffness reduction of the flexural member.

Figure 6 illustrates the variation of temperature with time for three different points chosen on the cross-section of the beam. The nonlinearity in temperature variation can be described from there. Point 3 shows a lesser magnitude of temperature with respect to point 1 and point 2.

A dynamic explicit analysis is performed to understand the typical flexural damage behavior of the T-beam. Here red contours show the damaged region and evolution of cracks. Primarily, it can be seen that maximum damage of the beam occurs at the bottom part of the beam underneath the loading cross-section and continues to propagate up to the entire span between the boundary conditions, mid-span of the beam is more susceptible to damage or failure. After the initiation of damage, it continues to propagate toward the boundary conditions. The accuracy of the crack patterns can be increased using finer meshes. When a concrete specimen is unloaded from a point on a stress–strain curve, the elastic stiffness of the material comes up to be degraded which further lead to the initiation of damage or cracks. Figure 7 shows the typical tensile damage contour of the T-beam after analysis.

This particular stiffness degradation can be characterized by the damage index. The damage index for this case can be classified as tensile and compressive damage variables. These variables are considered to be a function of plastic strain, temperature, and field variables [1]. Figure 8 illustrates the variation of tensile damage with time for the RCC T-beam. The cracks in concrete induce very high-stress values in the rebars, which can further cause catastrophic failure of the structure for the subsequent distress in rebars. Regular monitoring is very essential for these types of failures of RCC flexural structural components.

The rapid damage due to the brittleness of concrete member can be seen in the plot in Fig. 8. All these considerations are made without applying temperature boundary

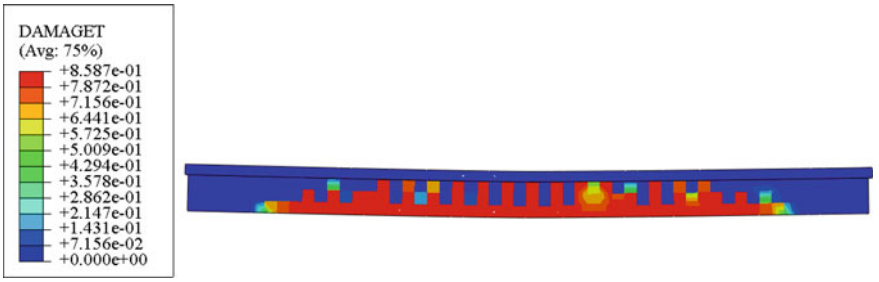

Fig. 7 Tensile damage pattern of the T-beam post analysis

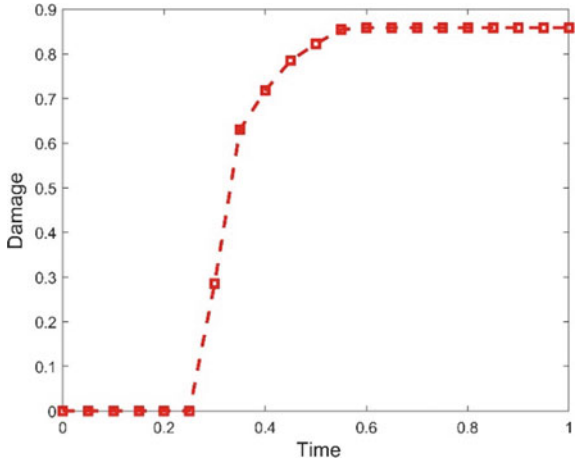

Fig. 8 Tensile damage variable relation with time

conditions. But, the CDP model does not consider the degradation of material properties with a change in temperature. Hence, a fully coupled temperature–displacement analysis is necessary to understand this phenomenon. Also, the degradation can be observed from the viewpoint of stress redistribution on material fiber due to fire exposure. This analysis is carried out with a constant amplitude and frequency loading as mentioned earlier in the FE modeling section. Mechanical boundary conditions are employed along with the thermal boundary condition.

The displacement contour shown in Fig. 9 shows maximum displacement at the mid-span of the T-beam and it has a good agreement with the displacement contours of the dynamic explicit step of the analysis. Figure 10 shows the increment in the magnitude of displacement at a selected nodal point at the mid-span of the T-beam under fire attack. Different magnitudes of thermal boundary conditions are incorporated along with the ambient temperature is shown. The significant increment in displacement over time can be seen with increasing temperature. which represents the effect of induced thermal stress on the displacement of the flexural member under fire exposure.

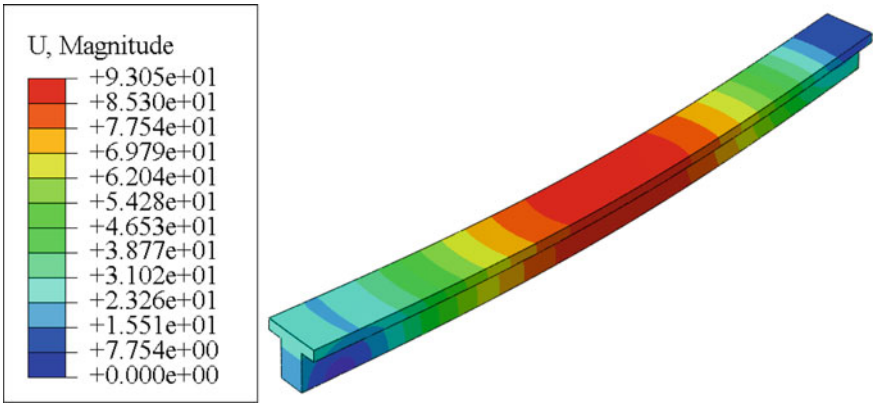

Fig. 9 Displacement contour of the RCC T-beam post analysis

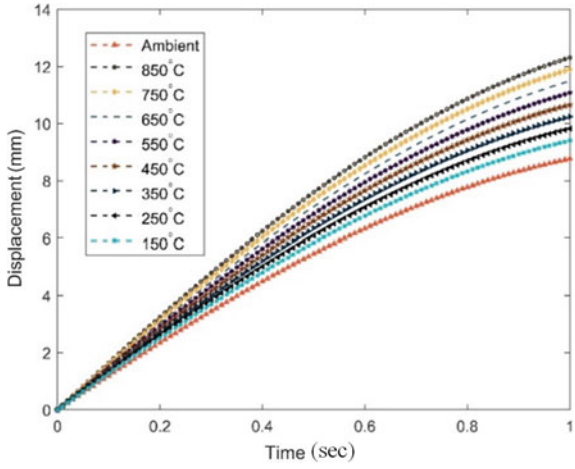

Fig. 10 Displacement variations with time of fire exposure at different temperature zones

The nonlinear temperature variation shown in Fig. 6 results in stress redistribution inside the structural member. The involvement of thermal stress is described using self-equilibrating stress. The involvement of thermal boundary conditions is neglected for the evaluation of the continuity stress of the T-beam. The total stress is calculated on the basis of applied periodic loading and thermal boundary conditions. Variations of these stresses are described on the basis of induced stresses at the top and the bottom fiber of the concrete member. Figures 11 and 12 illustrate the variation of different stresses with distance for the top and bottom fibers, respectively, for the considered RCC T-beam. The effect of induced thermal stress can be illustrated in the graphs shown below, which leads to the massive stiffness degradation of the structural member.

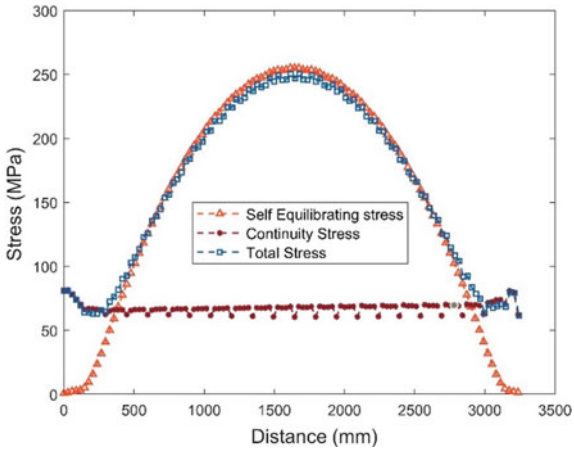

Fig. 11 Stress variations with distance at the top concrete fiber along the beam

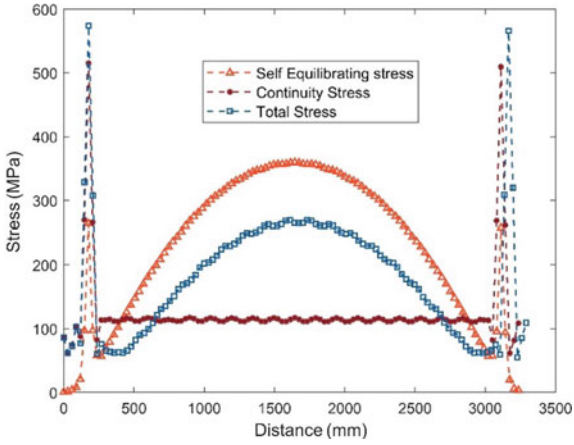

Fig. 12 Stress variations with distance at the bottom concrete fiber along the beam

Higher stresses reduce the rigidity and stiffness of the structure along with degrading the mechanical performance of the constituent materials. With a change in time of fire exposure, the stiffness degradation may lead to the initiation of thermal cracks into the structure. The mid-span of the T-beam is more susceptible to facing the initiation of a thermal crack. The formation of thermal cracks inside the concrete will induce higher stresses in the rebars. So, it seems to be very essential to understand the stress distribution on the rebar fibers.

The next part of the study explores the distributions of self-equilibrating stress, continuity stress, and total stress at the top and bottom reinforcement fibers of the RCC T-beam.

Figures 13 and 14 describe variation in these stresses at the top and bottom fiber of the reinforcement. Significant variations in normal stress and thermal stress can be easily seen along with incremental total stress for rebars.

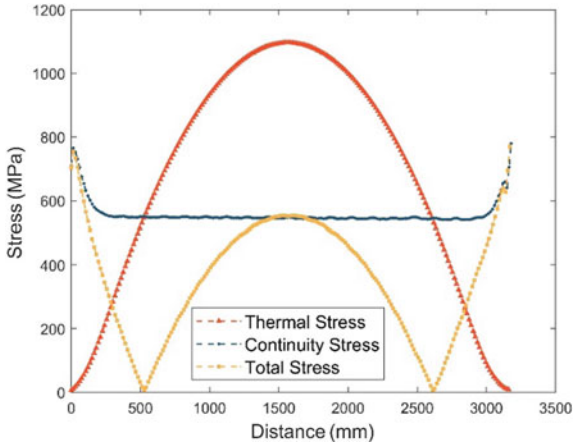

Fig. 13 Stress variations with distance at the top fiber of the reinforcement along the beam

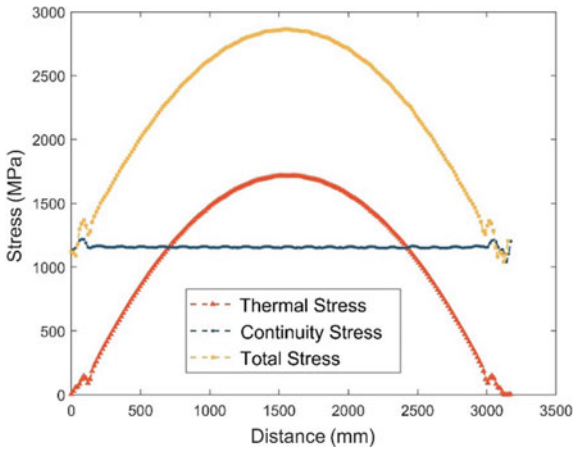

Fig. 14 Stress variations with distance at the bottom fiber of the reinforcement along the beam

The mechanical strength of an RCC T-beam seems to get weaker with higher temperature zones and higher stress generation inside the rebar and concrete fibers. Especially the rebars seem to get higher stress due to their higher thermal expansion coefficient. The higher stress generation inside reinforcements can be reduced with greater concrete cover thickness. This will also increase the durability and service life of the structure, and that should be accounted for in design codes.

6 Conclusions

The prediction of fire resistance of RCC structures is indeed very critical. The cross-sectional temperature method followed in the present study can be concluded to be

the most useful method for the evolution of fire resistance of RCC structures. This particular method has not considered the redistributions of internal forces under fire attack. The thermomechanical model adopted in the present work seems to be accurate for the prediction of fire resistance of a real-life multi-span bridge girder. Here, a small-scale model of an RCC bridge girder is considered for computational efficiency purposes. The heat transfer analysis carried out in the first step of the study describes the temperature field contour and nonlinear temperature variation relation plot with time. The nonlinearity of temperature variation causes stress redistribution inside the structure. The stress variations are recorded with a coupled thermal–displacement analysis, and the effect of thermal stress and its comparison with normal stress and total stress is elaborated. Very high stresses are developed at the top and bottom rebar fibers, which shows that proper precautions should be taken prior to designing the concrete cover thickness, ratio of longitudinal reinforcements. It can also be observed that higher concrete cover thickness ensures higher fire resistance to RCC flexural members like T-beam. The typical flexural damage pattern is observed using the popular CDP model in ABAQUS. The future scope of study may include a parametric study with changing the mechanical and thermal material properties of steel and concrete; and their effect on stress and stiffness of the structure after a fire hazard. The entire study seems to be very significant to evaluate the fire resistance of real-life RCC bridge girders.

References

1. Abaqus User's manual, version 6.10. Dassault systems Simulia Corp, France (2016)
2. Cai B, Li B, Fu F (2020) Finite element analysis and calculation method of residual flexural capacity of post-fire RC beams. Int J Concr Struct Mater
3. El-Hawary MM, Ragab AM, El-Azim AA, Elibiari S (1997) Effect of fire on shear behavior of RC beams. Comput Struct
4. El-Tayeb E, El-Metwally SE, Askar HS, Yousef Ahmed M (2015) Thermal analysis of reinforced concrete beams and frames. HBRC J
5. Fu CG, Liu W, Kong WY, Wang YZ (2015) The temperature field analysis of reinforced concrete beam based on heating and cooling whole curve. J Shandong Jianzhu Univ
6. Giuliani L, Crosti C, Gentili F (2012) Vulnerability of bridges to fire. In: Biondini, Frangopol (eds) Bridge maintenance, safety, management, resilience and sustainability
7. Joo S, Kim S, Kim Y, Park C (2017) Fire risk evaluation of bridge underneath conditions based on field investigation. In: Procedia engineering, Elsevier
8. Kodur VKR, Agarwal A (2017) Effect of temperature-induced bond degradation on fire response of reinforced concrete beams. Eng Struct
9. Kodur VKR, Naser MZ (2021) Classifying bridges for the risk of fire hazard via competitive machine learning. Adv Bridge Eng (Springer Open)
10. Kodur VKR, Wang TC, Cheng FP (2004) Predicting the fire resistance behavior of high strength concrete columns. Cement Concr Compos
11. Kodur VKR, Yu B, Dwaikat MMS (2013) A simplified approach for predicting temperature in reinforced concrete members exposed to standard fire. Fire Saf J
12. Liao JH, Lu ZD, Su L (2013) Experimental and finite element analysis of shear strength of concrete beams subjected to elevated temperature. J Tongji Univ

13. Shi XD, Guo ZH (2000) Investigation on the behavior of reinforced concrete at elevated temperature. China Civil Eng J
14. Song Y, Fu C, Liang S, Yin A, Dang L (2019) Fire resistance investigation of simple supported RC Beams with varying reinforcement configurations. Adv Civil Eng (Hindawi)
15. Wickstrom U (1986) A very simple method for estimating temperature in fire exposed concrete structures. Fire technology technical report, Swedish National Testing Institute

Collection of Municipal Solid Waste by Clustering of Dynamic Nodes for Vehicle Path Optimization

P. Sughosh, G. Savitha, S. Girisha, and S. B. Dattatreya

Abstract Collection and transportation of municipal solid waste (MSW) is a critical factor that governs the overall cost of the MSW management system. With the help of various technological interventions, optimal usage of available resources could bring about a considerable amount of savings. In this study, an attempt has been made to optimize the MSW collection vehicle route path to reduce the fuel, distance, and overall workload in local municipalities by adopting dynamic graph modeling. The optimization problem is addressed from three different perspectives, namely, (a) analyzing the dynamic nature of the user requests, (b) the influence of the number of waste collection vehicles available in a given area, and (c) determining the optimum number of vehicles for which the overall cost is minimized. Relevant simulation studies are carried out to validate the proposed approach.

Keywords Vehicle outing problem · Municipal solid waste · Clustering · Optimum route · Efficient deployment

1 Introduction

The increase in the per capita waste generation rate is mainly attributed to the rising global population, globalization, consumption, and improved quality of life. By the year 2050, the global municipal solid waste (MSW) generation is predicted to reach 3.4 billion tons (BT) from the current levels of 2.01 BT [1]. In order to prevent severe repercussions on the environment, the waste management sector has to look for an effective and sustainable way of collecting, disposing, and treating the generated

P. Sughosh (✉) · S. B. Dattatreya
Jawaharlal Nehru New College of Engineering, Shimoga, Karnataka 577204, India
e-mail: sughosh.p@gmail.com

G. Savitha · S. Girisha
Manipal Institute of Technology, Manipal Academy of Higher Education, Manipal, Karnataka 576104, India

L. Nandagiri et al. (eds.), *Recent Advances in Civil Engineering*, Lecture Notes in Civil Engineering 256, https://doi.org/10.1007/978-981-19-1862-9_68

waste. Upgradation of the current MSW management systems by adapting appropriate waste collection, transportation, and treatment technologies would help in mitigating its negative impacts on the environment.

The collection and transportation of MSW is the critical component of the system, which incurs about 60–80% of the total cost [2]. Optimizing the travel path of waste collection vehicles based on the real-time end-user data would help in reducing labor and fuel cost, operation time, and greenhouse gas emissions. It would also help in the reallocation of funds for implementing essential MSW treatment processes.

The solid waste management rules of 2016 have mandated the collection of segregated waste from individual households [3]. Urban local bodies (ULB) have the responsibility for collection, segregation, disposal, and treatment of MSW. Due to various initiatives such as the Swachh Bharat Mission (SBM), many UBLs have the basic infrastructural capabilities for waste collection and transportation from individual households (like a tricycle, e-rickshaws, and mini-trucks). But efficient utilization of these resources can only be ensured with proper technological interventions such as the application of optimization and soft computing techniques (for suggesting the optimal vehicle path) and the use of Internet of Things (smart bins) for estimating and transmitting the precise amount of MSW generated at each household's level in real-time.

The approach presented in this study would help the ULBs in the dynamic allocation of waste collection vehicles based on the demand exerted by the individual houses of a given area and in optimizing the traveling path of vehicles.

2 Literature Review

The objective of vehicle routing problems (VRP) is to minimize the distance, time, and cost of a vehicle traversing between the source (individual households) and destination (depot or waste collection centers). A few major variants of VRPs reported in the literature are as follows: (a) capacitated VRP (CVRP): VRP with a constraint on the maximum waste holding capacity, (b) VRP with time window (VRPTW): VRP with a constraint on the scheduled time of operation, (c) Stochastic VRP (SVRP): VRP in which the problem data such as the amount of waste generated, capacity of the vehicle or the time window are random variables.

Dantzig and Ramser [4] applied the traveling salesman problem (TSP) to determine the optimum route between a bulk gasoline terminal and a large number of service stations. The mathematical models for waste collection using principles of operation research were presented by Marks and Liebman [5]. Levin [6] proposed models based on integer linear programming to solve the problems related to fleet routing and scheduling. Marks and Stricker [7] presented the routing of public service vehicles used for trash collection, snow plowing, and street-cleaning purposes in the city of Cambridge. Algorithms for VRP with time window constraints were given by Solomon [8] and Tung and Pinnoi [9] further developed and applied them to solve the waste collection problem in Vietnam.

Numerous other researchers have also worked on similar problems and some of the latest approaches such as simulated annealing, ant colony optimization, and particle swarm optimization techniques have also been used in this regard. Babaee Tirkolaee et al. [10] developed a mathematical model for the capacitated arc routing problem and applied a hybrid simulated annealing technique to solve it. Hannan et al. [11] used a modified particle swarm optimization algorithm on a CVRP model for a scheduled MSW collection and route optimization problem. Studies on various web-based technologies and real-time monitoring systems collecting information from MSW generation nodes are also reported [12, 13].

As most of the ULBs in our country have the basic infrastructure for the collection of MSW (vehicles), there is a huge scope for implementation of these techniques and improving the overall system performance. Application of TSP along with the real-time waste generation and monitoring systems would be helpful to most of the ULBs in optimizing the utilization of available resources. Therefore, in this study an attempt has been made to bring out the following:

- An approach for allocation of a given number of vehicles depending on the real-time data (waste generation) of a given area.
- To identify the efficient route based on the number of available vehicles using the clustering technique.
- An approach for selecting the optimum number of vehicles given any number of nodes.

3 Methodology

The proposed approach utilizes the K-Means algorithm to cluster spatially neighboring users. Subsequently, an optimized route for deploying MSW vehicles to each cluster is determined.

3.1 Overview

The overview of the proposed system is shown in Fig. 1. In general, sending MSW collection vehicles to all the houses in a given area is redundant and inefficient as it increases the workload and fuel consumption. To this end, the work proposes a simple solution to facilitate the efficient deployment of vehicles by defining a constraint on users who can request service. The users are allowed to request for service only if the waste generated G by the user is greater than the threshold λ. Only these users are considered for providing service. This reduces the traversing path and fuel consumption substantially. A distance graph is constructed by considering R nodes that have raised an alarm. Further, all the nodes that have raised an alarm requesting service are clustered so that the given area is divided into different groups (sub-areas). Subsequently, MSW collection vehicles are then assigned to each of the sub-areas.

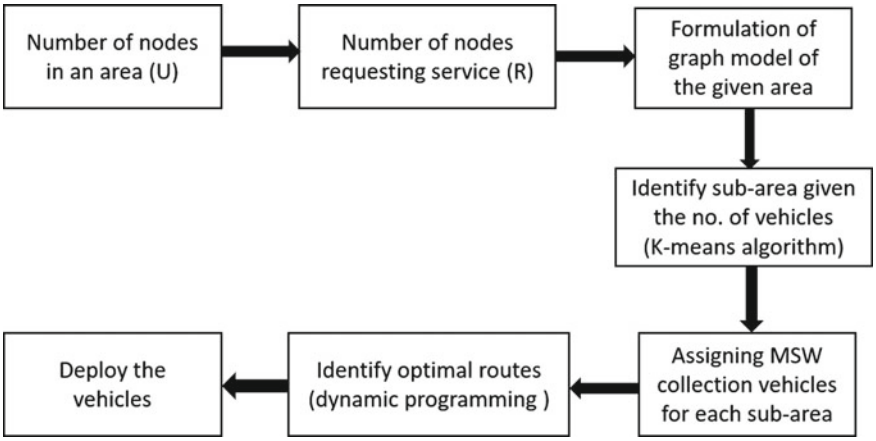

Fig. 1 Overview of the proposed system

Finally, dynamic programming is used for determining an optimum route for each sub-area.

3.2 Identifying the Sub-area

The given area is divided into multiple sub-areas to facilitate the efficient deployment of MSW collection vehicles. In this context, the proposed algorithm uses K-means clustering to divide the areas into sub-areas. K-means is an unsupervised learning algorithm that learns to identify clusters based on the data. Also, K-means is a parameterized modeling algorithm, where the identified groups depend on the K value determined by the user.

The K-means algorithm utilizes the spatial locations of the nodes to determine the clusters. This is an iterative algorithm that initializes K cluster centroids. Subsequently, the Euclidean distance between the nodes and the K cluster centroids is estimated. Finally, a node is assigned to the cluster with a minimum Euclidean distance to the cluster centroids. The objective function of the K-means algorithm is given as follows:

$$D_{\mathrm{e}} = \sum_{q=1}^{K} \sum_{p=1}^{R} \|x_p - y_q\| \tag{1}$$

where D_{e} represents the objective function, x represents the user nodes, and y represents the cluster centroids. The $\|x_p - y_q\|$ represents the distance function.

This results in dividing the given area into sub-areas. Each sub-area has spatially nearby user nodes. Hence, deploying the vehicles to these spatial nearby user nodes reduce fuel consumption. The K value is determined based on the number of available MSW collection vehicles.

3.3 Identifying Optimum Routes

After identifying K clusters, MSW collection vehicles need to be deployed for collecting wastes. A cluster may have multiple nodes. Hence, an optimum traversing path should be identified for deploying vehicles. This problem can be formulated as a TSP, where the objective is to efficiently traverse all the cities once, with minimum cost. Similarly, the MSW collection vehicles need to visit all the nodes (R) that have raised a service request. TSP problems can be solved using various approaches. In the present study, Bellman–Held–Karp dynamic programming [14] approach is utilized to identify the optimum route with a cluster. Dynamic programming is an iterative algorithm that dissolves a problem into sub-problems and then estimates an optimum solution to these sub-problems. A cost function ($F(T, j)$) is defined to estimate the minimum cost of visiting the node j from the depot such that all the nodes in set T are visited at least once. This is recursively performed by considering all the subsets of size 2 and then incrementing the size of subsets.

4 Results and Discussion

The proposed approach is evaluated and validated by adopting a simulation study. The solution obtained is simulated on randomly generated 80 nodes (U) in the range of 0–100, which represents the spatial distance of the nodes. This scenario is depicted in Fig. 2. In all these simulations, the depot position (starting point) is considered to be (30, 40).

4.1 Dynamic Variation of User Requests

Given U nodes and K waste collection vehicles, an effective approach is identified for routing the vehicles in a dynamically generated scenario. All the users may not need service in a typical real-time case. Hence, a subset of U, i.e., "R" users may request for service. Since the structure of the graph changes each time the user requests the service, this problem relates itself to the dynamic routing problem. Several methods are proposed in the literature that considers static graphs [2]. To this end, this work demonstrates the proposed solution on dynamically generated graphs.

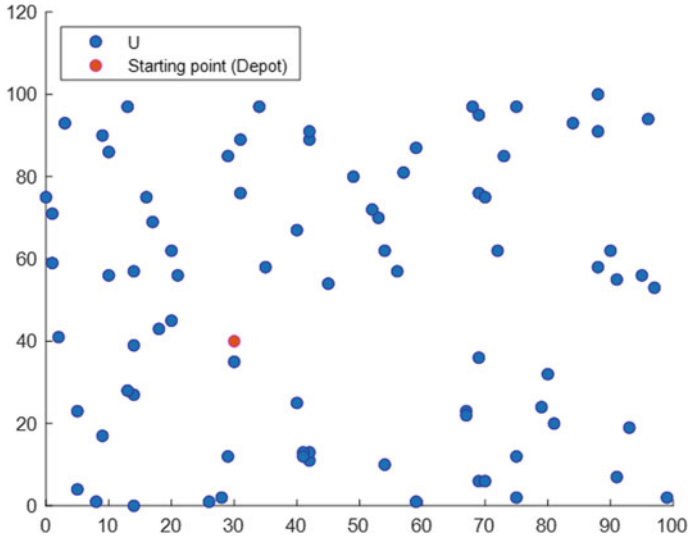

Fig. 2 The plot of U nodes

To simulate this scenario, the total nodes (U) is set to 80 with the number of waste collection vehicles (K) set to 3. Subsequently, R nodes ($R \leq U$), dynamically raise an alarm requesting for service. Hence, the K vehicles need to be deployed to these R dynamically generated nodes in an optimum way such that the fuel consumption is minimized. This is achieved by adopting the K-Means algorithm along with TSP (dynamic programming). This experiment is simulated twice with varying R values ($R = \{15; 30\}$). Initially, the experiment is simulated with R set to 15. The U nodes and the dynamically generated R nodes along with the depot position are shown in Fig. 3. These nodes are initially clustered using the K-Means algorithm, which groups the spatially nearby nodes. Consequently, the traversing path is reduced along with fuel consumption as vehicles are assigned to nearby nodes. The K value is set to 3 indicating that 3 vehicles are available for providing service. Subsequently, each vehicle is assigned one cluster. Finally, an optimum route is identified for each K vehicle using dynamic programming. Similarly, the same experiment is repeated with R value set to 30. It is observed that, in both cases, the optimum routes are identified effectively. Simulating the solution on dynamically generated graphs validates the proposed solution as it is more similar to a real-time scenario.

4.2 Influence of Number of Vehicles (K)

The study aims at identifying an effective way of deploying K vehicles for a given number of nodes (R) that have requested the service. In this case, identifying and grouping nearby user nodes (R) facilitates the effective deployment of vehicles. In

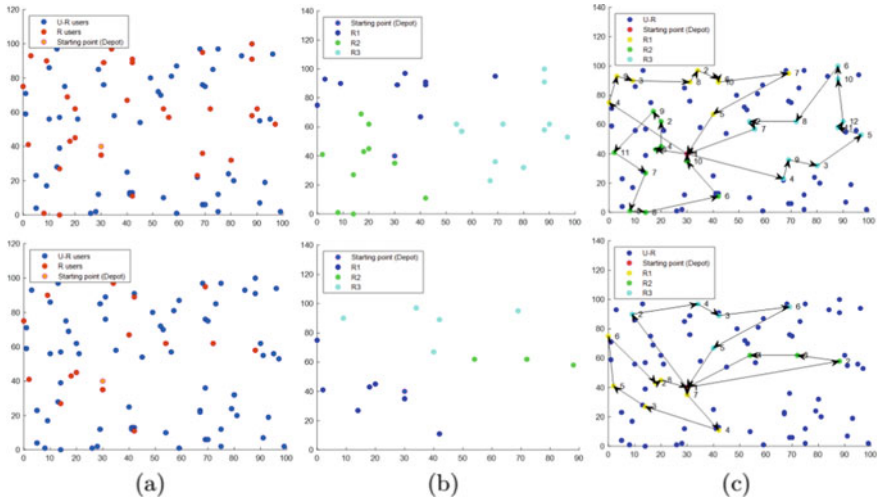

Fig. 3 **a** Total number of nodes (U), the nodes requesting service (R), and position of the depot. **b** The K clusters in R nodes. **c** Identified optimum path in K clusters

this context, the present study proposes to utilize the K-means clustering algorithm to group the nearby user nodes. The K value is dependent on the number of vehicles available for providing the service. Hence, an experiment is carried out by considering the scenario with the number of vehicles (K) as 3, 5, and 7. Figures 4, 5, and 6 represent the optimal route for the deployment of vehicles to provide service for the requested users R. The optimized routes for each cluster are indicated by the arrows.

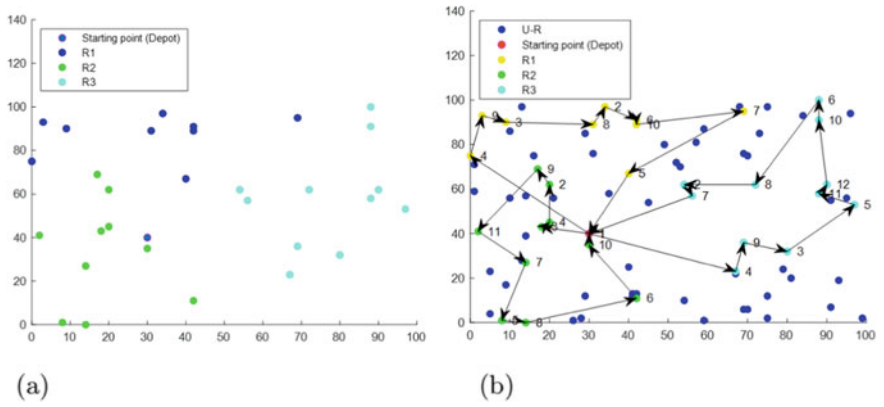

Fig. 4 **a** The clustered R nodes, $K = 3$. **b** Identified optimum path for $K = 3$

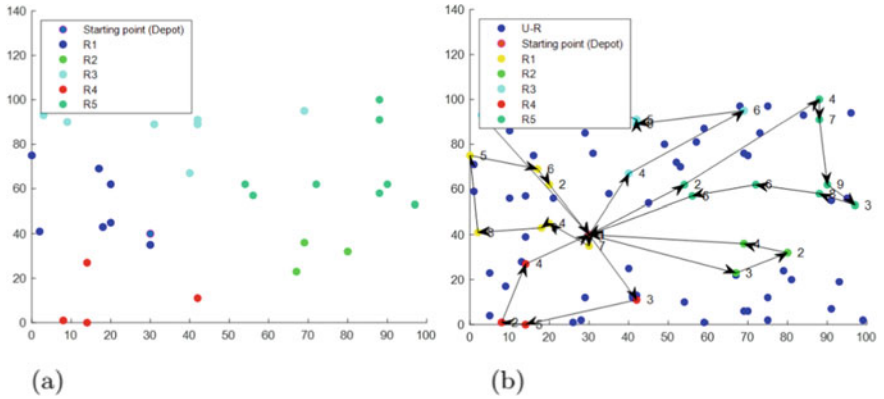

Fig. 5 **a** The clustered R nodes, $K = 5$. **b** Identified optimum path for $K = 5$

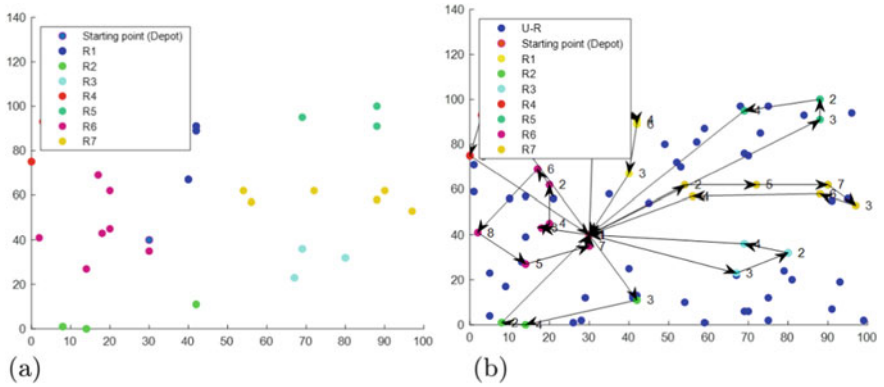

Fig. 6 **a** The clustered R nodes, $K = 7$. **b** Identified optimum path for $K = 7$

4.3 Selection of Optimum Number of Vehicles

Generally, a sufficient number of vehicles are available for municipal waste collection. But, deploying all vehicles at an instance would be redundant and inefficient.

Hence, there is a need for the deployment of an appropriate number of vehicles. It is observed that there are hardly any reports available in the literature that address this scenario. The proposed solution uses the elbow method to identify the optimum K value (number of vehicles). This approach iteratively evaluates the cost of selecting different values of K and suggests the best K for given R nodes. This simulation is carried out by considering $U = 80$ and $R = 30$. Subsequently, the elbow method is applied to determine the optimum K value. Figure 7 shows the cost of selecting different K values on R. It is observed that, at $K = 3$, the elbow occurs, and hence,

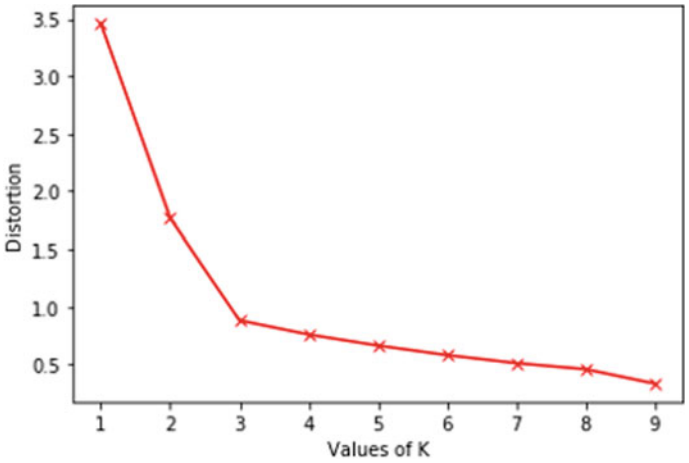

Fig. 7 The plot of the cost function with different values of K

Table 1 The minimum cost of traversing with the varying value of K

	Cluster							Total cost/distance
	1	2	3	4	5	6	7	
For $K = 3$	210.3	184.6	241.1					636.0
For $K = 5$	121.9	107.4	205.5	114.8	207.6			757.2
For $K = 7$	120.4	112.3	107.4	125.2	173.3	112.9	153.3	904.8

for $R = 30$, the optimum number of vehicles required is 3. The minimum cost of traversing through all the R nodes with different values of K is given in Table 1. It is observed that, for $K = 3$, the cost of traversing is minimum as compared to $K = 5$ and 7.

This further validates the proposed approach for selecting the optimum number of vehicles. This is an important result as it suggests the optimum number of vehicles required to provide service which can further reduce the fuel consumption and workload thereby improving the economy and efficiency of municipal waste collection.

5 Conclusion

The optimal routing of MSW collection vehicles is validated for the user requests which vary dynamically. Further, the study successfully demonstrates the effectiveness of the K-means clustering algorithm in demarking the given area into sub-areas based on the availability of waste collection vehicles. This ensures the efficient

deployment of MSW collection vehicles thereby increasing the overall collection efficiency. Additionally, a method is proposed and validated for selecting the optimum number of MSW collection vehicles for any given number of active nodes. This enhances the decision-making capabilities of the local municipalities leading to an overall reduction in the consumption of available resources.

References

1. Kaza S, Yao L, Bhada-Tata P, Van Woerden F (2018) What a waste 2.0: a global snapshot of solid waste management to 2050. World Bank Publications
2. Beliën J, De Boeck L, Van Ackere J (2014) Municipal solid waste collection and management problems: a literature review. Transp Sci 48(1):78–102
3. Mission SB (2016) Municipal solid waste management manual. Central Public Health and Environmental Engineering Organisation (CPHEEO), Ministry of Urban Development, Government of India
4. Dantzig GB, Ramser JH (1959) The truck dispatching problem. Manage Sci 6(1):80–91
5. Marks DH, Liebman JC (1970) Mathematical analysis of solid waste collection (No. 2104). US Bureau of Solid Waste Management
6. Levin A (1971) Scheduling and fleet routing models for transportation systems. Transp Sci 5(3):232–255
7. Marks DH, Stricker R (1971) Routing for public service vehicles. J Urban Plan Dev Div 97(2):165–178
8. Solomon M (1987) Algorithms for vehicle scheduling routing problem with time windows. Oper Res 35(2):254–265
9. Tung DV, Pinnoi A (2000) Vehicle routing–scheduling for waste collection in Hanoi. Eur J Oper Res 125(3):449–468
10. Babaee Tirkolaee E, Alinaghian M, Bakhshi Sasi M, Seyyed Esfahani MM (2016) Solving a robust capacitated arc routing problem using a hybrid simulated annealing algorithm: a waste collection application. J Ind Eng Manage Stud 3(1):61–76
11. Hannan MA, Akhtar M, Begum RA, Basri H, Hussain A, Scavino E (2018) Capacitated vehicle-routing problem model for scheduled solid waste collection and route optimization using PSO algorithm. Waste Manage 71:31–41
12. Rada EC, Grigoriu M, Ragazzi M, Fedrizzi P (2010) Web oriented technologies and equipments for MSW collection. In Proceedings of the International conference on risk management, assessment and mitigation-RIMA, vol 10, pp 150–153
13. Al Mamun MA, Hannan MA, Hussain A, Basri H (2016) Theoretical model and implementation of a real time intelligent bin status monitoring system using rule based decision algorithms. Expert Syst Appl 48:76–88
14. Agarwal S, Jain N, Choudhury T, Singh UV, Tomar R (2021) E-commerce delivery routing system using Bellman–Held–Karp algorithm. In: Advances in electromechanical technologies. Springer, Singapore, pp 277–285

Assessment of Seasonal Variation of Groundwater Quality Due to Heavy Metal Pollution in an Industrial Suburb

B. H. Anitha, C. Nanjundaswamy, S. N. Maya Naik, and M. S. Divyanand

Abstract Heavy metals concentration in groundwater, even at low concentrations affects human health severely. The objective of this study is to assess the seasonal variations of groundwater quality and to determine the concentration of heavy metal pollution in the Peenya industrial area, Bengaluru. The heavy metal concentrations in pre-monsoon were found in the order: Cr > Cr^{+6} > Pb > Ni > Fe > Cu > Cd, whereas for post-monsoon the order was Cr > Cr^{+6} > Fe > Cu > Ni > Pb > Cd. Powerful tools like MI (metal index) and HPI (heavy metal pollution index), which emphasize quality were used for the system of ranking. As per HPI and MI analysis, about 83% and 73% of groundwater samples, respectively, in pre-monsoon, about 57% and 50% in post-monsoon were not suitable for domestic usage. The mean HPI concentration for pre- and post-monsoon are 846 and 336.7, respectively, which is considered to be very high (critical value >100). The mean concentration of MI for pre and post-monsoon are 27.2 and 12.62, respectively, is also high (critical value >6) and is categorized as seriously affected. The overall status of water in the Peenya Industrial Area is highly polluted and not suitable for any domestic and industrial usage.

Keywords Groundwater quality · Pollution indices · Heavy metal pollution · Peenya industrial area

1 Introduction

Water is an elixir of life and earth's most distinctive feature, which is essential for every living organism on the planet. It is a crucial environmental resource and has

B. H. Anitha (✉) · S. N. Maya Naik
BMS College of Engineering, Bengaluru, Karnataka, India
e-mail: anidivy@gmail.com

C. Nanjundaswamy
Dr. Ambedkar Institute of Technology, Bengaluru, Karnataka, India

M. S. Divyanand
Advanced Micro Devices, Bengaluru, Karnataka, India

L. Nandagiri et al. (eds.), *Recent Advances in Civil Engineering*, Lecture Notes in Civil Engineering 256, https://doi.org/10.1007/978-981-19-1862-9_69

played a significant role in the social and economic growth of human civilization [1]. It is estimated that the largest user of groundwater in the world is India, with 248 cubic kilometers of groundwater usage per year [2]. Due to the rapid growth of the human population, industrialization, urbanization, and improvement in the standard of living, the water demand is extended. Over the past few decades, there has been a massive increase in the demand for freshwater [3], leading to the shortage of surface water and greater dependency on groundwater. The demand for groundwater resources has gone up [4].

Groundwater is a natural source of potable water. It is less vulnerable to pollution than the earth's surface water, but cleaning up groundwater, once contaminated is difficult [2]. Due to the increase in per capita demand for water, the dependency on groundwater has increased rapidly [4]. The various anthropogenic activities affected the quality of groundwater and are more susceptible to contamination from various sources such as improper and untreated wastewater disposal [3] leakage from landfills, municipal sewers, septic tanks, infiltration of fertilizers, and chemicals from industrial activity, saltwater intrusion, etc. [4]. Groundwater pollution and its overexploitation has been observed as localized contamination in major industrial zones [2].

The quality of groundwater in a particular region not only depends on factors like the nature of rocks present, the composition of the soil, and residence time but also on the recharge water. It also depends on the geology of the region, topography, climate, soil, etc. [5]. When groundwater contamination occurs in aquifers, it perseveres for a long time as a result of the slow movement [6], and also some major ions induced by geological features disperse over a large area [4]. So, regular monitoring of the quality of groundwater ensures water is safe, usable, and in an acceptable form. Monitoring groundwater is not only time taking and costly process but also difficult [5]. The groundwater quality varies seasonally and identifying the cause for quality deterioration leads to possible remediation [7].

The current work proposes the status of groundwater quality in Peenya industrial area, Bengaluru district of Karnataka state. Bengaluru has got the name 'silicon city' due to boom in the information technology. For the past many decades, it has overgrown in its size and the district administration is struggling to provide the necessary infrastructure and required demand for water supply [2].

Heavy metals are toxic and cause carcinogenic effects on living organisms [4]. Non-biodegradable, stable, and toxic heavy metals penetrate the food chain and increase the toxic levels, causing health problems [5]. If heavy metal exposure is for the long term, it causes health problems like damage to organs such as the brain, heart, kidney, liver, lungs. In extreme cases, the possibility and risk of cancer increases.

Heavy metals usage in the field of industrial, domestic, medical, and technology has resulted in large distribution and occurrence of metal ions in the environment [8]. The pollution of heavy metals is the most prominent cause of threatening water quality.

Several factors influence the toxicity of heavy metals such as the age of the person, gender, level of exposure, dosage, etc. [8]. The existence of toxic heavy metals in groundwater is a clear indication of anthropogenic activities. The industries which

use metals as raw materials for metal plating, chemical processing, finishing, and decorative purposes add a significant amount of trace metals into the environment. Groundwater contamination with chromium (Cr) has severe and toxic impacts on the environment and humans. The presence of Cr in groundwater is mainly derived from industrial wastewater discharge, which causes elevated concentrations of Cr in water bodies. Chromium in trivalent form is less soluble in water and less toxic but when it is oxidized to Cr (VI), it becomes highly toxic and more mobile in both groundwater and surface water [9]. Metals with high toxicity have led to chronic diseases like brain tumors, nerve damage, high blood pressure, lung cancer, and skeletal and kidney disorders [10].

The investigations made by many researchers found that the origin of trace metals and their transport, the rise of epidemiological issues, biomagnification of these toxic elements in the food chain, which has altered the life process severely.

Investigations are done concerning the concentration of heavy metals in the Bazman basin [11], southeastern Iran revealed a high concentration of Arsenic and selenium. Few researchers, [8, 12, 13] have investigated the groundwater quality and heavy metal contamination in Peenya industrial area using WQI, GIS interpolation techniques, bacteriological investigations like gram staining, heavy metal pollution index, and found heavy metals like chromium, lead, cadmium, mercury, copper, nickel, iron, etc. From the literature review, it has revealed that the Peenya is highly polluted since the past decades due to industrialization. The criteria for selection of wells for groundwater analysis is the excessive concentration of heavy metals due to increased industrial activity and its pollution in and around Peenya.

In recent times, an extensively used method for the qualitative detection of heavy metals in groundwater is pollution indices i.e., heavy metal index (HPI) and metal index (MI). These indices are useful tools for environmentalists, civil executives, and concerned authorities. The overall level of pollution of groundwater resources can be studied through these recent advanced methods. In pollution indices, considering overall parameters and the results can be converted into a single number. In MI, the total evaluation of the present state of quality and comparing the high concentration of heavy metals to its standard permissible limit for each element. HPI is an effective tool and also rating technique for assessing the quality of groundwater with special reference to heavy metals [14, 15].

An attempt has been made to analyze the seasonal variations of heavy metals in the groundwater of the study area for pre and post-monsoon seasons. The assessment of groundwater quality was not carried out during the monsoon season due to changes in rainfall patterns, which may lead to alterations in the level of groundwater. In a city like Bangalore, it is difficult to predict the rainfall pattern which varies seasonally [16]. The focus of research using the metal index (MI) and heavy metal pollution index (HPI) is to determine groundwater quality based on the concentration level of heavy metal presence in groundwater of PIA, Bengaluru.

2 Materials and Methodology

2.1 Description of the Study Area

Bengaluru city of Karnataka covers an area of 400 km^2, which lies between 12° 58′ N latitude and 77° 35′ E longitude. The PIA (Peenya Industrial Area) has a latitude of 13° 01′ N and a longitude of 77° 30′ E which is located in the northwest suburbs. The main aim of the current work is to evaluate seasonal variations of groundwater samples for heavy metal detection from PIA. Peenya is considered the largest industrial region in Asia and is approximately 40 km^2 covering 1800 active industries [17].

Dominating industries are electroplating, textile, leather, pharmaceutical, power coating, locomotives, etc. With less scientific knowledge and carelessness of the concerned authorities, PIA is polluted for many decades. Effluents are discharged into nearby rivers or lakes, and also due to heavy rainfall leaching and runoff of chemicals enter into the subsurface. Unorganized factories dump wastewater without any treatment into nearby vicinity. The detailed literature survey revealed that Peenya is highly affected by heavy metal contamination due to the largest manufacturing industries present in that area. The main objective of the present study is to assess the seasonal variations of heavy metal pollution of selected groundwater samples in the PIA, Bengaluru, using HPI and MI. It provides an overview of current groundwater quality for domestic and industrial usage.

Figures 1 and 2 map showing the location of the study area [15, 18].

2.2 Geology and Climate

The area is a part of the peninsular gneissic complex consists of reddish sandy soil. It is non-clayey, non-sticky, but porous which is common in the Peenya suburb region. It usually consists of granite, gneiss, and rock dykes. The study area has a highly undulating topography with sub-dendritic nature with varying hydrological characteristics [19]. The rainfall in Bengaluru for the past 20 years was 900 to 1056 mm and the temperature lies between 15 °C min and a maximum of 35 °C. The geology of the study area is depicted in Table 1.

2.3 Collection of Sample and Analysis

The sampling sites were identified in the study area and the 30 groundwater samples were collected according to the ‘grab sampling’ method in the pre-monsoon (January–February 2020) and post-monsoon (November 2020) seasons which is depicted in Fig. 3. The criteria for selection of wells are based on the existence of

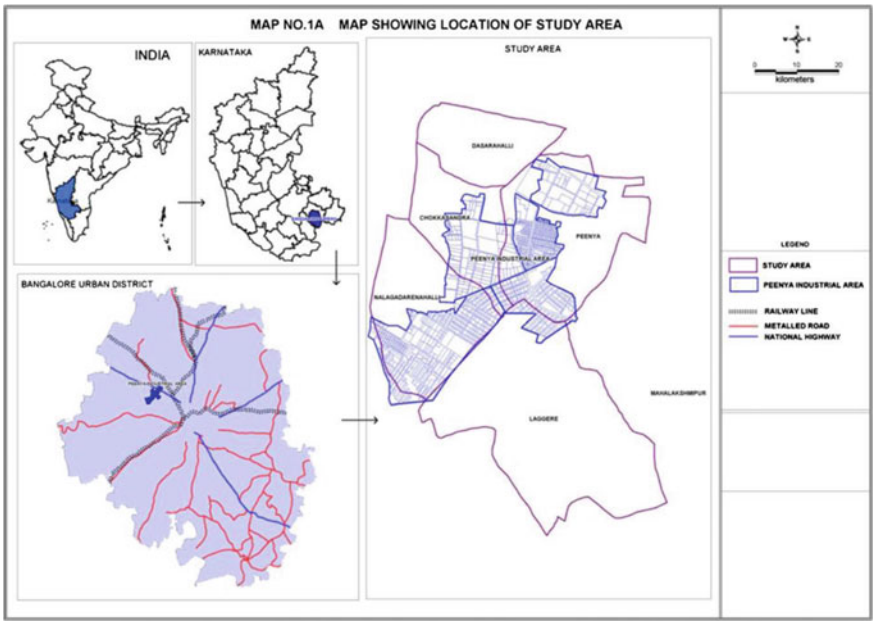

Fig. 1 Location of PIA

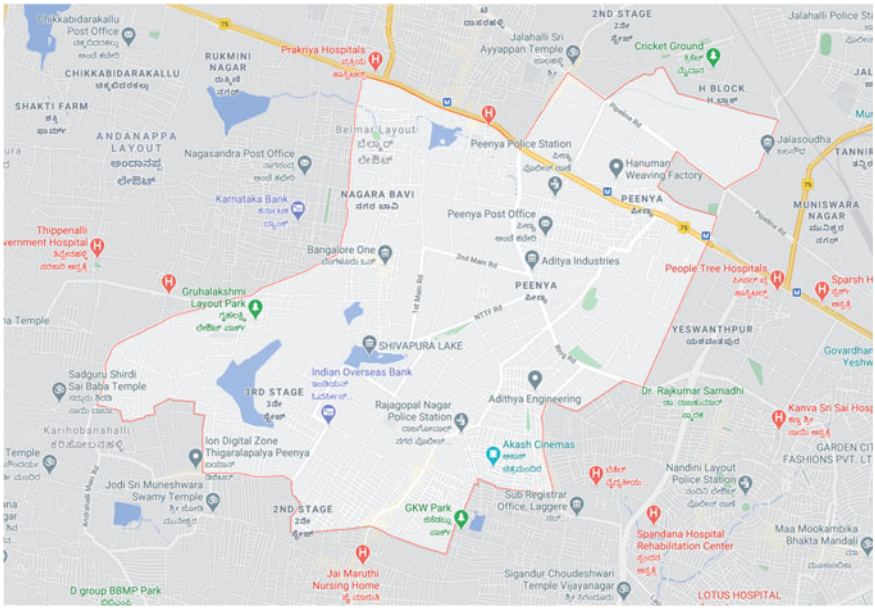

Fig. 2 Map showing PIA. *Source* From Google Maps

Table 1 Geological characteristics [15]

Type of characteristics	Details
Topography	Highly undulating topography with sub-dendritic nature and varying hydrological characteristics
Watershed	South Pinakini toward the eastern portion and Arkavathi toward the western portion
Water bodies	Nelagedranalli, Shivapura, Dasarahalli, and Karihobanahalli

Fig. 3 Locations of sampling points. *Source* From Google Maps

wells near the major industries, which have been established a long time ago to know the contamination level. The samples were collected in cleaned high-density polyethylene (HDPE) cans that had been washed with distilled water and acidic solution such as 1 N nitric acid, which follows the sampling protocols. The local impurities were washed out before collecting the samples. The samples collected in cans were taken to the laboratory carefully and analysis was done using standard APHA [20] methods. All the reagents were of analytical grade and instruments were calibrated before taking readings. Based on the availability of sources, the selected seven toxic heavy metals in the study area are hexavalent chromium, total chromium, nickel, copper, lead, cadmium, and iron. The selection of these heavy metals is based on the type of major industries present, raw materials used, processing, and type of wastewater generated in the study area. The clear indication of the presence of a high concentration of heavy metals in PIA is referred from the literature survey [8, 12, 13]. Analysis of the samples was carried out using an effective graphite furnace Perkin Elmer PinAAcle 900z atomic absorption spectrometer (AAS). The fuel used here is acetylene and the processing of samples includes digestion with concentrated

nitric acid and dilution directly injected into graphite furnace AAS [21]. To ensure accurate and precise readings, measurements were repeated twice. The results of the analysis followed the standard specifications under the Bureau of Indian Standards [22].

2.4 Estimation of Heavy Metal Pollution Index (HPI)

The term heavy metal pollution index (HPI) refers to the overall quality of water for assessing the level of concentration of heavy metal pollution. It is an effective tool that is considered for the overall influence of particular heavy metals on the total quality of groundwater. This useful tool is used by the public sector and regulatory agencies for pollution reduction and decision-making, related to resource management [6].

HPI was first proposed by Mohan et al. [23] as

$$\mathrm{HPI} = \frac{\sum_{i=1}^{n} Qi\,Wi}{\sum_{i=1}^{n} Wi} \tag{1}$$

where
n = total number of parameters,
Wi = unit weightage, and
Qi = sub-index of ith parameter, respectively, is as shown in Eq. (1).
The calculation of the sub-index, Qi, is given by

$$Qi = \sum_{i=1}^{n} \frac{Mi - Ii}{Si - Ii} * 100 \tag{2}$$

where
Mi = monitored value,
Ii = ideal values, and
Si = the standard value indicating the ith parameter is as shown in Eq. (2).

2.5 Estimation of Metal Index (MI)

MI is defined as the presence of a heavy metal concentration of each element in the solution to the maximum permissible limit of each element.

It has been proposed by Tamasi and Cini [24].

$$\mathrm{MI} = \sum_{i=1}^{n} \frac{Ci}{(\mathrm{MAC})i} \tag{3}$$

where *Ci* is the concentration of each element in the given sample, *i* represents the *i*th sample, whereas MAC is the maximum allowable concentration for each element as shown in Eq. (3).

3 Results and Discussions

3.1 Result of Analysis of Heavy Metals

The results of concentrations of heavy metals such as hexavalent chromium, total chromium, copper, nickel, lead, cadmium, and iron for pre-monsoon and post-monsoon in 30 groundwater samples are as shown in Figs. 4 and 5. The hexavalent chromium and total chromium concentrations range from 0.01 to 16.5 mg/l and 0.1 to 25.6 mg/l for pre-monsoon season, whereas it varies from 0.03 to 7.5 mg/l and 0.02 to

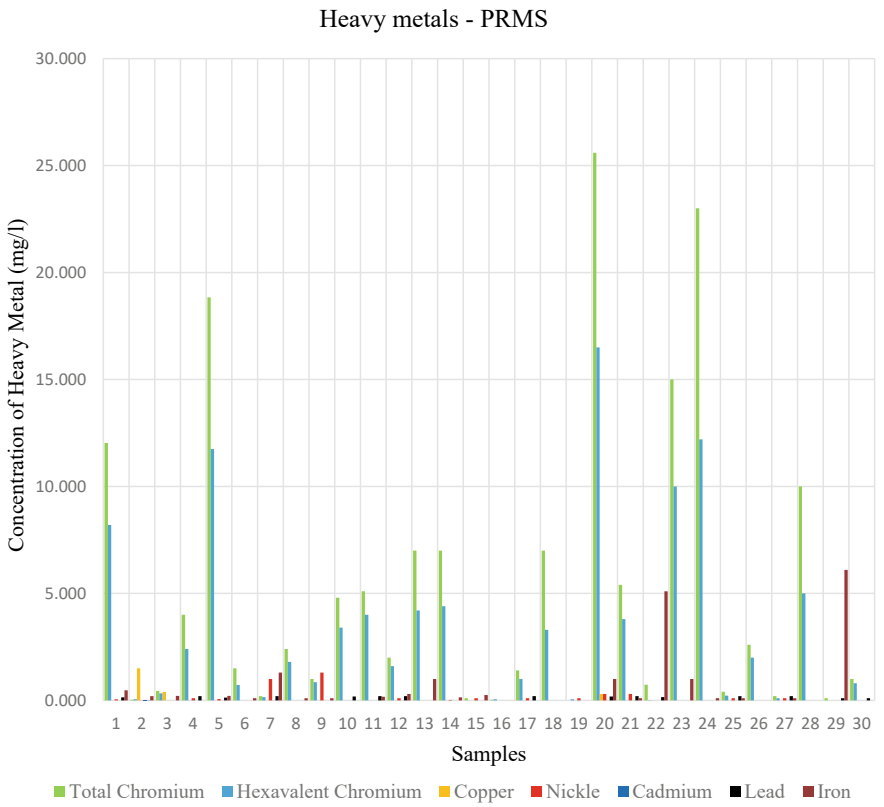

Fig. 4 Variation of heavy metal concentration for pre-monsoon season (PRMS)

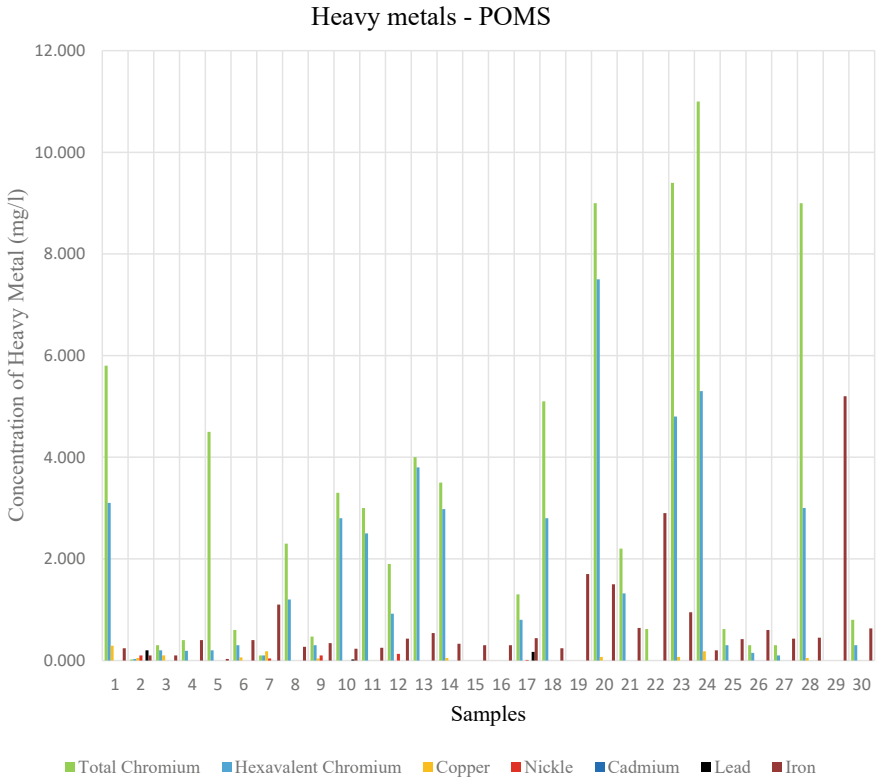

Fig. 5 Variation of heavy metal concentration for post-monsoon season (POMS)

11 mg/l for post-monsoon season, respectively. The concentration of total chromium was detected in 29 out of 30 sampling stations and 26 out of 30 sampling points in pre and post-monsoon seasons, respectively. The concentration of hexavalent chromium was detected in 28 out of 30 sampling stations and 25 out of 30 sampling stations in pre and post-monsoon season, respectively. The results revealed that the concentration of hexavalent and total chromium exceeded the permissible limit of 0.05 mg/l of BIS Standard. The detection of copper, in the case of pre-monsoon, is seen only in three sampling points and in 11 sampling points for the post-monsoon season, but within the permissible limit of 1.5 mg/l. The concentration of nickel in 14 stations exceeds the permissible limit of 0.02 mg/l, but it is seen below the detection level in sixteen sampling points in case of pre-monsoon. During post-monsoon season, the nickel concentration is detected only in 5 sampling points, and in 4 sampling points, it is exceeding the permissible limit. The lead concentration in the case of pre-monsoon exceeds the permissible limit of 0.01 mg/l in 15 sampling points. During post-monsoon, the lead concentration was detected in only three sampling points. In pre-monsoon, the cadmium concentration was detected at only one sampling point (sampling station 2), and during post-monsoon, it is detected in none of the sampling

points. Out of 30, in 21 sampling points, iron concentration was detected and in 14 stations it is within the permissible limit of 0.3 mg/l during pre-monsoon. But in post-monsoon, it was detected in all the sampling points and exceeded the maximum permissible limit in 19 sampling points.

Figures 4 and 5 show the graphical representation of variations in concentration of heavy metals in the study area for pre-monsoon and post-monsoon seasons. The co-occurrence of multi-elements in groundwater is due to the solubility of minerals, geology of the area, precipitation, semi-arid and arid conditions, presence of type of industries like chromium plating industries, textile industries, leather industries and its waste products, overexploitation of groundwater, contribution of anthropogenic activities, etc. [25]. From the above results, it is clear that high concentrations of heavy metals depict higher pollution due to the anthropogenic activities [17] that may include the leather industry and its waste products, electroplating industry and its applications, tanneries, textiles, etc. The toxicity of these metals may have entered groundwater through leaching, drainage leakage, corrosion of pipes that carry wastewater, etc.

From the analysis, it is clear that groundwater samples are highly contaminated with total chromium, hexavalent chromium, lead, nickel, and iron exceeding the BIS standards, which are at high risk of cancer in children and adults. Long-term exposure to these heavy metals may lead to potential health effects like kidney damage, high blood pressure, speech impairment, nerve damage, weak immune system, cancer, etc. Hexavalent chromium toxicity is severe compared to total chromium which mainly targets the respiratory tract and causes shortness of breath, nose irritation, wheezing, cough, and in severe cases lung cancer. It affects mainly body cells and damages DNA [26].

3.2 Evaluation of HPI and MI

The present study is to determine the seasonal variations in the given study area and to apply the pollution indices such as HPI and MI for the detection of the level of concentration of heavy metals. In Table 2, the specimen calculation of sample 1 for metal index and heavy metal pollution index in the case of post-monsoon is depicted. In Table 3, the results of HPI and MI of pre and post-monsoon seasons along with its latitude and longitude coordinates are shown, while Figs. 6 and 7 show the graphical representation of seasonal variations of HPI and MI in PIA. From the revealed results, the mean HPI was 846 for pre-monsoon and 336.7 for the post-monsoon season, which indicates an excessive level of contamination and a higher critical value of 100. The high amount of pollution content in groundwater shows a higher value of HPI. The percentage of the higher critical value of the heavy metal is 83% and 57 for pre- and post-monsoon in PIA. The mean MI concentration was found to be 27.2 in pre-monsoon and 12.62 in case of post-monsoon, and it was observed that 73 and 50% of samples were “Seriously Affected”, which is above the range of 6.

Table 2 The specimen calculation for heavy metal pollution index and metal index (first sample of post-monsoon)

Heavy metals	Monitored value (*Mi*)/concentration (*Ci*) in mg/l	Standard value (*Si*)/MAC in mg/l	Ideal value (*Ii*) in mg/l	Unit weightage (*Wi*)	Sub-index (*Qi*)	*Wi* * *Qi*	HPI = $\frac{\sum_{i=1}^{n} \mathrm{QiWi}}{\sum_{i=1}^{n} \mathrm{Wi}}$	$\boldsymbol{MI} = \sum_{i=1}^{n} \frac{Ci}{(\mathrm{MAC})i}$
Cr	5.8	0.05		20.0	11,600	232,000	654.8	26.4
Cr^{+6}	3.1	0.05		20.0	6200	124,000		
Cu	0.29	0.05	1.5	20.0	83.5	1669		
Ni	–	0.02		50.0	0	0		
Cd	–	0.003		333.3	0	0		
Pb	–	0.01		100.0	0	0		
Fe	0.24	0.3		3.3	80	266.7		

Table 3 Results of HPI, MI analysis

Sample station	Latitude	Longitude	HPI (PRMS)	HPI (POMS)	MI (PRMS)	MI (POMS)
1	13.0222	77.5229	1760.16	654.76	60.38	26.37
2	13.0162	77.5007	29.33	419.11	4.69	3.90
3	13.0286	77.5195	59.57	40.32	3.41	1.76
4	13.0188	77.5133	879.88	43.98	21.86	1.88
5	13.0189	77.5131	2503.96	343.96	89.79	13.44
6	13.0103	77.5007	162.64	70.30	6.39	2.93
7	13.0198	77.5135	851.42	38.49	11.62	1.90
8	13.0155	77.5027	307.52	256.65	12.05	10.13
9	13.0146	77.5031	730.08	106.45	14.62	3.19
10	13.0286	77.5197	929.27	483.39	26.00	17.82
11	13.0242	77.5099	1032.05	402.95	28.94	15.83
12	13.0147	77.5029	675.61	266.67	14.00	9.19
13	13.0392	77.5271	821.54	571.83	32.48	22.54
14	13.0227	77.5111	843.58	478.48	32.78	18.81
15	13.0163	77.5013	53.56	0.61	1.12	0.14
16	13.0345	77.5085	5.85	0.61	0.23	0.14
17	13.0161	77.5033	587.20	470.10	10.43	8.71
18	13.0313	77.5179	753.66	578.54	29.43	22.69
19	13.0235	77.5269	49.39	3.46	0.86	0.81
20	13.0215	77.5109	3552.01	1213.97	126.33	48.06
21	13.0313	77.5196	1176.42	258.86	31.33	10.36
22	13.0317	77.5192	338.90	51.26	6.69	3.15
23	13.0304	77.5193	1831.30	1044.56	71.90	41.22
24	13.0207	77.5143	2575.81	1196.42	100.62	47.18
25	13.0164	77.4971	457.15	68.17	5.39	2.83
26	13.0203	77.5105	336.59	34.15	13.14	1.57
27	13.0085	77.4996	433.74	30.14	4.48	1.35
28	13.0151	77.5094	1097.56	882.62	42.86	34.64
29	13.0306	77.5202	202.64	10.57	4.62	2.48
30	13.0212	77.5137	314.63	81.77	6.57	3.44

PRMS—Pre-monsoon season
POMS—post-monsoon season

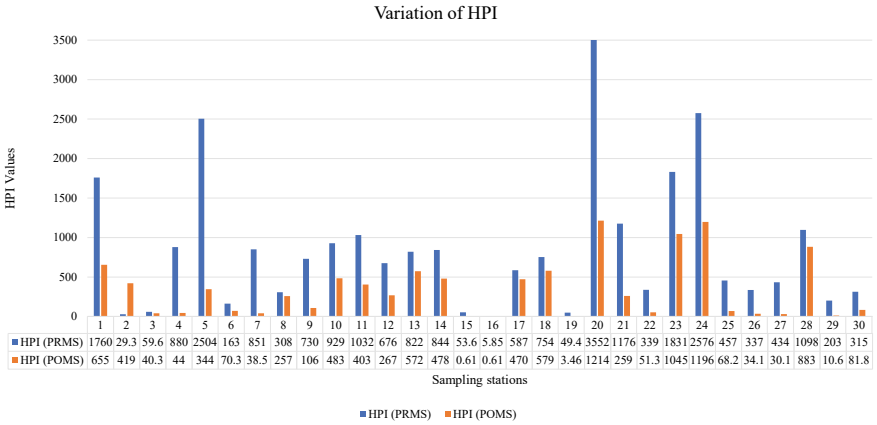

Fig. 6 Variation of HPI in the groundwater of PIA

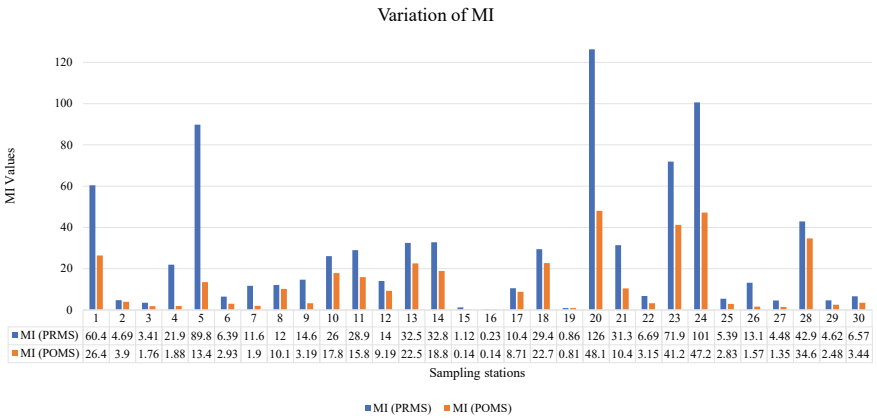

Fig. 7 Variation of MI in the groundwater of PIA

The higher value of HPI is due to the presence of a high concentration of heavy metals in groundwater samples.

In the selected seven toxic heavy metals, the highest concentration level was total chromium and then it was followed by the order hexavalent chromium, lead, nickel, iron, copper, and cadmium in pre-monsoon. In post-monsoon, total chromium remains to be highest like in the case of pre-monsoon and later followed by hexavalent chromium, iron, copper, nickel, lead, and cadmium. The depth of water in wells varies from 45 to 49 m during pre-monsoon and 55–60 m during post-monsoon [17].

Results have exhibited significantly a high concentration of heavy metals in pre-monsoon compared to a moderate concentration in post-monsoon. It is because of the effect of high precipitation that dissolves the minerals and influence of groundwater recharge, which leads to the improvement of the quality and quantity of groundwater.

The quality of groundwater depends on the quantity of groundwater recharge that occurs from rainfall and climate variations [27]. The dilute effect of monsoon season results in the consequent reduction of toxic metals. Sometimes, surface contaminants may take the path into the deep aquifer through leaching, and also due to runoff, the addition of contaminants during monsoon will increase concentration levels in post-monsoon.

Table 4 shows the range, characteristics, number of samples, and percentage of groundwater quality based on HPI and MI for pre- and post-monsoon is as shown in Table 4. Figures 8 and 9 show the pie chart of seasonal variation of groundwater quality distribution and its percentage based on HPI and MI results for pre and post-monsoon.

According to this classification, for pre and post-monsoon season the percentage of samples falls into the different categories as follows: 3.33 and 13.33 percentage of samples lie in the "Excellent category", the samples with the percentage of 6.70 and

Table 4 Groundwater quality classification

Index method	Range	Characteristics	PRMS number of samples (%)	POMS samples count (%)
HPI	>100	Unsuitable	25 (83.30%)	17 (56.67%)
	76–100	Very poor	0 (0.00%)	1 (3.30%)
	51–75	Poor	2 (6.70%)	3 (10.00%)
	26–50	Good	2 (6.70%)	5 (16.67%)
	<25	Excellent	1 (3.30%)	4 (13.30%)
MI	>6.0	Seriously affected	22 (73.30%)	15 (50.00%)
	4.0–6.0	Strongly affected	4 (13.30%)	0 (0.00%)
	2.0–4.0	Moderately affected	1 (3.30%)	7 (23.30%)
	1.0–2.0	Slightly affected	1 (3.30%)	5 (16.67%)
	0.3–1.0	Pure	1 (3.30%)	1 (3.30%)
	<0.3	Very pure	1 (3.30%)	2 (6.67%)

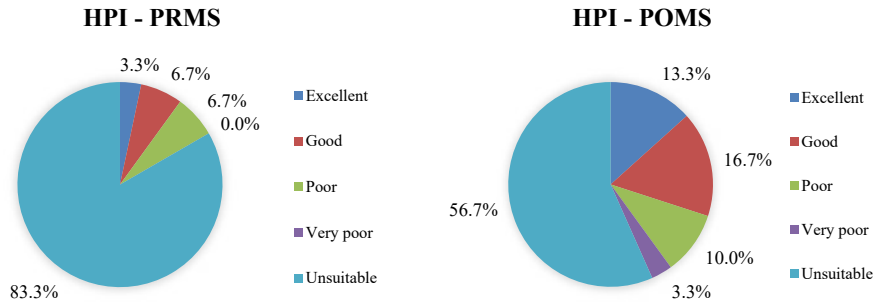

Fig. 8 Seasonal variation of HPI-based groundwater quality

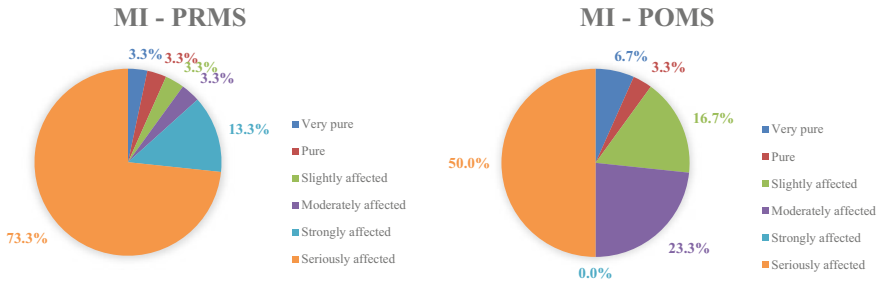

Fig. 9 Seasonal variation of MI-based groundwater quality

16.6 lie in the "Good category", whereas 6.70 and 10% of samples lies under "Poor category". None of the samples fall under the category "very poor" in pre-monsoon and 3.33% of samples fall into "Very Poor" in post-monsoon. Out of 30 sampling stations, 83% during pre-monsoon and 56.6% during post-monsoon are deemed completely "Unsuitable". Excessive HPI values are mainly due to the presence of industries in the study area like textile industries, nickel plating, decorative items, pharmaceutical industries, garment washing, electroplating manufacturers, etc.

The concentration mean value of MI in pre and post-monsoon was found to be 27.166 and 12.62, respectively. Just 3.33 and 6.3% of samples in pre- and post-monsoon are categorized as "Very pure", which are considered for portable usage and domestic activities. The samples with 93.3% in pre-monsoon and 90.0% in post-monsoon season fall above the threshold alert (1.0). It means that the range above 0.3–1.0 falls under threshold alert and the total percentage of samples above 1.0 (slightly affected) gives the alert note of contamination of groundwater. So, the samples that fall above threshold alert 1.0 are not suitable for domestic or industrial usage. Only 3.3% of the samples are classified under the "pure" category in both pre and post-monsoon. Around 3.30% of samples were found to be classified under the category "slightly" and "moderately" affected in pre-monsoon. Whereas, it is observed that 16.66% and 23.33% of samples are "Slightly" and "Moderately affected" in post-monsoon. In pre-monsoon, the samples of 13.30% are classified as "Strongly affected" but none of the samples falls under the category "Strongly affected" in post-monsoon. About 73.3% and 50% of samples in pre and post-monsoon are "Seriously affected".

4 Conclusion

The observations drawn from the obtained results indicate the high pollution contamination in groundwater in PIA. The concentration of heavy metals was high in the pre-monsoon study. The post-monsoon study revealed a decrease in concentration compared to the pre-monsoon. The high level of Cr, Cr^{+6}, Pb, Ni, and Fe are exceeding

the permissible limits of BIS in both seasons. The effective tool for heavy metal detection is HPI and metal index. From the above investigations, the work carried out for heavy metals is as follows: 83.3% of samples are unsuitable and have a mean HPI value of 846 for pre-monsoon whereas 56.7% of samples are unsuitable and have a mean HPI value of 336.7 for post-monsoon. In both seasons, it is exceeding the critical index value of 100 significantly. For MI analysis, 73% of samples lie under the category "seriously affected" with a mean MI concentration of 27.2 in pre-monsoon season. But in post-monsoon 50% of samples lies under "seriously affected" with a mean concentration of 12.62. Comparatively the high concentration of heavy metals in pre-monsoon has reduced significantly in post-monsoon due to the dilution effect of precipitation. The study emphasizes PIA is highly polluted and the reason may be due to excess toxic contents from many years. So, from the above results, it is highly recommended not to use contaminated water for any further domestic or industrial usage which may lead to severe health effects. The remedial measures such as bioremediation of heavy metals through microorganisms, biosorption, phytobial remediation, adsorption process, which are inexpensive and eco-friendly methods should be implemented. Toxicity reduction like immobilization, integrated approach like the soil washing process should be adopted to avoid further contamination. So, periodic monitoring of groundwater pollution from concerned authorities, and regular monitoring from the pollution control board is necessary to mitigate the level of intensity of pollution. Further contamination of heavy metal pollution in groundwater should be prevented for sustainable development.

References

1. Park's textbook of preventive and social medicine (Book, 2015)
2. CGWB (2013) Ground Water Information Booklet, Bangalore Urban District
3. Shivaprasad, H, Ravichandra K, Mallanna K, Kubakaddi S (2018) An assessment of groundwater quality index in Bommasandra, Bengaluru City, Karnataka State, India. Int J Eng Res Technol (Ahmedabad) 3
4. Luo W, Gao X, Zhang X (2018) Geochemical processes controlling the groundwater chemistry and fluoride contamination in the Yuncheng Basin, China—an area with complex hydrogeochemical conditions. PLOS ONE. 13:e0199082
5. Dev R, Bali M (2019) Evaluation of groundwater quality and its suitability for drinking and agricultural use in district Kangra of Himachal Pradesh, India. J Saudi Soc Agric Sci 18:462–468
6. Gulgundi MS, Shetty A (2018) Groundwater quality assessment of urban Bengaluru using multivariate statistical techniques. Appl Water Sci 8
7. Lerner DN (2007) Groundwater in the environment: an introduction. Ground Water. 45:253–253
8. Shankar BS (2019) A critical assay of heavy metal pollution index for the groundwaters of Peenya Industrial Area, Bangalore, India. Environ Monit Assess 191
9. Matta G, Nayak A, Student A, Kumar Student P, Student A, Tiwari A, Naik P (2020) Evaluation of heavy metals contamination with calculating the pollution index for Ganga River System 恆河河流系統之重金屬污染評估與污染 指數計算 68

10. Keshav Krishna A, Rama Mohan K (2016) Distribution, correlation, ecological and health risk assessment of heavy metal contamination in surface soils around an industrial area, Hyderabad, India. Environ Earth Sci 75
11. Rezaei A, Hassani H, Hassani S, Jabbari N, Fard Mousavi SB, Rezaei S (2019) Evaluation of groundwater quality and heavy metal pollution indices in Bazman basin, southeastern Iran. Groundwater Sustain Dev 9:100245
12. Pius A, Jerome C, Sharma N (2011) Evaluation of groundwater quality in and around Peenya industrial area of Bangalore, South India using GIS techniques. Environ Monit Assess 184:4067–4077
13. Baby Mathew B, Krishnamurthy NA study on the groundwater of Peenya industrial area and its related elements in Bengaluru region of Karnataka State, India. Environ Socio-Econ Stud 6(2):1–12
14. Reza R, Singh G (2011) Assessment of heavy metal contamination and its indexing approach for pond water in Angul District, Orissa, India. Asian J Water Environ Pollut 8:77–83
15. Anitha BH, Naik M, Nanjundaswamy C, Divyanand MS (2021) Application of heavy metal pollution index and metal index for the assessment of groundwater quality in Peenya Industrial Area. IOP Conf Ser: Earth Environ Sci 822:012033
16. Azad S, Debnath S, Rajeevan M (2015) Analysing predictability in Indian Monsoon Rainfall: a data analytic approach. Environ Process 2:717–727. https://doi.org/10.1007/s4071001501080
17. Dhakate R, Mohanty A, Ratnalu G, Mishra P, Rajkumar K (2018) Assessment of groundwater conditions and water quality around Peenya Industrial Development Areas Phase I & Phase II in Bangalore Sponsored by Karnataka State Pollution Control Board (KSPCB)
18. Nagaraja Gupta MS, Sadashivaiah C, Ranganna G, Inayathulla, Chandrashekar H (2018) On assessment of heavy metals in water sources of Peenya Industrial Area, Bengaluru, India. Int J Eng Res Technol 3
19. Ramakrishnaiah CR, Manasa N (2016) Distribution and migration of heavy metals in Peenya Industrial Area, Bangalore, Karnataka, India—a case study. J Geogr, Environ Earth Sci Int 6:1–13
20. APHA (2005) Standard methods for the examination of water and wastewater, 21st edn. American Public Health Association/American Water Works Association/Water Environment Federation, Washington DC
21. Bader N (2011) Sample preparation for trace element analysis by graphite furnace atomic absorption spectroscopy (GFAAS): an overview. Der Chem Sin 2:211–219
22. Bureau of Indian Standards: IS 10500 (2012): Drinking water (2013)
23. Mohan SV, Nithila P, Reddy SJ (1996) Estimation of heavy metals in drinking water and development of heavy metal pollution index. J Environ Sci Health. Part A: Environ Sci Eng Toxicol 31(2):283–289
24. Tamasi G, Cini R (2004) Heavy metals in drinking waters from Mount Amiata (Tuscany, Italy). Possible risks from arsenic for public health in the Province of Siena. Sci Total Environ 327:41–51
25. Kumar M, Goswami R, Patel AK, Srivastava M, Das N (2020) Scenario, perspectives and mechanism of arsenic and fluoride co-occurrence in the groundwater: a review. Chemosphere 249:126126. https://doi.org/10.1016/j.chemosphere.2020.126126
26. Momodu MA, Anyakora C (2010) Heavy metal contamination of ground water: the surulere case study. Res J Environ Earth Sci 2:39–43
27. Isa NM, Aris AZ, Lim WY, Sulaiman WNAW, Praveena SM (2013) Evaluation of heavy metal contamination in groundwater samples from Kapas Island, Terengganu, Malaysia. Arab J Geosci 7:1087–1100